RECENT SYNTHETIC AND STRUCTURAL DEVELOPMENTS IN NOBLE-GAS, CHLORINE, BROMINE, IRIDIUM, AND GROUP 6 FLUORINE CHEMISTRY

MARK R. BORTOLUS

RECENT SYNTHETIC AND STRUCTURAL DEVELOPMENTS IN NOBLE-GAS, CHLORINE, BROMINE, IRIDIUM, AND GROUP 6 FLUORINE CHEMISTRY

By MARK R. BORTOLUS, B.Sc.

A Thesis Submitted to the School of Graduate Studies in Partial Fulfillment of the Requirements for the Degree Doctor of Philosophy

DOCTOR OF PHILOSOPHY (2022) McMaster University

(Chemistry) Hamilton, Ontario

TITLE: Recent Synthetic and Structural Developments in Noble-Gas, Chlorine, Bromine, Iridium, and Group 6 Fluorine Chemistry

AUTHOR: Mark R. Bortolus, B. Sc. (McMaster University)

SUPERVISOR: Professor Gary J. Schrobilgen

NUMBER OF PAGES: xl, 679

ABSTRACT

The noble-gas difluorides, NgF_2 (Ng = Kr, Xe), are moderate-strength fluoride-ion donors which react with strong fluoride-ion acceptors to form salts of $[NgF]^+$ and $[Ng_2F_3]^+$. Although $[Xe_2F_3]^+$ and $[Kr_2F_3]^+$ salts had been synthesized and structurally characterized, the mixed Kr^{II}/Xe^{II} analogue, $[FKrFXeF]^+$, had not been reported. Reaction of $[XeF][AsF_6]$ with excess KrF_2 at −78 °C in anhydrous hydrogen fluoride (aHF) solvent yielded the first mixed Kr^{II}/Xe^{II} noble-gas compound, $[FKrFXeF][AsF_6]\cdot 0.5KrF_2\cdot 2HF$, a salt of the $[FKrFXeF]^+$ cation. In the course of the redox decomposition of $[FKrFXeF]^+$, the potent oxidative fluorinating properties of the Kr^{II} fluoride species resulted in oxidation of Xe^{II} to Xe^{IV} in aHF at −60 °C to form the mixed Kr^{II}/Xe^{IV} cocrystals, $([Kr_2F_3][AsF_6])_2\cdot XeF_4$ and $XeF_4\cdot KrF_2$. Further decomposition at 22 °C resulted in oxidation of Xe^{IV} to Xe^{VI} to give the recently reported Kr^{II}/Xe^{VI} complexes, $[F_5Xe(FKrF)_n][AsF_6]$ (n = 1, 2), $[F_5Xe][AsF_6]$, and a new Kr^{II}/Xe^{VI} complex, $[(F_5Xe)_2(\mu\text{-}FKrF)(AsF_6)_2]$, which was characterized by low-temperature (LT) Raman spectroscopy. The $[FKrFXeF][AsF_6]\cdot 0.5KrF_2\cdot 2HF$, $([Kr_2F_3][AsF_6])_2\cdot XeF_4$, and $XeF_4\cdot KrF_2$ compounds were characterized by LT Raman spectroscopy and single-crystal X-ray diffraction. Quantum-chemical calculations were used to assess the bonding in $[FKrFXeF]^+$, $[Kr_2F_3]^+$, and $[Xe_2F_3]^+$ and to assist in their vibrational assignments.

Although the fluoride-ion donor chemistries of the neutral X(V) (X = Cl, Br) fluorides and oxide fluorides are developed, the coordination chemistries of the X(V) cations $[XF_4]^+$, $[XOF_2]^+$, and $[XO_2]^+$ were largely unknown. The synthesis and structural characterization of the first Cl(V) coordination complex of XeF_2, $[O_2Cl(FXeF)_2][AsF_6]$, is

described. The reaction of α-$[ClO_2][AsF_6]$ with XeF_2 at −78 °C in anhydrous HF (aHF) solvent yields $[O_2Cl(FXeF)_2][AsF_6]$, which constitutes a rare example of noble-gas difluoride coordination to a main-group Lewis acid center. The low-temperature (LT) phase of β-$[ClO_2][AsF_6]$ was obtained for the first time upon recrystallization of α-$[ClO_2][AsF_6]$ from aHF solvent at –10 °C. The compounds were characterized by LT single-crystal X-ray diffraction and LT Raman spectroscopy. Quantum-chemical calculations were carried out for the model gas-phase $(O_2Cl(FXeF)_2][AsF_6]_2)^-$ anion to aid in the assignments of fundamental vibrational frequencies and $^{35/37}Cl$ isotopic shifts for $[O_2Cl(FXeF)_2][AsF_6]$ and to assess chemical bonding in $[O_2Cl(FXeF)_2]^+$ by use of an NBO analysis. The $[O_2Cl(FXeF)_2]^+$ cation and $[AsF_6]^-$ anion of $[O_2Cl(FXeF)_2][AsF_6]$ exist as intimate ion-pairs with secondary Cl---F_{As} and Cl---F_{Xe} bonds that are significantly shorter than the sums of the Cl and F van der Waals radii, and are predominantly electrostatic in nature. MEPS and NBO analyses were also carried out for the gas-phase $[XO_2]^+$ (X = Cl, Br, I) cations in order to assess the possibilities of analogous $[BrO_2]^+$ and $[IO_2]^+$ coordination complexes.

In a related study, the reactions of $[BrO_2][PnF_6]$ with XeF_2 in aHF were shown to yield $[O_2Br(FXeF)_n][AsF_6]$ (n = 1, 2) and $[O_2Br(FXeF)_2][SbF_6]$. The complexes were characterized by low-temperature Raman spectroscopy and single-crystal X-ray diffraction (SCXRD) and provided the first examples of coordination complexes between a noble-gas difluoride and $[BrO_2]^+$. The fluorine atoms of XeF_2 and $[PnF_6]^-$ interact with $[BrO_2]^+$ to form primarily electrostatic Br---F bonds by coordination of F atoms to

regions of high electrostatic potential on the Br(V) atom of $[BrO_2]^+$, with contact trajectories that avoid the stereo-active valence electron lone pair of Br(V).

The neutral interhalogen chlorine fluorine compounds ClF, ClF_3, and ClF_5 are potent oxidative fluorinating agents, and their applications as such have been well documented. The Cl(III) and Cl(V) fluorides also undergo O/F metathesis, which makes them useful synthetic reagents for the fluorination of oxides. Metatheses with ClF_3 yield unstable OClF, which rapidly dismutates to ClF and ClO_2F and had not been directly observed in these reactions. Although the oxides and fluorides of many heavy transition metals (TMs) had been established, there were no structurally characterized oxide fluorides of the noble metals, i.e., Rh, Pd, Ag, Ir, Pt, or Au. The apparent anomaly was investigated by the candidate, who synthesized and structurally characterized the first iridium oxide fluoride, the oxygen-bridged $[cyclo\text{-}(\mu\text{-}OIrF_4)_3]^{2-}$ anion, and iridium(V) fluoride adduct, $F_5Ir\text{---}OClF$, by reaction of IrO_2 with ClF_5 and ClF_3, respectively, in anhydrous hydrogen fluoride (aHF). The $[cyclo\text{-}(\mu\text{-}OIrF_4)_3]^{2-}$ anion provides the only example of a mixed-oxidation-state 2 x Ir(V) and 1 x Ir(VI) oxyfluoro-species. The formation of $F_5Ir\text{---}OClF$ prevents thermodynamically unstable OClF from rapidly disproportionating to yield ClF and ClO_2F, providing the first crystallographically characterized OClF coordination complex, and the first direct evidence for the formation of OClF in the reaction of ClF_3 with a metal oxide.

The coordination chemistries of the Group 6 oxide tetrafluorides, MOF_4 (M = Mo, W), have been developed by the structural characterizations of their coordination complexes with the noble-gas difluorides, NgF_2 (Ng = Kr, Xe). The $NgF_2 \cdot MOF_4$ (M =

Mo, W) and $XeF_2 \cdot 2MOF_4$ complexes have been previously synthesized in anhydrous HF (aHF) solvent and melts, respectively. However, $KrF_2 \cdot 2MoOF_4$ and $KrF_2 \cdot nWOF_4$ (n = 1, 2) had not been characterized by X-ray diffraction because they decomposed prior to crystallization. The candidate's contribution to this study was to synthesize $KrF_2 \cdot WOF_4$ and the solvate, $[\text{--}(F_4OMo)(\mu_3\text{-}F)H\text{---}(\mu\text{-}F)H\text{--}]_\infty$, in aHF and to characterize them by SCXRD. The SCXRD structures of the series of complexes show $NgF_2 \cdot MOF_4$ and $XeF_2 \cdot 2MOF_4$ have $F_t{-}N_g{-}F_b\text{---}M$ arrangements, in which the NgF_2 ligands coordinate to MOF_4 through μ-F_b bridges. The XeF_2 ligands of $XeF_2 \cdot 2MOF_4$ also coordinate to $F_3OM{-}F_b'\text{---}M'OF_4$ moieties through $F_t{-}Xe{-}F_b\text{---}M$ bridges to form $F_t{-}Xe{-}F_b\text{---}M(OF_3){-}F_b'\text{---}M'OF_4$, where XeF_2 coordinates trans to O of M and F_b' is trans coordinated to O of M'. The Ng–F_t, Ng–F_b, and M---F_b bond lengths of $NgF_2 \cdot nMOF_4$ are consistent with MOF_4 and $F_3OM{-}F_b'\text{---}M'OF_4$ fluoride-ion affinity trends: $CrOF_4 < MoOF_4 < WOF_4 \approx F_3OMo{-}F_b'\text{---}Mo'OF_4 < F_3OW{-}F_b'\text{---}W'OF_4$. Quantum-chemical calculations show the M---F_b bonds of $NgF_2 \cdot MOF_4$ and $XeF_2 \cdot 2MOF_4$ are predominantly electrostatic, σ-hole type bonds, with a significant orbital contribution that accounts for their bent Ng–F_b---M bond angles.

The coordination complex, $F_3XeF_b\text{---}WOF_4$, was synthesized in $CFCl_3$ solvent by reaction of the weak fluoride-ion donor and strong oxidative fluorinating agent, XeF_4, with the intermediate-strength fluoride-ion acceptor, WOF_4. The complex was characterized at low temperatures by single-crystal X-ray diffraction and Raman spectroscopy, and is the only TM coordination complex of Xe(IV). Xenon tetrafluoride and WOF_4 coordinate trans to the W=O bond through a W---F_b bond. The XeF_3 moiety of

F_3XeF_b---WOF_4 acquires a degree of $[XeF_3]^+$ character upon coordination that is reflected by its stretching frequencies that are intermediate with respect to XeF_4 and $[XeF_3]^+$. Quantum-chemical calculations show W---F_b is predominantly an electrostatic, σ-hole bond with a significant orbital contribution that accounts for the bent Xe–F_b---W angle of this complex, and that F_3XeF_b---MOF_4 (M = Cr, Mo) are less stable than the W analogue, which is consistent with failed attempts to synthesize F_3XeF_b---$MoOF_4$.

The oxide, fluoride, and oxide fluoride chemistries of Cr(VI) are significantly less developed than Mo(VI) and W(VI). Xenon hexafluoride is the most fluorobasic fluoride-ion donor among the noble-gas difluorides. Its reactions with the weak fluoride-ion acceptor, $CrOF_4$, were explored with the aim to synthesize novel Cr(VI) oxyfluoro-anion salts. Unpublished work from this group revealed that molten mixtures of XeF_6 and $CrOF_4$ react by means of F_2 elimination and reduction of Cr(VI) to Cr(V) and Cr(IV) to form $[XeF_5][Xe_2F_{11}][Cr^{V}OF_5]\cdot 2CrOF_4$, $[XeF_5]_2[Cr_2{}^{V}O_2F_8]$, $[XeF_5]_2[Cr^{IV}F_6]\cdot 2CrOF_4$, and $[Xe_2F_{11}]_2[Cr^{IV}F_6]$. The present work showed that their reactions in anhydrous hydrogen fluoride (aHF) and $CFCl_3$/aHF yield $[XeF_5]_2[Cr_2O_2F_8]\cdot 2HF$ and $[XeF_5]_2[Cr_2O_2F_8]\cdot 2XeOF_4$. Their reaction pathways involve redox transformations that give $[XeF_5]^+$ and/or $[Xe_2F_{11}]^+$ salts of the known $[CrOF_5]^{2-}$ and $[CrF_6]^{2-}$ anions, and the novel $[Cr_2O_2F_8]^{2-}$ anion. A low-temperature Raman spectroscopic study of an equimolar mixture of solid XeF_6 and $CrOF_4$ revealed that $[Xe_2F_{11}][CrOF_5]$ is formed as a reaction intermediate. The salts were structurally characterized by LT SCXRD and LT Raman spectroscopy and provide the first structural characterizations of the $[CrOF_5]^{2-}$ and $[Cr_2O_2F_8]^{2-}$ anions in which $[Cr_2O_2F_8]^{2-}$ represents a new structural motif among the

known oxyfluoro-anions of Group 6. The X-ray crystal structures show that $[XeF_5]^+$ and $[Xe_2F_{11}]^+$ form intimate ion-pairs with their respective through electrostatic Xe---F–Cr secondary bonding interactions. Quantum-chemical calculations were carried out to obtain the energy-minimized, gas-phase geometries and the vibrational frequencies and intensities of the anions as their gas-phase ion-pairs to aid in the assignments of their Raman spectra and to assess their bonding.

Recent advances in high-oxidation-state Cr(VI) and Cr(V) oxide fluoride chemistry have exploited the fluorobasicity of XeF_6 and resistance of the $[XeF_5]^+$ and $[Xe_2F_{11}]^+$ cations to oxidation for the preparation of the first examples of Cr(VI) and Cr(V) oxyfluoro-anions to be characterized by SCXRD. This provided impetus to attempt the synthesis and structural characterization of new Cr(VI)/Cr(V) oxyfluoro-anions derived from the reaction of CrO_2F_2 with XeF_6. The syntheses and structural characterizations of the first dinuclear Cr(VI) oxyfluoro-anion salts, $[XeF_5]_2[Cr_2O_4F_6]$, $[XeF_5]_2[Cr_2O_4F_6]\cdot 4HF$, $[XeF_5]_2[Cr_2O_4F_6]\cdot 2XeOF_4$, and the mononuclear anion $[XeF_5][Xe_2F_{11}][CrO_2F_4]$ by LT Raman spectroscopy and single-crystal X-ray diffraction are described. The salts were prepared by reaction of XeF_6 with CrO_2F_2 in the oxidatively resistant solvents, aHF and $CFCl_3$, and by their direct reaction in melts at elevated temperatures (ca. 50 °C). The $[Cr_2O_4F_6]^{2-}$ dianion is a dimer of $[CrO_2F_3]^-$. Quantum-chemical calculations show that the salts are strongly ion-paired and interact by means of primarily electrostatic Xe---F secondary bonding interactions. Quantum-chemical calculations were carried out to obtain the energy-minimized, gas-phase geometries and the vibrational frequencies and intensities of the gas-phase ion-pairs to aid in vibrational

frequency assignments and NBO and MEPS analyses were carried to assess their bonding.

In related studies, the reactions of XeF_6 with the fluoride-ion acceptors $M'OF_4$ (M' = Cr, Mo, W) yielded $[XeF_5]^+$ and $[Xe_2F_{11}]^+$ salts of the Group 6 oxyfluoro-anions $[M'OF_5]$ and $[M_2O_2F_9]$ (M = Mo, W). Xenon hexafluoride and MOF_4 react in aHF solution to give equilibrium mixtures of $[Xe_2F_{11}]^+$, $[XeF_5]^+$, $[(HF)_nF]^-$, $[MOF_5]^-$, and $[M_2O_2F_9]^-$ from which the salts crystallized. The $[XeF_5][CrOF_5]$ and $[Xe_2F_{11}][CrOF_5]$ salts did not form when attempts were made to react $CrOF_4$ with XeF_6 in aHF at low temperatures owing to the low fluoride-ion affinity of $CrOF_4$, but form $[XeF_5][HF_2]\cdot CrOF_4$ instead. Unlike $CrOF_4$, $MoOF_4$ and WOF_4 are sufficiently Lewis acidic to abstract F^- ion from $[(HF)_nF]^-$ in aHF to form $[MOF_5]^-$ and $[M_2O_2F_9]^-$ salts of the $[XeF_5]^+$ and $[Xe_2F_{11}]^+$ cations. Hydrolysis of $[Xe_2F_{11}][WOF_5]$ by small amounts of water contaminant in aHF solvent yielded $[XeF_5][WOF_5]\cdot XeOF_4$. To circumvent $[(HF)_nF]^-$ formation, $[Xe_2F_{11}][CrOF_5]$ was synthesized at LT in the oxidatively resistant solvent, CF_2ClCF_2Cl. The salts were characterized by LT SCXRD and LT Raman spectroscopy to give the first X-ray crystal structure of the $[CrOF_5]^-$ anion. Quantum-chemical calculations were carried out for gas-phase $M'OF_4$, $[M'OF_5]^-$, $[M'_2O_2F_9]^-$, $\{[Xe_2F_{11}][CrOF_5]\}_2$, $[Xe_2F_{11}][MOF_5]$, and $\{[XeF_5][M_2O_2F_9]\}_2$ to obtain their energy-minimized, gas-phase geometries and vibrational frequencies to aid in vibrational mode assignments and discussions of their chemical bonding.

ACKNOWLEDGEMENTS

I wholeheartedly thank Professor Gary J. Schrobilgen for his mentorship and friendship over the past several years. I could not have asked for a better supervisor. I look forward to what the years ahead bring for us both. I will forever be grateful for the kindness and patience you have shown me, and how you have pushed me to be a better scientist.

A special thank you to Dr. Helene P. A. Mercier, not only for the countless hours she spent teaching me to analyze X-ray, Raman, and computational data, and improve my writing, but for her unwavering support, guidance, and patience as a colleague and friend.

I would also like to thank my Ph.D. committee members, Prof. David J. H. Emslie and Prof. Yurij Mozharivskyj, for their guidance and support throughout my degree.

To past members of the research group, thank you! My time in the lab was made all the better for having worked with you. Thank you also to Brianna Nyugen and Griffin LaChapelle for being such great undergraduate Thesis students.

To my family, thank you for your love and support throughout my degree. It is from you that I found the courage to pursue this path. To my grandparents, Carl, Sylvia, Elizabeth, and Bruno, whom I love with all my heart. To my parents; Anna and Glenn Bortolus, who have given me the courage and drive to pursue this path. To my siblings and their partners, who were always willing to listen during stressful times. Thank you.

Finally, thank you to my wife, Jessica. You have been with me from first year Life Science to the end of my Ph.D. and have supported me at each turn. Thank you for being patient with me during this past decade, and for always listening when I talk about work, especially when you have no idea what I am talking about.

DECLARATION OF ACADEMIC ACHIEVEMENT

Dr. Hélène P. A. Mercier, a research scientist in the Schrobilgen group, is acknowledged for her contributions to the candidates training as highly-qualified-personnel, and for her assistance with structure solutions and refinements for problematic single-crystal X-ray diffraction data sets, Raman assignments and vibrational mode interpretations, and quantum-chemical calculations. She has also provided editing/proofreading services for the authors published works, and for the unpublished chapters of this Thesis. She is a co-author for the published chapters in which her contributions to the work were significant. During her 4th year undergraduate thesis in the Schrobilgen group, Brianna Nyugen assisted with experimental work leading to $[FKrFXeF][AsF_6]\cdot 0.5KrF_2\cdot 2HF$ (Chapter 3) and is a co-author on the published paper. Jamie Haner, a former graduate student in the Schrobilgen group, initially identified the $[O_2Cl(FXeF)_2][AsF_6]$ and $[O_2Br(FXeF)_2][SbF_6]$ coordination complexes (Chapters 4 and 5). During his 4th year undergraduate thesis in the Schrobilgen group, Griffin LaChapelle assisted with experimental work leading to the synthesis and characterization of the XeF_2 coordination complexes with $[BrO_2][PnF_6]$ (Pn = As, Sb) (Chapter 5) and will be a co-author on the published work. Dr. Jamie Goettel, a former graduate student in the Schrobilgen group, initially prepared the iridium oxide-fluoride anion species $[ClO_2]_2[cyclo\text{-}(\mu\text{-}OIrF_4)_3]$, which was misidentified at the time as $[ClO_2][cyclo\text{-}(\mu\text{-}OIrF_4)_3]$ (Chapter 6). He also synthesized $[XeF_5]_2[CrF_6]\cdot 2CrOF_4$, $[Xe_2F_{11}]_2[CrF_6]$, $[XeF_5]_2[Cr_2O_2F_8]$, and $[XeF_5][Xe_2F_{11}][CrOF_5]\cdot 2CrOF_4$, which are described in Chapter 9. Dr. Jim Britten, the X-Ray Manager at McMaster University, assisted with the solution of the crystal structure of $[XeF_5][Xe_2F_{11}][CrOF_4]$.

PREFACE

The following Chapters have been published.

Chapter 3: **Bortolus, M. R.**; Mercier, H. P. A.; Nyugen, B.; Schrobilgen, G. J. *Angew. Chem. Int. Ed.* **2021**, *60*, 23678–23686.

Chapter 4: **Bortolus, M. R.**; Ellwanger, M.; Haner, J.; Schrobilgen, G. J. *J. Fluor. Chem.* **2021**, *250*, 109814.

Chapter 7: **Bortolus, M. R.**; Mercier, H. P. A.; Brock, D. S.; Schrobilgen, G. J. *Chem. Eur. J*. **2022**, *28*, e202103729.

and,

Mercier, H. P. A.; Breddemann, U.; Brock, D. S.; **Bortolus, M. R.**; Schrobilgen, G. J. *Chem. Eur. J*. **2019**, *25*, 12105–12119.

Chapter 8: **Bortolus, M. R.**; Mercier, H. P. A.; Schrobilgen, G. J. *Angew. Chem. Int. Ed.* **2022**, *61*, e202211699.

Chapter 9: Goettel, J. T.; **Bortolus, M. R.**; Stuart, D. G.; Mercier, H. P. A.; Schrobilgen, G. J. *Chem. Eur. J*. **2019**, *25*, 15815–15829.

Chapter 11: **Bortolus, M. R**.; Mercier, H. P. A.; Schrobilgen, G. J. *Chem. Eur. J*. **2020**, *26*, 8935–8950.

Chapters 5, 6, and 10 will be submitted for publication as their own individual papers.

CANDIDATE'S SPECIFIC CONTRIBUTIONS TO PUBLISHED PAPERS

Chapters 3, 4, 8, and 11. The candidate carried out all low-temperature (LT) syntheses, LT structural characterizations (Raman spectroscopy and single-crystal X-ray diffraction), and experimental data analyses described in these papers. He also worked with co-authors to carry out the quantum-chemical analyses described in the paper, assign the Raman spectra of the title compounds with the aid of calculated vibrational frequency assignments, and to draft the paper for publication.

Chapter 7. The candidate carried out the LT syntheses and structural characterizations of $XeF_2 \cdot CrOF_4$, $KrF_2 \cdot WOF_4$, and $[\text{--}(F_4OMo)(\mu_3\text{-}F)H\text{---}(\mu\text{-}F)H\text{--}]_\infty$. He analyzed the experimental data (Raman, X-ray, syntheses) for all of the compounds described in both papers (*Chem. Eur. J.* **2022**, *28*, e202103729, and *Chem. Eur. J.* **2019**, *25*, 12105–12119.), and collaborated with the co-authors to draft the manuscripts for publication. He also contributed to carrying out quantum-chemical calculations and writing the discussion of the quantum-chemical calculation results for these papers. Only the most recent article in which the candidate is first-author, *Chem. Eur. J.* **2022**, *28*, e202103729, is reproduced because it draws comparisons with and refers to the other published paper and to $XeF_2 \cdot CrOF_4$ throughout the text.

Chapter 9. The candidate carried out the LT syntheses of $[XeF_5]_2[Cr_2O_2F_8] \cdot 2XeOF_4$ and $[XeF_5]_2[Cr_2O_2F_8] \cdot 2HF$, and structurally characterized both compounds by LT Raman spectroscopy and LT single-crystal X-ray diffraction. He analyzed the experimental data for all the compounds described in the paper, contributed to carrying out the quantum-chemical calculations, and drafted the manuscript for publication with the co-authors.

LIST OF ABBREVIATIONS AND SYMBOLS

General

ax	axial
eq	equatorial
FEP	perfluoroethylene/perfluoropropylene copolymer
IR	infrared
Kel-F	chlorotrifluoroethylene
VSEPR	valence shell electron pair repulsion
N.A.	natural abundance (isotopic)
i.d.	inner diameter
o.d.	outer diameter
in.	inch
LT	low temperature
RT	room temperature
CN	coordination number

Raman Spectroscopy

$\Delta\nu$	frequency
cm^{-1}	wavenumber
ν	stretching mode
δ	in-plane bend
δ_{umb}	umbrella mode
ρ_w	wagging mode
ρ_r	rocking mode
ρ_t	twisting mode
o.o.p.	out-of-plane
i.p.	in-plane

X-ray Crystallography

$\alpha, b, c, \alpha, \beta, \gamma$	unit cell parameters
V	unit cell volume
λ	wavelength
μ	absorption coefficient
ρ	density
Z	molecules per unit cell
mol. wt.	molecular weight
F	structure factor
R_1	conventional agreement index
wR_2	weighted agreement index

Computational

DFT	density functional theory
ADF	amsterdam density functional
NBO	natural bond orbital
AIM	atoms in molecules
ELF	electron localization function
MEPS	molecular electrostatic potential surface
EDA	energy decomposition analysis
ETS-NOCV	extended-transition-state natural orbitals for chemical valence
SOC	spin orbit coupling
VELP	valence electron lone pair
EP	electrostatic potential
QC	quantum-chemical

TABLE OF CONTENTS

page

LIST OF TABLES

page

LIST OF FIGURES

page

CHAPTER 1

INTRODUCTION

The chapters of this Thesis have either been published or are in press and contain their own introductions. This general introductory chapter focuses on noble-gas chemistry, with emphasis on the chemistries of the binary noble-gas fluorides, which are the synthetic precursors of all new noble-gas compounds described in this Thesis.

1.1. Discovery of Noble-gas Reactivity

Noble-gas reactivity was discovered by Neil Bartlett on March 23, 1962.[1] Bartlett, then at the University of British Columbia, hypothesized that because PtF_6 oxidized molecular oxygen to $[O_2]^+$ (IP_1, 12.2 eV), it should also oxidize xenon gas (IP_1, 12.13 eV) to Xe^+.[1] The reaction was carried out at room temperature (Eq **1.1**) and resulted in a yellow-orange powder which coated the inside of the Pyrex glass reaction vessel. Bartlett

$$Xe_{(g)} + PtF_{6(g)} \longrightarrow Xe[PtF_6]_{(s)} \qquad (\mathbf{1.1})$$

formulated the solid as $Xe[PtF_6]$, but it was later shown to be a mixture of $[XeF][PtF_6]$ and $[XeF][Pt_2F_{11}]$.[2] The discovery of noble-gas reactivity contradicted the preexisting dogma of noble-gas inertness. Research in this field has proven instrumental in the development of our current understanding of chemical bonding, particularly in relation to hyper-valent bonding and the nature of secondary and σ-hole bonding.

Within three years of Bartlett's discovery, the precursors for most noble-gas compounds, KrF_2,[3] XeF_2,[4] XeF_4,[5] and XeF_6,[6] as well as XeO_3,[7] and $XeOF_4$,[8] had been synthesized. Among the noble-gas (Group 18) elements, only xenon and krypton form

compounds in macroscopic quantities. Several reviews on noble-gas chemistry have been published,[9–20] as well as a historical account of the events leading up to the discovery of noble-gas reactivity and its impact on modern chemistry.[21] Most recently, the candidate has co-authored a chapter in *Comprehensive Inorganic Chemistry III* (ca. 100 pages) titled "Noble-gas Chemistry" which provides a review of developments in noble-gas chemistry since 2013. This article is in-press and highlights several published chapters in this Thesis. The latter reviews should be consulted for a more comprehensive background relating to synthetic and structural noble-gas chemistry.

1.2. Chemical Properties of the Noble-gas Fluorides

1.2.1. Noble-gas Difluorides NgF_2 (Ng = Kr, Xe)

Xenon difluoride has been prepared by reaction of Xe and F_2 gas in the presence of several different types of energy, such as heat, UV light, sun light, electric discharge, and high-energy irradiation.[22–24] The high-yield synthesis of bulk quantities of XeF_2 can be achieved by reaction of excess Xe with F_2 at ca. 400 °C,[24] or by UV irradiation of a gaseous Xe : F_2 mixture in a mole ratio of 1 : 2 with addition of ca. 1 mol % HF as a catalyst. Xenon difluoride is a colorless crystalline solid that is stable at room temperature (ΔH_f^o = –162.8 ±0.9 kJ mol^{-1};[25] m.p., 129.03 ±0.05 °C;[26] vapor pressure at 298.15 K, 4.55 torr[26]), and is an accessible and easy to handle noble-gas compound that has found important synthetic applications as a gas-phase etchant for microelectromechanical systems[27] and as an electrophilic and oxidative fluorinating agent that has found

application in ^{18}F positron emission tomography (PET),[28–30] main-group chemistry,[31–33] transition-metal chemistry,[34–36] and organic chemistry.[23,37,38]

Krypton difluoride is a colorless crystalline solid that is thermodynamically unstable at room temperature (ΔH_f^o = 60.2 ±3.3 kJ mol^{-1}, gas at 93 °C).[17] Due to its thermodynamic instability and the difficulty atomizing F_2 at low temperatures, the preparation of synthetically useful amounts of KrF_2 is technically challenging and difficult to scale. Gram quantities of KrF_2 may be prepared by electric glow discharge,[3,39,40] UV-photolysis,[41–45] or by use of a hot wire reactor,[45,46] and may be stored indefinitely at −78 °C.[3] Krypton difluoride has a significant vapour pressure at low temperatures (vapor pressure at 273.0 K, 29±2 torr)[17] which allows it to be sublimed under static or dynamic vacuum without appreciable decomposition.

All krypton chemistry is derived from KrF_2.[17] Although the oxidative fluorinating strength of the binary xenon fluorides increases with formal oxidation state, i.e., XeF_2 < XeF_4 < XeF_6,[47] KrF_2 is the strongest neutral oxidative fluorinating agent presently known, and is capable of oxidizing xenon gas to XeF_6 and gold metal to $[Kr_2F_3][AuF_6]$ below room temperature.[17] In addition to its thermal instability, the substantial difference between the oxidizer strengths of KrF_2 and XeF_2 can be attributed to substantially higher first and second ionization potentials for krypton (13.999 eV, 24.359 eV) relative to xenon (12.130 eV, 21.21 eV).[47]

The linear triatomic ($D_{\infty h}$) structures of NgF_2 have been established in the solid-, liquid-, and gas-phases by many characterization techniques[17,48] and are consistent with

AX_2E_3 valence shell electron lone pair (VSEPR) arrangements of bond-pairs (X) and valence electron lone pairs (E) around the central Ng atoms (A), with solid-state Ng–F bond distances of 1.894(5) (α-KrF_2)[46] and 1.999(4) (XeF_2)[48] Å (SCXRD, Figure 1.1). Although XeF_2 is soluble and stable in a variety of oxidatively resistant solvents, i.e., BrF_5, anhydrous HF, and CH_3CN, it undergoes hydrogen and halogen exchange reactions with CH_2Cl_2, $CHCl_3$, CCl_4, $CFCl_3$, CH_2Br_2, $CFCl_2CF_2Cl$.[49] Krypton difluoride is generally handled in only the most oxidatively resistant solvents such as aHF and BrF_5 to circumvent or reduce oxidative fluorination of the solvent medium.[17]

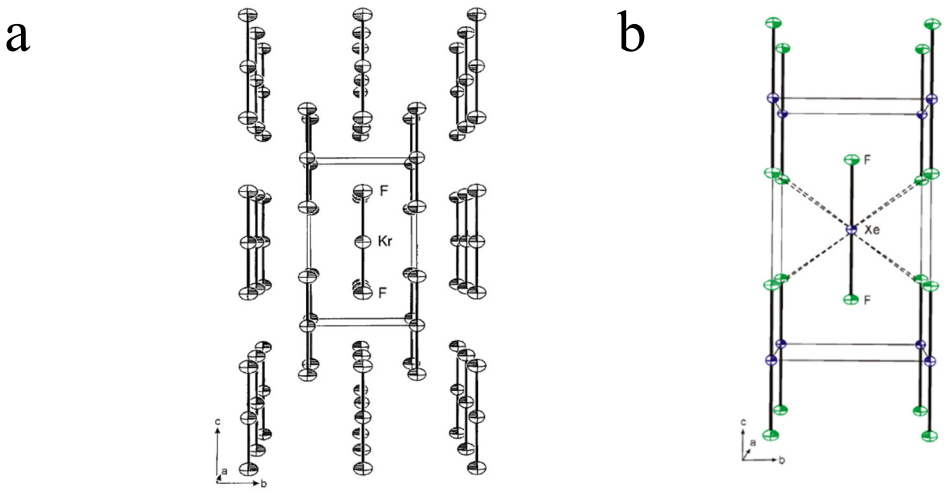

Figure 1.1. The X-ray crystal structures of (a) α-KrF_2[46] and (b) the low-temperature phase of XeF_2,[48] with thermal ellipsoids drawn at the 50% probability level. Dashed lines in (b) indicate secondary Xe---F secondary bonding interactions. Reprinted with permission from (a) Lehmann, J. F.; Dixon, D. A.; Schrobilgen, G. J. *Inorg. Chem.* **2001**, *40*, 3002–3017 (Copyright 2001 American Chemical Society), and (b) Elliot, H. S. A.; Lehmann, J. F.; Mercier, H. P. A.; Jenkins, H. D. B.; Schrobilgen, G. J. *Inorg. Chem.* **2010**, *49*, 8504–8523 (Copyright 2010 American Chemical Society).

The bonding in NgF_2 has been described in terms of a three-center, four electron (3c-4e) molecular orbital model in which the Xe $5p_z$ or Kr $4p_z$ atomic orbitals interact with the F $2p_z$ atomic orbitals to form bonding, non-bonding, and antibonding molecular orbitals (Figure 1.2).[17,50] The bonding and non-bonding orbitals are fully occupied, and give rise to a total bonding interaction that has formal Ng–F bond orders of 1/2. The charge distributions in NgF_2 have been investigated by ^{19}F-NMR[3,51,52] and Mössbauer spectroscopies,[53,54] which reveal that there is significantly more negative charge transfer to the F atoms of XeF_2 relative to KrF_2, indicating a greater degree of covalent character for the Ng–F bonds of KrF_2.

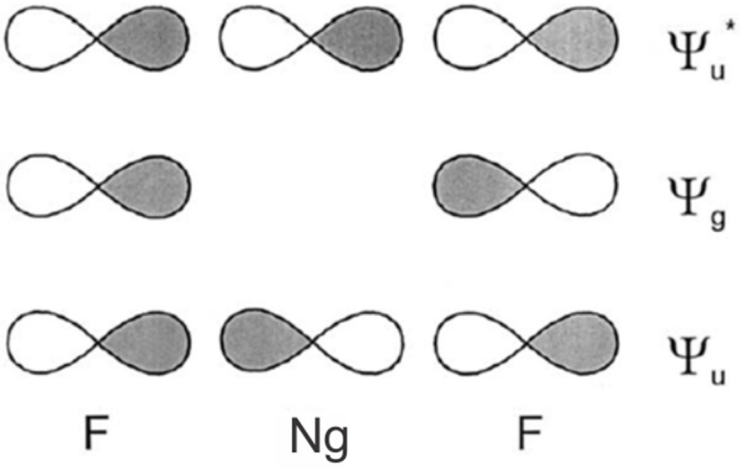

Figure 1.2. Molecular orbital diagrams for NgF_2. Modified with permission from Reprinted with permission from Lehmann, J. F.; Mercier, H. P. A.; Schrobilgen, G. J. *Coord. Chem. Rev.* **2002**, *233–234*, 1–39. Copyright 2002 American Chemical Society.

The covalent nature of the Kr–F bonds in KrF_2 has also been established through exposure of solid KrF_2 to γ-irradiation which yielded the F· and KrF· radicals by homolytic cleavage of the Kr–F bond.[55] The radicals were characterized by EPR

spectroscopy,[55] and their formation indicates that F· and KrF· have similar electron affinities. These observations in addition to the low mean thermochemical bond energy (48.9 kJ mol^{-1})[56,57] and energy of atomization (97.9 kJ mol^{-1})[56,57] for KrF_2 provide rationales for the ability of KrF_2 to serve as a good low-temperature source of F·.

The Ng–F (Ng = Kr, Xe) bonding of NgF_2 may also be represented by a 3c-4e valence bond description in accordance with resonance Structures I and II.

$$F–Ng^+\ F^- \longleftrightarrow F–Ng–F \longleftrightarrow F^-\ {}^+Ng–F$$

I II I

The high ionic characters of the polar-covalent Ng–F bonds implied by Structures I and II account for the fluoride-ion donor behavior of NgF_2 towards strong to moderate strength Lewis acids such as TiF_4[58] and MF_5 (M = As,[17,46,48] Sb,[17,46,48] Bi,[17] V,[17] Nb,[17] Ta,[17] Au[17]). These fluoride-ion transfer reactions may be carried out in the oxidatively resistant solvent, anhydrous HF (aHF), to form $[NgF][MF_6]$ and $[NgF][M'_2F_{11}]$ (M′ = Sb,[17,46,48] Bi,[17] Nb,[17] Ta,[17] Ir,[17] Pt[17]) salts [Eq. (**1.2**)].

$$NgF_2 + nMF_5 \longrightarrow [NgF][M_nF_{5n+1}]\ (n = 1 \text{ or } 2) \qquad (\mathbf{1.2})$$

The $[NgF]^+$ cations are potent oxidizers, with $[KrF]^+$ being the strongest oxidative fluorinating agent currently known.[17,46] The $[NgF]^+$ cations are also moderately strong Lewis acids which form intimate ion-pairs that interact through Ng---F_b–M fluorine bridges between the cation and a fluorine atom of $[M_nF_{5n+1}]^-$.[17,46,48] The ionic character of the secondary Ng---F_b bridge bond increases with the Lewis acidity of MF_5,[48] resulting in

a longer Ng---F_b bond, a shorter terminal Ng–F_t bond, greater $[NgF]^+$ character, and enhanced oxidizer strength.

The reaction of NgF_2 with a $[NgF]^+$ salt in aHF yields the planar V-shaped $[Ng_2F_3]^+$ (Ng = Kr or Xe) cations [Eq. (**1.3**)].[17,46,48,58,59]

$$NgF_2 + [NgF][MF_6] \longrightarrow [Ng_2F_3][MF_6] \qquad (\mathbf{1.3})$$

The formal Ng–F_t bond orders of $[Ng_2F_3]^+$ lie between ½ (NgF_2) and 1 ($[NgF]^+$), in accordance with the 5c-6e valence bond description given by resonance Structures III–V.

$$[F–Ng–F–Ng–F]^+ \leftrightarrow F–Ng–F\ {}^{+}Ng–F \leftrightarrow F–Ng^{+}\ F^{-}\ {}^{+}Ng–F \leftrightarrow F–Ng^{+}\ F–Ng–F \leftrightarrow [F–Ng–F–Ng–F]^+$$

III IV V IV III

The $[Ng_2F_3]^+$ cations do not form intimate ion-pairs with their anions and have oxidizer strengths that lie between those of NgF_2 (1/2) and $[NgF]^+$ (1), consistent with the formal Ng–F_t bond orders.[17,51]

The ligand behaviors of KrF_2 and XeF_2 are well established and have been described in several reviews.[17,19,22] To stabilize terminal NgF_2 coordination complexes, i.e., complexes with the general formula A---$F_b^{\delta-}$–$Ng^{\delta+}$–F_t, the fluoride-ion affinity of the fluoride-ion acceptor must be closely matched with the fluorobasicity of NgF_2, and the acceptor (A) must be resistant to oxidative fluorination by the polarized NgF_2 ligand which has enhanced $[NgF]^+$ character. Xenon difluoride forms terminal and bridging coordination complexes with a considerable number of fluoride-ion acceptors that include

main-group and transition-metal cations (i.e., Li^+, Mg^{2+}, Ca^{2+}, Cu^{2+}, Zn^{2+}, Sr^{2+}, Ag^+, Cd^{2+}, Ba^{2+}, La^{3+}, Nd^{3+}, Pb^{2+},[15,19] La^{3+}, Ce^{3+}, Pr^{3+}, Nd^{3+}, Sm^{3+}, Eu^{3+}, Gd^{3+}, Tb^{3+}, and Dy^{3+}, Y^{3+}[60]), the halogen (V) cations, $[ClO_2]^+$ [61] and $[BrOF_2]^+$,[62,63] the noble-gas cation $[XeF_5]^+$,[19,64] and the neutral TM oxide tetrafluorides MOF_4 (M = Cr,[65–67] Mo,[67] W[67]). Molecular addition compounds of XeF_2 also have been synthesized and structurally characterized that include $XeOF_4 \cdot XeF_2$,[68] $IF_5 \cdot XeF_2$,[69] and $XeF_4 \cdot XeF_2$.[70,71] The descriptions of these compounds as molecular addition compounds are based on the similarity of the vibrational frequencies and geometrical parameters of these compounds to those of their component molecules.

In contrast, crystallographically characterized examples of KrF_2 coordination compounds are very rare due to the thermodynamic instability and exceptional oxidative fluorinating strength of KrF_2 and its derivatives. The only KrF_2 coordination complexes that have been structurally characterized by SCXRD were all characterized within the past decade: $[F_2OBr(FKrF)_2AsF_6]$,[62] $Hg(FKrF)_{1.5}(OTeF_5)_2$,[72] $KrF_2 \cdot MOF_4$ (M = Cr,[65] Mo,[67] W[67]), $KrF_2 \cdot 2CrOF_4$,[65] $[F_5Xe(FKrF)_nAsF_6]$ (n = 1, 2),[73] $[Mg(FKrF)_4(AsF_6)_2]$,[74] and $[Mg(FKrF)_4(AsF_6)_2] \cdot 2BrF_5$.[74] The $[F_5Xe(FKrF)_nAsF_6]$ (n = 1, 2) complexes are the only examples of mixed Xe/Kr noble-gas compounds where the KrF_2 ligands are coordinated to Xe^{VI} in $[XeF_5]^+$ through primarily electrostatic σ-hole type Xe---F_b bonds.

1.2.2. Xenon Tetrafluoride

The chemistry of Xe(IV) is significantly less developed than the chemsitries of Xe(II) and Xe(VI).[20] Several factors contribute to the scarcity of Xe(IV) species which include their

strong oxidizing properties, and the endothermic natures of Xe(IV) oxides and oxide fluorides and their propensities to undergo redox eliminations and disproportionations.[20] A comprehensive review of developments pertaining to the syntheses, properties, structures, and bonding of Xe(IV) compounds ranging from the discovery of noble-gas reactivity in 1962 to 2014 inclusive is provided in *Chemical Reviews* (2015), and should be consulted for a more detailed overview of Xe(IV) chemistry.[20]

Shortly after the discovery of noble-gas reactivity, the high-temperature and pressure reaction of Xe and F_2 was investigated, which led to the discovery of the first binary noble-gas fluoride, XeF_4.[75,76] Xenon tetrafluoride is the precursor for all Xe(IV) compounds, and is difficult to synthesize in high purity by the thermal method due to the formation of equilibrium mixtures of XeF_2, XeF_4, and XeF_6 (Eqs **1.4–1.6**).[20,75,76] Gas-phase equilibrium constants have been determined for the formation of the binary xenon fluorides from the reaction of their elements at elevated temperature and pressure (Figure 1.3), which emphasize the importance of rigorous experimental control of Xe : F_2 stoichiometry, temperature, and pressure in the preparation of pure xenon fluorides.[20]

$$Xe + F_2 \rightleftharpoons XeF_2 \qquad (\mathbf{1.4})$$

$$XeF_2 + F_2 \rightleftharpoons XeF_4 \qquad (\mathbf{1.5})$$

$$XeF_4 + F_2 \rightleftharpoons XeF_6 \qquad (\mathbf{1.6})$$

The synthesis of high purity XeF_4 has been achieved by reaction of a ca. 1 : 5 molar mixture of Xe : F_2 at 400 °C in a 130 mL welded nickel reactor for 1 h followed by rapid cooling to RT in a water bath. The vessel is then cooled to −78 °C, and excess F_2 is pumped away to yield essentially pure XeF_4. Small amounts of volatile XeF_6, F_2, Xe, and

HF may then be removed under vacuum. More complex mixtures of XeF_2, XeF_4, and XeF_6 may also be chemically purified by reaction with AsF_5 to afford pure XeF_4.[77] Xenon tetrafluoride is calculated to be stable to disproportionation into XeF_2 and XeF_6 by ~5 kcal mol^{-1} under standard conditions and is a potent oxidative fluorinating agent.[20,78] Its square-planar structure has been unambiguously established by single-crystal X-ray diffraction (SCXRD), neutron diffraction, and infrared (IR), Raman, and NMR spectroscopies, and is consistent with an AX_4E_2 VSEPR arrangement around the central xenon atom.[20]

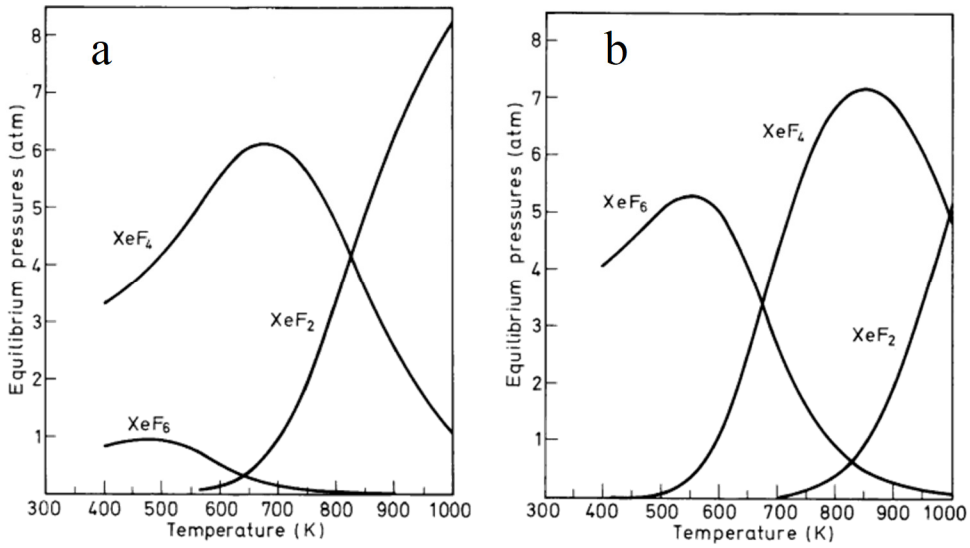

Figure 1.3. (a) Equilibrium pressures of xenon fluorides as a function of temperature. Initial conditions: 125 mmol of Xe, 275 mmol of F_2 per 1000 mL. (b) Equilibrium pressures of xenon fluorides as a function of temperature. Initial conditions: 125 mmol of Xe, 1225 mmol of F_2 per 1000 mL. Reprinted with permission from Reprinted from Haner, J.; Schrobilgen, G. J. *Chem. Rev.*, **2015**, *115*, 1255–1295. Copyright 2015, with permission from Elsevier.

Xenon tetrafluoride reacts with strong Lewis acids such as MF_5 (M = As,[79] Sb,[79–82] Bi[83]) in aHF solvent and in melts to form $[XeF_3][MF_6]$ and $[XeF_3][M'_2F_{11}]$ (M′ = Sb,[79,84,85] Bi[86]) salts [Eq. (**1.7**)].

$$XeF_4 + nMF_5 \longrightarrow [XeF_3][M_nF_{5n+1}] \ (n = 1 \text{ or } 2) \qquad (\mathbf{1.7})$$

The reactions of XeF_4 with the alkali metal fluorides MF (M = Na^+, K^+, Rb^+, and Cs^+), NOF, and with the "naked" and anhydrous fluoride-ion donor $[N(CH_3)_4]F$[20,87] yield salts of the $[XeF_5]^-$ anion (Eqs. (**1.8–1.10**)).

$$XeF_4 + MF \longrightarrow M[XeF_5] \ (M = Na^+, K^+, Rb^+, \text{and } Cs^+) \qquad (\mathbf{1.8})$$

$$XeF_4 + NOF \longrightarrow [NO][XeF_5] \qquad (\mathbf{1.9})$$

$$XeF_4 + [N(CH_3)_4]F \longrightarrow [N(CH_3)_4][XeF_5] \qquad (\mathbf{1.10})$$

The solid-state and solution structures of the $[XeF_3]^+$ and $[XeF_5]^-$ ions have been determined by SCXRD and Raman and multi-NMR spectroscopies.[20] The coordination environment around the Xe atom in the T-shaped $[XeF_3]^+$ cation is an AX_3E_2 VSEPR arrangement[88] in which two bond-pair domains occupy axial positions, and one bond-pair domain and two lone-pair domains occupy equatorial positions of a trigonal bipyramid. In the case of $[XeF_3]^+$ salts, the cation is strongly ion-paired with its respective anion, and their primary Xe–F bonds have increased covalent character relative to XeF_4 (Figure 1.4).[20]

The F atom arrangement of the $[XeF_5]^-$ anion is a regular pentagon (D_{5h}), which provided the first example of a structurally characterized AX_5E_2 VSEPR arrangement (Figure 1.5).[87]

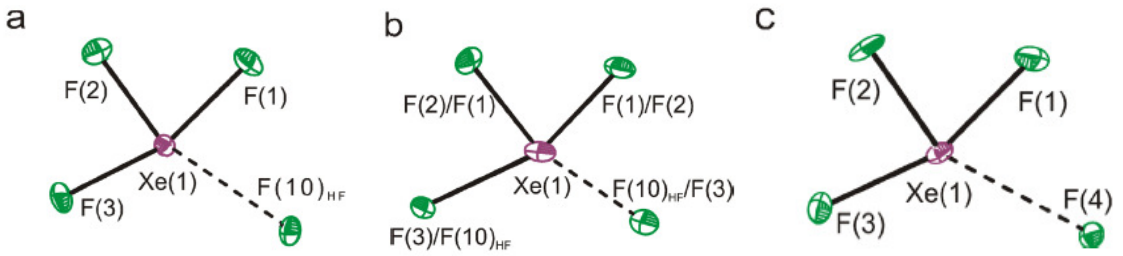

Figure 1.4. The coordination environments of the $[XeF_3]^+$ cations in the X-ray crystal structures of (a) $[H_5F_4][SbF_6]\cdot 2[XeF_3\cdot HF][Sb_2F_{11}]$, (b) $[XeF_3\cdot HF][Sb_2F_{11}]$, and (c) $[XeF_3][SbF_6]$. Thermal ellipsoids are drawn at the 50% probability level. Secondary Xe---F_b bridge bond interactions between $[XeF_3]^+$ and nearby anions and/or cocrystallized HF molecules are indicated by dashed lines. Reprinted with permission from Brock, D. S.; Mercier, H. P. A.; Schrobilgen, G. J. *J. Am. Chem. Soc.* **2013**, *135*, 5089–5104. Copyright 2013 American Chemical Society.

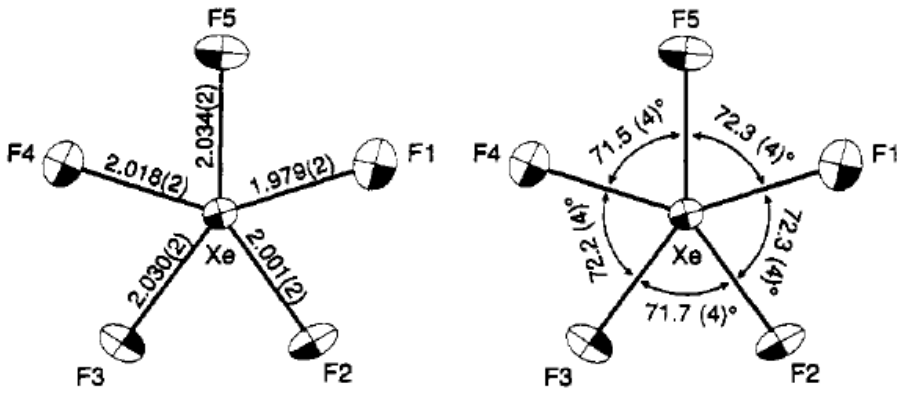

Figure 1.5. The atom numbering scheme, bond lengths (Å) and angles (deg) for $[XeF_5]^-$ at −86 °C in $[N(CH_3)_4][XeF_5]$. Thermal ellipsoids are drawn at the 50% probability level. Reprinted with permission from Reprinted with permission from Christe, K. O.; Curtis, E. C.; Dixon, D. A.; Mercier, H. P. A.; Sanders, J. C. P.; Schrobilgen, G. J. *J. Am. Chem. Soc.* **1991**, *113*, 3351–3361. Copyright 1991 American Chemical Society.

The coordination chemistry of Xe(IV) is very limited relative to that of Ng(II) (Ng = Kr, Xe). This is attributed to the low fluorobasicity of XeF_4, which is significantly less

than NgF_2 and XeF_6, i.e., $XeF_4 << KrF_2 \approx XeF_2 < XeF_6$,[20,89] The potent oxidative fluorinating strength of the $[XeF_3]^+$ cation which is the highest among xenon cations derived from the binary fluorides as determined from calculated F^+ detachment energies, i.e., $[XeF_5]^+ < [XeF]^+ < [XeF_3]^+$.[90] Presently, there is only one structurally characterized example of an XeF_4 coordination complex, $[Mg(XeF_2)(XeF_4)][AsF_6]_2$ (Figure 1.6),[91] which was formed by reaction of a 1:1:1 molar mixture of XeF_2, XeF_4, and $Mg[AsF_6]_2$ in aHF solvent at room temperature. The coordinated XeF_4 molecule is polarized by its interaction with Mg^{2+} in the crystal structure of the complex such that the primary coordination environment of Xe(IV) is intermediate with respect to XeF_4 and ion-paired salts of $[XeF_3]^+$.

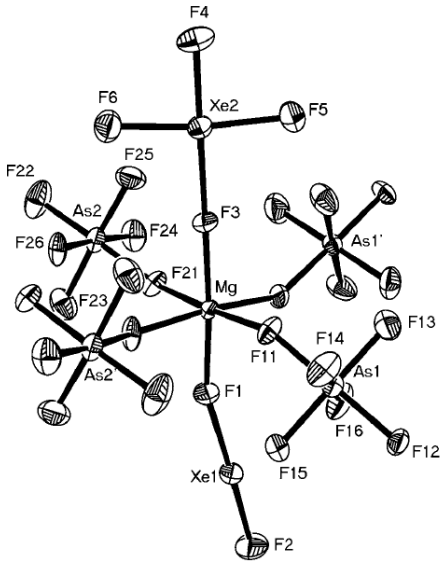

Figure 1.6. Coordination of the Mg atom in the crystal structure of $[Mg(XeF_2)(XeF_4)][AsF_6]_2$. Thermal ellipsoids are drawn at the 50% probability level. Reprinted with permission from Tavčar, G.; Žemva, B. *Angew. Chem. Int. Ed.* **2009**, *48*, 1432–1343. Copyright 2009 John Wiley and Sons.

Xenon tetrafluoride also forms two molecular addition compounds (cocrystals) that have been structurally characterized; $XeF_4 \cdot XeF_2$[70,92] and $([XeF_5][CrF_4])_4 \cdot XeF_4$,[93] where the geometric parameters of XeF_4 in their X-ray crystal structures are comparable to those of solid XeF_4. Although the oxide-fluorides and oxides of Xe(IV) have their own interesting chemistries, they are not directly related to the focus of this Thesis and are not discussed.

1.2.3. Xenon Hexafluoride

Xenon hexafluoride is prepared in high yield and purity by the reaction of Xe with 20 or more equivalents of F_2 at ca. 300 °C and pressures above 50 atm (Eq. **1.4–1.6**).[94] The oxide and oxide fluorides of Xe(VI), $XeOF_4$,[68,95] XeO_2F_2,[96] and XeO_3,[97,98] are prepared by the controlled hydrolysis of XeF_6 with stoichiometric amounts of water (Eqs **1.11–1.13**). The treacherously shock-sensitive and explosive nature of XeO_3[97] highlights the challenges associated with noble-gas chemistry, where strictly anhydrous reaction conditions are of paramount importance. Although the oxide-fluorides and oxides of Xe(VI) have their own interesting chemistries, they are not directly related to the focus of this Thesis and are not discussed in further detail. Instead, the focus is on the structure of XeF_6 and its use as a fluoride-ion donor.

$$XeF_6 + H_2O \longrightarrow XeOF_4 + 2HF \qquad (\mathbf{1.11})$$

$$XeOF_4 + H_2O \longrightarrow XeO_2F_2 + 2HF \qquad (\mathbf{1.12})$$

$$XeO_2F_2 + H_2O \longrightarrow XeO_3 + 2HF \qquad (\mathbf{1.13})$$

The structures of XeF_6 and stereo-activity of its VELP in the solid, liquid, and gas-phases have been the subject of considerable discussion over the past 50 years. The

possible geometries of monomeric gas-phase XeF_6 are an octahedral structure (O_h) with a stereo-inactive VELP or a monocapped octahedron (C_{3v}) with a stereo-active VELP. The VSEPR model of molecular geometry predicted a monocapped octahedral geometry (C_{3v}) for XeF_6 very early in the history of noble-gas chemistry.[88,99] Although seven crystal phases of XeF_6 have been characterized by LT SCXRD,[100] none of these phases contain well-isolated XeF_6 molecules that exhibit C_{3v} symmetry. Rather, five of their phases are ionic oligomers of the form $([XeF_5]^+F^-)_n$ (n = 4 (Figure 1.7), 6), and two phases are comprised of $([XeF_5]^+F^-)_3 \cdot XeF_6$ structural units that may be described as $([XeF_5]^+F^-)_3$ trimers that are coordinated to an XeF_6 molecule that exhibit local C_{2v} symmetry.

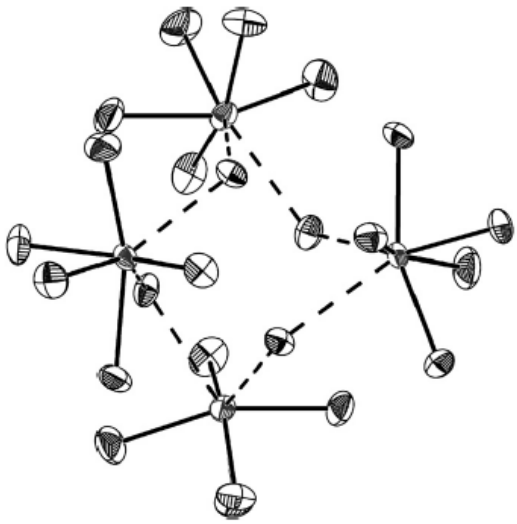

Figure 1.7. The tetrameric unit $([XeF_5]^+F^-)_4$ in the low-temperature phases of XeF_6 (*mP*16). Thermal ellipsoids are drawn at the 50% probability level. The tetrameric of phase XeF_6 (*oP*16, not shown) is very similar to the *mP*16 phase, except with poorer crystallographic resolution. Reprinted from Hoyer, S.; Emmler, T.; Seppelt, K. *J. Fluor. Chem.* **2006**, *127*, 1415–1422. Copyright 2006, with permission from Elsevier.

Recently, a joint synthetic and computational study reported the syntheses and structural characterizations of the F_6Xe---$NCCH_3$ and F_6Xe---$(NCCH_3)_2$ coordination complexes (Figure 1.8), which conclusively showed the presence of a diffuse stereochemically active VELP for XeF_6 in the solid-state.[101,102]

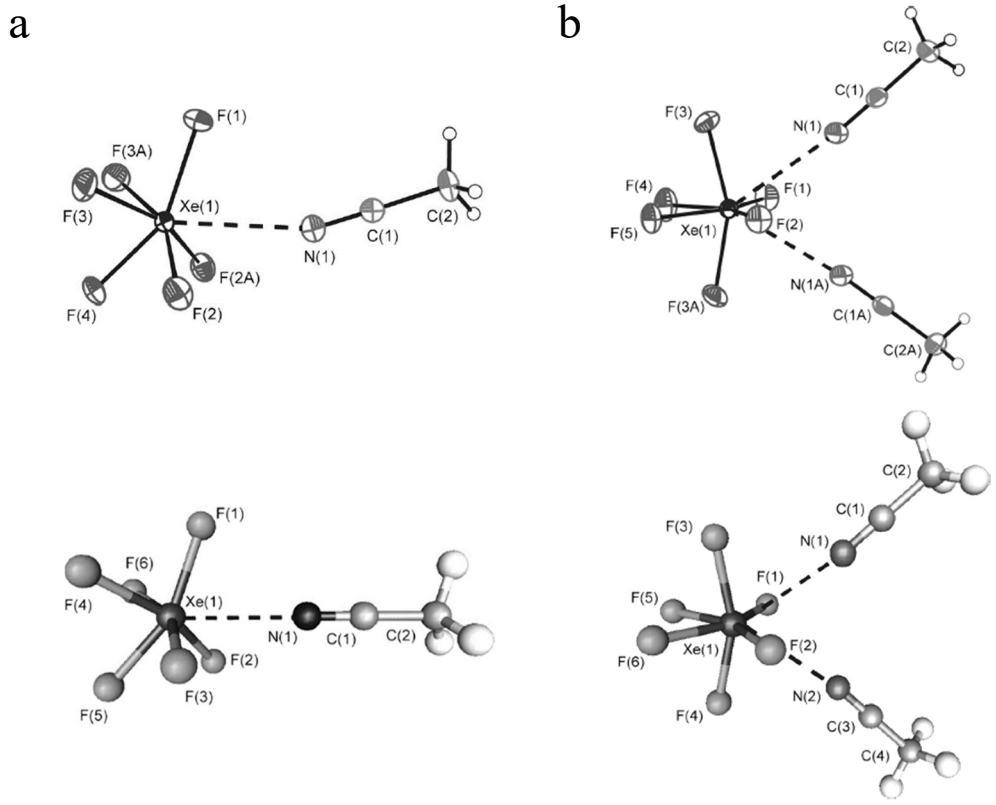

Figure 1.8. (a) X-ray crystal structure of F_6Xe---$NCCH_3$ (top). Ellipsoids are shown at the 50% probability level. The calculated geometry (PBE1PBE/aug-cc-pVTZ(-PP)) for $F_6XeNCCH_3$ (bottom) is also shown. (b) X-ray crystal structure of $F_6Xe(NCCH_3)_2 \cdot CH_3CN$. The lattice CH_3CN molecule is not shown (top). Ellipsoids are shown at the 50% probability level. The calculated geometry (PBE1PBE/aug-cc-pVTZ(-PP)) for $F_6Xe(NCCH_3)_2$ (bottom) is also shown. Reprinted from Matsumoto, K.; Haner, J.; Mercier, H. P. A.; Schrobilgen, G. J. *Angew. Chem. Int. Ed.* **2015**, *54*, 14169–14173. Copyright 2015 John Wiley and Sons.

The LT solution structure of XeF_6 has been shown by ^{19}F and ^{129}Xe NMR spectroscopy to be a fluxional tetramer, Xe_4F_{24}, in which the four Xe and 24 F atoms undergo rapid intramolecular exchange on the NMR time scale[103,104] and therefore do not provide definitive stereochemical information about the VELPs of the xenon atoms in solution. The gas-phase structure of monomeric XeF_6 has been shown by electron diffraction,[105–108] and by far-infrared,[109] Raman,[110,111] UV-visible absorption,[111] and photoelectron spectroscopies[112,113] to have C_{3v} symmetry, consistent with XeF_6 having a stereo-active VELP. Recent coupled-cluster quantum-chemical calculations indicate that the O_h and C_{3v} conformers (Figure 1.9) correspond to local minima, whereas the higher energy C_{2v} geometry is a transition state between C_{3v} conformers.[114,115]

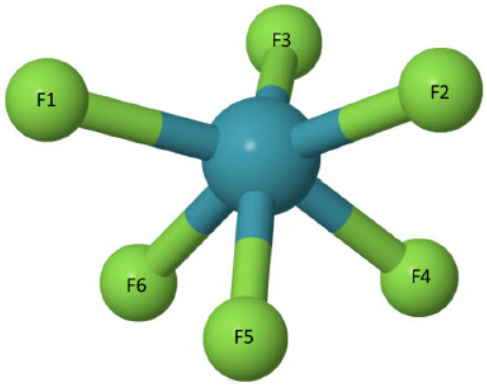

Figure 1.9. Schematic representation of the C_{3v} structure of XeF_6 optimized at the CCSD(T) level. Reprinted from Gawrilow, M.; Beckers, H.; Riedel, S.; Cheng, L. *J. Phys. Chem. (A)* **2018**, *122*, 119–129. Copyright 2018 American Chemical Society.

The ionic character implied by the solid-state and solution structures of XeF_6 are consistent with its highly fluorobasic behavior. Solutions of XeF_6, the strongest fluoride-

ion donor among the binary noble-gas fluorides, were studied as a function of concentration by Raman spectroscopy in aHF, and provided principal equilibria that describe the ionization of XeF_6 to the strong-oxidant cations, $[XeF_5]^+$ and $[Xe_2F_{11}]^+$, in aHF solvent (eqs **1.14**, **1.15**).[116]

$$([XeF_5]^+F^-)_4 + 2nHF \rightleftharpoons 2[Xe_2F_{11}]^+ + 2[(HF)_nF]^- \quad (n \geq 1) \qquad \textbf{(1.14)}$$

$$[Xe_2F_{11}]^+ + nHF \rightleftharpoons 2[XeF_5]^+ + [(HF)_nF]^- \ (n \geq 1) \qquad \textbf{(1.15)}$$

The geometry of the $[XeF_5]^+$ cation is a square-pyramidal AX_5E VSEPR arrangement (Figure 1.10), where the Xe VELP occupies the open square face of the square pyramid which, in turn, displaces the equatorial fluorine atoms towards the axial fluorine due to lone pair-bond pair repulsions between the Xe VELP domain and the $Xe{-}F_{eq}$ bond-pair domains.

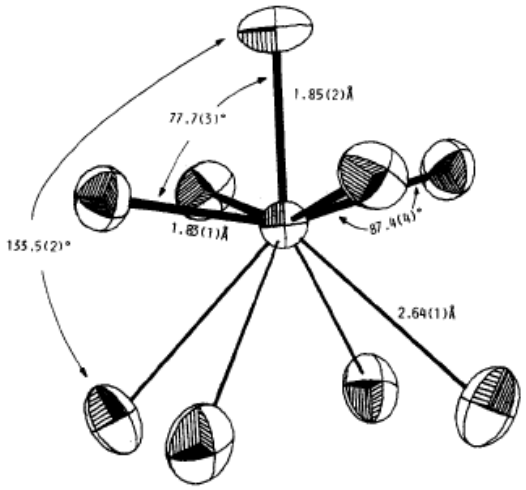

Figure 1.10. The coordination environment of the $[XeF_5]^+$ cation in $[XeF_5][AgF_4]$,[117] where thermal ellipsoids are drawn at the 50% probability level. Reprinted with permission from Lutar, K.; Jesih, A.; Leban, I.; Žemva, B.; Bartlett, N. *Inorg. Chem.* **1989**, *28*, 3467–3471. Copyright 1989 American Chemical Society.

The $[Xe_2F_{11}]^+$ cation may be described as two $[XeF_5]^+$ cations bridged by a fluoride-ion (Figure 1.11). As observed for $[XeF_5]^+$, the F_{eq} ligands of $[Xe_2F_{11}]^+$ are displaced by the Xe VELPs towards their respective F_{ax} ligands. The primarily electrostatic Xe---F secondary bonding interactions between $[XeF_5]^+/[Xe_2F_{11}]^+$ and their fluoro- and oxyfluoro-anions are directed towards regions of high positive electrostatic potential (σ-holes) on the Xe atoms of $[XeF_5]^+$ and $[Xe_2F_{11}]^+$.[73] The regions are located at the intersections of the equatorial Xe–F bond-pair domains on the base of the square-based pyramids formed by their axial and equatorial F atoms.

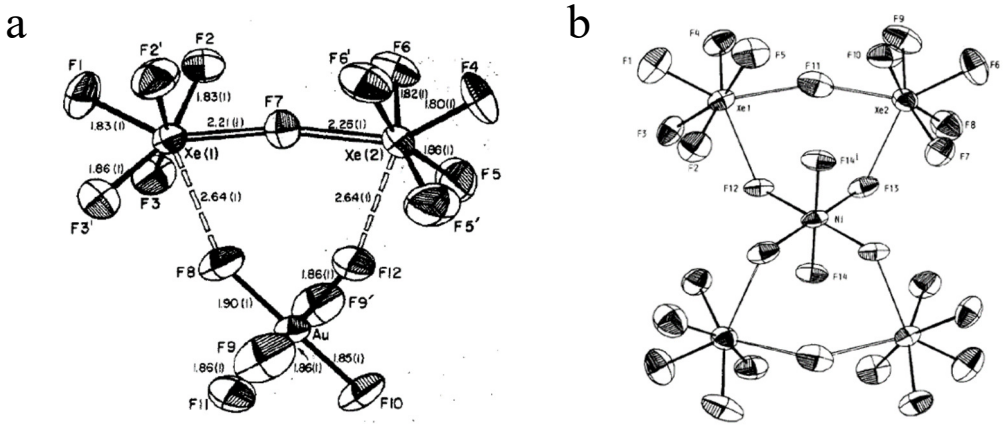

Figure 1.11. (a) The structural unit in the SCXRD structure of $[Xe_2F_{11}]_2[NiF_6]$[118] with thermal ellipsoids drawn at the 50% probability level. Reprinted with permission from Jesih, A.; Lutar, K.; Leban, I.; Žemva, B. *Inorg. Chem.* **1989**, *28*, 2911–2914. Copyright 1989 American Chemical Society. (b) The structural unit in the SCXRD structure of $[Xe_2F_{11}]_2[AuF_6]$[119] with thermal ellipsoids drawn at the 50% probability level. Reprinted with permission from Leary, K.; Zalkin, A.; Bartlett, N. *Inorg. Chem.* **1974**, *13*, 775–779. Copyright 1974 American Chemical Society.

The +6 oxidation state of xenon in the $[XeF_5]^+$ and $[Xe_2F_{11}]^+$ cations results in electronic environments that are sufficiently electron poor to enable stabilization of a variety of high-oxidation state transition-metal oxyfluoro-anions. These include the Tc(VII) and Os(VIII) oxyfluoro-anion salts $[XeF_5][TcO_2F_4]$,[120] $[XeF_5][\mu\text{-}(OsO_3F_2)_2]$, $[XeF_5][OsO_3F_3]$, and $[Xe_2F_{11}][fac\text{-}OsO_3F_3]$ (Figure 1.12).[121]

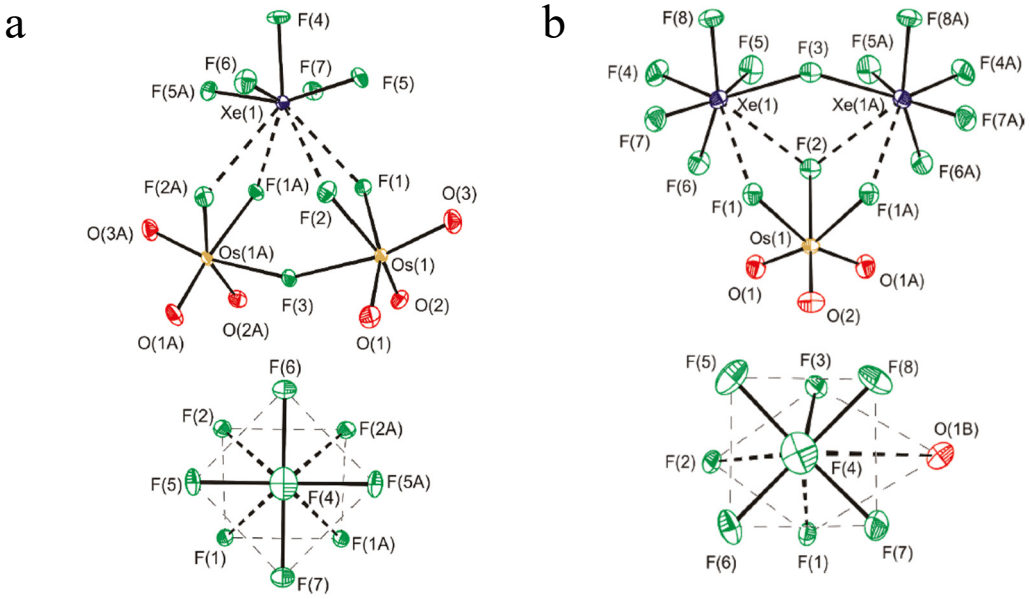

Figure 1.12. (a) The structural unit in the SCXRD structure of $[XeF_5][\mu\text{-}F(OsO_3F_2)_2]$ with thermal ellipsoids drawn at the 70% probability level (top), and (b) the primary and secondary coordination spheres of Xe(VI) in $[XeF_5]^+$ showing the four Xe---F secondary bonding interactions (bottom). (b) The structural unit in the SCXRD structure of $[Xe_2F_{11}][fac\text{-}OsO_3F_3]$ with thermal ellipsoids drawn at the 70% probability level (top), and the primary and secondary coordination spheres of Xe(VI) in the XeF_5-units of the $[Xe_2F_{11}]^+$ cation showing the Xe---F/O secondary bonding interactions (bottom).[121] Reprinted with permission from Hughes, M. J.; Mercier, H. P. A.; Schrobilgen, G. J. *Inorg. Chem.* **2010**, *49*, 3501–3515. Copyright 2010 American Chemical Society.

Purpose and Scope of the Thesis Research

The research described in this Thesis is in the field of synthetic inorganic fluorine chemistry with emphases the application of noble-gas compounds towards the syntheses and structural characterizations of fluoro- and oxyfluoro-derivatives of main-group and transition-metal (TM) elements in their highest oxidation states and at the limits of coordination. This work advances our understanding of structure and chemical bonding over a broad range of noble-gas and TM compounds which include hyper-valent species and weak covalent/electrostatic bonds that exemplify trends within the Periodic Table.

A goal of this Thesis research has been to address the absence of mixed Xe(II)/Kr(II) and Xe(IV)/Kr(II) noble-gas compounds. Chapter 3 describes a thorough synthetic, structural, and computational study of the first mixed Kr^{II}/Xe^{II} species, the $[FKrFXeF]^+$ cation (as the $[AsF_6]^-$ salt), and the first mixed Kr^{II}/Xe^{IV} compounds, obtained as the cocrystals $([Kr^{II}_2F_3][AsF_6])_2 \cdot Xe^{IV}F_4$ and $Xe^{IV}F_4 \cdot Kr^{II}F_2$. The isolation and structural characterization of mixed Kr^{II}/Xe^{II} and Kr^{II}/Xe^{IV} noble-gas compounds pose formidable synthetic challenges, and could only be isolated and structurally characterized at low temperatures under rigorously anhydrous and oxygen-free conditions owing to the propensity of KrF_2, $[KrF]^+$, and $[Kr_2F_3]^+$ to oxidize Xe^{II} to Xe^{IV} and Xe^{VI} at low temperatures. For these reasons, the study also delves into the redox reaction pathway of $[FKrFXeF]^+$ by monitoring the reaction between KrF_2 and $[XeF][AsF_6]$ and the subsequent redox decomposition of $[FKrFXeF][AsF_6]$ by means of low-temperature (LT) Raman spectroscopy. The structures of $[FKrFXeF]^+$ and the mixed Kr^{II}/Xe^{IV} and Kr^{II}/Xe^{VI} redox products and their bonding were determined by LT single-crystal X-ray

diffraction, LT Raman spectroscopy, and by quantum-chemical (QC) analyses. QC calculations were also used to assess bonding and to aid in the assignments of Raman spectra.

This Thesis also describes examples in which noble-gas fluorides have been used to significantly extend high-oxidation state main-group coordination chemistry. Chapters 4 and 5 describe advancements in the coordination chemistries of cationic X(V) (X = Cl, Br) species, which had been limited to four structurally characterized Br(V) examples; $[F_2OBr(FNgF)_2][AsF_6]$ (Ng = Kr, Xe), $[F_2OBrFXeF][AsF_6]$, and $[O_2Br(BrO_2F)_2][AsF_6]$. Utilization of the known ligand behavior of XeF_2, the syntheses and structural characterizations of the first coordination complexes between the $[XO_2]^+$ cations and XeF_2 has significantly advanced the coordination chemistry of X(V) (X = Cl, Br) cations and has provided further examples of noble-gas difluorides coordinated to strong oxidant main-group Lewis acid centers. The studies also provided insight into the nature of secondary X(V)---FXeF bonds.

A further expansion of main-group fluoride chemistry is provided in Chapter 6, which describes the application of the neutral chlorine fluorides ClF_3 and ClF_5 as oxidative fluorinating and O/F metathesis reagents in their reactions with IrO_2. The main objective of the study was to prepare novel iridium oxyfluoro compounds. This work resulted in the syntheses of the first iridium oxyfluoro-anion, $[cyclo\text{-}(\mu\text{-}OIrF_4)_3]^{2-}$, as the $[ClO_2]^+$ salt, and the first neutral Ir(V) coordination complex, F_5Ir---OClF. The syntheses and structural characterizations of these compounds by SCXRD has significantly advanced TM oxyfluoride and fluoride chemistry and represents a breakthrough in

fundamental noble-metal chemistry, in addition to providing the first direct evidence for the formation of highly unstable OClF in the reaction of ClF_3 with a metal fluoride.

Another focus of this Thesis has been to exploit the chemistries of the binary noble-gas fluorides to develop high-oxidation-state Group 6 TM oxyfluoride chemistry (Chapters 7–11). The Group 6 oxide tetrafluorides, MOF_4 (M = Cr, Mo, W), are intermediate-strength fluoride-ion acceptors that had been previously shown to form complexes with the noble-gas difluorides, NgF_2 (Ng = Kr, Xe), having the general formulae $NgF_2 \cdot nMOF_4$ (n = 1, 2). At the outset of this Thesis research, $FKrF_b$---WOF_4, and $FKrF_b$---MOF_3F_b'---MOF_4' (M = Mo, W) had not been characterized by X-ray diffraction because these complexes rapidly decompose prior to crystallization. Chapter 7 describes the syntheses of $FXeF_b$---$CrOF_4$, $FKrF_b$---WOF_4, and the [--$(F_4OMo)(\mu_3$-F)H---(μ-F)H--]$_\infty$ solvate in aHF solvent and their structural characterizations. Accompanying quantum-chemical calculations provide a detailed description of the nature of the M---F_b bonds in the $FNgF_b$---MOF_4 and $FNgF_b$---MOF_3F_b'---MOF_4' adduct series.

In a related study (Chapter 8), the first TM adduct of XeF_4, F_3XeF_b---WOF_4, was synthesized and structurally characterized by LT SCXRD and Raman spectroscopy. The study represents a significant development in XeF_4 coordination chemistry, which had been previously limited to one structurally characterized example, $[Mg(XeF_2)(XeF_4)][AsF_6]_2$, and includes detailed QC calculations that describe the nature of the bonding in F_3XeF_b---WOF_4.

The reactions of MOF_4 (M = Cr, Mo, W) with XeF_6 were also studied and are described in Chapters 9–11 – the objective was to synthesize high-oxidation state Group 6

oxyfluoro-anion salts of $[XeF_5]^+$ and/or $[Xe_2F_{11}]^+$. The room-temperature reaction of XeF_6 and $CrOF_4$ in aHF and $CFCl_3$ (Chapter 9) led to reductive elimination of F_2 along with the novel formations of the Cr(V) oxyfluoro-anion salts, $[XeF_5]_2[Cr_2O_2F_8]\cdot 2XeOF_4$ and $[XeF_5]_2[Cr_2O_2F_8]\cdot 2HF$. The reaction of CrO_2F_2 and XeF_6 gave $[XeF_5][Cr_2O_4F_6]$, $[XeF_5][Cr_2O_4F_6]\cdot 4HF$, $[XeF_5][Cr_2O_4F_6]\cdot 2XeOF_4$, and $[XeF_5][Xe_2F_{11}][CrO_2F_4]$, which provided the first structural characterizations of a dinuclear Cr(VI) oxyfluoro-anion, $[Cr_2O_4F_6]^{2-}$, and of $[CrO_2F_4]^{2-}$ (Chapter 10). In contrast with NgF_2 and XeF_4, reactions of MOF_4 (M = Mo, W) with XeF_6 in aHF solvent yielded oxyfluoro-anion salts, i.e., $[XeF_5][M_2O_2F_9]$ and $[Xe_2F_{11}][MOF_5]$ (Chapter 11). The low-temperature (LT) reaction of XeF_6 and $CrOF_4$ in aHF yielded $[XeF_5][HF_2]\cdot CrOF_4$, which demonstrated that $CrOF_4$ is too weak of a Lewis acid to abstract fluoride-ion from $[HF_2]^-$ at LT in aHF. To circumvent $[HF_2]^-$ formation, $[Xe_2F_{11}][CrOF_5]$ was synthesized in Freon-114, which provided the first X-ray crystal structure of $[CrOF_5]^-$.

CHAPTER 2

EXPERIMENTAL SECTION

2.1. Standard Techniques

Cautionary Statement. *Anhydrous HF (aHF) must be handled using appropriate protective gear with ready access to proper treatment procedures*[122–124] *in the event of contact with the liquid, vapor, solutions, and HF formed by the hydrolysis of the moisture-sensitive compounds encountered in this study. The noble-gas fluorides are potent oxidative fluorinators and highly energetic materials that are generally only stable under the rigorously anhydrous conditions. They react vigorously or may detonate upon hydrolysis or contact with organic materials. Furthermore, the hydrolyses of Xe(VI) compounds may form* XeO_3*, a highly endothermic, shock-sensitive detonator when dry, and highly toxic HF. The syntheses of noble-gas compounds are therefore generally restricted to small amounts (<100 mg) and their syntheses and other manipulations are most often carried out in FEP (perfluoroethylene/perfluoropropylene copolymer) vessels to avoid sharp fragments in the event of a detonation. The use of adequate protective apparel and shielding are crucial for the safe handling of all these compounds. The utmost precautions must be taken when disposing of these materials and their derivatives.*

2.1.1. Drybox and Vacuum Line Techniques

The compounds used and prepared in this work are moisture- and temperature-sensitive and were handled under rigorously anhydrous conditions on glass and metal vacuum line systems or in the nitrogen atmosphere of a dry box (Vacuum Atmospheres Model DLX, oxygen and moisture <0.1 ppm) equipped with a glass cryowell. Low-

temperature additions of potentially reactive solids were carried out in the dry box by use of a metal Dewar filled with 4.5 mm copper plated steel spheres (air rifle shot) that had been previously cooled to ca. –140 °C in the glass cryowell (–196 °C) of the dry box.

Transfers of volatile corrosive compounds and aggressively fluorinating solvents (e.g., HF and AsF_5) were carried out on metal vacuum lines constructed mainly from nickel and 316 stainless steel and fitted with 316 stainless steel valves (Autoclave Engineers Inc., Figure 2.1),[125] which were themselves fitted with grease-free PTFE packings. Pressures were measured at ambient temperatures using MKS Model PDR-5B pressure transducers having inert wetted surfaces constructed of Inconel. The dynamic range of the pressure transducers was 0 – 1150 torr with an accuracy of ±0.5 torr over the entire pressure range. Two Edwards two-stage E2M8 direct-drive vacuum pumps functioned as a rough pump and as a high vacuum pump. The rough pump was primarily used to remove volatile fluoride compounds by pumping through a fluoride/fluorine trap consisting of a stainless-steel column packed with a soda lime absorbent (Fisher Scientific, 4-8 mesh), followed by a glass liquid nitrogen trap to remove any CO_2, water and other volatile products generated in the soda lime trap. The second vacuum pump provided a high vacuum source (ca. 10^{-4} torr) and was fitted with a glass liquid nitrogen trap and copper column, immediately before the pump, packed with activated charcoal (Norit)

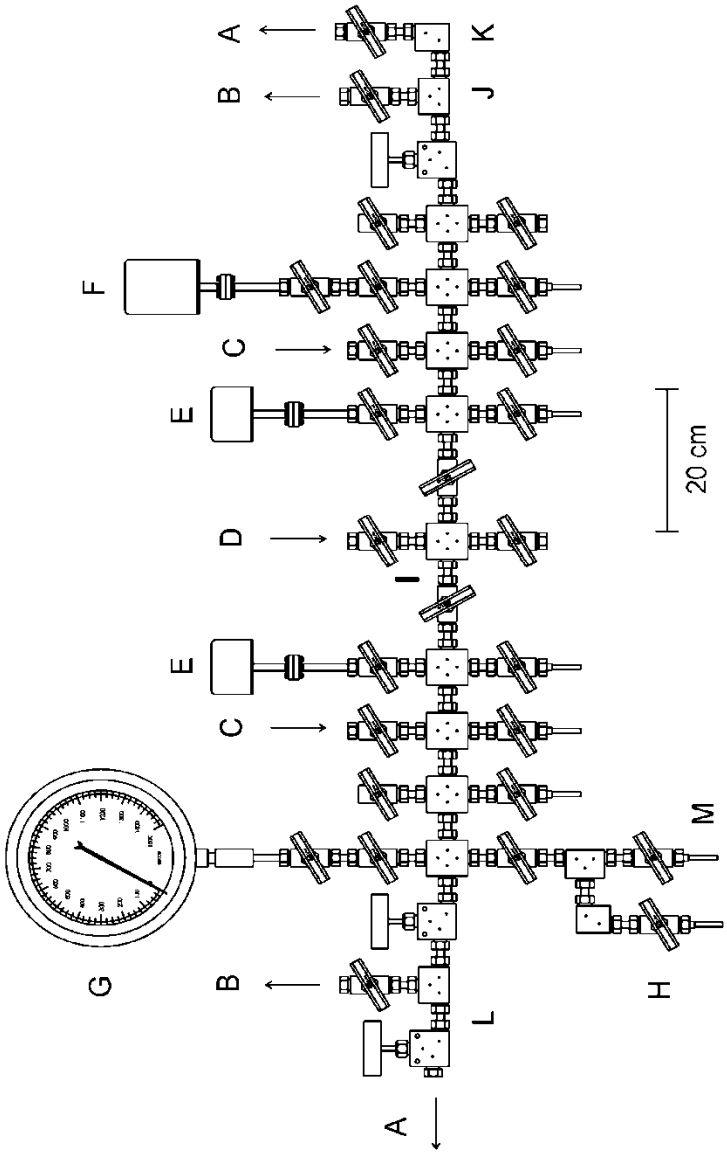

Figure 2.1. Schematic Diagram of the Metal Vacuum Line System: (A) outlet to liquid nitrogen and charcoal (Norit) traps followed by a two-stage direct-drive rotary vacuum pump (Edwards, E2M8) – hard vacuum, (B) outlet to soda lime and liquid nitrogen traps followed by a two-stage direct-drive rotary vacuum pump (Edwards, E2M8) – rough vacuum, (C) dry nitrogen inlet, (D) fluorine inlet, (E) MKS Model PDR-5B pressure transducer (0 –1000 torr), (F) MKS Model PDR-5B pressure transducer (0 – 10 torr), (G) Bourdon pressure gauge (0 – 1500 torr), (H) $^{3}/_{8}$-in. 316 stainless steel high pressure valve (Autoclave Engineers, 30BM6071), (I) 316 stainless steel cross, (J) 316 stainless steel T-piece, (K) 316 stainless steel L-piece, (L) nickel connectors, (M) ¼-in. o.d., $^{1}/_{8}$-in. i.d. nickel tube, (N) hot-wire reactor connection. Reproduced with permission from Leblond, N. Ph. D. Thesis, McMaster University, Hamilton, Canada, **1998**.

Transfers of volatile compounds that did not attack glass were carried out on Pyrex glass vacuum lines (Figure 2.2) equipped with grease-free 6-mm J. Young glass stopcocks which were fitted with PTFE barrels. Vacuum (ca. 10^{-4} torr) was achieved using a single vacuum pump (Edwards two-stage E2M8 direct-drive) connected through a glass liquid nitrogen trap. Pressures inside the glass vacuum lines were monitored using a mercury manometer when backfilling reaction vessels.

2.1.2. Preparative Apparatus and Sample Vessels

All synthetic work was carried out in reactors constructed from lengths of ¼-in. o.d. FEP tubing which were heat-sealed at one end and heat-flared (45° SAE) at the other. The tubing was connected to Kel-F valves, encased in aluminum housings, using brass flare fittings. All vessels were then connected to a glass vacuum line using ¼-in. stainless steel Swagelok Ultra-torr unions fitted with Viton O-rings and were rigorously dried by pumping (a minimum of 6 h) under dynamic vacuum. Vessels were then connected to the metal vacuum line using Swagelok Ultra-torr unions and passivated with ca. 1000 torr of F_2 for ca. 12 h. Once passivated, vessels were evacuated under dynamic vacuum to remove all volatile impurities and back-filled with dry N_2 (ca. 1000 torr) prior to use. Similarly, connections made to a metal vacuum line were dried under dynamic vacuum and passivated with F_2 gas overnight. Connections made to a glass vacuum line were dried under dynamic vacuum overnight. Glass vessels used to handle less corrosive materials were dried under dynamic vacuum for a minimum of 8 hr and were periodically heated (flamed out) with a Bunsen burner while under vacuum.

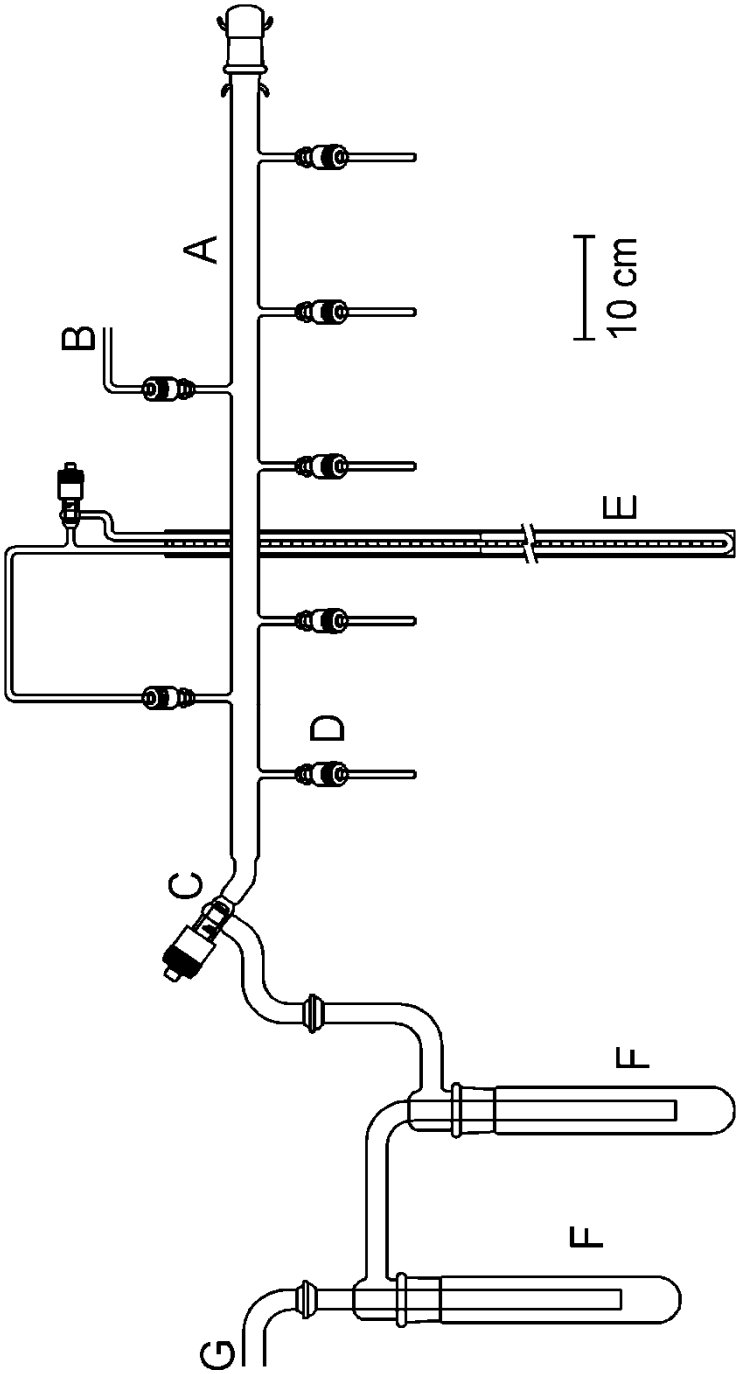

Figure 2.2. Glass vacuum line used for the manipulation of non-corrosive volatile materials. (A) Main vacuum manifold. (B) Dry N_2 inlet. (C) 15-mm greaseless J. Young valve with PTFE barrel. (D) 6-mm greaseless J. Young valve with PTFE barrel. (E) Mercury manometer. (F) Liquid N_2 cold traps. (G) Outlet to vacuum pump. Reproduced with permission from Leblond, N. Ph. D. Thesis, McMaster University, Hamilton, Canada, **1998**.

Low-temperature Raman spectra of solids (ca. −140 to −150 °C) were recorded on samples prepared in thin-walled ¼-in. o.d. FEP tubing.

All connections to vacuum lines were made using thick-walled ¼-in. o.d. $^{3}/_{16}$-in i.d. FEP tubing in conjunction with ¼-in. stainless steel Swagelock Ultra-torr connectors outfitted with stainless steel compression fittings and Viton rubber O-rings.

2.2. Synthesis and Purification of Starting Materials

2.2.1. Sources and Purification of Gases: N_2, Ar, F_2, Xe, and Kr

House nitrogen gas was generated by boiling off liquid nitrogen (Air Liquide) and was further dried through a freshly regenerated bed of type 4 Å molecular sieves. High-purity nitrogen gas (Praxair, 99.999%) and argon gas (VitalAire, 99.999%) were also employed for the back pressuring of reaction vessels and were used without further purification. Technical grade fluorine gas (Air Products, >98 %) and ultra-high purity Xe (Air Products, 99.995%) and Kr (Air Products, 99.995%) were used without further purification.

2.2.2. Purification of Solvents: Anhydrous HF, $CFCl_3$ (Freon-11), CF_2ClCF_2Cl (Freon-114)

HF. Commercial anhydrous hydrogen fluoride (Harshaw Chemical Co.) was purified by addition of ca. 5 atm of F_2 gas to a commercial HF sample contained in a nickel can that was allowed to stand for a minimum of ca. 48 h prior to use, converting residual water to HF and O_2. The reactor was subsequently cooled to −196 °C and all volatiles, such as O_2 and F_2, were removed under dynamic vacuum. Alternatively, aHF was dried over K_2NiF_6 in a 3/4 in. o.d. FEP vessel outfitted with Kel-F valve. After drying, the vessel was cooled

to −196 °C and placed under dynamic vacuum to remove any non-condensable gases (O_2 and F_2). Anhydrous HF (aHF) was then distilled into a dry Kel-F storage vessel equipped with a Kel-F valve and stored at room temperature for future use. Transfer of aHF was accomplished by vacuum distillation from the Kel-F storage vessel, on a metal vacuum line, through a vacuum submanifold constructed from FEP, as shown in Figure 2.3.

Freon-114 (CF_2ClCF_2Cl, Matheson) and Freon-11 ($CFCl_3$, Matheson) were dried over P_4O_{10} for several days and distilled into 175-mL glass dispensing vessels outfitted with grease-free 6-mm J. Young glass/Teflon stopcocks for storage. Small quantities (ca. 0.5 mL) were transferred under static vacuum on a glass vacuum line through a glass submanifold into individual reaction vessels.

2.2.3. Syntheses and Purification of Reagents

AsF_3. Arsenic trifluoride was prepared according to the literature method.[126]

AsF_5. Arsenic pentafluoride was prepared as previously described[127,128] by direct fluorination of AsF_3 with purified F_2 in a nickel can. The AsF_5 was used from the reaction can without further purification.

SbF_3. Antimony trifluoride (Aldrich, 98%) was purified by sublimation at ca. 350–400 °C under dynamic vacuum. The SbF_3 was then transferred to the dry box and stored in a ¼ in. o.d. FEP storage vessel fitted with a Kel-F valve until used.

SbF_5. Antimony pentafluoride was prepared *in situ* by direct fluorination of SbF_3 with F_2 in aHF as previously described.[129]

IrO_2. Iridium dioxide powder was obtained from abcr (99% purity).

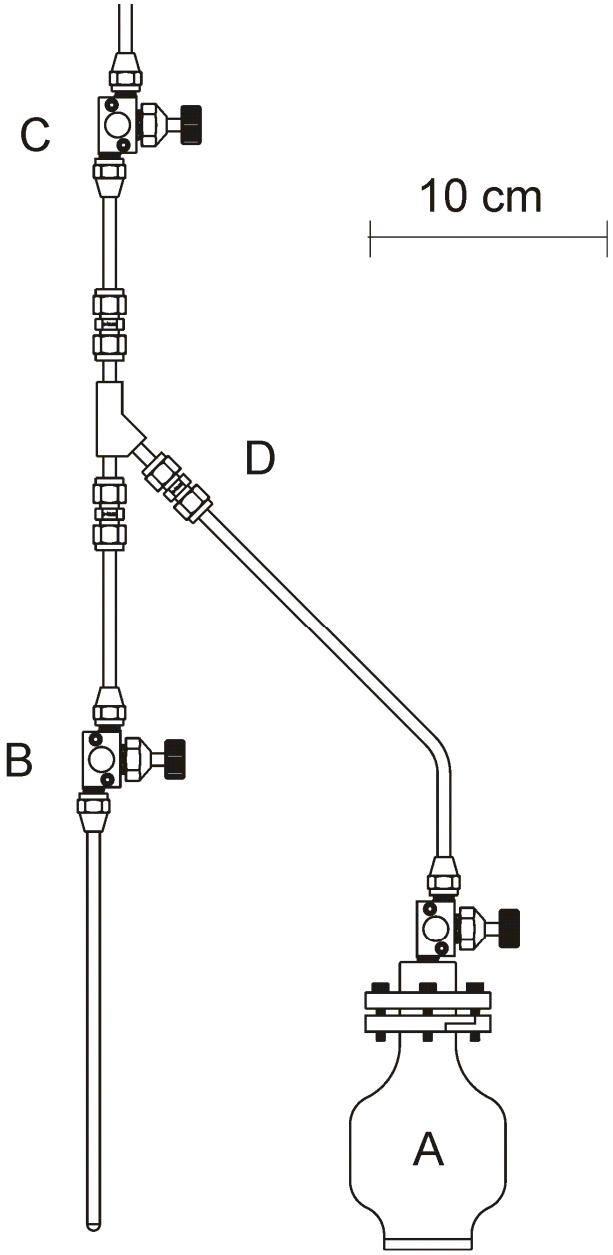

Figure 2.3. Hydrogen fluoride distillation apparatus. (A) Kel-F storage vessel containing HF. (B) FEP reaction vessel fitted with a Kel-F valve. (C) Kel-F valve connected to vacuum manifold. (D) ¼-in. Teflon union. Reproduced with permission from Leblond, N. Ph. D. Thesis, McMaster University, Hamilton, Canada, **1998**.

ClF_3. Chlorine trifluoride was synthesized using a modification of the literature method described by Brauer.[130] The nickel reaction vessel was first passivated by synthesizing a small amount of ClF_3 and allowing it to stand overnight in the reactor, followed by removal of Cl_2 and unreacted ClF_3 under vacuum. Chlorine trifluoride was synthesized by condensing 108 mmol of Cl_2 and 340 mmol of F_2 into a 1.377-liter nickel reaction vessel and heating it to 240–260 °C for 24 h. Excess F_2 was removed at −196 °C, and ClF_3 was transferred into a smaller nickel storage vessel. The LT Raman spectrum of an aliquot of colorless ClF_3 in an FEP sample tube showed bands only assigned to ClF_3.

ClF_5 and BrF_5. Spectroscopically pure ClF_5 (Raman spectroscopy) was obtained in a stainless-steel cylinder from Prof. K. O. Christe (University of Southern California) and was used without further purification. Bromine pentafluoride (Ozark-Mahoning Co) was purified in an FEP vessel equipped with a Kel-F valve and loaded with 20 g of KF (to complex HF as $K[HF_2 \cdot nHF]$. Bromine and BrF_3 impurities were eliminated by directly fluorinating them to BrF_5 at ambient temperature as previously described.[131] The product was stored in the purification vessel under 1000 torr of a 1:1 mixture of N_2 (or Ar) and F_2 at −78 °C until transferred under dynamic vacuum for use.

XeF_2, XeF_4, and XeF_6. Xenon difluoride[127] and XeF_4[132] were prepared according to the literature methods and stored in a Kel-F tube inside a dry box until needed. Xenon hexafluoride was prepared by the reaction of Xe and F_2 similar to the method described by Malm and Chernick.[133]

KrF_2. Krypton difluoride was prepared by use of a 316-stainless steel hot-wire reactor (Figure 2.4) equipped with a nickel filament, similar to that originally described[134] and

subsequently modified.[45] The filament was fabricated from a 1/16-in. diameter nickel wire tightly wound about a second length of 1/16-in. nickel wire that was, in turn, coiled and stretched into a helix. The hot-wire reactor was pressurized with ca. 1000 torr (50 mmol) of krypton and then cooled to –196 °C in a 20-L Dewar. After reaching thermal equilibrium, the reactor was pressurized with 25 torr of F_2 and the DC power supply for the nickel filament was adjusted to ca. 6 V and 30 A (the filament was dull red in color under these conditions). The F_2 pressure increased to ca. 45 torr after the power supply was turned on and was regulated between 25 and 45 torr by the periodic addition of F_2 during the synthesis. The decreasing F_2 pressure was used to qualitatively monitor the production of KrF_2, and additional aliquots of Kr (1.0 to 2.0 mmol) were condensed into the reactor when the rate of KrF_2 production slowed. Upon completion of the reaction (*ca.* 14 h), excess F_2 was removed under dynamic vacuum at –196 °C. The excess Kr and crude KrF_2 were recovered as a colorless solid by rapidly warming the reactor with compressed air to room temperature while dynamically pumping the volatile contents through a ½-in. o.d. FEP U-trap (–196 °C). The Kr/KrF_2 mixture was then warmed to –78 °C under dynamic vacuum to remove the unreacted Kr. The remaining colorless KrF_2 was finally warmed to room temperature and rapidly sublimed into a 3/8-in. o.d. FEP tube equipped with a Kel-F valve, where it was stored under 1000 torr of N_2 at –78 °C until used. The yield was ca. 5 g of pure KrF_2.

CrO_2F_2 and $MoOF_4$. Chromyl fluoride (CrO_2F_2) and $MoOF_4$ were synthesized by reaction of CrO_3 with MoF_6 according to the published procedure.[135]

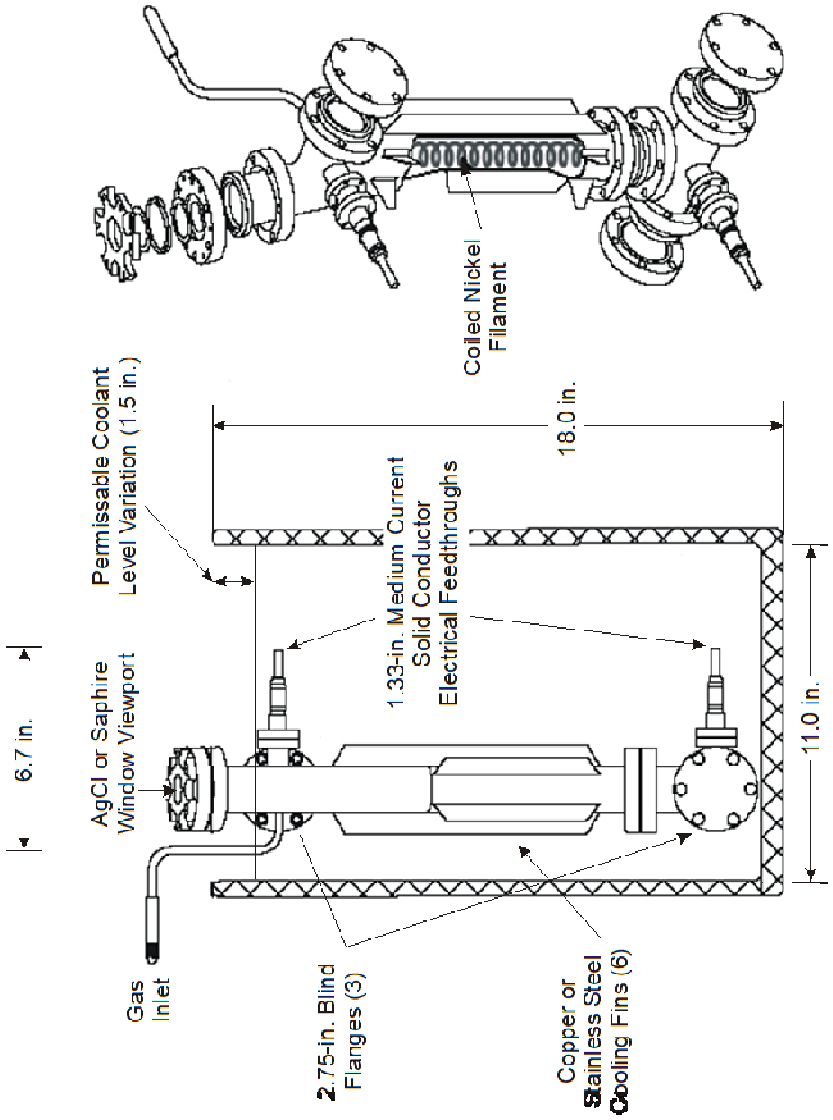

Figure 2.4. The stainless steel hot-wire reactor used for the preparation of KrF_2. (a) An external view and dimensions of a hot-wire reactor submerged in a liquid nitrogen coolant bath. (b) A perspective drawing of the hot-wire reactor showing the flange assembly and nickel filament (cut away region). Reproduced with permission from Gerken, M. Ph. D. Thesis, McMaster University, Hamilton, Canada, **2000**.

$CrOF_4$. Chromium oxide tetrafluoride was synthesized by the reaction of KrF_2 and $CrOF_4$ in aHF using a modification[65] of a previously published procedure.[66]

WOF_4. Tungsten oxide tetrafluoride was synthesized as previously described.[136]

ClO_2F. Chloryl fluoride (ClO_2F) was prepared by the literature method.[137] Prior to transfer, pale yellow ClO_2F was decolorized by direct fluorination of the Cl_2 contaminant by addition of a mixture of ~400 torr F_2 and ~500 torr N_2 to the sample at −196 °C, followed by warming with agitation to −78 °C. Oxidative fluorination of Cl_2 contaminant to ClF_3 and/or ClF_5 prevented partial reduction of XeF_2. The purity of ClO_2F was confirmed by recording a LT Raman spectrum, which was in good agreement with the literature and showed no bands attributable to Cl_2, ClF_3, or ClF_5.[138]

BrO_2F. Bromyl fluoride (BrO_2F) was synthesized using a modification of a published literature procedure.[139] Sodium bromate (31.4 mg, 0.208 mmol) was weighed into an FEP reaction vessel and dried for 24 h under dynamic vacuum. Approximately 0.3 mL of aHF was condensed into the reactor under static vacuum at −196 °C. The sample was warmed to −20 °C with agitation to effect dissolution and cooled to −196 °C whereupon ca. 0.1 mL of BrF_5 was condensed into the reaction vessel under static vacuum. The sample was slowly warmed to −78 °C, whereupon the aHF liquified and a vigorous reaction was observed which yielded a light orange precipitate. The Raman spectrum (−150 °C) of this precipitate was recorded under frozen aHF which revealed a mixture of BrO_2F and unreacted BrF_5. Additional $NaBrO_3$ (20.5 mg, 0.136 mmol) was dried and added at LT (ca. −150 °C) to the vessel in the dry box. The sample was reacted as previously described. Excess BrF_5 and the aHF solvent were then removed under dynamic vacuum at

−40 °C, whereupon the light orange precipitate became white. Pure BrO_2F (assessed by LT Raman spectroscopy) was then transferred under static vacuum at −10 to 30 °C into an empty FEP reaction vessel at −196 °C. A LT Raman spectrum of pure BrO_2F was collected and compared with its previously reported spectra.[139] The sample was then stored under ca. 1000 torr of Ar at −78 °C until needed.

2.3. Syntheses and Characterizations of the Mixed Noble-Gas Compounds, $[FKr^{II}FXe^{II}F][AsF_6]\cdot 0.5Kr^{II}F_2\cdot 2HF$, $([Kr^{II}_2F_3][AsF_6])_2\cdot Xe^{IV}F_4$, and $Xe^{IV}F_4\cdot Kr^{II}F_2$

The salt, $[XeF][AsF_6]$, was synthesized in aHF by reaction of XeF_2 with a stoichiometric excess of AsF_5 according to the literature method[48] and was stored in a dry box at room temperature in a ¼-in. o.d. FEP vessel until used.

Samples for a Variable-temperature Raman Spectroscopic Study of the Redox Decomposition of $[FKrFXeF][AsF_6]\cdot 0.5KrF_2\cdot 2HF$. Two samples containing $[XeF][AsF_6]$ and KrF_2 in aHF were prepared as previously described using the following quantities of reagents: (a) $[XeF][AsF_6]$, 18.23 mg, 0.054 mmol; KrF_2, 31.4 mg, 0.258 mmol, (b) $[XeF][AsF_6]$, 17.4 mg, 0.051 mmol; KrF_2, 35.3 mg, 0.290 mmol. Samples (a) and (b) were then warmed, in stages and for varying periods of time, from –78 to 0 °C and from –65 to 22 °C, respectively. Product distributions were periodically monitored by LT Raman spectroscopy as described in the discussion of the variable-temperature Raman spectroscopic studies in the Results and Discussion; Syntheses and Reactivities and in Tables A1.1 and A1.2 of Appendix 1.

Sample for the Raman Spectrum of ($[Kr_2F_3][AsF_6])_2 \cdot XeF_4$ (2). A sample containing 11.8 mg (0.035 mmol) $[XeF][AsF_6]$ and 24.4 mg (0.200 mmol) KrF_2 in aHF was prepared as previously described and warmed from –78 to 0 °C in stages over ca. 30 min. The sample was cooled to –196 °C and subsequently warmed to –78 °C, whereupon white solids precipitated from solution. The LT Raman spectrum (Figure A1.13) of the solid mixture was recorded under frozen aHF at –150 °C and was shown to be primarily $([Kr_2F_3][AsF_6])_2 \cdot XeF_4$ with minor amounts of $[FKrFXeF][AsF_6] \cdot 0.5KrF_2 \cdot 2HF$, $XeF_4 \cdot KrF_2$, and XeF_4.

2.3.1. Syntheses and Crystal Growth

2.3.1.1. $[FKrFXeF][AsF_6] \cdot 0.5KrF_2 \cdot 2HF$ (1). Inside a dry box, 35.6 mg (0.105 mmol) of $[XeF][AsF_6]$ was added to a ¼-in. o.d. h-shaped FEP reaction vessel equipped with a Kel-F valve. Approximately 0.5 mL of aHF and 22.8 mg (0.187 mmol) of KrF_2 was then condensed into the reaction vessel under static vacuum at –196 °C through an FEP submanifold attached to a metal vacuum line. The reaction vessel was backfilled with 1000 torr of Ar and the sample was warmed in stages from –78 to –45 °C, whereupon all $[XeF][AsF_6]$ and KrF_2 dissolved to give a colorless solution. The sample was maintained at –45 °C for ca. 1 h before it was quenched at –196 °C and subsequently warmed to –78 °C, whereupon a fine white precipitate deposited from the solution. The LT Raman spectrum of the solid was recorded under frozen aHF at –150 °C and was shown to be primarily $[FKrFXeF][AsF_6] \cdot 0.5KrF_2 \cdot 2HF$ (**1**), with minor amounts of $[Kr_2F_3][AsF_6]$ and $XeF_4 \cdot KrF_2$ (**4**) formed from the redox decomposition of **1**. The sample was warmed from –150 to –45 °C with agitation to effect dissolution, and colorless, block-shaped crystals of

1 were grown by slow cooling of the reaction vessel from –45 to –78 °C over ca. 6 h. The crystals were isolated by decanting the aHF supernatant at –78 °C into the side arm of the FEP reaction vessel, which was subsequently cooled to –196 °C and heat-sealed off under dynamic vacuum. Residual aHF was removed from the crystalline sample under dynamic vacuum at –78 °C. All subsequent crystalline samples were isolated in a similar manner. A single crystal of **1** having the dimensions 0.078 x 0.098 x 0.300 mm^3 was selected and mounted (vide infra*)* for a LT SCXRD determination.

2.3.1.2. $([Kr_2F_3][AsF_6])_2 \cdot XeF_4$ (2). Inside a dry box, 30.68 mg (0.09045 mmol) of $[XeF][AsF_6]$ was loaded into a ¼-in. o.d. h-shaped FEP reaction vessel equipped with a Kel-F valve. Approximately 0.5 mL of aHF and 35.6 mg (0.292 mmol) of KrF_2 were condensed into the reaction vessel under static vacuum at –196 °C. The reaction vessel was backfilled with 1000 torr of N_2 at –196 °C and warmed to –78 °C, whereupon the aHF melted. The reaction mixture was then warmed to –40 °C for ca. 10 min with agitation to effect dissolution. The sample was slowly cooled to –50 °C over ca. 2 h, during which time colorless, block-shaped crystals of **1** grew. Slow gas evolution was also observed during crystal growth. Slow cooling of the reaction vessel from –50 to –60 °C over ca. 1 h resulted in a second crystal growth which yielded colorless, plate-shaped crystals of $([Kr_2F_3][AsF_6])_2 \cdot XeF_4$ (**2**). A single crystal of **2** having the dimensions 0.042 x 0.216 x 0.931 mm^3 was selected and mounted (vide infra) for a LT SCXRD determination.

2.3.1.3. $[Xe_2F_3][SbF_6]$ (3). In a typical synthesis, 170.84 mg (1.009 mmol) of XeF_2 was added to an aHF/SbF_5 (0.518 mmol SbF_5) mixture at –150 °C inside a dry box. The

reactor was then warmed to 0 °C with agitation to effect dissolution. Slow cooling of the sample from –39 °C to –42 °C over 4 h yielded pale yellow, block-shaped crystals of $[Xe_2F_3][SbF_6]$. A single crystal of **3** having the dimensions 0.079 x 0.085 x 0.380 mm^3 was selected and mounted (vide infra) for a LT SCXRD determination.

2.3.1.4. $XeF_4 \cdot NgF_2$ (Ng = Kr (4), Xe (5)) and XeF_4 (6). Crystalline XeF_4 (26.21 mg, 0.1264 mmol (Kr); 42.82 mg, 0.2066 mmol (Xe)) was transferred inside a dry box into ¼-in. o.d. FEP reaction vessels outfitted with Kel-F valves. Approximately 0.5 mL $CFCl_3$ solvent was condensed into each reaction vessel under static vacuum on a glass vacuum line at –196 °C. The samples were warmed to room temperature for ca. 5 min with agitation, whereupon approximately half of the crystalline XeF_4 dissolved. Because crystalline XeF_4 is partially soluble in $CFCl_3$ at room-temperature, the samples were rapidly quenched to –196 °C and warmed to –78 °C to precipitate powdered XeF_4. After two further warming/quenching cycles, all crystalline XeF_4 was converted to a white powder. In the case of $XeF_4 \cdot KrF_2$, 37.7 mg (0.310) mmol) of KrF_2 was condensed into the reactor under static vacuum at –196 °C through an FEP submanifold that was attached to a metal vacuum line. In the case of $XeF_4 \cdot XeF_2$, powdered XeF_4 under frozen $CFCl_3$ was transferred into a dry box and maintained at −150 °C[140] while XeF_2 (29.52 mg, 0.174 mmol) was added to the reaction vessel. The samples were then slowly warmed to 22 °C to effect dissolution. Gentle bubbling was observed for the XeF_4/KrF_2 sample at this temperature and the solvent became pale yellow in color, indicating some oxidative fluorination of $CFCl_3$ with the liberation of Kr and Cl_2 gas had occurred. Slow cooling of the reaction vessels from 22 to 10 °C (Xe) and 0 °C (Kr) over ca. 30 min led to the

formation of colorless, plate-shaped crystals of $XeF_4 \cdot KrF_2$ (**4**) and $XeF_4 \cdot XeF_2$ (**5**), and colorless, block-shaped crystals of XeF_4 (**6**). Single crystals of **4**, **5**, and **6** having the dimensions 0.016 x 0.028 x 0.220 mm^3, 0.073 x 0.140 x 0.253 mm^3, and 0.156 x 0.162 x 0.713 mm^3, respectively, were selected and mounted (vide infra) for LT SCXRD determinations.

2.3.1.5. [XeF$_5$][AsF$_6$] (7). Single-crystals of $[XeF_5][AsF_6]$ (**7**) were crystallized from aHF solution between 22 and –30 ℃ over ca. 4 h from sample (b) of the *Variable-temperature Raman Spectroscopic Study of the Redox Decomposition of [FKrFXeF][AsF$_6$]·0.5KrF$_2$·2HF* (vide supra). A single crystal of **7** having the dimensions 0.063 x 0.136 x 0.213 mm^3 was selected and mounted (vide infra) for a LT SCXRD determination.

2.4. Syntheses and Structural Characterizations of the Cl(V) Coordination Complex, [O$_2$Cl(FXeF)$_2$][AsF$_6$], and *β*-[ClO$_2$][AsF$_6$]

2.4.1. β-[ClO$_2$][AsF$_6$] (1) and α-[ClO$_2$][AsF$_6$]. In a typical synthesis, ca. 100 mg (ca. 1.14 mmol) of ClO_2F and 1.05 mmol of AsF_5 were added to ca. 0.5 mL aHF at −196 °C. The reactor and contents were warmed to 22 °C for ca. 5 min and subsequently cooled to −196 °C, whereupon a voluminous white precipitate formed. The LT Raman spectrum of this precipitate under frozen aHF was assigned to previously unknown *β*-$[ClO_2][AsF_6]$. The aHF solvent and excess ClO_2F were removed under dynamic vacuum at −78. The Raman spectrum of the resulting fine white precipitate was consistent with that of compound (**1**). The sample was warmed to 22 °C, agitated for ca. 5 min, and then cooled to −196 ℃. The LT Raman spectrum of the sample was consistent with the known phase, *α*-$[ClO_2][AsF_6]$,

and was assigned by comparison with previously published spectra.[141,142] The sample was stored in a 1/4-inch o.d. FEP storage vessel in a dry box until used.

2.4.2. β-[ClO₂][AsF₆] (1) crystal growth. Approximately 0.5 mL of aHF and 23.2 mg of *α*-$[ClO_2][AsF_6]$ were added to a 1/4-in. o.d. FEP reaction vessel equipped with a Kel-F valve. The reactor and contents were warmed to 22 °C to effect dissolution and subsequently cooled to −78 °C, whereupon a white solid precipitated from solution. The LT Raman spectrum of the precipitate, recorded under frozen aHF, corresponded to *β*-$[ClO_2][AsF_6]$. The sample was then warmed with agitation to 0 °C to effect dissolution. The resulting solution, which was slowly cooled from 0 to −10 °C over ca. 4 h, yielded colorless, block-shaped crystals of *β*-$[ClO_2][AsF_6]$. The crystals were isolated by removal of the aHF solvent under dynamic vacuum at −78 °C. The LT Raman spectrum was obtained for the dry crystalline sample. A single crystal of *β*-$[ClO_2][AsF_6]$ having the dimensions 0.048 × 0.123 × 0.242 mm^3 was selected and mounted (see *Sec. 4.4.1*) for a LT SCXRD determination.

2.4.3. [ClO₂][SbF₆]. The salt, $[ClO_2][SbF_6]$, was synthesized by a procedure similar to that described for *β*-$[ClO_2][AsF_6]$ (*Sec. 4.3.2*). Approximately 82 mg (0.94 mmol) of ClO_2F was added to an HF/SbF_5 mixture containing 0.58 mmol of SbF_5 at −196 °C. The reactor was slowly warmed to −78 °C and agitated, whereupon a white precipitate formed. The LT Raman spectrum of the precipitate, recorded under frozen aHF, was consistent with that previously reported for $[ClO_2][SbF_6]$.[143] The aHF solvent and excess ClO_2F were removed under dynamic vacuum at −78 °C to give $[ClO_2][SbF_6]$ as a dry powder, which was stored in a 1/4-inch o.d. FEP vessel inside a dry box until used.

2.4.4. $[O_2Cl(FXeF)_2][AsF_6]$ (2). Approximately 0.5 mL of aHF was added to a 1/4-in. o.d. straight FEP reaction vessel equipped with a Kel-F valve. Inside a dry box, 5.51 mg (0.0217 mmol) of α-$[ClO_2][AsF_6]$ and 13.21 mg (0.0780 mmol) of XeF_2 were loaded into the reactor which was maintained at −150 °C by means of copper-plated steel air rifle shot that had been cooled inside the cryowell of the dry box. The reaction vessel was then warmed from −150 to −20 °C, whereupon $[ClO_2][AsF_6]$ and XeF_2 dissolved to give a colorless solution. The sample was quenched at −196 °C and subsequently warmed to −78 °C, whereupon a fine white precipitate deposited. The LT Raman spectrum of the solid, recorded under frozen aHF, was shown to consist of **2** and excess XeF_2. The sample was then warmed to −30 °C to effect dissolution and colorless, block-shaped crystals of **2** were grown by slow cooling of the solution from −30 to −65 °C over ca. 5 h. The crystals were isolated as described in *Sec. 4.3.2* and a LT Raman spectrum was obtained for the dry crystalline material. A single crystal of **2** having the dimensions 0.132 × 0.142 × 0.470 mm^3 was selected and mounted (see *Sec. 4.4.1*) for a LT SCXRD determination.

2.4.5. Attempted Synthesis of $[O_2Cl(FXeF)_2][SbF_6]$. Approximately 1:3 and 1:8 molar mixtures of $[ClO_2][SbF_6]$ (1:3, 15.21 mg, 0.0502 mmol; 1:8, 16.8 mg, 0.0554 mmol) and XeF_2 (1:3, 22.2 mg, 0.1311 mmol; 1:8, 71.3 mg, 0.4211 mmol) were prepared as described above. Both samples were warmed with agitation to 22 °C for ca. 5 min and subsequently quenched at −196 °C. Warming the quenched samples to −78 °C yielded white precipitates, which were identified by recording their LT Raman spectra under frozen aHF. The 1:3 molar mixture showed only unreacted starting materials, whereas the 1:8 molar mixture consisted of $[Xe_2F_3][SbF_6]$ and ClO_2F. The aHF solvent was then

removed from the 1:3 molar mixture under dynamic vacuum at −78 °C, and ca. 0.5 mL $CFCl_3$ was condensed into the reactor at −196 °C. The sample was then slowly warmed from −196 to −30 °C with agitation to dissolve the reactants. Upon warming to −30 °C, vigorous gas evolution ensued and the $CFCl_3$ solvent turned yellow due to Cl_2 formation. The sample was quenched at −196 °C and warmed to −78 °C, whereupon a white precipitate formed. The LT Raman spectrum of the precipitate corresponded to that of $[ClO_2][SbF_6]$,[143] with no bands observed for XeF_2 or an XeF_2 coordination complex. The $CFCl_3$ solvent was removed under dynamic vacuum at −78 °C, and the LT Raman spectrum of the remaining white solid showed it to be pure $[ClO_2][SbF_6]$.[143]

2.5. Syntheses and Structural Characterizations of the Br(V) Coordination Complexes, $[O_2Br(FXeF)_n][AsF_6]$ (n = 1, 2), and $[O_2Br(FXeF)_2][SbF_6]$

2.5.1. Synthesis of $[BrO_2][AsF_6]$. Approximately 0.5 mL of aHF was condensed into an FEP reaction vessel containing 40 mg (0.31 mmol) of BrO_2F at −196 °C. The sample was then warmed to −20 °C with agitation to effect dissolution, and subsequently cooled to −196 °C whereupon 310 torr (0.317 mmol) of AsF_5 was condensed into the reaction vessel under static vacuum. The sample was slowly warmed to −20 °C, mixed, and then cooled to −78 °C, whereupon an orange precipitate formed. The LT Raman spectrum of the precipitate recorded under frozen aHF was identical to the published spectrum of $[BrO_2][AsF_6]$.[139] The sample was stored under 1000 torr of Ar at −78 °C until used.

2.5.2. Synthesis of $[BrO_2][SbF_6]$. In a typical reaction, 25 mg (0.191 mmol) of BrO_2F was transferred into an FEP reaction vessel containing a frozen (−196 °C) solution of SbF_5 (0.16 mmol) dissolved in ca. 0.5 mL of aHF. The reaction mixture was then warmed

to −10 °C to effect dissolution, and upon cooling to −78 °C, a pale orange precipitate formed. The LT Raman spectrum of the precipitate, recorded under frozen aHF solvent, was identical to the previously reported LT spectrum of $[BrO_2][SbF_6]$.[143] The aHF solvent was removed at −78 °C by pumping through a −196 °C FEP U-trap, and excess BrO_2F was removed under static vacuum at −10 °C by sublimation and condensed into an FEP storage vessel maintained at −196 °C. The FEP vessel containing dry $[BrO_2][SbF_6]$ was then backfilled with 1000 torr Ar at −78 °C and stored at RT in the dry box until used. Alternatively, $[BrO_2][SbF_6]$ that had been freshly prepared in aHF solvent was transferred into the dry box for reaction with XeF_2, without removal of excess BrO_2F, SbF_5, or HF under dynamic vacuum.

2.5.3. Syntheses of $[O_2Br(FXeF)_n][AsF_6]$ (n = 1, 2) and Crystal Growth. A freshly prepared sample of $[BrO_2][AsF_6]$ (91.9 mg, 0.306 mmol) was dissolved in ca. 0.5 mL of aHF and was transferred into the dry box through a cryowell, where XeF_2 (79.9 mg, 0.472 mmol) was added to the FEP reaction vessel at −150 °C. The valved vessel and contents were removed from the dry box and the reaction mixture was warmed to ca. −10 °C with agitation to effect dissolution. Subsequent cooling of the sample to −78 °C yielded an orange precipitate and a small amount of white precipitate. The LT Raman spectrum of the sample, recorded under frozen aHF at −150 °C, showed two new $[BrO_2]^+$ coordination complexes of XeF_2 had formed, as well as the presence of unreacted $[BrO_2][AsF_6]$, XeF_2, and a small amount of $[Xe_2F_3][AsF_6]$. The formation of $[Xe_2F_3][AsF_6]$ is attributed to the reaction of XeF_2 with excess AsF_5 used for the synthesis of $[BrO_2][AsF_6]$ (Section 2.5.1.). The mixture was redissolved in aHF at 0 °C, and the solution was slowly cooled to −8 °C

over a period of ca. 1 h, which resulted in crystallization of $[Xe_2F_3][AsF_6]$ (identified by a SCXRD unit cell determination). Further cooling to −42 °C over ca. 7 h yielded dark orange crystals of $[O_2Br(FXeF)_2][AsF_6]$, and orange crystals of $[O_2Br(FXeF)][AsF_6]$ grew over ca. 3 h at −46 °C. The aHF solvent was removed under dynamic vacuum at −78 °C, and crystals suitable for SCXRD structure determinations were mounted at low temperature on an X-ray diffractometer.

2.5.4. Synthesis of $[O_2Br(FXeF)_2][SbF_6]$ and Crystal Growth. A valved FEP reaction vessel containing ca. 0.5 mL aHF solvent was transferred into a dry box through a glass cryowell and dry crystalline $[BrO_2][SbF_6]$ (66.4 mg, 0.191 mmol) was loaded into the vessel at ca. −150 °C. The sample was warmed to RT to dissolve $[BrO_2][SbF_6]$ and subsequently cooled to ca. −150 °C, and XeF_2 (88.2 mg, 0.521 mmol) was added to the frozen sample. The reaction mixture was slowly warmed to RT with agitation outside the dry box, which resulted in dissolution of the reactants to give a light orange solution. Cooling the reaction mixture to 18 °C led to crystallization of amber $[BrO_2][SbF_6]$. Further cooling to −50 °C over ca. 10 h resulted in the growth of orange, needle-shaped crystals of $[O_2Br(FXeF)_2][SbF_6]$. Excess XeF_2 crystallized upon cooling the sample to −78 °C. The aHF solvent was removed under dynamic vacuum at −78 °C, and the resulting crystalline mixture was shown to consist of XeF_2, $[BrO_2][SbF_6]$, and $[O_2Br(FXeF)_2][SbF_6]$ by LT Raman spectroscopy (Figure 5.5) and LT SCXRD.

2.5.5. Attempted Synthesis of $[O_2Br(FXeF)][SbF_6]$. A valved FEP reaction vessel containing 25.0 mg (0.0719 mmol) of $[BrO_2][SbF_6]$ and 12.9 mg (0.0762 mmol) of XeF_2 in ca. 0.5 mL aHF solvent was prepared as described in Section 2.5.3. The reaction

mixture was warmed to 0 °C outside the dry box to effect dissolution. Upon cooling to −78 °C, orange and colorless solids precipitated from solution. The LT Raman spectrum of the precipitate, recorded under frozen aHF solvent, showed unreacted $[BrO_2][SbF_6]$, $[O_2Br(FXeF)_2][SbF_6]$, and a small amount of colorless $[Xe_2F_3][SbF_6]$. Following addition of more XeF_2 (15.0 mg, 0.089 mmol), the LT Raman spectrum showed the sample consisted of a mixture of $[O_2Br(FXeF)_2][SbF_6]$, $[BrO_2][SbF_6]$, XeF_2, and $[Xe_2F_3][SbF_6]$.

2.6. Syntheses and Structural Characterizations of $[ClO_2]_2[cyclo\text{-}\mu\text{-}(OIrF_4)_3]$ and the Coordination Complex $F_5Ir{-}{-}{-}OClF$

2.6.1. Syntheses of $F_5Ir{-}{-}{-}OClF$ and $[ClO_2][IrF_6]$. Iridium dioxide (23.20 mg, 0.1034 mmol) was weighed into the main arm of a ¼-in. o.d. FEP h-shaped reaction vessel that was outfitted with a stainless-steel valve and was dried under dynamic vacuum for over 24 h on a glass vacuum line. Anhydrous HF (ca 0.5 mL) and ClF_3 (ca. 0.3 mL) were condensed into the reaction vessel under static vacuum at –196 °C. The sample was then backfilled with ca. 1000 torr of N_2 gas and warmed to RT, whereupon vigorous gas-evolution ensued that originated from black, solid IrO_2 at the bottom of the reaction vessel along with simultaneous formation of a brown-black precipitate that was likely IrF_4. Continued reaction at RT for ca. 4 h resulted in the consumption of IrO_2 and the brown-black precipitate with the formation of a dark amber solution. The sample was then cooled to and stored at –78 °C, whereupon amber, needle-shaped crystals of $F_5Ir{-}{-}{-}OClF$ and purple, plate-shaped crystals of $[ClO_2][IrF_6]$ deposited overnight from solution. The aHF solvent was removed under dynamic vacuum at −78 °C by pumping through an FEP U-trap maintained at −196 °C. Crystals of $F_5Ir{-}{-}{-}OClF$ and $[ClO_2][IrF_6]$ that were

suitable for SCXRD structure determinations were selected and mounted at low temperatures on an X-ray diffractometer.

2.6.2. Synthesis of [ClO$_2$]$_2$[cyclo-μ-(OIrF$_4$)$_3$]. In a typical reaction, IrO_2 (14.60 mg, 0.0651 mmol) was weighed into the main arm of a ¼-in. o.d. FEP h-shaped reactor outfitted with a stainless-steel valve and dried for 24 h on a glass vacuum line. Anhydrous HF solvent (ca. 0.5 mL) and ClF_5 (ca. 0.2 mL) were condensed onto IrO_2 under static vacuum at –196 °C. The reaction vessel was then backfilled to a pressure of ca. 1000 torr with N_2 gas at –78 °C. Upon warming to RT, gas evolution occurred that originated from solid IrO_2 at the bottom of the reaction vessel, and a brown-black precipitate simultaneously formed in the solution above IrO_2 which was likely IrF_4. The colorless solution slowly turned an intense dark-brown color that became opaque over a period of ca. 4 h. The sample was allowed to react at room temperature for an additional 4 days and yielded a brown-black supernatant and a brown-black precipitate. The sample was cooled to –24 °C, and brown-black, needle-shaped crystals of $[ClO_2]_2[cyclo\text{-}\mu\text{-}(OIrF_4)_3]$ and purple, plate-shaped crystals of $[ClO_2][IrF_6]$ grew from the solution between –24 and –30 °C over a period of 1 h. Crystals of $[ClO_2]_2[cyclo\text{-}\mu\text{-}(OIrF_4)_3]$ and $[ClO_2][IrF_6]$ that were suitable for SCXRD structure determinations were selected and mounted at LT on an X-ray diffractometer.

2.7. Noble-Gas Difluoride Complexes of $CrOF_4$ and MOF_4 (M = Mo, W); $NgF_2 \cdot CrOF_4$ (Ng = Kr, Xe), $NgF_2 \cdot MOF_4$, $NgF_2 \cdot 2CrOF_4$, and $XeF_2 \cdot 2M'OF_4$ (M′ = Mo, W).

2.7.1. $KrF_2 \cdot WOF_4$. Tungsten oxide tetrafluoride was weighed into the main arm of a passivated ¼-in. o.d. FEP h-shaped reactor in a dry box. Anhydrous HF solvent (ca 0.5 mL) and KrF_2 were condensed into the reaction vessel under static vacuum at −196 °C and the vessel was backfilled with ca. 1000 torr N_2 gas at −78 °C. The sample was maintained at −78 °C for ca. 5 min with periodic agitation, which yielded a flocculant, white precipitate. Upon warming to −65 °C, the white precipitate dissolved after ca. 10 min with agitation, and the solution was immediately poured into the side arm of the reactor. The side arm was warmed to −55 °C for ca. 15 s to effect dissolution and immediately cooled to −60 °C. Slow cooling of the side arm from −60 to −66 °C over ca. 1 h yielded colorless, needle-shaped crystals of $KrF_2 \cdot WOF_4$. A Raman spectrum was obtained on the crystals under solid aHF at −150 °C.

2.7.2. [--(F_4OMo)(μ_3-F)H---(μ-F)H--]$_\infty$. In the dry box, $MoOF_4$ (ca. 50 mg) was weighed into a ¼-in. o.d. FEP reactor equipped with a Kel-F valve. The reactor was then removed from the dry box and moved to a metal vacuum line where aHF (ca. 0.5 mL) was transferred into the reactor at −196 °C. The sample was warmed to room temperature for ca. 10 min, whereupon all $MoOF_4$ dissolved. Slow cooling of the sample from room temperature to −60 °C over ca. 4 h yielded colorless plates of [--(F_4OMo)(μ_3-F)H---(μ-F)H--]$_\infty$. The crystalline samples were isolated by decanting the aHF supernatant at −78 °C into the side arm of the reaction vessel, which was cooled to −196 °C and heat-sealed

off under dynamic vacuum. Residual aHF was removed from the crystalline sample under dynamic vacuum at −78 °C. All crystalline samples described in subsequent subsections were isolated in a similar manner. The attempted synthesis of [--(F_4OW)(μ_3-F)H---(μ-F)H--]$_\infty$ was carried out in a similar manner to the synthesis of [--(F_4OMo)(μ_3-F)H---(μ-F)H--]$_\infty$ using 47.46 mg WOF_4 and ca. 0.5 mL aHF in a ¼-in. o.d. FEP reactor equipped with a Kel-F valve.

2.7.3. XeF_2·$CrOF_4$. In a typical synthesis, $CrOF_4$ (74.0 mg; 0.521 mmol) and XeF_2 (103.1 mg; 0.609 mmol) were weighed into an FEP reaction vessel at –150 °C in a dry box. The reaction vessel was warmed to ca. 76 °C for 2 min, whereupon the sample melted and a red vapor attributable to gaseous $CrOF_4$ was visible above the melt. Upon melting, pale-red, $CrOF_4$-stained crystals of XeF_2 (identified by a unit cell determination) sublimed directly above the heated region of the reactor. The molten sample was quenched at –78 °C and its LT (–150 °C) Raman spectrum was shown to correspond to XeF_2·$CrOF_4$ and a small amount of excess XeF_2.

2.8. Synthesis, Structure, and Bonding of a Xe(IV) Transition-Metal Coordination Complex, F_3XeF_b---WOF_4

2.8.1. F_3XeF_b---WOF_4. Crystalline XeF_4 (43.46 mg, 0.2097 mmol) was transferred inside a dry box into a ¼-in. o.d. FEP reaction vessel outfitted with a Kel-F valve. Approximately 0.5 mL $CFCl_3$ solvent was condensed into the reaction vessel at –196 °C under static vacuum on a glass vacuum line. The sample was warmed to RT for ca. 5 min with agitation, whereupon approximately half of the crystalline XeF_4 dissolved. Because crystalline XeF_4 is only partially soluble in $CFCl_3$ at room temperature, the sample was

rapidly quenched to –196 °C and warmed to –78 °C to precipitate a microcrystalline powder. After two further warming/quenching cycles, the original XeF_4 sample was converted to a microcrystalline powder. The powdered XeF_4 under frozen $CFCl_3$ was transferred into a dry box and maintained at −150 °C while WOF_4 (48.09 mg, 0.1743 mmol) was added to the reaction vessel. A Kel-F valve was connected to the reaction vessel, which was then slowly warmed to 22 °C to effect dissolution. Slow gas evolution was observed at this temperature as the colorless solution became pale yellow in color, indicating some oxidative fluorination of $CFCl_3$ with the liberation of Xe and Cl_2 gas had occurred. Slow cooling of the reaction vessel from 22 to −20 °C over ca. 1 h led to the formation of colorless, plate-shaped crystals of F_3XeF_b---WOF_4 and colorless, block-shaped crystals of XeF_4 (identified by single-crystal X-ray unit cell determinations). A single crystal of F_3XeF_b---WOF_4 having the dimensions 0.050 x 0.171 x 0.287 mm^3 was selected and mounted (vide infra) for a LT SCXRD determination.

2.8.2. Attempted Synthesis of F_3XeF_b---WOF_4 in a Melt. Xenon tetrafluoride (40.70 mg, 0.1963 mmol) and WOF_4 (36.50 mg, 0.1323 mmol) were added at −150 °C to an FEP reaction vessel inside a dry box. The reaction vessel was closed with a Kel-F valve and the sample was warmed to ca. 50 °C, whereupon the solids fused and rapid gas evolution ensued. The sample was cooled to room temperature, whereupon the molten mixture solidified to yield a white polycrystalline solid. Upon cooling to −78 °C, a white solid (WF_6) formed on the cooled walls of the FEP reaction vessel. The LT Raman spectrum of the solid mixture showed bands due to $FXeF_b$---WOF_4, XeF_4, and WF_6 (324, 328, 670,

673, and 771 cm^{-1}) consistent with oxidative fluorination of WOF_4 to WF_6 and O_2, and reduction of Xe(IV) to Xe(II).

2.8.3. Attempted Synthesis of F_3XeF_b---WOF_4 in aHF. Approximately 0.5 mL of aHF solvent was transferred into a ¼-in o.d. FEP reaction vessel under static vacuum. The reactor was transferred into a dry box, maintained at ca. −150 °C using liquid-nitrogen cooled air-rifle shot, and XeF_4 (27.85 mg, 0.1344 mmol) and WOF_4 (45.11 mg, 0.1635 mmol) were added. The reaction vessel and contents were warmed to 22 °C for ca 5 min with agitation, and upon cooling to −78 °C, a white precipitate formed. The LT (−150 °C) Raman spectrum of the precipitate was recorded under frozen aHF solvent and showed bands due to unreacted XeF_4 and WOF_4. The sample was then allowed to react at room temperature over a period of 6 h followed by cooling to −78 °C, which yielded crystalline $FXeF_b$---WOF_4 that was identified by LT Raman spectroscopy.

2.8.4. Attempted Syntheses of F_3XeF_b---$MoOF_4$ in $CFCl_3$ Solvent and in a Melt. Using the synthetic procedure described for F_3XeF_b---WOF_4, XeF_4 (47.45 mg, 0.2288 mmol) and $MoOF_4$ (56.63 mg, 0.2053 mmol) were allowed to react in 0.5 mL of $CFCl_3$ solvent in a ¼-in. o.d FEP reaction vessel equipped with a Kel-F valve. After warming to 22 °C with periodic agitation for ca. 15 min, the reaction vessel and contents were cooled to −78 °C, whereupon a white solid formed that remained suspended in the solvent. The LT (−150 °C) Raman spectrum of the solid under frozen $CFCl_3$ solvent showed bands due to unreacted XeF_4 and $MoOF_4$, which indicated no reaction had occurred.

The direct reaction of XeF_4 with $MoOF_4$ in a melt was also attempted. Xenon tetrafluoride (59.20 mg, 0.2856 mmol) and $MoOF_4$ (52.70 mg, 0.2804 mmol) were

weighed out and loaded into a ¼-in. o.d. FEP reaction vessel at ca. −150 °C inside a dry box. The reaction vessel was closed with a Kel-F valve and the solid mixture was warmed to ca. 75 °C, whereupon the solids fused to give a colorless liquid. The sample was then allowed to cool and solidify at 22 °C. The resulting white polycrystalline mass was shown by LT Raman spectroscopy to correspond to a mixture of unreacted XeF_4 and $MoOF_4$.

2.8.5. Attempted Synthesis of F_3XeF_b---$W(OF_3)$–F_b'---$W'OF_4$ in $CFCl_3$. Xenon tetrafluoride (32.30 mg, 0.1559 mmol) and WOF_4 (96.50 mg, 0.3499 mmol) were added at −150 °C to an FEP reaction vessel containing ca 0.5 mL $CFCl_3$ inside a dry box. The reaction vessel was closed with a Kel-F valve and allowed to react as previously described to give a mixture of F_3XeF_b---WOF_4 and unreacted WOF_4 (determined from the Raman spectrum of the frozen sample at −150 °C).

2.9. Chromium Oxide Tetrafluoride and Its Reactions with Xenon Hexafluoride; the $[XeF_5]^+$ and $[Xe_2F_{11}]^+$ Salts of the $[Cr^{VI}OF_5]^-$, $[Cr^{V}OF_5]^{2-}$, $[Cr^{V}{}_2O_2F_8]^{2-}$, and $[Cr^{IV}F_6]^{2-}$ Anions

2.9.1. $[XeF_5]_2[Cr_2O_2F_8]\cdot 2HF$. Xenon hexafluoride (56.0 mg, 0.223 mmol) was transferred under static vacuum at –196 °C into a fluorine-passivated FEP reaction vessel containing HF-wetted $CrOF_4$ (ca. 36 mg, 0.25 mmol) in $CFCl_3$ solvent (ca. 0.4 mL). The sample was warmed to room temperature, whereupon $CrOF_4$ and XeF_6 rapidly dissolved to give a clear, colorless solution. Pale yellow-green, block-shaped crystals of $[XeF_5]_2[Cr_2O_2F_8]\cdot 2HF$ were grown from the solution at –78 °C over a period of 48 h. A single crystal of $[XeF_5]_2[Cr_2O_2F_8]\cdot 2HF$ (dimensions, 0.17 x 0.31 x 0.55 mm^3) was selected and mounted for a LT X-ray crystal structure determination. Amber, block-

shaped crystals of $[XeF_5]_2[Cr_2O_2F_8]\cdot 2XeOF_4$ were also obtained, as confirmed by unit cell determinations.

2.9.2. $[XeF_5]_2[Cr_2O_2F_8]\cdot 2XeOF_4$. Using a procedure similar to that used for the synthesis of $[XeF_5]_2[Cr_2O_2F_8]\cdot 2HF$, XeF_6 (64.5 mg, 0.263 mmol) and $CrOF_4$ (ca. 55 mg, 0.38 mmol) were combined in aHF solvent (ca. 0.4 mL). The sample was warmed to room temperature, whereupon $CrOF_4$ and XeF_6 rapidly dissolved to give an amber solution. Amber, block-shaped crystals of $[XeF_5]_2[Cr_2O_2F_8]\cdot 2XeOF_4$ were grown from solution overnight at –78 °C. A Raman spectrum of the dry crystalline sample was recorded at −150 °C. A single crystal (dimensions, 0.13 x 0.17 x 0.21 mm^3) was selected and mounted for a LT X-ray crystal structure determination.

2.10. Syntheses and Structural Characterizations of $[Cr_2O_4F_6]^{2-}$ and $[CrO_2F_4]^{2-}$ salts.

2.10.1. $[XeF_5]_2[Cr_2O_4F_6]$ (1) and $[XeF_5]_2[Cr_2O_4F_6]\cdot 4HF$ (2). Approximately 0.5 mL of aHF, 17.5 mg (0.143 mmol) of CrO_2F_2, and 90.7 mg (0.536 mmol) of XeF_6 were condensed at −196 °C through an FEP submanifold into a ¼-in. o.d. FEP reaction vessel equipped with a sidearm and outfitted with a Kel-F valve. The reaction mixture was warmed to RT and agitated, whereupon the reactants dissolved to give an amber solution. Upon cooling the solution to −78 °C, a dark amber solid and a small amount (ca. < 5%) of a yellow solid precipitated from solution. The LT Raman spectrum of the solid showed it was a mixture of **1** and **3**, where **1** was the dominant component (Figure 10.6). The solution was warmed to RT to dissolve the solids, and amber, block-shaped crystals of $[XeF_5]_2[Cr_2O_4F_6]$ (**1**) and $[XeF_5]_2[Cr_2O_4F_6]\cdot 4HF$ (**2**) and yellow to amber, block-shaped

crystals of $[XeF_5]_2[Cr_2O_4F_6]\cdot 2XeOF_4$ (**3**) (identified by LT Raman spectroscopy, Figure 10.7) grew when the solution was cooled from 22 to −47 °C over 6 h. The crystals were isolated by decanting the HF supernatant into the side arm of the reaction vessel at –78 °C. The side-arm and contents were cooled to –196 °C and heat-sealed off under dynamic vacuum. Residual HF was removed from the crystalline sample under dynamic vacuum at –78 °C by pumping through an FEP U-trap that was maintained at −196 °C. The LT Raman spectrum of the sample was obtained, and suitable single crystals of **1** and **2** were mounted on a goniometer for SCXRD structure determinations. Crystals of **3** were of poor quality, so another sample was prepared by purposely allowing a mixture of XeF_6 and CrO_2F_2 in aHF to hydrolyze by exposure to trace amounts of moisture which diffused into the reaction vessel over ca. 7 days at −78 °C (vide infra).

2.10.2. $[XeF_5]_2[Cr_2O_4F_6]\cdot 2XeOF_4$ (3). A sample was prepared as previously described in Section 2.10.1 using ca. 0.5 mL of aHF, 30.5 mg (0.250 mmol) of CrO_2F_2, and 112.3 mg (0.663 mmol) of XeF_6. The sample was allowed to stand at −78 °C for one week, and was then warmed to RT and agitated, to give a amber solution. Light yellow, block-shaped crystals of $[XeF_5]_2[Cr_2O_4F_6]\cdot 2XeOF_4$ and colorless, block-shaped crystals of $[XeF_5][HF_2]\cdot 1.5HF$ (identified by LT SCXRD unit cell determinations)[100] were grown by slowly cooling the sample from 22 to −30 °C over 2 h. The crystals were isolated as previously described and the LT Raman spectrum of the crystalline sample was obtained. A single crystal of **3** was selected and mounted for a LT X-ray crystal structure determination.

2.10.3. [XeF$_5$][Xe$_2$F$_{11}$][CrO$_2$F$_4$] (4). A mixture of 12.0 mg (0.098 mmol) of CrO_2F_2 and 29.5 mg (0.1202 mmol) of XeF_6 was obtained by statically subliming individual components into a ¼-in. o.d. FEP reaction vessel at −196 ºC. The sample was warmed to 22 ºC to give a light red liquid. The sample was placed in a water bath (ca. 50 ºC) and crystals of $[XeF_5][Xe_2F_{11}][CrO_2F_4]$ were grown by allowing the bath to slowly cool to room temperature overnight. The crystals were isolated as previously described (see Section 2.10.1. and the LT Raman spectrum of the crystalline sample was obtained. Several attempts to grow high-quality crystals of **4** yielded twinned crystals. The propensity for crystals of **4** to twin is likely due to the packing arrangement in its crystal structure (see Section 10.2.2.2). A single crystal of **4** was selected and mounted for a LT X-ray crystal structure determination.

2.11. Group 6 Oxyfluoro-anion Salts of $[XeF_5]^+$ and $[Xe_2F_{11}]^+$; Syntheses and Structures of $[XeF_5][M_2O_2F_9]$ (M = Mo, W), $[Xe_2F_{11}][M'OF_5]$ (M' = Cr, Mo, W), $[XeF_5][HF_2]\cdot CrOF_4$, and $[XeF_5][WOF_5]\cdot XeOF_4$

2.11.1. [Xe$_2$F$_{11}$][CrOF$_5$]. Inside a dry box, $CrOF_4$ (20.20 mg, 0.1403 mmol) was loaded into a passivated ¼-in. FEP reactor equipped with a Kel-F valve and maintained at −150 °C by copper-plated steel air rifle shot that had been previously cooled inside the cryowell of a dry box. The reaction vessel was then attached to a glass vacuum manifold, cooled to −196 °C, and ca. 0.45 mL of CF_2ClCF_2Cl was condensed into the reaction vessel under static vacuum. The reaction vessel was backfilled with dry N_2 (ca. 800 torr), closed, connected to a FEP XeF_6 storage vessel through an FEP submanifold on a high-vacuum metal vacuum line. Xenon hexafluoride (76.4 mg, 0.311 mmol) was sublimed under static

vacuum into the reaction vessel at −196 °C. The reactor and contents were slowly warmed to −78 °C and agitated for ca. 5 min to dissolve XeF_6 and $CrOF_4$. The sample was immediately quenched at −196 °C and subsequently warmed to −78 °C, whereupon an orange-colored precipitate formed. The LT Raman spectrum (−150 °C) of the precipitate was identical to that previously reported for $[Xe_2F_{11}][CrOF_5]$ (see Chapter 9), which was obtained by reaction of XeF_6 and $CrOF_4$ between −78 and 18 °C. The sample was slowly warmed to −28 °C, whereupon the orange precipitate dissolved, with agitation, after ca. 10 min. Dark purple, trapezoid-shaped crystals of $[Xe_2F_{11}][CrOF_5]$ (**1**) that were suitable for a single-crystal X-ray structure determination were grown by slowly cooling the reaction vessel and contents from −28 to −43 °C over ca. 2 h and were isolated by decanting the CF_2ClCF_2Cl supernatant at –78 °C into the side arm of the reaction vessel, which was subsequently cooled to –196 °C and heat-sealed off under dynamic vacuum. Residual CF_2ClCF_2Cl was removed from the crystalline sample under dynamic vacuum at –78 °C, after which a Raman spectrum was recorded on the crystalline product at –150 °C. All crystalline samples described in subsequent subsections were isolated in a similar manner. A single crystal of **1** (dimensions, 0.212 x 0.385 x 0.560 mm^3) was selected and mounted (vide infra) for a LT single-crystal X-ray structure determination.

2.11.2. $[XeF_5][HF_2]\cdot CrOF_4$. Approximately 0.5 mL of aHF was condensed under static vacuum into a passivated 1/4-in o.d. FEP reactor equipped with a Kel-F valve, which was then cooled to and maintained at ca. −150 °C inside a dry box and loaded with $CrOF_4$ (15.20 mg, 0.1056 mmol). Xenon hexafluoride (60.2 mg, 0.245 mmol) was then sublimed

under static vacuum into the reaction vessel at −196 °C, which was warmed to −78 °C with agitation, but showed no evidence of reaction after ca. 5 min. The reaction vessel was slowly warmed from −78 to 0 °C, whereupon all material dissolved to give a light red solution. Violet, trapezoid-shaped crystals of $[XeF_5][HF_2]\cdot CrOF_4$ (**2**) and colorless, block-shaped crystals of XeF_6 (confirmed by a unit cell determination) were grown by slowly cooling the reaction vessel from 0 to −53 °C over ca. 3 h. A single crystal of **2** (dimensions, 0.178 x 0.306 x 0.379 mm^3) was selected and mounted (vide infra) for a LT single-crystal X-ray structure determination.

2.11.3. $[Xe_2F_{11}][MOF_5]$ (M = Mo, W). Inside a dry box, MOF_4 (Mo, 30.5 mg, 0.162 mmol; W, 38.7 mg, 0.140 mmol) was loaded into a passivated ¼-in. FEP reactor equipped with a Kel-F valve. The reaction vessel was cooled to −196 °C and ca. 0.5 mL aHF was condensed into the reaction vessel under static vacuum. Xenon hexafluoride (Mo, 45.2 mg, 0.184 mmol; W, 88.7 mg, 0.361 mmol) was then sublimed under static vacuum into the reaction vessel at −196 °C. The samples were slowly warmed from −196 to −20 (Mo) and 0 °C (W), whereupon all material dissolved to give colorless solutions. Colorless, block-shaped crystals of $[Xe_2F_{11}][MoOF_5]$ (**3**) and $[Xe_2F_{11}][WOF_5]$ (**4**) were grown by slowly cooling the solutions from −20 to −53 °C (Mo) and from 0 to −31 °C (W) over ca. 3 and 6 h, respectively. Single crystals of **3** and **4** having the dimensions 0.148 x 0.158 x 0.284 mm^3 (Mo) and 0.052 x 0.121 x 0.141 mm^3 (W) were selected and mounted (vide infra) for LT single-crystal X-ray structure determinations.

2.11.4. $[XeF_5][M_2O_2F_9]$ (M = Mo, W). The syntheses of **5** and **6** followed a procedure similar to that described for **3** and **4** using 48.0 mg (0.255 mmol) of $MoOF_4$ and 19.2 mg

(0.078 mmol) of XeF_6 for the synthesis of $[XeF_5][Mo_2O_2F_9]$ (**5**) and 36.7 mg (0.133 mmol) of WOF_4 and 51.1 mg (0.208 mmol) of XeF_6 for the synthesis of $[XeF_5][W_2O_2F_9]$ (**6**). The samples were slowly warmed from −196 to −30 (Mo) and −35 °C (W), whereupon all material dissolved to give colorless solutions. Colorless, block-shaped crystals of **5** and **6** were grown by slow cooling of the solutions from −30 to −55 °C and from −35 to −45 °C, respectively, over ca. 4 h. Single crystals of **5** and **6** having the dimensions 0.071 x 0.099 x 0.157 mm^3 (Mo) and 0.080 x 0.291 x 0.382 mm^3 (W), were selected and mounted (*vide infra*) for LT single-crystal X-ray structure determinations.

2.11.5. $[XeF_5][WOF_5]\cdot XeOF_4$. The formation of $[XeF_5][WOF_5]\cdot XeOF_4$ (**7**) resulted from a synthetic procedure similar to that described for **4** using 67.8 mg (0.246 mmol) of WOF_4 and 104.6 mg (0.426 mmol) of XeF_6. The sample was stored for one week at −78 °C, during which time small amounts of H_2O diffused through the walls of the FEP reaction vessel. The sample was then slowly warmed to room temperature, whereupon all material dissolved to give a colorless solution. Colorless, block-shaped crystals of $[XeF_5][WOF_5]\cdot XeOF_4$ (**7**) were grown by slowly cooling the solution from room temperature to −40 °C over ca. 3 h. A single crystal of **7** having the dimensions 0.059 x 0.137 x 0.301 mm^3 was selected and mounted (vide infra) for a LT single-crystal X-ray structure determination.

2.11.6. Attempted Syntheses of $[XeF_5][MOF_5]$ (M = Mo, W) in $CFCl_3$. Xenon hexafluoride (Mo, 17.8 mg, 0.07 mmol; W, 46.4 mg, 0.19 mmol) was sublimed into passivated ¼-in. FEP reaction vessels equipped with Kel-F valves. The reaction vessels were then attached to a glass vacuum manifold, cooled to −196 °C, and ca. 0.55 mL

quantities of $CFCl_3$ onto XeF_6 under static vacuum. The vessels were transferred into a dry box through a cryowell, where they were maintained at −150 °C and loaded with MOF_4 (Mo, 13.5 mg, 0.07 mmol; W, 49.7 mg, 0.18 mmol). The reaction mixtures were slowly warmed outside the dry box from −196 to −15 (Mo) and 23 °C (W) and dissolved to give colorless solutions. Samples were cooled to −196 °C and subsequently warmed to −78 °C, whereupon a white powder precipitated from solution. The LT Raman spectra of these powders were obtained at −150 °C in their frozen aHF solutions. The samples were then briefly warmed to room temperature to effect dissolution and colorless, block-shaped crystals of **6** were grown by slow cooling of the XeF_6/WOF_4 sample from −30 to −45 °C over ca. 5 h, which were characterized by an X-ray unit cell determination.

2.12. X-ray Crystallography

2.12.1. Low-Temperature Crystal Mounting

Because most compounds investigated in this work were thermally unstable and/or moisture sensitive, their crystals were mounted at low temperature using the apparatus depicted in Figure 2.5. The reaction vessels containing the samples were first cut open below the Kel-F valve while maintaining the sample at –78 °C. The sample was then quickly dumped into the aluminum trough of the crystal mounting apparatus under a stream of dry nitrogen, precooled (–104 ±2 °C) by the regulated passage of dry nitrogen gas flow through a 5-L dewar filled with liquid N_2. The temperature inside the trough was measured using a copper-constantan thermocouple positioned in the sample region of the trough. Crystals were then selected using a stereo-zoom microscope and mounted on a

nylon cryoloop (MiTiGen MicroMounts^{TM}) using perfluorinated polyether oil (Ausimont Inc., Fomblin Z25) which served as an adhesive upon freezing at low temperature. The cryloop was fitted to a magnetic base and affixed to the end of a magnetic wand (Hampton Research). The magnetic wand could be fastened to an adjustable support stage such that samples could be inspected in the dry nitrogen cold stream under the stereo-zoom microscope. The mounted crystal and magnetic head were quickly (ca. 5 to 10 s) transferred from the crystal mounting apparatus to the magnetic mount of the goniometer by means of a cryotongs (Hampton Research) which had been precooled in liquid N_2 prior to use. The crystals were maintained at low temperature on the goniometer head by a cold N_2 gas flow provided by a Molecular Structure Corporation cryostat system.

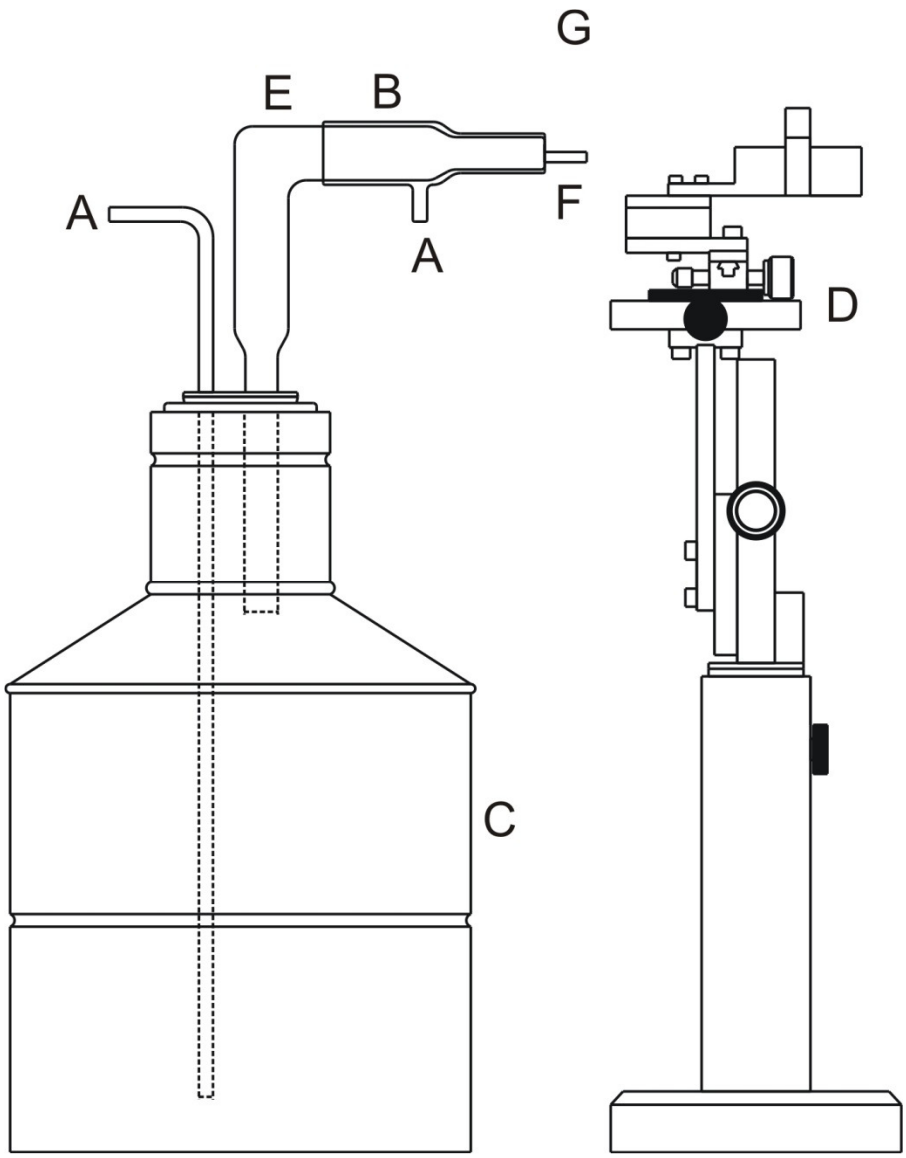

Figure 2.5. Low-temperature crystal mounting apparatus. (A) Nitrogen inlet. (B) Glass sleeve for ambient nitrogen flow. (C) Liquid N_2 dewar. (D) Adjustable support stage. (E) Silvered dewar (glass). (F) Aluminum trough. (G) Stereo-zoom microscope. Reproduced with permission from Leblond, N. Ph. D. Thesis, McMaster University, Hamilton, Canada, **1998**.

2.12.2. Data Collection

2.12.2.1. Bruker SMART APEX II Diffractometer

With the exception of $[O_2Br(FXeF)][AsF_6]$, $[O_2Br(FXeF)_2][AsF_6]$, and $[O_2Br(FXeF)_2][SbF_6]$, the crystallographic data acquired for this Thesis was collected using a Bruker SMART APEX II diffractometer equipped with Oxford Cryosystems low-temperature cryostream accessory that provided a stream of cold, gaseous N_2 for low-temperature data collection. The instrument was controlled by a Cryostream Controller 700 (Oxford Cryosystems). The Bruker SMART APEX II X-ray diffractometer is equipped with an APEX II 4K CCD (charge-coupled device) area detector and a triple-axis goniometer that is controlled by the APEX II Graphical User Interface (GUI) software.[144] A Bruker Triumph curved crystal monochromator was used with a $Mo_{K\alpha}$ (λ = 0.71073 Å) radiation source for all compounds. Diffraction data collection at −173 °C consisted of ω- and ϕ-scans collected at 0.5° intervals. The crystal-to-detector distance was 4.960 cm and the data collection was carried out in 512 x 512 pixel mode using 2 x 2 pixel binning. The raw data sets were processed by use of either the APEX II[144] or APEX III GUI software.[145,146] Scaling of the diffraction data was done using the SADABS[146] or TWINABS[147] programs.

2.12.2.2. STOE IPDS II X-ray diffractometer

Crystals of $[O_2Br(FXeF)][AsF_6]$, $[O_2Br(FXeF)_2][AsF_6]$, and $[O_2Br(FXeF)_2][SbF_6]$ were characterized on a STOE IPDS II X-ray diffractometer equipped with Dectris Pilatus detector and a triple-axis goniometer that was controlled by X-Area software. A $Mo_{K\alpha}$ (λ = 0.71073 Å) radiation source was used for all compounds, and diffraction data collection at −173 °C consisted of Ω-scans collected at 0.5° intervals. The crystal-to-detector distance was 6.000 cm. The raw STOE data sets were converted by use of

di2bruker software into Bruker image files which were then processed by the APEX III GUI software.[145] Scaling of the diffraction data was done using the SADABS[146] or TWINABS[147] programs.

2.12.2.3. Solution and Refinement of Structures

The XPREP program[148] was used to confirm unit cell dimensions and the crystal lattice. The crystal structures were solved with *SHELXT*[149] and refined with *SHELXL*[150] programs, within the *Olex2* software.[151] The space group choice was confirmed using Platon.[152] The final refinement was obtained by introducing anisotropic thermal parameters and the recommended weightings for all of the atoms. The maximum electron densities in the final difference Fourier maps were most often located near heavy atoms, i.e., Kr, Xe, W, etc.

The unit cell of $[FKrFXeF][AsF_6]\cdot 0.5KrF_2\cdot 2HF$ contains two voids (26.2 $Å^3$ and 8.9 e^- each) which are occupied by disordered HF molecules. Attempts to model the fluorine atoms of the HF molecules using an atomistic disorder model led to non-positive F atom thermal parameters because their positions in the crystal lattice are not well defined. Instead, the disordered HF molecules were modelled using the PLATON SQUEEZE function for disordered solvents embedded in crystal lattices, as implemented in OLEX2, prior to refinement.

The crystal structures of $[Xe_2F_3][SbF_6]$ and $[XeF_5][AsF_6]$ were refined as two-component twins using the twin laws −1 0 0 0 1 0 0 0 −1 (BASF, 0.50(2)) and −1 0 0 0 1 0 0 0 −1 (BASF 0.03(2)), respectively. Attempts to model the elongated F-atom ellipsoids in the structural solution of $[XeF_5][AsF_6]$ by means of an atomistic disorder model resulted in non-positive F-atom thermal parameters and F-atom ellipsoids that could not be split.

The crystal structure of β-$[ClO_2][AsF_6]$ was refined as a merohedral twin using the twin law −1 0 0 0 1 0 0 0 −1 with a BASF value of 0.498(14). The crystal structure of $[O_2Cl(FXeF)_2][AsF_6]$ was refined as a merohedral twin using the twin law −1 0 0 0 1 0 0 0 −1 with a BASF value of 0.0029(5).

The crystal structure of $[O_2Br(FXeF)_2][AsF_6]$ was refined as a merohedral twin using the twin law (−1 0 0 0 0 −1 0 −1 0) with a BASF value of 0.0693(8). The crystal structure of $[O_2Br(FXeF)_2][SbF_6]$ was refined as a merohedral twin using the twin law (−1 0 0 0 0 −1 0 −1 0) with a BASF value of 0.1718(9).

The crystal structure of $XeF_2 \cdot CrOF_4$ was refined as a two-component twin (BASF, 0.0044). The hydrogen atoms of $[--(F_4OMo)(\mu_3\text{-}F)H---(\mu\text{-}F)H--]_\infty$ were placed at positions derived from a difference map.

The crystal structure of $F_3XeF---WOF_4$ was refined as a non-merohedral twin with a BASF value of 0.3678(14).

The crystal structure of $[XeF_5]_2[Cr_2O_4F_6]$ was refined as a non-merohedral twin with a BASF value of 0.328(3). The crystal structure of $[XeF_5][Xe_2F_{11}][CrO_2F_4]$ was refined as a merohedral twin using the twin law (1 0 1 0 −1 0 0 0 −1) with a BASF value of 0.499(3).

The crystal structure of $[XeF_5][W_2O_2F_9]$ was refined as a two-component twin (BASF, 0.4070). The crystal structure of $[XeF_5][WOF_5] \cdot XeOF_4$ was refined as a merohedral twin using the twin law −1 0 1 0 −1 0 0 0 1 with a BASF value of 0.0038(3).

2.13. Raman Spectroscopy

Raman spectra were recorded on a Bruker RFS 100 FT Raman spectrometer using 1064-nm excitation, 300 mW laser power, and ±0.5 cm^{-1} resolution. The spectra were recorded at −150 °C in the macrosample chamber of the spectrometer as previously described[73] using 1028 scans on samples contained in FEP reaction vessels. Product distributions in aHF and $CFCl_3$ solvents were periodically monitored by LT Raman spectroscopy. Reaction mixtures were quenched at −196 °C and subsequently warmed to −78 °C, whereupon white solids precipitated from solution. Raman spectra were either recorded on the dry solids or on solids under frozen solvent.

2.14. Quantum-Chemical Calculations

All basis sets were obtained online from the EMSL Basis Set Exchange (https://bse.pnl.gov/bse/portal).[153] Quantum-chemical calculations (density functional theory) were carried out by using the program Gaussian 09[154] for geometry optimizations, vibrational frequencies, and vibrational band intensities. All geometries were fully optimized by using analytical gradient methods. The program GaussView[155] was used to visualize the vibrational mode descriptions and MEPS isosurface contours. Natural Bond Orbital analyses were carried out by use of NBO program version 6.0.[156] AIM and ELF analyses were carried out by use of the Multiwfn package[157] and the formatted G09 wavefunction files as input. ELF basins were also analyzed by use of the program Chimera.[158]

The gas-phase geometries used for EDA and ETS-NOCV analyses were optimized using the Amsterdam Density Functionals (ADF) package in Software for Chemistry and Materials (SCM, version 2016.106).[159] The calculations were carried

out at the DFT level using the hybrid form of PBE (25% HF exchange) by Ernzerhof-Scuseria[160] and by Adamo-Barone[161] with the triple-ζ double-polarization all-electron basis set (TZ2P). Relativistic effects were considered by use of the zero-order regular approximation (ZORA)[162] and the GrimmeD4 correction was used to account for dispersion effects.[163] The computational results were visualized using the ADF Graphical User Interface (SCM).

CHAPTER 3

Syntheses and Characterizations of the Mixed Noble-Gas Compounds, $[FKr^{II}FXe^{II}F][AsF_6]\cdot 0.5Kr^{II}F_2\cdot 2HF$, $([Kr^{II}_2F_3][AsF_6])_2\cdot Xe^{IV}F_4$, and $Xe^{IV}F_4\cdot Kr^{II}F_2$

Adapted with permission from: Bortolus, M. R.; Mercier, H. P. A.; Nyugen, B.; Schrobilgen, G. J. *Angew. Chem. Int. Ed.* **2021**, *60*, 23678–23686.

3.1. Introduction

Xenon compounds exhibit a wide range of formal oxidation states: 0, +½, +2, +4, +6, and +8, but krypton compounds are presently limited to the +2-oxidation state. All known krypton compounds are derived from KrF_2,[17] an endothermic compound (ΔH_f = 60.2 kJ mol^{-1}, gas phase, 93 °C)[56,57] and potent oxidative fluorinating agent that is capable of oxidizing Xe to XeF_6 at (RT).[17]

Although $[Ng_2F_3]^+$ salts have been synthesized and structurally characterized at low temperatures (LT) by single-crystal X-ray diffraction (SCXRD),[17,48,58,59] Raman spectroscopy,[17,46,48,51,58,59] and multi-NMR spectroscopy,[17] the mixed Kr^{II}/Xe^{II} analogue, $[FKrFXeF]^+$, had not been reported. The isolation and structural characterization of mixed Kr^{II}/Xe^{II} and Kr^{II}/Xe^{IV} noble-gas compounds pose a formidable synthetic challenge owing to the ability of KrF_2, $[KrF]^+$, and $[Kr_2F_3]^+$ to oxidize Xe^{II} and Xe^{IV} to Xe^{VI}. The $[F_5Xe(FKrF)_nAsF_6]$ (n = 1, 2) complexes[73] are the only reported examples of mixed noble-gas compounds in which the KrF_2 ligands are bound to Xe^{VI} by means of weak electrostatic interactions, i.e., σ-hole bonds.[164]

The present work describes the synthesis and structural characterization of the first mixed Kr^{II}/Xe^{II} noble-gas compound, $[FKrFXeF][AsF_6]\cdot 0.5KrF_2\cdot 2HF$, and its redox decomposition in aHF to known mixed Kr^{II}/Xe^{VI} complexes and the first Kr^{II}/Xe^{IV} complexes.

3.2. Results and Discussion

3.2.1. Syntheses

[FKrFXeF][AsF$_6$]·0.5KrF$_2$·2HF (1). The reaction of [XeF][AsF_6] with KrF_2 in aHF solvent at −78 °C yielded [FKrFXeF][AsF_6], which cocrystallized with HF and KrF_2 between −40 and −78 °C to give **1** [Eq. (**3.3**)]. Compound **1** was stable at −78 °C in aHF but underwent redox decomposition at −60 °C in aHF in the presence of excess KrF_2.

$$[FKrFXeF][AsF_6] + 0.5KrF_2 + 2HF \rightleftharpoons [FKrFXeF][AsF_6]\cdot 0.5KrF_2\cdot 2HF \quad (\mathbf{3.3})$$

Redox Decomposition of 1 in aHF. The redox decomposition of **1** was periodically monitored by LT Raman spectroscopy to identify reaction products, semi-quantitatively determine their relative distributions, and to determine reaction pathways for the redox decomposition of **1**. The decomposition of **1** in the presence of excess KrF_2 in aHF solution was monitored for two samples; (a) −78 to 0 °C, and (b) −65 to 22 °C. Both samples were warmed in successive stages (vide infra) for varying periods of time followed by quenching to −196 °C to halt decomposition. The quenched samples were then warmed to −78 °C, whereupon aHF melted and finely divided white solids precipitated from their respective solutions. Samples were then mechanically agitated at −78 °C to homogenize the solid mixtures, allowed to settle for ca. 1 min, and quenched again to −196 °C before acquiring their Raman spectra at −150 °C. Raman frequencies and assignments are provided in Tables A1.1 and A1.2 of Appendix 1.

Sample (a): A 5:1 molar ratio of KrF_2 : [XeF][AsF_6] was dissolved at −78 °C, agitated for ca. 5 min, and shown by LT Raman spectroscopy to contain unreacted

$[XeF][AsF_6]$,[48] KrF_2,[165] and to exhibit a new set of bands that was assigned to **1**. Warming the solution from −78 to −42 °C led to consumption of $[XeF][AsF_6]$, a set of new bands that was assigned to $[Kr_2F_3][AsF_6]\cdot n KrF_2$,[46] and a dominant set of bands due to **1**. Upon warming to −38 °C, the band intensities of KrF_2 and **1** decreased, the intensities of the $[Kr_2F_3][AsF_6]\cdot n KrF_2$ bands increased, and three sets of new bands appeared that were assigned to $([Kr_2F_3][AsF_6])_2\cdot XeF_4$ (**2**), $XeF_4\cdot KrF_2$ (**4**), and XeF_4 (**6**)[20] Further warming from −38 to −10 °C led to decreased band intensities for **1** and increased band intensities for **2**, **4**, $[Kr_2F_3][AsF_6]\cdot n KrF_2$,[46] and **6**, where the $[Kr_2F_3][AsF_6]\cdot n KrF_2$ bands were the most intense. At −20 °C, weak bands assigned to $[O_2][AsF_6]$[166] were also observed (Table A1.1, footnote [a]). Upon warming from −10 to 0 °C, the $[Kr_2F_3][AsF_6]\cdot n KrF_2$ and **6** bands decreased in intensity and those of **2** and **4** increased in intensity, where the bands of **4** were the most intense.

Sample (b): The reaction of an 8:1 molar ratio of KrF_2 : $[XeF][AsF_6]$ in aHF at −65 °C for ca. 15 min yielded a mixture of $[XeF][AsF_6]$, KrF_2, and **1**. Further reaction at −55 °C for ca. 15 min resulted in consumption of $[XeF][AsF_6]$, increased intensities for bands assigned to **1**, and the appearance of new bands assigned to **2, 4**, $[Kr_2F_3][AsF_6]\cdot n KrF_2$, and **6**. Warming of the sample to 0 °C for ca. 5 min resulted in complete reaction of $[XeF][AsF_6]$, a significant decrease in the band intensities of **1,** and increased band intensities for **2**, **4**, $[Kr_2F_3][AsF_6]\cdot n KrF_2$, and **6**. Warming from 0 °C to RT for ca. 15 min resulted in complete decomposition of **1** and partial decomposition of **2** with the formation of $[F_5Xe][AsF_6]$,[73] the Kr^{II}/Xe^{VI} complexes, $[F_5Xe(FKrF)_nAsF_6]$ (n = 1, 2),[73] and minor amounts of $[O_2][AsF_6]$ (Table A1.1, footnote [a]).[166] A weak band at 485 cm^{-1} was assigned to the new Kr^{II}/Xe^{VI} complex, $[(F_5Xe)_2(\mu\text{-}FKrF)(AsF_6)_2]$ (vide infra). The sample was then warmed to RT for ca. 10

min and slowly cooled to −50 °C over a period of ca. 4 h, whereupon colorless, block-shaped crystals grew. The crystals and a white, polycrystalline solid were isolated upon removal of the aHF solvent under dynamic vacuum at −78 °C. The LT Raman spectrum of the dry solid mixture exhibited bands due to the aforementioned crystals, $[F_5Xe(FKrF)AsF_6]$,[73] $[F_5Xe][AsF_6]$ (**7**), and **6** (confirmed by single-crystal unit cell determinations), and a set of intense bands that were assigned to polycrystalline $[(F_5Xe)_2(\mu\text{-}FKrF)(AsF_6)_2]$ (Table A1.2). Although $[(F_5Xe)_2(\mu\text{-}FXeF)(AsF_6)_2]$[64] had been previously synthesized and characterized, the Kr^{II} analogue, $[(F_5Xe)_2(\mu\text{-}FKrF)(AsF_6)_2]$, was unknown.

Reaction pathways for the redox decomposition of **1** in aHF solvent in the presence of excess KrF_2 are proposed in Eqs. (**3.4**–**3.9**) that are based on LT Raman spectroscopic studies of the decompositions of samples (a) and (b) between −78 and 22 °C:

$$2[FKrFXeF][AsF_6]\cdot 0.5KrF_2\cdot 2HF + 3KrF_2 \xrightarrow{-60\ ^\circ C} 2[Kr_2F_3][AsF_6] + 2XeF_4 + 2Kr + 4HF \quad (\mathbf{3.4})$$

$$2[Kr_2F_3][AsF_6] + XeF_4 \overset{-60\ ^\circ C}{\rightleftharpoons} ([Kr_2F_3][AsF_6])_2\cdot XeF_4 \quad (\mathbf{3.5})$$

$$[Kr_2F_3][AsF_6] + n KrF_2 \overset{-60\ ^\circ C}{\rightleftharpoons} [Kr_2F_3][AsF_6]\cdot n KrF_2 \quad (\mathbf{3.6})$$

$$XeF_4 + KrF_2 \overset{-60\ \text{to}\ 0\ ^\circ C}{\rightleftharpoons} XeF_4\cdot KrF_2 \quad (\mathbf{3.7})$$

$$[Kr_2F_3][AsF_6] + XeF_4 \xrightarrow{22\ ^\circ C} [F_5Xe][AsF_6] + Kr + KrF_2 \quad (\mathbf{3.8})$$

$$[F_5Xe][AsF_6] + n KrF_2 \overset{22\ ^\circ C}{\rightleftharpoons} [F_5Xe(FKrF)_nAsF_6]\ (n = 0.5, 1, 2) \quad (\mathbf{3.9})$$

The $XeF_4\cdot NgF_2$ adducts were also synthesized by direct reaction of XeF_4 and NgF_2 (see Appendix 1).

3.2.2. X-ray Crystallography

Details of the data collection parameters and other crystallographic information for $[FKrFXeF][AsF_6]\cdot 0.5KrF_2\cdot 2HF$ (**1**), $([Kr_2F_3][AsF_6])_2\cdot XeF_4$ (**2**), $[Xe_2F_3][SbF_6]$ (**3**), $XeF_4\cdot KrF_2$ (**4**), $XeF_4\cdot XeF_2$ (**5**), XeF_4 (**6**), and $[XeF_5][AsF_6]$ (**7**) are summarized in Table 3.1. Experimental geometric parameters are given for **1**–**7** in Table 3.2 and Tables A1.3–A1.7. The structural units and packing diagrams for the crystal structures of **1**–**7** are provided in Figures 3.1–3.3 and Figures A1.1–A1.9. The structure of **3** was re-determined at −173 °C to obtain more precise structural parameters to enable comparison of $[Xe_2F_3]^+$ with $[FKrFXeF]^+$ in (**1**), and $[Kr_2F_3]^+$ in (**2**). The structure of **6** was also re-determined at −173 °C to provide a better comparison with cocrystallized XeF_4 in **2**, **4**, and **5**. The structures of **6** and **7** are discussed in Appendix 1.

[FKrFXeF][AsF₆]·0.5KrF₂·2HF (1), ([Kr₂F₃][AsF₆])₂·XeF₄ (2), and [Xe₂F₃][SbF₆] (3). The structures of **1**, **2**, and **3** consist of discrete $[FKrFXeF]^+$ or $[Ng_2F_3]^+$ (Ng = Kr or Xe) cations and $[MF_6]^-$ (M = As (**1**, **2**), Sb (**3**)) anions that are cocrystallized with KrF_2 (**1**) or XeF_4 (**2**). The shortest cation-anion distances (**1**, Xe---F_{As}, 3.124(6) Å; Kr---F_{As}, 3.086(2) Å; **2**, Kr---F_{As}, 2.986(3); **3**, Xe---F_{Sb}, 3.077(3) Å) and the shortest Ng---F distances (**1**, Xe---F_{KrF2}, 3.198(2) Å; **2**, Kr---F_{XeF4}, 3.271(4) Å) are shorter than but close to the sums of the Ng and F van der Waals radii (Kr···F, 3.49 Å;[167] 3.71 Å;[168] Xe···F, 3.63 Å;[167] 3.52 Å[168]). The geometric parameters of KrF_2 in **1** (Table A1.3) are equal to α-KrF_2,[46] and those of XeF_4 in **2** (Table A1.4) are similar to XeF_4 (**6**). The bond lengths and bond angles of $[MF_6]^-$ in **2** and **3** (Tables A1.4, A1.5) are comparable to other $[Ng_2F_3][MF_6]$ salts, e.g., monoclinic $[Xe_2F_3][AsF_6]$,[59] $[Kr_2F_3][AsF_6]\cdot[KrF][AsF_6]$,[46] $[Kr_2F_3][SbF_6]\cdot KrF_2$,[46] and $([Kr_2F_3][AsF_6])_2\cdot KrF_2$.[46] The

same is true for the $[AsF_6]^-$ anion in **1,** however, it is positionally disordered (Figure A1.1b).

The terminal Ng–F_t bonds of $[FKrFXeF]^+$ in **1** (Kr, 1.806(4) Å; Xe, 1.882(4) Å) are significantly shorter than the Ng---F_b bridge bonds (Kr, 2.055(4) Å; Xe, 2.172(4) Å), consistent with the greater covalent characters for the terminal Ng–F_t bonds as inferred from resonance Structures III–V (see Section 1.2.1.). The Kr–F_t and Kr---F_b bonds are significantly more polarized than the Kr–F bonds of $[F_5Xe(FKrF)_nAsF_6]$ (n = 1, 2) (Kr–F_t: 1.8393(12)–1.8505(15) Å; Kr---F_b: 1.9167(15)–1.9367(9) Å),[73] which is consistent with the greater covalent character of the Xe---F_b bond in **1** and contrasts with the electrostatic Xe---F_b bonds in $[F_5Xe(FKrF)_nAsF_6]$ (n = 1, 2) (2.550(2)–2.576(2) Å).[73] The Kr–F_t and Kr---F_b bond lengths of **1** are similar to those of **2** (Kr–F_t, 1.793(3) and 1.797(3) Å; Kr---F_b, 2.054(3) and 2.069(3) Å), and lie within the Kr–F bond length ranges of other $[Kr_2F_3]^+$ salts (Kr–F_t, 1.780(7)–1.805(5) Å; Kr---F_b, 2.027(5)–2.065(4) Å),[17,46] but are significantly longer and shorter, respectively, than in intimately ion-paired $[KrF]^+$ salts (Kr–F_t, 1.765(3)–1.774(6) Å; Kr---F_b, 2.090(6)–2.140(3) Å).[17,46]

The Xe–F_t bond in **1** is somewhat shorter than in $[Xe_2F_3]^+$ salts (1.901(4)–1.929(6) Å) and lies within the range of Xe–F_t bonds that have been reported for intimately ion-paired $[XeF]^+$ salts (1.854(4)–1.913(7) Å).[48,58] This indicates a greater degree of $[XeF]^+$ character in $[FKrFXeF]^+$ than in $[Xe_2F_3]^+$, in accordance with the enhanced covalent characters of the Kr–F_t and Kr---F_b bonds of $[FKrFXeF]^+$ relative to its Xe–F_t and Xe---F_b bonds. These trends are also observed in the QTAIM, NBO, MEPS, and ELF analyses of $[FKrFXeF]^+$ and $[Ng_2F_3]^+$ (see Computational Results).

Table 3.1. Summary of crystal data and refinement results for [FKrFXeF][AsF_6]·0.5KrF_2·2HF (1), ([Kr_2F_3][AsF_6])$_2$·XeF_4 (2), [Xe_2F_3][SbF_6] (3), XeF_4·KrF_2 (4), XeF_4·XeF_2 (5), XeF_4 (6), and [XeF_5][AsF_6] (7)

Compound	**1**	**2**	**3**	**4**	**5**	**6**	**7**
Space group	*Pbam*	$P2_1/n$	*Cc*	*Cmce*	$P2_1/c$	$P2_1/n$	*Ama*2
a (Å)	11.7093(5)	7.7079(13)	14.542(4)	12.1734(8)	6.4389(5)	4.9474(3)	9.796(2)
b (Å)	15.0296(6)	9.1056(16)	8.129(3)	10.4910(7)	7.2692(6)	5.7792(4)	13.272(2)
c (Å)	5.5794(2)	13.723(3)	9.971(3)	8.7562(6)	6.2293(5)	5.7872(4)	11.578(2)
β (°)	90	95.366(7)	130.421(9)	90	92.577(3)	100.279(2)	90
V (Å^3)	981.90(7)	958.9(3)	897.4(5)	1118.26(13)	291.27(4)	162.81(2)	1505.2(4)
Z	4	2	4	8	2	2	8
M_W (g mol^{-1})	521.92	1034.34	555.35	329.10	376.60	207.30	415.22
ρ_{calcd} (g cm^{-3})	3.531	3.582	4.111	3.910	4.294	4.229	3.665
T (°C)	–173	–173	–173	–173	–173	–173	–173
μ (mm^{-1})	13.678	14.581	10.592	14.057	11.665	10.498	9.103
R_1[a]	0.0442	0.0467	0.0244	0.0382	0.0181	0.0098	0.0356
wR_2[b]	0.1261	0.1177	0.0524	0.1409	0.0516	0.0249	0.0759

[a] $R_1 = \Sigma||F_o| - |F_c||/\Sigma|F_o|$. [b] $wR_2 = [\Sigma(w(F_o^2 - F_c^2)^2)/\Sigma(w(F_o^2)^2)]^{1/2}$.

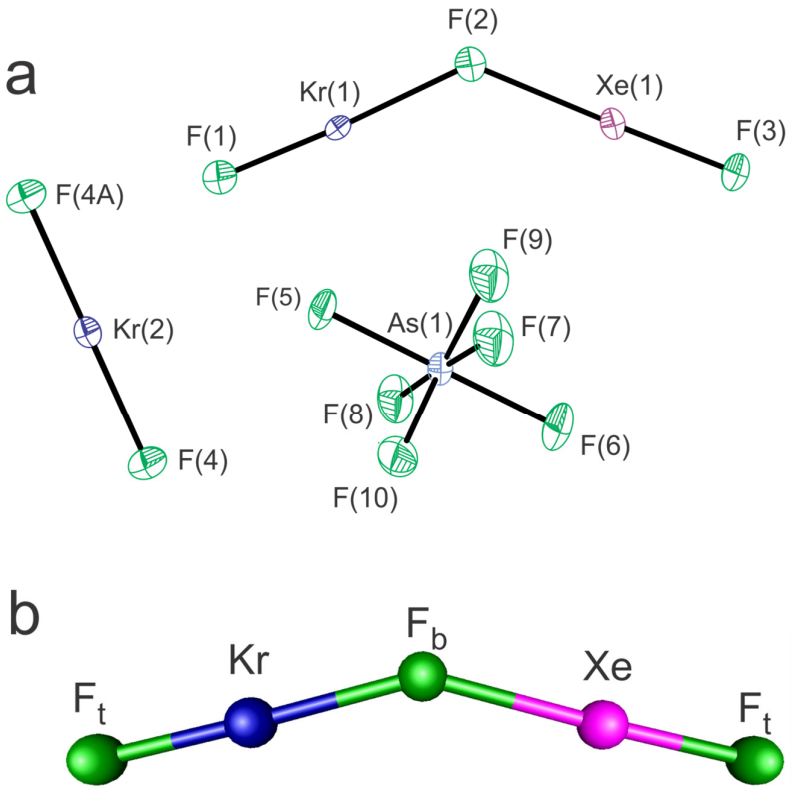

Figure 3.1. (a) The structural unit in the crystal structure of $[FKrFXeF][AsF_6]\cdot 0.5KrF_2\cdot 2HF$ (1), where one of two orientations of the disordered $[AsF_6]^-$ anion is shown (see Figure A1.1). Thermal ellipsoids are drawn at the 50% probability level. (b) The gas-phase optimized geometry of $[FKrFXeF]^+$ (B2PLYP-D3/Def2-TZVPD).

The Xe---F_b bond of **1** is somewhat longer than those of **3** (2.152(3) Å, 2.155(3) Å) and intermediate with respect to other $[Xe_2F_3]^+$ salts (2.139(7)–2.194(4) Å),[17,48,58] but shorter and more covalent than the Xe---F_b bonds of ion-paired $[XeF]^+$ salts (2.204(7)–2.343(4) Å).[48,58]

The Kr---F_b---Xe (131.8(2)°) angle of $[FKrFXeF]^+$ is notably smaller than the Xe---F_b---Xe angles of $[Xe_2F_3]^+$ salts (139.8(8)°–164.3(3)°),[17,48,58,59] and is intermediate with respect to the Kr---F_b---Kr angles of $[Kr_2F_3]^+$ salts (126.0(2)°–142.5(3)°).[17,46] The variations of Ng---F_b---Ng angles are consistent with their low experimental and calculated gas-phase vibrational frequencies (see Raman Spectroscopy) and their associated deformabilities, which are influenced by crystal packing.[46,48,59] The F_b---Ng–F_t angles of **1**–**3** (**1**, Kr, 177.1(2)° and Xe, 178.8(2)°; **2**, Kr, 177.0(1)° and 178.3(1)°; **3**, Xe, 176.3(1)° and 179.1(1)°) display small, but significant deviations from linearity that are consistent with other $[Ng_2F_3]^+$ salts.[17,46,48,59] Similar near-linear F_b---Ng–F_t angles were reproduced by the calculated gas-phase geometries of $[FKrFXeF]^+$ and $[Ng_2F_3]^+$ (see Computational Results).

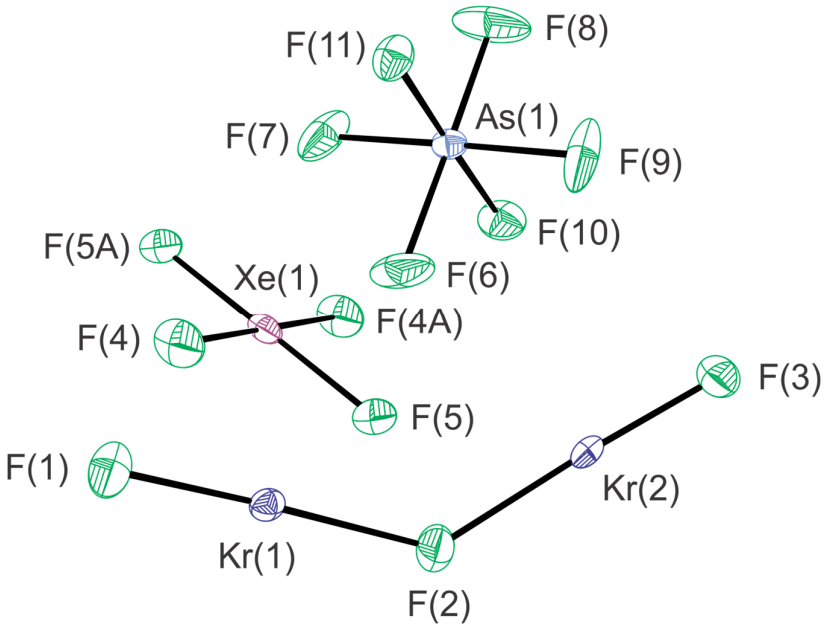

Figure 3.2. The structural unit in the crystal structure of $([Kr_2F_3][AsF_6])_2 \cdot XeF_4$ (**2**). Thermal ellipsoids are drawn at the 50% probability level.

Table 3.2. Experimental and calculated geometric parameters for the cations of $[FKrFXeF][AsF_6]\cdot 0.5KrF_2\cdot 2HF$ (**1**), $([Kr_2F_3][AsF_6])_2\cdot XeF_4$ (**2**), and $[Xe_2F_3][SbF_6]$ (**3**)[a]

	Exptl			Calcd[b]		
	$[Kr_2F_3]^+$ (**2**)	$[FKrFXeF]^+$ (**1**)	$[Xe_2F_3]^+$ (**3**)	$[Kr_2F_3]^+$ (**2′**)	$[FKrFXeF]^+$ (**1′**)	$[Xe_2F_3]^+$ (**3′**)
			Bond Lengths (Å)			
Kr–F_t	1.797(3) 1.793(3)	1.806(4)		1.797	1.795	
Kr---F_b	2.054(3) 2.069(3)	2.055(4)		2.092	2.075	
Xe–F_t		1.882(4)	1.924(3) 1.924(3)		1.912	1.914
Xe---F_b		2.172(4)	2.155(3) 2.152(3)		2.232	2.213
			Bond Angles (deg)			
F_t–Kr---F_b	178.3(1) 177.0(1)	177.1(2)		177.95	178.49	
F_t–Xe---F_b		178.8(2)	179.1(1) 176.3(1)		178.18	179.07
Kr---F_b---Kr	131.8(2)			142.12		
Kr---F_b---Xe		131.8(2)			149.89	
Xe---F_b---Xe			158.3(2)			162.58

[a] Geometric parameters for $[AsF_6]^-$ and $[SbF_6]^-$ are given in Tables A1.3–A1.5. [b] B2PLYP-D3/Def2-TZVPD (F, Kr, Xe).

$XeF_4 \cdot NgF_2$ (Ng = Kr (4), Xe (5)). A low-precision, RT SCXRD structure of **5** was previously reported[92] without an accompanying structural diagram. The LT, high-precision SCXRD structures of cocrystals **4** (Figures 3.3, A1.4a, and A1.5a) and **5** (Figures A1.4b, and A1.5b) are not isotypic and are comprised of XeF_4 and NgF_2 molecules that are weakly coordinated through electrostatic, σ-hole type fluorine-bridge interactions, where the shortest Xe^{IV}---F contact distances in **4** (3.219(1) Å) and **5** (3.083(2) Å) are close to the sums of the Xe and F van der Waals radii (vide supra). The XeF_4 and NgF_2 molecules of **4** and **5** both form columns along the *c*-axes and alternating layers of XeF_4 and NgF_2 molecules along the *a*- and *b*-axes of their unit cells (Figure A1.5).

The Xe^{IV}–F bond lengths in **4** (1.946(2)–1.950(2) Å) are equal to those of XeF_4 in **6** (1.9449(6), 1.9509(6) Å), whereas the Xe^{IV}–F bonds in **5** (1.937(1)–1.9412(9) Å) are somewhat shorter than those of **4** and **6**. There are two crystallographically nonequivalent XeF_4 molecules in the structural unit of **4**. The Xe atom of one XeF_4 molecule lies on a special position and has four symmetry-related long Xe^{IV}---F_{Kr} contacts (3.083(2) Å) with four neighboring KrF_2 molecules and two symmetry-related long Xe^{IV}---F_{Xe} contacts (3.508(2) Å) with two adjacent XeF_4 molecules (CN_{XeIV} = 4 + 6, Figure 3.3). The Xe atom of the second XeF_4 molecule has four symmetry-related long Xe^{IV}---F_{Kr} contacts (3.367(2) Å) with four neighboring KrF_2 molecules, and four symmetry-related long Xe^{IV}---F_{Xe} contacts (3.341(2) Å) with two neighboring XeF_4 molecules (CN_{XeIV} = 4 + 8, Figure A1.4a).

The Kr–F bonds of **4** (1.922(2) Å) are somewhat longer than those of α-KrF_2 (1.894(5) Å)[46] due to long Xe^{IV}---F_{Kr} contacts (2 x 3.083(2) Å), which polarize these bonds. In contrast, the Xe^{II}–F bonds of **5** (1.9940(9) Å) are equal to those of

crystalline XeF_2 (1.999(4) Å)[48] due to the less polarizing, longer Xe^{IV}---F_{XeII} contacts of **5** (2 x 3.219(1) Å).

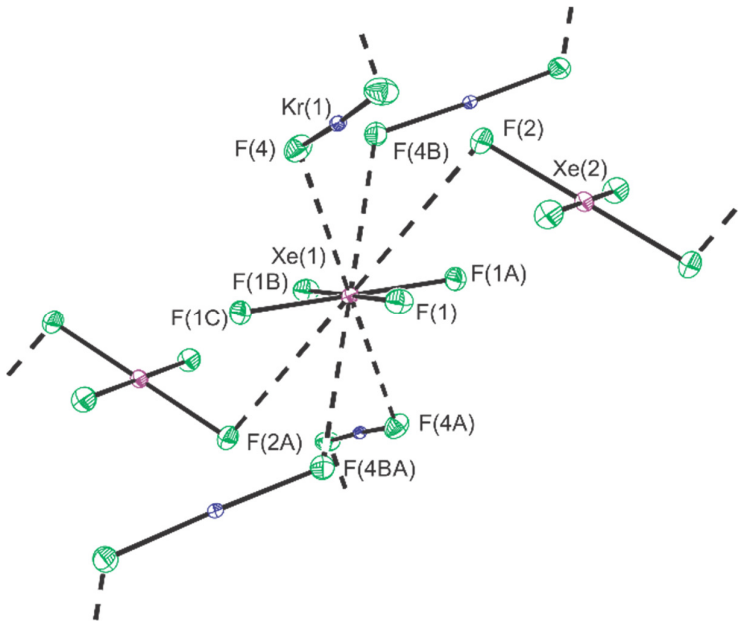

Figure 3.3. The coordination environment around $Xe_{(1)}F_4$ in the crystal structure of $XeF_4 \cdot KrF_2$ (**4**). Thermal ellipsoids are drawn at the 50% probability level. Diagrams showing the coordination environments around the $Xe_{(2)}F_4$ molecule of **4** (Figure A1.4a) and the XeF_4 molecule of $XeF_4 \cdot XeF_2$ (**5**) (Figure A1.4b) are provided in Appendix 1.

3.2.3. Raman Spectroscopy

The factor-group analysis of $[FKrFXeF][AsF_6] \cdot 0.5KrF_2 \cdot 2HF$ (**1**) and vibrational assignments of $[AsF_6]^-$ are provided in Appendix 1 (Figures A1.10– A1.12 and Table A1.8) along with those of $([Kr_2F_3][AsF_6])_2 \cdot XeF_4$ (**2**) (Figures A1.13– A1.16 and Table A1.9), $XeF_4 \cdot KrF_2$ (**4**) (Figures A1.17–S19, and Table A1.10), and $[(F_5Xe)_2(\mu\text{-}FKrF)(AsF_6)_2]$ (Figure A1.20 and Table A1.11).

The LT Raman spectrum of **1** is shown in Figure 3.4. Spectral assignments for the $[FKrFXeF]^+$ cation were made by comparison with the calculated gas-phase vibrational frequencies, mode displacements, and Raman intensities of the energy-minimized geometry of $[FKrFXeF]^+$ (**1'**, Table 3.3). The vibrational assignments for $[FKrFXeF]^+$ were also aided by comparison with the experimental and calculated vibrational frequencies of the related $[Ng_2F_3]^+$ cations (see Computational Results). Overall, the vibrational frequency trends are well reproduced by the calculations.

All vibrational bands of $[FKrFXeF]^+$ are split into two components that are attributed to vibrational mode coupling within the crystallographic unit cell, i.e., factor-group splitting. The origin of these splittings was verified by a factor-group analysis that is based on the X-ray crystal structure of **1** and was carried out using the "correlation method" [169] (Figure A1.10).

In addition to factor-group splitting, the calculated vibrational displacements of gas-phase $[FKrFXeF]^+$ reveal significant intra-ionic vibrational coupling between the Kr–F_t and Xe–F_t stretching modes and the Kr–F_b and Xe–F_b stretching modes, where similar couplings have been observed for $[Kr_2F_3]^+$ and $[Xe_2F_3]^+$.[17,48,59] The ν(Ng-F_t) and ν(Ng-F_b) modes each in-phase and out-of-phase couple to give a total of four stretching modes. The coupled ν(Ng-F_t) stretches occur at significantly higher frequencies than the coupled ν(Ng-F_b) stretches, which is consistent with their relative Ng–F bond lengths and formal bond orders deduced from resonance Structures III–V and NBO analyses (see Computational Results). Thus, the in-phase coupled mode, [ν(Kr-F_t) + ν(Xe-F_t)], occurs at higher frequency (exptl, 598/607 cm^{-1}; calcd, 613 cm^{-1}) than the out-of-phase coupled mode, [ν(Kr-F_t) − ν(Xe-F_t)] (exptl, 558/562 cm^{-1}; calcd, 595 cm^{-1}). The observed and calculated frequencies of the [ν(Kr-F_t) ± ν(Xe-F_t)]

modes are intermediate with respect to those of the [ν(Ng-F_t) ± ν(Ng′-F_t)] modes of $[Kr_2F_3]^+$ (exptl, 594–610 and 555–570 cm^{-1}; calcd, 616 and 589 cm^{-1}) and $[Xe_2F_3]^+$ (exptl, 589–596 and 570–578 cm^{-1}; calcd, 610 and 600 cm^{-1}). The in-phase coupled Ng–F_b stretching mode, [ν(Kr-F_b) + ν(Xe-F_b)], occurs at lower frequency (exptl, 304/308; calcd, 247 cm^{-1}) than its out-of- phase counterpart, [ν(Kr-F_b) − ν(Xe-F_b)] (exptl, 448/452 cm^{-1}; calcd, 422 cm^{-1}). The observed and calculated frequencies of the coupled [ν(Kr-F_b) ± ν(Xe-F_b)] modes are also intermediate with respect to the [ν(Ng-F_b) ± ν(Ng′-F_b)] modes of $[Kr_2F_3]^+$ (exptl, 330–358 and 437–462 cm^{-1}; calcd, 280 and 426 cm^{-1}) and $[Xe_2F_3]^+$ (exptl, 243–275 and 400–420 cm^{-1}; calcd, 200 and 416 cm^{-1}).[17,48,59]

The δ(F_tNgF_b) bending modes occur at much lower frequencies and are predicted to be weaker in intensity. The in-plane δ(F_tKrF_b)$_{i.p.}$ and δ(F_tXeF_b)$_{i.p.}$ bends couple in-phase (exptl, 160/162; calcd, 139 cm^{-1}) and out-of-phase (exptl, 181/183; calcd, 158 cm^{-1}), as do the out-of-plane δ(F_tKrF_b)$_{o.o.p.}$ and δ(F_tXeF_b)$_{o.o.p.}$ bends (i.p.: exptl, 172/174; calcd, 146 cm^{-1}; o.o.p.: exptl, 187/191; calcd, 199 cm^{-1}). These frequencies are comparable to those observed and calculated for $[Kr_2F_3]^+$ (exptl, 158–190 cm^{-1}; calcd, 163, 166, 164, 203 cm^{-1}) and $[Xe_2F_3]^+$ (exptl, 154–182 cm^{-1}; calcd, 132, 139, 140, 180 cm^{-1}).[17,48,59]

The δ(KrF_bXe) bending mode occurs at lowest frequency (calcd, 30 cm^{-1}), and could not be observed. The calculated frequency is comparable to and higher than those calculated for $[Kr_2F_3]^+$ (36 cm^{-1}) and $[Xe_2F_3]^+$ (15 cm^{-1}), respectively.

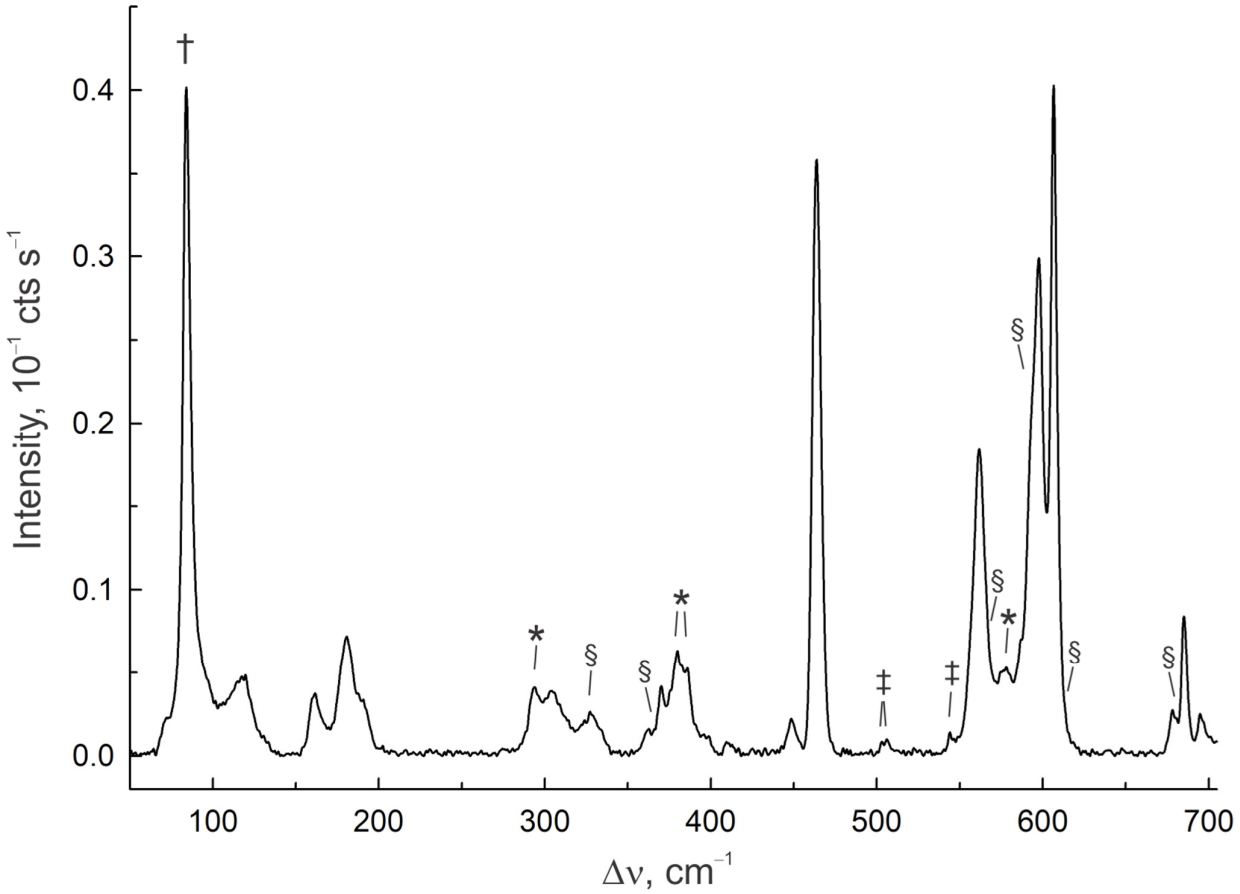

Figure 3.4. Raman spectrum of $[FKrFXeF][AsF_6]\cdot 0.5KrF_2\cdot 2HF$ (**1**) recorded under frozen aHF at −150 °C using 1064-nm excitation. The symbols denote $[Kr_2F_3][AsF_6]$ (§) and XeF_4 (‡) contaminant formed by redox decomposition of **1**, FEP sample tube bands (*), and an instrumental artifact (†).

Table 3.3. Experimental Raman frequencies of $[FKrFXeF]^+$ in $[FKrFXeF][AsF_6]\cdot 0.5KrF_2\cdot 2HF$ (**1**) and calculated vibrational frequencies, intensities, and assignments for $[FKrFXeF]^+$ (**1'**)

Exptl [a,b]	Calcd [a,c,d]	Assgnts [e]
607(100) 598(75) [f]	613(202)[7]	ν_1(A'), ν(Kr-F_t) + ν(Xe-F'$_t$)
562(45) 558(sh)	595(15)[194]	ν_2(A'), ν(Kr-F_t) − ν(Xe-F'$_t$)
452(sh) 448(5)	422(23)[608]	ν_3(A'), ν(Kr-F_b) − ν(Xe-F_b)
308(sh) 304(10)	247(9)[16]	ν_4(A'), ν(Kr-F_b) + ν(Xe-F_b)
191(8) 187(sh)	199(<1)[12]	ν_8(A''), $\delta(F_tKrF_b)_{o.o.p.}$ − $\delta(F'_tXeF_b)_{o.o.p.}$
183(15) [f] 181(18)	158(4)[2]	ν_5(A'), $\delta(F_tKrF_b)_{i.p.}$ − $\delta(F'_tXeF_b)_{i.p.}$
173(13) [f] 171(sh)	146(2)[2]	ν_9(A''), $\delta(F_tKrF_b)_{o.o.p.}$ + $\delta(F'_tXeF_b)_{o.o.p.}$
162(10) 160(sh) [f]	139(2)[1]	ν_6(A'), $\delta(F_tKrF_b)_{i.p.}$ + $\delta(F'_tXeF_b)_{i.p.}$
	30(3)[<0.1]	ν_7(A'), $\delta(KrF_bXe)$

[a] Frequencies are given in cm^{-1}. [b] Values in parentheses denote relative Raman intensities. Abbreviations denote shoulder (sh). The Raman spectrum was recorded under frozen aHF in an FEP sample tube at −150 °C using 1064-nm excitation. [c] B2PLYP-D3/Def2-TZVPD (F, Kr, Xe). [d] Values in parentheses and square brackets denote calculated Raman intensities ($Å^4$ amu^{-1}) and infrared intensities (km mol^{-1}), respectively. [e] Assignments are for the energy-minimized geometry of gas-phase $[FKrFXeF]^+$ (C_s). Abbreviations denote stretch (ν), bend (δ), in-plane (i.p.), out-of-plane (o.o.p.), terminal fluorine (F_t), bridging fluorine (F_b). [f] The band overlaps with a $[Kr_2F_3][AsF_6]$ band.

3.2.4. Computational Results

Quantum-chemical calculations were used to assess the bonding of $[FKrFXeF]^+$ (**1'**), $[Kr_2F_3]^+$ (**2'**), and $[Xe_2F_3]^+$ (**3'**). The NgF_2 molecules and $[NgF]^+$ cations were also calculated for comparison. Among the levels tested (Tables A1.12–A1.15), the B2PLYP-D3/Def2-TZVPD (F, Kr, Xe) level of theory gave the best agreement with experiment.

The NBO, QTAIM, ELF, and MEPS analyses were also carried out, with a fuller discussion of the QTAIM and ELF analyses given in Appendix 1 (Tables A1.16– A1.19 and Figures A1.21– A1.31).

3.2.4.1. Calculated Geometries

The calculated gas-phase geometries of **1'**, **2'**, and **3'** reproduce the V-shaped experimental geometries.

The calculated Kr–F_t [1.797 (**1'**), 1.795 (**2'**) Å] and Xe–F_t [1.912 (**1'**), 1.914 (**3'**) Å] bonds are significantly shorter than their respective Kr---F_b [2.075 (**1'**), 2.092 (**2'**) Å] and Xe---F_b [2.232 (**1'**), 2.213 (**3'**) Å] bonds, in accordance with their crystal structures (Table 3.2). The bond length trends, Kr–F_t (**1'**) < Xe–F_t (**1'**) and Kr---F_b (**1'**) < Xe---F_b (**1'**), agree with experiment and follow the relative covalent radii of Kr and Xe. Other bond length trends are also reproduced: Kr–F_t (**1'**) ≥ Kr–F_t (**2'**), Xe–F_t (**1'**) < Xe–F_t (**3'**), Kr---F_b (**1'**) ≈ Kr---F_b (**2'**), Xe---F_b (**1'**) ≥ Xe---F_b (**3'**).

The poorer agreement between the calculated and experimental Ng---F_b---Ng angles is related to their low calculated δ(NgF_bNg) bending frequencies (Tables A1.12–A1.13) and their high deformabilities, which render them susceptible to crystal packing.[48,59] Although comparisons of calculated and experimental Ng---F_b---Ng angles are complicated by the deformabilities of these angles, the calculated Kr---F_b---Kr and Kr---F_b---Xe angles are very similar, but smaller than the Xe---F_b---Xe angles [149.89° (**1'**), 142.12° (**2'**), 162.58° (**3'**)].

The small deviations of the calculated F_t–Ng---F_b angles from linearity well reproduce the experimental deviations [178.49 and 178.18° (**1'**), 177.95° (**2'**), 179.07°

(**3'**)]. Thus, the small deviations of these angles are not solely a consequence of crystal packing.

3.2.4.2. Natural Bond Orbital (NBO) Analyses

The NAO analyses (Table A1.16) show that the Ng, F_t, and F_b atoms of **1'**, **2'**, and **3'** have NPA charge distributions, Wiberg valences, and Wiberg bond indices that are consistent with resonance Structures III–V of $[Ng_2F_3]^+$ (See Section 1.2.1. of the Introduction).

The Kr and Xe charges of **1'** (Kr, 1.144; Xe, 1.341), **2'** (1.143), and **3'** (1.343) are very similar to those of $[NgF]^+$ (Kr, 1.166; Xe, 1.348) and are somewhat more positive than in NgF_2 (Kr, 1.071; Xe, 1.276) (Table A1.17). The F_t atom charges of **1'** (F_t (Kr), −0.330; F_t (Xe), −0.475) are nearly equal to those of **2'** (−0.323), **3'** (−0.480) and to the average F atom charges of NgF_2 and $[NgF]^+$ (Kr, −0.351; Xe −0.493). The F_b atom charge of **1'** (−0.679) is the average (−0.682) of the F_b atom charges in **2'** (−0.639) and **3'** (−0.725).

The Ng valences of **1'** (Kr, 1.040; Xe, 0.934) are equal to those of $[Ng_2F_3]^+$ (Kr, 1.039; Xe, 0.931) and, in turn, to the average Ng valences of $[NgF]^+$ and NgF_2 (Kr, 1.041; Xe, 0.947). The $F_{t(Kr)}$ (0.909) and $F_{t(Xe)}$ (0.792) valences of **1'** are nearly equal to those of $[Ng_2F_3]^+$ (Kr, 0.914; Xe, 0.786), whereas the $F_{b(Ng)}$ valence of **1'** (0.591) is the mean of the $F_{b(Kr)}$ (0.658) and $F_{b(Xe)}$ (0.516) valences in **2'** and **3'** (0.587). The Ng–F_t and Ng–F_b Wiberg bond indices of $[NgF]^+$, NgF_2, **1'**, **2'**, and **3'** show that Kr–F bonds are consistently more covalent than Xe–F bonds, in accordance with the higher electronegativity of krypton.[170,171]

3.2.4.3. Atoms in Molecules (AIM) Analyses

In general, indicators of bond covalency are provided by several AIM properties evaluated at the bond critical points[172] (see discussion and Tables A1.18, A1.19 in Appendix 1). The charge density contour maps of the Laplacian distributions ($\nabla^2\rho$) are provided for **1'**, **2'**, **3'**, NgF_2, and $[NgF]^+$ in Figure A1.21.

Overall, the Ng–F_t and Ng---F_b bond properties are consistent with their relative Ng–F_t and Ng---F_b bond lengths and Wiberg bond indices. Likewise, the AIM parameters of **1'**, **2'**, and **3'** are in accordance with Kr–$F_{t/b}$ bonds that are more covalent than Xe–$F_{t/b}$ bonds.

3.2.4.4. Electron Localization Function (ELF) Analyses

ELF analyses[173,174] were carried out for **1'**, **2'**, **3'**, NgF_2, and $[NgF]^+$ to visualize the behaviors of the Ng valence electron lone pairs (VELPs) of these species. ELF parameters are provided in Tables A1.18 and A1.19 and ELF isosurface plots are shown for the localization domains of **1'**, **2'**, **3'**, NgF_2, and $[NgF]^+$ (Figure 3.5 and Figures A1.22 and A1.23). In the ensuing discussion and figures, the abbreviations denote atomic basin populations, $\overline{N}$[A]; electron localization function, $\eta(\mathbf{r})$; core basin, C(A); monosynaptic valence basin, V(A); and closed isosurface, $\eta(\mathbf{r}) = f$, where $\eta(\mathbf{r})$ is defined as the isosurface contour.

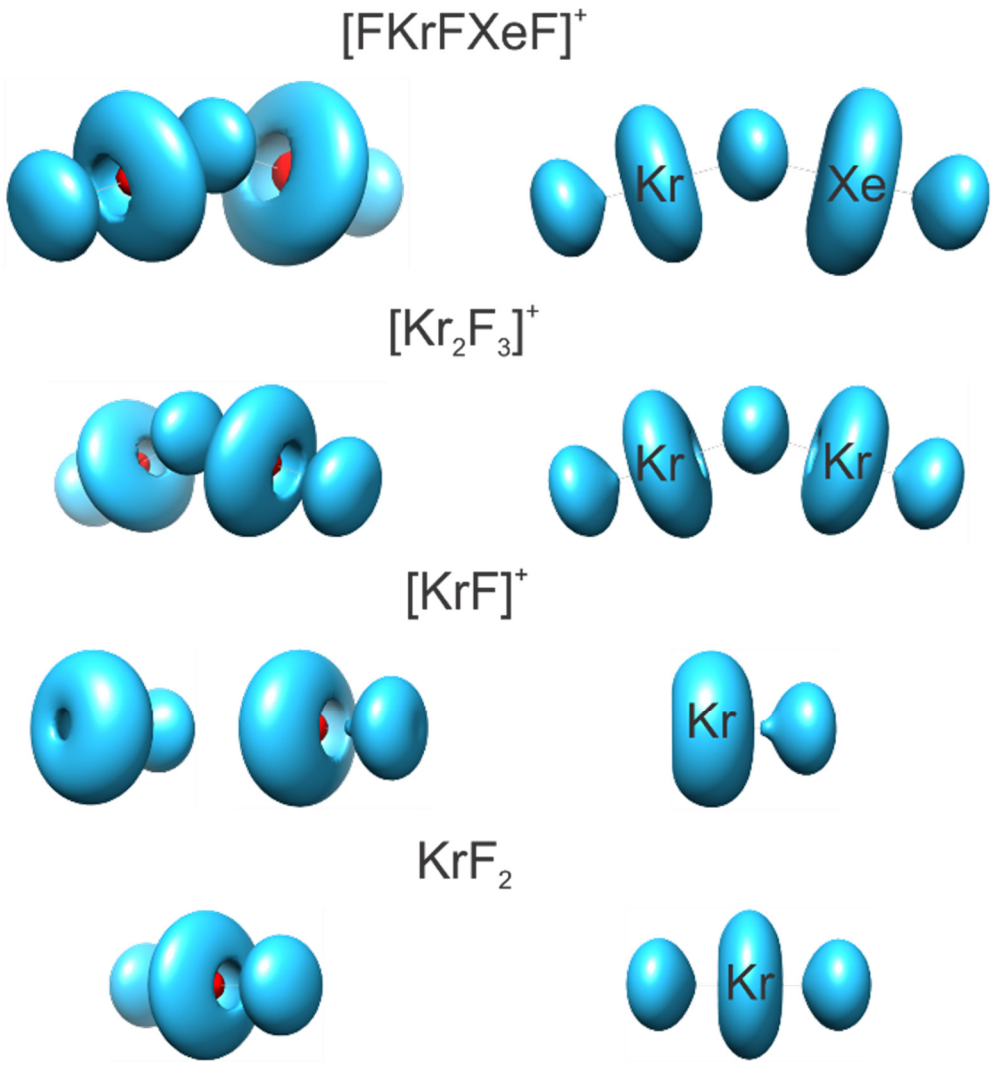

Figure 3.5. ELF isosurface plots at $\eta(r)$ = 0.60 (B2PLYP-D3/Def2-TZVPD) for $[FKrFXeF]^+$, $[Kr_2F_3]^+$, $[KrF]^+$, and KrF_2. Color code: red = core; blue = monosynaptic basin.

The ELF basin populations of the Kr and Xe cores are comparable for **1'**, **2'**, **3'**, NgF_2, and $[NgF]^+$. The ELF valence population analyses suggest an interpretation of bonding in which there is significant delocalization of electron density between the valence shells of the Ng atoms and those of its neighboring F atoms. The ELF analyses of **1'**, **2'**, **3'**, NgF_2, and $[NgF]^+$ only display monosynaptic Ng and F valence basins, in accordance with their polar-covalent bonds. The toroidal shapes of their Ng valence basins (Figure 3.5) result from the combination of the three-valence electron lone pair domains of Ng, with the atomic core electron basin (C(Ng)) lying at the center of the torus. Similar toroidal valence basins have been noted for the Ng (Ng = Kr or Xe) atoms of XeF_2,[175] $[XeF_3]^-$,[175] $[XeOTeF_5][Sb(OTeF_5)_6]\cdot SO_2ClF$,[176] $F_4OCrFNgF$,[65] $F_4OCrFNgF$-$CrOF_4$,[65] and $[F_5Xe(FKrF)_nAsF_6]$.[73] The small perturbations of the V(Ng) toroidal basins of **1'**, **2'**, and **3'** arise from accommodation of the V(Ng) basins to the asymmetries of their immediate environments.[65,73]

The V(Ng) basin perturbations of the $[NgF]^+$ cations are noteworthy because the VSEPR rules[88] predict a trigonal pyramidal AXE_3 arrangement of one electron bond pair (X) and three VELPs (E), where A is the Ng atom. Owing to strong mutual repulsions among the VELPs of Ng, the toroidal shape of the V(Ng) basin is maintained, with only a slightly closed toroidal hole on the side of the V(Ng) basin opposite to the Ng–F bond. Correspondingly, a region of high electrostatic potential occurs opposite to the Ng–F bond in the molecular electrostatic potential surfaces (MEPS) of $[KrF]^+$ and $[XeF]^+$ (vide infra).

The ELF reduction of localization diagrams for **1'**, **2'**, **3'**, NgF_2, and $[NgF]^+$ (Figures A1.24–A1.26), which provide the hierarchies of ELF basins and the corresponding basin separation values (f_{sep}), are discussed in Appendix 1.

3.2.4.5. Molecular Electrostatic Potential Surface (MEPS) Analyses

The MEPS isosurfaces of **1'**, **2'**, **3'**, NgF_2, and $[NgF]^+$ are depicted in Figure 3.6 and Figures A1.27– A1.31. The isosurfaces of NgF_2 confirm XeF_2 is more fluorobasic than KrF_2,[17] as reflected in the electrostatic potential (EP) minima of their fluorine ligand atoms (F_{Xe}, −92 kJ mol^{-1}; F_{Kr}, −74 kJ mol^{-1}) and in accordance with the relative electrophilicities of Xe and Kr and their EP maxima (Xe, 105 kJ mol^{-1}; Kr, 116 kJ mol^{-1}). Regions of most negative EP occur on the F ligands as rings around the C_∞-axes of NgF_2 (Figures 3.6 and A1.30). The most positive EPs of **1'**, **2'**, and **3'** lie between their respective Ng atoms (Kr 573 kJ mol^{-1}, Xe 568 kJ mol^{-1}; Kr 596 kJ mol^{-1}; Xe 537 kJ mol^{-1}) and are opposed to the lowest EP values of their F_t atoms (Kr 314 kJ mol^{-1}, Xe 277 kJ mol^{-1}; Kr 322 kJ mol^{-1}; Xe 269 kJ mol^{-1}).

The higher EP values of Kr relative to those of Xe are consistent with the greater electronegativity of Kr. Correspondingly, the maximum EP values of F_b in **2'** (358 kJ mol^{-1}), **1'** (370 kJ mol^{-1}) and **3'** (399 kJ mol^{-1}) increase with decreasing total electrophilicities of the Ng atoms. The Ng atoms of $[KrF]^+$ and $[XeF]^+$ display the most positive EP maxima in the series of noble-gas species examined in this study and are opposite to the Ng–F bonds and nearly equal for both cations. These regions correspond to highly directional σ-holes[164] that are aligned with the exposed Ng cores situated at the centers of the near-toroidal Ng valence basins (see ELF Analyses). Like NgF_2 (vide

supra), regions of lowest EP on the F ligands (Figures 3.6 and A1.30) occur as rings around the C_∞-axes of $[KrF]^+$ (503 kJ mol^{-1}) and $[XeF]^+$ (431 kJ mol^{-1}).

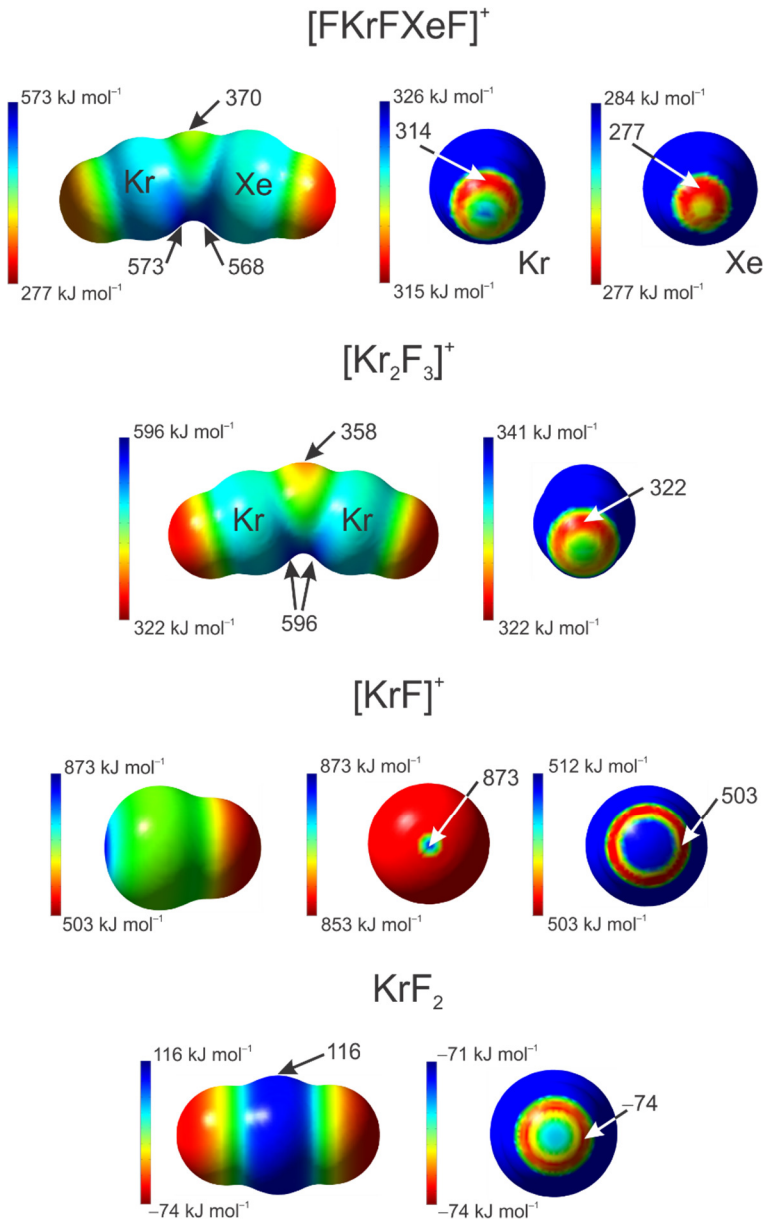

Figure 3.6. Molecular electrostatic potentials of $[FKrFXeF]^+$, $[Kr_2F_3]^+$, $[KrF]^+$, and KrF_2 are depicted at their 0.001 e a_0^{-3} isosurfaces where extrema are indicated by arrows (B2PLYP-D3/Def2-TZVPD).

3.3. Conclusion

The synthesis and structural characterization of $[FKrFXeF][AsF_6]\cdot 0.5KrF_2\cdot 2HF$ by LT single-crystal X-ray diffraction and LT Raman spectroscopy provides a unique example of a mixed Kr^{II}/Xe^{II} compound. The propensity of $[KrF]^+$, $[FKrFXeF]^+$, and KrF_2 to oxidatively fluorinate Xe^{II} to Xe^{IV} and Xe^{VI} at the low temperatures required the synthesis and structural characterization of the $[FKrFXeF]^+$ cation to be carried out in aHF solvent below −60 °C under rigorously anhydrous conditions. The thermally sensitive $[FKrFXeF][AsF_6]\cdot 0.5KrF_2\cdot 2HF$ salt undergoes rapid redox decomposition in the presence of excess KrF_2 between −60 and −38 °C in aHF solvent to yield XeF_4, $[Kr_2F_3][AsF_6]$, and Kr gas. The cocrystals, $([Kr_2F_3][AsF_6])_2\cdot XeF_4$ and $XeF_4\cdot KrF_2$; which crystallized from equilibrium mixtures of the decomposition products; KrF_2, XeF_4, and $[Kr_2F_3][AsF_6]$ in aHF solvent between −38 and 0 °C; provided the first examples of mixed Kr^{II}/Xe^{IV} compounds. The $([Kr_2F_3][AsF_6])_2\cdot XeF_4$ cocrystal underwent further redox decomposition at RT to yield $[F_5Xe][AsF_6]$, KrF_2, Kr gas, the known Kr^{II}/Xe^{VI} complexes, $[F_5Xe(FKrF)_nAsF_6]$ (n = 1, 2), and a new Kr^{II}/Xe^{VI} complex, $[(F_5Xe)_2(\mu\text{-}FKrF)(AsF_6)_2]$, which was characterized by LT Raman spectroscopy. Quantum-chemical calculations were employed to obtain gas-phase geometries, vibrational assignments. QTAIM, NBO, MEPS, and ELF analyses were employed to assess the nature of bonding in $[FKrFXeF]^+$ and $[Ng_2F_3]^+$, and show that their terminal Ng–F_t and Ng---F_b bonds are polar covalent, where the Ng–F_t bonds are significantly more covalent than Ng---F_b bonds, and Kr–F_t and Kr---F_b are more covalent than Xe–F_t and Xe---F_b.

CHAPTER 4

Syntheses and Structural Characterizations of the Cl(V) Coordination Complex, $[O_2Cl(FXeF)_2][AsF_6]$, and β-$[ClO_2][AsF_6]$

Adapted with permission from: Bortolus, M. R.; Ellwanger, M.; Haner, J.; Schrobilgen, G. J. *J. Fluor. Chem.* **2021**, *250*, 109814.

4.1. Introduction

Although the fluoride-ion donor properties of neutral Cl(V) and Br(V) fluorides and oxide fluorides have been studied,[141,143,177,178] the coordination chemistries of their cations have not been as extensively explored. The Lewis acidic $[XF_4]^+$, $[XOF_2]^+$, and $[XO_2]^+$ (X = Cl, Br) cations form intimate ion-paired fluoro-anion salts and therefore may be expected to form complexes with oxidatively resistant Lewis bases and polar-covalent fluorides. The noble-gas difluorides, NgF_2 (Ng = Kr, Xe), are moderate-strength fluoride-ion donors, which readily transfer fluoride ion to strong fluoride-ion acceptors such as PnF_5 (Pn = As, Sb, Bi)[46,48,51,179–181] to form intimately ion-paired $[NgF][PnF_6]$ salts. In contrast, the intermediate strength fluoride-ion acceptors, MOF_4 (M = Cr, Mo, W),[65,66,182–184] do not fully transfer fluoride ion but form neutral coordination complexes with NgF_2 by means of Ng–F---M bridges, e.g., $FNgF{---}CrOF_4$ and $F_4OCr{---}FNgF{---}CrOF_4$.

The fluoride-ion donor ability of NgF_2 has been exploited to synthesize the first examples of Br(V) adduct-cations, $[F_2OBr(FNgF)_2][AsF_6]$ (Ng = Xe, Kr)[62,63] and $[F_2OBr(FXeF)][AsF_6]$.[63] More recently, the reaction of excess BrO_2F with AsF_5 has provided a further example of a Br(V) complex cation, $[O_2Br(BrO_2F)_2][AsF_6]$.[139] To the authors' knowledge, there are no prior examples of structurally characterized Cl(V) or

I(V) cation coordination complexes. A prior attempt to synthesize $[F_2OCl(FXeF)_2][AsF_6]$ in aHF solvent by the reaction of $[ClOF_2][AsF_6]$ with XeF_2 resulted in fluoride-ion transfer with the formation of $ClOF_3$ and $[Xe_2F_3][AsF_6]$.[63]

The $[ClO_2]^+$ cation is anticipated to be a weaker fluoride-ion acceptor than $[ClOF_2]^+$, and may therefore form isolable coordination complexes with NgF_2 that do not readily dissociate or undergo fluoride-ion transfer reactions. The present work describes such a synthesis and the structural characterization of a Cl(V) coordination complex, $[O_2Cl(FXeF)_2][AsF_6]$, as well as a new low-temperature modification, β-$[ClO_2][AsF_6]$. Both salts were characterized by LT single-crystal X-ray diffraction (SCXRD) and LT Raman spectroscopy. Gas-phase geometry optimizations and NBO and MEPS analyses were employed to aid in the discussion of chemical bonding and calculated vibrational frequencies were used to aid with assignments of fundamental vibrational frequencies and $^{35/37}Cl$ isotopic shifts.

4.2. Results and discussion

4.2.1. Syntheses and properties

4.2.1.1. β-[ClO₂][AsF₆] (1) and α-[ClO₂][AsF₆].

The reaction of a 1:1 molar mixture of ClO_2F and AsF_5 in aHF at 22 °C yielded α-$[ClO_2][AsF_6]$ according to [Eq. (**4.1**)]. Rapid cooling of the sample from 22 to −196 °C followed by warming to −78 °C yielded a white polycrystalline solid that was shown to be

$$ClO_2F + AsF_5 \xrightarrow{aHF} \beta\text{-}[ClO_2][AsF_6] \xrightarrow{RT} \alpha\text{-}[ClO_2][AsF_6] \qquad (\mathbf{4.1})$$

β-$[ClO_2][AsF_6]$ (**1**) by recording its LT Raman spectrum under frozen aHF. Removal of the aHF at −78 °C yielded dry β-$[ClO_2][AsF_6]$, which underwent an irreversible phase

transition to the known α-$[ClO_2][AsF_6]$ phase upon warming to room temperature (RT). The α-phase had been previously synthesized by the RT reactions of ClO_2F with AsF_5,[142] and ClF_3 with As_2O_5.[178] Dissolution of α-$[ClO_2][AsF_6]$ in aHF at 0 °C followed by rapid cooling to −78 °C afforded **1** in quantitative yield. Single-crystals of **1** were grown by dissolution of α-$[ClO_2][AsF_6]$ (ca. 23 mg) in ca. 0.5 mL of aHF solvent at 22 °C and slowly cooling the sample to −10 °C over ca. 4 h.

4.2.1.2. $[O_2Cl(FXeF)_2][AsF_6]$ (2)

The reaction of $[ClO_2][AsF_6]$ with 3.59 equiv of XeF_2 at −20 °C in aHF solvent yielded **2** [Eq. (**4.2**)]. Although aHF solutions of $[O_2Cl(FXeF)_2][AsF_6]$ (**2**) were stable at RT, single crystals had to be grown by slow cooling of the aHF solution from −30 to −65 °C over ca. 5 h.

$$[ClO_2][AsF_6] + 2XeF_2 \xrightarrow{-20\ ^\circ C\ in\ aHF} [O_2Cl(FXeF)_2][AsF_6] \qquad (\mathbf{4.2})$$

4.2.1.3. Attempted Syntheses of $[O_2Cl(FXeF)_2][SbF_6]$

No reaction was observed when a ~1:3 molar ratio of $[ClO_2][SbF_6]$ and XeF_2 in aHF was warmed to 22 °C for ca. 5 min. In contrast, a ~1:8 molar ratio of $[ClO_2][SbF_6]$ and XeF_2 in aHF solution yielded $[Xe_2F_3][SbF_6]$ and ClO_2F when warmed to 22 °C for ca. 1 min [Eq. (**4.3**)]. Equation (**4.3**) is consistent with the lower fluorobasicity of $[SbF_6]^-$

$$[ClO_2][SbF_6] + 2XeF_2 \xrightarrow{aHF} [Xe_2F_3][SbF_6] + ClO_2F \qquad (\mathbf{4.3})$$

relative to that of $[AsF_6]^-$ in aHF, which results in sufficient enhancement of the Lewis acidity of $[ClO_2]^+$ to favor fluoride-ion abstraction from XeF_2 in preference to $[O_2Cl(FXeF)_n]^+$ (n = 1, 2) formation. Analogous fluoride-ion abstraction reactions occur

for $[XOF_2][AsF_6]$ (X = Cl, Br) and XeF_2 in aHF solution which have been shown to yield $[Xe_2F_3][AsF_6]$ and XOF_3.[63]

No reaction was observed when a ~1:3 molar mixture of $[ClO_2][SbF_6]$ and XeF_2 was dissolved in $CFCl_3$ at −78 °C. Upon warming to −30 °C, vigorous gas evolution ensued, and the solution color turned yellow, indicative of Cl_2 formation. When gas evolution ceased after ca. 15 s, the sample was immediately quenched at −196 °C. The LT Raman spectrum of the sample under frozen $CFCl_3$ showed only $[ClO_2][SbF_6]$ and solvent bands. Removal of $CFCl_3$ solvent under dynamic vacuum at −78 °C yielded a white solid, which had a LT Raman spectrum that corresponded to $[ClO_2][SbF_6]$.[143] A prior study has shown that XeF_2 slowly fluorinates $CFCl_3$ over 14 d at RT to yield CF_2Cl_2, CF_3Cl, Xe, and Cl_2, whereas the reaction rate was dramatically increased and went to completion within several hours in the presence of catalytic amounts of HF.[49] The aggressive redox fluorination of $CFCl_3$ by $XeF_2/[ClO_2][SbF_6]$ in the present study is likely attributable to a Lewis-acid catalyzed fluorination of $CFCl_3$ by XeF_2 that is activated by coordination of XeF_2 to the $[ClO_2]^+$ cation, e.g., $[O_2Cl\text{---}FXeF]^+$.

4.2.2. X-ray crystallography

Details of the data acquisition parameters and other crystallographic information for *β*-$[ClO_2][AsF_6]$ (**1**) and $[O_2Cl(FXeF)_2][AsF_6]$ (**2**) are provided in Table 4.1. The crystal structure of **1** is not isotypic with other $[ClO_2][MF_6]$ (M = P, As, Sb, Ir) salts.[141,143] Key experimental and calculated geometric parameters are given in Table 4.2 and Table A2.1 of Appendix 2 and the crystal structures of **1** and **2** are depicted in Figures 4.1 and 4.2, respectively. The geometry of $[ClO_2]^+$ may be described in terms of an AX_2E VSEPR[88]

arrangement of two double-bond domains (X) and a valence electron lone pair domain (E) around Cl (A) which result in a trigonal planar geometry in which the Cl valence electron lone pair (VELP) domain occupies one vertex of the triangle formed by the VELP and the Cl−O double-bond pair domains.

The As–F bond lengths of $[AsF_6]^-$ in **1** are similar to those of other ion-paired $[AsF_6]^-$ salts.[46,48] The short Cl---F_{As} secondary bonds between the cation and anion are significantly polarized so that the longest As–F bonds (1.731(3)–1.747(3) Å) correspond to the F atoms of the shortest Cl---F_{As} secondary bonds. The geometric parameters of $[AsF_6]^-$ in **2** are similar to those of **1**, and also show similar As–F bond length differences that result from short Cl---F_{As} secondary bonds.

4.2.2.1. β-[ClO_2][AsF_6] (1)

The geometric parameters of $[ClO_2]^+$ in **1** (Cl–O, 1.407(4), 1.408(4) Å; O–Cl–O, 119.2(2)°) occur within the ranges of Cl–O bond lengths (1.379(9)–1.418(4) Å) and O–Cl–O bond angles (117.2(9)–119.75(5)°) observed in other $[ClO_2]^+$ salts.[141,143,185–187]

The cations and anions of **1** are intimately ion-paired through four secondary Cl---F_{As} bonds (2.500(3)–2.758(3) Å), which are significantly shorter than the sum of the Cl and F van der Waals radii (3.22 Å,[167] 3.28 Å[168]) and avoid the stereo-active VELP domain of chlorine. The Cl---F_{As} bonds are directed towards four σ-holes on the Cl atom of $[ClO_2]^+$ (see 4.2.4.3. Molecular Electrostatic Potential Surface (MEPS) Analyses). The coordination environment of the Cl atom in **1** (CN_{Cl} = 2 + 4) is similar to those of X (X = Cl, Br) in $[XO_2][SbF_6]$[143] (Figure 4.1a). The ion-pairs of **1** pack in columns along the *b*-

axis with the cations and anions lying in separate *bc*-planes that alternate along the *a*-axis of the crystallographic unit cell (Figure 4.1b).

4.2.2.2. $[O_2Cl(FXeF)_2][AsF_6]$ (2)

The geometric parameters of $[ClO_2]^+$ in **2** are equal, within ±3σ, to those observed for **1** (Table 4.2 and Table A2.1 of Appendix 2). Terminal coordination of XeF_2 to the Cl atom of $[ClO_2]^+$ polarizes the Xe–F bonds and results in Xe–F_t bond contraction (1.9721(11) Å) and Xe–F_b bond elongation (2.0381(10) Å) relative to the Xe–F bonds of XeF_2 (1.999(2) Å).[48] The Xe–F_t bonds of **2** are comparable to those of $XeF_2{\cdot}CrOF_4$ (1.969(2) Å) and are somewhat longer than those of $[F_2OBr(FXeF)_2][AsF_6]$ (1.956(5), 1.960(4) Å),[63] whereas the Xe–F_b bonds are significantly shorter than in $XeF_2{\cdot}CrOF_4$ (2.057(2) Å)[65] and $[F_2OBr(FXeF)_2][AsF_6]$ (2.052(4), 2.053(4) Å).[63] The Xe–F bonds of **2** are significantly less polarized than those of $[XeF][AsF_6]$ (Xe–F_t, 1.888(3) Å; Xe–F_b, 2.208(3) Å),[48] which is consistent with the formation of a terminally coordinated XeF_2 complex. The bent Cl---F–Xe bond angles of **2** (125.45(4)°) are similar to the Cr---F–Ng bond angles of $NgF_2{\cdot}CrOF_4$ (Kr, 123.51(4)°; Xe, 118.50(8)°) and $NgF_2{\cdot}2CrOF_4$ (Kr, 119.77(3)°; Xe, 126.44(7)°],[65] and are significantly smaller than the Br---F–Xe bond angles of $[F_2OBr(FXeF)_2][AsF_6]$ (134.1(2) and 142.1(2)°).[63] The F–Xe–F bond angles of **2** (178.11(7)°) show small deviations from 180° that are similar to those of $[F_2OBr(FXeF)_2][AsF_6]$ (178.4(2), 179.8(2)°)[63] and $XeF_2{\cdot}CrOF_4$ (179.81(8)°).[65]

The $[ClO_2]^+$ cation of **2** interacts with the coordinated XeF_2 molecules and neighboring $[AsF_6]^-$ anions through Cl---F secondary bonds (Figure 4.2a, Table 4.2, and Figure A2.1, Table A2.1 of Appendix 2) that are significantly less than the sum of the Cl

and F van der Waals radii (*vide supra*) and avoid the stereo-active VELP domain on Cl. As in the case of **1**, the trajectories of the Cl---F secondary bonds are directed towards regions of high positive electrostatic potential (EP), σ-holes, on the Cl atom. The two shortest Cl---F_{Xe} secondary bonds result from terminal coordination of two XeF_2 molecules (2 x 2.4242(10) Å) into σ-holes located on both faces of the triangle defined by the two Cl–O double-bond domains and the VELP domain of Cl. The longest Cl---F secondary bonds are formed with the F atoms of neighboring $[AsF_6]^-$ anions (2.6350(13), 3.0307(13), 3.0307(13) Å) and are directed towards σ-holes on Cl which are trans to Cl–O double bond domains. This is presently the only example of a seven-coordinate, CN_{Cl} = 2 + 5, salt of $[ClO_2]^+$, whereas CN_{Cl} = 2 + 4 and CN_{Cl} = 2 + 6 have been observed for other $[ClO_2]^+$ salts.[141] Although the atomic radii increase from Cl to Br, the Cl---F_{Ng} bonds of **2** are significantly longer than the Br---F_{Ng} bonds of $[F_2OBr(FXeF)_2][AsF_6]$,[63] and the Xe–F bonds of the coordinated XeF_2 molecules of **2** are correspondingly less polarized, in accordance with the greater Lewis acidity of $[BrOF_2]^+$ relative to that of $[ClO_2]^+$.

Table 4.1. Summary of crystal data and refinement results for β-$[ClO_2][AsF_6]$ (**1**) and $[O_2Cl(FXeF)_2][AsF_6]$ (**2**)

	1	**2**
space group	*Pc*	$Cmc2_1$
a (Å)	5.6418(15)	13.7150(8)
b (Å)	5.0245(13)	9.4147(5)
c (Å)	9.985(3)	8.3911(5)
α (deg)	90	90
β (deg)	102.863(12)	90
γ (deg)	90	90
V (Å^3)	275.94(13)	1083.48(11)
Z (Molecules/unit cell)	2	4
M_W (g mol$^{-1)}$	256.37	594.97
ρ_{calcd} (g cm^{-3})	3.086	3.647
T (°C)	−173 °C	−173 °C
μ (mm^{-1})	6.720	9.657
R_1[a]	0.0448	0.0153
wR_2[b]	0.1149	0.0370

[a] $R_1 = \Sigma||F_o| - |F_c||/\Sigma|F_o|$. [b] $wR_2 = [\Sigma(w(F_o^2 - F_c^2)^2)/\Sigma(w(F_o^2)^2)]^{1/2}$.

Table 4.2. Experimental bond lengths (Å) for β-$[ClO_2][AsF_6]$ (**1**) and $[O_2Cl(FXeF)_2][AsF_6]$ (**2**) and calculated bond lengths (Å) for gas-phase $([O_2Cl(FXeF)_2][AsF_6]_2)^-$ (**2′**)[a]

	1		**2**	**2′**
	exptl		exptl	calcd[b]
Cl(1)–O(1)	1.407(4)	Cl(1)–O(1)	1.4107(16)	1.414
Cl(1)–O(2)	1.408(4)	Cl(1)–O(2)	1.4045(15)	1.415
		Xe(1)–F(5)	2.0381(10)	2.087
		Xe(1)–F(6)	1.9721(11)	1.977
Cl(1)---F(1)	2.500(3)	Cl(1)---F(5A)	2.4242(10)	2.331
Cl(1)---F(6B)	2.515(3)	Cl(1)---F(5B)	2.4242(10)	2.331
Cl(1)---F(3C)	2.728(3)	Cl(1)---F(1A)	2.6350(13)	2.689
Cl(1)---F(2A)	2.758(3)	Cl(1)---F(4)	3.0307(13)	3.069
		Cl(1)---F(4A)	3.0307(13)	3.069
As(1)–F(1)	1.734(3)	As(1)–F(1)	1.7283(12)	1.743
As(1)–F(2)	1.729(3)	As(1)–F(2)	1.7124(11)	1.738
As(1)–F(3)	1.731(3)	As(1)–F(2A)	1.7124(11)	1.738
As(1)–F(4)	1.701(3)	As(1)–F(3)	1.7194(13)	1.744
As(1)–F(5)	1.708(3)	As(1)–F(4)	1.7274(10)	1.774
As(1)–F(6)	1.747(3)	As(1)–F(4A)	1.7274(10)	1.774
		As(1A)–F(1A)	1.7283(12)	1.794
		As(1A)–F(2B)	1.7124(11)	1.744
		As(1A)–F(2BA)	1.7124(11)	1.744
		As(1A)–F(3A)	1.7194(13)	1.732
		As(1A)–F(4B)	1.7274(10)	1.749
		As(1A)–F(4BA)	1.7274(10)	1.749

[a] The labeling scheme corresponds to that used in Figure 4.2. Experimental bond angles for **1** and **2** and the calculated bond angles for the model anion, **2′**, are provided in Table A2.1 of Appendix 2. [b] B3LYP/Def2-TZVPD.

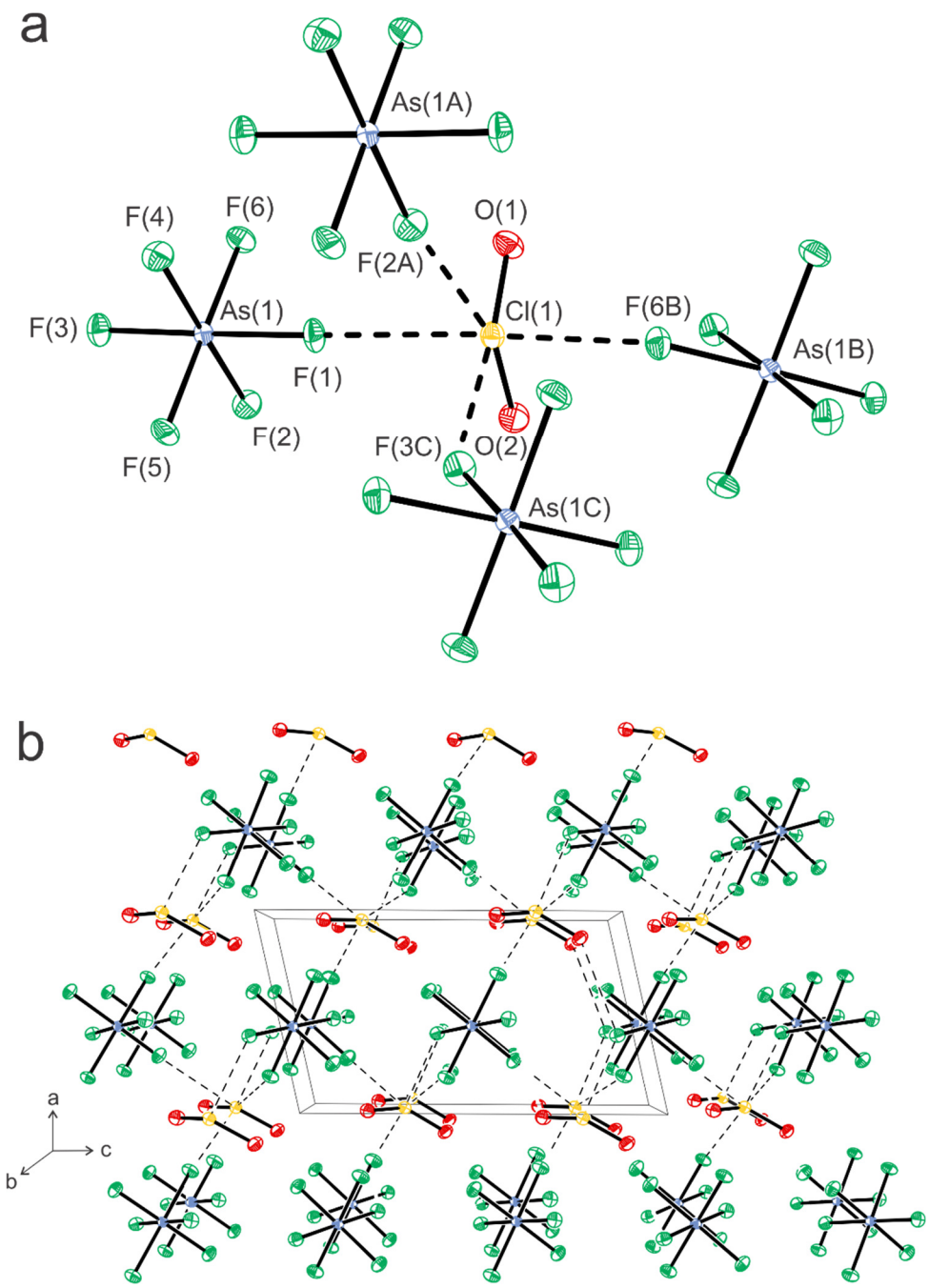

Figure. 4.1. (a) The coordination environment (CN_{Cl} = 2 + 4) of $[ClO_2]^+$ in *β*-$[ClO_2][AsF_6]$ (**1**). (b) A packing diagram showing the unit cell of **1** viewed along the *b*-axis of the unit cell. Thermal ellipsoids are drawn at the 50% probability level and secondary Cl---F bonding interactions are indicated by dashed lines.

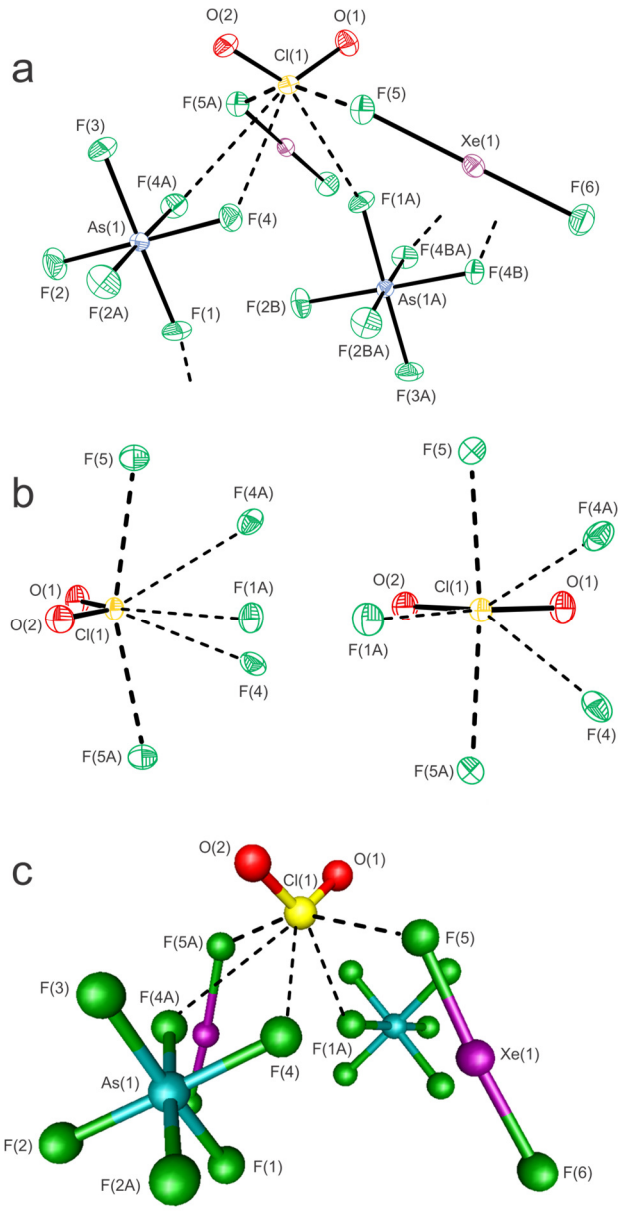

Figure. 4.2. (a) The structural unit in the crystal structure of $[O_2Cl(FXeF)_2][AsF_6]$ (**2**). Thermal ellipsoids are drawn at the 50% probability level and secondary Cl---F bonding interactions are indicated by dashed lines. (b) Expanded views of the chlorine coordination environment (CN_{Cl} = 2 + 5) of $[ClO_2]^+$ in $[O_2Cl(FXeF)_2][AsF_6]$ (**2**) from different perspectives. (c) The calculated (B3LYP/Def2-TZVPD (O, F, As, Cl, Xe)) gas-phase geometry of the model $([O_2Cl(FXeF)_2][AsF_6]_2)^-$ (**2′**) anion.

4.2.3. Raman spectroscopy

4.2.3.1. β-[ClO_2][AsF_6] (1) and α-[ClO_2AsF_6]

The solid-state, LT Raman spectra of *β*-[ClO_2][AsF_6] (**1**) and *α*-[ClO_2][AsF_6] are shown in Figure 4.3 and Figure A2.2 of Appendix 2, respectively. Spectral assignments (Table 4.3) were made by comparison with the Raman spectra of *α*-[ClO_2][AsF_6] (RT)[142] and [ClO_2][SbF_6] (−163 °C).[143]

The stretching bands of $[ClO_2]^+$ are split into two components having ca. ~3:1 relative intensity ratios due to chlorine isotope shifts ($\Delta\nu^{35/37}$) that arise from the natural abundance chlorine isotopes, ^{35}Cl (75.8%) and ^{37}Cl (24.2%).[143] The $^{35/37}Cl$ isotopic shifts resolved for **1** [$\Delta\nu_{as}(^{35/37}ClO_2)$, 14.4 cm^{-1}; $\Delta\nu_s(^{35/37}ClO_2)$, 5.6 cm^{-1}; $\Delta\delta(^{35/37}OClO)$, 5.4] are in good agreement with those of [ClO_2][SbF_6] [$\Delta\nu_{as}(^{35/37}ClO_2)$, 14.8 cm^{-1}; $\Delta\nu_s(^{35/37}ClO_2)$, 5.3 cm^{-1}; $\Delta\delta(^{35/37}OClO)$, not observed][143] and the calculated isotopic shifts of gas-phase $[ClO_2]^+$ [$\Delta\nu_{as}(^{35/37}ClO_2)$, 15.5 cm^{-1}; $\Delta\nu_s(^{35/37}ClO_2)$, 5.9 cm^{-1}; $\Delta\delta(^{35/37}OClO)$, 4.1 cm^{-1}]. The $\Delta\nu_{as}(^{35/37}ClO_2)$ and $\Delta\nu_s(^{35/37}ClO_2)$ bands also exhibit factor-group splittings. The formally Raman-inactive bands [$\nu_3(T_{1u})$, $\nu_4(T_{1u})$, $\nu_6(T_{2u})$] and Raman-active bands [$\nu_1(A_{1g})$, $\nu_2(E_g)$, $\nu_5(T_{2g})$] of $[AsF_6]^-$ were also observed as factor-group split bands in the Raman spectrum of **1**. Separate factor-group analyses were carried out for $[ClO_2]^+$ and $[AsF_6]^-$ (Figures A2.3 and A2.4, respectively, of Appendix 2) based on the X-ray crystal structure of **1** using the "correlation method".[169] The factor-group analysis predicts splitting of the $[ClO_2]^+$ vibrational bands into 3A′ and 3A″ components under unit cell symmetry, C_s, which were resolved on the $\nu_s(^{35/37}ClO_2)$ and $\nu_{as}(^{35}ClO_2)$ stretching bands. Site symmetry lowering of $[AsF_6]^-$ under crystal site symmetry (C_1) removes the

degeneracy of its $\nu_2(E_g)$, $\nu_3(T_{1u})$, $\nu_5(T_{2g})$, and $\nu_6(T_{2u})$ vibrational modes which, along with $\nu_1(A_{1g})$, vibrationally couple under C_s unit cell symmetry to give 15A′ and 15 A″ Raman-active modes, of which only 17 bands were observed (Table 4.3).

The fundamental vibrations of $[ClO_2]^+$ occur within the frequency ranges of other $[ClO_2][MF_6]$ (M = Sb,[143] Ru,[185] Ir[141,188]) salts: $\nu_s(ClO_2)$, 1056–1065 cm^{-1}; $\nu_{as}(ClO_2)$, 1287–1308 cm^{-1}; and δ(OClO), 518–519 cm^{-1}, and exhibit significant solid-state packing dependencies that are more pronounced for the $\nu_s(ClO_2)$ and $\nu_{as}(ClO_2)$ stretching modes than for the δ(OClO) bending mode. Accordingly, the ClO_2 stretching bands of **1** occur at significantly higher frequencies than those of *α*-$[ClO_2][AsF_6]$,[142] whereas δ(OClO) occurs at a similar frequency (Table 4.3).

4.2.3.2. $[O_2Cl(FXeF)_2][AsF_6]$ (2)

The LT Raman spectrum of **2** is shown in Figure 4.4. Spectral assignments were made by comparison with the calculated vibrational frequencies and Raman intensities of the energy-minimized, gas-phase geometry of the model anion, $([O_2Cl(FXeF)_2][AsF_6]_2)^-$ (**2′**) (Table 4.4 and Table A2.2 of Appendix 2), and well reproduced the experimental vibrational frequencies of **2**. The $[AsF_6]^-$ anion modes of **2**, which do not couple with $[ClO_2]^+$ or XeF_2 modes, are assigned under O_h symmetry in Table 4.4. More detailed anion mode assignments and descriptions that correspond to those of **2′** are provided in Table A2.2 of Appendix 2.

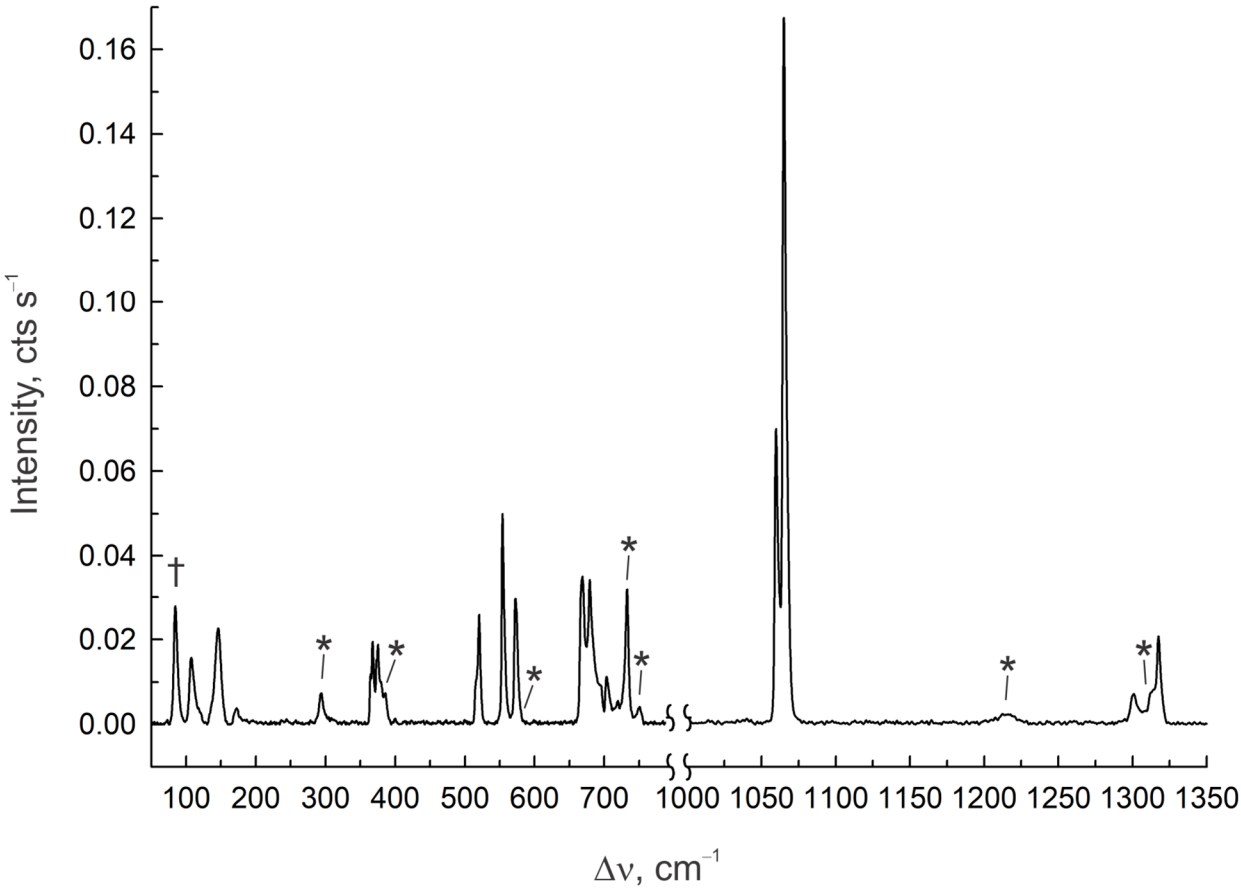

Figure. 4.3. Raman spectrum of β-$[ClO_2][AsF_6]$ (**1**) recorded on a dry powder at −150 °C using 1064-nm excitation. The symbols denote FEP sample tube bands (*) and an instrumental artifact (†).

Table 4.3. Experimental Raman frequencies (cm^{-1}), intensities, and assignments for α-$[ClO_2][AsF_6]$ and β-$[ClO_2][AsF_6]$ (**1**)

α-$[ClO_2][AsF_6]$ [a,b]	$\Delta\nu^{35/37}$ [c]	β-$[ClO_2][AsF_6]$ [b,d]	$\Delta\nu^{35/37}$ [c]	assgnts [e]
		1317.6(13)		
1293.9(14)	12.2	1312.7(sh)	14.4	$\nu_3(B_2)$, $\nu_{as}(^{35}ClO_2)$
1281.7(5)		1300.8(4)		$\nu_3(B_2)$, $\nu_{as}(^{37}ClO_2)$
		1067.5(sh)		
1044.9(100)	5.8	1065.2(100)	5.6	$\nu_1(A_1)$, $\nu_s(^{35}ClO_2)$
		1061.7(sh)		$\nu_1(A_1)$, $\nu_s(^{37}ClO_2)$
1039.1(27)		1059.9(42)		
728.1(11)		719.3(4)		
		703.3(8)		$\nu_3(T_{1u})$ ($[AsF_6]^-$)
693.2(8)		695.3(sh)		
		679.3(21)		$\nu_1(A_{1g})$ ($[AsF_6]^-$)
684.0(74)		668.7(21)		
575.5(18)		572.7(18)		$\nu_2(E_g)$ ($[AsF_6]^-$)
570.0(30)		554.1(30)		
		521.6(15)	5.4	$\nu_2(A_1)$, $\delta(O^{35}ClO)$
519.0(15)		516.2(sh)		$\nu_2(A_1)$, $\delta(O^{37}ClO)$
		400.1(1)		$\nu_4(T_{1u})$ ($[AsF_6]^-$)
		380.4(sh)		
372.1(23)		375.5(11)		
		373.1(sh)		$\nu_5(T_{2g})$ ($[AsF_6]^-$)
		368.7(12)		
		364.8(7)		
		256.7(1)		
		244.1(1)		
		239.3(sh)		$\nu_6(T_{2u})$ ($[AsF_6]^-$)
		235.8(1)		

[a] This work. The Raman spectrum was recorded in an FEP sample tube at −150 °C on a dry powder using 1064-nm excitation. Vibrational bands were also observed at 104.3(9), 117.0(5), 123.7(4), and 140.0(14) cm^{-1}, which are tentatively assigned to lattice modes. [b] Values in parentheses denote relative Raman intensities. The abbreviation (sh) denotes a shoulder. [c] $\Delta\nu^{35/37} = \nu(^{35}ClO_2) - \nu(^{37}ClO_2)$. [d] The Raman spectrum was recorded on a dry crystalline sample in an FEP sample tube at −150 °C. Bands were also observed at 107.4(10), 117.9(2), 146.2(14), 172.4(2), 186.7(sh), and 195.6(sh) cm^{-1} that are tentatively assigned to lattice modes. [e] Assignments were made under C_{2v} symmetry for the $[ClO_2]^+$ cation and O_h symmetry for the $[AsF_6]^-$ anion. Abbreviations denote stretch (ν), bend (δ), symmetric (s), and asymmetric (as).

The ion-paired formula unit of **2** possesses C_s symmetry in its crystal structure and in the calculated model anion (**2′**). Site symmetry lowering alone does not account for the Raman band splittings observed for the non-degenerate $[ClO_2]^+$ and $[AsF_6]^-$ modes of **2**. Consequently, a factor-group analysis (Figure A2.5 of Appendix 2), based on the X-ray crystal structure of **2,** was carried out by use of the "correlation method"[169] (see Appendix 2). Of the 84 coupled modes predicted by the factor-group analysis of **2**, only 27 were observed in the Raman spectrum, indicating that the majority of predicted splittings are too small to be resolved.

Chlorine isotopic shifts were resolved for the $[ClO_2]^+$ stretching modes of **2** [$\Delta\nu_{as}(^{35/37}ClO_2)$, 14.7 cm^{-1} and $\Delta\nu_s(^{35/37}ClO_2)$, 6.0 cm^{-1}] which are comparable to those of **1** (see Sec. 2.3.1), and are in excellent agreement with the calculated isotopic shifts of the cation stretching modes of **2′** [$\Delta\nu_{as}(^{35/37}ClO_2)$, 14.6 cm^{-1}; $\Delta\nu_s(^{35/37}ClO_2)$, 6.7 cm^{-1}]. The $\Delta\nu_s(^{35/37}ClO_2)$ stretches (1071.2, 1077.2 cm^{-1}) of **2** occur at significantly higher frequencies than the $\Delta\nu_s(^{35/37}ClO_2)$ stretches of **1** (1059.9/1061.7, 1065.2/1067.5 cm^{-1}), whereas the $\Delta\nu_{as}(^{35/37}ClO_2)$ stretches of **2** (1301.2, 1315.9 cm^{-1}) occur at frequencies comparable to the $\Delta\nu_{as}(^{35/37}ClO_2)$ stretches of **1** (1300.8, 1315.2 cm^{-1}). The in-plane bending mode, $\delta(O_1ClO_2)_{i.p.}$, occurs at significantly higher frequency (536.1 cm^{-1}) than the bending mode of **1** (516.2, 521.6 cm^{-1}). The out-of-plane bending mode, $\delta(O_1ClO_2)_{o.o.p.}$, was calculated at 305.9 cm^{-1}, but was not observed.

Terminal coordination of XeF_2 to $[ClO_2]^+$ results in two polarized XeF_2 molecules which do not display in-phase and out-of-phase coupling between their $\nu(Xe\text{-}F_t)$ and $\nu(Xe\text{-}F_b)$ stretches. Instead, the $\nu(Xe\text{-}F_t)$ stretching modes in-phase and out-of-phase

couple, as do the $\nu(Xe\text{-}F_b)$ modes, to give two in-phase and two out-of-phase Xe–F stretching modes: $\nu_s(Xe\text{-}F_t) = [\nu(Xe_1\text{-}F_6) + \nu(Xe_{1A}\text{-}F_{6A})]$, $\nu_{as}(Xe\text{-}F_t) = [\nu(Xe_1\text{-}F_6) - \nu(Xe_{1A}\text{-}F_{6A})]$, $\nu_s(Xe\text{-}F_b) = [\nu(Xe_1\text{-}F_5) + \nu(Xe_{1A}\text{-}F_{5A})]$, and $\nu_{as}(Xe\text{-}F_b) = [\nu(Xe_1\text{-}F_5) - \nu(Xe_{1A}\text{-}F_{5A})]$. Analogous couplings have been observed and assigned for the $\nu(Ng\text{-}F_t)$ and $\nu(Ng\text{-}F_b)$ stretching modes of $[F_2OBr(FNgF)_2][AsF_6]$,[62,63] $[Mg(FXeF)_4(AsF_6)_2]$,[189] $[Hg(KrF_2)_8][AsF_6]_2$,[190] and $[F_5Xe(FKrF)_2AsF_6]$,[73] which also do not exhibit cross coupling of their $\nu(Ng\text{-}F_t)$ and $\nu(Ng\text{-}F_b)$ stretches. The $\nu_s(Xe\text{-}F_t)$ (519 cm^{-1}) and $\nu_{as}(Xe\text{-}F_t)$ (531, 481 cm^{-1}) modes of **2** occur at significantly higher frequencies than their $\nu_s(Xe\text{-}F_b)$ (447 cm^{-1}) and $\nu_{as}(Xe\text{-}F_b)$ (436/439 cm^{-1}) modes, in accordance with the greater covalent characters of the Xe–F_t bonds. The $\nu_s(Xe\text{-}F_t)$ mode is weakly in-phase coupled with the $\delta(O_1ClO_2)_{i.p.}$ mode and occurs at a frequency (519.0 cm^{-1}) that is intermediate with respect to its asymmetric counterpart, $\nu_{as}(Xe\text{-}F_t)$. The latter mode is in-phase and out-of-phase coupled with $[\nu(As_1\text{-}F_2) + \nu(As_1\text{-}F_{4A})] - [\nu(As_1\text{-}F_{2A}) + \nu(As_1\text{-}F_4)]$ (530.9 cm^{-1}) and $[\nu(As_1\text{-}F_{2A}) + \nu(As_1\text{-}F_4)] - [\nu(As_1\text{-}F_2) + \nu(As_1\text{-}F_{4A})]$ (481.1 cm^{-1}), respectively. The symmetric $\nu_s(Xe\text{-}F_b)$ mode also occurs at higher frequency (446.7 cm^{-1}) than the asymmetric $\nu_{as}(Xe\text{-}F_b)$ mode (435.6/439.4 cm^{-1}), which is weakly in-phase coupled with $\delta(O_1ClO_2)_{o.o.p.}$.

The $\delta(FXeF)$ bending modes are also in-phase and out-of-phase coupled to give four modes: $\delta_s(FXeF)_{i.p.} = [\delta(F_5Xe_1F_6)_{i.p} + \delta(F_5Xe_1F_6)_{i.p}]$, $\delta_s(FXeF)_{o.o.p.} = [\delta(F_5Xe_1F_6)_{o.o.p} + \delta(F_5Xe_1F_6)_{o.o.p}]$, $\delta_{as}(FXeF)_{i.p.} = [\delta(F_5Xe_1F_6)_{i.p} - \delta(F_5Xe_1F_6)_{i.p}]$ and $\delta_{as}(FXeF)_{o.o.p.} = [\delta(F_5Xe_1F_6)_{o.o.p} - \delta(F_5Xe_1F_6)_{o.o.p}]$. Only the $\delta_s(FXeF)_{o.o.p.}$ band (233.7 cm^{-1}) was observed,

with a frequency similar to those of the δ(FXeF) bending modes of $[F_2OBr(FXeF)][AsF_6]$ (244 cm^{-1}) and $[F_2OBr(FXeF)_2][AsF_6]$ (232, 299 cm^{-1}).[63]

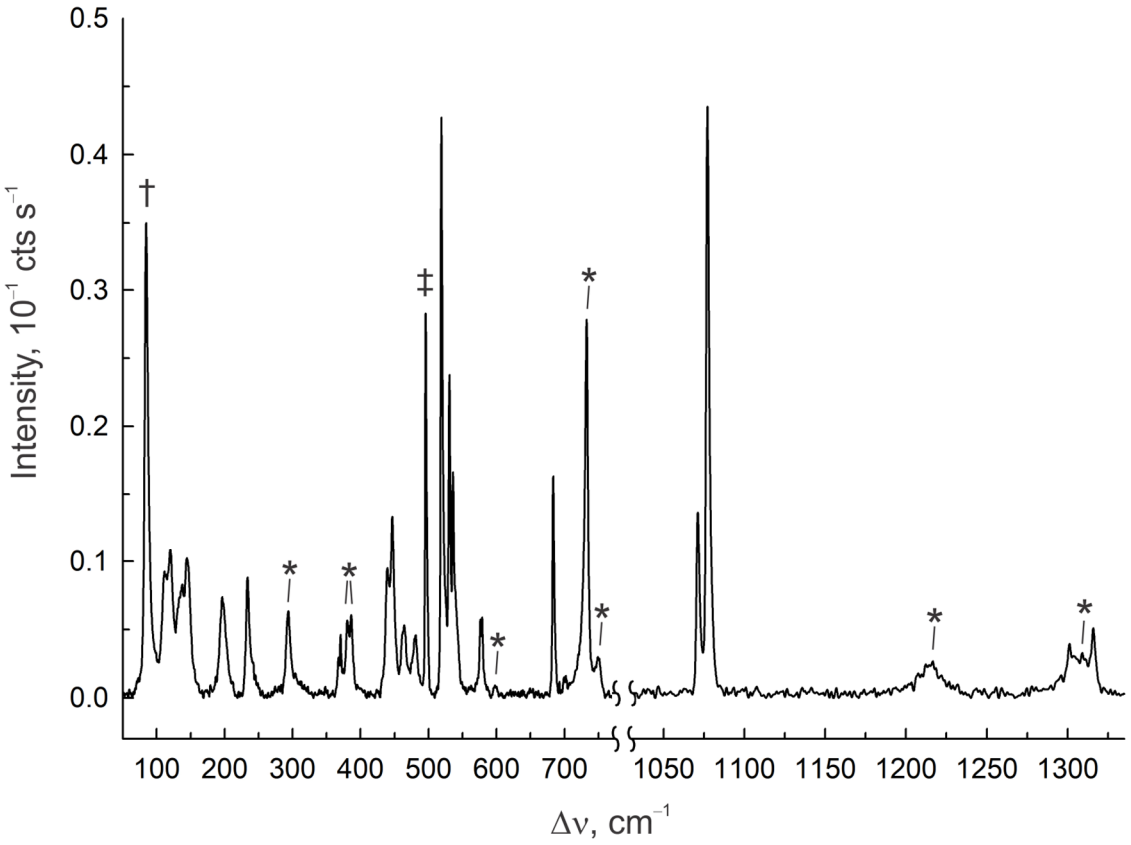

Figure. 4.4. Raman spectrum of $[O_2Cl(FXeF)_2][AsF_6]$ (**2**) recorded on a dry crystalline sample at −150 °C using 1064-nm excitation. Symbols denote bands assigned to excess XeF_2 (‡), FEP sample tube bands (*), and an instrumental artifact (†).

Table 4.4. Experimental Raman frequencies (cm^{-1}) and intensities for $[O_2Cl(FXeF)_2][AsF_6]$ (**2**),[a] and the calculated vibrational frequencies (cm^{-1}), intensities, and assignments for the model anion, $([O_2Cl(FXeF)_2][AsF_6]_2)^-$ (**2′**)[b]

2		**2′**			
exptl [a]	$\Delta\nu^{35/37}$ [c]	^{35}Cl calcd [b]	^{37}Cl calcd [b]	$\Delta\nu^{35/37}$ [c]	**assgnts** [d]
1315.9(11)	14.7	1335.6(16)[139]	1320.9(16)[134]	14.7	$[\nu(Cl–O_1) - \nu(Cl–O_2)]$
1301.2(9)					
1077.2(100)	6.0	1133.0(237)[64]	1126.3(236)[61]	6.7	$[\nu(Cl–O_1) + \nu(Cl–O_2)]$
1071.2(32)					
		702.3(<1)[205]	702.3(<1)[205]		$\nu_3(T_{1u})$ ($[AsF_6]^-$)
701.9(5)		696.5(1)[270]	696.5(1)[269]		
699.4(5)		693.6(5)[172]	693.6(5)[172]		
692.1(3)		690.4(7)[19]	690.4(7)[19]		
		686.0(<1)[339]	686.0(<1)[339]		
		684.0(1)[114]	684.0(1)[113]		
685.6(sh)		648.6(29)[32]	648.6(29)[32]		$\nu_1(A_{1g})$ ($[AsF_6]^-$)
683.5(36)		646.8(5)[77]	646.8(5)[77]		
578.9(14)		564.1(3)[1]	564.1(3)[1]		$\nu_2(E_g)$ ($[AsF_6]^-$)
576.3(14)					
539.4(sh)		562.0(6)[9]	561.5(6)[13]	0.5	$[\nu(As_1\text{-}F_1) + \nu(As_1\text{-}F_3)] - [\nu(As_1\text{-}F_2) + \nu(As_1\text{-}F_{2A}) + \nu(As_1\text{-}F_4) + \nu(As_1\text{-}F_{4A})] + [\delta(O_1ClO_2)_{i.p.}]_{small}$
536.1(39)		551.0(4)[18]	548.7(8)[18]	2.3	$\delta(O_1ClO_2)_{i.p.}$
530.9(55)		545.5(9)[8]	545.4(29)[192]	0.1	$[\nu(Xe_1\text{-}F_6) - \nu(Xe_{1A}\text{-}F_{6A})] + [\nu(As_1\text{-}F_2) + \nu(As_1\text{-}F_{4A})] - [\nu(As_1\text{-}F_{2A}) + \nu(As_1\text{-}F_4)]$
519.0(98)		542.2(33)[198]	541.5(26)[186]	0.7	$[\nu(Xe_1\text{-}F_6) + \nu(Xe_{1A}\text{-}F_{6A})] + [\delta(O_1ClO_2)_{i.p.}]_{small}$
481.1(11)		535.9(11)[71]	535.9(11)[72]		$[\nu(Xe_1\text{-}F_6) - \nu(Xe_{1A}\text{-}F_{6A})] - [\nu(As_1\text{-}F_2) + \nu(As_1\text{-}F_{4A})] + [\nu(As_1\text{-}F_{2A}) + \nu(As_1\text{-}F_4)]$
464.2(11)		520.7(4)[28]	520.3(4)[28]	0.4	$[\nu(As_{1A}\text{-}F_{1A}) + \nu(As_{1A}\text{-}F_{3A})] + [\delta(O_1ClO_2)_{i.p.}]_{small}$
446.7(30)		440.0(3)[241]	440.0(3)[242]		$[\nu(Xe_1\text{-}F_5) + \nu(Xe_{1A}\text{-}F_{5A})]$
439.4(23)	3.8	426.9(2)[84]	426.0(2)[95]	0.9	$[\nu(Xe_1\text{-}F_5) - \nu(Xe_{1A}\text{-}F_{5A})] + [\delta(O_1ClO_2)_{o.o.p.}]_{small}$
435.6(sh)					
		393.3(<0.01)[151]	393.1(<0.01)[142]	0.2	
		392.2(<1)[<1]	392.2(<1)[<1]		$\nu_4(T_{1u})$ $[AsF_6]^-$
400.2(1)		389.8(<1)[63]	389.8(<1)[63]		
394.0(2)		388.8(<1)[<1]	388.8(<1)[<1]		
		388.0(<1)[53]	388.0(<1)[53]		
		387.0(<1)[81]	387.0(<1)[82]		
		356.7(<1)[<1]	356.7(<1)[<1]		$\nu_5(T_{2g})$ $[AsF_6]^-$
		354.3(<1)[1]	354.3(<1)[1]		
370.7(11)		353.4(<1)[<1]	353.4(<1)[<1]		
367.6(7)		351.6(1)[<1]	351.5(1)[<1]	0.1	
		351.4(<1)[2]	351.4(<1)[2]		
		349.4(1)[<1]	349.1(1)[<1]	0.3	

continued …

Table 4.4 (continued)

2		**2′**			
exptl [a]	$\Delta\nu^{35/37}$ [c]	^{35}Cl calcd [b]	^{37}Cl calcd [b]	$\Delta\nu^{35/37}$ [c]	**assgnts** [d]
233.7(20)		246.0(4)[<1]	246.0(4)[<1]		$[\delta(F_5Xe_1F_6)_{o.o.p.} + \delta(F_{5A}Xe_{1A}F_{6A})_{o.o.p.}]$
		305.9(18)[315]	302.2(18)[305]	3.7	$\delta(O_1ClO_2)_{o.o.p.}$
		235.9(<0.1)[<1]	235.9(<0.1)[<1]		$\nu_6(T_{2u})$ $[AsF_6]^-$
		234.1(<0.1)[<1]	234.1(<0.1)[<1]		
		232.9(<0.1)[<0.1]	232.9(<0.1)[<0.1]		
		229.2(<0.1)[<1]	229.2(<0.1)[<1]		
		225.3(<0.1)[<1]	225.3(<0.1)[<1]		
		225.0(<0.1)[2]	225.0(<0.1)[2]		
196.3(16)					Lattice mode
		219.7(<1)[19]	219.6(<1)[18]	0.1	$[\delta(F_5Xe_1F_6)_{o.o.p.} - \delta(F_{5A}Xe_{1A}F_{6A})_{o.o.p.}]$
		208.6(<1)[38]	208.5(<1)[38]	0.1	$[\delta(F_5Xe_1F_6)_{i.p.} + \delta(F_{5A}Xe_{1A}F_{6A})_{i.p.}]$
		206.6(<1)[<1]	206.5(<1)[<1]	0.1	$[\delta(F_5Xe_1F_6)_{i.p.} - \delta(F_{5A}Xe_{1A}F_{6A})_{i.p.}]$
		155.8(<1)[<1]	155.5(<1)[<1]	0.3	Deformation modes
		132.9(1)[5]	131.9(1)[4]		
		127.2(4)[7]	126.5(3)[7]	0.7	
		116.8(2)[27]	116.3(2)[27]	0.5	
		103.0(5)[<1]	103.0(5)[<1]		
		82.6(1)[<1]	82.5(1)[<1]	0.1	
		71.7(3)[2]	71.6(3)[2]	0.1	
		66.9(<1)[15]	66.6(<1)[15]	0.3	
		61.4(2)[<1]	61.3(2)[<1]	0.1	
		52.6(<0.1)[<1]	52.6(<0.1)[<1]		
		52.4(<1)[2]	52.3(<1)[2]	0.1	
		49.6(<1)[3]	49.6(<1)[3]		
		43.0(<1)[<1]	43.0(<1)[<1]		
		36.4(<1)[2]	36.4(<1)[2]		
		29.3(<1)[<1]	29.3(<0.1)[<1]		
		29.3(<0.1)[<1]	29.3(<1)[<1]		
		18.2(<0.1)[<1]	18.2(<1)[<1]		
		14.9(<1)[1]	14.9(<1)[1]		
		13.2(<1)[1]	13.2(<0.1)[<1]		
		11.8(<0.1)[<1]	11.8(<0.1)[<1]		
		−22.6(<1)[<0.1]	−22.6(<0.1)[<1]		

continued …

Table 4.4. (continued) [a] The Raman spectrum was recorded on a dry crystalline sample in an FEP sample tube at −150 °C using 1064-nm excitation. Vibrational bands were also observed at 101.6(7), 111.4(20), 113.7(20), 120.0(25), 133.5(16), 137.6(18), 144.1(23), and 196.3(16) cm^{-1} that are tentatively assigned to lattice modes. Abbreviation denotes a shoulder (sh). [b] B3LYP/Def2-TZVPD. The atom labeling scheme is the same as that shown in Figure 4.2b. Values in parentheses and square brackets denote calculated Raman intensities ($Å^4$ amu^{-1}) and infrared intensities (km mol^{-1}), respectively. [c] $\Delta\nu^{35/37}$ = $\nu(^{35}Cl)$ − $\nu(^{37}Cl)$. [d] General assignments were made under O_h symmetry for the $[AsF_6]^-$ anion, however, more detailed vibrational assignments for the $[AsF_6]^-$ anion are provided in Table A2.2 of Appendix 2. Abbreviations denote stretch (ν), bend (δ), in-plane (i.p.), and out-of-plane (o.o.p.). The ClO_2-plane lies in the *bc*-mirror plane of the crystallographic unit cell.

4.2.4. Computational results

Quantum-chemical calculations were used to assess the bonding in the model $([O_2Cl(FXeF)_2][AsF_6]_2)^-$ (**2′**) anion. The calculation at the B3LYP/Def2-TZVPD level of theory resulted in a stationary point with one imaginary frequency (-22.6 cm^{-1}). The calculated geometry of gas-phase **2′** well reproduced the coordination environment of the $[ClO_2]^+$ cation in the crystal structure of **2** (Figure 4.2c, Table 4.2, and Table A2.1 of Appendix 2). Parallel calculations for $[ClO_2]^+$ and XeF_2 at the same level of theory (Tables A2.3–A2.5 of Appendix 2) resulted in stationary points with all frequencies real and enabled comparisons with **2′**. An NBO (Table A2.6 of Appendix 2) analysis of **2′** was also carried out to aid in the discussion of the chemical bonding in **2**, and NBO (Tables A2.7 and A2.8 of Appendix 2) and MEPS (Figure 4.5) analyses of $[XO_2]^+$ (X = Cl, Br, I) were implemented to help assess the feasibility of synthesizing $[O_2X(FNgF)_2][AsF_6]$ (X = Br, I; Ng = Kr, Xe) analogues.

4.2.4.1. Geometry optimizations of $[XO_2]^+$ (X = Cl, Br, I) and $([O_2Cl(FXeF)_2][AsF_6]_2)^-$ (2′)

The initial geometries of $[ClO_2]^+$ and **2′** were obtained starting from the X-ray crystal structures of **1** and **2**, respectively, and the initial geometry used for $[BrO_2]^+$ was obtained from the X-ray crystal structure of $[BrO_2][SbF_6]$.[143] Because no structurally characterized $[IO_2]^+$ salts had been reported, the initial geometry in the optimization of $[IO_2]^+$ was approximated from the optimized geometry of $[BrO_2]^+$ by replacement of the Br atom by an I atom. The calculated gas-phase $[XO_2]^+$ cations have V-shaped geometries as observed in the crystal structures of $[ClO_2]^+$ and $[BrO_2]^+$,[143] where their X–O bonds

elongate and their O-X-O bond angles compress upon descending the Group 17 (Table A2.6 of Appendix 2).

The gas-phase geometry of **2′** optimized to C_s symmetry (Table 4.2, Figure 4.2b, and Table A2.1 of Appendix 2) and was compared with gas-phase $[ClO_2]^+$ (Table A2.3 of Appendix 2) to assess the effects of secondary bonding. The calculated structural parameters of **2′**, although slightly overestimated, are in good agreement with and reproduce the most important features in the crystal structure of **2**: (1) the CN_{Cl} = 2 + 5 coordination environment of $[ClO_2]^+$, (2) the directionality of the Cl---F secondary bond interactions, which avoid the stereo-active VELP domain of Cl and are directed towards σ-holes of Cl, and (3) the elongation of the Xe–F_t bonds and contraction of the Xe–F_b bonds of the coordinated XeF_2 molecules. Ion-pair formation significantly weakens and elongates the Cl–O bonds in the calculated geometry of **2′** (1.414, 1.415 Å) relative to gas-phase $[ClO_2]^+$ (1.4090 Å), and results in a significantly smaller O–Cl–O bond angle for **2′** (115.87°) than for gas-phase $[ClO_2]^+$ (121.49°).

4.2.4.2. Natural Bond Orbital (NBO) analyses

The natural atomic orbital (NAO) analyses of $[XO_2]^+$ (X = Cl, Br, I) (Table A2.7 of Appendix 2) show increases in positive (X) and negative (O) charges, and decreases in Wiberg bond indices and valence indices for all atoms upon descending Group 17.

The Cl and O atoms of $[ClO_2]^+$ in **2′** display high valence indices (Cl, 3.320; O, 2.069, 2.070) and Cl–O Wiberg bond indices (2 x 1.559) (Table A2.6 of Appendix 2) that are consistent with significant Cl–O double bond character. When compared with gas-phase $[ClO_2]^+$ (Table A2.7 of Appendix 2), **2′** has greater positive Cl and negative O

charges and significantly lower O valence indices and Cl–O Wiberg bond indices due to the polarizing effect of the Cl---F secondary bonds. The Wiberg bond indices of the Cl---F_{Xe} secondary bonds of **2′** are very low (0.004–0.081), indicating that these bonds are primarily electrostatic in nature and are best described as σ-hole bonds (see Section 4.2.4.3. Molecular Electrostatic Potential Surface (MEPS) Analyses). Polarization of the Xe–F bonds in **2′** is consistent with terminal XeF_2 coordination. Thus, the F_b atoms of the adducted XeF_2 molecules that form short Cl---F_{Xe} secondary bonds have smaller negative charges, lower Xe–F_b Wiberg bond indices, and greater F atom valence indices than XeF_2 (Table A2.8 of Appendix 2), and the F atom charges of the terminal F_t atoms are more negative and have greater valence indices and Xe–F Wiberg bond indices than free XeF_2 and the F_b atoms of adducted XeF_2. The F atoms of $[AsF_6]^-$, which form secondary bonds with the Cl atom of $[ClO_2]^+$ in **2′**, have higher negative charges, lower valence indices, and lower As–F Wiberg bond indices than F atoms that do not interact with $[ClO_2]^+$.

4.2.4.3. Molecular electrostatic potential surface (MEPS) analyses

The MEPS isosurfaces for the $[XO_2]^+$ (X = Cl, Br, I) cations are compared in Figure 4.5. Their relative Lewis acid strengths are reflected in their global EP maxima (Cl, 782 kJ mol^{-1}; Br, 767 kJ mol^{-1}; I, 761 kJ mol^{-1}), which decrease from Cl to I and are located on both faces of the triangle defined by the two X–O double-bond domains and the VELP domain of X and correspond to σ-holes. These σ-holes and those located trans to the X–O bonds (Cl, 740 kJ mol^{-1}; Br, 754 kJ mol^{-1}; I, 756 kJ mol^{-1}) form a band of high positive EP that encircles the VELP domain of X. The Cl---F secondary bonds in the crystal structures of **1** and **2** are directed towards σ-holes within this band, where the O–Cl---F

contact angles (92.34(3)–97.16(3)°) of the shortest secondary bonds are closer to 90° and the O–Cl---F contact angles (149.69(6)–153.99(8)°) of the longest secondary bonds are directed towards σ-holes that are trans to the Cl–O bonds. The global EP minima are located on the O atoms (Cl, 478 kJ mol^{-1}; Br, 423 kJ mol^{-1}; I, 362 kJ mol^{-1}) and become less positive upon descending Group 17.

The trends are in accordance with decreasing valence indices and Wiberg bond indices and increased positive (X) and negative (O) NPA charges (Table A2.7 of Appendix 2) upon descending Group 17. The high positive EP maxima on the halogen isosurfaces of $[BrO_2]^+$ and $[IO_2]^+$ suggest they may be candidates for complex formation with NgF_2 (Ng = Kr, Xe) under reaction conditions similar to those employed for the synthesis of **2**.

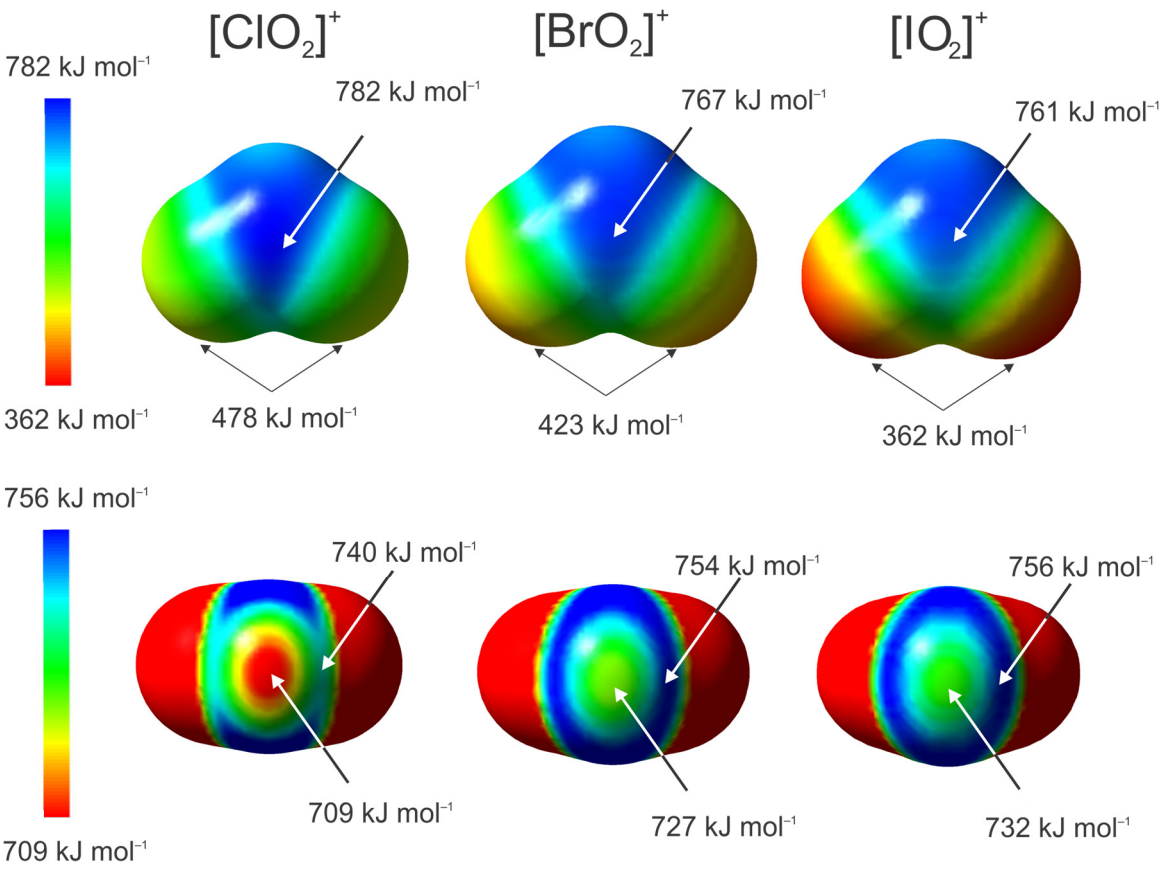

Figure 4.5. The molecular electrostatic potential surface (MEPS) contours calculated at the 0.001 e a_0^{-3} isosurfaces of $[ClO_2]^+$, $[BrO_2]^+$ and $[IO_2]^+$. The extrema of selected electrostatic potentials are indicated by arrows. The optimized geometries and MEPS were calculated at the B3LYP/Def2-TZVPD (O, Cl, Br, I) level of theory.

4.3. Conclusion

The moderate Lewis acid strength and oxidative resistance of the $[ClO_2]^+$ cation has been exploited to synthesize the first Cl(V) coordination complex of XeF_2. The reaction of α-$[ClO_2][AsF_6]$ with XeF_2 in aHF afforded $[O_2Cl(FXeF)_2][AsF_6]$, which was structurally characterized by LT Raman spectroscopy and LT SCXRD. The LT phase, β-$[ClO_2][AsF_6]$, was obtained by crystallization or precipitation from aHF solution and was also characterized by LT Raman spectroscopy and LT SCXRD. The irreversible conversion of β-$[ClO_2][AsF_6]$ to the known α-phase was shown to occur upon warming to RT. The α-phase was converted to the β-phase by dissolution in aHF followed by precipitation at −78 °C. The cation stretching frequencies of α-$[ClO_2][AsF_6]$ occur at significantly lower frequency than those of β-$[ClO_2][AsF_6]$ which is likely due to crystal packing differences. The $[ClO_2]^+$ cations of β-$[ClO_2][AsF_6]$ and $[O_2Cl(FXeF)_2][AsF_6]$ form short Cl---F secondary bonds with neighboring $[AsF_6]^-$ anions or XeF_2 molecules in the solid-state that are significantly less than the sums of the Cl and F van der Waals radii and are best described as σ-hole bonds. The NBO analysis of the model anion, $([O_2Cl(FXeF)_2][AsF_6]_2)^-$, affirms that the Cl---$F_{Xe}$ and Cl---F_{As} secondary bonds are primarily electrostatic, noncovalent bonds, and a MEPS analysis of gas-phase $[ClO_2]^+$ shows that these bonds are directed towards regions of high positive electrostatic potential (EP), σ-holes, on the isosurface of Cl. The synthesis of a $[O_2Cl(FXeF)_2]^+$ salt represents a significant extension of Cl(V) coordination chemistry and suggests the syntheses of other high-oxidation-state $[XO_2]^+$ (X = Cl, Br, I) coordination complexes of NgF_2, such as $[O_2X(FNgF)_2][AsF_6]$ (Ng = Kr, Xe), may also be achievable.

CHAPTER 5

Syntheses and Structural Characterizations of the Br(V) Coordination Complexes, $[O_2Br(FXeF)_n][AsF_6]$ (n = 1, 2), and $[O_2Br(FXeF)_2][SbF_6]$

5.1. Introduction

The highest Cl and Br oxidation state for which cationic coordination complexes have been synthesized and structurally characterized is the +5 oxidation state.[62,63,139] This is due, in part, to the scarcity of known X(VII) cation salts, which is attributed to their aggressive oxidizing characters and to the inability to prepare the neutral XOF_5 and BrO_2F_3 precursors.[177,191–198] Furthermore, attempts to synthesize salts of $[XO_3]^+$ cations by reaction of XO_3F (X = Cl, Br) with SbF_5 and with SbF_5/aHF superacid mixtures resulted in redox elimination of O_2 and formation of $[XO_2][SbF_6]$ salts.[143] Of the known X(VII) cations $[ClO_2F_2]^+$ [199] and $[XF_6]^+$,[200–203] $[ClO_2F_2]^+$ has the greatest potential to form coordination complexes because it is coordinatively unsaturated and is known to react with NO_2F to yield the extremely reactive neutral Cl(VII) oxyfluoride, ClO_2F_3.[199] However, $[ClO_2F_2]^+$ has only been prepared as the minor product (ca. 10 % yield) in the reaction of ClO_2F with the strong oxidant PtF_6, which makes the preparation of synthetically useful amounts of $[ClO_2F_2]^+$ and/or ClO_2F_3 very challenging and difficult to scale.[199] Although the strong oxidant fluoro-cations, $[ClF_6]^+$ and $[BrF_6]^+$, have been synthesized and structurally characterized,[200–203] their syntheses also require strong oxidants (Cl, $[KrF]^+$ or PtF_6; Br, $[KrF]^+$), and their Lewis acidities are expected to be significantly diminished owing to steric crowding in their valence shells.[143] Thus, $[BrF_6][AsF_6]$ does not react with strongly fluorobasic NOF to form BrF_7, but undergoes

redox disproportionation to form $[NO][AsF_6]$, $[NO][BrF_6]$, and F_2.[201] The chemistries of Cl(VII) and Br(VII) are significantly more limited than that of I(VII), for which IF_7, IOF_5, IO_2F_3, and IO_3F are known.

In contrast with the chemistries of Cl(VII), Br(VII), and I(VII), the fluoride-ion donor-acceptor properties of Br(V), Cl(V), and I(V) fluorides and oxyfluorides have been extensively studied.[177,191–198,204,205] Reactions of amphoteric XF_5, XO_2F, and XOF_3 (X = Cl, Br) with strong fluoride-ion donors such as anhydrous $[N(CH_3)_4]F$, NOF, and alkali metal fluorides yield the $[XF_6]^-$,[206–210] $[XO_2F_2]^-$,[191,211–213] and $[XOF_4]^-$ anions,[143,191–196,214] whereas their reactions with fluoride-ion acceptors such as AsF_5, and SbF_5 result in fluoride-ion abstraction to afford salts of the Lewis acidic $[XF_4]^+$,[215–217] $[XO_2]^+$,[139,142,143,185–188,218–222] and $[XOF_2]^+$ [63,143,191,192,194,195,223,224] cations, respectively. Reactions of $[BrOF_2][AsF_6]$ with the oxidatively resistant noble-gas difluorides NgF_2 (Ng = Kr, Xe) in aHF solvent have been shown to form the $[F_2OBr(FNgF)_2][AsF_6]$ (Ng = Kr,[62] Xe[63]) and $[F_2OBr(FXeF)][AsF_6]$ coordination complexes (Eqs. **5.1** and **5.2**).

$$[BrOF_2][AsF_6] + XeF_2 \xrightarrow[RT]{aHF} [F_2OBr(FXeF)][AsF_6] \qquad (\mathbf{5.1})$$

$$[BrOF_2][AsF_6] + 2NgF_2 \xrightarrow[RT]{aHF} [F_2OBr(FNgF)_2][AsF_6] \qquad (\mathbf{5.2})$$

Coordination of NgF_2 to Lewis acidic p-block elements is challenging because the Lewis acid must be resistant to oxidative fluorination, but not Lewis acidic enough to abstract fluoride-ion to form $[NgF]^+$ salts. The $[BrOF_2]^+$ cation meets these criteria, and these studies provided the first examples of structurally characterized cationic Br(V) coordination complexes.

More recently, the synthesis of $[O_2Cl(FXeF)_2][AsF_6]$[61] provided the first example of a cationic Cl(V) coordination complex which was structurally characterized by LT Raman spectroscopy and LT SCXRD.[61] This study showed that XeF_2 terminally coordinates to the Lewis acidic Cl(V) center through primarily electrostatic Cl---F_{Xe} bonds that are directed towards regions of high electrostatic potential on the Cl(V) atom of $[ClO_2]^+$. MEPS analyses for $[BrO_2]^+$ and $[IO_2]^+$ indicated that these cations are expected to form coordination complexes with XeF_2. Prior to this work, only one cationic Br(V) coordination complex of $[BrO_2]^+$, $[O_2Br(BrO_2F)][AsF_6]$,[139] had been synthesized and structurally characterized. However, the adducted BrO_2F molecules exhibited an O/F positional disorder, and no discussion was provided concerning the nature of the bonding in this complex. Thus, the reactions of XeF_2 with $[BrO_2]^+$ salts in aHF solvent were investigated with the view to synthesize and structurally characterize $[BrO_2]^+$ coordination complexes by analogy with those of $[ClO_2]^+$.[61]

5.2. RESULTS AND DISCUSSION

5.2.1. Syntheses

The syntheses of XeF_2 coordination complexes of $[BrO_2][PnF_6]$ employed small quantities of $[BrO_2][PnF_6]$ (<100 mg) to avoid handling and transfer of hazardous quantities of thermally unstable and potentially explosive BrO_2F (calcd. ΔH_f = 18.8 kJ mol^{-1}, CCSD-DTQ; 12.6 kJ mol^{-1}, CCSD-Q5).[177] To circumvent transfer of small quantities of dry $[BrO_2][PnF_6]$ salts in a dry box, the salts were synthesized in aHF solvent and allowed to react in situ with XeF_2. Consequently, small excesses of PnF_5 used

for the syntheses of $[BrO_2][PnF_6]$ in aHF reacted with XeF_2 to form small amounts of $[Xe_2F_3][PnF_6]$.

Final products and distributions were monitored by recording the LT (−150 °C) Raman spectra of precipitated solids under frozen aHF solvent. Dry crystalline material was also characterized by LT SCXRD and/or LT Raman spectroscopy.

5.2.1.1. $[O_2Br(FXeF)_2][AsF_6]$ and $[O_2Br(FXeF)][AsF_6]$

The reaction of a ca. 1.0 : 1.5 molar mixture of freshly prepared $[BrO_2][AsF_6]$ with XeF_2 at –10 °C in aHF solvent led to a mixture of $[O_2Br(FXeF)][AsF_6]$, $[O_2Br(FXeF)_2][AsF_6]$, unreacted $[BrO_2][AsF_6]$ and XeF_2 (Eqs. **5.3** and **5.4**).

$$[BrO_2][AsF_6] + XeF_2 \underset{-10\ °C}{\overset{aHF}{\rightleftharpoons}} [O_2Br(FXeF)][AsF_6] \qquad (\mathbf{5.3})$$

$$[O_2Br(FXeF)][AsF_6] + XeF_2 \underset{-10\ °C}{\overset{aHF}{\rightleftharpoons}} [O_2Br(FXeF)_2][AsF_6] \qquad (\mathbf{5.4})$$

The sample was warmed to 0 °C to effect dissolution of all solid materials. Dark orange, needle-shaped crystals of $[O_2Br(FXeF)_2][AsF_6]$ grew upon cooling the sample to –42 °C over ca. 7 h, and light orange, needle-shaped crystals of $[O_2Br(FXeF)][AsF_6]$ grew upon cooling from –42 to –46 °C over 3 h. Crystals of $[BrO_2][SbF_6]$, XeF_2, and $[Xe_2F_3][AsF_6]$ also grew from aHF solution (see Section 2.5.3.).

5.2.1.2. $[O_2Br(FXeF)_2][SbF_6]$

The reaction of a 1.0 : 2.5 molar mixture of dry $[BrO_2][SbF_6]$ and XeF_2 in aHF solvent at –10 °C yielded $[O_2Br(FXeF)_2][SbF_6]$ and unreacted starting materials (Eq. **5.5**), indicating that $[O_2Br(FXeF)_2][SbF_6]$, XeF_2, and $[BrO_2][SbF_6]$ exist in equilibrium in aHF solvent.

$$[BrO_2][SbF_6] + 2XeF_2 \underset{-10\ °C}{\overset{aHF}{\rightleftharpoons}} [O_2Br(FXeF)_2][SbF_6] \qquad (\mathbf{5.5})$$

Dark red-orange, needle-shaped crystals of $[O_2Br(FXeF)_2][SbF_6]$ (**3**) were grown by slowly cooling the reaction mixture from 22 to –50 °C over ca. 10 h. Crystals of $[BrO_2][SbF_6]$ and XeF_2 also grew from aHF solution (see Section 2.5.4.).

5.2.1.3. Attempted Synthesis of $[O_2Br(FXeF)][SbF_6]$

The reaction of an approximately equimolar mixture of freshly prepared $[BrO_2][SbF_6]$ with XeF_2 in aHF yielded $[O_2Br(FXeF)_2][SbF_6]$, unreacted $[BrO_2][SbF_6]$, and a small amount of $[Xe_2F_3][SbF_6]$. Addition of another equivalent of XeF_2 yielded a mixture of $[O_2Br(FXeF)_2][SbF_6]$, XeF_2, and $[BrO_2][SbF_6]$. The absence of $[O_2Br(FXeF)][SbF_6]$ is presumably due to of the lower fluorobasicity of $[SbF_6]^-$ relative to that of $[AsF_6]^-$. This enhances the Lewis acidity of $[BrO_2]^+$ sufficiently to favor $[O_2Br(FXeF)_2][SbF_6]$ formation. Preferential formation of $[F_2OBr(FKrF)_2][AsF_6]$ was also reported when the synthesis of $[F_2OBr(FKrF)][AsF_6]$ was attempted.[62]

5.2.2. X-ray Crystallography

A summary of X-ray crystallographic data and refinement results for $[O_2Br(FXeF)_2][AsF_6]$ (**1**), $[O_2Br(FXeF)_2][SbF_6]$ (**2**), and $[O_2Br(FXeF)][AsF_6]$ (**3**) is provided in Table 5.1. The X-ray crystal structures and key bond lengths and angles of **1**–**3** are provided in Figures 5.1–5.3 and Tables 5.1–5.3.

The coordinated $[BrO_2]^+$ cations in **1**–**3** have the bent geometry that is predicted for an AX_2E VSEPR arrangement of two bond pair domains (X) and one valence electron lone-pair domain (E) around the central Br(V) atom (A). The $[PnF_6]^-$ anions have octahedral AX_6 VSEPR geometries that are slightly distorted by ion-pair interactions. The structural parameters of the $[PnF_6]^-$ anions are similar to those of other ion-paired $[PnF_6]^-$

salts,[17,46,48,61,143] including the slight elongation of the Pn–F bonds for F atoms that form Br---F_{Pn} secondary bonds relative to those Pn–F bonds corresponding to F atoms that do not engage in secondary bond formation with Br(V).

5.2.2.1. $[O_2Br(FXeF)_2][AsF_6]$ (1) and $[O_2Br(FXeF)_2][SbF_6]$ (2)

Both $[O_2Br(FXeF)_2][AsF_6]$ (**1**) and $[O_2Br(FXeF)_2][SbF_6]$ (**2**) crystallize in the $P\bar{1}$ space group and are isotypic. The salts are intimate ion-pairs that are extensively fluorine bridged in the solid-state through secondary Br---F_{Xe} and Br---F_{Pn} bonds. The geometric parameters of $[BrO_2]^+$ in **1** (1.584(4) and 1.597(4) Å; 111.9(2)°) and **2** (1.589(5) and 1.593(4) Å; 111.1(2) °) are equal within ±3σ to those of $[BrO_2][PnF_6]$ (As: 1.590(3) Å, 112.1(3)°;[139] Sb: 1.595(2) Å, 111.9(1)°).[143] Unlike $[O_2Cl(FXeF)_2][AsF_6]$[61] and $[F_2OBr(FXeF)_2][AsF_6]$,[63] where both XeF_2 ligands are terminally coordinated, complexes **1** and **2** have one asymmetrically and two symmetrically bridged XeF_2 ligands that each interact with two Br(V) atoms. The differences among XeF_2 coordination modalities in **1**, **2**, $[O_2Cl(FXeF)_2][AsF_6]$,[61] and $[F_2OBr(FXeF)_2][AsF_6]$[63] are attributed to the larger covalent radius of Br(V) relative to that of Cl(V), and to the lower fluoride-ion affinity and less congested coordination sphere of $[BrO_2]^+$ relative to $[BrOF_2]^+$. The two symmetrically bridged XeF_2 ligands of **1** and **2** have bond lengths (2.001(3) Å and 1.997(3) Å) that are equal within ±3σ to those of the low-temperature phase of XeF_2 (1.999(2) Å).[48] In contrast, asymmetric bridging of XeF_2 results in contraction of one Xe–F bond (**1**, 1.965(3) Å; **2**, 1.970(4) Å) and elongation of the other Xe–F bond (**1**, 2.026(3) Å; **2**, 2.039(3) Å) relative to the Xe–F bond lengths of symmetrically bridged XeF_2 (vide supra). The Xe–F bonds of the asymmetrically bridged XeF_2 ligands of **1** and **2** are more

asymmetric than those of $[Cd(FXeF)_5][PF_6]_2$ (1.990(7) and 2.010(8) Å),[225] $[Ca(FXeF)_4][AsF_6]_2$ (1.973(8) and 2.030(8) Å),[226] and $Hg(OTeF_5)_2 \cdot 1.5XeF_2$ (1.991(4) and 2.012(4) Å).[72] The F–Xe–F bond angles of the asymmetrically bridged XeF_2 ligands (**1**, 179.0(2)°; **2**, 178.7(2)°) are essentially linear and are similar to those in other asymmetrically bridged coordination complexes ($[Cd(FXeF)_5][PF_6]_2$, 178.7(4)°;[225] $[Ca(FXeF)_4][AsF_6]_2$ (176.5(5) Å);[226] $Hg(OTeF_5)_2 \cdot XeF_2$, 179.4(2)°).[72]

Table 5.1. Summary of X-ray crystal data and refinement results for $[O_2Br(FXeF)_2][AsF_6]$ (**1**), $[O_2Br(FXeF)_2][SbF_6]$ (**2**), and $[O_2Br(FXeF)][AsF_6]$ (**3**)

	1	**2**	**3**
space group	$P\bar{1}$	$P\bar{1}$	$P\bar{1}$
a (Å)	7.0662(4)	7.1159(5)	6.1219(4)
b (Å)	8.7302(5)	8.8756(7)	9.3670(6)
c (Å)	8.7948(5)	8.9035(6)	14.7903(10)
α (deg)	92.417(2)	90.560(4)	91.719(3)
β (deg)	92.112(2)	91.595(3)	92.563(2)
γ (deg)	92.048(3)	91.794(4)	90.658(2)
V (Å^3)	541.32(5)	561.80(7)	846.83(10)
Z[a]	2	2	4
M_W[b]	639.43	686.26	470.13
ρ_{calcd}[c]	3.923	4.057	3.687
T (°C)	−173 °C	−173 °C	−173 °C
μ [d]	13.109	12.061	12.771
R_1[e]	0.0381	0.0349	0.0379
wR_2[f]	0.0883	0.0839	0.0991

[a] Molecules/unit cell. [b] g mol^{-1}. [c] g cm^{-3}. [d] mm^{-1}. [e] $R_1 = \Sigma||F_o| - |F_c||/\Sigma|F_o|$. [f] $wR_2 = [\Sigma(w(F_o^2 - F_c^2)^2)/\Sigma(w(F_o^2)^2)]^{1/2}$.

The $[BrO_2]^+$ cations of **1** and **2** interact with neighboring XeF_2 ligands and with the $[PnF_6]^-$ (Pn = As, Sb) anions through secondary Br---F_{Xe} bonds (**1**, 2.531(3)–2.860(3) Å; **2**, 2.527(3)–2.902(3) Å) and Br---F_{Pn} bonds (**1**, 2.814(3) and 2.951(3) Å; **2**, 2.468(3)

and 2.873(3) Å) that are significantly shorter than the sum of the Br and F van der Waals radii (3.30, 3.32 Å).[167] The Br---F_{Xe} secondary bonds of **1** and **2** are significantly longer than those of $[F_2OBr(FXeF)_2][AsF_6]$ (2.292(4), 2.306(4) Å),[63] which is consistent with the lower anticipated fluoride-ion affinity of $[BrO_2]^+$ relative to that of $[BrOF_2]^+$. These primarily electrostatic, σ-hole interactions avoid the stereo-active valence electron lone pair on Br(V) and are directed towards regions of high positive electrostatic potential on Br(V) that are cis and trans to the Br–O bonds, in accordance with the previously reported MEPS analysis of $[BrO_2]^+$.[61] The shorter Br---F_{Xe} secondary bonds of **1** and **2** are directed towards regions of highest positive EP on $[BrO_2]^+$ that are cis to the Br–O bonds, whereas the longer Br---F_{Xe} secondary bonds are directed towards localized regions of high positive EP (σ-holes) that are trans to Br–O bonds. This results in a distorted bicapped trigonal prismatic (CN_{Br} = 2 + 6) coordination sphere for Br(V) in **1** and **2**.

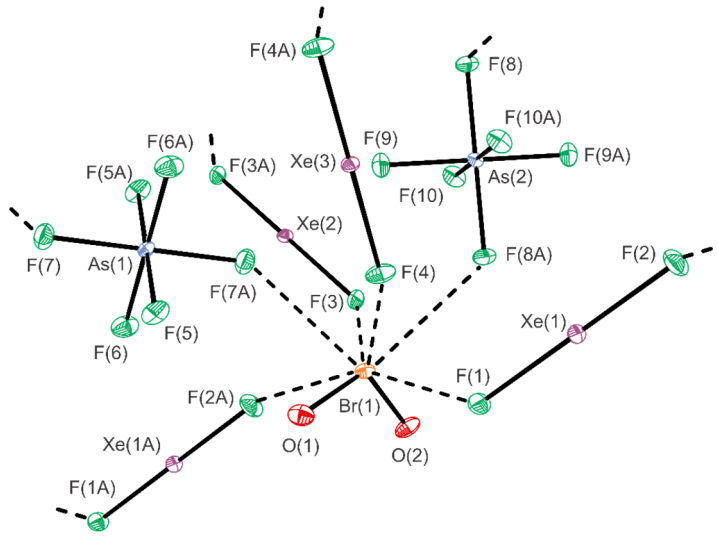

Figure 5.1. Structural unit in the X-ray crystal structure of $[O_2Br(FXeF)_2][AsF_6]$ (**1**). Thermal ellipsoids are drawn at the 50% probability level and secondary Br---F_{Xe} and Br---F_{As} bonds are indicated by dashed lines.

Table 5.2. Experimental geometric parameters for $[O_2Br(FXeF)_2][AsF_6]$ (**1**) and $[O_2Br(FXeF)_2][SbF_6]$ (**2**)

Bond Lengths (Å)					
	1	**2**		**1**	**2**
Br(1)–O(1)	1.584(4)	1.589(5)	Xe(3)–F(4)	2.001(3)	1.999(3)
Br(1)–O(2)	1.597(4)	1.593(4)	Xe(3)–F(4A)	2.001(3)	1.999(3)
Br(1)---F(1)	2.531(3)	2.527(3)	Pn(1)–F(5)	1.723(3)	1.872(3)
Br(1)---F(2A)	2.860(3)	2.902(3)	Pn(1)–F(5A)	1.723(3)	1.872(3)
Br(1)---F(3)	2.584(4)	2.610(3)	Pn(1)–F(6)	1.718(3)	1.882(3)
Br(1)---F(4)	2.685(3)	2.708(4)	Pn(1)–F(6A)	1.718(3)	1.882(3)
Br(1)---F(7A)	2.814(3)	2.768(3)	Pn(1)–F(7)	1.743(3)	1.897(3)
Br(1)---F(8A)	2.951(3)	2.873(3)	Pn(1)–F(7A)	1.743(3)	1.897(3)
Xe(1)–F(1)	2.026(3)	2.039(3)	Pn(2)–F(8)	1.737(3)	1.898(3)
Xe(1)–F(2)	1.965(3)	1.970(4)	Pn(2)–F(8A)	1.737(3)	1.898(3)
			Pn(2)–F(9)	1.714(3)	1.873(3)
Xe(2)–F(3)	1.997(3)	2.000(3)	Pn(2)–F(9A)	1.714(3)	1.873(3)
Xe(2)–F(3A)	1.997(3)	2.000(3)	Pn(2)–F(10)	1.724(3)	1.876(3)
			Pn(2)–F(10A)	1.724(3)	1.876(3)
Bond Angles (°)					
O(1)–Br(1)–O(2)	111.9(2)	111.1(2)	F(5A)–Pn(1)–F(6)	89.82(17)	90.57(16)
F(1)---Br(1)–O(1)	92.61(17)	92.52(19)	F(5A)–Pn(1)–F(6A)	90.18(17)	89.44(16)
F(2A)---Br(1)–O(1)	76.17(17)	76.74(18)	F(5A)–Pn(1)–F(7)	89.78(16)	90.23(15)
F(3)---Br(1)–O(1)	132.55(17)	133.47(18)	F(5A)–Pn(1)–F(7A)	90.22(16)	89.77(15)
F(4)---Br(1)–O(1)	83.47(17)	84.26(18)	F(6)–Pn(1)–F(6A)	180.00	180.00
F(7A)---Br(1)–O(1)	77.01(16)	77.46(17)	F(6)–Pn(1)–F(7)	90.11(18)	89.62(15)
F(8A)---Br(1)–O(1)	153.57(16)	153.51(18)	F(6)–Pn(1)–F(7A)	89.89(17)	90.38(15)
F(1)---Br(1)–O(2)	84.68(17)	86.58(17)	F(6A)–Pn(1)–F(7)	89.88(17)	90.38(15)
F(2A)---Br(1)–O(2)	79.00(17)	77.80(17)	F(6A)–Pn(1)–F(7A)	90.11(18)	89.62(15)
F(3)---Br(1)–O(2)	80.22(17)	79.94(17)	F(7)–Pn(1)–F(7A)	180.00	180.00
F(4)---Br(1)–O(2)	145.13(16)	147.24(17)	F(8)–Pn(2)–F(8A)	180.00	180.00
F(7A)---Br(1)–O(2)	144.53(17)	141.72(17)	F(8)–Pn(2)–F(9)	90.28(16)	89.49(14)
F(8A)---Br(1)–O(2)	89.70(17)	89.54(18)	F(8)–Pn(2)–F(9A)	89.72(16)	90.51(14)
F(1)–Xe(1)–F(2)	179.01(17)	178.73(16)	F(8)–Pn(2)–F(10)	90.45(16)	89.55(15)
F(3)–Xe(2)–F(3A)	180.00	180.00	F(8)–Pn(2)–F(10A)	89.55(16)	90.45(15)
F(4)–Xe(3)–F(4A)	180.00	180.00	F(8A)–Pn(2)–F(9)	89.72(16)	90.51(14)
F(5)–Pn(1)–F(5A)	180.00	180.00	F(8A)–Pn(2)–F(9A)	90.28(16)	89.49(14)
F(5)–Pn(1)–F(6)	90.18(17)	89.44(16)	F(8A)–Pn(2)–F(10)	89.56(16)	90.45(15)
F(5)–Pn(1)–F(6A)	89.82(17)	90.56(16)	F(8A)–Pn(2)–F(10A)	90.44(16)	89.55(15)
F(5)–Pn(1)–F(7)	90.22(17)	89.77(15)	F(9)–Pn(2)–F(9A)	180.00	180.00
F(5)–Pn(1)–F(7A)	89.78(16)	90.23(15)	F(9)–Pn(2)–F(10)	89.70(16)	90.06(15)
			F(9)–Pn(2)–F(10A)	90.30(16)	89.93(15)
			F(10)–Pn(2)–F(10A)	180.00	180.00

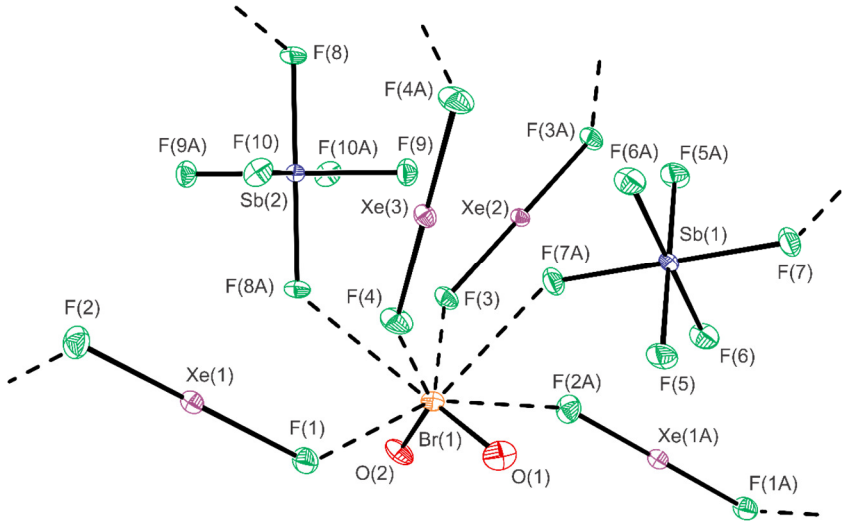

Figure 5.2. Structural unit in the X-ray crystal structure of $[O_2Br(FXeF)_2][SbF_6]$ (**2**). Thermal ellipsoids are drawn at the 50% probability level and secondary Br---F_{Xe} and Br---F_{Sb} bonds are indicated by dashed lines.

5.2.2.2. $[O_2Br(FXeF)][AsF_6]$ (3).

The X-ray crystal structure of $[O_2Br(FXeF)][AsF_6]$ (**3**) is extensively fluorine bridged and consists of two crystallographically inequivalent structural units (Figure 5.3 and Table 5.3). The $[BrO_2]^+$ cations have Br–O bond lengths (1.588(4) and 1.602(4) Å) and O-Br-O bond angles (111.1(2) and 111.6(2)°) that are equal within ±3σ to those of **1** and **2**. The XeF_2 ligands are located on general positions and are asymmetrically coordinated between two Br(V) centers (Xe_1–F: 1.971(3) and 2.014(3) Å; Xe_2–F: 1.978(3) and 2.007(3) Å), where the Xe–F bond lengths are similar to those of **1** and **2**.

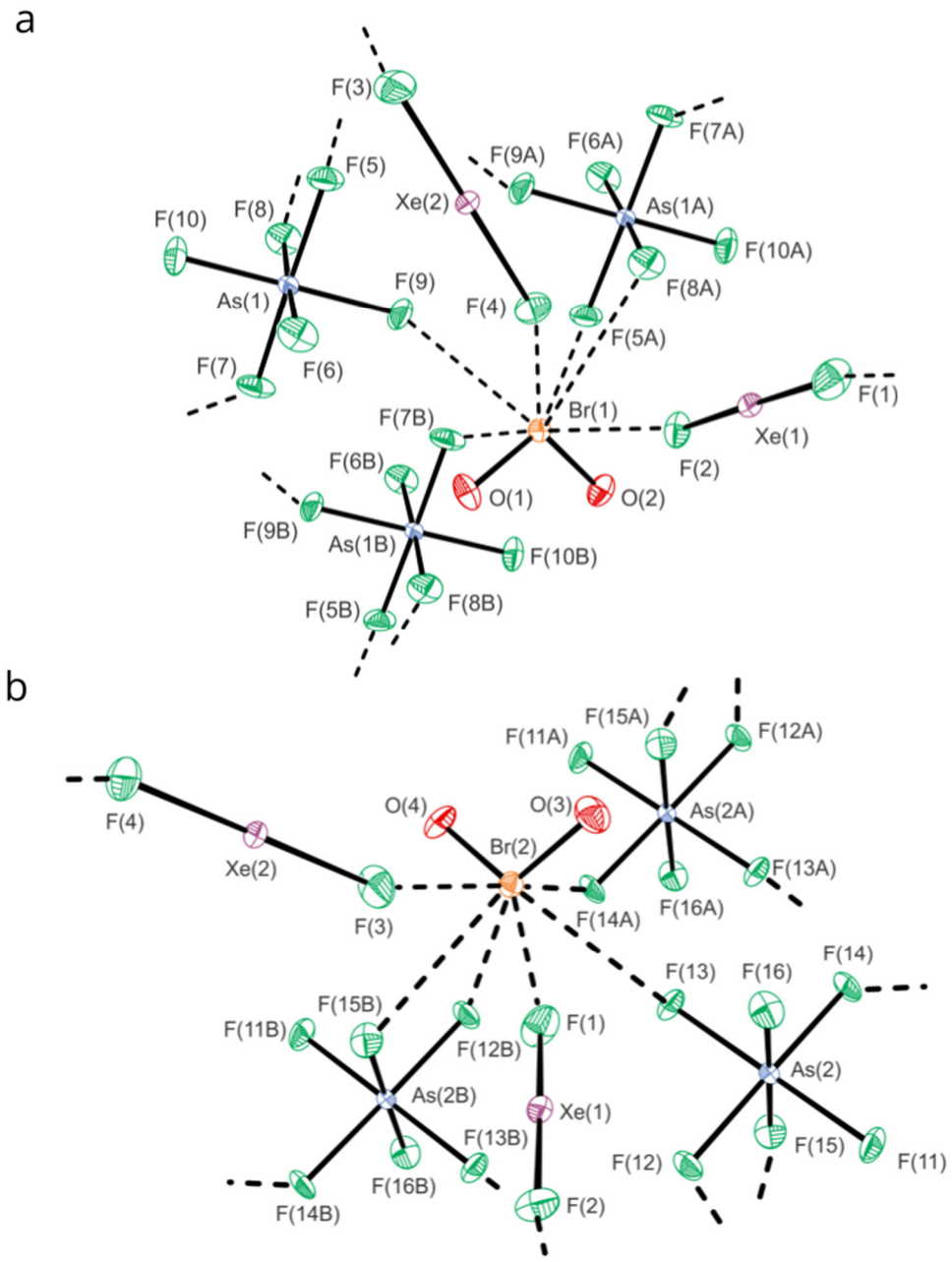

Figure 5.3. The structural units (a) and (b) in the X-ray crystal structure of $[O_2Br(FXeF)][AsF_6]$ (**3**) showing the Br(V) coordination environments. Thermal ellipsoids are drawn at the 50% probability level and secondary Br---F_{Xe} and Br---F_{As} bonds are indicated by dashed lines.

Table 5.3. Experimental geometric parameters for $[O_2Br(FXeF)][AsF_6]$ (**3**)

Bond Lengths (Å)			
Br(1)–O(1)	1.588(4)	Xe(1)–F(1)	1.971(3)
Br(1)–O(2)	1.594(3)	Xe(1)–F(2)	2.014(3)
Br(1)---F(2)	2.438(3)	Xe(2)–F(3)	2.007(3)
Br(1)---F(4)	2.777(3)	Xe(2)–F(4)	1.978(3)
Br(1)---F(5A)	3.018(3)		
Br(1)---F(7B)	2.866(3)	As(1)–F(5)	1.724(3)
Br(1)---F(8A)	2.944(3)	As(1)–F(6)	1.717(3)
Br(1)---F(9)	2.707(3)	As(1)–F(7)	1.726(3)
		As(1)–F(8)	1.722(3)
Br(2)–O(3)	1.602(4)	As(1)–F(9)	1.728(3)
Br(2)–O(4)	1.598(3)	As(1)–F(10)	1.704(3)
Br(2)---F(1)	2.599(3)	As(2)–F(11)	1.721(3)
Br(2)---F(3)	2.532(3)	As(2)–F(12)	1.728(3)
Br(2)---F(12B)	2.851(3)	As(2)–F(13)	1.729(3)
Br(2)---F(13)	2.796(3)	As(2)–F(14)	1.726(3)
Br(2)---F(14A)	2.876(3)	As(2)–F(15)	1.728(3)
Br(2)---F(15B)	2.907(3)	As(2)–F(16)	1.711(3)
Bond Angles (°)			
O(1)–Br(1)–O(2)	111.6(2)	F(1)–Xe(1)–F(2)	179.2(1)
F(2)---Br(1)–O(1)	101.8(2)	F(3)–Xe(2)–F(4)	179.7(1)
F(4)---Br(1)–O(2)	145.9(2)		
F(7B)---Br(1)–O(1)	84.5(2)	F(5)–As(1)–F(6)	91.1(2)
F(8A)---Br(1)–O(1)	148.1(2)	F(5)–As(1)–F(7)	177.6(2)
F(9)---Br(1)–O(2)	138.3(2)	F(5)–As(1)–F(8)	88.0(2)
F(5A)---Br(1)–O(1)	151.8(2)	F(5)–As(1)–F(9)	89.2(2)
		F(5)–As(1)–F(10)	91.1(2)
O(3)–Br(2)–O(4)	111.1(2)		
		F(11)–As(1)–F(12)	90.1(2)
F(1)---Br(2)–O(4)	149.8(2)	F(11)–As(1)–F(13)	179.5(2)
F(3)---Br(2)–O(4)	89.6(2)	F(11)–As(1)–F(14)	89.8(2)
F(12B)---Br(2)–O(3)	149.7(2)	F(11)–As(1)–F(15)	90.1(2)
F(13)---Br(2)–O(4)	138.1(2)	F(11)–As(1)–F(16)	90.4(1)
F(14A)---Br(2)–O(3)	98.2(2)		
F(15B)---Br(2)–O(4)	152.5(2)		

The $[BrO_2]^+$ cations of **3** interact with the asymmetrically coordinated XeF_2 ligands and nearby $[AsF_6]^-$ anions through primarily electrostatic Br---F_{Xe} (Br(1), 2.438(3), 2.777(3) Å; Br(2), 2.532(3), 2.599(3) Å) and Br---F_{As} (Br(1), 2.707(3), 2.866(3), 2.944(3), 3.018(3) Å; Br(2), 2.795(3), 2.851(3), 2.876(3), 2.907(3) Å) secondary bonds. As in **1** and **2**, these secondary bonds avoid the stereo-active lone pair on Br(V), and are directed towards regions of high electrostatic potential on $[BrO_2]^+$ that are cis and trans to the Br–O bonds. These interactions are significantly shorter than the sum of the Br and F van der Waals radii (vide supra),[167] and give rise to distorted bicapped trigonal prismatic Br(V) coordination spheres (CN_{Br} = 2 + 6) for both Br(V) centers. The shortest Br---$F_{Xe/As}$ contacts (Br(1), 2.438(3) Å; Br(2), 2.532(3) Å) coordinate cis to the Br–O bonds, whereas the longer Br---$F_{Xe/As}$ contacts are trans to the Br–O bonds (Br(1), 2.777(3) Å; Br(2), 2.599(3) Å).

5.2.3. Raman Spectroscopy

Calculated gas-phase geometries and frequencies of compounds **1**–**3** were not obtained because they are extensively fluorine bridged. Attempts to optimize oligomeric models failed at the B3LYP/Def2-TZVPD, APFD/Def2-TZVPD, and PBE1PBE/Def2-TZVPD levels of theory. The calculated gas-phase optimized geometry of $[BrO_2]^+$ and associated vibrational frequencies and isotopic shifts are provided in Chapter 4.[61] Spectral assignments (Tables 5.4 and 5.5) for $[BrO_2]^+$ and the terminal and bridging XeF_2 ligands were therefore made by comparison with $[BrO_2][AsF_6]$,[139] $[BrO_2][SbF_6]$,[143] $[BrO_2][BF_4]$,[191] $[O_2Cl(FXeF)_2][AsF_6]$,[61] $[F_2OBr(FXeF)_2][AsF_6]$, $[F_2OBr(FXeF)][AsF_6]$,[63]

and $Hg(OTeF_5)_2 \cdot 1.5XeF_2$.[72] Quantum-chemical calculations for XeF_2 coordination complexes $[O_2Cl(FXeF)_2][AsF_6]$,[61] $[F_2OBr(FNgF)_2][AsF_6]$,[62,63] and $[F_2OBr(FXeF)][AsF_6]$,[63] have shown that little or no intermolecular vibrational coupling occurs among the Ng–F stretching modes of coordinated NgF_2 and the cation and anion stretching modes within the unit cell. It is therefore reasonable to assume that this also applies to compounds **1**, **2**, and **3**. Thus, tentative assignments were made assuming no significant vibrational coupling occurs among the vibrational modes of XeF_2, $[BrO_2]^+$, and $[PnF_6]^-$. Previous QC calculations have also shown that when two or more XeF_2 ligands are present in a complex that have the same coordination modality, terminal or bridging, intermolecular coupling of the Xe–F stretches occurs for these ligands within the crystallographic unit cell.[61–63] It was therefore assumed that intermolecular coupling also occurs between the two symmetrically bridged XeF_2 ligands of **1** and **2** (F_3, F_{3A} and F_4, F_{4A}) and between the two asymmetrically bridged XeF_2 ligands of **3** (F_1, F_2 and F_3, F_4).

Vibrational assignments for $[PnF_6]^-$ (Pn = As, Sb) were made by comparison with other $[PnF_6]^-$ salts[17,46,48,61,143] and under assumed O_h symmetry. Symmetry lowering of the $[PnF_6]^-$ anions from the gas-phase O_h symmetry to C_i site symmetry in the crystal structures of **1** and **2** accounts for the splitting of the degenerate E_g and T_{2g} modes, and is consistent with the observation of no formally Raman inactive ungerade modes in the Raman spectra of their anions (Table 5.4). In contrast, the $[AsF_6]^-$ anion in the crystal structure of **3** exhibits C_1 site symmetry, which results in observation of the formally Raman inactive T_{1u} modes in addition to splittings arising from site-symmetry-lowering

for the E_g, T_{2g}, and T_{1u} modes (Table 5.5). Correlation of the site symmetries of **1** (C_i), **2** (C_i), and **3** (C_1) to the space group symmetries (C_i) does not predict band splitting. However, the occurrence of two crystallographically inequivalent $[AsF_6]^-$ anions in **3** gives rise to splitting of the symmetric A_{1g} band of $[AsF_6]^-$.

5.2.3.1. $[O_2Br(FXeF)_2][AsF_6]$ (1) and $[O_2Br(FXeF)_2][SbF_6]$ (2)

The low-temperature Raman spectra of **1** and **2** are shown in Figures 5.4 and 5.5, respectively. The Raman frequencies of $[BrO_2]^+$ of **1** ($\nu_{as}(BrO_2)$, 944.2/947.3 cm^{-1}; $\nu_s(BrO_2)$, 885.9 cm^{-1}; δ(OBrO), 379.2 cm^{-1}), and **2** ($\nu_{as}(BrO_2)$, 943.7/946.1; $\nu_s(BrO_2)$, 886.6; δ(OBrO), 377.0 cm^{-1}) are similar to those of $[BrO_2][SbF_6]$ (942.8/940.5, 877.9, 371.9 cm^{-1}),[143] $[BrO_2][AsF_6]$ (931, 862, 382 cm^{-1}), and $[BrO_2][BF_4]$ (947, 884, 379 cm^{-1}).[191] The $^{79/81}$Br isotopic shift, $\Delta\nu = \nu(^{79}Br) - \nu(^{81}Br)$, was only resolved for the $\Delta\nu_{as}(^{79/81}BrO_2)$ modes (**1**, 3.1 cm^{-1}; **2**, 2.4 cm^{-1}) and are comparable to the $\Delta\nu_{as}(^{79/81}BrO_2)$ isotopic shift of $[BrO_2][SbF_6]$ (2.3 cm^{-1}).[143]

The bands at 515.5 cm^{-1} (**1**) and 513.3 cm^{-1} (**2**) are assigned to the in-phase coupled stretching modes of the two symmetrically bridged XeF_2 ligands, [$\nu(Xe_2\text{-}F_3)$ + $\nu(Xe_2\text{-}F_{3A})$] + [$\nu(Xe_3\text{-}F_4)$ + $\nu(Xe_3\text{-}F_{4A})$], and are similar to those of the symmetrically bridged XeF_2 complexes $[Pb_3(FXeF)_{11}][PF_6]_6$ (514 cm^{-1}) and $[Pb(FXeF)_3][PF_6]_2$ (513 cm^{-1}).[227] The bands at 464.4, 535.5 (**1**) and 458.4, 533.9 (**2**) cm^{-1} are similar to those observed for terminally coordinated XeF_2 in $[O_2Cl(FXeF)_2][AsF_6]$ (435.6, 439.4, 446.7, and 481.1, 519.0, 530.9 cm^{-1}),[61] $[F_2OBr(FXeF)_2][AsF_6]$ (409, 460, 467, and 540, 543, 548, 552 cm^{-1}), and $[F_2OBr(FXeF)][AsF_6]$ (426, 447, and 531, 543, 559 cm^{-1}),[63] where

the lower frequencies correspond to the longer bridging Xe–F_b bonds and the higher frequencies correspond to the shorter terminal Xe–F_t bonds. Thus, the bands around 460 and 530 cm^{-1} of **1** and **2** were assigned to the $\nu(Xe_1\text{-}F_1)$ and $\nu(Xe_1\text{-}F_2)$ stretching modes. The bands display significant shifts to lower and higher frequency, respectively, relative to the $\nu_1(\Sigma_g^+)$ band of solid XeF_2 (496 cm^{-1}).[48] A similar, but less pronounced, frequency asymmetry has been reported for the asymmetrically bridged XeF_2 ligand of $Hg(OTeF_5)_2 \cdot 1.5XeF_2$ (489 and 518 cm^{-1}).[72]

The bands at 230.7 (**1**) and 228.6 (**2**) cm^{-1} are assigned to overlapping $\delta(F_1Xe_1F_2)$, $\delta(F_3Xe_2F_{3A})$, and $\delta(F_4Xe_3F_{4A})$ bending modes by analogy with those reported for $[O_2Cl(FXeF)_2][AsF_6]$ (234 cm^{-1}),[61] $[F_2OBr(FXeF)_2][AsF_6]$ (232, 299 cm^{-1}), and $[F_2OBr(FXeF)][AsF_6]$ (244 cm^{-1}).[63] These bands are shifted to higher frequency relative to $\nu_2(\Pi_u)$ of XeF_2 (213 cm^{-1}).[48]

5.2.3.2. $[O_2Br(FXeF)][AsF_6]$ (3)

The LT Raman spectrum of $[O_2Br(FXeF)][AsF_6]$ (**3**) is shown in Figure 5.5. The occurrence of two crystallographically inequivalent $[BrO_2]^+$ cations in **3** results in additional splittings of the $[BrO_2]^+$ Raman bands ($\nu_{as}(BrO_2)$; 943.5/945.7 and 934.4/937.2 cm^{-1}; $\nu_s(BrO_2)$, 883.8 and 876.8 cm^{-1}; $\delta(OBrO)$, 376.2 and 371.0 cm^{-1}) in addition to isotopic splittings, $\Delta\nu_{as}(^{79/81}BrO_2)$ = 2.2 and 2.8 cm^{-1}, that are similar to those of **1** and **2**.

The Xe–F bond length asymmetries of **3** are similar to those of **1**, **2**, and the terminally coordinated XeF_2 coordination complex, $[F_2OBr(FXeF)_2][AsF_6]$.[63] The ν(Xe-F) stretching modes of the two XeF_2 ligands in **3** are therefore expected to in- and out-of-

phase (i.p. and o.o.p.) couple to give four modes, [ν(Xe_1-F_1) ± ν(Xe_2-F_4)] and [ν(Xe_1-F_2) ± ν(Xe_2-F_3)]. The assignment of specific bands to the i.p. and o.o.p. coupled modes were made by analogy with [$F_2OBr(FXeF)_2$][AsF_6], which increase in frequency in the order [ν(Xe-F_b) − ν(Xe-F_b)] < [ν(Xe-F_b) + ν(Xe-F_b)] < [ν(Xe-F_t) − ν(Xe-F_t)] < [ν(Xe-F_t) + ν(Xe-F_t)].[61] The highest frequency bands (i.p., 545.9; o.o.p., 525.6 cm^{-1}) are therefore assigned to the [ν(Xe_1-F_1) ± ν(Xe_2-F_4)] stretching modes, whereas the lower frequency bands (i.p., 497.0; o.o.p., 458.8 cm^{-1}) are assigned to the [ν(Xe_1-F_2) ± ν(Xe_2-F_3)] stretching modes. These bands occur at frequencies that are comparable to those of the asymmetrically bridged XeF_2 ligands of **1** and **2** (vide supra). The band at 214.7 cm^{-1} is assigned to the in-phase coupled [δ($F_1Xe_1F_2$) + δ($F_3Xe_2F_4$)] bending mode of **3** by comparison with the bending modes of **1** and **2**.

Table 5.4. Experimental[a] vibrational frequencies, intensities, and assignments for $[O_2Br(FXeF)_2][AsF_6]$ (**1**) and $[O_2Br(FXeF)_2][SbF_6]$ (**2**)

exptl			assgnts[c]
1[a]	**2**[b]		
947.3(16)	946.1(14)	^{79}Br	$\nu_{as}(BrO_2)$
944.2(sh)	943.7(13)	^{81}Br	
885.9(73)	886.6(65)	^{79}Br, ^{81}Br	$\nu_s(BrO_2)$
681.3(24)	649.3(26)		$\nu_1(A_{1g})$ ($[PnF_6]^-$)
587.6(2)	560.2(sh)		$\nu_2(E_g)$ ($[PnF_6]^-$)
581.2(1)	556.8(4)		
535.5(41)	533.9(51)		$\nu(Xe_1\text{-}F_2)$
515.5(100)	513.3(100)		$[\nu(Xe_2\text{-}F_3) + \nu(Xe_2\text{-}F_{3A})] + [\nu(Xe_3\text{-}F_4) + \nu(Xe_3\text{-}F_{4A})]$
464.4(18)	458.4(27)		$\nu(Xe_1\text{-}F_1)$
379.2(13)	377.0(12)		δ(OBrO)
370.8(4)[d]			$\nu_3(T_{2g})$ $[PnF_6]^-$
367.6(6)	284.4(10)[e]		
364.9(6)[d]	278.8(6)[e]		
230.7(4)	228.8(4)		$\delta(F_1Xe_1F_2) + \delta(F_3Xe_2F_{3A}) + \delta(F_4Xe_3F_{4A})$
	160.5(sh)		deformation/lattice modes
152.8(12)	145.3(11)		
137.8(9)	127.5(8)		
119.5(30)	114.8(sh)		
110.3(26)	108.2(18)		

[a] The Raman spectrum was recorded for a dry crystalline mixture of **1**, $[BrO_2][AsF_6]$, and XeF_2 in an FEP sample tube at −150 °C using 1064-nm excitation, where **1** was the dominant species. The band assigned to the symmetric stretching frequency of unreacted XeF_2 occurred at 496(89) cm^{-1}. Vibrational bands due to $[BrO_2][AsF_6]$ were observed at 932(1), 863(5), 687(sh), 580(1), 575(1), 553(3), 371(sh), and 365(sh) cm^{-1} (this work; assigned by comparison with ref. 136). [b] The Raman spectrum was recorded for a dry crystalline mixture of **2**, $[BrO_2][SbF_6]$, and XeF_2 in an FEP sample tube at −150 °C using 1064-nm excitation, where **2** was the dominant species. The band assigned to the symmetric stretching mode of unreacted XeF_2 occurred at 496(89) cm^{-1}. The vibrational bands of $[BrO_2][SbF_6]$ were observed at 940(sh), 878(27), 637(19), 563(5), 551(12), 372(6), 284(10), and 279(6) cm^{-1} (this work; assigned by comparison with ref. 139). [c] Assignments were made under O_h symmetry for the $[PnF_6]^-$ anions. Abbreviations denote stretch (ν) and bend (δ). [d] The band overlaps with $[BrO_2][AsF_6]$ ($\nu_3(T_{2g})$ $[AsF_6]^-$, 365, 371 cm^{-1}). [e] The band overlaps with $[BrO_2][SbF_6]$ ($\nu_3(T_{2g})$ $[SbF_6]^-$, 284, 279 cm^{-1}).

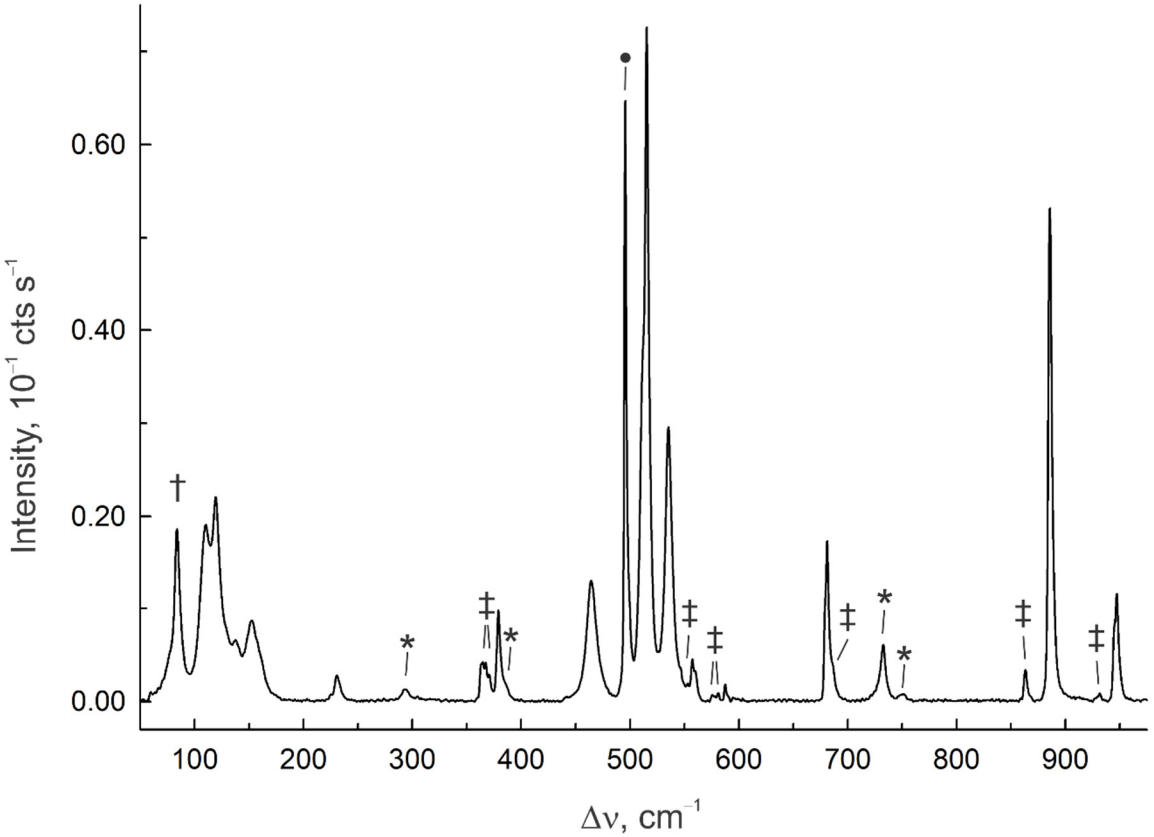

Figure 5.4. Raman spectrum of dry crystalline $[O_2Br(FXeF)_2][AsF_6]$ (**1**) recorded at −150 °C using 1064-nm excitation. Symbols denote bands assigned to unreacted $[BrO_2][AsF_6]$ (‡) and XeF_2 (•), FEP sample tube bands (*), and an instrumental artifact (†).

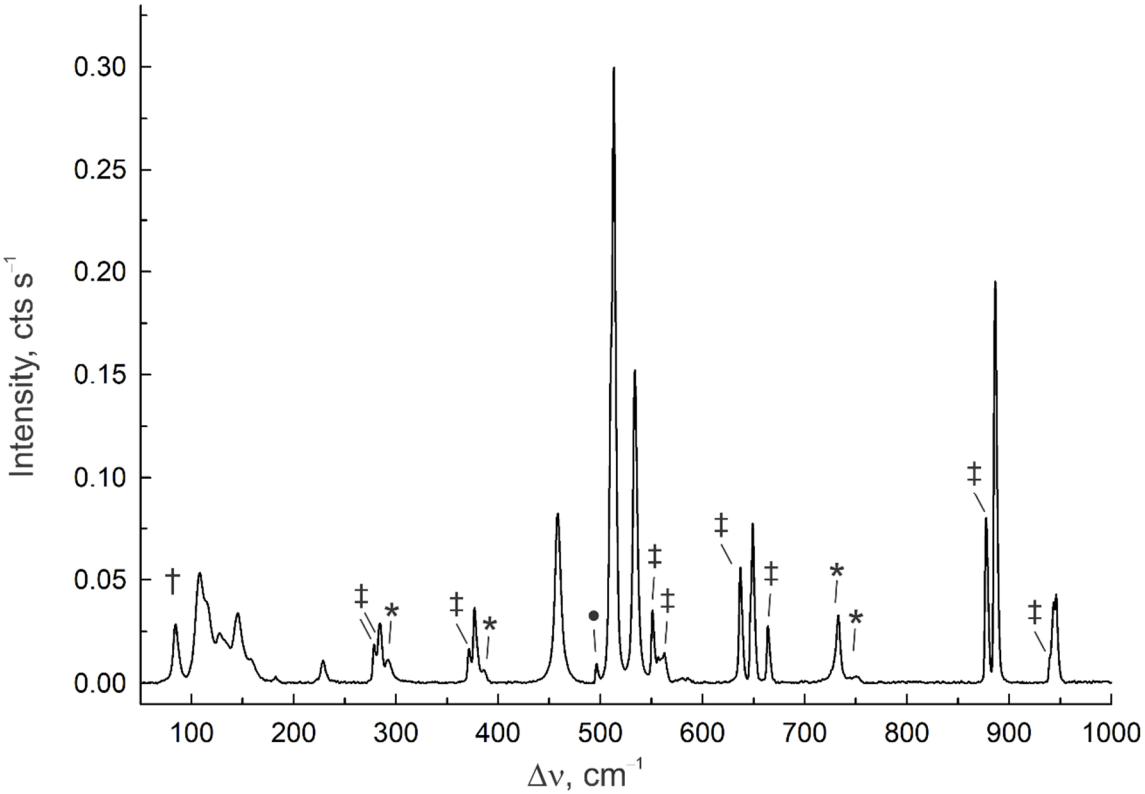

Figure 5.5. Raman spectrum of dry crystalline $[O_2Br(FXeF)_2][SbF_6]$ (**2**) recorded at −150 °C using 1064-nm excitation. Symbols denote bands assigned to unreacted $[BrO_2][SbF_6]$ (‡) and XeF_2 (•), FEP sample tube bands (*), and an instrumental artifact (†).

Table 5.5. Experimental[a] vibrational frequencies, intensities, and assignments for $[O_2Br(FXeF)][AsF_6]$ (**3**)

exptl		assgnts[b]
945.7(13)	^{79}Br	$\nu_{as}(BrO_2)$
943.5(sh)	^{81}Br	
937.2(13)	^{79}Br	
934.4(sh)	^{81}Br	
883.8(49)	^{79}Br	$\nu_s(BrO_2)$
	^{81}Br	
876.8(51)	^{79}Br	
	^{81}Br	
700.1(12)[c]		$\nu_4(T_{1u})$ ($[AsF_6]^-$)
685.4(29)[c]		$\nu_1(A_{1g})$ ($[AsF_6]^-$)
682.6(31)[d]		
577.8(15)[d]		$\nu_2(E_g)$ ($[AsF_6]^-$)
572.6(13)[d]		
545.9(50)		$[\nu(Xe_1\text{-}F_1) + \nu(Xe_2\text{-}F_4)]$
525.6(100)		$[\nu(Xe_1\text{-}F_1) - \nu(Xe_2\text{-}F_4)]$
497.0(44)[e]		$[\nu(Xe_1\text{-}F_2) + \nu(Xe_2\text{-}F_3)]$
458.8(23)		$[\nu(Xe_1\text{-}F_2) - \nu(Xe_2\text{-}F_3)]$
402.8(3)		$\nu_5(T_{1u})$ $[AsF_6]^-$
397.5(4)		
393.6(4)		
376.2(12)[d]		δ(OBrO)
371.0(11)		
366.5(21)[d]		$\nu_3(T_{2g})$ $[AsF_6]^-$
214.7(2)		$\delta(F_1Xe_1F_2) + \delta(F_3Xe_2F_4)$
155.7(10)		deformation/lattice modes
133.4(12)		
111.7(10)		
95.9(6)		

[a] The Raman spectrum was recorded for a dry crystalline mixture of **3**, $[BrO_2][AsF_6]$, and $[Xe_2F_3][AsF_6]$ in an FEP sample tube at −150 °C using 1064-nm excitation, where **3** was the dominant species. Vibrational bands of $[BrO_2][AsF_6]$ occurred at 931(sh), 862(12), and 554(5) cm^{-1}. Vibrational bands of $[Xe_2F_3][AsF_6]$ occurred at 596(14), 589(14), and 166(sh) cm^{-1}. [b] Assignments for the $[AsF_6]^-$ anions were made under O_h symmetry. Abbreviations denote stretch (ν), bend (δ). [c] The band overlaps with $[BrO_2][AsF_6]$ ($\nu_4(T_{1u})$ ($[AsF_6]^-$), 700; $\nu_1(A_{1g})$ ($[AsF_6]^-$), 685 cm^{-1}). [d] The band overlaps with $[Xe_2F_3][AsF_6]$ (683, 577, 572, and 376 cm^{-1}). [e] The band overlaps with $\nu_1(\Sigma_g^+)$ of XeF_2 (496 cm^{-1}).

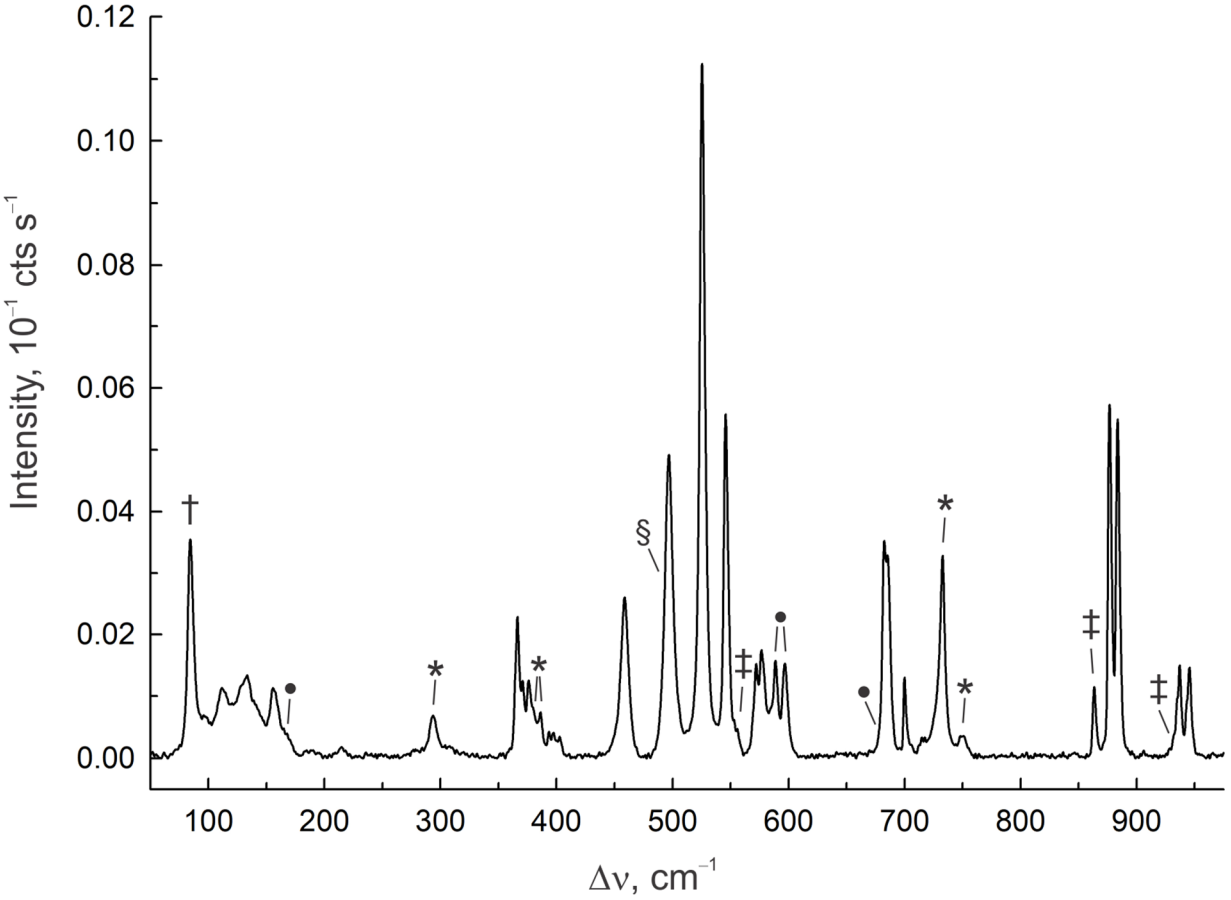

Figure 5.6. Raman spectrum of dry crystalline $[O_2Br(FXeF)][AsF_6]$ (**3**) recorded at −150 °C using 1064-nm excitation. Symbols denote a band that overlaps with the $\nu_1(\Sigma_g^+)$ of unreacted solid XeF_2 (496 cm^{-1}) (§); and bands assigned to unreacted $[BrO_2][AsF_6]$ (‡), $[Xe_2F_3][AsF_6]$ (•), FEP sample tube bands (*), and an instrumental artifact (†).

5.3. CONCLUSIONS

The coordination chemistry of cationic Br(V) species had been limited to four structurally characterized complexes; $[F_2OBr(FXeF)][AsF_6]$, $[F_2OBr(FNgF)_2][AsF_6]$ (Ng = Kr, Xe), and $[O_2Br(BrOF_2)_2][AsF_6]$. Three new Br(V) coordination complexes have now been synthesized by reactions of $[BrO_2][PnF_6]$ (Pn = As, Sb) with XeF_2 in aHF, namely $[O_2Br(FXeF)_2][PnF_6]$ and $[O_2Br(FXeF)][AsF_6]$, which were structurally characterized by LT Raman spectroscopy and LT SCXRD and provide the first examples of $[BrO_2]^+$ coordination complexes with a noble-gas fluoride. In contrast with $[O_2Br(FXeF)_2][PnF_6]$, which displays both symmetrically and asymmetrically bridged XeF_2 ligands, $[O_2Br(FXeF)][AsF_6]$ displays only an asymmetrically bridged XeF_2 ligand. The $[O_2Br(FXeF)_2][PnF_6]$ salts are not isotypic with $[O_2Cl(FXeF)_2][AsF_6]$, which is attributed to the larger covalent radius of Br(V) relative to that of Cl(V), where Br(V) can accommodate a larger primary plus secondary coordination sphere. The Br(V) atoms of these complexes have total Br(V) coordination numbers of eight ($CN_{Br} = 2 + 6$). The complex salts are intimately ion-paired, and are extensively fluorine bridge in the solid-state through secondary Br---F_{Xe} and Br---F_{Pn} bonds that are predominantly electrostatic in character.

CHAPTER 6

Syntheses and Structural Characterizations of $[ClO_2]_2[cyclo\text{-}\mu\text{-}(OIrF_4)_3]$ and the Coordination Complex $F_5Ir\text{---}OClF$

6.1. Introduction

Historically, the noble metals (Ru, Rh, Pd, Ag, Os, Ir, Pt, and Au) have been characterized by their resistance to chemical attack and propensity to favor oxidation state 0, much like the noble gases. Although the chemistries of the oxides and fluorides of the noble metals are well established,[228] there are no structurally characterized examples of Rh, Pd, Ag, Ir, Pt, and Au oxide fluorides.[228] This may be rationalized, in part, by the *oxo-wall* rule: transition metals in tetragonal coordination environments that have more than five d electrons cannot form M–O (M = transition metal) π-bonds because their π* antibonding orbitals are fully occupied.[229] The MO diagram of the d^1 vanadyl ion, $[VO(H_2O)_5]^{2+}$ (Figure 6.1), provides an illustration of an early-row TM in a tetragonal coordination sphere that obeys the *oxo-wall* rule that has fully populated π bonding orbitals which gives rise to a V≡O triple bond.[230] Transition metals having more than five d electrons must reduce their coordination numbers and/or adopt different geometries to make orbitals available that can accommodate nonbonding electrons. Consequently, late-row TMs, especially the noble-metals, do not form metal-oxygen double bonds in tetragonal coordination environments unless they are in their highest oxidation states, which renders them prone to O_2, F_2, and OF redox eliminations owing to their high electron affinities. Thus, compounds of Rh/Ir(IV,V,VI), Pd/Pt(V,VI), and Au(V) are candidates for noble-metal oxide fluoride formation because their d-orbital occupancies fall short of the *oxo-wall* regardless of their coordination geometries.

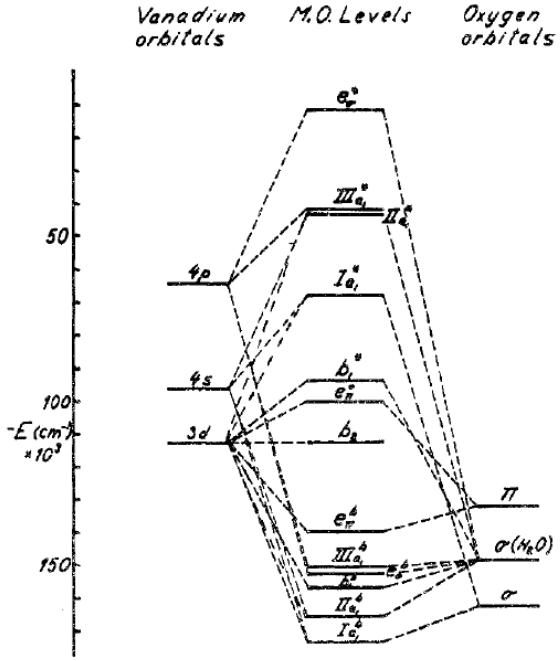

Figure 6.1. Molecular orbital (MO) scheme for $[VO(H_2O)_5]^{2+}$ (C_{4v}). Energy levels are drawn to scale. The MOs are labeled according to their respective symmetries under C_{4v} point group symmetry. The prefixes I, II, and III denote different MO's that have a_1 symmetry. Reproduced with permission from Ballhausen, C. J.; Gray, H. B. *Inorg. Chem.* **1962**, *1*, 111–122.

Among the elements in the Periodic Table, iridium has the greatest range of documented oxidation states (−3, −1, 0, +1, +2, +3, +4, +5, +6, +7, +8, and +9).[231] The highest iridium oxidation state for which macroscopic amounts of compounds have been isolated is Ir(VI), as exemplified by IrF_6[232] and the $[IrO_6]^{6-}$ anion.[233] Quantum-chemical calculations indicate that the highest oxidation state iridium fluoride or oxide fluoride that has a realistic chance of existing is Ir(VII), e.g., IrF_7, $IrOF_5$, and $[IrF_6]^+$.[234] The $[IrF_6]^+$ cation has been observed in the gas phase by mass spectrometry (Schrobilgen *et al.*, unpublished work). Both $Ir^{VII}OF_5$ and $Ir^{VI}OF_4$ have

fewer than five d electrons and are predicted to be stable with respect to O_2, F_2, or OF elimination,[234] and are therefore reasonable synthetic goals for the syntheses of iridium oxide fluoride species. Oxidative fluorination or O/F metathesis of IrO_2 may therefore yield an isolable iridium oxide fluoride species.

Like the noble-gas fluorides, ClF_3 is an aggressive oxidative fluorinating agent which has diverse applications as an O/F metathesis reagent and amphoteric fluoride-ion donor/acceptor (Figure 6.2).[178]

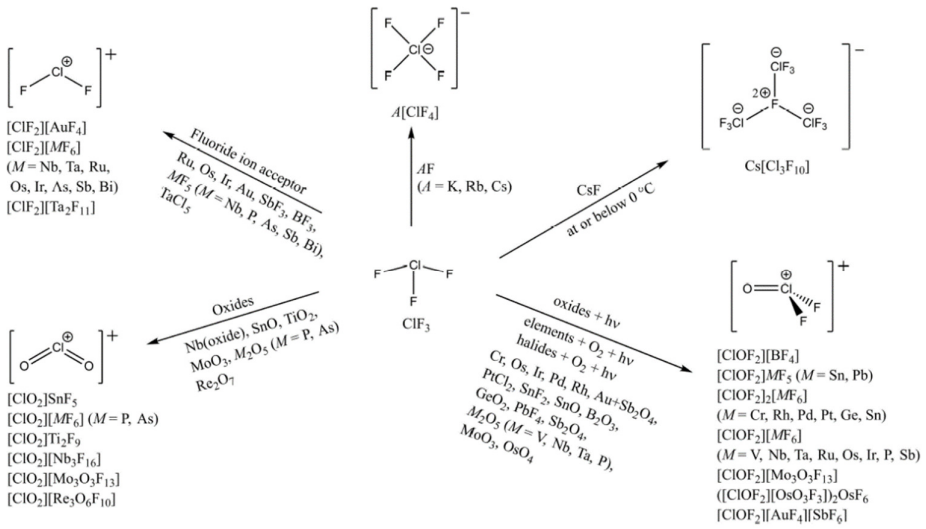

Figure 6.2. Overview of selected compounds obtained from reactions with ClF_3. Reproduced with permission from Scheibe, B.; Karttunen, A. J.; Kraus, F. *Z. Anorg. Allg. Chem.* **2022**, e202200106.

Reactions of ClF_3 with metal oxides are known to yield $[ClO_2]^+$ salts of high-oxidation-state fluoro- and oxyfluoro-anions by means of oxidative fluorination and O/F metathesis.[141] The latter reactions yield endothermic OClF (calcd. ΔH^o_f = 27.6 kJ mol^{-1}, CCSD-DTQ; 24.3 kJ mol^{-1}, CCSD-Q5),[177] which rapidly disproportionates to ClO_2F and ClF at room temperature.[235–238] Salts of $[ClO_2]^+$ form by reactions of ClO_2F

with Lewis acidic metal fluorides and/or oxide fluorides that are formed by fluorination of metal oxides.[141] Although OClF is proposed as an unstable intermediate in the reaction of ClF_3 with metal oxides, it has not been directly observed in these reactions.[141] However, it has been synthesized and isolated by hydrolysis of ClF_3,[236,238] photolysis of ClF and O_3 in an argon matrix,[237] and exposure of ClF_3 and O_2 to an electric discharge.[238] The structure of OClF has been shown by vibrational[235–238] and microwave spectroscopies[238] to be bent, and the analysis of its ground-state rotational spectrum has provided high-precision gas-phase structural parameters.[238] The half-life of gaseous OClF in a stainless steel absorption cell pressurized to 100 Pa with an equimolar mixture of ClF_3 and H_2O is ca. 3 min.[236] Thus, OClF is surprisingly long-lived in the gas-phase, and may therefore have sufficient kinetic stability in an acidic medium such as aHF to react with fluoride-ion acceptors. However, attempts to abstract fluoride-ion from OClF formed by controlled hydrolysis of $[ClF_2][AsF_6]$ in aHF were unsuccessful. Instead of $[ClO][AsF_6]$, $[ClO_2][AsF_6]$ was obtained as the only product after volatile compounds had been removed under dynamic vacuum.[239] More recently, the hydrolysis of $[ClF_2][IrF_6]$ in aHF solvent in the presence of ClF_3 was shown to yield $[ClO_2][IrF_6]$.[141] Thus, no $[ClO]^+$ salts or neutral coordination complexes of OClF have been reported.

Although ClF_5[240,241] is a weaker oxidative fluorinating agent than ClF_3, it fluorinates second and third row non-metals[241] and may react with metal oxides to yield $[ClO_2]^+$ salts of high-oxidation-state metal fluoro- and oxyfluoro-anions. The present study therefore investigates the reactions of IrO_2 with ClF_3 and ClF_5 in aHF solvent with the goals to synthesize an iridium oxide fluoride species and monitor the products of these reactions to obtain direct evidence for OClF formation.

6.2. Results and Discussion

6.2.1. Syntheses

6.2.1.1. Syntheses of F_5Ir---OClF and $[ClO_2][IrF_6]$

The reaction of IrO_2 with excess ClF_3 in aHF solvent was carried out at room temperature in an FEP reaction vessel equipped with a stainless steel valve. Excess ClF_3 was condensed onto a sample of IrO_2 under frozen aHF solvent at −196 °C. Upon warming to room temperature, vigorous gas evolution ensued that originated from the IrO_2 powder at the bottom of the reaction vessel. A brown-black precipitate, likely IrF_4, initially formed which was subsequently consumed as the reaction progressed. The solution turned dark amber in color upon complete consumption of IrO_2 and IrF_4 within ca. 4 h. The sample was cooled to –78 °C, whereupon amber, needle-shaped crystals of F_5Ir---OClF and purple, plate-shaped crystals of $[ClO_2][IrF_6]$ grew from solution overnight. Crystals suitable for single-crystal X-ray structure determinations were isolated by removal of the aHF solvent at –78 °C and were characterized by LT SCXRD.

The synthesis and crystallographic characterization of F_5Ir---OClF (Eqs. **6.1–6.3**) provides the first evidence for the formation of OClF as an intermediate in the reaction of ClF_3 with a metal oxide.

$$IrO_2 + 2ClF_3 \xrightarrow{aHF} IrF_4 + 2OClF \quad (\mathbf{6.1})$$

$$2IrF_4 + ClF_3 \xrightarrow{aHF} 2IrF_5 + ClF \quad (\mathbf{6.2})$$

$$IrF_5 + OClF \xrightarrow{aHF} F_5Ir\text{---}OClF \quad (\mathbf{6.3})$$

Excess OClF disproportionates to ClF and ClO_2F (Eq. **6.4**), and ClO_2F reacts with IrF_5 to form $[ClO_2][IrF_6]$ (Eq. **6.5**).

$$2\mathrm{OClF} \xrightarrow{\mathrm{aHF}} \mathrm{ClF} + \mathrm{ClO_2F} \quad (\mathbf{6.4})$$

$$\mathrm{ClO_2F} + \mathrm{IrF_5} \xrightarrow{\mathrm{aHF}} [\mathrm{ClO_2}][\mathrm{IrF_6}] \quad (\mathbf{6.5})$$

Examination of the crystalline sample under a stereomicroscope during LT SCXRD crystal mounting showed that the product consisted of approximately equal amounts of F_5Ir---OClF and $[ClO_2][IrF_6]$.

Attempts to obtain a LT Raman spectrum of the dry crystalline mixture of amber F_5Ir---OClF and purple $[ClO_2][IrF_6]$ resulted in pyrolysis of the sample at the focal point of the laser beam and the formation of a yellow solid that was likely IrF_5. The Raman spectrum exhibited seven intense, broad fluorescence bands between 2175–3662 cm^{-1} with no perceptible bands at lower frequencies other than those of the FEP sample tube.

6.2.1.2. Synthesis of $[ClO_2]_2[cyclo\text{-}\mu\text{-}(OIrF_4)_3]$

The reaction of IrO_2 with excess ClF_5 in aHF solvent was carried out in an FEP reaction vessel equipped with a stainless-steel valve. The reaction required up to 4 days to go to completion at ambient temperature. The faster reaction time for ClF_3 relative to that of ClF_5 is consistent with their relative oxidative fluorinating strengths. Upon warming to room temperature, slow gas evolution occurred that originated from solid IrO_2 at the bottom of the reaction vessel and coincided with the formation of a brown-black precipitate that was likely IrF_4. As the reaction proceeded, the solution changed from colorless to brown-black and was accompanied by dissolution of solid IrO_2 and IrF_4 and gas evolution. The brown-black solution was olive-green in color when a thin film of the solution coated the FEP reaction vessel. After reaction at RT for 4 days, the sample was cooled to −22 °C, whereupon black, needle-shaped crystals of $[ClO_2]_2[cyclo\text{-}\mu\text{-}(OIrF_4)_3]$ and purple, plate-shaped crystals of $[ClO_2][IrF_6]$ grew

from the solution between −22 and –30 °C over a period of 8 h. Crystals suitable for LT SCXRD structure determinations were mounted on a X-ray diffractometer.

The LT Raman spectrum of a dry crystalline mixture of $[ClO_2]_2$[*cyclo*-μ-$(OIrF_4)_3$] and $[ClO_2][IrF_6]$ resulted in strong fluorescence bands in the 2100–3600 cm^{-1} region. Absorption of the laser beam (1064-nm) by black crystalline $[ClO_2]_2$[*cyclo*-μ-$(OIrF_4)_3$] resulted in rapid decomposition with the formation of a yellow spot, possibly IrF_5, where the laser beam struck the sample.

A plausible reaction pathway that leads to the formation of the mixed oxidation state 2 x Ir(V)/1 x Ir(VI) dianion, [*cyclo*-μ-$(OIrF_4)_3]^{2-}$, is provided in the ensuing discussion.

The formation of $[ClO_2][IrF_6]$ (characterized by a LT SCXRD unit cell determination) is slow, and may occur by reaction of ClF_5 with IrO_2 (Eqs. **6.6**–**6.8**).

$$IrO_2 + ClF_5 \xrightarrow{aHF} IrF_4 + ClO_2F \qquad (\mathbf{6.6})$$

$$2IrF_4 + ClF_5 \xrightarrow{aHF} 2IrF_5 + ClF_3 \qquad (\mathbf{6.7})$$

$$IrF_5 + ClO_2F \xrightarrow{aHF} [ClO_2][IrF_6] \qquad (\mathbf{6.8})$$

Formation of ClF_3 in Eq. **6.7**. necessitates that its reaction with IrO_2 to give $[ClO_2][IrF_6]$ and F_5Ir---OClF must also be considered (Eqs. **6.1**–**6.5**). Although F_5Ir---OClF is stable in aHF solvent at room temperature for up to ca. 4 h, the longer reaction time employed for this reaction (4 days) may have allowed the slower competing redox disproportionation of F_5Ir---OClF to proceed to completion (Eq. **6.9**).

$$F_5Ir^{V}\text{---}OClF \xrightarrow{4\ d} Ir^{VI}OF_4 + ClF + \tfrac{1}{2}F_2 \qquad (\mathbf{6.9})$$

Redox decomposition of F_5Ir---OClF accounts for the presence of Ir(VI) in [*cyclo*-μ-$(OIrF_4)_3]^{2-}$, because ClF_3 and ClF_5 are not expected to oxidize iridium above the +5 oxidation state given that the room temperature reaction of the stronger oxidative fluorinating agent, ClF_3, with Ir metal in aHF solvent yields $[ClF_2][IrF_6]$.[242] Lewis acidic $IrOF_4$ is expected to abstract fluoride ion from ClO_2F in aHF solution to form $[ClO_2][Ir^{VI}OF_5]$ (Eq. **6.10**).

$$IrOF_4 + ClO_2F \xrightarrow{aHF} [ClO_2][IrOF_5] \qquad (\mathbf{6.10})$$

By analogy with $[CrOF_5]^-$ in its $[Xe_2F_{11}]^+$ salt (see Chapters 9 and 11),[243,244] the $[Ir^{VI}OF_5]^-$ anion may undergo redox elimination of F_2 in aHF solvent at RT to form the more stable $[Ir^{V}OF_4]^-$ intermediate (Eq. **6.11**). The $[Ir^{V}OF_4]^-$ anion has an unsaturated primary coordination sphere and may be expected to dimerize to form $[ClO_2]_2[Ir^{V}_2O_2F_8]$ (Eq. **6.12**) by analogy with $[CrOF_4]^-$ [244] and $[AsOF_4]^-$ [245] which dimerize to form the F-bridged $[Cr_2O_2F_8]^{2-}$ dianion[244] (see Chapter 9) and O-bridged $[As_2O_2F_8]^{2-}$ dianion.[245]

$$[ClO_2][IrOF_5] \xrightarrow{aHF} [ClO_2][IrOF_4] + \tfrac{1}{2}F_2 \qquad (\mathbf{6.11})$$

$$2[ClO_2][IrOF_4] \xrightarrow{aHF} [ClO_2]_2[Ir_2O_2F_8] \qquad (\mathbf{6.12})$$

Reaction of $[ClO_2]_2[Ir^{V}_2O_2F_8]$ and $IrOF_4$ in aHF would then yield the observed mixed-oxidation-state product, $[ClO_2]_2$[*cyclo*-μ-$(OIrF_4)_3]$ (Eq. **6.13**), in which two Ir(V) and one Ir(VI) O-bridge to form a six-membered Ir_3O_3-ring.

$$[ClO_2]_2[Ir_2O_2F_8] + IrOF_4 \xrightarrow{aHF} [ClO_2]_2[cyclo\text{-}\mu\text{-}(OIrF_4)_3] \qquad (\mathbf{6.13})$$

6.2.2. X-ray Crystallography.

A summary of the X-ray crystallographic data and refinement results for $[ClO_2]_2$[*cyclo*-μ-$(OIrF_4)_3]$ and F_5Ir---OClF is provided in Table 6.1. The experimental

and calculated geometric parameters for $[ClO_2]_2[cyclo\text{-}\mu\text{-}(OIrF_4)_3]$ (**1**) and F_5Ir---OClF (**2**) are listed in Tables 6.2, 6.3, and A3.1–A3.3.

Table 6.1. Summary of crystal data and refinement results for $[ClO_2]_2[cyclo\text{-}(\mu\text{-}OIrF_4)_3]$ (**1**) and F_5Ir---OClF (**2**)

	1	**2**
space group	*Fdd*2	$P2_1/n$
a (Å)	15.6155(9)	5.1257(7)
b (Å)	11.9737(6)	19.739(3)
c (Å)	14.3621(8)	10.8299(15)
α (deg)	90	90
β (deg)	90	99.673(5)
γ (deg)	90	90
V (Å^3)	2685.4(3)	1080.2(3)
Z[a]	8	8
M_W[b]	987.50	357.65
ρ_{calcd}[c]	4.885	4.399
T (°C)	–173	–173
μ [d]	30.24	25.270
R_1[e]	0.0110	0.0433
wR_2[f]	0.0243	0.0856

[a] Molecules/unit cell. [b] g mol^{-1}. [c] g cm^{-3}. [d] mm^{-1}. [e] $R_1 = \Sigma||F_o| - |F_c||/\Sigma|F_o|$. [f] $wR_2 = [\Sigma(w(F_o^2 - F_c^2)^2)/\Sigma(w(F_o^2)^2)]^{1/2}$.

6.2.2.1. $[ClO_2]_2[cyclo\text{-}\mu\text{-}(OIrF_4)_3]$ (1)

The crystal structure of $[ClO_2]_2[cyclo\text{-}\mu\text{-}(OIrF_4)_3]$ (**1**) provides the first structurally characterized example of a iridium oxide fluoride dianion and of a mixed Ir(V)/Ir(VI) species (Figure 6.3, Table 6.2). The cations and dianions are strongly ion-paired, with each dianion forming twelve secondary Cl---F_{Ir} bonds with neighboring $[ClO_2]^+$

cations (2.548(2)–3.174(1) Å) that are significantly shorter than the sum of the chlorine and fluorine van der Waals radii (3.22, 3.28 Å).[167] This gives rise to a three-dimensional fluorine-bridged network of intimately ion-paired cations and dianions. The $[ClO_2]^+$ cations in **1** occupy general positions, and have Cl–O bond lengths (1.409(3), 1.409(3) Å) that are somewhat longer than those of $[ClO_2][RuF_6]$ (1.379(9) Å),[185] and $[ClO_2][SbF_6]$ (1.385(5) Å).[143] The O–Cl–O bond angle (118.7(2)°) is bent and equal within ±3σ to those of $[ClO_2][RuF_6]$ (117.2(9)°)[185] and $[ClO_2][SbF_6]$ (117.8(9)°).[143]

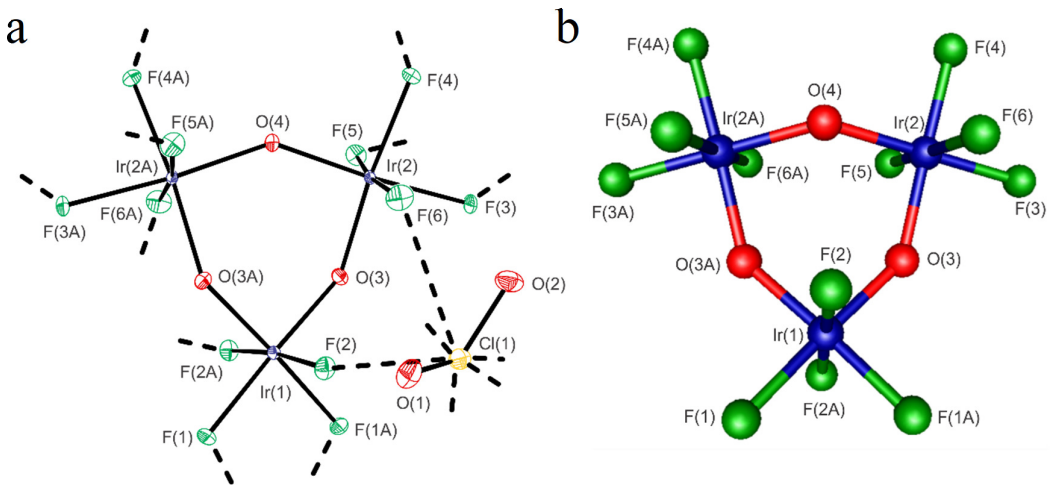

Figure 6.3. (a) The $[cyclo\text{-}\mu\text{-}(OIrF_4)_3]^{2-}$ dianion in the X-ray crystal structure of $[ClO_2]_2[cyclo\text{-}\mu\text{-}(OIrF_4)_3]$. Thermal ellipsoids are drawn at the 50% probability level. Secondary Cl---F bonds are indicated by dashed lines. (b) The gas-phase geometry of $[cyclo\text{-}\mu\text{-}(OIrF_4)_3]^{2-}$ (C_1) was optimized at the uPBE1PBE/aug-cc-pVTZ-(Ir)-Def2-TZVPD-(O, F) level of theory.

The [*cyclo*-(μ-OIrF$_4$)$_3$]$^{2-}$ dianion is a six-membered ring (C_2 symmetry, Figure 6.4) comprised of two symmetry-equivalent Ir(V) atoms and one Ir(VI) atom that are bridged by O atoms (Figure 6.1) in which the Ir$_1$, Ir$_2$, Ir$_{2A}$, and O$_4$ atoms are coplanar and the O$_3$ and O$_{3A}$ atoms are positioned 0.385 Å above and below the plane. The dianion of **1** is O-bridged like that of [*cyclo*-μ-(OSbF$_4$)$_3$]$^{3-}$ in its Cs$^+$ salt, except that [*cyclo*-μ-(OSbF$_4$)$_3$]$^{3-}$ has a boat-shaped Sb$_3$O$_3$-ring structure with C_s symmetry.[246]

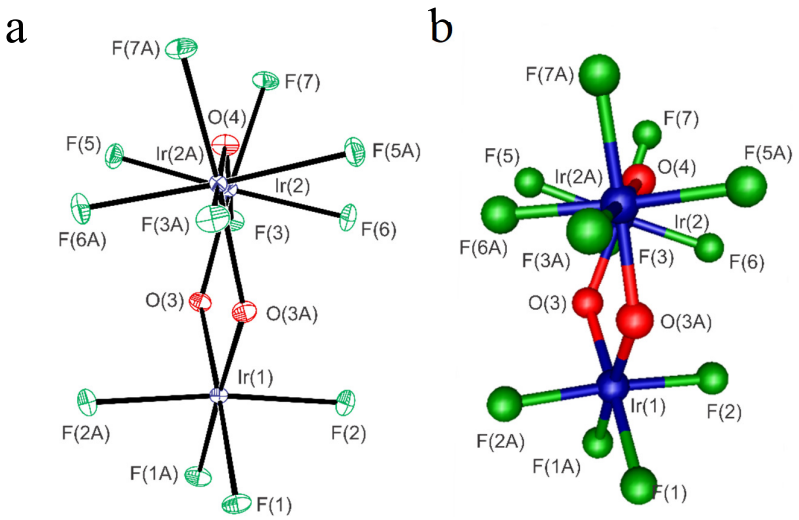

Figure 6.4. Side-on views of the (a) experimental and (b) calculated (uPBE1PBE/aug-cc-pVTZ-(Ir)-Def2-TZVPD-(O, F)) structures of [*cyclo*-μ-(OIrF$_4$)$_3$]$^{2-}$. Thermal ellipsoids are drawn at the 50% probability level.

Each Ir atom of [*cyclo*-(μ-OIrF$_4$)$_3$]$^{2-}$ has two terminal Ir–F bonds that are trans to Ir–O bridge bonds and two terminal Ir–F bonds that are trans to one another. The Ir coordination spheres are distorted octahedra in which the Ir–F bonds are bent away from the Ir–O bridge bonds (O–Ir–F$_{cis}$, 90.41(10)–93.90(10)^o). The terminal Ir–F bonds (1.883(2)–1.923(2) Å) are significantly longer than the Ir–O bridge bonds

(1.8479(13), 1.851(2), 1.861(2) Å). This supports assignment of the bridging atoms to oxygen rather than to fluorine because Ir–F bridge bonds would have greater degrees of ionic character and would therefore be significantly longer than terminal Ir–F bonds. Furthermore, the average Ir–O bond length of $[cyclo\text{-}\mu\text{-}(OIrF_4)_3]^{2-}$ (1.853(2) Å) is somewhat shorter than the bridging Ir–O bonds of the symmetrically bridged dinuclear iridium oxo-complexes $Cl(pyalk)_2Ir–O–Ir(pyalk)_2Cl$ (pyalk = 2-(2-pyridinyl)-2-propanolate), which contract upon oxidation of iridium from Ir(IV)/ Ir(IV) (1.917(5) Å) in Cl(pyalk)Ir–O–Ir(pyalk)Cl to Ir(IV)/Ir(V) (1.876(4) Å) in $[Cl(pyalk)_2Ir–O–Ir(pyalk)_2Cl][PF_6]$ and Ir(V)/Ir(V) (1.8621(4) Å) in $[Cl(pyalk)_2Ir–O–Ir(pyalk)_2Cl][PF_6]_2$.[247] The shorter average Ir–O bridge bond length of **1** (1.853(2) Å) relative to that of $[Cl(pyalk)_2Ir–O–Ir(pyalk)_2Cl]^{2+}$ is consistent with a description of $[cyclo\text{-}\mu\text{-}(OIrF_4)_3]^{2-}$ as a 2 x Ir(V) / 1 x Ir(VI) mixed-oxidation-state dianion.

Table 6.2. Experimental and calculated[a] bond lengths (Å) for $[cyclo\text{-}\mu\text{-}(OIrF_4)_3]^{2-}$

	exptl	calcd		exptl	
Ir(1)–O(3)	1.861(2)	1.851	Ir(1)–O(3A)	1.861(2)	1.851
Ir(1)–F(1)	1.883(2)	1.895	Ir(1)–F(1A)	1.883(2)	1.895
Ir(2)–F(2)	1.910(2)	1.897	Ir(2)–F(2A)	1.910(2)	1.886
Ir(2)–O(3)	1.851(2)	1.897	Ir(2A)–O(3A)	1.851(2)	1.897
Ir(2)–O(4)	1.8479(13)	1.873	Ir(2A)–O(4)	1.8479(13)	1.872
Ir(2)–F(3)	1.923(2)	1.879	Ir(2A)–F(3A)	1.923(2)	1.879
Ir(2)–F(4)	1.911(2)	1.900	Ir(2A)–F(4A)	1.911(2)	1.900
Ir(2)–F(5)	1.895(2)	1.882	Ir(2A)–F(5A)	1.895(2)	1.888
Ir(2)–F(6)	1.884(2)	1.888	Ir(2A)–F(6A)	1.884(2)	1.882

[a] uPBE1PBE/aug-cc-pVTZ(Ir)-Def2TZPVD-(O, F). The labeling scheme is the same as in Figure 6.3. Table A3.1 lists the complete set of experimental geometric parameters for $[ClO_2]_2[cyclo\text{-}\mu\text{-}(OIrF_4)_3]$ and Table A3.2 lists the complete set of calculated geometric parameters for $[cyclo\text{-}\mu\text{-}(OIrF_4)_3]^{2-}$.

The shortest Ir–O bridge bonds of **1** are trans to the longest Ir–F bonds, which form the shortest secondary Cl---F bonds, and vice versa. The polar-covalent Ir–F bonds of $[ClO_2]_2$[*cyclo*-μ-$(OIrF_4)_3$] occur within the range for the Ir–F bond lengths of the intimately ion-paired [XeF][IrF_6] salt (1.854(5)–1.961(4) Å).[248]

6.2.2.2. F_5Ir---OClF (2)

The structural characterization of F_5Ir---OClF (**2**) provides the first crystal structure of a TM coordination complex with OClF and of the OClF ligand. The asymmetric unit of **2** (Table 6.3, Figure 6.5) consists of two crystallographically unique F_5Ir---OClF structural units.

Table 6.3. Experimental and calculated bond lengths (Å) for F_5Ir---OClF

exptl				calcd	
				Gaussian[a]	ADF[b]
Cl(1)–O(1)	1.548(4)	Cl(2)–O(2)	1.548(3)	1.513	1.520
Cl(1)–F(1)	1.594(4)	Cl(2)–F(7)	1.600(3)	1.611	1.622
Ir(1)–F(2)	1.879(3)	Ir(2)–F(8)	1.867(3)	1.895	1.867
Ir(1)–F(3)	1.870(3)	Ir(2)–F(9)	1.864(3)	1.842	1.869
Ir(1)–F(4)	1.873(3)	Ir(2)–F(10)	1.874(3)	1.875	1.851
Ir(1)–F(5)	1.855(4)	Ir(2)–F(11)	1.885(3)	1.830	1.854
Ir(1)–F(6)	1.885(3)	Ir(2)–F(12)	1.879(3)	1.844	1.844
Ir(1)---O(1)	2.029(4)	Ir(2)---O(2)	2.028(3)	2.066	2.073

The labeling scheme is the same as in Figure 6.5. [a] uPBE1PBE/aug-cc-pVTZ-pp(Ir)-Def2-TZVPD-(O, F, Cl). [b] PBE0-D4/TZ2P (including collinear SOC). Table A3.3 lists the complete set of experimental and calculated geometric parameters for F_5Ir---OClF.

The Cl^{III} atoms of the OClF ligands in **2** each have six nearby F_{Ir} atoms that are within the sum of the Cl and F van der Waals radii (3.22, 3.28 Å). However, not all of these contacts are considered significant secondary bonding interactions. The total primary bond valences of the Cl^{III} atoms in **2** are 2.822 and 2.845 vu (vu = bond valence units; Cl–O, R_0 = 1.71; Cl–F, R_0 = 1.69; B = 0.37).[249,250] Inclusion of three Cl---F secondary bonds for $Cl_{(1)}$ (2.659(3), 2.749(3), and 2.885(3) Å) and two Cl---F secondary bonds for $Cl_{(2)}$ (2.565(3) and 2.587 Å) to the total bond valences of $Cl_{(1)}$ (3.015 vu) and $Cl_{(2)}$ (3.001 vu) give values that are close to the formal +3 oxidation state of Cl. The secondary bonds result in an extended three-dimensional solid-state packing arrangement (Figure A7.1).

The primary iridium coordination sphere in **2** may be described as an AX_5Y VSEPR arrangement[88] of one axial Ir---O bond (Y) and one axial and four equatorial Ir–F bonds (X) around the central Ir atom that constitutes the distorted octahedral primary coordination sphere of Ir(V). The O atom of OClF interacts with Ir at the center of the basal face of the square pyramid formed by the four equatorial F atoms and the axial F atom of the IrF_5 moiety. The Ir---O bonds of **2** (2.028(3), 2.029(4) Å) are significantly longer than the Ir–O bridge bonds of **1** (vide supra), which is consistent with their greater electrostatic character. The Ir---O–Cl bond angles of **2** (120.4(2), 119.8(2)º) are more acute than the Xe---F_b–M (M = Cr, Mo, W) bond angles of F_tNgF_b---MOF_4 (134.33(5)–148.09(7)º). The M---F_b bonds of F_tNgF_b---MOF_4 are predominantly electrostatic with small but significant degrees of covalent character that contribute to their bent Xe---F_b–M bond angles along with contributions from crystal packing. Thus, the Ir---O bonds of **2** are expected to have a higher degree of covalent character than the M---F_b bonds of F_tNgF_b---MOF_4. The Ir–F bonds of

F_5Ir---OClF (1.855(4)–1.885(3) Å) are polarized by short Cl---F secondary bonds (2.565(3)–2.885(3) Å) with neighboring OClF ligands and are comparable to the Ir–F bond lengths of $[ClO_2][IrF_6]$ (1.868(2)–1.892(2) Å).[141] The shortest Ir–F bonds (1.855(4), 1.864(3) Å) correspond to two equatorial F atoms from different F_5Ir---OClF molecules that do not have significant Cl---F secondary bonding interactions. In contrast, the longest Ir–F bonds (1.885(3), 1.885(3) Å) correspond to F atoms on Ir that have the shortest Cl---F secondary bonds.

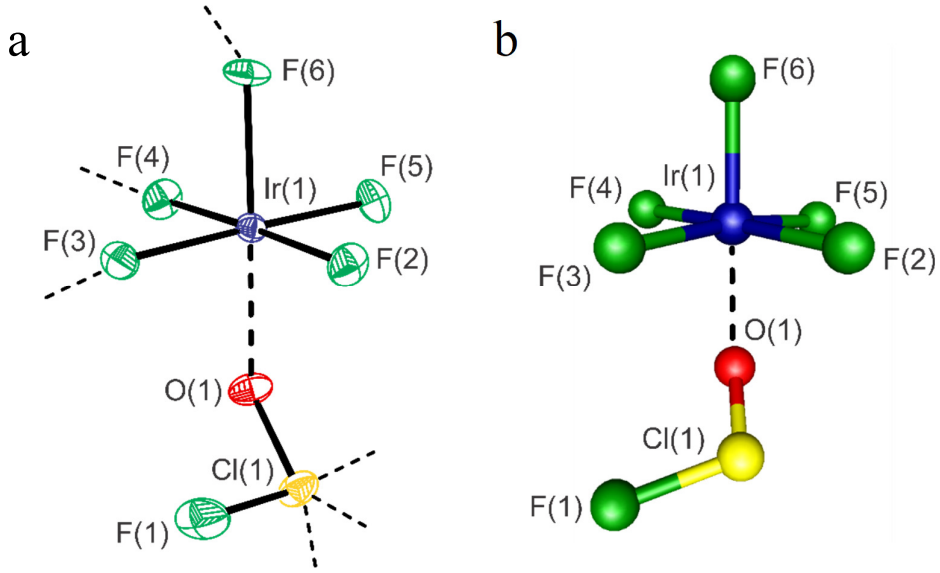

Figure 6.5. (a) One of two structural units in the X-ray crystal structure of F_5Ir---OClF (**2**). Thermal ellipsoids are drawn at the 50% probability level. (b) The calculated gas-phase geometry of F_5Ir---OClF was calculated at the uPBE1PBE/aug-cc-pVTZ-(Ir)-Def2-TZVPD-(O, F, Cl) level of theory. Secondary Ir---O and Cl---F bonds are indicated by dashed lines. The second structural unit in the X-ray crystal structure of **2** is depicted in Figure A7.2.

The Cl–O (1.548(4), 1.548(4) Å) and Cl–F (1.594(4), 1.600(3) Å) bonds of the OClF ligands of **2** are significantly elongated and shortened, respectively, relative to those of gas-phase OClF (Cl–O, 1.488(5) Å; Cl–F, 1.693(4) Å).[238] The O–Cl–F bond angle (106.7(2)°) of **2** is also somewhat more acute relative to that of gas-phase OClF (110.6(8)°)[238] which, in part, may be attributable to solid-state packing.

6.2.3. Quantum-chemical Calculations

Recent computational studies of the neutral iridium fluorides IrF_n (n = 1–6) at the scalar relativistic CCSD(T)/triple-ζ level and two-component quasi-relativistic DFT levels of theory show that SOC dominates in IrF_5 and is required to achieve a triplet ground state solution with C_{4v} symmetry.[251] In the absence of SOC, IrF_5 distorts to a $^3B_1/C_{2v}$ ground-state structure with two longer and two shorter $Ir–F_{eq}$ bonds.[251]

In the present study, the gas-phase geometries of OClF (C_s), IrF_5 (C_{4v}) and F_5Ir---OClF (C_1) were optimized at the PBE0-D4/TZ2P level of theory with relativistic SOC included (Tables A3.2-A3.5). Attempts to optimize the gas-phase geometry of $[cyclo\text{-}\mu\text{-}(OIrF_4)_3]^{2-}$ at the PBE0-D4/TZ2P level of theory with relativistic SOC included are in progress. The geometries of OClF, IrF_5, F_5Ir---OClF, and $[cyclo\text{-}\mu\text{-}(OIrF_4)_3]^{2-}$ were also calculated at the uPBE1PBE/aug-cc-PVTZ-(Ir)-Def2-TZVPD-(F,O,Cl) level of theory without inclusion of SOC because the desired bonding analysis, NBO, is incompatible with SOC corrections.

The distortion of IrF_5 to C_{2v} symmetry in the absence of SOC is reproduced in this study at the uPBE1PBE/aug-cc-PVTZ-(Ir)-Def2-TZVPD-(F,O,Cl) level of theory, with a similar distortion observed for the Ir–F bond lengths in F_5Ir---OClF. Other than this difference, the gas-phase geometries of F_5Ir---OClF calculated at PBE0-D4/TZ2P

and uPBE1PBE/aug-cc-PVTZ-(Ir)-Def2-TZVPD-(F,O,Cl) levels of theory are comparable, including their Ir---O bond lengths and Ir---O–Cl bond angles. To facilitate comparisons of F_5Ir---OClF and [*cyclo*-*μ*-$(OIrF_4)_3]^{2-}$ with each other, discussions pertaining to their calculated geometries and NBO analyses were limited to the uPBE1PBE/aug-cc-PVTZ-(Ir)-Def2-TZVPD-(F,O,Cl) level of theory. The MEPS of OClF, IrF_5, and F_5Ir---OClF were calculated at the PBE0-D4/TZ2P level of theory.

6.2.3.1. Gas-phase Geometry Optimization

The gas-phase geometries of [*cyclo*-*μ*-$(OIrF_4)_3]^{2-}$ (Figure 6.3, C_1), F_5Ir---OClF (Figure 6.5, C_1), IrF_5 (Figure A3.3, C_{2v}), and OClF (Figure A3.4. C_s) optimized at the uPBE1PBE/aug-cc-PVTZ-(Ir)-Def2-TZVPD-(F,O,Cl) level of theory with all frequencies real (Tables A3.2–A3.8). The starting geometries used for the gas-phase optimizations of [*cyclo*-*μ*-$(OIrF_4)_3]^{2-}$ (C_1) and F_5Ir---OClF (C_1) were the crystallographic geometries obtained from **1** and **2**, respectively. Attempts to optimize the geometry of [*cyclo*-*μ*-$(OIrF_4)_3]^{2-}$ at a higher symmetry (C_2) resulted in a large negative frequency (−223 cm^{-1}). The geometry of [*cyclo*-*μ*-$(OIrF_4)_3]^{2-}$ was optimized with spin multiplicities 2, 4, 6, and 8, where multiplicity 8 gave the lowest energy solution. The geometry of F_5Ir---OClF was optimized with spin multiplicities 1 and 3, where multiplicity 3 gave the lower energy solution. The initial geometries for OClF and IrF_5 were obtained from their ground-state rotational spectrum,[238] and X-ray crystal structure of F_5Ir---OClF, respectively.

The calculated gas-phase geometry of [*cyclo*-*μ*-$(OIrF_4)_3]^{2-}$ exhibits the following bond length differences relative to the ion-pair in its X-ray crystal structure: (**1**) the Ir–F bonds of F atoms that form the shortest secondary bonds in the solid state

(Ir_1–$F_{2,2A}$, Ir_2–$F_{3–5}$, Ir_{2A}–$F_{3A–5A}$) are shorter in the calculated gas-phase structure; (**2**) the Ir_2–O_3, Ir_{2A}–O_{3A}, Ir_2–O_4, and Ir_2–O_{4A} bonds that are trans to the contracted Ir–F bonds are elongated relative to those of **1**; and (**3**) the Ir_1–$O_{3,3A}$ bonds that are trans to the Ir–$F_{1,1A}$ bonds are contracted in the calculated gas-phase structure.

The experimental bond lengths and bond angles of F_5Ir---OClF are well reproduced at both levels of theory. The energy-minimized gas-phase geometries of F_5Ir---OClF have staggered conformations (∠Cl–O---Ir–$F_{(2)}$ dihedral angle: Gaussian, 41.8°; ADF, 52.7°), whereas the experimental geometry is closer to an eclipsed conformation (11.0(3)°, 22.1(2)°) (Figure 6.5). The differences between the calculated and the experimental structures are likely due to crystal packing and the tendency for Cl(III) to complete its valence shell through intra- and intermolecular secondary Cl---F_{Ir} interactions.[250] This is exemplified by the formation of two intramolecular Cl---$F_{2,3}$ secondary bonds between coordinated OClF and IrF_5 in the calculated gas-phase geometry (Gaussian, 2.887, 2.966 Å; ADF, 2.873, 3.004 Å) which are significantly shorter than the sums of the Cl and F van der Waals radii (vide supra).

6.2.3.2. Natural Bond Order (NBO) Analyses

The chemical bonding in [*cyclo*-μ-$(OIrF_4)_3]^{2-}$, F_5Ir---OClF, IrF_5, and OClF was assessed by NBO analyses (uPBE1PBE/aug-cc-PVTZ-(Ir)-Def2-TZVPD-(F,O,Cl)) to provide semi-quantitative descriptions of their bonding (Tables A3.9–A3.12). The O atom valences of [*cyclo*-μ-$(OIrF_4)_3]^{2-}$ are somewhat greater than 2 (2.088, 2.106, 2.016) and their associated O atom charges (−0.580, −0.581, −0.613) and Ir–O WBIs (0.683, 0.765, 0.852, and 0.852) are consistent with polar-covalent Ir–O bridge bonds. The F-atom charges (−0.516 to −0.550) and associated Ir–F WBIs (0.500–0.556) of

Ir–F bonds that are trans to Ir–O bonds indicate these bonds have greater ionic characters than Ir–F bonds that are cis to Ir–O bonds (charges, −0.507 to −0.541; WBIs, 0.523–0.579). The Ir atom charges (2.032, 2.032, and 2.042) and atom valences (3.937, 3.937, and 4.102) of [*cyclo*-*μ*-$(OIrF_4)_3]^{2-}$ are consistent with polar-covalent Ir–O and Ir–F bonds.

The NBO analyses of F_5Ir---OClF, IrF_5, and OClF show that complex formation results in significant negative charge transfer from OClF to IrF_5, as indicated by the IrF_5 and OClF group charges (IrF_5, −0.240; OClF, 0.240). The Ir---O bond has a significantly lower WBI (0.338) than the Ir–F bonds (0.547–0.719), which indicates that the Ir---O coordinate bond has greater electrostatic character. Complexation enhances the ionic character of the Cl–O bond and the covalent character of the Cl–F bond upon coordination of OClF, as shown by differences between the Cl–O and Cl–F WBIs of OClF (Cl–O, 1.519; Cl–F, 0.679) and F_5Ir---OClF (Cl–O, 1.287; Cl–F, 0.794). This is also reflected in the O and F atom charges for OClF, which become more negative and positive, respectively, upon complexation. The Ir---O bond is therefore predominantly electrostatic with a significant degree of covalent character, and the OClF ligand is polarized to a significant extent upon coordination.

Coordination also enhances the ionic characters of the Ir–F bonds in F_5Ir---OClF relative to the Ir–F bonds in IrF_5, as shown by decreased Ir–F WBIs (IrF_5, 0.601–0.857; F_5Ir---OClF, 0.547–0.719) and F atom valences (IrF_5, 0.834–1.006; F_5Ir---OClF, 0.789–0.999), and more negative F-atom charges (IrF_5, −0.345 to −0.512; F_5Ir---OClF, −0.418 to −0.545). The formation of two Cl---$F_{2,3}$ secondary bonds (WBIs, 0.050 and 0.140) also slightly increase the ionic characters of the Ir–$F_{2,3}$

bonds. The low WBIs of these secondary bonds are consistent with primarily electrostatic, σ-hole bonds that are directed towards regions of high positive electrostatic potential on Cl (vide infra).

6.2.3.3. Molecular Electrostatic Potential Surface Analyses

The MEPS isosurfaces (PBE0-D4/TZ2P) of gas-phase OClF, IrF_5, and F_5Ir---OClF are depicted in Figure 6.6 along with their EP extrema. Electrostatic potential values provided in parentheses are in kJ mol^{-1}.

The MEPS isosurface of OClF is consistent with coordination through O instead of F based on their relative EP minima (F, −40; O, −76). The isosurface of IrF_5 has a maximum positive EP on Ir (438) that is located trans to the axial Ir–F bond. The O atom of the OClF ligand in F_5Ir---OClF coordinates into their region of high charge depletion on Ir, a σ-hole, to give a predominantly electrostatic Ir---O bond. The OClF ligand has two σ-holes on the isosurface of Cl that are located trans to the Cl–O (163) and Cl–F (176) bonds, respectively. The EP isosurface minima on the equatorial F atoms of IrF_5 (−29) are significantly more negative than the EP maximum of its axial F atom (4).

Coordination of OClF to IrF_5 significantly enhances regions of high positive EP on Cl that are trans to the Cl–O (296) and Cl–F (275) bonds relative to those of free OClF (Cl–O, 163; Cl–F, 176). The Cl---F_{Ir} secondary bonds in the experimental and calculated geometries of F_5Ir---OClF are directed towards the σ-holes on Cl. The EP maxima of the O and F atom isosurfaces of the OClF ligand in F_5Ir---OClF change their polarities from negative in OClF (F, −40; O, −76) to positive in F_5Ir---OClF (F, 86; O, 53). The EP minima of the equatorial F atom isosurfaces of IrF_5 in F_5Ir---OClF (F_{eq}, −71, −85; F_{ax}, 78) are significantly more negative than in IrF_5 (F_{eq}, −29; F_{ax}, 4).

In particular, the EP of the axial F atom is negative for F_5Ir---OClF (−78) and positive for IrF_5 (4). This is in accordance with transfer of significant negative charge from OClF to IrF_5 as shown by the NBO analyses (vide supra).

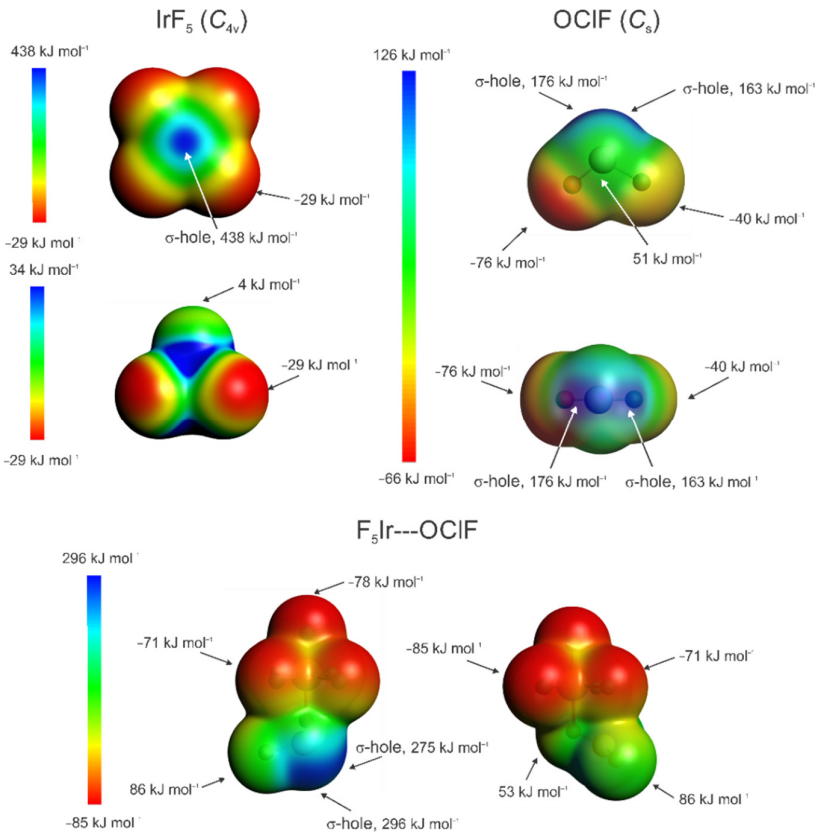

Figure 6.6. The MEPS calculated at the 0.001 e a_0^{-3} isosurface value for IrF_5, OClF, and F_5Ir---OClF. Electrostatic potential extrema are indicated by arrows. The optimized geometries and MEPs were calculated at the PBE0-D4/TZ2P level of theory and include collinear SOC.

6.3. Conclusions

Although the oxides and fluorides of the majority of heavy transition metal elements were known, there have been no structurally characterized examples of oxide fluorides reported for the noble metals Rh, Pd, Ag, Ir, Pt, or Au. Now, the synthesis and structural characterization of the first iridium oxide fluoride species, the [*cyclo*-(μ-$OIrF_4)_3$]$^{2-}$ dianion, is reported. Furthermore, the F_5Ir---OClF coordination complex was synthesized by reaction of IrO_2 with ClF_5 or ClF_3 in aHF solvent. The structural characterization of F_5Ir---OClF provides the first direct evidence for the formation of OClF in the reaction of ClF_3 with a metal oxide, IrO_2, and the first crystallographic characterization of a OClF species. Formation of the F_5Ir---OClF complex also stabilizes endothermic OClF with respect to disproportionation to ClF and ClO_2F. The [*cyclo*-(μ-$OIrF_4)_3$]$^{2-}$ dianion is oxygen bridged and provides a rare example of a mixed high-oxidation-state iridium species [2 x Ir(V) and 1 x Ir(VI)]. The oxo-wall is circumvented by the high-oxidation-states and non-tetragonal coordination spheres of Ir in [*cyclo*-(μ-$OIrF_4)_3$]$^{2-}$ and by the formation of Ir–O single bonds. Both $[ClO_2]_2$[*cyclo*-(μ-$OIrF_4)_3$] and F_5Ir---OClF exhibit extended three-dimensional networks in the solid-state that result from primarily electrostatic Cl---F_{Ir} secondary bonds. Quantum-chemical calculations show that the Ir–F bonds of [*cyclo*-(μ-$OIrF_4)_3$]$^{2-}$ and F_5Ir---OClF and the Ir–O bridge bonds of [*cyclo*-(μ-$OIrF_4)_3$]$^{2-}$ are polar-covalent in nature. The Ir---O bond of F_5Ir---OClF is predominantly electrostatic in character and may be described as a σ-hole bond. However, the Ir---O bond also has a significant degree of covalent character that accounts for its bent Ir---O–Cl bond angles in its calculated gas-phase and X-ray crystal structures.

CHAPTER 7

Noble-Gas Difluoride Complexes of $CrOF_4$ and MOF_4 (M = Mo, W); $NgF_2 \cdot CrOF_4$ (Ng = Kr, Xe), $NgF_2 \cdot MOF_4$, $NgF_2 \cdot 2CrOF_4$, and $XeF_2 \cdot 2M'OF_4$ (M′ = Mo, W).

Adapted with permission from: Bortolus, M. R.; Mercier, H. P. A.; Brock, D. S.; Schrobilgen, G. J. *Chem. Eur. J.* **2022***, 28,* e202103729. and Mercier, H. P. A.; Breddemann, U.; Brock, D. S.; **Bortolus, M. R.;** Schrobilgen, G. J. *Chem. Eur. J.* **2019**, *25*, 12105–12119.

7.1. Introduction

The noble-gas difluorides NgF_2 (Ng = Kr, Xe) are fluoride-ion donors and potent oxidative fluorinating agents that react with strong fluoride-ion acceptors such as PnF_5 (Pn = As, Sb, Bi) to form $[NgF]^+$ and $[Ng_2F_3]^+$ salts of $[PnF_6]^-$ and $[Pn_2F_{11}]^-$.[46,48,58,59] In contrast, the Group 6 oxide tetrafluorides, MOF_4 (M = Cr, Mo, W), are significantly weaker fluoride-ion acceptors that form two series of neutral complexes with NgF_2 (Ng = Kr, Xe) having the general formulae $NgF_2 \cdot MOF_4$ (M = Cr, Mo, W) and $NgF_2 \cdot 2MOF_4$.[65,66,182–184]

Although $NgF_2 \cdot CrOF_4$ and $NgF_2 \cdot 2CrOF_4$ have been thoroughly characterized by low-temperature (LT) single-crystal Xray diffraction (SCXRD) and Raman spectroscopy,[65] $XeF_2 \cdot WOF_4$ was the only $NgF_2 \cdot nMOF_4$ (n = 1, 2; M = Mo, W) complex to have been structurally characterized by SCXRD, but at low precision.[182] Low-temperature solution ^{19}F and ^{129}Xe NMR studies in both BrF_5 and SO_2ClF solvents showed F_tXeF_b---MOF_4, F_tXeF_b---$M(OF_3)$–F_b'---M_t'OF_4, F_tXeF_b---$M(OF_3)$–F_b'---$M'(OF_3)$–F_b"---M_t"OF_4, and F_tXeF_b---$M(OF_3)$–F_b'---$M'(OF_3)$–F_b"---$M"(OF_3)$–F_b'''---M_t'''OF_4 have Xe–F_b---M bridges and metal–fluorine–metal bridges that are non-labile on the NMR time scale, with structures having *trans*, *trans*-arrangements of the M=O and M_t'=O/M_t"=O/M_t'''=O bonds with respect to F_b'/F_b"/ F_b'''.[183] The

$XeF_2{\cdot}nMOF_4$ (n = 1, 2) complexes have also been characterized in the solid state by Raman spectroscopy and their spectra tentatively assigned. The $KrF_2{\cdot}nMoOF_4$ (n = 1–3) and $KrF_2{\cdot}WOF_4$ complexes were formed in SO_2ClF solution at LT.[184] Their solution ^{19}F NMR spectra provided definitive proof for the formation of F_tKrF_b---$MoOF_4$, F_tKrF_b---WOF_4, F_tKrF_b---$Mo(OF_3)$–F_b'---$Mo_t'OF_4$, and F_tKrF_b---$Mo(OF_3)$–F_b'---$Mo'(OF_3)$–F_b"---$Mo_t"OF_4$ complexes having non-labile Kr–F_b---Mo/W bridges and metal–fluorine–metal bridges that are assigned *trans*, *trans*-arrangements of the Mo=O and Mo_t'=O/ Mo_t"=O bonds with respect to F_b'/F_b''.[184] The Raman spectra of the solid $KrF_2{\cdot}MoOF_4$ and $KrF_2{\cdot}WOF_4$ complexes are consistent with their ^{19}F solution NMR studies and their xenon analogues.[184]

The present work provides solid-state structural characterizations of $NgF_2{\cdot}MOF_4$ (Ng = Kr, Xe; M = Mo, W) and $XeF_2{\cdot}2MOF_4$ by LT SCXRD and Raman spectroscopy. The HF solvate, [--$(F_4OMo)(\mu_3$-F)H---(μ-F)H--]$_\infty$, was also characterized by LT SCXRD and Raman spectroscopy. Quantum-chemical calculations (QC) were employed to arrive at definitive assignments of the Raman spectra of the NgF_2 complexes, and to assess and compare bonding in $NgF_2{\cdot}MOF_4$ and $XeF_2{\cdot}2MOF_4$.

7.2. Results and Discussion

7.2.1. Syntheses and Reactivities

7.2.1.1. $NgF_2{\cdot}MOF_4$ (Ng = Kr, Xe) (M = Mo, W) and $XeF_2{\cdot}CrOF_4$. In typical reactions, 1:1 molar mixtures of NgF_2 (Ng = Kr, Xe) and MOF_4 (M = Mo, W) were allowed to react at −78 °C in aHF solvent for ca. 5 min with periodic agitation to give flocculent white precipitates of the $NgF_2{\cdot}MOF_4$ complexes [Eq. (7.1)].

$$NgF_2 + MOF_4 \xrightarrow{aHF} NgF_2{\cdot}MOF_4 \qquad \textbf{(7.1)}$$

Colorless, needle-shaped crystals of $KrF_2 \cdot MoOF_4$ (**1**) were grown by dissolving a 1:1 molar mixture of KrF_2 and $MoOF_4$ in aHF at −35 °C, followed by slow cooling from −35 to −55 °C over ca. 4 h. Crystalline samples were isolated by decanting the aHF supernatant at −78 °C into the side arm of an FEP h-shaped reaction vessel, which had been cooled to −196 °C, and heat-sealed off under dynamic vacuum. Residual aHF was removed from the crystalline sample under dynamic vacuum at −78 °C. Except for $KrF_2 \cdot WOF_4$ (**2**), all crystalline samples described in the ensuing subsections were isolated in a similar manner.

Crystals of $KrF_2 \cdot WOF_4$ (**2**) were particularly challenging to grow owing to the propensity of KrF_2 to oxidatively fluorinate WOF_4 to WF_6 and O_2 in aHF solution at the crystallization temperature (−60 °C). This difficulty was overcome by partially dissolving a sample of $KrF_2 \cdot WOF_4$, with agitation, in aHF at −65 °C over a ca. 10 min period. The supernatant was then carefully decanted into the cooled (−62 °C) side arm of the h-shaped reactor, warmed to −55 °C for ca. 15 s to ensure complete solubility, and then cooled to and maintained at −60 °C for ca. 1 min to initiate crystal growth. Slow cooling of the sample from −60 to −66 °C for ca. 1 h yielded colorless, needle-shaped crystals of $KrF_2 \cdot WOF_4$ (**2**). The LT Raman spectrum of the crystalline sample was obtained under solid HF at −150 °C prior to decanting HF into the main arm of the reactor at −78 °C. The decanted solvent was isolated by cooling the supernatant to −196 °C and heat-sealing off the side arm under dynamic vacuum. Residual HF was removed from the crystalline sample under dynamic vacuum at −78 °C.

Colorless, needle-shaped crystals of $XeF_2 \cdot MOF_4$ (M = Mo (**3**), W (**4**)) were grown by dissolving 1:1 molar mixtures of XeF_2 and $MoOF_4$ or WOF_4 in aHF at room

temperature, followed by slow cooling of these samples from 25 to −69 °C and 25 to −78 °C, respectively.

7.2.1.2. $XeF_2{\cdot}2MOF_4$ (M = Mo (5), W (6)). The reactions of 1:2 molar mixtures of molten XeF_2 and MOF_4 at 50 °C resulted in colorless liquids [Eq. (**7.2**)]. Slow cooling of these melts from 50 to 12 °C and from 50 to 21 °C respectively, resulted in colorless, plate-shaped crystals of $XeF_2{\cdot}2MoOF_4$ (**5**) and $XeF_2{\cdot}2WOF_4$ (**6**).

$$XeF_2 + 2MOF_4 \xrightarrow{50\,^{\circ}C} XeF_2{\cdot}2MOF_4 \qquad (\mathbf{7.2})$$

An attempt to synthesize $KrF_2{\cdot}2MoOF_4$ in aHF yielded crystalline $KrF_2{\cdot}MoOF_4$ and the HF solvate, [--$(F_4OMo)(\mu_3$-F)H---(μ-F)H--]$_\infty$ (**7**) [Equation (**7.3**)] (see Appendix 4, Figure A4.1 and Table A4.1). Attempts to form the solvated WOF_4 analogue of **7** by dissolution of WOF_4 in aHF were unsuccessful and only yielded unreacted WOF_4 upon removal of aHF solvent.

$$MoOF_4 + 2HF \longrightarrow [\text{--}(F_4OMo)(\mu_3\text{-F})H\text{---}(\mu\text{-F})H\text{--}]_\infty \qquad (\mathbf{7.3})$$

7.2.2. X-ray Crystallography

Data collection parameters and other crystallographic information for $KrF_2{\cdot}MoOF_4$ (**1**), $KrF_2{\cdot}WOF_4$ (**2**), $XeF_2{\cdot}MoOF_4$ (**3**), $XeF_2{\cdot}WOF_4$ (**4**), $XeF_2{\cdot}2MoOF_4$ (**5**), $XeF_2{\cdot}2WOF_4$ (**6**), and [--$(F_4OMo)(\mu_3$-F)H---(μ-F)H--]$_\infty$ (**7**) are provided in Table 7.1.

7.2.2.1. $NgF_2{\cdot}MOF_4$ (M = Mo, W). The crystal structures of $NgF_2{\cdot}MOF_4$ are isotypic (P21/c) and are best described as complexes in which an F atom of NgF_2 coordinates into the σ-hole region of M that is trans to the axial M=O bond (Figure 7.1 and Figure A4.2, Appendix 4) to give near-eclipsed conformations (∠Kr–F_b---Mo–$F_{(1)}$, 14.34(7)°; ∠Kr–Fb---W–$F_{(1)}$, 16.1(2)°, ∠Xe–F_b---Mo–$F_{(1)}$, 7.55(6)°; ∠Xe–F_b---W–$F_{(1)}$, 5.9(2)°). The structural units are well-isolated, where the shortest O···F and F···F intermolecular contacts of $KrF_2{\cdot}MOF_4$ and $XeF_2{\cdot}MOF_4$ (Tables A4.2 and A4.3) are

somewhat longer and shorter, respectively, than the sums of their van der Waals radii (O···F, 2.99,[167] 2.96[168] Å; F···F, 2.94,[167] 2.92[168] Å).

The Kr–F_t (Mo, 1.8202(9); W, 1.805(2) Å), Kr–F_b (Mo, 1.9653(9); W, 1.989(2) Å), Xe–F_t (Mo, 1.9369(12); W, 1.929(3) Å) and Xe–F_b (Mo, 2.0813(12); W, 2.102(3) Å) bonds of $NgF_2{\cdot}MOF_4$ (Table 7.2) are significantly shorter and longer, respectively, than those of α-KrF_2 (Kr–F: 1.894(5) Å)[46] and XeF_2 (Xe–F: 1.999(4) Å),[48] as observed in $NgF_2{\cdot}CrOF_4$ (Kr–F_t, 1.8489(9), Kr–F_b, 1.9279(9); Xe–F_t, 1.945(3), 1.969(2), Xe–F_b, 2.035(3), 2.057(2) Å).[65] The Ng–F bonds of the NgF_2 ligand become more polarized, consistent with the calculated FIAs of the Group 6 oxide tetrafluorides ($CrOF_4$, −285; $MoOF_4$, −355 WOF_4, −386 kJ mol^{-1}),[252] which result in progressively longer Ng–F_b bridge bonds and shorter Ng–F_t terminal bonds (see above). Because the Ng–F_t and Ng–F_b bonds of $NgF_2{\cdot}MOF_4$ are significantly longer and shorter, respectively, than those of $[NgF][PnF_6]$,[46,48,58] the relative degree of fluoride-ion transfer from NgF_2 to MOF_4 is correspondingly smaller. The F–Kr–F bond angles are near-linear (178.3(2)–179.19(5)°), and are comparable to those of $NgF_2{\cdot}CrOF_4$ (Kr: 179.91(5)°; Xe: 179.1(1), 179.81(8)°),[65] The Ng–F_b---M bond angles in $KrF_2{\cdot}MOF_4$ (Mo, 134.33(5); W, 135.22(12)°) and $XeF_2{\cdot}MOF_4$ (Mo, 148.09(7); W, 150.6(2)°) are bent and are in good agreement with those of $NgF_2{\cdot}CrOF_4$ (Kr: 123.51(4)°; Xe: 133.1(1), 118.50(8)°).[65] Similar trends have been noted for other terminally coordinated NgF_2 (Ng = Kr, Xe) adducts: $[F_2OBr(FNgF)_2AsF_6]$,[62,63] $[Mg(FKrF)_4(AsF_6)_2]$,[74] $[F_5Xe(FNgF)_nAsF_6]$ (n = 1, 2),[64,73] and $[Hg(FKrF)_8][AsF_6]_2$.[190]

The Mo–O (Kr, 1.6508(12); Xe, 1.6492(14) Å), W–O (Kr, 1.679(3); Xe, 1.677(3) Å), Mo–F (Kr, 1.8400(9)–1.8562(8); Xe, 1.8396(12)–1.8524(11) Å), and W–

F (Kr, 1.852(2)–1.862(2); Xe, 1.846(3)–1.862(3) Å) bond lengths are comparable to those of the infinite-chain $MoOF_4$[253] and tetrameric WOF_4 structures,[254] and gaseous monomeric MOF_4 (Mo,[255,256] W[256]). The secondary Mo---F_b (Kr, 2.2473(9); Xe, 2.2352(12) Å) and W---F_b (Kr, 2.217(2); Xe, 2.199(3) Å) bonds are significantly longer than M–F_t bonds (see above) owing to their dominant electrostatic characters. The M---F_b bond lengths of $NgF_2 \cdot MOF_4$ (Ng = Kr, Xe; M = Cr,[65] Mo, W) decrease with increasing FIA upon descending Group 6,[252] in accordance with primarily electrostatic σ-hole type M---Fb bonds (see Computational Results).

7.2.2.2. $XeF_2 \cdot 2MOF_4$ (M = Mo, W). The crystal structures of $XeF_2 \cdot 2MOF_4$ are isotypic (*Pbcn*) and consist of well-isolated structural units (Figure 7.2 and Figure A4.3). The shortest O···F and F···F intermolecular contacts in $XeF_2 \cdot 2MOF_4$ (Table A4.4) are slightly less than the sums of their van der Waals radii (see above). The F_b' atom of the F_tXeF_b---$M(OF_3)$–F_b' moieties in $XeF_2 \cdot 2MOF_4$ are *trans*-coordinated to the M'=O bond of a second $M'OF_4$ molecule to give F_tXeF_b---$M(OF_3)$–F_b'---$M'OF_4$. The M–F_b'---M' bridge bond angles (Mo, 159.02(7); W, 159.5(2)°) are significantly less than 180° (see Computational Results). The F_tXeF_b---$M(OF_3)$–F_b' moieties adopt nearly eclipsed conformations (∠Xe–F_b---Mo–$F_{(9)}$, 7.19(7)°; ∠Xe–F_b---W–$F_{(9)}$, 2.3(3)°), similar to those of $NgF_2 \cdot MOF_4$ (see above). The crystal structures reveal *cis, trans*-arrangements of M=O/M'=O bonds relative to F_b' instead of the *trans, trans*-arrangements previously assigned based on LT solution ^{19}F NMR studies.[183] Both arrangements have been observed for the $[Mo_3O_3F_{13}]^-$ anion in the crystal structure of $[ClO_2][Mo_3O_3F_{13}]$.[141]

Table 7.1. Summary of crystal data and refinement results for $KrF_2 \cdot MoOF_4$ (**1**), $KrF_2 \cdot WOF_4$ (**2**), $XeF_2 \cdot MoOF_4$ (**3**), $XeF_2 \cdot WOF_4$ (**4**), $XeF_2 \cdot 2MoOF_4$ (**5**), $XeF_2 \cdot 2WOF_4$ (**6**), and [--(F_4OMo)(μ_3-F)H---(μ-F)H--]$_\infty$ (**7**)

	1	**2**	**3**	**4**	**5**	**6**	**7**
space group	$P2_1/c$	$P2_1/c$	$P2_1/c$	$P2_1/c$	*Pbcn*	*Pbcn*	$P2_1/c$
a (Å)	5.2881(1)	5.3024(3)	5.2334(1)	5.2105(3)	16.9762(3)	17.1091(8)	7.226(1)
b (Å)	10.1495(2)	10.1808(6)	9.5634(2)	9.6408(6)	8.24267(1)	8.4664(4)	6.9321(12)
c (Å)	10.9750(2)	10.9945(7)	12.3165(3)	12.3383(8)	13.9290(2)	13.9364(7)	10.3917(18)
α	90	90	90	90	90	90	90
β (deg)	93.630(1)	94.058(2)	90.494(1)	90.736(2)	90	90	97.670(3)
γ	90	90	90	90	90	90	90
V (Å^3)	587.86(2)	592.02(6)	616.41(2)	619.74(7)	1992.59(5)	2018.7(2)	515.84(16)
Z	4	4	4	4	8	8	4
*M*w (g mol^{-1})	309.74	397.65	357.24	445.15	545.18	721.00	227.96
ρ_{calcd} (g cm^{-3})	3.500	4.461	3.849	4.771	3.635	4.745	2.935
T (°C)	−173	−173	−173	−173	−173	−173	−173
μ (mm^{-1})	9.758	26.986	7.580	24.063	5.990	26.203	2.592
R_1[a]	0.0283	0.0325	0.0191	0.0277	0.0244	0.0381	0.0234
wR_2[b]	0.0519	0.0804	0.0357	0.0664	0.0448	0.0928	0.0463

[a] $R_1 = \sum \| F_o | - | F_c \| / \sum | F_o |$ for $I > 2\sigma(I)$. [b] $wR_2 = [\sum[w(F_o^2 - F_c^2)^2] / \sum w(F_o^2)^2]^{1/2}$ for $I > 2\sigma(I)$.

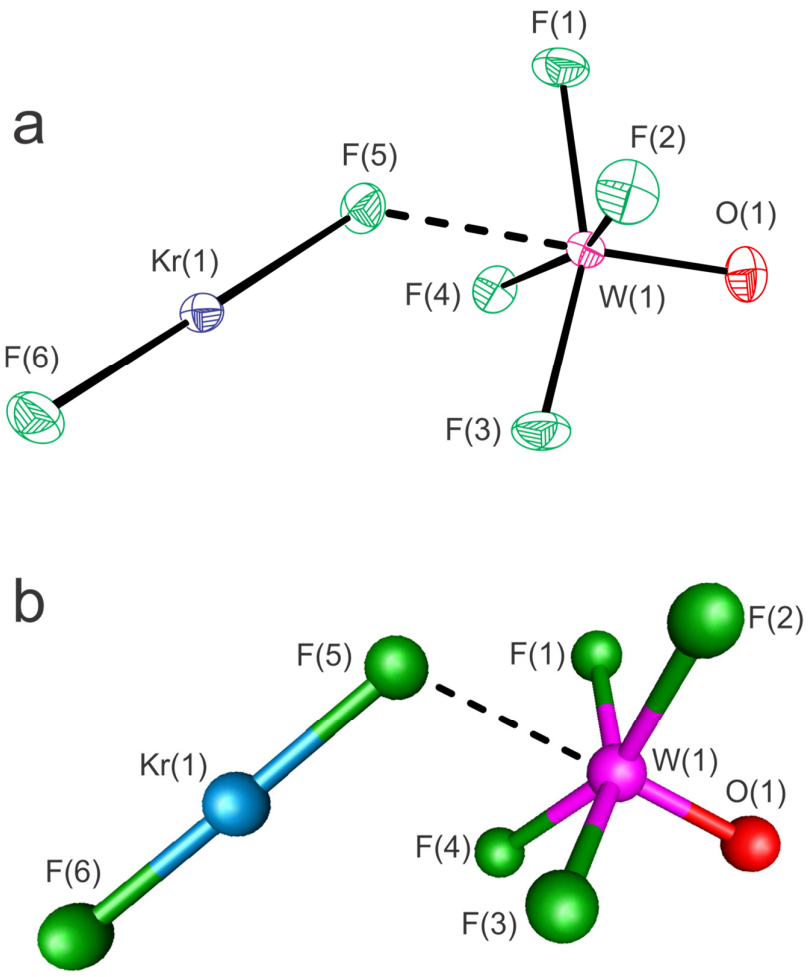

Figure 7.1. (a) The X-ray crystal structure of $KrF_2 \cdot WOF_4$ (near-eclipsed conformation) with thermal ellipsoids drawn at the 50% probability level; and (b) its calculated staggered conformation.

The Xe–F_t (Mo, 1.9283(10); W, 1.922(4) Å) and Xe–F_b (Mo, 2.1153(10); W, 2.136(4) Å) bonds of $XeF_2 \cdot 2MOF_4$ (M = Mo, W) (Table 7.2) are somewhat shorter and longer, respectively, than those of $XeF_2 \cdot MOF_4$ (M=Mo, W), indicating that $M(OF_3)–F_b$'---M'OF_4 is a stronger fluoride-ion acceptor than MOF_4. As expected, the longest Ng–F_b bridge bonds and shortest Ng–F_t terminal bonds are observed for $XeF_2 \cdot 2WOF_4$, consistent with the greater calculated FIA of WOF_4 relative to $MoOF_4$.[252] As in $XeF_2 \cdot MOF_4$, the Ng–F_t and Ng–F_b bonds of $XeF_2 \cdot 2MOF_4$ are significantly longer and shorter, respectively, than those of $[XeF][AsF_6]$.[48] Although $M(OF_3)–F_b$'---M'OF_4 is expected to be a stronger fluoride-ion acceptor than MOF_4, it is incapable of complete fluoride-ion transfer from NgF_2 to form $[NgF][M_2O_2F_9]$ salts. The F_t–Xe–F_b bond angles are nearly linear (Mo, 178.85(4); W, 178.1(2)°), and are comparable to those of other terminally coordinated NgF_2 ligand complexes (see above). The Xe–F_b---M bond angles of $XeF_2 \cdot 2MOF_4$ (Mo, 130.84(5); W, 131.7(2)°) are comparable to those of $NgF_2 \cdot MOF_4$ (M = Cr,[65] Mo, W) and other terminally coordinated NgF_2 complexes (see above).

The M=O (Mo, 1.6432(12), 1.6461(12); W, 1.660(5), 1.662(6) Å) and M–F (Mo, 1.8208(10)–1.8456(10); W, 1.825(4)–1.848(4) Å) bond lengths of $XeF_2 \cdot 2MOF_4$ are comparable to those of $XeF_2 \cdot MOF_4$ (see above). As expected, the shortest M–F_t bond is trans to the M–F_b'---M' bridge, and the longest M–F_t bond nearly eclipses (see above) the XeF_2 ligand. The M---F_b bridge bonds with NgF_2 (Mo, 2.1980(9); W, 2.177(4) Å) are significantly shorter than in $XeF_2 \cdot MOF_4$ (see above) and indicate, when combined with the trends observed for Ng–F_t and Ng–F_b, the order of increasing FIA for the XeF_2 ligand is: $MoOF_4 < WOF_4 \approx Mo(OF_3)–F_b$'---Mo'$OF_4 < W(OF_3)–F_b$'---W'$OF_4$. The asymmetric M–$F_b$'---M' bridge bonds are consistent with polar-

Table 7.2. Key experimental and calculated bond lengths (Å) and bond angles (deg) for $KrF_2{\cdot}MoOF_4$ (**1**), $KrF_2{\cdot}WOF_4$ (**2**), $XeF_2{\cdot}MoOF_4$ (**3**), $XeF_2{\cdot}WOF_4$ (**4**), $XeF_2{\cdot}2MoOF_4$ (**5**), $XeF_2{\cdot}2WOF_4$ (**6**) [a]

	Exptl						Calcd[b]					
	$NgF_2{\cdot}MOF_4$			$XeF_2{\cdot}2MOF_4$			$NgF_2{\cdot}MOF_4$			$XeF_2{\cdot}2MOF_4$		
	1	**2**	**3**	**4**	**5**	**6**	**1'**	**2'**	**3'**	**4'**	**5'**	**6'**
Ng–F_t	1.8202(9)	1.805(2)	1.937(12)	1.929(3)	1.928(10)	1.922(4)	1.834	1.829	1.955	1.951	1.950	1.944
Ng–F_b	1.9653(9)	1.989(2)	2.081(12)	2.102(3)	2.115(10)	2.136(4)	1.926	1.935	2.048	2.058	2.059	2.072
M---F_b	2.2473(9)	2.217(2)	2.235(12)	2.199(3)	2.1980(9)	2.177(4)	2.416	2.405	2.389	2.378	2.339	2.321
F_t–Ng–F_b	179.19(5)	178.8(11)	178.35(6)	178.3(2)	178.85(4)	178.1(2)	178.8	178.8	178.3	178.3	178.4	177.9
Ng–F_b---M	134.33(5)	135.2(12)	148.09(7)	150.6(2)	130.84(5)	131.7(2)	114.2	114.5	116.8	117.2	125.6	123.8

[a] Geometric parameters for the MOF_4 (M = Mo, W) groups are provided in Tables A4.3–A4.5 of Appendix 4. [b] APFD/Def2TZVPD.

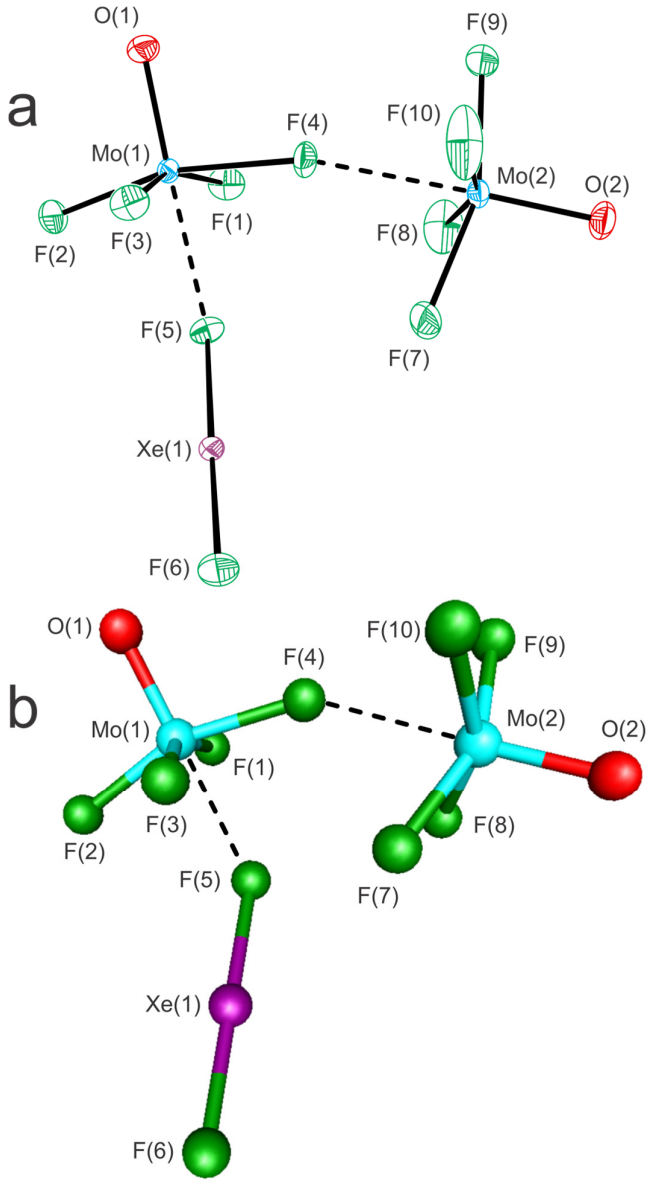

Figure 7.2. The X-ray crystal structure of (a) $XeF_2 \cdot 2MoOF_4$ (**5**) with the thermal ellipsoids drawn at the 50% probability level; and (b) its calculated geometry (**5'**). The X-ray crystal structure of $XeF_2 \cdot 2WOF_4$ (**6**) and its calculated geometry (**6'**) are depicted in Figure A4.4, Appendix 4.

covalent M–F_b' bonds (Mo–F_b', 1.9350(10), W–F_b', 1.929(4) Å) and primarily electrostatic F_b'---Mo (2.2990(10) Å) and F_b'---W (2.313(4) Å) bonds. The shorter M–F_b' and longer F_b'---M' bonds observed in $XeF_2 \cdot 2WOF_4$ are consistent with the higher FIA of WOF_4 relative to that of $MoOF_4$, which has less fluorobasic F ligands. This is consistent with the fact that F_tXeF_b---$W(OF_3)$–F_b'---Mo'OF_4 cannot be synthesized in solutions or melts (see Experimental Section) apparently owing to the lower FIA of $MoOF_4$ and its inability to coordinate to an F ligand of WOF_4 in $XeF_2 \cdot WOF_4$.

7.2.2.3. [--(F_4OMo)(μ_3-F)H---(μ-F)H--]$_\infty$ (7). The crystal structure of **7** is a coordination complex in which the F atom of an HF molecule interacts with the σ-hole of Mo that is *trans* to the axial Mo=O bond of $MoOF_4$, and the H atom of adducted HF forms an H-bonded, infinite-chain structure that incorporates a second equivalent of HF (Figure 7.3). The chains are well separated, with the shortest O···F and F···F intermolecular contacts between chains being only somewhat shorter than the sums of their van der Waals radii (Table A4.5).

The F_H---F_H distance (2.465(2) Å) between neighboring HF molecules in **7** is very similar to the F_H---F_H distance in the crystal structure of HF (2.49(1) Å).[257] The Mo=O (1.650(2) Å) and Mo–F (1.8427(14)–1.8875(14) Å) bond lengths are like those of $NgF_2 \cdot MoOF_4$. The Mo---F bridge bond of **7** (2.1527(14) Å) is intermediate with respect to the Mo–F_{ax} bond of $[Xe_2F_{11}][MoOF_5]$ (2.061(2) Å)[243] and the Mo---F_b bridge bond of $NgF_2 \cdot MoOF_4$ (Kr: 2.2470(9); Xe: 2.2352(12) Å), in accordance with the description of **7** as a coordination complex rather than a salt, and the greater fluorobasicity of HF relative to that of NgF_2.

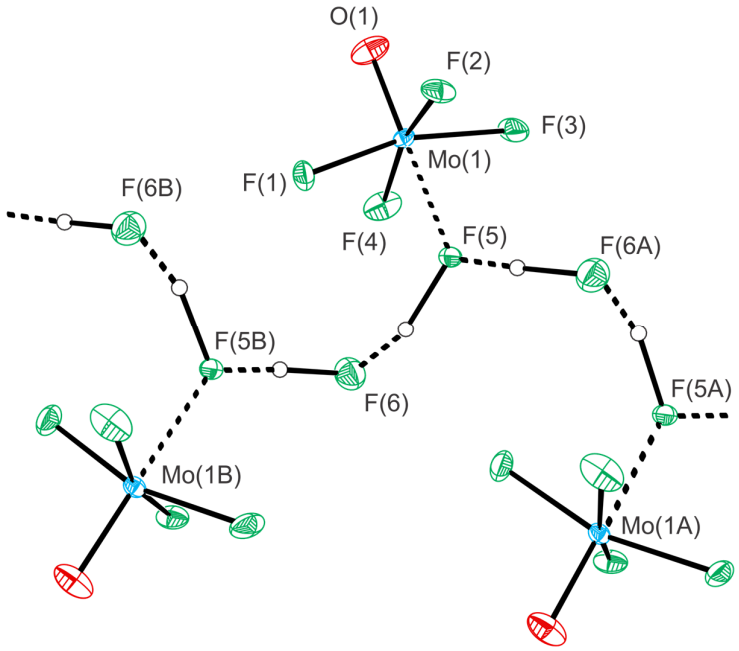

Figure 7.3. A portion of the X-ray crystal structure of [--(F_4OMo)(μ_3-F)H---(μ-F)H--]$_\infty$ (**7**) showing its infinite-chain structure. Thermal ellipsoids are drawn at the 50% probability level.

7.2.3. Raman Spectroscopy

The LT Raman spectra of $XeF_2 \cdot MOF_4$ and $XeF_2 \cdot 2MOF_4$ (Ng = Kr, Xe; M = Mo, W) (Figures A4.4 and A4.5, Appendix 4) have been re-recorded to provide more precise assignments and descriptions of the vibrational modes that are based on their calculated vibrational frequencies and the atomic displacements of gas-phase structures 1'–6' (Tables A4.6–A4.8). The previously published Raman spectra of $KrF_2 \cdot MOF_4$ (M = Mo, W) were recorded at −196 °C[184] and were of very good quality; they did not need to be re-recorded. The Raman spectra of $XeF_2 \cdot 2MOF_4$ were previously assigned to a *trans, trans*-arrangement of M=O bonds based on solution ^{19}F NMR studies,[183] and are now re-assigned based on the *cis, trans*-arrangements of

M=O bonds in their crystal structures (see above). A detailed discussion of the vibrational assignments for $NgF_2 \cdot MOF_4$ is provided in Appendix 4 along with factor-group analyses for $NgF_2 \cdot MOF_4$ and $XeF_2 \cdot 2MOF_4$ (Figures A4.6 and A4.7).

7.2.3.1. $XeF_2 \cdot 2MOF_4$ (M = Mo, W). The high-frequency bands at 1036 (Mo) and 1050/1053 (W) cm^{-1} (calcd, 1094 (Mo) and 1073 (W) cm^{-1}) are assigned to the in-phase $\nu(M_1\text{-}O_1) + \nu(M_2\text{-}O_2)$ mode, whereas the out-of-phase $\nu(M_1\text{-}O_1) - \nu(M_2\text{-}O_2)$ mode occurs at lower frequency, 1028 (Mo) and 1041/1044 (W) cm^{-1} (calcd, 1028 (Mo) and 1070 (W) cm^{-1}). The bands between 589–724 (Mo) and 610–719 (W) cm^{-1} are assigned to coupled $\nu(M_1\text{-}F_t)$ and $\nu(M_2\text{-}F_t)$ stretches (calcd, 595–716 (Mo) and 612–711 (W) cm^{-1}) and are comparable to the $\nu(M\text{-}F_t)$ stretching frequencies of the 1:1 complex (Tables A4.7 and A4.8). The bands at 525/527 (Mo) and 535/537 (W) cm^{-1} (calcd, 564 (Mo) and 563 (W) cm^{-1}) occur at significantly lower frequencies than the terminal $\nu(M\text{-}F_t)$ stretches and are assigned to the bridging out of- phase, $\nu(M_1\text{-}F_6) - \nu(M_2\text{-}F_6)$ mode, consistent with longer $M_1\text{–}F_6$ and $M_2\text{–}F_6$ bonds. The calculations show no intraligand coupling between $\nu(Xe\text{-}F_t)$ and $\nu(Xe\text{-}F_b)$. The $XeF_2 \cdot 2MOF_4$ bands at 572/574(5) and 582/585(6) cm^{-1} are assigned to $\nu(Xe\text{-}F_t)$ and occur at slightly higher frequency than those of $XeF_2 \cdot MOF_4$ (562/567(3); 571/574(4) cm^{-1}), in accordance with the experimental bond length trends, $Xe\text{–}F_t$ (1:2) < $Xe\text{–}F_t$ (1:1). The $XeF_2 \cdot 2MOF_4$ bands at 421 (Mo) and 408 (W) cm^{-1} are assigned to $\nu(Xe\text{-}F_b)$ and occur at slightly lower frequency than those of $XeF_2 \cdot MOF_4$ (449/466 (Mo); 437/466 (W) cm^{-1}), in agreement with the experimental bond length trends, $Xe\text{–}F_b$ (1:2) > $Xe\text{–}F_b$ (1:1). These trends were reproduced by the calculations: $\nu(Xe\text{-}F_t)$: 557 (5'); 567 (6') cm^{-1} > 551 (3'); 556 (4') cm^{-1}; $\nu(Xe\text{-}F_b)$: 460 (5'); 445 (6') cm^{-1} < 472 (3'); 462 (4') cm^{-1}.

Deformation modes that involve XeF_2 ligand coupling with the $M_2O_2F_8$ ($M(OF_3)–F_b$'---M'OF_4) moiety occur at frequencies that are similar to the non-coupled modes of the 1:1 adduct. The in-plane bends, $\delta(F_5Xe_1F_6)$, occur at higher frequencies (exptl: 259, 276 (Mo); 248, 270[6] (W) cm^{-1}; calcd: 251, 288 (Mo); 249, 287 (W) cm^{-1}) than the out-of-plane bends (exptl: 193/198, 236 (Mo); 193/201, 235/237 (W) cm^{-1}; calcd: 196, 238 (Mo); 192, 231 (W) cm^{-1}). The rocking modes, $\rho_r(F_5Xe_1F_6)$, occur at higher frequencies (exptl: 141/146 (Mo); 139/142 (W) cm^{-1}; calcd: 133 (Mo); 134 (W) cm^{-1}) than the torsional modes, which were not observed (calcd: 84 (Mo); 86 (W) cm^{-1}). The $\delta(M_1F_5Xe_1)$ bending modes occur at very low frequencies (calcd: 43 (Mo); 42 (W) cm^{-1}) and also could not be observed.

7.2.4. Computational Results

The gas-phase geometries of $NgF_2 \cdot MOF_4$ and $XeF_2 \cdot 2MOF_4$ (Ng = Kr, Xe; M = Mo, W) were optimized with all frequencies real at the APFD/Def2-TZVPD (F, O, Mo, W, Kr, Xe) and B3LYP/ Def2-TZVPD (O, F, Mo, W)/aug-cc-pVTZ(-PP) (Kr, Xe) levels of theory. Calculated vibrational frequencies, intensities, and geometric parameters are given in Table 7.2 and Tables A4.2–A4.4 and A4.6–A4.8 of Appendix 4. The APFD results provide gas-phase structures that better reproduce the experimental geometric parameters and are therefore referred to in the ensuing discussion, where comparisons are also made with the $NgF_2 \cdot n CrOF_4$ (n = 1, 2) complexes, calculated at the same level of theory.[65]

7.2.4.1. Calculated Geometries

The energy-minimized gas-phase geometries of $NgF_2 \cdot MOF_4$ have staggered conformations (Cs symmetry) as observed for $NgF_2 \cdot CrOF_4$[65] and are discussed in Appendix 4. The energy-minimized gas-phase geometry of $XeF_2 \cdot 2MoOF_4$ (**5'**) has a

near-eclipsed conformation, with a small ∠Xe–F_b---Mo–$F_{(1)}$ dihedral angle, similar to the experimental value of **5** (calcd: 1.4°; exptl: 7.55(6)°) (Figure 7.2). The energy-minimized gas-phase geometry of $XeF_2 \cdot 2WOF_4$ (**6'**) has a gauche conformation, with a larger ∠Xe–F_b---W–$F_{(1)}$ dihedral angle, contrasting with the experimental near-eclipsed conformation of **6** (calcd: 24.1°; exptl: 5.9(2)°) (Figure A4.3, Appendix 4). As observed in their crystal structures, the calculated Xe–F_t bonds are shorter than the Xe–F_b bonds (Table 7.2), with average calculated Xe–$F_{t/b}$ bond lengths that are very similar to the calculated bond lengths of free NgF_2 (Kr, 1.869; Xe, 1.986 Å).[65] The near linear F_t–Xe–F_b bond angles and the bent Xe–F_b---M bond angles (calcd: **5'**, 125.6; **6'**, 123.8°; exptl: **5**, 130.84(5); **6**, 131.7(2)°) of **5'** and **6'** are reproduced by the calculations. The latter angles are expected to be highly deformable[65] and susceptible to crystal packing, which is consistent with the calculated low frequencies of δ(Xe–F_b---M) (Tables A4.6–A4.8, Appendix 4).

All experimental bond length and bond angle trends for the $F_3OM_{(1)}$–$F_{(4)}$---$M_{(2)}OF_4$ moieties are well reproduced by the calculations (Table A4.4); including the asymmetries of the bridge bonds, $M_{(2)}$---$F_{(4)}$ > $M_{(1)}$–$F_{(4)}$, (calcd: **5'**, 2.426 and 1.897 Å; **6'**, 2.416 and 1.909 Å; exptl: **5**, 2.2990(10) and 1.9350(10) Å; 6, 2.313(4) and 1.929(4) Å), and the $M_{(1)}$–$F_{(4)}$---$M_{(2)}$ angles (calcd: **5'**, 145.8; **6'**, 145.6°; exptl: **5**, 159.02(7); **6**, 159.5(2)°).

7.2.4.2. Natural Bond Orbital (NBO) Analyses

The NAO analyses (Table A4.9) show that the Kr and Xe atom NPA charges of $NgF_2 \cdot CrOF_4$, $NgF_2 \cdot 2CrOF_4$,[65] $NgF_2 \cdot MOF_4$, and $XeF_2 \cdot 2MOF_4$ are slightly more positive than those of free NgF_2. The small degrees of charge transfer from NgF_2 to $CrOF_4$, MOF_4, and $M_2O_2F_8$ are consistent with coordination complexes in which the

$CrOF_4$, MOF_4, and $M_2O_2F_8$ group charges are some-what less negative for $NgF_2{\cdot}CrOF_4$ (Xe, −0.072; Kr, −0.067)[65] and $NgF_2{\cdot}MOF_4$ (Mo: Xe, −0.074; Kr, −0.077; W: Xe, −0.077; Kr, −0.074) than for $XeF_2{\cdot}2MOF_4$ (Mo: Xe, −0.090; W: Xe, −0.096). These charges, which are equal in magnitude to the small positive charges of the coordinated NgF_2 ligands, follow the fluoride-ion acceptor strength trend, $M_2O_2F_8$ > MOF_4 > $CrOF_4$ (see MEPS Analyses). The relative F_b and F_t atom charges of $NgF_2{\cdot}CrOF_4$ (Kr, −0.517, F_b and −0.471, F_t; Xe, −0.599, F_b and −0.576, F_t), $NgF_2{\cdot}MOF_4$ (Mo: Kr, −0.541, F_b and −0.449, F_t; Xe, −0.621, F_b and −0.561, F_t; W: Kr, −0.550, F_b and −0.442, F_t; Xe, −0.627, F_b and −0.554, F_t), and $XeF_2{\cdot}2MOF_4$ (Mo: −0.625, F_b and −0.553, F_t; W: −0.632, F_b and −0.544, F_t) reflect the degrees of ligand polarization, with F atom charges that are more negative for F_b and less negative for F_t relative to the F atom charges of NgF_2 (Kr, −0.509; Xe, −0.605). The Ng–F_t and Ng–F_b Wiberg bond indices of $NgF_2{\cdot}CrOF_4$ (Kr–F_t, 0.599; Kr–F_b, 0.483; Xe–F_t, 0.557; Xe–F_b 0.441)[65] $NgF_2{\cdot}MOF_4$ (Mo: Kr–F_t, 0.625, Kr–F_b, 0.452; Xe–F_t, 0.581; Xe–F_b, 0.410; W: Kr–F_t, 0.637; Kr–F_b, 0.438; Xe–F_t, 0.591; Xe–F_b, 0.397) and $XeF_2{\cdot}2MOF_4$ (Mo: Xe–F_t, 0.592; Xe–F_b, 0.387; W: Xe–F_t, 0.606; Xe–F_b, 0.368) are greater and smaller, respectively, than those of NgF_2 (Xe, 0.521; Kr, 0.555) and also reflect the degrees of ligand polarization in these complexes. The atomic charges and Wiberg bond indices are consistent with polar-covalent NgF_2 ligand bonds in their $CrOF_4$, MOF_4, and $M_2O_2F_8$ complexes. The small Wiberg bond indices of Cr---F_b and M---F_b are also in accordance with the fluoride-ion acceptor strength trend deduced from MEPS isosurface extrema (see below): $NgF_2{\cdot}CrOF_4$ (Kr, 0.090; Xe, 0.098),[65] $NgF_2{\cdot}MOF_4$ (Mo: Kr, 0.101; Xe, 0.109; W: Kr, 0.110; Xe, 0.117), $XeF_2{\cdot}2MOF_4$ (Mo: 0.128; W: 0.141).

7.2.4.3. Atoms in Molecules (AIM) Analysis

Detailed discussions of the AIM analyses[172] for MOF_4, $NgF_2{\cdot}MOF_4$, and $XeF_2{\cdot}2MOF_4$ are provided in Appendix 4. Upon adduct formation, the AIM properties of the M=O and M–F bonds in MOF_4 and $NgF_2{\cdot}MOF_4$ (Table A4.10) show trends that are similar to those of $NgF_2{\cdot}n CrOF_4$.[65] The AIM properties for the Ng–F bonds of $NgF_2{\cdot}CrOF_4$ and $NgF_2{\cdot}MOF_4$ (Table A4.10) indicate increased degrees of Ng–F bond polarization upon descending Group 6 that are in accordance with the relative fluoride-ion affinities of $CrOF_4$ and MOF_4. The primarily electrostatic Cr---F_b and M---F_b bonds of $NgF_2{\cdot}CrOF_4$ and $NgF_2{\cdot}MOF_4$ become more covalent as evidenced by their increased Laplacian of electron densities ($\nabla^2\rho_b$), densities of all electrons (ρ_b), and delocalization densities (δ) when descending Group 6. AIM analyses of $XeF_2{\cdot}2MOF_4$ (Table A4.11) reveal that coordination of M'OF_4 to $XeF_2{\cdot}MOF_4$ to give F_tXeF_b---M(OF_3)–F_b'---M'OF_4 significantly polarizes the M–F and Xe–F bonds. The M---F_b, Xe–F_t, and M–F_t bonds of F_tXeF_b---M(OF_3)–F_b'---M'OF_4 have greater covalent character than $XeF_2{\cdot}MOF_4$, with increased ρ_b, $\nabla^2\rho_b$, and δ-values, and decreased energy densities, H_b. In contrast, the Xe–F_b and M–F_b' bonds are more ionic, having decreased ρ_b, $\nabla^2\rho_b$, and δ-values, and increased *Hb*-values. The AIM parameters of the M'---F_b' bonds are consistent with primarily electrostatic, σ-hole interactions, and indicate that the M'---F_b' bonds of $XeF_2{\cdot}2MOF_4$ are less covalent than the M---F_b bonds. These observations are consistent with the relative FIAs for MOF_4 and M(OF_3)–F_b'---M'OF_4 that follow the order $CrOF_4 < MoOF_4 < WOF_4 \approx$ Mo(OF_3)–F_b'---Mo'OF_4 < W(OF_3)–F_b'---W'OF_4, and are also in accordance with the NBO, MEPS, ELF, and EDA analyses of $XeF_2{\cdot}MOF_4$ and $XeF_2{\cdot}2MOF_4$ (vide infra).

7.2.4.4. Electron Localization Function (ELF) Analysis

ELF analyses[173,174] were carried out for MOF_4, $NgF_2{\cdot}MOF_4$, and $XeF_2{\cdot}2MOF_4$. ELF parameters are provided in Tables A4.10 and A4.11 and ELF isosurface plots are shown for the localization domains of MOF_4, $NgF_2{\cdot}MOF_4$, and $XeF_2{\cdot}2MOF_4$ in Figure A4.8. The ELF valence basins of MOF_4, $NgF_2{\cdot}MOF_4$, and $XeF_2{\cdot}2MOF_4$ are monosynaptic, consistent with the highly polar-covalent nature of the bonding in these compounds. Coordination of NgF_2 to MOF_4 results in perturbation of the toroidal V(Ng) basins, similar to those in $NgF_2{\cdot}n CrOF_4$,[65] where bond critical points are observed between the V(Ng) and the equatorial V(F) basins of adducted MOF_4. These perturbations are more pronounced in $XeF_2{\cdot}2MOF_4$, where the toroidal V(Xe) basin must also accommodate the V(F) basins of coordinated M'OF_4.

The $\bar{N}$[C(Ng)], $\bar{N}$[C(F)], and $\bar{N}$[C(O)] ELF core basin populations are close to the ideal charges, and do not differ significantly upon complex formation. Coordination of NgF_2 to MOF_4 results in no changes in $\bar{N}[V(F_t)]$, but enhancement of $\bar{N}[V(F_b)]$ relative to NgF_2, which is more pronounced for $NgF_2{\cdot}WOF_4$. The F_b basin populations follow the order Cr < Mo < W. Coordination of M'OF_4 to $XeF_2{\cdot}MOF_4$ to give F_tXeF_b---$M(OF_3)$–F_b'---M'OF_4 follows a similar trend, with an even greater increase in $\bar{N}[V(F_b)]$ for $XeF_2{\cdot}2WOF_4$. Increases in the $\bar{N}[V(F_b')]$-values of the coordinated F_b' atoms of MOF_4 relative to those of $XeF_2{\cdot}MOF_4$ are also observed. The localization domain reduction tree diagrams for MOF_4, $NgF_2{\cdot}MOF_4$, and $XeF_2{\cdot}2MOF_4$ (Figure A4.9) provide the hierarchies of ELF basins and their basin separation values (*f*sep). The ELF reduction of the localization diagrams of $NgF_2{\cdot}MOF_4$ follow an order like those described for $NgF_2{\cdot}n CrOF_4$,[65] and are not discussed in detail. Upon descending Group 6, the $NgF_2{\cdot}CrOF_4$ and $NgF_2{\cdot}MOF_4$

adducts separate into NgF_2 and $CrOF_4/MOF_4$ *f*-localization domains in the order Cr < Mo < W, consistent with the relative Cr---F_b and M---F_b bond covalencies. For the $XeF_2{\cdot}2MOF_4$ complexes, M'OF_4 separates from $XeF_2{\cdot}MOF_4$ at somewhat lower *f*-sep-values (Mo, 0.05; W, 0.06) than $XeF_2{\cdot}MOF_4$ separates into XeF_2 and MOF_4 (*f*-sep: Mo, 0.08; W, 0.09), in accordance with the relative bond strengths of M---F_b and M'---F_b'.

7.2.4.5. Molecular Electrostatic Potential Surface (MEPS) Analyses

The MEPS isosurfaces of gas-phase $CrOF_4$, MOF_4 (C_{4v}), NgF_2, NgF_2 ·$CrOF_4$, and $NgF_2{\cdot}MOF_4$ (M = Mo, W) are depicted in Figure 7.4 and Figure A4.10 along with selected electrostatic potential extrema (EP, kJ mol^{-1}). The MEPS isosurfaces of $CrOF_4$ and $NgF_2{\cdot}CrOF_4$, obtained from a related study, were calculated at the same level of theory.[65] The MEPS isosurfaces of KrF_2 and XeF_2 confirm XeF_2 is somewhat more fluorobasic than KrF_2.[65] The isosurfaces of $CrOF_4$ and MOF_4 have regions of high positive EP with maxima (Cr, 247; Mo, 350; W, 354) located on the metal atoms, trans to the Cr=O and M=O bonds that are in accordance with the calculated FIAs (kJ mol^{-1}) of $CrOF_4$ (285), $MoOF_4$ (355), and WOF_4 (387).[252] The fluorine ligands of NgF_2 in $NgF_2{\cdot}n CrOF_4$ (n = 1, 2), $NgF_2{\cdot}MOF_4$, and $XeF_2{\cdot}2MOF_4$ coordinate into these regions of high charge depletion to give Cr---F and M---F bonds that are predominantly electrostatic with small covalent contributions as revealed by NBO, AIM, ELF, and EDA analyses (see below). The higher EP maxima of the Ng and the terminal F atoms of Ng in $NgF_2{\cdot}CrOF_4$ (Xe, 113; F_{Xe}, −55; Kr, 125; F_{Kr}, −39), $NgF_2{\cdot}MoOF_4$ (Xe, 136; F_{Xe}, −34; Kr, 150; F_{Kr}, −18), $NgF_2{\cdot}WOF_4$ (Xe, 147; F_{Xe}, −24; Kr 160; F_{Kr}, −6), $XeF_2{\cdot}2MoOF_4$ (Xe, 141; F_{Xe}, −26), and $XeF_2{\cdot}2WOF_4$ (Xe, 155; F_{Xe},

−14) relative to those of free NgF_2 (XeF_2: Xe, 95; F_{Xe}, −78; KrF_2: 104; F_{Kr}, −64) are consistent with polarization of the coordinated NgF_2 molecule by the Group 6 metal.

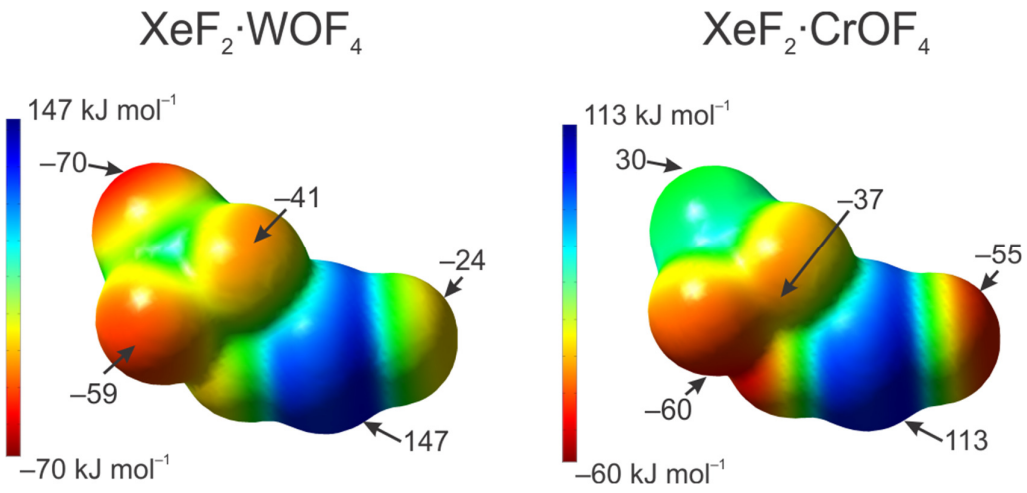

Figure 7.4. The MEPS calculated at the 0.001 $e \cdot a_0^{-3}$ isosurfaces for $XeF_2 \cdot WOF_4$ and $XeF_2 \cdot CrOF_4$. Selected electrostatic potentials are indicated by arrows. The optimized geometries and MEPs were calculated at the APFD/Def2-TZVPD (F, O, Cr, W, Xe) level of theory.

Correspondingly, the EP extrema of the O and F atoms on the metal of $NgF_2 \cdot CrOF_4$ (Xe: O, 30; $F_{av.}$, −48; Kr: O, 32; $F_{av.}$, −46), $NgF_2 \cdot MoOF_4$ (Xe: O, −37; $F_{av.}$, −48; Kr: O, −34; $F_{av.}$, −48), and $NgF_2 \cdot WOF_4$ (Xe: O, −70; $F_{av.}$, −50; Kr: O, −67; $F_{av.}$, −49), and the O atoms of $XeF_2 \cdot 2MoOF_4$ (O_t, −31; O_b, −16), and $XeF_2 \cdot 2WOF_4$ (O_t, −61; O_b, −45) are significantly less than those of free $CrOF_4$ (O, 51; F, −30), $MoOF_4$ (O, −7; F, −31), and WOF_4 (O, −34; F, −30), respectively. Comparisons of the Xe and Ft EP maxima of $XeF_2 \cdot 2MOF_4$ with those of $XeF_2 \cdot MOF_4$ are consistent with greater XeF_2 ligand polarization for $XeF_2 \cdot 2MOF_4$ complexes and the relative fluoride-ion acceptor

strengths: $M(OF_3)–F_b'---M'OF_4 > MOF_4$ and $W(OF_3)–F_b'---W'OF_4 > Mo(OF_3)–F_b'---Mo'OF_4$. The EP extrema of $XeF_2·MOF_4$ show the fluorine atoms on the metals are significantly more basic than the terminal fluorine of XeF_2. Thus, when a second $M'OF_4$ molecule coordinates to $XeF_2·MOF_4$, it preferentially coordinates to a more basic fluorine atom of the MOF_4 moiety in $F_tNgF_b---MOF_4$ rather than to F_t of the XeF_2 ligand, thereby providing rationales for (1) why coordination of a second MOF_4 molecule does not result in XeF_2-bridged complexes analogous to $OF_4Cr---FNgF---CrOF_4$,[65] and (2) why the O ligands of the $O=M–F_b'---M'=O$ moiety are cis to one another and XeF_2 coordinates trans to the M=O bond as in $XeF_2·MOF_4$.

7.2.4.6. Energy Decomposition Analysis (EDA)

The bonding in gas-phase $NgF_2·nCrOF_4$ (n = 1, 2), $NgF_2·MOF_4$ (Ng = Kr, Xe; M = Mo, W), and $XeF_2·2MOF_4$ was analyzed by use of EDA,[258] at the PBE0-D4/TZ2P level of theory (Tables A4.12–A4.18). A more detailed discussion of the EDA is provided in Appendix 4. Trends among the EDA terms of $NgF_2·nCrOF_4$, $NgF_2·MOF_4$, and $XeF_2·2MOF_4$ indicate that the orbital and electrostatic contributions to the $M---F_b$ and $M'---F_b'$ bonds increase upon descending Groups 6 and 18. Orbital mixing comprises 26.9–35.8% of the total attractive contributions for the $M---F_b$ bonds of $NgF_2·MOF_4$, and accounts for the non-linear $Ng–F_b---M$ bond angles in their crystal structures.[65] Symmetric bridging of two $CrOF_4$ molecules to a NgF_2 ligand in $NgF_2·2CrOF_4$ results in weaker $Cr---F_b$ bonding interactions relative to $NgF_2·CrOF_4$, whereas the $M---F_b$ bonds of terminally coordinated $XeF_2·2MOF_4$ are stronger than those of $XeF_2·MOF_4$. The $M'---F_b'$ bonds of $M(OF_3)–F_b'---M'OF_4$ are weaker than, but similar to the $M---F_b$ bonds of $F_tXeF_b---MOF_4$, with small but significant degrees

of covalency that may account for the nonlinear M–F_b'---M' bond angles observed in their crystal structures. These angles are, however, highly deformable and susceptible to crystal packing (see above).

7.2.4.7. Natural Orbitals for Chemical Valence (ETS-NOCV) Analysis

Detailed ETS-NOCV analyses[259] of $NgF_2 \cdot n CrOF_4$, $NgF_2 \cdot MOF_4$, and $XeF_2 \cdot 2MOF_4$ are provided in Appendix 4 (Figures A4.11–A4.17 and Tables A4.19–A4.21). The analysis of $KrF_2 \cdot MoOF_4$ is provided as a representative example. Breakdown of the orbital energy contribution, ΔE_{orb}, for $KrF_2 \cdot MoOF_4$ into individual pairwise contributions of orbitals reveals two significant interactions (Table A4.19) between KrF_2 and $MoOF_4$: (1) σ-type donation from the HOMO, HOMO−1, and HOMO−2 SFOs of KrF_2 to the LUMO+3 SFO of $MoOF_4$ ($\Psi_{1/-1} = \pm 0.22091$, −32.9 kJ mol^{-1}) (Figure 7.5), and (2) σ-type donation from the HOMO−6 SFO of $MoOF_4$ into the HOMO−6 SFO of KrF_2 ($\Psi_{1/-1} = \pm 0.11636$, −8.6 kJ mol^{-1}) (Figure A4.12).

Similar σ-type donations from NgF_2 to $CrOF_4$ and MOF_4 are observed for all coordination complexes, where the degrees of charge delocalization and energy gain increase down Groups 6 and 18 (Table A4.19). It is likely that similar σ-bond interactions from MOF_4 to NgF_2 also occur in other coordination complexes described in this work, however, their individual energetic contributions do not meet the threshold energy requirement (>8.6 kJ mol^{-1}) to be described by the ETS-NOCV method.

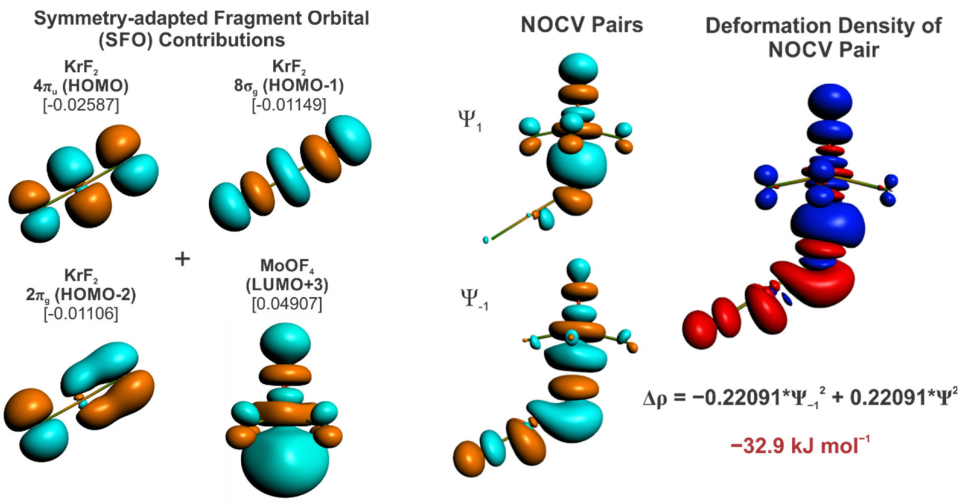

Figure 7.5. The major contribution in the ETS-NOCV analysis of $KrF_2 \cdot MoOF_4$ (PBE0-D4/TZ2P). The isosurface values used for SFO depictions and deformation densities are 0.03 and 0.0002 a.u, respectively. Relative contributions of the SFOs are given in square brackets. Phases of SFOs and NOCV pairs are indicated in light blue and orange. Deformation density colors indicate increased (red) and decreased (blue) electron density relative to the parent fragments.

7.3. Conclusion

The coordination chemistries of NgF_2 and the Group 6 oxide tetrafluorides, $MoOF_4$ and WOF_4, have been significantly extended by the syntheses and detailed structural characterizations of $NgF_2 \cdot MOF_4$ (Ng = Kr, Xe; M = Mo, W) and $XeF_2 \cdot 2MOF_4$ and the complementary QC calculations presented in this study. The NgF_2 molecules terminally coordinate to the metal atom of MOF_4 in $NgF_2 \cdot MOF_4$ and $XeF_2 \cdot 2MOF_4$ (M = Mo, W) to form F_tNgF_b---MOF_4 and F_tXeF_b---$M(OF_3)$–F_b'---M'OF_4, whereas two $CrOF_4$ molecules coordinate to give a symmetrically bridged NgF_2 ligand in the F_4OCr---$FNgF$---$CrOF_4$ complex. In the cases of Mo and W, the second MOF_4

molecule preferentially coordinates to the MOF_4 moiety of $XeF_2 \cdot MOF_4$ instead of to F_t of the XeF_2 ligand. This is consistent with the observed and calculated *cis, trans*-arrangements of M=O and M'=O bonds relative to F_b' and with the greater fluorobasicities of the F atoms of coordinated MOF_4 relative to the F_t atom of the XeF_2 ligand. The geometries of F_tXeF_b---$M(OF_3)$–F_b'---M'OF_4 are unusual and contrast with the related $[F_4OM$---F_b'---$MOF_4]^-$ anions where both M=O bonds are trans to F_b'. The Ng–Ft, Ng–Fb, and M---F_b bond lengths of $XeF_2 \cdot nMOF_4$ (n = 1, 2) and the FIAs follow the trend: $CrOF_4 < MoOF_4 < WOF_4 \approx Mo(OF_3)$–$F_b$'---Mo'$OF_4 <$ $W(OF_3)$–F_b'---W'OF_4. The crystal structures, Raman spectra, and quantum-chemical analyses (AIM, ELF, NAO, MEPS, EDA, and ETS-NOCV) demonstrate that the M---F_b and M'---F_b' bonds of the Ng–F_b---M and M–F_b'---M' fluorine bridges are predominantly electrostatic with small degrees of covalency. The M---F_b and M'---F_b' bonds are dominated by σ-hole type interactions in which the highly nucleophilic F_b atom interacts with the electrophilic region of the transition metal of MOF_4 that is trans to the oxygen atom, with a small covalent component, which accounts for the bent M---F_b–Ng bridge bond angles that are observed and calculated for $NgF_2 \cdot MOF_4$ and $XeF_2 \cdot 2MOF_4$.

CHAPTER 8

Synthesis, Structure, and Bonding of a Xe(IV) Transition-Metal Coordination Complex, F_3XeF_b---WOF_4

Adapted with permission from: **Bortolus, M. R.**; Mercier, H. P. A.; Schrobilgen, G. J. *Angew. Chem. Int. Ed.* **2022**, *61*, e202211699.

8.1. Introduction

Xenon tetrafluoride is the weakest fluoride-ion donor among the binary noble-gas fluorides (relative fluoride-ion donor strengths: $XeF_6 > XeF_2 \approx KrF_2 >> XeF_4$)[20,260] and a powerful oxidative fluorinating agent.[20] The reactions of XeF_4 with the strong fluoride-ion acceptors, liquid SbF_5 or SbF_5 and BiF_5 in anhydrous HF (aHF) solvent, result in intimately ion-paired $[XeF_3][Pn_nF_{5n+1}]$ (n = 1, 2, Pn = Sb, Bi) salts.[20] Xenon tetrafluoride also reacts with liquid AsF_5 at −100 °C to form $[XeF_3][AsF_6]$, which is stable in the presence of excess AsF_5 at −78 °C but dissociates under vacuum at this temperature.[20] The $[XeF_3]^+$ cation is a stronger oxidative fluorinating agent than XeF_4 whose salts are only stabilized by oxidatively resistant, weakly fluorobasic fluoro-anions.[20]

Although several $[XeF_3]^+$ salts have been synthesized and structurally characterized,[20] only one example of a neutral XeF_4 coordination complex, $[Mg(XeF_2)(XeF_4)][AsF_6]_2$, has been reported in which Mg^{2+} is coordinated to XeF_4 through a fluorine bridge, Xe–F_b---Mg.[91] The synthesis of an XeF_4 coordination complex is challenging owing to the low fluorobasicity of XeF_4. Stabilization requires coordination of XeF_4 to an oxidatively resistant Lewis acid center (A) through an Xe–F_b---A bridge. The oxidizer strength of coordinated XeF_4 is enhanced due to its $XeF_3]^+$ character. Thus, a suitable fluoride-ion acceptor for the synthesis of a XeF_4

coordination complex must be oxidatively resistant and have an FIA that is significantly less that of AsF_5 (FIA = 443 kJ mol^{-1}, MP2/PDZ).[261]

The latter criteria are met by the Group 6 oxide tetrafluorides, MOF_4 (Cr, Mo, W), which are oxidatively resistant, moderate-strength fluoride-ion acceptors (FIAs: $CrOF_4$, 285; $MoOF_4$, 355; WOF_4, 387 kJ mol^{-1}; CCSD(T)/aug-cc-pVQZ-PP)[252] that readily abstract fluoride-ion from XeF_6 to yield ion-paired Group 6 oxyfluoro-anion salts of $[XeF_5]^+$ and $[Xe_2F_{11}]^+$.[243,244] In contrast, members of the MOF_4 series are incapable of fluoride-ion abstraction from NgF_2, and form neutral coordination complexes instead, e.g., $FNgF_b$---MOF_4 and F_4OCr---F_bNgF_b---$CrOF_4$.[65,67] The present study explores the fluoride-ion donor behavior of XeF_4 towards the strongest fluoride-ion acceptors among the Group 6 oxide tetrafluorides, $MoOF_4$ and WOF_4. The substantial FIA of WOF_4 and its resistance to oxidation are exploited to synthesize the first transition-metal coordination complex with the weak fluoride-ion donor and potent oxidative fluorinating agent, XeF_4.

8.2. Results and Discussion

8.2.1. Syntheses

Synthetic details are provided in Appendix 5; reaction products were determined by LT Raman spectroscopy.

Reaction of a 1.20:1.00 molar ratio of XeF_4:WOF_4 in $CFCl_3$ solvent at 22 °C yielded a mixture of F_3XeF_b---WOF_4 and unreacted starting materials [Eq. (**8.1**)].

$$XeF_4 + WOF_4 \rightleftarrows F_3XeF_b\text{---}WOF_4 \qquad (\mathbf{8.1})$$

Reaction of a 1.48:1.00 molar ratio of XeF_4:WOF_4 in a melt at ca. 50 °C resulted in rapid oxidative fluorination of WOF_4 and reduction of Xe(IV) to Xe(II) to yield $FXeF_b$---WOF_4 and WF_6, and O_2 gas [Eqs. (**8.2**) and (**8.3**)].

$$XeF_4 + WOF_4 \longrightarrow XeF_2 + WF_6 + \tfrac{1}{2}O_2 \quad (\mathbf{8.2})$$

$$XeF_2 + WOF_4 \longrightarrow FXeF_b\text{---}WOF_4 \quad (\mathbf{8.3})$$

Attempts to synthesize F_3XeF_b---WOF_4 in aHF by reaction of a 1.00:1.21 molar ratio of XeF_4:WOF_4 for 5 min at 22 °C yielded unreacted starting materials. Further reaction at RT for 6 h resulted in oxidative fluorination of WOF_4 and Xe(IV) reduction to give $FXeF_b$---WOF_4, WF_6, and O_2 gas [Eqs. (**8.2**) and (**8.3**)].

The attempted synthesis of F_3XeF_b---$MoOF_4$ in a melt and in $CFCl_3$ solvent under similar reaction conditions yielded unreacted starting materials, in accordance with the lower FIA of $MoOF_4$. The synthesis of F_3XeF_b---$W(OF_3)$–F_b'---$W'OF_4$ was also attempted in $CFCl_3$ solvent. The RT reaction of a 1.00:2.24 molar ratio of XeF_4:WOF_4 in $CFCl_3$ yielded F_3XeF_b---WOF_4 and unreacted WOF_4.

8.2.2. X-ray Crystallography

The F_3XeF_b---WOF_4 complex is a colorless crystalline solid that was characterized by SCXRD ($P\bar{1}$, a = 5.555(11) Å, b = 7.607(10) Å, c = 8.361(16) Å, α = 79.76(6)°, β = 73.64(5)°, γ = 86.74(5)°, Z = 2, V = 333.6(10) Å^3, T = −173 °C, R_1 = 4.16, and wR_2 = 11.85). The F_3XeF_b---WOF_4 molecules pack in columns (Figure A5.1, Appendix 5), with the shortest F···F distance (2.609(5) Å) between adjacent columns being somewhat less than the sum of the fluorine van der Waals radii (2.94 Å,[167] 2.92 Å[168]). Key experimental and calculated geometric parameters are provided in Table A5.1, Appendix 5.

The F_3XeF_b---WOF_4 structural unit is best described as a coordination complex in which an F atom of XeF_4 coordinates trans to the W=O bond of the WOF_4 moiety (Figures 8.1 and A5.2). Four long Xe···F_W contacts (3.043(4)–3.120(4) Å) occur between the equatorial F atoms of four neighboring WOF_4 groups and the Xe

atom of XeF_4, two above and two below the XeF_4-plane, that avoid the stereo-active valence electron lone pairs (VELPs) on Xe(IV). The Xe(IV) coordination sphere of F_3XeF_b---WOF_4 may be described as a distorted square-planar AX_3YE_2 valence shell electron lone pair (VSEPR)[88] arrangement of VELP (E) domains and Xe–F bond-pair (X/Y) domains. The Xe–F_1 bond (1.872(5) Å) trans to the Xe–F_b bridge bond is contracted whereas the Xe–F_b bond (2.068(5) Å) is elongated relative to the Xe–$F_{2,3}$ bonds (1.912(5), 1.917(5) Å). Similar bond length trends were observed for the coordinated XeF_4 molecule of $[Mg(XeF_2)(XeF_4)][AsF_6]_2$ (1.871(7) Å), 1.906(7), 1.916(7), and 2.083(6) Å, respectively).[91] The Xe–$F_{2,3}$ bond lengths of F_3XeF_b---WOF_4 are equal, within ±3σ, to those of the ion-paired *β*-$[XeF_3][SbF_6]$ salt (1.893(2), 1.901(2) Å),[82] but longer than its Xe–F_{eq} bond (1.840(2) Å). The Xe–F_b bridge bond is intermediate with respect to the Xe–F bonds of XeF_4 (1.9449(6), 1.9509(6) Å)[20] and the Xe---F_b bonds of the *β*-$[XeF_3][SbF_6]$ ion-pair (2.484(2), 2.645(2) Å).[82] The F_1–Xe–$F_{2,3}$ (87.3(2), 87.7(2)°) and F_b–Xe–F_1 (178.5(2)°) bond angles are similar to those of $[Mg(XeF_2)(XeF_4)][AsF_6]_2$ (85.4, 87.1, 179.0°)[91] but differ markedly from those of *β*-$[XeF_3][SbF_6]$ (79.62(8), 79.77(8), 152.71(7)°).[82] The F_1–Xe–$F_{2,3}$ bond angles of F_3XeF_b---WOF_4 are somewhat less than for XeF_4 (89.74(3), 90.26(3)°).[262] The geometric parameters of the WOF_4 moiety (Table A5.1) in F_3XeF_b---WOF_4 are comparable to those of $FNgF_b$---WOF_4.[67] The W---F_b bond (2.239(5) Å) is primarily electrostatic and is best described as a σ-hole bond that is longer and somewhat weaker than the W---F_b bonds of $FNgF_b$---WOF_4 (Kr, 2.217(2); Xe, 2.199(3) Å),[67] in accordance with the lower fluorobasicity of XeF_4 relative to NgF_2.[260] However, compression of the O–W–$F_{5–8}$ bond angles (100.0(2)–100.3(2)°) in the complex

relative to gas-phase WOF_4 (104.8(6)°)[256] and its bent W---F_b–Xe bond angle (145.2(2)°) indicates that the W---F_b bond contains some degree of orbital interaction.

The gas-phase geometry of F_3XeF_b---WOF_4 was optimized at the APFD/Def2-TZVPD level of theory to assess the bonding in this complex (Table A5.1). The experimental bond lengths and bond angles are generally well reproduced, whereas the calculated conformation (C_s) differs from experiment (C_1); i.e., the dihedral ∠F(5)-W-Xe-F(2) angle in the crystal structure (97.1(2)°) is much larger than in the calculated structure (35.12°). The conformational difference (Figure 8.1) likely arises from crystal packing and the tendency for Xe(IV) to complete its valence shell through weak intermolecular secondary Xe---F bonds.[250]

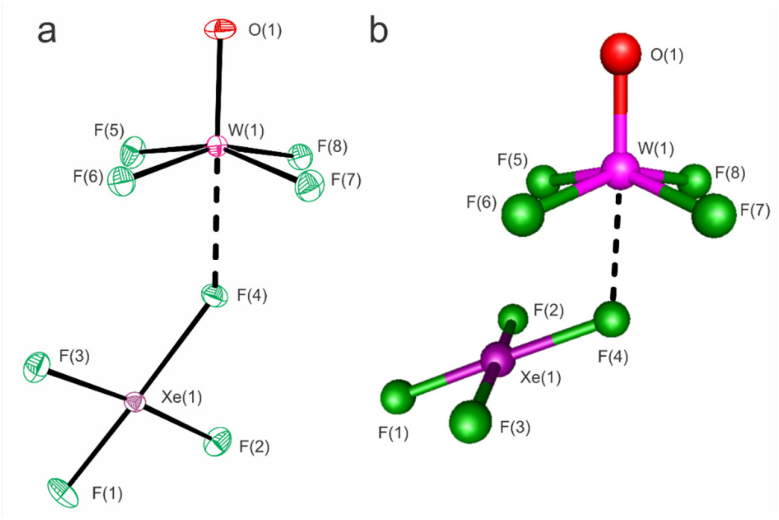

Figure 8.1. (a) The structural unit in the X-ray crystal structure of F_3XeF_b---WOF_4, where thermal ellipsoids are drawn at the 50% probability level. (b) The calculated energy-minimized, gas-phase geometry of F_3XeF_b---WOF_4.

8.2.3. Raman Spectroscopy

Vibrational assignments for the LT Raman spectrum of F_3XeF_b---WOF_4 (Figure A5.3 and Table A5.2, Appendix 5) were made by comparison with the calculated gas-phase

vibrational frequencies (square brackets) and atomic displacements for the calculated vibrational modes of F_3XeF_b---WOF_4, XeF_4 (Table A5.3), WOF_4 (Table A5.4); and the Raman spectra of WOF_4,[263] XeF_4,[20] β-$[XeF_3][SbF_6]$,[79] and $FNgF_b$---WOF_4.[67]

The calculated vibrational frequencies and relative Raman intensities for gas-phase F_3XeF_b---WOF_4 are in good agreement with experiment. The calculated vibrational displacements show that intraligand coupling among the ν(Xe-F_1), $\nu(XeF_{2,3})$, and ν(Xe-F_b) stretches is insignificant. The most intense band at 614 [604] cm^{-1} is assigned to the ν(Xe-F_1), which is similar to that of $[Mg(XeF_2)(XeF_4)][AsF_6]_2$ (605 cm^{-1}),[91] but occurs at significantly lower frequency than the factor-group (FG) split ν(Xe-F_{eq}) stretch of β-$[XeF_3][SbF_6]$ (643/663 cm^{-1}).[79] The $\nu(XeF_{2,3})$ stretches are in- and out-of-phase coupled to give two modes, [ν(Xe-F_2) + ν(Xe-F_3)] and [ν(Xe-F_2) − ν(Xe-F_3)], where the latter mode is also weakly coupled to [ν(W-F_5) − ν(W-F_6)]. These modes are assigned to bands at 580 [564] and 610 [600] cm^{-1}, respectively, and occur at frequencies similar to those of $[Mg(XeF_2)(XeF_4)][AsF_6]_2$ (552, 596 cm^{-1}),[91] and the FG-split $\nu(XeF_{2ax})$ stretches of β-$[XeF_3][SbF_6]$ (564/576, 604/612 cm^{-1}),[79] consistent with the similar Xe–$F_{2,3}$ bond lengths of F_3XeF_b---WOF_4, $[Mg(XeF_2)(XeF_4)][AsF_6]_2$,[91] and β-$[XeF_3][SbF_6]$.[79] The ν(Xe-F_1) and $\nu(XeF_{2,3})$ stretches of F_3XeF_b---WOF_4 occur at higher frequencies than $\nu_s(XeF_4)$ and $\nu_{as}(XeF_4)$ of XeF_4 (533/544 and 503/506 cm^{-1}),[262] which is consistent with enhancement of $[XeF_3]^+$ character upon XeF_4 coordination. The band at 422 [472] cm^{-1} is assigned to the ν(Xe-F_b), and is similar to an unassigned band at 460 cm^{-1} in the Raman spectrum of $[Mg(XeF_2)(XeF_4)][AsF_6]_2$.[91] The bands at 331 [333], 248 [239], and 161 [153] cm^{-1} are respectively assigned to the deformation modes, $\delta_{umb}(XeF_1F_2F_3F_4)$, [$\delta(F_1XeF_2)$ + $\delta(F_3XeF_4)$], and $\delta(F_2XeF_3)$.

The vibrational bands at 1044 [1096] cm^{-1} and 712 [727], 637 [631] cm^{-1} are respectively assigned to the W-O and W-F stretching modes of the WOF_4 moiety and are similar to those of $FNgF_b$---WOF_4.[67] The deformation band at 315 [321] cm^{-1} is assigned to [$\delta(F_6WF_7) + \delta(F_5WF_8)$] and those at 302 [309] and 296 [307] cm^{-1} are assigned to the out-of-plane [$\delta(OWF_5F_6)_{o.o.p.} - \delta(OWF_7F_8)_{o.o.p.}$] and in-plane [$\delta(OWF_5F_6)_{i.p.} - \delta(OW_7F_8)_{i.p.}$] bends. Low-frequency bands at 265 [257], 200 [186], and 156 [150] cm^{-1} are assigned to coupled XeF_4 and WOF_4 deformation modes.

8.2.4. Quantum-chemical Calculations

The bonding of F_3XeF_b---WOF_4 was assessed by NBO (Table A5.5, Appendix 5), MEPS (Figure 8.2), and ELF analyses (Figure 8.3, and Figure A5.4 and Table A5.6) (APFD/Def2-TZVPD). AIM analyses (Table A5.6) are exclusively discussed in Appendix 5. An energy decomposition (EDA) analysis and natural orbitals for a chemical valence extended transition state (ETS-NOCV) analysis were also carried out for the M---F_{Xe} bonds (M = Cr, Mo, W) of F_3XeF_b---WOF_4 and those of the hypothetical F_3XeF_b---$CrOF_4$ and F_3XeF_b---$MoOF_4$ analogues (PBE0-D4/TZ2P) (Tables 8.1, A5.1, A5.7 and A5.8). Parallel analyses for XeF_4 and WOF_4 (Table A5.1) enabled comparisons with F_3XeF_b---WOF_4 and assessment of the effects of complex formation. More in-depth discussions pertaining to these analyses are provided in Appendix 5.

The NBO analyses show coordination of XeF_4 to WOF_4 results in significant bond polarity changes for the Xe–F, W–F, and W–O bonds of F_3XeF_b---WOF_4. The atom charges, Wiberg bond indices, and valences of the Xe–F bonds (Table A5.5) reflect their relative covalencies, i.e., $F_b < F_{2,3} < F_1$. The Wiberg bond index of W---F_b (0.097) is somewhat less than the W---F_b bond indices of $FNgF_b$---WOF_4 (Xe, 0.117;

Kr, 0.110) and consistent with the lower fluorobasicity of XeF_4 relative to NgF_2. In the MEPS analysis (Figure 8.2), the electrostatic potential (EP) minima of the F atoms of XeF_4 (−34 kJ mol^{-1}) are significantly less negative than those of NgF_2 (Xe, −78 kJ mol^{-1}; Kr, −64 kJ mol^{-1} [67]), in accordance with the higher formal oxidation state of Xe(IV) and the lower fluorobasicity of XeF_4.

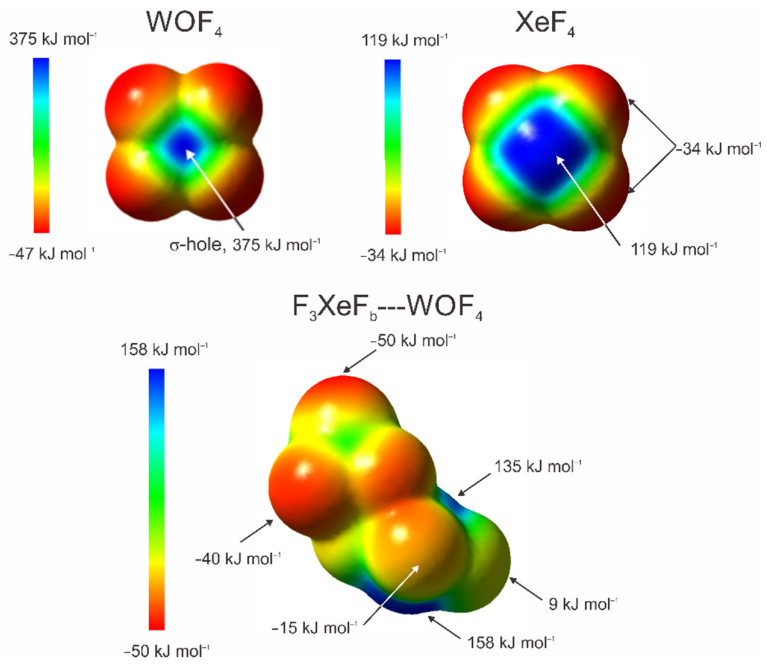

Figure 8.2. The MEPS contours calculated at the 0.001 e a_o^{-3} isosurfaces of WOF_4, XeF_4, and F_3XeF_b---WOF_4. The extrema of selected electrostatic potentials are indicated by arrows.

The MEPS analysis of F_3XeF_b---WOF_4 (Figure 8.2) shows that the F_b atom interacts with a region of high electrostatic potential on W (375 kJ mol^{-1}), that is trans to the W=O double bond, to form a primarily electrostatic W---F_b σ-hole bond and slightly elongated Xe–F_b and contracted Xe–F_1 bonds. The EP maxima on the MEPS isosurfaces of the Xe, F_1, and $F_{2,3}$ atoms are more positive than those of XeF_4, and correspondingly the EP extrema of the O and F atoms of coordinated WOF_4 are more

negative than those of free WOF_4. These trends are consistent with polarization of XeF_4 upon complex formation that is accompanied by a small degree of charge transfer from XeF_4 to WOF_4 (NBO Analysis, Table A5.5).

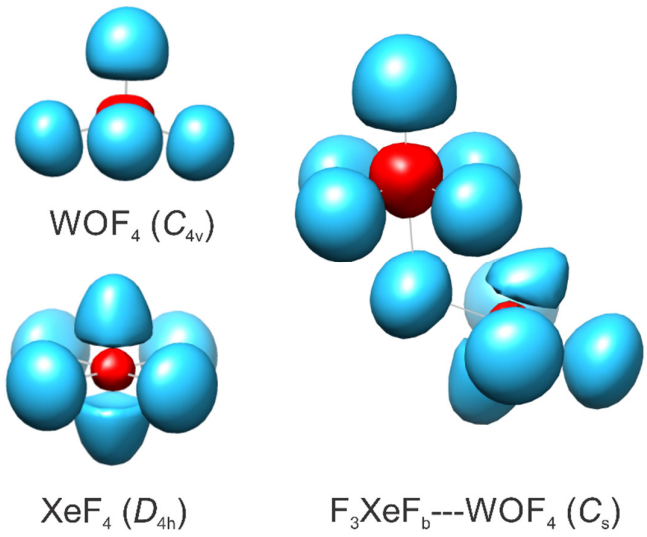

Figure 8.3. ELF isosurface plots (η(r) = 0.60) for WOF_4, XeF_4, and F_3XeF_b---WOF_4. Color code: core basins (red); C(W), C(Xe); monosynaptic valence basins (blue); V(F), V(O), V(Xe).

The F and Xe electron localization function (ELF) valence basins of XeF_4, WOF_4, and F_3XeF_b---WOF_4 are monosynaptic, in accord with the polar-covalent bond characters of this compound (Figure 8.3). The ELF isosurface plot of XeF_4 is consistent with an AX_4E_2 VSEPR arrangement around xenon, where the stereo-active VELPs of Xe occupy axial positions and the Xe–F bond domains occupy equatorial positions. Coordination of XeF_4 to WOF_4 distorts the AX_4E_2 arrangement such that the axial V(Xe) lone pair basin proximate to the $V(F_{5,6})$ basins of WOF_4 is perturbed. The ELF reduction of localization diagram (Figure A5.4) for F_3XeF_b---WOF_4 separates into XeF_4 and WOF_4 domains at $f_{sep} = 0.07$, which is marginally less than for

$FXeF_b$---WOF_4 (0.08) and consistent with a primarily electrostatic W---F_b bond. The V(F) basins of F_3XeF_b---WOF_4 separate from V(Xe) in accord with the relative polar-covalent characters of its Xe–F bonds, i.e., $V(F_b) < V(F_{2,3}) < V(F_4)$.

Energy decomposition analyses (EDA) for the M---F_b bonds of F_3XeF_b---WOF_4, the hypothetical F_3XeF_b---$CrOF_4$ and F_3XeF_b---$MoOF_4$ analogues, and the known $FXeF_b$---MOF_4 analogues[67] are compared in Tables 8.1 and A5.7. The W---F_b bond dissociation energy (D_E) of F_3XeF_b---WOF_4 (36.90 kJ mol^{-1}) is substantially less than those of $FNgF_b$---WOF_4 (Kr, 49.18; Xe, 55.17 kJ mol^{-1}), in accordance with the lower fluorobasicity of XeF_4. Electrostatic interactions contribute 57.4% to the total attractive terms for the W---F_b bond, whereas orbital mixing contributes 35.4% and dispersion effects provide the remaining 7.2%. The EDA analysis shows the W---F_b bond is primarily electrostatic with a smaller orbital contribution, and intermediate with respect to the D_E values for the Cr---F_b and Mo---F_b bonds of $FXeF_b$---$CrOF_4$ and $FXeF_b$---$MoOF_4$. The D_E values of the M---F_b bonds for both complex series follow the FIA trend, $WOF_4 > MoOF_4 > CrOF_4$. The percent electrostatic and orbital contributions to the M---F_b bonds of $FXeF_b$---MOF_4 and F_3XeF_b---MOF_4 are similar in both series, where electrostatic contributions to the M---F_b bonds (57 – 64%) dominate orbital contributions (27 – 35%). The orbital contribution to the W---F_b bond accounts for the non-linear Xe–F_b---W bond angle in the gas-phase,[67] which significantly contributes, along with crystal packing effects, to its non-linearity in the crystal structure of F_3XeF_b---WOF_4. The calculated Xe–F_b---M bond angles of F_3XeF_b---$CrOF_4$ (116.90°), F_3XeF_b---$MoOF_4$ (122.53°), and F_3XeF_b---WOF_4 (122.64°) are very similar to those of $FXeF_b$---$CrOF_4$ (120.45°), $FXeF_b$---$MoOF_4$ (122.86°), and

$FXeF_b$---WOF_4 (123.68°),[67] in accordance with similar percentage orbital contributions to the M---F_b bonds of both series of complexes (Table 8.1).

Table 8.1. Energy Decomposition Analyses (EDA)[a] for the M---F_b Bonds of F_3XeF_b---MOF_4 (M = Cr, Mo, W) and $FXeF_b$---MOF_4

Attractive Energy Terms [a] →	ΔE_{orb}[b]	ΔE_{elstat}[b]	ΔE_{disp}[b]	D_E[b,c]
$FXeF_b$---WOF_4 [d]	−71.24 (34.4 %)	−126.87 (61.2 %)	−9.13 (4.4 %)	55.17
$FXeF_b$---$MoOF_4$ [d]	−58.37 (33.3 %)	−107.94 (61.7 %)	−8.73 (5.0 %)	48.88
F_3XeF_b---WOF_4	**−52.15 (35.4 %)**	**−84.32 (57.4 %)**	**−10.64 (7.2 %)**	**36.90**
F_3XeF_b---$MoOF_4$	−39.89 (33.8 %)	−68.03 (57.7 %)	−9.97 (8.5 %)	32.93
$FXeF_b$---$CrOF_4$ [d]	−26.11 (26.9 %)	−62.12 (64.1 %)	−8.73 (9.0 %)	28.43
F_3XeF_b---$CrOF_4$	−17.02 (26.6 %)	−37.14 (57.9 %)	−9.93 (15.5 %)	20.94

[a] Calculated at the PBE0-D4/TZ2P level of theory. The attractive energy terms are ΔE_{orb} = orbital mixing (covalency) between fragments, ΔE_{elstat} = electrostatic interaction energy between fragment charge densities, ΔE_{disp} = dispersion energy. [b] kJ mol^{-1}. [c] $-D_E = \Delta E_{int} + \Delta E_{prep}$, where D_E is the M---F_b bond dissociation energy, ΔE_{int} is the interaction energy, and ΔE_{prep} is the preparation energy. [d] Ref. [67].

An ETS-NOCV analysis was carried out to determine and visualize the most significant attractive orbital contributions in the EDA analysis for the W---F_b bond of F_3XeF_b---WOF_4. The most significant orbital interaction between XeF_4 and WOF_4 is σ-donation from the HOMO and HOMO−3 symmetry fragment orbitals (SFOs) of XeF_4 into the LUMO+3 of WOF_4 ($\Psi_{1/-1} = \pm 0.21194$) (Figure 8.4), which contributes −31.62 kJ mol^{-1} (61% of the total orbital interaction energy) to the W---F_b bond. The deformation of electron density that results from this interaction is also depicted in Figure 8.4. Similar σ-bond interactions were obtained from ETS-NOCV analyses for

the M---F_b bonds of $FNgF_b$---MOF_4 (Ng = Kr, Xe; M = Cr, Mo, W).[67] The $FNgF_b$---WOF_4 complexes have greater degrees of charge delocalization ($\Psi_{1/-1}$: Xe, 0.24840; Kr, 0.23953) and total orbital energy gains (Xe, −44.0 kJ mol^{-1}; Kr, −40.6 kJ mol^{-1}) than F_3XeF_b---WOF_4 (vide supra). The energy contribution to the W---F_b bond of F_3XeF_b---WOF_4 from all other orbital interactions is −20.53 kJ mol^{-1}, where no single contribution meets the threshold energy (> 8.6 kJ mol^{-1}) required for explicit description by the ETS-NOCV method.

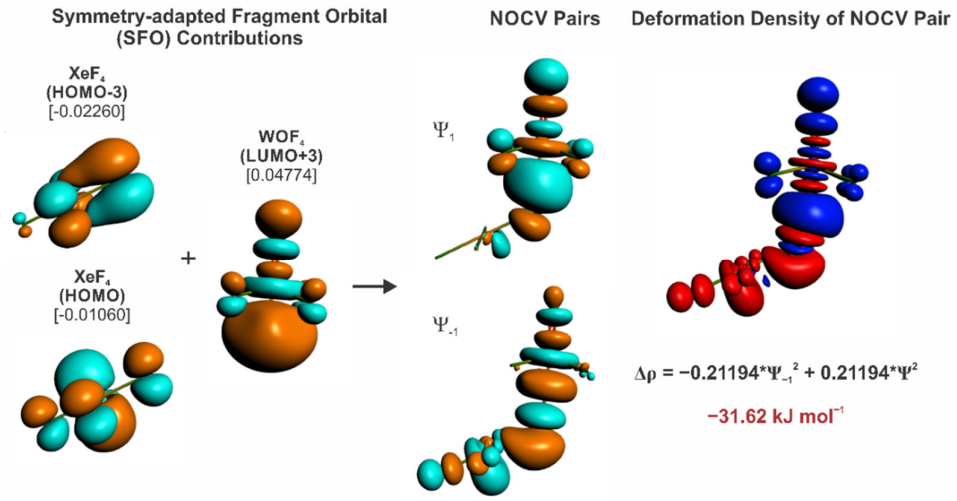

Figure 8.4. The ETS-NOCV analysis for F_3XeF_b---WOF_4 (PBE0/TZ2P) showing the SFO combinations for the XeF_4 (HOMO−3 and HOMO) and WOF_4 (LUMO+3) orbital combinations. Phases of SFO combinations and NOCV pairs are denoted by light blue and orange colors. Deformation density colors denote increased (blue) and decreased (red) electron densities relative to the parent fragments. Isosurface values used for orbital depictions are SFOs (XeF_4, WOF_4) and NOCV pairs (0.03 a.u.), and deformation densities (0.003 a.u.).

CHAPTER 9

Chromium Oxide Tetrafluoride and Its Reactions with Xenon Hexafluoride; the $[XeF_5]^+$ and $[Xe_2F_{11}]^+$ Salts of the $[Cr^{VI}OF_5]^-$, $[Cr^{V}OF_5]^{2-}$, $[Cr^{V}_2O_2F_8]^{2-}$, and $[Cr^{IV}F_6]^{2-}$ Anions

Adapted with permission from: Goettel, J. T.; **Bortolus, M. R.;** Stuart, D. G.; Mercier, H. P. A.; Schrobilgen, G. J. *Chem. Eur. J.* **2019**, *29*, 15815–15829.

9.1. Introduction

The chromium(VI) oxide fluorides, CrO_2F_2[135] and $CrOF_4$,[66,264] and salts of the $[CrO_3F]^-$,[265–267] $[CrO_2F_3]^-$,[268] *cis*-$[CrO_2F_4]^{2-}$,[269–271] and $[CrOF_5]^-$ [66,264] anions, have been synthesized and characterized. Recent synthetic and structural studies have shown that $CrOF_4$ is sufficiently Lewis acidic to form stable adducts with the noble-gas difluorides NgF_2 (Ng = Kr,[65,66] Xe[65]). However, CrF_6 is presently nonexistent, although its synthesis and characterization by elemental analysis was reported in 1963[272] and its low-temperature (LT) IR spectrum was reported in 1966.[273] The IR spectrum was later shown to arise from a mixture of CrF_5, CrO_2F_2, $CrOF_4$, and other compounds.[274] Subsequent reports, which appeared in 1984,[275] 1985,[276] and 1991,[277] claimed to have substantiated the existence of CrF_6 based on matrix-isolation IR and UV-visible spectroscopic studies. However, further matrix-isolation IR studies reported in 1990[274] and 1992[278] showed that the spectrum previously attributed to CrF_6 was due to CrF_5. A more recent matrix-isolation IR and computational study[279] concurred with the latter findings and the present nonexistence of CrF_6.

Both $MoOF_4$ and WOF_4 were initially synthesized and described in 1907 by Ruff and Eisner,[280] but it was not until 1963 that the synthesis of $CrOF_4$ was reported by Edwards,[281] which was subsequently improved to provide higher purities and

yields.[66,264,282] The fluoride-ion acceptor properties of $MoOF_4$ and WOF_4 have been the subjects of studies which have resulted in the syntheses of numerous $[MoOF_5]^-$ [283–287] and $[WOF_5]^-$ [283–285,288–296] salts that have been well characterized in the solid state by IR and Raman spectroscopy,[283,285,288,290,293,294,296] elemental analyses,[283,286,287,290,292–294] and powder X-ray diffraction;[283,287] and in solution by ^{19}F NMR spectroscopy[283,284,291–295] and cyclic voltammetry.[286] X-ray crystal structures of the $[AsPh_4]^+$,[290] $[Cs(15\text{-crown-}5)_2]^+$,[290] and Ag^{2+} [288] salts of $[WOF_5]^-$, in which the O/F positions are disordered, have also been reported. The crystal structures of $[Xe_2F_{11}][MoOF_5]$ and $[XeF_5][Mo_2O_2F_9]$ have recently been reported (see Chapter 11), and the X-ray crystal structures of the Li^+–Cs^+ salts of $[Mo_2O_2F_9]^-$[297] and $[MoOF_5]^-$ in $K_3[MoOF_7]$[298] were subsequently published.

Although several $[CrOF_5]^-$ salts have been synthesized and characterized by vibrational spectroscopy, no X-ray crystal structure of a $[CrOF_5]^-$ salt has been reported. The $[CrOF_5]^-$ anion has been synthesized as its Cs^+ salt by heating a 1:1 molar ratio of CsF and $CrOF_4$ to 100 °C (eq **9.1**).[264] Elemental analysis and the IR spectrum of the product were in good agreement with the formulation, $Cs[CrOF_5]$. The $[NO]^+$ salt was subsequently prepared by reaction of $CrOF_4$ with NOF at room temperature (eq **9.1**),[66]

$$CrOF_4 + MF \xrightarrow{aHF} [M][CrOF_5] \quad M = Cs^+ \text{ or } [NO]^+ \qquad (\mathbf{9.1})$$

The $[CrOF_5]^-$ anion of $[NO][CrOF_5]$ was characterized by low-temperature IR and Raman spectroscopy and its spectrum was assigned under C_{4v} point symmetry.[66] Controlled pyrolysis of $[NO][CrOF_5]$ resulted in a mixture which was shown to consist of $[NO][CrOF_5]$ and $[NO][CrOF_5]\cdot nCrOF_4$ by IR spectroscopy. These findings suggested that salts such as $[NO][Cr_2O_2F_9]$ are thermally more stable than

$[NO][CrOF_5]$.[66] The $Cs[CrOF_5]$ and $[NO][CrOF_5]$ salts were subsequently synthesized by the reaction of equimolar amounts of CrO_2F_2 with excess F_2 and either NOF or CsF at 80 °C (eq **9.2**) and the $Cs[CrOF_5]$ salt was also prepared by reaction of CrO_3 with CsF and COF_2 at 90 °C (eq **9.3**).[270] The $[(CH_3)_2SnF]^+$ salt of $[CrOF_5]^-$ was prepared by reaction of $(CH_3)_2SnF_2$ with $CrOF_4$ in aHF solvent (eq **9.4**).[270]

$$CrO_2F_2 + MF + F_2 \xrightarrow{aHF} [M][CrOF_5] + 1/2O_2 \qquad (\mathbf{9.2})$$

$$CrO_3 + CsF + COF_2 \xrightarrow{aHF} Cs[CrOF_5] + 2CO_2 \qquad (\mathbf{9.3})$$

$$(CH_3)_2SnF_2 + CrOF_4 \xrightarrow{aHF} [(CH_3)_2SnF][CrOF_5] \qquad (\mathbf{9.4})$$

The chemistries of Cr(V) and Cr(IV) oxide fluorides are more limited. The synthesis and vibrational spectra have been reported for pure $CrOF_3$[299–301] and the syntheses of the K^+ and Cs^+ salts of $[CrOF_4]^-$ and their characterizations by mass balance measurements,[302] X-ray powder diffraction,[301] and by infrared[300] and UV-vis spectroscopies[300] have also been reported. A LT ESR study of $K[CrOF_4]$ reported the observation of both $[CrOF_4]^-$ and $[CrOF_5]^{2-}$ in frozen 48% aqueous HF glasses.[303] The $[(C_2H_5)_4N]^+$ salt of $[CrOF_5]^{2-}$ was synthesized by the reaction of $[(C_2H_5)_4N][CrOCl_4]$ with AgF in a $HF_{(aq)}/CH_2Cl_2$ mixture and was characterized by ESR and IR spectroscopy.[304] The neutral Cr(IV) oxide fluoride, $CrOF_2$, was synthesized by the thermal decomposition of CrO_2F_2 at 500 °C, and is insoluble in water,[305] aqueous acids (HCl, HF, HNO_3), aqueous bases (NH_4OH, NaOH, KOH), and common organic solvents. The only Cr(IV) oxyfluoro-anion that has been reported is $[CrO_2F]^-$, which was obtained as a reduction product in the reaction of $[(CH_3)_4N][CrO_3F]$ with organic alcohols and was characterized by elemental analysis and IR spectroscopy.[266] To date,

there have been no crystal structures reported for $[CrOF_5]^-$, $[Cr_2O_2F_9]^-$, $[CrOF_4]^-$, and $[CrOF_5]^{2-}$.

The noble-gas difluorides, NgF_2 (Ng = Kr, Xe), are sufficiently fluorobasic to form adducts with the Group 6 d^0 metal oxide tetrafluorides, MOF_4 (M = Cr, Mo, W), having the general formulae $NgF_2 \cdot nMOF_4$ (n = 1, 2).[65,183,184,306] Members of the MOF_4 series are intermediate strength fluoride-ion acceptors which do not fully transfer fluoride ion to form $[NgF][MOF_5]$ or $[NgF][M_2O_2F_9]$ salts. Instead, NgF_2 coordinates to the metal by means of Ng–F---M bridges.[65] Xenon hexafluoride is more fluorobasic than XeF_2,[260] and is therefore more likely to donate fluoride ion to $CrOF_4$ to form $[XeF_5]^+$ and $[Xe_2F_{11}]^+$ salts of $[CrOF_5]^-$. The +6 oxidation state of xenon in $[XeF_5]^+$ and $[Xe_2F_{11}]^+$ provides the electron-poor environments that are needed to stabilize high-oxidation state transition-metal oxyfluoro-anions such as in the case of the stable Os(VIII) salts, $[XeF_5][OsO_3F_3]$, $[Xe_2F_{11}][fac\text{-}OsO_3F_3]$, and $[XeF_5][\mu\text{-}F(OsO_3F_2)_2]$.[121]

A prior attempt to synthesize Cr(V) fluoro-anion salts by use of XeF_6 as a fluoride ion donor led to Cr(V) reduction and F_2 elimination.[307] Instead of the anticipated $[XeF_5][Cr^VF_6]$ salt, the reaction of XeF_6 with CrF_5 yielded $[XeF_5][Cr^{IV}F_5]$ which was characterized by single-crystal X-ray diffraction (eq **9.5**).[307]

$$XeF_6 + CrF_5 \xrightarrow{aHF} [XeF_5][CrF_5] \qquad (\mathbf{9.5})$$

The present study examines the reactions between $CrOF_4$ and XeF_6 in melts and in the oxidatively resistant solvents, aHF and $CFCl_3$. The reaction pathways involve redox transformations that give rise to several chromium oxide fluoride anions in the +6 and +5 oxidation states and $[CrF_6]^{2-}$. The latter anions were isolated as $[XeF_5]^+$ and $[Xe_2F_{11}]^+$ salts and structurally characterized by LT single-crystal X-ray diffraction and LT Raman spectroscopy. Quantum-chemical calculations were

employed to calculate the gas-phase geometries and to aid in the vibrational frequency assignments of several compounds synthesized in this study.

9.2. Results and Discussion

9.2.1. Syntheses

9.2.1.1. $[XeF_5][Xe_2F_{11}][CrOF_5]\cdot 2CrOF_4$ (6) and $[Xe_2F_{11}][CrOF_5]$. Equimolar mixtures of XeF_6 and $CrOF_4$ liquified near room temperature to form a dark purple liquid with the vigorous evolution of a gas that was noncondensible at −196 °C (eq **9.6**). The gas was identified as F_2 by rapid tarnishing of a drop of mercury upon exposure to it. Slow cooling of the reaction product from 20 to 0 °C resulted in the growth of large, rod-shaped crystals (m.p. 18 °C) which were shown to be $[XeF_5][Xe_2F_{11}][CrOF_5]\cdot 2CrOF_4$ (**6**) (see X-ray Crystallography). The net equation for the reaction of XeF_6 with $CrOF_4$ in a melt near ambient temperature is given by eq **9.6**.

$$3XeF_6 + 3CrOF_4 \xrightarrow{\text{melt}} [XeF_5][Xe_2F_{11}][CrOF_5]\cdot 2CrOF_4 + \tfrac{1}{2}F_2 \qquad (\mathbf{9.6})$$

and likely proceeds by the following pathway (eqs 9.6a-9.6c):

$$\left.\begin{array}{l} XeF_6 + CrOF_4 \xrightarrow{\text{melt}} [XeF_5][CrOF_5] \\ \text{and/or} \\ 2XeF_6 + CrOF_4 \xrightarrow{\text{melt}} [Xe_2F_{11}][CrOF_5] \end{array}\right\} \qquad (\mathbf{9.6a})$$

$$\left.\begin{array}{l} XeF_6 + [XeF_5][CrOF_5] \xrightarrow{\text{melt}} [XeF_5]_2[CrOF_5] + \tfrac{1}{2}F_2 \\ \text{and/or} \\ [Xe_2F_{11}][CrOF_5] \xrightarrow{\text{melt}} [XeF_5]_2[CrOF_5] + \tfrac{1}{2}F_2 \end{array}\right\} \qquad (\mathbf{9.6b})$$

$$XeF_6 + [XeF_5]_2[CrOF_5] \xrightarrow{\text{melt}} [XeF_5][Xe_2F_{11}][CrOF_5] \qquad (\mathbf{9.6c})$$

Upon crystallization, $CrOF_4$ is introduced into the coordination sphere of the $[CrOF_5]^{2-}$ anion in **6** (see X-ray Crystallography).

To establish whether $[CrOF_5]^-$ salts are formed as intermediates in eqs **9.6a** and **9.6b**, the reaction between XeF_6 and $CrOF_4$ was monitored as a function of time and temperature by Raman spectroscopy. Equimolar amounts of solid XeF_6 and $CrOF_4$ were mixed at –78 °C and then warmed to –50 °C, whereupon the color of the mixture changed from red to orange. The sample was thereafter successively warmed to higher temperatures in steps ranging from –30 °C to ambient temperature and was allowed to react at each temperature stage for a sufficient length of time to produce a notable change in the Raman spectrum. The sample was intermittently agitated during each reaction period, and then quenched to –196 °C. Reaction progress was monitored by recording the low-temperature (–91 to –120 °C) Raman spectrum after each warm/quench cycle (see footnotes [i–m] in Table A6.1).

The Raman spectra of the orange solid (Table A6.1) showed that bands corresponding to free $CrOF_4$ persisted while a new set of bands appeared and grew in intensity until the sample reached 0 °C. The new bands arose from $[Xe_2F_{11}][CrOF_5]$ (eq **9.6a**) and were assigned by comparison with those of $Cs[CrOF_5]$,[264] $[NO][CrOF_5]$,[66] and the calculated frequencies of the gas-phase $[CrOF_5]^-$ anion listed in footnote [g] of Table A6.1. The experimental Raman bands of $[CrOF_5]^-$ (Table A6.1) occurred at: ν(Cr-O), 951 cm^{-1}; $[\nu_s(Cr\text{-}F_{4e}) + \nu(Cr\text{-}F_{ax})]$, 640 cm^{-1}; $\nu_{as}(Cr\text{-}F_{4e})$, 568 cm^{-1}; $\nu(Cr\text{-}F_{ax})$, 527 cm^{-1}; $[\delta(OCrF_e) + \delta(F_eCrF_{ax})]$, 341 cm^{-1}; $[\delta(F_eCrF_e) + \delta(F_eCrF_e)]$, 323/314 cm^{-1}; $[\rho_w(OCrF_{ax}) + \rho_w(F_eCrF_e)]$, 275 cm^{-1}; $[\rho_t(F_eCrF_e) + \rho_t(F_eCrF_e)]$, 216 cm^{-1} . The $[Xe_2F_{11}]^+$ cation bands (Table A6.1) were assigned by comparison with known $[Xe_2F_{11}]^+$ salts.[121,308] The sample was then warmed in stages

until fusion occurred at ca. 18 °C and then immediately quenched at –196 °C, whereupon weak bands due to $[XeF_5][Xe_2F_{11}][CrOF_5]\cdot 2CrOF_4$ (**6**) (see Raman Spectroscopy) began to appear in addition to those of $[Xe_2F_{11}][CrOF_5]$ and free $CrOF_4$. The sample was then re-melted and held at ambient temperature for ca. 1 min with no apparent sign of gas evolution and then quenched at –196 °C. The Raman spectrum showed $[Xe_2F_{11}][CrOF_5]$ and increased amounts of **6**, but no free $CrOF_4$ could be detected. Upon continued reaction for one additional hour at ambient temperature, gas evolution was clearly evident and predominantly compound **6** and a small amount of $[Xe_2F_{11}][CrOF_5]$ were observed in the Raman spectrum of the quenched sample. Crystals of $[Xe_2F_{11}][CrOF_5]$ that were suitable for an X-ray crystal structure determination could not be obtained from the melts during the course of these studies.

9.2.1.2. ***$[XeF_5]_2[CrF_6]\cdot 2CrOF_4$ (1).*** When ca. 1.5 equivalents of $CrOF_4$ were allowed to react with one equivalent of XeF_6 at room temperature, the mixture fused to give a dark-purple liquid that contained undissolved $CrOF_4$. The reaction mixture was warmed to approximately 60 °C and the contents were agitated to effect dissolution of the remaining $CrOF_4$ (eq **9.5**). Upon slow cooling of the melt to room temperature, dark-red, needle-shaped crystals of $[XeF_5]_2[CrF_6]\cdot 2CrOF_4$ deposited on the walls of the reaction vessel.

The proposed pathway for the reaction of XeF_6 with $CrOF_4$ (eq **9.7**) at elevated temperature (60 °C) initially proceeds via eq **9.6a** to give $[XeF_5][CrOF_5]$, which then undergoes F_2 elimination to form $[XeF_5][CrOF_4]$ (eq **9.7a**). The latter salt undergoes fluorine/oxygen metathesis with XeF_6 (eq **9.7b**), with introduction of $CrOF_4$ into the

coordination sphere of $[CrF_6]^{2-}$ occurring upon crystallization of the melt (see compound **1** in X-ray Crystallography).

$$3XeF_6 + 3CrOF_4 \xrightarrow[60\ ^\circ C]{melt} [XeF_5]_2[CrF_6]\cdot 2CrOF_4 + \tfrac{1}{2}F_2 + XeOF_4 \qquad (\mathbf{9.7})$$

$$[XeF_5][CrOF_5] \longrightarrow [XeF_5][CrOF_4] + \tfrac{1}{2}F_2 \qquad (\mathbf{9.7a})$$

$$2XeF_6 + [XeF_5][CrOF_4] \longrightarrow [XeF_5]_2[CrF_6] + XeOF_4 + \tfrac{1}{2}F_2 \qquad (\mathbf{9.7b})$$

9.2.1.3. $[Xe_2F_{11}]_2[CrF_6]$ (2) and $[XeF_5]_2[Cr_2O_2F_8]$ (3). Approximately four equivalents of XeF_6 were allowed to react with one equivalent of $[XeF_5]_2[CrF_6]\cdot 2CrOF_4$ in a melt at 30 °C. Slow cooling from 30 °C to room temperature resulted in the formation of crystalline $[Xe_2F_{11}]_2[CrF_6]$ (colorless needles) and $[XeF_5]_2[Cr_2O_2F_8]$ (red-orange blocks).

The overall reactions leading to the formation of **2** and **3** are provided by eqs (**9.8**) and (**9.9**), respectively. Compound **2** arises from the addition of XeF_6 to $[XeF_5]^+$ of the starting compound, $[XeF_5]_2[CrF_6]\cdot 2CrOF_4$ (**1**) in eq **9.8**. Compound **3** is

$$2XeF_6 + [XeF_5]_2[CrF_6]\cdot 2CrOF_4 \longrightarrow [Xe_2F_{11}]_2[CrF_6] + 2CrOF_4 \qquad (\mathbf{9.8})$$

formed by the reaction of co-crystallized $CrOF_4$ in **1** with XeF_6 (eq **9.9**). The overall reaction presumably occurs in two consecutive steps, eqs **9.6a** and **9.9a**, which yield $[CrOF_4]^-$ as a transient species that dimerizes to form $[Cr_2O_2F_8]^{2-}$.

$$2XeF_6 + 2CrOF_4 \longrightarrow [XeF_5][Cr_2O_2F_8] + F_2 \qquad (\mathbf{9.9})$$

$$2[XeF_5][CrOF_5] \longrightarrow F_2 + 2[XeF_5][CrOF_4] \longrightarrow [XeF_5]_2[Cr_2O_2F_8] \qquad (\mathbf{9.9a})$$

9.2.1.4. $[XeF_5]_2[Cr_2O_2F_8]\cdot 2HF$ (4) and $[XeF_5]_2[Cr_2O_2F_8]\cdot 2XeOF_4$ (5). The reaction of equimolar amounts of XeF_6 with HF-wetted $CrOF_4$ in $CFCl_3$ solvent at room temperature yielded a mixture of $[XeF_5]_2[Cr_2O_2F_8]\cdot 2HF$ (**4**) and $[XeF_5]_2[Cr_2O_2F_8]\cdot 2XeOF_4$ (**5**), where compound **4** was the major component. Xenon

hexafluoride was transferred onto a sample containing $CrOF_4$ and aHF in $CFCl_3$ solvent at –196 °C. Upon warming to room temperature, $CrOF_4$ and XeF_6 rapidly dissolved to give a clear, amber solution. Transparent, pale yellow-green, block-shaped crystals of $[XeF_5]_2[Cr_2O_2F_8]\cdot 2HF$ (**4**) and amber, block-shaped crystals of $[XeF_5]_2[Cr_2O_2F_8]\cdot 2XeOF_4$ (**5**) slowly grew from solution when the sample was allowed to stand at –78 °C for 48 h.

The reaction of equimolar amounts of XeF_6 and $CrOF_4$ in aHF at –78 °C initially yielded crystalline $XeF_6\cdot 1.5HF$[100] and α-$CrOF_4$,[65] which were confirmed by unit cell determinations. Upon warming to room temperature, α-$CrOF_4$ and $XeF_6\cdot 1.5HF$ rapidly dissolved in aHF to give an amber solution. Quenching the sample at –196 °C yielded a white precipitate, which readily redissolved in aHF at room temperature. Amber, block-shaped crystals of **5** slowly grew from solution upon standing overnight at –78 °C.

The products resulting from the reactions of XeF_6 and $CrOF_4$ in aHF and in $CFCl_3$/aHF suggest the overall reaction proceeds according to eq **9.9** which may be understood in terms of the reaction pathway represented by eqs **9.6a** and **9.9a**. The formation of $XeOF_4$ arises via eqs **9.7a** and **9.7b**. Co-crystallized HF and $XeOF_4$ are presumably introduced into the coordination spheres of $[XeF_5]^+$ and $[Cr_2O_2F_8]^{2-}$ upon crystallization (see compounds **4** and **5** in X-ray Crystallography).

9.2.2. X-ray Crystallography

Details of data collection and crystallographic information pertaining to $[XeF_5]_2[CrF_6]\cdot 2CrOF_4$ (**1**), $[Xe_2F_{11}]_2[CrF_6]$ (**2**), $[XeF_5]_2[Cr_2O_2F_8]$ (**3**),

$[XeF_5]_2[Cr_2O_2F_8]\cdot 2HF$ (**4**), $[XeF_5]_2[Cr_2O_2F_8]\cdot 2XeOF_4$ (**5**), and $[XeF_5][Xe_2F_{11}][CrOF_5]\cdot 2CrOF_4$ (**6**) are provided in Table 9.1.

The crystal structures contain $[XeF_5]^+$ and/or $[Xe_2F_{11}]^+$ cations which interact with their respective anions by means of Xe---F secondary bonds (Tables A6.2–A6.6). In cases here the cations interact with more than one anion (compounds **1**–**3**), the formula units form columns by ion-pair formation between neighboring cations and anions (Figures 9.1–9.3 and A6.2–A6.4). The columns run parallel to the *b*-axis (**1** and **2**) or to the *c*-axis (**3**) of their unit cells. The $[XeF_5]_2[Cr_2O_2F_8]$ ion pairs of **4** are bridged through HF molecules and form well-separated columns that run parallel to the *c*-axis (Figures 9.4 and A6.5). Additional Cr---F interactions occur between the $CrOF_4$ molecule and the fluorine atoms of their anions in $[XeF_5]_2[CrF_6]\cdot 2CrOF_4$ (**1**) and $[XeF_5][Xe_2F_{11}][CrOF_5]\cdot 2CrOF_4$ (**6**) (Figures 9.1 and 9.5, Tables A6.2 and A6.6). In contrast, $[XeF_5]_2[Cr_2O_2F_8]\cdot 2XeOF_4$ (**5**) and $[XeF_5][Xe_2F_{11}][CrOF_5]\cdot 2CrOF_4$ (**6**) do not form extended structures but consist of well-isolated units having no significant intermolecular interactions to one another (Figures 9.5, 9.6, A6.6, and A6.7).

Structural units that are in common for the crystal structures are compared in separate sections of the ensuing discussion.

9.2.2.1. $[XeF_5]^+$ and $[Xe_2F_{11}]^+$. The bond lengths, bond angles, and Xe---F contact distances of $[XeF_5]^+$ and $[Xe_2F_{11}]^+$ in all six salts (Tables A6.2−A6.6) are comparable to those observed in $[Xe_2F_{11}][AuF_6]$,[308] $[Xe_2F_{11}]_2[NiF_6]$,[118] $[XeF_5]_3[Ti_4F_{19}]$,[309] $[XeF_5][OsO_3F_3]$, $[Xe_2F_{11}][OsO_3F_3]$, and $[XeF_5][\mu\text{-}F(OsO_3F_2)_2]$.[121]

The $[XeF_5]^+$ cation geometry may be described in terms of an AX_5E VSEPR arrangement of five bond pairs (X) and a valence electron lone pair (E) around Xe (A) which result in its square-pyramidal geometry.[88] The Xe valence electron lone pair is

located in the open square face of the square pyramid, and displaces the equatorial fluorine atoms towards the axial fluorine atom due to repulsions between the axial electron lone pair and Xe−F_{eq} bond-pair domains. Consequently, the negatively charged fluorine ligands, which contact the positively charged Xe atom, avoid the Xe−F_{eq} bond pairs and valence electron lone pair of Xe in the manner previously noted and described for $[XeF_5][PtF_6]$.[310] The $[XeF_5]^+$ cations of compounds **1** and **3**–**6**

Table 9.1. Summary of X-ray crystal data and refinement results for $[XeF_5]_2[CrF_6]\cdot 2CrOF_4$ (**1**), $[Xe_2F_{11}]_2[CrF_6]$ (**2**), $[XeF_5]_2[Cr_2O_2F_8]$ (**3**), $[XeF_5]_2[Cr_2O_2F_8]\cdot 2HF$ (**4**), $[XeF_5]_2[Cr_2O_2F_8]\cdot 2XeOF_4$ (**5**), and $[XeF_5][Xe_2F_{11}][CrOF_5]\cdot 2CrOF_4$ (**6**)

	1	**2**	**3**	**4**	**5**	**6**
space group	$P\bar{1}$	$C2/c$	$C2/c$	$P2_1/c$	$P\bar{1}$	$Pbca$
a (Å)	5.3742(3)	21.866(1)	16.4840(7)	10.7873(7)	7.435(1)	17.3003(9)
b (Å)	9.3138(5)	5.5211(2)	9.1198(4)	9.1928(6)	8.750(1)	9.1104(5)
c (Å)	9.3642(5)	17.3538(8)	8.9772(4)	8.5616(5)	8.993(1)	27.7020(15)
α (deg)	106.091(3)	90	90	90	90.920(2)	90
β (deg)	98.974(3)	115.183(2)	93.122(2)	106.870(2)	108.392(2)	90
γ (deg)	95.973(3)	90	90	90	97.838(2)	90
V (Å^3)	439.45(4)	1895.9(1)	1347.6(1)	812.48(9)	548.9(1)	4366.2(4)
Z	1	4	4	4	1	8
M_W[a]	906.60	1109.20	740.60	410.32	1187.20	1148.90
ρ_{calcd}[b]	3.426	3.886	3.650	3.354	3.591	3.496
T (ºC)	–173	–173	–173	–173	–173	–173
μ [c]	5.853	7.887	6.777	5.672	7.285	6.294
R_1[d]	0.0398	0.0574	0.0229	0.0248	0.0304	0.0384
wR_2[e]	0.0996	0.1175	0.0515	0.0653	0.0753	0.0634

[a] g mol^{-1}. [b] g cm^{-3}. [c] (mm^{-1}). [d] $R_1 = \Sigma||F_o| - |F_c||/\Sigma|F_o|$. [e] $wR_2 = [\Sigma(w(F_o^2 - F_c^2)^2)/\Sigma(w(F_o^2)^2)]^{½}$.

interact with their respective anions through Xe---F secondary bonding interactions (Tables A6.2−A6.6) that are significantly less than the sum of the Xe and F van der Waals radii (3.61 Å,[167] 3.52 Å[168]). Each $[XeF_5]^+$ cation of structure **4** also interacts with the fluorine atom of a HF molecule through a Xe---$F_{(H)}$ contact (2.7985(9) Å) that is significantly less than those of $[XeF_5]_2[H_2F]\cdot HF$ (Xe---$F_{(H)}$, 3.006(5)–3.096(6) Å).[100] With the exception of $[Xe_2F_{11}][AuF_6]$,[308] which has a coordination number of 7, the common coordination numbers of Xe in $[XeF_5]^+$ and $[Xe_2F_{11}]^+$ salts are CN = 8: e.g., $[XeF_5]_2[PdF_6]$,[311] $[XeF_5][AsF_6]$,[312] $[XeF_5]_2[NiF_6]$,[313] and $[XeF_5][OsO_3F_3]$,[121] and

CN = 9: e.g., $[XeF_5][SbF_6]\cdot XeOF_4$,[314] $[XeF_5][PtF_6]$,[310] $[XeF_5][AgF_4]$,[117] $[XeF_5][\mu\text{-}F(OsO_3F_2)_2]$,[121] $[Xe_2F_{11}][OsO_3F_3]$,[121] and $[Xe_2F_{11}]_2[NiF_6]$.[118]

The Xe atom (CN = 8) of $[XeF_5]^+$ in $[XeF_5][Xe_2F_{11}][CrOF_5]\cdot 2CrOF_4$ (**6**) (Figure 9.4) has three Xe---F contacts with the axial and equatorial fluorine atoms of the $[CrOF_5]^{2-}$ anion (Xe(1)---F(3), 2.632(2) Å; Xe(1)---F(4), 2.624(2) Å; Xe(1)---F(1), 2.463(2) Å). The Xe atoms (CN = 9) of $[XeF_5]_2[CrF_6]\cdot 2CrOF_4$ (**1**) (Figure 9.1) each have two Xe---F contacts with two fluorine atoms of two $[CrF_6]^{2-}$ anions (Xe(1)---F(3A), 2.436(3) Å; Xe(1)---F(2), 2.447(3) Å) and with two fluorine atoms of two $CrOF_4$ molecules (Xe(1)---F(4), 3.084(3) Å; Xe(1)---F(5A), 3.044(3) Å). Each Xe atom (CN = 9) of $[XeF_5]_2[Cr_2O_2F_8]$ (**3**) (Figure 9.3) has two Xe---F contacts with one $[Cr_2O_2F_8]^{2-}$ anion (Xe(1)---F(4), 2.4272(8) Å; Xe(1)---F(2A), 3.0227(9) Å) and two Xe---F contacts with a second $[Cr_2O_2F_8]^{2-}$ anion (Xe(1)---F(2B), 2.6560(9) Å; Xe(1)---F(3B), 2.6573(9) Å). The Xe atoms are also nine-coordinate in $[XeF_5]_2[Cr_2O_2F_8]\cdot 2HF$ (**4**) and $[XeF_5]_2[Cr_2O_2F_8]\cdot 2XeOF_4$ (**5**), with each Xe atom having two shorter and one longer Xe---F contact with a single $[Cr_2O_2F_8]^{2-}$ anion (**4**: Xe(1)---F(2), 2.4581(8) Å; Xe(1)---F(4A), 2.4837(8) Å; Xe(1)---F(3), 3.0718(8) Å and **5**: Xe(1)---F(2A), 2.518(1) Å; Xe(1)---F(4), 2.475(1) Å; Xe(1)---F(3), 3.039(1) Å) and one longer Xe---F contact with the fluorine atom of an HF molecule (**4**: Xe(1)---F(11), 2.7985(9) Å) or an $XeOF_4$ molecule (**5**: Xe(1)---F(12), 3.262(1) Å).

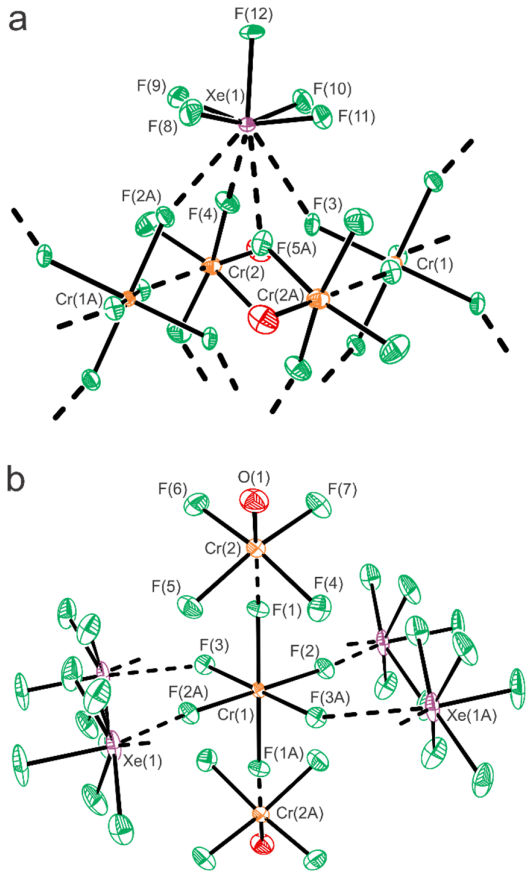

Figure 9.1. The X-ray crystal structure of $[XeF_5]_2[CrF_6]\cdot 2CrOF_4$ (**1**) with thermal ellipsoids drawn at the 50% probability level. The coordination spheres of (a) the $[XeF_5]^+$ cation and (b) the $[CrF_6]^{2-}$ anion are depicted. Secondary Xe---F and Cr---F bonding interactions are indicated by dashed lines.

The $[Xe_2F_{11}]^+$ cations are comprised of two $[XeF_5]^+$ cations that are asymmetrically fluorine-bridged by a fluoride ion. As in $[XeF_5]^+$, the F_{eq} atoms are displaced towards their respective F_{ax} atoms due to repulsions between the axial valence electron lone pair of Xe and their Xe–F_{eq} bond pairs. The Xe atoms (CN = 8) of $[Xe_2F_{11}]_2[CrF_6]$ (**2**) (Figure 9.2) have Xe---F contacts with one axial fluorine atom (Xe(1)---F(14B), 2.711(5) Å; (Xe(2)---F(14), 2.712(5) Å) and one equatorial fluorine atom (Xe(1)---F(12), 2.588(6) Å; Xe(2)---F(13), 2.583(6) Å) of two different $[CrF_6]^{2-}$

anions. The Xe atoms (CN = 8) of $[Xe_2F_{11}]^+$ in $[XeF_5][Xe_2F_{11}][CrOF_5]\cdot 2CrOF_4$ (**6**) have contacts with the axial fluorine ligand (Xe(2)---F(1), 2.822(2) Å; Xe(3)---F(1), 2.826(2) Å) and one equatorial fluorine ligand (Xe(2)---F(2), 2.575(2) Å; Xe(3)---F(5), 2.660(2) Å) of the same $[CrOF_5]^{2-}$ anion. Although the Xe---F cation-anion contact distances of compounds **2** and **6** are significantly shorter than the sum of the Xe and F van der Waals radii, they are longer than the Xe---F_b bridge bonds of $[Xe_2F_{11}]^+$ (**2**: Xe(1)–F(11), 2.262(6) Å; Xe(2)–F(11), 2.250(6) Å; **6**: Xe(2)–F(16), 2.333(2) Å; Xe(3)–F(16), 2.247(2) Å).

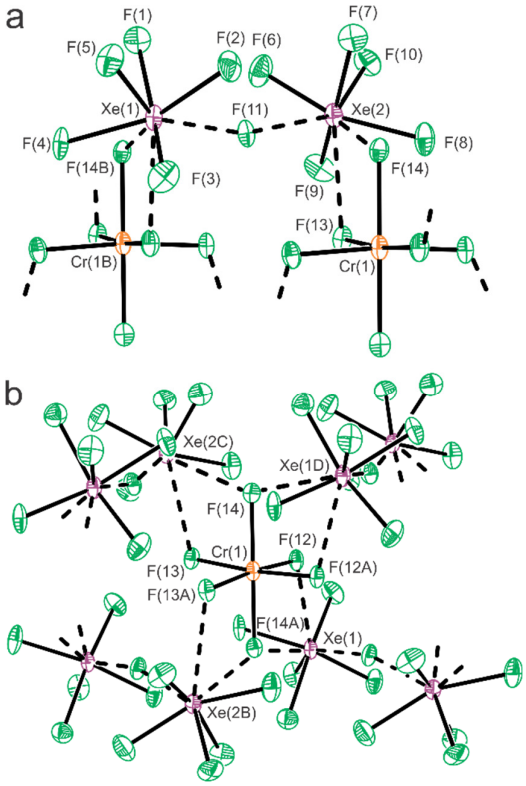

Figure 9.2. The X-ray crystal structure of $[Xe_2F_{11}]_2[CrF_6]$ (**2**) with thermal ellipsoids drawn at the 50% probability level. The coordination spheres of (a) the $[Xe_2F_{11}]^+$ cation and (b) the $[CrF_6]^{2-}$ anion are depicted. Secondary Xe---F bonding interactions are indicated by dashed lines.

9.2.2.2. $XeOF_4$. The bond lengths and bond angles around the Xe atom of $XeOF_4$ in **5** are comparable to those of $XeOF_4 \cdot XeF_2$.[68] As is the case of the isoelectronic $[XeF_5]^+$ cation (*vide supra*) and $XeOF_4 \cdot XeF_2$, the four Xe---F contacts with the Xe atom of $XeOF_4$ in $[XeF_5]_2[Cr_2O_2F_8] \cdot 2XeOF_4$ (**5**) (2.968(1) Å, 2.986(1) Å, 3.337(1) Å, 3.496(1) Å) occur in the open square face of the square-pyramidal $XeOF_4$ molecule and avoid the valence electron lone pair of Xe that is trans to the oxygen atom.

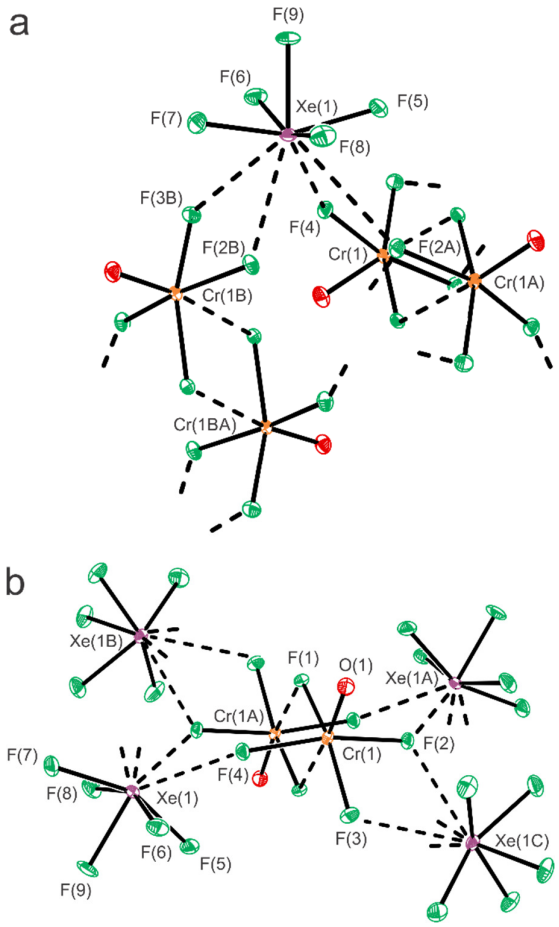

Figure 9.3. The X-ray crystal structure of $[XeF_5]_2[Cr_2O_2F_8]$ (**3**) with thermal ellipsoids drawn at the 50% probability level. The coordination spheres of (a) the $[XeF_5]^+$ cation and (b) the $[Cr_2O_2F_8]^{2-}$ anion are depicted. Secondary Xe---F bonding interactions are indicated by dashed lines.

9.2.2.3. $CrOF_4$. The geometric parameters of the co-crystallized $CrOF_4$ molecules in $[XeF_5]_2[CrF_6]\cdot 2CrOF_4$ (**1**) (Figure 9.1) and $[XeF_5][Xe_2F_{11}][CrOF_5]\cdot 2CrOF_4$ (**6**) (Figure 9.6) are very similar to those of α- and β-$CrOF_4$ and $XeF_2\cdot 2CrOF_4$.[65] The co-crystallized $CrOF_4$ molecules of both salts interact with a fluorine ligand of the anion through a Cr---F contact that is trans to the Cr–O bond. The $CrOF_4$ molecules of $[XeF_5][Xe_2F_{11}][CrOF_5]\cdot 2CrOF_4$ (**6**) interact with two adjacent equatorial fluorine ligands of the $[CrOF_5]^{2-}$ anion (Cr(2)---F(3), 2.393(2) Å; Cr(3)---F(4), 2.483(2) Å). The $CrOF_4$ molecules of $[XeF_5]_2[CrF_6]\cdot 2CrOF_4$ (**1**) are trans to one another, and interact with the axial fluorine ligands of $[CrF_6]^{2-}$ through Cr---F contacts (Cr(1)---F(1), 2.216(3) Å), and with neighboring $[XeF_5]^+$ cations through short Xe---F contacts (*vide supra*). The Cr---F contacts in **1** and **6** are comparable to those of α-$CrOF_4$ (2.274(3)–2.333(3) Å), β-$CrOF_4$ (2.3659(6) Å),[65] and $XeF_2\cdot 2CrOF_4$ (Cr(2)---F(1), 2.386(1) Å).[65] The Cr–O bonds of $[XeF_5]_2[CrF_6]\cdot 2CrOF_4$ (**1**) (1.571(4) Å) and $[XeF_5][Xe_2F_{11}][CrOF_5]\cdot 2CrOF_4$ (**6**) (1.547(3) Å, 1.530(3) Å) have significant double bond character and are comparable in length to those of α-$CrOF_4$ (1.539(3)–1.558(4) Å), β-$CrOF_4$ (1.5490(7) Å), and $XeF_2\cdot 2CrOF_4$ (1.545(2) Å).[65] The fluorine ligands of $CrOF_4$ are bent away from the sterically more demanding Cr–O double bond domains of this non-VSEPR molecule.[88]

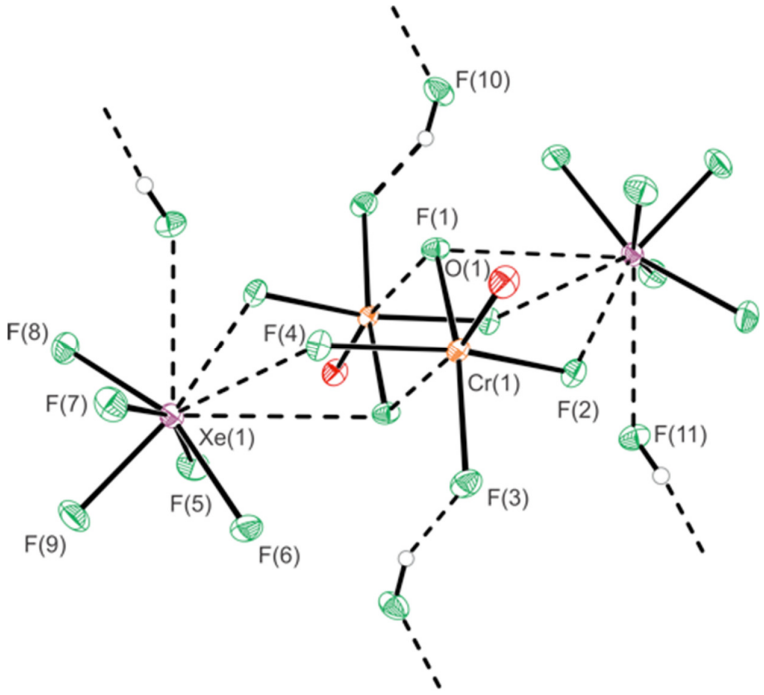

Figure 9.4. The X-ray crystal structure of $[XeF_5]_2[Cr_2O_2F_8]\cdot 2HF$ (**4**) with thermal ellipsoids drawn at the 50% probability level. Secondary Xe---F bonding interactions are indicated by dashed lines.

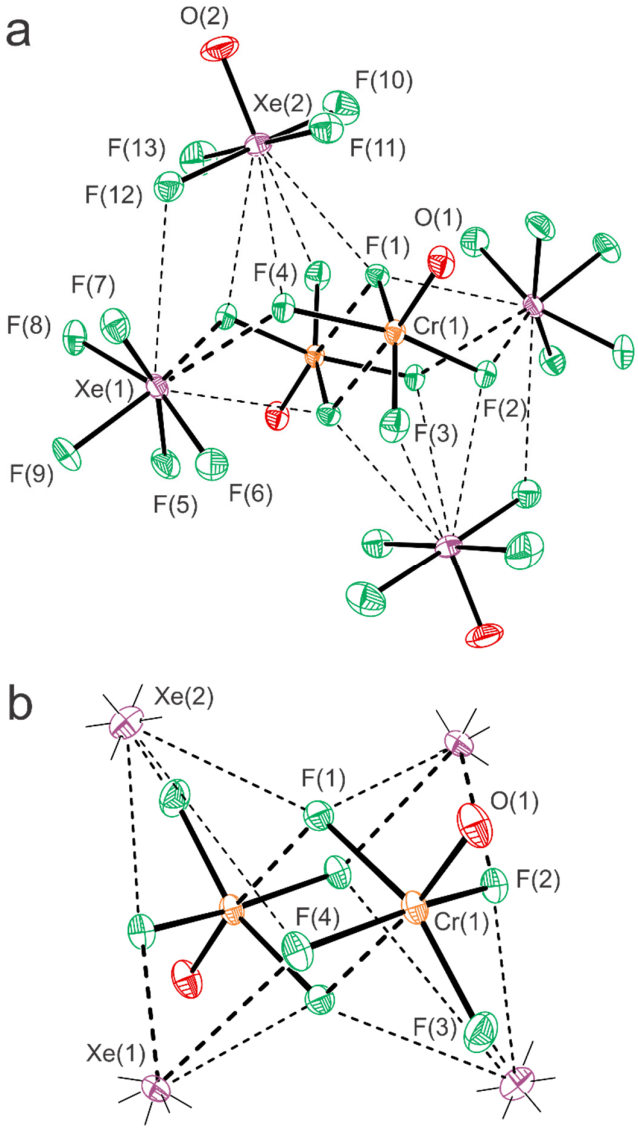

Figure 9.5. Depictions of (a) the X-ray crystal structure of $[XeF_5]_2[Cr_2O_2F_8]\cdot 2XeOF_4$ (**5**), and (b) the coordination environment around the $[Cr_2O_2F_8]^{2-}$ anion; thermal ellipsoids are drawn at the 50% probability level. Secondary Xe---F bonding interactions are indicated by dashed lines.

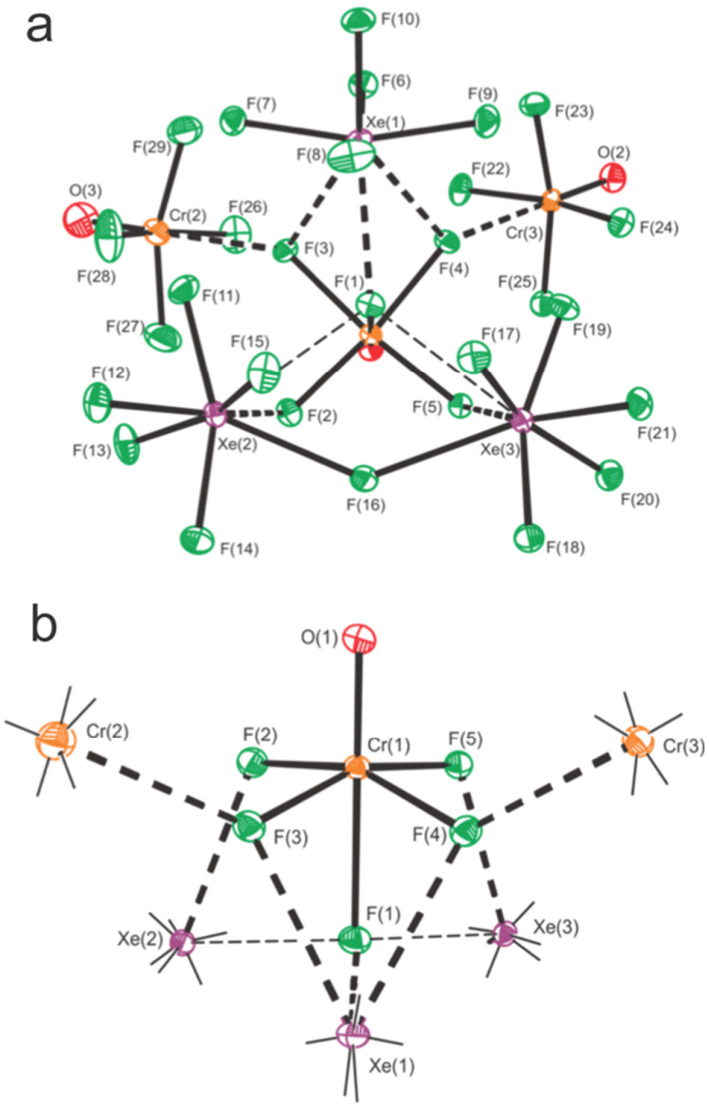

Figure 9.6. Depictions of (a) the asymmetric unit in the X-ray crystal structure of $[XeF_5][Xe_2F_{11}][CrOF_5]\cdot 2CrOF_4$ (**6**) and (b) the coordination environment around the $[CrOF_5]^{2-}$ anion; thermal ellipsoids are drawn at the 50% probability level. Secondary bonding interactions are indicated by dashed lines.

9.2.2.4. $[CrF_6]^{2-}$. The Cr–F bonds of the $[CrF_6]^{2-}$ anion in $[XeF_5]_2[CrF_6]\cdot 2CrOF_4$ (**1**) (Figure 9.1) are essentially equal resulting in a Cr coordination sphere that is close to octahedral (Table 9.2). This contrasts with the $[CrF_6]^{2-}$ anion of $[Xe_2F_{11}]_2[CrF_6]$ (**2**) (Figure 9.2) where two trans Cr−F_{ax} bonds (Cr(1)−F(14), 1.855(6) Å) are significantly longer than the four Cr−F_{eq} bonds (Cr(1)−F(12), 1.797(5) Å; Cr(1)−F(13) 1.798(5) Å), resulting in a local Cr environment that is close to D_{4h} symmetry (Table 9.3). The Cr−F_{eq} bond lengths of $[Xe_2F_{11}]_2[CrF_6]$ (**2**) are equal, within ±3σ, to those of $[XeF_5]_2[CrF_6]\cdot 2CrOF_4$ (**1**). The longer Cr−F_{ax} bonds of $[Xe_2F_{11}]_2[CrF_6]$ (**2**) are a consequence of short intermolecular contacts between the F_{ax} ligands and the Xe atoms of two different $[Xe_2F_{11}]^+$ cations (*vide supra*). The Cr−F_{eq} and Cr−F_{ax} bond lengths of the $[CrF_6]^{2-}$ anions in **2** are significantly shorter and longer, respectively, than those of $Li_2[CrF_6]$ (Cr−F_{eq}, 1.829(3) Å; Cr−F_{ax}, 1.812(4) Å),[315] and are intermediate with respect to the terminal and bridging Cr–F bonds of known Cr(IV) fluoride species in which the Cr atom is coordinated to six fluorine ligands, namely, $XeF_2\cdot CrF_4$ (Cr–F_t, 1.683(3)–1.750(2) Å; Cr–F_b, 1.839(2)–2.099(2) Å) and $[XeF_5][CrF_5]$ (Cr–F_t, 1.675(11)−1.825(10) Å; Cr–F_b, 1.900(9)− 1.971(10) Å).[307]

Table 9.2. Experimental geometric parameters for the $[CrF_6]^{2-}$ anion of $[XeF_5]_2[CrF_6]\cdot 2CrOF_4$ (**1**)

Bond Lengths (Å)			
Cr(1)−F(1)	1.812(3)	Cr(1)−F(3)	1.820(3)
Cr(1)−F(2)	1.816(3)		
Bond Angles (deg)			
F(1)−Cr(1)−F(2)	90.1(1)	F(2)−Cr(1)−F(3)	90.7(1)
F(1)−Cr(1)−F(3)	89.8(1)	F(2)−Cr(1)−F(2A)	180.0(1)
F(1)−Cr(1)−F(2A)	89.9(1)	F(2)−Cr(1)−F(3A)	89.3(1)
F(1)−Cr(1)−F(3A)	90.2(1)	F(3)−Cr(1)−F(3A)	180.0(2)
F(1)−Cr(1)−F(1A)	180.0(2)		

Table 9.3. Experimental geometric parameters for the $[CrF_6]^{2-}$ anion of $[Xe_2F_{11}]_2[CrF_6]$ (**2**).

Bond Lengths (Å)			
Cr(1)−F(12)	1.797(5)	Cr(1)−F(14)	1.855(6)
Cr(1)−F(13)	1.798(5)		
Bond Angles (deg)			
F(12)−Cr(1)−F(13)	89.89(2)	F(13)−Cr(1)−F(14)	87.1(3)
F(12)−Cr(1)−F(14)	92.93(3)	F(13)−Cr(1)−F(14A)	92.8(3)
F(12)−Cr(1)−F(12A)	90.2(4)	F(13)−Cr(1)−F(13A)	90.6(4)
F(12)−Cr(1)−F(13A)	174.3(3)	F(14)−Cr(1)−F(14A)	179.8(4)
F(12)−Cr(1)−F(14A)	87.2(3)		

9.2.2.4. $[Cr_2O_2F_8]^{2-}$. The $[Cr_2O_2F_8]^{2-}$ anion (Figures 9.3–9.5, Tables 9.4 and 9.5) can be described as two symmetry-equivalent $[CrOF_4]^-$ anions which share two fluorine bridge atoms, F(1) and F(1A). As expected, the Cr−F_b bridge bonds (2.1177(8) Å (**3**), 2.2237(8) Å (**4**), 2.265(1) Å (**5**)) are disposed trans to the O-ligand due to the *trans*-influence and are significantly longer than the equatorial Cr−F_{eq} bonds (1.7940(9)–1.8519(8) Å (**3**), 1,7940(8)–1.8739(7) Å (**4**), and 1.733(1)–1.904(1) Å (**5**)). The shortest Cr−F_{eq} bond in **5** (1.733(1) Å) corresponds to the only F_{eq} atom that has no Xe---F bonding interaction (Table A6.5) and has a bond length that is comparable to the Cr−F_{eq} bond lengths of α-$CrOF_4$ (1.707(2)–1.729(2) Å) and β-$CrOF_4$ (1.7212(6)–1.7372(6) Å).[65] The Cr−O bond lengths (1.567(1) Å (**3**), 1.5438(9) Å (**4**), 1.549(1) Å (**5**)) are characteristic of Cr–O double bonds, and are slightly longer than those of $CrOF_3$ (1.542(5) Å),[299] α-$CrOF_4$ (1.539(3)–1.558(4) Å), and β-$CrOF_4$ (1.5490(7) Å).[65] The four equatorial fluorine ligands of the coordinated $CrOF_4$ molecule are bent away from the Cr−O double bond domain, as indicated by their large O−Cr−F_{eq} angles (97.01(5)−102.56(5)° (**3**), 97.32(4)−103.20(5)° (**4**), 98.92(6)−105.63(7)° (**5**)). The F−Cr−F and F---Cr−F bond angles of the $[Cr_2O_2F_8]^{2-}$ anions in **3**–**5** are comparable.

9.2.2.5. $[CrOF_5]^{2-}$. The primary chromium coordination sphere of $[CrOF_5]^{2-}$ (Figure 9.6, Table 9.6) in $[XeF_5][Xe_2F_{11}][CrOF_5]\cdot 2CrOF_4$ (**6**) consists of four equatorial fluorine ligands and an axial fluorine ligand trans to the oxygen ligand. The Cr−F_{ax} bond (2.121(2) Å) is significantly longer than the Cr−F_{eq} bonds (1.814(2)−1.879(2) Å). The elongated bond is attributed to the *trans*-influence of oxygen and to three Xe---F_{ax} contacts (Xe(1)---F(1), 2.463(2) Å; Xe(2)---F(1), 2.822(2) Å; Xe(3)---F(1), 2.826(2) Å) with the xenon atoms of neighboring cations (*vide supra*).

Table 9.4. Experimental geometric parameters for $[XeF_5]_2[Cr_2O_2F_8]$ (**3**) and $[XeF_5]_2[Cr_2O_2F_8]\cdot 2HF$ (**4**)

	(3)	**(4)**		**(3)**	**(4)**
Bond Lengths and Contacts (Å)					
Cr(1)−O(1)	1.567(1)	1.5438(9)	Cr(1)−F(3)	1.7940(9)	1.7940(8)
Cr(1)−F(1)	1.8519(8)	1.8730(7)	Cr(1)−F(4)	1.8330(8)	1.8398(8)
Cr(1)−F(2)	1.8497(8)	1.8362(8)	Cr(1)---F(1A)	2.1177(8)	2.2237(8)
Bond Angles (deg)					
O(1)−Cr(1)−F(1)	98.27(5)	98.85(4)	O(1)−Cr(1)−F(4)	97.11(5)	97.32(4)
O(1)−Cr(1)−F(2)	97.01(5)	99.55(5)	O(1)−Cr(1)---F(1A)	171.34(5)	169.75(4)
O(1)−Cr(1)−F(3)	102.56(5)	103.20(5)	F(1)−Cr(1)−F(4)	90.33(4)	89.89(4)
F(1)−Cr(1)−F(2)	90.35(4)	86.03(4)	F(1)−Cr(1)---F(1A)	73.14(4)	72.03(3)
F(1)−Cr(1)−F(3)	159.07(4)	157.85(4)	F(2)−Cr(1)−F(4)	165.61(4)	163.06(4)
F(2)−Cr(1)−F(3)	85.17(4)	88.28(4)	F(2)−Cr(1)---F(1A)	84.38(4)	84.75(3)
F(3)−Cr(1)−F(4)	89.10(4)	89.37(4)	F(4)−Cr(1)---F(1A)	82.07(4)	78.35(3)
F(3)−Cr(1)---F(1A)	86.07(4)	86.15(3)	Cr(1)---F(1A)−Cr(1A)	106.83(4)	107.97(3)

Table 9.5. Experimental and calculated geometric parameters for $[XeF_5]_2[Cr_2O_2F_8]\cdot 2XeOF_4$ (**5**) and $[Cr_2O_2F_8]^{2-}$ (**5'**)

	exptl	calcd[a]			exptl	calcd[a]	
Bond Lengths and Contacts (Å)							
	(5)	**(5)**	**(5')**		**(5)**	**(5)**	**(5')**
Cr(1)−O(1)	1.549(1)	1.493	1.526	Cr(1)−F(3)	1.733(1)	1.725	1.779
Cr(1)−F(1)	1.904(1)	1.839	1.827	Cr(1)−F(4)	1.840(1)	1.833	1.771
Cr(1)−F(2)	1.854(1)	1.851	1.771	Cr(1)---F(1A)	2.265(1)	2.354	2.373
Bond Angles (deg)							
O(1)−Cr(1)−F(1)	100.92(6)	105.53	100.79	O(1)−Cr(1)−F(4)	99.17(6)	100.70	102.63
O(1)−Cr(1)−F(2)	98.92(6)	101.43	100.95	O(1)−Cr(1)---F(1A)	172.40(6)	176.56	172.19
O(1)−Cr(1)−F(3)	105.63(7)	106.71	102.63	F(1)−Cr(1)−F(4)	87.20(5)	86.74	88.50
F(1)−Cr(1)−F(2)	84.17(4)	84.44	88.53	F(1)−Cr(1)---F(1A)	71.63(5)	71.06	71.40
F(1)−Cr(1)−F(3)	153.22(5)	147.64	156.58	F(2)−Cr(1)−F(4)	161.13(4)	157.66	158.07
F(2)−Cr(1)−F(3)	88.24(5)	86.58	87.05	F(2)−Cr(1)---F(1A)	82.05(4)	78.79	79.24
F(3)−Cr(1)−F(4)	92.01(5)	90.01	87.05	F(4)−Cr(1)---F(1A)	79.31(4)	78.93	79.24
F(3)−Cr(1)---F(1A)	81.91(5)	76.72	85.18	Cr(1)---F(1)−Cr(1A)	108.37(5)	108.94	108.60

[a] The uPBE1PBE/aug-cc-pVDZ (Xe)-Def2-SVP (F, O, Cr) level of theory was used.

Table 9.6. Experimental and Calculated Geometric Parameters of $[XeF_5][Xe_2F_{11}][CrOF_5]\cdot 2CrOF_4$ (**6**) and $[CrOF_5]^{2-}$ (**6'**)

	exptl	calcd[a]			exptl	calcd[a]	
			Bond Lengths and Contacts (Å)				
	(6)	**(6)**	**(6')**		**(6)**	**(6)**	**(6')**
Cr1−O1	1.546(2)	1.491	1.559	Cr1−F3	1.879(2)	1.836	1.844
Cr1−F1	2.121(2)	2.233	1.887	Cr1−F4	1.872(2)	1.825	1.844
Cr1−F2	1.823(2)	1.807	1.844	Cr1−F5	1.814(2)	1.814	1.844
			Bond Angles (deg)				
O1−Cr1−F1	176.93(11)	178.12	180.0	F1−Cr1−F5	81.62(8)	79.98	85.79
O1−Cr1−F2	100.59(11)	102.51	94.21	F2−Cr1−F3	90.16(8)	88.86	89.69
O1−Cr1−F3	99.21(10)	102.27	94.21	F2−Cr1−F4	160.40(8)	153.37	171.58
O1−Cr1−F4	98.65(11)	103.98	94.21	F2−Cr1−F5	90.98(9)	88.59	89.69
O1−Cr1−F5	100.57(11)	101.89	94.21	F3−Cr1−F4	83.14(8)	83.00	89.69
F1−Cr1−F2	81.45(8)	77.64	85.79	F3−Cr1−F5	159.62(8)	155.69	171.58
F1−Cr1−F3	78.43(8)	75.85	85.79	F4−Cr1−F5	89.09(9)	88.57	89.69
F1−Cr1−F4	79.17(8)	75.79	85.79				

[a] The uPBE1PBE/aug-cc-pVDZ (Xe)-Def2-SVP (F, O, Cr) level of theory was used.

The equatorial fluorine ligands of $[CrOF_5]^{2-}$ interact with $[XeF_5]^+$, $[Xe_2F_{11}]^+$, and $CrOF_4$ through a number of Xe---F_{eq} and Cr---F_{eq} contacts. These secondary bonding interactions account for the large Cr−F_{eq} bond length range (1.814(2)– 1.879(2) Å) observed for $[CrOF_5]^{2-}$, where shorter distances correspond to a single contact with the $[Xe_2F_{11}]^+$ cation and longer distances correspond to contacts with the $[XeF_5]^+$ and $[Xe_2F_{11}]^+$ cations and two Cr---F_{eq} contacts with the co-crystallized $CrOF_4$ molecules. The Cr−O bond length of $[CrOF_5]^{2-}$ (1.546(2) Å) is comparable to those of $CrOF_3$ (1.542(5) Å),[299] α-$CrOF_4$ (1.539(3)–1.558(4) Å), and β-$CrOF_4$ (1.5490(7) Å).[65]

9.2.3. Raman Spectroscopy

The low-temperature Raman spectra of $[XeF_5]_2[Cr_2O_2F_8]\cdot 2XeOF_4$ (**5**) and $[XeF_5]Xe_2F_{11}][CrOF_5]\cdot 2CrOF_4$ (**6**) are shown in Figures 9.7a and 9.7b, respectively. The Raman spectra were recorded on crystalline samples of **5** and **6** which were subsequently characterized by single-crystal X-ray structure determinations (see X-ray Crystallography). Spectral assignments were made by comparison with the calculated

vibrational frequencies and intensities of the energy-minimized, gas-phase geometries of $[XeF_5]_2[Cr_2O_2F_8]\cdot 2XeOF_4$ (**5**) and $[XeF_5][Xe_2F_{11}][CrOF_5]\cdot 2CrOF_4$ (**6**) at the uPBE1PBE/aug-cc-pVDZ-Def2SVP level of theory. Vibrational assignments for $CrOF_4$, $XeOF_4$, and the $[XeF_5]^+$ and $[Xe_2F_{11}]^+$ cations were also aided by comparison with polymeric $CrOF_4$,[65] $XeOF_4\cdot XeF_2$,[68] $[XeF_5][OsO_3F_3]$,[121] $[XeF_5][AsF_6]$,[316] $[XeF_5][BF_4]$,[316] $[Xe_2F_{11}][AuF_6]$,[308] $[Xe_2F_{11}][PdF_6]$,[308] and $[Xe_2F_{11}][OsO_3F_3]$.[121] The observed and calculated frequencies, their detailed assignments, and mode descriptions are provided in Tables A6.7 and A6.8. Except for the overestimated ν(Cr-O) and underestimated ν(Xe-O) stretching frequencies, the experimental vibrational frequencies and their trends are well reproduced by the calculated frequencies.

A Raman spectrum (Figure A6.8) was also recorded on a crystalline sample obtained by reaction of four equivalents of XeF_6 with one equivalent of **6**. Unit cell parameters showed the sample contained primarily compound **2**; however, the occurrence of a weak, broad band at 1002 cm^{-1} in the Raman spectrum suggested the sample was not entirely homogeneous. This band was assigned to a small amount of unreacted **6**.

9.2.3.1. $[XeF_5]_2[Cr_2O_2F_8]\cdot 2XeOF_4$ (5). Several bands exhibit splittings in the Raman spectrum of $[XeF_5]_2[Cr_2O_2F_8]\cdot 2XeOF_4$ (Table A6.7). Consequently, a factor-group analysis based on the X-ray crystal structure of **5** (Figure A6.9) was carried out using the "correlation method"[169] to determine if these splittings arise from vibrational coupling within the crystallographic unit cell. A total of 102 vibrational modes are predicted for gas-phase $[XeF_5]_2[Cr_2O_2F_8]\cdot 2XeOF_4$ under C_i symmetry. The vibrations belong to the irreducible representations $\Gamma = 51A_g + 51A_u$, where the A_g and A_u modes are Raman- and infrared-active, respectively. The A_g and A_u representations of

gas-phase vibrational modes of **5** correlate to A irreducible representations under C_1 site symmetry in the solid state and to A representations under the C_1 unit cell symmetry. Therefore, all 102 modes are predicted to be both Raman and infrared active (Figure A6.9) under the unit cell symmetry. Consequently, any band splittings that occur in the solid-state Raman spectrum do not arise from vibrational coupling within the unit cell but are due to intramolecular vibrational coupling.

The band observed at 1026 cm^{-1} is assigned to the symmetric stretch, [$\nu(Cr_1\text{-}O_1) + \nu(Cr_{1A}\text{-}O_{1A})$] of the $[Cr_2O_2F_8]^{2-}$ anion, and occurs at higher frequency than in $Cr^{V}OF_3$ (Ra) (1000 cm^{-1})[301] and $Cs[Cr^{V}OF_4]$ (IR) (1005 cm^{-1}).[300] The calculated ν(Cr-O) stretching frequency increases upon ion-pair formation (anion: 1148 cm^{-1}; ion pair: 1209 cm^{-1}). The asymmetric stretch, [$\nu(Cr_1\text{-}O_1) - \nu(Cr_{1A}\text{-}O_{1A})$], is Raman inactive under C_i symmetry and was not observed. The diversity of Cr–F and Cr---F bond lengths results in ν(Cr-F) stretching modes that range from 398 to 700 cm^{-1} (calcd: 369–731 cm^{-1}) (Table A6.7). The band at 398 cm^{-1} involves the bridging F atoms and corresponds to [$\nu(Cr_1\text{-}F_1) + \nu(Cr_1\text{-}F_{1A})$] + [$\nu(Cr_{1A}\text{-}F_1) + \nu(Cr_{1A}\text{-}F_{1A})$]; however, the out-of-phase counterpart, [$\nu(Cr_1\text{-}F_1) + \nu(Cr_1\text{-}F_{1A})$] – [$\nu(Cr_{1A}\text{-}F_1) + \nu(Cr_{1A}\text{-}F_{1A})$], which is predicted to be weak and to occur at much lower frequency (231 cm^{-1}), was not observed. The bands at 370 and 375 cm^{-1} are assigned to δ(FCrO) deformation modes (calcd: 358, 359, 365 cm^{-1}) by comparison with analogous modes in α- and β-$CrOF_4$.[65]

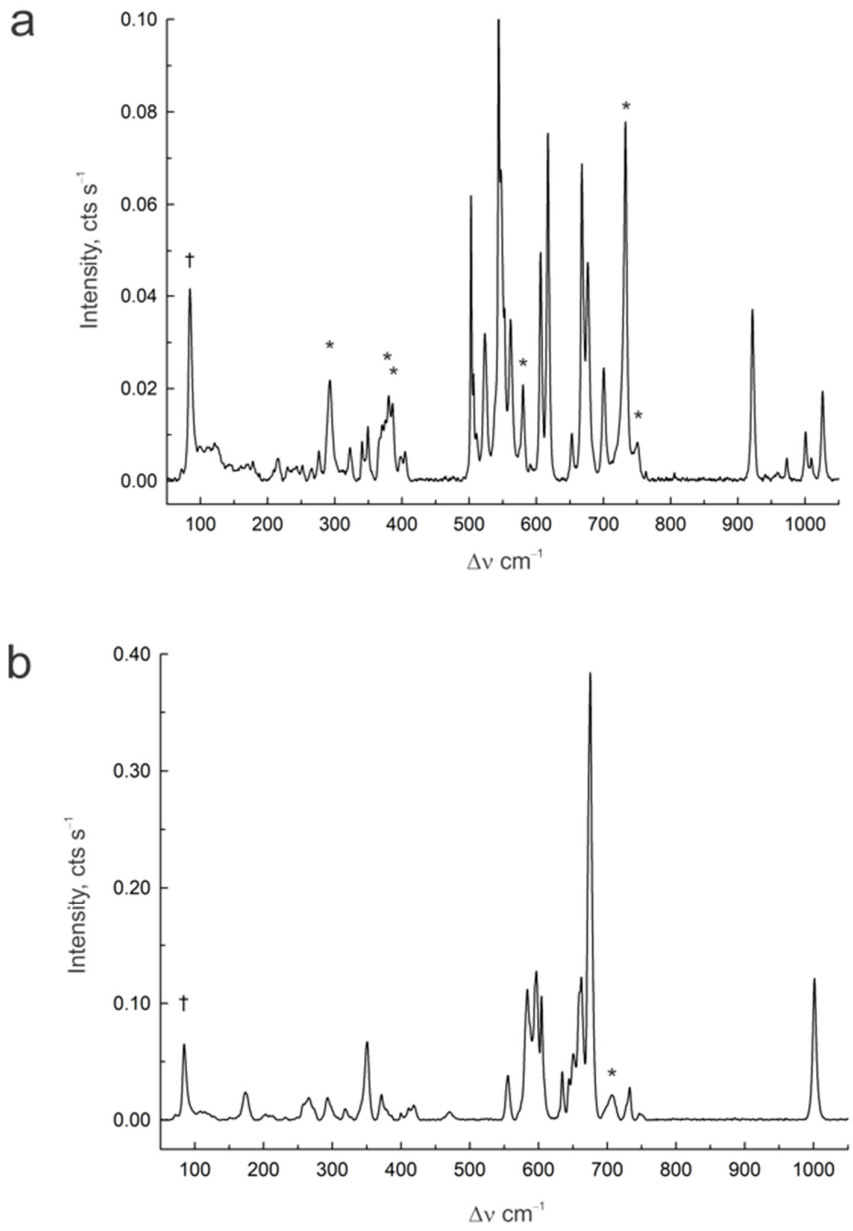

Figure 9.7. Raman spectra of (a) $[XeF_5]_2[Cr_2O_2F_8]\cdot 2XeOF_4$ (**5**) and (b) $[XeF_5][Xe_2F_{11}][CrOF_5]\cdot 2CrOF_4$ (**6**) recorded at −140 °C using 1064-nm excitation. The symbol (†) denotes an instrumental artifact. Asterisks (*) denote FEP sample tube bands.

9.2.3.2. $[XeF_5][Xe_2F_{11}][CrOF_5]\cdot 2CrOF_4$ (6). Unlike compound (**5**), band splittings were not observed in the Raman spectrum. The medium-intensity band at 1000 cm^{-1} (Table A6.8) is assigned to overlapping Cr-O stretches of $CrOF_4$ (calcd: 1230, 1232 cm^{-1}) and $[CrOF_5]^{2-}$ (calcd: 1192 cm^{-1}), which is consistent with the very similar Cr−O bond lengths of $CrOF_4$ (1.526(3), 1.545(3) Å) and $[CrOF_5]^{2-}$ (1.545(3) Å) in the crystal structure of **6**. The calculated ν(Cr-O) stretching frequency of $[CrOF_5]^{2-}$ increases significantly upon ion-pair formation (free anion: 1009 cm^{-1}; ion-pair: 1192 cm^{-1}). The bands between 700 and 750 cm^{-1} (calcd: 722−762 cm^{-1}) are assigned to the Cr-F stretching modes of the coordinated $CrOF_4$ molecules and do not couple with the cation or anion modes. The Cr-F_{eq} stretching modes of $[CrOF_5]^{2-}$ occur at lower frequencies, which are consistent with the longer Cr−F_{eq} bonds of the anion (1.813(2)–1.875(2) Å) than in the coordinated $CrOF_4$ molecules (1.734(2)–1.745(2) Å) of **6**. The latter stretching modes are coupled to the Xe-F stretching modes of the cations. The bands at 555–608 cm^{-1} (calcd: 562−602 cm^{-1}) arise from the Cr-F stretches of $[CrOF_5]^{2-}$ and $CrOF_4$, which are coupled to the Xe-F stretches of both $[XeF_5]^+$ and $[Xe_2F_{11}]^+$. The band at 470 cm^{-1} (calcd: 469 cm^{-1}) results from coupling of the Cr-F_e stretches of $[CrOF_5]^{2-}$ to the Xe-F_e stretches of $[Xe_2F_{11}]^+$. The bands at 372–419 cm^{-1} are mainly assigned to δ(FCrO) and δ(FCrF) deformation modes (calcd: 357−413 cm^{-1}) arising from both $[CrOF_5]^{2-}$ and $CrOF_4$. The umbrella modes, $\delta_{umb}(CrF_{4e})$, of $CrOF_4$ occur at lower frequencies (exptl: 343, 351 cm^{-1}; calcd: 344−354 cm^{-1}) and are coupled to the δ(FXeF) deformation modes of $[XeF_5]^+$ and $[Xe_2F_{11}]^+$.

9.2.4. COMPUTATIONAL RESULTS

9.2.4.1. Calculated Geometries

The optimized gas-phase structures of $CrOF_4$ and $[CrOF_5]^-$ were optimized at the PBE1PBE/aug-cc-pVDZ (Xe)-Def2-SVP (F, O, Cr) level of theory and resulted in stationary points with all frequencies real (Tables A6.7–A6.10). The calculated frequencies of the $[CrOF_5]^-$ anion (Table A6.1, footnote g) are consistent with the observed values provided in the *Syntheses* section of the Results and Discussion and in Table A6.1.

The geometries of $[XeF_5]_2[Cr_2O_2F_8]\cdot 2XeOF_4$ (**5**), $[XeF_5][Xe_2F_{11}][CrOF_5]\cdot 2CrOF_4$ (**6**), $[Cr_2O_2F_8]^{2-}$ (**5'**), and $[CrOF_5]^{2-}$ (**6'**) were fully optimized, with no imaginary frequencies, by employing a broken symmetry approach (uPBE1PBE/def2-TZVP), which used different orbitals for α- and β-spin electrons. In the case of the gas-phase $[Cr_2O_2F_8]^{2-}$ anion, the Cr···Cr distance was fixed to that calculated for $[XeF_5]_2[Cr_2O_2F_8]\cdot 2XeOF_4$ (3.43 Å) to find a minimum. In the absence of this constraint, the $[CrOF_4]^-$ anions separated at this level of theory. The geometries of the triplet-state adducts and corresponding anions optimized, and a stability analysis showed that the final unrestricted wavefunctions were stable. The starting geometries used for $[XeF_5]_2[Cr_2O_2F_8]\cdot 2XeOF_4$, $[Cr_2O_2F_8]^{2-}$, $[XeF_5][Xe_2F_{11}]$-$[CrOF_5]\cdot 2CrOF_4$, and $[CrOF_5]^{2-}$ were the crystallographic geometries obtained from their respective $[XeF_5]^+$ salts. All trends observed in the crystal structures are reproduced by the calculated geometries of **5** and **6**, including the secondary bond lengths and their associated contact angles. The greatest discrepancies occur for the Cr−O and Cr−F bond lengths, which are underestimated, and for the Xe−F bond lengths, which are overestimated.

***9.2.4.1.1. $[XeF_5]_2[Cr_2O_2F_8]\cdot 2XeOF_4$ and $[Cr_2O_2F_8]^{2-}$* (5').** The $[Cr_2O_2F_8]^{2-}$ anion optimized to C_i symmetry (Figure 9.8). The Cr−F_t bond that is trans to the Cr-F_b bridge bond is slightly shorter (1.771 Å) than the Cr−F_t bonds (1.779 Å) that are cis to the Cr–F_b bridge bond (1.827 Å). As expected, the Cr−F_t bonds are significantly shorter than the Cr---F_b contact distances (2.373 Å). Upon salt formation, the Cr−F_b and Cr---F_b bonds of $[XeF_5]_2[Cr_2O_2F_8]\cdot 2XeOF_4$ (1.839 and 2.354 Å) change very little (Figure 9.8). Three of the terminal Cr−F_t bonds are elongated due to Xe---F contacts with $XeOF_4$ and $[XeF_5]^+$, whereas the Cr−F_t bond, with no significant contacts, and the Cr–O bond are significantly shorter (1.725 and 1.493 Å, respectively) than in the isolated anion (1.779 and 1.526 Å). Bond length contractions are only observed for bonds where the fluorine/oxygen atoms do not have significant secondary bonding interactions. The contractions are induced by increased polarization of the Cr–F_t and Cr−O bonds when they are trans to terminal fluorine ligands that have short contacts with neighboring Xe or Cr atoms.

***9.2.4.1.2. $[XeF_5][Xe_2F_{11}][CrOF_5]\cdot 2CrOF_4$ and $[CrOF_5]^{2-}$* (6').** The $[CrOF_5]^{2-}$ anion optimized to C_{4v} symmetry, with the Cr−F_{ax} bond being significantly longer (1.887 Å) than the Cr−F_{eq} bonds (1.844 Å) (Figure 9.9). The Cr−O bond (1.559 Å) is also longer than that of the calculated $[Cr_2O_2F_8]^{2-}$ anion (1.526 Å). Unlike $[Cr_2O_2F_8]^{2-}$, the $[CrOF_5]^{2-}$ anion of $[XeF_5][Xe_2F_{11}][CrOF_5]\cdot 2CrOF_4$ is severely distorted in the gas-phase ion-pair (Figure 9.9), with the Cr−F_{ax} bond (2.233 Å) being significantly elongated in comparison with the free $[CrOF_5]^{2-}$ anion (1.887 Å). The elongation results from interactions between F_{ax} and Xe_1 (2.351 Å), Xe_2 (2.752 Å), and Xe_3 (3.047 Å), and is also accompanied by shortening of the Cr−F_{eq} bonds (1.807−1.836 Å), increases in the O−Cr−F_{eq} angles (101.9−102.5° relative to 94.5° in **6'**), and

decreases in the F_{ax}–Cr–F_{eq} angles (75.8–80.0° relative to 85.8° in **6'**). As observed for gas-phase $[Cr_2O_2F_8]^{2-}$ and $[XeF_5]_2[Cr_2O_2F_8]\cdot 2XeOF_4$, the Cr–O bond of gas-phase $[CrOF_5]^{2-}$ (1.491 Å) in $[XeF_5][Xe_2F_{11}][CrOF_5]\cdot 2CrOF_4$ is significantly shorter than in the free $[CrOF_5]^{2-}$ anion (1.559 Å).

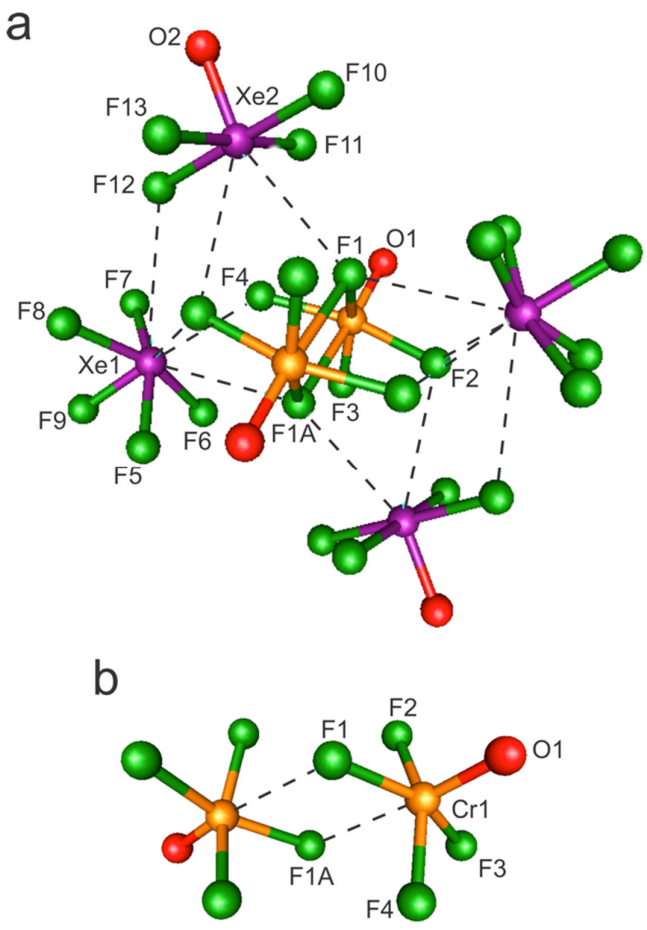

Figure 9.8. Calculated geometries of (a) $[XeF_5]_2[Cr_2O_2F_8]\cdot 2XeOF_4$ and (b) $[Cr_2O_2F_8]^{2-}$. The uPBE1PBE/aug-ccpVDZ (Xe)-Def2-SVP (F, O, Cr) level of theory was used.

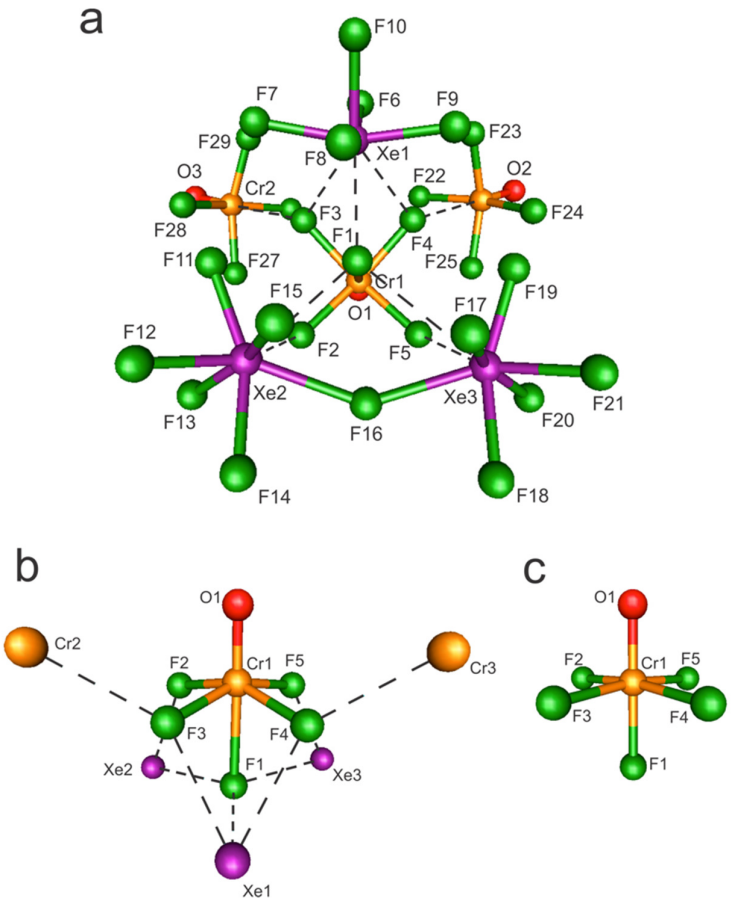

Figure 9.9. Calculated geometries of (a) $[XeF_5][Xe_2F_{11}][CrOF_5]\cdot 2CrOF_4$, (b) the coordination environment around $[CrOF_5]^{2-}$, and (c) $[CrOF_5]^{2-}$. The uPBE1PBE/aug-ccpVDZ (Xe)-Def2-SVP (F, O, Cr) level of theory was used.

9.3. Conclusions

The reactions of XeF_6 with $CrOF_4$ in melts and in the oxidatively resistant solvents, aHF and $CFCl_3$, resulted in the formation of $[XeF_5]_2[CrF_6]\cdot 2CrOF_4$(**1**), $[Xe_2F_{11}]_2[CrF_6]$ (**2**), $[XeF_5]_2[Cr_2O_2F_8]$ (**3**), $[XeF_5]_2[Cr_2O_2F_8]\cdot 2HF$ (**4**), $[XeF_5]_2[Cr_2O_2F_8]\cdot 2XeOF_4$ (**5**), and $[XeF_5][Xe_2F_{11}][CrOF_5]\cdot 2CrOF_4$ (**6**), which were characterized by LT single-crystal X-ray diffraction. Reduction of Cr(VI) to Cr(V)

and Cr(VI) is accompanied by F_2 elimination, a common feature of this chemistry. The reaction of XeF_6 with $CrOF_4$ to give $[XeF_5][Xe_2F_{11}][CrOF_5]\cdot 2CrOF_4$ was shown by LT Raman spectroscopy to proceed through the intermediate Cr(VI) salt, $[Xe_2F_{11}][CrOF_5]$. The syntheses of the salts provide the first X-ray crystal structures of the previously known $[CrOF_5]^{2-}$ and the novel $[Cr_2O_2F_8]^{2-}$ anions. The $[XeF_5]^+$ and $[Xe_2F_{11}]^+$ cations of $[XeF_5]_2[CrF_6]\cdot 2CrOF_4$, $[Xe_2F_{11}]_2[CrF_6]$, and $[XeF_5]_2[Cr_2O_2F_8]$ interact with their anions and $CrOF_4$ through Xe---F and Cr---F secondary bonding interactions to give well-separated chains in their crystal structures, whereas the solid-state structures of $[XeF_5][Xe_2F_{11}][CrOF_5]\cdot 2CrOF_4$ and $[XeF_5]_2[Cr_2O_2F_8]\cdot 2XeOF_4$ are comprised of well-isolated formula units that have no significant intermolecular interactions. The $[Cr_2O_2F_8]^{2-}$ anion has C_i symmetry and consists of two symmetry-equivalent $[CrOF_4]^-$ anions that interact through two asymmetric Cr---F_b–Cr bridges. The $[XeF_5]_2[Cr_2O_2F_8]\cdot 2XeOF_4$ and $[XeF_5][Xe_2F_{11}][CrOF_5]\cdot 2CrOF_4$ salts were also characterized by low-temperature Raman spectroscopy. Quantum-chemical calculations were carried out for $[XeF_5]_2[Cr_2O_2F_8]\cdot 2XeOF_4$, $[Cr_2O_2F_8]^{2-}$, $[XeF_5][Xe_2F_{11}][CrOF_5]\cdot\ 2CrOF_4$, and $[CrOF_5]^{2-}$ in order to obtain their gas-phase optimized geometries, and to aid in their vibrational frequency assignments. Other than the $[OsO_3F_3]^-$ and $[\mu\text{-}F(OsO_3F_2)]^-$ anions, the $[CrOF_5]^-$, $[CrOF_5]^{2-}$, and $[Cr_2O_2F_8]^{2-}$ anions are the only other high-oxidation-state transition-metal oxide fluoride anions that are known to form stable salts with noble-gas cations.

CHAPTER 10

Syntheses and Structural Characterizations of $[Cr_2O_4F_6]^{2-}$ and $[CrO_2F_4]^{2-}$ Salts

10.1. Introduction.

Until recently, the $[N(CH_3)_4]^+$,[267] K^+, Rb^+, and Cs^+ salts of $[CrO_3F]^-$,[265] prepared by reaction of CrO_3 with MF (M = $[N(CH_3)_4]^+$, K^+, Rb^+, Cs^+), provided the only crystallographically characterized examples of a Cr(VI) oxide fluoride anion. Furthermore, although salts of $[MO_3F_2]^{2-}$ (M = Mo, W) are known,[317,318] the Cr analogue is unknown. In Chapters 9 and 11, the syntheses of high-oxidation-state Cr(VI) and Cr(V) oxide fluorides exploited the fluorobasicity of XeF_6 and the oxidative resistance of the $[XeF_5]^+$ and $[Xe_2F_{11}]^+$ cations to prepare the first examples of stable $[Cr^{VI}OF_5]^-$, $[Cr^{V}OF_5]^{2-}$, and $[Cr^{V}_2O_2F_8]^{2-}$ salts to be characterized by SCXRD, namely; $[Xe_2F_{11}][Cr^{VI}OF_5]$,[243] $[XeF_5]_2[Cr^{V}_2O_2F_8]$, $[XeF_5]_2[Cr^{V}_2O_2F_8]\cdot 2HF$, $[XeF_5]_2[Cr^{V}_2O_2F_8]\cdot 2XeOF_4$, and $[XeF_5][Xe_2F_{11}][Cr^{V}OF_5]\cdot 2CrOF_4$.[244] The salts were prepared by the reaction of XeF_6 with $CrOF_4$ in melts and in the oxidatively resistant solvents aHF, $CFCl_3$, and Freon-114 under rigorously anhydrous reaction conditions.[244] Like $[MO_3F_2]^{2-}$, salts of $[MOF_6]^{2-}$ (M = Mo, W) have been reported but $[CrOF_6]^{2-}$ is unknown.

No crystal structures have been reported which contain Cr(VI) oxyfluoro-anions derived from CrO_2F_2, namely the $[CrO_2F_3]^-$ and $[CrO_2F_4]^{2-}$ anions. This contrasts with Mo and W, where salts of $[M_2O_4F_6]^{2-}$ [286,319,320] and $[MO_2F_4]^{2-}$ [321–324] have been characterized by SCXRD. The $[M_2O_4F_6]^{2-}$ dianions are dimers of the $[MO_2F_3]^-$ anions which have *cis*-dioxo arrangements and fluorine-bridged structures.[286,319,320] The fluoride-ion donor-acceptor properties of chromyl fluoride (CrO_2F_2)

were studied by Gard *et al.* in 1975 and 1978. The products of the reactions of CrO_2F_2 with the fluoride-ion donors M′F (M′ = $[NO]^+$,[268] $[NO_2]^+$,[268] Li^+, Na^+, K^+, and Cs^+)[269] and M″F_2 (M″ = Mg^{2+}, Ca^{2+});[269] the Lewis acids SO_3, TaF_5, SbF_5, and $(CF_3CO)_2O$, as well as the salts $NaOOCCF_3$ and $NaNO_3$ were characterized by vibrational spectroscopy,[268,269] powder X-ray diffraction,[269] magnetic susceptibility measurements,[269] and chemical analysis.[268,269] Although these studies resulted in the RT characterizations of $[NO][CrO_2F_3]$,[268] $[NO_2][CrO_2F_3]$,[268] M′$_2[CrO_2F_4]$, M″$[CrO_2F_4]$, $CrO_2(CF_3COO)_2$, $CrO_2(SO_3F)_2$, $[CrO_2F][TaF_6]$, $[CrO_2F][SbF_6]$, $[CrO_2F][Sb_2F_{11}]$, $Na_2[CrO_2F_2(CF_3COO)_2]$, and $Na_2[CrO_2F_2(NO_3)_2]$;[269] no detailed structural studies, including SCXRD structure determinations, have been forthcoming for these compounds.

The SCXRD characterizations of $[Cr_2O_4F_6]^{2-}$ and $[CrO_2F_4]^{2-}$ salts alone would provide a significant extension of the very limited chemistry of Cr(VI) oxyfluorides, complete the series of structurally characterized $[M_2O_4F_6]^{2-}$ and $[MO_2F_4]^{2-}$ (M = Cr, Mo, W) anions, and the series of known Cr(VI) oxyfluoro-anions; $[CrO_3F]^-$, $[CrOF_5]^-$, $[Cr_2O_4F_6]^{2-}$ ($[CrO_2F_3]^-$ dimer), and $[CrO_2F_4]^{2-}$. This provided impetus to investigate the reaction of CrO_2F_2 with the fluoride-ion donor, XeF_6, with the aim to synthesize and structurally characterize $[XeF_5]^+$ and/or $[Xe_2F_{11}]^+$ salts of the $[CrO_2F_3]^-$ and $[CrO_2F_4]^{2-}$ anions by LT Raman spectroscopy, LT SCXRD, and QC calculations.

10.2. Results and Discussion

10.2.1. Syntheses

Reaction product distributions were monitored by recording the LT Raman spectra of precipitated solids under frozen aHF solvent or dry solids obtained from reactions in melts.

10.2.1.1. *$[XeF_5]_2[Cr_2O_4F_6]$ (1), $[XeF_5]_2[Cr_2O_4F_6]\cdot 4HF$ (2), and $[XeF_5]_2[Cr_2O_4F_6]\cdot 2XeOF_4$ (3).*

The reaction of a 3.7 : 1.0 molar ratio of XeF_6 with CrO_2F_2 in aHF solvent at 22 °C followed by slow cooling to –47 °C over 6 h resulted in the formation of amber, block-shaped crystals of $[XeF_5]_2[Cr_2O_4F_6]$ (**1**) and $[XeF_5]_2[Cr_2O_4F_6]\cdot 4HF$ (**2**) (Eq. **10.1**), and trace amounts of light yellow $[XeF_5]_2[Cr_2O_4F_6]\cdot 2XeOF_4$ (**3**), where the $[Cr_2O_4F_6]^{2-}$ dianion is the dimer of the $[CrO_2F_3]^-$ anion.

Four equivalents of HF were incorporated into the crystal lattice of $[XeF_5]_2[Cr_2O_4F_6]$ when this salt was crystallized from aHF to give **2** (Eq. **10.2**).

$$2XeF_6 + 2CrO_2F_2 \longrightarrow 2[XeF_5][CrO_2F_3] \longrightarrow [XeF_5]_2[Cr_2O_4F_6] \qquad (\mathbf{10.1})$$

$$[XeF_5]_2[Cr_2O_4F_6] + 4HF \longrightarrow [XeF_5]_2[Cr_2O_4F_6]\cdot 4HF \qquad (\mathbf{10.2})$$

Samples of XeF_6 in aHF solvent hydrolyzed in the presence of trace amounts of H_2O which diffused into the reaction vessels over prolonged periods of sample storage at −78 ºC to form $XeOF_4$ and HF (Eqs. **10.3** and **10.4**). Yellow to amber, block-shaped crystals of $[XeF_5]_2[Cr_2O_4F_6]\cdot 2XeOF_4$ (**3**) grew from a sample which contained a 2.5 : 1.0 molar ratio of XeF_6 : CrO_2F_2 in aHF that had been stored at −78 °C for approximately one week. The reaction mixture was subsequently warmed to 22 °C followed by slow cooling to –30 °C over ca. 2 h. The formation of **3** is described by Eq. **10.5**, where two equivalents of $XeOF_4$ are incorporated into the crystal lattice of $[XeF_5]_2[Cr_2O_4F_6]$ upon crystallization from aHF.

$$XeF_6 + H_2O \longrightarrow XeOF_4 + 2HF \qquad (\mathbf{10.3})$$

and/or

$$[XeF_5]^+ + H_2O \longrightarrow XeOF_4 + [H_2F]^+ \qquad (\mathbf{10.4})$$

$$[XeF_5]_2[Cr_2O_4F_6] + 2XeOF_4 \longrightarrow [XeF_5]_2[Cr_2O_4F_6]\cdot 2XeOF_4 \qquad (\mathbf{10.5})$$

10.2.1.2. ***[XeF5][Xe2F11][CrO2F4] (4).*** Reaction of a 1.2 : 1.0 molar mixture of XeF_6 and CrO_2F_2 in a melt at ca. 50 °C yielded the mixed cation salt $[XeF_5][Xe_2F_{11}][CrO_2F_4]$ (**4**) (Eqs. **10.6** and **10.7**).

$$2XeF_6 + 2CrO_2F_2 \longrightarrow [XeF_5]_2[Cr_2O_4F_6] \qquad (\mathbf{10.6})$$

$$[XeF_5]_2[Cr_2O_4F_6] + XeF_6 \longrightarrow [XeF_5][Xe_2F_{11}][CrO_2F_4] + CrO_2F_2 \qquad (\mathbf{10.7})$$

Amber colored, plate-shaped crystals of **4** were grown from the melt when it was slowly cooled from 50 to 22 °C overnight in a water bath.

10.2.2. ***X-ray Crystallography***

Details of data collection and crystallographic information pertaining to $[XeF_5]_2[Cr_2O_4F_6]$ (**1**), $[XeF_5]_2[Cr_2O_4F_6]\cdot 4HF$ (**2**), $[XeF_5]_2[Cr_2O_4F_6]\cdot 2XeOF_4$ (**3**), and $[XeF_5][Xe_2F_{11}][CrO_2F_4]$ (**4**) are provided in Table 10.1. The experimental geometric parameters of $[XeF_5]^+$ and $[Xe_2F_{11}]^+$ in **1**–**4** (Table A7.1–A7.5 of Appendix 7) are comparable to those of other fluoro- and oxyfluoro-anion salts of $[XeF_5]^+$ and $[Xe_2F_{11}]^+$ [121,243,244,307–312] and are not discussed. The geometric parameters of $XeOF_4$ in **3** are comparable to those in $[XeF_5]_2[Cr_2O_2F_8]\cdot 2XeOF_4$[244] and $XeOF_4\cdot XeF_2$[68] and are also not discussed.

10.2.2.1. ***[XeF5]2[Cr2O4F6] (1), [XeF5]2[Cr2O4F6]·4HF (2), and [XeF5]2[Cr2O4F6]·2XeOF4 (3).*** The $[XeF_5]^+$ cations in **1**–**3** interact with their respective anions and with coordinated HF (**2**) or $XeOF_4$ (**3**) by means of primarily electrostatic Xe---F secondary bonds (Tables A7.1–A7.3) that avoid the stereo-active Xe VELP. The $[XeF_5]^+$ cation in **1** has a total coordination number of eight, with five primary Xe–F bonds and three Xe---F_{Cr} secondary bonding interactions with the F atoms of the anion. Coordination of four HF molecules in **2** results in hydrogen-

Table 10.1. Summary of X-ray crystal data and refinement results for $[XeF_5]_2[Cr_2O_4F_6]$ (**1**), $[XeF_5]_2[Cr_2O_4F_6]\cdot 4HF$ (**2**), $[XeF_5]_2[Cr_2O_4F_6]\cdot 2XeOF_4$ (**3**), and $[XeF_5][Xe_2F_{11}][CrO_2F_4]$ (**4**)

	1	**2**	**3**	**4**
space group	$P2_1/n$	$P2_1/c$	$P\bar{1}$	$P2/c$
a (Å)	6.347(2)	7.6348(5)	7.6308(8)	17.560(5)
b (Å)	11.968(4)	10.6633(6)	8.4310(9)	12.610(4)
c (Å)	8.691(4)	10.3706(6)	9.3022(10)	15.550(6)
α (deg)	90	90	116.654(4)	90
β (deg)	99.373(18)	104.519(3)	90.954(3)	116.321(11)
γ (deg)	90	90	97.757(4)	90
V (Å^3)	651.4(4)	817.33(9)	527.95(10)	3086.3(17)
Z	2	2	2	8
MW[a]	734.60	814.63	593.60	857.90
calcd density[b]	3.746	3.310	3.734	3.693
T (°C)	–173	–173	–173	–173
μ [c]	6.999	5.629	7.574	7.438
R_1[d]	0.0453	0.0287	0.0226	0.0991
wR_2[e]	0.1256	0.0726	0.0584	0.2684

[a] g mol^{-1}. [b] g cm^{-3}. [c] (mm^{-1}). [d] $R_1 = \Sigma||F_o|-|F_c||/\Sigma|F_o|$. [e] $wR_2 = [\Sigma(w(F_o^2-F_c^2)^2)/\Sigma(w(F_o^2)^2)]^{1/2}$.

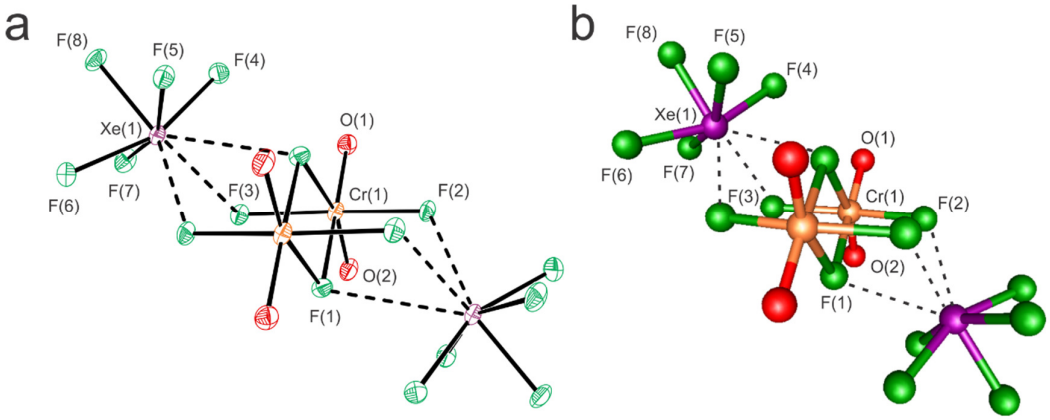

Figure 10.1. (a) The X-ray crystal structure of $[XeF_5]_2[Cr_2O_4F_6]$ (**1**) with thermal ellipsoids drawn at the 50% probability level. Secondary Xe---F bonds are indicated by dashed lines. (b) The gas-phase geometry of $[XeF_5]_2[Cr_2O_4F_6]$ (**1′**) was calculated at the PBE1PBE/Def2-SVP level of theory.

bonded HF bridges between the cations and dianion. One HF molecule forms a Xe---F_H secondary bond with the Xe atom of $[XeF_5]^+$ (2.7868(11) Å) and a H-bond with a neighboring HF molecule (F_H···F_H, 2.5431(17) Å). The additional Xe---F_H interactions reduce the Lewis acidities of the $[XeF_5]^+$ cations so that the Xe---$F_{1,1A}$ secondary bonds formed with the bridging fluorines ($F_{1,1A}$) of the dianion in **2** (2 x 3.1624(9) Å) are significantly longer than in **1** (2 x 2.762(3) Å). The proximate HF molecules interact through a H_F---$F_{1,1A}$ secondary bonds with the bridging $F_{1,1A}$ atoms of $[Cr_2O_4F_6]^{2-}$ (F···F, 2 x 2.4774(15) Å) and serve to complete the Xe---F–H---F–H---$F_{1,1A}$ bridges between the cations and dianion.

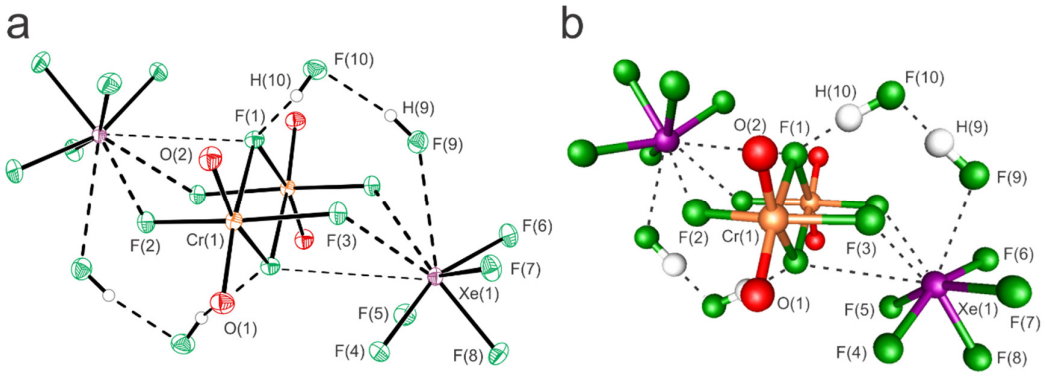

Figure 10.2. (a) The X-ray crystal structure of $[XeF_5]_2[Cr_2O_4F_6]\cdot 4HF$ (**2**) with thermal ellipsoids drawn at the 50% probability level. Secondary Xe---F bonds are indicated by dashed lines. (b) The gas-phase geometry of $[XeF_5]_2[Cr_2O_4F_6]\cdot 4HF$ (**2′**) was calculated at the PBE1PBE/Def2-SVP level of theory.

The coordinated $XeOF_4$ molecules of **3** also bridge the cations and dianion through long $F_{Xe_{2,2A}}$---$Xe_{1,1A}$ (2 x 3.3940(11), $Xe_{2,2A}$---$F_{1,1A}$ (2 x 2.9965(8) Å), $Xe_{2,2A}$---$F_{2,2A}$ (2 x 3.0036(9) Å) and $Xe_{2,2A}$---$F_{3,3A}$ (2 x 3.2685(9) Å) secondary bonds. The

secondary $Xe_{2,2A}$---$F_{1,1A–3,3A}$ bonds are directed towards the open square face of the square-pyramidal $XeOF_4$ molecules and avoid the stereo-active VELPs of $Xe_{2,2A}$ that are trans to the $Xe_{2,2A}$–O bonds.

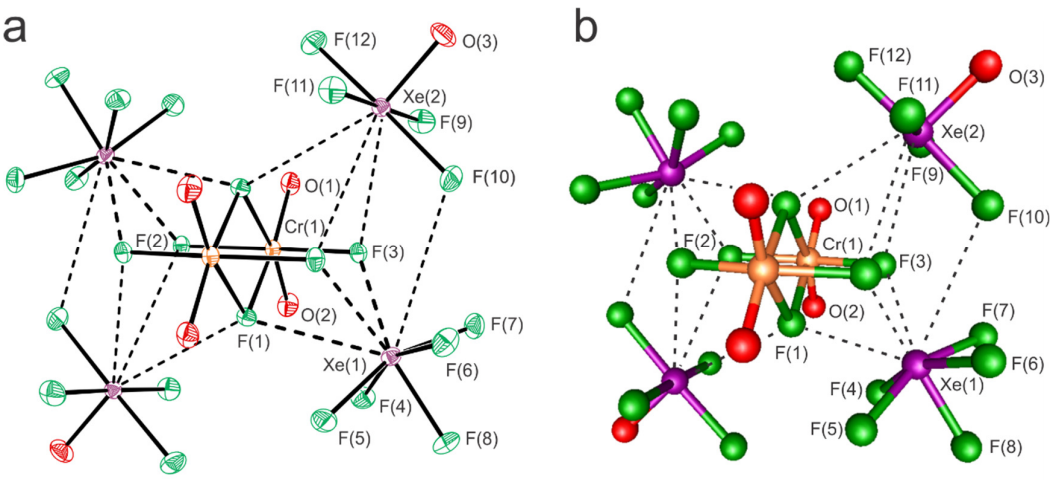

Figure 10.3. (a) The X-ray crystal structure of $[XeF_5]_2[Cr_2O_4F_6]\cdot 2XeOF_4$ (**3**) with thermal ellipsoids drawn at the 50% probability level. Secondary Xe---F bonds are indicated by dashed lines. (b) The gas-phase geometry of $[XeF_5]_2[Cr_2O_4F_6]\cdot 2XeOF_4$ (**3′**) was calculated at the PBE1PBE/Def2-SVP level of theory.

The dimeric $[Cr_2O_4F_6]^{2-}$ dianion (Figures 10.1–10.3, Tables A7.1–A7.3) is comprised of two symmetry-equivalent $[CrO_2F_3]^-$ anions that have *cis*-dioxo arrangements of terminal Cr–O bonds and bridge through two fluorine atoms, F_1 and F_{1A}. The primary coordination spheres of the Cr(VI) atoms may be described in terms of AX_2Y_4 VSEPR arrangements[88] that give rise to a distorted octahedral coordination spheres around each Cr(VI) atom (A) that consists of two Cr–O double bonds that are cis to one another (X) and four Cr–F single bonds (Y), where two Cr–F bonds are

trans to one another and two bridging Cr–F bonds are cis to one another. The Cr–$F_{2,3}$ bonds are bent away from the Cr–O double bonds, as indicated by O−Cr–$F_{2,3}$ bond angles that are greater than 90°; (93.2(2)–97.1(2) (**1**), 95.12(5)–97.66(5) (**2**), 94.26(5)–96.93(5)° (**3**). The more open angles are attributed to bond-pair double-bond-pair repulsions.

The Cr–O bond lengths (1.585(5), 1.590(5) (**1**), 1.5765(11), 1.5822(11) (**2**), 1.5758(10), 1.5822(10) (**3**) Å) have significant double-bond character but are somewhat elongated relative to those of the Cr(V) oxyfluoro-anion salts $[XeF_5]_2[Cr_2O_2F_8]$ (1.567(1) Å), $[XeF_5]_2[Cr_2O_2F_8]\cdot 2HF$ (1.5438(9) Å), and $[XeF_5]_2[Cr_2O_2F_8]\cdot 2XeOF_4$ (1.549(1) Å);[244] the Cr(VI) oxyfluoro-anion salt $[Xe_2F_{11}][CrOF_5]$ (1.565(1) Å); and the neutral Cr(VI) oxide fluorides α-$CrOF_4$ (1.539(3)–1.558(4) Å),[65] β-$CrOF_4$ (1.5490(7) Å),[65] and CrO_2F_2 (1.574(1), 1.576(1) Å).[325]

The *trans*-influences of the Cr–O bonds result in greater degrees of ionic character in the asymmetric Cr–$F_{1,1A}$ bridge bonds (2.065(4), 2.082(5) (**1**), 2.1146(9), 2.1314(9) (**2**), and 2.0660(8), 2.1337(8) (**3**) Å), that are cis to one another and trans to Cr–O bonds. The Cr–$F_{1,1A}$ bridge bonds are significantly longer than the terminal Cr–$F_{2,3}$ bonds (1.861(4), 1.870(4) (**1**), 1.8451(9), 1.8509(9) (**2**), and 1.8488(8), 1.8668(8) (**3**) Å), which is consistent with their relative degrees of covalent character, Cr–$F_{2,3}$ > Cr–$F_{1,1A}$. The geometries of the $[Cr_2O_4F_6]^{2-}$ dianions in **1**–**3** are isostructural with $[Mo_2O_4F_6]^{2-}$ in its protonated piperazine ($[o\text{-}N_2C_4H_{12}]^+$),[320] pyridine ($[C_5H_5NH]^+$),[320] and *N*-butylpyridinium ($[C_9H_{14}N]^+$)[286] salts, and $[W_2O_4F_6]^{2-}$ in [Na-15-crown-5]$_2[W_2O_4F_6]\cdot 2CH_3CN$.[319]

Table 10.2. Experimental and Calculated[a] Geometric Parameters for $[Cr_2O_4F_6]^{2-}$ in $[XeF_5]_2[Cr_2O_4F_6]$ (1,1′), $[XeF_5]_2[Cr_2O_4F_6]\cdot 4HF$ (2,2′), and $[XeF_5]_2[Cr_2O_4F_6]\cdot 2XeOF_4$ (3,3′)

	1	**1′**	**2**	**2′**	**3**	**3′**
	exptl	**calcd**	**exptl**	**calcd**	**exptl**	**calcd**
Bond Lengths (Å)						
Cr(1)−O(1)	1.585(5)	1.520	1.5765(11)	1.5202	1.5822(10)	1.5185
Cr(1)−O(2)	1.590(5)	1.520	1.5822(11)	1.5202	1.5758(10)	1.5185
Cr(1)−F(1)	2.082(5)	2.135	2.1146(9)	2.1501	2.0660(8)	2.1499
Cr(1)−F(1A)	2.065(4)	2.135	2.1314(9)	2.1501	2.1337(8)	2.1499
Cr(1)−F(2)	1.861(4)	1.831	1.8509(9)	1.8180	1.8488(8)	1.8281
Cr(1)−F(3)	1.870(4)	1.831	1.8451(9)	1.8180	1.8668(8)	1.8281
Bond Angles (°)						
O(1)−Cr(1)−O(2)	104.5(2)	105.5	104.82(6)	105.74	104.69(6)	105.64
O(1)−Cr(1)−F(1)	163.4(2)	160.9	161.65(5)	161.71	160.23(5)	161.59
O(1)−Cr(1)−F(1A)	93.4(2)	92.7	91.40(5)	92.50	90.00(5)	92.44
O(1)−Cr(1)−F(2)	94.2(2)	95.6	95.12(5)	96.94	97.00(5)	96.90
O(1)−Cr(1)−F(3)	96.0(2)	98.7	97.66(5)	98.45	94.26(5)	98.64
O(2)−Cr(1)−F(1)	91.5(3)	92.7	93.43(5)	92.50	94.75(5)	92.44
O(2)−Cr(1)−F(1A)	161.2(3)	160.9	163.75(5)	161.71	165.26(5)	161.59
O(2)−Cr(1)−F(2)	97.1(2)	98.7	96.67(5)	98.45	96.93(5)	98.64
O(2)−Cr(1)−F(3)	93.2(2)	95.6	95.73(5)	96.94	96.73(5)	96.90
F(1)−Cr(1)−F(1A)	71.29(14)	70.0	70.39(4)	69.30	70.69(4)	69.77
F(1)−Cr(1)−F(2)	79.18(18)	75.5	80.67(4)	78.70	84.03(4)	82.26
F(1)−Cr(1)−F(3)	87.36(18)	85.1	82.09(4)	80.27	79.63(3)	76.56
F(1A)−Cr(1)−F(2)	87.31(18)	85.1	82.59(4)	80.27	79.74(3)	76.56
F(1A)−Cr(1)−F(3)	78.85(18)	75.5	80.87(4)	78.70	83.16(3)	82.26
F(2)−Cr(1)−F(3)	163.23(15)	156.4	159.29(4)	154.37	159.47(4)	154.15
Cr(1)−F(1)−Cr(1A)	108.71(14)	110.0	110.24(5)	110.70	109.31(4)	110.23

[a] PBE1PBE/Def2-SVP.

10.2.2.2. $[XeF_5][Xe_2F_{11}][CrO_2F_4]$ (4). The unit cell of **4** is comprised of two crystallographically inequivalent structural units that are well separated from one another (Table 10.3, Figures 10.4 and 10.5). The structural units stack in columns along the *c*-axis of the unit cell, and these columns pack in the *bc*-plane to form ordered layers. The spaces between the layers are solely occupied by F-atoms bound to Xe and provide a "slippery" interface over which adjacent layers may translate

relative to one another. This likely serves as an interface that accounts for why $[XeF_5][Xe_2F_{11}][CrO_2F_4]$ crystals have a propensity to twin and exhibit diffuse X-ray scattering indicative of a loss of order in one dimension. Both structural units in the crystal structure of **4** exhibit the same geometric trends, thus only one unit considered in the ensuing discussion.

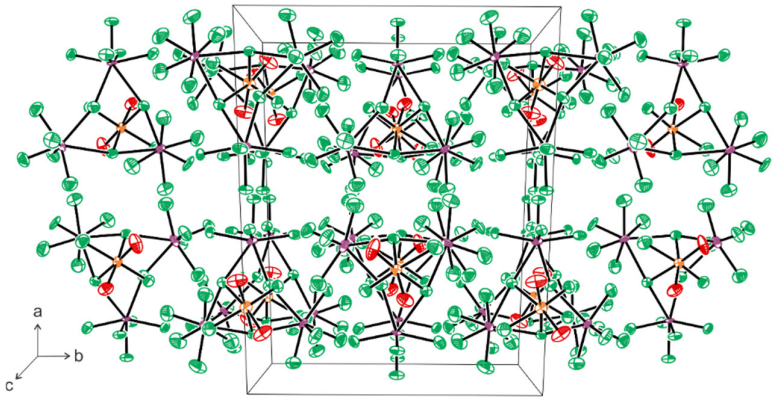

Figure 10.4. A packing diagram showing the unit cell of **4** viewed along the *c*-axis of the unit cell.

The structural units in **4** are intimately ion-paired salts in which the $[CrO_2F_4]^{2-}$ dianions form short Xe---F_{Cr} secondary bonds (2.368(13)–2.830(13) Å) with $[XeF_5]^+$ and $[Xe_2F_{11}]^+$ that avoid the stereo-active VELPs on their Xe atoms (Figure 10.5). The $[XeF_5]^+$ cations form two short Xe_1---$F_{1,2}$ secondary bonds with $[CrO_2F_4]^{2-}$ (2.414(12) and 2.447(12) Å) and one longer bond with F_3 (2.687(14) Å). The $[Xe_2F_{11}]^+$ cations also form two short $Xe_{2,3}$---$F_{1,2}$ secondary bonds (2.417(11) and 2.544(13) Å) and two longer $Xe_{2,3}$---F_4 bonds (2.779(12) and 2.830(13) Å). The Xe---F bond lengths reflect the relative fluorobasicities of the F atoms in $[CrO_2F_4]^{2-}$, which increase in the order $F_4 \approx F_3 < F_1 \approx F_2$.

Table 10.3. Experimental and Calculated[a] Geometric Parameters for $[CrO_2F_4]^{2-}$

	exptl (4)			calcd (4′)
Bond Lengths (Å)				
Cr(1)−O(1)	1.504(16)	Cr(2)−O(3)	1.560(16)	1.5198
Cr(1)−O(2)	1.595(16)	Cr(2)−O(4)	1.520(17)	1.5198
Cr(1)−F(1)	2.105(12)	Cr(2)−F(21)	2.178(12)	2.2079
Cr(1)−F(2)	2.081(13)	Cr(2)−F(22)	2.146(12)	2.2079
Cr(1)−F(3)	1.812(14)	Cr(2)−F(23)	1.834(14)	1.7968
Cr(1)−F(4)	1.838(13)	Cr(2)−F(24)	1.823(12)	1.7985
Bond Angles (°)				
O(1)–Cr(1)–O(2)	101.2(11)	O(3)–Cr(2)–O(4)	107.2(10)	105.4
O(1)–Cr(1)–F(1)	94.3(9)	O(3)–Cr(2)–F(21)	90.4(8)	91.3
O(1)–Cr(1)–F(2)	169.8(9)	O(3)–Cr(2)–F(22)	164.3(7)	163.2
O(1)–Cr(1)–F(3)	103.1 (10)	O(3)–Cr(2)–F(23)	104.2(9)	100.6
O(1)–Cr(1)–F(4)	97.4(9)	O(3)–Cr(2)–F(24)	96.3(8)	100.8
O(2)–Cr(1)–F(1)	164.5(8)	O(4)–Cr(2)–F(21)	162.0(8)	163.2
O(2)–Cr(1)–F(2)	89.0(8)	O(4)–Cr(2)–F(22)	88.5(7)	91.3
O(2)–Cr(1)–F(3)	98.8(8)	O(4)–Cr(2)–F(23)	96.2(10)	100.6
O(2)–Cr(1)–F(4)	98.2(8)	O(4)–Cr(2)–F(24)	104.1(9)	100.8
F(1)–Cr(1)–F(2)	75.5(5)	F(21)–Cr(2)–F(22)	74.0(5)	71.9
F(1)–Cr(1)–F(3)	78.0(5)	F(21)–Cr(2)–F(23)	75.4(6)	74.4
F(1)–Cr(1)–F(4)	79.1(5)	F(21)–Cr(2)–F(24)	77.0(5)	76.8
F(2)–Cr(1)–F(3)	75.6(6)	F(22)–Cr(2)–F(23)	74.4(5)	74.4
F(2)–Cr(1)–F(4)	80.4(6)	F(22)–Cr(2)–F(24)	78.4(5)	76.8
F(3)–Cr(1)–F(4)	150.2(6)	F(23)–Cr(2)–F(24)	145.4(6)	144.2

[a] PBE1PBE/Def2-SVP.

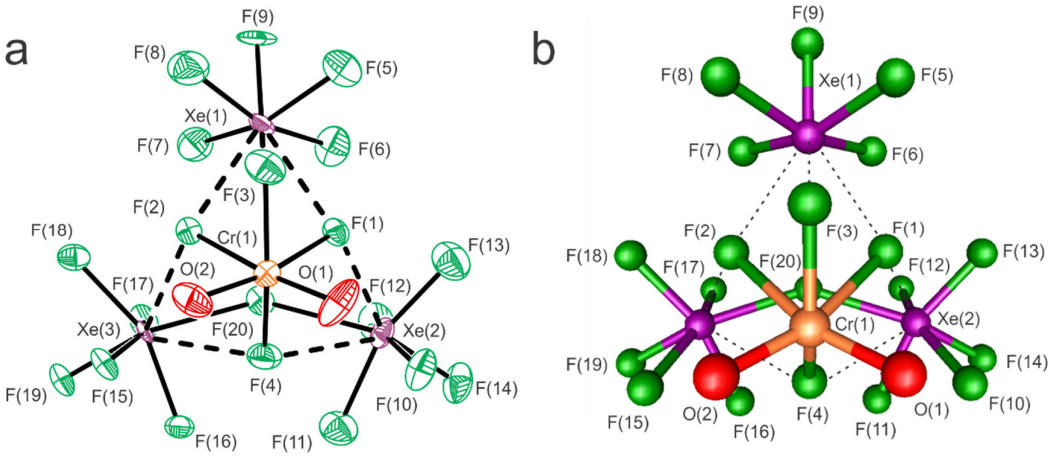

Figure 10.5. (a) One of two crystallographically unique structural units in the X-ray crystal structure of $[XeF_5][Xe_2F_{11}][CrO_2F_4]$ (**4**), where thermal ellipsoids are drawn at the 50% probability level, and secondary Xe---F bonds are indicated by dashed lines. (b) The calculated gas-phase geometry of $[XeF_5][Xe_2F_{11}][CrO_2F_4]$ (**4′**) (PBE1PBE/Def2-SVP).

The primary coordination sphere of Cr(VI) in $[CrO_2F_4]^{2-}$ may be described as an AX_2Y_4 VSEPR arrangement[88] of two Cr–O double bond-pair domains (X) and four Cr–F single bond-pair domains (Y) around the central Cr atom (A) and is similar to the Cr(VI) coordination environments of $[Cr_2O_4F_6]^{2-}$. The Cr–O double-bond pairs interact with the Cr–F single-bond pairs and with each other to give more open O–Cr–F (89.0(8)–103.1(10)°) and O–Cr–O bond angles (101.2(11)°) when compared with the *cis*-F–Cr–F bond angles (75.5(5)–80.4(6)°). The $Cr–F_{1,2}$ bonds (2.105(12) and 2.081(13) Å, respectively) are significantly elongated relative to the $Cr–F_{3,4}$ bonds (1.812(14) and 1.838(13) Å, respectively) due to the *trans*-influences of the Cr–O bonds (1.504(16)–1.560(16) Å), where the relative Cr–F bond lengths reflect the relative fluorobasicities, $F_4 \approx F_3 < F_1 \approx F_2$. The $[CrO_2F_4]^{2-}$ anion geometries in **4** are

similar to those of the ordered $[M'O_2F_4]^{2-}$ (M′ = Mo, W) anions in $[pyH]_2[Cu(py)_4(MoO_2F_4)_2]$,[326] $Na_2[WO_2F_4]$,[327] and $[HNC_6H_6OH]_2[Cu(NC_5H_5)_4(WO_2F_4)_2]$,[324] and complete the series of crystallographically characterized $[MO_2F_4]^{2-}$ anions (M = Cr, Mo, W).

10.2.3. Raman Spectroscopy

The low-temperature Raman spectra of $[XeF_5]_2[Cr_2O_4F_6]$ (**1**), $[XeF_5]_2[Cr_2O_4F_6]\cdot 4HF$ (**2**), $[XeF_5]_2[Cr_2O_4F_6]\cdot 2XeOF_4$ (**3**), and $[XeF_5][Xe_2F_{11}][CrO_2F_4]$ (**4**) (Figures 10.6, 10.7, 10.8, and 10.9, respectively) are the first fully assigned vibrational spectra reported for salts of the $[Cr_2O_4F_6]^{2-}$ and $[CrO_2F_4]^{2-}$ anions. Spectral assignments were made by comparison with the calculated vibrational frequencies and intensities of the energy-minimized, gas-phase geometries of $[XeF_5]_2[Cr_2O_4F_6]$ (**1′**), $[XeF_5]_2[Cr_2O_4F_6]\cdot 4HF$ (**2′**), $[XeF_5]_2[Cr_2O_4F_6]\cdot 2XeOF_4$ (**3′**), and $[XeF_5][Xe_2F_{11}][CrO_2F_4]$ (**4′**) at the PBE1PBE/Def2-SVP level of theory. The observed and calculated frequencies, their detailed assignments, and vibrational mode descriptions for **1**–**4** are provided in Tables A7.6–A7.9. Except for the overestimated ν(Cr-O) stretching frequencies, the experimental vibrational frequencies and their trends are well reproduced by the calculations. Vibrational assignments for the cocrystallized $XeOF_4$ and the $[XeF_5]^+$ and $[Xe_2F_{11}]^+$ cations were also aided by comparison with vibrational spectra of $XeOF_4$,[68] $XeOF_4\cdot XeF_2$,[68] $[XeF_5][OsO_3F_3]$,[121] $[XeF_5][AsF_6]$,[316] $[XeF_5][BF_4]$,[316] $[Xe_2F_{11}][OsO_3F_3]$,[121] $[XeF_5]_2[Cr_2O_2F_8]\cdot 2XeOF_4$, and $[XeF_5][Xe_2F_{11}][CrOF_5]\cdot 2CrOF_4$.[244] The latter assignments are in good agreement with the literature and are not discussed. Tables A7.6–A7.9 show that many of the

vibrational modes are coupled to some extent. Therefore, only the predominant components in the mode descriptions are used as the basis for ensuing discussions.

10.2.3.1. $[XeF_5]_2[Cr_2O_4F_6]$ (1), $[XeF_5]_2[Cr_2O_4F_6]\cdot 2XeOF_4$ (2), and $[XeF_5]_2[Cr_2O_4F_6]\cdot 2XeOF_4$ (3). The $[Cr_2O_4F_6]^{2-}$ anions in the SCXRD structures of **1**–**3** have C_i symmetry. Factor-group analyses based on the crystal structures of **1**–**3** were carried out using the "correlation method" (Figures A7.1–A7.3).[169] Correlation of the gas-phase ion-pair symmetries of **1′**–**3′** (C_{2h}) to the crystal site symmetries (C_i) and space group symmetries (**1**, **2**, C_{2h}; **3**, C_i) do not result in symmetry lowering. The unit cells of all three salts have centers of symmetry so that mutual exclusion applies. Accordingly, no formally Raman inactive modes were observed in the Raman spectra of **1**–**3**.

The highest frequency Raman bands are assigned to the in-phase symmetric $[\nu(Cr_1\text{-}O_1) + \nu(Cr_1\text{-}O_2)] + [\nu(Cr_{1A}\text{-}O_{1A}) + \nu(Cr_{1A}\text{-}O_{2A})]$ (**1**, 940 cm^{-1}; **2**, 951 cm^{-1}; **3**, 951 cm^{-1}) and asymmetric $[\nu(Cr_1\text{-}O_1) - \nu(Cr_1\text{-}O_2)] + [\nu(Cr_{1A}\text{-}O_{1A}) - \nu(Cr_{1A}\text{-}O_{2A})]$ (**1**, 919 cm^{-1}; **2**, 912 cm^{-1}; **3**, 922 cm^{-1}) stretches. The ν(Cr-O) stretching modes of **1**–**3** occur at somewhat lower frequencies than the ν(Cr-O) stretching modes of CrO_2F_2 (Ra: 935 and 955 cm^{-1}),[328] $CrOF_4$ (Ra: β, 995; α, 1001 cm^{-1}),[65] and $[Xe_2F_{11}][CrOF_5]$ (Ra: 951 cm^{-1}).[243] The calculated gas-phase (Cr-O) stretching frequencies of $[Cr_2O_4F_6]^{2-}$ increase upon ion-pair formation (anion: 1075–1106 cm^{-1} and ion-pair: **1**, 1148–1182 cm^{-1}; **2**, 1153–1189 cm^{-1}; **3**, 1151–1185 cm^{-1}), indicating that ion-pairing strengthens the Cr–O bonds somewhat.

The in-phase symmetric stretches, $[\nu(Cr_1\text{-}F_2) + \nu(Cr_1\text{-}F_3)] + [\nu(Cr_{1A}\text{-}F_{2A}) + \nu(Cr_{1A}\text{-}F_{3A})]$, occur at (**1**) 534, (**2**) 585, and (**3**) 563 cm^{-1}, whereas the in-phase asymmetric stretches, $[\nu(Cr_1\text{-}F_2) - \nu(Cr_1\text{-}F_3)] + [\nu(Cr_{1A}\text{-}F_{2A}) - \nu(Cr_{1A}\text{-}F_{3A})]$, occur at

lower frequencies (**1**, 520 cm^{-1}; **2**, 540 cm^{-1}; **3**, 542 cm^{-1}). The symmetric and asymmetric modes occur at lower frequency than the ν(Cr-F) stretching modes of liquid CrO_2F_2 (Ra: 770 and 708 cm^{-1}).[328] The in-phase symmetric stretches that involve the bridging F atoms, F_1 and F_{1A}, [ν(Cr_1-F_1) + ν(Cr_1-F_{1A})] + [ν(Cr_{1A}-F_1) + ν(Cr_{1A}-F_{1A})], occur at even lower frequency (**1**, 408 cm^{-1}; **2**, 397 cm^{-1}; **3**, 405 cm^{-1}), consistent with their relative experimental and calculated Cr–F bond lengths which increase in the order $Cr–F_{1,1A} > Cr–F_{2,3}$. The in-phase asymmetric stretches, [ν(Cr_1-F_1) − ν(Cr_1-F_{1A})] + [ν(Cr_{1A}-F_1) − ν(Cr_{1A}-F_{1A})], occur at somewhat lower frequency (**1**, 401; **2**, 339; **3**, 373 cm^{-1}).

The symmetric [δ($O_1Cr_1O_2$) + δ($O_{1A}Cr_{1A}O_{2A}$)] bending modes of **1**–**3** were observed at (**1**) 445, (**2**) 439, and (**3**) 440 cm^{-1} (calcd: **1′**, 481; **2′**, 483; **3′**, 481 cm^{-1}). These bands occur at somewhat higher frequencies than the δ(OCrO) bending mode of liquid CrO_2F_2 (403 cm^{-1}).[328] The bands at 296 (**1**), 261 (**2**), and 272 (**3**) cm^{-1} are assigned to the bending modes, [δ($F_2Cr_1F_3$) + δ($F_{2A}Cr_{1A}F_{3A}$)]. The corresponding calculated values (**1′**, 294 cm^{-1}; **2′**, 265 cm^{-1}; **3′**, 275 cm^{-1}) are comparable to those calculated for gas-phase $[Cr_2O_4F_6]^{2-}$ (275 cm^{-1}).

The symmetric [ρ_w($O_1Cr_1O_2$) + ρ_w($O_{1A}Cr_{1A}O_{2A}$)] deformation modes of **1**–**3** are assigned to the bands at (**1**) 356, (**2**) 339, and (**3**) 353 cm^{-1} (calcd: **1′**, 363; **2′**, 373; **3′**, 360 cm^{-1}). The symmetric [ρ_t($O_1Cr_1O_2$) + ρ_t($O_{1A}Cr_{1A}O_{2A}$)] twisting modes give rise to bands at (**1**) 356, (**2**) 339, and (**3**) 353 cm^{-1}. The [ρ_t($O_1Cr_1O_2$) + ρ_t($O_{1A}Cr_{1A}O_{2A}$)] modes are assigned to bands at 242 (**1**) and 239 (**2**) cm^{-1}, respectively. The same coupled mode of **2′** is calculated to be lower in frequency (202 cm^{-1}) and likely overlaps with the lattice modes of **2** (114–187 cm^{-1}).

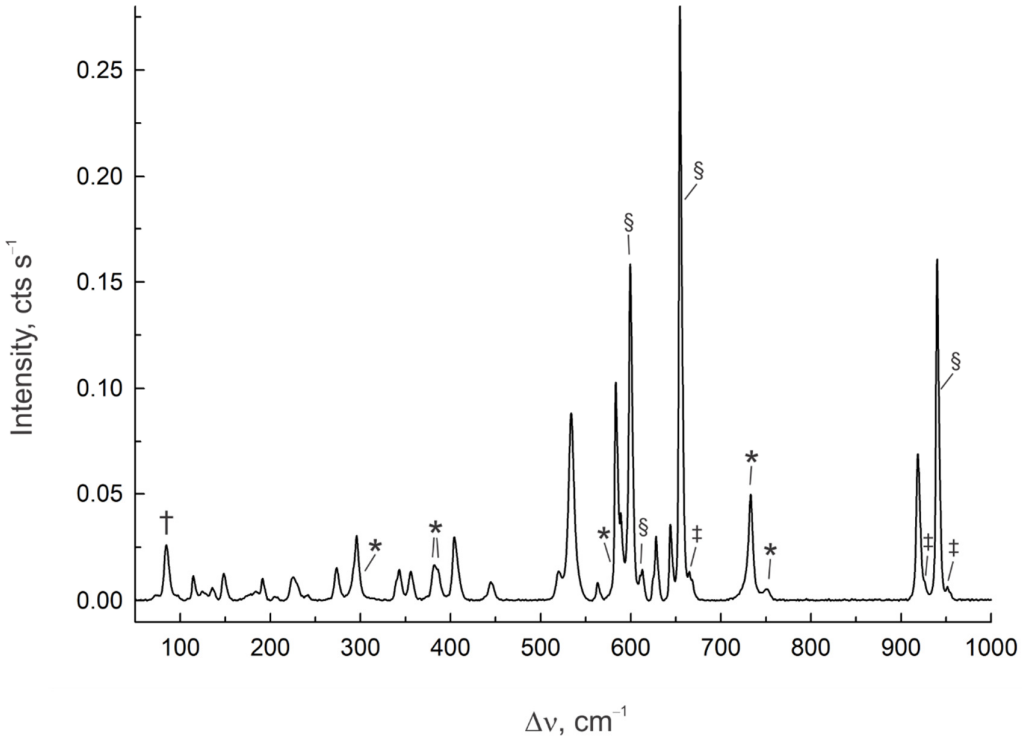

Figure 10.6. The Raman spectrum of a mixture of solid $[XeF_5]_2[Cr_2O_4F_6]$ (**1**), $[XeF_5]_2[Cr_2O_4F_6]\cdot 4HF$ (**2**), and $[XeF_5]_2[Cr_2O_4F_6]\cdot 2XeOF_4$ (**3**), where **1** was dominant. The spectrum was recorded under a frozen aHF solution at −150 ºC using 1064-nm excitation. The symbols denote Raman bands of **1** which overlap with those of **2** (§), bands due to **3** (‡), FEP sample tube bands (*), and an instrumental artifact (†).

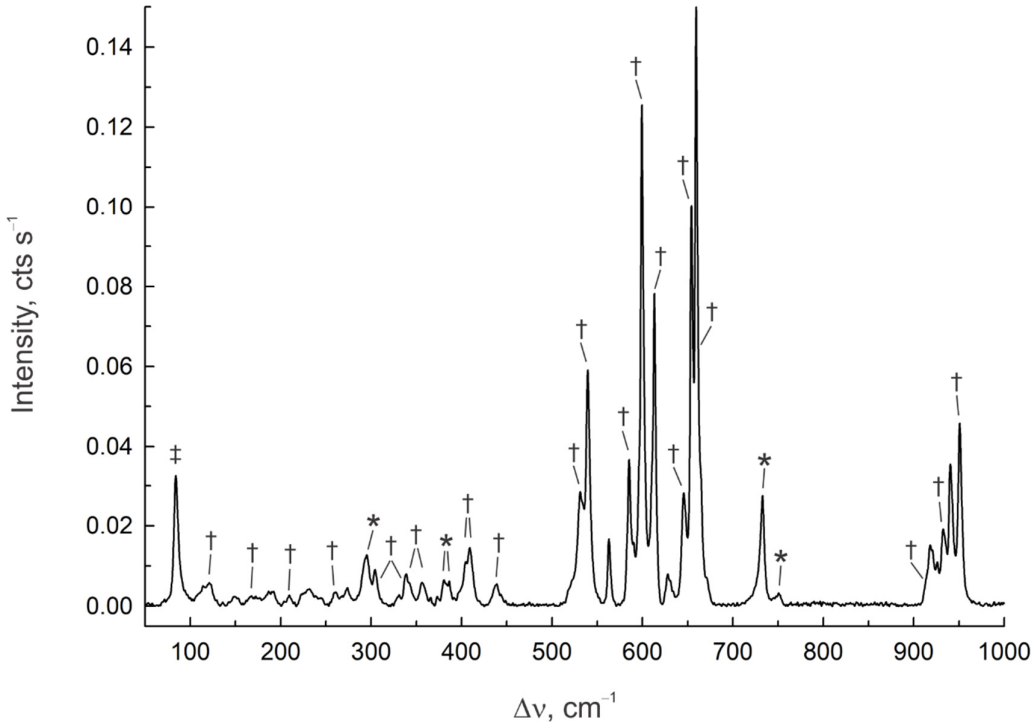

Figure 10.7. The Raman spectrum of a mixture of $[XeF_5]_2[Cr_2O_4F_6]$ (**1**), $[XeF_5]_2[Cr_2O_4F_6]\cdot 4HF$ (**2**), and $[XeF_5]_2[Cr_2O_4F_6]\cdot 2XeOF_4$ (**3**) recorded under a frozen aHF solution at −150 ºC using 1064-nm excitation, where **2** was the dominant component. The symbols denote bands assigned to **2** (†), FEP sample tube bands (*), and an instrumental artifact (‡). Unmarked bands corresponding to **1** and **3** are listed in footnote [a] of Table A7.7.

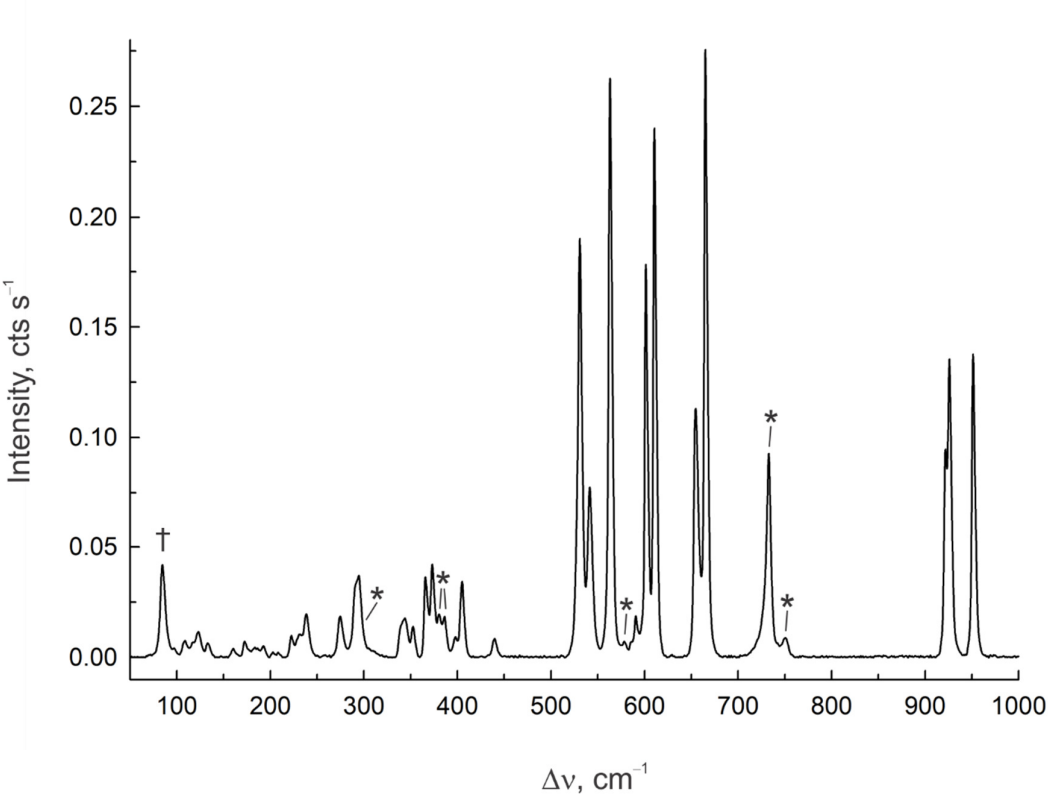

Figure 10.8. The Raman spectrum of $[XeF_5]_2[Cr_2O_4F_6]\cdot 2XeOF_4$ (**3**) recorded under a frozen aHF solution at −150 ºC using 1064-nm excitation. The symbols denote an instrumental artifact (†) and FEP sample tube bands (*).

10.2.3.2. [XeF₅][Xe₂F₁₁][CrO₂F₄] (4). A factor-group analysis based on the crystal structure of **4** was carried out using the "correlation method" (Figure A7.4).[169] Seventy-two vibrational modes are predicted for gas-phase $[XeF_5][Xe_2F_{11}][CrO_2F_4]$ (C_s). The vibrations belong to the irreducible representations Γ = 39 A′ + 33 A″, where all modes are Raman- and infrared-active. The A′ and A″ representations of

gas-phase $[XeF_5][Xe_2F_{11}][CrO_2F_4]$ correlate to A representations under C_1 site symmetry in the crystal structure of **4**. When correlated to the space group symmetry (C_i), each of the 72 A modes splits into Raman-active A_g and infrared-active A_u components (Figure A7.4). Thus, all 72 vibrational bands in the calculated Raman spectra of **4** are predicted to be Raman active (Table A7.9). Of the 72 predicted bands, 25 were observed.

The Raman bands observed at 954 and 950 cm^{-1} are assigned to the symmetric [$\nu(Cr_1\text{-}O_1) + \nu(Cr_1\text{-}O_2)$] and asymmetric [$\nu(Cr_1\text{-}O_1) - \nu(Cr_1\text{-}O_2)$] stretches, respectively. The calculated ν(Cr-O) stretches of **4′** (1183 and 1164 cm^{-1}) occur at higher frequencies than in the free gas-phase $[CrO_2F_4]^{2-}$ anion (1058 and 1042 cm^{-1}), indicating that ion-pair formation strengthens the Cr–O double bonds.

The bands observed at 579 and 573 cm^{-1} are assigned to the symmetric, [$\nu(Cr_1\text{-}F_3) + \nu(Cr_1\text{-}F_4)$] and asymmetric, [$\nu(Cr_1\text{-}F_3) - \nu(Cr_1\text{-}F_4)$], stretches, respectively; whereas the band at 283 cm^{-1} is assigned to the symmetric stretch, [$\nu(Cr_1\text{-}F_1) + \nu(Cr_1\text{-}F_2)$]. This observed frequency difference is reproduced for the calculated ion-pair **4′** (591 and 583 cm^{-1} versus 305 cm^{-1}). These values bracket the ν(Cr-F) stretching frequencies calculated for gas-phase $[CrO_2F_4]^{2-}$ (558, 501, 404, 397 cm^{-1}) where $\nu(Cr\text{-}F_{3,4})$ and $\nu(Cr\text{-}F_{1,2})$ in-phase and out-of-phase couple (558 and 404 cm^{-1}), reflecting decreases in the Cr–$F_{3,4}$ bond lengths and increases in the Cr–$F_{1,2}$ bond lengths upon ion-pair formation.

The band at 441 cm^{-1} is assigned to the $\delta(O_1Cr_1O_2)$ bending mode (calcd: 441 cm^{-1}), a frequency similar to the δ(OCrO) modes of **1**–**3** (vide supra). The $\rho_w(O_1Cr_1O_2)$, $\rho_r(O_1Cr_1O_2)$, and $\rho_r(O_1Cr_1O_2)$ deformation modes are strongly coupled to other deformation modes but could be assigned to the bands observed at 358/323,

344, and 294 cm^{-1}, respectively (calcd: 365/359, 361, and 316 cm^{-1}). Note that the frequencies calculated for **4′** are comparable to those of gas-phase $[CrO_2F_4]^{2-}$ (453, 361, 336, and 340 cm^{-1}).

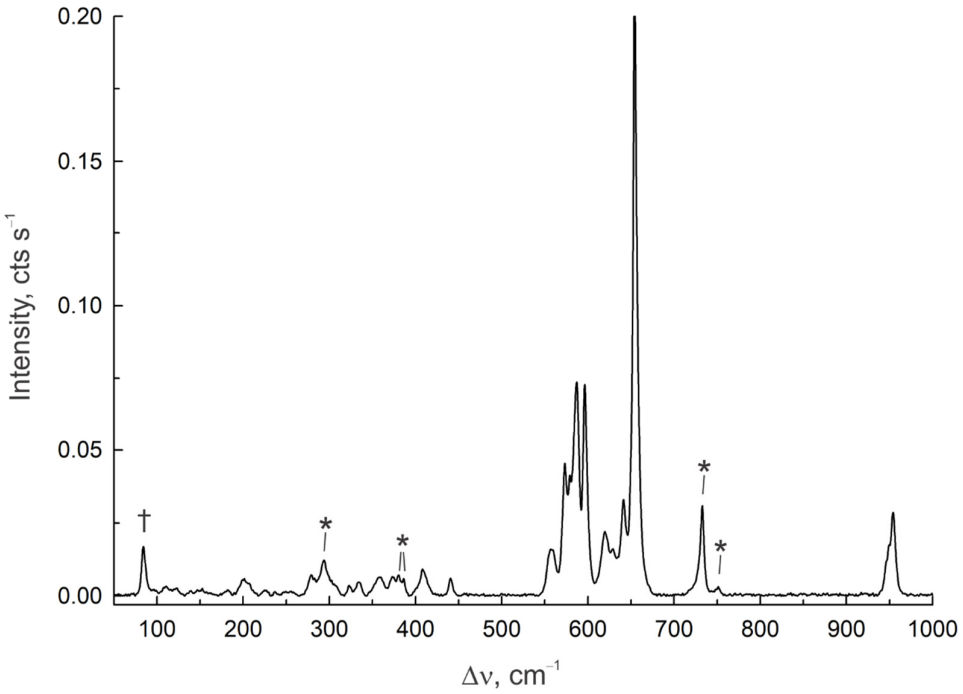

Figure 10.9. The Raman spectrum of $[XeF_5][Xe_2F_{11}][CrO_2F_4]$ (**4**) recorded under a frozen aHF solution at −150 °C using 1064-nm excitation. The symbols denote an instrumental artifact (†) and FEP sample tube bands (*).

10.2.4. COMPUTATIONAL RESULTS

10.2.4.1. Calculated Geometries

The gas-phase structures of $[XeF_5]^+$, $[Xe_2F_{11}]^+$, CrO_2F_2, $[CrO_2F_4]^{2-}$, and $[Cr_2O_4F_6]^{2-}$, and the ion-pairs $[XeF_5]_2[Cr_2O_4F_6]$ (**1′**), $[XeF_5]_2[Cr_2O_4F_6]\cdot 4HF$ (**2′**),

$[XeF_5]_2[Cr_2O_4F_6]\cdot 2XeOF_4$ (**3′**), and $[XeF_5][Xe_2F_{11}][CrO_2F_4]$ (**4′**) were optimized at the PBE1PBE/Def2-SVP level of theory which resulted in stationary points with all frequencies real (Tables A7.1–A7.3, A7.5–A7.15, Figures 10.1–10.4 and A7.5–A7.9). The gas-phase structure of $[Cr_2O_4F_6]^{2-}$ (C_{2h}) optimized with one imaginary frequency (−46 cm^{-1}). The imaginary frequency persisted when geometry optimizations were carried out using lower symmetry starting geometries (C_s, −47; C_i, −48; C_1, −48 cm^{-1}). The $[Cr_2O_4F_6]^{2-}$ dimer did not separate into discrete $[CrO_2F_3]^-$ anions during any geometry optimization cycle. The starting geometries used for $[XeF_5]^+$ and $[Xe_2F_{11}]^+$ and for $[Cr_2O_4F_6]^{2-}$ and $[CrO_2F_4]^{2-}$ were the crystallographic geometries obtained from **1** and **4**, respectively. The starting geometries used for CrO_2F_2[325] and ion-pairs **1′–4′** were the crystallographic geometries, **1–4**. The experimental geometries of **1–4** are well reproduced by the calculated ion-pair geometries of **1′–4′**.

10.2.4.1.1. CrO_2F_2, $[Cr_2O_4F_6]^{2-}$, $[XeF_5]_2[Cr_2O_4F_6]$ (1′), $[XeF_5]_2[Cr_2O_4F_6]\cdot 4HF$ (2′), and $[XeF_5]_2[Cr_2O_4F_6]\cdot 2XeOF_4$ (3′). The gas-phase geometries of CrO_2F_2 and $[Cr_2O_4F_6]^{2-}$ optimized to C_{2v} and C_{2h} symmetries, respectively. The Cr–O (1.552 Å) and Cr–$F_{2,3}$ (1.781 Å) bond lengths of $[Cr_2O_4F_6]^{2-}$ are elongated relative to those of CrO_2F_2 (Cr–O, 1.525 Å; Cr–F, 1.685 Å), consistent with the enhanced Cr–O and Cr–F bond polarities of the $[Cr_2O_4F_6]^{2-}$ dianion. The Cr–O bond elongations are in part attributable to localization of the dianion charge on the oxygen atoms, which may be rationalized in terms of Cr=O ⟷ Cr–O^- resonance contributions. The Cr–$F_{1,1A}$ bridge bonds of $[Cr_2O_4F_6]^{2-}$ are significantly longer (2.068 Å) than its terminal Cr–$F_{2,3}$ bonds (1.781 Å) owing to the *trans*-influences of the Cr–O bonds, and to the different coordination number of the bridged and terminal fluorine atoms.

The F atoms of the $[Cr_2O_4F_6]^{2-}$ dianions in the gas-phase ion-pairs **1′**–**3′** form secondary Xe---F bonds with the $[XeF_5]^+$ cations (**1′**, 2.421 and 2.522 Å; **2′**, 2.4798 and 3.1502 Å; **3′**, 2.4642 and 2.6655 Å) that are significantly shorter than the sum of the Xe and F van der Waals radii (vide supra). In the cases of **2′** and **3′**, secondary Xe---F_H and Xe---F_{XeOF_4} bonds are also formed (**2′**, 2.4771 Å; **3′**, 3.3951 Å). These interactions significantly elongate the Cr–$F_{1,1A}$ bridge bonds (**1′**, 2.135 Å; **2′**, 2.150 Å; **3′**, 2.150 Å) and terminal Cr–$F_{2,3}$ bonds (**1′**, 1.831 Å; **2′**, 1.818 Å; **3′**, 1.828 Å) relative to the gas-phase values of $[Cr_2O_4F_6]^{2-}$ (Cr–$F_{1,1A}$: 2.068 Å; Cr–$F_{2,3}$: 1.781 Å). The elongations are accompanied by contracted Cr–O bonds (**1′**, 1.520 Å; **2′**, 1.520 Å; **3′**, 1.519 Å) relative to gas-phase $[Cr_2O_4F_6]^{2-}$ (1.552 Å). Thus, ion-pair formation elongates the Cr–F bonds and contracts the Cr–O bonds of **1′–3′** relative to those of gas-phase $[Cr_2O_4F_6]^{2-}$. Hydrogen bonding of HF to the $F_{1,1A}$ atoms in **2′** and coordination of $XeOF_4$ in **3′** result in longer Cr–$F_{1,1A}$ bridge bonds and shorter Cr–$F_{2,3}$ terminal bonds relative to **1′** (vide supra).

10.2.4.1.2. $[CrO_2F_4]^{2-}$ and $[XeF_5][Xe_2F_{11}][CrO_2F_4]$ (4′). The gas-phase geometries of $[CrO_2F_4]^{2-}$ and **4′** optimized to C_{2v} and C_s symmetries, respectively. The Cr–$F_{1,2}$ bonds of gas-phase $[CrO_2F_4]^{2-}$ (1.930 Å) are significantly longer than the Cr–$F_{3,4}$ bonds (1.856 Å) due to the *trans*-influence of the Cr–O double bonds (1.570 Å). The $[CrO_2F_4]^{2-}$ anion in **4′** ion-pairs with $[XeF_5]^+$ and $[Xe_2F_{11}]^+$ through short secondary Xe---F_{Cr} bonds (Xe---$F_{1,2}$, 2.387 and 2.398 Å; Xe---$F_{3,4}$, 2.3872–2.8574 Å) that are comparable in length to those calculated for **1′**–**3′**. Ion-pairing significantly elongates the Cr–$F_{1,2}$ bonds (2.208 Å) and shortens the Cr–$F_{3,4}$ bonds (1.7797, 1.799 Å) and Cr–O bonds (1.520 Å) relative to gas-phase $[CrO_2F_4]^{2-}$ (vide supra).

10.2.4.2. Natural Bond Orbital (NBO) Analysis

The natural atomic orbital (NAO) analyses of gas-phase CrO_2F_2, $[Cr_2O_4F_6]^{2-}$, and $[CrO_2F_4]^{2-}$ (Tables A7.16–A7.22) show trends of decreasing natural population analysis (NPA) charges for all atoms with increasing net negative charge: CrO_2F_2 > $[Cr_2O_4F_6]^{2-}$ > $[CrO_2F_4]^{2-}$. The Cr atom valences increase and the O atom valences and Cr–O WBIs decrease in the same order. The Cr–O WBIs of $[CrO_2F_4]^{2-}$ (1.809) are less than those of $[Cr_2O_4F_6]^{2-}$ (1.860), in accord with the greater WBIs of the *trans*-Cr–$F_{1,2}$ bonds of $[CrO_2F_4]^{2-}$ (0.460) relative to those of the *trans*-Cr–$F_{1,1A}$ bonds of $[Cr_2O_4F_6]^{2-}$ (0.268). In contrast, the WBIs of the Cr–$F_{2,3}$ bonds of $[Cr_2O_4F_6]^{2-}$ (0.654) are greater than those of Cr–$F_{3,4}$ in $[CrO_2F_4]^{2-}$ (0.540). Thus, the Cr–O and *cis*-Cr–F bonds in $[Cr_2O_4F_6]^{2-}$ and $[CrO_2F_4]^{2-}$ become more ionic as the covalent characters of the *trans*-Cr–F bonds increase.

The cations and dianions of **1′–3′** are intimately ion-paired (Tables A7.17–A7.19), as exemplified by the net charges of the ions ($[XeF_5]^+$, 0.759–0.807; $[Cr_2O_4F_6]^{2-}$, −1.520 to −1.604) which indicate significant degrees of charge transfer from the dianion to cation. The ions pair through primarily electrostatic Xe---$F_{1,1A}$ and Xe---$F_{2,3}$ bridge bonds that have correspondingly small WBIs (0.011–0.085 and 0.084–0.108, respectively). Ion-pairing in **1′–3′** increases the WBIs of the Cr–O bonds (2.037–2.053) and decreases the WBIs of the Cr–$F_{2,3}$ (0.501–0.515) and Cr–$F_{1,1A}$ (0.181–0.203) bonds relative to gas-phase $[Cr_2O_4F_6]^{2-}$. These interactions also result in more positive NPA charges on Cr and O and more negative charges on the bridging $F_{1,1A}$ and terminal $F_{2,3}$ atoms of **1′–3′**, which is consistent with more covalent Cr–O bonds and more ionic Cr–F bonds relative to the free $[Cr_2O_4F_6]^{2-}$ dianion. The

valences of O and $F_{1,1A}$ in **1′–3′** also increase relative to those of $[Cr_2O_4F_6]^{2-}$, whereas the Cr and $F_{2,3}$ valences decrease.

The coordinated HF molecules of **2′** interact with the cations through secondary Xe---F_H bonds (WBI, 0.103), and interact with one another (WBI, 0.148) and with the anion (WBI, 0.131) through F---H_F hydrogen bonds. These interactions result in more positive NPA charges on O, higher valences for O and $F_{2,3}$, and greater WBIs for the Cr–O and Cr–$F_{2,3}$ bonds of **2′** relative to those of **1′**. This is accompanied by more negative charges on $F_{1,1A}$ and $F_{2,3}$, and decreased Cr–$F_{1,1A}$ WBIs and Cr and $F_{1,1A}$ atom valences for **2′** relative to **1′**. Thus, HF coordination in **2′** increases the ionic characters of the Cr–$F_{1,1A}$ bonds and the covalent characters of the Cr–O and Cr–$F_{2,3}$ bonds relative to **1′**. In the case of **3′**, coordination of $XeOF_4$ through secondary Xe---F bonding interactions (WBIs 0.061 and 0.090) results in more positive O atom charges, increased Cr, O, and $F_{2,3}$ valences and Cr–O WBIs, more negative $F_{1,1A}$ charges, and decreased $F_{1,1A}$ valences and Cr–F WBIs relative to **1′**. This indicates greater degrees of ionic characters for the Cr–F bonds and covalent characters for the Cr–O bonds of **3′** relative to **1′**.

The cations and dianion of **4′** are intimately ion-paired (Table A7.19), with calculated charges that indicate a significant degree of dianion to cation charge transfer ($[XeF_5]^+$, 0.712; $[Xe_2F_{11}]^+$, 0.761; $[CrO_2F_4]^{2-}$, −1.472). The WBIs of the secondary Xe---F bonds of **4′** (Xe---$F_{1,2}$, 0.125, 0.134; Xe---$F_{3,4}$, 0.026, 0.079) are consistent with primarily electrostatic interactions. The WBIs of the highly polar-covalent Cr–$F_{1,2}$ bonds (0.151) of **4′** are significantly lower than in gas-phase $[CrO_2F_4]^{2-}$ (vide supra) due to polarization by strong secondary Xe---$F_{1,2}$ bonds. Consequently, the WBIs of the Cr–O (2.024) and Cr–$F_{3,4}$ (0.566 and 0.568) bonds of

4′ are greater than in gas-phase $[CrO_2F_4]^{2-}$ (vide supra). Ion pairing also results in more positive charges on Cr, O, and $F_{3,4}$; more negative charges on $F_{1,2}$; increased atom valences for O and $F_{3,4}$; and decreased Cr and $F_{1,2}$ valences for **4′** relative to $[CrO_2F_4]^{2-}$. These observations are consistent with more covalent Cr–O and Cr–$F_{3,4}$ bonds and more ionic Cr–$F_{1,2}$ bonds for **4′** relative to gas-phase $[CrO_2F_4]^{2-}$.

10.2.4.3. Molecular Electrostatic Potential Surface (MEPS) Analyses

The MEPS of CrO_2F_2, $[Cr_2O_4F_6]^{2-}$, and $[CrO_2F_4]^{2-}$ are depicted in Figure 10.10. The negative electrostatic potential (EP) maxima (kJ mol^{-1}) of CrO_2F_2 are located on the F atom isosurfaces (−42) and are similar in magnitude to those calculated for the F atom isosurfaces of MOF_4 (M = Cr, Mo, W, i.e., Cr, −33; Mo, −46; and W, −47)[243] at the same level of theory. Two positive EP maxima (151) on Cr are trans to the Cr–O double bonds and are significantly less than the EP maximum of $CrOF_4$ (218), consistent with a lower fluoride affinity of CrO_2F_2 relative to that of $CrOF_4$.

The EP minima of $[Cr_2O_4F_6]^{2-}$ (−979) and $[CrO_2F_4]^{2-}$ (−1124) lie at the intersections of the $F_{1,1A}$ and $F_{2,3}$ isosurfaces of $[Cr_2O_4F_6]^{2-}$ and at the intersections of the $F_{1,2}$ and $F_{3,4}$ isosurfaces of $[CrO_2F_4]^{2-}$. Local EP minima are also located on the $F_{1,1A}$ (−858) and $F_{2,3}$ (−774) isosurfaces of $[Cr_2O_4F_6]^{2-}$ and the $F_{1,2}$ (−885) and $F_{3,4}$ (−827) isosurfaces of $[CrO_2F_4]^{2-}$, which reflect their relative F-atom fluorobasicities.

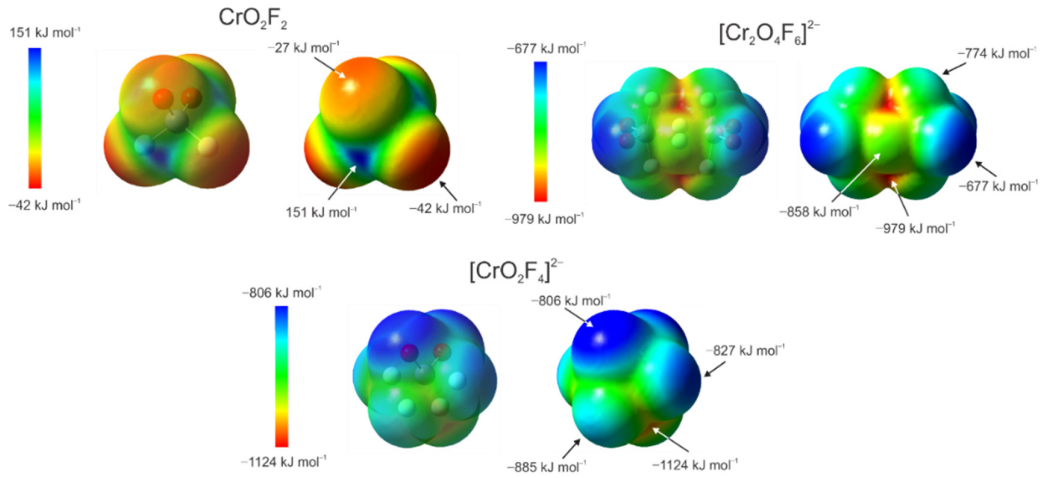

Figure 10.10. The molecular electrostatic potential surface (MEPS) contours at the 0.001 e bohr^{-3} isosurface were calculated at the PBE1PBE/Def2-SVP level of theory for CrO_2F_2, $[Cr_2O_4F_6]^{2-}$, and $[CrO_2F_4]^{2-}$. Positive and negative electrostatic potential extrema are indicated by arrows.

The MEPS isosurfaces of $[XeF_5]^+$ and $[Xe_2F_{11}]^+$ are depicted in Figure 10.11. Examination of a narrow range of high positive EP values for $[XeF_5]^+$ (735–780) shows four localized EP maxima (780) on the Xe isosurface that are located trans to the Xe–F_{ax} bond at the intersections of the F_{eq} isosurfaces. A similar examination of a narrow range of high positive EP values for $[Xe_2F_{11}]^+$ (603–643) shows only one maximum on each Xe atom isosurface (643) that is located at the intersection of the F_b and F_{eq} isosurfaces. Comparison of the EP maxima on the Xe atoms of $[XeF_5]^+$ and $[Xe_2F_{11}]^+$ indicates that $[XeF_5]^+$ is more Lewis acidic. The trajectories of the secondary Xe---F bonds of **1**–**4** and **1′**–**4′** are directed towards regions of highest positive EP on $[XeF_5]^+$ and $[Xe_2F_{11}]^+$, and supports their description as predominantly electrostatic, σ-hole bonds.

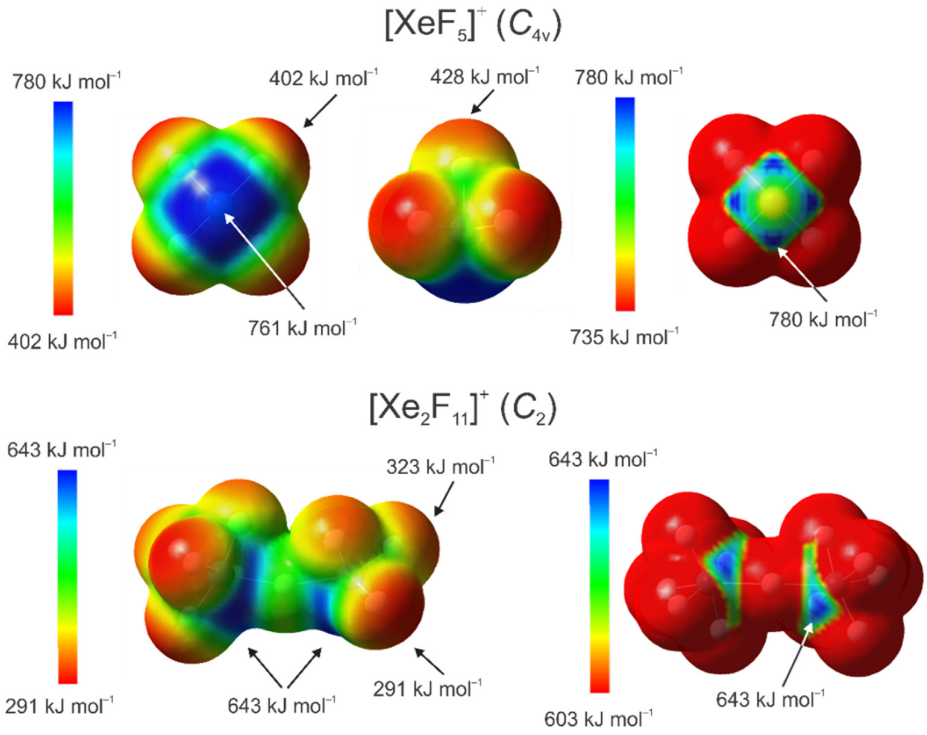

Figure 10.11. The molecular electrostatic potential surface (MEPS) contours at the 0.001 e bohr^{-3} isosurfaces were calculated at the PBE1PBE/Def2-SVP level of theory for $[XeF_5]^+$ and $[Xe_2F_{11}]^+$. The positive electrostatic potential extrema are indicated by arrows.

10.3. Conclusions

The chemistry of Cr(VI) oxide fluoride species is more limited than that of M(VI) (M = Mo, W). Although salts of the $[M_2O_4F_6]^{2-}$ and $[MO_2F_4]^{2-}$ anions have been characterized by SCXRD, no salts of $[Cr_2O_4F_6]^{2-}$ or $[CrO_2F_4]^{2-}$ had been crystallographically characterized. The syntheses and structural characterizations of $[XeF_5]_2[Cr_2O_4F_6]$, $[XeF_5]_2[Cr_2O_4F_6]\cdot 4HF$, $[XeF_5]_2[Cr_2O_4F_6]\cdot 2XeOF_4$, and $[XeF_5][Xe_2F_{11}][CrO_2F_4]$ by LT Raman spectroscopy and SCXRD described in this work completes the series of structurally characterized Cr(VI) oxide fluoride anions

$[CrO_3F]^-$, $[CrOF_5]^-$, $[Cr_2O_4F_6]^{2-}$, and $[CrO_2F_4]^{2-}$, and the series of crystallographically characterized $[M_2O_4F_6]^{2-}$ and $[MO_2F_4]^{2-}$ (M = Cr, Mo, W) anions. Their characterization by vibrational spectroscopy also provides the first Raman spectroscopic study of salts containing the $[Cr_2O_4F_6]^{2-}$ and $[CrO_2F_4]^{2-}$ anions that have been fully assigned with the aid of quantum-chemical calculations. The $[Cr_2O_4F_6]^{2-}$ (dimer of $[CrO_2F_3]^-$) and $[CrO_2F_4]^{2-}$ anions were stabilized by the oxidatively resistant noble-gas cations $[XeF_5]^+$ and $[Xe_2F_{11}]^+$, which have previously been used to isolate other high-oxidation-state transition-metal oxyfluoro-anion salts.[121,243,244] The Cr(VI) oxyfluoro-anion salts were prepared by reaction of XeF_6 with CrO_2F_2 in the oxidatively resistant solvent aHF and by direct reaction in melts at elevated temperatures (ca. 50 °C). NBO analyses show that the salts are intimately ion-paired through primarily electrostatic Xe---F_{Cr} bonds. Quantum-chemical calculations indicate significant degrees of negative charge transfer from the dianions to the cations in their ion-pairs, and that secondary Xe---F_{Cr} bonds influence the covalent characters of the Cr–O and Cr–F bonds. MEPS analyses show the secondary Xe---F_{Cr} bonds are directed towards regions of high positive EP on $[XeF_5]^+$ and $[Xe_2F_{11}]^+$.

CHAPTER 11

Group 6 Oxyfluoro-anion Salts of $[XeF_5]^+$ and $[Xe_2F_{11}]^+$; Syntheses and Structures of $[XeF_5][M_2O_2F_9]$ (M = Mo, W), $[Xe_2F_{11}][M'OF_5]$ (M' = Cr, Mo, W), $[XeF_5][HF_2]\cdot CrOF_4$, and $[XeF_5][WOF_5]\cdot XeOF_4$

Adapted with permission from: Bortolus, M. R.; Mercier, H. P. A.; Schrobilgen, G. J. *Chem. Eur. J.* **2020**, *26*, 8935–8950.

11.1. Introduction

The Group 6 oxide tetrafluorides, M′OF_4 (M = Cr, Mo, W), are significantly weaker Lewis acids and fluoride-ion acceptors than PF_5, AsF_5, SbF_5, and BiF_5. The Group 15 pentafluorides abstract fluoride ion from NgF_2 (Ng = Kr, Xe) to form ion-paired $[NgF]^+$ salts of the $[PnF_6]^-$ (Pn = P[46] As,[46,48,51] Sb,[46,48,51,179] Bi[46,48]) and $[Pn'_2F_{11}]^-$ (Pn′ = Sb,[48,51,179–181] Bi[48]) anions. This contrasts with the Group 6 oxide tetrafluorides which do not abstract fluoride ion from NgF_2, but form series of adducts having the general formulae $NgF_2\cdot n$M′OF_4 (n = 1, 2).[65,67] In both $NgF_2\cdot$M′OF_4 (M′ = Mo, W, Cr) and $XeF_2\cdot 2MOF_4$ (M = Mo, W), a single fluorine atom of NgF_2 coordinates to the metal, trans to the axial M′–O bond and trans to an M–O bond, to form FNgF---M′(O)F_4 [65–67,182–184,306] and FXeF---M(O)F_3F---M(O)F_4,[67,183,184,306] respectively. In contrast, both F atoms of NgF_2 coordinate to two $CrOF_4$ molecules in $NgF_2\cdot 2CrOF_4$ to give F_4(O)Cr---FNgF---Cr(O)F_4.[65]

The Group 6 oxide tetrafluorides readily abstract F^- from strong fluoride-ion donors such as NOF and the alkali metal fluorides to form salts of the $[M'OF_5]^-$ (Cr,[66,264,270] Mo,[283–287,298] W[283–285,288,292–296,329–331]), $[M_2O_2F_9]^-$ (Mo,[283,297,332,333] W[283,293,297,334–338]), and $[MOF_6]^{2-}$ [283] anions, which have been characterized in the solid state and in solution (Table 11.1). Although the $[WOF_5]^-$ [288,290,292,331] and

$[W_2O_2F_9]^-$ [336–338] anions have been previously characterized by Xray crystallography, several structures suffer from O/F positional disorders and/or are of low precision. Subsequent to the authors′ preliminary reports of $[Xe_2F_{11}][M'OF_5]$ and $[XeF_5][M_2O_2F_9]$, the structural characterization of the $[MOF_5]^-$ anions in $K_3[MOF_7]$,[298,331] and the $[M_2O_2F_9]^-$ anions in their Li^+-Cs^+ salts were reported.[297,339] Although the Cs^+,[264] $[NO]^+$,[66] and $[Sn(CH_3)_2F]^+$ [270] salts of $[CrOF_5]^-$ have been characterized by vibrational spectroscopy,[66,264,270] elemental analysis,[66,264,270] and X-ray powder diffraction (unindexed d-spacings were reported for $[NO][CrOF_5]$),[66] no crystal structures of $[CrOF_5]^-$ or $[Cr_2O_2F_9]^-$ salts have been forthcoming. Thermal decomposition of $[NO][CrOF_5]$ was reported to yield polyanion salts of Cr^{VI}, $[NO][CrOF_5]\cdot n CrOF_4$, based on the observation of new Cr-O and Cr-F stretching bands in the infrared spectrum of the pyrolysis product.[66] In contrast, a recent study showed that thermal decomposition of $[Xe_2F_{11}][CrOF_5]$ in melts and in aHF and $CFCl_3$ solutions resulted in F_2 elimination and salts of the Cr^V oxyfluoro-anions, $[CrOF_5]^{2-}$ and $[Cr_2O_2F_8]^{2-}$, which were characterized by single-crystal X-ray diffraction, low-temperature Raman spectroscopy, and quantum-chemical calculations.[244]

Anhydrous hydrogen fluoride (aHF) solutions of $MoOF_4$ and WOF_4 have been shown by Raman and ^{19}F NMR spectroscopy to partially self-ionize to form $[M_2O_2F_9]^-$ and $[H_2F]^+$.[283] The latter study also demonstrated that addition of the strong F^- ion donor, NOF, resulted in equilibrium mixtures of the $[NO]^+$ salts of $[M_2O_2F_9]^-$, $[MOF_5]^-$, and $[MOF_6]^{2-}$. Subsequent Raman and ^{19}F NMR spectroscopic studies of $CrOF_4$ in aHF solution[66] suggested that self-ionization may also give rise to $[Cr_2O_2F_9]^-$ and $[H_2F]^+$. These studies were inconclusive and did not provide

unambiguous proof for the formation of $[Cr_2O_2F_9]^-$ in aHF, nor were discrete salts of $[CrOF_5]^-$ and $[Cr_2O_2F_9]^-$ isolated from aHF solution.

Table 11.1. Summary of methods previously used for the characterizations of the $[M'OF_5]^-$ (M′ = Cr, Mo, W), $[M_2O_2F_9]^-$, and $[MOF_6]^{2-}$ (M = Mo, W) anions

Anion	Characterization Methods[a]
$[CrOF_5]^-$	Ra,[66,270] IR,[264] EA,[66,264,270] PXRD[66,b]
$[MoOF_5]^-$	Ra,[283,285,286] IR,[269,271] EA,[284,286,287] ^{19}F NMR,[283,284] CV,[286] PXRD,[283] LT PXRD[298]
$[WOF_5]^-$	Ra,[283,286,288,293,294,296] IR,[283,285,292–294,296,331] EA,[283,293,294,296] ^{19}F NMR,[283,293–295,329] PXRD,[283,296,331] RT SCXRD[288,290,292,294]LT PXRD[331]
$[Mo_2O_2F_9]^-$	Ra,[283,297] IR,[283,297] EA,[269] ^{19}F NMR,[283,332,333] PXRD,[283] LT SCXRD[297]
$[W_2O_2F_9]^-$	Ra,[283,293,339] IR,[283,293,339] EA,[283,293,339] ^{19}F NMR,[283,293,334–336] RT SCXRD[334,336–338], LT SCXRD[339]
$[MOF_6]^{2-}$ (M = Mo, W)	Ra, IR, PXRD[283]

[a] Abbreviations denote Raman spectroscopy (Ra), infrared spectroscopy (IR), elemental analysis (EA), solution nuclear magnetic resonance spectroscopy (NMR), cyclic voltammetry (CV), powder X-ray diffraction (PXRD), and single-crystal X-ray diffraction (SCXRD). [b] d-spacings were reported for $[NO][CrOF_5]$, but a unit cell was not determined.

Xenon hexafluoride is considerably more fluorobasic in aHF solution than either XeF_2 or XeF_4.[116] Raman[116] and ^{19}F NMR spectroscopic studies[340] have shown that XeF_6 ionizes in aHF to give equilibrium mixtures of $[XeF_5]^+$, $[Xe_2F_{11}]^+$, $([XeF_5]^+F^-)_4$, and $[(HF)_nF]^-$, whereas XeF_2 and XeF_4 do not ionize to a significant extent.[99] Several examples of $[XeF_5]^+$ and $[Xe_2F_{11}]^+$ transition-metal oxyfluoro-anion salts are known for Os^{VIII} and Cr^V, which have been structurally characterized by single-crystal Xray diffraction: $[XeF_5][OsO_3F_3]$,[121] $[Xe_2F_{11}][fac\text{-}OsO_3F_3]$,[121] $[XeF_5][\mu\text{-}F(OsO_3F_2)_2]$,[121] $[XeF_5]_2[Cr_2O_2F_8]$,[244] $[XeF_5]_2[Cr_2O_2F_8]\cdot 2HF$,[244] $[XeF_5]_2[Cr_2O_2F_8]\cdot 2XeOF_4$,[244] and $[XeF_5][Xe_2F_{11}][CrOF_5]\cdot 2CrOF_4$.[244] The recent LT Raman spectroscopic characterization of $[Xe_2F_{11}][CrOF_5]$ as a reaction intermediate in the synthesis of $[XeF_5][Xe_2F_{11}][CrOF_5]\cdot 2CrOF_4$ suggests that the $[MOF_5]^-$ (M = Mo, W) salts of $[XeF_5]^+$ and $[Xe_2F_{11}]^+$ should also form owing to the greater calculated fluoride-ion affinities (FIAs) of $MoOF_4$ (−355 kJ mol^{-1}) and WOF_4 (−386 kJ mol^{-1}) compared with that of $CrOF_4$ (−285 kJ mol^{-1}).[252] The high fluorobasicity of XeF_6 and

its extensive ionization in aHF solvent make it a viable fluoride-ion donor for the syntheses of stable $[XeF_5]^+$ and $[Xe_2F_{11}]^+$ salts of $[M'OF_5]^-$ and $[M_2O_2F_9]^-$ in aHF.

The present study reports the syntheses and structural characterizations of $[Xe_2F_{11}][CrOF_5]$ (**1**), $[XeF_5][HF_2]\cdot CrOF_4$ (**2**), $[Xe_2F_{11}][MoOF_5]$ (**3**), $[Xe_2F_{11}][WOF_5]$ (**4**), $[XeF_5][Mo_2O_2F_9]$ (**5**), $[XeF_5][W_2O_2F_9]$ (**6**), and $[XeF_5][WOF_5]\cdot XeOF_4$ (**7**) by LT single-crystal Xray diffraction and Raman spectroscopy. The study also provides the first structural characterization of a $[CrOF_5]^-$ salt and precise crystal structures of the $[MOF_5]^-$ and $[M_2O_2F_9]^-$ anions. Quantum-chemical calculations are employed to aid in the vibrational frequency assignments and discussions of the primary and secondary bonding in these salts.

11.2. Results and Discussion

11.2.1. Syntheses

11.2.1.1. $[Xe_2F_{11}][MOF_5]$ (M = Mo (3), W (4)), $[XeF_5][M_2O_2F_9]$ (M = Mo (5), W (6)), and $[XeF_5][WOF_5]\cdot XeOF_4$ (7).

Equilibria arising from the ionization of MOF_4 in aHF solvent have been previously investigated [Eqs. (**11.1**)–(**11.3**)][283] and shown to shift to the right with increasing $[(HF)_nF]^-$ concentration.

$$2MOF_4 + [(HF)_nF]^- \rightleftharpoons nHF + [M_2O_2F_9]^- \quad (n \geq 1) \qquad (\mathbf{11.1})$$

$$[M_2O_2F_9]^- + [(HF)_nF]^- \rightleftharpoons nHF + 2[MOF_5]^- \quad (n \geq 1) \qquad (\mathbf{11.2})$$

$$[MOF_5]^- + [(HF)_nF]^- \rightleftharpoons nHF + [MOF_6]^{2-} \quad (n \geq 1) \qquad (\mathbf{11.3})$$

In an unrelated study, the Raman spectra of XeF_6 in aHF solutions were studied as a function of initial XeF_6 concentration (ca. 0.3 to 5.0 M).[116] The XeF_6 tetramer, $([XeF_5]^+F^-)_4$, was shown to be the dominant species at high initial molar ratios (XeF_6/HF = 1:10), whereas solutions having intermediate initial molar ratios

(XeF_6/HF = 1:20) had $[Xe_2F_{11}]^+$ as the dominant cation, and dilute solutions (XeF_6/HF = 1:150) had $[XeF_5]^+$ as the dominant cation. The principal equilibria which describe the ionization of XeF_6 in aHF are given by Equations (**11.4**) and (**11.5**).

$$([XeF_5]^+F^-)_4 + 2n\text{HF} \rightleftharpoons 2[Xe_2F_{11}]^+ + 2[(\text{HF})_nF]^- \quad (n \geq 1) \qquad (\mathbf{11.4})$$

$$[Xe_2F_{11}]^+ + n\text{HF} \rightleftharpoons 2[XeF_5]^+ + [(\text{HF})_nF]^- \quad (n \geq 1) \qquad (\mathbf{11.5})$$

In the present work, $[Xe_2F_{11}][MOF_5]$ (Mo (**3**), W (**4**)) and $[XeF_5][M_2O_2F_9]$ (Mo (**5**), W (**6**)) were obtained by varying the initial molar ratios of XeF_6 and MOF_4 in dilute aHF solutions (XeF_6/HF molar ratios ranged from 1:70 to 1:313), in accordance with Equations (**11.1**)–(**11.5**). When a stoichiometric excess of XeF_6 was employed, the equilibria shifted to favor $[Xe_2F_{11}]^+$ and $[MOF_5]^-$, whereas a stoichiometric or limiting amount of XeF_6 favored $[XeF_5]^+$ and $[M_2O_2F_9]^-$ formation. The hydrolysis of $[Xe_2F_{11}][WOF_5]$ in aHF yielded HF, $[XeF_5]^+$, and $XeOF_4$ [Eq. (**11.6**)], which crystallized in the presence of $[WOF_5]^-$ to give **7**.

$$[Xe_2F_{11}][WOF_5] + H_2O \rightarrow [XeF_5][WOF_5] + XeOF_4 + 2\text{HF} \qquad (\mathbf{11.6})$$

11.2.1.2. Attempted Syntheses of $[XeF_5][MOF_5]$ (M = Mo, W) in $CFCl_3$.

In an attempt to circumvent $[Xe_2F_{11}][MOF_5]$ and $[XeF_5][M_2O_2F_9]$ formation, the syntheses of $[XeF_5][MOF_5]$ were attempted in $CFCl_3$ solvent and reactions were periodically monitored by LT (−150 °C) Raman spectroscopy in order to semiquantitatively determine the dominant species in the frozen (quenched) samples (see Experimental Section). The reaction of equimolar amounts of XeF_6 and $MoOF_4$ in $CFCl_3$ at −78 to −15 °C yielded a mixture of $MoOF_4$, XeF_6, and $[Xe_2F_{11}][MoOF_5]$ in which $[Xe_2F_{11}][MoOF_5]$ dominated. Further reaction at −15 to 25 °C yielded a mixture of $MoOF_4$, $[Xe_2F_{11}][MoOF_5]$, and $[XeF_5][Mo_2O_2F_9]$ in which $[Xe_2F_{11}][MoOF_5]$ dominated, but XeF_6 was not detected in the Raman spectrum. The

reaction of XeF_6 and WOF_4 in $CFCl_3$ at RT yielded a mixture of WOF_4, $[Xe_2F_{11}][WOF_5]$, and $[XeF_5][W_2O_2F_9]$ in which $[Xe_2F_{11}][WOF_5]$ was the dominant species. Crystalline $[XeF_5][W_2O_2F_9]$ was also identified by unit cell determinations.

Xenon hexafluoride is not expected to ionize in $CFCl_3$, but is likely present as its tetramer, $([XeF_5]^+F^-)_4$.[104] A plausible equilibrium describing fluoride-ion abstraction from the tetramer to yield the strongly ion-paired salts, $[Xe_2F_{11}][MOF_5]$ (M = Mo, W), is given by Eq. (**11.7**). Dominance of $[Xe_2F_{11}][MOF_5]$ in the reaction of XeF_6 with MOF_4 in $CFCl_3$ solvent and consumption of XeF_6 upon warming the reaction mixture to 25 °C indicated that the proposed equilibrium [Eq. (**11.7**)] favors $[Xe_2F_{11}][MOF_5]$ formation. Fluoride-ion abstraction from $[Xe_2F_{11}][MOF_5]$ by MOF_4 presumably yields two equivalents of $[XeF_5][MOF_5]$ according to Eq. (**11.8**) which, in turn, react with MOF_4 to form $[XeF_5][M_2O_2F_9]$ according to Eq. (**11.9**). Because $[XeF_5][MOF_5]$ was not observed and reaction mixtures that had been warmed to room temperature yielded $[Xe_2F_{11}][MOF_5]$, $[XeF_5][M_2O_2F_9]$, and MOF_4; it may be inferred that the equilibria [Eqs. (**11.8**) and (**11.9**)] lie to the left and to the right, respectively.

$$([XeF_5]^+F^-)_4 + 2MOF_4 \rightarrow [Xe_2F_{11}][MOF_5] \quad (\mathbf{11.7})$$

$$[Xe_2F_{11}][MOF_5] + MOF_4 \rightarrow 2[XeF_5][MOF_5] \quad (\mathbf{11.8})$$

$$[XeF_5][MOF_5] + MOF_4 \rightarrow [XeF_5][M_2O_2F_9] \quad (\mathbf{11.9})$$

11.2.1.3. $[Xe_2F_{11}][CrOF_5]$ (1) and $[XeF_5][HF_2]\cdot CrOF_4$ (2).

Unlike $MoOF_4$ and WOF_4, the reaction of $CrOF_4$ with XeF_6 in aHF did not yield either a $[CrOF_5]^-$ or a $[Cr_2O_2F_9]^-$ salt. The room-temperature reaction of XeF_6 and $CrOF_4$ in aHF was recently shown to form the Cr^V oxyfluoro-anion salt, $[XeF_5]_2[Cr_2O_2F_8]\cdot 2XeOF_4$, through a multi-step pathway which involved reductive

elimination of F_2 and O/F metathesis.[244] In an attempt to prevent Cr^{VI} reduction, the LT (−78 to 0 °C) reaction of XeF_6 and $CrOF_4$ in aHF was carried out, however, only α-$CrOF_4$, β-$CrOF_4$, and $[XeF_5][HF_2]$ were identified in the reaction mixture by determinations of their unit cells. When a 2.21:1 molar ratio of $XeF_6/CrOF_4$ was allowed to react at 0 °C in aHF (initial molar ratio of XeF_6/HF = 1:100), the Cr^{VI} adduct, **2**, formed as the sole product, which was isolated from solution along with a small quantity of unreacted crystalline XeF_6 (identified by unit cell determinations). Unlike $MoOF_4$ and WOF_4, $CrOF_4$ is incapable of abstracting F^- from $[(HF)_nF]^-$ at 0 °C in aHF solution, and forms **2** instead, in accordance with the low fluoride-ion affinity of $CrOF_4$.

To avoid $[XeF_5][HF_2]$ formation, the reaction of XeF_6 and $CrOF_4$ was carried out in the oxidatively resistant solvent, CF_2ClCF_2Cl. This reaction resulted in fluoride-ion abstraction from XeF_6 by $CrOF_4$ to give **1** [Eq. (**11.7**)]. The room-temperature reactions of XeF_6 and $CrOF_4$ in aHF and in $CFCl_3$/HF mixtures had been previously shown to yield Cr^V oxyfluoro-anion salts by reductive elimination of F_2.[244] Consequently, the synthesis of $[XeF_5][Cr_2O_2F_9]$ by reaction of $[Xe_2F_{11}][CrOF_5]$ with excess $CrOF_4$ at room temperature in CF_2ClCF_2Cl was not investigated.

11.2.2. X-ray Crystallography

Details of X-ray data collection and crystallographic information pertaining to $[Xe_2F_{11}][CrOF_5]$ (**1**), $[XeF_5][HF_2]\cdot CrOF_4$ (**2**), $[Xe_2F_{11}][MoOF_5]$ (**3**), $[Xe_2F_{11}][WOF_5]$ (**4**), $[XeF_5][Mo_2O_2F_9]$ (**5**), $[XeF_5][W_2O_2F_9]$ (**6**), and $[XeF_5][WOF_5]\cdot XeOF_4$ (**7**) are provided in Table 11.2.

The crystal structures of **1**–**7** (Figures 11.1–11.5 and Figures A8.1–A8.3 of Appendix 8) are best described as ion-pairs in which the Lewis acidic $[XeF_5]^+$ and

$[Xe_2F_{11}]^+$ cations form fluorine bridges with their respective anions by means of Xe---F secondary bonds. The latter bonds are significantly shorter than the sum of the Xe and F van der Waals radii (3.61 Å,[167] 3.52 Å)[168] (Tables A8.1–A8.6 of Appendix 8). Each cation and anion of **1**, **2**, **5**, and **6** interacts with two anions and two cations, respectively, to form dimeric structural units that pack along the *a*-axes of their unit cells. The dimeric units of **1**, **5**, and **6** are well-separated with no significant intermolecular contacts, whereas compound **2** crystallizes in sheets that are bridged by long Xe---F_{CrOF4} contacts to neighboring sheets (Figure A8.4). Compounds **3** and **4** are isotypic and form six-membered rings (lying in the *bc*-planes of their unit cells) that interact with one another through long Xe---F_{eq} contacts to form columns which stack parallel to the *a*-axes of their unit cells (Figure A8.5). Although **1** has a molecular formula that is analogous to those of **3** and **4**, its crystal structure is not isotypic with the crystal structures of the latter compounds (Table 11.2). Compound **7** crystallizes in chains that result from short secondary bonding interactions between $[XeF_5]^+$ and $[WOF_5]^-$. The chains run parallel to the *a*-axis and alternate with columns of cocrystallized $XeOF_4$ molecules that are parallel to the *b*-axis (Figure A8.6).

Table 11.2. Summary of X-ray crystal data and refinement results for $[Xe_2F_{11}][CrOF_5]$ (1), $[XeF_5][HF_2]\cdot CrOF_4$ (2), $[Xe_2F_{11}][MoOF_5]$ (3), $[Xe_2F_{11}][WOF_5]$ (4), $[XeF_5][Mo_2O_2F_9]$ (5), $[XeF_5][W_2O_2F_9]$ (6), and $[XeF_5][WOF_5]\cdot XeOF_4$ (7)

	1	**2**	**3**	**4**	**5**	**6**	**7**
space group	$P\bar{1}$	$P\bar{1}$	$P2_1/n$	$P2_1/n$	$P\bar{1}$	$P\bar{1}$	$P2_1/m$
a (Å)	7.5409(6)	6. 3011(4)	8.6130(7)	8.6465(3)	8.0652(4)	8.105(5)	5.5727(5)
b (Å)	9.4357(6)	7.8902(6)	8.7822(9)	8.8270(3)	8.9035(5)	8.919(5)	8.6980(7)
c (Å)	9.7089(6)	8.6923(5)	15.6503(14)	15.6220(6)	8.9681(5)	8.971(8)	12.1256(11)
α (deg)	63.205(2)	92.315(3)	90	90	85.270(2)	85.00(7)	90
β (deg)	89.251(3)	102.700(3)	94.716(5)	94.994(2)	74.702(2)	75.46(5)	101.422(4)
γ (deg)	68.274(2)	100.824(3)	90	90	70.945(2)	71.12(5)	90
V (Å^3)	562.90(7)	412.57(5)	1179.80(19)	1187.79(7)	587.13(6)	593.9(8)	576.10(9)
Z[a]	2	2	4	4	2	2	2
M_W[b]	634.60	409.31	678.54	766.45	621.18	797.00	744.45
ρ_{calcd}[c]	3.744	3.295	3.820	4.286	3.514	4.457	4.292
T (ºC)	–173	–173	–173	–173	–173	–173	–173
μ [d]	7.147	5.584	6.963	15.537	5.153	22.336	15.992
R_1[e]	0.0238	0.0209	0.0384	0.0340	0.0236	0.0448	0.0442
wR_2[f]	0.0581	0.0547	0.0922	0.0786	0.0519	0.1392	0.0989

[a] Molecules/unit cell. [b] g mol^{-1}. [c] g cm^{-3}. [d] mm^{-1}. [e] $R_1 = \Sigma||F_o| - |F_c||/\Sigma|F_o|$. [f] $wR_2 = [\Sigma(w(F_o^2 - F_c^2)^2)/\Sigma(w(F_o^2)^2)]^{1/2}$.

11.2.2.1. $[XeF_5]^+$ and $[Xe_2F_{11}]^+$. The primary bond lengths and bond angles of $[XeF_5]^+$ and $[Xe_2F_{11}]^+$ in all seven salts (Tables A8.1–A8.6 of Appendix 8) are comparable to those of other fluoro- and oxyfluoro-anion salts of $[XeF_5]^+$ and $[Xe_2F_{11}]^+$, e.g., $[Xe_2F_{11}][AuF_6]$,[308] $[Xe_2F_{11}]_2[NiF_6]$,[118] $[Xe_2F_{11}][SbF_6]$,[341] $[XeF_5]_3[Ti_4F_{19}]$,[309] $[XeF_5]_2[PdF_6]$,[311] $[XeF_5][AsF_6]$,[312] $[XeF_5][SbF_6]\cdot XeOF_4$,[314] $[XeF_5][PtF_6]$,[310] $[XeF_5][AgF_4]$,[117] $[XeF_5][CrF_5]\cdot XeF_4$,[93] $[XeF_5][BF_4]$,[341] $[XeF_5][OsO_3F_3]$, $[Xe_2F_{11}][fac\text{-}OsO_3F_3]$, $[XeF_5][\mu\text{-}F(OsO_3F_2)_2]$,[121] $[XeF_5]_2[CrF_6]\cdot 2CrOF_4$, $[Xe_2F_{11}]_2[CrF_6]$, $[XeF_5]_2[Cr_2O_2F_8]$, $[XeF_5]_2[Cr_2O_2F_8]\cdot 2XeOF_4$, and $[XeF_5][Xe_2F_{11}][CrOF_5]\cdot 2CrOF_4$,[244] and are not discussed further.

Each Xe atom of both $[Xe_2F_{11}]^+$ cations in the dimeric structural unit of $[Xe_2F_{11}][CrOF_5]$ (**1**) has one short Xe---F_{ax} (2.5065(9) Å, 2.5687(9) Å) and one long Xe---F_{eq} (2.814(1) Å, 2.862(1) Å) contact with a $[CrOF_5]^-$ anion of the dimeric unit. In contrast, the $[Xe_2F_{11}]^+$ cations of $[Xe_2F_{11}][MoOF_5]$ (**3**) and $[Xe_2F_{11}][WOF_5]$ (**4**) (CN_{Xe} = 8) have short Xe---F secondary bonding interactions with the F_{ax} ligand (Mo, 2.348(2) Å; W, 2.405(2) Å) and one F_{eq} ligand (Mo, 2.640(2) Å; W, 2.661(2) Å) of $[MOF_5]^-$ (M = Mo, W), and two long interionic Xe---F_{eq} contacts (Mo, 2.969(2) Å, 3.072(2) Å; W, 2.966(2) Å, 3.057(2) Å) with two F_{eq} ligands of two neighboring $[MOF_5]^-$ anions. The $[XeF_5]^+$ cations of **5** and **6** (CN_{Xe} = 9) have two short (Mo, 2.6438(9) Å, 2.6553(8) Å; W, 2.677(5) Å, 2.681(5) Å) and two long (Mo, 2.8987(9) Å, 2.9828(9) Å; W, 2.888(5) Å, 2.990(5) Å) interionic Xe---F_{eq} contacts with two adjacent $[M_2O_2F_9]^-$ anions. In contrast, the $[XeF_5]^+$ cation of **7** has two short Xe---F secondary bonding interactions with one F_{ax} ligand (2.357(4) Å) and one F_{eq} ligand (2.689(4) Å) of two neighboring $[WOF_5]^-$ anions (next nearest Xe---F distance is 3.131(3) Å), and provides the first example of an $[XeF_5]^+$ cation for which CN_{Xe} = 7.

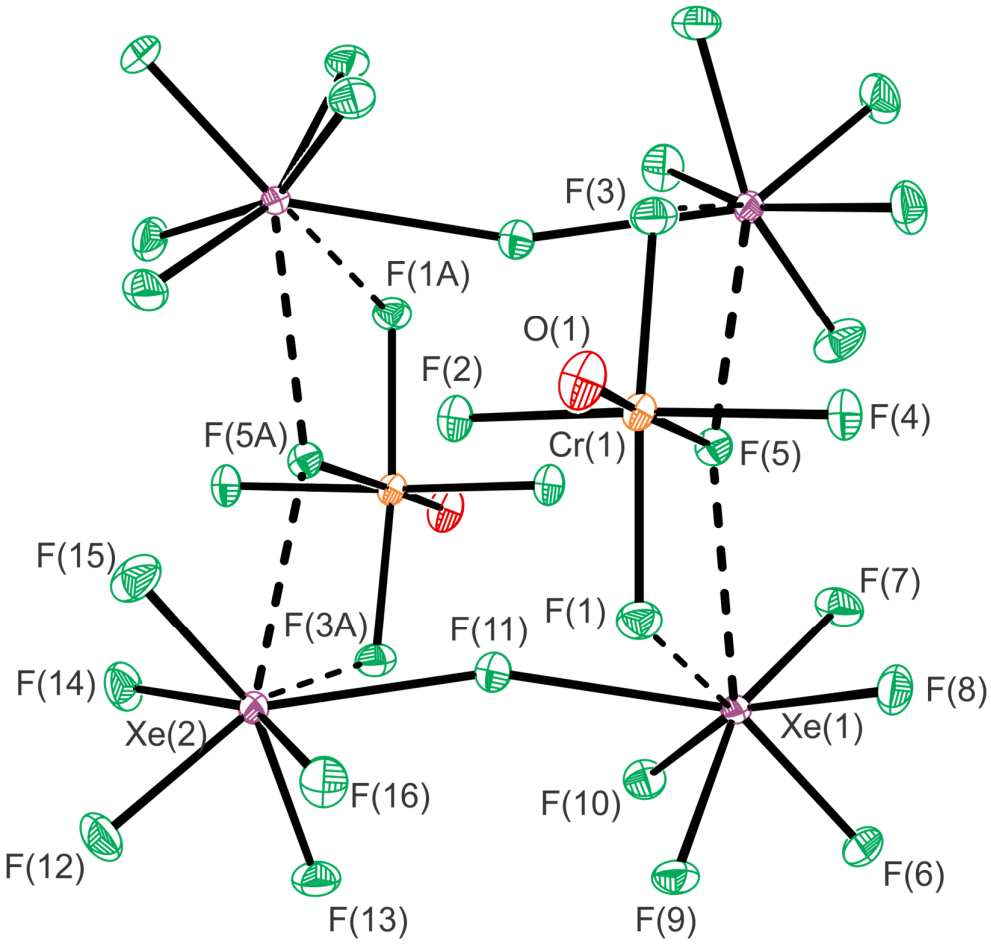

Figure 11.1. The dimeric structural unit in the X-ray crystal structure of $[Xe_2F_{11}][CrOF_5]$ (**1**) with thermal ellipsoids drawn at the 50% probability level. Secondary Xe---F and Cr---F bonding interactions are indicated by dashed lines.

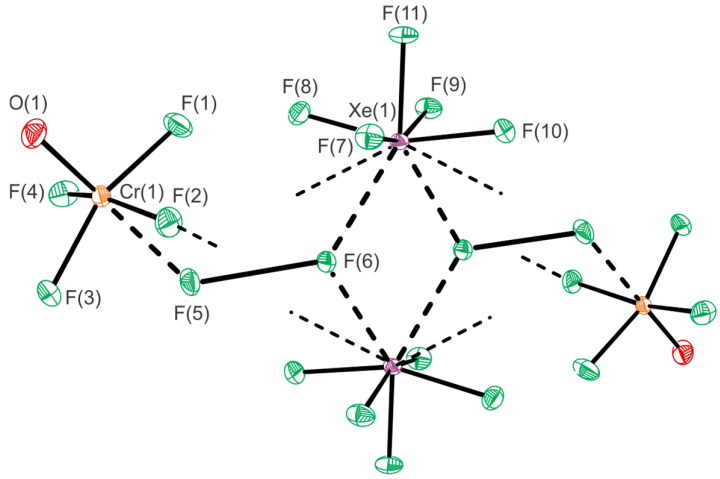

Figure 11.2. The dimeric structural unit in the X-ray crystal structure of $[XeF_5][HF_2]\cdot CrOF_4$ (**2**) with thermal ellipsoids drawn at the 50% probability level. Secondary Xe---F and Cr---F bonding interactions are indicated by dashed lines.

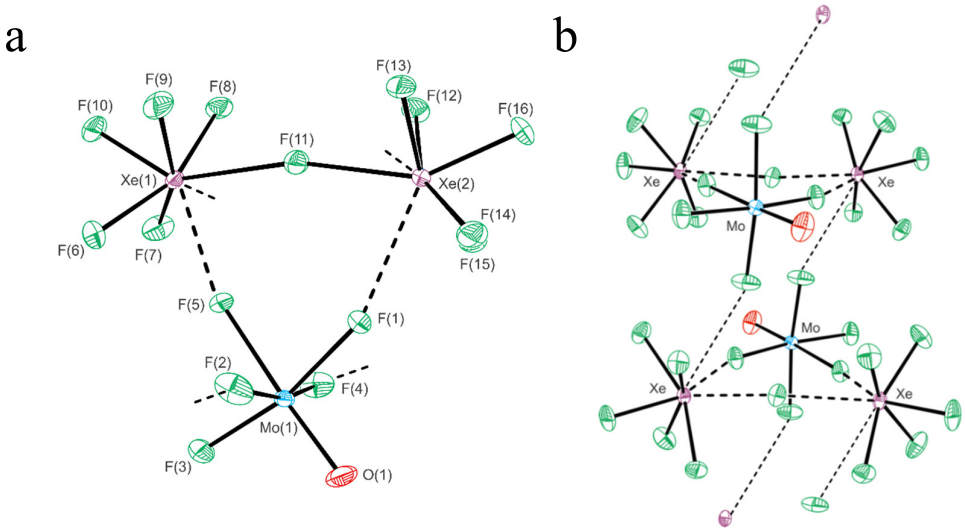

Figure 11.3. (a) The structural unit in the X-ray crystal structure of $[Xe_2F_{11}][MoOF_5]$ (**3**) with thermal ellipsoids drawn at the 50% probability level. (b) A diagram showing the stacking of the structural units of **3** in columns along the *a*-axis of the unit cell. Secondary Xe---F and Mo---F bonding interactions are indicated by dashed lines. The structural unit in the X-ray crystal structure of the isotypic $[Xe_2F_{11}][WOF_5]$ (**4**) salt is shown in Figure A8.1 of Appendix 8.

11.2.2.2. ***[M′OF$_5$]$^-$ (M′ = Cr, Mo, W).*** The crystal structure of **1** (Figure 11.1) provides the only X-ray crystal structure of the $[CrOF_5]^-$ anion; and **3** (Figure 11.2), **4** (Figure A8.1), and **7** (Figure 11.5) provide precise crystal structures for the $[MoOF_5]^-$ and $[WOF_5]^-$ anions (Tables 11.3 and A8.6). The primary coordination spheres of the $[M'OF_5]^-$ anions are distorted octahedra comprised of four M′–F_{eq} bond domains that are bent away from the M′–O double-bond domain, and a F_{ax} ligand trans to the M′–O bond. The M′–F_{eq} bonds vary in length, where the shortest M′–F_{eq} bonds correspond to the F_{eq} ligands that have the longest Xe---F_{eq} contacts, and vice versa (vide supra). The short M′–O bonds (Cr, 1.565(1) Å; Mo, 1.664(3) Å; W, 1.697(3) Å, 1.686(5) Å) are consistent with significant double bond character. The M′–F_{ax} bonds (Cr, 2.1059(9) Å; Mo, 2.061(2) Å); W, 2.047(2) Å, 2.063(4) Å) are significantly longer than the M′–F_{eq} bonds (Cr, 1.7437(9)–1.7712(9) Å; Mo, 1.835(3)–1.898(2) Å; W, 1.848(2)–1.900(2) Å, 1.862(4)–1.890(4) Å) (Tables 11.3 and A8.6). Their elongations are attributed to the *trans*-influence of their M′–O bonds and the existence of short Xe---F_{ax} contacts (vide supra) with the Xe atoms of nearby $[Xe_2F_{11}]^+$ cations. The covalent radii of the Group 6 metals increase from Cr to W, which is reflected by commensurate M′–O and M′–F_{eq} bond length increases. In contrast, the M′–F_{ax} bond lengths decrease from Cr to W, consistent with the trend of increasing FIA for M′OF_4 upon descending the Group 6 triad.[252]

The M–F and M–O bond lengths of **3** and **4** are comparable to the $[MOF_5]^-$ anions in $K_3[MOF_7]$[298,331] and to the $[WOF_5]^-$ anion of **7**, respectively. The W–F_{eq} bonds of **4** (vide supra) are significantly longer than in $Ag[WOF_5]_2$ (W–F_{eq}, 1.826(7)–1.873(7) Å),[288] whereas the W–O and W–F_{ax} bonds of **4** are significantly shorter than those of $Ag[WOF_5]_2$ (1.729(8) Å and 2.075(7) Å, respectively).

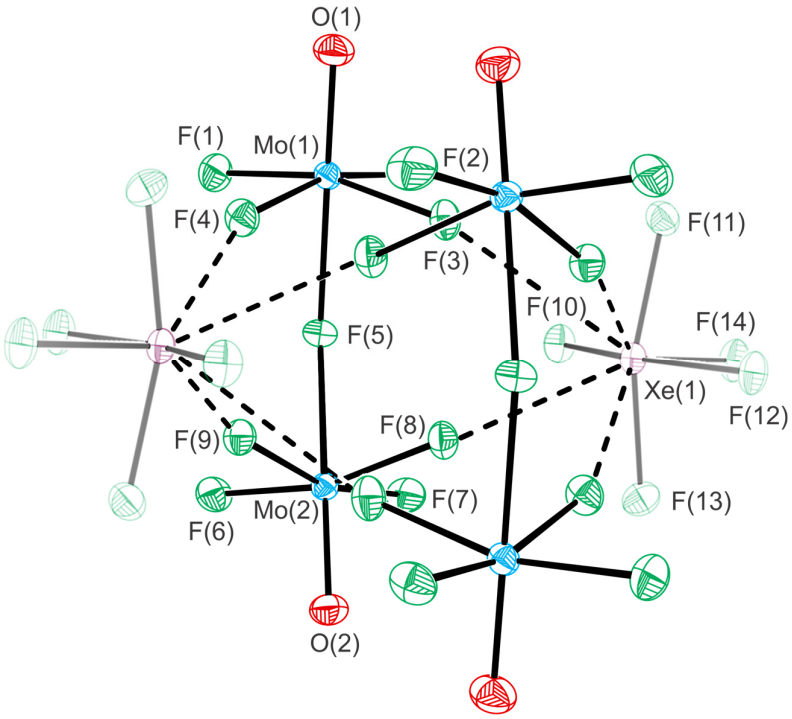

Figure 11.4. The dimeric structural unit in the X-ray crystal structure of $[XeF_5][Mo_2O_2F_9]$ (**5**) with thermal ellipsoids drawn at the 50% probability level. The $[XeF_5]^+$ cations have been faded to emphasize the anions. Secondary Xe---F and Mo---F bonding interactions are indicated by dashed lines. The dimeric structural unit of the isotypic $[XeF_5][W_2O_2F_9]$ (**6**) salt is shown in Figure A8.2 of Appendix 8.

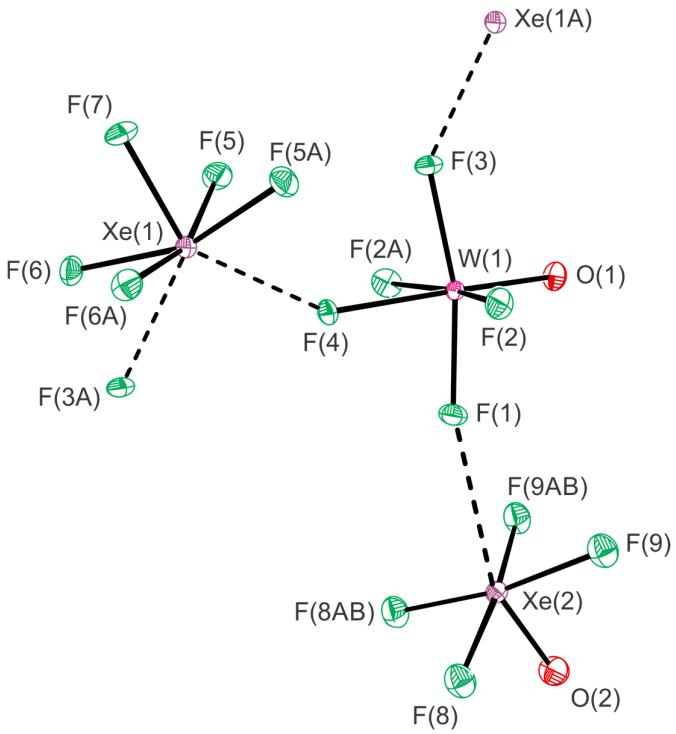

Figure 11.5. The structural unit in the X-ray crystal structure of $[XeF_5][WOF_5]\cdot XeOF_4$ (**7**) with thermal ellipsoids drawn at the 50% probability level. Only one of two orientations for $XeOF_4$ is shown. Secondary Xe---F and W---F bonding interactions are indicated by dashed lines. A figure depicting both $XeOF_4$ orientations may be found in Appendix 8 (Figure A8.3).

Table 11.3. Experimental and calculated[a] geometric parameters for $[M'OF_5]^-$ (M′ = Cr, Mo, W) in **1**, **3**, and **4**

	1		**3**		**4**	
	exptl	calcd	exptl	calcd	exptl	calcd
Bond Lengths (Å)						
M′1−O1	1.565(1)	1.498	1.664(3)	1.665	1.698(3)	1.693
M′1–F1	1.7717(9)	1.733	1.898(2)	1.943	1.900(2)	1.958
M′1−F2	1.7560(9)	1.726	1.855(3)	1.843	1.873(2)	1.913
M′1−F3	1.7712(9)	1.733	1.835(3)	1.844	1.848(2)	1.863
M′1−F4	1.7437(9)	1.699	1.863(3)	1.899	1.867(2)	1.864
M′1−F5	2.1059(9)	2.315	2.061(2)	2.153	2.047(2)	2.148
Bond Angles (deg)						
O1–M′1–F1	98.43(6)	101.6	94.8(1)	96.4	95.1(1)	96.7
O1–M′1–F2	97.14(5)	100.1	97.4(2)	100.2	96.6(2)	98.8
O1–M′1–F3	97.79(6)	101.6	98.0(2)	98.7	97.6(1)	98.4
O1–M′1–F4	96.93(5)	100.8	96.5(2)	98.7	97.4(2)	99.8
O1–M′1–F5	178.16(5)	178.6	176.9(1)	176.7	177.1(1)	176.9
F1–M′1–F2	88.38(4)	87.3	88.0(1)	87.2	88.0(1)	81.0
F1–M′1–F3	163.77(5)	156.9	167.2(1)	164.1	167.3(1)	164.1
F1–M′1–F4	88.98(5)	88.5	88.1(1)	81.7	88.1(1)	87.2
F1–M′1–F5	82.02(4)	78.5	82.1(1)	82.0	81.93(9)	82.0
F2–M′1–F3	88.95(5)	87.3	90.2(1)	94.9	90.5(1)	91.6
F2–M′1–F4	165.92(5)	159.0	165.8(1)	159.1	165.7(1)	158.9
F2–M′1–F5	84.65(4)	81.2	83.0(1)	82.7	83.0(1)	78.2
F3–M′1–F4	89.74(5)	88.5	90.6(1)	91.1	90.3(1)	95.3
F3–M′1–F5	81.80(4)	78.5	85.1(1)	82.7	85.4(1)	82.7
F4–M′1–F5	81.29(4)	77.8	83.0(1)	78.2	82.9(1)	82.9

[a] The PBE1PBE/Def2-SVP (F, O, M, Xe) level of theory was used.

The O–M′–F_{eq} bond angles of $[M'OF_5]^-$ in **1** (Cr, 96.93(5)–98.43(6)°), **3** (Mo, 94.8(1)–98.0(2)°), **4** (W, 95.1(1)–97.4(2)°), and **7** (W, 95.8(2)–98.3(2)°) are significantly more closed than in $[XeF_5][HF_2]\cdot CrOF_4$ (98.87(5)–100.11(5)°), $XeF_2\cdot CrOF_4$ (99.72(8)–100.9(1)°), $XeF_2\cdot 2CrOF_4$ (100.24(9)–102.04(9)°),[65] and $WOF_4\cdot(o\text{-}NC_5FH_4)$ (98.2(5)–100.3(5)°);[342] and are comparable to those of $MOF_4\cdot OPPh_3$ (Mo, 95.47(9)–97.97(8)°;[343] W, 96.0(2)–98.0(2)°).[344] The O–M′–F_{eq} bond angles of gas-phase $M'OF_4$ are more open[345–347] than in $[M'OF_5]^-$ because their M′–F_{eq} single bond domains only interact with an axial M′–O double bond domain. In the cases of the neutral $[XeF_5][HF_2]\cdot CrOF_4$ and $MOF_4\cdot OPPh_3$ adducts, the Cr–F_{eq} and M–F_{eq} bond domains also interact with their respective Cr---F_{HF2-} and M–O bond

domains, which result in smaller O–Cr–F_{eq} and O–M–F_{eq} bond angles relative to those of M′OF_4.

11.2.2.3. ***$[M_2O_2F_9]^-$ (M = Mo, W).*** The bond lengths and angles of $[M_2O_2F_9]^-$ in the isotypic crystal structures of **5** (Figure 11.4) and **6** (Figure A8.2) are comparable. The anions are comprised of two asymmetrically fluorine-bridged MOF_4 molecules, $[F_4(O)M\text{---}F_b\text{---}M(O)F_4]^-$, where the M---$F_b$ bridge bonds (Mo, 2.1060(8), 2.1420(8) Å; W, 2.113(5), 2.167(5) Å) are trans to the M–O double bonds (Table 11.4) and are significantly longer than the terminal M–F_{eq} bonds (Mo, 1.8327(9)–1.9043(9) Å; W, 1.839(5)–1.907(5) Å) due to the dicoordinate F_b atom and the combined trans-influences of two M–O bonds. The longest M–F_{eq} bonds (Mo, 1.8787(9)–1.9043(9) Å; W, 1.881(5)–1.907(5) Å) correspond to the shortest Xe---F_{eq} contacts (vide supra), whereas the F_{eq} atoms of the shortest M–F_{eq} bonds (Mo, 1.8327(9)–1.8407(9) Å; W, 1.839(5)–1.851(5) Å) have no significant contacts. The short M–O bonds (Mo, 1.657(1) Å, 1.659(1) Å; W, 1.681(6) Å, 1.696(5) Å) are consistent with significant double-bond character and are very similar to those of $[MOF_5]^-$ (vide supra). The M---F_b---M bond angles (Mo, 147.40(4)°; W, 147.6(2)°) and $F_{eq}MMF_{eq}$ dihedral angles (Mo, 0.30(4)–2.07(5)°; W, 0.4(3)–2.6(3)°) are expected to be highly deformable based on their low calculated deformation frequencies (see Raman Spectroscopy) and are likely bent or nearly eclipsed to accommodate Xe---F ion-pair interactions within the crystal lattice. The primary bond lengths and angles of the $[M_2O_2F_9]^-$ anions in **5** and **6** lie within the range of values reported for their Li^+–Cs^+ salts.[297,339] The $F_{eq}MMF_{eq}$ dihedral angles of the latter salts increase with cation size and have a broad range of M---F_b---M bond angles (Mo, 137.98(11)–158.89(12)°; W, 138.7(2)–152.0(2)°).[297,339]

11.2.2.4. $[XeF_5][HF_2]\cdot CrOF_4$. The $[XeF_5]^+$ cations (CN_{Xe} = 9) of compound **2** (Figure 11.2) have two short interionic Xe---F_{HF2-} contacts (2.4231(7) Å, 2.4320(7) Å) with two $[HF_2]^-$ anions that result in a dimeric structural unit in which the F···F distance of $[HF_2]^-$ (2.386(1) Å) is comparable to those of $[XeF_5][HF_2]\cdot HF$ (2.383(4) Å, 2.445(4) Å).[100] The dimeric structural unit of **2** also contains two adducted $CrOF_4$ molecules which have primary bond lengths and angles that are comparable to those of polymeric α-$CrOF_4$, β-$CrOF_4$, and $NgF_2\cdot 2CrOF_4$ (Ng = Kr, Xe).[65] The Cr atom coordinates to the F ligand of $[HF_2]^-$ that is not coordinated to the Xe atom. The Cr---F_{HF2-} distance (2.2378(7) Å) is somewhat shorter than the Cr---F_{NgF2} distances in $NgF_2\cdot CrOF_4$ (Kr, 2.3265(9) Å; Xe, 2.314(2) Å) and $NgF_2\cdot 2CrOF_4$ (Kr, 2.4293(6) Å; Xe, 2.385(1) Å),[65] and is consistent with the greater fluorobasicity of $[HF_2]^-$ relative to that of NgF_2, and with the dominant electrostatic character of the Cr---F bond, a σ-hole type interaction similar to those observed for $NgF_2\cdot n CrOF_4$ (n = 1, 2).[65]

11.2.2.5. $XeOF_4$. The bond lengths and bond angles of cocrystallized $XeOF_4$ in **7** (Table A8.6) are very similar to those of $[XeF_5]_2[Cr_2O_2F_8]\cdot 2XeOF_4$ [244] and $XeOF_4\cdot XeF_2$.[68] There is one Xe---F_{eq} secondary bond with the $[WOF_5]^-$ anion (2.890(7) Å) that avoids the stereo-active xenon valence electron lone pair trans to the O atom of $XeOF_4$ (CN_{Xe} = 6). The next nearest Xe···F and Xe···O distances are 3.829(4) Å and 3.371(5) Å, respectively.

Table 11.4. Experimental and calculated[a] geometric parameters of $[M_2O_2F_9]^-$ (M = Mo, W) in 5 and 6

	5		6	
	exptl	calcd	exptl	calcd
	Bond Lengths (Å)			
M(1)−O(1)	1.657(1)	1.643	1.681(6)	1.676
M(1)–F(1)	1.8327(9)	1.821	1.851(5)	1.843
M(1)−F(2)	1.8355(9)	1.822	1.843(5)	1.844
M(1)−F(3)	1.9043(9)	1.904	1.887(5)	1.918
M(1)−F(4)	1.8947(8)	1.898	1.881(5)	1.916
M(1)---F(5)	2.1060(8)	2.116	2.167(5)	2.130
M(2)–O(2)	1.659(1)	1.643	1.696(5)	1.676
M(2)---F(5)	2.1420(8)	2.116	2.113(5)	2.130
M(2)–F(6)	1.840(1)	1.821	1.846(5)	1.844
M(2)–F(7)	1.8407(9)	1.822	1.839(5)	1.844
M(2)–F(8)	1.8787(9)	1.904	1.907(5)	1.917
M(2)–F(9)	1.8822(9)	1.898	1.892(4)	1.916
	Bond Angles (deg)			
M(1)---F(5)---M(2)	147.40(4)	148.2	147.6(2)	148.9
O(1)–M(1)–F(1)	98.57(5)	99.4	99.4(3)	99.1
O(1)–M(1)–F(2)	99.27(5)	99.2	99.6(3)	99.1
O(1)–M(1)–F(3)	95.90(5)	96.4	98.6(3)	96.9
O(1)–M(1)–F(4)	95.30(5)	96.4	97.4(3)	96.9
O(1)–M(1)---F(5)	175.37(5)	175.5	178.2(3)	175.6
F(1)–M(1)–F(2)	91.89(5)	92.9	89.9(3)	92.9
F(1)–M(1)–F(3)	165.34(4)	163.8	161.9(3)	163.5
F(1)–M(1)–F(4)	89.96(4)	89.2	88.9(2)	88.9
F(1)–M(1)---F(5)	84.17(4)	83.8	81.4(2)	83.9
F(2)–M(1)–F(3)	88.08(4)	88.3	88.6(2)	88.6
F(2)–M(1)–F(4)	164.87(4)	163.7	162.9(2)	163.5
F(2)–M(1)---F(5)	84.31(4)	83.8	82.0(2)	83.9
F(3)–M(1)–F(4)	86.37(4)	85.4	87.4(2)	85.1
F(3)–M(1)---F(5)	81.24(4)	80.2	80.5(2)	79.9
F(4)–M(1)---F(5)	80.93(3)	80.4	81.0(2)	79.9
O(2)–M(2)---F(5)	178.60(5)	175.5	176.0(3)	175.6
O(2)–M(2)–F(6)	98.68(6)	99.4	99.2(3)	99.1
O(2)–M(2)–F(7)	98.46(5)	99.2	99.8(3)	99.1
O(2)–M(2)–F(8)	97.43(6)	96.4	97.2(3)	96.9
O(2)–M(2)–F(9)	97.15(5)	96.4	96.7(3)	96.9
F(5)---M(2)–F(6)	82.28(4)	83.8	82.9(2)	83.9
F(5)---M(2)–F(7)	82.52(4)	83.8	83.5(2)	83.9
F(5)---M(2)–F(8)	81.59(4)	80.2	80.6(2)	80.0
F(5)–M(2)–F(9)	81.83(4)	80.4	79.9(2)	79.9
F(6)–M(2)–F(7)	90.55(5)	92.9	91.7(3)	92.9
F(6)–M(2)–F(8)	163.84(4)	163.8	163.5(2)	163.4
F(6)–M(2)–F(9)	89.01(4)	89.2	89.8(2)	88.8
F(7)–M(2)–F(8)	88.42(4)	88.3	87.6(2)	88.7
F(7)–M(2)–F(9)	164.27(4)	163.7	163.0(2)	163.5
F(8)–M(2)–F(9)	87.66(4)	85.4	86.2(2)	85.1
$F_{eq}MMF_{eq}$	0.30(4), 2.07(5)	0.10, 0.07	0.4(3), 2.6(3)	0.01, 0.03

[a] The PBE1PBE/Def2-SVP (F, O, M, Xe) level of theory was used.

11.2.3. Raman Spectroscopy

The LT Raman spectra of $[Xe_2F_{11}][M'OF_5]$ (M′ = Cr (**1**), Mo (**3**), W (**4**)), $[XeF_5][M_2O_2F_9]$ (M = Mo (**5**), W (**6**)), and $[XeF_5][WOF_5]\cdot XeOF_4$ (**7**) are shown in Figures 11.6–11.8 and Figures A8.7–A8.9 of Appendix 8. Spectral assignments for **1** and **3**–**6** were made by comparison with the calculated vibrational frequencies of the energy-minimized, gas-phase geometries of $\{[Xe_2F_{11}][CrOF_5]\}_2$, $[Xe_2F_{11}][MOF_5]$, and $\{[XeF_5][M_2O_2F_9]\}_2$ at the PBE1PBE/Def2-SVP level of theory. The observed and calculated frequencies, their detailed vibrational band assignments, and mode descriptions are provided in Tables A8.7–A8.9 of Appendix 8. The vibrational frequencies of the free gas-phase $[M'OF_5]^-$ and $[M'_2O_2F_9]^-$ anions were also calculated (Tables A8.10 and A8.11 of Appendix 8). The vibrational assignments for $[XeF_5]^+$ and $[Xe_2F_{11}]^+$ were also aided by comparison with the vibrational frequencies and band intensities of $[XeF_5][AsF_6]$,[316] $[XeF_5][BF_4]$,[116,316] $[XeF_5][fac\text{-}OsO_3F_3]$, $[Xe_2F_{11}][fac\text{-}OsO_3F_3]$, $[XeF_5][\mu\text{-}F(OsO_3F_2)_2]$,[121] $[XeF_5]_2[Cr_2O_2F_8]\cdot 2XeOF_4$, and $[XeF_5][Xe_2F_{11}][CrOF_5]\cdot 2CrOF_4$.[244] Overall, the vibrational frequency trends are well reproduced by the calculations. Because the gas-phase geometry of **7** was not optimized, its Raman spectrum was assigned by comparison with those of **4**, **6**, and $XeOF_4$ [348] (Table A8.12 of Appendix 8). Several vibrational bands in the Raman spectra of $[Xe_2F_{11}][MOF_5]$ (M = Mo, W) are split into two components (Table A8.8). The band splittings are attributed to vibrational mode coupling within the crystallographic unit cells of both salts, i.e., factor-group splitting. To confirm the origins of these splittings, a factor-group analysis (Figure A8.10), based on the isotypic crystal structures of $[Xe_2F_{11}][MOF_5]$, was carried out using the "correlation method".[169] Fifty-four vibrational modes are predicted for gas-phase $[Xe_2F_{11}][MOF_5]$

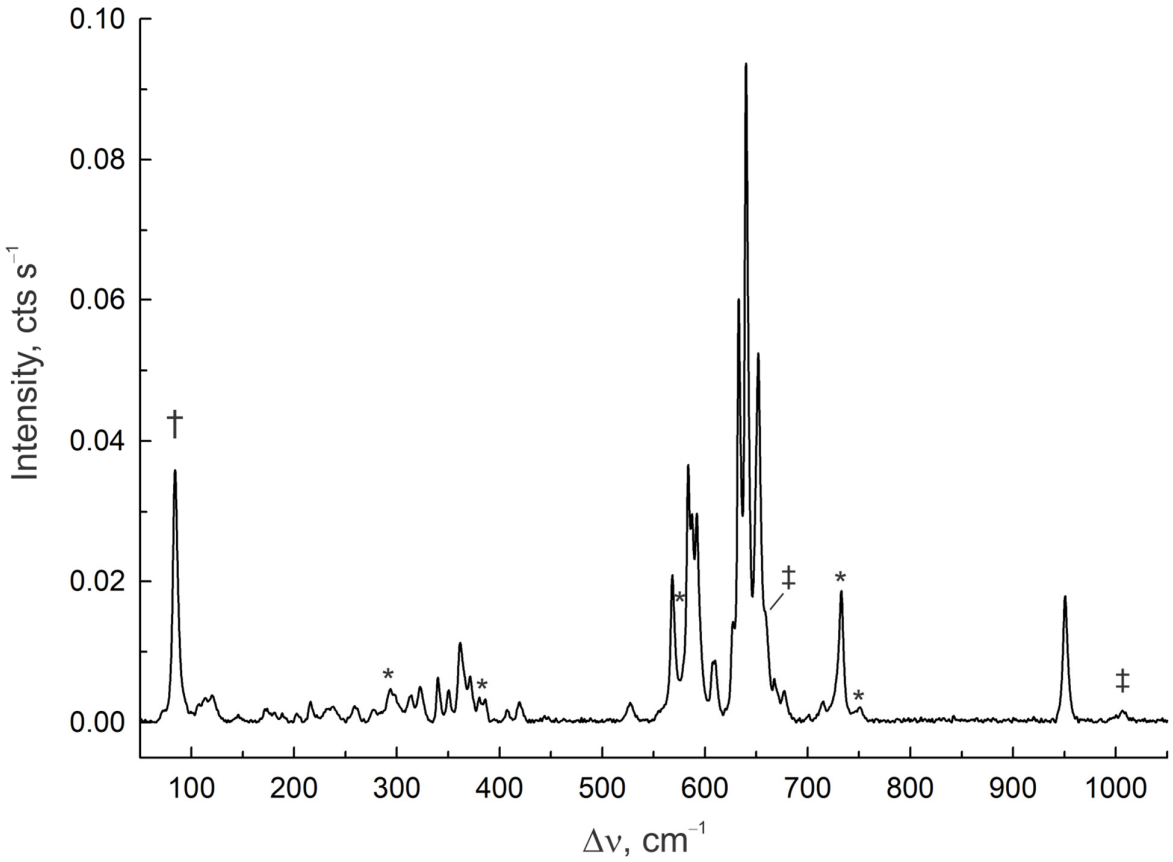

Figure 11.6. Raman spectrum of $[Xe_2F_{11}][CrOF_5]$ (**1**) recorded at −140 °C using 1064-nm excitation. The symbols denote the ν(Cr-O) band of an unidentified chromium oxyfluoride reduction product (‡), FEP sample tube bands (*), and an instrumental artifact (†).

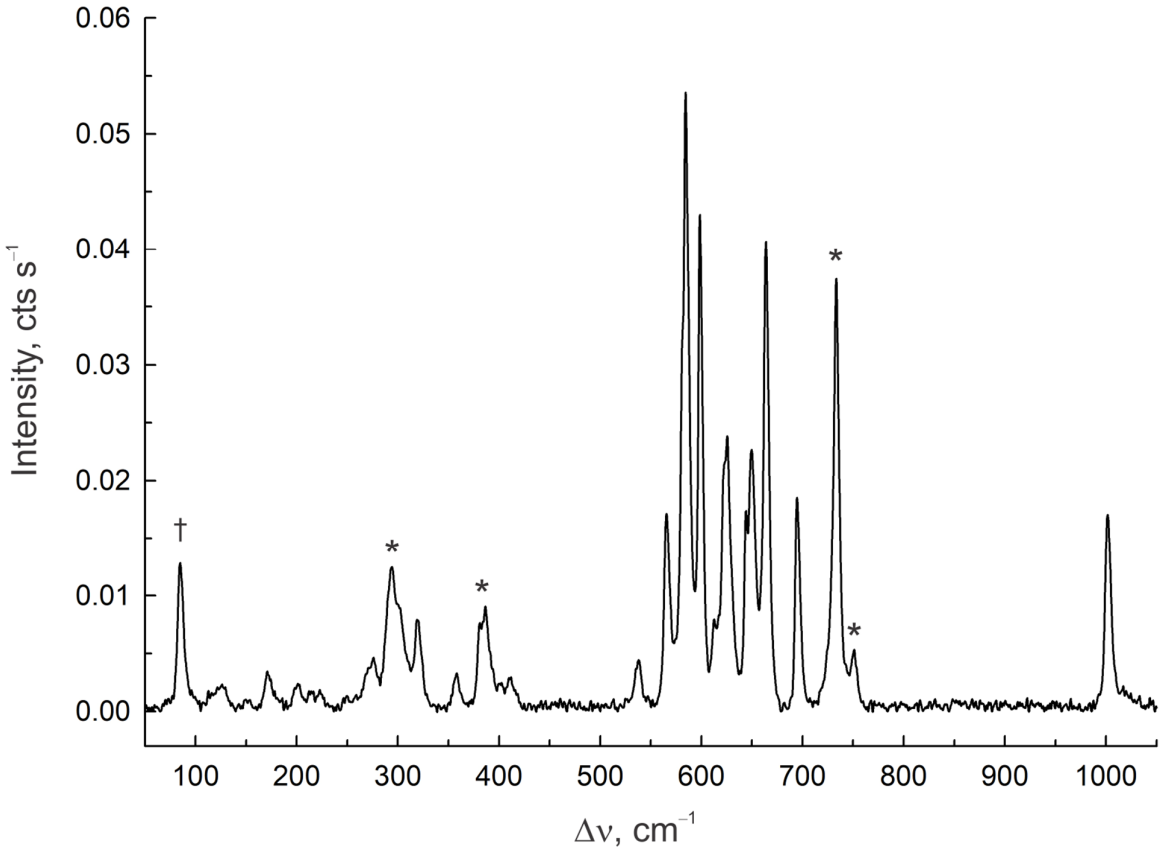

Figure 11.7. Raman spectrum of $[Xe_2F_{11}][MoOF_5]$ (**3**) recorded at −140 °C using 1064-nm excitation. The symbols denote FEP sample tube bands (*) and an instrumental artifact (†). The Raman spectrum of isotypic $[Xe_2F_{11}][WOF_5]$ (**4**) is given in Figure A8.7 of Appendix 8

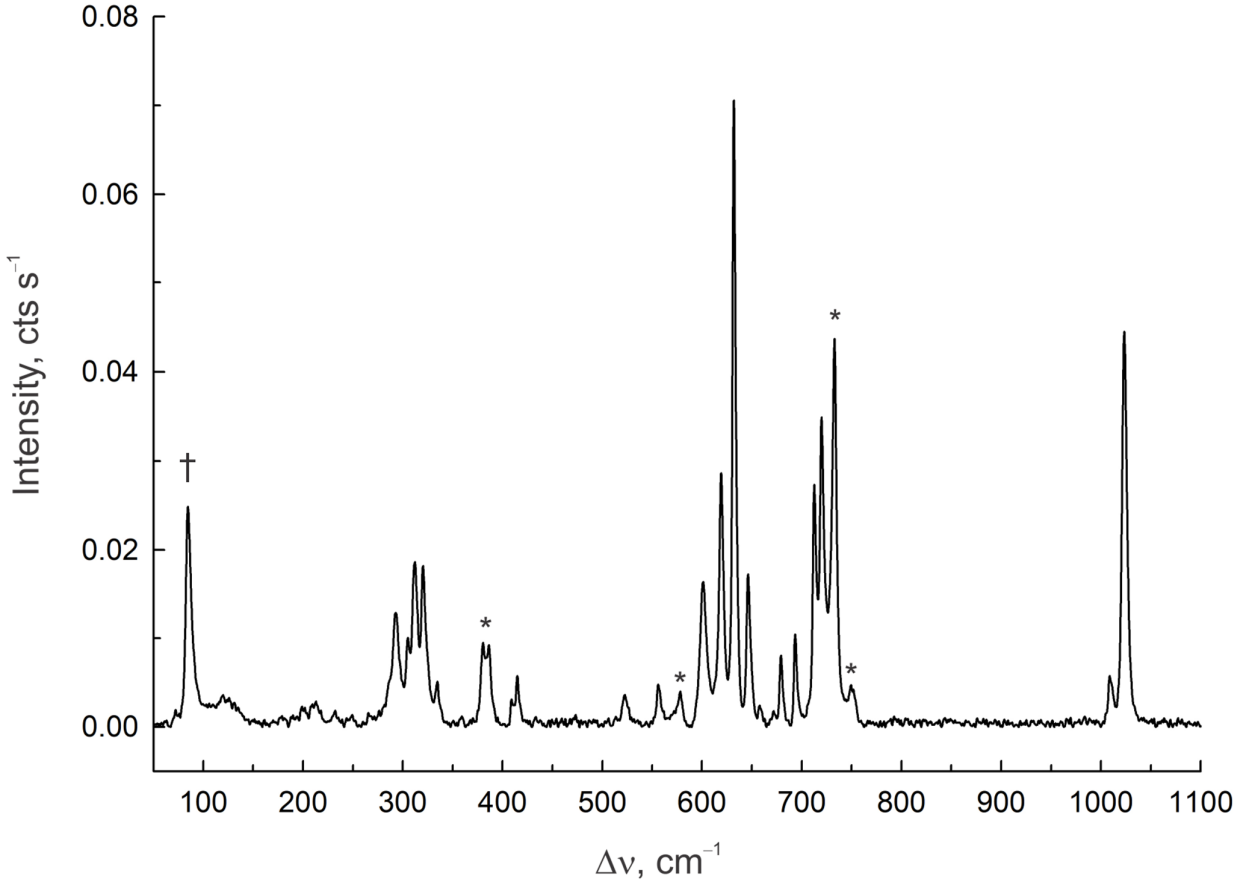

Figure 11.8. Raman spectra of $[XeF_5][Mo_2O_2F_9]$ (**5**) recorded at −140 °C using 1064-nm excitation. The symbols denote FEP sample tube bands (*) and an instrumental artifact (†). The Raman spectrum of isotypic $[XeF_5][W_2O_2F_9]$ (**6**) is given in Figure A8.8 of Appendix 8.

under C_1 symmetry. The vibrations belong to the irreducible representations Γ = 54 A, where the A modes are Raman- and infrared-active. The A representations of gas-phase $[Xe_2F_{11}][MOF_5]$ correlate to A representations under C_1 site symmetry in the solid state. When correlated to the crystal symmetry (C_{2h}), each of the 54 modes splits into Raman-active A_g and B_g components and infrared-active A_u and B_u components (Figure A8.10). Factor-group splittings were resolved for many of the vibrational bands in the Raman spectra of $[Xe_2F_{11}][MOF_5]$ (Table A8.8).

11.2.3.1. [Xe₂F₁₁][CrOF₅] (1). Preliminary assignments were recently provided for $[Xe_2F_{11}][CrOF_5]$ that are based on the calculated frequencies of the gas-phase $[CrOF_5]^-$ anion.[244] The assignments have now been improved by use of a model that closely resembles the crystal structure of the title compound. Unlike $[Xe_2F_{11}][MOF_5]$, no vibrational band splittings are observed in the Raman spectrum of $[Xe_2F_{11}][CrOF_5]$, in accordance with the factor-group analysis (Figure A8.11), which predicts each vibrational band is split into a Raman-active A_g and an infrared- active A_u component. Thus, only the A_g components are observed as unsplit bands in the Raman spectrum (Table A8.7). The highest frequency band at 951 cm^{-1} is assigned to ν(Cr-O), and occurs at a frequency that is very similar to that of $Cs[CrOF_5]$ (IR) (955 cm^{-1}),[264] but is lower than those of $[NO][CrOF_5]$ (Ra) (993 cm^{-1})[66] and $[(CH_3)_2SnF][CrOF_5]$ (IR) (997 cm^{-1}).[270] The bands at 527, 652, 677, and 715 cm^{-1} arise from $\nu(Cr\text{-}F_{eq})$ stretching modes (see Table A8.8), with the intense band at 652 cm^{-1} assigned to the in-phase $[\nu(Cr_1\text{-}F_{4eq}) + \nu(Cr_{1A}\text{-}F_{4eq})]$ mode. The large frequency range observed for the $\nu(Cr\text{-}F_{eq})$ stretching modes is reproduced by the calculations (553, 698, 699, and 750 cm^{-1}). The coupled $\nu(Cr\text{-}F_{ax})$ stretching modes

are predicted at lower frequencies, where one out-of-phase [$\nu(Cr_1\text{-}F_5) - \nu(Cr_{1A}\text{-}F_{5A})$] mode couples with $[Xe_2F_{11}]^+$ stretches and two in-phase [$\nu(Cr_1\text{-}F_5) + \nu(Cr_{1A}\text{-}F_{5A})$] modes couple with $CrOF_4$ deformation modes. The bands at 216 and 233 cm^{-1} are assigned to the in-phase modes (calcd, 209 and 227 cm^{-1}) whereas the out-of-phase mode was not observed because it is only infrared active (calcd, 353 cm^{-1}). The band at 407 cm^{-1} (calcd, 401 cm^{-1}) is assigned to the $\delta(F_{eq}CrF_{eq})$ bending mode, the bands at 365 and 371 cm^{-1} (calcd, 377 and 393 cm^{-1}) are assigned to $\delta(OCrF_{eq})$ bending modes, and the band at 362 cm^{-1} (calcd, 373 cm^{-1}) is assigned to the $\delta_{umb}(MF_{4eq})$ umbrella mode. The band at 323 cm^{-1} (calcd, 318 cm^{-1}) is assigned to the $\rho_w(F_{eq}CrF_{eq})$ wag, which is also coupled to $[Xe_2F_{11}]^+$ bending modes.

11.2.3.2. $[Xe_2F_{11}][MoOF_5]$ (3) and $[Xe_2F_{11}][WOF_5]$ (4). The ν(M-O) stretches at 1002 (Mo) and 1015 (W) cm^{-1} are comparable to those observed in the Raman spectra of $[ClOF_2][MoOF_5]$ (1011 cm^{-1}),[283] $[NO][MOF_5]$ (Mo, 985; W, 1001 cm^{-1}),[283] and $Cs[MOF_5]$ (Mo, 973; W, 989 cm^{-1}).[285] The $\nu(M\text{-}F_{eq})$ stretches, which involve F_{eq} atoms that do not have significant secondary Xe---F_{eq} bonding interactions, occur at higher frequencies (exptl: Mo, 623/626, 695/698 cm^{-1}; W, 626/630, 700/703 cm^{-1}; calcd: Mo, 637, 727/733 cm^{-1}; W, 637, 705/715 cm^{-1}) than those which involve F_{eq} atoms that are coordinated to the cation. In the latter case, out-of-phase (exptl: Mo, 535/538 cm^{-1}; W, 545/554 cm^{-1}; calcd: Mo, 525 cm^{-1}; W, 538 cm^{-1}) and in-phase (exptl: Mo, 323 cm^{-1}; W, 324/327 cm^{-1}; calcd: Mo, 326 cm^{-1}; W, 325 cm^{-1}) modes are predicted. The coupled $\nu(M\text{-}F_{ax})$ stretching modes have out-of-phase components, which occur at higher frequencies (exptl: Mo, 412 cm^{-1}; W, 411 cm^{-1}; calcd: Mo, 405 cm^{-1}; W, 411 cm^{-1}), and

in-phase components, which occur at lower frequencies (exptl: Mo, 358 cm^{-1}; W, 358 cm^{-1}; calcd: Mo, 350 cm^{-1}; W, 349 cm^{-1}). The out-of-phase and in-phase $\nu(M\text{-}F_{eq})$ and $\nu(M\text{-}F_{ax})$ stretches are also coupled with cation modes and other anion modes. Except for three deformation modes (exptl: Mo, 127, 301, 319, cm^{-1}; W, 121, 301, 324 cm^{-1}; calcd: Mo, 126, 312, 320, cm^{-1}; W, 121, 308, 324 cm^{-1}), all anion deformation modes couple with cation modes (Table A8.8). The calculated $\nu(M'\text{-}O)$ stretching frequencies (M′ = Cr, Mo, W) of the ion-pairs (Cr (**1′**), 1225 cm^{-1}; Mo (**2′**), 1018 cm^{-1}; W (**3′**), 994 cm^{-1}) are higher than those of free $[M'OF_5]^-$ (Cr, 1127 cm^{-1}; Mo, 1087 cm^{-1}; W, 1060 cm^{-1}). The same trend is observed for the $\nu(M'\text{-}F_{eq})$ stretching frequencies (ion-pairs: Cr (**1′**), 553, 696–750 cm^{-1}; Mo (**2′**), 525, 637, 727, 733 cm^{-1}; W (**3′**), 538, 637, 705, 717 cm^{-1}; free $[M'OF_5]^-$: Cr, 514, 634, 659 cm^{-1}; Mo, 580, 664, 671 cm^{-1}; W, 605, 649, 673 cm^{-1}). In contrast, the $\nu(M'\text{-}F_{ax})$ stretches decrease upon ion-pair formation (free $[M'OF_5]^-$: Cr, 492 cm^{-1}; Mo, 556 cm^{-1}; W, 565 cm^{-1}; ion-pairs: Cr (**1′**), 227 and 209 cm^{-1}; Mo (**2′**), 405 and 350 cm^{-1}; W (**3′**), 411 and 349 cm^{-1}), whereas the deformation modes of the free $[M'OF_5]^-$ anions and their ion-pairs (**1′**, **2′**, **3′**) are predicted to occur in similar frequency ranges.

11.2.3.4. $[XeF_5][Mo_2O_2F_9]$ (5) and $[XeF_5][W_2O_2F_9]$ (6). No band splittings were observed in the Raman spectra of $[XeF_5][M_2O_2F_9]$, which is consistent with their factor-group analyses (Figure A8.12) and the predicted absence of vibrational coupling within the crystallographic unit cell. In accordance with the factor-group analysis, the A_u components are infrared-active and only the unsplit A_g components are observed in the Raman spectrum (Table A8.9). The bands at 1009, 1023 cm^{-1} (Mo) and 1027, 1040 cm^{-1}

(W) are assigned to the asymmetric and symmetric ν(M-O) stretches, respectively, and occur at frequencies comparable to those of $[Xe_2F_{11}][MOF_5]$. The ν(M-O) stretching frequencies are in good agreement with those of $[ClOF_2][Mo_2O_2F_9]$ (1020 cm^{-1}),[283] $[NO][M_2O_2F_9]$ (Mo, 1025 cm^{-1}; W, 1041 cm^{-1}),[283] $[NF_4][W_2O_2F_9]$ (1034 cm^{-1}),[293] and $[Cs][W_2O_2F_9]$ (1036 cm^{-1}).[293] As noted for **3** and **4**, the ν(M-F_{eq}) stretches which involve F_{eq} atoms that are not coordinated to $[XeF_5]^+$ occur at higher frequencies (exptl: Mo, 694, 713, 720 cm^{-1}; W, 701, 711, 716 cm^{-1}; calcd: Mo, 729, 735, 750 cm^{-1}; W, 719, 736, 743 cm^{-1}) than those which involve F_{eq} atoms that are coordinated to $[XeF_5]^+$ (exptl: Mo, 523, 556, 632, 646, 679 cm^{-1}; W, 549, 593, 633, 643, 683 cm^{-1}; calcd: Mo, 523, 529, 620, 648, 682 cm^{-1}; W, 545, 597, 615, 649, 684 cm^{-1}). The latter frequencies are assigned to ν(M-F_{eq}) stretches that are weakly coupled to ν(Xe-F) stretching modes of both $[XeF_5]^+$ cations. The coupled ν(M-F_b) stretching modes are predicted at lower frequencies. Of the four predicted modes, only the band corresponding to the in-phase [ν(Mo_1-F_5) + ν(Mo_2-F_5)] + [ν(Mo_{1A}-F_{5A}) + ν(Mo_{2A}-F_{5A})] mode is observed at 131 cm^{-1} (calcd, 131 cm^{-1}) for **5**, whereas the in-phase [ν(W_1-F_5) + ν(W_2-F_5)] + [ν(W_{1A}-F_{5A}) + ν(W_{2A}-F_{5A})] and the out-of-phase [ν(W_1-F_5) + ν(W_2-F_5)] − [ν(W_{1A}-F_{5A}) + ν(W_{2A}-F_{5A})] bands are observed at 127 and 121 cm^{-1} (calcd, 122 and 116 cm^{-1}), respectively, for **6**. Other than the latter bands, all bands that occur below 419 (Mo) and 412 (W) cm^{-1} arise from cation and anion deformation modes. The medium-intensity bands observed at 319 and 322 (Mo) cm^{-1} and 315 and 320 (W) cm^{-1}, are assigned to δ(OMF) bending modes (calcd: Mo, 312 and 320 cm^{-1}; W, 313 and 323 cm^{-1}). As in the case of the $[MOF_5]^-$ anions, the calculated ν(M-O) stretching frequencies increase for the $[XeF_5][M_2O_2F_9]$ ion-pairs (free $[M_2O_2F_9]^-$: Mo,

1053 and 1069 cm^{-1}; W, 1068 and 1073 cm^{-1}; ion-pairs: Mo (**5′**), 1102 and 1123 cm^{-1}; W (**6′**), 1088 and 1103 cm^{-1}), whereas the ν(M-F_b) stretching frequencies are relatively insensitive to ion-pair formation (free $[M_2O_2F_9]^-$: Mo, 123 and 468 cm^{-1}; W, 108 and 484 cm^{-1}; ion-pairs: Mo (**5′**), 131 and 440 cm^{-1}; W (**6′**), 127 and 459 cm^{-1}). Upon ion-pair formation, many ν(M-F_{eq}) stretching modes couple with ν(Xe-F) stretching modes, resulting in greater frequency ranges for the calculated ion-pairs (Mo (**5′**), 512–750 cm^{-1}; W (**6′**), 537–716 cm^{-1}) than for the free $[M_2O_2F_9]^-$ anions (Mo, 606–714 cm^{-1}; W, 649–716 cm^{-1}).

11.2.4. Computational Results

11.2.4.1. Calculated Geometries. The gas-phase structures of $[Xe_2F_{11}][MOF_5]$ and $\{[XeF_5][M_2O_2F_9]\}_2$ (M = Mo, W) were optimized at the PBE1PBE/Def2-SVP level of theory and resulted in stationary points with all frequencies real (Tables A8.7–A8.9). The geometries of $\{[Xe_2F_{11}][CrOF_5]\}_2$ and $[Cr_2O_2F_9]^-$ were optimized at the same level of theory (Table 11.3 and Table A8.13), each with one imaginary frequency (−24 cm^{-1} and −4 cm^{-1}, respectively). The gas-phase geometries of the $[M'OF_5]^-$ (M′ = Cr, Mo, W) and $[M_2O_2F_9]^-$ (M = Mo, W) anions optimized to C_{4v} and C_4 symmetries, respectively, with all frequencies real (Table A8.13 and Figure A8.13), and were compared to assess the effects of ion-pair formation. The gas-phase geometries of M′OF_4 optimized to C_{4v} symmetry (Table A8.14) with all frequencies real (Table A8.15). The initial geometries of M′OF_4 were obtained from gas-phase electron diffraction studies[345–347] and those used for $[M'OF_5]^-$, $\{[Xe_2F_{11}][CrOF_5]\}_2$, $[M_2O_2F_9]^-$, $[Xe_2F_{11}][MOF_5]$, and $\{[XeF_5][M_2O_2F_9]\}_2$ were obtained from the X-ray crystal structures of $[Xe_2F_{11}][M'OF_5]$ and $[XeF_5][M_2O_2F_9]$

described in the present work. The initial geometry used for $[Cr_2O_2F_9]^-$ was the optimized geometry of the $[Mo_2O_2F_9]^-$ anion where the Mo atoms had been replaced by Cr atoms. The calculated Cr–O and Cr–F_{eq} bond lengths of the $\{[Xe_2F_{11}][CrOF_5]\}_2$ ion-pair are, on average, underestimated by 0.07 and 0.04 Å, respectively, relative to their experimental values. The calculated terminal Xe–F bond lengths of $[XeF_5]^+$ and $[Xe_2F_{11}]^+$ in the $\{[Xe_2F_{11}][CrOF_5]\}_2$, $[Xe_2F_{11}][MOF_5]$, and $\{[XeF_5][M_2O_2F_9]\}_2$ ion-pairs are, on average, overestimated by 0.02 Å relative to their experimental values.

11.2.4.1.1. $\{[Xe_2F_{11}][CrOF_5]\}_2$, $[CrOF_5]^-$, $[Xe_2F_{11}][MOF_5]$ (M = Mo, W), and $[MOF_5]^-$.

The gas-phase geometry of the dimeric $\{[Xe_2F_{11}][CrOF_5]\}_2$ ion pair optimized to C_i symmetry (Figure 11.9). The calculated geometry reproduces the crystallographic trends for **1**, i.e., the F_{ax} atom of the Cr–F_{ax} bond (2.315 Å) trans to the Cr–O bond (1.498 Å) has short interionic Xe---F_{ax} contacts (2.246, 2.247 Å) with the Xe atoms of two $[Xe_2F_{11}]^+$ cations, and the Cr–F_{ax} bond is significantly longer than the Cr–F_{eq} bonds (1.699–1.733 Å). The two shortest Cr–F_{eq} bonds of **1** have no significant interionic contacts, whereas the two longest Cr–F_{eq} bonds have two Xe---F_{eq} contacts with two $[Xe_2F_{11}]^+$ cations (2.849, 2.850 Å) which result in CN_{Xe} = 8. Ion-pair formation results in short interionic Xe---F_{ax} contacts with $[CrOF_5]^-$ that significantly weaken the Cr–F_{ax} bond and polarize the Cr–O and Cr–F_{eq} bonds, leading to elongation of the Cr–F_{ax} bond and contraction of the Cr–O and Cr–F_{eq} bonds. The preference for coordination of a second $[Xe_2F_{11}]^+$ cation to the F_{ax} atom of $[CrOF_5]^-$ rather than to a F_{eq} atom in the gas-phase ion-pair is consistent with the lower relative basicities of the F_{eq} atoms. This contrasts with what is observed in the crystal structures and calculated gas-phase ion-pairs of **3** and **4** in which

$[Xe_2F_{11}]^+$ has short Xe---F contacts with both the F_{ax} and the F_{eq} fluorine atoms of $[MOF_5]^-$. The gas-phase geometries of the $[Xe_2F_{11}][MOF_5]$ ion-pairs optimized to C_1 symmetry and reproduce the trends observed in the crystal structures of **3** and **4** (Figures 11.10 and A8.14a). The short M–O bonds (Mo, 1.665 Å; W, 1.693 Å) are indicative of double-bond character. The M–F_{ax} bonds (Mo, 2.153 Å; W, 2.148 Å) are significantly longer than the M–F_{eq} bonds (Mo, 1.843–1.943 Å; W, 1.863–1.958 Å) owing to short Xe---F_{ax} contacts (vide supra) and the trans-influences of their M–O bonds. The M–F_{ax} bonds of $[MOF_5]^-$ (vide supra) in the ion-pairs are significantly elongated with respect to gas-phase $[MOF_5]^-$ (Mo, 1.955 Å; W, 1.972 Å). The longest M–F_{eq} bonds correspond to the shortest Xe---F_{eq} contacts (vide supra), and vice versa. Each Xe atom in the crystal structures of $[Xe_2F_{11}][MOF_5]$ forms a Xe---F_{eq}–M bridge with the anion of a neighboring ion-pair to give $CN_{Xe} = 8$, whereas the Xe atoms of the calculated gas phase ion-pairs achieve $CN_{Xe} = 8$ by reorientation of the $[MOF_5]^-$ anion so that one F_{eq} atom interacts with both Xe atoms of the $[Xe_2F_{11}]^+$ cation (Mo, 3.146, 3.232 Å; W, 3.157, 3.353 Å). The Xe coordination environments of the calculated gas-phase ion-pair of $[Xe_2F_{11}][MOF_5]$ are reminiscent of the Xe coordination environments in the crystal structure and the calculated gas-phase ion-pair of $[Xe_2F_{11}][fac\text{-}OsO_3F_3]$.[121] The M′−$F_{ax}$, M′–$F_{eq}$, and M′–O bond lengths of the gas-phase $[M'OF_5]-$ anions significantly increase with the covalent radii of the metal (Cr < Mo < W),[349] whereas the M′–F_{ax} bond lengths of their ion-pairs decrease from Cr to W, in accordance with their crystal structures and calculated fluoride-ion affinities.[252]

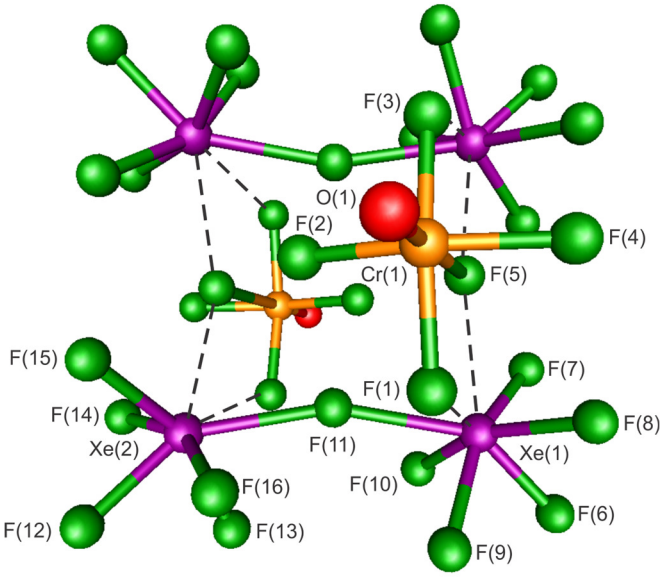

Figure 11.9. The calculated gas-phase geometry of $\{[Xe_2F_{11}][CrOF_5]\}_2$. The PBE1PBE/Def2-SVP (F, O, Cr, Xe) level of theory was used.

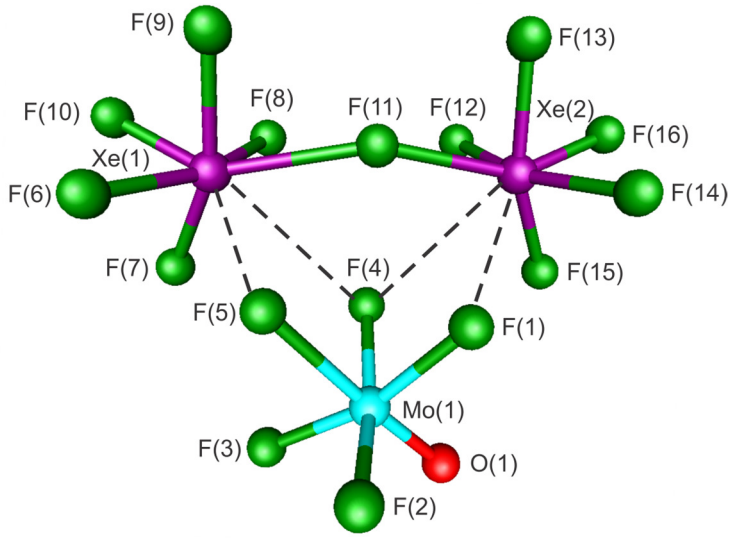

Figure 11.10. The calculated gas-phase geometry of $[Xe_2F_{11}][MoOF_5]$. The PBE1PBE/Def2-SVP (F, O, Mo, W, Xe) level of theory was used. The calculated gas phase geometry of $[Xe_2F_{11}][WOF_5]$ may be found in Appendix 8 (Figure A8.14a).

11.2.4.1.2. ***{[XeF$_5$][M$_2$O$_2$F$_9$]}$_2$ and [M$_2$O$_2$F$_9$]$^-$ (M = Mo, W).*** In contrast with their experimental C_i symmetries, the gas phase geometries (Figures 11.11 and A8.14b) of the {[XeF$_5$][M$_2$O$_2$F$_9$]}$_2$ dimers optimized to C_{2h} (Mo) and C_2 (W) symmetries. The calculated gas-phase geometries of {[XeF$_5$][M$_2$O$_2$F$_9$]}$_2$ accurately reproduce the experimental bond lengths, angles, and trends (Tables 11.4 and A8.5). The greatest differences between the calculated and experimental geometries are consequences of the higher symmetries of their optimized geometries, which result in four very similar Xe---F$_{eq}$ secondary bonds (Mo, 2.635–2.645 Å; W, 2.645–2.657 Å) instead of the two short and two long Xe---F$_{eq}$ bonds observed in the crystal structures of **5** (Mo, 2.6438(9)–2.9828(9) Å) and **6** (W, 2.677(5)–2.990(5) Å). In contrast with the experimental M–F$_{eq}$---Xe angles (Mo, 147.14(4)–164.14(4)°; W, 148.0(2)–164.5(2)°), the calculated M–F$_{eq}$---Xe contact angles are very similar (Mo, 158.7–168.9°; W, 165.7–169.9°). Two F$_{eq}$ ligands of the MOF$_4$ moieties in the [F$_4$(O)M---F$_b$---M(O)F$_4$]$^-$ anions of {[XeF$_5$][M$_2$O$_2$F$_9$]}$_2$ form short Xe---F$_{eq}$ secondary bonds with neighboring [XeF$_5$]$^+$ cations (vide supra) which result in CN$_{Xe}$ = 9 for each [XeF$_5$]$^+$ cation. The calculated M---F$_b$ bond lengths (Mo, 2.116 Å; W, 2.130 Å) are very similar to the average experimental M---F$_b$ bond lengths (Mo, 2.124(3) Å; W, 2.140(7) Å) and are also significantly longer than the M–F$_{eq}$ (Mo, 1.821–1.904 Å; W, 1.843–1.918 Å) and M–O bonds (Mo, 1.643 Å; W, 1.676 Å). The primary bond lengths of the gas-phase [M′$_2$O$_2$F$_9$]$^-$ anions increase with the covalent radii of the metals, similar to the trends observed for the gas-phase [M′OF$_5$]$^-$ anions. The gas-phase [F$_4$(O)M′---F$_b$---M′(O)F$_4$]$^-$ anions have linear M′---F$_b$---M′ bond angles with near-staggered F$_{eq}$M′M′F$_{eq}$ dihedral angles (Cr, 40.8–49.2°; Mo, 39.2–50.8°; W, 44.6–45.4°). Ion-pair formation

results in bent M---F_b---M bond angles (Mo, 148.2°; W, 148.9°), and eclipsed (Mo, 0°; W, 0.3°) $F_{eq}MMF_{eq}$ dihedral angles in order to optimize secondary bonding interactions with the Xe atoms of neighboring $[XeF_5]^+$ cations, in agreement with the crystal structures of **5** and **6**. As observed for all other ion-pairs discussed in this study, M–F_{eq} bonds, which have F_{eq} atoms that have secondary contacts with Xe, are significantly elongated relative to M–F_{eq} bonds that have no Xe---F_{eq} interactions. The M---F_b bond lengths of the free anions and their ion-pairs are comparable, whereas the M–O bonds are slightly shorter in the gas-phase ion-pairs.

11.2.4.2. Natural Bond Orbital (NBO) Analyses. The natural atomic orbital (NAO) analyses of M′OF_4 (M′ = Cr, Mo, W) (Table A8.16) show trends of increasing positive (M′) and negative (O, F) natural population analysis (NPA) charges, and decreasing valence indices for all atoms upon descending Group 6. These trends are also observed for the M′, M, O, F_{ax}, and F_{eq} atoms of gas-phase $[M'OF_5]^-$, $[M'_2O_2F_9]^-$, $\{[Xe_2F_{11}][CrOF_5]\}_2$, $[Xe_2F_{11}][MOF_5]$, and $\{[XeF_5][M_2O_2F_9]\}_2$. The charge and valence index differences between $CrOF_4$ and $MoOF_4$ are significantly greater than between $MoOF_4$ and WOF_4, and follow a similar trend for the $[M'OF_5]^-$ anions. A parallel trend also occurs among the calculated fluoride-ion affinities (FIAs) of M′OF_4,[252] where the FIA of $CrOF_4$ is significantly less negative than those of $MoOF_4$ and WOF_4.

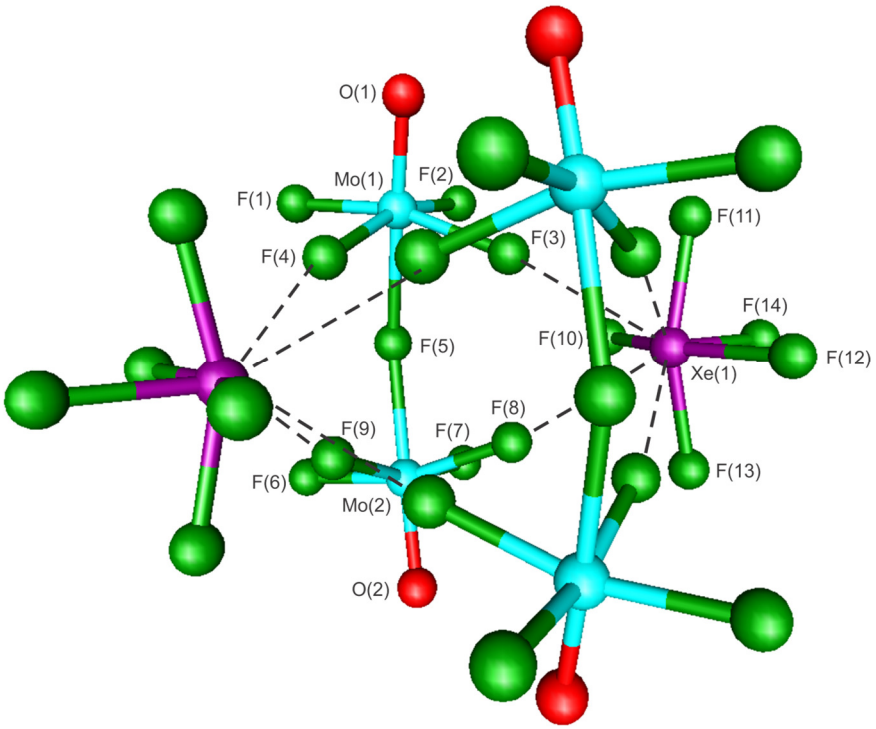

Figure 11.11. The calculated gas-phase geometry of $[XeF_5][Mo_2O_2F_9]$. The PBE1PBE/Def2-SVP (F, O, Mo, W, Xe) level of theory was used. The calculated gas-phase geometry of $[XeF_5][W_2O_2F_9]$ may be found in Appendix 8 (Figure A8.14b).

The NPA charges of $[M'OF_5]^-$ are more negative, the valence indices of the M′ atoms are greater, and the valence indices of the O and F_{eq} atoms are smaller than those of $M'OF_4$. The F_{ax} atom charges become more negative upon descending Group 6 and have more negative charges and lower valence indices than their F_{eq} atoms, consistent with their greater fluorobasicities. The O and F_{eq} valence indices and M′–O and M′–F_{eq} Wiberg bond indices of $[M'_2O_2F_9]^-$ are greater than those of $[M'OF_5]^-$, which is attributable to greater delocalization of the net charge in $[M'_2O_2F_9]^-$.

The F_{eq} atoms of $[MOF_5]^-$ and $[M_2O_2F_9]^-$ in $[Xe_2F_{11}][MOF_5]$ and $\{[XeF_5][M_2O_2F_9]\}_2$ that form Xe---F_{eq} secondary bonds in their ion-pairs are more polarized and exhibit more negative NPA charges, lower valence indices, and lower M–F_{eq} Wiberg bond indices than the free gas-phase anions, whereas the F_{eq} atoms, which lack significant secondary bonding interactions, show the opposite trends. The F_{ax} atoms of ion-paired $[Xe_2F_{11}][MOF_5]$ also display significantly more negative charges, lower valences, and lower M–F_{ax} bond indices than those of the free gas-phase $[MOF_5]^-$ anions. The relative basicities of the F_{ax} and F_{eq} atoms of $[Xe_2F_{11}][MOF_5]$ are reflected in the differences between the Wiberg bond indices of the shortest Xe---F_{ax} contacts (Mo, 0.207; W, 0.191) and Xe---F_{eq} contacts (Mo, 0.064, W; 0.063). The M–F_{ax} Wiberg bond indices of $[Xe_2F_{11}][MOF_5]$ (Mo, 0.278; W, 0.282) are comparable to the M---F_b bond indices of $\{[XeF_5][M_2O_2F_9]\}_2$ (Mo, 0.282; W, 0.272). The high charges, low valence indices, and low Wiberg bond indices of the M–F_{ax} bonds in $[Xe_2F_{11}][MOF_5]$ and the M---F_b bonds in $\{[XeF_5][M_2O_2F_9]\}_2$ show they are best described as highly polar-covalent bonds.

When compared with gas-phase $[CrOF_5]^-$, the $[CrOF_5]^-$ anion in $\{[Xe_2F_{11}][CrOF_5]\}_2$ displays significant negative charge increases (F_{ax}) and decreases (O and F_{eq}). The F_{eq} atoms that form short Xe---F_{eq} secondary bonds have more negative charges, lower valence indices, and lower Cr–F_{eq} bond indices relative to F_{eq} atoms that do not have significant secondary bonding interactions. The trends indicate significant polarization of the Cr–F_{ax} bond owing to short interionic Xe---F_{ax} contacts, which reduce the F_{eq} atom basicities in $[CrOF_5]^-$. This trend is not observed for the gas-phase

$[Xe_2F_{11}][MOF_5]$ ion-pairs, and likely accounts for the formation of the dimeric structural unit in the crystal structure of $[Xe_2F_{11}][CrOF_5]$ by favoring a second Xe---F_{ax} contact instead of an additional Xe---F_{eq} contact.

11.2.4.3. Molecular Electrostatic Potential Surface (MEPS) Analyses

The MEPS of $M'OF_4$ and the $[M'OF_5]^-$ anions (M′ = Cr, Mo, W) are depicted in Figures 11.12 and 11.13. The differences between the electrostatic potential (EP) minima and maxima of the MEPS for $CrOF_4$, $MoOF_4$, and WOF_4 are greater for $CrOF_4$ and $MoOF_4$/WOF_4 than for $MoOF_4$ and WOF_4, in accordance with their NBO analyses. Similar trends are observed among the $[M'OF_5]^-$ anions.

The EP maxima of the $M'OF_4$ isosurfaces trans to the M′–O bonds become more positive (Cr, 218 kJ mol^{-1}; Mo, 340 kJ mol^{-1}; W, 375 kJ mol^{-1}) when going from $CrOF_4$ to WOF_4, in accordance with their calculated FIAs.[252] Their relative fluorobasicities are also reflected in their F atom EP minima (Cr, −39 kJ mol^{-1}; Mo, −46 kJ mol^{-1}; W, −47 kJ mol^{-1}), which become more negative in going from Cr to W. The EP minima of the O atoms also become more negative in going from Cr to W (Cr, 34 kJ mol^{-1}; Mo, −6 kJ mol^{-1}; W, −9 kJ mol^{-1}). These trends are in accordance with increasing positive (M′) and negative (O, F) NPA charges (Table A8.16) upon descending Group 6.

The global EP minima of the MEPS for the $[M'OF_5]-$ anions (Cr, −567 kJ mol^{-1}; Mo, −512 kJ mol^{-1}; W, −499 kJ mol^{-1}) (Figure A8.15) lie at the intersections of their respective F_{ax} and F_{eq} isosurfaces, and are approximately 11 to 17 times more negative than the global EP minima of $M'OF_4$ (Cr, −33 kJ mol^{-1}; Mo, −46 kJ mol^{-1}; W, −47 kJ mol^{-1}). The EPs of the F_{ax} atoms in $[M'OF_5]^-$ (Cr, −509 kJ mol^{-1}; Mo, −486 kJ mol^{-1}; W,

−486 kJ mol^{-1}) become more positive when going from Cr to Mo/W, consistent with the relative FIAs of M′OF_4 [252] and the F_{ax} atom basicities of [M′OF_5]$^-$. The EPs of the F_{ax} atoms are also significantly more negative than those of the F_{eq} atoms, which accords with the relative basicities of the F_{ax} and F_{eq} ligands. The EP minima of the O atoms become more negative when going from Cr to W (Cr, −389 kJ mol^{-1}; Mo, −412 kJ mol^{-1}; W, −438 kJ mol^{-1}) and parallel the trend observed for M′OF_4 (Cr, 34 kJ mol^{-1}; Mo, −6 kJ mol^{-1}; W, −9 kJ mol^{-1}), which is opposite to the trend that occurs for the EP minima of the F_{eq} atoms (Cr, −446 kJ mol^{-1}; Mo, −433 kJ mol^{-1}; W, −431 kJ mol^{-1}).

The MEPS of {[Xe_2F_{11}][$CrOF_5$]}$_2$ and [Xe_2F_{11}][MOF_5] were also calculated (Figures A8.16 and A8.17) to assess the effects of ion-pair formation on the EP isosurfaces of the F_{eq} atoms in [MOF_5]$^-$. The EP minima of two equivalent F_{eq} atoms of [$CrOF_5$]$^-$ in {[Xe_2F_{11}][$CrOF_5$]}$_2$, which are well-separated from neighboring MEPS isosurfaces and can be reliably evaluated (−53 kJ mol^{-1}), are approximately one-eighth that of gas-phase [$CrOF_5$]$^-$ (−446 kJ mol^{-1}) and are comparable to the EP minimum of F_{eq} in $CrOF_4$ (−33 kJ mol^{-1}). Parallel trends are observed for the F_{eq} isosurfaces of [Xe_2F_{11}][MOF_5] (Mo, −64 kJ mol^{-1}; W, −74 kJ mol^{-1}) and free [MOF_5]$^-$ (Mo, −433 kJ mol^{-1}; W, −431 kJ mol^{-1}), consistent with polarization of the electron density of these strongly ion-paired salts away from their terminal F_{eq} atoms towards F_{eq} atoms that form secondary Xe---F_{eq} bonds in their ion-pairs. These observations are in accordance with the NPA charges, bond valences, and Wiberg bond indices of the F_{eq} atoms in {[Xe_2F_{11}][$CrOF_5$]}$_2$ and [Xe_2F_{11}][MOF_5].

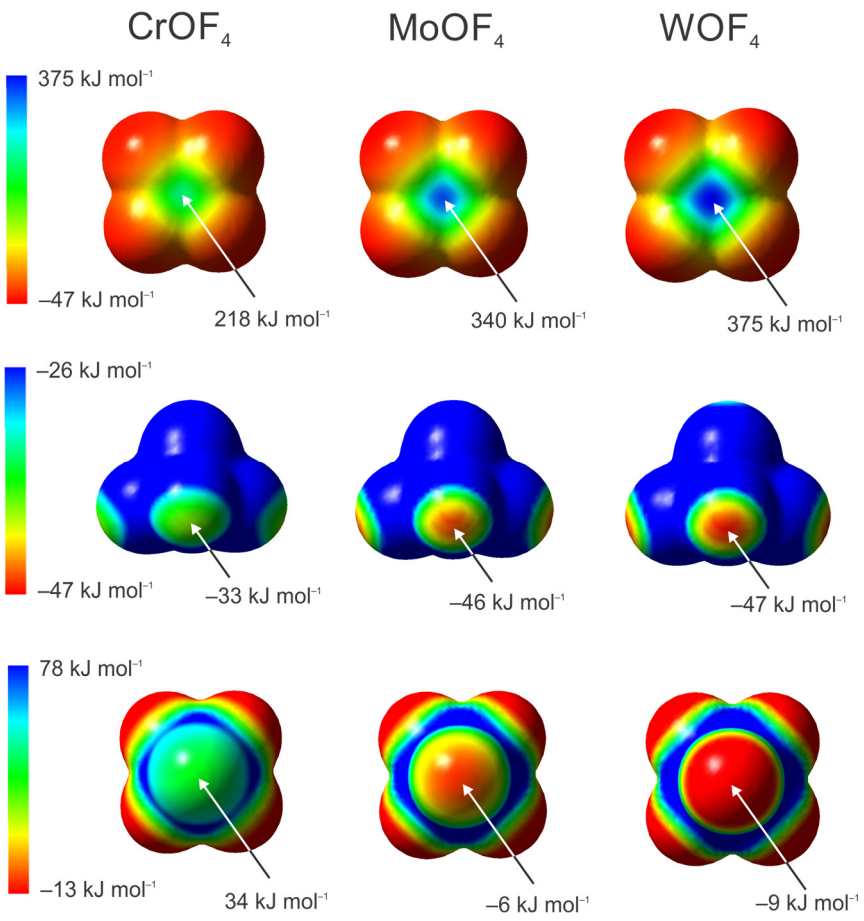

Figure 11.12. The molecular electrostatic potential surface (MEPS) contours calculated at the 0.001 e bohr^{-3} isosurfaces of $CrOF_4$, $MoOF_4$ and WOF_4. The extrema of selected electrostatic potentials are indicated by arrows. The optimized geometries and MEPS were calculated at the PBE1PBE/Def2-SVP (O, F, Cr, Mo, W) level of theory.

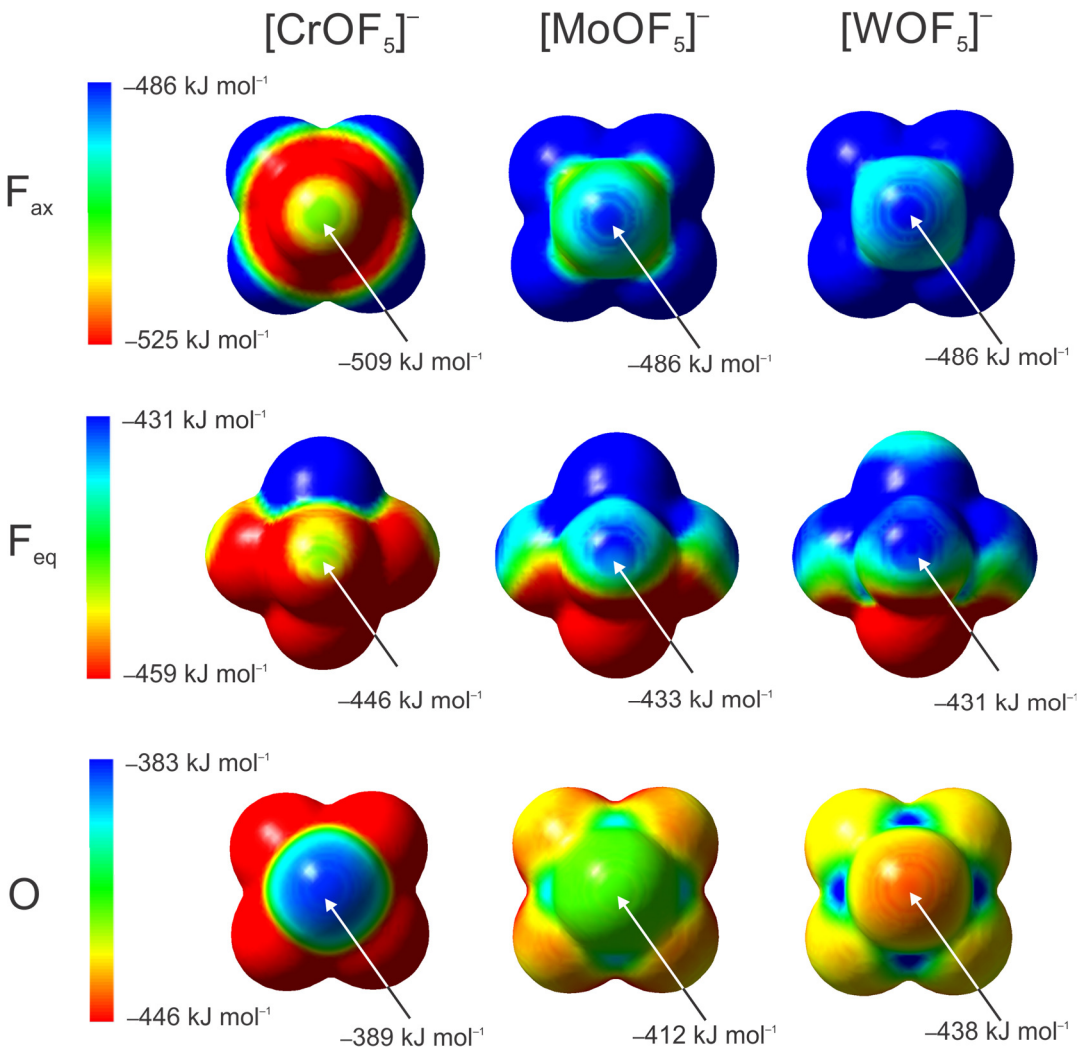

Figure 11.13. The molecular electrostatic potential surface (MEPS) contours calculated at the 0.001 e bohr^{-3} isosurfaces of $[CrOF_5]^-$, $[MoOF_5]^-$ and $[WOF_5]^-$. The extrema of selected electrostatic potentials are indicated by arrows. The optimized geometries and MEPS were calculated at the PBE1PBE/Def2-SVP (O, F, Cr, Mo, W) level of theory.

11.3. Conclusion

Prior work has shown that the oxide tetrafluorides of the Group 6 triad form neutral adducts with KrF_2 and XeF_2.[65,67,182–184,306] In the present work, the room-temperature reactions of MOF_4 (M = Mo, W) with XeF_6, the strongest fluoride-ion donor among the noble-gas fluorides, in aHF and $CFCl_3$ solvents have provided the ion-paired salts, $[Xe_2F_{11}][MOF_5]$ and $[XeF_5][M_2O_2F_9]$. Hydrolysis of $[Xe_2F_{11}][WOF_5]$ in HF was shown to form $[XeF_5][WOF_5]\cdot XeOF_4$. In an earlier related study,[244] the room-temperature reaction of XeF_6 and $CrOF_4$ in melts and in aHF and $CFCl_3$ solvents yielded Cr^{V} and Cr^{IV} fluoro- and oxyfluoro-anion salts that resulted from F_2 elimination reactions. The salt, $[Xe_2F_{11}][CrOF_5]$, was identified by LT Raman spectroscopy as an intermediate in the reaction between XeF_6 and $CrOF_4$ that led to the reduction of Cr^{VI} to Cr^{V} by means of F_2 elimination and formation of $[XeF_5][Xe_2F_{11}][CrOF_5]\cdot 2CrOF_4$.[244] The present study has shown that the low-temperature reaction of XeF_6 with $CrOF_4$ in aHF yielded $[XeF_5][HF_2]\cdot CrOF_4$ and revealed that $CrOF_4$ is incapable of abstracting F^- from $[(HF)_nF]^-$ at 0 °C in aHF, in accordance with the calculated FIAs of the Group 6 oxide tetrafluorides.[252] Bifluoride formation was circumvented by the low-temperature reaction of XeF_6 and $CrOF_4$ in CF_2ClCF_2Cl solvent, which provided $[Xe_2F_{11}][CrOF_5]$. The $[Xe_2F_{11}][CrOF_5]$, $[XeF_5][HF_2]\cdot CrOF_4$, $[Xe_2F_{11}][MoOF_5]$, $[Xe_2F_{11}][WOF_5]$, $[XeF_5][Mo_2O_2F_9]$, $[XeF_5][W_2O_2F_9]$, and $[XeF_5][WOF_5]\cdot XeOF_4$ salts were synthesized and structurally characterized by low-temperature single-crystal X-ray diffraction and Raman spectroscopy. The present study has provided the first crystal structure determination of the $[CrOF_5]^-$ anion, precise crystal structures of $[MOF_5]^-$ and

$[M_2O_2F_9]^-$, and the first adduct of $CrOF_4$ with a fluoro-anion, $[XeF_5][HF_2]\cdot CrOF_4$. The crystal structures of the strongly ion-paired salts and their calculated gas-phase ion-pairs reflect the relative fluorobasicities of their anions and the calculated fluoride-ion affinities of M′OF_4 (M′ = Cr, Mo, W). The NBO analyses of gas-phase M′OF_4, $[M'OF_5]^-$, $\{[Xe_2F_{11}][CrOF_5]\}_2$, $[M_2O_2F_9]^-$, $[Xe_2F_{11}][MOF_5]$, and $\{[XeF_5][M_2O_2F_9]\}_2$ show that the F_{eq} ligands of $[CrOF_5]^-$ in $\{[Xe_2F_{11}][CrOF_5]\}_2$ are significantly less fluorobasic than those of $[MOF_5]^-$ in $[Xe_2F_{11}][MOF_5]$, as indicated by two Xe---F_{ax} secondary bonds in the structural unit of $[Xe_2F_{11}][CrOF_5]$ (**1**) in contrast to one Xe---F_{ax} secondary bond in the structural units of $[Xe_2F_{11}][MOF_5]$ (**3**, **4**). Detailed vibrational frequency assignments and mode descriptions for the Raman spectra of $[Xe_2F_{11}][M'OF_5]$ and $[XeF_5][M_2O_2F_9]$ have been obtained and fully assigned with the aid of quantum-chemical calculations.

CHAPTER 12

Conclusions

The first example of a mixed Kr^{II}/Xe^{II} compound, $[FKrFXeF][AsF_6]\cdot 0.5KrF_2\cdot 2HF$, was synthesized in aHF solvent below −60 °C under rigorously anhydrous conditions and structurally characterized by LT SCXRD and LT Raman spectroscopy. Redox decomposition of the thermally sensitive $[FKrFXeF][AsF_6]\cdot 0.5KrF_2\cdot 2HF$ salt was monitored by LT Raman spectroscopy and showed oxidative fluorination of Xe^{II} to Xe^{VI} had occurred with the formation of $([Kr_2F_3][AsF_6])_2\cdot XeF_4$ and $XeF_4\cdot KrF_2$. The latter were the first examples of mixed Kr^{II}/Xe^{IV} compounds. Further reaction at room temperature yielded the known Kr^{II}/Xe^{VI} complexes, $[F_5Xe(FKrF)_nAsF_6]$ (n = 1, 2), and a new Kr^{II}/Xe^{VI} complex, $[(F_5Xe)_2(\mu\text{-}FKrF)(AsF_6)_2]$, which was characterized by LT Raman spectroscopy. Quantum-chemical analyses of $[FKrFXeF]^+$ revealed that the terminal Ng–F bonds are polar covalent, where the Ng–F_t bonds have a greater degree of covalent character than the Ng---F_b bonds, and the Kr–F_t and Kr---F_b bonds were shown to be more covalent than the Xe–F_t and Xe---F_b bonds.

The first Cl(V) coordination complex of XeF_2 was prepared by exploiting the Lewis acid character and oxidative resistance of the $[ClO_2]^+$ cation. The reaction of α-$[ClO_2][AsF_6]$ with XeF_2 in aHF afforded $[O_2Cl(FXeF)_2][AsF_6]$, which was structurally characterized by LT Raman spectroscopy and LT SCXRD. The LT β-$[ClO_2][AsF_6]$ phase was obtained for the first time by crystallization or precipitation from aHF solution and was also characterized by LT Raman spectroscopy and LT SCXRD. An NBO analysis of the model anion, $([O_2Cl(FXeF)_2][AsF_6]_2)^-$, shows that the Cl---$F_{Xe}$ and Cl---F_{As} bonds are

primarily electrostatic, and a MEPS analysis of gas-phase $[ClO_2]^+$ showed that these bonds are directed towards regions of high positive electrostatic potential, σ-holes, on the isosurface of Cl. The synthesis of a salt of the $[O_2Cl(FXeF)_2]^+$ cation is a significant extension of Cl(V) coordination chemistry and indicated that the syntheses of other high-oxidation state $[XO_2]^+$ (X = Cl, Br, I) coordination complexes of NgF_2, such as $[O_2X(FNgF)_2][AsF_6]$ (Ng = Kr, Xe), may also be possible.

In a follow-up and related study, the reactions of $[BrO_2][PnF_6]$ (Pn = As, Sb) with XeF_2 in aHF were investigated and shown to yield $[O_2Br(FXeF)_n][AsF_6]$ (n = 1, 2) and $[O_2Br(FXeF)_2][SbF_6]$. The complexes were characterized by low-temperature Raman spectroscopy and SCXRD and provided the first examples of coordination complexes between a noble-gas difluoride and $[BrO_2]^+$. The F atoms of XeF_2 and $[PnF_6]^-$ interact with regions of high electrostatic potential on the bromine atom of $[BrO_2]^+$ such that their contact trajectories avoid the stereo-active valence electron lone pair of Br(V).

Prior to the present work, there were no structurally characterized examples of oxide fluorides of the noble metals Rh, Pd, Ag, Ir, Pt, or Au. Chlorine trifluoride and ClF_5 are oxidative fluorinating agents which are also known to undergo O/F metathesis reactions, and their reactions with IrO_2 were investigated with the aim to prepare the first iridium oxide fluoride species. The neutral iridium(V) fluoride coordination complex, F_5Ir---OClF, was prepared by reaction of IrO_2 with ClF_3 in aHF solvent. The characterization of F_5Ir---OClF by SCXRD provided the first experimental evidence for the formation of OClF as an unstable reaction intermediate in the reaction of ClF_3 with a metal oxide, and the first example of an OClF coordination complex. The first iridium

oxyfluoro-anion salt, $[ClO_2]_2[cyclo\text{-}(\mu\text{-}OIrF_4)_3]$, was synthesized by reaction of IrO_2 with ClF_5 in aHF solvent at room temperature over a period of four days. The $[cyclo\text{-}(\mu\text{-}OIrF_4)_3]^{2-}$ anion is a six-membered Ir_3O_3-ring in which the Ir coordination sphere of 4 x Ir–F and 2 x Ir–O bonds is octahedral with cis-oriented Ir–O bonds. This salt provides a rare example of a high-oxidation-state, mixed-valence (2 x Ir(V) and 1 x Ir(VI)) species, and the first structurally characterized high-oxidation-state iridium oxide fluoride. Quantum-chemical calculations showed that the Ir---O bond in F_5Ir---OClF is predominantly electrostatic in nature.

The coordination chemistries of the Group 6 oxide tetrafluorides with NgF_2 were significantly extended by the syntheses and detailed structural characterizations of F_tNgF_b---$M(O)F_4$ (Ng = Kr, Xe; M = Mo, W) and F_tXeF_b---$M(O)F_3F_b'$---$M'(O)F_4$ by SCXRD. In this study, KrF_2 was shown to coordinate to the electrophilic center of the transition metal through fluorine in its complexes: F_tKrF_b---$Mo(O)F_4$ and F_tKrF_b---$W(O)F_4$. The synthesis and characterization of the tungsten complex with KrF_2 proved to be particularly challenging owing to the propensity of this complex to decompose by oxidative fluorination to WF_6, Kr, and O_2 at low temperatures (−65 °C). The study also provided the first definitive structural characterizations of the F_tXeF_b---$M(O)F_3F_b'$---$M'(O)F_4$ complexes, which have *cis-, trans*-arrangements of M=O and M'=O bonds with respect to F_b', by LT SCXRD structure determinations and low-temperature Raman spectroscopy. The preference for the *cis-, trans*-isomer over the *trans-, trans*-isomer is attributed to the greater fluorobasicities of the F atoms of coordinated MOF_4 relative to the F_t atom of the XeF_2 ligand, as shown by NBO, AIM, and MEPS analyses. The nature

of M---F_b and M'---F_b' in F_tNgF_b---$M(O)F_4$ and F_tXeF_b---$M(O)F_3F_b'$---$M'(O)F_4$ were investigated by quantum-chemical calculations and were shown to be σ-hole bonds. These bonds have small but significant degrees of covalent character which account for the bent Ng–F_b---M bond angles and staggered dihedral O=M---F_b–Ng–F_t angles that are observed in the crystal structures of these compounds and are calculated for the gas-phase molecules.

The chemistry of XeF_4 is the least developed among the binary xenon fluorides XeF_2, XeF_4, and XeF_6. The absence of an XeF_4 coordination complex with a TM center underscores the relative dearth of synthetic and structural information and highlights the experimental challenges associated with Xe(IV) chemistry. Now, a thorough synthetic, structural, and computational investigation has led to the synthesis and characterization of the first TM complex of Xe(IV), F_3XeF_b---WOF_4 by LT Raman spectroscopy and LT SCXRD. This provided only the second structurally characterized example of XeF_4 ligand behavior. The complex was synthesized by reaction of XeF_4, one of the most potent oxidative fluorinators known, with the oxidatively resistant Lewis acid, WOF_4, in $CFCl_3$ solvent. Quantum-chemical calculations were used to assist with the assignments of the Raman spectrum and to provide insight into the bonding of the complex. Chemical bonding was thoroughly assessed using NBO, AIM, ELF, MEPS, EDA, and ETS-NOCV analyses, which show that the W---F_b bonds in F_3XeF_b---WOF_4 and the M---F_b bonds in the hypothetical F_3XeF_b---MOF_4 (M = Cr, Mo) complexes are best described as σ-hole bonds which have small but significant degrees of covalent character.

The chemistry of chromium in its highest oxidation state, +6, is severely limited relative to molybdenum and tungsten. Because CrF_6 is unknown, $CrOF_4$ provides the most highly fluorinated neutral Cr compound. The chemistry of $CrOF_4$ had been limited to the vibrationally characterized Cs^+ and $[NO]^+$ salts of $[CrOF_5]^-$, and the crystallographically and vibrationally characterized F_tNgF_b---$CrOF_4$ and F_4OCr---F_bNgF_b---$CrOF_4$ coordination complexes. Reactions of $CrOF_4$ with XeF_6, the strongest fluoride-ion donor among the noble-gas fluorides, in melts and in the oxidatively resistant solvents aHF and $CFCl_3$ were investigated with the aim to synthesize and structurally characterize Cr(VI) oxyfluoro-anion salts. The reaction pathways involve redox transformations that result in F_2 gas elimination and reduction of Cr(VI) to Cr(V) and Cr(IV) and/or oxygen/fluorine metatheses to yield: $[XeF_5]_2[Cr^{IV}F_6]\cdot 2CrOF_4$, $[Xe_2F_{11}]_2[Cr^{IV}F_6]$, $[XeF_5]_2[Cr^{V}{}_2O_2F_8]$, $[XeF_5]_2[Cr^{V}{}_2O_2F_8]\cdot 2HF$, $[XeF_5]_2[Cr^{V}{}_2O_2F_8]\cdot 2XeOF_4$, and $[XeF_5][Xe_2F_{11}][Cr^{V}OF_5]\cdot 2CrOF_4$, which were characterized by LT single-crystal X-ray diffraction. This provided the first crystal structure of the $[Cr^{V}OF_5]^{2-}$ anion and the first syntheses and crystal structures of the $[Cr^{V}{}_2O_2F_8]^{2-}$ anion. The reaction of XeF_6 with $CrOF_4$ to give $[XeF_5][Xe_2F_{11}][CrOF_5]\cdot 2CrOF_4$ was also shown by LT Raman spectroscopy to proceed through the intermediate Cr(VI) salt, $[Xe_2F_{11}][CrOF_5]$. Quantum-chemical calculations were employed to calculate the gas-phase geometries, and aid in vibrational frequency assignments and discussions of chemical bonding.

Like $CrOF_4$, the chemistry of CrO_2F_2 is also limited. This is exemplified by the fact that salts of the $[M_2O_4F_6]^{2-}$ [286,319,320] and $[MO_2F_4]^{2-}$ [321–324] anions (M = Mo, W) have

been characterized by SCXRD, whereas their Cr analogues had not. Salts of the high-oxidation-state oxyfluoro-anions $[Cr_2O_4F_6]^{2-}$ and $[CrO_2F_4]^{2-}$ have now been synthesized by reactions of XeF_6 with CrO_2F_2 in aHF solvent and by their direct reaction in melts at elevated temperatures (ca. 50 °C), namely $[XeF_5]_2[Cr_2O_4F_6]$, $[XeF_5]_2[Cr_2O_4F_6]\cdot 4HF$, $[XeF_5]_2[Cr_2O_4F_6]\cdot 2XeOF_4$, and $[XeF_5][Xe_2F_{11}][CrO_2F_4]$. The salts were characterized by LT Raman spectroscopy and SCXRD and provide the first crystallographic characterizations of $[Cr_2O_4F_6]^{2-}$ and $[CrO_2F_4]^{2-}$. The $[Cr_2O_4F_6]^{2-}$ anions are fluorine-bridged dimers of $[CrO_2F_3]^-$ which have terminal cis-dioxo Cr–O double bonds. Quantum-chemical calculations show that the Cr–F_b bonds in $[Cr_2O_4F_6]^{2-}$ are highly polar-covalent, and that ion-pair formation as well as HF and $XeOF_4$ coordination significantly effects the covalent characters of the Cr–O and Cr–F bonds in $[Cr_2O_4F_6]^{2-}$ and $[CrO_2F_4]^{2-}$.

In a related study, the RT reactions of MOF_4 (M = Mo, W) with XeF_6 in aHF and $CFCl_3$ solvents yielded the ion-paired salts, $[Xe_2F_{11}][MOF_5]$ and $[XeF_5][M_2O_2F_9]$, and hydrolysis of $[Xe_2F_{11}][WOF_5]$ in HF gave $[XeF_5][WOF_5]\cdot XeOF_4$. In contrast, the LT reaction of XeF_6 with $CrOF_4$ in aHF yielded $[XeF_5][HF_2]\cdot CrOF_4$, which demonstrated that $CrOF_4$ is incapable of abstracting F^- from $[(HF)_xF]^-$ at 0 °C in aHF, in accordance with the calculated FIAs of $CrOF_4$, $MoOF_4$, and WOF_4. Bifluoride formation was circumvented by the low-temperature reaction of XeF_6 and $CrOF_4$ in CF_2ClCF_2Cl (Freon-114) solvent and yielded $[Xe_2F_{11}][CrOF_5]$. The salts were characterized by low-temperature single-crystal X-ray diffraction and Raman spectroscopy, which provided the first crystal structure determination of the $[CrOF_5]^-$ anion, precise and non-disordered

geometric parameters for $[MOF_5]^-$ and $[M_2O_2F_9]^-$, and the first structurally characterized coordination complex of $CrOF_4$ with a fluoro-anion, $[XeF_5][HF_2]\cdot CrOF_4$. Quantum-chemical calculations show that structural differences between dimeric $[Xe_2F_{11}][CrOF_5]$ and monomeric $[Xe_2F_{11}][MOF_5]$ may be attributed to the significantly lower and higher basicities of the F_{eq} and F_{ax} atoms of $[CrOF_5]^-$ in $\{[Xe_2F_{11}][CrOF_5]\}_2$ relative to those of $[MOF_5]^-$ in $[Xe_2F_{11}][MOF_5]$.

CHAPTER 13

Future Work

13.1. Extending X(V) (X = Cl, Br, I) Coordination Chemistry

The advances in X(V) coordination chemistry described in Chapters 4 and 5 of this Thesis provide the basis for further research in this field. Presently, $[O_2Cl(FXeF)_2][AsF_6]$ is the only cationic Cl(V) coordination complex that has been structurally characterized,[61] and the $[O_2Br(FXeF)_n][AsF_6]$ (n = 1, 2), $[O_2Br(FXeF)_2][SbF_6]$, $[F_2OBrFXeF][AsF_6]$, $[F_2OBr(FNgF)_2][AsF_6]$, and $[O_2Br(BrO_2F)][AsF_6]$ complexes represent the known Br(V) cationic coordination complexes. An obvious extension of this work would be to use KrF_2 as the coordinating ligand, which has previously been demonstrated for $[BrOF_2]^+$ [62] but not for $[XO_2]^+$ (X = Cl, Br, I) (Eq. **13.1**).

$$[XO_2][PnF_6] + nKrF_2 \longrightarrow [O_2X(FKrF)_n][PnF_6] \text{ (Pn = As, Sb; } n = 1 \text{ or } 2) \quad (\mathbf{13.1})$$

There are presently no structurally characterized examples of cationic I(V) coordination complexes. Recent molecular electrostatic potential surface analyses of the $[XO_2]^+$ (X = Cl, Br, I) cations have demonstrated that the global electrostatic potential maxima, which correlate with Lewis acidity, are similar for the $[BrO_2]^+$ (767 kJ mol^{-1}) and $[IO_2]^+$ (762 kJ mol^{-1}) cations.[61] Thus, it is likely that $[IO_2]^+$ coordination complexes of NgF_2 (Ng = Kr, Xe) can be synthesized by analogy with those of $[ClO_2]^+$ and $[BrO_2]^+$ (Eq. **13.1**). It would also be interesting to see if $[O_2X(FKrF)_n]^+$ undergoes intramolecular oxidative fluorination to the +7 oxidation state of X to form $[XO_2F_2]^+$ salts according to Eq. **13.2**.

$$[O_2X(FKrF)][PnF_6] \longrightarrow [XO_2F_2][PnF_6] + Kr \quad (\mathbf{13.2})$$

No nitrogen- or oxygen-base complexes of the X(V) (X = Cl, Br, I) cations $[XF_4]^+$, $[XOF_2]^+$, and $[XO_2]^+$ have been reported. Attempts to form X---N/O bonded cationic coordination complexes of $[XO_2]^+$ by coordination of oxidatively resistant Lewis bases such as acetonitrile, pentafluoropyridine, and thiazyl trifluoride should be attempted in efforts to form $[O_2X(L)_2][PnF_6]$ (L = $NCCH_3$, C_5F_5N, NSF_3) (Eq. **13.3**).

$$[XO_2][PnF_6] + nL \longrightarrow [O_2X(L)_n][PnF_6] \text{ (Pn = As, Sb; } n = 1 \text{ or } 2) \quad (\mathbf{13.3})$$

This work may also be expanded to the oxyfluoro-cations $[XF_4]^+$ [215–217] and $[XOF_2]^+$,[139,142,143,185–188,218–222] which are more Lewis acidic than $[XO_2]^+$ and are expected to form coordination complexes with noble-gas fluorides. Prior attempts to synthesize $[F_2OCl(FXeF)_2][AsF_6]$ by analogy with $[F_2OBr(FXeF)_2][AsF_6]$ resulted in fluoride-ion abstraction to give $[Xe_2F_3][AsF_6]$ and $ClOF_3$, which can be attributed to the greater Lewis acidity of $[ClOF_2]^+$ relative to that of $[BrOF_2]^+$. To reduce the propensity for NgF_2 to transfer fluoride-ion and form a neutral coordination complex instead, the $[ClOF_2]^+$ cation, and more Lewis acidic Cl(V), Br(V), and I(V) cations, should be paired with anions that are more fluorobasic than $[PnF_6]^-$ (Pn = As, Sb) such as the $[MOF_5]^-$ and $[M_2O_2F_9]^-$ (M = Mo, W) counterions (Eqs. **13.4** and **13.5**). This is expected to reduce the effective Lewis acidity of the cations and may facilitate the formation of stable $[XOF_2]^+$ and $[XF_4]^+$ coordination complexes with NgF_2.

$$[XOF_2][M_nO_nF_{4n+1}] \ (n = 1 \text{ or } 2) + mNgF_2 \longrightarrow [F_2OX(FNgF)_m][M_nO_nF_{4n+1}] \ (\mathbf{13.4})$$

$$[XF_4][M_nO_nF_{4n+1}] \ (n = 1 \text{ or } 2) + mNgF_2 \longrightarrow [F_4X(FNgF)_m][M_nO_nF_{4n+1}] \quad (\mathbf{13.5})$$

13.2. Syntheses and Structural Characterizations of Inorganic Derivatives of MO_2F_2 (M = Cr, Mo, W) and their Related Ions.

As highlighted in Chapters 9–11, the high-oxidation state oxide, fluoride, and oxide fluoride chemistries of Group 6, particularly those of chromium, are limited. Although the research described in Chapters 9–11 has advanced the aforementioned research areas, significant gaps remain that are mainly related to the syntheses and structural characterizations of inorganic derivatives of high-oxidation state Group 6 oxide, fluoride, and oxide fluoride species. For example, chromyl fluoride (CrO_2F_2) reacts with $(CF_3CO)_2O$ and SO_3 to give $CrO_2(OCCF_3)_2$ and $CrO_2(SO_3F)_2$,[269] and undergoes ligand exchange with $Hg(OSeF_5)_2$ to yield $CrO_2(OSeF_5)_2$ and HgF_2,[350] however, no crystal structures of the reaction products have been forthcoming.

The pseudo-octahedral F_5TeO-ligand (teflate) is a highly electronegative, oxidatively resistant ligand that is often employed as a bulky analogue of fluorine.[351–355] The group electronegativity of the F_5TeO-ligand is similar to that of fluorine, except that it forms bonds through its oxygen atom, is isoelectronic with $[SbF_6]^-$, and its salts are tend to be very soluble in non-polar solvents because the F_5TeO-ligands generally do not engage in bridging, unlike fluorine compounds. The high electronegativity, oxidative resistance, steric bulk, and high solubilities of F_5TeO-derivatives have resulted in extensive use of the F_5TeO-ligand as a fluorine analogue in main-group chemistry, and especially for noble-gas compounds.

Reactions of MO_2X_2 (M = Cr, Mo, W; X = Cl or F) with $HOTeF_5$ in $CFCl_3$ or CF_2ClCF_2Cl solvent are expected to yield $MO_2(OTeF_5)_2$ and HX according to Eq. **13.6**.

Alternatively, $MO_2(OTeF_5)_2$ may be prepared by reaction of MO_2X_2 with $Hg(OTeF_5)_2$ or $B(OTeF_5)_3$ according to Eqs. **13.7** and **13.8**.

$$MO_2X_2 + 2HOTeF_5 \longrightarrow MO_2(OTeF_5)_2 + 2HX \quad (\mathbf{13.6})$$

$$MO_2X_2 + Hg(OTeF_5)_2 \longrightarrow MO_2(OTeF_5)_2 + HgX_2 \quad (\mathbf{13.7})$$

$$3MO_2X_2 + 2B(OTeF_5)_3 \longrightarrow 3MO_2(OTeF_5)_2 + 2BX_3 \quad (\mathbf{13.8})$$

Nitrogen base adducts of Lewis acidic $MO_2(OTeF_5)_2$ may also be prepared by reaction of $MO_2(OTeF_5)_2$ with oxidatively resistant nitrogen bases such as acetonitrile to obtain the $MO_2(OTeF_5)_2L_2$ (L = CH_3CN, CH_3CH_2CN) series of adducts (Eqs. **13.9**).

$$MO_2(OTeF_5)_2 + 2CH_3CN \longrightarrow MO_2(OTeF_5)_2L_2 \quad (\mathbf{13.9})$$

Reactions of $MO_2(OTeF_5)_2$ (M = Cr, Mo, W) with M′[$OTeF_5$] (M′ = TMA, Cs, Ag) may be expected to yield salts of novel monomeric $[MO_2(OTeF_5)_3]^-$ and $[MO_2(OTeF_5)_4]^{2-}$ anions, or of the dimerized $[M_2O_4(OTeF_5)_6]^{2-}$ anions. This work may also be extended to other oxidatively resistant electron-withdrawing functional groups such as $–OC(CF_3)_3$, $–OC(O)CF_3$, $–OSO_2F$, and $–OSO_2CF_3$, provided suitable ligand transfer reagents can be found.

CHAPTER 14

REFERENCES

1. Bartlett, N. *Proc. Chem. Soc.* **1962**, *218*.
2. Graham, L.; Graudejus, O.; Jha, N. K.; Bartlett, N. *Coord. Chem. Rev.* **2000**, *197*, 321–334.
3. Schreiner, F.; Malm, J. G.; Hindman, J. C. *J. Am. Chem. Soc.* **1965**, *87*, 25–28.
4. Hoppe, R.; Dähne, W.; Mattauch, H.; Rödder, K. *Angew. Chem. Int. Ed.* **1962**, *1*, 599.
5. Claassen, H. H.; Selig, H.; Malm, J. G. *J. Am. Chem. Soc.* **1962**, *84*, 3593.
6. Malm, J. G.; Sheft, I.; Chernick, C. L. *J. Am. Chem. Soc*. **1963**, *85*, 110–111.
7. Smith, D. F. *J. Am. Chem. Soc*. **1963**, *85*, 816–817.
8. Smith, D. F. *Science* **1963**, *140*, 899–900.
9. Schrobilgen, G. J. "Lewis Acid Properties of Noble Gas Cations", In *Synthetic Fluorine Chemistry*, Chambers, R. D.; Olah G. A.; Prakash, G. K. S. eds., New York: Wiley and Sons, 1992, Chapter 1, pp. 1−30.
10. Gomila, R. M.; Frontera, A. *Front. Chem.* **2020**, *8*, 395.
11. Saha, R.; Jana, G.; Pan, S.; Merino, G.; Chattaraj, P. K. *Molecules* **2019**, *24*, 2933.
12. Nabiev, S. S.; Sokolov, V. B.; Chaivanov, B. B. *Russ. Chem. Rev*. **2014**, *83*, 1135–1180.
13. Mazej, Z. *Molecules* **2020**, *25*, 3014.
14. Pan, S.; Jana, G.; Merino, G.; Chattaraj, P. K. *ChemistryOpen* **2019**, *8*, 173–187.
15. Hope, E. G. *Coord. Chem. Rev.* **2013**, *257*, 902–909.

16. Grandinetti, F. *Noble Gas Chemistry: Structure, Bonding, and Gas-Phase Chemistry*; John Wiley & Sons, **2018**.

17. Lehmann, J. F.; Mercier, H. P. A.; Schrobilgen, G. J. *Coord. Chem. Rev.* **2002**, *233–234*, 1–39.

18. Tavčar, G.; Tramšek, M. *J. Fluor. Chem*. **2015**, *174*, 14–21.

19. Brock, D. S.; Schrobilgen, G. J.; Žemva, B. "Noble-Gas Chemistry" In *Comprehensive Inorganic Chemistry II (Second Edition): From Elements to Applications*; Elsevier Ltd, 2013; Vol. 1, pp 755–822.

20. Haner, J.; Schrobilgen, G. J. *Chem. Rev*. **2015**, *115*, 1255–1295.

21. a) Laszlo, P.; Schrobilgen, G. J. *Angew. Chem. Int. Ed.* **1988**, *27*, 479–489. b) Schrobilgen, G. J. "Chemistry at the Edge of the Periodic Table: The Importance of Periodic Trends on the Discovery of the Noble Gases and the Development of Noble-Gas Chemistry", In *The Periodic Table I – Historical Development and Essential Features*, Mingos, D. M. P. Ed.; Structure and Bonding 181, Springer Nature, Zurich, **2019**, Chapter 49, pp.157–196.

22. Tramšek, M.; Žemva, B. *Acta. Chim. Slov.* **2006**, *55*, 105–116.

23. Halpern, D. F.; Tavčar, G.; Tramšek, M. "Xenon(II) Fluoride" In *Encyclopedia of Reagents for Organic Synthesis*; John Wiley & Sons Ltd, 2017; pp 1–5.

24. Falconer, W. E.; Sunder, W. A. *J. Inorg. Nucl. Chem.* **1967**, *29*, 1380–1381.

25. Johnson, G. K.; Malm, J. G.; Hubbard, W. N. *J. Chem. Thermodyn.* **1972**, *4*, 879–891.

26. Schreiner, F.; McDonald, G. N.; Chernick, C. L. *J. Phys. Chem.* **1968**, *72*, 1162–1166.

27. Easter, C.; O'Neal, C. B. *J. Microelectromech. Syst.* **2009**, *18*, 1054–1061.

28. Schrobilgen, G. J.; Firnau, G.; Chirakal, R.; Garnett, E. S. *J. Chem. Soc. Chem. Commun.* **1981**, *4*, 198–199.

29. Lu, S.; Pike, V. W. *J. Fluor. Chem.* **2010**, *131*, 1032–1038.

30. Vasdev, N.; Pointner, B. E.; Chirakal, R.; Schrobilgen, G. J. *J. Am. Chem. Soc.* **2002**, *124*, 12863–12868.

31. Yamaguchi, S.; Shirasaka, T.; Tamao, K. *Organometallics* **2002**, *21*, 2555–2558.

32. Yamaguchi, S.; Akiyama, S.; Tamao, K. *J. Organomet. Chem.* **2002**, *646*, 277–281.

33. Klapötke, T. M.; Krumm, B.; Mayer, P.; Piotrowski, H.; Ruscitti, O. P.; Schiller, A. *Inorg. Chem.* **2002**, *41*, 1184–1193.

34. Yahav, A.; Goldberg, I.; Vigalok, A. *J. Am. Chem. Soc.* **2003**, *125*, 13634–13635.

35. Bernhardt, E.; Bach, C.; Bley, B.; Wartchow, R.; Westphal, U.; Sham, I. H. T.; von Ahsen, B.; Wang, C.; Willner, H.; Thompson, R. C.; Aubke, F. *Inorg. Chem.* **2005**, *44*, 4189–4205.

36. Yahav, A.; Goldberg, I.; Vigalok, A. *Inorg. Chem*. **2005**, *44*, 1547–1553.

37. Jeon, K. J.; Lee, Z.; Pollak, E.; Moreschini, L.; Bostwick, A.; Park, C. M.; Mendelsberg, R.; Radmilovic, V.; Kostecki, R.; Richardson, T. J.; Rotenberg, E. *ACS Nano.* **2011**, *5*, 1042–1046.

38. Patrick, T. B.; Mortezania, R. *J. Org. Chem.* **1988**, *53*, 5153–5155.

39. Sessa, P. A.; McGee, H. A. *J. Phys. Chem*. **1969**, *73*, 2078–2080.

40. Prusakov, V. N.; Sokolov, V. B. *Sov. At. Energy* **1971**, *31*, 990–999.

41. Turner, J. J.; Pimentel, G. C. *Science* **1963**, *140*, 974–975.

42. Streng, L. V.; Streng, A. G. *Inorg. Chem.* **1966**, *5*, 328–329.

43. Slivnik, J.; Šmalc, A.; Lutar, K.; Žemva, B.; Frlec, B. *J. Fluor. Chem*. **1975**, *5*, 273–274.

44. Šmalc, A.; Lutar, K.; Žemva, B.; Kinkead, S. A. *Inorg. Synth.* **2007**, *29*, 11–15.

45. Kinkead, S. A.; FitzPatrick, J. R.; Foropoulos, J.; Kissane, R. J.; Purson, J. D. *ACS Symposium Series,* **1994**, *555*, 40–55.

46. Lehmann, J. F.; Dixon, D. A.; Schrobilgen, G. J. *Inorg. Chem*. **2001**, *40*, 3002–3017.

47. Liebman, J. F. *Struct. Chem*. **2000**, *11*, 261–263.

48. Elliott, H. St. A.; Lehmann, J. F.; Mercier, H. P. A.; Jenkins, H. D. B.; Schrobilgen, G. J. *Inorg. Chem.* **2010**, *49*, 8504–8523.

49. Dukat, W. W.; Holloway, J. H.; Hope, E. G.; Townson, P. J.; Powell, R. L. *J. Fluor. Chem.* **1993**, *62*, 293–296.

50. Rundle, R. E. *J. Am. Chem. Soc.* **1963**, *85*, 112–113.

51. Gillespie, R. J.; Schrobilgen, G. J. *Inorg. Chem*. **1976**, *15*, 22–31.

52. Gillespie, R. J.; Netzer, A.; Schrobilgen, G. J. *Inorg. Chem*. **1974**, *13*, 1455–1459.

53. Ruby, S. L.; Selig, H. *Phys. Rev.* **1966**, *147*, 348–354.

54. Holloway, J. H.; Schrobilgen, G. J.; Bukshpan, S.; Hilbrants, W.; de Waard, H. *J. Chem. Phys.* **1976**, *66*, 2627–2630.

55. Falconer, W. E.; Morton, J. R.; Streng, A. G. *J. Chem. Phys.* **1964**, *41*, 902–903.

56. Gunn, S. R. *J. Chem. Phys*. **1967**, *71*, 2934–2937.

57. Gunn, S. R. *J. Am. Chem. Soc.* **1966**, *88*, 5924.

58. Radan, K.; Goreshnik, E.; Žemva, B. *Angew. Chem. Int. Ed.* **2014**, *53*, 13715–13719.

59. Fir, B. A.; Gerken, M.; Pointner, B. E.; Mercier, H. P. A.; Dixon, D. A.; Schrobilgen, G. J. *J. Fluor. Chem.* **2000**, *105*, 159–167.

60. Mazej, Z.; Goreshnik, E. *Eur. J. Inorg. Chem*. **2021**, *2021*, 2669–2681.

61. Bortolus, M. R.; Ellwanger, M.; Haner, J.; Schrobilgen, G. J. *J. Fluor. Chem*. **2021**, *250*, 109814.

62. Brock, D. S.; Casalis de Pury, J. J.; Mercier, H. P. A.; Schrobilgen, G. J.; Silvi, B. *J. Am. Chem. Soc.* **2010**, 132, 3533–3542.

63. Brock, D. S.; Casalis de Pury, J. J.; Mercier, H. P. A.; Schrobilgen, G. J.; Silvi, B. *Inorg. Chem.* **2010**, *49*, 6673–6689.

64. Žemva, B.; Jesih, A.; Templeton, D. H.; Zalkin, A.; Cheetham, A. K.; Bartlett, N. *J. Am. Chem. Soc.* **1987**, *109*, 7420–7427.

65. Mercier, H. P. A.; Breddemann, U.; Brock, D. S.; Bortolus, M. R.; Schrobilgen, G. J. *Chem. Eur. J.* **2019**, *25*, 12105–12119.

66. Christe, K. O.; Wilson, W. W.; Bougon, R. A. *Inorg. Chem.* **1986**, *25*, 2163–2169.

67. Bortolus, M. R.; Mercier, H. P. A.; Brock, D. S.; Schrobilgen, G. J. *Chem. Eur. J.* **2022**, *28*, e202103729.

68. Hughes, M. J.; Brock, D. S.; Mercier, H. P. A.; Schrobilgen, G. J. *J. Fluor. Chem.* **2011**, *132*, 660–668.

69. Jones, G. R.; Burbank, R. D.; Bartlett, N. *Inorg. Chem*. **1970**, *9*, 2264–2268.

70. Adams, C. J. *J. Raman Spectrosc*. **1974**, *2*, 391–397.

71. Burns, J. H. *J. Phys. Chem.* **1963**, *67*, 536.

72. Debackere, J. R.; Mercier, H. P. A.; Schrobilgen, G. J. *J. Am. Chem. Soc.* **2014**, *136*, 3888–3903.

73. Lozinšek, M.; Mercier, H. P. A.; Schrobilgen, G. J. *Angew. Chem. Int. Ed.* **2021**, *60*, 8149–8156.

74. Lozinšek, M.; Mercier, H. P. A.; Brock, D. S.; Žemva, B.; Schrobilgen, G. J. *Angew. Chem. Int. Ed.* **2017**, *56*, 6251–6254.

75. Claassen, H. H.; Selig, H.; Malm, J. G. *J. Am. Chem. Soc.* **1962**, *84*, 3593.

76. Chernick, C. L.; Claassen, H. H.; Fields, P. R.; Hyman, H. H.; Malm, J. G.; Manning, W. M.; Matheson, M. S.; Quarterman, L. A.; Schreiner, F.; Selig, H. H.; Sheft, I.; Siegel, S.; Sloth, E. N.; Stein, L.; Studier, M. H.; Weeks, J. L.; Zirin, M. H. *Science* **1962**, *138*, 136–138.

77. Malm, J. G.; Chernick, C. L.; Williamson, S. M. *Inorg. Synth.* **1966**, *8*, 254–258.

78. Bartlett, N.; Sladky, F. O. "The Chemistry of Krypton, Xenon and Radon" In *The Chemistry of the Monatomic Gases*; Elsevier, 1973; pp 213–330.

79. Gillespie, R. J.; Landa, B.; Schrobilgen, G. J. *Inorg. Chem*. **1976**, *15*, 1256–1263.

80. Gillespie, R. J.; Schrobilgen, G. J. *Inorg. Chem.* **1974**, *13*, 2370–2374.

81. Boldrini, P.; Gillespie, R. J.; Ireland, P. R.; Schrobilgen, G. J. *Inorg. Chem*. **1974**, *13*, 1690–1694.

82. Brock, D. S.; Mercier, H. P. A.; Schrobilgen, G. J. *J. Am. Chem. Soc.* **2013**, *135*, 5089–5104.

83. Gillespie, R. J.; Martin, D.; Schrobilgen, G. J.; Slim, D. R. *J. Chem. Soc., Dalton Trans*. **1977**, *22*, 2234–2237.

84. Gillespie, R. J.; Landa, B.; Schrobilgen, G. J. *J. Chem. Soc. (D).* **1971**, *23*, 1543–1544.

85. McKee, D. E.; Zalkin, A.; Bartlett, N. *Inorg. Chem*. **1973**, *12*, 1713–1717.

86. Gillespie, R. J.; Martin, D.; Schrobilgen, G. J. *J. Chem. Soc., Dalton Trans.* **1980**, *10*, 1898–1903.

87. Christe, K. O.; Curtis, E. C.; Dixon, D. A.; Mercier, H. P. A.; Sanders, J. C. P.; Schrobilgen, G. J. *J. Am. Chem. Soc.* **1991**, *113*, 3351–3361.

88. Gillespie, R. J.; Hargittai, I. *The VSEPR Model of Molecular Geometry*; Allyn and Bacon: Boston, MA, 1991.

89. Gillespie, R. J.; Landa, B.; Schrobilgen, G. J. *J. Inorg. Nucl. Chem. Supplement* **1976**, *28*, 179–182.

90. Grant, D. J.; Wang, T. H.; Dixon, D. A.; Christe, K. O. *Inorg. Chem.* **2010**, *49*, 261–270.

91. Tavčar, G.; Žemva, B. *Angew. Chem. Int. Ed.* **2009**, *48*, 1432–1434.

92. Burns, J. H. *J. Phys. Chem.* **1963**, *67*, 536.

93. Mazej, Z.; Darriet, J.; Grannec, J.; Lutar, K.; Tressaud, A.; Žemva, B. *J. Fluor. Chem*. **1999**, *99*, 25–28.

94. Chernic, C. L.; Malm, J. G.; Williamson, S. M. *Inorg. Chem.* **1966**, *8*, 258–260.

95. Selig, H. *Inorg. Chem.* **1966**, *5*, 183–186.

96. Huston J. L. *J. Phys. Chem.* **1967**, *71*, 3339–3341.

97. Goettel, J. T.; Schrobilgen, G. J. *Inorg. Chem*. **2016**, *55*, 12975–12981.

98. Templeton, D. H.; Zalkin, A.; Forrester, J. D.; Wiliamson, S. M. *J. Am. Chem. Soc.* **1963**, *85*, 817.

99. Bartlett, N.; Jha, N. K. *Noble Gas Compounds*; H. H. Hyman, Ed.; University of Chicago Press: Chicago, **1963**; p 23.

100. Hoyer, S.; Emmler, T.; Seppelt, K. *J. Fluor. Chem.* **2006**, *127*, 1415–1422.

101. Matsumoto, K.; Haner, J.; Mercier, H. P. A.; Schrobilgen, G. J. *Angew. Chem. Int. Ed.* **2015**, *54*, 14169–14173.

102. Haner, J.; Matsumoto, K.; Mercier, H. P. A.; Schrobilgen, G. J. *Chem Eur. J.* **2016**, *22*, 4833–4842.

103. Schrobilgen, G. J.; Holloway, J. H.; Granger, P.; Brevard, C. *Inorg. Chem.* **1978**, *17*, 980–987.

104. Seppelt, K.; Bartlett, N. *Z. Anorg. Allg. Chem.* **1977**, *436*, 122–126.

105. Bartell, L. S.; Gavin, R. M.; Thompson, H. B.; Chernick, C. L. *J. Chem. Phys.* **1965**, *43*, 2547–2548.

106. Harshbarger, W.; Bohn, R. K.; Bauer, S. H. *J. Am. Chem. Soc.* **1967**, *89*, 6466–6469.

107. Gavin, R. M.; Bartell, L. S. *J. Chem. Phys.* **1968**, *48*, 2460–2465.

108. Bartell, L. S.; Gavin, R. M. *J. Chem. Phys.* **1968**, *48*, 2466–2483.

109. Hyunyong K.; Claassen, H. H.; Pearson, E. F. *Inorg. Chem.* **1968**, *7*, 616–617.

110. Gasner, E. L.; Claassen, H. H. *Inorg. Chem*. **1967**, *6*, 1937–1938.

111. Claassen, H. H.; Goodman, G. L.; Hyunyong, K. *J. Chem. Phys*. **1972**, *56*, 5042–5053.

112. Cutler, J. N.; Bancroft, G. M.; Bozek, J. D.; Tan, K. H.; Schrobilgen, G. J. *J. Am. Chem. Soc.* **1991**, *113*, 9125–9131.

113. Bancroft, G. M.; Bristow, D. J.; Tse, J. S.; Schrobilgen, G. J. *Inorg. Chem.* **1983**, *22*, 2673– 2677.

114. Peterson, K. A.; Dixon, D. A.; Stoll, H. *J. Phys. Chem.* **2012**, *116*, 9777–9782.

115. Gawrilow, M.; Beckers, H.; Riedel, S.; Cheng, L. *J. Chem. Phys.* **2018**, *122*, 119–129.

116. Adams, C. J.; Bartlett, N. *Isr. J. Chem.* **1978**, *17*, 114–125.

117. Lutar, K.; Jesih, A.; Leban, I.; Žemva, B.; Bartlett, N. *Inorg. Chem.*, **1989**, *28*, 3467–3471.

118. Jesih, A.; Lutar, K.; Leban, I.; Žemva, B. *Inorg. Chem.* **1989**, *28*, 2911–2914.

119. Leary, Z.; Zalkin, A.; Bartlett, N. *Inorg. Chem.* **1974**, *13*, 775–779.

120. Mercier, H. P. A.; Schrobilgen, G. J. *Inorg. Chem.* **1993**, *32*, 145–151.

121. Hughes, M. J.; Mercier, H. P. A.; Schrobilgen, G. J. *Inorg. Chem*. **2010**, *49*, 3501–3515.

122. Bertolini, J. C. *J. Emerg. Med.* **1992**, *10*, 163–168.

123. Peters, D.; Miethchen, R. *J. Fluor. Chem.* **1996**, *79*, 161–165.

124. Segal, E. B. *Chem. Health Saf.* **2000**, *7*, 18–23.

125. Nicolas LeBlond. Ph.D. Thesis, McMaster, Hamilton, 1998.

126. Breuer, G. *Handbook of Preparative Inorganic Chemistry*, vol. 1, Ed. Riley, R. F. Academic Press Inc., **1963**, pp. 197.

127. Mercier, H. P. A.; Sanders, J. C. P.; Schrobilgen, G. J.; Tsai, S. S. *Inorg. Chem.* **1993**, *32*, 386–393.

128. Emara, A. A. A.; Lehmann, J. F.; Schrobilgen, G. J. *J. Fluor. Chem*. **2005**, *126*, 1373–1376.

129. Kinkead, S. A; FitzPatrick, J. R.; Foropoulos, J. J.; Kissane, R. J.; Purson, J. D. In *Fluorine Chemistry Toward the 21st Century*; Thrasher, J. S.; Strauss, S. H., Eds.; ACS Symposium Series 555; American Chemical Society: Washington, DC, 1994; Chapter 3, pp 40−55.

130. Breuer, G. *Handbook of Preparative Inorganic Chemistry*, vol. 1, Ed. Riley, R. F. Academic Press Inc., **1963**, pp. 155.

131. Gillespie, R. J.; Schrobilgen, G. J. *Inorg. Chem*. **1976**, *15*, 22–31.

132. Malm, J. G.; Chernick, C. L. *Inorg. Synth.* **1966**, *3*, 254–258.

133. Malm, J. G.; Chernick, C. L. *Inorg. Synth.* **1966**, *8*, 258–260.

134. Bezmel'nitsyn V. N.; Legasov V. A.; Chaivanov B. B. *Dokl. Akad. Nauk. SSSR* **1997**, *235*, 96–98.

135. Green, P. J.; Gard, G. L. *Inorg. Chem.* **1977**, *16*, 1243–1245.

136. Burns, R. C.; O'Donnell, T. A.; Waugh, A. B. *J. Fluor. Chem*. **1978**, *12*, 505–517.

137. Christe, K. O.; Wilson, R. D.; Schack, C. J.; Desmarteau, D. D. *Inorg. Synth.* **1986**, *24*, 3.

138. Tantot, G.; Joubert, P.; Bougon, R. *Can. J. Chem*. **1978**, *56*, 1634–1637.

139. Seppelt, K. *Angew. Chem. Int. Ed.* **2019**, *58*, 18928–18930.

140. Casteel, W. J.; Dixon, D. A.; Mercier, H. P. A.; Schrobilgen, G. J. *Inorg. Chem*. **1996**, *35*, 4310–4322.

141. Scheibe, B.; Karttunen, A. J.; Kraus, F. *Eur. J. Inorg. Chem*. **2021**, *2021*, 405–421.

142. Christe, K. O.; Schack, C. J.; Pilipovich, D.; Sawodny, W. *Inorg. Chem*. **1969**, *8*, 2489–2494.

143. Lehmann, J. F.; Riedel, S.; Schrobilgen, G. J. *Inorg. Chem.* **2008**, *47*, 8343–8356.

144. APEX2, v.2014.9-0, Bruker AXS Inc.; Madison, WI, **2005**–**2014**.

145. APEX3, release v2017.3-0; Bruker AXS Inc.; Madison, WI, **1995**.

146. Sheldrick, G. M. *SADABS* (Siemens Area Detector Absorption Corrections), version 2.03; Siemens Analytical X-ray Instruments, Inc.; Madison, WI, **1999**.

147. *TWINABS* – Bruker AXS Scaling for Twinned Crystals, v.2012/1, Madison, WI, 2014.

148. *XPREP* – Reciprocal Space Exploration, v.2014/2, Bruker AXS Inc., Madison, WI, 2014.

149. Sheldrick, G. M. *Acta Crystallogr.* **2015**, *A71*, 3–8.

150. Sheldrick, G. M. *Acta Crystallogr.* **2015**, *C71*, 3–8.

151. Dolomanov, O. V.; Bourhis, L. J.; Gildea, R. J.; Howard, J. A. K.; Puschmann, H. *J. Appl. Crystallogr.* **2009**, *42*, 339–341.

152. Spek, A. L. *J. Appl. Crystallogr*. **2003**, *36*, 7–13.

153. EMSL Basis Set Exchange, v.1.2.2, https://bse.pnl.gov/bse/portal, Environmental Molecular Science Laboratory, Pacific Northwest National Laboratory, Richland, WA.

154. Gaussian 09, Revision D.01, Frisch, M. J.; Trucks, G. W.; Schlegel, H. B.; Scuseria, G. E.; Robb, M. A.; Cheeseman, J. R.; Scalmani, G.; Barone, V.; Mennucci, B.; Petersson, G. A.; Nakatsuji, H.; Caricato, M.; Li, X.; Hratchian, H. P.; Izmaylov, A. F.; Bloino, J.; Zheng, G.; Sonnenberg, J. L.; Hada, M.; Ehara, M.; Toyota, K.; Fukuda, R.; Hasegawa, J.; Ishida, M.; Nakajima, T.; Honda, Y.; Kitao, O.; Nakai, H.; Vreven, T.; Montgomery, J. A.; Peralta, J. E.; Ogliaro, F.; Bearpark, M.; Heyd, J. J.; Brothers, E.; Kudin, K. N.; Staroverov, V. N.; Kobayashi, R.; Normand, J.; Raghavachari, K.; Rendell, A.; Burant, J. C.; Iyengar, S. S.; Tomasi, J.; Cossi, M.; Rega, N.; Millam, N. J.; Klene, M.; Knox, J. E.; Cross, J. B.; Bakken, V.; Adamo, C.; Jaramillo, J.; Gomperts, R.; Stratmann, R. E.; Yazyev, O.; Austin, A. J.; Cammi, R.; Pomelli, C.; Ochterski, J. W.; Martin, R. L.; Morokuma, K.; Zakrzewski, V. G.; Voth, G. A.; Salvador, P.; Dannenberg, J. J.; Dapprich, S.; Daniels, A. D.; Farkas, J.; Foresman, J. B.; Ortiz, J. V.; Cioslowski, J.; Fox, D. J. Gaussian, Inc: Wallingford, CT, **2009**.

155. GaussView, version 3.0; Gaussian Inc.: Pittsburgh, PA, 2003.

156. NBO 6.0. Glendening, E. D.; Badenhoop, J. K.; Reed, A. E.; Carpenter, J. E.; Bohmann, J. A.; Morales, C. M.; Landis, C. R.; Weinhold, F. Theoretical Chemistry Institute, University of Wisconsin, Madison, **2013**.

157. Multiwfn, version 3.3.8; Lu, T.; Chen, F. *J. Comput. Chem.* **2012**, *33*, 580−592.

158. Pettersen, E. F.; Goddard, T. D.; Huang, C. C.; Couch, G. S.; Greenblatt, D. M. Meng, E. C.; Ferrin, T. E. *J. Comput. Chem.* **2004**, *25*, 1605–1612.

159. a) ADF 2016, SCM, Theoretical Chemistry, Vrije Universiteit, Amsterdam, The Netherlands, http://www.scm.com; b) Guerra, F. C.; Snijders, J. G.; te Velde, G.; Baerends, E. J. *Theor. Chem. Acc.* **1998**, *99*, 391–403; c) te Velde, G.; Bickelhaupt, F. M.; Baerends, E. J.; Guerra, C. J.; van Gisbergen, S. J. A.; Snijders, J. G.; Ziegler, T. *J. Comput. Chem.* **2001**, *22*, 931–967.

160. Ernzerhof, M.; Scuseria, G. E. *J. Chem. Phys.* **1999**, *110*, 5029–5036.

161. Adamo, C.; Barone, V. *J. Chem. Phys.* **1999**, *110*, 6158–6170.

162. a) van Lenthe, E.; Baerends, E. J.; Snijders, J. G. *J. Chem. Phys.* **1993**, *99,* 4597−4610; b) van Lenthe, E.; Baerends, E. J.; Snijders, J. G. *J. Chem. Phys.* **1994**, *101*, 9783−9792; c) van Lenthe, E.; Ehlers, A.; Baerends, E. *J. Chem. Phys.* **1999**, *110*, 8943−8953; d) van Lenthe, E.; Snijders, J. G.; Baerends, E. J. *J. Chem. Phys.* **1996**, *105*, 6505−6516; e) van Lenthe, E.; van Leeuwen, R.; Baerends, E. J.; Snijders, J. G. *Int. J. Quantum Chem.* **1996**, *57*, 281−293.

163. Grimme, S.; Ehrlich, S.; Goerigk, L. *J. Comput. Chem*. **2011**, *32*, 1456−1465.

164. Politzer, P.; Murray, J. S.; Clark, T.; Resnati, G. *Phys. Chem. Chem. Phys.* **2017**, *19*, 32166–32178

165. Al-Mukhtar, M.; Holloway, J. H.; Hope, E. G.; Schrobilgen, G. J. *J. Chem. Soc., Dalton Trans.*, **1991**, 2831–2834.

166. Griffiths, J. E.; Sunder, W. A. *J. Chem. Phys*. **1982**, *77*, 1087–1092.

167. Bondi, A. *J. Phys. Chem.* **1964**, *68*, 441–451.

168. Alvarez, S. *J. Chem. Soc., Dalton Trans*. **2013**, *42*, 8617–8636.

169. Fateley, W. G.; McDevitt, N. T.; Bentley, F. F. *Appl. Spectrosc.* **1971**, *25*, 155–173.

170. Allen, L. C. *Int. J. Quantum Chem*. **1994**, *49*, 253–277.

171. Rahm, M.; Zeng, T.; Hoffmann, R. *J. Am. Chem. Soc.* **2019**, *141*, 342–351.

172. Bader, R. F. W. *Atoms in Molecules: A Quantum Theory*; Oxford University Press; Clarendon Press, 1990.

173. Becke, A. D.; Edgecombe, K. E. *J. Chem. Phys*. **1990**, *92*, 5397–5403.

174. Silvi, B.; Savin, A. *Nature* **1994**, *371*, 683–686.

175. Vasdev, N.; Moran, M. D.; Tuononen, H. M.; Chirakal, R.; Suontamo, R. J.; Bain, A. D.; Schrobilgen, G. J. *Inorg. Chem.* **2010**, *49*, 8997–9004.

176. Mercier, H. P. A.; Moran, M. D.; Sanders, J. C. P.; Schrobilgen, G. J.; Suontamo, R. J. *Inorg. Chem.* **2005**, *44*, 49–60.

177. Thanthiriwatte, K. S.; Vasiliu, M.; Dixon, D. A.; Christe, K. O. *Inorg. Chem.* **2012**, *51*, 10966–10982.

178. Scheibe, B.; Karttunen, A. J.; Weigend, F.; Kraus, F. *Chem. Eur. J.* **2021**, *27*, 2381–2392.

179. Frlec, B.; Holloway, J. H. *Inorg. Chem.* **1976**, *15*, 1263–1270.

180. Burgess, J.; Fraser, C. J. W.; McRae, V. M.; Peacock, R. D.; Russell, D. R. *J. Inorg. Nucl. Chem.* **1976**, *28*, 183–188.

181. Mcrae, V. M.; Peacock, R. D.; Russell, D. R. *J. Chem. Soc. (D).* **1969**, 62–63.

182. Tucker, P. A.; Taylor, P. A.; Holloway, J. H.; Russell, D. R. *Acta Crystallogr.* **1975**, *B31*, 906–908.

183. Holloway, J. H.; Schrobilgen, G. J.; Holloway, J. H.; Schrobilgen, G. J. *Inorg. Chem.* **1980**, *19*, 2632–2640.

184. Holloway, J. H.; Schrobilgen, G. J. *Inorg. Chem.* **1981**, *20*, 3363–3368.

185. Bougon, R.; Cicha, W. V.; Lance, M.; Meublat, L.; Nierlich, M.; Vigner, J. *Inorg. Chem.* **1991**, *30*, 102–109.

186. Antipin, M. Y.; Ehllern, A. M.; Sukhoverkhov, V. F.; Struchkov, Y. T.; Buslaev, Y. A. *Dokl. Akad. Nauk. SSSR* **1987**, *293*, 1152–1155.

187. Tobias, K. M.; Jansen, M. *Z. Anorg. Allg. Chem.* **1987**, *550*, 16–26.

188. Christe, K. O. *Inorg. Chem.* **1973**, *12*, 1580–1587.

189. Tramšek, M.; Benkič, P.; Žemva, B. *Inorg. Chem.* **2004**, *43*, 699–703.

190. DeBackere, J. R.; Schrobilgen, G. J. *Angew. Chem. Int. Ed.* **2018**, *57*, 13167–13171.

191. Gillespie, R. J.; Spekkens, P. H. *Isr. J. Chem.* **1978**, *17*, 11–19.

192. Christe, K.; Curtis, E. C.; Schack, C. J. *Inorg. Chem.* **1972**, *11*, 2212–2215.

193. Christe, K. O.; Curtis, E. C. *Inorg. Chem.* **1972**, *11*, 2209–2211.

194. Christe, K. O.; Schack, C. J.; Pilipovich, D. *Inorg. Chem.* **1972**, *11*, 2205–2208.

195. Schack, C. J.; Lindahl, C. B.; Pilipovich, D.; Christe, K. O. *Inorg. Chem.* **1972**, *11*, 2201–2205.

196. Christe, K. O.; Curtis, E. C. *Inorg. Chem*. **1972**, *11*, 2196–2201.

197. Pilipovich, D.; Rogers, H. H.; Wilson, R. D. *Inorg. Chem.* **1972**, *11*, 2192–2195.

198. Pilipovich, D.; Lindahl, C. B.; Schack, C. J.; Wilson, R. D.; Christe, K. O. *Inorg. Chem*. **1972**, *11*, 2189–2192.

199. Christe, K. O.; Wilson, R. D. *Inorg. Chem.* **1973**, *12*, 1356–1357.

200. Schroer, T.; Christe, K. O. *Inorg. Chem.* **2001**, *40*, 2415–2419.

201. Gillespie, R. J.; Schrobilgen, G. J. *Inorg. Chem.* **1974**, *13*, 1230–1235.

202. Wilson, W. W.; Christe, K. O. *J. Fluor. Chem.* **1982**, *21*, 7.

203. Christe, K. O.; Wilson, W. W.; Curtis, E. C. *Inorg. Chem.* **1983**, *22*, 3056–3060.

204. Scheibe, B.; Ivlev, S. I.; Karttunen, A. J.; Kraus, F. *Eur. J. Inorg. Chem.* **2020**, *2020*, 1319–1324.

205. Christe, K. O; Curtis, E. C.; Dixon, D. A. *J. Am. Chem. Soc.* **1993**, *115*, 1520–1526.

206. Christe, K. O.; Wilson, W. W. *Inorg. Chem.* **1989**, *28*, 3275–3277

207. Mahjoub, A. R.; Hoser, A.; Fuchs, J.; Seppelt, K. *Angew. Chem. Int. Ed.* **1989**, *28*, 1526–1527.

208. Mahjoub, A. R.; Zhang, X.; Seppelt, K. *Chem. Eur. J.* **1995**, *1*, 261–265.

209. Dixon, D. A.; Grant, D. J.; Christe, K. O.; Peterson, K. A. *Inorg. Chem*. **2008**, *47*, 5485–5494.

210. Christe, K. O.; Wilson, W. W.; Chirakal, R. V.; Sanders, J. C. P.; Schrobilgen, G. J.; Chirakal, R. V. *Inorg. Chem*. **1990**, *29*, 3506–3511.

211. Gillespie, R. J.; Spekkens, P. *J. Chem. Soc., Dalton Trans*. **1976**, 2391–2396.

212. Huggins, D. K.; Fox, W. B. *Inorg. Nucl. Chem. Letters* **1970**, *6*, 337–339.

213. Christe, K. O.; Curtis, E. C. *Inorg. Chem.* **1972**, *11*, 35–39.

214. Ellern, A.; Boatz, J. A.; Christe, K. O.; Drews, T.; Seppelt, K. *Z. Anorg. Allg. Chem*. **2002**, *628*, 1991–1999.

215. Christe, K. O.; Zhang, X.; Sheehy, J. A.; Bau, R. *J. Am. Chem. Soc*. **2001**, *123*, 6338–6348.

216. Vij, A.; Tham, F. S.; Vij, V.; Wilson, W. W.; Christe, K. O. *Inorg. Chem*. **2002**, *41*, 6397–6403.

217. Lind, M. D.; Christe, K. O.; Lind, M. D.; Christe, K. O. *Inorg. Chem.* **1972**, *11*, 608–612.

218. Mallouk, T. E.; Rosenthal, G. L.; Müller, G.; Brusasco, R.; Bartlett, N. *Inorg. Chem*. **1984**, *23*, 3167–3173.

219. Edwards, A. J.; Sills, R. J. C. *J. Chem. Soc., Dalton Trans*. **1974**, 1726–1729.

220. Schmeisser, M.; Brändle, K. *Adv. Inorg. Chem. Radiochem.* **1963**, *5*, 41–89.

221. Nabiev, S. S. *Russ. Chem. Bull.* **1999**, *48*, 711–717.

222. Jacob, E. *Angew. Chem. Int. Ed.* **1976**, *15*, 158–158.

223. Bougon, R.; Huy, T. B.; Charpin, P.; Gillespie, R. J.; Spekkens, P. H. *J. Chem. Soc., Dalton Trans.* **1979**, 6–12.

224. Adelhelm, M.; Jacob, E. *Angew. Chem. Int. Ed.* **1977**, *16*, 461.

225. Bunič, T.; Tavčar, G.; Tramšek, M.; Žemva, B. *Inorg. Chem*. **2006**, *45*, 1038–1042.

226. Benkič, P.; Tramšek, M.; Žemva, B. *Solid State Sci.* **2002**, *4*, 1425–1434.

227. Bunič, T.; Tramšek, M.; Goreshnik, E.; Tavčar, G.; Žemva, B. *Inorg. Chem*. **2007**, *46*, 5276–5282.

228. Riedel, S. "High-Valent Fluorides and Fluoro-Oxidizers." In *Comprehensive Inorganic Chemistry II (Second Edition): From Elements to Applications*; Elsevier Ltd, 2013; Vol. 2, pp 187–221.

229. Winkler, J. R.; Gray, H. B. *Electronic Structures of Oxo-Metal Ions. Structure and Bonding*; Springer, Berlin, Heidelberg 2012, pp 17–28.

230. Ballhausen, C. J.; Gray, H. B. *Inorg. Chem.* **1962**, *1*, 111–122.

231. Pyykkö, P.; Xu, W.-H. *Angew. Chem. Int. Ed.* **2015**, *54*, 1080–1081.

232. Drews, T.; Supeł, J.; Hagenbach, A.; Seppelt, K. *Inorg. Chem*. **2006**, *45*, 3782–3788.

233. Choy, J. -H.; Kim, D. -K.; Hwang, S. -H.; Demazeau, G.; Jung, D. -Y. *J. Am. Chem. Soc.* **1995**, *117*, 8557–8566.

234. Riedel, S.; Kaupp, M. *Angew. Chem. Int. Ed.* **2006**, *45*, 3708–3711.

235. Cooper, T. D.; Dost F. N.; Wang, C. H. *J. Inorg. Nucl. Chem.* **1972**, *34*, 3564–3567.

236. Muller, H. S. P. *Chem. Phys. Lett.* **1999**, *314*, 396–402.

237. Andrews, L.; Chi, F. K.; Arkell, A. *J. Am. Chem. Soc.* **1974**, *96*, 1997–2000.

238. Müller, H. S. P.; Cohen, E. A. *J. Chem. Phys.* **2002**, *116*, 2407–2416.

239. Christe, K. O. *Inorg. Chem.* **1972**, *11*, 1220–1222.

240. Gatti, R.; Krieger, R. L.; Sicre, J. E.; Schumacher, H. J. *J. Inorg. Nucl. Chem.* **1966**, *28*, 647–658.

241. Pilipovich, D.; Maya, W.; Lawton, E. A.; Bauer, H. F.; Sheehan, D. F.; Ogimachi, N. N.; Wilson, R. D.; Gunderloy, F. C.; Bedwell, V. E. *Inorg. Chem.* **1967**, *6*, 1918–1919.

242. Scheibe, B.; Haiges, R.; Ivlev, S. I.; Karttunen, A. J.; Müller, U.; Christe, K. O.; Kraus, F. *Eur. J. Inorg. Chem.* **2020**, *2020*, 4483–4496.

243. Bortolus, M. R.; Mercier, H. P. A.; Schrobilgen, G. J. *Chem. Eur. J.* **2020**, *26*, 8935–8950.

244. Goettel, J. T.; Bortolus, M. R.; Stuart, D. G.; Mercier, H. P. A.; Schrobilgen, G. J. *Chem. Eur. J.* **2019**, *25*, 15815–15829.

245. Haase, W. *Chem. Ber.* **1974**, *107*, 1009–1018.

246. Haase, W. *Acta Crystallogr.* **1974**, B30, 2465–2469.

247. Shopov, D. Y.; Sharninghausen, L. S.; Sinha, S. B.; Mercado, B. Q.; Balcells, D.; Brudvig, G. W.; Crabtree, R. H. *Inorg. Chem.* **2018**, *57*, 5684–5691.

248. Tamadon, F.; Seidel, S.; Seppelt, K. *Acta. Chim. Slov*. **2013**, *60*, 491–494.

249. Brown, I. D. *The Chemical Bond in Inorganic Chemistry. The Bond Valence Model*; Oxford University Press, 2006.

250. Brown, I. D. *Private Communication.* (Cl–O, R_0 = 1.71; Cl–F, R_0 = 1.69; B = 0.37).

251. Lu, Y.; Tsegaw, Y. A.; Wodyński, A.; Li, L.; Beckers, H.; Kaupp, M.; Riedel, S. *Chem. Eur. J.* **2022**, *28*, e202104005.

252. Craciun, R.; Dixon, D. A. *Private Communication.* Calculated fluoride-ion affinities of $CrOF_4$ (−285 kJ mol^{-1}), $MoOF_4$ (−355 kJ mol^{-1}), and WOF_4 (−386 kJ mol^{-1}).

253. Edwards, A. J.; Steventon, B. R. *J. Chem. Soc. (A)*, **1971**, 21–25.

254. Turnbull, D.; Chaudhary, P.; Leenstra, D.; Hazendonk, P.; Wetmore, S. D.; Gerken, M. *Inorg. Chem*. **2020**, *59*, 17544–17554.

255. Iijima, K. *Bull. Chem. Soc. Jpn.* **1977**, *50*, 373–375.

256. Robiette, A. G.; Hedberg, K.; Hedberg, L. *J. Mol. Struct.* **1977**, *37*, 105–112.

257. Atoji, M.; Lipscomb, W. N. *Acta. Crystallogr.* **1954**, *7*, 173–175.

258. Ziegler, T.; Rauk, A. *Theor. Chim. Acta.* **1977**, *46*, 1–10.

259. Mitoraj, M. P.; Michalak, A.; Ziegler, T. *J. Chem. Theory. Comput*. **2009**, *5*, 962–975.

260. Gillespie, R. J.; Landa, B.; Schrobilgen, G. J. *J. Inorg. Nucl. Chem.* **1976**, *28*, 179–182.

261. Christe, K. O.; Dixon, D. A.; Mclemore, D.; Wilson, W. W.; Sheehy, J. A.; Boatz, J. A. *J. Fluor. Chem.* **2000**, *101*, 151–153.

262. Bortolus, M. R.; Mercier, H. P. A.; Nguyen, B.; Schrobilgen, G. J. *Angew. Chem. Int. Ed.* **2021**, *60*, 23678–23686.

263. Beattie, I. R.; Livingston, K. M. S.; Reynolds, D. J.; Ozin, G. A. *J. Chem. Soc. (A)* **1970**, 1210–1216.

264. Hope, E. G.; Jones, P. J.; Levason, W.; Ogden, J. S.; Tajik, M.; Turff, J. W. *J. Chem. Soc., Dalton Trans.* **1985**, 529–533.

265. Granier, W.; Vilminot, S.; Vidal, J. D.; Cot, L. *J. Fluor. Chem*. **1981**, *19*, 123–134.

266. Ghammamy, S.; Baghy, M. R. *Transit. Met. Chem.* **2007**, *32*, 456–460.

267. Ghammamy, S.; Dastpeyman, S.; Sadjadi, S. A. S. *Trans. Met. Chem*. **2006**, *31*, 482–486.

268. Green, P. J.; Gard, G. L. *Inorg. Nucl. Chem. Lett.* **1978**, *14*, 179–182.

269. Brown, S. D.; Green, P. J.; Gard, G. L. *J. Fluor. Chem.* **1975**, *5*, 203–219.

270. Mallela, S. P.; Shreeve, J. M. *Organometallics* **1989**, *8*, 2751–2754.

271. Brown, S. D.; Gard, G. L. *Inorg. Chem.* **1973**, *12*, 483–484.

272. Glemser, O.; Roesky, H.; Hellberg, K. -H. *Angew. Chem.* **1963**, *75*, 346–347.

273. Hellberg, K. H.; Müller, A.; Glemser, O. *Z. Naturforsch. B.* **1966**, *21*, 118–121.

274. Jacob, E.; Willner, H. *Chem. Ber.* **1990**, *123*, 1319–1321.

275. Hope, E. G.; Jones, P. J.; Levason, W.; Ogden, J. S.; Tajik, M. *J. Chem. Soc. Chem. Commun*. **1984**, *20*, 1355–1356.

276. Hope, E. G.; Jones, P. J.; Levason, W.; Ogden, J. S.; Tajik, M.; Turff, J. W. *J. Chem. Soc., Dalton Trans.* **1985**, *7*, 1443–1449.

277. Hope, E. G.; Levason, W.; Ogden, J. S. *Inorg. Chem*. **1991**, *30*, 4873–4874.

278. Jacobs, J.; Müller, H. S. P.; Willner, H.; Jacob, E.; Bürger, H. *Inorg. Chem*. **1992**, *31*, 5357–5363.

279. Schlöder, T.; Brosi, F.; Freyh, B. J.; Vent-Schmidt, T.; Riedel, S. *Inorg. Chem.* **2014**, *53*, 5820–5829.

280. Ruff, O.; Eisner, F. *Ber. Dtsch. Chem. Ges.* **1907**, *40*, 2926–2935.

281. Edward A. J. *Proc. Chem. Soc.* **1960**, 205.

282. Mallela, S. P.; Shreeve, J. M. *Inorg. Synth*. **1992**, *29*, 124–127.

283. Bougon, R.; Huy, T. B.; Charpin, P. *Inorg. Chem*. **1975**, *14*, 1822–1830.

284. Buslaev Y. A.; Kokunov T. V.; Bochkareva, V. A.; Shustorovish, E. M. *Dokl. Akad. Nauk. SSSR* **1971**, *201*, 355–358.

285. Beuter, V. A.; Sawodny, W. *Z. Anorg. Allg. Chem.* **1976**, *427*, 37–44.

286. Kanatani, T.; Matsumoto, K.; Hagiwara, R. *Eur. J. Inorg. Chem.* **2010**, 1049–1055.

287. Hargreaves, G. B.; Peacock, R. D. *J. Chem. Soc.* **1958**, 4390–4393.

288. Mazej, Z.; Gilewski, T.; Goreshnik, E. A.; Jagličić, Z.; Derzsi, M.; Grochala, W. *Inorg. Chem.* **2017**, *56*, 224–233.

289. Turnbull, D.; Gerken, M. *Acta Crystallogr.* **2020**, *E76*, 1345–1348.

290. Nuszhär, D.; Weller, F.; Dehnicke, K.; Hiller, W. *J. Alloy. Compd.,* **1992**, *183*, 30–44.

291. Il'in, E. G.; Golovanov, B. V.; Ignatov, M. E.; Butskii, V. D.; Buslaev, Y. A. *Dokl. Akad. Nauk. SSSR,* **1986**, *289*, 624–627.

292. Massa, W.; Hermann, S.; Dehnicke, K. *Z. Anorg. Allg. Chem*. **1982**, *493,* 33–40.

293. Wilson, W. W.; Christe, K. O. *Inorg. Chem.* **1981**, *20*, 4139–4143.

294. Selig, H.; Sunder, W. A.; Schilling, F. C.; Falconer, W. E. *J. Fluor. Chem.* **1978**, *11*, 629–635.

295. Buslaev, Yu. A.; Kokunov, Yu. V.; Gustyakova, M. P.; Chubar, Yu. D.; Moiseev, I. I. *Dokl. Akad. Nauk. SSSR,* **1977**, *233*, 357−360.

296. Bagnall, K. W.; du Preez, J. G. H.; Gellatly, B. J.; Holloway, J. H. *J. Chem. Soc., Dalton Trans.* **1975**, *19*, 1963–1968.

297. Stene, R. E.; Scheibe, B.; Karttunen, A. J.; Petry, W.; Kraus, F. *Eur. J. Inorg. Chem.* **2019**, *2019*, 3672–3682.

298. Stoll, C.; Seibald, M.; Baumann, D.; Huppertz, H. *Eur. J. Inorg. Chem.* **2019**, *2019*, 3383–3388.

299. McHughes, M.; Willett, R. D.; Davis, H. B.; Gard, G. L. *Inorg. Chem*. **1986**, *25*, 426–427.

300. Hope, E. G.; Jones, P. J.; Levason, W.; Ogden, J. S.; Tajik, M.; Turff, J. W. *J. Chem. Soc., Dalton Trans.* **1984**, *11*, 2445–2447.

301. Green, P. J.; Johnson, B. M.; Loehr, T. M.; Gard, G. L. *Inorg. Chem.* **1982**, *21*, 3562–3565.

302. Clark, H. C.; Sadana, Y. N. *Can. J. Chem.* **1964**, *42*, 702–704

303. Manoharan, P. T.; Rogers, M. T. *J. Chem. Phys.* **1968**, *49*, 5510–5519.

304. Ziebarth, O. V.; Selbin, J. *J. Inorg. Nucl. Chem.* **1970**, *32*, 849–865.

305. Rochat, W. V.; Gerlach, J. N.; Gard, G. L. *Inorg. Chem.* **1970**, *9*, 998–999.

306. Holloway, J. H.; Schrobilgen, G. J.; Taylor, P. *J. Chem. Soc., Chem. Commun.* **1975**, 40–41.

307. Lutar, K.; Borrmann, H.; Žemva, B. *Inorg. Chem.* **1998**, *37*, 3002–3006.

308. Leary, K.; Zalkin, A.; Bartlett, N. *Inorg. Chem*. **1974**, *13*, 775−779.

309. Mazej, Z.; Goreshnik, E. *Eur. J. Inorg. Chem.* **2009**, 4503–4506.

310. Bartlett, N.; Einstein, F.; Stewart, D. F.; Trotter, J. *J. Chem. Soc. (A),* **1967**, 1190–1193.

311. Leary, K.; Templeton, D. H.; Zalkin, A.; Bartlett, N. *Inorg. Chem*. **1973**, *12*, 1726–1730.

312. Bartlett, N.; DeBoer, B. G.; Hollander, F. J.; Sladky, F. O.; Templeton, D. H.; Zalkin, A. *Inorg. Chem.* **1974**, *13*, 780–785.

313. Jesih, A.; Lutar, K.; Leban, I.; Žemva, B. *Eur. J. Solid State Inorg. Chem.* **1991**, *28*, 829–840.

314. Pointner, B. E.; Suontamo, R. J.; Schrobilgen, G. J. *Inorg. Chem*. **2006**, *45*, 1517–1534.

315. Mazej, Z.; Goreshnik, E. *Eur. J. Inorg. Chem.* **2008**, *11*, 1795–1812.

316. Christe, K. O.; Curtis, E. C.; Wilson, R. D. *J. Inorg. Nucl. Chem.* **1976**, *28*, 159–165.

317. Hou, Y.; Wu, H.; Yu, H.; Hu, Z.; Wang, J.; Wu, Y. *Angew. Chem. Int. Ed.* **2021**, *60*, 25302–25306.

318. Hou, Y.; Li, H.; Wu, H.; Yu, H.; Hu, Z.; Wang, J.; Wu, Y. *Dalton Trans.* **2022**, *51*, 14036–14040.

319. Barth, J. A.; Wollert, R.; Rentschler, E.; Massa, W.; Dehnicke, K. *Z. Anorg. Allg. Chem.* **1991**, *596*, 121–132.

320. Veryasov, G.; Morozov, D.; Goreshnik, E.; Jesih, A. *J. Fluor. Chem.* **2013**, *156*, 240–245.

321. Sergienko, V. S.; Porai-Koshits, M. A.; Khodashova, T. S.; Kurnakov, N. S. *J. Struct. Chem.* **1972**, *13*, 431–436.

322. Laptash, N. M.; Udovenko, A. A. *J. Struct. Chem.* **2016**, *57*, 390–398.

323. Shi, T.; Zhang, F.; Li, Y.; Gao, L.; Yang, Z.; Pan, S. *Inorg. Chem.* **2020**, *59*, 3034–3041.

324. Welk, M. E.; Norquist, A. J.; Stern, C. L.; Poeppelmeier, K. R. *Inorg. Chem.* **2001**, *40*, 5479–5480.

325. Supeł, J.; Abram, U.; Hagenbach, A.; Seppelt, K. *Inorg. Chem.* **2007**, *46*, 5591–5595.

326. Heier, K. R.; Norquist, A. J.; Wilson, C. G.; Stern, C. L.; Poeppelmeier, K. R. *Inorg. Chem.* **1998**, *37*, 76–80.

327. Chaminade, J. P.; Moutou, J. M.; Villeneuve, G.; Couzi, M.; Pouchard, M.; Hagenmuller, P. *J. Solid State Chem.* **1986**, *65*, 27–39.

328. Brown, S. D.; Gard, G. L.; Loehr, T. M. *J. Chem. Phys.* **1976**, *64*, 1219–1222.

329. Il'in, E. G.; Golovanov, B. V.; Ignatov, M. E.; Butskil, V. D.; Buslaev, Y. A. *Dokl. Akad. Nauk. SSSR* **1986**, *289*, 624–627.

330. Nuszhär, D.; Weller, F.; Dehnicke, K.; Hiller, W. *J. Alloys. Compd.* **1992**, *183*, 30–44.

331. Stoll, C.; Heymann, G.; Seibald, M.; Baumann, D.; Huppertz, H. *J. Fluor. Chem.* **2019**, *226*, 109356.

332. Buslaev, Y. A.; Kokunov, Y. V.; Bochkareva, V. A.; Shustorovich, E. M. *J. Struct. Chem.* **1972**, *13*, 491–492.

333. Beuter, A.; Sawodny, W. *Angew. Chem*. **1972**, *84*, 1099–1100.

334. Buslaev, Y. A.; Kokunov, Y. V.; Bochkareva, V. A. *Dokl. Akad. Nauk. SSSR* **1972**, *13*, 611–616.

335. McFarlane, W.; Noble, A. M.; Winfield, J. M. *J. Chem. Soc. (A)* **1971**, 948–953.

336. Arnaudet, L.; Bougon, R.; Ban, B.; Lance, M.; Navaza, A.; Nierlich, M.; Vigner, J. *J. Fluor. Chem.* **1992**, *59*, 141–152.

337. Crossman, M. C.; Fawcett, J.; Hope, E. G.; Russell, D. R. *J. Organomet. Chem.* **1996**, *514*, 87–91.

338. Hoskins, B. F.; Linden, A.; O'Donnell, T. A. *Inorg. Chem.* **1987**, *26*, 2223–2228.

339. Stene, R. E.; Scheibe, B.; Karttunen, A. J.; Petry, W.; Kraus, F. *Eur. J. Inorg. Chem.* **2020**, *2020*, 2260–2269.

340. Gillespie, R. J.; Schrobilgen, G. J. *Inorg. Chem.* **1974**, *13*, 765–770.

341. Mazej, Z.; Goreshnik, E. *Eur. J. Inorg. Chem.* **2017**, *2017*, 2800–2807.

342. Arnaudet, L.; Bougon, R.; Buu, B.; Lance, M.; Nierlich, M.; Vigner, J. *Inorg. Chem.* **1993**, *32*, 1142–1146.

343. Levason, W.; Monzittu, F. M.; Reid, G.; Zhang, W.; Hope, E. G. *J. Fluor. Chem.* **2017**, *200*, 190–197.

344. Levason, W.; Reid, G.; Zhang, W. *J. Fluor. Chem.* **2016**, *184*, 50–57.

345. Robiette, A. G.; Hedberg, K.; Hedberg, L. *J. Mol. Struct.* **1977**, *37*, 105–112.

346. Iijima, K. *Bull. Chem. Soc. Jpn.* **1977**, *50*, 373–375.

347. Huang, J.; Hedberg, K.; Shreeve, J. M.; Mallela, S. P. *Inorg. Chem.* **1988**, *27*, 4633–4635.

348. Tsao, P.; Cobb, C. C.; Claassen, H. H. *J. Chem. Phys.* **1971**, *54*, 5247–5253.

349. Cordero, B.; Gómez, V.; Platero-Prats, A. E.; Revés, M.; Echeverría, J.; Cremades, E.; Barragán, F.; Alvarez, S. *J. Chem. Soc. Dalton Trans.* **2008**, *21*, 2832–2838.

350. Seppelt, K. *Chem Ber* **1975**, *108*, 1823–1829.

351. Strauss, S. H. *Chem. Rev.* **1993**, *93*, 927–942.

352. Krossing, I.; Raabe, I. *Angew. Chem. Int. Ed.* **2004**, *43*, 2066–2090.

353. Seppelt, K. *Angew. Chem. Int. Ed.* **1993**, *32*, 1025–1027.

354. Damerius, R.; Huppmann, P.; Lentz, D.; Seppelt, K. *J. Chem. Soc., Dalton Trans.* **1984**, 2821–2826.

355. Birchall, T.; Myers, R. D.; de Waard, H.; Schrobilgen, G. J. *Inorg. Chem.* **1982**, *21*, 1068–1073.

APPENDIX 1

Chapter 3 Supporting Information

Syntheses and Characterizations of the Mixed Noble-Gas Compounds, $[FKr^{II}FXe^{II}F][AsF_6]\cdot 0.5Kr^{II}F_2\cdot 2HF$, $([Kr^{II}_2F_3][AsF_6])_2\cdot Xe^{IV}F_4$, and $Xe^{IV}F_4\cdot Kr^{II}F_2$

Adapted with permission from: Bortolus, M. R.; Mercier, H. P. A.; Nyugen, B.; Schrobilgen, G. J. *Angew. Chem. Int. Ed.* **2021**, *60*, 23678–23686.

Table of Contents

Table A1.1. Raman frequencies and intensities for sample (a); the redox decomposition of [FKrFXeF][AsF_6]·0.5KrF_2·2HF (**1**) at various temperatures [a]

Sample (a); redox decomposition of (1)							
–78 °C	**–50 °C**	**–42 °C**	**–38 °C**	**–30 °C**	**–20 °C**	**–10 °C**	**0 °C**
					1857(5)	*1856(14)*	*1865(11)*
723(sh)							
	698(sh)	698(4)					
	695(9)	695(8)	694(sh)	694(sh)	694(sh)	694(sh)	694(sh)
					690(10) [b]	*691(14)* [b]	*691(11)* [b]
684(sh)	684(22)	685(19)	685(24) [b]	684(17) [b]	685(19) [b]	685(21) [b]	**685(14)** [b]
			682(sh)	682(sh)	682(sh)	682(sh)	
680(25)							
	678(9)	678(8)					
610(71)							
606(100) [c]	**606(100)**	**606(100)**	**606(sh)**	**606(sh)**	**606(sh)**	**606(sh)**	**606(36)**
	603(sh)	603(sh)	603(100)	603(100)	604(100)	604(100)	603(sh)
			600(sh)	**600(sh)**	**600(sh)**	**600(79)**	**600(89)**
597(42)	**597(65)**	**597(69)**	**597(sh)**	**597(sh)**	**597(sh)**	**597(sh)**	**597(sh)**
	594(sh)	594(sh)	594(sh)	594(sh)	594(sh)	594(sh)	
			590(sh)	**590(17)**	**590(19)**	**590(21)**	**590(sh)**
			588(sh)	**588(sh)**	**588(sh)**	**588(sh)**	**588(sh)** [c]
586(4)	586(17)	586(sh)	586(18) [c]	586(sh) [c]	**586(19)** [c]	**586(21)** [c]	**586(11)** [c]
			582(24)	**582(sh)**	**582(sh)**	**582(21)**	**582(sh)**
			580(sh)	**580(sh)**	**580(sh)**	**580(sh)**	
579(6)	578(13)	579(sh)	578(29) [b]	578(26) [b]	578(sh) [b]	578(sh) [b]	578(sh) [b]
	576(13)	576(15)	576(sh)	576(22)	576(24)	576(29)	576(14)
572(sh)	571(sh)	571(sh)	572(sh)	572(sh)	572(sh)		
						570(14)	**570(7)**
			564(sh)	**564(13)**	**564(sh)**		**564(sh)**
562(17)	**563(43)**	**563(42)**	**562(24)**	**562(sh)**	**562(sh)**	**562(sh)**	
			561(sh)	**560(sh)**	**560(sh)**	**560(21)**	**560(21)**
	558(sh)	**558(sh)**					
	555(sh)	555(sh)	555(sh)	555(sh)	555(sh)	555(sh)	

continued …

Table A1.1. (continued)

Sample (a); redox decomposition of (1)							
–78 °C	**–50 °C**	**–42 °C**	**–38 °C**	**–30 °C**	**–20 °C**	**–10 °C**	**0 °C**
	554(sh)	554(sh)	554(35)	553(48)	553(57)	553(71)	554(sh)
			548(sh)	**548(sh)**	**546(sh)**	**547(sh)**	**548(82)**
			544(12) [d]	**544(48)** [d]	**544(52)** [d]	**544(100)** [d]	**543(100)** [d]
			540(6)	**540(sh)**	**540(sh)**	**540(sh)**	**540(sh)**
			510(6)	**509(13)**	**509(sh)**	**509(sh)**	**509(sh)**
				507(17)	**507(24)**	**507(50)**	**507(75)**
				503(30)	503(29)	503(57)	
				500(sh)	**500(sh)**	**500(sh)**	**500(14)**
468(sh)	468(178)	468(142)	468(441) [e]	468(230) [e]	468(214) [e]	469(221) [e]	469(261) [e]
464(3813) [c]	**464(178)** [c]	**464(112)** [c]	**464(sh)** [c]	**464(sh)** [c]	**464(sh)** [c]	**464(sh)** [c]	**464(sh)** [c]
	452(sh)	**452(4)**					
	448(9)	**449(4)**					
421(4)							
		410(2)					
		408(2)					
		400(3)					
		398(3)					
	382(sh)	382(sh)	382(sh)	382(sh)	382(sh)		
378(sh) [f]							
	376(sh) [f]	376(sh) [f]	375(6) [f]	375(9) [f]	375(10) [f]	375(sh) [f]	
372(4)	372(9)		373(sh) [b]	372(9) [b]	372(10) [b]	372(sh) [b]	**373(sh)** [c]
370(4)	370(13)	370(12)	370(sh) [b]	369(4) [b]	369(10) [b]	**369(7)** [b]	**370(7)** [b]
			365(sh)	**365(sh)**	**365(10)**	**365(7)**	**365(7)**
	364(4)	363(4)	363(sh)	363(4)	363(sh)	362(sh)	
			360(sh)	**360(4)**	**359(10)**	**359(14)**	**359(7)**
			353(3)	353(9)	353(10)		353(4)
				350(9)	349(10)	350(14)	

continued …

Table A1.1. (continued)

Sample (a); redox decomposition of (1)							
–78 °C	**–50 °C**	**–42 °C**	**–38 °C**	**–30 °C**	**–20 °C**	**–10 °C**	**0 °C**
344(17)							
						333(7)	**332(7)**
	308(9) [f]	**308(sh)** [f]		**309(4)** [f]	**308(5)** [f]		
	304(9) [f]	**304(12)** [f]	**303(6)** [f]	**304(sh)** [f]	**304(5)** [f]		
							278(4)
							270(4)
							236(sh)
							228(7)
							223(7)
						216(7)	
			197(6)	**197(sh)**		**197(7)**	
			193(12) [c]	**193(9)** [c]	**193(14)** [c]	**193(sh)** [c]	**193(sh)** [c]
190(3)	**191(9)**	**191(8)**	190(12) [b]	190(9) [b]	191(14) [b]	**190(21)** [b]	**189(14)** [c]
		188(sh) [c]	**188(12)** [c]	**188(sh)** [c]	**189(14)** [c]	**188(21)**	**188(sh)**
	186(sh)	**186(sh)**					
			185(12)	185(sh)	185(sh)	186(sh)	185(sh)
182(4)	**182(17)**	**182(sh)**	**182(sh)**	**182(sh)**	**182(sh)**	**182(sh)**	**182(sh)**
180(4)	**180(sh)**	**180(19)**	**180(12)**	**180(9)**	**180(sh)**	**180(7)**	**180(4)**
	178(sh)	178(sh)	178(12)	178(sh)	178(5)	178(7)	178(4)
						176(7)	
173(sh)	**172(9)**	**172(sh)**					
	170(9)	**170(8)**					
164(sh)							
162(sh)	**162(13)**	**162(8)**	**162(sh)**				
160(8) [c]	**160(13)**	**160(sh)**					

continued …

Table A1.1. (continued)

Sample (a); redox decomposition of (1)							
–78 °C	**–50 °C**	**–42 °C**	**–38 °C**	**–30 °C**	**–20 °C**	**–10 °C**	**0 °C**
							149(sh)
148(sh)							
						147(sh)	**147(sh)**
						144(7)	**143(21)**
						141(7)	**141(sh)**
						137(7)	**137(sh)**
						135(sh)	**135(sh)**
	133(4)	133(4)	133(sh)		133(5)		
130(238) [b]	130(sh) [h]	131(4) [h]	130(12) [c,h]	131(4) [c,h]		131(14) [c,h]	131(7) [c,h]
	128(9)	128(sh)			128(sh)	128(sh)	128(sh)
	124(sh)	125(sh)	**125(12)** [c]	**126(sh)** [c]	**126(sh)** [c]	**126(sh)** [c]	**126(sh)** [c]
	122(sh)	122(sh)	**122(sh)** [c]	**122(sh)** [c]	**122(sh)** [c]	**122(sh)** [c]	**122(sh)** [c]
	120(17)	120(sh)	**120(24)** [c]	**120(sh)** [c]	**120(sh)** [c]	**120(29)** [c]	**120(29)** [c]
	118(13)	118(sh)		**119(17)** [c]	**119(24)** [c]	**119(sh)** [c]	**119(sh)** [c]
	116(sh)	115(15)	115(15) [b]	**115(13)** [c]	**116(24)** [c]	**117(29)** [c]	**118(18)** [c]
	114(13)	114(sh)	112(18) [b]	**112(13)** [c]	**112(19)** [c]	**112(sh)** [c]	**112(sh)** [c]
	111(13)	111(12)					
	109(13)	109(sh)	**110(sh)** [c]	**109(13)** [c]	**109(14)** [c]	**109(21)** [c]	**108(sh)** [c]
	107(sh)	106(12)	107(18)		**107(14)** [c]	**107(21)** [c]	
				105(13)	**105(14)**	**105(21)**	**105(sh)**
	103(13)	103(sh)	**102(24)** [c]	**102(sh)** [c]	**102(sh)** [c]	**101(sh)** [c]	**101(sh)** [c]
	100(sh)	100(sh)		99(sh)	99(sh)	99(sh)	
	98(sh)	98(sh)		97(sh)	97(sh)	97(sh)	97(sh)

continued …

Table A1.1. (continued)

[a] Frequencies are given in cm^{-1}. The abbreviation (sh) denotes a shoulder. Color code: $[XeF][AsF_6]$,[S1] **$[FKrFXeF][AsF_6]\cdot 0.5KrF_2\cdot 2HF$ (1)**, β-KrF_2,[S2] ***α*-KrF_2**,[S2] **$([Kr_2F_3][AsF_6])_2\cdot XeF_4$ (2)**, $[Kr_2F_3][AsF_6]\cdot n KrF_2$,[S3] **$XeF_4\cdot KrF_2$ (4)**, XeF_4, *$[O_2][AsF_6]$*.[S4] Values in parentheses are relative Raman intensities. Bolded blue values correspond to the **$[FKrFXeF]^+$** bands of **1**. The Raman spectra were recorded at –150 °C under a frozen aHF solution in an FEP sample tube using 1064-nm excitation. Reaction conditions are provided in the "Results and Discussion" section of the manuscript under "**Syntheses and Reactivities; *Redox Decomposition of 1 in aHF***". Oxidation of small amounts of H_2O and/or O_2 contaminants by $[Kr_2F_3][AsF_6]$ during the redox decomposition of **1** likely led to the formation of $[O_2][AsF_6]$ (ν(O-O), 1856–1865 cm^{-1}). The contaminants likely resulted from diffusion through the walls of the FEP sample tube when the sample was stored at –78 °C. [b] The band overlaps with a band of **2**. [c] The band overlaps with a band of **1**. [d] The band overlaps with a XeF_4 band. [e] The band overlaps with a band of **4**. [f] The band overlaps with an FEP sample tube band. [g] The band overlaps with a $[Kr_2F_3][AsF_6]\cdot n KrF_2$ band. [h] The band overlaps with an **α-KrF_2** band.

Table A1.2. Raman frequencies and intensities for sample (b); the redox decomposition of $[FKrFXeF][AsF_6]\cdot 0.5KrF_2\cdot 2HF$ (**1**) at various temperatures [a]

Sample (b): redox decomposition of (1)					
–65 °C [b]	**–55 °C** [b]	**0 °C** [b]	**RT 15 min** [b]	**RT 30 min**[b]	**dry crystals** [c]
					1864(4)
			1857(11)	*1857(15)*	*1857(10)*
			749(1)		**748(9)**
			743(1)		***742(sh)***
			740(1)		**740(5)**
731(sh)					
					727(sh)
724(16)					
			723(sh)		**723(sh)**
			720(sh)		720(sh)
			708(1)		**708(1)**
	696(4)				
					694(sh)
			691(11)	*691(13)*	***691(15)*** [d]
		690(sh)			
684(6)	685(19)	**685(18)** [e]	**685(5)** [e,f,g]	685(1) [g]	**685(16)** [f]
680(30)	680(13)				
678(sh)	678(sh)	678(1)			
			675(sh)	675(sh)	675(53)
			670(3, br)	***670(4, br)***	**669(19)**
			661(1)	661(1)	661(15) [g]
					651(1)
			630(sh)	***630(sh)***	***630(50)***
			625(4) [g]	***625(6)*** [g]	**625(100)** [h]
			623(8)	***623(6)***	***623(sh)***

continued …

Table A1.2. (continued)

Sample (b); redox decomposition of (1)					
–65 °C [b]	**–55 °C** [b]	**0 °C** [b]	**RT 15 min** [b]	**RT 30 min**[b]	**dry crystals** [c]
610(82)	610(sh)				
				609(sh)	609(20)
606(100) [h]	**606(100)**	**606(100)**			
	603(sh)	603(sh)			
	600(sh)	**600(sh)**	**600(19)**	**600(sh)**	
597(26)	**597(69)**	**597(32)**			**598(sh)**
594(sh)	594(sh)	594(sh)			
		590(sh)	**590(5)**		
					589(5)
		588(14) [e]	**588(5)**		
585(6)	585(15)	585(sh) [j]			
	582(sh)	**582(sh)**	*581(8)*	*581(7)*	*581(2)*
		580(sh)	**578(11)**		
578(8)	578(17)	578(23) [j]			
572(4)	572(15)	572(sh)			
		570(sh)	**571(6)**		
			568(8)	*568(7)*	*567(3)*
563(13)	**563(35)**	**563(16)** [j]	**564(5)** [e]	564(sh) [g,j]	**564(2)**
	561(sh)	**561(sh)**	**560(8)**	**560(4)**	**560(sh)**
559(8)	**559(sh)**	**559(sh)**			**559(3)**
		556(sh)			
	554(sh)	554(45)	554(24) [i]	554(20) [i]	***554(sh)*** [m]
	548(3)	**548(68)**	549(sh)	549(sh)	549(36)
	544(1) [m]	**544(95)** [m]	544(100) [i]	544(100) [i]	***544(28)*** [m]
		541(sh)	541(22) [j]		540(sh)
			532(2)		533(3)
					530(sh)
		510(sh)			
	508(1)	**508(55)**			
				507(sh)	507(sh)

continued …

Table A1.2. (continued)

Sample (b); redox decomposition of (1)					
–65 °C	**–55 °C**	**0 °C**	**RT 15 min**	**RT 30 min**	**dry crystals**
	506(sh)				
	503(sh)	503(sh)	503(68)	503(67)	503(17)
		500(27)	**500(sh)**		
			484(3)	**484(sh)**	**485(69)**
			473(5)		
468(sh)	468(219)	468(368) [k]	*468(5,br)*	*468(5,br)*	
464(313)	**464(192)**	**464(768)**			
			455(4)	455(4)	454(68)
	452(sh)				
	448(4)				
					421(sh)
420(5)	420(2)				
					417(sh)
					412(sh)
					411(5)
	409(1)				***409(sh)***
					407(4)
					405(sh)
					402(sh)
					401(5)
	398(1)	399(1)			
					397(4)
	395(sh)				
					393(sh)
	392(sh)	391(sh)			
					389(6)
	382(sh)	382(sh)			
					381(1)
					379(sh)
					376(sh)

continued …

Table A1.2. (continued)

Sample (b); redox decomposition of (1)					
–65 °C	**–55 °C**	**0 °C**	**RT 15 min**	**RT 30 min**	**dry crystals**
375(sh) [l]	375(8) [l]	375(sh) [l]			
					374(sh) [l]
	373(8) [e]	**373(9)** [e]	**373(4)** [l]	**373(sh)** [l]	**373(6)** [l]
370(5) [j]	370(8) [j]	370(9) [j]			
			369(sh)	369(sh)	369(6)
	365(2)	**366(5)**			
					364(2)
	363(2)	363(9)			
	360(2)	**360(9)**			
	357(2)	357(9)			
	353(2)	353(9)			
	350(3)	350(9)			
					347(5)
344(23)	344(6)				344(sh)
		342(5)			
		339(5)			
		330(5)			
306(sh)	**306(8)**	**305(2)**			
304(sh)	**304(8)**				
					302(7) [l]
					298(9) [l]
					294(4) [l]
		277(9)			
					265(1)
					238(1)
		228(5)			
					226(1)
			214(5)	214(4)	214(1)
			199(3)	**199(4)**	
		195(sh)			

continued …

Table A1.2. (continued)

Sample (b); redox decomposition of (1)					
–65 °C	**–55 °C**	**0 °C**	**RT 15 min**	**RT 30 min**	**dry crystals**
190(3)	**190(8)**	**190(14)**			
			188(8)	**188(6)**	
186(sh)	**186(sh)**	**186(9)**			
183(sh)	**183(sh)**	**183(9)**			
181(5)	**181(15)**	**180(9)**			
	178(sh)	178(sh)			
175(sh)	**175(sh)**	**175(sh)**			
172(sh)	**172(sh)**				
162(7)	**162(sh)**				
160(7) [o]	**160(8)**				
150(sh)				**150(4)**	**150(sh)**
				144(sh)	**144(sh)**
	142(sh)	**142(18)**	143(5)	142(sh)	142(12)
				137(sh)	**137(11)**
					134(sh)
131(20) [e]	**130(sh)**	**130(50)** [e]	130(5)	130(sh)	130(sh)
				125(sh)	**125(sh)**
124(8)					
					123(sh)
122(8)					
120(8)		120(23)	**120(sh)**	**121(sh)**	**120(7)**
			118(14)	118(9)	118(sh)
117(6)	**117(13)** [f]	**117(18)** [f]			
				115(8)	**115(sh)**
113(sh)		114(18)			
				112(sh)	**112(4)**
108(3)				109(sh)	109(4)
				107(4)	**107(4)**
105(3)		105(9)		105(sh)	105(4)
				103(sh)	**103(4)**

continued …

Table A1.2. (continued)

[a] Frequencies are given in cm^{-1}. The abbreviation (sh) denotes a shoulder. Color code: [XeF][AsF_6],[S1] **[FKrFXeF]**[AsF_6]·0.5KrF_2·2HF (**1**), β-KrF_2,[S2] **α-KrF_2**,[S2] **([Kr_2F_3][AsF_6])$_2$·XeF_4** (**2**), [Kr_2F_3][AsF_6]·*n*KrF_2,[S3] **XeF_4·KrF_2** (**4**), XeF_4, *[O_2][AsF_6]*,[S4] [F_5Xe(FKrF)AsF_6],[S5] *[F_5Xe(FKrF)$_2AsF_6$]*,[S5] **[(F_5Xe)$_2$(μ-FKrF)(AsF_6)$_2$]**, ***[XeF_5][AsF_6]***.[S5] Values in parentheses are relative Raman intensities. Bolded blue values denote the $[FKrFXeF]^+$ bands of **1**. Reaction conditions are provided in the "Results and Discussion" section of the manuscript under "**Syntheses and Reactivities; *Redox Decomposition of 1 in aHF***". Oxidation of small amounts of H_2O and/or O_2 contaminants by [Kr_2F_3][AsF_6] during the redox decomposition of **1** likely led to the formation of [O_2][AsF_6] (ν(O-O), 1856–1865 cm^{-1}). The contaminants likely resulted from diffusion through the walls of the FEP sample tube when the sample was stored at –78 °C. [b] The Raman spectrum was recorded at –150 °C under a frozen aHF solution in an FEP sample tube using 1064-nm excitation. [c] The Raman spectrum was recorded at –150 °C on dry crystals in an FEP sample tube using 1064-nm excitation. [d] The band overlaps with a [O_2][AsF_6] band. [e] The band overlaps with a band of **1**. [f] The band overlaps with a *[F_5Xe(FKrF)$_2AsF_6$]* band. [g] The band overlaps with a **[(F_5Xe)$_2$(μ-FKrF)(AsF_6)$_2$]** band. [h] The band overlaps with a band of [XeF][AsF_6] band. [i] The band overlaps with a ***[XeF_5][AsF_6]*** band. [j] The band overlaps with a **([Kr_2F_3][AsF_6])$_2$·XeF_4** (**2**) band. [k] The band overlaps with a [Kr_2F_3][AsF_6]·*n*KrF_2 band. [l] The band overlaps with an FEP band. [m] The band overlaps with a XeF_4 band. [n] The band overlaps with a **XeF_4·KrF_2** band. [o] The band overlaps with a [XeF][AsF_6] band.

Syntheses and Reactivities (continued)

Syntheses of $XeF_4 \cdot NgF_2$ (Ng = Kr, Xe). The $XeF_4 \cdot XeF_2$ cocrystal was initially obtained when it was fortuitously formed when the synthesis of pure XeF_4 was attempted by direct reaction of Xe with F_2 at high temperature.[S6] The cocrystal was also obtained by the fusion of an equimolar mixture of XeF_4 and XeF_2.[S7] The latter approach is not suitable for the synthesis of $XeF_4 \cdot KrF_2$ because KrF_2 rapidly oxidatively fluorinates XeF_4 to XeF_6 at room temperature. In efforts to circumvent Xe(IV) oxidation, the synthesis of $XeF_4 \cdot KrF_2$ was attempted in aHF and in $CFCl_3$ solvents.

Reaction of XeF_4 with ca. 2 molar equivalents of XeF_2 in aHF solvent at 22 °C only resulted in unreacted starting reagents. Thus, XeF_4 and XeF_2 are strongly favored by equilibrium (Eq. **A1.1**) in aHF solvent. This is consistent with the formation of $XeF_4 \cdot KrF_2$

$$XeF_4 + NgF_2 \rightleftharpoons XeF_4 \cdot NgF_2 \qquad \textbf{(A1.1)}$$

in the redox decomposition of **1** in aHF when a large excess of KrF_2 is present, and a mixture of XeF_4, KrF_2, and $XeF_4 \cdot KrF_2$ is formed as the concentration of KrF_2 decreases and XeF_4 increases (see Table A1.2).

When XeF_4 was allowed to react with 2.45 or 0.84 molar equivalents of KrF_2 or XeF_2, respectively, at room temperature (RT) in $CFCl_3$, equilibrium mixtures of XeF_4, NgF_2, and $XeF_4 \cdot NgF_2$ were obtained. In contrast with aHF solvent, $XeF_4 \cdot NgF_2$ formation [Eq. (A1.1)] was favorable in $CFCl_3$. Single-crystals of $XeF_4 \cdot NgF_2$ were obtained by slowly cooling the reaction mixtures from RT to 10 °C (Xe) and to 0 °C (Kr) over a

period of ca. 30 min. The Raman spectra, recorded at –150 °C under frozen $CFCl_3$, showed mixtures of crystalline $XeF_4 \cdot NgF_2$, XeF_4, and NgF_2.

Table A1.3. Experimental geometric parameters for $[AsF_6]^-$ and cocrystalized KrF_2 in $[FKrFXeF][AsF_6]\cdot 0.5KrF_2\cdot 2HF$ (**1**)

Bond Lengths (Å)			
Kr(2)–F(4)	1.893(4)	Kr(2)–F(4A)	1.893(4)
As(1)–F(5)	1.701(4)	As(1)–F(8A)	1.671(7)
As(1)–F(6)	1.712(4)	As(1)–F(9)	1.689(6)
As(1)–F(7)	1.764(7)	As(1)–F(9A)	1.689(6)
As(1)–F(7A)	1.764(7)	As(1)–F(10)	1.775(6)
As(1)–F(8)	1.671(7)	As(1)–F(10A)	1.775(6)

Bond Angles (deg)			
F(3)–Kr(2)–F(4)	180.0		
F(5)–As(1)–F(6)	179.9(3)	F(7)–As(1)–F(10A)	87.2(4)
F(5)–As(1)–F(7)	95.7(2)	F(7A)–As(1)–F(8)	67.1(4)
F(5)–As(1)–F(7A)	95.7(2)	F(7A)–As(1)–F(8A)	177.3(4)
F(5)–As(1)–F(8)	85.0(3)	F(7A)–As(1)–F(9)	87.1(5)
F(5)–As(1)–F(8A)	85.0(3)	F(7A)–As(1)–F(9A)	31.3(3)
F(5)–As(1)–F(9)	85.5(3)	F(7A)–As(1)–F(10)	87.2(4)
F(5)–As(1)–F(9A)	85.5(3)	F(7A)–As(1)–F(10A)	154.4(4)
F(5)–As(1)–F(10)	93.8(3)	F(8)–As(1)–F(8A)	110.3(6)
F(5)–As(1)–F(10A)	93.8(3)	F(8)–As(1)–F(9)	151.4(4)
F(6)–As(1)–F(7)	84.2(2)	F(8)–As(1)–F(9A)	95.6(4)
F(6)–As(1)–F(7A)	84.2(2)	F(8)–As(1)–F(10)	22.9(4)
F(6)–As(1)–F(8)	95.2(3)	F(8)–As(1)–F(10A)	90.1(5)
F(6)–As(1)–F(8A)	95.2(3)	F(8A)–As(1)–F(9)	95.6(4)
F(6)–As(1)–F(9)	94.3(3)	F(8A)–As(1)–F(9A)	151.4(4)
F(6)–As(1)–F(9A)	94.3(3)	F(8A)–As(1)–F(10)	90.1(5)
F(6)–As(1)–F(10)	86.5(3)	F(8A)–As(1)–F(10A)	22.9(4)
F(6)–As(1)–F(10A)	86.5(3)	F(9)–As(1)–F(9A)	57.7(6)
F(7)–As(1)–F(7A)	115.4(5)	F(9)–As(1)–F(10)	174.1(4)
F(7)–As(1)–F(8)	177.3(4)	F(9)–As(1)–F(10A)	117.4(4)
F(7)–As(1)–F(8A)	67.1(4)	F(9A)–As(1)–F(10)	117.4(4)
F(7)–As(1)–F(9)	31.3(3)	F(9A)–As(1)–F(10A)	174.1(4)
F(7)–As(1)–F(9A)	87.1(5)	F(10)–As(1)–F(10A)	68.4(5)
F(7)–As(1)–F(10)	154.4(4)		

Table A1.4. Experimental geometric parameters for $[AsF_6]^-$ and cocrystalized XeF_4 in $([Kr_2F_3][AsF_6])_2 \cdot XeF_4$ (**2**)

Bond Lengths (Å)			
Xe(1)–F(4)	1.931(3)	Xe(1)–F(5)	1.940(4)
Xe(1)–F(4A)	1.931(3)	Xe(1)–F(5A)	1.940(4)
As(1)–F(6)	1.716(3)	As(1)–F(9)	1.712(3)
As(1)–F(7)	1.711(3)	As(1)–F(10)	1.717(3)
As(1)–F(8)	1.692(3)	As(1)–F(11)	1.728(3)

Bond Angles (deg)			
F(4)–Xe(1)–F(4A)	180.0(2)	F(4A)–Xe(1)–F(5)	90.3(2)
F(4)–Xe(1)–F(5)	89.7(2)	F(4A)–Xe(1)–F(5A)	89.7(2)
F(4)–Xe(1)–F(5A)	90.3(2)	F(5)–Xe(1)–F(5A)	180.0
F(6)–As(1)–F(7)	89.0(2)	F(7)–As(1)–F(11)	89.6(2)
F(6)–As(1)–F(8)	179.7(2)	F(8)–As(1)–F(9)	90.3(3)
F(6)–As(1)–F(9)	89.6(2)	F(8)–As(1)–F(10)	90.8(2)
F(6)–As(1)–F(10)	89.4(2)	F(8)–As(1)–F(11)	89.3(2)
F(6)–As(1)–F(11)	90.4(2)	F(9)–As(1)–F(10)	89.0(2)
F(7)–As(1)–F(8)	91.1(2)	F(9)–As(1)–F(11)	90.4(2)
F(7)–As(1)–F(9)	178.5(2)	F(10)–As(1)–F(11)	179.4(2)
F(7)–As(1)–F(10)	91.0(2)		

Table A1.5. Experimental geometric parameters for $[SbF_6]^-$ in $[Xe_2F_3][SbF_6]$ (**3**)

Bond Lengths (Å)			
Sb(1)–F(4)	1.716(3)	Sb(1)–F(7)	1.712(3)
Sb(1)–F(5)	1.711(3)	Sb(1)–F(8)	1.717(3)
Sb(1)–F(6)	1.692(3)	Sb(1)–F(9)	1.728(3)

Bond Angles (deg)			
F(4)–Sb(1)–F(5)	179.0(1)	F(5)–Sb(1)–F(9)	89.5(1)
F(4)–Sb(1)–F(6)	89.8(1)	F(6)–Sb(1)–F(7)	89.1(1)
F(4)–Sb(1)–F(7)	89.8(1)	F(6)–Sb(1)–F(8)	178.8(1)
F(4)–Sb(1)–F(8)	91.1(1)	F(6)–Sb(1)–F(9)	91.2(1)
F(4)–Sb(1)–F(9)	91.5(1)	F(7)–Sb(1)–F(8)	90.1(1)
F(5)–Sb(1)–F(6)	90.6(1)	F(7)–Sb(1)–F(9)	178.7(1)
F(5)–Sb(1)–F(7)	89.2(1)	F(8)–Sb(1)–F(9)	89.6(1)
F(5)–Sb(1)–F(8)	88.6(1)		

Table A1.6. Experimental geometric parameters for $XeF_4 \cdot KrF_2$ (**4**), $XeF_4 \cdot XeF_2$ (**5**), and XeF_4 (**6**)

Bond Lengths (Å)					
$XeF_4 \cdot KrF_2$		$XeF_4 \cdot XeF_2$		XeF_4	
Xe(1)–F(1)	1.950(2)	Xe(1)–F(1)	1.9412(9)	Xe(1)–F(1)	1.9509(6)
Xe(1)–F(1A)	1.950(2)	Xe(1)–F(1A)	1.9412(9)	Xe(1)–F(1A)	1.9509(6)
Xe(1)–F(1B)	1.950(2)	Xe(1)–F(2)	1.937(1)	Xe(1)–F(2)	1.9449(6)
Xe(1)–F(1C)	1.950(2)	Xe(1)–F(2A)	1.937(1)	Xe(1)–F(2A)	1.9449(6)
Xe(2)–F(2)	1.950(2)				
Xe(2)–F(2A)	1.950(2)	Xe(2)–F(3)	1.9940(9)	Xe(1)---F(1B)	3.1507(6)
Xe(2)–F(3)	1.946(2)	Xe(2)–F(3A)	1.9940(9)	Xe(1)---F(1C)	3.4075(6)
Xe(2)–F(3A)	1.946(2)			Xe(1)---F(2B)	3.1962(6)
		Xe(1)---F(1B)	3.262(1)		
Kr(1)–F(4)	1.922(2)	Xe(1)---F(3)	3.290(1)		
Kr(1)–F(4A)	1.922(2)	Xe(1)---F(3B)	3.219(1)		
		Xe(2)---F(2)	3.236(1)		
Xe(1)---F(4)	3.083(2)				
Xe(2)---F(1)	3.341(2)				
Xe(2)---F(4)	3.367(2)				
Kr(1)---F(1D)	3.083(2)				
Bond Angles (deg)					
F(1)–Xe(1)–F(1A)	92.1(1)	F(1)–Xe(1)–F(1A)	180.0	F(1)–Xe(1)–F(1A)	180.0
F(1)–Xe(1)–F(1B)	180.0	F(1)–Xe(1)–F(2)	90.47(5)	F(1)–Xe(1)–F(2)	90.26(3)
F(1)–Xe(1)–F(1C)	87.9(1)	F(1)–Xe(1)–F(2A)	89.53(5)	F(1)–Xe(1)–F(2A)	89.74(3)
F(1A)–Xe(1)–F(1B)	87.9(1)	F(1A)–Xe(1)–F(2)	89.53(5)	F(1A)–Xe(1)–F(2)	89.74(3)
F(1A)–Xe(1)–F(1C)	180.0	F(1A)–Xe(1)–F(2A)	90.47(5)	F(1A)–Xe(1)–F(2A)	90.26(3)
F(1B)–Xe(1)–F(1C)	92.1(1)	F(2)–Xe(1)–F(2A)	180.0	F(2)–Xe(1)–F(2A)	180.0
F(2)–Xe(1)–F(2A)	180.0	F(3)–Xe(2)–F(3A)	180.0		
F(2)–Xe(1)–F(3)	90.0				
F(2)–Xe(1)–F(3A)	90.0				
F(2A)–Xe(1)–F(3)	90.0				
F(2A)–Xe(1)–F(3A)	90.0				
F(3)–Xe(1)–F(3A)	180.0				
F(4)–Kr(1)–F(4A)	178.2(1)				

Table A1.7. Experimental and calculated geometric parameters for $[XeF_5][AsF_6]$ (**7**)

Bond Lengths (Å)			
Xe(1)–F(1)	1.800(8)	Xe(2)–F(4)	1.815(7)
Xe(1)–F(2)	1.840(6)	Xe(2)–F(5)	1.844(5)
Xe(1)–F(2A)	1.840(6)	Xe(2)–F(6)	1.833(8)
Xe(1)–F(3)	1.839(6)	Xe(2)–F(6A)	1.833(8)
Xe(1)–F(3A)	1.839(6)	Xe(2)–F(7)	1.832(8)
Xe(1)---F(8)	2.615(6)	Xe(2)---F(10)	2.767(6)
Xe(1)---F(8A)	2.615(6)	Xe(2)---F(10A)	2.767(6)
Xe(1)---F(13)	2.793(6)	Xe(2)---F(14)	2.705(5)
		Xe(2)---F(14A)	2.705(5)
As(1)–F(8)	1.712(6)	As(2)–F(11)	1.710(7)
As(1)–F(8A)	1.712(6)	As(2)–F(12)	1.709(5)
As(1)–F(9)	1.657(7)	As(2)–F(12A)	1.709(5)
As(1)–F(9A)	1.657(7)	As(2)–F(13)	1.741(6)
As(1)–F(10)	1.699(6)	As(2)–F(14)	1.749(5)
As(1)–F(10A)	1.699(6)	As(2)–F(14A)	1.749(5)

Bond Angles (deg)			
F(1)–Xe(1)–F(2)	80.6(3)	F(4)–Xe(2)---F(10)	134.2(3)
F(1)–Xe(1)–F(2A)	80.6(3)	F(4)–Xe(2)---F(10A)	134.2(3)
F(1)–Xe(1)–F(3)	79.6(3)	F(4)–Xe(2)---F(14)	138.3(2)
F(1)–Xe(1)–F(3A)	79.6(3)	F(4)–Xe(2)---F(14A)	138.2(2)
F(1)–Xe(1)---F(8)	146.0(3)	F(5)–Xe(2)–F(6)	88.3(2)
F(1)–Xe(1)---F(8A)	146.0(3)	F(5)–Xe(2)–F(6A)	88.3(2)
F(1)–Xe(1)---F(13)	130.0(3)	F(5)–Xe(2)–F(7)	158.0(3)
F(2)–Xe(1)–F(2A)	87.2(5)	F(5)–Xe(2)---F(10)	68.9(2)
F(2)–Xe(1)–F(3)	160.2(3)	F(5)–Xe(2)---F(10A)	68.9(2)
F(2)–Xe(1)–F(3A)	88.4(3)	F(5)–Xe(2)---F(14)	129.6(2)
F(2)–Xe(1)---F(8)	114.5(3)	F(5)–Xe(2)---F(14A)	129.6(2)
F(2)–Xe(1)---F(8A)	70.5(3)	F(6)–Xe(2)–F(6A)	160.0(5)
F(2)–Xe(1)---F(13)	130.2(3)	F(6)–Xe(2)–F(7)	88.0(3)
F(2A)–Xe(1)–F(3)	88.4(3)	F(6)–Xe(2)---F(10)	68.0(4)
F(2A)–Xe(1)–F(3A)	160.2(3)	F(6)–Xe(2)---F(10A)	68.0(4)
F(2A)–Xe(1)---F(8)	70.5(3)	F(6)–Xe(2)---F(14)	72.2(2)
F(2A)–Xe(1)---F(8A)	114.5(3)	F(6)–Xe(2)---F(14A)	72.2(2)
F(2A)–Xe(1)---F(13)	130.2(3)	F(6A)–Xe(2)–F(7)	88.0(3)
F(3)–Xe(1)–F(3A)	89.3(4)	F(6A)–Xe(2)---F(10)	128.4(4)
F(3)–Xe(1)---F(8)	82.0(4)	F(6A)–Xe(2)---F(10A)	128.4(4)
F(3)–Xe(1)---F(8A)	128.6(3)	F(6A)–Xe(2)---F(14)	124.1(2)
F(3)–Xe(1)---F(13)	65.7(2)	F(6A)–Xe(2)---F(14A)	124.1(2)
F(3A)–Xe(1)---F(8)	128.6(3)	F(7)–Xe(2)---F(10)	128.8(3)
F(3A)–Xe(1)---F(8A)	82.0(4)	F(7)–Xe(2)---F(10A)	128.8(3)
F(3A)–Xe(1)---F(13)	65.7(2)	F(7)–Xe(2)---F(14)	69.2(3)
F(8)---Xe(1)---F(8A)	65.9(6)	F(7)–Xe(2)---F(14A)	69.2(3)
F(8)---Xe(1)---F(13)	64.6(2)	F(10)---Xe(2)---F(10A)	60.7(3)
F(8A)---Xe(1)---F(13)	64.6(2)	F(10)---Xe(2)---F(14)	60.7(3)
F(4)–Xe(2)–F(5)	78.5(3)	F(10)---Xe(2)---F(14A)	87.5(3)
F(4)–Xe(2)–F(6)	80.0(3)	F(10A)---Xe(2)---F(14)	60.7(3)
F(4)–Xe(2)–F(6A)	80.0(3)	F(10A)---Xe(2)---F(14A)	87.5(3)
F(4)–Xe(2)–F(7)	79.5(4)	F(14)---Xe(2)---F(14A)	60.7(3)

continued …

Table A1.7. (continued)

F(8)–As(1)–F(8A)	90.3(6)	F(11)–As(2)–F(12)	91.6(3)
F(8)–As(1)–F(9)	87.8(5)	F(11)–As(2)–F(12A)	91.6(3)
F(8)–As(1)–F(9A)	92.0(6)	F(11)–As(2)–F(13)	176.5(3)
F(8)–As(1)–F(10)	178.7(6)	F(11)–As(2)–F(14)	90.0(3)
F(8)–As(1)–F(10A)	89.0(5)	F(11)–As(2)–F(14A)	90.0(3)
F(8A)–As(1)–F(9)	92.0(5)	F(12)–As(2)–F(12A)	93.0(3)
F(8A)–As(1)–F(9A)	87.8(5)	F(12)–As(2)–F(13)	90.9(2)
F(8A)–As(1)–F(10)	89.0(5)	F(12)–As(2)–F(14)	90.7(3)
F(8A)–As(1)–F(10A)	178.7(6)	F(12)–As(2)–F(14A)	176.0(3)
F(9)–As(1)–F(9A)	179(1)	F(12A)–As(2)–F(13)	90.9(2)
F(9)–As(1)–F(10)	91.1(5)	F(12A)–As(2)–F(14)	176.0(3)
F(9)–As(1)–F(10A)	89.1(5)	F(12A)–As(2)–F(14A)	90.7(3)
F(9A)–As(1)–F(10)	89.1(5)	F(13)–As(2)–F(14)	87.6(2)
F(9A)–As(1)–F(10A)	91.1(5)	F(13)–As(2)–F(14A)	87.6(2)
F(10)–As(1)–F(10A)	91.8(7)	F(14)–As(2)–F(14A)	85.6(4)

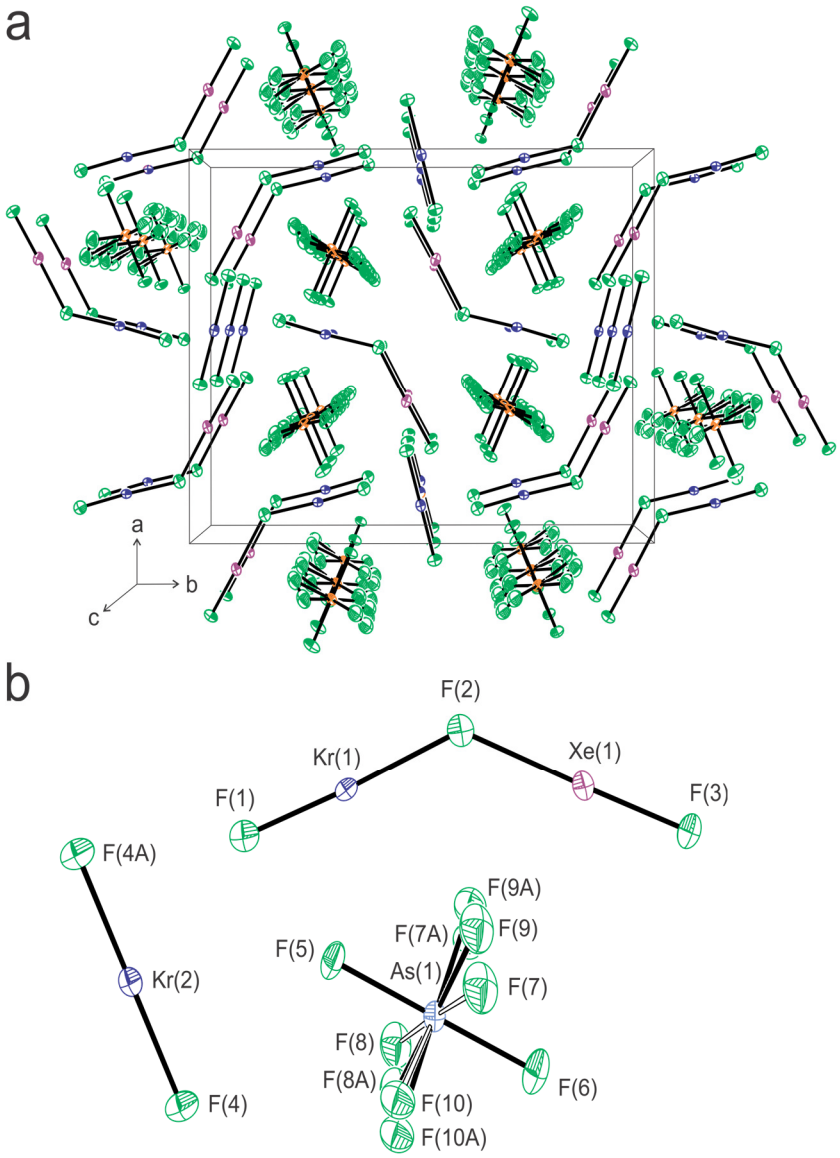

Figure A1.1. (a) A packing diagram showing the X-ray crystal structure of $[FKrFXeF][AsF_6]\cdot 0.5KrF_2\cdot 2HF$ (**1**) viewed along the *c*-axis of the unit cell. (b) The structural unit in the X-ray crystal structure of $[FKrFXeF][AsF_6]\cdot 0.5KrF_2\cdot 2HF$ (**1**) showing both orientations of the disordered $[AsF_6]^-$ anion. Thermal ellipsoids are drawn at the 50% probability level.

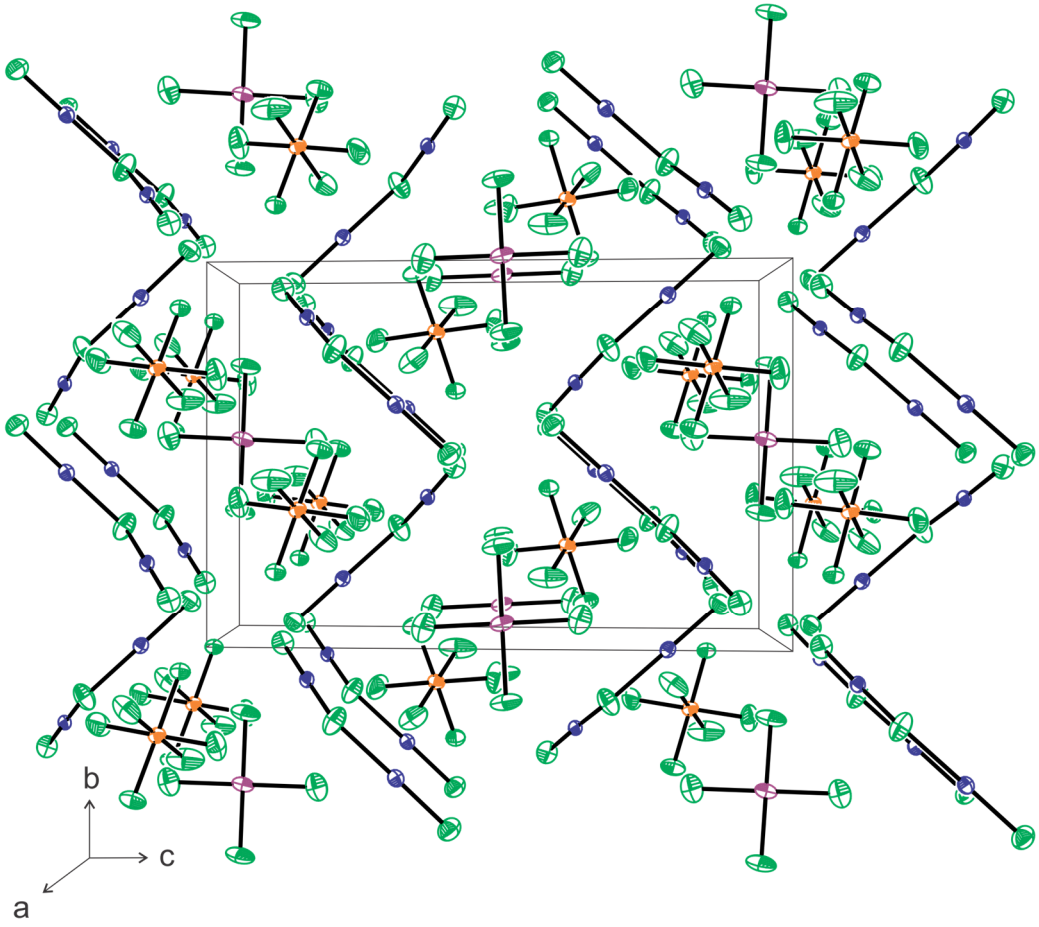

Figure A1.2. A packing diagram showing the X-ray crystal structure of $([Kr_2F_3][AsF_6])_2 \cdot XeF_4$ (**2**) viewed along the *a*-axis of the unit cell; thermal ellipsoids are drawn at the 50% probability level.

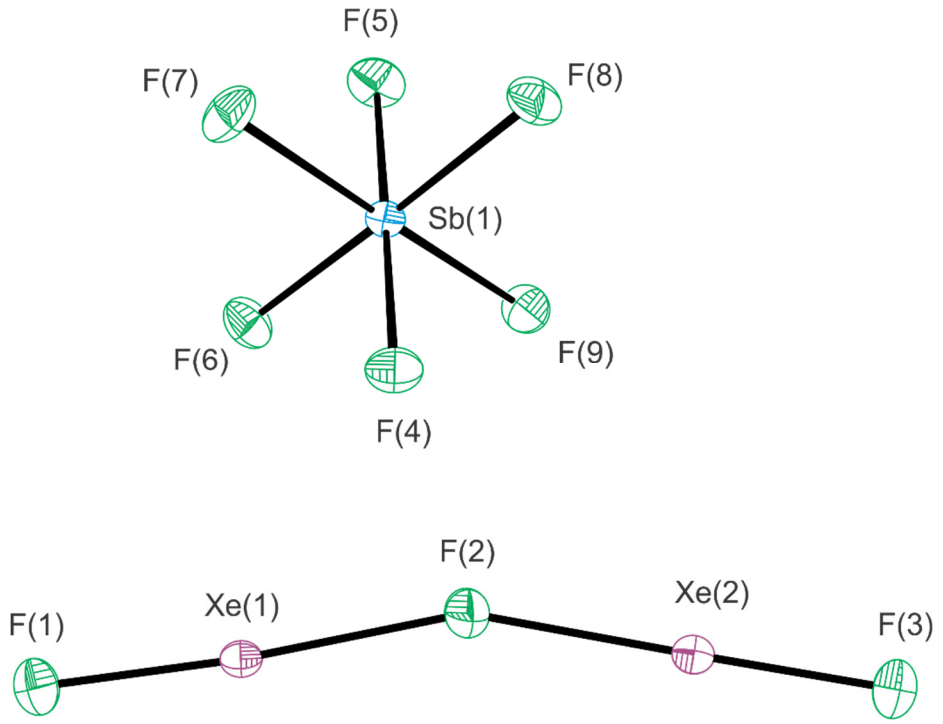

Figure A1.3. The structural unit in the X-ray crystal structure of $[Xe_2F_3][SbF_6]$ (**3**). Thermal ellipsoids are drawn at the 50% probability level.

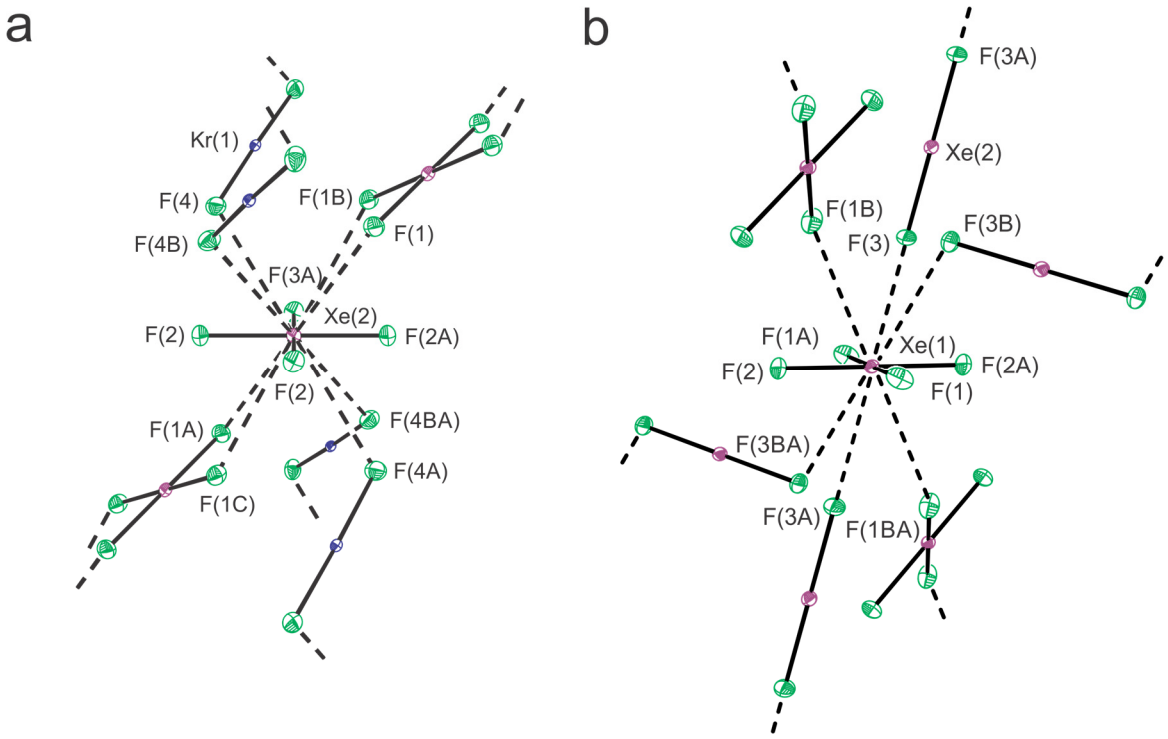

Figure A1.4. (a) A portion of the X-ray crystal structure of $XeF_4 \cdot KrF_2$ (**4**) showing the coordination environment around the xenon atom of $Xe_{(2)}F_4$. A structural diagram depicting the coordination environment around $Xe_{(1)}F_4$ in **4** is provided in Figure 3.3. (b) A portion of the X-ray crystal structure of $XeF_4 \cdot XeF_2$ (**5**) showing the coordination environment of XeF_4. Thermal ellipsoids are drawn at the 50% probability level.

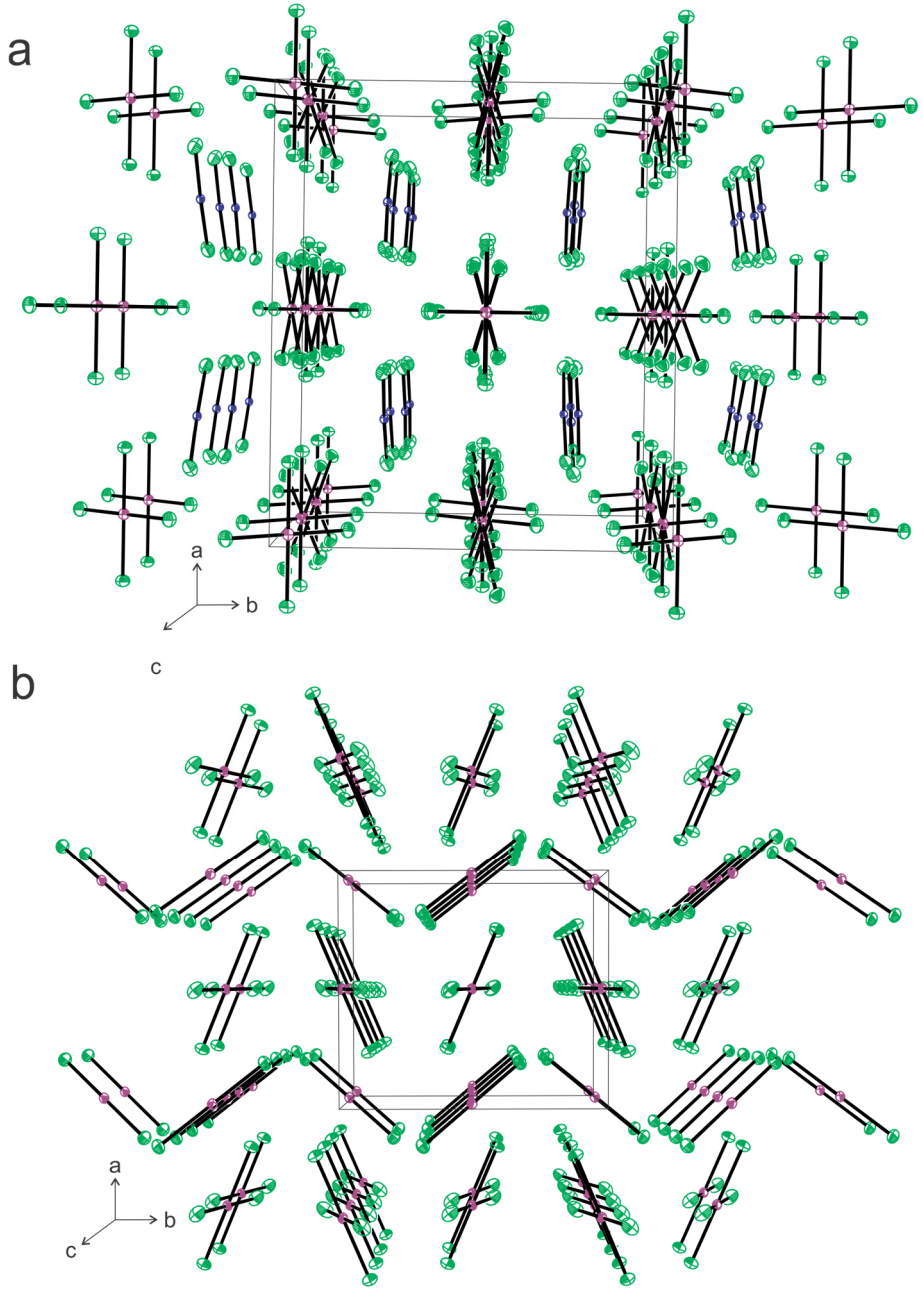

Figure A1.5. (a) A packing diagram showing the X-ray crystal structure of $XeF_4 \cdot KrF_2$ (**4**) viewed along the *c*-axis of the unit cell. (b) A packing diagram showing the X-ray crystal structure of $XeF_4 \cdot XeF_2$ (**5**) viewed along the *c*-axis of the unit cell. Thermal ellipsoids are drawn at the 50% probability level.

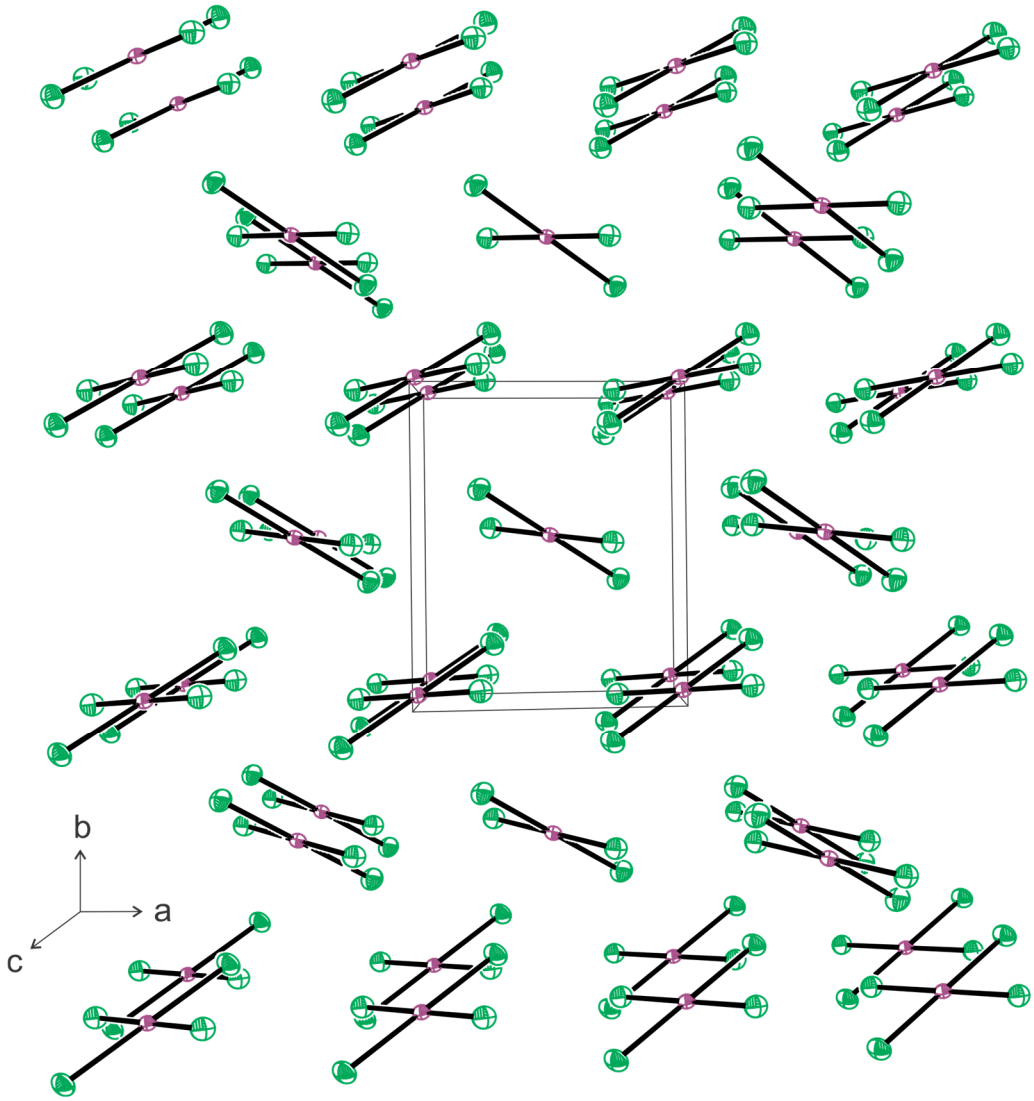

Figure A1.6. A packing diagram showing the X-ray crystal structure of XeF_4 (**6**) viewed along the *c*-axis of the unit cell; thermal ellipsoids are drawn at the 50% probability level.

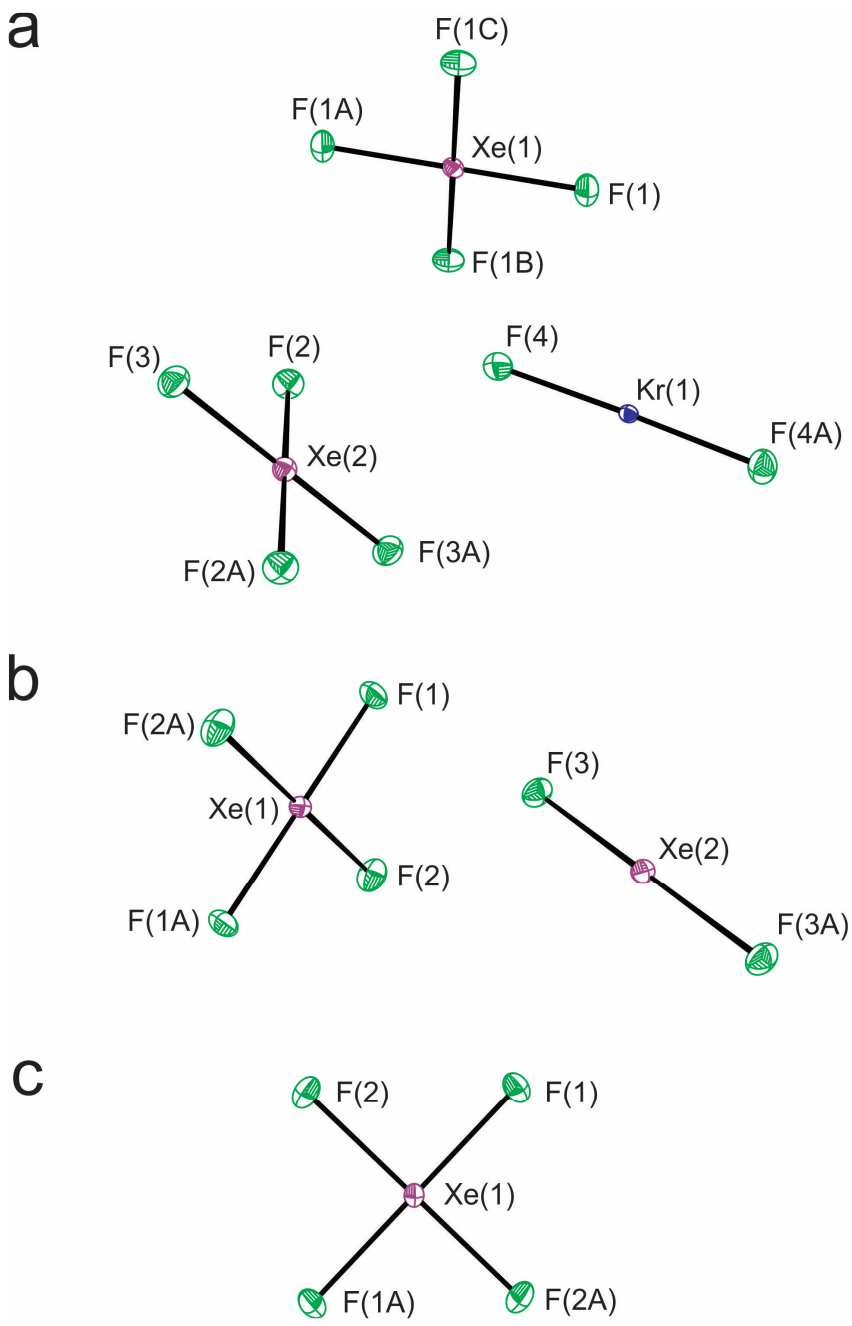

Figure A1.7. The structural units in the X-ray crystal structures of (a) $XeF_4 \cdot KrF_2$ (**4**), (b) $XeF_4 \cdot XeF_2$, (**5**) and (c) XeF_4 (**6**). Thermal ellipsoids are drawn at the 50% probability level.

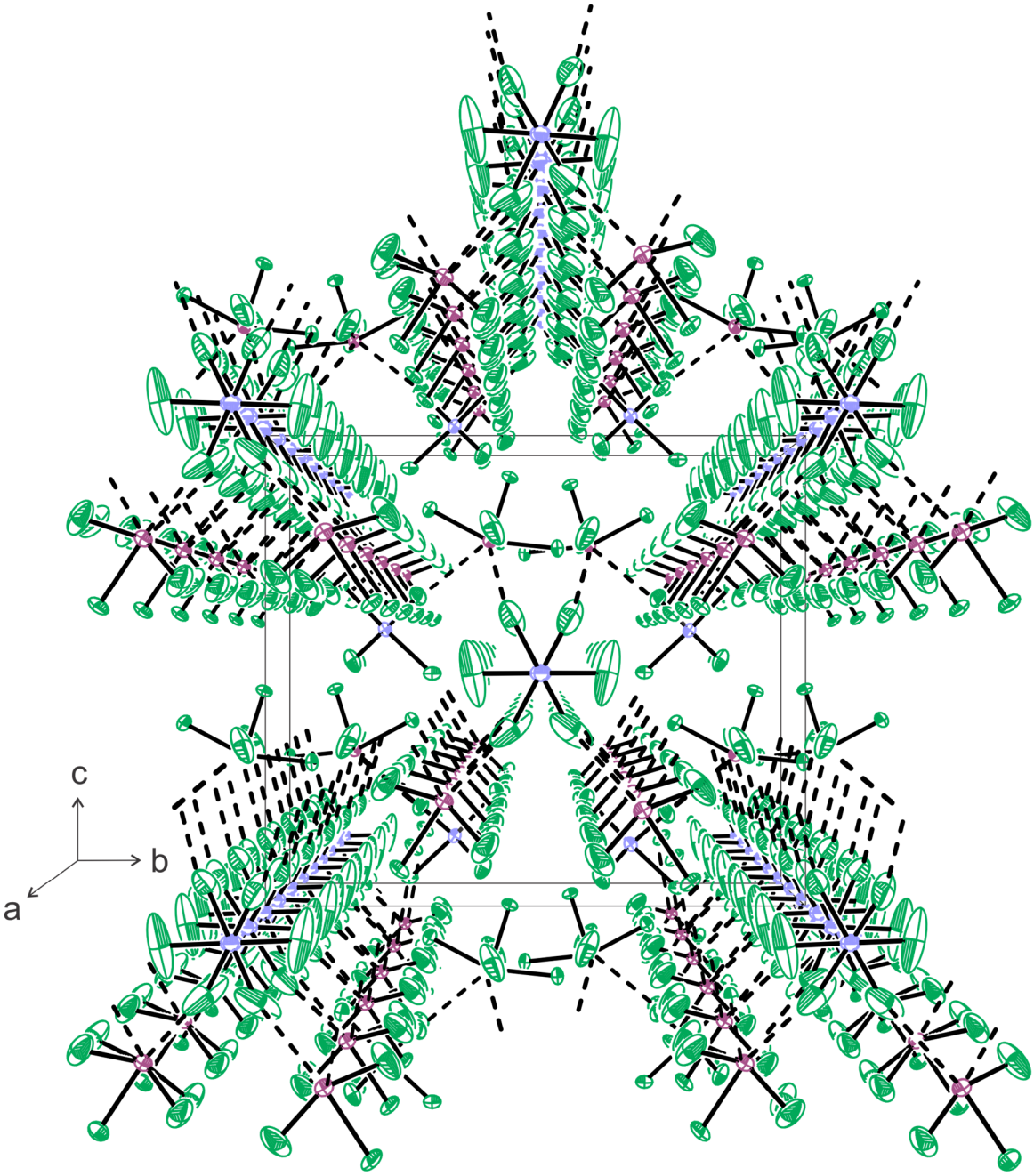

Figure A1.8. A packing diagram showing the X-ray crystal structure of $[XeF_5][AsF_6]$ (**7**) viewed along the *a*-axis of the unit cell. Thermal ellipsoids are drawn at the 50% probability level.

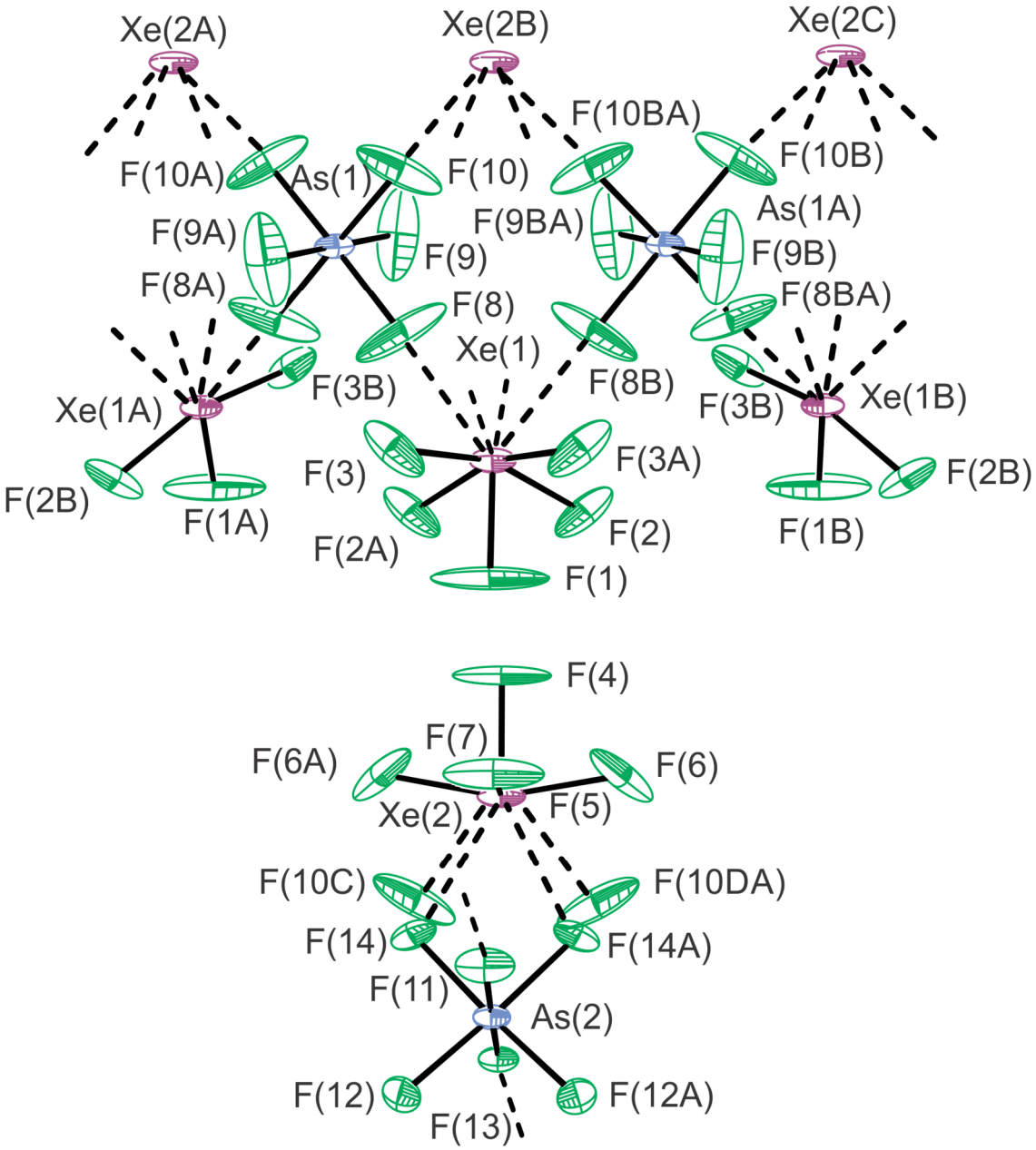

Figure A1.9. The coordination environments around Xe(1) and Xe(2) in the X-ray crystal structure of $[XeF_5][AsF_6]$ (**7**). Thermal ellipsoids are drawn at the 50% probability level.

X-ray Crystallography (continued)

XeF_4 (6). A low-precision RT single-crystal X-ray diffraction (SCXRD) structure of XeF_4 was reported in 1963.[S8] In the same year, a RT single-crystal neutron diffraction study of XeF_4 reported significantly more precise Xe–F bond lengths (1.951(2) and 1.954(2) Å) and *cis*-F–Xe–F bond angles (90.0(1)°).[S9] In both cases, the local symmetry of XeF_4 was C_i due to crystallographic site-symmetry lowering, with Xe–F bond lengths and *cis*-F–Xe–F bond angles that are equal within ±3σ. In both studies, the structure was described as a molecular solid comprised of square-planar XeF_4 molecules. In 1996, very precise Xe–F bond lengths were obtained for gas-phase XeF_4 by high-resolution gas-phase infrared spectroscopy (1.93487(3) Å, D_{4h}).[S10] The present work reports the high-precision, LT SCXRD structure of XeF_4. Xenon tetrafluoride crystallizes in the same space group at LT (Figures A1.6 and A1.7c) and RT. However, in the present study, the Xe–F bond lengths (1.9449(6) and 1.9509(6) Å) and *cis*-F–Xe–F bond angles (89.74(3) and 90.26(3)°) are significantly different within ±3σ. The Xe–F bond lengths of crystalline XeF_4 are longer than those of gas-phase XeF_4 due to long Xe---F intermolecular contacts (3.1507(6) and 3.1962(6) Å) in the crystal lattice (Table A1.6), where the longer Xe–F bonds correspond to shorter Xe---F contacts and the shorter Xe–F bonds correspond to longer Xe---F contacts.

[XeF_5][AsF_6] (7). The low-precision RT SCXRD structure of $[XeF_5][AsF_6]$ was reported in 1974.[S12] The structure was solved in the $P2_1/c$ space group and consisted of well isolated dimeric structural units in which each $[XeF_5]^+$ cation forms one short Xe---F_{As} secondary bond (2.65(2) Å) to the fluorine atom of one of the two $[AsF_6]^-$ anions and two

longer Xe---F_{As} secondary bonds (2.73(2) and 2.83(2) Å) to two fluorine atoms of the second $[AsF_6]^-$ anion in the dimeric unit.[S12] In contrast, the present unit cell consists of two crystallographically inequivalent $[XeF_5]^+$ and $[AsF_6]^-$ that are extensively bridged through Xe---F_{As} secondary bonds so that they form columns along the *a*-axis that are diagonally linked in the *bc*-plane (Figure A1.8). The $[Xe_{(1)}F_5]^+$ cation forms three short Xe---F_{As} secondary bonds (2.615(6), 2.615(6), and 2.796(6) Å) to three fluorine atoms of neighboring $[As_{(1)}F_6]^-$ and $[As_{(2)}F_6]^-$ anions, whereas the $[Xe_{(2)}F_5]^+$ cation forms two shorter symmetry-related Xe---F_{As} secondary bonds (2 x 2.705(5) Å) with two fluorine atoms of a single $[As_{(2)}F_6]^-$ anion, and two longer symmetry-related Xe---F_{As} secondary bonds (2 × 2.767(6) Å) with two fluorine atoms of two different neighboring $[As_{(1)}F_6]^-$ anions (Figure A1.9).

The primary bond lengths and bond angles of $[XeF_5]^+$ in **7** (Table A1.7) are comparable to those of other fluoro- and oxyfluoro-anion salts of $[XeF_5]^+$, e.g., $[XeF_5]_3[Ti_4F_{19}]$,[S12] $[XeF_5]_2[PdF_6]$,[S13] $[XeF_5][AsF_6]$,[S11] $[XeF_5]_2[NiF_6]$,[S14] $[XeF_5][SbF_6]\cdot XeOF_4$,[S15] $[XeF_5][PtF_6]$,[S16] $[XeF_5][AgF_4]$,[S17] $[XeF_5][CrF_5]\cdot XeF_4$,[S18] $[XeF_5][OsO_3F_3]$,[S19] $[XeF_5][\mu\text{-}F(OsO_3F_2)_2]$,[S19] $[XeF_5]_2[CrF_6]\cdot 2CrOF_4$,[S20] $[XeF_5]_2[Cr_2O_2F_8]$,[S20] $[XeF_5]_2[Cr_2O_2F_8]\cdot 2HF$,[S20] $[XeF_5]_2[Cr_2O_2F_8]\cdot 2XeOF_4$,[S20] and $[XeF_5][Xe_2F_{11}][CrOF_5]\cdot 2CrOF_4$,[S20] and are not discussed further.

Raman Spectroscopy (continued)

[FKrFXeF][AsF₆]·0.5KrF₂·2HF (1).

[FKrFXeF]$^+$. The vibrational modes of gas-phase $[FKrFXeF]^+$ under C_s symmetry belong to the irreducible representations $\Gamma = 7A' + 2A''$, where the A' and A" modes are Raman- and infrared-active. The A' and A" irreducible representations of gas-phase $[FKrFXeF]^+$ correlate to A' and A" irreducible representations under the C_s site symmetry in the solid state. When correlated to the unit cell symmetry of **1** (D_{2h}), each vibrationally coupled A' mode splits into two Raman-active bands, A_g and B_{1g}, and two infrared-active bands, B_{2u} and B_{3u}. Each A" mode splits into two Raman-active bands, B_{2g} and B_{3g}, and two infrared-active bands, A_u and B_{1u} (Figure A1.10).

Figure A1.10. Factor-group analysis of $[FKrFXeF]^+$ in **1** [a]

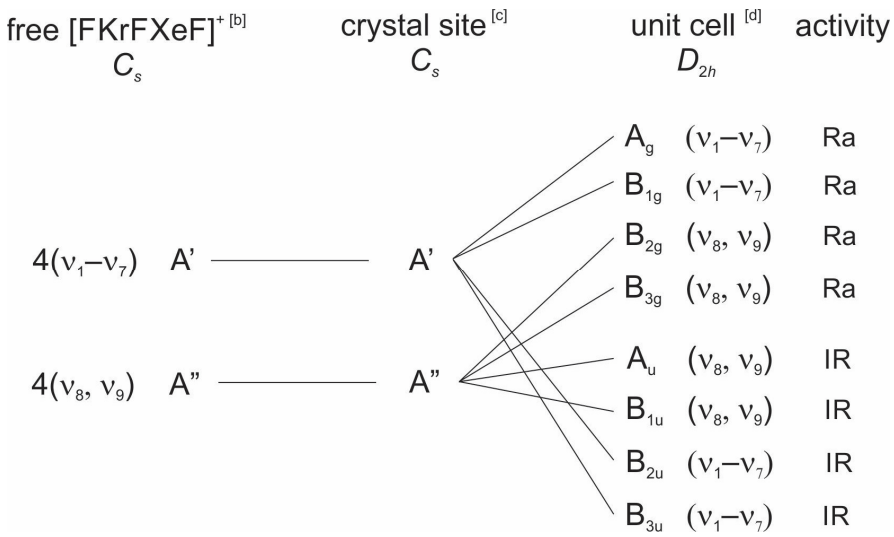

[a] The external modes are not treated in this analysis. [b] The vibrational irreducible representation for gas-phase $[FKrFXeF]^+$ (C_s) is $\Gamma = 7A' + 2A''$. [c] The σ(*xy*)-plane of gas-phase $[FKrFXeF]^+$ (C_s) is maintained under the crystal site symmetry of **1** (C_s) and was selected to correlate the crystal site symmetry to the unit cell symmetry (D_{2h}). [d] Space group; *Pbam*, $Z = 4$.

[AsF$_6$]$^-$. The $[AsF_6]^-$ bands of **1** were assigned by comparison with $[Kr_2F_3][AsF_6]$,[S3] $[Kr_2F_3][AsF_6]\cdot n KrF_2$,[S3] and $[Xe_2F_3][AsF_6]$.[S21] All $[AsF_6]^-$ bands are split into two or more bands in the Raman spectrum of **1**. To account for these splittings, a factor-group analysis based on the X-ray crystal structure of **1** was carried out using the "correlation method" [S22] (Figure A1.11).

Six vibrational modes are predicted for gas-phase $[AsF_6]^-$ under O_h symmetry. The vibrations belong to the irreducible representations $\Gamma = A_{1g} + E_g + T_{2g} + 2T_{1u} + T_{2u}$, where the A_{1g}, E_g, and T_{2g} modes are Raman-active, the T_{1u} modes are infrared-active, and the T_{2u} mode is inactive. All irreducible representations of $[AsF_6]^-$ under O_h symmetry correlate to A′ and A″ irreducible representations under the C_s crystal site symmetry of $[AsF_6]^-$ in **1**. When correlated to the D_{2h} unit cell symmetry of **1**, each vibrationally coupled A′ mode splits into two Raman-active bands, A_g and B_{1g}, and two infrared-active bands, B_{2u} and B_{3u}. The A″ modes also split into two Raman-active bands, B_{2g} and B_{3g}, and two infrared-active bands, A_u and B_{1u}. Band splittings were resolved for $\nu_1(A_{1g})$, $\nu_2(E_g)$, $\nu_3(T_{2g})$, $\nu_4(T_{1u})$, and $\nu_5(T_{1u})$ (Table A1.8).

Figure A1.11. Factor-group analysis of $[AsF_6]^-$ in **1** [a]

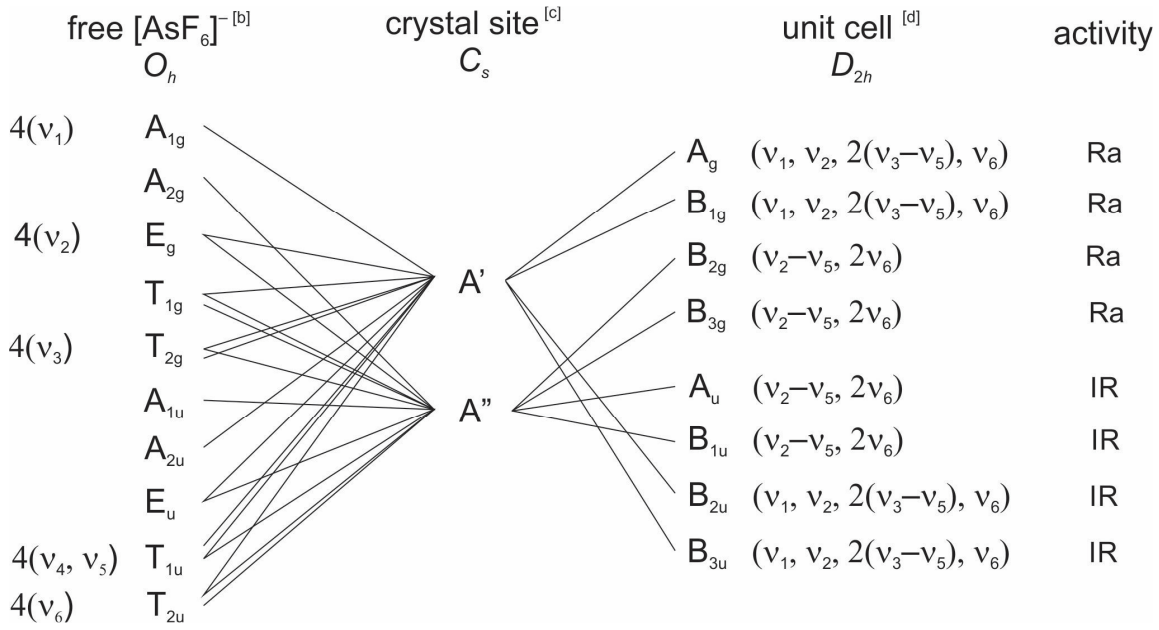

[a] The external modes are not treated in this analysis. [b] The vibrational irreducible representation for gas-phase $[AsF_6]^-$ (O_h) is $\Gamma = A_{1g} + E_g + T_{2g} + 2T_{1u} + T_{2u}$. [c] A σ_d-plane ($\sigma(xy)$) of the gas-phase $[AsF_6]^-$ anion (O_h) is maintained under the crystal site symmetry of **1** (C_s) and was selected for correlation of the crystal site symmetry to the unit cell symmetry (D_{2h}). [d] Space group; *Pbam*, $Z = 4$.

KrF_2. The ν_s(Kr–F) mode of cocrystallized KrF_2 in **1** was observed at 464 cm^{-1}. Although the factor-group analysis of KrF_2 in **1** (Figure A1.12) predicts that this mode is split, band splitting was not resolved.

Figure A1.12. Factor-group analysis of KrF_2 in **1** [a]

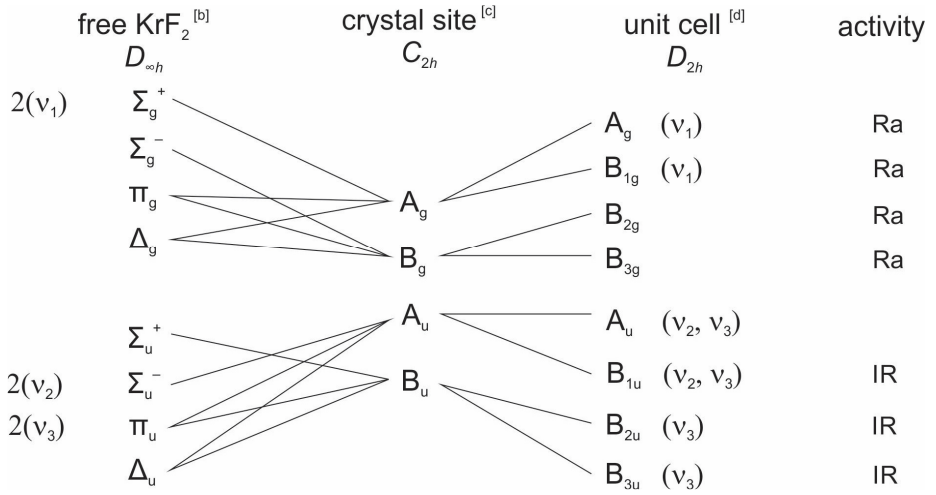

[a] The external modes have not been treated in this analysis. [b] The vibrational irreducible representation for gas-phase KrF_2 ($D_{\infty h}$) is $\Gamma = \Sigma_g^+ + \Sigma_u^- + \Pi_u$. [c] A C_2''-axis ($C_2(z)$) of gas-phase KrF_2 ($D_{\infty h}$) is maintained under the crystal site symmetry of **1** (C_{2h}) and was selected to correlate the crystal site symmetry to the unit cell symmetry (D_{2h}). [d] Space group; *Pbam*, $Z = 4$. There are 0.5 KrF_2 molecules in the formula unit of **1**, which gives rise to two KrF_2 molecules in the unit cell.

Table A1.8. Experimental Raman frequencies, intensities, and general assignments for $[AsF_6]^-$ in $[FKrFXeF][AsF_6]\cdot 0.5KrF_2\cdot 2HF$ (**1**)

exptl [a]	assgnts (O_h) [b]
697(sh)	$\nu_4(T_{1u})$
695(8)	
685(20)	$\nu_1(A_{1g})$
678(8) [c]	
594(sh) [c]	$\nu_2(E_g)$
586(sh) [c]	
578(sh)	
572(sh)	
413(3)	$\nu_5(T_{1u})$
411(3)	
409(3)	
399(3)	
396(3)	
391(sh)	
382(sh)	$\nu_3(T_{2g})$
375(sh)	
370(10)	
363(5)	

[a] Frequencies are given in cm^{-1}. The ν_s(Kr–F) mode of cocrystallized KrF_2 in **1** was observed at 464(90) cm^{-1}. Weak bands and shoulders were observed at 174(sh), 183(sh), 330(8), 366(5), 567(sh), 594(sh), 600(sh), 610(sh), and 680(sh) cm^{-1} and 503(3), 506(3), and 546(sh) cm^{-1} that were assigned to $[Kr_2F_3][AsF_6]$ [S3] and XeF_4 (**4**), respectively, which formed from the redox decomposition of **1**. The lattice modes of **1**, $[Kr_2F_3][AsF_6]$, and XeF_4 (**4**) were observed at 95(sh), 97(sh), 101(8), 104(8), 106(8), 109(sh), 111(sh), 115(10), 117(13), 120(13), 122(sh), 124(sh), 127(sh), 130(3), and 133(3) cm^{-1}. Values in parentheses denote relative Raman intensities. Abbreviations denote shoulder (sh) and not observed (n.o.). The Raman spectrum was recorded in a FEP sample tube at −150 °C using 1064-nm excitation under frozen aHF. [b] Assignments are made under O_h symmetry for the $[AsF_6]^-$ anion. [c] The band overlaps with a $[Kr_2F_3][AsF_6]$ band.

([Kr$_2$F$_3$][AsF$_6$])$_2$·XeF$_4$ (2). The solid-state, LT Raman spectrum of **2** is reproduced in Figure A1.13. The vibrational assignments for $[Kr_2F_3]^+$ were made by comparison with (a) the calculated gas-phase vibrational frequencies and Raman intensities of the energy-minimize geometry of $[Kr_2F_3]^+$ (Table A1.9) and (b) the experimental frequencies of $[Kr_2F_3]^+$ in $[Kr_2F_3][AsF_6]$,[S3] $[Kr_2F_3][AsF_6]\cdot n KrF_2$,[S3] and $[Kr_2F_3][SbF_6]$.[S3] The $[AsF_6]^-$ bands of **2** were assigned under O_h symmetry by comparison with those observed in the latter salts (Table A1.9, footnote b). The bands of cocrystallized XeF_4 in **2** were assigned under D_{4h} symmetry by comparison with XeF_4,[S23] $XeF_4\cdot XeF_2$,[S23] and $XeF_4\cdot KrF_2$. Several bands in the Raman spectrum of **2** are split into two or more components. To account for these splittings, factor-group analyses based on the X-ray crystal structure of **2** were carried out using the "correlation method" [S22] (Figures A1.14– A1.16).

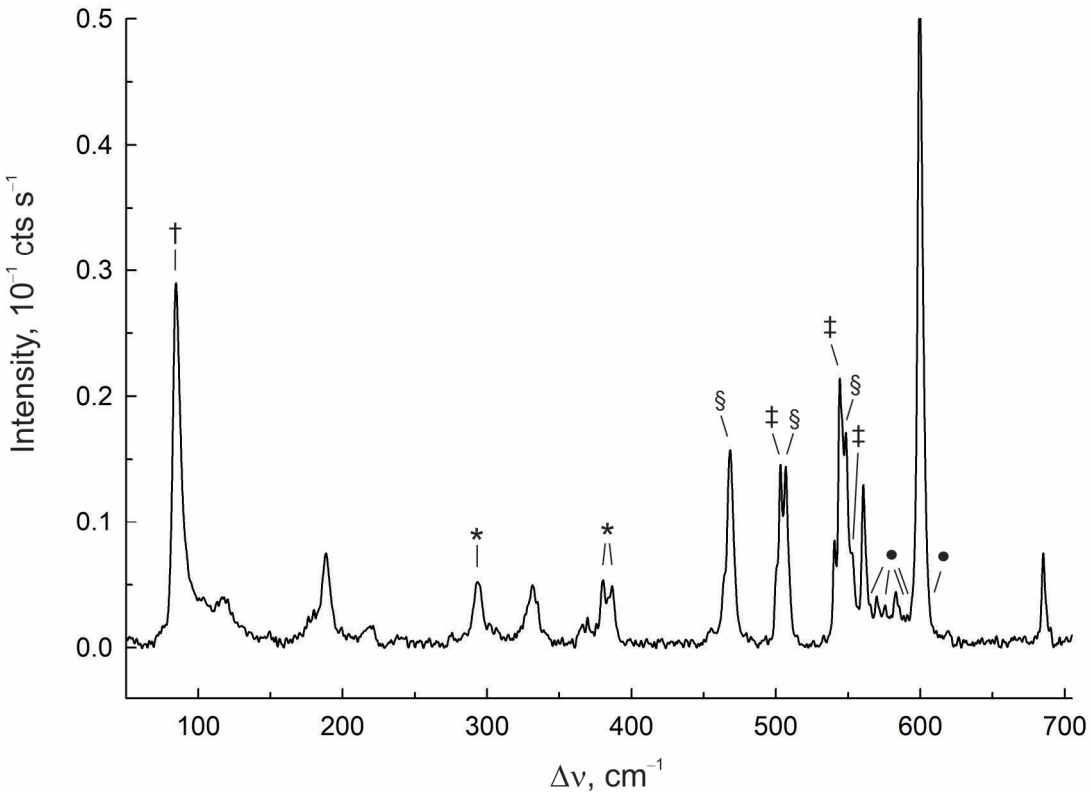

Figure A1.13. Raman spectrum of $([Kr_2F_3][AsF_6])_2{\cdot}XeF_4$ (**2**) recorded at −150 °C under frozen aHF using 1064-nm excitation. The symbols denote bands assigned to $[FKrFXeF][AsF_6]{\cdot}0.5KrF_2{\cdot}2HF$ (**1**) (•), bands assigned to $XeF_4{\cdot}KrF_2$ (**4**) (§), bands assigned to XeF_4 (**6**) (‡), FEP sample tube bands (*), and an instrumental artifact (†).

Table A1.9. Experimental Raman frequencies and calculated vibrational frequencies, intensities, and assignments for $[Kr_2F_3]^+$ in $([Kr_2F_3][AsF_6])_2{\cdot}XeF_4$ (**2**)

exptl [a,b]	calcd [a,c]		assgnts [d]
	B2PLYP-D3[e]	B3PW91 GD3BJ[f]	
600(100)	616(216)[10]	648(181)[10]	$\nu_1(A_1)$, $\nu(NgF_t) + \nu(Ng'F'_t)$
564(sh) 561(24) [g]	589(16)[230]	627(15)[236]	$\nu_7(B_2)$, $\nu(NgF_t) - \nu(Ng'F'_t)$
455(4)	426(<1)[583]	431(<1)[437]	$\nu_8(B_2)$, $\nu(NgF_b) - \nu(Ng'F_b)$
335(7) 331(9)	280(20)[12]	302(11)[13]	$\nu_2(A_1)$, $\nu(NgF_b) + \nu(Ng'F_b)$
199(4)	203(0)[12]	203(<0.1)[12]	$\nu_6(B_1)$, $\delta(F_tNgF_b)_{i.p.} - \delta(F'_tNg'F_b)_{i.p.}$
188(13) [g]	166(2)[0]	164(3)[0]	$\nu_5(A_2)$, $\delta(F_tNgF_b)_{o.o.p.} + \delta(F'_tNg'F_b)_{o.o.p.}$
180(6) [g]	164(7)[<1]	167(3)[<1]	$\nu_3(A_1)$, $\delta(F_tNgF_b)_{i.p.} + \delta(F'_tNg'F_b)_{i.p.}$
176(4) [g]	163(2)[2]	162(2)[<1]	$\nu_9(B_2)$, $\delta(F_tNgF_b)_{i.p.} - \delta(F'_tNg'F_b)_{i.p.}$
n.o.	36(5)[<0.1]	42(5)[<1]	$\nu_4(A_1)$, $\delta(NgF_bNg')$

[a] Frequencies are given in cm^{-1}. [b] Values in parentheses denote relative Raman intensities. Abbreviations denote shoulder (sh), not observed (n.o.). The Raman spectrum was recorded in a FEP sample tube at −150 °C using 1064-nm excitation under frozen aHF. The ν(Xe–F) bands of cocrystallized XeF_4 in **2** were observed at: $\nu_3(B_{2g})$; 500(4) and 509(sh) cm^{-1}, and $\nu_1(A_{1g})$; 540(15) cm^{-1}. The $[AsF_6]^-$ bands of **2** were observed at: $\nu_5(T_{2g})$; 360(sh), 366(4), 370(4) and 376(4) cm^{-1}, $\nu_2(E_g)$; 570(7), 582(7), 588(6), and 591(6) cm^{-1}, $\nu_1(A_{1g})$; 685(13) cm^{-1}, and $\nu_3(T_{1u})$); 690(4) cm^{-1}. Weak bands and shoulders were observed at 562(sh), 576(6), 578(sh), 580(6), 585(sh), 598(sh), and 606(sh) cm^{-1} that were assigned to $[FKrFXeF][AsF_6]{\cdot}0.5KrF_2{\cdot}2HF$ (**1**). Bands and shoulders were also observed at 219(4), 221(4), 507(26), 544(39), and 549(31) cm^{-} that were assigned to $XeF_4{\cdot}KrF_2$ (**4**)[1], and 503(28), 549(31), and 554(sh) cm^{-1} that were assigned to XeF_4. Lattice modes corresponding to the mixture of the aforementioned compounds were observed at 101(7), 103(7), 113(7), 116(7), 118(7), 120(7), 124(6), and 130(4) cm^{-1}. [c] Values in parentheses and square brackets denote calculated Raman intensities ($Å^4$ amu^{-1}) and infrared intensities (km mol^{-1}), respectively. [d] Assignments are for the energy-minimized geometry of $[Kr_2F_3]^+$ (C_{2v}) calculated using the B2PLYP-D3 and B3PW91-GD3BJ methods. Abbreviations denote stretch (ν), bend (δ), in-plane (i.p.), out-of-plane (o.o.p.), terminal fluorine (F_t), bridging fluorine (F_b). [e] The Def2-TZVPD (F, Kr, Xe) basis set was used. [f] The aug-ccpVDZ(-PP)(F, Kr)/aug-ccpVTZ(-PP) (Xe) basis sets were used. [g] This band overlaps with a band of **1**.

[Kr$_2$F$_3$]$^+$. Nine vibrational modes are predicted for gas-phase $[Kr_2F_3]^+$ under C_{2v} symmetry. The vibrations belong to the irreducible representations $\Gamma = 4A_1 + 3B_1 + A_2 + B_2$, where the A_1, B_1, and B_2 modes are both Raman- and infrared-active, and the A_2 mode is Raman-active. In the factor-group analysis, all irreducible representations of gas-phase $[Kr_2F_3]^+$ under C_{2v} symmetry correlate to A irreducible representations under the C_1 crystal site symmetry of $[Kr_2F_3]^+$ in **2**. When correlated to its unit cell symmetry, C_{2h}, each vibrationally coupled A mode splits into two Raman active bands, A_g and B_g, and into two infrared-active bands, A_u and B_u. Band splittings were only resolved for the $\nu_7(B_2)$ and $\nu_2(A_1)$ bands (Table A1.9).

The calculated vibrational displacements reveal the ν(Ng–F$_t$) and ν(Ng–F$_b$) modes of $[Kr_2F_3]^+$ are strongly coupled, giving rise to four modes, $\nu_1(A_1)$, $\nu_7(B_1)$, $\nu_8(B_2)$, and $\nu_2(A_1)$. The in-phase coupled $\nu_1(A_1)$ mode [ν(Ng–F$_t$) + ν(Ng′–F$_t$)], occurs at higher frequency (exptl, 600 cm^{-1}; calcd, 616 cm^{-1}) than the out-of-phase coupled $\nu_7(B_1)$ mode [ν(Ng–F$_t$) − ν(Ng′–F$_t$)] (exptl, 561, 564 cm^{-1}; calcd, 589 cm^{-1}), whereas the out-of-phase coupled bridge $\nu_8(B_2)$ mode, [ν(Ng–F$_b$) − ν(Ng′–F$_b$)] (exptl, 455 cm^{-1}; calcd, 426 cm^{-1}), occurs at higher frequency than the in-phase coupled bridge $\nu_2(A_1)$ mode [ν(Ng–F$_b$) + ν(Ng′–F$_b$)] (exptl, 331, 335 cm^{-1}; calcd, 280 cm^{-1}).

The calculated in- and out-of-plane coupled deformation modes are in good agreement with experiment (Table A1.9). The in-plane $\nu_4(A_1)$ mode, δ(NgF$_b$Ng'), is predicted to occur at very low frequency (36 cm^{-1}) and was not observed. The potential energy surface corresponding to this bend has been previously described as “flat”,

indicating that the Kr---F_b---Kr bond angle of $[Kr_2F_3]^+$ is highly deformable and may be influenced by secondary bonding interactions within the crystal lattice.[S3]

Figure A1.14. Factor-group analysis of $[Kr_2F_3]^+$ in $([Kr_2F_3][AsF_6])_2{\cdot}XeF_4$ (**2**) [a]

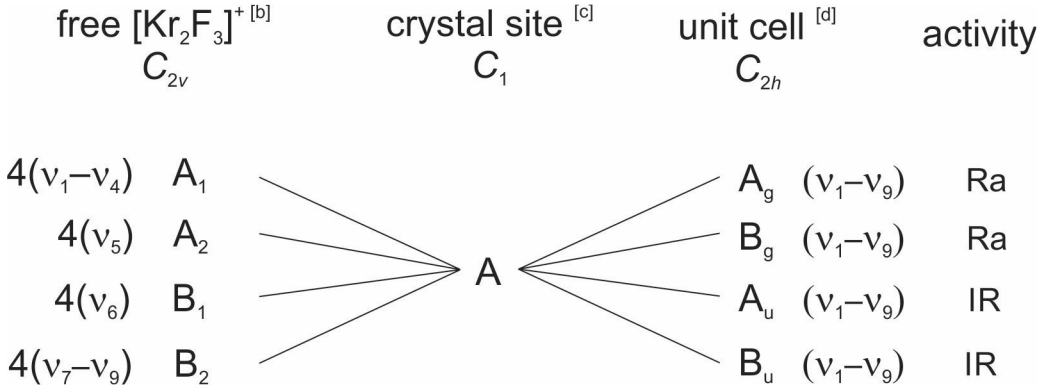

[a] The external modes are not treated in this analysis. [b] The vibrational irreducible representation for gas-phase $[Kr_2F_3]^+$ is $\Gamma = 4A_1 + 3B_1 + A_2 + B_2$. [c] All atoms of $[Kr_2F_3]^+$ occupy general positions in the crystal structure of **2**. [d] Space group; $P2_1/n$, $Z = 2$. There are two $[Kr_2F_3]^+$ cations in the formula unit of **2**, giving rise to four cations in the unit cell.

[AsF₆]⁻. In the factor-group analysis, all irreducible representations of gas-phase $[AsF_6]^-$ under O_h symmetry correlate to A irreducible representations under the C_1 crystal site symmetry of the $[AsF_6]^-$ ion in **2**. When correlated to its unit cell symmetry, C_{2h}, each vibrationally coupled A mode splits into two Raman-active bands, A_g and B_g, and two infrared-active bands, A_u and B_u. Band splittings were only resolved on the $\nu_2(E_g)$ and $\nu_5(T_{2g})$ bands (Table A1.9, footnote b).

Figure A1.15. Factor-group analysis of $[AsF_6]^-$ in $([Kr_2F_3][AsF_6])_2 \cdot XeF_4$ (**2**) [a]

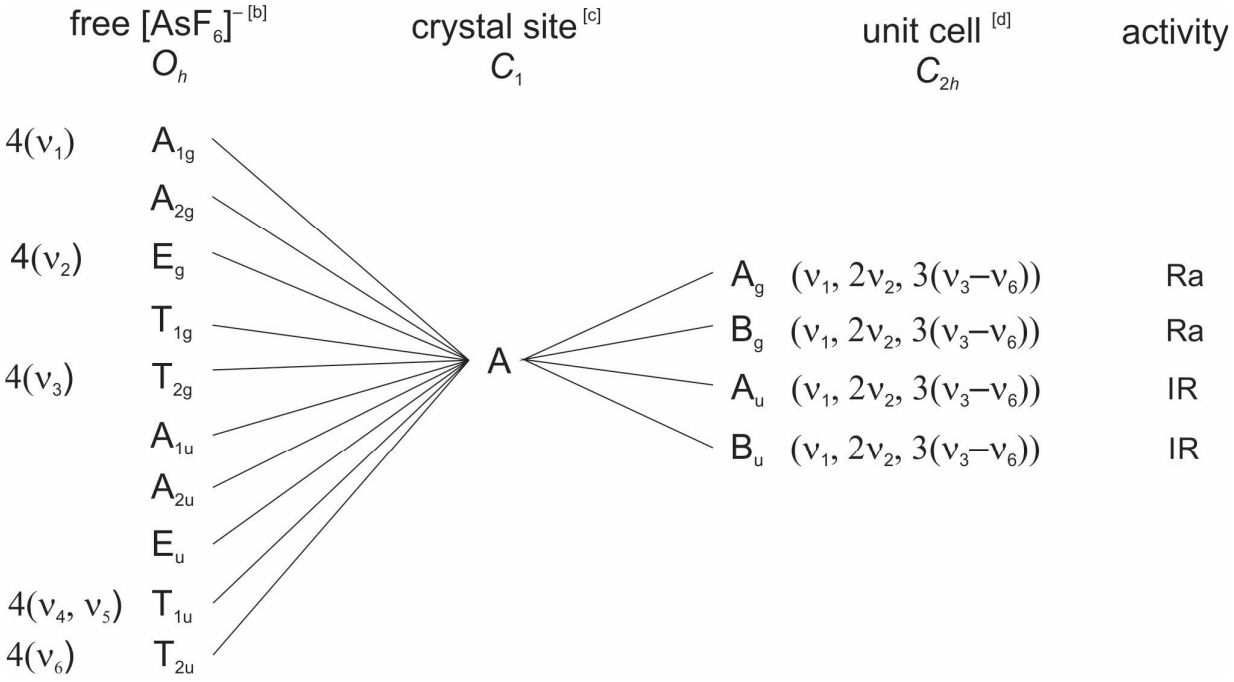

[a] The external modes are not treated in this analysis. [b] The vibrational irreducible representation for gas-phase $[AsF_6]^-$ (O_h) is $\Gamma = A_{1g} + E_g + T_{2g} + 2T_{1u} + T_{2u}$. [c] All atoms of $[AsF_6]^-$ occupy general positions in the crystal structure of **2**. [d] Space group; $P2_1/n$, $Z = 2$. There are two $[AsF_6]^-$ anions in the formula unit of **2**, giving rise to four anions in the unit cell.

XeF₄. Seven vibrational modes are predicted for gas-phase XeF_4 under D_{4h} symmetry. The vibrations belong to the irreducible representations $\Gamma = A_{1g} + B_{1g} + B_{2g} + A_{2u} + B_{2u} + 2E_u$, where the A_{1g}, B_{1g}, and B_{2g} modes are Raman-active, the A_{2u} and E_u modes are infrared-active, and the B_{2u} mode is inactive. The gerade and ungerade irreducible representations of gas-phase XeF_4 under D_{4h} symmetry correlate to A_g and A_u irreducible

representations, respectively, under the C_i crystal site symmetry of XeF_4 in **2**. When correlated to its unit cell symmetry, D_{2h}, each vibrationally coupled A_g mode splits into two Raman-active bands, A_g and B_g, and each A_u band splits into two infrared-active components, A_u and B_u. Band splitting was resolved for the $\nu_3(B_{2g})$ band (500/509 cm^{-1}) in the Raman spectrum of **2**. The unsplit $\nu_1(A_{1g})$ band was observed at 540 cm^{-1}, but the $\nu_2(B_{1g})$ band was not observed.

Figure A1.16. Factor-group analysis of cocrystallized XeF_4 in $([Kr_2F_3][AsF_6])_2 \cdot XeF_4$ (**2**) [a]

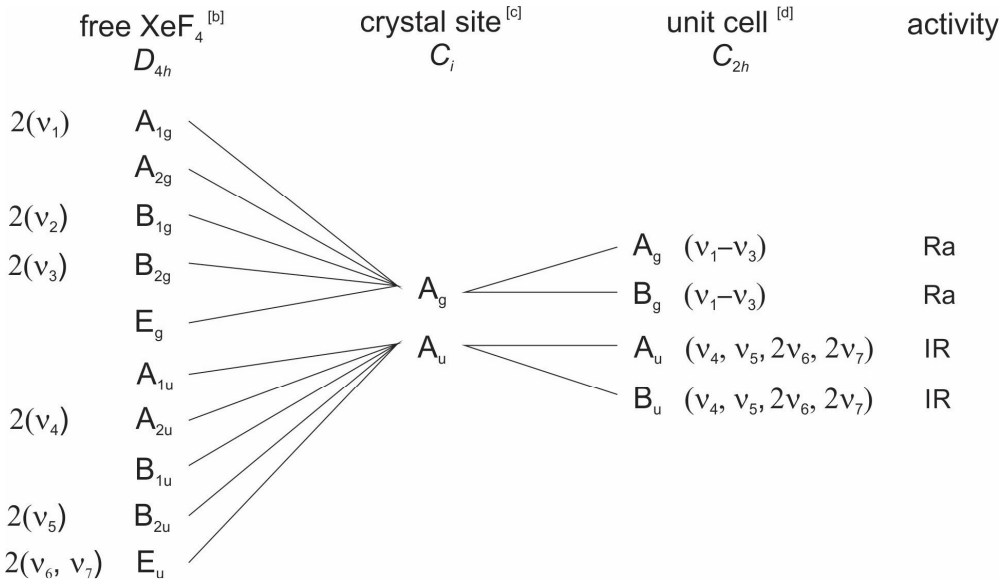

[a] The external modes are not treated in this analysis. [b] The vibrational irreducible representation for gas-phase XeF_4 (D_{4h}) is $\Gamma = A_{1g} + B_{1g} + B_{2g} + A_{2u} + B_{2u} + 2E_u$. [c] The inversion center of gas-phase XeF_4 (D_{4h}) is maintained under the crystal site symmetry of **2** (C_i) and was used to correlate the crystal site symmetry to the unit cell symmetry (D_{2h}). [d] Space group; $P2_1/n$, $Z = 2$.

$XeF_4 \cdot KrF_2$ (4). The Raman spectrum of **4** (Figure A1.17) can be analyzed as the composite of the vibrational spectra of XeF_4 and KrF_2, in accordance with the weak Xe---F secondary bonding interactions observed its crystal structure.

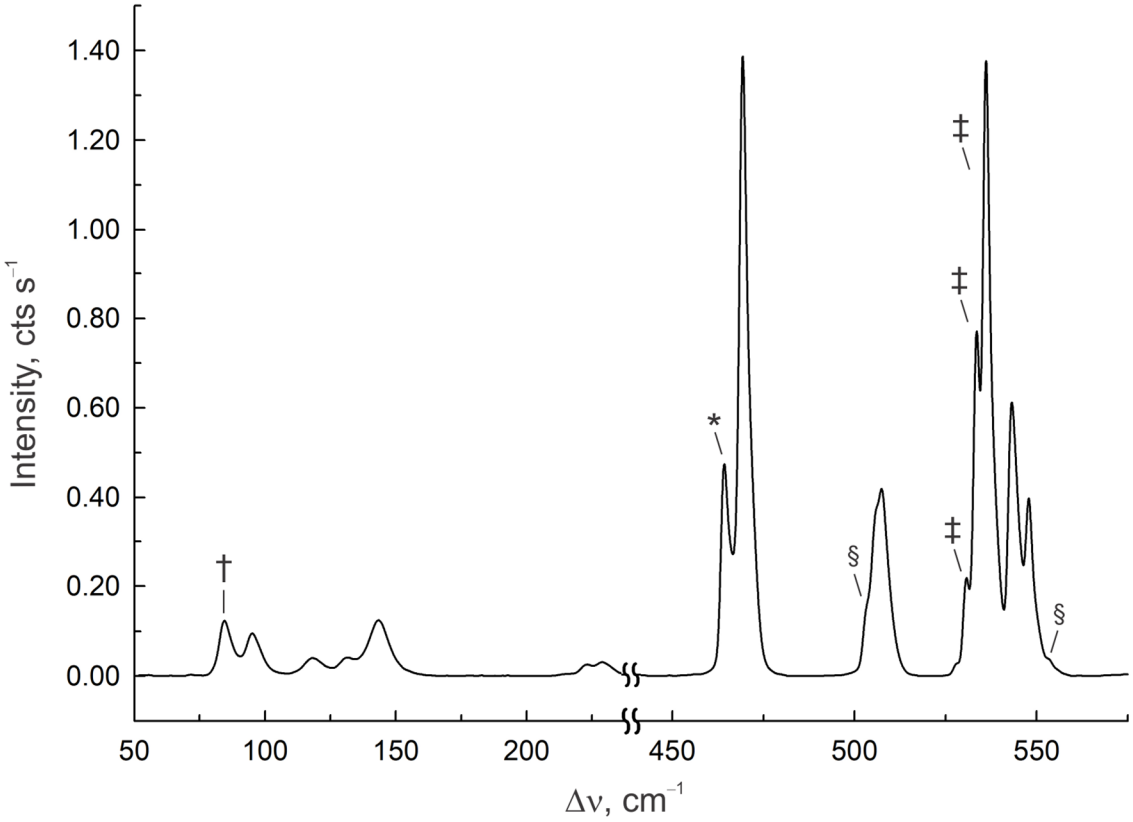

Figure A1.17. Raman spectrum of $XeF_4 \cdot KrF_2$ (**4**) recorded at −150 °C under frozen $CFCl_3$ using 1064-nm excitation. The symbols denote bands assigned to XeF_4 (§), $CFCl_3$ (‡), the $\nu_1(\Sigma_g^+)$ band of α-KrF_2 (*), and an instrumental artifact (†).

Table A1.10. Raman frequencies, intensities, and assignments for $XeF_4 \cdot KrF_2$ (**4**)

exptl [a]	assgnts [b]
548(29) 543(44) [c]	$\nu_1(A_{1g})_{XeF_4}$
507(30) [c] 505(30) [c]	$\nu_3(B_{2g})_{XeF_4}$
469(100) [d]	ν_s(Kr–F)
229(2) 223(2)	$\nu_2(B_{1g})_{XeF_4}$
143(9) 132(3) 118(3) 95(7)	lattice modes

[a] The Raman spectrum was recorded in an FEP sample tube at −150 °C using 1064-nm excitation under frozen $CFCl_3$. Frequencies are given in cm^{-1}. Values in parentheses denote relative Raman intensities. Abbreviations denotes stretch (ν). Weak shoulders were observed at 215(sh), 503(sh), and 553(sh) cm^{-1} that were assigned to XeF_4.[S23] Bands observed at 129(sh), 246(50), 294(sh), 352(33), 398(39), 531(16), 534(56), 536(99), 817(10), 822(9), 830(6), 839(8), 1065(2), 1076(4), 1634(<1), and 2098(<1) cm^{-1} were assigned to $CFCl_3$. [b] Assignments for XeF_4 and KrF_2 were made under D_{4h} and $D_{\infty h}$ symmetry, respectively. [c] The band overlaps with a XeF_4 band. [d] The band overlaps with a β-KrF_2 band.

KrF₂. The band of cocrystallized KrF_2 (469 cm^{-1}) in **4** was assigned to the ν_s(Kr–F) mode by comparison with α-KrF_2 (465 cm^{-1}),[S2] β-KrF_2 (468, 469 cm^{-1}),[S2] and cocrystallized KrF_2 in $[Kr_2F_3][PnF_6]\cdot n KrF_2$ (Sb: 456 cm^{-1}; As: 462 cm^{-1}).[S3] Although the factor-group analysis predicts this mode should be split (Figure A1.18), the band splitting was not resolved.

Figure A1.18. Factor-group analysis of KrF_2 in $XeF_4\cdot KrF_2$ (**4**) [a]

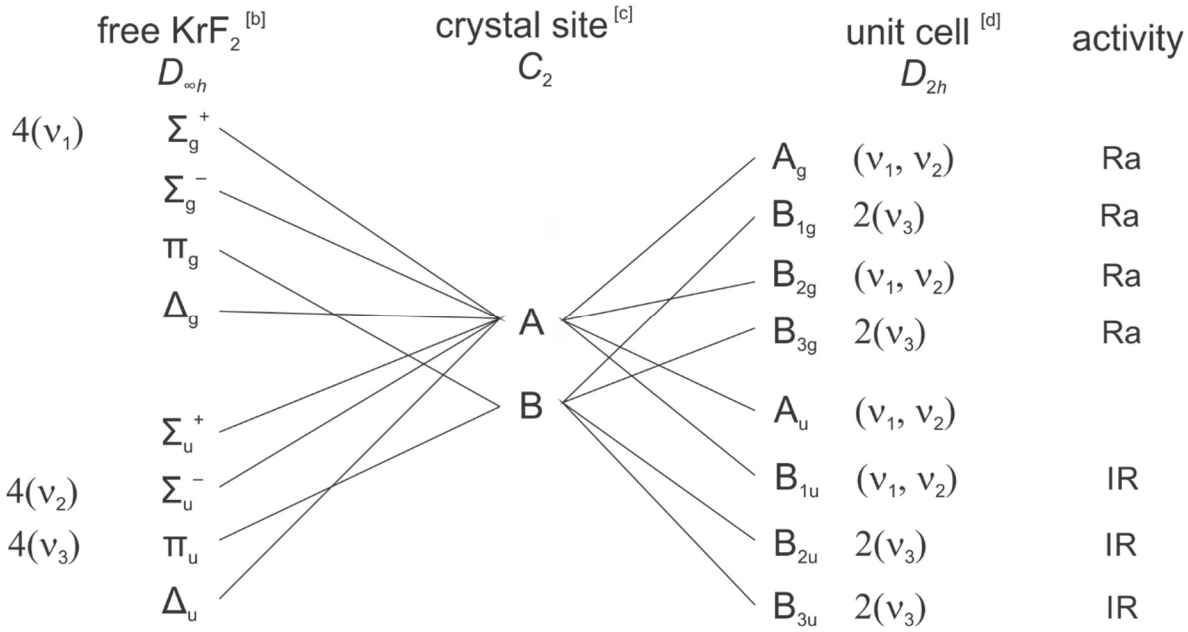

[a] The external modes are not treated in this analysis. [b] The vibrational irreducible representation for gas-phase KrF_2 ($D_{\infty h}$) is $\Gamma = \Sigma_g^+ + \Sigma_u^- + \pi_u$. [c] The $C_2(y)$ axis of gas-phase KrF_2 ($D_{\infty h}$) is maintained under the crystal site symmetry (C_2) and was selected for correlation of the crystal site symmetry to the unit cell symmetry (D_{2h}). [d] Space group; *Cmce*, $Z = 8$. The number of molecules contributing to the total number of lattice vibrations for a *C*-centered unit cell is equal to *Z* divided by two (ref. S22, pp. 2-4).

XeF_4. Bands of cocrystallized XeF_4 in **4** were assigned under D_{4h} symmetry by comparison with XeF_4[S23] and $XeF_4 \cdot XeF_2$.[S23] All the XeF_4 bands of **4** are split into two components ($\nu_1(A_{1g})$, 543/548 cm^{-1}, $\nu_3(B_{2g})$, 505/507 cm^{-1}, $\nu_2(B_{1g})$, 223/229 cm^{-1}) contrary to what was observed for $XeF_4 \cdot XeF_2$ ($\nu_1(A_{1g})$, 548 cm^{-1}, $\nu_3(B_{2g})$, 508 or 511 cm^{-1}, $\nu_2(B_{1g})$, 219 cm^{-1}).[S23] A factor-group analysis was carried out (Figure A1.19) to account for band splitting. In the factor-group analysis of 4, the symmetry of gas-phase XeF_4 (D_{4h} symmetry) is lowered under its crystal site symmetry to C_{2h}. When correlated to the unit cell symmetry, D_{2h}, the $\nu_1(A_{1g})$, $\nu_2(B_{1g})$, and $\nu_3(B_{2g})$ bands of XeF_4 are each predicted to split into two Raman-active bands; these splittings were observed in the Raman spectrum (Table A1.10).

Figure A1.19. Factor-group analysis of XeF_4 in $XeF_4 \cdot KrF_2$ (**4**) [a]

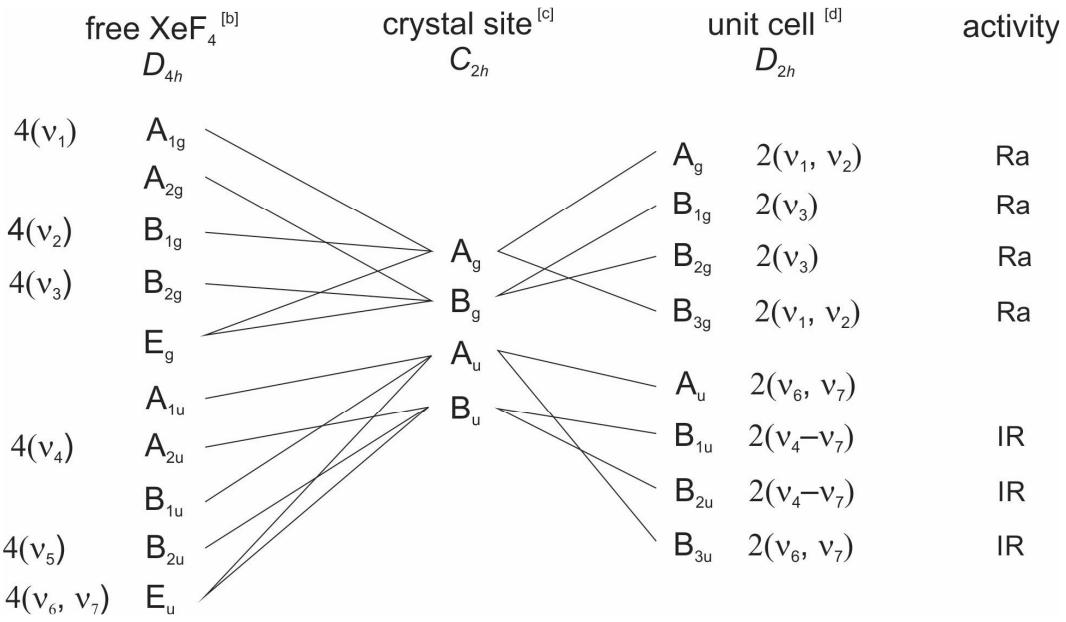

[a] The external modes are treated in this analysis. [b] The vibrational irreducible representation for gas-phase XeF_4 (D_{4h}) is $\Gamma = A_{1g} + B_{1g} + B_{2g} + A_{2u} + B_{2u} + 2E_u$. [c] The $C_2(x)$-axis of gas-phase XeF_4 (D_{4h}) is maintained under the crystal site symmetry (C_{2h}) and was selected for correlation of the crystal site symmetry to the unit cell symmetry (D_{2h}). [d] Space group; *Cmce*, $Z = 8$. The number of molecules contributing to the total number of lattice vibrations for a *C*-centered unit cell is equal to Z divided by two (ref. S22, pp. 2-4).

[(F$_5$Xe)$_2$(μ-FKrF)(AsF$_6$)$_2$]. The solid-state, LT Raman spectrum of [(F$_5$Xe)$_2$(*μ*-FKrF)(AsF$_6$)$_2$] is shown in Figure A1.20. The spectrum has bands (Table A1.11) that are very similar to those assigned to [XeF$_5$]$^+$ and [AsF$_6$]$^-$ in [XeF$_5$][AsF$_6$] and [F$_5$Xe(FKrF)$_n$AsF$_6$] (*n* = 1, 2),[5] as well as a strong band at 485 cm^{-1} that is intermediate with respect to the ν(Kr–F$_b$) and ν(Kr–F$_t$) stretching frequencies of [F$_5$Xe(FKrF)AsF$_6$] (454 and 533 cm^{-1}) and [F$_5$Xe(FKrF)$_2$AsF$_6$] (466, 472/474 and 543, 564/567 cm^{-1}). The 485 cm^{-1} band is slightly shifted to higher frequency than the symmetric ν$_s$(Kr–F) stretching modes of *α*-KrF$_2$ (465 cm^{-1})[2] and *β*-KrF$_2$ (468, 469 cm^{-1}),[2] and those of the symmetrically bridged KrF$_2$ in KrF$_2$·2CrOF$_4$ (465 cm^{-1})[24] and Hg(OTeF$_5$)$_2$·1.5KrF$_2$ (468 cm^{-1}).[25] The observation of a single ν(Ng–F) stretching band in the Raman spectrum is consistent with a symmetrically bridged KrF$_2$ ligand that is similar to the known XeF$_2$ bridged analogue, [(F$_5$Xe)$_2$(*μ*-FXeF)(AsF$_6$)$_2$].[26] Although not observed in the latter complex, shifts to higher frequency relative to XeF$_2$ (496 cm^{-1})[27] have been reported for the ν$_s$(Xe–F) bands of the symmetrically bridged XeF$_2$ molecules in [Ca(FXeF)$_5$(PF$_6$)$_2$] (522 cm^{-1}),[28] [Cd(FXeF)$_5$(PF$_6$)$_2$] (521 cm^{-1}),[28] [Sr$_3$(FXeF)$_3$(PF$_6$)$_2$] (532 cm^{-1}),[29] [Pb$_3$(FXeF)$_3$(PF$_6$)$_2$] (513 cm^{-1}),[29] and [Ba(FXeF)$_4$(PF$_6$)$_2$] (525 cm^{-1}).[30]

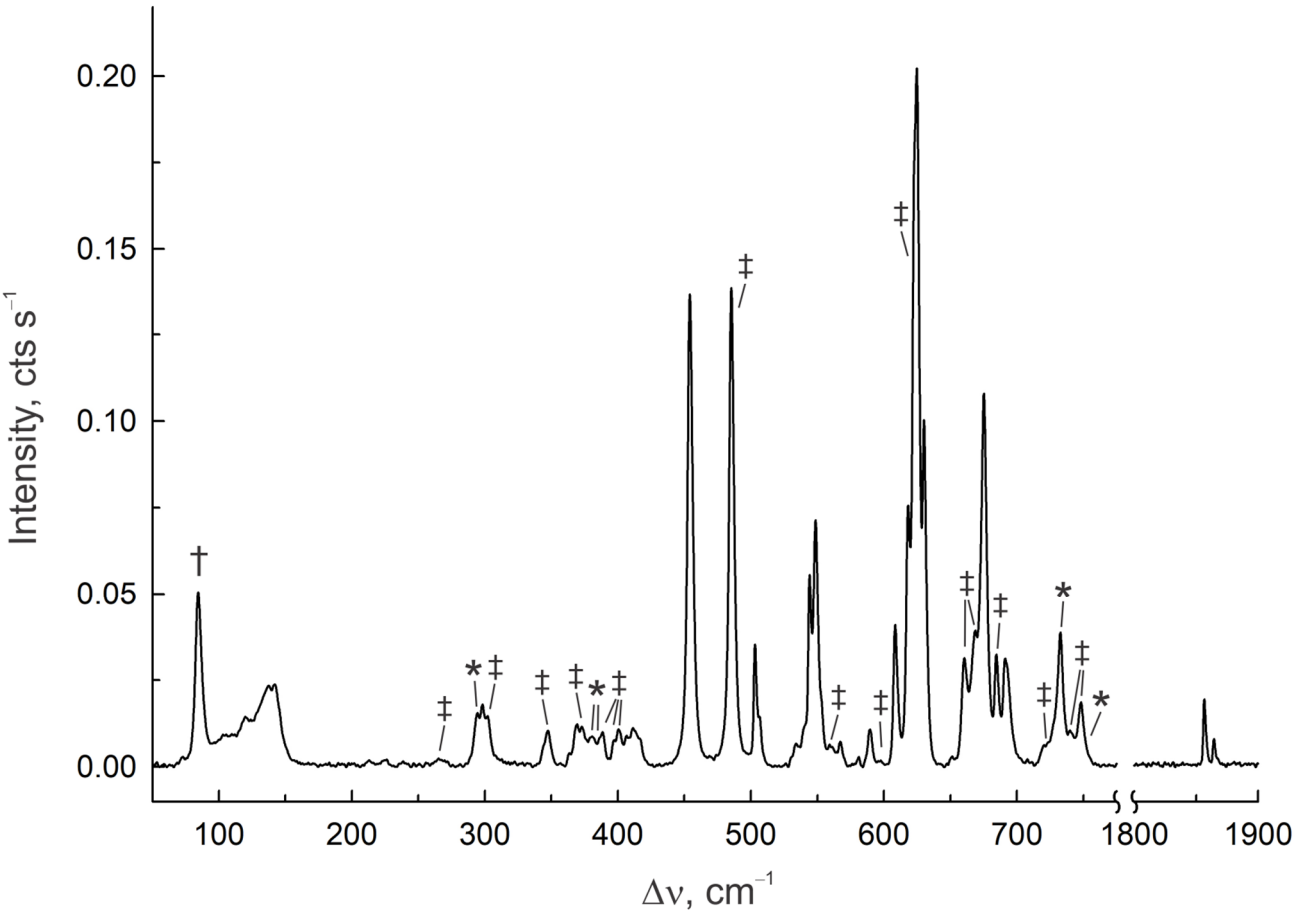

Figure A1.20. Raman spectrum of a solid mixture of $[(F_5Xe)_2(\mu\text{-}FKrF)(AsF_6)_2]$ (Table A1.11), $[XeF_5][AsF_6]$, $[F_5Xe(FKrF)AsF_6]$, XeF_4, and $[O_2][AsF_6]$, formed from the redox decomposition of **1** in aHF, and recorded at −150 °C using 1064-nm excitation. The symbols denote bands assigned to $[(F_5Xe)_2(\mu\text{-}FKrF)(AsF_6)_2]$ (‡), FEP sample tube bands (*), and an instrumental artifact (†). Band assignments for $[XeF_5][AsF_6]$,[S5] $[F_5Xe(FKrF)AsF_6]$,[S5] XeF_4,[S23] and $[O_2][AsF_6]$ [S4] are given, along with their relative intensities, in Table A1.2.

Table A1.11. Raman frequencies, intensities, and assignments for $[(F_5Xe)_2(\mu\text{-}FKrF)(AsF_6)_2]$

exptl [a]	assgnts [b]		
	$[XeF_5]^+$	$[AsF_6]^-$	KrF_2
748(9) 740(5) 723(sh) 708(1)		$\nu_4(T_{1u})$	
685(16) [c]		$\nu_1(A_{1g})$	
669(19)	$\nu_1(A_1)$		
661(15) [c]	$\nu_7(E)$		
625(100) [d]	$\nu_2(A_1)$		
598(sh)	$\nu_4(B_1)$		
567(3) 564(2) [c] 560(sh) [c] 559(3)		$\nu_2(E_g)$	
485(69)			ν_s(Kr–F)
417(sh)	$\nu_8(E)$		
405(sh) 402(sh) 397(4)		$\nu_5(T_{1u})$	
389(6) 381(1) 373(6) [e]		$\nu_3(T_{2g})$	
347(5)	$\nu_3(A_1)$		
302(7) [e]	$\nu_6(B_2)$		
265(1)	$\nu_5(B_1)$		

continued…

Table A1.11. (continued) [a] Frequencies are given in cm^{-1}. Lattice modes of $[(F_5Xe)_2(\mu\text{-}FKrF)(AsF_6)_2]$ were observed at 103(4), 107(4), 112(4), 115(sh), 120(sh), 123(sh), 125(sh), 134(sh), 137(11), 144(sh) and 150(sh) cm^{-1}. Values in parentheses denote relative Raman intensities. Abbreviations denote shoulder (sh). The Raman spectrum was recorded in a FEP sample tube at −150 °C using 1064-nm excitation on a dry crystalline sample. [b] Assignments are made under D_{4h} symmetry for the $[XeF_5]^+$ cation, O_h symmetry for the $[AsF_6]^-$ anion, and $D_{\infty h}$ symmetry for KrF_2. [c] The band overlaps with a band of $[F_5Xe(FKrF)AsF_6]$. [d] The band overlaps with a $[XeF_5][AsF_6]$ band. [e] The band overlaps with an FEP sample tube band.

Computational Results (continued)

Quantum-chemical calculations have been used to assess the bonding in $[FKrFXeF]^+$, $[Kr_2F_3]^+$, and $[Xe_2F_3]^+$. The NgF_2 molecules and $[NgF]^+$ cations were also calculated for comparison. The DFT functionals, B3LYP, PBE1PBE, and B3PW91, all with and without inclusion of GD3BJ dispersion, and the B2PLYP-D3, APFD, and WB97XD functionals, which include dispersion, were employed using the Def2-TZVPD, aug-cc-pVDZ(-PP), and/or aug-cc-pVTZ(-PP) basis sets. All calculations resulted in stationary points with all frequencies real (Tables A1.12– A1.15). Statistical analyses were carried out to determine which levels of theory best reproduce the experimental Ng–F_t and Ng---F_b bond lengths and the Ng---F_b---Ng and F_t–Ng---F_b bond angles of $[FKrFXeF]^+$, $[Kr_2F_3]^+$, and $[Xe_2F_3]^+$ and their vibrational frequencies and intensities. The analyses showed that the B2PLYP-D3/Def2-TZVPD (F, Kr, Xe) level of theory gave the best agreement with experiment, followed by B3PW91-D3/aug-ccpVDZ(-PP) (F, Kr)/aug-ccpVTZ(-PP) (Xe). Although the $[Kr_2F_3]^+$ and $[Xe_2F_3]^+$ cations had been previously studied by computational methods,[S3] the calculations were repeated for $[Kr_2F_3]^+$ and $[Xe_2F_3]^+$ at the aforementioned levels of theory to enable valid comparisons to be made

among the $[FKrFXeF]^+$, $[Kr_2F_3]^+$, and $[Xe_2F_3]^+$ cations. The calculated geometrical parameters of the $[Ng_2F_3]^+$ cations were compared with the most precise experimental values currently available (Table 3.2). The NBO (Tables A1.16 and A1.17), QTAIM (Tables A1.18 and A1.19, Figure A1.21), ELF, and MEPS analyses were also carried out at the B2PLYP-D3/Def2-TZVPD and B3PW91-D3/aug-ccpVDZ(-PP)/aug-ccpVTZ(-PP) levels of theory. The ensuing discussions refer to B2PLYP-D3/Def2-TZVPD values.

Atoms in a Molecule (AIM) Analyses

In general, indicators of bond covalency are provided by several AIM properties evaluated at the bond critical points[S31] (see Tables A1.18, A1.19). Significantly negative values for the Laplacian of electron density ($\nabla^2\rho_b$) and the Cremer-Kraka total energy density (H_b), and densities of all electrons (ρ_b) greater than 0.2 au are associated with strong covalent bonding. In the case of polar-covalent bonds, it has been shown that the signs or the small absolute values of the above properties can be ambiguous, and it is necessary to consider the combined properties in order to characterize the nature of the bond.[S31] The bond delocalization indices (δ), which provide the number of electron pairs shared by two atoms, are also considered in this study. Contour maps of the charge densities showing the bond paths, intersections of atomic surfaces, and the charge density contour maps of the Laplacian distributions ($\nabla^2\rho$) are provided for $[FKrFXeF]^+$, $[Ng_2F_3]^+$, NgF_2, and $[NgF]^+$ (Figure A1.21).

The small positive ρ_b (Kr–F_t, 0.137–0.200 au; Xe–F_t, 0.121–0.161 au) and $\nabla^2\rho_b$ values (Kr–F_t, 0.051–0.237 au; Xe–F_t, 0.225–0.248 au) of the Ng–F_t bonds in $[NgF]^+$, NgF_2, $[FKrFXeF]^+$, and $[Ng_2F_3]^+$ are consistent with polar-covalent bonds. This

description is supported by their delocalization indices δ (Kr–F_t, 0.742–1.089 au; Xe–F_t, 0.759–1.035 au; and by their very small negative H_b-values (Kr–F_t, –0.141 to –0.0061 au; Xe–F_t, –0.096 to –0.056 au). The corresponding values for the Ng---F_b bridge bonds of $[FKrFXeF]^+$ and $[Ng_2F_3]^+$ are notably smaller than their Ng–F_t values and consistent with their greater ionic characters; ρ_b (Kr---F_b, 0.081, 0.084 au; Xe---F_b, 0.067, 0.070 au), δ (Kr---F_b, 0.472, 0.457 au; Xe---F_b, 0.435, 0.449 au), and H_b (Kr---F_b, –0.018, –0.016 au; Xe---F_b, –0.015, –0.014 au). The Ng–F_t and Ng---F_b bond properties are consistent with their relative Ng–F_t and Ng---F_b bond lengths and Wiberg bond indices. Likewise, the AIM parameters of $[FKrFXeF]^+$ and $[Ng_2F_3]^+$ are in accordance with Kr–$F_{t/b}$ bonds that are more covalent than Xe–$F_{t/b}$ bonds.

The Kr and/or Xe valence electron lone pair (VELP) charge densities are readily discernible on the contour maps of $\nabla^2\rho$ (Figure A1.21). The charge densities of the Kr and/or Xe VELPS combine to form tori around the Kr and/or Xe atoms (see ELF Analyses). The tori lie in planes that are perpendicular to the molecular planes of $[FKrFXeF]^+$, $[Ng_2F_3]^+$, NgF_2, and $[NgF]^+$ so that the plane of the charge density contour map depicted in Figure A1.21 passes through each torus to give two VELP charge concentrations on either side of the Ng cores. The tori of $[NgF]^+$ cations are off-center, which conform with the perturbations of the toroidal V(Ng) basins observed in their ELF isosurface plots (vide infra). In all cases, the F-atom VELP charge densities are nearly spherical. A common feature in the plots of the Laplacian distributions of $[FKrFXeF]^+$ and $[Ng_2F_3]^+$ is that the F_b and Ng contours are not joined or are very weakly joined, whereas contour lines enclosing F_t and Kr and/or Xe are clearly visible. This is in

accordance with more covalent terminal Ng–F_t bonds relative to the Ng---F_b bridge bonds. Contour lines enclosing F_t and Ng are also visible for NgF_2 and $[NgF]^+$.

Electron Localization Function (ELF) Analyses

ELF analyses [S32,S33] were carried out for $[FKrFXeF]^+$ $[Ng_2F_3]^+$, NgF_2, and $[NgF]^+$ to visualize the behaviors of the Ng VELPs of these species. In the ensuing discussion, the abbreviations denote atomic basin populations, $\overline{N}$[A]; electron localization function, $\eta(\mathbf{r})$; core basin, C(A); monosynaptic valence basin, V(A); and closed isosurface, $\eta(\mathbf{r}) = f$, where $\eta(\mathbf{r})$ is defined as the isosurface contour. ELF parameters are provided in Tables A1.18 and A1.19 and ELF isosurface plots are shown for the localization domains of $[FKrFXeF]^+$ $[Ng_2F_3]^+$, NgF_2, and $[NgF]^+$ in Figures 3.5, A1.22 and A1.23.

The ELF population analyses (Tables A1.18 and A1.19) are in agreement with the QTAIM results (vide supra). The ELF basin populations of the Kr and Xe cores are comparable for $[FKrFXeF]^+$, $[Ng_2F_3]^+$, NgF_2, and $[NgF]^+$. In all cases, the Kr and Xe core populations are close to the ideal core population of the Kr atom, [Ar] $3d^{10}$ = 28 e and Xe atom, [Kr] $4d^{10}$ = 46 e. The ELF valence population analyses suggest an interpretation of the bonding in terms of a significant delocalization of electron density between the valence shells of the Ng atoms and those of its neighboring F atoms.

The ELF analyses of $[FKrFXeF]^+$, $[Ng_2F_3]^+$, NgF_2, and $[NgF]^+$ only display monosynaptic Ng and F valence basins, in accordance with the polar-covalent characters of their bonds. The toroidal shapes of their Ng valence basins result from the combination of the three valence electron lone pair domains of Ng, with the atomic core electron basin (C(Ng)) lying at the center of the torus. The small perturbations of the toroidal V(Ng)

basins of $[FKrFXeF]^+$ and $[Ng_2F_3]^+$ arise from accommodation of the V(Ng) basins to the asymmetries of their immediate environments (Figures 3.5 and A1.22).[S34–S36] Similar toroidal-shaped valence basins have been noted for XeF_2,[S34,S37] $[XeF_3]^-$,[S37] $[XeOTeF_5][Sb(OTeF_5)_6]\cdot SO_2ClF$,[S38] and for the NgF_2 (Ng = Kr or Xe) ligands of $[BrOF_2][AsF_6]\cdot 2NgF_2$,[S34,S35] $NgF_2\cdot CrOF_4$,[S24] $NgF_2\cdot 2CrOF4$,[S24] and $[F_5Xe(FKrF)_nAsF_6]$ (n = 1, 2).[S5]

The V(Ng) basin perturbations of the $[NgF]^+$ cations are noteworthy because the VSEPR rules [S39] predict a trigonal pyramidal AXE_3 arrangement of one electron bond pair (X) and three VELPS (E), where A is the Ng atom. Owing to strong mutual repulsions among the VELPS of Ng, the toroidal shape of the V(Ng) basin is maintained, with only a slightly closed toroidal hole on the side of the V(Ng) basin opposite the Ng–F bond. Correspondingly, a region of high electrostatic potential also occurs opposite to the Ng–F bond in the molecular electrostatic potential surfaces (MEPS) of $[KrF]^+$ and $[XeF]^+$ (vide infra).

The localization domain reduction tree diagrams[S40] provide the hierarchies of the ELF basins and the corresponding basin separation values (f_{sep}) for $[FKrFXeF]^+$ $[Ng_2F_3]^+$, NgF_2, and $[NgF]^+$ (Figures A1.24– A1.26). The ELF reduction of localization diagrams of $[FKrFXeF]^+$, $[Kr_2F_3]^+$, and $[Xe_2F_3]^+$ reveal that the three cations initially separate at the same value (f_{sep} = 0.10) into F_tKrF_b and/or F_tXeF_b *f*-localization domains. In $[FKrFXeF]^+$, the core basin of Kr separates at a lower value (f_{sep} = 0.15) than the core basin of Xe (f_{sep} = 0.23), and the F_tKrF_b and F_tXeF *f*-localization domains ultimately separate into V(Ng) and V($F_{b/t}$) basins at f_{sep} values (Kr, 0.26(b) and 0.49(t); Xe, 0.21(b) and 0.35(t)) that are

similar to those encountered for $[Kr_2F_3]^+$ (0.25(b) and 0.49(t)) and $[Xe_2F_3]^+$ (0.22(b) and 0.34(t)). In all cases, the separations of the V(Ng) and V(F_t) valence basins occur at much higher f_{sep} values than the V(Ng) and V(F_b) valence basins, which is consistent with Ng–F_t bonds that are more covalent than the Ng---F_b bonds. The f_{sep} values are also consistent with Kr–$F_{t/b}$ bonds that are more covalent than Xe–$F_{t/b}$ bonds. The V(Ng) and V(F_t) basins in $[FKrFXeF]^+$ and $[Ng_2F_3]^+$ separate at f_{sep} values similar to those of $[NgF]^+$ (Kr, 0.51; Xe, 0.36). These results are also consistent with the Wiberg bond indices obtained from NBO analyses (Table A1.16 and A1.17) and the QTAIM analyses (Table A1.18 and A1.19).

Table A1.12. Calculated geometrical parameters and key frequencies for $[FKrFXeF]^+$

	$Xe\text{-}F_t$	$Xe\text{---}F_b$	$Kr\text{---}F_b$	$Kr\text{-}F_t$	F_tXeF_b	XeF_bKr	F_tKrF_b	ν_1	ν_2	ν_3	ν_4
B3LYP											
aVDZa	1.951	2.249	2.092	1.823	177.64	148.39	178.11	622	603	418	250
aVTZa	1.925	2.235	2.081	1.798	178.23	154.45	178.58	625	606	422	232
aVTDZa	1.928	2.242	2.091	1.823	177.79	149.80	178.27	622	602	416	244
Def2TZVP	1.917	2.237	2.092	1.799	178.09	152.97	178.46	620	601	409	234
B3LYP-D3[a]											
aVDZa	1.951	2.245	2.089	1.824	177.76	144.65	178.25	621	603	420	263
aVTZa	1.924	2.230	2.078	1.798	178.08	151.26	178.49	625	606	423	243
aVTDZa	1.928	2.237	2.089	1.823	177.81	146.24	178.30	622	602	417	257
Def2TZVP	1.917	2.232	2.089	1.799	178.00	149.95	178.39	620	601	410	244
PBE1PBE											
aVDZa	1.930	2.222	2.067	1.797	177.84	147.66	178.18	654	632	435	264
aVTZa	1.902	2.205	2.055	1.770	178.42	154.56	178.62	661	638	435	243
aVTDZa	1.907	2.213	2.067	1.797	177.97	149.18	178.31	655	632	431	258
Def2TZVP	1.895	2.207	2.065	1.771	178.30	153.06	178.54	657	634	422	245
PBE1PBE-D3[a]											
aVDZa	1.930	2.220	2.066	1.797	177.89	146.00	178.25	654	632	436	270
aVTZa	1.902	2.203	2.053	1.770	178.37	153.16	178.59	661	637	436	247
aVTDZa	1.907	2.212	2.066	1.797	177.97	147.72	178.31	654	632	432	263
Def2TZVP	1.895	2.205	2.063	1.771	178.29	151.57	178.53	657	634	423	251
B3PW91											
aVDZa	1.939	2.232	2.077	1.809	177.65	146.00	178.10	637	617	425	264
aVTZa	1.912	2.216	2.065	1.783	178.11	152.20	178.44	643	622	427	244
aVTDZa	1.916	2.224	2.076	1.809	177.73	147.68	178.17	638	618	422	257
Def2TZVP	1.905	2.218	2.075	1.784	178.00	150.82	178.36	638	618	414	247
B3PW91-D3[a]											
aVDZa	1.939	2.228	2.074	1.809	177.78	142.66	178.24	639	618	428	277
aVTZa	1.912	2.212	2.062	1.783	178.05	148.99	178.41	643	621	429	256
aVTDZa	1.916	2.220	2.074	1.809	177.83	144.08	178.31	639	618	424	270
Def2TZVP	1.905	2.214	2.072	1.784	177.98	147.52	178.35	636	617	417	259
B2PLYPD3											
aVDZa	1.947	2.245	2.081	1.826	177.90	143.92	178.30	612	594	433	265
aVTZa	1.917	2.225	2.066	1.795	178.27	151.60	178.56	620	603	436	244
aVTDZa	1.926	2.238	2.081	1.826	177.98	145.08	178.36	612	594	431	260
Def2TZVP	1.912	2.232	2.075	1.797	178.18	149.89	178.49	613	596	422	247
APFD											
aVDZa	1.934	2.221	2.067	1.802	177.92	142.39	178.32	649	626	433	282
aVTZa	1.906	2.205	2.055	1.775	178.20	149.43	178.50	653	630	434	258
aVTDZa	1.911	2.214	2.067	1.802	177.99	143.88	178.38	648	626	430	275
Def2TZVP	1.899	2.207	2.066	1.776	181.87	147.97	181.57	647	626	422	261
wB97XD											
aVDZa	1.927	2.231	2.074	1.790	178.34	151.78	178.54	662	644	423	249

[a] The GD3BJ dispersion was used.

aVDZa	1.952	2.232	178.54	149.57	610	599	422	237
aVTZa	1.926	2.216	180.00	169.35	614	604	428	183
aVTDZa	1.930	2.224	178.79	151.81	612	601	413	229
Def2TZVP	1.919	2.219	180.00	166.68	611	600	415	186
PBE1PBE								
aVDZa	1.932	2.211	178.62	152.38	639	628	431	235
aVTZa	1.904	2.194	179.30	168.40	645	634	434	194
aVTDZa	1.909	2.203	178.85	155.97	640	629	422	223
Def2TZVP	1.896	2.197	179.08	164.52	642	631	421	199
PBE1PBE-D3[a]								
aVDZa	1.932	2.209	178.60	150.48	640	628	432	243
aVTZa	1.904	2.192	179.11	164.61	645	634	436	202
aVTDZa	1.909	2.201	178.84	153.38	641	630	422	232
Def2TZVP	1.897	2.196	178.95	159.14	642	631	421	214
B3PW91								
aVDZa	1.941	2.221	178.47	150.92	625	614	424	236
aVTZa	1.913	2.204	178.97	163.68	629	619	428	199
aVTDZa	1.918	2.213	178.73	154.03	626	615	416	225
Def2TZVP	1.906	2.208	178.83	158.73	626	615	414	209
B3PW91-D3[a]								
aVDZa	1.941	2.217	178.44	147.40	626	614	427	250
aVTZa	1.914	2.201	178.87	154.81	630	619	426	225
aVTDZa	1.918	2.209	178.69	149.74	628	616	417	241
Def2TZVP	1.906	2.204	178.78	152.09	628	616	413	231
B2PLYPD3								
aVDZa	1.949	2.227	178.66	151.64	609	598	428	232
aVTZa	1.919	2.207	179.31	167.72	611	601	430	201
aVTDZa	1.928	2.219	178.87	153.28	609	598	419	227
Def2TZVP	1.914	2.213	179.07	162.58	610	600	416	200
APFD								
aVDZa	1.935	2.210	178.51	147.10	634	623	431	254
aVTZa	1.908	2.194	178.94	155.58	639	628	431	226
aVTDZa	1.913	2.202	178.75	149.46	636	625	420	245
Def2TZVP	1.901	2.197	178.85	152.41	637	625	416	233
wB97XD								
aVDZa	1.929	2.220	178.96	159.99	651	640	428	211

[a] The GD3BJ dispersion was used.

Table A1.14. Calculated geometrical parameters and key frequencies for $[Kr_2F_3]^+$

	Kr-F_t	**Kr---F_b**	**F_tKrF_b**	**KrF_bKr**	**ν_1**	**ν_6**	**ν_7**	**ν_2**
B3LYP								
aVDZa	1.821	2.104	177.69	142.41	630	609	422	279
aVTZa	1.795	2.093	177.86	147.78	631	610	421	261
aVTDZa	1.821	2.104	177.69	142.41	630	609	422	279
Def2TZVP	1.797	2.103	177.80	147.02	625	603	409	261
B3LYP-D3[a]								

aVDZa	1.821	2.101	177.79	139.93	631	610	425	289
aVTZa	1.795	2.090	177.91	144.93	631	610	424	272
aVTDZa	1.821	2.101	177.79	139.93	631	610	425	289
Def2TZVP	1.797	2.100	177.90	144.14	625	603	412	272
PBE1PBE								
aVDZa	1.795	2.078	177.83	142.09	663	642	437	293
aVTZa	1.768	2.064	178.03	148.36	668	647	436	273
aVTDZa	1.795	2.078	177.83	142.09	663	642	437	293
Def2TZVP	1.769	2.074	177.99	147.40	663	641	424	274
PBE1PBE-D3[a]								
aVDZa	1.795	2.076	177.88	141.00	664	642	438	298
aVTZa	1.768	2.063	178.04	147.18	668	646	438	278
aVTDZa	1.795	2.076	177.88	141.00	664	642	438	298
Def2TZVP	1.769	2.072	178.00	146.12	663	641	425	279
B3PW91								
aVDZa	1.806	2.088	177.72	140.57	647	626	429	293
aVTZa	1.780	2.075	177.85	145.67	649	628	428	276
aVTDZa	1.806	2.088	177.72	140.57	647	626	429	293
Def2TZVPD	1.782	2.085	177.82	144.83	644	621	416	276
B3PW91-D3[a]								
aVDZa	1.806	2.085	177.81	138.34	648	627	431	302
aVTZa	1.780	2.073	177.91	143.16	650	628	430	285
aVTDZa	1.806	2.085	177.81	138.34	648	627	431	302
Def2TZVPD	1.782	2.082	177.91	142.24	645	622	419	286
B2PLYPD3								
aVDZa	1.823	2.098	177.81	137.62	615	589	439	295
aVTZa	1.792	2.082	177.96	143.31	622	597	439	279
aVTDZa	1.823	2.098	177.81	137.62	615	589	439	295
Def2TZVP	1.795	2.092	177.95	142.12	616	589	426	280
APFD								
aVDZa	1.799	2.078	177.92	138.14	658	636	436	306
aVTZa	1.773	2.065	178.01	143.64	661	639	436	288
aVTDZa	1.799	2.078	177.92	138.14	658	636	436	306
Def2TZVPD	1.774	2.075	178.01	142.75	656	633	424	288
wB97XD								
aVDZa	1.789	2.085	178.08	146.09	667	646	413	275

[a] The GD3BJ dispersion was used.

Table A1.15. Calculated geometrical parameters and frequencies for $[NgF]^+$ and NgF_2

	$[NgF]^+$	
	Kr-F	ν_1
B2PLYP-D3/Def2TZVP	1.737	693(9)[<1]
B3PW91-D3/aVTDZa[a]	1.755	701(10)[<1]
	Xe-F	ν_1
B2PLYP-D3/Def2TZVP	1.873	656(11)[6]

B3PW91-D3/aVTDZa[a]	1.878	671(11)[7]		
		NgF_2		
	Kr-F	ν_1	ν_2	ν_3
B2PLYP-D3/Def2TZVP	1.897	578(0)[235]	460(51)[0]	234(0)[13]
B3PW91-D3/aVTDZa[a]	1.895	605(0)[13]	505(51)[0]	235(0)[13]
	Xe-F	ν_1	ν_2	ν_3
B2PLYP-D3/Def2TZVP	2.002	544(0)[245]	499(54)[0]	208(0)[16]
B3PW91-D3/aVTDZa[a]	2.002	558(0)[245]	517(44)[0]	208(0)[15]

[a] The GD3BJ dispersion was used.

Table A1.16. Natural population analysis (NPA) charges, Wiberg valences, and Wiberg bond indices for $[FKrFXeF]^+$ (C_s), and $[Ng_2F_3]^+$ (C_{2v}) (Ng = Xe, Kr)

B2PLYP-D3/Def2-TZVPD (F, Kr, Xe)

$[FKrFXeF]^+$					**$[Xe_2F_3]^+$**				**$[Kr_2F_3]^+$**			
Bond Indices		NPA Charges [Valences]			Bond Indices		NPA Charges [Valences]		Bond Indices		NPA Charges [Valences]	
$Xe-F_{t(Xe)}$	0.720	Xe	1.341	[0.934]	$Xe-F_t$	0.714	Xe	1.343 [0.931]				
$Xe-F_b$	0.196	Kr	1.144	[1.040]	$Xe-F_b$	0.200					Kr	1.143 [1.039]
$Kr-F_b$	0.234	$F_{t(Xe)}$	–0.475	[0.792]			F_t	–0.480 [0.786]	$Kr-F_b$	0.227		
$Kr-F_{t(Kr)}$	0.790	F_b	–0.679	[0.591]			F_b	–0.725 [0.516]	$Kr-F_t$	0.797	F_b	–0.639 [0.658]
		$F_{t(Kr)}$	–0.330	[0.909]							F_t	–0.323 [0.914]
		$\sum_{[FKrFXeF]^+}$	**1.001**				$\sum_{[Xe_2F_3]^+}$	**1.001**			$\sum_{[Kr_2F_3]^+}$	**1.001**
Ng---Ng	0.009				Ng---Ng	0.010			Ng---Ng	0.008		

B3PW91-GD3BJ/aug-ccpVDZ(-PP) (F, Kr)/aug-ccpVTZ(-PP) (Xe)

$[FKrFXeF]^+$					**$[Xe_2F_3]^+$**				**$[Kr_2F_3]^+$**			
Bond Indices		NPA Charges [Valences]			Bond Indices		NPA Charges [Valences]		Bond Indices		NPA Charges [Valences]	
$Xe-F_{t(Xe)}$	0.737	Xe	1.249	[1.014]	$Xe-F_t$	0.730	Xe	1.247 [1.010]				
$Xe-F_b$	0.252	Kr	1.051	[1.066]	$Xe-F_b$	0.257					Kr	1.054 [1.066]
$Kr-F_b$	0.286	$F_{t(Xe)}$	–0.430	[0.836]			F_t	–0.437 [0.830]	$Kr-F_b$	0.280		
$Kr-F_{t(Kr)}$	0.758	F_b	–0.562	[0.762]			F_b	–0.620 [0.676]	$Kr-F_t$	0.766	F_b	–0.509 [0.844]
		$F_{t(Kr)}$	–0.307	[0.926]							F_t	–0.299 [0.931]
		$\sum_{[FKrFXeF]^+}$	**1.001**				$\sum_{[Xe_2F_3]^+}$	**1.003**			$\sum_{[Kr_2F_3]^+}$	**1.001**
Ng---Ng	0.013				Ng---Ng	0.013			Ng---Ng	0.011		

Table A1.17. Natural population analysis (NPA) charges, Wiberg valences, and Wiberg bond indices for $[NgF]^+$ ($C_{\infty v}$) and NgF_2 ($D_{\infty h}$) (Ng = Xe, Kr)

B2PLYP-D3/Def2-TZVPD (F, Kr, Xe)

Bond Indices		NPA Charges [Valences]			Bond Indices		NPA Charges [Valences]		
		$[XeF]^+$					**$[KrF]^+$**		
Xe−F_t	0.896	Xe	1.348	[0.896]	Kr−F_t	0.993	Kr	1.166	[0.993]
		F_t	–0.348	[0.896]			F_t	–0.166	[0.993]
		$\sum_{[XeF]^+}$	**0.000**				$\sum_{[KrF]^+}$	**0.000**	
		XeF_2					**KrF_2**		
Xe−F_t	0.499	Xe	1.276	[0.997]	Kr−F_t	0.544	Kr	1.071	[1.089]
Xe−F_t	0.499	F_t	–0.638	[0.608]	Kr−F_t	0.544	F_t	–0.536	[0.723]
		F_t	–0.638	[0.608]			F_t	–0.536	[0.723]
		$\sum_{XeF_2}$	**0.000**				$\sum_{KrF_2}$	**–0.001**	

B3PW91-GD3BJ/aug-ccpVDZ(-PP) (F, Kr)/aug-ccpVTZ(-PP) (Xe)

Bond Indices		NPA Charges [Valences]			Bond Indices		NPA Charges [Valences]		
		$[XeF]^+$					**$[KrF]^+$**		
Xe−F_t	0.926	Xe	1.310	[0.926]	Kr−F_t	0.999	Kr	1.147	[0.999]
		F_t	–0.310	[0.926]			F_t	–0.147	[0.999]
		$\sum_{[XeF]^+}$	**0.000**				$\sum_{[KrF]^+}$	**0.000**	
		XeF_2					**KrF_2**		
Xe−F_t	0.538	Xe	1.164	[1.077]	Kr−F_t	0.550	Kr	0.974	[1.101]
Xe−F_t	0.538	F_t	–0.582	[0.676]	Kr−F_t	0.550	F_t	–0.487	[0.777]
		F_t	–0.582	[0.676]			F_t	–0.487	[0.777]
		$\sum_{XeF_2}$	**0.000**				$\sum_{KrF_2}$	**0.000**	

Table A1.18. QTAIM density of all electrons (ρ_b), Laplacian of electron density ($\nabla^2\rho_b$), energy density (H_b), QTAIM delocalization Indices (δ), QTAIM atomic populations ($\bar{N}$), and ELF basin populations ($\bar{N}$[A]) for $[FKrFXeF]^+$ (C_s) and $[Ng_2F_3]^+$ (C_{2v}) (Ng = Xe, Kr) [a]

B2PLYP-D3/Def2-TZVPD (F, Kr, Xe)

Bond	ρ_b	$\nabla^2\rho_b$	H_b	δ	$\bar{N}$		$\bar{N}$[A]	
				$[FKrFXeF]^+$				
$Xe-F_{t(Xe)}$	0.148	0.248	−0.083	0.908	$\bar{N}$(Xe)	52.69	$\bar{N}$[C(Xe)] [b]	46.87
$Xe-F_b$	0.067	0.190	−0.014	0.435	$\bar{N}$(Kr)	34.94	$\bar{N}$[V(Xe)]	6.80
$Kr-F_b$	0.084	0.237	−0.018	0.472	$\bar{N}(F_{t(Xe)})$	9.47	$\bar{N}$[C(Kr)]	27.79
$Kr-F_{t(Kr)}$	0.174	0.144	−0.104	0.912	$\bar{N}(F_b)$	9.59	$\bar{N}$[V(Kr)]	6.93
					$\bar{N}(F_{t(Kr)})$	9.31	$\bar{N}[C(F_{t(Xe)})]$	2.15
							$\bar{N}[V(F_{t(Xe)})]$	7.45
							$\bar{N}[C(F_b)]$	2.13
							$\bar{N}[V(F_b)]$	7.42
							$\bar{N}[C(F_{t(Kr)})]$	2.14
							$\bar{N}[V(F_{t(Kr)})]$	7.31
				$[Xe_2F_3]^+$				
$Xe-F_t$	0.147	0.248	−0.082	0.904	$\bar{N}$(Xe)	52.69	$\bar{N}$[C(Xe)] [c]	46.28
$Xe-F_b$	0.070	0.195	−0.015	0.449	$\bar{N}(F_t)$	9.48	$\bar{N}$[V(Xe)]	6.80
					$\bar{N}(F_b)$	9.66	$\bar{N}[C(F_{t(Xe)})]$	2.15
							$\bar{N}[V(F_{t(Xe)})]$	7.46
							$\bar{N}[C(F_b)]$	2.13
							$\bar{N}[V(F_b)]$	7.50
				$[Kr_2F_3]^+$				
$Kr-F_b$	0.081	0.232	−0.016	0.457	$\bar{N}$(Kr)	34.94	$\bar{N}$[C(Kr)]	27.77
$Kr-F_t$	0.175	0.141	−0.105	0.917	$\bar{N}(F_t)$	9.30	$\bar{N}$[V(Kr)]	6.93
					$\bar{N}(F_b)$	9.52	$\bar{N}[C(F_{t(Kr)})]$	2.14
							$\bar{N}[V(F_{t(Kr)})]$	7.30
							$\bar{N}[C(F_b)]$	2.14
							$\bar{N}[V(F_b)]$	7.35

continued …

Table A1.18. (continued)

B3PW91-GD3BJ/aug-ccpVDZ(-PP) (F, Kr)/aug-ccpVTZ(-PP) (Xe)

Bond	ρ_b	$\nabla^2\rho_b$	H_b	δ	$\bar{N}$		$\bar{N}$[A]	
				$[FKrFXeF]^+$				
$Xe-F_{t(Xe)}$	0.144	0.292	−0.065	1.072	$\bar{N}(Xe)$	52.73	$\bar{N}$[C(Xe)] [b]	47.39
$Xe-F_b$	0.069	0.198	−0.011	0.517	$\bar{N}(Kr)$	34.96	$\bar{N}$[V(Xe)]	6.85
$Kr-F_b$	0.082	0.253	−0.010	0.547	$\bar{N}(F_{t(Xe)})$	9.45	$\bar{N}$[C(Kr)]	27.25
$Kr-F_{t(Kr)}$	0.160	0.258	−0.065	1.078	$\bar{N}(F_b)$	9.56	$\bar{N}$[V(Kr)]	7.02
					$\bar{N}(F_{t(Kr)})$	9.31	$\bar{N}$[C($F_{t(Xe)}$)]	2.15
							$\bar{N}$[V($F_{t(Xe)}$)]	7.44
							$\bar{N}$[C(F_b)]	2.16
							$\bar{N}$[V(F_b)]	7.38
							$\bar{N}$[C($F_{t(Kr)}$)]	2.15
							$\bar{N}$[V($F_{t(Kr)}$)]	7.21
				$[Xe_2F_3]^+$				
$Xe-F_t$	0.143	0.292	−0.065	1.066	$\bar{N}(Xe)$	52.73	$\bar{N}$[C(Xe)] [c]	46.25
$Xe-F_b$	0.071	0.203	−0.012	0.529	$\bar{N}(F_t)$	9.46	$\bar{N}$[V(Xe)]	6.85
					$\bar{N}(F_b)$	9.62	$\bar{N}$[C($F_{t(Xe)}$)]	2.16
							$\bar{N}$[V($F_{t(Xe)}$)]	7.44
							$\bar{N}$[C(F_b)]	2.16
							$\bar{N}$[V(F_b)]	7.44
				$[Kr_2F_3]^+$				
$Kr-F_b$	0.079	0.247	−0.009	0.535	$\bar{N}(Kr)$	34.96	$\bar{N}$[C(Kr)]	27.80
$Kr-F_t$	0.161	0.256	−0.066	1.086	$\bar{N}(F_t)$	9.30	$\bar{N}$[V(Kr)]	7.01
					$\bar{N}(F_b)$	9.49	$\bar{N}$[C($F_{t(Kr)}$)]	2.16
							$\bar{N}$[V($F_{t(Kr)}$)]	7.19
							$\bar{N}$[C(F_b)]	2.16
							$\bar{N}$[V(F_b)]	7.32

[a] The atomic unit (au) for $\nabla^2\rho_b$ is e/a_0^5 (1 au = 24.098 e Å^{-5}). The au for ρ_b is e/a_0^3 (1 au = 6.748 e Å^{-3}). The au for H is e^2/a_0^4 (1 au = E_h/a_0^3 = 6.748 E_h/Å^3). a_0 = Bohr radius = 0.52918 Å. e = charge on an electron. E_h = hartree = e^2/a_0. [b] $\bar{N}$[C(Xe)] = 117 – {$\bar{N}$[C(Kr)] + $\bar{N}$[C($F_{t(Xe)}$)] + $\bar{N}$[C(F_b)] + $\bar{N}$[C($F_{t(Kr)}$)] + $\bar{N}$[V(Xe)] + $\bar{N}$[V(Kr)] + $\bar{N}$[V($F_{t(Xe)}$)] + $\bar{N}$[V(F_b)] + $\bar{N}$[V($F_{t(Kr)}$)]}. [c] $\bar{N}$[C(Xe)] = 135 – {2x$\bar{N}$[C($F_{t(Xe)}$)] + $\bar{N}$[C(F_b)] + 2x$\bar{N}$[V(Xe)] + 2x$\bar{N}$[V($F_{t(Xe)}$)] + $\bar{N}$[V(F_b)]}.

Table A1.19. QTAIM density of all electrons (ρ_b), Laplacian of electron density ($\nabla^2\rho_b$), energy density (H_b), QTAIM delocalization indices (δ), QTAIM atomic populations ($\bar{N}$), and ELF basin populations ($\bar{N}$[A]) in $[NgF]^+$ ($C_{\infty v}$) and NgF_2 ($D_{\infty h}$) (Ng = Xe, Kr) [a]

B2PLYP-D3/Def2-TZVPD (F, Kr, Xe)

Bond	ρ_b	$\nabla^2\delta_b$	H_b	δ	$\bar{N}$		$\bar{N}$[A]	
				$[XeF]^+$				
Xe−F_t	0.161	0.256	−0.096	1.035	$\bar{N}$(Xe)	52.64	$\bar{N}$[C(Xe)] [b]	46.76
					$\bar{N}$(F_t)	9.36	$\bar{N}$[V(Xe)]	6.72
							$\bar{N}$[C(F_t)]	2.15
							$\bar{N}$[V(F_t)]	7.37
				$[KrF]^+$				
Kr−F_t	0.200	0.051	−0.141	1.089	$\bar{N}$(Kr)	34.84	$\bar{N}$[C(Kr)]	27.30
					$\bar{N}$(F_t)	9.16	$\bar{N}$[V(Kr)]	7.13
							$\bar{N}$[C(F_t)]	2.13
							$\bar{N}$[V(F_t)]	6.86
				XeF_2				
Xe−F_t	0.121	0.225	−0.056	0.759	$\bar{N}$(Xe)	52.78	$\bar{N}$[C(Xe)] [c]	45.81
Xe−F_t	0.121	0.225	−0.056	0.759	$\bar{N}$(F_t)	9.61	$\bar{N}$[V(Xe)]	6.86
					$\bar{N}$(F_t)	9.61	$\bar{N}$[C(F_t)]	2.12
							$\bar{N}$[V(F_t)]	7.54
							$\bar{N}$[C(F_t)]	2.12
							$\bar{N}$[V(F_t)]	7.54
				KrF_2				
Kr−F_t	0.137	0.222	−0.061	0.742	$\bar{N}$(Kr)	35.05	$\bar{N}$[C(Kr)]	27.19
Kr−F_t	0.137	0.222	−0.061	0.742	$\bar{N}$(F_t)	9.48	$\bar{N}$[V(Kr)]	7.20
					$\bar{N}$(F_t)	9.48	$\bar{N}$[C(F_t)]	2.14
							$\bar{N}$[V(F_t)]	7.32
							$\bar{N}$[C(F_t)]	2.14
							$\bar{N}$[V(F_t)]	7.32

continued …

Table A1.19. (continued)

B3PW91-GD3BJ/aug-ccpVDZ(-PP) (F, Kr)/aug-ccpVTZ(-PP) (Xe)

Bond	ρ_b	$\nabla^2\rho_b$	H_b	δ	$\bar{N}$		$\bar{N}$[A]	
				$[XeF]^+$				
Xe−F_t	0.157	0.298	−0.076	1.247	$\bar{N}$(Xe)	52.66	$\bar{N}$[C(Xe)] [b]	46.76
					$\bar{N}$(F_t)	9.34	$\bar{N}$[V(Xe)]	6.75
							$\bar{N}$[C(F_t)]	2.14
							$\bar{N}$[V(F_t)]	7.38
				$[KrF]^+$				
Kr−F_t	0.179	0.200	−0.085	1.301	$\bar{N}$(Kr)	34.85	$\bar{N}$[C(Kr)]	27.29
					$\bar{N}$(F_t)	9.15	$\bar{N}$[V(Kr)]	7.10
							$\bar{N}$[C(F_t)]	2.14
							$\bar{N}$[V(F_t)]	6.87
				XeF_2				
Xe−F_t	0.119	0.263	−0.044	0.892	$\bar{N}$(Xe)	52.81	$\bar{N}$[C(Xe)] [c]	45.77
Xe−F_t	0.119	0.263	−0.044	0.892	$\bar{N}$(F_t)	9.59	$\bar{N}$[V(Xe)]	6.91
					$\bar{N}$(F_t)	9.59	$\bar{N}$[C(F_t)]	2.16
							$\bar{N}$[V(F_t)]	7.50
							$\bar{N}$[C(F_t)]	2.16
							$\bar{N}$[V(F_t)]	7.50
				KrF_2				
Kr−F_t	0.137	0.222	−0.061	0.886	$\bar{N}$(Kr)	35.04	$\bar{N}$[C(Kr)]	27.11
Kr−F_t	0.137	0.222	−0.061	0.886	$\bar{N}$(F_t)	9.48	$\bar{N}$[V(Kr)]	7.17
					$\bar{N}$(F_t)	9.48	$\bar{N}$[C(F_t)]	2.14
							$\bar{N}$[V(F_t)]	7.32
							$\bar{N}$[C(F_t)]	2.14
							$\bar{N}$[V(F_t)]	7.32

[a] The atomic unit (au) for $\nabla^2\rho_b$ is e/a_0^5 (1 au = 24.098 e Å^{-5}). The au for ρ_b is e/a_0^3 (1 au = 6.748 e Å^{-3}). The au for H is e^2/a_0^4 (1 au = E_h/a_0^3 = 6.748 E_h/Å^3). a_0 = Bohr radius = 0.52918 Å. e = charge on an electron. E_h = hartree = e^2/a_0. [b] $\bar{N}$[C(Xe)] = 63 – {$\bar{N}$[C(F_t)] + $\bar{N}$[V(Xe)] +$\bar{N}$[V(F_t)]}. [c] $\bar{N}$[C(Xe)] = 72 – {2x$\bar{N}$[C(F_t)] + $\bar{N}$[C(F_b)] + $\bar{N}$[V(Xe)] + 2x$\bar{N}$[V($F_{t(Xe)}$)] + $\bar{N}$[V(F_b)]}.

$[Kr_2F_3]^+$

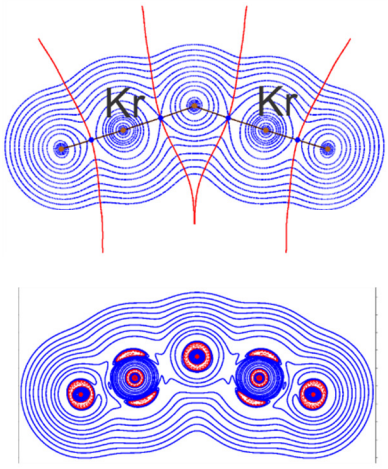

$[FKrFXeF]^+$

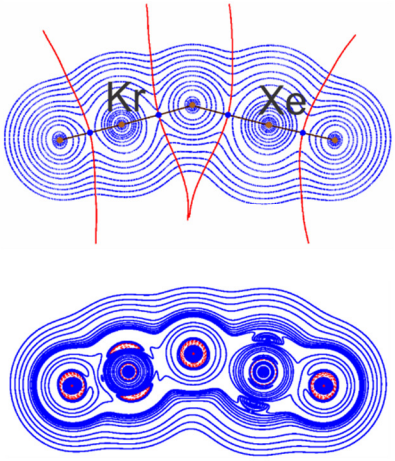

$[Xe_2F_3]^+$

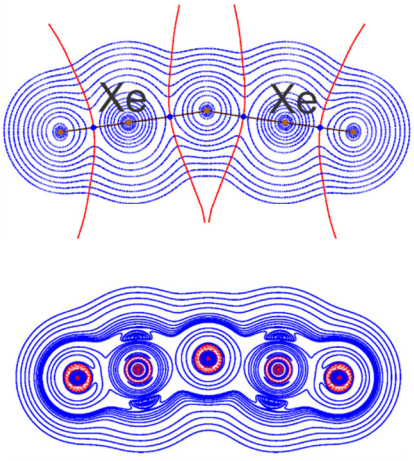

$[KrF]^+$

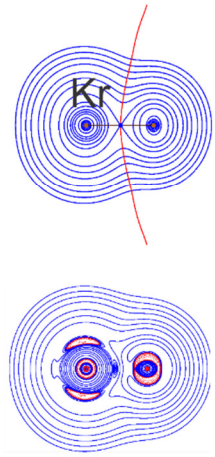

$[XeF]^+$

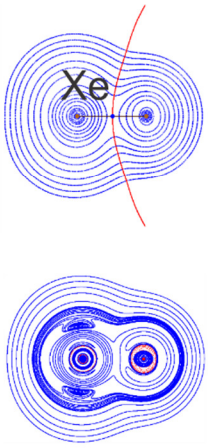

KrF_2

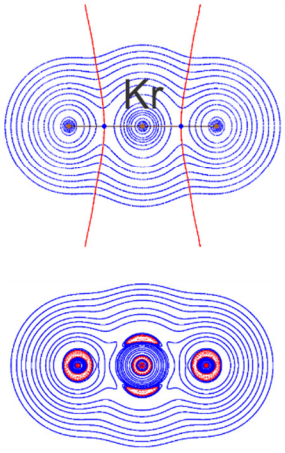

XeF_2

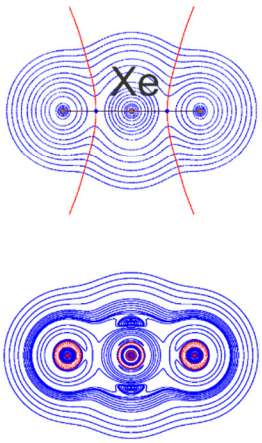

Figure A1.21. Contour maps of the charge density showing the bond paths and the intersection of the interatomic surfaces (top) and charge density contour maps of the Laplacian distribution (bottom) in $[FKrFXeF]^+$, $[Ng_2F_3]^+$, $[NgF]^+$ and NgF_2 (Ng = Kr, Xe). The nuclear positions in the contour maps of the charge density are identical to those in the contour maps of the Laplacian distribution. The contour values start at ±0.001 a.u. and increase in the order ±2 x 10^n, ±4 x 10^n, and ±8 x 10^n with n starting at −3 and increasing in increments of 1 to give a maximum contour value of 8 x 10^6 with several additional contour values on the contour maps of the Laplacian distribution ($[FKrFXeF]^+$ and $[Xe_2F_3]^+$: ±0.072, ±0.07, ±0.06, ±0.05, ±0.03 a.u.; $[XeF]^+$: ±0.07, ±0.06, ±0.055, ±0.05, ±0.045, ±0.038, ±0.035, ±0.0347 a.u.; XeF_2: ±0.069, ±0.065, ±0.060, ±0.05, ±0.032, ±0.025 a.u.). Bond critical points are denoted by blue dots. Solid blue contours denote positive and dashed red contours denote negative values of $\nabla^2\rho$.

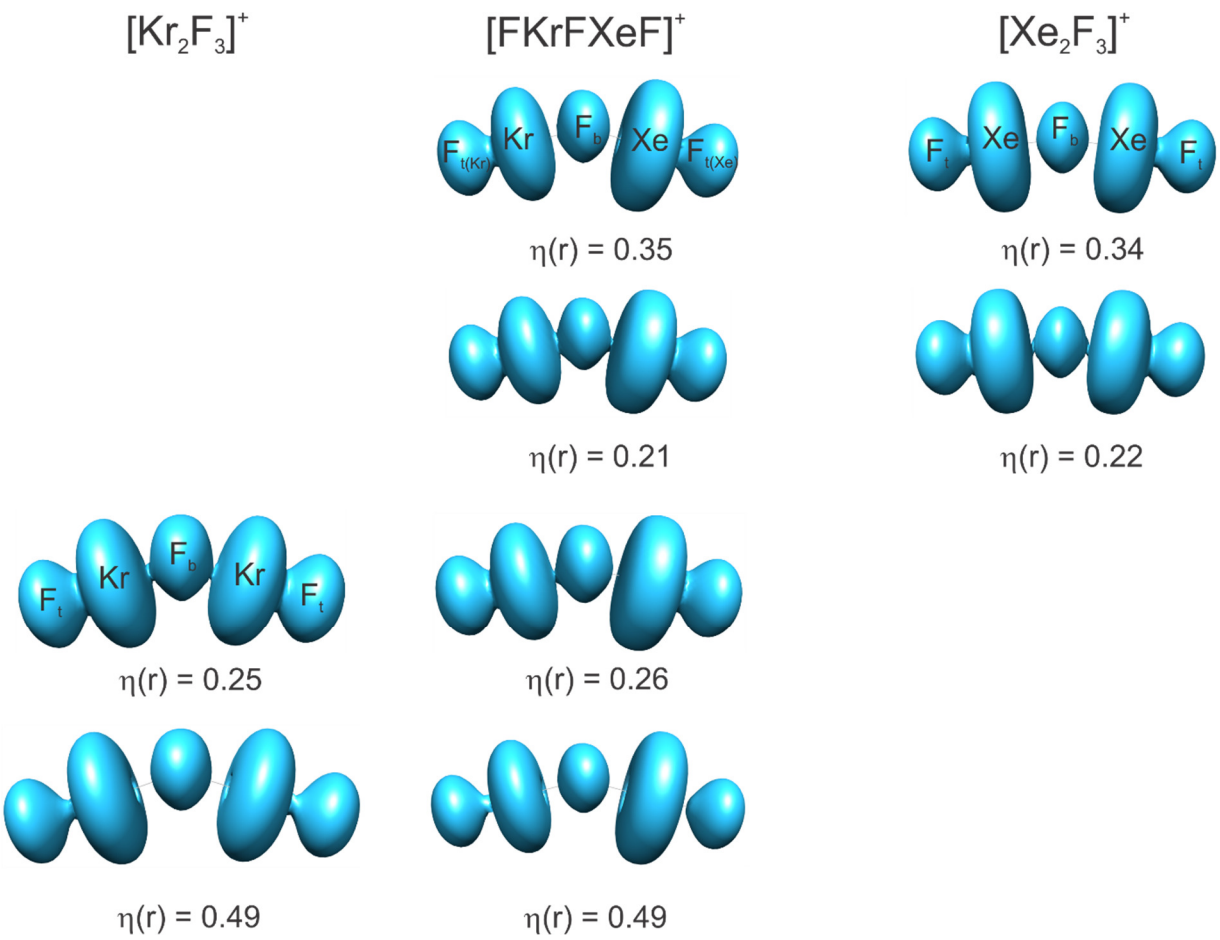

Figure A1.22. ELF isosurface plots at the $\eta(\mathbf{r})$ values the F_tNgF_b *f*-localization domains separate into V(Ng) and V($F_{b/t}$) basins; note the similarities and differences between the isosurfaces of $[FKrFXeF]^+$ and $[Ng_2F_3]^+$ (Ng = Xe, Kr). Color code: red = core; blue = monosynaptic basin. See Figure A1.23 for other orientations and for the ELF isosurface plots of $[NgF]^+$ and NgF_2 and consult the Computational Results in Appendix 1.

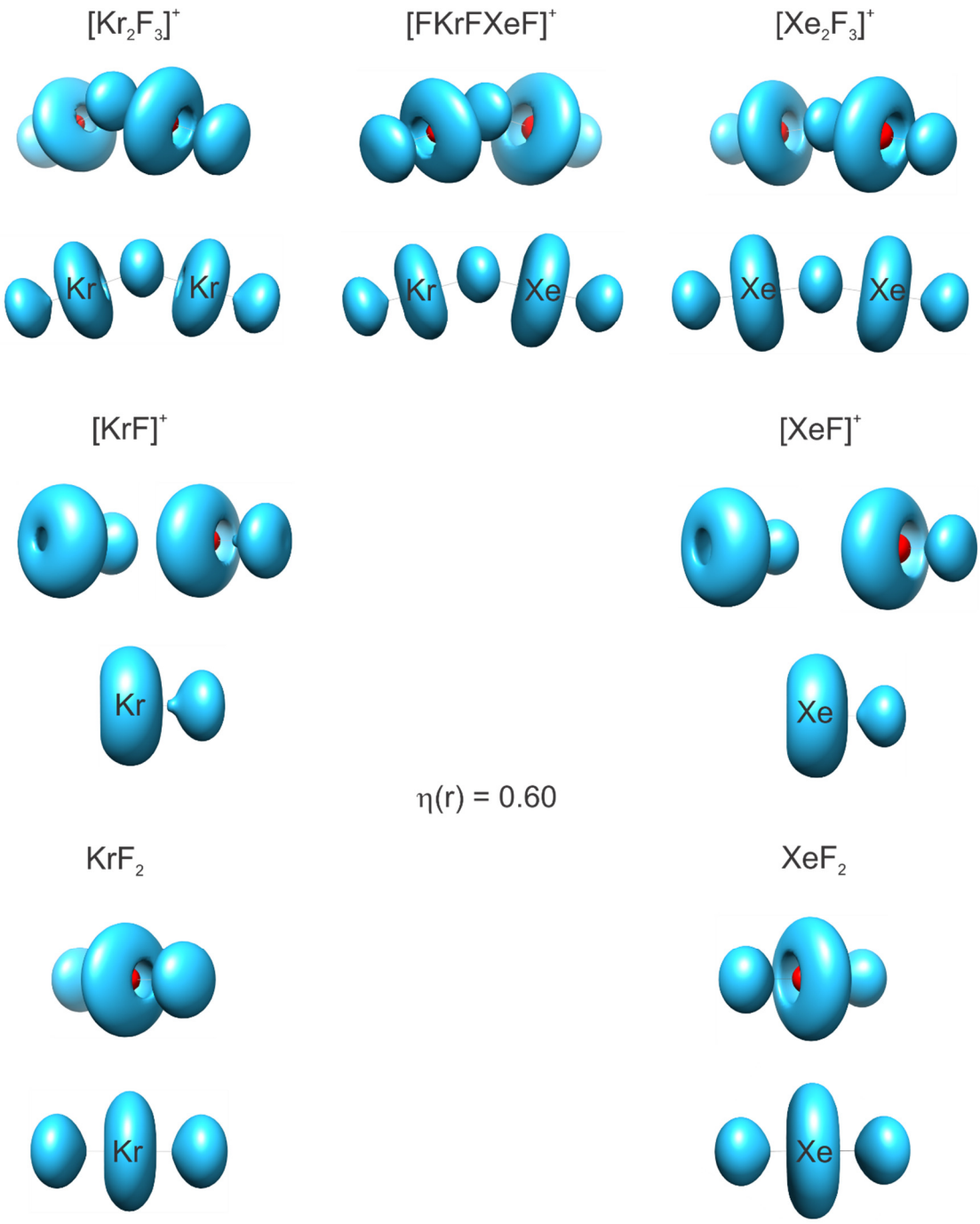

Figure A1.23. ELF isosurface plots at $\eta(\mathbf{r})$ = 0.60 (B2PLYP-D3/Def2-TZVPD) for $[FKrFXeF]^+$, $[Ng_2F_3]^+$, $[NgF]^+$, and NgF_2 (Ng = Xe, Kr). Color code: red = core; blue = monosynaptic basin. Two orientations are shown for the $[Ng_2F_3]^+$ cations and NgF_2, and three orientations are shown for the $[NgF]^+$ cations.

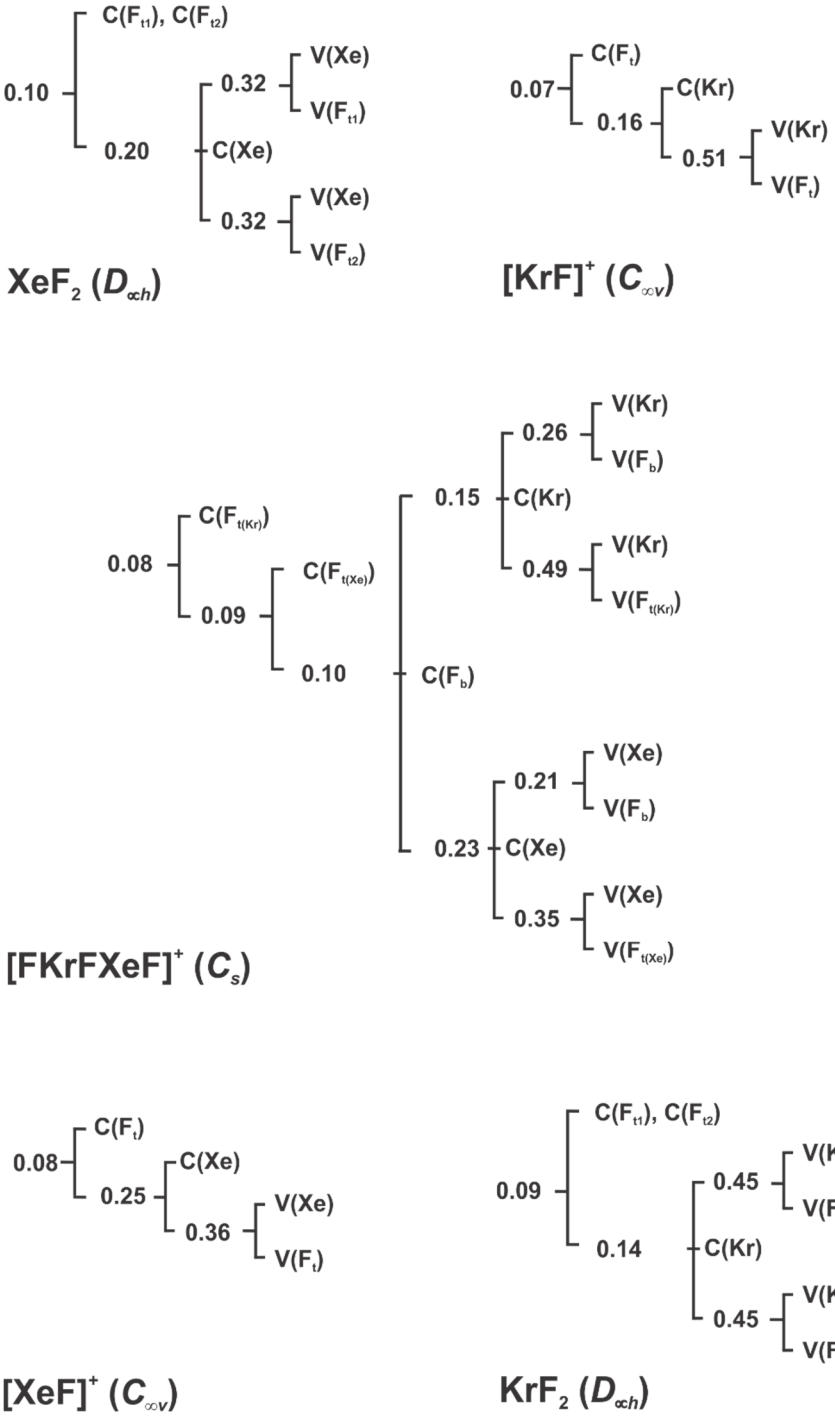

Figure A1.24. ELF reduction of the localization diagrams (B2PLYP-D3/Def2-TZVPD) for $[FKrFXeF]^+$, NgF_2, and $[NgF]^+$ showing the ordering of localization nodes and the boundary isosurface values, $\eta(\mathbf{r})$ (also referred to as f_{sep}-values), at which the reducible domains split.

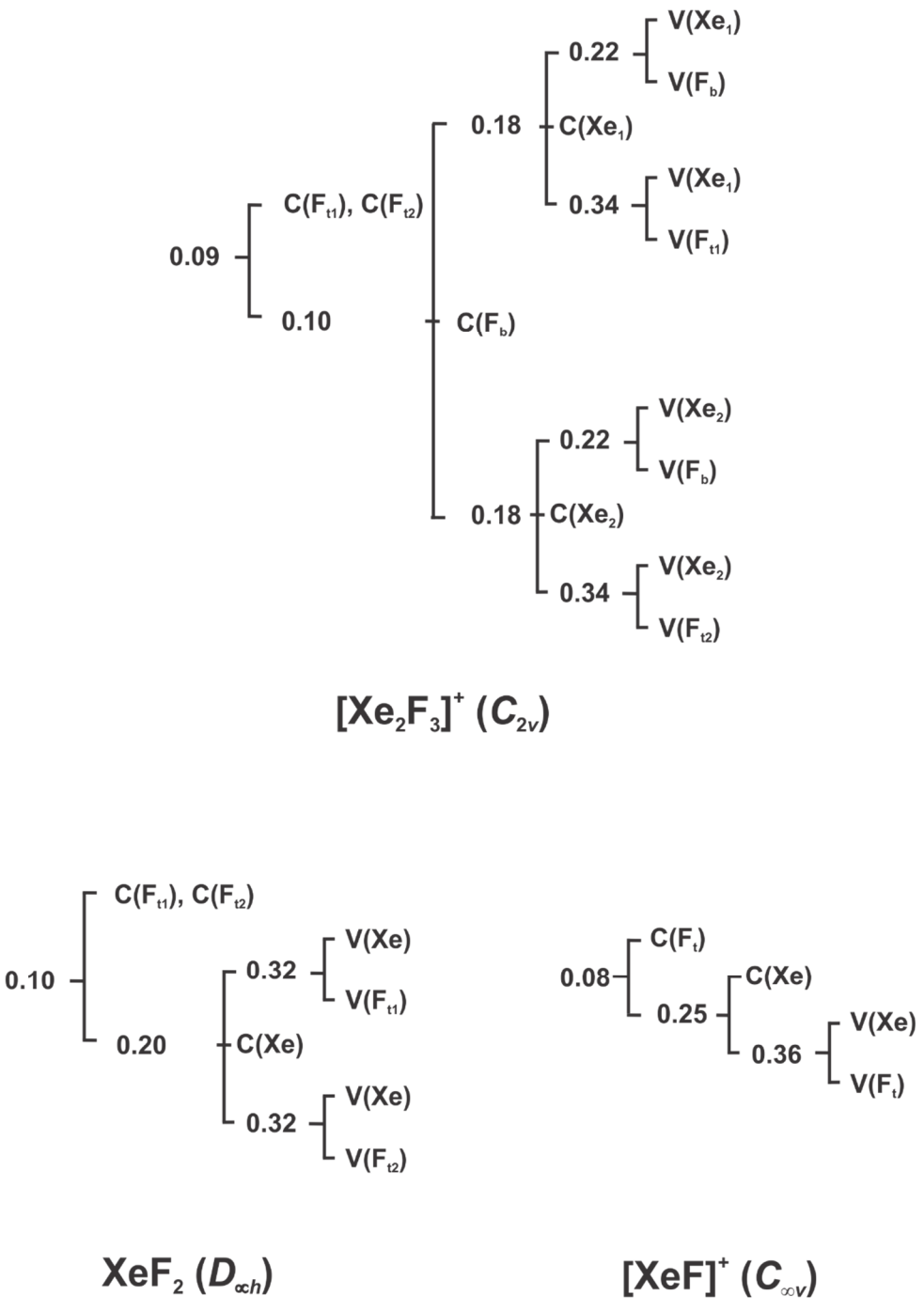

Figure A1.25. ELF reduction of the localization diagrams (B2PLYP-D3/Def2-TZVPD) for $[Xe_2F_3]^+$, XeF_2, and $[XeF]^+$ showing the ordering of localization nodes and the boundary isosurface values, $\eta(\mathbf{r})$ (also referred to as f_{sep}-values), at which the reducible domains split.

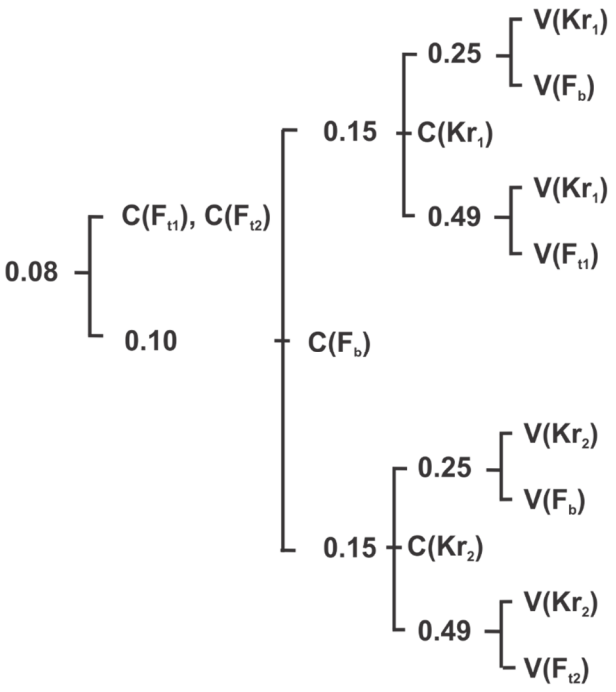

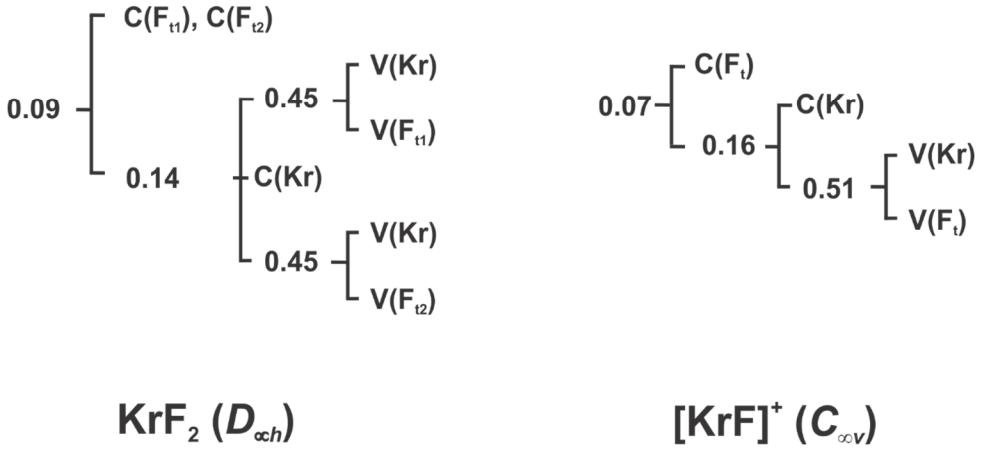

Figure A1.26. ELF reduction of the localization diagrams (B2PLYP-D3/Def2-TZVPD) for $[Kr_2F_3]^+$, KrF_2, and $[KrF]^+$ showing the ordering of localization nodes and the boundary isosurface values, $\eta(\mathbf{r})$ (also referred to as f_{sep}-values), at which the reducible domains split.

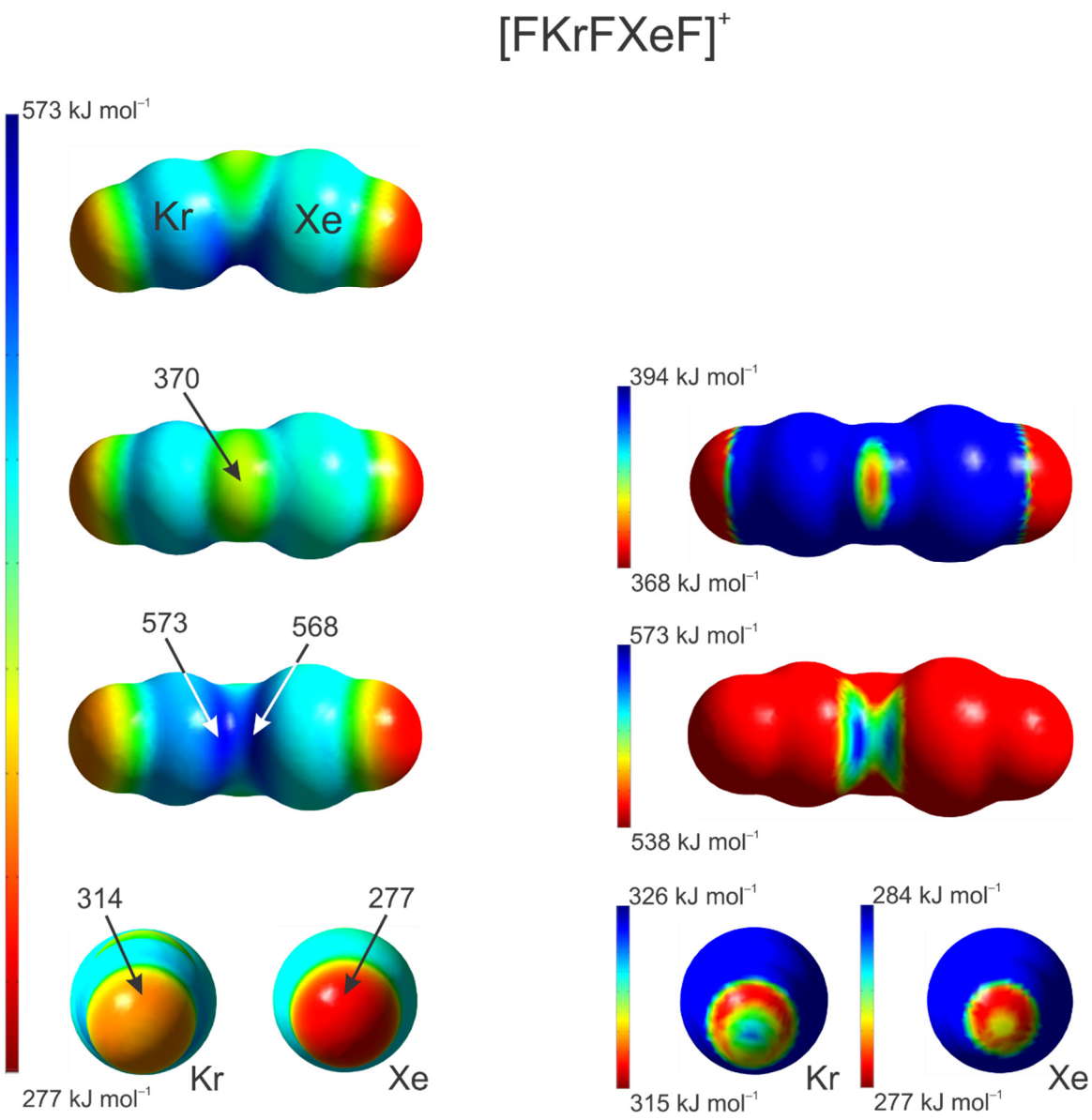

Figure A1.27. The calculated molecular electrostatic potentials of the $[FKrFXeF]^+$ cation at the 0.001 e a_0^{-3} isosurface, where the extrema of selected electrostatic potentials are indicated by arrows. The optimized geometries and MEPS were calculated at the B2PLYP-D3/Def2-TZVPD level of theory.

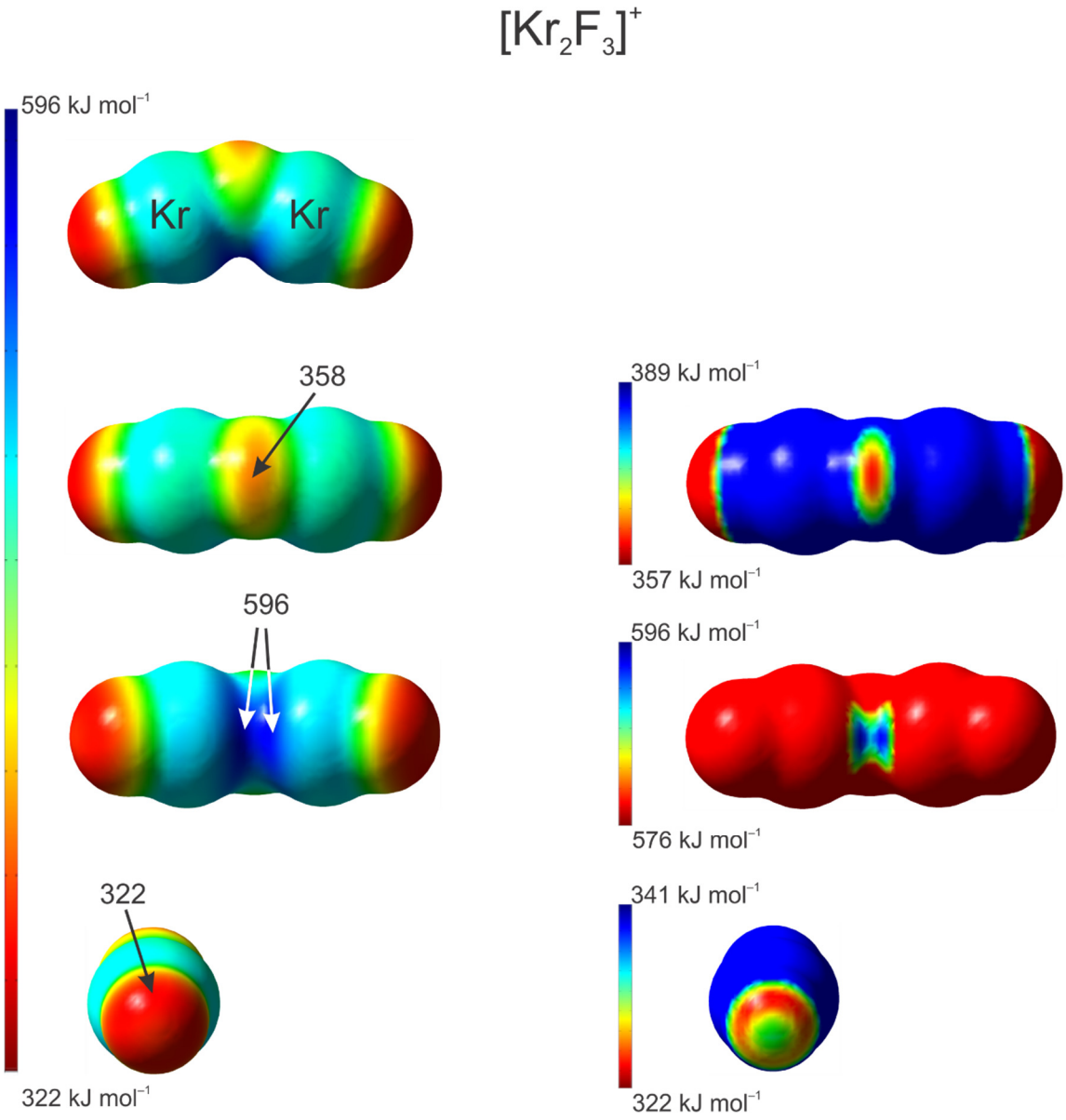

Figure A1.28. The calculated molecular electrostatic potentials of the $[Kr_2F_3]^+$ cation at the 0.001 e a_0^{-3} isosurface, where the extrema of selected electrostatic potentials are indicated by arrows. The optimized geometries and MEPS were calculated at the B2PLYP-D3/Def2-TZVPD level of theory.

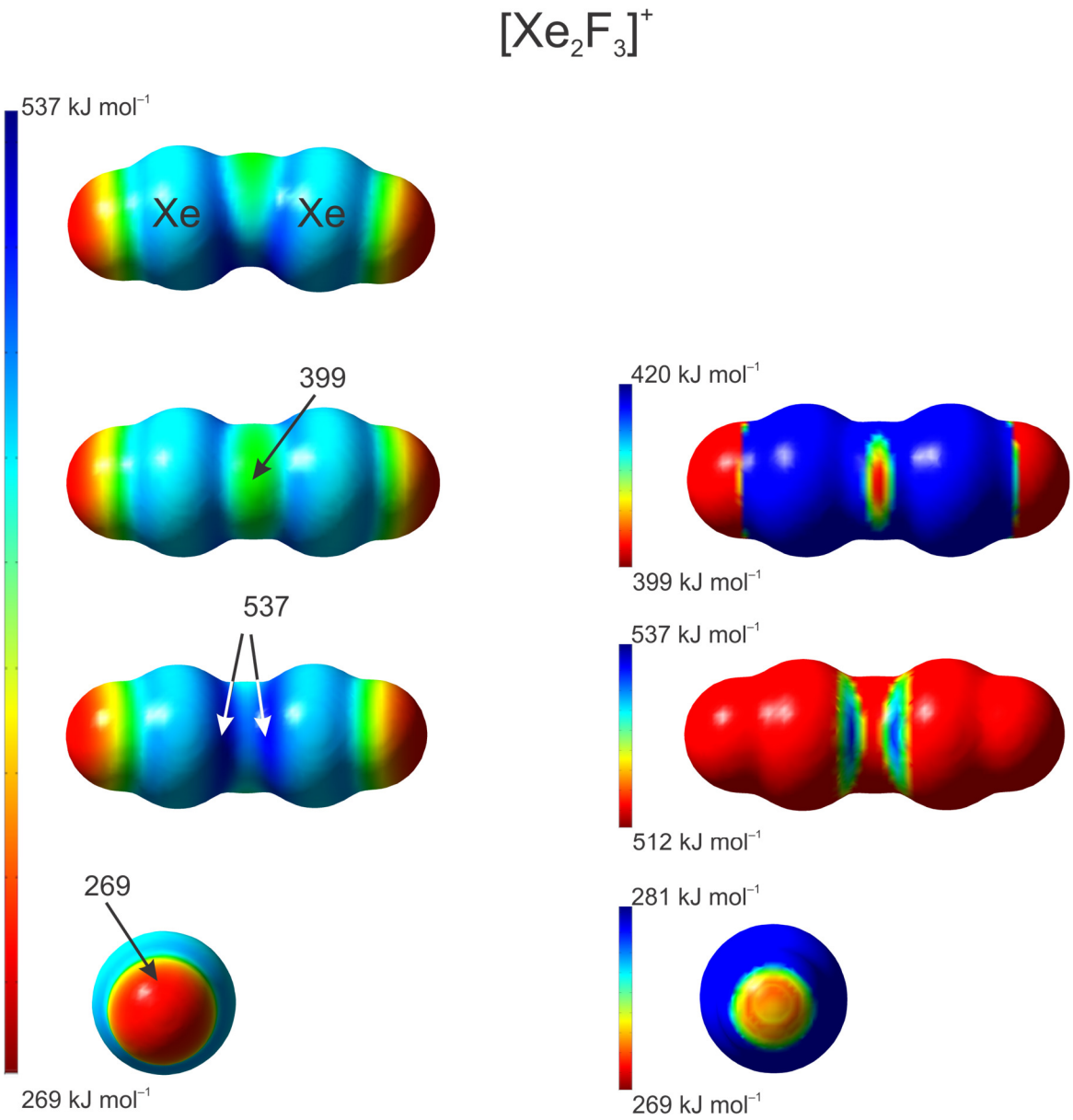

Figure A1.29. The calculated molecular electrostatic potentials of the $[Xe_2F_3]^+$ cation at the 0.001 e a_0^{-3} isosurface, where the extrema of selected electrostatic potentials are indicated by arrows. The optimized geometries and MEPS were calculated at the B2PLYP-D3/Def2-TZVPD level of theory.

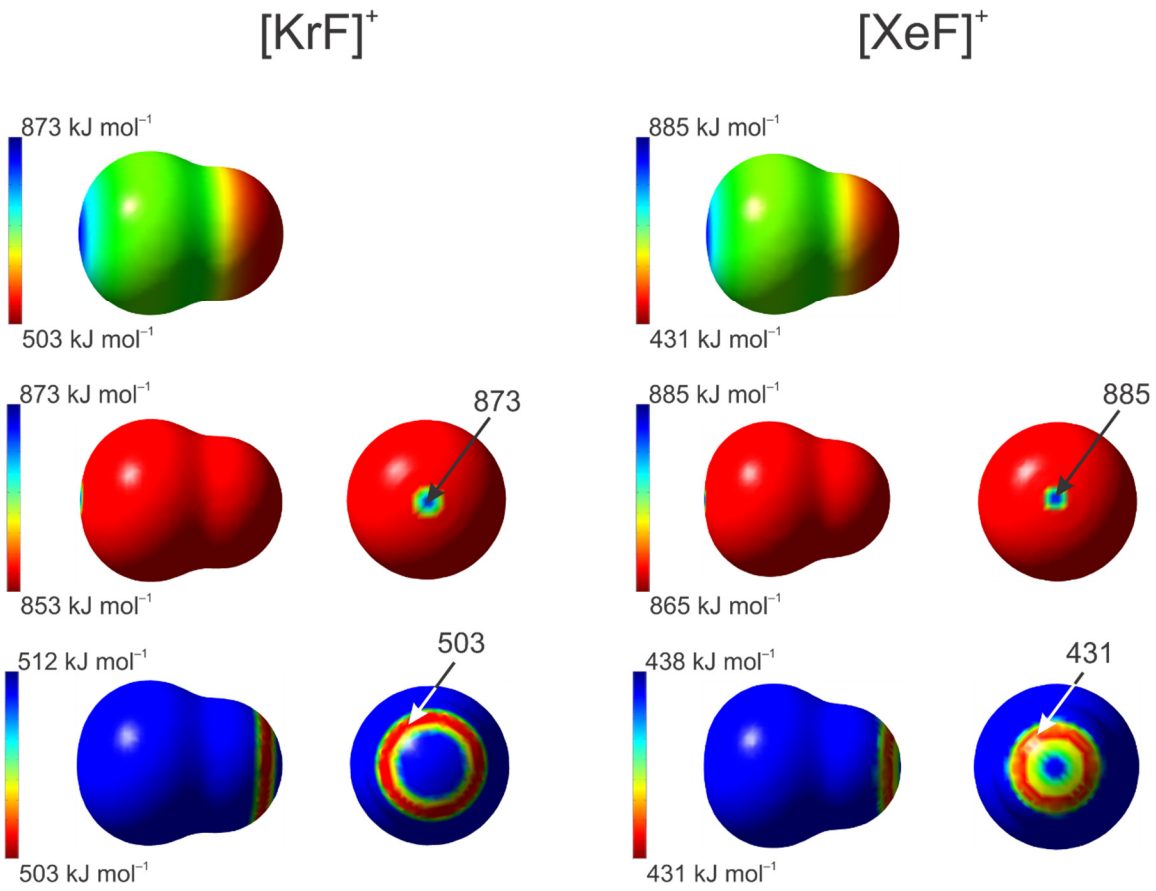

Figure A1.30. Calculated molecular electrostatic potentials at the 0.001 e a_0^{-3} isosurfaces of the $[NgF]^+$ cations (Ng = Kr, Xe), where the extrema of selected electrostatic potentials are indicated by arrows. The optimized geometries and MEPS were calculated at the B2PLYP-D3/Def2-TZVPD level of theory.

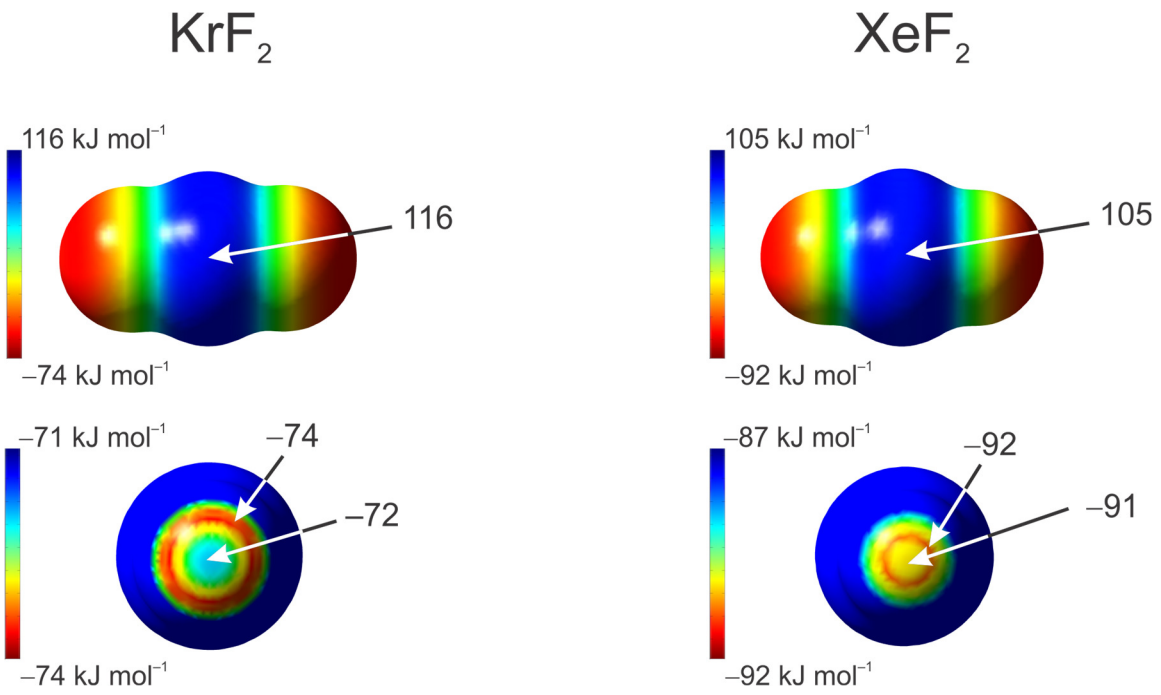

Figure A1.31. Calculated molecular electrostatic potentials at the 0.001 e a_0^{-3} isosurfaces of NgF_2 (Ng = Kr, Xe). The extrema of selected electrostatic potentials are indicated by arrows. The optimized geometries and MEPS were calculated at the B2PLYP-D3/Def2-TZVPD level of theory.

References

[S1] Elliot, H. S. A.; Lehmann, J. F.; Mercier, H. P. A.; Jenkins, D. B.; Schrobilgen, G. J. *Inorg. Chem.* **2010**, *49*, 8504–8523.

[S2] Mukhtar, M. A-.; Holloway, J. H.; Hope, E. G.; Schrobilgen, G. J. *J. Chem. Soc. Dalton Trans.* **1991**, 2831–2834.

[S3] Lehmann, J. F.; Dixon, D. A.; Schrobilgen, G. J. *Inorg. Chem.* **2001**, *40*, 3002–3017, and references therein.

[S4] Griffiths, J. E.; Sunder, W. A. *J. Chem. Phys.* **1982**, *77*, 1087–1092.

[S5] Lozinšek, M.; Mercier, H. P. A.; Schrobilgen, G. J. *Angew. Chem. Int. Ed.* **2021**, *60*, 8149–8156.

[S6] Burns, J. H. *J. Phys. Chem*. **1963**, *67*, 536.

[S7] Burns, J. H.; Ellison, R. D.; Levy, H. A. *J. Phys. Chem.* **1963**, *67*, 1569–1570.

[S8] Ibers, J. A.; Hamilton, W. C. *Science*, **1963**, *139*, 106–107.

[S9] Burns, H. H.; Agron, P. A.; Levy, H. A. *Science*, **1963**, *139*, 1208–1209.

[S10] Bürger, H.; Ma, S.; Breidung, J.; Thiel, W. *J. Chem. Phys.* **1996**, *104*, 4945–4953.

[S11] Bartlett, N.; DeBoer, B. G.; Hollander, F. J.; Sladky, F. O.; Templeton, D. H.; Zalkin, A. *Inorg. Chem.* **1974**, *13*, 780–785.

[S12] Mazej, Z.; Goreshnik, E. *Eur. J. Inorg. Chem.* **2009**, *29*, 4503–4506.

[S13] Leary, K.; Templeton, D. H.; Zalkin, A.; Bartlett, N. *Inorg. Chem.* **1973**, *12*, 1726–1730.

[S14] Jesih, A.; Lutar, K.; Leban, I.; Žemva, B. *Eur. J. Solid State Inorg. Chem.* **1991**, *28*, 829–840.

[S15] Pointner, B. E.; Suontamo, R. J.; Schrobilgen, G. J. *Inorg. Chem.* **2006**, *45*, 1517–1534.

[S16] Bartlett, N.; Einstein, F.; Stewart, D. F.; Trotter, J. *J. Chem. Soc. (A),* **1967**, 1190–1193.

[S17] Lutar, K.; Jesih, A.; Leban, I.; Žemva, B.; Bartlett, N. *Inorg. Chem.* **1989**, *28*, 3467–3471.

[S18] Mazej, Z.; Darriet, J.; Grannec, J.; Lutar, K.; Tressaud, A.; Žemva, B. *J. Fluor. Chem.* **1999**, *99*, 25–28.

[S19] Hughes, M. J.; Mercier, H. P. A.; Schrobilgen, G. J. *Inorg. Chem.* **2010**, *49*, 3501–3515.

[S20] Goettel, J. T.; Bortolus, M. R.; Stuart, D. G.; Mercier, H. P. A.; Schrobilgen, G. J. *Chem. Eur. J.* **2019**, *25*, 15815–15829.

[S21] Fir, B. A.; Gerken, M.; Pointner, B. E.; Mercier, H. P. A.; Dixon, D. A.; Schrobilgen, G. J. *J. Fluor. Chem.* **2000**, *105*, 159–167, and references therein.

[S22] Fateley, W. G.; Dollish, F. R.; McDevitt, N. T.; Bentley, F. F. *Infrared and Raman Selection Rules for Molecular and Lattice Vibrations: The Correlation Method*, Wiley, New York, **1972**.

[S23] Adams, C. J. *J. Raman Spectrosc.* **1974**, *2*, 391–397.

[S24] Mercier, H. P. A.; Breddemann, U.; Brock, D. S.; Bortolus, M. R.; Schrobilgen, G. J. *Chem. Eur. J.* **2019**, *25*, 12105–12119.

[S25] Debackere, J. R.; Mercier, H. P. A.; Schrobilgen, G. J. *J. Am. Chem. Soc.* **2014**, *136*, 3888–3903.

[S26] Žemva, B.; Jesih, A.; Templeton, D. H.; Zalkin, A.; Cheetham, A. K.; Bartlett, N. *J. Am. Chem. Soc.* **1987**, *109*, 7420–7427.

[S27] Tramšek, M.; Žemva, B. *Acta. Chem. Slov.* **2006**, *53*, 105–116.

[S28] Bunič, T.; Tavčar, G.; Tramšek, M.; Žemva, B. *Inorg. Chem.* **2006**, *45*, 1038–1042.

[S29] Bunič, T.; Tramšek, M.; Goreshnik, E.; Tavčar, G.; Žemva, B. *Inorg. Chem.* **2007**, *46*, 5276–5282.

[S30] Bunič, T.; Tramšek, M.; Goreshnik, E.; Žemva, B. *Inorg. Chem.* **2008**, *10*, 1511–1516.

[S31] Bader, R. F. W. *Atoms in Molecules: A Quantum Theory*; Oxford University Press, Oxford, **1990**.

[S32] Becke, A. D.; Edgecombe, K. E. *J. Chem. Phys.* **1990**, *92*, 5397–5403.

[S33] Silvi, B.; Savin, A. *Nature*, **1994**, *371*, 683–686.

[S34] Brock, D. S.; Casalis de Pury, J. J.; Mercier, H. P. A.; Schrobilgen, G. J.; Silvi, B. *Inorg. Chem.* **2010**, *49*, 6673–6689.

[S35] Brock, D. S.; Casalis de Pury, J. J.; Mercier, H. P. A.; Schrobilgen, G. J.; Silvi, B. *J. Am. Chem. Soc.* **2010**, *132*, 3533–3542.

[S36] Ivanova, M. V.; Mercier, H. P. A.; Schrobilgen, G. J. *J. Am. Chem. Soc.* **2015**, *137*, 13398–13413.

[S37] Vasdev, N.; Moran, M. D.; Tuononen, H. M.; Chirakal, R.; Suontamo, R. J.; Bain, A. D.; Schrobilgen, G. J. *Inorg. Chem.* **2010**, *49*, 8997–9004.

[S38] Mercier, H. P. A.; Moran, M. D.; Sanders, J. C. P.; Schrobilgen, G. J.; Suontamo, R. J. *Inorg. Chem.* **2005**, *44*, 49–60.

[S39] Gillespie, R. J.; Hargittai, I. *The VSEPR Model of Molecular Geometry*; Allyn and Bacon: Boston, MA, **1991**.

[S40] Savin, A.; Silvi, B.; Colonna, F. *Can. J. Chem.* **1996**, *74*, 1088–1096.

APPENDIX 2

CHAPTER 4 Supporting Information

Syntheses and Structural Characterizations of the Cl(V) Coordination Complex, $[O_2Cl(FXeF)_2][AsF_6]$, and β-$[ClO_2][AsF_6]$

Adapted with permission from: Bortolus, M. R.; Ellwanger, M.; Haner, J.; Schrobilgen, G. J. *J. Fluor. Chem.* **2021**, *250*, 109814.

Table of Contents

Table A2.1. Experimental bond angles for β-$[ClO_2][AsF_6]$ (**1**) and $[O_2Cl(FXeF)_2][AsF_6]$ (**2**) and calculated [a] bond angles for $([O_2Cl(FXeF)_2][AsF_6]_2)^-$ (**2′**)

β-$[ClO_2][AsF_6]$ exptl		$[O_2Cl(FXeF)_2][AsF_6]$ exptl		$([O_2Cl(FXeF)_2][AsF_6]_2)^-$ calcd [a]
Bond Angles (deg)				
O(1)–Cl(1)–O(2)	119.2(2)	O(1)–Cl(1)–O(2)	118.8(1)	115.87
O(1)–Cl(1)---F(1)	95.6(2)	O(1)–Cl(1)---F(1A)	92.34(3)	86.57
O(1)–Cl(1)---F(2A)	85.1(2)	O(1)–Cl(1)---F(4)	149.69(6)	154.61
O(1)–Cl(1)---F(3A)	154.2(2)	O(1)–Cl(1)---F(4A)	149.69(6)	154.61
O(1)–Cl(1)---F(6A)	95.8(2)	O(1)–Cl(1)---F(5)	92.34(3)	93.02
O(2)–Cl(1)---F(1)	97.9(2)	O(1)–Cl(1)---F(5A)	92.34(3)	93.02
O(2)–Cl(1)---F(2A)	155.5(2)	O(2)–Cl(1)---F(1A)	153.99(8)	157.56
O(2)–Cl(1)---F(3A)	85.5(2)	O(2)–Cl(1)---F(4)	81.76(7)	75.30
O(2)–Cl(1)---F(6A)	92.4(2)	O(2)–Cl(1)---F(4A)	81.76(7)	75.30
F(1)---Cl(1)---F(2A)	74.5(1)	O(2)–Cl(1)---F(5)	97.16(3)	100.85
F(1)---Cl(1)---F(3A)	87.5(1)	O(2)–Cl(1)---F(5A)	97.16(3)	100.85
F(1)---Cl(1)---F(6A)	158.4(1)	F(4)---Cl(1)---F(4A)	46.78(4)	47.08
F(2A)---Cl(1)---F(3A)	71.1(1)	F(4)---Cl(1)---F(5)	107.74(3)	61.84
F(2A)---Cl(1)---F(6A)	88.3(1)	F(4)---Cl(1)---F(5A)	61.46(3)	107.67
F(3A)---Cl(1)---F(6A)	74.4(1)	F(4A)---Cl(1)---F(5)	61.46(3)	61.61
F(1)–As(1)–F(2)	90.1(2)	F(4A)---Cl(1)---F(5A)	107.74(3)	107.67
F(1)–As(1)–F(3)	178.0(2)	F(5)---Cl(1)---F(5A)	160.46(5)	152.17
F(1)–As(1)–F(4)	89.9(2)	F(1)–As(1)–F(2)	90.23(6)	90.86
F(1)–As(1)–F(5)	90.6(2)	F(1)–As(1)–F(2A)	90.23(6)	90.86
F(1)–As(1)–F(6)	89.4(2)	F(1)–As(1)–F(3)	179.2(1)	177.48
F(2)–As(1)–F(3)	89.1(2)	F(1)–As(1)–F(4)	89.53(6)	88.98
F(2)–As(1)–F(4)	178.9(2)	F(1)–As(1)–F(4A)	89.53(6)	88.98
F(2)–As(1)–F(5)	90.3(2)	F(2)–As(1)–F(2A)	92.1(1)	92.07
F(2)–As(1)–F(6)	88.7(2)	F(2)–As(1)–F(3)	90.36(7)	90.89
F(3)–As(1)–F(4)	90.9(2)	F(2)–As(1)–F(4)	178.11(7)	177.68
F(3)–As(1)–F(5)	91.3(2)	F(2)–As(1)–F(4A)	89.83(6)	90.25
F(3)–As(1)–F(6)	88.7(2)	F(2A)–As(1)–F(3)	90.36(7)	90.89
F(4)–As(1)–F(5)	90.8(2)	F(2A)–As(1)–F(4)	89.83(6)	90.25
F(4)–As(1)–F(6)	90.2(2)	F(2A)–As(1)–F(4A)	178.11(7)	177.68
F(5)–As(1)–F(6)	179.0(2)	F(3)–As(1)–F(4)	89.86(6)	89.20
		F(3)–As(1)–F(4A)	89.86(6)	89.20
		F(4)–As(1)–F(4A)	88.30(8)	87.43
		F(5)–Xe(1)–F(6)	179.47(5)	175.60
		Xe(1)–F(5)---Cl(1)	125.45(4)	126.94
		F(1A)–As(1A)–F(2B)		88.44
		F(1A)–As(1A)–F(2BA)		88.44
		F(1A)–As(1A)–F(3A)		179.75
		F(1A)–As(1A)–F(4B)		88.26

continued …

Table A2.1. (continued)

β-$[ClO_2][AsF_6]$ exptl	$[O_2Cl(FXeF)_2][AsF_6]$ exptl	$([O_2Cl(FXeF)_2][AsF_6]_2)^-$ calcd [a]
	Bond Angles (deg)	
	F(1A)–As(1A)–F(4BA)	88.26
	F(2B)–As(1A)–F(2BA)	90.53
	F(2B)–As(1A)–F(3A)	91.74
	F(2B)–As(1A)–F(4B)	176.69
	F(2B)–As(1A)–F(4BA)	89.62
	F(2BA)–As(1A)–F(3A)	91.74
	F(2BA)–As(1A)–F(4B)	89.62
	F(2BA)–As(1A)–F(4BA)	176.69
	F(3A)–As(1A)–F(4B)	91.56
	F(3A)–As(1A)–F(4BA)	91.56
	F(4B)–As(1A)–F(4BA)	90.04

[a] B3LYP/Def2-TZVPD.

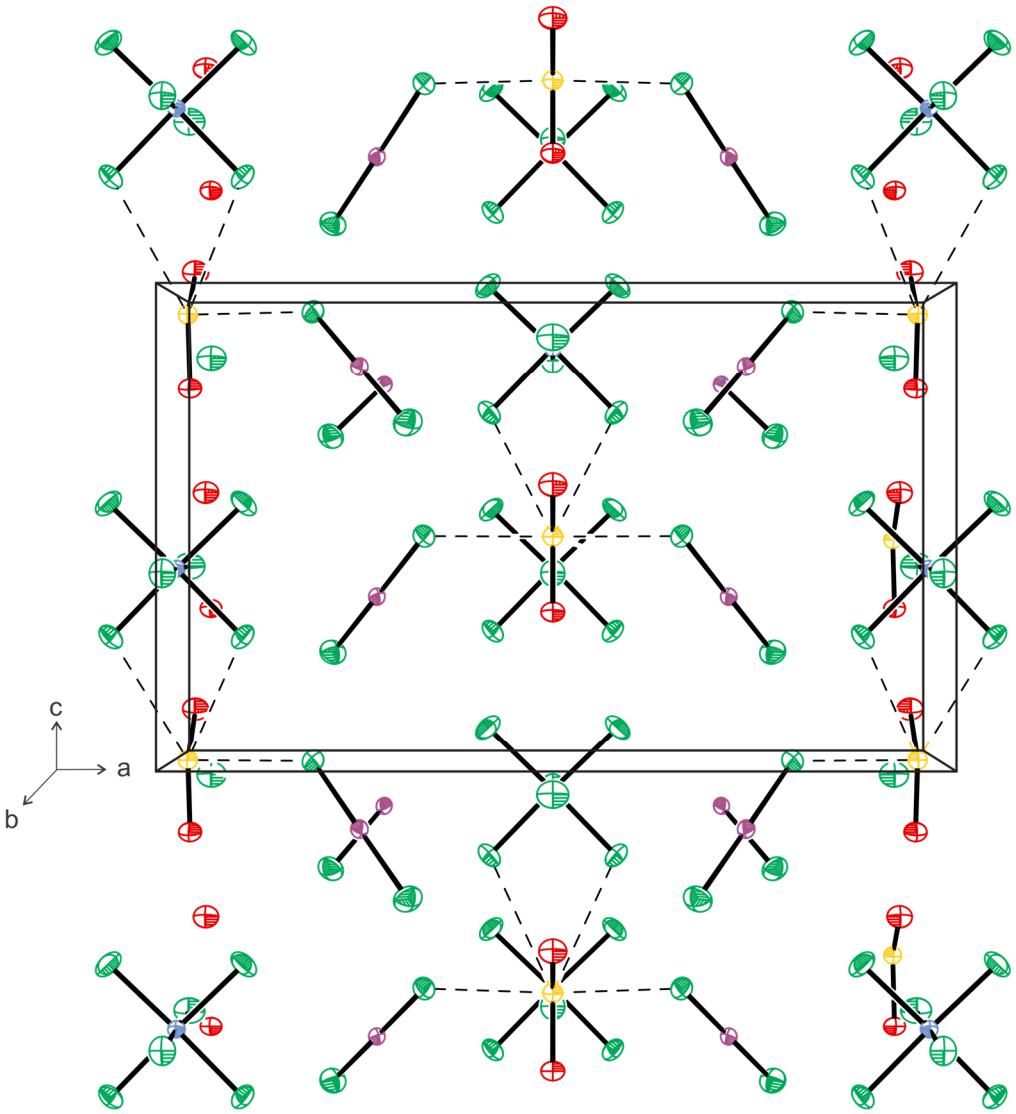

Figure A2.1. A packing diagram showing the X-ray crystal structure of $[O_2Cl(FXeF)_2][AsF_6]$ (**2**) viewed along the *b*-axis of the unit cell; thermal ellipsoids are drawn at the 50% probability level.

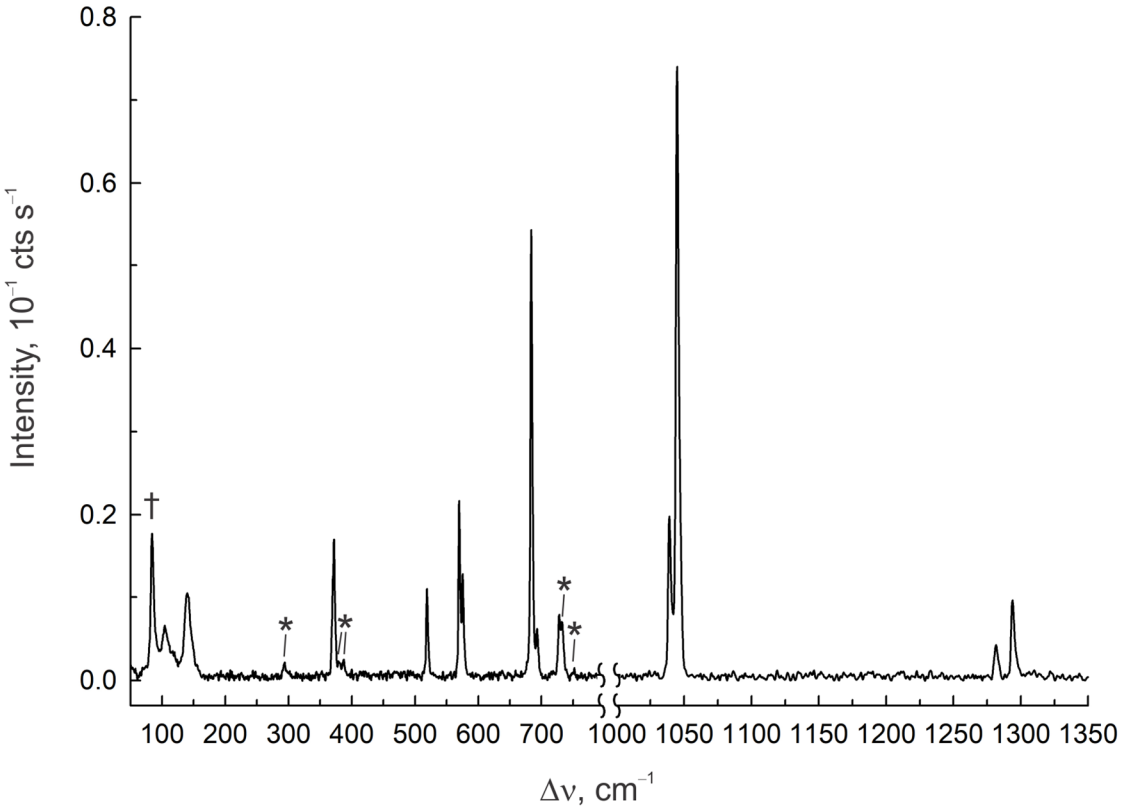

Figure A2.2. Raman spectrum of α-$[ClO_2][AsF_6]$ recorded on a dry powder at −150 °C using 1064-nm excitation. The symbols denote FEP sample tube bands (*) and an instrumental artifact (†).

Figure A2.3. Factor-group analysis for $[ClO_2]^+$ in β-$[ClO_2][AsF_6]$ (**1**)[a]

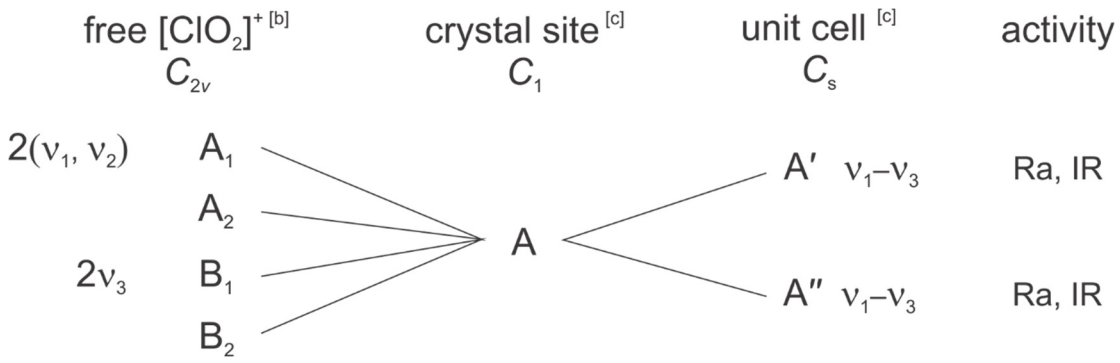

[a] The external modes have not been treated in this analysis. [b] The vibrational irreducible representation for gas-phase $[ClO_2]^+$ (C_{2v}) is $\Gamma = 2A_1 + A_2$. [c] Space group; *Pc*, Z = 2.

Figure A2.4. Factor-group analysis for $[AsF_6]^-$ in β-$[ClO_2][AsF_6]$ (**1**)[a]

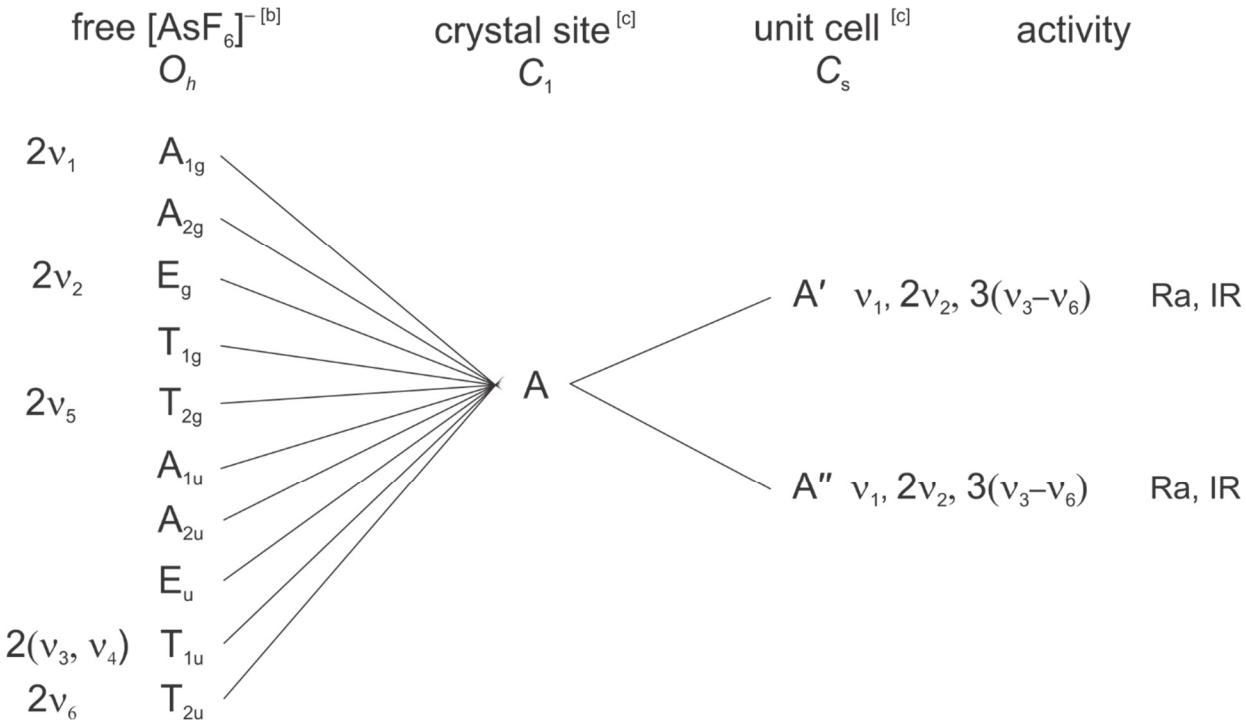

[a] The external modes have not been treated in this analysis. [b] The vibrational irreducible representation for gas-phase $[AsF_6]^-$ (O_h) is $\Gamma = A_{1g} + E_g + T_{2g} + 2T_{1u} + T_{2u}$. [c] Space group; *Pc*, Z = 2.

Raman Spectroscopy (continued)

β-[ClO₂][AsF₆] (1). The gas-phase symmetries of $[ClO_2]^+$ (C_{2v}) and $[AsF_6]^-$ (O_h) are lowered to C_1 site symmetry in the crystal structure of **1**, so that all vibrational modes of both ions are Raman and infrared active. Although this accounts for the observation of $[AsF_6]^-$ bands that are derived from ungerade modes in the Raman spectrum, it does not account for splitting of the non-degenerate cation and anion modes. The latter splittings result from vibrational couplings within the unit cell. To account for these splittings, separate factor-group analyses for $[ClO_2]^+$ and $[AsF_6]^-$ using the "correlation method" [S1] and the X-ray crystal structure of **1** (Figures A2.2 and A2.3) were carried out.

The vibrational modes of gas-phase $[ClO_2]^+$ (C_{2v}) belong to the irreducible representations $\Gamma = 2A_1 + B_2$, where the A_1 and B_2 modes are both Raman- and IR-active in the gas phase. The A_1 and B_2 irreducible representations correlate to A irreducible representations under C_1 site symmetry in the solid state. When correlated to the unit cell symmetry (C_s), each vibrationally coupled A mode splits into a A′ and a A″ mode for a total of 3A′ and 3A″ modes that are both Raman- and IR-active,

All irreducible representations of gas-phase $[AsF_6]^-$ (O_h), $\Gamma = A_{1g} + E_g + T_{2g} + 2T_{1u} + T_{2u}$, correlate to A irreducible representations under the crystal site symmetry (C_1) of $[AsF_6]^-$. When correlated to the unit cell symmetry (C_s), each vibrationally coupled A mode splits into two Raman- and two IR-active A′ and A″ modes to give 15A′ and 15A″ modes.

[O₂Cl(FXeF)₂][AsF₆] (2). A total of 42 vibrational modes are predicted for $[O_2Cl(FXeF)_2][AsF_6]$ (**2**) based on C_s symmetry in its X-ray crystal structure. The

vibrations belong to the irreducible representations $\Gamma = 24A' + 18A''$, where the modes are both Raman- and IR-active. The latter modes correlate to A' and A" irreducible representations under C_s site symmetry in the solid state. When correlated to the unit cell symmetry (C_{2v}), each vibrationally coupled A' mode splits into an A_1 and a B_2 component that are both Raman and infrared active; and each coupled A″ mode splits into an A_2 (Raman-active) and a B_1 (Raman- and IR-active) component to give a total of 84 Raman-active modes and 66 IR-active modes.

Table A2.2. Experimental Raman frequencies and intensities for $[O_2Cl(FXeF)_2][AsF_6]$ (**2**),[a] and calculated[b] vibrational frequencies, intensities, and assignments for the Hypothetical ($[O_2Cl(FXeF)_2][AsF_6]_2)^-$ (**2′**) anion

2		**2′**			**assgnts** [c]	
exptl [a]	Δν	^{35}Cl calcd [b]	^{37}Cl calcd [b]	Δν		$[AsF_6]^-$ (O_h)
1315.9(11) 1301.2(9)	14.7	1335.6(16)[139]	1320.9(16)[134]	14.7	$[\nu(Cl–O_1) - \nu(Cl–O_2)]$	
1077.2(100) 1071.2(32)	6.0	1133.0(237)[64]	1126.3(236)[61]	6.7	$[\nu(Cl–O_1) + \nu(Cl–O_2)]$	
		702.3(<1)[205]	702.3(<1)[205]		$\nu(As_1\text{-}F_3) - \nu(As_1\text{-}F_1)$	
701.9(5)		696.5(1)[270]	696.5(1)[269]		$[\nu(As_{1A}\text{-}F_{2B}) + \nu(As_{1A}\text{-}F_{4BA})] - [\nu(As_{1A}\text{-}F_{2BA}) + \nu(As_{1A}\text{-}F_{4B})]$	
699.4(5)		693.6(5)[172]	693.6(5)[172]		$[\nu(As_{1A}\text{-}F_{2B}) + \nu(As_{1A}\text{-}F_{2BA})] - [\nu(As_{1A}\text{-}F_{4B}) + \nu(As_{1A}\text{-}F_{4BA})]$	
		690.4(7)[19]	690.4(7)[19]		$\nu(As_1\text{-}F_2) + \nu(As_1\text{-}F_{2A}) + \nu(As_{1A}\text{-}F_{3A})$	$\nu_3(T_{1u})$ ($[AsF_6]^-$)
692.1(3)		686.0(<1)[339]	686.0(<1)[339]		$[\nu(As_1\text{-}F_2) + \nu(As_1\text{-}F_{2A})] - \nu(As_{1A}\text{-}F_{3A})$	
		684.0(1)[114]	684.0(1)[113]		$[\nu(As_1\text{-}F_2) + \nu(As_1\text{-}F_{4A})] - [\nu(As_1\text{-}F_{2A}) + \nu(As_1\text{-}F_4)]$	
685.6(sh)		648.6(29)[32]	648.6(29)[32]		$\nu(As_1\text{-}F) + \nu(As_{1A}\text{-}F)$	$\nu_1(A_{1g})$ ($[AsF_6]^-$)
683.5(36)		646.8(5)[77]	646.8(5)[77]		$\nu(As_1\text{-}F) - \nu(As_{1A}\text{-}F)$	
578.9(14) 576.3(14)		564.1(3)[1]	564.1(3)[1]		$\nu(As_{1A}\text{-}F_{2B}) + \nu(As_{1A}\text{-}F_{4B}) - \nu(As_{1A}\text{-}F_{2BA}) + \nu(As_{1A}\text{-}F_{4BA})$	$\nu_2(E_g)$ ($[AsF_6]^-$)
539.4(sh)		562.0(6)[9]	561.5(6)[13]	0.5	$[\nu(As_1\text{-}F_1) + \nu(As_1\text{-}F_3)] - [\nu(As_1\text{-}F_2) + \nu(As_1\text{-}F_{2A}) + \nu(As_1\text{-}F_4) + \nu(As_1\text{-}F_{4A})] + [\delta(O_1ClO_2)_{i.p.}]_{small}$	
536.1(39)		551.0(4)[18]	548.7(8)[18]	2.3	$\delta(OClO)_{i.p.}$	
530.9(55)		545.5(9)[8]	545.4(29)[192]	0.1	$[\nu(Xe_1\text{-}F_6) - \nu(Xe_{1A}\text{-}F_{6A})] + [\nu(As_1\text{-}F_2) + \nu(As_1\text{-}F_{4A})] - [\nu(As_1\text{-}F_{2A}) + \nu(As_1\text{-}F_4)]$	
519.0(98)		542.2(33)[198]	541.5(26)[186]	0.7	$[\nu(Xe_1\text{-}F_6) + \nu(Xe_{1A}\text{-}F_{6A})] + [\delta(O_1ClO_2)_{i.p.}]_{small}$	
481.1(11)		535.9(11)[71]	535.9(11)[72]		$[\nu(Xe_1\text{-}F_6) - \nu(Xe_{1A}\text{-}F_{6A})] - [\nu(As_1\text{-}F_2) + \nu(As_1\text{-}F_{4A})] + [\nu(As_1\text{-}F_{2A}) + \nu(As_1\text{-}F_4)]$	
464.2(11)		520.7(4)[28]	520.3(4)[28]	0.4	$[\nu(As_{1A}\text{-}F_{1A}) + \nu(As_{1A}\text{-}F_{3A})] + [\delta(O_1ClO_2)_{i.p.}]_{small}$	
446.7(30)		440.0(3)[241]	440.0(3)[242]		$[\nu(Xe_1\text{-}F_5) + \nu(Xe_{1A}\text{-}F_{5A})]$	
439.4(23) 435.6(sh)		426.9(2)[84]	426.0(2)[95]	0.9	$[\nu(Xe_1\text{-}F_5) - \nu(Xe_{1A}\text{-}F_{5A})] + [\delta(O_1ClO_2)_{o.o.p.}]_{small}$	

continued…

Table A2.2. (continued)

2	**2′**			**assgnts** [d]	
exptl [a]	^{35}Cl calcd [b]	^{37}Cl calcd [b]	Δν [c]		$[AsF_6]^-$ (O_h)
	393.3(<0.01)[151]	393.1(<0.01)[142]	0.2	$\delta(F_1As_1F_3) + \delta(F_{1A}As_{1A}F_{3A}) + \delta(F_2As_1F_{4A}) + \delta(F_{2B}As_1F_{4BA}) + \delta(F_{2A}As_1F_4) + \delta(F_{2BA}As_{1A}F_{4B})$	
	392.2(<1)[<1]	392.2(<1)[<1]		$[\delta(F_2As_1F_4) + \delta(F_{2A}As_1F_{4A}) + \delta(F_1As_1F_3)] - [\delta(F_{2B}As_{1A}F_{4B}) + \delta(F_{2BA}As_{1A}F_{4BA}) + \delta(F_{1A}As_{1A}F_{3A})]$	
400.2(1)	389.8(<1)[63]	389.8(<1)[63]		$[\delta(F_1As_1F_3) + \delta(F_2As_1F_4) + \delta(F_{2A}As_1F_{4A})]$	
394.0(2)	388.8(<1)[<1]	388.8(<1)[<1]		$[\delta(F_2As_1F_{4A}) + \delta(F_{2BA}As_1F_{4B}) + \delta(F_1As_1F_3)] - [\delta(F_{2A}As_1F_4) + \delta(F_{2B}As_{1A}F_{4BA}) + \delta(F_{1A}As_{1A}F_{3A})]$	$\nu_4(T_{1u})$ $[AsF_6]^-$
	388.0(<1)[53]	388.0(<1)[53]		$[\delta(F_1As_1F_3) + \delta(F_{1A}As_{1A}F_{3A}) + \delta(F_2As_1F_4) + \delta(F_{2A}As_{1A}F_{4A})] - [\delta(F_{2B}As_{1A}F_{4B}) + \delta(F_{2BA}As_{1A}F_{4BA})]$	
	387.0(<1)[81]	387.0(<1)[82]		$\delta(F_{1A}As_{1A}F_{3A}) + \delta(F_{2B}As_{1A}F_{4B}) + \delta(F_{2BA}As_{1A}F_{4BA})$	
	356.7(<1)[<1]	356.7(<1)[<1]		$\rho_t(F_{2B}As_{1A}F_{4B})_{o.o.p.} + \rho_t(F_{2BA}As_{1A}F_{4BA})_{o.o.p.}$	
	354.3(<1)[1]	354.3(<1)[1]		$\rho_t(F_1As_1F_3)_{i.p.} + \rho_t(F_2As_1F_4)_{i.p.} + \rho_t(F_{2A}As_1F_{4A})_{i.p.}$	
370.7(11)	353.4(<1)[<1]	353.4(<1)[<1]		$\rho_t(F_1As_1F_3)_{o.o.p.} + \rho_t(F_2As_1F_4)_{i.p.} + \rho_t(F_{2A}As_1F_{4A})_{i.p.}$	
367.6(7)	351.6(1)[<1]	351.5(1)[<1]	0.1	$\rho_t(F_{1A}As_{1A}F_{3A})_{o.o.p.} + \rho_t(F_{2B}As_{1A}F_{4B})_{i.p.} + \rho_t(F_{2BA}As_{1A}F_{4BA})_{i.p.}$	$\nu_5(T_{2g})$ $[AsF_6]^-$
	351.4(<1)[2]	351.4(<1)[2]		$\rho_t(F_{1A}As_{1A}F_{3A})_{i.p.} + \rho_t(F_{2B}As_{1A}F_{4B})_{i.p.} + \rho_t(F_{2BA}As_{1A}F_{4BA})_{i.p.}$	
	349.4(1)[<1]	349.1(1)[<1]	0.3	$\rho_t(F_2As_1F_4)_{o.o.p.} + \rho_t(F_{2A}As_1F_{4A})_{o.o.p.}$	
233.7(20)	246.0(4)[<1]	246.0(4)[<1]		$[\delta(F_5Xe_1F_6)_{o.o.p.} + \delta(F_{5A}Xe_{1A}F_{6A})_{o.o.p.}]$	
	305.9(18)[315]	302.2(18)[305]	3.7	$\delta(OClO)_{o.o.p.}$	
	235.9(<0.1)[<1]	235.9(<0.1)[<1]		$\rho_t(F_{1A}As_{1A}F_{3A})_{o.o.p.} + \rho_t(F_{2B}As_{1A}F_{4B})_{o.o.p.} + \rho_t(F_{2BA}As_{1A}F_{4BA})_{o.o.p.}$	
	234.1(<0.1)[<1]	234.1(<0.1)[<1]		$\rho_t(F_2As_1F_4)_{i.p.} + \rho_t(F_{2A}As_AF_{4A})_{i.p.}$	
	232.9(<0.1)[<0.1]	232.9(<0.1)[<0.1]		$\rho_t(F_{1A}As_{1A}F_{3A})_{i.p.} + \rho_t(F_{2B}As_{1A}F_{4B})_{o.o.p.} + \rho_t(F_{2BA}As_{1A}F_{4BA})_{o.o.p.}$	
	229.2(<0.1)[<1]	229.2(<0.1)[<1]		$\rho_t(F_1As_1F_3)_{i.p.} + \rho_t(F_2As_1F_4)_{o.o.p.} + \rho_t(F_{2A}As_1F_{4A})_{o.o.p.}$	$\nu_6(T_{2u})$ $[AsF_6]^-$
	225.3(<0.1)[<1]	225.3(<0.1)[<1]		$\rho_t(F_{2B}As_{1A}F_{4B})_{i.p.} + \rho_t(F_{2BA}As_{1A}F_{4BA})_{i.p.}$	
	225.0(<0.1)[2]	225.0(<0.1)[2]		$\rho_t(F_1As_1F_3)_{o.o.p.} + \rho_t(F_2As_1F_4)_{o.o.p.} + \rho_t(F_{2A}As_1F_{4A})_{o.o.p.}$	
196.3(16)				Lattice modes	
	219.7(<1)[19]	219.6(<1)[18]	0.1	$[\delta(F_5Xe_1F_6)_{o.o.p.} - \delta(F_{5A}Xe_{1A}F_{6A})_{o.o.p.}]$	
	208.6(<1)[38]	208.5(<1)[38]	0.1	$[\delta(F_5Xe_1F_6)_{i.p.} + \delta(F_{5A}Xe_{1A}F_{6A})_{i.p.}]$	
	206.6(<1)[<1]	206.5(<1)[<1]	0.1	$[\delta(F_5Xe_1F_6)_{i.p.} - \delta(F_{5A}Xe_{1A}F_{6A})_{i.p.}]$	

continued…

Table A2.2. (continued)

2	**2′**			**assgnts** [d]
exptl [a]	^{35}Cl calcd [b]	^{37}Cl calcd [b]	Δν [c]	
	155.8(<1)[<1]	155.5(<1)[<1]	0.3	Deformation modes
	132.9(1)[5]	131.9(1)[4]		
	127.2(4)[7]	126.5(3)[7]	0.7	
	116.8(2)[27]	116.3(2)[27]	0.5	
	103.0(5)[<1]	103.0(5)[<1]		
	82.6(1)[<1]	82.5(1)[<1]	0.1	
	71.7(3)[2]	71.6(3)[2]	0.1	
	66.9(<1)[15]	66.6(<1)[15]	0.3	
	61.4(2)[<1]	61.3(2)[<1]	0.1	
	52.6(<0.1)[<1]	52.6(<0.1)[<1]		
	52.4(<1)[2]	52.3(<1)[2]	0.1	
	49.6(<1)[3]	49.6(<1)[3]		
	43.0(<1)[<1]	43.0(<1)[<1]		
	36.4(<1)[2]	36.4(<1)[2]		
	29.3(<1)[<1]	29.3(<0.1)[<1]		
	29.3(<0.1)[<1]	29.3(<1)[<1]		
	18.2(<0.1)[<1]	18.2(<1)[<1]		
	14.9(<1)[1]	14.9(<1)[1]		
	13.2(<1)[1]	13.2(<0.1)[<1]		
	11.8(<0.1)[<1]	11.8(<0.1)[<1]		
	−22.6(<1)[<0.1]	−22.6(<0.1)[<1]		

continued…

Table A2.2. (continued) [a] The Raman spectrum was recorded on dry crystals in a FEP sample tube at −150 °C using 1064-nm excitation. Lattice modes were observed at 101.6(7), 111.4(20), 113.7(20), 120.0(25), 133.5(16), 137.6(18), and 144.1(23) cm^{-1}. Values in parentheses denote relative Raman intensities. Abbreviations denote shoulder (sh). [b] B3LYP/Def2-TZVPD. The atom labeling scheme is the same as that shown in Figure 2b. Values in parentheses and square brackets denote calculated Raman intensities ($Å^4$ amu^{-1}) and infrared intensities (km mol^{-1}), respectively. [c] $\Delta\nu^{35/37} = \nu(^{35}Cl) - \nu(^{37}Cl)$. [d] Assignments are made under O_h symmetry for the $[AsF_6]^-$ anion in this table. Abbreviations denote stretch (ν), bend (δ), symmetric (s), asymmetric (as), equatorial (eq), axial (ax), in-plane (i.p.), and out-of-plane (o.o.p.). The "plane" refers to the *bc*-mirror plane in the crystal structure of **2** which the $[ClO_2]^+$ cation lies in.

Figure A2.5. Factor-group analysis of $[O_2Cl(FXeF)_2][AsF_6]$ (**2**) [a]

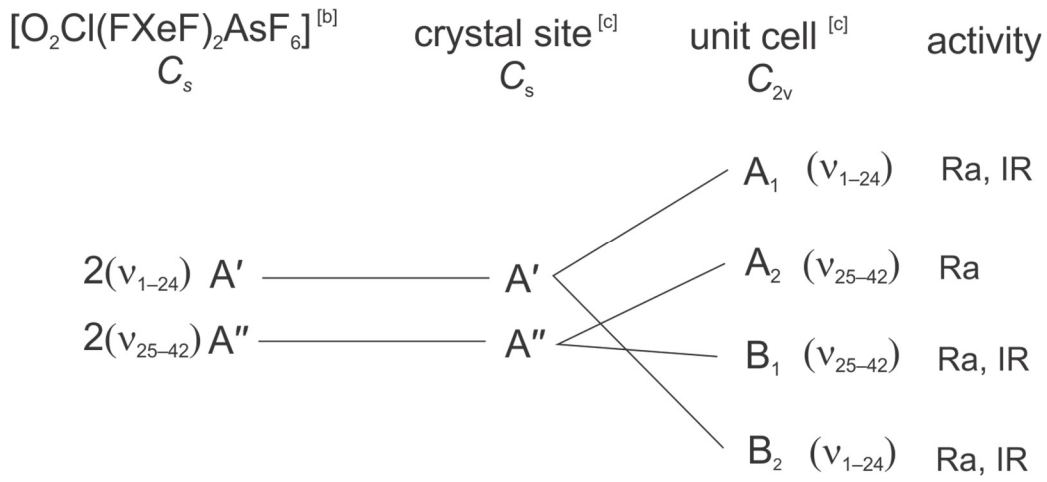

[a] The external modes have not been treated in this analysis. [b] The vibrational irreducible representation for $[O_2Cl(FXeF)_2][AsF_6]$ (**2**) (C_s) is $\Gamma = 24A' + 18A''$. [c] Space group; $Cmc2_1$, $Z = 4$. The number of molecules contributing to the total number of vibrational modes for a *C*-centered unit cell is equal to $^{Z}/_{2}$ (ref. S1, pp. 2–4).

Table A2.3. Calculated [a] geometric parameters for $[XO_2]^+$ (X = Cl, Br, I) (C_{2v})

	$[ClO_2]^+$ [b]	**$[BrO_2]^+$ [b]**	**$[IO_2]^+$ [b]**
Bond Lengths (Å)			
X–O (Å)	1.4090	1.5884	1.7606
Bond Angles (deg)			
O-X-O (°)	121.49	115.51	110.25

[a] B3LYP/Def2-TZVPD.

Table A2.4. Calculated [a] vibrational frequencies, intensities, and assignments for $[XO_2]^+$ (X = Cl, Br, I)

	$[ClO_2]^+$ [b]	Δν [b]	$[BrO_2]^+$ [b]	Δν [b]	$[IO_2]^+$ [b]	assgnts (C_{2v}) [c]
^{35}Cl / ^{79}Br	1382.3(5)[68]		1028.8(8)[22]			
^{37}Cl / ^{81}Br	1366.8(5)[65]	15.5	1026.0(7)[22]	2.8	923(11)[16]	$\nu_3(B_1)$, $\nu_{as}(XO_2)$
^{35}Cl / ^{79}Br	1119.2(30)[6]		949.8(32)[<0.1]			
^{37}Cl / ^{81}Br	1113.3(30)[6]	5.9	948.5(32)[<0.1]	1.3	887(37)[<0.1]	$\nu_1(A_1)$, $\nu_s(XO_2)$
^{35}Cl / ^{79}Br	521.8(2)[21]		364.6(3)[13]			
^{37}Cl / ^{81}Br	517.7(2)[20]	4.1	363.8(3)[13]	0.8	294(4)[13]	$\nu_2(A_1)$, δ(OXO)

[a] B3LYP/Def2-TZVPD. [b] Frequencies are given in cm^{-1}. Values in parentheses and square brackets denote calculated Raman intensities ($Å^4$ amu^{-1}) and infrared intensities (km mol^{-1}), respectively. [c] Abbreviations denote stretch (ν), and bend (δ).

Table A2.5. Calculated [a] geometrical parameters and frequencies for XeF_2

Xe-F	ν_1 [b]	ν_2 [b]	ν_3 [b]
2.0065	541(0)[248]	503(47)[0]	205(0)[16]

[a] B3LYP/Def2-TZVPD. [b] Frequencies are given in cm^{-1}. Values in parentheses and square brackets denote calculated Raman intensities ($Å^4$ amu^{-1}) and infrared intensities (km mol^{-1}), respectively.

Table A2.6. Natural population analysis (NPA) charges, valence indices, and Wiberg bond indices for $([O_2Cl(FXeF)_2][AsF_6]_2)^{-}$ [a]

Bond Indices		NPA Charges [Valence Indices]		
Cl1−O1	1.559	Cl1	1.895	[3.320]
Cl1−O2	1.559	O1	−0.541	[2.069]
Cl1---F5	0.081	O2	−0.540	[2.070]
Cl1---F5A	0.081			
Cl1---F1A	0.012			
Cl1---F4	0.004			
Cl1---F4A	0.004			
		$\sum_{[ClO_2]^+}$	**0.814**	
As1–F1	0.544	As1	2.804	[3.165]
As1–F2	0.549	F1	−0.621	[0.659]
As1–F2A	0.549	F2	−0.618	[0.663]
As1–F3	0.542	F2A	−0.618	[0.663]
As1–F4	0.488	F3	−0.623	[0.657]
As1–F4A	0.488	F4	−0.659	[0.606]
		F4A	−0.659	[0.606]
		$\sum_{[As_{(1)}F_6]^-}$	**−0.994**	
As1A–F1A	0.458	As1A	2.801	[3.167]
As1A–F2B	0.540	F1A	−0.674	[0.589]
As1A–F2BA	0.540	F2B	−0.624	[0.656]
As1A–F3A	0.556	F2BA	−0.624	[0.656]
As1A–F4B	0.534	F3A	−0.614	[0.670]
As1A–F4BA	0.534	F4B	−0.628	[0.650]
		F4BA	−0.628	[0.650]
		$\sum_{[As_{(1A)}F_6]^-}$	**−0.991**	
Xe1–F5	0.391	Xe1	1.274	[0.999]
Xe1–F6	0.582	F5	−0.561	[0.670]
		F6	−0.627	[0.701]
		$\sum_{Xe_{(1)}F_2}$	**0.086**	
Xe1A–F5A	0.391	Xe1A	1.274	[0.999]
Xe1A–F6A	0.582	F5A	–0.561	[0.670]
		F6A	–0.627	[0.701]
		$\sum_{Xe_{(1A)}F_2}$	**0.086**	
		$\sum_{total}$	**−0.999**	

[a] B3LYP/Def2-TZVPD.

Table A2.7. Natural population analysis (NPA) charges, Wiberg valences, and Wiberg bond indices for $[XO_2]^+$ (C_{2v}) (X = Cl, Br, I)[a]

Bond Indices		NPA Charges [Valences]		
		$[ClO_2]^+$		
Cl−O	1.659	Cl	1.789	[3.317]
Cl−O	1.659	O	−0.394	[2.202]
		O	−0.394	[2.202]
		$\sum_{[ClO_2]^+}$	**1.001**	
		$[BrO_2]^+$		
Br−O	1.539	Br	2.001	[3.078]
Br−O	1.539	O	−0.500	[2.073]
		O	−0.500	[2.073]
		$\sum_{[BrO_2]^+}$	**1.001**	
		$[IO_2]^+$		
I−O	1.504	I	2.347	[3.008]
I−O	1.504	O	−0.673	[1.930]
		O	−0.673	[1.930]
		$\sum_{[IO_2]^+}$	**1.001**	

[a] B3LYP/Def2-TZVPD.

Table A2.8. Natural population analysis (NPA) charges, Wiberg valences, and Wiberg bond indices for XeF_2 ($D_{\infty h}$)[a]

Bond Indices		NPA Charges [Valences]		
		XeF_2		
Xe−F_t	0.518	Xe	1.207	[1.037]
Xe−F_t	0.518	F_t	−0.604	[0.650]
		F_t	−0.604	[0.650]
		$\sum_{XeF_2}$	**−0.001**	

[a] B3LYP/Def2-TZVPD.

References

[1] Fateley, W. G.; Dollish, F. R.; McDevitt, N. T.; Bentley, F. F. Infrared and Raman selection rules for molecular and lattice vibrations: The Correlation Method, Wiley, New York, 1972.

APPENDIX 3

Chapter 6 Supporting Information

Syntheses and Structural Characterizations of $[ClO_2]_2[cyclo\text{-}(\mu\text{-}OIrF_4)_3]$ and the Coordination Complex, $F_5Ir\text{---}OClF$

Table A3.1. Experimental geometric parameters for $[ClO_2]_2[cyclo\text{-}(\mu\text{-}OIrF_4)_3]$

Bond Lengths (Å)			
Cl(1)–O(1)	1.409(3)	Ir(1)–O(3)	1.861(2)
Cl(1)–O(2)	1.409(3)	Ir(1)–F(1)	1.883(2)
Cl(1)---F(1A)	3.106(2)	Ir(2)–F(2)	1.910(2)
Cl(1)---F(2)	2.557(2)	Ir(2)–O(3)	1.851(2)
Cl(1)---F(3B)	2.548(2)	Ir(2)–O(4)	1.8479(13)
Cl(1)---F(7C)	2.588(2)	Ir(2)–F(3)	1.923(2)
Cl(1)---F(5D)	2.722(2)	Ir(2)–F(4)	1.911(2)
Cl(1)---F(6)	3.174(2)	Ir(2)–F(5)	1.895(2)
		Ir(2)–F(6)	1.884(2)

Bond Angles (°)			
O(1)–Cl(1)–O(2)	118.7(2)	F(1)–Ir(1)–F(1A)	86.70(14)
O(1)–Cl(1)---F(1A)	60.71(13)	F(1)–Ir(1)–F(2)	86.82(9)
O(1)–Cl(1)---F(2)	89.65(14)	F(1)–Ir(1)–F(2A)	88.59(10)
O(1)–Cl(1)---F(3B)	91.96(13)	F(1A)–Ir(1)–F(2)	88.59(10)
O(1)–Cl(1)---F(7C)	86.62(14)	F(1A)–Ir(1)–F(2A)	86.82(09)
O(1)–Cl(1)---F(5D)	151.48(14)	F(2)–Ir(1)–F(2A)	173.69(14)
O(1)–Cl(1)---F(6)	111.55(13)	O(3)–Ir(2)–O(4)	94.19(14)
O(2)–Cl(1)---F(1A)	82.90(14)	O(3)–Ir(2)–F(3)	90.12(10)
O(2)–Cl(1)---F(2)	117.36(13)	O(3)–Ir(2)–F(4)	174.26(10)
O(2)–Cl(1)---F(3B)	91.97(13)	O(3)–Ir(2)–F(5)	93.86(11)
O(2)–Cl(1)---F(7C)	148.16(15)	O(3)–Ir(2)–F(6)	90.41(11)
O(2)–Cl(1)---F(5D)	82.66(14)	O(4)–Ir(2)–F(3)	175.22(14)
O(2)–Cl(1)---F(6)	54.90(12)	O(4)–Ir(2)–F(4)	90.61(13)
		O(4)–Ir(2)–F(5)	92.11(8)
O(3)–Ir(1)–O(3A)	92.49(16)	O(4)–Ir(2)–F(6)	93.75(8)
O(3)–Ir(1)–F(1)	177.00(11)	F(3)–Ir(2)–F(4)	85.19(9)
O(3)–Ir(1)–F(1A)	90.41(10)	F(3)–Ir(2)–F(5)	85.55(10)
O(3)–Ir(1)–F(2)	93.90(10)	F(3)–Ir(2)–F(6)	88.26(11)
O(3)–Ir(1)–F(2A)	90.47(10)	F(4)–Ir(2)–F(5)	89.09(10)
O(3A)–Ir(1)–F(1)	90.41(10)	F(4)–Ir(2)–F(6)	86.14(10)
O(3A)–Ir(1)–F(1A)	177.00(11)	F(5)–Ir(2)–F(6)	172.48(10)
O(3A)–Ir(1)–F(2)	90.47(10)	Ir(1)–O(3)–Ir(2)	141.62(15)
O(3A)–Ir(1)–F(2A)	93.90(10)	Ir(2)–O(4)–Ir(2A)	142.1(2)
Ir(1)–O(3)–Ir(2)–O(4)	−38.1(2)	Ir(2)–O(4)–Ir(2A)–O(3A)	11.94(8)

[a] The labeling scheme is the same as in Figure 6.3.

Table A3.2. Calculated[a] geometric parameters for [*cyclo*-(μ-$OIrF_4$)$_3$]$^{2-}$ (C_1)

Bond Lengths (Å)			
Ir(1)–O(3)	1.851	Ir(1)–O(3A)	1.851
Ir(1)–F(1)	1.895	Ir(1)–F(1A)	1.895
Ir(1)–F(2)	1.897	Ir(1)–F(2A)	1.886
Ir(2)–O(3)	1.897	Ir(2A)–O(3A)	1.897
Ir(2)–O(4)	1.873	Ir(2A)–O(4)	1.872
Ir(2)–F(3)	1.879	Ir(2A)–F(3A)	1.879
Ir(2)–F(4)	1.900	Ir(2A)–F(4A)	1.900
Ir(2)–F(5)	1.882	Ir(2A)–F(5A)	1.888
Ir(2)–F(6)	1.888	Ir(2A)–F(6A)	1.882

Bond Angles (°)			
O(3)–Ir(1)–O(3A)	92.37	F(3)–Ir(2)–F(4)	88.36
O(3)–Ir(1)–F(1)	177.36	F(3)–Ir(2)–F(5)	87.67
O(3)–Ir(1)–F(1A)	90.06	F(3)–Ir(2)–F(6)	89.05
O(3)–Ir(1)–F(2)	92.95	F(4)–Ir(2)–F(5)	88.36
O(3)–Ir(1)–F(2A)	90.71	F(4)–Ir(2)–F(6)	88.07
O(3A)–Ir(1)–F(1)	90.04	F(5)–Ir(2)–F(6)	175.22
O(3A)–Ir(1)–F(1A)	177.34	Ir(1)–O(3)–Ir(2)	141.36
O(3A)–Ir(1)–F(2)	92.95	Ir(2)–O(4)–Ir(2A)	140.50
O(3A)–Ir(1)–F(2A)	90.71	O(3A)–Ir(2A)–O(4)	90.32
F(1)–Ir(1)–F(1A)	87.51	O(3A)–Ir(2A)–F(3A)	89.47
F(1)–Ir(1)–F(2)	87.99	O(3A)–Ir(2A)–F(4A)	177.39
F(1)–Ir(1)–F(2A)	88.18	O(3A)–Ir(2A)–F(5A)	90.45
F(1A)–Ir(1)–F(2)	88.00	O(3A)–Ir(2A)–F(6A)	93.00
F(1A)–Ir(1)–F(2A)	88.18	O(4)–Ir(2A)–F(3A)	178.17
F(2)–Ir(1)–F(2A)	174.71	O(4)–Ir(2A)–F(4A)	91.90
O(3)–Ir(2)–O(4)	90.30	O(4)–Ir(2A)–F(5A)	92.77
O(3)–Ir(2)–F(3)	89.48	O(4)–Ir(2A)–F(6A)	90.53
O(3)–Ir(2)–F(4)	177.41	F(3A)–Ir(2A)–F(4A)	88.36
O(3)–Ir(2)–F(5)	92.99	F(3A)–Ir(2A)–F(5A)	89.05
O(3)–Ir(2)–F(6)	90.45	F(3A)–Ir(2A)–F(6A)	87.67
O(4)–Ir(2)–F(3)	178.17	F(4A)–Ir(2A)–F(5A)	88.07
O(4)–Ir(2)–F(4)	91.90	F(4A)–Ir(2A)–F(6A)	88.36
O(4)–Ir(2)–F(5)	90.52	F(5A)–Ir(2A)–F(6A)	175.22
O(4)–Ir(2)–F(6)	92.77	Ir(1)–O(3A)–Ir(2A)	141.34
Ir(1)–O(3)–Ir(2)–O(4)	-47.12	Ir(2)–O(4)–Ir(2A)–O(3A)	11.55

[a] uPBE1PBE/aug-cc-pVTZ(Ir)-Def2TZPVD-(O, F). The labeling scheme is the same as in Figure 6.3.

Table A3.3. Experimental and calculated geometric parameters for F_5Ir---OClF[a]

	exptl	calcd			exptl	calcd	
		Gaussian[b]	ADF[c]			Gaussian[b]	ADF[c]
Bond Lengths (Å)							
Cl(1)–O(1)	1.548(4)	1.513	1.520	Cl(2)–O(2)	1.548(3)	1.513	1.520
Cl(1)–F(1)	1.594(4)	1.611	1.622	Cl(2)–F(7)	1.600(3)	1.611	1.622
Ir(1)–F(2)	1.879(3)	1.895	1.867	Ir(2)–F(8)	1.867(3)	1.895	1.867
Ir(1)–F(3)	1.870(3)	1.842	1.869	Ir(2)–F(9)	1.864(3)	1.842	1.869
Ir(1)–F(4)	1.873(3)	1.875	1.851	Ir(2)–F(10)	1.874(3)	1.875	1.851
Ir(1)–F(5)	1.855(4)	1.830	1.854	Ir(2)–F(11)	1.885(3)	1.830	1.854
Ir(1)–F(6)	1.885(3)	1.844	1.844	Ir(2)–F(12)	1.879(3)	1.844	1.844
Ir(1)---O(1)	2.029(4)	2.066	2.073	Ir(2)---O(2)	2.028(3)	2.066	2.073
Cl(1)---F(12A)	2.659(3)			Cl(2)---F(6)	2.565(3)		
Cl(1)---F(4B)	2.749(3)			Cl(2)---F(11F)	2.587(3)		
Cl(1)---F(3C)	2.885(3)						
Bond Angles (°)							
O(1)–Cl(1)–F(1)	106.7(2)	106.67	108.39	O(2)–Cl(2)–F(7)	105.0(2)	106.67	108.39
O(1)---Ir(1)–F(2)	90.71(15)	85.68	85.65	O(2)---Ir(2)–F(8)	88.93(14)	85.68	85.65
O(1)---Ir(1)–F(3)	87.87(15)	86.77	87.29	O(2)---Ir(2)–F(9)	90.14(14)	86.77	87.29
O(1)---Ir(1)–F(4)	87.18(15)	92.42	89.36	O(2)---Ir(2)–F(10)	88.62(14)	92.42	89.36
O(1)---Ir(1)–F(5)	90.52(16)	85.77	87.81	O(2)---Ir(2)–F(11)	88.33(15)	85.77	87.81
O(1)---Ir(1)–F(6)	178.12(16)	178.91	178.17	O(2)---Ir(2)–F(12)	178.54(14)	178.91	178.17
F(2)–Ir(1)–F(3)	89.68(15)	88.88	87.82	F(8)–Ir(2)–F(9)	89.78(16)	88.88	87.82
F(2)–Ir(1)–F(4)	177.87(15)	177.87	174.92	F(8)–Ir(2)–F(10)	177.20(14)	177.87	174.92
F(2)–Ir(1)–F(5)	90.47(16)	89.61	91.12	F(8)–Ir(2)–F(11)	90.00(15)	89.61	91.12
F(2)–Ir(1)–F(6)	90.89(15)	93.55	92.53	F(8)–Ir(2)–F(12)	92.51(15)	93.55	92.53
F(3)–Ir(1)–F(4)	89.98(15)	90.05	91.05	F(9)–Ir(2)–F(10)	91.59(15)	90.05	91.05
F(3)–Ir(1)–F(5)	178.39(15)	172.48	175.05	F(9)–Ir(2)–F(11)	178.46(15)	172.48	175.05
F(3)–Ir(1)–F(6)	91.14(15)	93.99	87.82	F(9)–Ir(2)–F(12)	90.08(14)	93.99	87.82
F(4)–Ir(1)–F(5)	89.81(16)	91.21	92.79	F(10)–Ir(2)–F(11)	88.57(14)	91.21	92.79
F(4)–Ir(1)–F(6)	91.22(15)	88.37	89.58	F(10)–Ir(2)–F(12)	89.93(14)	88.37	89.58
F(5)–Ir(1)–F(6)	90.46(16)	93.46	92.47	F(11)–Ir(2)–F(12)	91.45(15)	93.46	92.47
Cl(1)–O(1)---Ir(1)	120.4(2)	116.47	92.09	Cl(2)–O(2)---Ir(2)	119.8(2)	116.47	92.09
Dihedral angles (°)							
Cl(1)–O(1)---Ir(1)–F(2)	11.0(3)	41.75	52.68	Cl(2)–O(2)---Ir(2)–F(8)	22.1(2)	41.75	52.68

[a] The labeling scheme is the same as shown in Figure 6.5. [b] uPBE1PBE/aug-cc-pVTZ-pp(Ir)-Def2-TZVPD-(O, F, Cl). [c] PBE0-D4/TZ2P. The calculation also includes collinear SOC.

Table A3.4. Calculated geometric parameters for gas-phase OClF

	Gaussian[a]	ADF[b]
Cl–O	1.4752	1.4851
Cl–F	1.6647	1.6800
O–Cl–F	110.24	110.57

[a] PBE1PBE/Def2-SVP-(F, O, Cl). [b] PBE0-D4/TZ2P. The calculation also includes collinear SOC.

Table A3.5. Calculated geometric parameters[a] for IrF_5 (C_{2v})[b] and IrF_5 (C_{4v})[c]

	Gaussian[b]	ADF[c]
Bond Lengths (Å)		
Ir(1)–F(1)	1.8168	1.8358
Ir(1)–F(2)	1.8240	1.8453
Ir(1)–F(3)	1.8750	1.8453
Ir(1)–F(4)	1.8240	1.8453
Ir(1)–F(5)	1.8750	1.8453
Bond Angles (°)		
F(1)–Ir(1)–F(2)	98.16	94.22
F(1)–Ir(1)–F(3)	91.34	94.22
F(1)–Ir(1)–F(4)	98.16	94.22
F(1)–Ir(1)–F(5)	91.34	94.22
F(2)–Ir(1)–F(3)	89.81	89.69
F(2)–Ir(1)–F(4)	163.67	171.56
F(2)–Ir(1)–F(5)	89.81	89.69
F(3)–Ir(1)–F(4)	89.81	89.69
F(3)–Ir(1)–F(5)	177.31	171.56
F(4)–Ir(1)–F(5)	89.81	89.69

[a] The labeling scheme is the same as shown in Figure A3.3. [b] uPBE1PBE/aug-cc-pVTZ-pp(Ir)-Def2-TZVPD-(F). [c] PBE0-D4/TZ2P. The calculation also includes collinear SOC.

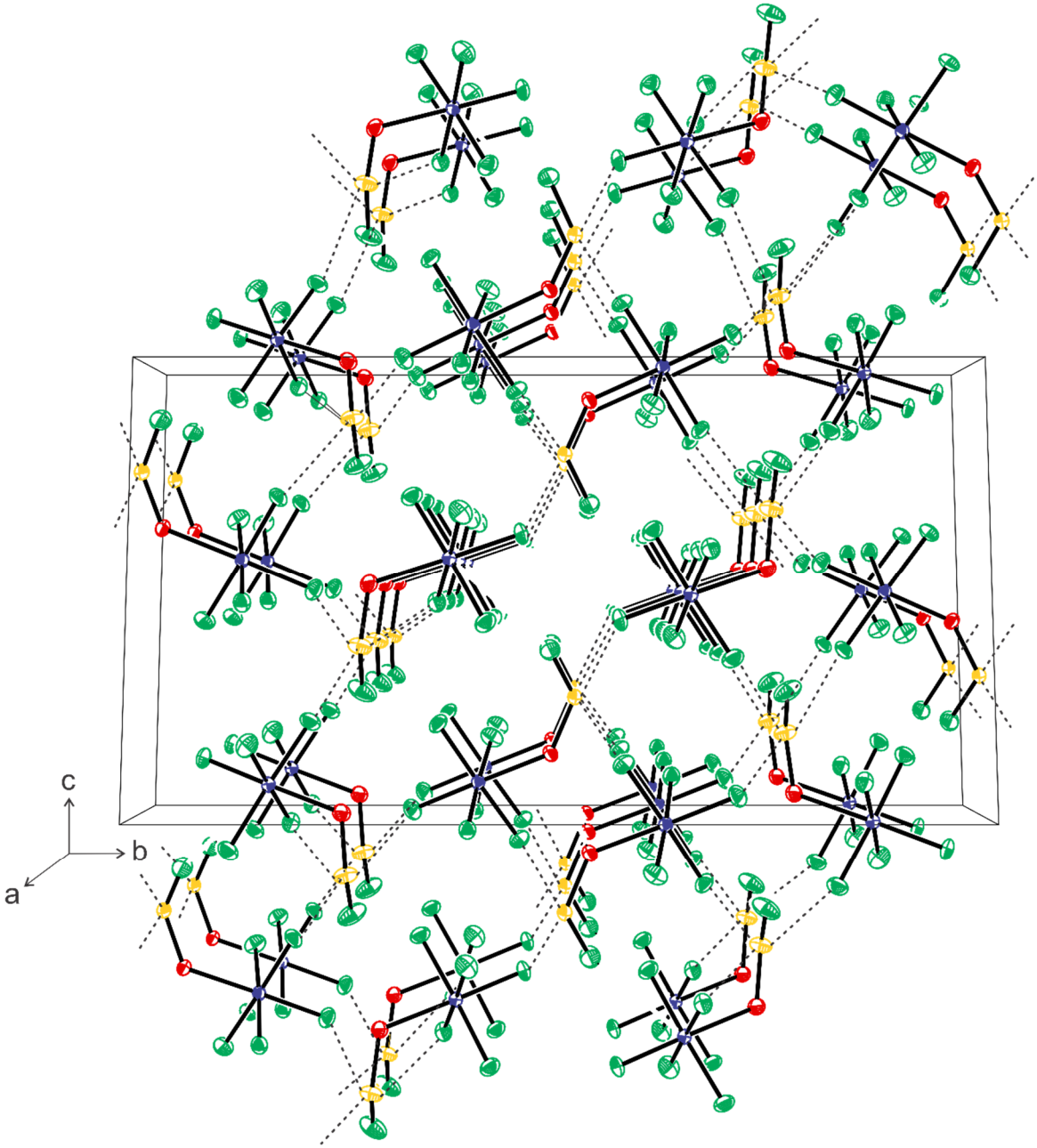

Figure A3.1. A packing diagram showing the X-ray crystallographic unit cell of F_5Ir---OClF (**2**) viewed along the *a*-axis. Thermal ellipsoids are drawn at the 50% probability level.

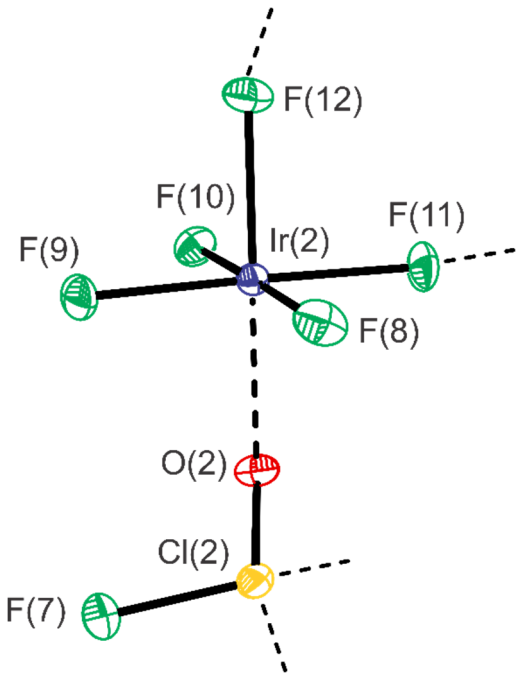

Figure A3.2. The second structural unit in the X-ray crystal structure of F_5Ir---OClF (**2**). The first structural unit is provided in Figure 6.5. Thermal ellipsoids are drawn at the 50% probability level and secondary Ir---O and Cl---F bonds are indicated by dashed lines.

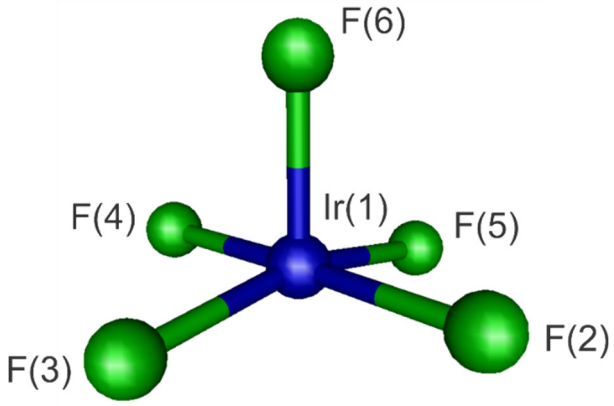

Figure A3.3. Calculated gas-phase geometry of IrF_5 (C_{2v}). uPBE1PBE/aug-cc-pVTZ-pp(Ir)-Def2-TZVPD-(F).

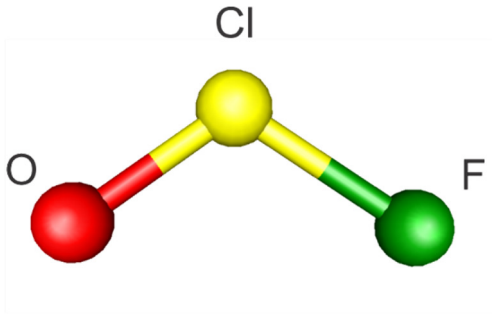

Figure A3.4. Calculated gas-phase geometry of OClF (C_s). PBE1PBE/Def2-TZVPD-(O, Cl, F).

Table A3.6. Calculated[a] vibrational frequencies,[b] intensities, and assignments for OClF

	assgnts [b]
1114(15)[82]	ν(Cl-O)
670(14)[130]	ν(Cl-F)
338(4)[8]	δ(OClF)

[a] PBE1PBE/Def2-TZVPD-(O, F, Cl). [b] Values in parentheses and square brackets denote calculated Raman intensities ($Å^4$ amu^{-1}) and infrared intensities (km mol^{-1}), respectively.

Table A3.7. Calculated[a] vibrational frequencies,[b] intensities, and assignments for IrF_5 (C_{2v})

	assgnts [b]
745(21)[16]	$\nu(Ir\text{-}F_1)$
726(<1)[194]	$\nu(Ir\text{-}F_1) - \nu(Ir\text{-}F_3)$
719(22)[18]	$\nu(Ir\text{-}F_1) - \nu(Ir\text{-}F_{2\text{-}5})$
684(<1)[210]	$\nu(Ir\text{-}F_2) - \nu(Ir\text{-}F_4)$
657(9)[<1]	$[\nu(Ir\text{-}F_2) + \nu(Ir\text{-}F_4)] - [\nu(Ir\text{-}F_2) + \nu(Ir\text{-}F_4)]$
270(<1)[8]	$\delta(F_2IrF_4)$
256(<1)[12]	$\delta_{umb}(IrF_{4eq})$
227(<1)[13]	$\delta(F_3IrF_5)$
224(2)[0]	$\delta(F_2IrF_3) - \delta(F_4IrF_5)$
169(<1)[1]	$\rho_w(F_2IrF_4) - \rho_w(F_3IrF_5)$
118(2)[<1]	$\delta(F_1IrF_2) - \delta(F_1IrF_4)$
85(1)[3]	$\delta(F_1IrF_3) - \delta(F_1IrF_5)$

[a] uPBE1PBE/aug-cc-pVTZ-pp(Ir)-Def2-TZVPD-(F). [b] Values in parentheses and square brackets denote calculated Raman intensities ($Å^4$ amu^{-1}) and infrared intensities (km mol^{-1}), respectively. The atom labeling scheme is the same as in Figure A3.3.

Table A3.8. Calculated[a] vibrational frequencies,[b] intensities, and assignments for F_5Ir---$OClF$

	assgnts [b]
972(28)[93]	$\nu(Cl_1\text{-}O_1)$
742(121)[137]	$\nu(Cl_1\text{-}F_2)$
714(16)[172]	$\nu(Ir_1\text{-}F_5) + \nu(Ir_1\text{-}F_6)$
701(5)[135]	$[\nu(Ir_1\text{-}F_4) + \nu(Cl_1\text{-}F_2)] - [\nu(Ir_1\text{-}F_6) + \nu(Ir_1\text{-}F_3)]$
685(18)[28]	$\nu(Ir_1\text{-}F_6) - [\nu(Ir_1\text{-}F_3) + \nu(Ir_1\text{-}F_4)]$
668(2)[153]	$\nu(Ir_1\text{-}F_2) - \nu(Ir_1\text{-}F_4)$
623(7)[17]	$[\nu(Ir_1\text{-}F_2) + \nu(Ir_1\text{-}F_4)] - [\nu(Ir_1\text{-}F_3) + \nu(Ir_1\text{-}F_5)]$
473(24)[16]	$\nu(Ir_1\text{---}O_1)$
369(3)[11]	$\delta(O_1Cl_1F_1)$
299(<1)[13]	$\delta_{umb}(IrF_{4eq})$
270(<1)[6]	$\delta(F_2Ir_1F_4) + \delta(F_3Ir_1F_5)$
243(1)[10]	$\delta(F_3Ir_1F_5) + \delta(F_5Ir_1F_6)$
236(<1)[8]	$\delta(F_3Ir_1F_5) - \delta(F_6Ir_1O_1)$
225(3)[<1]	$\delta(F_3Ir_1F_4) - \delta(F_2Ir_1F_5)$
206(<1)[2]	$\rho_t(F_2Ir_1F_3) + \rho_t(F_4Ir_1F_5)$
199(2)[<1]	$\delta(F_4Ir_1F_6) + \rho_t(F_2Ir_1F_5)$
187(3)[1]	$\rho_t(F_4Ir_1F_5)$
162(<1)[<1]	$\rho_w(F_6Ir_1O_1)$
106(<1)[5]	$\delta(Cl_1O_1Ir_1)$
82(1)[2]	$\rho_w(O_1Cl_1F_1) + \rho_r(IrF_5)$
52(<1)[<1]	$\rho_r(O_1Cl_1F_1) + \rho_r(IrF_5)$

[a] uPBE1PBE/aug-cc-pVTZ-pp(Ir)-Def2-TZVPD-(O, F, Cl). [b] Values in parentheses and square brackets denote calculated Raman intensities ($Å^4$ amu^{-1}) and infrared intensities (km mol^{-1}), respectively. The atom labeling scheme is the same as in Figure 6.5.

Table A3.9. Wiberg bond indices, natural population analysis (NPA) charges, and valence indices for OClF

Bond Indices		NPA Charges [Valence Indices]		
Cl−O	1.519	Cl	1.081	[2.199]
Cl−F	0.679	O	−0.667	[1.734]
		F	−0.414	[0.894]
		$\sum_{OClF}$	**0.000**	

[a] PBE1PBE/Def2-TZVPD-(O, F, Cl).

Table A3.10. Wiberg bond indices, natural population analysis (NPA) charges, and valence indices for IrF_5 (C_{2v})

Bond Indices		NPA Charges [Valence Indices]		
Ir1−F1	0.857	Ir1	2.212	[3.519]
Ir1−F2	0.730	F1	−0.345	[1.006]
Ir1−F3	0.601	F2	−0.421	[0.994]
Ir1−F4	0.730	F3	−0.512	[0.834]
Ir1−F5	0.601	F4	−0.421	[0.994]
		F5	−0.512	[0.834]
		$\sum_{IrF5}$	**0.001**	

[a] uPBE1PBE/aug-cc-pVTZ-pp(Ir)-Def2-TZVPD-(F). The atom labeling scheme is the same as in Figure A3.3.

Table A3.11. Wiberg bond indices, natural population analysis (NPA) charges, and valence indices for [*cyclo*-(μ-OIrF$_4$)$_3$]$^{2-}$ (C_1)

Bond Indices		NPA Charges [Valence Indices]		
Ir1−O3	0.852	Ir1	2.042	[4.102]
Ir1−O3A	0.852	Ir2	2.032	[3.937]
Ir1−F1	0.513	Ir2A	2.032	[3.937]
Ir1−F1A	0.513	F1	−0.541	[0.801]
Ir1−F2	0.523	F1A	−0.541	[0.801]
Ir1−F2A	0.543	F2	−0.542	[0.793]
Ir2−O3	0.683	F2A	−0.521	[0.824]
Ir2−O4	0.765	F3	−0.516	[0.842]
Ir2−F3	0.556	F3A	−0.516	[0.842]
Ir2−F4	0.500	F4	−0.550	[0.776]
Ir2−F5	0.565	F4A	−0.550	[0.776]
Ir2−F6	0.579	F5	−0.521	[0.825]
Ir2A−O3A	0.684	F5A	−0.507	[0.846]
Ir2A−O4	0.766	F6	−0.507	[0.847]
Ir2A−F3A	0.556	F6A	−0.521	[0.825]
Ir2A−F4A	0.500	O3	−0.581	[2.106]
Ir2A−F5A	0.579	O3A	−0.580	[2.106]
Ir2A−F6A	0.565	O4	−0.613	[2.088]
		$\sum_{\text{total}}$	**−2.001**	

[a] uPBE1PBE/aug-cc-pVTZ-pp(Ir)-Def2-TZVPD-(O, F). The atom labeling scheme is the same as in Figure 6.3.

Table A3.12. Wiberg bond indices, natural population analysis (NPA) charges, and valence indices for F_5Ir---OClF

Bond Indices		NPA Charges [Valence Indices]		
Ir1−F2	0.547	Ir1	2.099	[3.651]
Ir1−F3	0.675	F2	−0.545	[0.789]
Ir1−F4	0.616	F3	−0.456	[0.945]
Ir1−F5	0.719	F4	−0.496	[0.853]
Ir1−F6	0.703	F5	−0.418	[0.999]
Ir1---O1	0.338	F6	−0.424	[0.943]
		$\sum_{\mathbf{IrF5}}$	**−0.240**	
Cl1−O1	1.287	Cl1	1.210	[2.166]
Cl1−F1	0.794	O1	−0.634	[1.940]
Cl1---F2	0.140	F1	−0.336	[0.974]
Cl1---F3	0.050	$\sum_{\mathbf{OClF}}$	**0.240**	
		$\sum_{\mathbf{total}}$	**−0.000**	

[a] uPBE1PBE/aug-cc-pVTZ-pp(Ir)-Def2-TZVPD-(O, Cl, F). The atom labeling scheme is the same as in Figure 6.5.

APPENDIX 4

Chapter 7 Supporting Information

Noble-Gas Difluoride Complexes of MOF_4 (M = Mo, W); $NgF_2 \cdot MOF_4$ (Ng = Kr, Xe), and $XeF_2 \cdot 2MOF_4$; and the HF Solvate, $[--(F_4OMo)(\mu_3\text{-}F)H---(\mu\text{-}F)H--]_\infty$

Adapted with permission from: Bortolus, M. R.; Mercier, H. P. A.; Brock, D. S.; Schrobilgen, G. J. *Chem. Eur. J.* **2022**, *28*, e202103729.

Table of Contents **Page(s)**

Table of Contents (continued) **Page(s)**

Syntheses, Properties, and Crystal Growth

Attempted Syntheses of F_tXeF_b---$W(OF_3)$–F_b'---$Mo(O)F_4$. The reaction of a 1:1:1 molar mixture of XeF_2, $MoOF_4$, and WOF_4 in a melt (65 °C) and in $CFCl_3$ solution (RT) only yielded colorless, needle-shaped crystals of $XeF_2 \cdot WOF_4$ and $(MoOF_4)_4$, which were confirmed by LT Raman spectroscopy and unit cell determinations.

[--(F_4OMo)(μ_3-F)H---(μ-F)H--]$_\infty$ (7). In an attempt to synthesize $KrF_2 \cdot 2MoOF_4$, two equiv. of $MoOF_4$ and one equiv. of KrF_2 were allowed to react in aHF solvent at −35 °C, followed by immediate quenching at −196 °C. The sample was warmed to −78 °C, whereupon two distinct white precipitates formed. When allowed to stand at −78 °C for ca. 4 h, the precipitates formed discrete layers in the FEP reaction vessel. The Raman spectrum of the bottom layer was consistent with the known $KrF_2 \cdot MoOF_4$ complex,[S1] whereas the Raman spectrum of the top layer exhibited two new ν(Mo-O) stretching bands (1031, 1041 cm^{-1}) and several new ν(Mo-F) stretching bands (657, 688, 702, 715 cm^{-1}).

Following redissolution of the precipitates at −35 °C, crystals were grown by slow cooling from −35 to −65 °C over ca. 6 h and were mounted for SCXRD. The bulk crystalline sample was comprised of nearly equal amounts of $KrF_2 \cdot MoOF_4$ and the HF solvate, [--(F_4OMo)(μ_3-F)H---(μ-F)H--]$_\infty$ (**7**), which were confirmed by unit cell determinations and SCXRD (**7**). A sample of $MoOF_4$ was dissolved in aHF at RT [Eq. (**A4.1**)], and the Raman spectrum of the resulting white precipitate was obtained at −150 °C, which was identical to the spectrum of the sample that yielded crystalline [--(F_4OMo)(μ_3-F)H---(μ-F)H--]$_\infty$ (Figure A4.1 and Table A4.1).

$$MoOF_4 + 2HF \longrightarrow [\text{--}(F_4OMo)(\mu_3\text{-}F)H\text{---}(\mu\text{-}F)H\text{--}]_\infty \qquad (\mathbf{A4.1})$$

Attempted Synthesis of [--(F_4OW)(μ_3-F)H---(μ-F)H--]$_\infty$. Reaction of WOF_4 with aHF at room temperature over a period of ca. 10 min followed by slow removal aHF solvent at −78 °C yielded a white precipitate which was shown by LT (−150 °C) Raman spectroscopy to correspond to unreacted WOF_4.

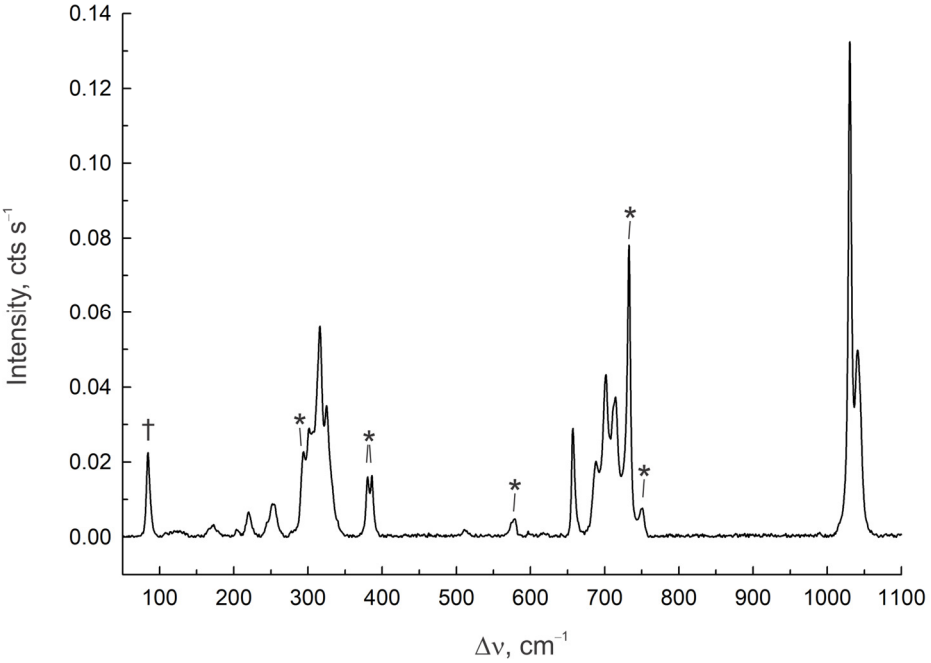

Figure A4.1. Raman spectrum of [--(F_4OMo)(μ_3-F)H---(μ-F)H--]$_\infty$ recorded at −150 °C using 1064-nm excitation. The symbols denote FEP sample tube bands (*) and an instrumental artifact (†).

Table A4.1. Experimental Raman frequencies and intensities, and tentative assignments for [--(F_4OMo)(μ_3-F)H---(μ-F)H--]$_\infty$

	assgnts
1041(38) 1031(100)	ν(Mo–O)
715(29)	[ν(Mo-F_1) + ν(Mo-F_4)] – [ν(Mo-F_2) + ν(Mo-F_3)]
702(34) 688(16)	[ν(Mo-F_1) + ν(Mo-F_2)]
657(22)	[ν(Mo-F_3) + ν(Mo-F_4)]
511(2)	ν(Mo-$F_{(HF)}$)
325(27)	[δ(F_1MoF_4) + δ(F_2MoF_3)]
316(43)	[δ(OMoF_1F_2) – δ(OMoF_3F_4)]
301(23)	[δ(OMoF_2F_3) – δ(OMoF_1F_4)]
252(7)	δ(Mo$F_{(4)}$)$_{umb}$
220(5)	[δ(F_1MoF_2) – δ(F_3MoF_4)]
173(2)	[δ(F_1MoF_4) – δ(F_2MoF_3)]

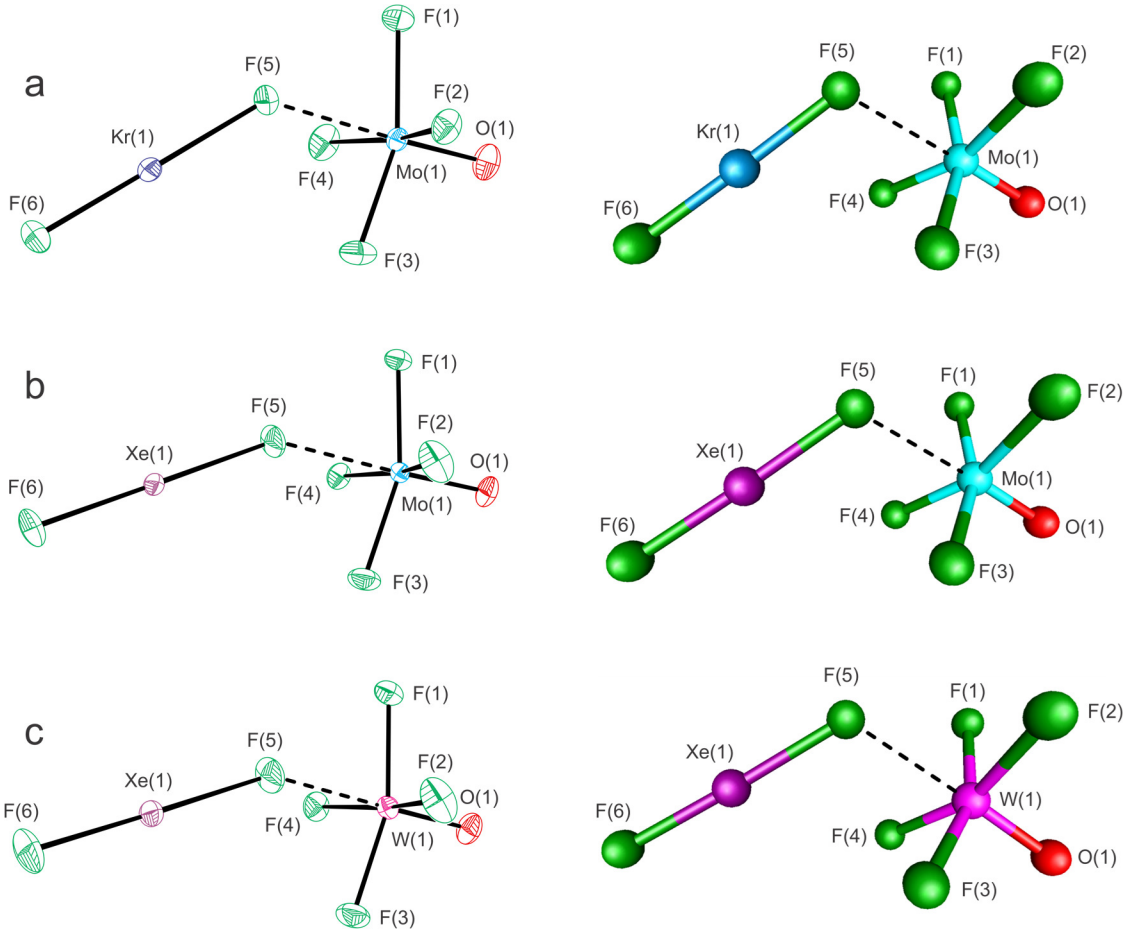

Figure A4.2. The X-ray crystal structures (left, near-eclipsed conformations) of (a) $KrF_2 \cdot MoOF_4$, (b) $XeF_2 \cdot MoOF_4$, and (c) $XeF_2 \cdot WOF_4$, with thermal ellipsoids drawn at the 50% probability level, and their structures calculated at the APFD/Def2-TZVPD level of theory (right, staggered conformations).

Table A4.2. Experimental and calculated geometric parameters for $KrF_2 \cdot MOF_4$ (M = Mo, W)

	$KrF_2 \cdot MoOF_4$			**$KrF_2 \cdot WOF_4$**		
	exptl	calcd (C_s)[a]		exptl	calcd (C_s)[a]	
		APFD	B3LYP		APFD	B3LYP
			Bond Lengths (Å)			
M(1)–O(1)	1.6508(12)	1.643	1.654	1.679(3)	1.674	1.684
M(1)–F(1)	1.8444(9)	1.833	1.848	1.853(2)	1.849	1.863
M(1)–F(2)	1.8562(8)	1.833	1.848	1.856(2)	1.849	1.863
M(1)–F(3)	1.8400(9)	1.853	1.864	1.852(2)	1.868	1.879
M(1)–F(4)	1.8425(9)	1.853	1.864	1.8620(19)	1.868	1.879
M(1)---F(5)	2.2473(9)	2.416	2.461	2.217(2)	2.405	2.411
Kr(1)–F(5)	1.9653(9)	1.926	1.945	1.989(2)	1.935	1.957
Kr(1)–F(6)	1.8202(9)	1.834	1.857	1.805(2)	1.829	1.850
			Bond Angles (deg)			
F(5)–Kr(1)–F(6)	179.19(5)	178.8	178.8	178.84(11)	178.8	178.7
Kr(1)–F(5)---M(1)	134.33(5)	114.2	120.9	135.22(12)	114.5	122.0
O(1)–M(1)–F(1)	100.60(6)	102.6	102.5	100.68(13)	102.2	102.0
O(1)–M(1)–F(2)	99.65(5)	102.6	102.5	99.75(13)	102.2	102.0
O(1)–M(1)–F(3)	101.21(6)	102.2	102.2	100.85(14)	101.9	101.7
O(1)–M(1)–F(4)	99.91(5)	102.2	102.2	99.49(12)	101.9	101.7
O(1)–M(1)---F(5)	177.87(5)	178.1	178.6	177.91(12)	177.9	178.6
F(1)–M(1)–F(2)	87.26(4)	88.7	88.5	89.22(12)	88.8	88.6
F(1)–M(1)–F(3)	158.14(5)	155.2	155.3	158.44(12)	155.8	156.2
F(1)–M(1)–F(4)	89.57(5)	87.6	87.6	87.30(11)	87.7	87.8
F(1)–M(1)---F(5)	77.28(4)	78.8	78.5	77.37(10)	79.2	79.0
F(2)–M(1)–F(3)	87.73(4)	87.6	87.6	88.37(12)	87.7	87.8
F(2)–M(1)–F(4)	160.44(5)	155.2	155.3	160.76(11)	155.8	156.2
F(2)–M(1)---F(5)	80.09(4)	78.8	78.5	81.04(11)	79.2	79.0
F(3)–M(1)–F(4)	88.07(5)	85.6	85.9	87.95(11)	85.7	86.1
F(3)–M(1)---F(5)	80.90(4)	76.5	76.8	81.09(10)	76.6	77.3
F(4)–M(1)---F(5)	80.39(4)	76.5	76.8	79.73(9)	76.6	77.3
			Dihedral Angles (deg)			
$Kr–F_{(5)}---M–F_{(1)}$	14.34(7)	44.3	44.4	16.1(2)	44.4	44.4
			Intermolecular Contacts (Å)			
O···F	3.021(3)			3.033(6)		
F···F	2.732(2)			2.731(5)		

[a] Calculated at the APFD/Def2-TZVPD and B3LYP/aVTZ(-PP)(Xe)/Def2-TZVPD(O, F)/def2-TZVPD(-PP)(Mo, W) levels of theory.

Table A4.3. Experimental and calculated geometric parameters for $XeF_2 \cdot MOF_4$ (M = Mo, W)

	$XeF_2 \cdot MoOF_4$			$XeF_2 \cdot WOF_4$		
	exptl	calcd (C_s)[a]		exptl	calcd (C_s)[a]	
		APFD	B3LYP		APFD	B3LYP
			Bond Lengths (Å)			
M(1)–O(1)	1.6492(14)	1.643	1.654	1.677(3)	1.676	1.685
M(1)–F(1)	1.8479(12)	1.833	1.848	1.858(3)	1.849	1.863
M(1)–F(2)	1.8435(12)	1.833	1.848	1.850(3)	1.849	1.863
M(1)–F(3)	1.8396(12)	1.856	1.866	1.846(3)	1.870	1.881
M(1)–F(4)	1.8524(11)	1.856	1.866	1.862(3)	1.870	1.881
M(1)---F(5)	2.2352(12)	2.389	2.420	2.199(3)	2.378	2.375
Xe(1)–F(5)	2.0813(12)	2.048	2.072	2.102(3)	2.058	2.085
Xe(1)–F(6)	1.9369(12)	1.955	1.981	1.929(3)	1.951	1.975
			Bond Angles (deg)			
F(5)–Xe(1)–F(6)	178.35(6)	178.3	178.6	178.32(15)	178.3	178.5
Xe(1)–F(5)---M(1)	148.09(7)	116.8	125.1	150.57(18)	117.2	126.1
O(1)–M(1)–F(1)	100.03(7)	102.4	102.1	100.10(16)	102.0	101.7
O(1)–M(1)–F(2)	100.00(7)	102.4	102.1	100.43(17)	102.0	101.7
O(1)–M(1)–F(3)	100.46(7)	101.9	101.8	99.71(16)	101.6	101.3
O(1)–M(1)–F(4)	98.45(6)	101.9	101.8	98.02(15)	101.6	101.3
O(1)–M(1)---F(5)	178.09(6)	177.7	178.4	178.12(15)	177.5	178.3
F(1)–M(1)–F(2)	89.28(6)	89.0	88.7	89.36(15)	89.0	88.8
F(1)–M(1)–F(3)	159.47(6)	155.7	156.0	160.14(14)	156.3	156.9
F(1)–M(1)–F(4)	88.09(6)	87.7	87.7	87.39(14)	87.8	87.9
F(1)–M(1)---F(5)	78.45(5)	79.3	79.0	78.98(13)	79.7	79.5
F(2)–M(1)–F(3)	88.37(6)	87.7	87.7	88.45(15)	87.8	87.9
F(2)–M(1)–F(4)	161.54(6)	155.7	156.0	161.56(15)	156.3	156.9
F(2)–M(1)---F(5)	81.18(6)	79.3	79.0	81.24(14)	79.7	79.5
F(3)–M(1)–F(4)	87.72(6)	85.6	86.0	88.46(13)	85.6	86.2
F(3)–M(1)---F(5)	81.03(6)	76.5	77.1	81.18(14)	76.6	77.4
F(4)–M(1)---F(5)	80.39(5)	76.5	77.1	80.32(13)	76.6	77.4
			Dihedral Angles (deg)			
$Xe–F_{(5)}$---$M–F_{(1)}$	7.55(6)	44.3	44.4	5.9(2)	44.3	44.4
			Intermolecular Contacts (Å)			
O···F	3.021(3)			3.033(6)		
F···F	2.732(2)			2.731(5)		

[a] Calculated at the APFD/Def2-TZVPD and B3LYP/aVTZ(-PP)(Xe)/Def2-TZVPD(O, F)/def2-TZVPD(-PP)(Mo, W) levels of theory.

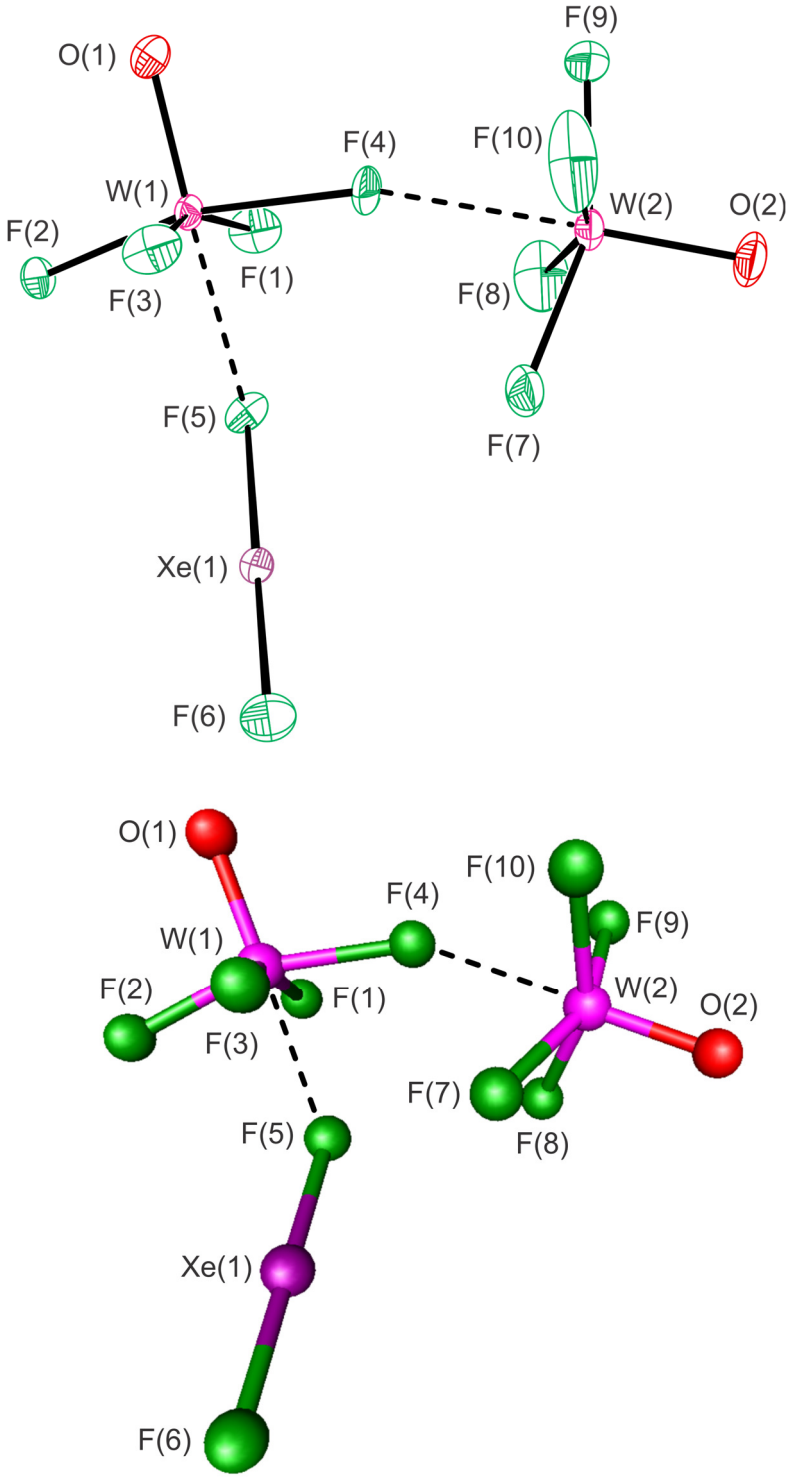

Figure A4.3. The X-ray crystal structure (top) of $XeF_2 \cdot 2WOF_4$ and its calculated geometry (bottom, APFD/def2TZVPD level of theory). Thermal ellipsoids are drawn at the 50% probability level.

Table A4.4. Experimental and calculated parameters for $XeF_2 \cdot 2MOF_4$ (M = Mo, W)

	$XeF_2 \cdot 2MoOF_4$			$XeF_2 \cdot 2WOF_4$		
	exptl	calcd (C_s)[a]		exptl	calcd (C_i)[a]	
		APFD	B3LYP		APFD	B3LYP
			Bond Lengths (Å)			
Xe(1)–F(5)	2.1153(10)	2.059	2.090	2.136(4)	2.072	2.110
Xe(1)–F(6)	1.9283(10)	1.950	1.973	1.922(4)	1.944	1.966
M(1)---F(5)	2.1980(9)	2.339	2.355	2.177(4)	2.321	2.305
M(1)–O(1)	1.6461(12)	1.640	1.651	1.660(5)	1.672	1.682
M(1)–F(1)	1.8285(10)	1.822	1.839	1.828(4)	1.842	1.855
M(1)–F(2)	1.8208(10)	1.827	1.842	1.825(4)	1.846	1.855
M(1)–F(3)	1.8456(10)	1.849	1.860	1.848(4)	1.859	1.874
M(1)–F(4)	1.9350(10)	1.897	1.907	1.929(4)	1.909	1.930
M(2)---F(4)	2.2990(10)	2.426	2.520	2.313(4)	2.416	2.450
M(2)–O(2)	1.6432(12)	1.642	1.653	1.662(6)	1.673	1.682
M(2)–F(7)	1.8398(12)	1.837	1.850	1.837(5)	1.851	1.865
M(2)–F(8)	1.8370(13)	1.861	1.870	1.841(5)	1.873	1.887
M(2)–F(9)	1.8238(12)	1.838	1.851	1.835(5)	1.855	1.866
M(2)–F(10)	1.8315(12)	1.835	1.846	1.839(5)	1.847	1.860
			Bond Angles (deg)			
F(5)–Xe(1)–F(6)	178.85(4)	178.4	178.5	178.06(19)	177.9	178.2
Xe(1)–F(5)---M(1)	130.84(5)	125.6	131.7	131.70(19)	123.8	133.9
O(1)–M(1)---F(5)	177.42(5)	178.5	178.7	176.9(2)	179.1	178.5
O(1)–M(1)–F(1)	100.74(6)	102.2	102.4	101.0(2)	101.8	101.7
O(1)–M(1)–F(2)	99.57(6)	101.2	100.7	99.3(2)	100.9	100.2
O(1)–M(1)–F(3)	99.21(5)	101.9	101.9	98.8(2)	101.5	101.3
O(1)–M(1)–F(4)	96.23(5)	99.3	99.1	96.4(2)	99.33	98.7
F(1)–M(1)–F(2)	92.16(5)	90.9	90.3	92.5(2)	90.8	90.7
F(1)–M(1)–F(3)	158.51(5)	155.4	155.4	158.6(2)	156.4	156.7
F(1)–M(1)–F(4)	85.78(5)	86.8	86.9	85.8(2)	86.7	86.7
F(2)–M(1)–F(3)	92.30(5)	88.9	88.9	92.3(2)	89.5	89.3
F(2)–M(1)–F(4)	164.18(5)	159.4	160.1	164.3(2)	159.7	161.0
F(3)–M(1)–F(4)	84.22(5)	84.9	85.6	84.0(2)	85.9	85.8
F(5)---M(1)–F(1)	79.91(4)	78.6	78.3	80.27(17)	78.7	79.1
F(5)---M(1)–F(2)	82.88(4)	80.0	80.4	83.51(19)	79.8	81.0
F(5)---M(1)–F(3)	79.81(4)	77.2	77.3	79.54(16)	78.0	77.9
F(5)---M(1)–F(4)	81.31(4)	79.5	79.8	80.80(18)	80.0	80.0

continued…

Table A4.4. (continued)

	$XeF_2 \cdot 2MoOF_4$			$XeF_2 \cdot 2WOF_4$		
	exptl	calcd (C_s)[a]		exptl	calcd (C_i)[a]	
		APFD	B3LYP		APFD	B3LYP
			Bond Angles (deg)			
O(2)–M(2)---F(4)	178.51(6)	179.6	179.1	178.5(2)	179.5	179.3
O(2)–M(2)–F(7)	100.09(6)	102.6	102.5	100.1(3)	102.2	102.0
O(2)–M(2)–F(8)	99.81(6)	101.6	102.2	100.9(3)	101.3	101.4
O(2)–M(2)–F(9)	100.94(7)	102.0	102.9	101.8(3)	102.0	102.0
O(2)–M(2)–F(10)	100.08(6)	102.5	102.6	100.6(3)	102.0	102.0
F(4)---M(2)–F(7)	79.51(5)	77.2	76.6	78.9(2)	77.3	77.9
F(4)---M(2)–F(8)	78.75(5)	78.1	77.6	78.0(2)	78.8	77.9
F(4)---M(2)–F(9)	79.46(5)	78.1	78.0	79.3(2)	78.4	78.2
F(4)---M(2)–F(10)	81.35(5)	77.8	77.6	80.5(2)	77.9	78.6
F(7)–M(2)–F(8)	88.06(7)	86.6	86.7	88.1(3)	86.8	86.8
F(7)–M(2)–F(9)	158.97(6)	155.3	154.6	158.2(3)	155.6	156.0
F(7)–M(2)–F(10)	87.89(7)	88.5	88.2	87.9(3)	88.8	88.5
F(8)–M(2)–F(9)	88.25(7)	86.4	86.3	87.7(3)	86.2	86.6
F(8)–M(2)–F(10)	160.10(6)	155.9	155.2	158.5(2)	156.7	156.6
F(9)–M(2)–F(10)	88.57(7)	88.2	88.1	88.2(3)	88.4	88.5
Mo(1)–F(4)---M(2)	159.02(6)	145.8	131.4	159.5(2)	145.6	164.8
			Dihedral Angles (deg)			
Xe–$F_{(5)}$---M–$F_{(3)}$	7.19(7)	1.4	3.5	2.3(3)	24.1	2.6
			Intermolecular Contacts (Å)			
O···F	2.929(2)			2.912(4)		
F···F	2.828(2)			2.867(4)		

[a] Calculated at the APFD/def2-TZVPD and B3LYP/aVTZ(-PP)(Xe)/Def2-TZVPD(O, F)/def2-TZVPD(-PP)(Mo, W) levels of theory.

Table A4.5. Experimental geometric parameters for [--(F_4OMo)(μ_3-F)H---(μ-F)H--]$_\infty$

Bond Lengths (Å)	
Mo(1)–O(1)	1.6500(19)
Mo(1)–F(1)	1.8541(14)
Mo(1)–F(2)	1.8875(14)
Mo(1)–F(3)	1.8427(14)
Mo(1)–F(4)	1.8456(15)
Mo(1)---F(5)	2.1527(14)
F(5)---F(6)	2.511(2)

Bond Angles (deg)	
O(1)–Mo(1)–F(1)	99.46(8)
O(1)–Mo(1)–F(2)	97.03(8)
O(1)–Mo(1)–F(3)	98.60(9)
O(1)–Mo(1)–F(4)	98.69(9)
O(1)–Mo(1)---F(5)	179.54(8)
F(1)–Mo(1)–F(2)	86.84(7)
F(1)–Mo(1)–F(3)	161.59(7)
F(1)–Mo(1)–F(4)	89.88(7)
F(1)–Mo(1)---F(5)	80.58(6)
F(2)–Mo(1)–F(3)	87.41(7)
F(2)–Mo(1)–F(4)	164.26(7)
F(2)–Mo(1)---F(5)	82.51(6)
F(3)–Mo(1)–F(4)	90.93(8)
F(3)–Mo(1)---F(5)	81.33(6)
F(4)–Mo(1)---F(5)	81.76(6)
Mo(1)---F(5)---F(6)	110.91(6)
O···F	2.859(2)
F···F	2.664(2)

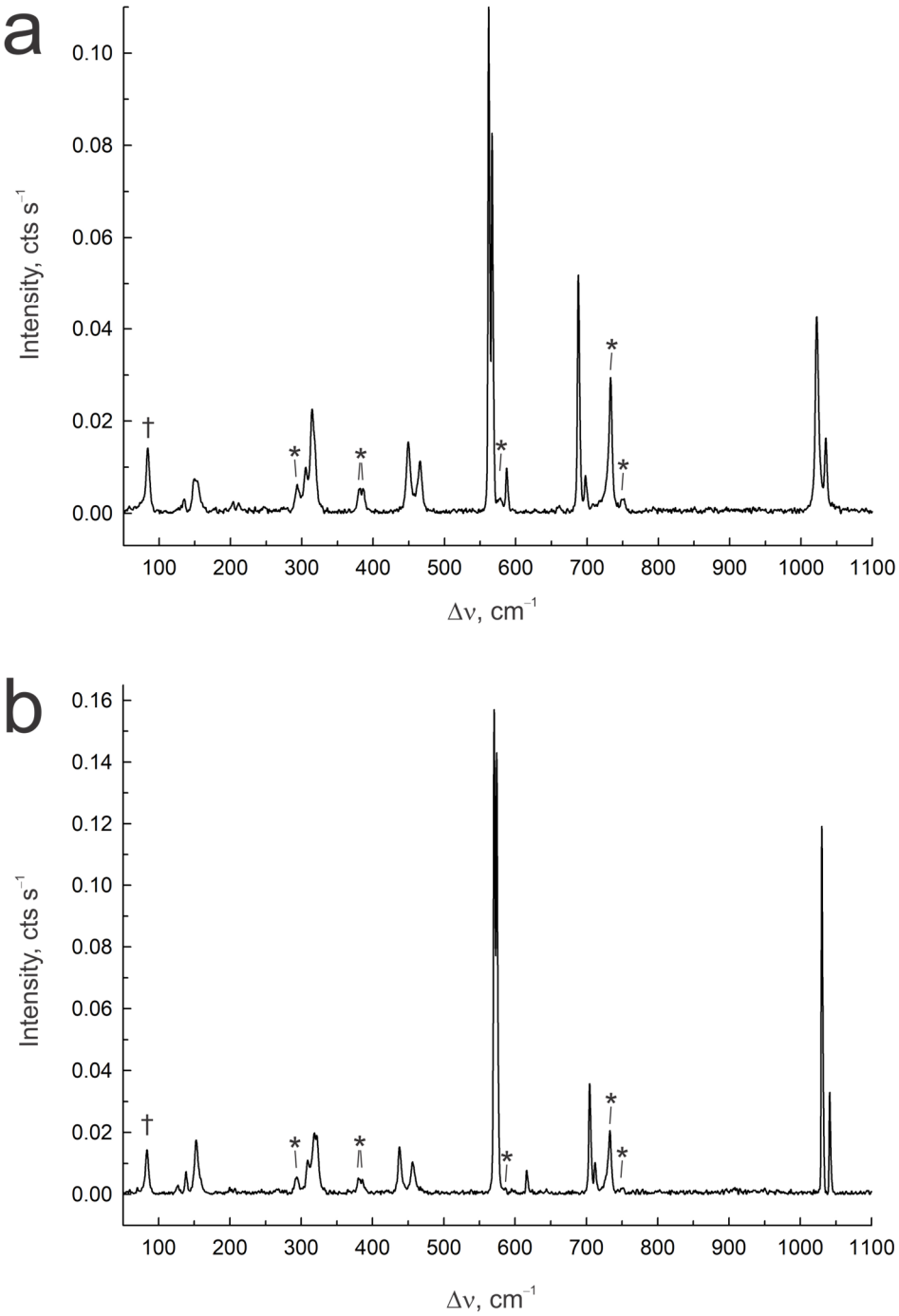

Figure A4.4. Raman spectra of (a) $XeF_2 \cdot MoOF_4$ and (b) $XeF_2 \cdot WOF_4$ recorded at −150 °C using 1064-nm excitation. The symbols denote FEP sample tube bands (*) and an instrumental artifact (†).

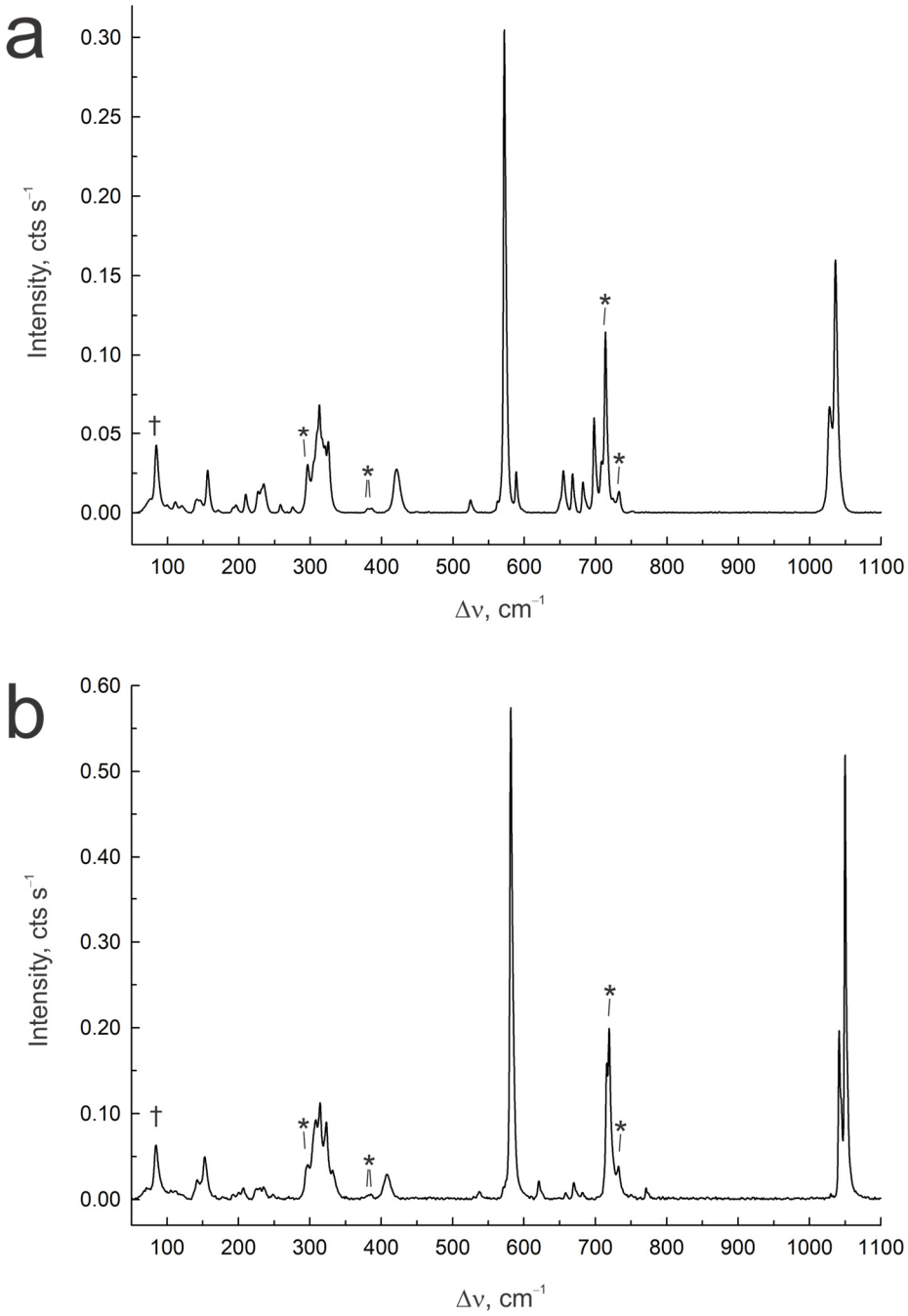

Figure A4.5. Raman spectra of (a) $XeF_2 \cdot 2MoOF_4$ and (b) $XeF_2 \cdot 2WOF_4$ recorded at −150 °C using 1064-nm excitation. The symbols denote FEP sample tube bands (*) and an instrumental artifact (†).

Raman Discussion (continued)

The Raman spectra of $NgF_2 \cdot MOF_4$ and $XeF_2 \cdot 2MOF_4$ (Ng = Kr, Xe; M = Mo, W) (Figures A4.4 and A4.5) have been re-examined in this work to provide more precise descriptions and assignments of the vibrational modes based on the calculated vibrational frequencies and atomic displacements of **1'**–**6'** (Tables A4.6–A4.8).

In a prior study,[S1] the assignments of the Raman spectra of $NgF_2 \cdot MOF_4$ were based on the observed geometry in the crystal structure of $XeF_2 \cdot WOF_4$, which was the only crystal structure of a Group 6 oxide tetrafluoride complex with a noble-gas fluoride then available,[S2] whereas the Raman spectra of $XeF_2 \cdot 2MOF_4$ were assigned assuming a *trans, trans*-isomer deduced from solution ^{19}F NMR studies.[S1,S3] The vibrational assignments were mainly made by comparison with assignments for MOF_4, $[MOF_5]^-$, $[M_2O_2F_9]^-$, $[Xe_2F_3]^+$, and NgF_2 that were available at that time. The present Raman assignments for $NgF_2 \cdot MOF_4$ and $XeF_2 \cdot 2MOF_4$ were made by comparison with the calculated gas-phase vibrational frequencies and Raman intensities for their energy-minimized geometries. The calculated gas-phase geometries of $XeF_2 \cdot 2MOF_4$ correspond to the *cis, trans*-isomers observed in their crystal structures. The vibrational assignments for $NgF_2 \cdot MOF_4$ were also aided by comparison with the experimental and calculated vibrational frequencies of the chromium analogue, $NgF_2 \cdot CrOF_4$.[S4] Notable improvements relating to the assignments of stretching and deformation modes that involve the NgF_2 ligands of $NgF_2 \cdot MOF_4$ and $XeF_2 \cdot 2MOF_4$ have been made in the present study. Overall, the vibrational frequency trends are well reproduced by the

calculations. Only the main contributions to the vibrational modes are considered in the following discussion.

$NgF_2 \cdot MOF_4$ (Ng = Kr, Xe; M = Mo, W). The previously published Raman spectra of $KrF_2 \cdot MOF_4$ (M = Mo, W) were recorded at −196 °C[S1] and are of very good quality and showed many of the vibrational bands that are predicted to be weak as well as many of the predicted factor-group splittings (vide infra and Tables A4.6 and A4.7). The published Raman spectra of $XeF_2 \cdot MOF_4$ (M = Mo, W) were also of very good quality, although they were recorded at −108 °C.[S1] They were also recorded at −150 °C in the present work, which improved the Raman spectra of these complexes (Figures A4.4a and A4.4b, Tables A4.6 and A4.7).

The splittings observed on many of the $NgF_2 \cdot MOF_4$ bands were originally correctly attributed to factor-group splittings based on the crystal structure of $XeF_2 \cdot WOF_4$.[S2] Determinations of the isotypic crystal structures of $KrF_2 \cdot MOF_4$ and $XeF_2 \cdot MoOF_4$ in the present study confirmed the previously published vibrational assignments and their factor-group splittings (vide infra).

In accordance with the calculated vibrational frequencies, the ν(Mo-O) and ν(W-O) stretching bands occur at essentially the same frequencies in $NgF_2 \cdot MoOF_4$ (calcd: 1090 (Kr) and 1089 (Xe) cm^{-1}; exptl: 1025/1034 (Kr) and 1022/1035 (Xe) cm^{-1}) and $NgF_2 \cdot WOF_4$ (calcd: 1068 (Kr) and 1067 (Xe) cm^{-1}; exptl: 1034/1041 (Kr) and 1030/1041 (Xe) cm^{-1}). Although the ν(Mo-O) stretches are expected to occur at higher frequencies than the ν(W-O) stretches, in accordance with the calculated bond length

trend, Mo–O < W–O, and the relative atomic masses of Mo and W; the ν(Mo-O) stretches occur at lower frequencies than the ν(W-O) stretches.

The ν(Ng-F_b) and ν(Ng-F_t) stretching frequencies occur at similar frequencies in $KrF_2 \cdot MOF_4$ (calcd: 580 and 477 (Mo), and 583 and 470 (W) cm^{-1}; exptl: 566/579 and 462/479 (Mo), and 571/581 and 450/469 (W) cm^{-1}) and in $XeF_2 \cdot MOF_4$ (calcd: 551 and 472 (Mo), and 556 and 462 (W) cm^{-1}; exptl: 562/567 and 449/466 (Mo) and 571/574 and 437/466 (W) cm^{-1}) complexes. These frequencies are in the same range as those of $NgF_2 \cdot CrOF_4$.[S4] In the earlier Raman spectroscopic study of the $NgF_2 \cdot MOF_4$ complexes,[S1] (i) the bands at 462, 466, 450, and 458 cm^{-1} were misassigned to ν(M-F_{ax}); instead, they are one of the two components of the factor-group split ν(Ng-F_b) bands and (ii) one component of the factor-group split ν(Xe-F_t) band of $XeF_2 \cdot MoOF_4$ at 567 cm^{-1} has now been reassigned, and occurs at lower frequency than was previously reported (575 cm^{-1}). The most intense component of the factor-group split ν(Xe-F_t) band is observed at 562 cm^{-1} compared to 566 cm^{-1} in the previous study.

Coordination of NgF_2 to MOF_4 results in in-plane, $\delta(F_5NgF_6)_{i.p.}$, and out-of-plane, $\delta(F_5NgF_6)_{o.o.p.}$, bending modes that are expected to be very weak. Only $\delta(F_5XeF_6)_{i.p.}$ (277 (Mo) and 274 (W) cm^{-1}) and $\delta(F_5XeF_6)_{o.o.p.}$ (241 (W) cm^{-1}) were observed, in good agreement with their calculated values (288, 286, and 239 cm^{-1}, respectively). Most bands below 300 cm^{-1} were incorrectly assigned in the earlier study.[S1]

$XeF_2 \cdot 2MOF_4$ (M = Mo, W). Acquisition of new Raman spectra at −150 °C for $XeF_2 \cdot 2MOF_4$ (M = Mo, W) in the present study compared to −109 °C (Mo) and −100 °C (W) in the previous study,[S1] resulted in enhanced spectral resolution. In accordance with

the predicted factor-group splittings (Figures A4.5a and A4.5b, and Table A4.8), most of the bands in the −150 °C spectra of $XeF_2 \cdot 2MOF_4$ are flanked by shoulders.

Table A4.6. Experimental (Raman) and calculated vibrational frequencies, intensities, and assignments for $NgF_2 \cdot MoOF_4$ (Ng = Kr, Xe)

$KrF_2 \cdot MoOF_4$						$XeF_2 \cdot MoOF_4$			
exptl[a,b]	calcd[a,c]			assgnts (C_s)[d]	calcd[a,c]		exptl[a,b]	
[e]	APFD	B3LYP			APFD	B3LYP	[e]	[f]
1034(12) 1025(33)	1118(42)[184]	1090(46)[175]	A′	ν(Mo-O)	1117(43)[190]	1089(48)[181]	1036(12) 1024(35)	1035(15) 1022(39)
698(7) 691(63)	725(12)[142]	706(12)[151]	A′	[ν(Mo-F_1) + ν(Mo-F_2)]	724(12)[138]	704(12)[147]	698(8) 689(47)	698(8) 689(47)
702(5)	713(<1)[267]	696(<1)[264]	A″	[ν(Mo-F_1) + ν(Mo-F_4)] − [ν(Mo-F_2) + ν(Mo-F_3)]	711(<1)[259]	694(<1)[261]	716(1)	709(2)
661(2)	698(6)[206]	684(7)[178]	A′	[ν(Mo-F_3) + ν(Mo-F_4)]	694(5)[206]	680(7)[180]	662(<1)	661(2)
582(16)	608(3)[8]	594(4)[6]	A″	[ν(Mo-F_1) + ν(Mo-F_3)] − [ν(Mo-F_2) + ν(Mo-F_4)]	605(3)[9]	591(4)[6]	588(9)	590, sh 587(9)
579(53) 566(100)	600(19)[220]	580(17)[226]	A′	ν(Ng-F_6) − ν(Kr-F_5)$_{small}$	572(28)[155]	551(30)[160]	575(75) 566(100)	567(74) 562(100)
479(40) 462(59)	496(42)[71]	477(54)[61]	A′	[ν(Ng-F_5) − ν(Mo-F_5)]	487(22)[132]	472(34)[132]	466(12) 451(16)	466(10) 449(14)
312(36)	321(2)[8]	315(2)[1]	A′	[δ(F_1MoF_4) + δ(F_2MoF_3)]	320(2)[<1]	314(2)[4]	316(24)	318, sh 314(21)
303(15)	311(2)[11] 313(3)[7]	311(4)[7] 310(3)[8]	A′ A″	[δ(OMoF_1F_2) − δ(OMoF_3F_4)] [δ(OMoF_2F_3) − δ(OMoF_1F_4)]	318(4)[9] 313(3)[8]	311(4)[5] 311(3)[8]	307(10)	306(8) 300, sh
[g]	322(3)[8]	294(2)[5]	A′	δ(F_5NgF_6)$_{i.p.}$ − (δ(Mo$F_{(4)}$)$_{umb}$)$_{small}$	308(1)[13]	288(1)[8]	277(1)	
260(1)	267(<1)[74]	250(<1)[80]	A′	δ(Mo$F_{(4)}$)$_{umb}$ + (δ(F_5NgF_6)$_{i.p.}$)$_{small}$	266(<1)[85]	243(<1)[83]	251(1)	
	260(<0.1)[19]	248(<0.1)[20]	A″	δ(F_5NgF_6)$_{o.o.p.}$ − [δ(F_1MoF_4) − δ(F_2MoF_3)]$_{small}$	248(<1)[22]	241(<1)[22]		
226(7) 220, sh	229(<1)[9]	225(<1)[12]	A′	[δ(F_1MoF_2) − δ(F_3MoF_4)]	227(<1)[9]	220(<1)[20]	212(2)	212(2)
210(4)	221(<1)[4]	216(<1)[2]	A″	[δ(F_1MoF_4) − δ(F_2MoF_3)] + (δ(F_5NgF_6)$_{o.o.p.}$)$_{small}$	206(<1)[<1]	200(<1)[<0.1]	204(2)	204(2)
155(8)	164(<1)[<1]	152(<1)[<1]	A″	[ρ_t(F_1MoF_2) − ρ_t(F_3MoF_4)]	164(<1)[<1]	154(<1)[<1]	152(10)	154(6)

continued …

Table A4.6. (continued)

$KrF_2 \cdot MoOF_4$					$XeF_2 \cdot MoOF_4$			
140(8)	160(2)[3]	134(3)[9]	A′	$[\rho_t(F_5NgF_6) - \rho_r(MoOF_{(4)})_{small}]$	143(2)[2]	126(2)[5]	136(5)	135(3)
	120(<1)[1]	114(<1)[1]	A″	$[\rho_t(F_5NgF_6) - \rho_t(MoOF_{(4)})]$	118(<1)[2]	114(<1)[2]		
	109[<1][<1]	99(<1)[2]	A′	$[\rho_r(MoOF_{(4)}) + \rho_r(F_5KrF_6)_{small}]$	108[<1][<1]	99(<1)[1]		
	61(<1)[<1]	44(1)[<1]	A′	$\delta(MoF_5Ng)_{i.p.}$	61(<1)[<1]	42(<1)[<1]		
	36(1)[<0.1]	17(1)[<0.1]	A″	$[\rho_t(F_5NgF_6) + \rho_t(MoOF_{(4)})]$	36(1)[<0.1]	16(<1)[<0.1]		
174, sh 170(20) 130(6) 116(2) 84, sh 79(17) 72(15) 69, sh 60(5) 52(30) 37(12) 29(6)				lattice modes			119(9) 74(5) 55(18) 46(17) 39(14) 31(16)	

continued …

Table A4.6. (continued) [a] Frequencies are given in cm^{-1}. [b] Values in parentheses denote relative Raman intensities. The abbreviation denotes a shoulder (sh). [c] Values in parentheses and square brackets denote calculated Raman intensities ($Å^4$ amu^{-1}) and infrared intensities (km mol^{-1}), respectively. Assignments are for the energy-minimized gas-phase geometry (C_s) calculated using the APFD/def2-TZVPD(O, F, Kr)/def2-TZVPD(-PP)(Mo, Xe) and the B3LYP/aVTZ(-PP)(Kr, Xe)/Def2-TZVPD(O, F)/def2-TZVPD(-PP)(Mo) levels of theory. [d] Abbreviations denote stretch (ν), bend (δ), rock (ρ_r), twist (ρ_t), and wag (ρ_w), umbrella (umb), $MoOF_{(4)}$ ($Mo_1O_1F_1F_2F_3F_4$), in-plane (i.p.), and out-of-plane (o.o.p.). Bond elongations and angle openings are denoted by plus (+) signs, and bond contractions and angle compressions are denoted by minus (−) signs. The in-plane and out-of-plane bending modes are relative to the $O_1Mo_1F_5Ng_1F_6$-plane, where the atom labeling scheme corresponds to that used in Figure A4.2. [e] From ref [S1]; the frequencies have been reassigned. Bands previously observed at 546(3) and 509(0.5) cm^{-1} were previously assigned to $XeF_2 \cdot MoOF_4$ but were not observed in the present work. [f] Present work. The Raman spectrum was recorded in an FEP sample tube at −150 °C using 1064-nm excitation. [g] The band may overlap with an FEP sample tube band.

Table A4.7. Experimental (Raman) and calculated vibrational frequencies, intensities, and assignments for $KrF_2 \cdot WOF_4$ and $XeF_2 \cdot WOF_4$

$KrF_2 \cdot WOF_4$					$XeF_2 \cdot WOF_4$			
exptl[a,b]	calcd[a,c]		assgnts (C_s)[d]		calcd[a,b]		exptl[a,c]	
[e]	APFD	B3LYP			APFD	B3LYP	[e]	[f]
1041(8) 1034(45)	1093(41)[153]	1068(47)[147]	A′	ν(W-O)	1092(41)[158]	1067(48)[153]	1043(14) 1033(56)	1041(21) 1030(76)
712(4) 706(18)	723(13)[55]	704(14)[51]	A′	$[\nu(W\text{-}F_1) + \nu(W\text{-}F_2)] + [\nu(W\text{-}F_3) + \nu(W\text{-}F_4)]_{small}$	723(13)[57]	703(13)[53]	714(6) 706(8)	712(7) 705(23)
	688(<1)[206]	671(<1)[208]	A″	$[\nu(W\text{-}F_1) + \nu(W\text{-}F_4)] - [\nu(W\text{-}F_2) + \nu(W\text{-}F_3)]$	687(<1)[197]	669(<1)[204]		
	679(<1)[242]	664(<1)[231]	A′	$[\nu(W\text{-}F_3) + \nu(W\text{-}F_4)] - [\nu(W\text{-}F_1) + \nu(W\text{-}F_2)]_{small}$	676(<1)[231]	661(<1)[224]		
611(3)	628(2)[19]	614(3)[14]	A″	$[\nu(W\text{-}F_1) + \nu(W\text{-}F_3)] - [\nu(W\text{-}F_2) + \nu(W\text{-}F_4)]$	625(2)[21]	611(2)[16]	618(4)	616(5)
581(45) 571(100)	603(23)[205]	583(24)[210]	A′	$\nu(Ng\text{-}F_6) - \nu(Kr\text{-}F_5)_{small}$	576(31)[146]	556(36)[146]	577(83) 573(100)	574(93) 571(100)
469(17) 450(42)	490(40)[90]	470(55)[87]	A′	$[\nu(Ng\text{-}F_5) - \nu(W\text{-}F_5)]$	479(21)[152]	462(32)[161]	458(8) 439(11)	466(7) 437(10)
312(16)	318(2)[1]	312(2)[<1]	A′	$[\delta(F_1WF_4) + \delta(F_2WF_3)]$	316(2)[2]	310(2)[<1]	320(17)	322(12) 319(13)
301(12)	307(2)[12]	310(4)[8]	A′	$[\delta(OWF_1F_2) - \delta(OWF_3F_4)]$	321(3)[13]	311(4)[8]	311, sh	309(7)
	310(3)[6]	308(3)[7]	A″	$[\delta(OWF_2F_3) - \delta(OWF_1F_4)]$	310(3)[7]	309(3)[7]		
[g]	326(3)[22]	293(2)[11]	A′	$\delta(F_5NgF_6)_{i.p.} - (\delta(WF_{(4)})_{umb})_{small}$	304(2)[15]	286(1)[10]	274(1)	
	252(<1)[69]	240(<1)[79]	A′	$\delta(WF_{(4)})_{umb} + (\delta(F_5NgF_6)_{i.p.})_{small}$	250(<1)[81]	235(<1)[89]	248(<1)	
	258(<0.1)[21]	247(<0.1)[23]	A″	$\delta(F_5NgF_6)_{o.o.p.} - [\delta(F_1WF_4) - \delta(F_2WF_3)]_{small}$	243(<0.1)[27]	239(<0.1)[27]	241(<1)	
221(4)	224(<1)[11]	220(<1)[13]	A′	$[\delta(F_1WF_2) - \delta(F_3WF_4)]$	222(<1)[11]	216(<1)[19]	206(1) 202(1)	207(1) 202(1)
206(2)	217(<1)[6]	212(<1)[3]	A″	$[\delta(F_1WF_4) - \delta(F_2WF_3)] + (\delta(F_5NgF_6)_{o.o.p.})_{small}$	205(<1)[<1]	199(<1)[<1]		199(1)

continued …

Table A4.7. (continued)

$KrF_2 \cdot WOF_4$					$XeF_2 \cdot WOF_4$			
158(6)	169(<1)[<1]	160(<1)[<1]	A″	$[\rho_t(F_1WF_2) - \rho_t(F_3WF_4)]$	168(<1)[<1]	162(<1)[<1]	153(14)	158, sh 153(12)
144(8)	161(2)[4]	138(3)[10]	A′	$\rho_r(F_5NgF_6)$	142(2)[2]	129(2)[5]	139(6)	138(5)
	121(<1)[<1]	118(1)[1]	A″	$[\rho_t(F_5NgF_6) - \rho_t(WOF_{(4)})]$	119(<1)[1]	118(<1)[2]	127(3)	127(2)
	108[<1)[<1]	103(<1)[1]	A′	$\rho_r(WOF_{(4)})$	106[<1)[<1]	101(<1)[<1]		
	60(1)[<1]	44(1)[<1]	A′	$\delta(WF_5Ng)_{i.p.}$	59(<1)[<1]	41(<1)[<1]		
	36(1)[<0.1]	16(1)[<0.1]	A″	$[\rho_t(F_5NgF_6) + \rho_t(WOF_{(4)})]$	36(<1)[<0.1]	16(<1)[<0.1]		
172(18)				lattice modes				70(5) 53(18) 35(25) 30, sh

[a] Frequencies are given in cm^{-1}. [b] Values in parentheses denote relative Raman intensities. The abbreviation denotes a shoulder (sh). [c] Values in parentheses and square brackets denote calculated Raman intensities ($Å^4$ amu^{-1}) and infrared intensities (km mol^{-1}), respectively. Assignments are for the energy-minimized gas-phase geometry (C_s) calculated at the APFD/def2-TZVPD(O, F, Kr)/def2-TZVPD(-PP)(W, Xe) and B3LYP/aVTZ(-PP)(Kr, Xe)/Def2-TZVPD(O, F)/def2-TZVPD(-PP)(W) levels of theory. [d] Abbreviations denote stretch (ν), bend (δ), rock (ρ_r), twist (ρ_t), and wag (ρ_w), umbrella (umb), $WOF_{(4)}$ ($W_1O_1F_1F_2F_3F_4$), in-plane (i.p.), and out-of-plane (o.o.p.). Bond elongations and angle openings are denoted by plus (+) signs, and bond contractions and angle compressions are denoted by minus (−) signs. The in-plane and out-of-plane bending modes are relative to the $O_1W_1F_5Kr_1F_6$-plane, where the atom labeling scheme corresponds to that used in Figure 1. [e] From ref [S1]; the frequencies have been reassigned. Previously reported bands at 544(5) and 504(4) cm^{-1} were assigned to $KrF_2 \cdot WOF_4$ but were not observed in the present work. [f] Present work. The Raman spectrum was recorded in an FEP sample tube at −150 °C using 1064-nm excitation. [g] The band may overlap with an FEP sample tube band.

Table A4.8. Experimental (Raman) and calculated vibrational frequencies, intensities, and assignments for $XeF_2 \cdot 2MoOF_4$ and $XeF_2 \cdot 2WOF_4$

$XeF_2 \cdot 2MoOF_4$					$XeF_2 \cdot 2WOF_4$			
exptl[a,b]		calcd[a,c]		assgnts[d]	calcd[a,b]		exptl[a,c]	
[e]	[f]	APFD	B3LYP		APFD	B3LYP	[g]	[f]
1036(53)	1039(43)	1122(65)[104]	1094(69)[111]	$[\nu(M_1\text{-}O_1) + \nu(M_2\text{-}O_2)]$	1098(56)[105]	1073(67)[102]	1053, sh 1050(89)	1052(50)
1028(22)	1030(20)	1119(18)[257]	1092(21)[224]	$[\nu(M_1\text{-}O_1) - \nu(M_2\text{-}O_2)]$	1094(22)[192]	1070(21)[179]	1044, sh 1041(34)	1044(24)
724(3)	726(4)	735(7)[349]	716(7)[354]	$[\nu(M_1\text{-}F_2) + \nu(M_1\text{-}F_3)] + [\nu(M_2\text{-}F_9) - \nu(M_2\text{-}F_7)]$	730(4)[75]	711(7)[71]	719(35) 716(28)	720(26)
714(38) 708(11)	715(37) 711, sh	726(4)[216]	708(4)[194]	$[\nu(M_1\text{-}F_2) + \nu(M_1\text{-}F_1)] - [\nu(M_2\text{-}F_{10}) + \nu(M_2\text{-}F_9)]$	726(21)[60]	707(21)[70]		
700, sh 698(20)	700(20)	719(14)[97]	704(14)[125]	$[\nu(M_1\text{-}F_2) + \nu(M_1\text{-}F_3)] + [\nu(M_2\text{-}F_7) - \nu(M_2\text{-}F_9)] + \nu(M_2\text{-}F_{10})$	702(1)[337]	685(1)[348]	682(1)	684(1)
685, sh 682(6)	684(8)	716(8)[179]	698(5)[135]	$[\nu(M_1\text{-}F_1) + \nu(M_1\text{-}F_2) - \nu(M_1\text{-}F_3)] + \nu(M_2\text{-}F_9)$	691(<1)[177]	674(<1)[102]	673, sh 670(3)	672(3)
671, sh 668(8)	669(8)	699(2)[139]	683(4)[142]	$[\nu(M_2\text{-}F_9) + \nu(M_2\text{-}F_7)] + [\nu(M_2\text{-}F_8) - \nu(M_2\text{-}F_{10})]$	682(1)[105]	665(1)[144]	658(1)	662(1)
655(9) 651, sh	656(9)	680(5)[237]	661(7)[226]	$[\nu(M_1\text{-}F_1) + \nu(M_1\text{-}F_2) + \nu(M_1\text{-}F_3)] - [\nu(M_1\text{-}F_4) - \nu(M_2\text{-}F_4)]_{small}$	671(1)[174]	653(2)[153]	625, sh 621(4)	624(3)
597, sh 589(8)	593(7)	611(2)[22]	595(3)[16]	$[\nu(M_2\text{-}F_9) + \nu(M_2\text{-}F_7)] - [\nu(M_2\text{-}F_8) + \nu(M_2\text{-}F_{10})]$	630(1)[50]	612(2)[46]		
527, sh 525(3)	528(2)	589(5)[69]	564(9)[126] [h]	$[\nu(M_1\text{-}F_4) - \nu(M_2\text{-}F_4)]$	598(3)[126]	563(15)[153] [i]	537(2) 535, sh	541(1)
574, sh 572(100)	575(100)	576(34)[153]	557(35)[129]	$\nu(Xe_1\text{-}F_6)$	583(37)[143]	567(34)[169] [j]	585, sh 581(100)	585(100)

continued …

Table A4.8. (continued)

$XeF_2 \cdot 2MoOF_4$					$XeF_2 \cdot 2WOF_4$			
421(9)	422(9)	485(20)[164]	460(29)[161]	$[\nu(Xe_1\text{-}F_5) - \nu(M_1\text{-}F_5)]$	474(18)[187]	445(27)[196]	408(5)	409(5)
325(15) 321(14)	324, sh	323(1)[4]	316(2)[2]	$[\delta(F_8M_2F_7) + \delta(F_9M_2F_{10})] / \delta(O_2M_2F_4)$	319(2)[1]	312(1)[<1]	334, sh 332(6)	332(4)
316, sh		321(3)[6]	316(2)[1]	$[\delta(O_1M_1F_1) - \delta(O_1M_1F_3)] + [\delta(O_2M_2F_9) - \delta(O_2M_2F_7)]_{small}$	324(1)[14]	315(3)[3]	323(16) 321, sh	324(12)
313(23)	314(20)	318(2)[3]	315(1)[8]	$[\delta(O_1M_1F_2) - \delta(O_1M_1F_4)] + [\delta(O_2M_2F_9) - \delta(O_2M_2F_7)]$	316(1)[3]	314(1)[5]	314(20)	317(28)
310, sh		313(3)[10]	313(2)[11]	$[\delta(O_1M_1F_2F_3) - \delta(O_1M_1F_1F_4)] + [\delta(O_2M_2F_9F_{10}) - \delta(O_2M_2F_8F_7)]$	308(3)[13]	313(1)[8]	308(16) 305, sh	310(15)
306, sh		315(4)[9]	312(5)[8]	$[\delta(O_1M_1F_2) - \delta(O_1M_1F_4)] + [\delta(O_2M_2F_8) - \delta(O_2M_2F_{10})]$	311(3)[9]	309(5)[9]		
297(9)	298(10)	324(2)[5]	308(3)[<1]	$[\delta(F_2M_1F_3) + \delta(F_1M_1F_4)]$	323(2)[<1]	303(3)[4]	297(6) 295, sh	299(6)
278, sh 275(1)	276(1)	311(1)[10]	288(<1)[10]	$\delta(F_6Xe_1F_5)_{i.p.} + \delta(M_1F_{(4)})_{umb}$	306(2)[10]	287(1)[13]		270(<1)
268(<1)		267(<1)[12]	260(<1)[58]	$\delta(M_2F_{(4)})_{umb}$	256(<1)[24]	248(<1)[29]		
261, sh 258(2)	259(2)	276(<1)[84]	251(<1)[43]	$[\delta(F_6Xe_1F_5)_{i.p.} - \delta(M_1F_{(4)})_{umb}]$	265(<1)[64]	249(<1)[70]	248(1)	251(<1)
235(6) 232, sh	236(6)	246(<1)[46]	238(<1)[66]	$\delta(F_6Xe_1F_5)_{o.o.p.} + \delta(M_1F_1F_2F_3)$	236(<1)[41]	231(<1)[82]	237(1) 235(3)	236(3)
		241(<1)[18]	234(<1)[24]	$\rho_w(F_2M_1F_4) + [\delta(F_8M_2F_7) - \delta(F_9M_2F_{10})]$	240(<1)[32]	232(<1)[22]	230(2) 228, sh	
227(4)	230, sh	225(<1)[14]	223(1)[3]	$[\delta(F_8M_2F_9) - \delta(F_{10}M_2F_7)]$	220(<1)[13]	217(<1)[3]	225(2)	226(3)
213, sh 210(4)	212(4)	219(<1)[3]	213(<1)[3]	$\rho_w(F_2M_1F_4) - [\delta(F_8M_2F_7) - \delta(F_9M_2F_{10})]$	214(<1)[6]	209(<1)[3]	210, sh 207(2)	208(3)
196(2) 192(1)	198(2) 193(1)	203(<1)[5]	196(<1)[<1]	$\delta(F_6Xe_1F_5)_{o.o.p.} - \rho_w(F_1M_1F_3)$	200(<0.1)[12]	192(<1)[1]	201(1) 193(1)	196, sh

continued …

Table A4.8. (continued)

$XeF_2 \cdot 2MoOF_4$					$XeF_2 \cdot 2WOF_4$			
173, sh 171(<1)	170(1)	187(<1)[4]	170(<1)[2]	$[\rho_t(F_1M_1F_2) - \rho_t(F_3M_1F_4)]$	192(<1)[3]	181(<1)[4]		
156(9)	156(10)	152(<1)[<0.1]	144(<1)[<0.1]	$[\rho_t(F_9M_2F_{10}) - \rho_t(F_8M_2F_7)]$	159(<1)[<0.1]	154(<1)[<0.1]	153(9) 149, sh	154(9)
146(3) 141(3)	142(4)	148(1)[2]	133(1)[4]	$\rho_r(F_6Xe_1F_5) + \rho_r(M_1O_1F_{(4)})_{small}$	146(1)[2]	134(1)[3]	142(4) 139, sh	144(5)
122, sh 120(1)		130(<1)[1]	121(<1)[2]	$[\rho_t(M_1O_1F_{(4)}) - \rho_t(F_6Xe_1F_5)]$	130(<1)[<1]	124(1)[1]		
111(2)	111(3)	126(<1)[<1]	114(<1)[1]	$\rho_r(M_1O_1F_{(4)})_{i.p.}$	123(<1)[<1]	117(<1)[<1]	111(2)	
		100(<1)[2]	88(<1)[1]	$[\rho_t(M_1O_1F_{(4)}) - \rho_t(M_2O_2F_{(4)})]$	99(<1)[<1]	91(<0.1)[<1]		
		83(<1)[<1]	84(<1)[1]	$[\rho_t(F_6Xe_1F_5) + \rho_r(M_2O_2F_{(4)})]$	82(<1)[<1]	86(<1)[<1]		
		95(<1)[2]	67(<1)[5]	$\delta(M_1O_1F_{(4)}) / \delta(M_2O_2F_{(4)})$	90(<0.1)[2]	66(<0.1)[6]		
		60(<1)[<1]	43(<1)[<1]	$\delta(M_1F_5Xe_1)_{i.p.}$	58(<1)[1]	42(<1)[<1]		
		55(<0.1)[<1]	33(<1)[<1]	$\delta(M_1F_4Mo_2)_{i.p.}$	55(<1)[<1]	35(<0.1)[<1]		
		373(<1)[<0.1]	22(1)[<0.1]	$\rho_t(F_6Xe_1F_5) + \rho_t(M_1O_1F_2F_4)$	41(<1)[<0.1]	26(1)[<0.1]		
		15(<1)[<0.1]	13(<0.1)[<0.1]	$\rho_t(M_2F_{(4)})$	17(<1)[<0.1]	8(<0.1)[[<0.1]		
		23(<0.1)[<0.1]	12(<0.1)[<0.1]	$[\rho_t(M_1F_{(4)}) + \rho_t(M_2O_2F_{(4)})]$	23(<0.1)[<0.1]	15(<0.1)[<0.1]		
99(2)	99(2) 68(12)			lattice modes			105(2)	66(15)

continued …

Table A4.8. (continued) [a] Frequencies are given in cm^{-1}. [b] Values in parentheses denote relative Raman intensities. The abbreviation denotes a shoulder (sh). [c] Values in parentheses and square brackets denote calculated Raman intensities ($Å^4$ amu^{-1}) and infrared intensities (km mol^{-1}), respectively. [d] Assignments are for the energy-minimized gas-phase geometry (C_1) calculated at the APFD/def2-TZVPD(O, F)/def2-TZVPD(-PP)(Mo, W, Xe) and B3LYP/aVTZ(-PP)(Xe)/Def2-TZVPD(O, F)/def2-TZVPD(--PP)(Mo,W) levels of theory. Abbreviations denote stretch (ν), bend (δ), rock (ρ_r), twist (ρ_t), and wag (ρ_w), umbrella (umb), $M_1F_{(4)}$ ($M_1F_3F_4F_5F_6$), $M_2F_{(4)}$ ($M_2F_7F_8F_9F_{10}$), in-plane (i.p.), and out-of-plane (o.o.p.). Bond elongations and angle openings are denoted by plus (+) signs; and bond contractions and angle compressions are denoted by minus (−) signs. The in-plane and out-of-plane bending modes are relative to the $O_1M_1F_5Xe_1F_6$-plane, where the atom labeling scheme corresponds to those used in Figures 7.2 and A4.3. [e] Present work. The Raman spectrum was recorded in an FEP sample tube at −150 °C using 1064-nm excitation. Weak bands previously reported at 546(1) and 504(<1) cm^{-1} were not observed in the present spectrum. [f] From ref [S1]. The bands at 750, 734, 388, and 382 cm^{-1} reported in the Raman spectrum of $XeF_2 \cdot 2MoOF_4$ were incorrectly assigned and are now reassigned to FEP sample tube bands. The band at 298 cm^{-1} was correctly assigned but overlaps with an FEP sample tube band. [g] Present work. The Raman spectrum was recorded in an FEP sample tube at −150 °C using 1064-nm excitation. In addition to bands due to $XeF_2 \cdot 2WOF_4$, weak bands were observed at 1030(1), 575(sh), and 571(3) cm^{-1} that are assigned to $XeF_2 \cdot WOF_4$. [h] $[\nu(M_1\text{-}F_6) - \nu(M_2\text{-}F_6)] - [\nu(Mo_1\text{-}F_3) + \nu(Mo_1\text{-}F_5)]_{small}$. [i] $[\nu(M_1\text{-}F_6) - \nu(M_2\text{-}F_6)] - [\nu(Xe_1\text{-}F_1)]_{small}$. [j] $\nu(Xe_1\text{-}F_1) + [\nu(W_1\text{-}F_6) - \nu(W_2\text{-}F_6)]_{small}$.

Figure A4.6. Factor-group analyses for $NgF_2 \cdot MOF_4$ (Ng = Kr, Xe; M = Mo, W)[a]

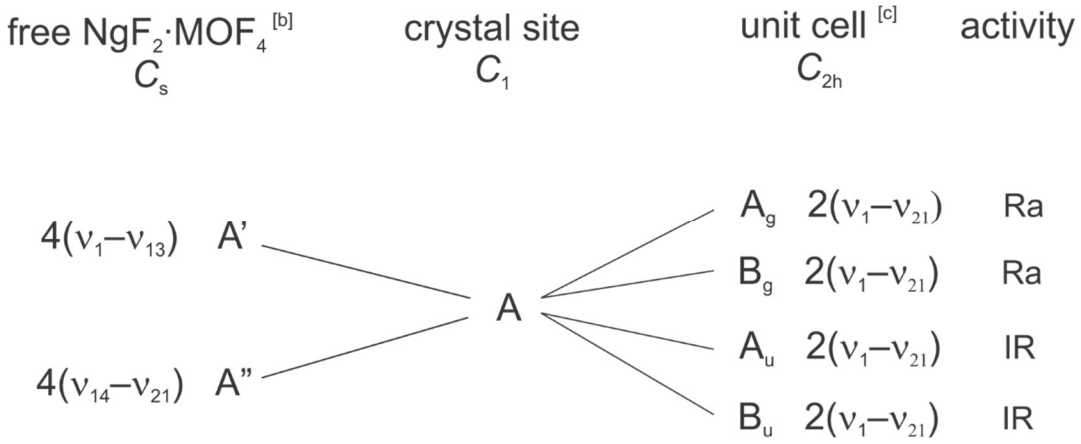

[a] The external modes have not been treated in this analysis. [b] The irreducible vibrational representation of gas-phase $NgF_2 \cdot MOF_4$ is Γ = 13A' + 8A". [c] Space group; $P2_1/c$, $Z = 4$.

$NgF_2 \cdot MOF_4$ (M = Mo, W). Twenty-one vibrational modes are predicted for gas-phase $NgF_2 \cdot MOF_4$ under C_s symmetry. The vibrations belong to the irreducible representations Γ = 13A' + 8A", where the A' and A" modes are Raman- and infrared-active. The A' and A" irreducible representations of $NgF_2 \cdot MOF_4$ under C_s symmetry in the gas phase correlate to A irreducible representations under C_1 site symmetry in the solid state. When correlated to its unit cell symmetry, the vibrationally coupled modes of $NgF_2 \cdot MOF_4$ split into 21 A_g and B_g Raman-active bands and 21 A_u and B_u infrared-active bands when correlated to C_{2h} crystal symmetry (Figure A4.6). The factor-group splittings observed in the Raman spectra are listed in Tables A4.6 and A4.7.

Figure A4.7. Factor-group analyses for $XeF_2 \cdot 2MOF_4$ (M = Mo, W)[a]

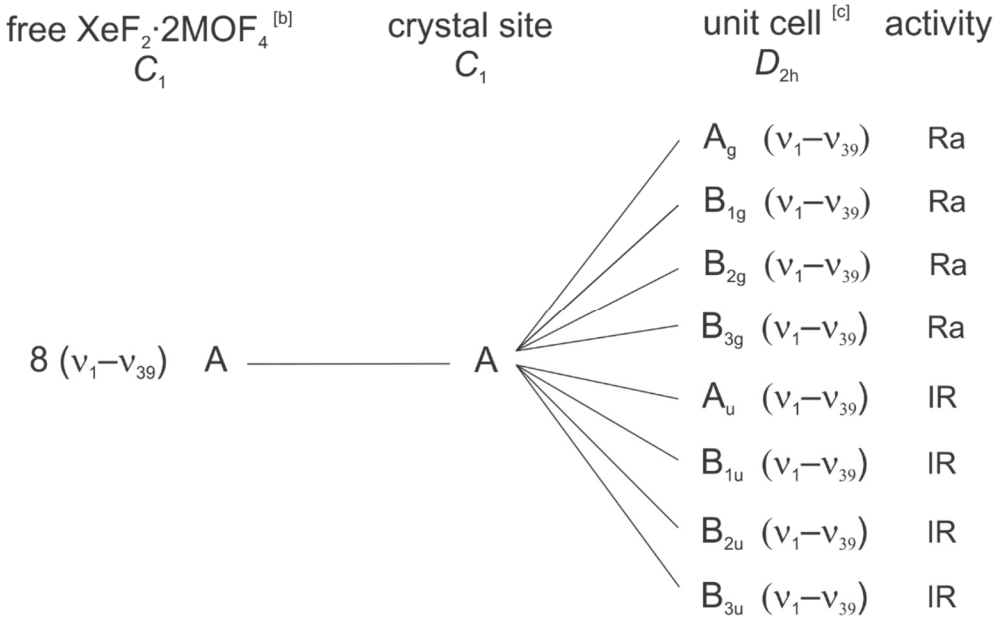

[a] The external modes have not been treated in this analysis. [b] The vibrational irreducible representation for gas-phase $XeF_2 \cdot 2MOF_4$ is Γ = 39 A. [c] Space group; *Pbcn*, $Z = 8$.

$XeF_2 \cdot 2MOF_4$ (M = Mo, W). Thirty-nine vibrational modes are predicted for gas-phase $XeF_2 \cdot 2MOF_4$ under C_1 symmetry. The vibrations belong to the irreducible representations Γ = 39 A, where the A modes are Raman- and infrared-active. The A representations of gas-phase $XeF_2 \cdot 2MOF_4$ correlate to A representations under C_1 site symmetry in the solid state. When correlated to the crystal symmetry (D_{2h}), each of the 39 modes splits into Raman-active A_g, B_{1g}, B_{2g}, and B_{3g} components and infrared-active A_u, B_{1u}, B_{2u}, and B_{3u} components (Figure A4.7). The factor-group splittings observed in the Raman spectra are listed in Table A4.8.

Computational Results (continued)

Calculated Geometries

$NgF_2 \cdot MOF_4$ and $XeF_2 \cdot 2MOF_4$ (Ng = Kr, Xe; M = Mo, W). The starting geometries used for the energy optimizations of **1'**–**4'** were the crystallographic geometries, where the $NgF_2 \cdot MOF_4$ complexes adopt a near-eclipsed conformation. As observed for $NgF_2 \cdot CrOF_4$,[S4] the energy-minimized gas-phase geometries correspond to staggered conformations (C_s symmetry), with all vibrational frequencies real (Figures 7.1 and A4.2). As a consequence, the Ng–F_b---M–$F_{(1)}$ dihedral angles are the geometric parameters that differ the most from experiment (exptl: ∠Kr–F_b---Mo–$F_{(1)}$, 14.34(2)°; ∠Kr–F_b---W–$F_{(1)}$, 16.1(2)°, ∠Xe–F_b---Mo–$F_{(1)}$, 7.55(6)°; ∠Xe–F_b---W–$F_{(1)}$, 5.9(2)°; calcd: ∠Kr–F_b---Mo–$F_{(1)}$, 44.3°; ∠Kr–F_b---W–$F_{(1)}$, 44.4°, ∠Xe–F_b---Mo–$F_{(1)}$, 44.3°; ∠Xe–F_b---W–$F_{(1)}$, 44.4°). The starting geometries used for the energy optimizations of **5'** and **6'** were the crystallographic geometries where the $XeF_2 \cdot MOF_4$ complexes adopt nearly eclipsed conformations (∠Xe–F_b---Mo–$F_{(3)}$, 7.19(7)°; ∠Xe–F_b---W–$F_{(3)}$, 2.3(3)°) that is only retained in the energy-minimized geometry of **5'** (∠Xe–F_b---Mo–$F_{(3)}$, 1.4°; ∠Xe–F_b---W–$F_{(3)}$, 24.1°) (Figures 7.2 and A4.3).

As observed in their crystal structures, the calculated Ng–F_t bonds (calcd: **1'**, 1.834; **2'**, 1.829, **3'**, 1.955; **4'**, 1.951, **5'**, 1.950; **6'**, 1.944 Å; exptl: **1**, 1.8202(9); **2**, 1.805(2), **3**, 1.9369(12); **4**, 1.929(3), **5**, 1.9283(10); **6**, 1.922(4) Å) are shorter than the Ng–F_b bonds (calcd: **1'**, 1.926; **2'**, 1.935, **3'**, 2.048; **4'**, 2.058, **5'**, 2.059; **6'**, 2.072 Å; exptl: **1**, 1.9653(9); **2**, 1.989(2), **3**, 2.0813(12); **4**, 2.102(3), **5**, 2.1153(10); **6**, 2.136(4) Å). The

bond length trend, Kr–F_t < Xe–F_t and Kr–F_b < Xe–F_b, is also reproduced. The average calculated Ng–$F_{t/b}$ bond lengths are very similar to the calculated bond lengths of free NgF_2 (Kr, 1.869; Xe, 1.986 Å).

The calculated F_t–Ng---F_b bond angles are nearly linear, as observed experimentally. The calculated Ng–F_b---M bond angles of **1'**–**4'** are slightly underestimated (calcd: **1'**, 114.2; **2'**, 114.5, **3'**, 116.8; **4'**, 117.2°; exptl: **1**, 134.33(5); **2**, 135.22(12), **3**, 148.09(7); **4**, 150.57(18)°), whereas the agreement is slightly better for **5'** and **6'** (calcd: **5'**, 125.6; **6'**, 123.8°; exptl: **5**, 130.84(5); **6**, 131.70(19)°). As previously noted,[S4] these angles are highly deformable, having very low calculated δ(Ng–F_b---M) frequencies (Tables A4.6–A4.8) and are therefore likely to be influenced by crystal packing.

The Mo–O/W–O and Mo–F/W–F bond lengths of **1'**–**4'** are nearly equal in both the $NgF_2 \cdot MoOF_4$ and $NgF_2 \cdot WOF_4$ complexes, with the two Mo–F/W–F bonds proximate to the Ng atom being somewhat longer than those that are further away (Tables A4.2 and A4.3). This trend is not evident in the experimental structures because of their different conformations. In contrast, **5** and **6**, which display similar calculated and experimental conformations, the $M_{(1)}$–$F_{(1)}$ bond, which is the terminal fluorine atom closest to the Xe atom, is longer than the other two terminal $M_{(1)}$–F_t bonds (Table A4.4). Other experimental trends are well reproduced by the calculations: Mo---F_b > W---F_b, Mo–O < W–O, and Mo–F_t < W–F_t.

The asymmetry observed for the bridge bonds in the $(F_3O)M_{(1)}$–$F_{(6)}$---$M_{(2)}OF_4$ moiety, $M_{(2)}$---$F_{(6)}$ > $M_{(1)}$–$F_{(4)}$, (**5**, 2.2990(10) and 1.9350(10) Å; **6**, 2.313(4) and 1.929(4)

Å) is reproduced (**5'**, 2.426 and 1.897 Å; **6'**, 2.416 and 1.909 Å), as well as the $M_{(1)}$–$F_{(6)}$---$M_{(2)}$ bond angle (calcd: **5'**, 145.8; **6'**, 145.6 °; exptl: **5**, 159.02(6); **6**, 159.5(2) °).

Atoms in Molecules (AIM) Analyses

In an AIM analysis, bond covalency may be assessed by evaluating the Laplacian of electron density ($\nabla^2\rho_b$), Cremer-Kraka total energy density (H_b), the densities of all electrons (ρ_b), and the bond delocalization indices (δ) at bond critical points.[S5] The chemical bonding in $NgF_2{\cdot}nCrOF_4$ (Ng = Kr, Xe; n = 1, 2) has previously been described by AIM analyses, which revealed that the Cr–O bonds have significant double bond character, the Cr–F and Ng–F bonds are highly polar covalent in nature, with coordination of NgF_2 to $CrOF_4$ resulting in enhanced polarization of the Ng–F and Cr–F bonds and the formation of a primarily electrostatic Cr---F_b bond.[S4]

The M−O bonds of MOF_4, $NgF_2{\cdot}MOF_4$, and $XeF_2{\cdot}2MOF_4$ (M = Mo, W) have large positive $\nabla^2\rho_b$ (0.958–1.070), ρ_b (0.309–0.423), δ (1.920–2.100), and negative H_b (−0.244 to −0.265), consistent with significant double bond character. The M−F bonds have smaller $\nabla^2\rho_b$ (0.713–0.984), ρ_b (0.143–0.262), and δ (0.615–0.959) values and less negative H_b-values (−0.048 to −0.077) than for the M−O bonds that are consistent with their highly polar-covalent characters. As observed in $NgF_2{\cdot}nCrOF_4$,[S4] the two M–F bonds orientated towards the Ng atoms in $NgF_2{\cdot}MOF_4$ and $XeF_2{\cdot}2MOF_4$ show decreased ρ_b, H_b, and δ values and slightly increased $\nabla^2\rho_b$ values that are consistent with their polar-covalent characters. Coordination of MOF_4 to $XeF_2{\cdot}MOF_4$ to give F_tXeF_b---$M(OF_3)$–F_b'---$M'OF_4$ significantly polarizes the M–F_b' bond, resulting in decreased $\nabla^2\rho_b$, ρ_b, δ, and less

negative H_b values relative to the M−F_t bonds of XeF_2·MOF_4. Opposite trends are observed for the AIM properties of the M−O bonds in XeF_2·2MOF_4, which indicate coordination of M′OF_4 strengthens the M−O double bonds.

The AIM parameters of the M---F_b bonds of the NgF_2·MOF_4 complexes have small positive $\nabla^2\rho_b$, ρ_b, and δ values, in addition to small positive or negative values of H_b, consistent with primarily electrostatic σ-hole type interactions (Tables A4.10 and A4.11). The M---F_b bonds become more covalent upon descending Group 6, as evidenced by their increasing Laplacian of electron densities ($\nabla^2\rho_b$: Cr, (Kr) 0.135, (Xe) 0.148;[S4] Mo, (Kr) 0.171, (Xe) 0.183; W, (Kr) 0.222, (Xe) 0.237), densities of all electrons (ρ_b: Cr, (Kr) 0.028, (Xe) 0.030;[S4] Mo, (Kr) 0.035, (Xe) 0.038; W, (Kr) 0.069, (Xe) 0.073), and delocalization densities (δ: Cr, (Kr) 0.084, (Xe) 0.093;[S4] Mo, (Kr) 0.122, (Xe) 0.131; W, (Kr) 0.206, (Xe) 0.219). Coordination of M′OF_4 to XeF_2·MOF_4 to give F_tXeF_b---M(OF_3)–F_b′---M′OF_4 results in primarily electrostatic M′---F_b′ bonds that are weaker than the M---F_b bonds of NgF_2·MOF_4 ($\nabla^2\rho_b$: Mo, 0.162, W, 0.220; ρ_b: Mo, 0.032, W, 0.064; δ: Mo, 0.104, W, 0.180; H_b: Mo, 0.003, W, −3.0 x 10^{-4}).

The Ng–F AIM properties of the terminally coordinated NgF_2 ligands of NgF_2·MOF_4 and XeF_2·2MOF_4 (Tables A4.10 and A4.11) show their Ng–F bond polarizations relative to free NgF_2 are comparable to those of NgF_2·$CrOF_4$,[S4] [F_2OBr(FNgF)$_2$][AsF_6],[S6,S7] and [F_5Xe(FNgF)$_n$][AsF_6] (n = 1, 2).[S8,S9] Upon coordination, ρ_b, and δ decrease for Ng–F_b and increase for Ng–F_t, whereas H_b decreases for Ng–F_t and increases for Ng–F_b. Coordination also increases and decreases $\nabla^2\rho_b$ for the Kr–F_b and Kr–F_t bonds in KrF_2·MOF_4, respectively, relative to KrF_2. The opposite

behavior is observed for the $\nabla^2\rho_b$ values of the Xe–F bonds in $XeF_2{\cdot}MOF_4$ and $XeF_2{\cdot}2MOF_4$ relative to XeF_2. Similar trends have been noted for the Ng–F bonds in $NgF_2{\cdot}CrOF_4$.[S4] In all instances, the AIM properties of the Ng–F_t and Ng–F_b bonds bracket those of free NgF_2. The NgF_2 molecules in $NgF_2{\cdot}MOF_4$ become increasingly more polarized upon descending Group 6 as the fluoride-ion affinities (FIAs) of MOF_4 and $M_2O_2F_8$ ($M(OF_3)$–F_b'---M'OF_4) increase, consistent with relative FIAs for MOF_4 and $M(OF_3)$–F_b′---M′OF_4 that follow the order $CrOF_4 < MoOF_4 < WOF_4 \leq Mo(OF_3)$–$F_b$′---Mo′$OF_4$ < $W(OF_3)$–F_b′---W′OF_4.

Electron Localization Function (ELF) Analyses

ELF analyses were carried out for MOF_4, $NgF_2{\cdot}MOF_4$, and $XeF_2{\cdot}2MOF_4$. ELF parameters are provided in Tables A4.10 and A4.11 and ELF isosurface plots are shown for the localization domains of MOF_4, $NgF_2{\cdot}MOF_4$, and $XeF_2{\cdot}2MOF_4$ (Figure A4.8). In the ensuing discussion and figures, the abbreviations denote atomic basin populations, $\bar{N}$[A]; electron localization function, $\eta(\mathbf{r})$; core basin, C(A); monosynaptic valence basin, V(A); and closed isosurface, $\eta(\mathbf{r}) = f$, where $\eta(\mathbf{r})$ is defined as the isosurface contour. Because the Def2-TZVPD basis set does not separate the sub-valence and valence electrons, they cannot be distinguished by ELF.

The ELF valence basins of MOF_4, $NgF_2{\cdot}MOF_4$, and $XeF_2{\cdot}2MOF_4$ are monosynaptic, consistent with the highly polar-covalent nature of the bonding in these compounds. Coordination of NgF_2 to MOF_4 results in a perturbation of the toroidal V(Ng) basins similar to those in $NgF_2{\cdot}n CrOF_4$,[S4] where bond critical points are observed

between the V(Ng) basins and the equatorial V(F) basins of complexed MOF_4. These perturbations become even more significant in $XeF_2{\cdot}2MOF_4$, where the toroidal V(Xe) basin must also accommodate the V(F) basins of complexed $M'OF_4$.

The $\bar{N}$[C(Ng)], $\bar{N}$[C(F)], and $\bar{N}$[C(O)] ELF core basin populations are close to the ideal core charges, and do not vary significantly upon coordination. Coordination of NgF_2 to MOF_4 increases $\bar{N}[V(F_b)]$ and $\bar{N}[V(F_t)]$ relative to NgF_2 following the order Cr < Mo < W, whereas coordination of $M'OF_4$ to $XeF_2{\cdot}MOF_4$ to give $F_tXeF_b{---}M(OF_3){-}F_b'{---}M'OF_4$ results in no change for $\bar{N}[V(F_b)]$ (Mo), a small increase for $\bar{N}[V(F_b)]$ (W), no change for $\bar{N}[V(F_t)]$ (Mo, W), and increases for $\bar{N}[V(F_b')]$ (Mo, W).

The localization domain reduction tree diagrams for MOF_4, $NgF_2{\cdot}MOF_4$, and $F_tXeF_b{---}M(OF_3){-}F_b'{---}M'OF_4$ (Figure A4.9) provide the hierarchies of ELF basins and the corresponding basin separation values (f_{sep}). The ELF reduction of the localization diagrams of $NgF_2{\cdot}MOF_4$ follow a similar order to those described for $NgF_2{\cdot}n CrOF_4$,[S4] and are not discussed. Upon descending Group 6, the $NgF_2{\cdot}MOF_4$ complexes separate into NgF_2 and MOF_4 *f*-localization domains in the order Cr < Mo < W, consistent with the relative degrees of M---F_b bond covalency, which increase in the same order. In the $F_tXeF_b{---}M(OF_3){-}F_b'{---}M'OF_4$ complexes, $M'OF_4$ separates from $XeF_2{\cdot}MOF_4$ at significantly lower f_{sep}-values (Mo, 0.05; W, 0.06) than $XeF_2{\cdot}MOF_4$ (f_{sep}: Mo, 0.08; W, 0.09) into XeF_2 and MOF_4, in accordance with the relative bond strengths, M---F_b > M′---F_b'.

Table A4.9. Natural Population Analysis (NPA) charges, wiberg valences, and wiberg bond indices for $NgF_2 \cdot MOF_4$, $XeF_2 \cdot 2MOF_4$, MOF_4, and NgF_2 (Ng = Kr, Xe; M = Mo, W)[a]

$KrF_2 \cdot MoOF_4$					$XeF_2 \cdot MoOF_4$				
Bond Indices		NPA Charges [Valences]			Bond Indices		NPA Charges [Valences]		
Kr1−F5	0.452	Kr1	1.060	[1.087]	Xe1−F5	0.410	Xe1	1.256	[1.005]
Kr1−F6	0.625	F5	−0.541	[0.781]	Xe1−F6	0.581	F5	−0.621	[0.681]
		F6	−0.449	[0.816]			F6	−0.561	[0.702]
		$\sum_{KrF_2}$	**0.070**				$\sum_{XeF_2}$	**0.074**	
Mo1---F5	0.101	Mo1	2.274	[4.995]	Mo1---F5	0.109	Mo1	2.274	[4.997]
Mo1−F1	0.757	F1	−0.456	[0.991]	Mo1−F1	0.759	F1	−0.456	[0.992]
Mo1−F2	0.757	F2	−0.456	[0.991]	Mo1−F2	0.759	F2	−0.456	[0.992]
Mo1−F3	0.702	F3	−0.497	[0.924]	Mo1−F3	0.697	F3	−0.500	[0.919]
Mo1−F4	0.702	F4	−0.497	[0.924]	Mo1−F4	0.697	F4	−0.500	[0.919]
Mo1−O1	1.971	O1	−0.437	[2.350]	Mo1−O1	1.973	O1	−0.436	[2.352]
		$\sum_{MoOF_4}$	**−0.070**				$\sum_{MoOF_4}$	**−0.074**	
$KrF_2 \cdot WOF_4$					$XeF_2 \cdot WOF_4$				
Bond Indices		NPA Charges [Valences]			Bond Indices		NPA Charges [Valences]		
Kr1−F5	0.438	Kr1	1.064	[1.086]	Xe1−F5	0.397	Xe1	1.258	[1.001]
Kr1−F6	0.637	F5	−0.550	[0.772]	Xe1−F6	0.591	F5	−0.627	[0.674]
		F6	−0.442	[0.823]			F6	−0.554	[0.709]
		$\sum_{KrF_2}$	**0.072**				$\sum_{XeF_2}$	**0.077**	
W1---F5	0.110	W1	2.498	[4.897]	W1---F5	0.117	W1	2.498	[4.897]
W1−F1	0.745	F1	−0.486	[0.940]	Cr1−F1	0.746	F1	−0.485	[0.940]
W1−F2	0.745	F2	−0.486	[0.940]	Cr1−F2	0.746	F2	−0.485	[0.940]
W1−F3	0.694	F3	−0.522	[0.879]	Cr1−F3	0.688	F3	−0.525	[0.874]
W1−F4	0.694	F4	−0.522	[0.879]	Cr1−F4	0.688	F4	−0.525	[0.874]
W1−O1	1.907	O1	−0.556	[2.223]	Cr1−O1	1.908	O1	−0.555	[2.224]
		$\sum_{WOF_4}$	**−0.074**				$\sum_{WOF_4}$	**−0.077**	
$XeF_2 \cdot 2MoOF_4$					$XeF_2 \cdot 2WOF_4$				
Bond Indices		NPA Charges [Valences]			Bond Indices		NPA Charges [Valences]		
Xe1−F5	0.387	Xe1	1.268	[0.998]	Xe1−F5	0.368	Xe1	1.272	[0.993]
Xe1−F6	0.592	F5	−0.625	[0.684]	Xe1−F6	0.606	F5	−0.632	[0.675]
		F6	−0.553	[0.711]			F6	−0.544	[0.721]
		$\sum_{XeF_2}$	**0.090**				$\sum_{XeF_2}$	**0.096**	
Mo1−F1	0.727	Mo1	2.278	[4.994]	W1−F1	0.715	W1	2.506	[4.889]
Mo1−F2	0.761	F1	−0.478	[0.955]	W1−F2	0.757	F1	−0.506	[0.907]
Mo1−F3	0.783	F2	−0.455	[0.991]	W1−F3	0.768	F2	−0.480	[0.947]
Mo1---F4	0.579	F3	−0.437	[1.023]	W1---F4	0.557	F3	−0.469	[0.968]
Mo1---F5	0.128	F4	−0.534	[0.889]	W1---F5	0.141	F4	−0.560	[0.839]
Mo1−O1	2.002	O1	−0.408	[2.378]	W1−O1	1.939	O1	−0.527	[2.253]
Mo2---F4	0.086	Mo2	2.279	[4.990]	W2---F4	0.092	W2	2.504	[4.890]
Mo2−F7	0.748	F7	−0.461	[0.981]	W2−F7	0.739	F7	−0.489	[0.933]
Mo2−F8	0.679	F8	−0.513	[0.900]	W2−F8	0.667	F8	−0.540	[0.852]
Mo2−F9	0.740	F9	−0.469	[0.971]	W2−F9	0.726	F9	−0.499	[0.918]
Mo2−F10	0.758	F10	−0.455	[0.991]	W2−F10	0.749	F10	−0.482	[0.944]
Mo2−O2	1.971	O2	−0.437	[2.349]	W2−O2	1.910	O2	−0.554	[2.223]
		$\sum_{2MoOF_4}$	**−0.090**				$\sum_{2WOF_4}$	**−0.096**	

continued …

Table A4.9. (continued)

KrF_2[b]					XeF_2[b]				
Bond Indices		NPA Charges [Valences]			Bond Indices		NPA Charges [Valences]		
Kr−F	0.555	Kr	1.018	[1.109]	Xe−F	0.521	Xe	1.210	[1.042]
		F	−0.509	[0.757]			F	−0.605	[0.650]
		$\sum_{KrF_2}$	**0.000**				$\sum_{XeF_2}$	**0.000**	

$MoOF_4$					WOF_4				
Bond Indices		NPA Charges [Valences]			Bond Indices		NPA Charges [Valences]		
Mo1−F1	0.743	Mo1	2.322	[4.921]	W1−F1	0.737	W1	2.534	[4.839]
Mo1−F2	0.743	F1	−0.466	[0.972]	W1−F2	0.737	F1	−0.491	[0.928]
Mo1−F3	0.743	F2	−0.466	[0.972]	W1−F3	0.737	F2	−0.491	[0.928]
Mo1−F4	0.743	F3	−0.466	[0.972]	W1−F4	0.737	F3	−0.491	[0.928]
Mo1−O1	1.947	F4	−0.466	[0.972]	W1−O1	1.892	F4	−0.491	[0.928]
		O1	−0.457	[2.321]			O1	−0.568	[2.201]
		$\sum_{MoOF_4}$	**0.000**				$\sum_{WOF_4}$	**0.000**	

[a] Calculated at the APFD/Def2-TZVPD(O, F)/Def2-TZVPD(-PP)(Mo, W, Kr, Xe) level of theory. [b] From ref [S4].

Table A4.10. Laplacian of electron density ($\nabla^2\rho_b$), the density of all electrons (ρ_b), the energy density (H_b), delocalization indices (δ), QTAIM atomic populations ($\overline{N}$), and ELF basin populations ($\overline{N}$) for $NgF_2{\cdot}MOF_4$, NgF_2, and MOF_4 (Ng = Kr, Xe; M = Mo, W)[a,b]

	$KrF_2{\cdot}MoOF_4$	$KrF_2{\cdot}WOF_4$	KrF_2	$XeF_2{\cdot}MoOF_4$	$XeF_2{\cdot}WOF_4$	XeF_2	$MoOF_4$	WOF_4
$\nabla^2\rho_b$ [c]								
Ng1−F6	0.188	0.179	0.210	0.243	0.245	0.233		
Ng1−F5	0.229	0.234	0.210	0.220	0.218	0.233		
M1---F5	0.171	0.222		0.183	0.237			
M1−F1	0.768	0.978		0.769	0.979		0.758	0.974
M1−F2	0.768	0.978		0.769	0.979		0.758	0.974
M1−F3	0.721	0.924		0.716	0.918		0.758	0.974
M1−F4	0.721	0.924		0.716	0.918		0.758	0.974
M1−O1	0.998	1.070		1.000	1.070		0.958	1.030
ρ_b [d]								
Ng1−F6	0.159	0.162	0.147	0.134	0.136	0.126		
Ng1−F5	0.126	0.124	0.147	0.108	0.106	0.126		
M1---F5	0.035	0.069		0.038	0.073			
M1−F1	0.170	0.258		0.170	0.258		0.170	0.258
M1−F2	0.170	0.258		0.170	0.258		0.170	0.258
M1−F3	0.161	0.246		0.160	0.245		0.170	0.258
M1−F4	0.161	0.246		0.160	0.245		0.170	0.258
M1−O1	0.310	0.422		0.309	0.421		0.312	0.423
H_b [e]								
Ng1−F6	−0.084	−0.089	−0.071	−0.069	−0.701	−0.061		
Ng1−F5	−0.050	−0.049	−0.071	−0.044	−0.421	−0.061		
M1---F5	0.002	−0.002		0.002	−0.003			
M1−F1	−0.069	−0.074		−0.069	−0.074		−0.070	−0.074
M1−F2	−0.069	−0.074		−0.069	−0.074		−0.070	−0.074
M1−F3	−0.063	−0.068		−0.062	−0.067		−0.070	−0.074
M1−F4	−0.063	−0.068		−0.062	−0.067		−0.070	−0.074
M1−O1	−0.244	−0.260		−0.244	−0.259		−0.247	−0.265

continued …

Table A4.10. (continued)

	$KrF_2 \cdot MoOF_4$	$KrF_2 \cdot WOF_4$	KrF_2	$XeF_2 \cdot MoOF_4$	$XeF_2 \cdot WOF_4$	XeF_2	$MoOF_4$	WOF_4
Delocalization Indices								
δ(Ng1−F6)	0.972	0.987	0.912	0.943	0.951	0.892		
δ(Ng1−F5)	0.768	0.754	0.912	0.741	0.722	0.892		
δ(M1---F5)	0.122	0.206		0.131	0.219			
δ(M1−F1)	0.784	0.938		0.785	0.938		0.792	0.948
δ(M1−F2)	0.784	0.938		0.785	0.938		0.792	0.948
δ(M1−F3)	0.730	0.883		0.724	0.876		0.792	0.948
δ(M1−F4)	0.730	0.883		0.724	0.876		0.792	0.948
δ(M1−O1)	1.929	2.097		1.929	2.098		1.930	2.114
QTAIM Atomic Populations								
$\bar{N}$(Ng1)	34.96	34.98	35.02	52.73	52.73	52.77		
$\bar{N}$(F6)	9.44	9.43	9.49	9.58	9.57	9.61		
$\bar{N}$(F5)	9.55	9.65	9.49	9.65	9.75	9.61		
$\bar{N}$(M1)	39.96	69.61		38.96	69.61		38.99	69.72
$\bar{N}$(F1)	9.58	9.82		9.58	9.82		9.58	9.82
$\bar{N}$(F2)	9.58	9.82		9.58	9.82		9.58	9.82
$\bar{N}$(F3)	9.61	9.84		9.62	9.84		9.58	9.82
$\bar{N}$(F4)	9.61	9.84		9.62	9.84		9.58	9.82
$\bar{N}$(O1)	8.67	9.00		8.68	8.99		8.68	8.99

Table A4.10. (continued)

	$KrF_2 \cdot MoOF_4$	$KrF_2 \cdot WOF_4$	KrF_2	$XeF_2 \cdot MoOF_4$	$XeF_2 \cdot WOF_4$	XeF_2	$MoOF_4$	WOF_4
ELF Basin Populations [f]								
$\bar{N}$[C(Ng1)] [g,h]	27.88	27.69	28.06	45.81	45.81	45.61		
$\bar{N}$[V(Ng1)]	7.03	7.03	7.03	6.82	6.83	6.83		
$\bar{N}$[C(F6)]	2.15	2.13	2.13	2.15	2.13	2.14		
$\bar{N}$[V(F6)]	7.39	7.39	7.34	7.52	7.53	7.54		
$\bar{N}$[C(F5)]	2.15	2.14	2.13	2.15	2.15	2.14		
$\bar{N}$[V(F5)]	7.40	7.61	7.34	7.55	7.76	7.54		
$\bar{N}$[C(F1)]	2.16	2.15		2.16	2.15		2.14	2.14
$\bar{N}$[V(F1)]	7.54	8.20		7.54	8.21		7.54	8.23
$\bar{N}$[C(F2)]	2.16	2.15		2.16	2.15		2.14	2.14
$\bar{N}$[V(F2)]	7.54	8.20		7.54	8.21		7.54	8.23
$\bar{N}$[C(F3)]	2.15	2.15		2.15	2.15		2.14	2.14
$\bar{N}$[V(F3)]	7.56	8.19		7.56	8.19		7.54	8.23
$\bar{N}$[C(F4)]	2.15	2.15		2.15	2.15		2.14	2.14
$\bar{N}$[V(F4)]	7.56	8.19		7.56	8.19		7.54	8.23
$\bar{N}$[C(O1)]	2.13	2.13		2.13	2.13		2.12	2.13
$\bar{N}$[V(O1)]	6.88	8.10		6.88	8.10		6.88	8.11

[a] APFD/Def2-TZVPD level of theory. [b] See Figures 7.1 and A4.2 for the atom labeling schemes. [c] The atomic unit (au) for $\nabla^2\rho_b$ is e/a_0^5 (1 au = 24.098 e Å^{-5}). [d] The au for ρ_b is e/a_0^3 (1 au = 6.748 e Å^{-3}, a_0 = Bohr radius = 0.52918 Å, e = charge on an electron). [e] The total energy density of Cremer and Kraka (H_b) is defined as the sum of G_b and V_b, in which G_b is the Lagrangian kinetic energy and V_b is the potential energy density. The au for H_b is e^2/a_0^4 (1 au = E_h/a_0^3 = 6.748 E_h/Å^3, E_h = hartree = e^2/a_0). In covalent bonds, G_b is dominated by V_b, which gives a negative value for H_b. [f] Because the Def2-TZVPD basis set does not separate the sub-valence and valence electrons, they cannot be distinguished by ELF. Consequently, $\bar{N}$[C(M)] and $\bar{N}$[V(M)] (M = Mo, W) are not reported. [g] $\bar{N}$[C(Kr)] = 54 − $\bar{N}$[V(Kr)] − $\Sigma\bar{N}$[($F_{5,6}$)] − $\Sigma\bar{N}$[V($F_{5,6}$)]. [h] $\bar{N}$[C(Xe)] = 72 − $\bar{N}$[V(Xe)] − $\Sigma\bar{N}$[C($F_{5,6}$)] − $\Sigma\bar{N}$[V($F_{5,6}$)].

Table A4.11. Laplacian of electron density ($\nabla^2\rho_b$), the density of all electrons (ρ_b), the energy density (H_b), delocalization indices (δ), QTAIM atomic populations (N), and ELF basin populations (N) for $XeF_2 \cdot 2MOF_4$, XeF_2, and MOF_4 (M = Mo, W)[a,b]

	$XeF_2 \cdot 2MoOF_4$	$XeF_2 \cdot 2WOF_4$	XeF_2	$MoOF_4$	WOF_4
$\nabla^2\rho_b$ [c]					
Ng1−F6	0.245	0.248	0.233		
Ng1−F5	0.220	0.218	0.233		
M1---F5	0.209	0.272			
M1−F1	0.788	0.100		0.758	0.974
M1−F2	0.768	0.981		0.758	0.974
M1−F3	0.743	0.950		0.758	0.974
M1−F4	0.657	0.831		0.758	0.974
M1−O1	1.019	1.090		0.958	1.030
M2---F4	0.162	0.220			
M2−F7	0.713	0.912			
M2−F8	0.754	0.960			
M2−F9	0.771	0.973			
M2−F10	0.761	0.984			
M2−O2	0.992	1.060			
ρ_b [d]					
Ng1−F6	0.136	0.138	0.126		
Ng1−F5	0.105	0.101	0.126		
M1---F5	0.044	0.083			
M1−F1	0.173	0.262		0.170	0.258
M1−F2	0.170	0.260		0.170	0.258
M1−F3	0.165	0.251		0.170	0.258
M1−F4	0.143	0.220		0.170	0.258
M1−O1	0.312	0.424		0.312	0.423
M2---F4	0.032	0.064			
M2−F7	0.159	0.242			
M2−F8	0.168	0.254			
M2−F9	0.170	0.257			
M2−F10	0.169	0.259			
M2−O2	0.310	0.423			

continued …

Table A4.11. (continued)

	$XeF_2{\cdot}2MoOF_4$	$XeF_2{\cdot}2WOF_4$	XeF_2	$MoOF_4$	WOF_4
H_b [e]					
Ng1−F6	−0.070	−0.072	−0.606		
Ng1−F5	−0.042	−0.039	−0.606		
M1---F5	0.0004	−0.005			
M1−F1	−0.072	−0.077		−0.070	−0.074
M1−F2	−0.069	−0.075		−0.070	−0.074
M1−F3	−0.066	−0.071		−0.070	−0.074
M1−F4	−0.048	−0.052		−0.070	−0.074
M1−O1	−0.247	−0.263		−0.247	−0.265
M2---F4	0.003	−0.00003			
M2−F7	−0.060	−0.065			
M2−F8	−0.067	−0.072			
M2−F9	−0.069	−0.073			
M2−F10	−0.068	−0.075			
M2−O2	−0.245	−0.262			
Delocalization Indices					
δ(Ng1−F6)	0.953	0.964	0.892		
δ(Ng1−F5)	0.712	0.685	0.892		
δ(M1---F5)	0.152	0.252			
δ(M1−F1)	0.807	0.959		0.792	0.948
δ(M1−F2)	0.783	0.943		0.792	0.948
δ(M1−F3)	0.752	0.903		0.792	0.948
δ(M1−F4)	0.615	0.739		0.792	0.948
δ(M1−O1)	1.941	2.118		1.930	2.114
δ(M2---F4)	0.104	0.180			
δ(M2−F7)	0.711	0.859			
δ(M2−F8)	0.768	0.918			
δ(M2−F9)	0.786	0.942			
δ(M2−F10)	0.777	0.932			
δ(M2−O2)	1.920	2.100			

continued …

Table A4.11. (continued)

	$XeF_2{\cdot}2MoOF_4$	$XeF_2{\cdot}2WOF_4$	XeF_2	$MoOF_4$	WOF_4
QTAIM Atomic Populations					
$\bar{N}$(Ng1)	52.71	52.72	52.77		
$\bar{N}$(F5)	9.66	9.77	9.61		
$\bar{N}$(F6)	9.57	9.56	9.61		
$\bar{N}$(M1)	38.94	69.60		38.99	69.72
$\bar{N}$(F1)	9.57	9.81		9.58	9.82
$\bar{N}$(F2)	9.59	9.82		9.58	9.82
$\bar{N}$(F3)	9.60	9.83		9.58	9.82
$\bar{N}$(F4)	9.66	9.96		9.58	9.82
$\bar{N}$(O1)	8.67	8.97		8.68	8.99
$\bar{N}$(M2)	38.94	69.61			
$\bar{N}$(F7)	9.63	9.86			
$\bar{N}$(F8)	9.59	9.83			
$\bar{N}$(F9)	9.58	9.82			
$\bar{N}$(F10)	9.59	9.83			
$\bar{N}$(O2)	8.69	8.99			

continued …

Table A4.11. (continued)

	$XeF_2{\cdot}2MoOF_4$	$XeF_2{\cdot}2WOF_4$	XeF_2	$MoOF_4$	WOF_4
ELF Basin Populations[f]					
$\bar{N}$[C(Ng1)][g,h]	45.83	45.55	45.61		
$\bar{N}$[V(Ng1)]	6.81	6.83	6.83		
$\bar{N}$[C(F5)]	2.15	2.15	2.24		
$\bar{N}$[V(F5)]	7.55	7.80	7.54		
$\bar{N}$[C(F6)]	2.14	2.15	2.14		
$\bar{N}$[V(F6)]	7.52	7.52	7.54		
$\bar{N}$[C(F1)]	2.14	2.15		2.14	2.14
$\bar{N}$[V(F1)]	7.53	8.21		7.54	8.23
$\bar{N}$[C(F2)]	2.15	2.14		2.14	2.14
$\bar{N}$[V(F2)]	7.54	8.20		7.54	8.23
$\bar{N}$[C(F3)]	2.15	2.15		2.14	2.14
$\bar{N}$[V(F3)]	7.55	8.19		7.54	8.23
$\bar{N}$[C(F4)]	2.15	2.15		2.14	2.14
$\bar{N}$[V(F4)]	7.60	8.34		7.54	8.23
$\bar{N}$[C(O1)]	2.13	2.13		2.12	2.13
$\bar{N}$[V(O1)]	6.87	8.09		6.88	8.11

continued …

Table A4.11. (continued)

	$XeF_2 \cdot 2MoOF_4$	$XeF_2 \cdot 2WOF_4$
$\bar{N}$[C(F7)]	2.15	2.15
$\bar{N}$[V(F7)]	7.57	8.20
$\bar{N}$[C(F8)]	2.15	2.16
$\bar{N}$[V(F8)]	7.55	8.20
$\bar{N}$[C(F9)]	2.15	2.15
$\bar{N}$[V(F9)]	7.54	8.20
$\bar{N}$[C(F10)]	2.15	2.15
$\bar{N}$[V(F10)]	7.54	8.21
$\bar{N}$[C(O2)]	2.13	2.13
$\bar{N}$[V(O2)]	6.89	8.11

[a] APFD/Def2-TZVPD level of theory. [b] See Figures 7.2 and A4.3 for the atom labeling schemes. [c] The atomic unit (au) for $\nabla^2\rho_b$ is e/a_0^5 (1 au = 24.098 e Å^{-5}). [d] The au for ρ_b is e/a_0^3 (1 au = 6.748 e Å^{-3}, a_0 = Bohr radius = 0.52918 Å, e = charge on an electron). [e] The total energy density of Cremer and Kraka (H_b) is defined as the sum of G_b and V_b, in which G_b is the Lagrangian kinetic energy and V_b is the potential energy density. The au for H_b is e^2/a_0^4 (1 au = E_h/a_0^3 = 6.748 E_h/Å^3, E_h = hartree = e^2/a_0). In covalent bonds, G_b is dominated by V_b, which gives a negative value for H_b. [f] Because the Def2-TZVPD basis set does not separate the sub-valence and valence electrons, they cannot be distinguished by ELF. Consequently, $\bar{N}$[C(M)] and $\bar{N}$[V(M)] (M = Mo, W) are not reported. [g] $\bar{N}$[C(Kr)] = 54 − $\bar{N}$[V(Kr)] − $\Sigma\bar{N}$[($F_{5,6}$)] − $\Sigma\bar{N}$[V($F_{5,6}$)]. [h] $\bar{N}$[C(Xe)] = 72 − $\bar{N}$[V(Xe)] − $\Sigma\bar{N}$[C($F_{5,6}$)] − $\Sigma\bar{N}$[V($F_{5,6}$)].

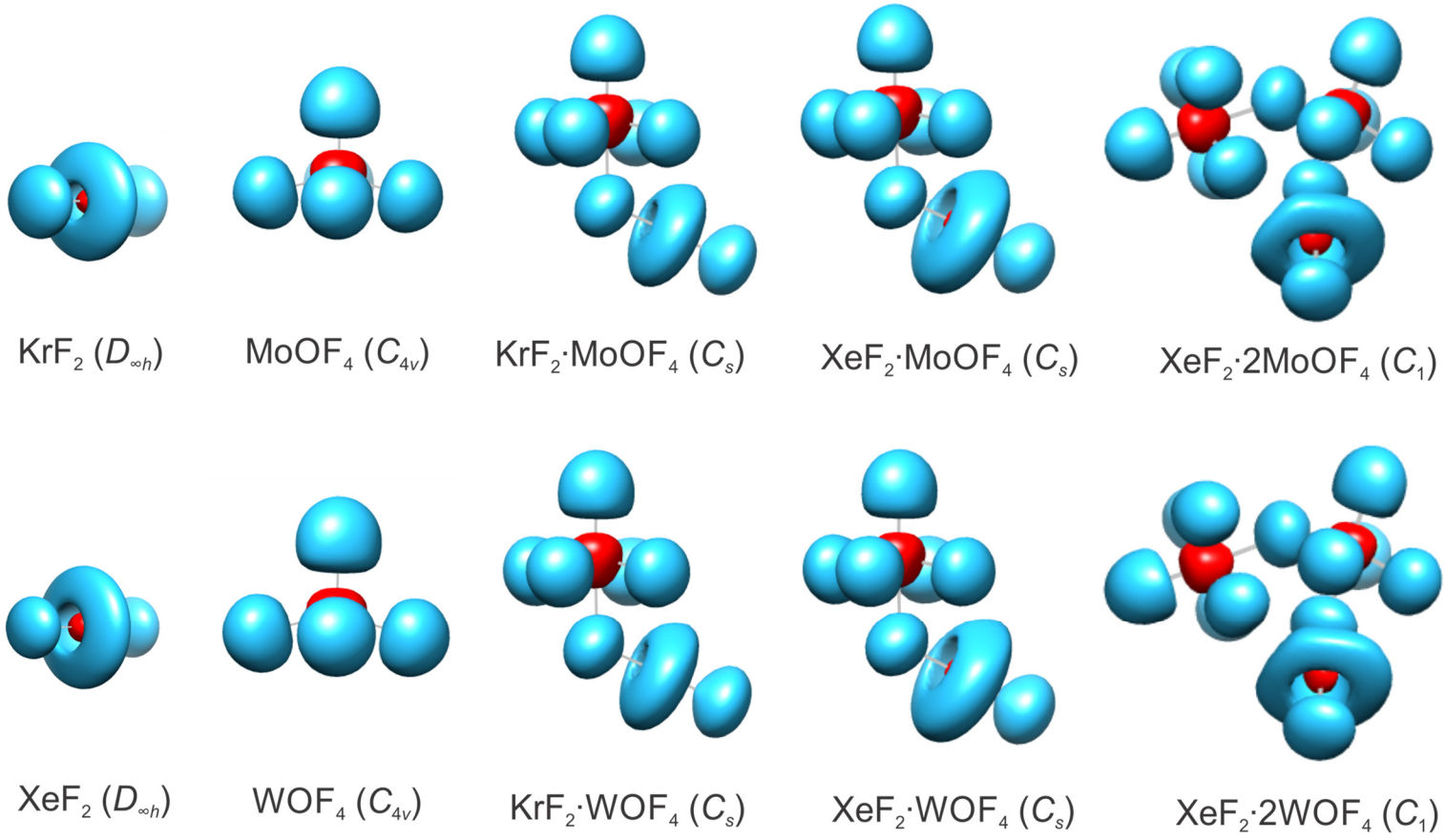

Figure A4.8. ELF isosurface plots, $\eta(r) = 0.60$ (APFD/Def2-TZVPD), for NgF_2, MOF_4, $NgF_2{\cdot}MOF_4$, and $XeF_2{\cdot}2MOF_4$ (Ng = Kr, Xe; M = Mo, W).

Figure A4.9. Reduction of localization diagrams for MOF_4 (C_{4v}), NgF_2 ($D_{\infty h}$), $NgF_2{\cdot}MOF_4$ (C_s), and $NgF_2{\cdot}2MOF_4$ (C_1) (Ng = Kr, Xe; M = Mo, W; see below) which show the ordering of localization nodes and the boundary isosurface values, η(r), at which the reproducible domains separate. Calculated at the APFD/Def2-TZVPD level of theory; the atom numbering schemes correspond to those used in Figures 7.1, 7.2, A4.2, and A4.3.

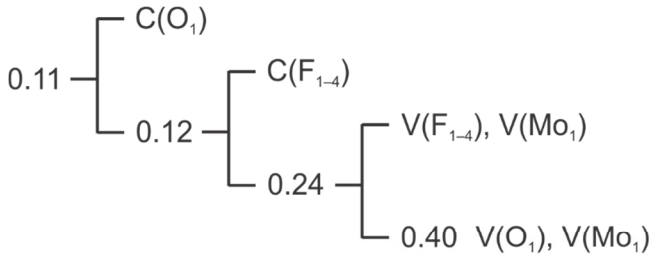

$MoOF_4$ (C_{4v})

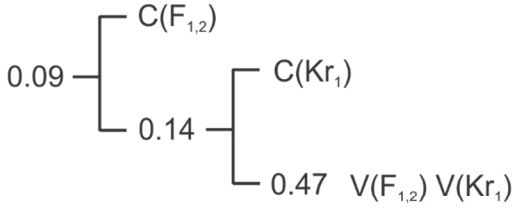

KrF_2 ($D_{\infty h}$)

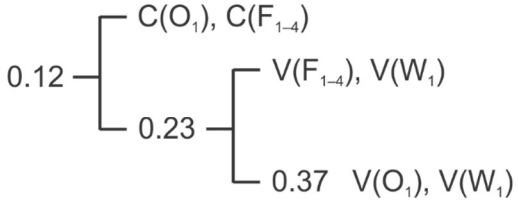

WOF_4 (C_{4v})

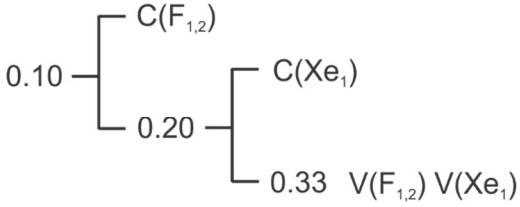

XeF_2 ($D_{\infty h}$)

continued …

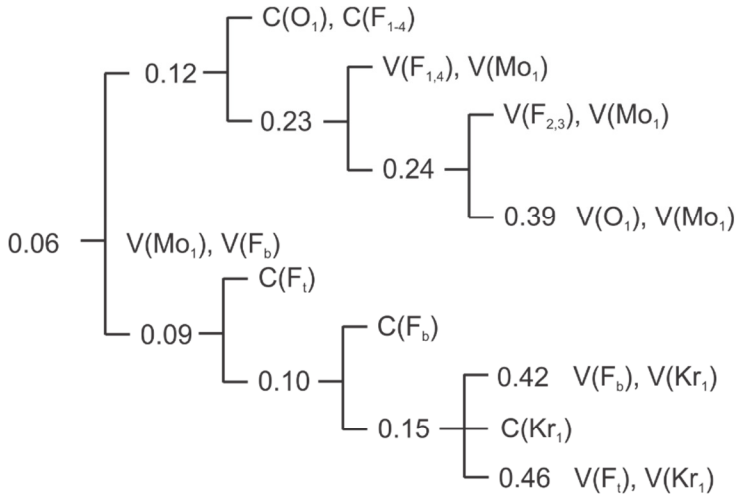

$KrF_2 \cdot MoOF_4$ (C_s)

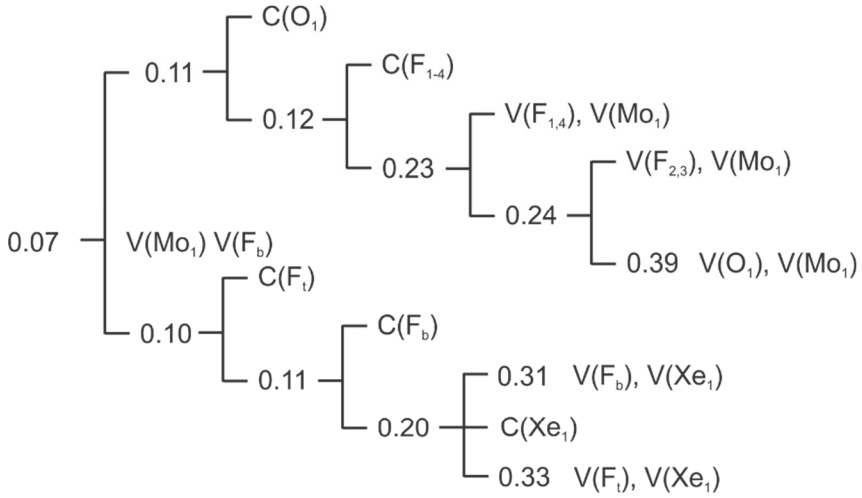

$XeF_2 \cdot MoOF_4$ (C_s)

continued …

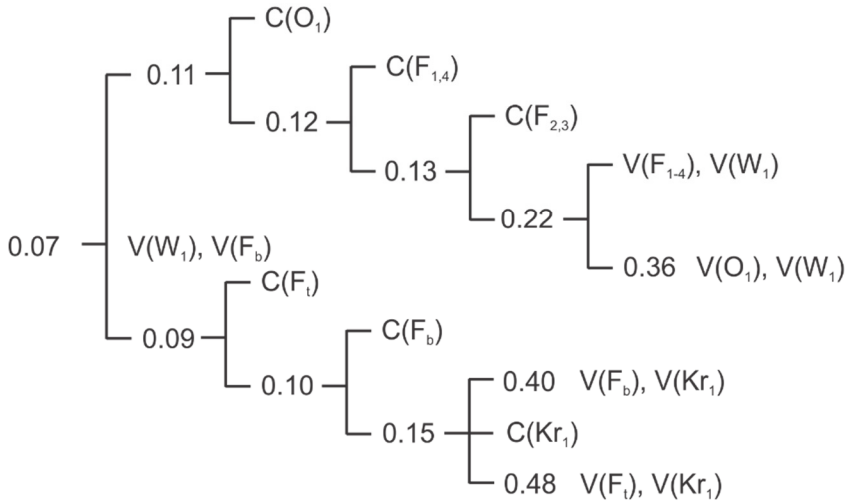

$KrF_2 \cdot WOF_4$ (C_s)

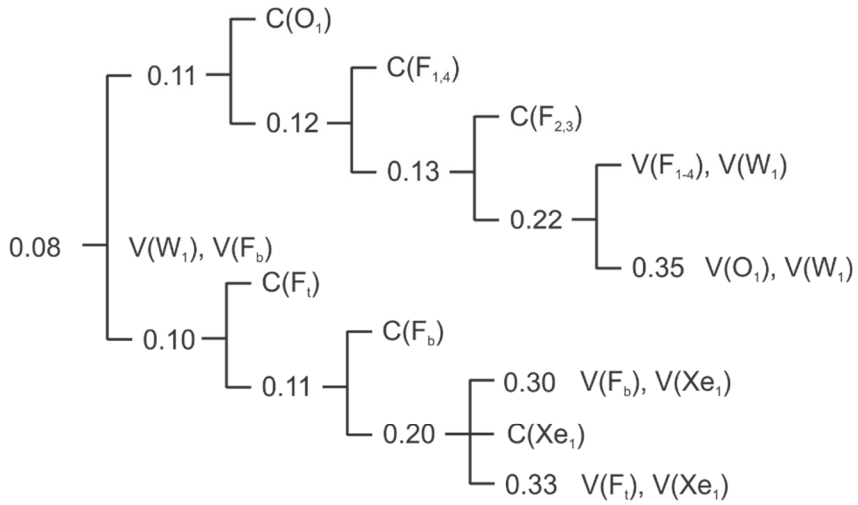

$XeF_2 \cdot WOF_4$ (C_s)

continued …

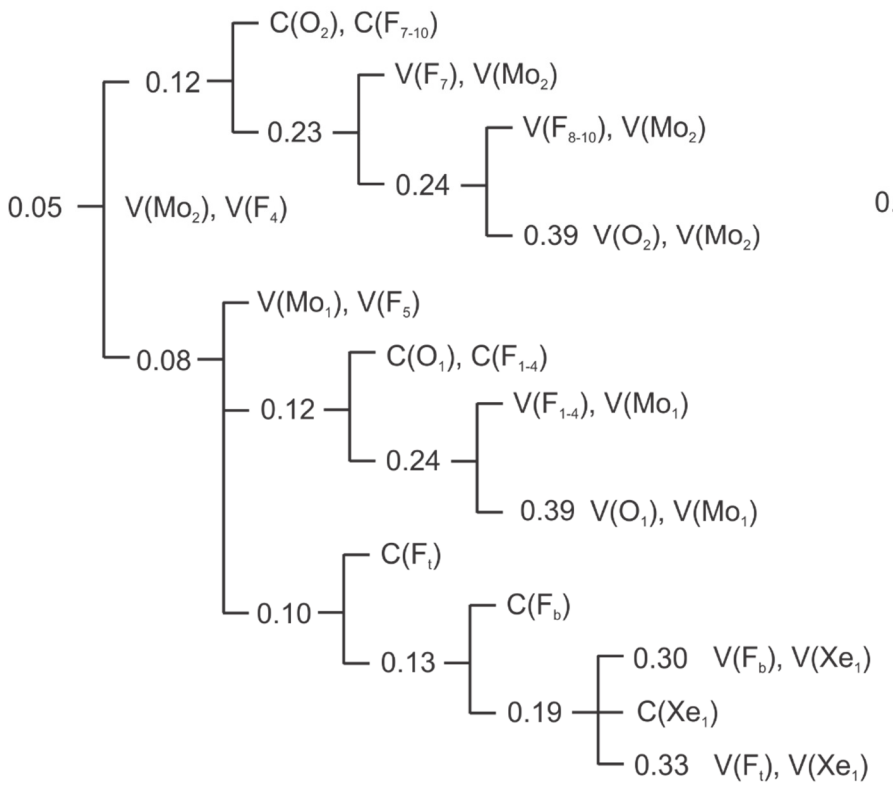

$XeF_2 \cdot 2MoOF_4$ (C_1)

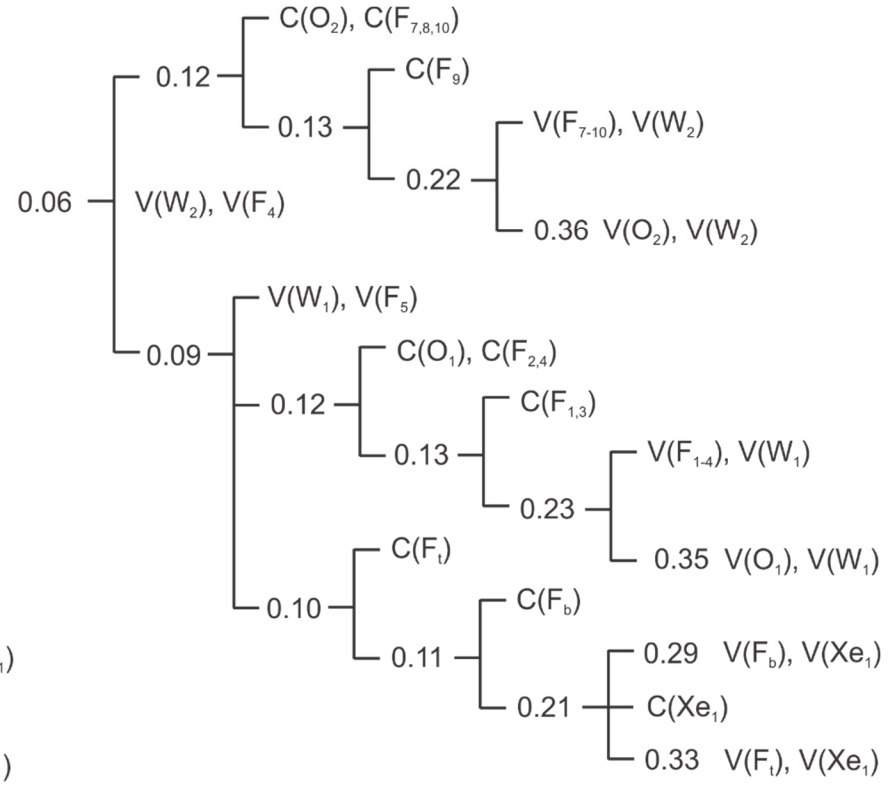

$XeF_2 \cdot 2WOF_4$ (C_1)

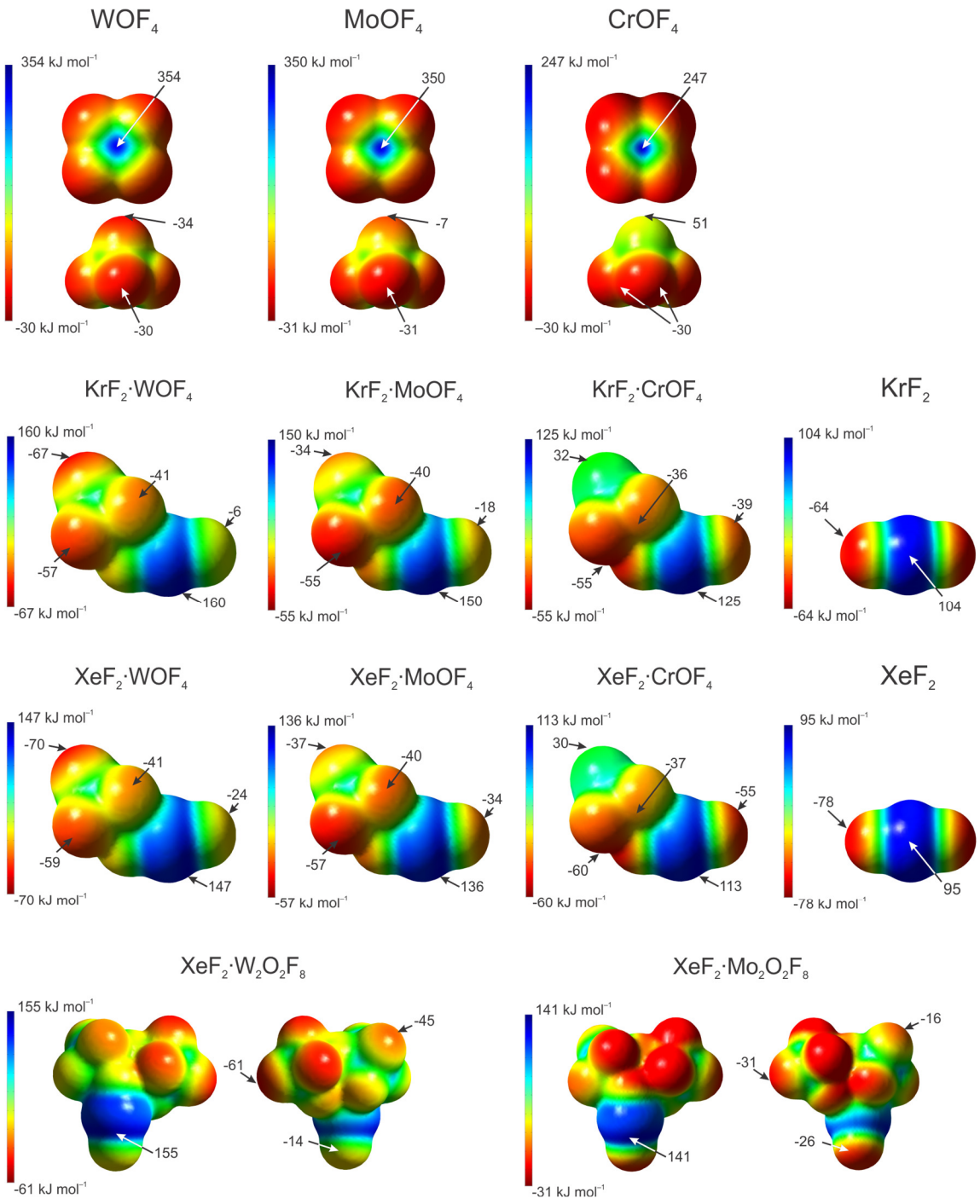

Figure A4.10. The molecular electrostatic potential surfaces (MEPS) calculated at the 0.001 e·a_0^{-3} isosurfaces of MOF_4, $NgF_2 \cdot MOF_4$, and NgF_2 (Ng = Kr, Xe; M = Mo, W, Cr), $XeF_2 \cdot 2MoOF_4$ and $XeF_2 \cdot 2WOF_4$. Selected electrostatic potential extrema are indicated by arrows. The optimized geometries and MEPs were calculated at the APFD/Def2-TZVPD (F, O, Mo, W, Kr, Xe) level of theory.

Table A4.12. Calculated[a] geometric parameters for $NgF_2 \cdot MOF_4$ (Ng = Kr, Xe; M = Cr, Mo, W)

	$KrF_2 \cdot CrOF_4$	$KrF_2 \cdot MoOF_4$	$KrF_2 \cdot WOF_4$	$XeF_2 \cdot CrOF_4$	$XeF_2 \cdot MoOF_4$	$XeF_2 \cdot WOF_4$
			Bond lengths (Å)			
M(1)–O(1)	1.5096	1.6424	1.6685	1.5098	1.6429	1.6692
M(1)–F(1)	1.7283	1.8581	1.8634	1.7308	1.8555	1.8654
M(1)–F(2)	1.7120	1.8454	1.8464	1.7129	1.8366	1.8466
M(1)–F(3)	1.7120	1.8352	1.8464	1.7129	1.8366	1.8466
M(1)–F(4)	1.7283	1.8405	1.8634	1.7308	1.8555	1.8654
M(1)---F(5)	2.5790	2.4132	2.3805	2.5071	2.3752	2.3514
Ng(1)–F(5)	1.9052	1.9313	1.9431	2.0161	2.0487	2.0599
Ng(1)–F(6)	1.8584	1.8401	1.8351	1.9689	1.9536	1.9496
			Bond angles (deg)			
F(5)–Ng(1)–F(6)	179.43	178.71	178.73	178.83	178.52	178.16
Ng(1)–F(5)---M(1)	114.03	122.35	119.15	120.45	122.86	123.68
O(1)–M(1)–F(1)	103.06	102.47	101.93	102.63	101.72	101.52
O(1)–M(1)–F(2)	103.31	101.80	102.24	103.02	102.08	102.07
O(1)–M(1)–F(3)	103.31	102.61	102.24	103.02	102.08	102.07
O(1)–M(1)–F(4)	103.06	101.98	101.93	102.63	101.72	101.52
O(1)–M(1)---F(5)	178.89	179.37	178.43	179.17	178.36	177.80
F(1)–M(1)–F(2)	87.08	86.25	87.71	87.24	87.75	87.81
F(1)–M(1)–F(3)	153.61	154.92	155.78	154.33	156.14	156.36
F(1)–M(1)–F(4)	86.00	86.86	85.80	86.00	85.93	86.01
F(1)–M(1)---F(5)	76.15	77.14	76.94	76.78	77.10	76.91
F(2)–M(1)–F(3)	87.90	88.18	88.73	88.23	88.81	88.79
F(2)–M(1)–F(4)	153.61	156.15	155.78	154.33	156.14	156.36
F(2)–M(1)–F(5)	77.47	77.70	78.86	77.57	79.06	79.47
F(3)–M(1)–F(4)	87.08	88.46	87.71	87.24	87.75	87.81
F(3)–M(1)---F(5)	77.47	77.78	78.86	77.57	79.06	79.47
F(4)–M(1)---F(5)	76.15	78.52	76.94	76.78	77.10	76.91
			Dihedral Angles (deg)			
$Ng–F_{(5)}---M–F_{(1)}$	44.62	13.14	44.33	44.47	44.36	44.45

[a] Calculated at the PBE0-D4/TZ2P level of theory.

Table A4.13. Calculated[a] geometric parameters for $XeF_2 \cdot 2MOF_4$ (M = Mo, W)

	$XeF_2 \cdot 2MoOF_4$	$XeF_2 \cdot 2WOF_4$		$XeF_2 \cdot 2MoOF_4$	$XeF_2 \cdot 2WOF_4$
			Bond lengths (Å)		
Ng(1)–F(5)	2.0664	2.0773	M(2)–O(2)	1.6418	1.6669
Ng(1)–F(6)	1.9463	1.9411	M(2)–F(7)	1.8378	1.8460
M(1)---F(5)	2.3069	2.2820	M(2)–F(8)	1.8616	1.8704
M(1)–O(1)	1.6399	1.6663	M(2)–F(9)	1.8418	1.8528
M(1)–F(1)	1.8473	1.8570	M(2)–F(10)	1.8343	1.8432
M(1)–F(2)	1.8315	1.8408	M(2)---F(4)	2.4315	2.4170
M(1)–F(3)	1.8280	1.8377			
M(1)–F(4)	1.9006	1.9126			
			Bond angles (deg)		
F(5)–Ng(1)–F(6)	177.68	178.05	O(2)–M(2)---F(4)	179.29	179.40
Ng(1)–F(5)---M(1)	132.18	133.02	O(2)–M(2)–F(7)	102.30	102.30
O(1)–M(1)–F(1)	101.75	101.57	O(2)–M(2)–F(8)	101.31	101.38
O(1)–M(1)–F(2)	100.90	100.57	O(2)–M(2)–F(9)	102.35	102.22
O(1)–M(1)–F(3)	102.02	101.82	O(2)–M(2)–F(10)	102.21	102.25
O(1)–M(1)–F(4)	98.89	99.11	F(7)–M(2)---F(4)	77.14	77.36
O(1)–M(1)---F(5)	178.34	178.60	F(7)–M(2)–F(8)	86.86	87.12
F(1)–M(1)–F(2)	88.67	89.11	F(7)–M(2)–F(9)	155.24	155.38
F(1)–M(1)–F(3)	155.90	156.23	F(7)–M(2)–F(10)	88.82	88.91
F(1)–M(1)–F(4)	85.68	85.59	F(8)–M(2)---F(4)	78.25	78.12
F(1)–M(1)–F(5)	77.75	77.92	F(8)–M(2)–F(9)	86.05	85.88
F(2)–M(1)–F(3)	90.64	90.74	F(8)–M(2)–F(10)	156.47	156.35
F(2)–M(1)–F(4)	160.13	160.27	F(9)–M(2)---F(4)	78.20	78.11
F(2)–M(1)–F(5)	80.69	80.74	F(9)–M(2)–F(10)	88.29	88.12
F(3)–M(1)–F(4)	86.87	86.60	F(10)–M(2)---F(4)	78.24	78.26
F(3)–M(1)–F(5)	78.37	78.60	M(1)–F(4)---M(2)	179.29	179.40
F(4)–M(1)–F(5)	79.51	79.57			
			Dihedral angles (deg)		
$Ng–F_{(5)}---M–F_{(1)}$	12.26	14.98			

[a] Calculated at the PBE0-D4/TZ2P level of theory.

Table A4.14. Calculated[a] geometric parameters for $NgF_2 \cdot 2CrOF_4$ (Ng = Kr, Xe)

	$KrF_2 \cdot 2CrOF_4$	$XeF_2 \cdot 2CrOF_4$		$KrF_2 \cdot 2CrOF_4$	$XeF_2 \cdot 2CrOF_4$
			Bond lengths (Å)		
Ng(1)–F(5)	1.8831	1.9970	M(2)–O(2)	1.5092	1.5093
Ng(1)–F(6)	1.8831	1.9970	M(2)–F(7)	1.7249	1.7276
M(1)---F(5)	2.6764	2.6029	M(2)–F(8)	1.7129	1.7123
M(1)–O(1)	1.5092	1.5093	M(2)–F(9)	1.7127	1.7126
M(1)–F(1)	1.7249	1.7276	M(2)–F(10)	1.7253	1.7284
M(1)–F(2)	1.7129	1.7123	M(2)---F(6)	2.6764	2.6029
M(1)–F(3)	1.7127	1.7126			
M(1)–F(4)	1.7253	1.7284			
			Bond angles (deg)		
Ng(1)–F(5)---M(1)	110.36	115.36	Ng(1)–F(6)---M(2)	110.36	115.36
O(1)–M(1)–F(1)	103.60	103.19	O(2)–M(2)---F(6)	178.61	178.69
O(1)–M(1)–F(2)	103.74	103.49	O(2)–M(2)–F(7)	103.60	103.19
O(1)–M(1)–F(3)	103.76	103.51	O(2)–M(2)–F(8)	103.74	103.49
O(1)–M(1)–F(4)	103.53	103.21	O(2)–M(2)–F(9)	103.76	103.51
O(1)–M(1)---F(5)	178.61	178.69	O(2)–M(2)–F(10)	103.53	103.21
F(1)–M(1)–F(2)	86.91	87.00	F(7)–M(2)---F(6)	75.52	75.89
F(1)–M(1)–F(3)	152.62	153.28	F(7)–M(2)–F(8)	86.91	87.00
F(1)–M(1)–F(4)	86.07	86.01	F(7)–M(2)–F(9)	152.62	153.28
F(1)–M(1)---F(5)	75.52	75.89	F(7)–M(2)–F(10)	86.07	86.01
F(2)–M(1)–F(3)	87.43	87.80	F(8)–M(2)---F(6)	77.33	77.44
F(2)–M(1)–F(4)	152.72	153.28	F(8)–M(2)–F(9)	87.43	87.80
F(2)–M(1)---F(5)	77.33	77.44	F(8)–M(2)–F(10)	152.72	153.28
F(3)–M(1)–F(4)	86.80	86.96	F(9)–M(2)---F(6)	77.10	77.40
F(3)–M(1)---F(5)	77.10	77.40	F(9)–M(2)–F(10)	86.80	86.96
F(4)–M(1)---F(5)	75.39	75.85	F(10)–M(2)---F(6)	75.39	75.85
F(5)–Ng(1)–F(6)	179.85	179.46			
			Dihedral angles (deg)		
$Ng–F_{(5)}---M_{(1)}–F_{(1)}$	44.27	43.49	$Ng–F_{(6)}---M_{(2)}–F_{(7)}$	44.27	43.49

[a] Calculated at the PBE0-D4/TZ2P level of theory.

Table A4.15. Calculated[a] geometric parameters for $CrOF_4$, MOF_4, and $M_2O_2F_8$ (M = Mo, W)

	$CrOF_4$	$MoOF_4$	WOF_4	$Mo_2O_2F_8$	$W_2O_2F_8$
Bond lengths (Å)					
M(1)–O(1)	1.5096	1.6411	1.6665	1.6375	1.6627
M(1)–F(1)	1.7153	1.8359	1.8448	1.8251	1.8370
M(1)–F(2)	1.7153	1.8359	1.8448	1.8268	1.8340
M(1)–F(3)	1.7153	1.8359	1.8448	1.8272	1.8351
M(1)–F(4)	1.7153	1.8359	1.8448	1.8761	1.8883
M(2)---F(4)				2.5813	2.5524
M(2)–O(2)				1.6411	1.6664
M(2)–F(5)				1.8382	1.8515
M(2)–F(6)				1.8459	1.8553
M(2)–F(7)				1.8417	1.8477
M(2)–F(8)				1.8363	1.8458
Bond angles (deg)					
O(1)–M(1)–F(1)	105.02	105.49	105.32	106.97	106.64
O(1)–M(1)–F(2)	105.02	105.49	105.32	103.62	103.93
O(1)–M(1)–F(3)	105.02	105.49	105.32	106.82	106.41
O(1)–M(1)–F(4)	105.02	105.49	105.32	102.69	103.26
F(1)–M(1)–F(2)	86.15	85.91	86.00	87.54	87.30
F(1)–M(1)–F(3)	149.97	149.02	149.35	146.10	146.82
F(1)–M(1)–F(4)	86.15	85.91	86.00	85.26	84.65
F(2)–M(1)–F(3)	86.15	85.91	86.00	87.24	87.63
F(2)–M(1)–F(4)	149.97	149.02	149.35	153.68	152.80
F(3)–M(1)–F(4)	86.15	85.91	86.00	84.79	85.07
O(2)–M(2)---F(4)				178.42	179.34
O(2)–M(2)–F(5)				103.60	103.47
O(2)–M(2)–F(6)				103.30	103.22
O(2)–M(2)–F(7)				103.32	103.30
O(2)–M(2)–F(8)				103.69	103.28
F(4)---M(2)–F(5)				76.87	76.08
F(4)---M(2)–F(6)				75.20	76.29
F(4)---M(2)–F(7)				76.19	77.15
F(4)---M(2)–F(8)				77.82	77.20
F(5)–M(2)–F(6)				86.12	86.07
F(5)–M(2)–F(7)				153.06	153.22
F(5)–M(2)–F(8)				87.16	86.76
F(6)–M(2)–F(7)				86.82	87.41
F(6)–M(2)–F(8)				153.01	153.48
F(7)–M(2)–F(8)				87.44	87.59
M(1)–F(4)---M(2)				151.53	151.31

[a] Calculated at the PBE0-D4/TZ2P level of theory.

Energy Decomposition Analyses (EDA)

The energy decomposition analysis (EDA) method developed by Ziegler and Rauk[S10] provides a quantitative interpretation of chemical bonding. The instantaneous interaction energy, ΔE_{int}, between two fragments A and B in molecule AB is described by (**1**) the quasiclassical electrostatic interaction energy between the charge densities of the fragments, ΔE_{elstat}, (**2**) the exchange repulsion between fragments due to the Pauli principle, ΔE_{Pauli}, and (**3**) the energy gain due to orbital mixing (covalency) between the fragments, ΔE_{orb}, in addition to a dispersion term, ΔE_{disp}, when dispersion energy corrections are included in the calculation (Eq **A4.1**).

$$\Delta E_{int} = \Delta E_{Pauli} + \Delta E_{elstat} + \Delta E_{orb} + \Delta E_{disp} \qquad \textbf{(A4.1)}$$

The total energy that is required to distort and electronically excite fragments A and B from their equilibrium geometries and wave functions to the states they possess in AB is the preparation energy, ΔE_{prep}. The sum of the interaction energy and preparation energy provides the bond dissociation energy, D_E, for the A−B bond (Eq **A4.2**).

$$-D_E = \Delta E_{int} + \Delta E_{prep} \qquad \textbf{(A4.2)}$$

Because ΔE_{prep} and ΔE_{Pauli} are positive, the stabilization of AB requires that the absolute value of the sum of the ΔE_{elstat}, ΔE_{orb}, and ΔE_{disp} terms exceeds the sum of the ΔE_{prep} and ΔE_{Pauli} terms. In general, the parameters described by the EDA method provide useful information related to ionicity, covalency, aromaticity, donation or backdonation, and hybridization.[S11]

The bonding in gas-phase $NgF_2{\cdot}CrOF_4$, $NgF_2{\cdot}MOF_4$, $NgF_2{\cdot}2CrOF_4$, and $XeF_2{\cdot}2MOF_4$ (Ng = Kr, Xe; M = Mo, W) was analyzed by the EDA method at the PBE0-

D4/TZ2P level of theory (Tables A4.12–A4.18). The $NgF_2{\cdot}CrOF_4$ and $NgF_2{\cdot}MOF_4$ complexes were described in terms of two fragments, NgF_2 and $CrOF_4$ or MOF_4, the $NgF_2{\cdot}2CrOF_4$ complexes were described in terms of three fragments, NgF_2, $CrOF_4$, and $Cr'OF_4$, and the $XeF_2{\cdot}2MOF_4$ complexes were described as either (1) XeF_2 and $M(OF_3)$–F_b'---$M'OF_4$, or (2) F_tXeF_b---MOF_4 and $M'OF_4$.

Table A4.16. EDA of the M---F_b bonds in $NgF_2{\cdot}MOF_4$ (Ng = Kr, Xe; M = Cr, Mo, W)[a]

	$KrF_2{\cdot}CrOF_4$	**$KrF_2{\cdot}MoOF_4$**	**$KrF_2{\cdot}WOF_4$**
ΔE_{int}	−29.83	−53.79	−63.67
ΔE_{orb}[b]	−22.10 (27.4%)	−52.53 (35.0%)	−66.23 (35.8%)
ΔE_{elstat}[b]	−50.82 (63.1%)	−90.33 (60.1%)	−110.81 (59.9%)
ΔE_{disp}[b]	−7.62 (9.5%)	−7.38 (4.9%)	−8.07 (4.3%)
ΔE_{Pauli}	50.7	96.45	121.43
Total ΔE_{prep}[c]	4.64	11.17	14.49
ΔE_{prep} (NgF_2)	1.13	3.85	5.32
ΔE_{prep} (MOF_4)	3.51	7.32	9.17
$-D_E$	−25.18	−42.61	−49.18
	$XeF_2{\cdot}CrOF_4$	**$XeF_2{\cdot}MoOF_4$**	**$XeF_2{\cdot}WOF_4$**
ΔE_{int}	−34.88	−62.57	−72.12
ΔE_{orb}[b]	−26.11 (26.9%)	−58.37 (33.3%)	−71.24 (34.4%)
ΔE_{elstat}[b]	−62.12 (64.1%)	−107.94 (61.7%)	−126.87 (61.2%)
ΔE_{disp}[b]	−8.73 (9.0%)	−8.73 (5.0%)	−9.13 (4.4%)
ΔE_{Pauli}	62.07	112.47	135.12
Total ΔE_{prep}[c]	6.45	13.69	16.95
ΔE_{prep} (NgF_2)	1.67	4.86	6.36
ΔE_{prep} (MOF_4)	4.77	8.83	10.59
$-D_E$	−28.43	−48.88	−55.17

[a] Calculated at the PBE0-D4/TZ2P level of theory. Values are given in kJ mol^{-1}. [b] Values in parentheses give the percentage of attractive interactions. [c] Total ΔE_{prep} ($NgF_2{\cdot}MOF_4$) = ΔE_{prep} (NgF_2) + ΔE_{prep} (MOF_4) where Ng = Kr, Xe and M = Cr, Mo, W.

Table A4.17. EDA of the Cr---F_b and M---F_b bonds in F_4OCr---$FNgF$---$CrOF_4$ and F_tXeF_b---$M(OF_3)$–F_b'---$M'OF_4$ (Ng = Kr, Xe; M = Mo, W)[a]

	$KrF_2{\cdot}2CrOF_4$	$XeF_2{\cdot}2CrOF_4$	$XeF_2{\cdot}2MoOF_4$	$XeF_2{\cdot}2WOF_4$
ΔE_{int}	−52.36	−60.26	−88.20	−101.87
ΔE_{orb}[b]	−32.66 (24.6%)	−39.73 (35.0%)	−80.74 (35.5%)	−97.82 (36.5%)
ΔE_{elstat}[b]	−81.67 (61.6%)	−102.75 (63.6%)	−133.71 (58.8%)	−156.07 (58.3%)
ΔE_{disp}[b]	−18.24 (13.8%)	−19.03 (11.8%)	−13.07 (5.7%)	−14.03 (5.2%)
ΔE_{Pauli}	80.21	101.25	139.33	166.04
Total ΔE_{prep}[c]	4.35	6.82	21.65	26.42
ΔE_{prep} (NgF_2)	0.25	0.88	7.45	9.13
ΔE_{prep} ($CrOF_4$)	2.05	2.97		
ΔE_{prep} ($NgF_2{\cdot}2CrOF_4$)	4.35	6.82		
ΔE_{prep} ($M(O)F_3F_b$---$M'(O)F_4$)			14.19	17.29
$-D_E$	−48.01	−53.44	−66.55	−75.45

[a] Calculated at the PBE0-D4/TZ2P level of theory. Values are given in kJ mol^{-1}. [b] Values in parentheses give the percentage of attractive interactions. [c] Total ΔE_{prep} ($NgF_2{\cdot}2CrOF_4$) = ΔE_{prep} (NgF_2) + $2\Delta E_{prep}$ ($CrOF_4$) and total ΔE_{prep} ($XeF_2{\cdot}2MOF_4$) = ΔE_{prep} (XeF_2) + ΔE_{prep} ($M(OF_3)$–F_b'---$M'OF_4$), where Ng = Kr, Xe and M = Mo, W.

Table A4.18. EDA of the M′---F_b' bond in F_tXeF_b---$M(OF_3)$–F_b'---$M'OF_4$ (M = Mo, W)[a]

	F_tXeF_b---$Mo(OF_3)$–F_b'---$Mo'OF_4$	F_tXeF_b---$W(OF_3)$–F_b'---$W'OF_4$
ΔE_{int}	−59.62	−67.78
ΔE_{orb}[b]	−48.43 (24.6%)	−56.27 (35.0%)
ΔE_{elstat}[b]	−82.67 (61.6%)	−95.76 (63.6%)
ΔE_{disp}[b]	−14.07 (13.8%)	−15.44 (11.8%)
ΔE_{Pauli}	85.55	99.69
Total ΔE_{prep}[c]	16.67	19.97
ΔE_{prep} (F_tXeF_b---MOF_4)	8.46	10.59
ΔE_{prep} ($M'OF_4$)	8.21	9.38
$-D_E$	−42.95	−47.81

[a] Calculated using the PBE0-D4/TZ2P level of theory. Values are given in kJ mol^{-1}. [b] Values in parentheses give the percentage of attractive interactions. [c] Total ΔE_{prep} (F_tXeF_b---$M(OF_3)$–F_b'---$M'OF_4$) = ΔE_{prep} (F_tXeF_b---MOF_4) + ΔE_{prep} ($M'OF_4$), where M = Mo, W.

Trends observed among the EDA terms of the $NgF_2{\cdot}CrOF_4$, $NgF_2{\cdot}MOF_4$, $NgF_2{\cdot}2CrOF_4$, and $XeF_2{\cdot}2MOF_4$ (M = Mo, W) complexes upon descending groups 6 and 18 of the Periodic Table provide a quantitative assessment of their relative M---F_b and M′---F_b' bond strengths. Moving down Group 18 from Kr to Xe or Group 6 from Cr to

Mo or W results in more negative ΔE_{elstat}, ΔE_{orb}, and ΔE_{disp} terms and more positive ΔE_{Pauli} terms, resulting in a more negative ΔE_{int} value overall. Prior AIM, ELF, and NBO analyses of $NgF_2 \cdot CrOF_4$ have shown that the C---F_b bonds are primarily electrostatic in nature, however the non-linear Cr---F_b–Ng bond angles in their crystal structures suggested the presence of a significant degree of covalency (orbital mixing).[S4] In this study, the EDA method quantitatively shows that orbital mixing comprises 26.9–35.8% of the total attractive contributions of the Cr---F_b and M---F_b bonds in $NgF_2 \cdot CrOF_4$ and $NgF_2 \cdot MOF_4$. Preparation energies (ΔE_{prep}) also become more positive upon descending Groups 6 and 18, consistent with greater distortions of the fragments from their equilibrium geometries, and bond dissociation energies become more negative because ΔE_{int} terms decrease faster than ΔE_{prep} terms increase. These trends indicate that the M---F_b bonds strengthen upon descending a group, in accordance with the relative fluoride-ion donor strengths of NgF_2 (Kr < Xe)[S4] and fluoride-ion affinities of the Group 6 oxide tetrafluorides (Cr < Mo < W). [S12]

To provide a quantitative comparison of the Cr---F_b bond strengths in $NgF_2 \cdot CrOF_4$ and $NgF_2 \cdot 2CrOF_4$, the EDA terms of $NgF_2 \cdot 2CrOF_4$ were divided by two to give the relative contributions for both symmetry-related Cr---F_b bonds. Symmetric bridging of two $CrOF_4$ molecules to a NgF_2 molecule results in weaker Cr---F_b bonding interactions with less negative ΔE_{elstat}, ΔE_{orb}, ΔE_{disp} terms, less positive ΔE_{prep} and ΔE_{Pauli} terms, and smaller bond dissociation energies. These observations are consistent with conclusions drawn from previously published crystallographic, Raman, and quantum-chemical (ELF, NBO, and MEPS) analyses.[S4] In contrast, the M---F_b bonds of $XeF_2 \cdot 2MOF_4$ are stronger

than those of $XeF_2{\cdot}MOF_4$, which further corroborates the relative fluoride-ion affinities of MOF_4 and $M(O)F_3F_b'$---$M'(O)F_4$: $CrOF_4 < MoOF_4 < WOF_4 \approx Mo(OF_3)–F_b'$---$Mo'OF_4 < W(OF_3)–F_b'$---$W'OF_4$. The EDA also confirm that the M'---F_b' bonds of $M(OF_3)–F_b'$---$M'OF_4$ are weaker than but analogous to the M---F_b bonds of $NgF_2{\cdot}MOF_4$ which are best described as predominantly electrostatic with small but significant degrees of covalency. The covalencies of these bonds likely account for the non-linear $M{-}F_b'$---M' bond angles in the crystal structures of $XeF_2{\cdot}2MOF_4$.

Extended Transition State Natural Orbitals for Chemical Valence (ETS-NOCV) Analyses

Recent advances combine the Energy Decomposition Analysis (EDA) partitioning scheme with the Natural Orbital for Chemical Valence (NOCV) method developed by Mitoraj and Michalak[S13] to give the ETS-NOCV method. The latter method divides the orbital interactions described by the EDA method into pairwise contributions of the most relevant fragment MOs. In an NOCV analysis, the difference between the electron densities of the interacting fragments before and after bond formation gives the deformation density, $\Delta\rho$, which is expressed in terms of pairs of NOCV eigenfunctions, Ψ_k and Ψ_{-k}, and their eigenvalues, ν_k and ν_{-k}, which have the same absolute value but opposite sign. The total charge deformation, $\Delta\rho(r)$, is the sum of pairwise contributions from NOCV orbitals which may be visualized to show changes in electronic structure upon bond formation. The total orbital interaction term from the EDA method, ΔE_{orb}, is derived from the sum of pairwise orbital interaction energies, ΔE^k_{orb}, associated with $\Delta\rho_k(r)$, which are obtained from the diagonal transition-state Kohn-Sham matrix elements

of the corresponding NOCV orbitals. Visual inspection of ΔE^{k}_{orb} allows assignment to a particular type of orbital interaction, i.e., σ, π, or δ. The eigenvalues, ν_k and ν_{-k}, measure the amount of electron density that is deformed by an interaction and provide the corresponding energy gain. The ETS-NOCV method therefore enables quantitative comparisons of the relative strengths of different types of covalent bonds. The results from this analysis, however, cannot be compared with numerical values derived from other EDA methods such as the Block-Localized Wave (BLW) function or Generalized Product Function (GPF) analyses.[S11]

In the ETS-NOCV analysis of $KrF_2 \cdot CrOF_4$, a breakdown of the ΔE_{orb} contributions into pairwise contributions shows there is only one significant interaction between KrF_2 and $CrOF_4$, i.e., σ-donation from the HOMO and HOMO−2 SFOs of the KrF_2 ligand into the LUMO+3 and LUMO+8 SFOs of $CrOF_4$ ($\Psi_{1/-1} = \pm 0.15216$) to give an energy gain of −12.7 kJ mol^{-1} (Table A4.19). The changes in electronic structure that result from pairwise orbital interactions are shown in Figure A4.11. The analogous interaction is observed for $XeF_2 \cdot CrOF_4$, where the charge delocalization ($\Psi_{1/-1} = \pm 0.17089$) and energy gain (−15.7 kJ mol^{-1}) are somewhat greater. Sigma-bonding in $NgF_2 \cdot MoOF_4$ and $KrF_2 \cdot WOF_4$ occurs between the HOMO, HOMO−1, and HOMO−2 SFOs of coordinated NgF_2 and the LUMO+3 SFO of MOF_4, whereas in the case of $XeF_2 \cdot WOF_4$, the HOMO−1 SFO of XeF_2 does not contribute significantly to the interaction (Table A4.19). The $KrF_2 \cdot MoOF_4$ complex is particularly noteworthy because it exhibits a second significant σ-type bonding interaction from the HOMO−6 SFO of $MoOF_4$ into the HOMO−6 SFO of KrF_2 (−8.6 kJ mol^{-1}) (Table A4.19, Figures 7.5 and

A4.12). Although it is likely that similar interactions occur for the remaining $NgF_2 \cdot MOF_4$ complexes, their individual energetic contributions do not meet the threshold energy requirement (> 8.6 kJ mol^{-1}) needed to be described by the ETS-NOCV method.[S13]

Analyses of the $NgF_2 \cdot 2CrOF_4$ complexes show that the Cr---F_b bonding interactions are best described as σ-type donations that are analogous to, but weaker than those of $NgF_2 \cdot CrOF_4$ and are not discussed further (Figures A4.13-A4.15, Table A4.20). A breakdown of the contributions to ΔE_{orb} in the ETS-NOCV analysis of the F_tXeF_b---$Mo(OF_3)$–F_b'---$Mo'OF_4$ complex shows that there is only one σ-type electron donation from the HOMO−5 SFO of $XeF_2 \cdot MoOF_4$ into the LUMO+3 SFO of $Mo'OF_4$ (Mo, $\Psi_{1/-1}$ = ± 0.19567), corresponding to an energy gain of −28.0 kJ mol^{-1} (Figure A4.16, Table A4.21). The deformation density shows electron density is primarily transferred from the Mo and F atoms of $MoOF_4$ to $Mo'OF_4$. Individual energy contributions from the remaining orbital interactions do not meet the threshold energy requirement (vide supra). A similar σ-type donation from the HOMO−7 and HOMO−8 SFOs of $XeF_2 \cdot WOF_4$ into the LUMO+3 SFO of $W'(O)F_4$ ($\Psi_{1/-1}$ = ± 0.20476, −32.3 kJ mol^{-1}) occurs for F_tXeF_b---$W(OF_3)$–F_b'---$W'OF_4$ (Figure A4.17, Table A4.21). These interactions are somewhat weaker than those of the M---F_b bonds of the $XeF_2 \cdot MOF_4$ complexes.

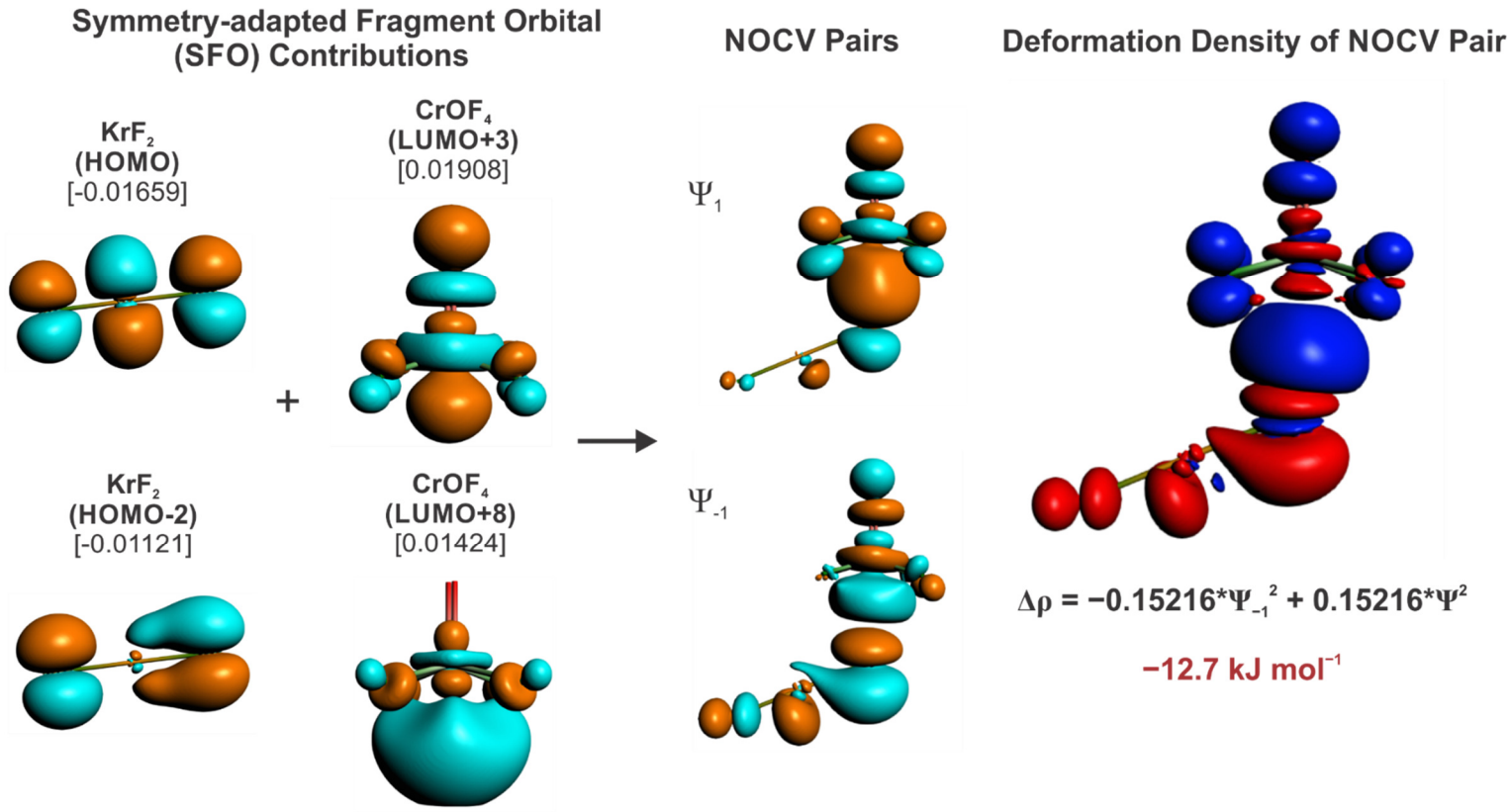

Figure A4.11. The major orbital contribution to the Cr---F_b bond in the ETS-NOCV analysis of $KrF_2 \cdot CrOF_4$ (PBE0-D4/TZ2P level of theory). The isosurface values used for orbital depictions are: KrF_2 SFOs (0.03 a.u.), $CrOF_4$ SFOs (0.05 a.u.), NOCV pairs (0.03 a.u.), and deformation densities (0.0002 a.u.). Contributions of the SFOs to the NOCV pairs are given in square brackets. Relative phases of SFOs and NOCV pairs are indicated in light blue and orange. The colors of the deformation densities indicate increased electron density (blue) and decreased electron density (red) relative to the parent fragments. The fragment orbitals, NOCV pairs, and deformation density pairs are viewed perpendicular to the (Kr, F_b, Cr)-plane.

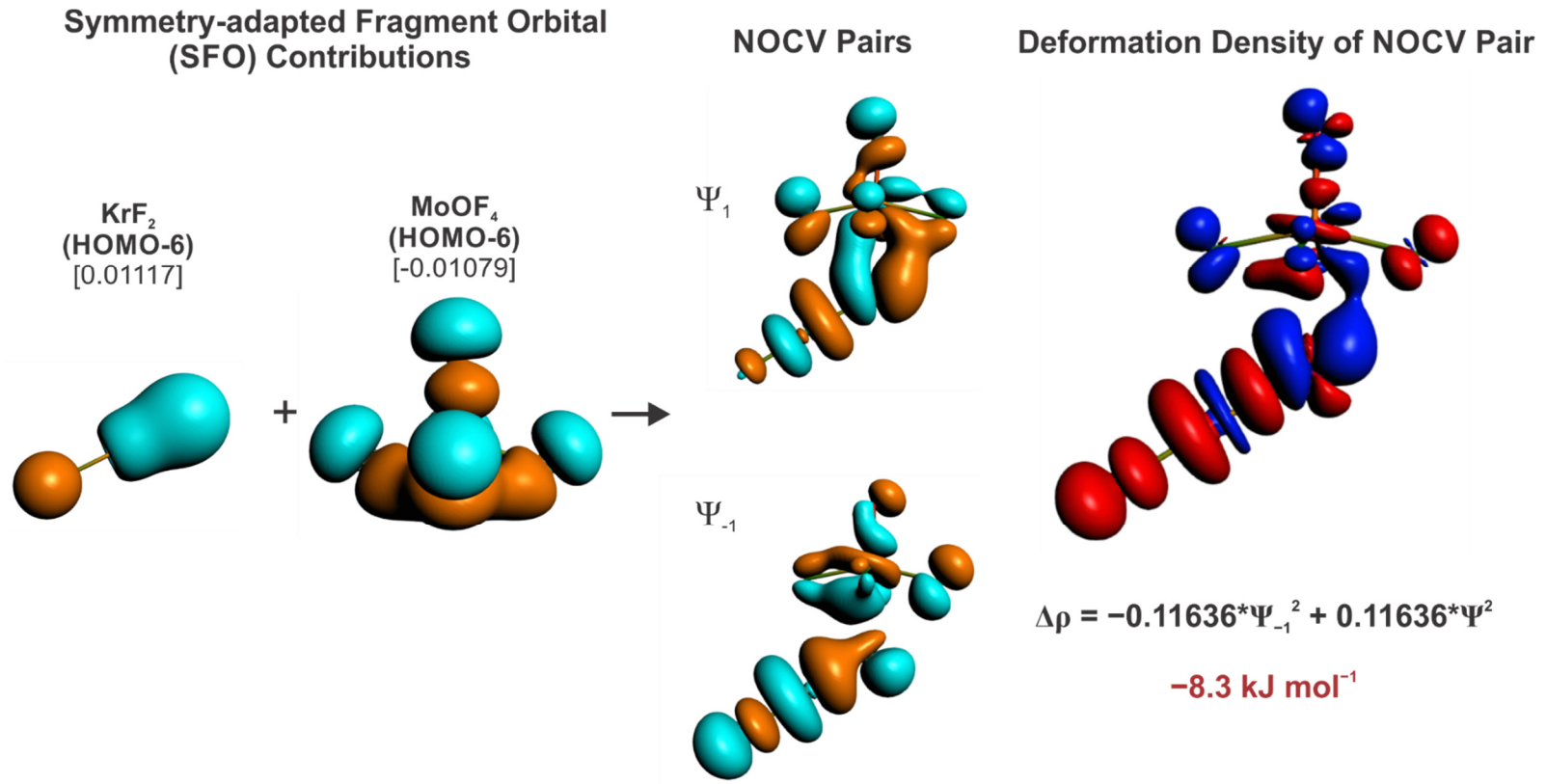

Figure A4.12. The second most significant orbital contribution to the Mo---F_b bond in the ETS-NOCV analysis of KrF_2·$MoOF_4$ (PBE0-D4/TZ2P level of theory). The isosurface values used for orbital depictions are: KrF_2 SFOs (0.03 a.u.), $MoOF_4$ SFOs (0.03 a.u.), NOCV pairs (0.03 a.u.), and deformation densities (0.0003 a.u.). Contributions of the SFOs to the NOCV pairs are given in square brackets. Relative phases of SFOs are indicated in light blue and orange. The colors of the deformation densities indicate increased electron density (blue) and decreased electron density (red) relative to the parent fragments. The fragment orbitals, NOCV pairs, and deformation density pairs are viewed perpendicular to the (Kr, F_b, Mo)-plane. The most significant orbital contribution is provided in Figure 7.5.

Table A4.19. ETS-NOCV analyses for the M---F_b bonds of $NgF_2{\cdot}MOF_4$ (Ng = Kr, Xe; M = Cr, Mo, W)[a]

	$KrF_2{\cdot}CrOF_4$	$KrF_2{\cdot}MoOF_4$		$KrF_2{\cdot}WOF_4$
		Major Contribution	**Minor Contribution**	
KrF_2				
$\Delta\rho(4\pi_u)$	−0.01659	−0.02587		−0.03476
$\Delta\rho(2\pi_g)$	−0.01121	−0.01106		−0.01637
$\Delta\rho(8\sigma_g)$		−0.01149		−0.01426
$\Delta\rho(4\sigma_u)$			0.01117	
MOF_4				
$\Delta\rho$(LUMO+3)	0.01908	0.04907		0.06472
$\Delta\rho$(LUMO+8)	0.01424			
$\Delta\rho$(HOMO−6)			−0.01079	
$\Psi_{1/-1}$	0.15216	0.22091	0.11636	0.23953
Energy (kJ mol^{-1})	−12.7	−32.9	−8.6	−40.6
	$XeF_2{\cdot}CrOF_4$	**$XeF_2{\cdot}MoOF_4$**		**$XeF_2{\cdot}WOF_4$**
XeF_2				
$\Delta\rho(4\pi_u)$	−0.02396	−0.01949		−0.02187
$\Delta\rho(2\pi_g)$	−0.01121	−0.01870		−0.02333
$\Delta\rho(8\sigma_g)$				−0.01524
MOF_4				
$\Delta\rho$(LUMO+3)	0.02396	0.04995		0.06199
$\Delta\rho$(LUMO+8)	0.01225			
$\Psi_{1/-1}$	0.17089	0.23180		0.24840
Energy (kJ mol^{-1})	−15.7	−36.5		−44.0

[a] Calculated at the PBE0-D4/TZ2P level of theory. Values are given in kJ mol^{-1}. The $NgF_2{\cdot}MOF_4$ complexes are described in terms of two fragments: NgF_2 and $CrOF_4$ or MOF_4.

Table A4.20. ETS-NOCV analyses for the Cr---F_b bonds of F_4OCr---F_b–Ng–F_b---$CrOF_4$ (Ng = Kr, Xe)[a]

	F_4OCr---F_b–Ng–F_b---$CrOF_4$		
	Kr	**Xe**	
		Major	**Minor**
NgF_2			
Δρ(HOMO)	−0.01838	−0.01813	
Δρ(HOMO−3)			−0.01916
$2CrOF_4$			
Δρ(LUMO+9)	0.01459	0.01956	
Δρ(LUMO+21)		0.01191	
Δρ(LUMO+10)			0.01426
$\Psi_{1/-1}$	0.13100	0.15284	0.12974
Energy (kJ mol^{-1})	−9.4	−11.9	−10.5

[a] Calculated at the PBE0-D4/TZ2P level of theory. Values are given in kJ mol^{-1}. The NgF_2·$2CrOF_4$ complexes are described in terms of two fragments: NgF_2 and ($2CrOF_4$); see Figures A4.13–A4.15.

Table A4.21. ETS-NOCV analyses for the M′---F_b′ bonds of F_tXeF_b---$M(OF_3)$–F_b′---M′OF_4 (M = Mo, W)[a]

	F_tXeF_b---$M(OF_3)$–F_b′---M′OF_4 (M = Mo, W)	
	Mo	**W**
XeF_2·MOF_4		
Δρ(HOMO−5)	−0.01727	
Δρ(HOMO−7)		−0.01011
Δρ(HOMO−8)		−0.01321
M′OF_4		
Δρ(LUMO+3)	0.04153	0.04705
$\Psi_{1/-1}$	0.19567	0.20476
Energy (kJ mol^{-1})	−28.0	−32.3

[a] Calculated at the PBE0-D4/TZ2P level of theory. Values are given in kJ mol^{-1}. The XeF_2·$2MOF_4$ complexes are described in terms of two fragments: F_tXeF_b---MOF_4 and M′OF_4.

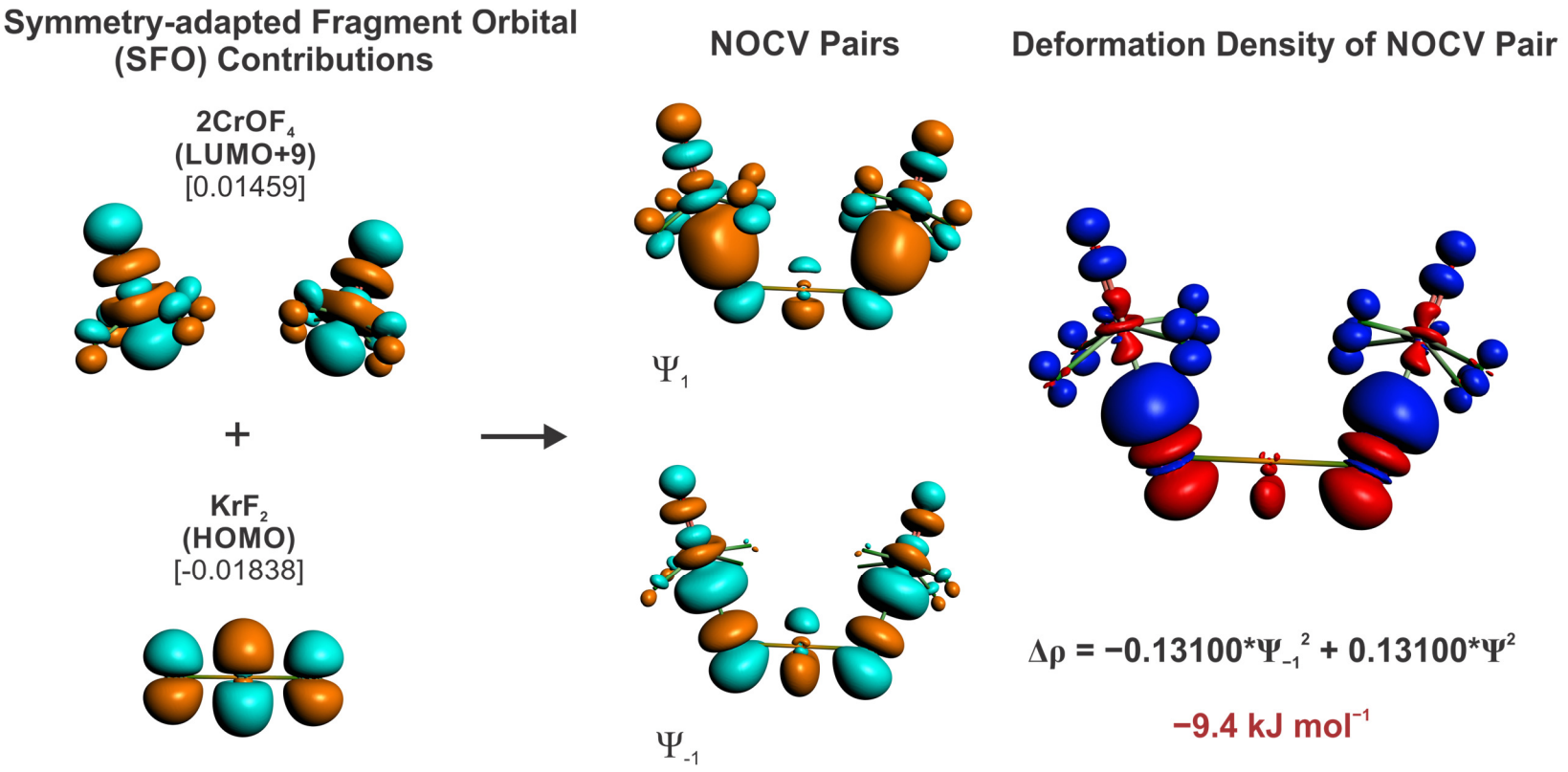

Figure A4.13. The major orbital contribution to the Cr---F_b bonds in the ETS-NOCV analysis of F_4OCr---F_b–Kr–F_b---$CrOF_4$ (PBE0-D4/TZ2P level of theory). The isosurface values used for orbital depictions are: $2CrOF_4$ SFOs (0.03 a.u.), KrF_2 SFOs (0.03 a.u.), NOCV pairs (0.03 a.u.), and deformation densities (0.0002 a.u.). Contributions of the SFOs to the NOCV pairs are given in square brackets. Relative phases of SFOs and NOCV pairs are indicated in light blue and orange. The colors of the deformation densities indicate increased electron density (blue) and decreased electron density (red) relative to the parent fragments. The fragment orbitals, NOCV pairs, and deformation density pairs are viewed perpendicular to the (Kr, F_b, Cr)-plane.

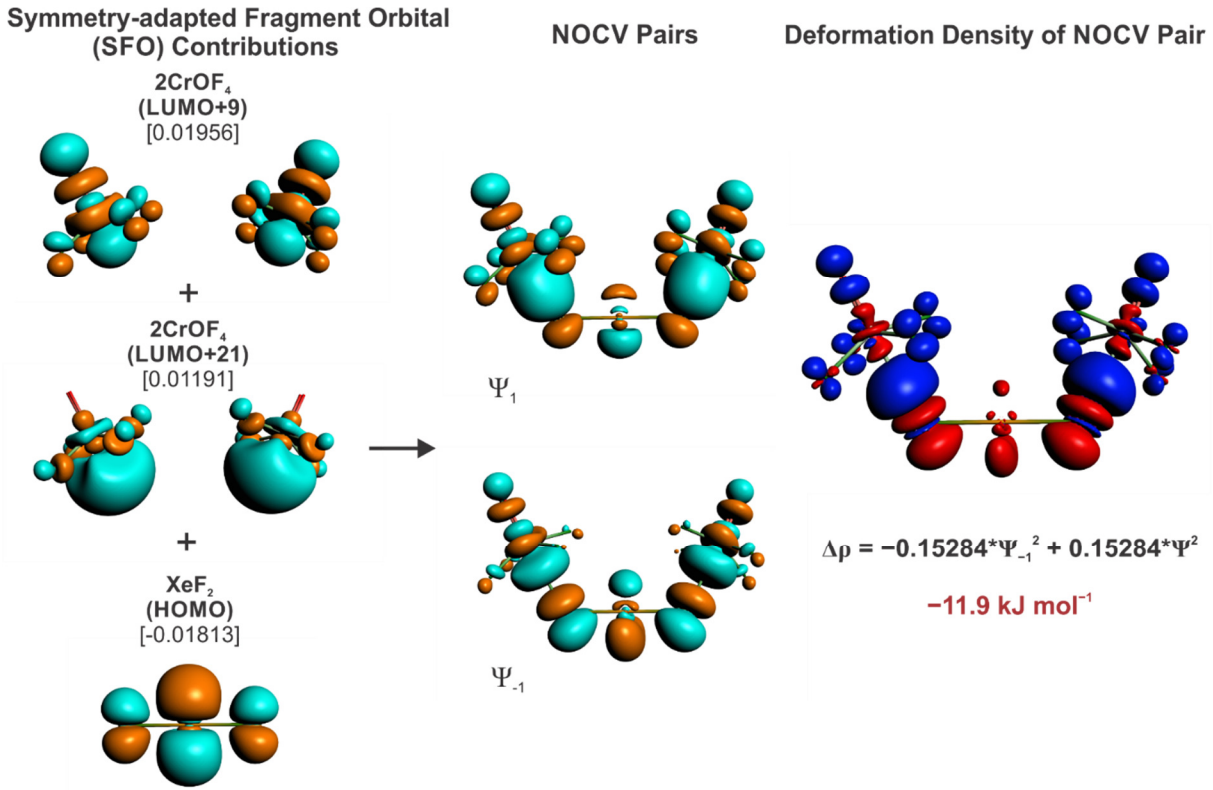

Figure A4.14. The most significant orbital contribution to the Cr---F_b bonds in the ETS-NOCV analysis of F_4OCr---F_b–Xe–F_b---$CrOF_4$ (PBE0-D4/TZ2P level of theory). The isosurface values used for orbital depictions are: $2CrOF_4$ SFOs (0.03 a.u.), XeF_2 SFOs (0.03 a.u.), NOCV pairs (0.03 a.u.), and deformation densities (0.0002 a.u.). Contributions of the SFOs to the NOCV pairs are given in square brackets. Relative phases of SFOs and NOCV pairs are indicated in light blue and orange. The colors of the deformation densities indicate increased electron density (blue) and decreased electron density (red) relative to the parent fragments. The fragment orbitals, NOCV pairs, and deformation density pairs are viewed perpendicular to the (Xe, F_b, Cr)-plane.

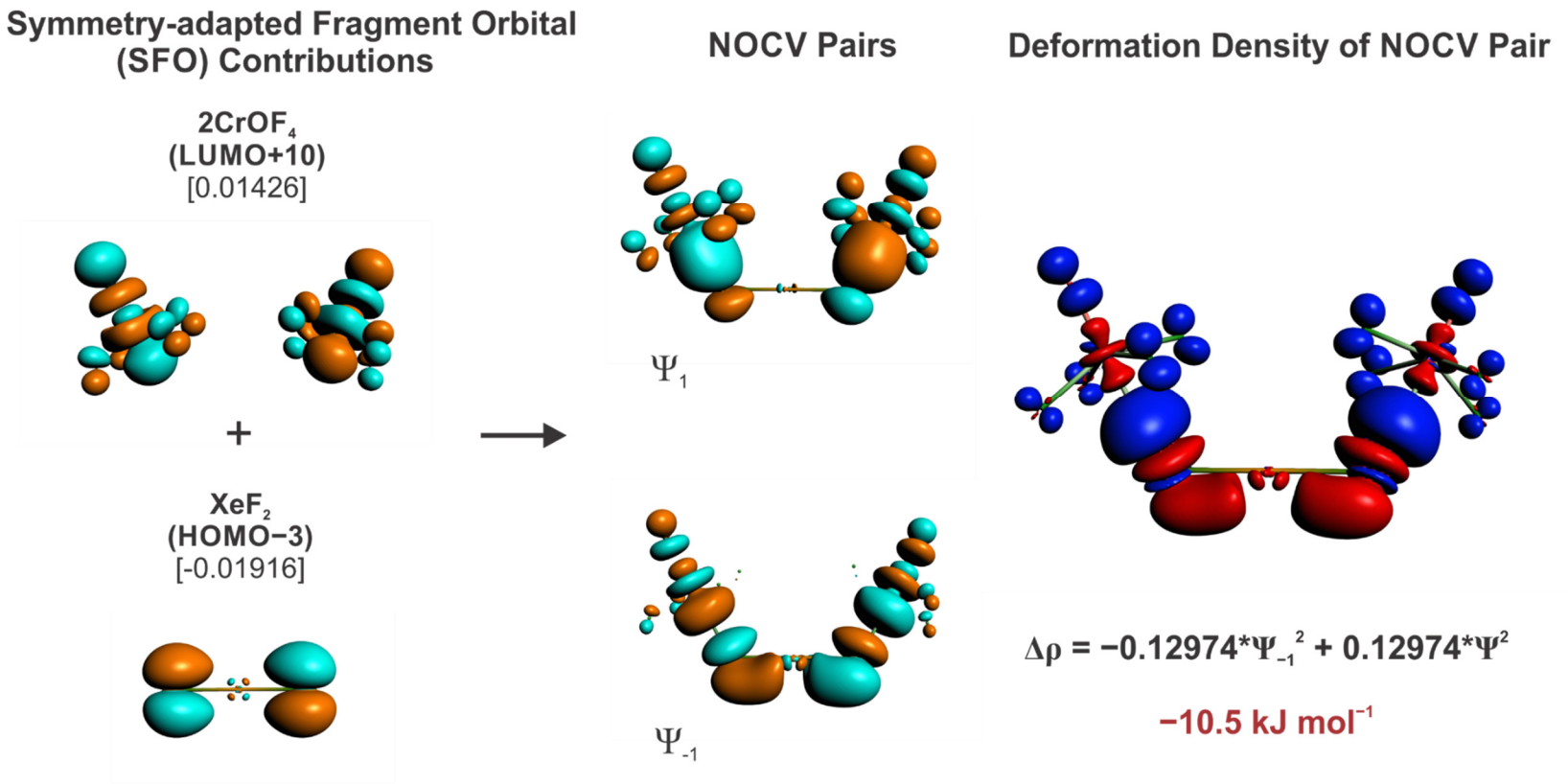

Figure A4.15. The second most significant orbital contribution to the Cr---F_b bonds in the ETS-NOCV analysis of F_4OCr---F_b–Xe–F_b---$CrOF_4$ (PBE0-D4/TZ2P level of theory). The isosurface values used for orbital depictions are: $2CrOF_4$ SFOs (0.03 a.u.), XeF_2 SFOs (0.03 a.u.), NOCV pairs (0.03 a.u.), and deformation densities (0.0002 a.u.). Contributions of the SFOs to the NOCV pairs are given in square brackets. Relative phases of SFOs and NOCV pairs are indicated in light blue and orange. The colors of the deformation densities indicate increased electron density (blue) and decreased electron density (red) relative to the parent fragments. The fragment orbitals, NOCV pairs, and deformation density pairs are viewed perpendicular to the (Xe, F_b, Cr)-plane.

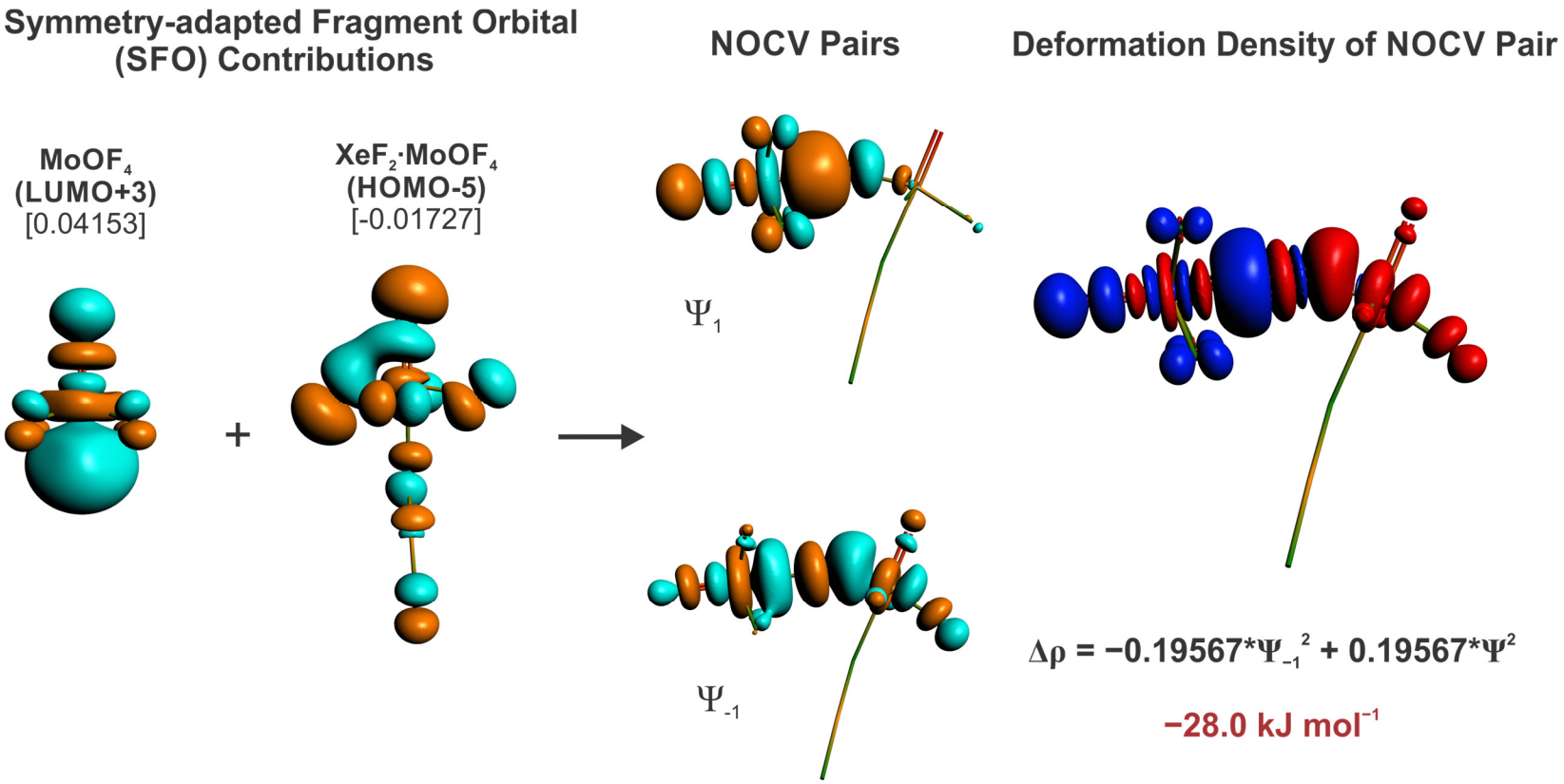

Figure A4.16. The major orbital contribution to the Mo---F_b bond in the ETS-NOCV analysis of F_tXeF_b---$Mo(OF_3)$–F_b'---Mo′OF_4 (PBE0-D4/TZ2P level of theory). The isosurface values used for orbital depictions are: XeF_2·$MoOF_4$ SFOs (0.03 a.u.), $MoOF_4$ SFOs (0.03 a.u.), NOCV pairs (0.03 a.u.), and deformation densities (0.0003 a.u.). Contributions of the SFOs to the NOCV pairs are given in square brackets. Relative phases of SFOs and NOCV pairs are indicated in light blue and orange. The colors of the deformation densities indicate increased electron density (blue) and decreased electron density (red) relative to the parent fragments. The fragment orbitals, NOCV pairs, and deformation density pairs are viewed perpendicular to the (Mo, F_b', Mo′)-plane.

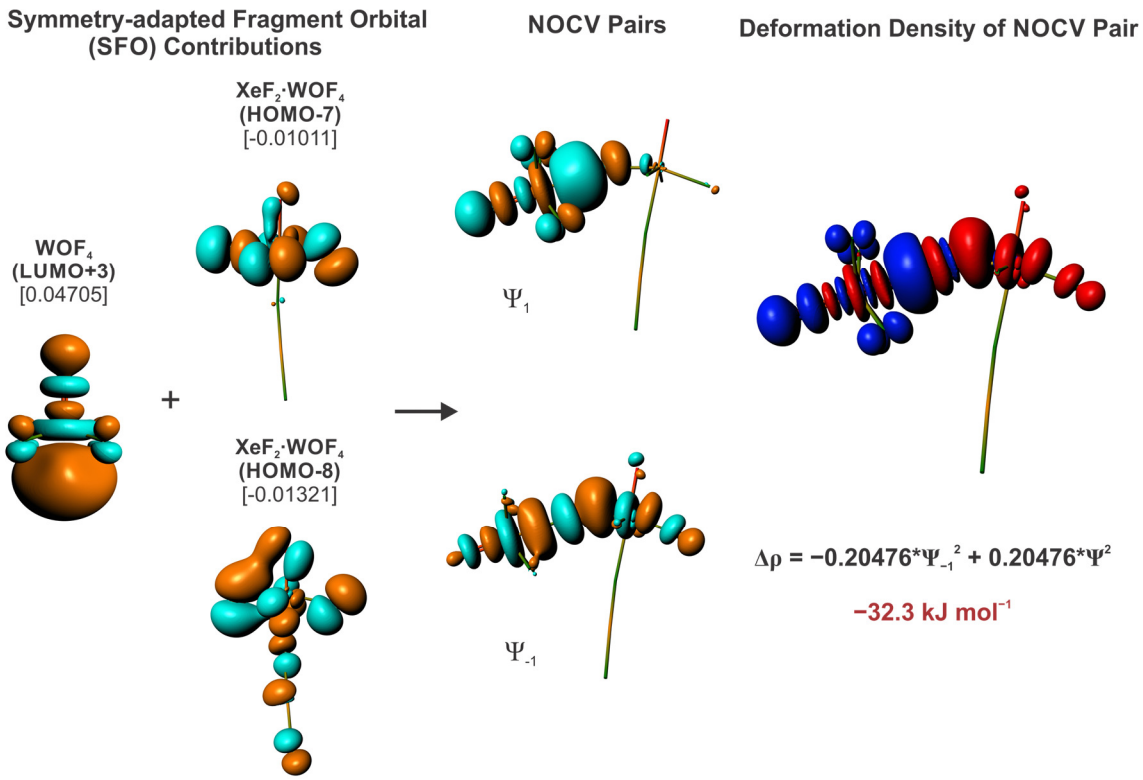

Figure A4.17. The major orbital contribution to the W---F_b' bond in the ETS-NOCV analysis of F_tXeF_b---$W(OF_3)$–F_b'---$W'OF_4$ (PBE0-D4/TZ2P level of theory). The isosurface values used for orbital depictions are: XeF_2·WOF_4 SFOs (0.03 a.u.), WOF_4 SFOs (0.03 a.u.), NOCV pairs (0.03 a.u.), and deformation densities (0.0003 a.u.). Contributions of the SFOs to the NOCV pairs are given in square brackets. Relative phases of SFOs and NOCV pairs are indicated in light blue and orange. The colors of the deformation densities indicate increased electron density (blue) and decreased electron density (red) relative to the parent fragments. The fragment orbitals, NOCV pairs, and deformation density pairs are viewed perpendicular to the (W, F_b', W′)-plane.

References

[S1] Holloway, J. H.; Schrobilgen, G. J. *Inorg. Chem.* **1981**, *20*, 3363–3368.

[S2] Tucker, P. A.; Taylor, P. A.; Holloway, J. H.; Russell, D. R. *Acta Crystallogr.* **1975**, *B31*, 906–908.

[S3] Holloway, J. H.; Schrobilgen, G. J. *Inorg. Chem.* **1980**, *19*, 2632–2640.

[S4] Mercier, H. P. A.; Breddemann, U.; Brock, D. S.; Bortolus, M. R.; Schrobilgen, G. J. *Chem. Eur. J.* **2019**, *25*, 12105–12119.

[S5] Bader, R. F. W. *Atoms in Molecules: A Quantum Theory*; Oxford University Press, Oxford, 1990.

[S6] Brock, D. S.; Casalis de Pury, J. J.; Mercier, H. P. A.; Schrobilgen, G. J.; Silvi, B. *Inorg. Chem.* **2010**, *49*, 6673–6689.

[S7] Brock, D. S.; Casalis de Pury, J. J.; Mercier, H. P. A.; Schrobilgen, G. J.; Silvi, B. *J. Am. Chem. Soc.* **2010**, *132*, 3533–3542.

[S8] Lozinšek, M.; Mercier, H. P. A.; Schrobilgen, G. J. *Angew. Chem. Int. Ed.* **2021**, *60*, 8149–8156; *Angew. Chem.* **2021**, *133*, 8230–8237.

[S9] Žemva, B.; Jesih, A.; Templeton, D. H.; Zalkin, A.; Cheetham, A. K.; Bartlett, N. *J. Am. Chem. Soc.* **1987**, *109*, 7420–7427.

[S10] Ziegler, T.; Rauk, A. *Theor. Chim. Acta* **1977**, *46*, 1–10.

[S11] Zhao, L.; Hopffgarten, M.; Andrada, D. M.; Frenking, G. *WIREs Comput. Mol. Sci.* **2018**, *8*, 1345.

[S12] Craciun, R.; Dixon, D. A. private communication.

[S13] Mitoraj, M. P.; Michalak, A.; Ziegler, T. *J. Chem. Theory Comput.* **2009**, *5*, 962–975.

APPENDIX 5

CHAPTER 8 Supporting Information

Synthesis, Structure, and Bonding of a Xe(IV) Transition-Metal Coordination Complex, F_3XeF_b---WOF_4

Adapted with permission from: Bortolus, M. R.; Mercier, H. P. A.; Schrobilgen, G. J. *Angew. Chem. Int. Ed.* **2022**, *61*, e202211699.

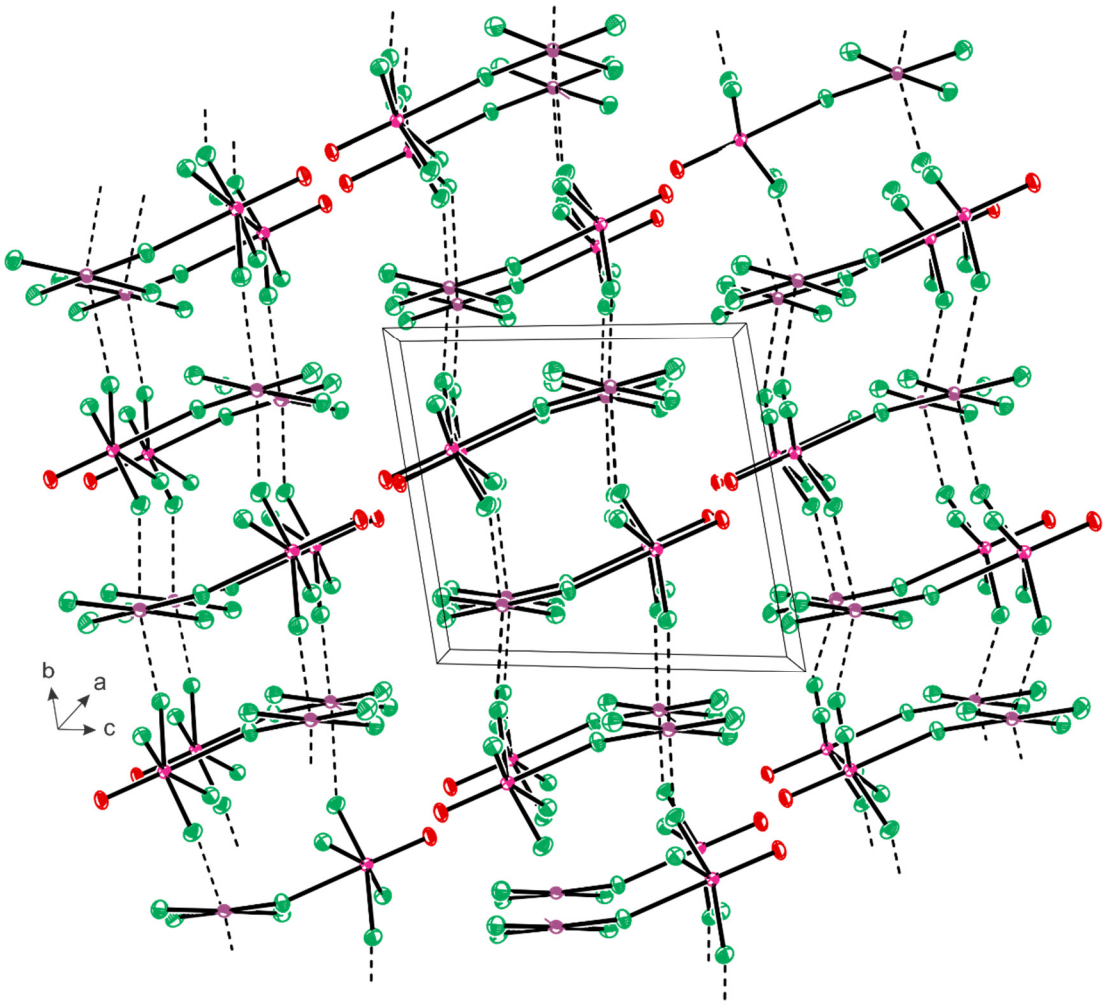

Figure A5.1. A packing diagram showing the X-ray crystal structure of F_3XeF_b---WOF_4 viewed along the *a*-axis of the crystallographic unit cell; thermal ellipsoids are drawn at the 50% probability level.

Table A5.1. Experimental and calculated geometric parameters for F_3XeF_b---WOF_4, and calculated geometric parameters for XeF_4, and WOF_4

	F_3XeF_b---WOF_4 [a]			XeF_4		WOF_4	
	exptl	DFT[b]	ADF[c]	DFT[b]	ADF[c]	DFT[b]	ADF[c]
			Bond Lengths (Å)				
Xe(1)–F(1)	1.872(5)	1.911	1.915	1.944	1.946		
Xe(1)–F(2)	1.912(5)	1.931	1.934	1.944	1.946		
Xe(1)–F(3)	1.917(5)	1.931	1.934	1.944	1.946		
Xe(1)–F(4)	2.068(5)	2.034	2.028	1.944	1.946		
W(1)---F(4)	2.239(5)	2.430	2.455				
W(1)–F(5)	1.842(4)	1.870	1.862			1.849	1.845
W(1)–F(6)	1.844(4)	1.870	1.862			1.849	1.845
W(1)–F(7)	1.840(4)	1.846	1.844			1.849	1.845
W(1)–F(8)	1.850(4)	1.846	1.844			1.849	1.845
W(1)–O(1)	1.665(5)	1.673	1.667			1.673	1.667
F(1)···F(1A)	2.609(5)						
Xe---F(7A)	3.043(5)						
Xe---F(8A)	3.080(5)						
Xe---F(5A)	3.093(5)						
Xe---F(6A)	3.120(5)						
			Bond Angles (º)				
F(1)–Xe(1)–F(2)	87.7(2)	88.1	88.4	90.0	90.0		
F(1)–Xe(1)–F(3)	87.3(2)	88.1	88.4	90.0	90.0		
F(1)–Xe(1)–F(4)	178.5(2)	178.9	179.6	180.0	180.0		
F(2)–Xe(1)–F(3)	175.0(2)	175.9	176.5	180.0	180.0		
F(2)–Xe(1)–F(4)	93.6(2)	91.9	91.6	90.0	90.0		
F(3)–Xe(1)–F(4)	91.4(2)	91.9	91.6	90.0	90.0		
Xe(1)–F(4)---W(1)	145.2(2)	114.5	122.6				
O(1)–W(1)---F(4)	179.2(2)	176.9	177.7				
O(1)–W(1)–F(5)	100.2(2)	102.6	102.8			105.0	105.3
O(1)–W(1)–F(6)	100.3(2)	102.3	102.7			105.0	105.3
O(1)–W(1)–F(7)	100.0(2)	102.3	102.7			105.0	105.3
O(1)–W(1)–F(8)	100.3(2)	102.6	102.8			105.0	105.3
F(6)–W(1)---F(4)	79.9(2)	75.5	75.7				
F(6)–W(1)–F(7)	88.6(2)	87.7	87.5			86.1	86.0
F(6)–W(1)–F(8)	159.4(2)	155.0	154.5			149.9	149.4
F(6)–W(1)–F(5)	87.4(2)	84.7	85.1			86.1	86.0
F(7)–W(1)---F(4)	79.2(2)	79.6	78.8				
F(7)–W(1)–F(8)	88.7(2)	89.2	88.7			86.1	86.0
F(7)–W(1)–F(5)	159.8(2)	155.0	154.5			149.9	149.4
F(8)–W(1)---F(4)	79.5(2)	79.6	78.8				
F(8)–W(1)–F(5)	88.1(2)	87.7	87.5			86.1	86.0
F(5)–W(1)---F(4)	80.5(2)	75.5	75.7				
			Dihedral Angle (º)				
F(5)-W-Xe-F(2)	97.1(2)	35.1	37.3				

[a] The labeling scheme corresponds to that used in Figure 8.1. [b] APFD/Def2-TZVPD. [c] PBE0-D4/TZ2P.

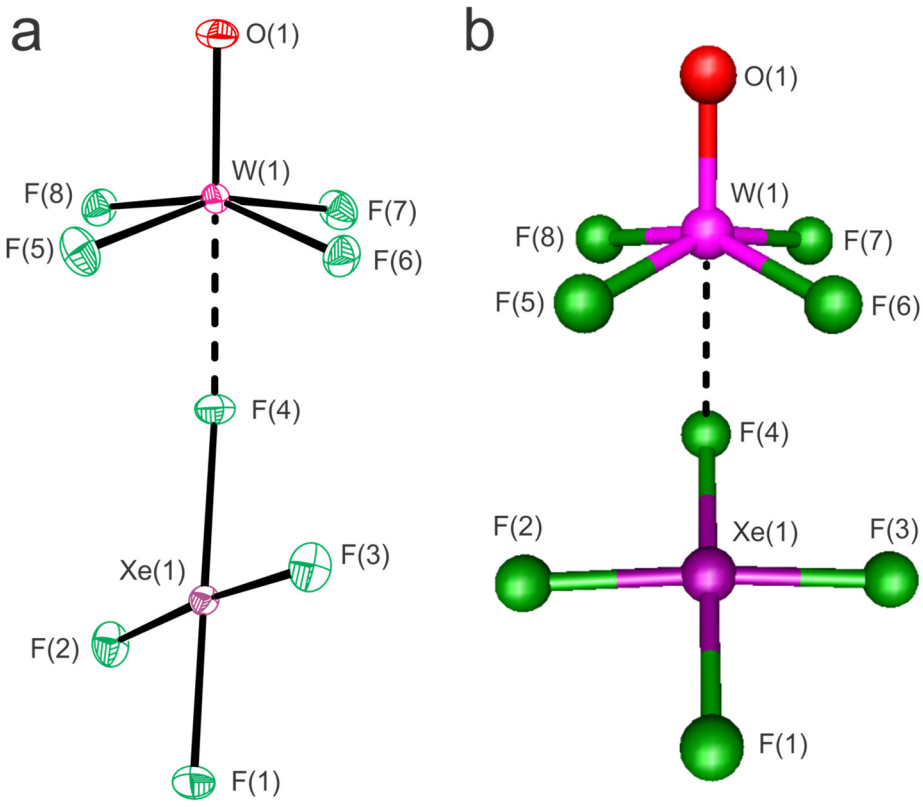

Figure A5.2. Alternative views of (a) the structural unit in the X-ray crystal structure of F_3XeF_b---WOF_4, viewed perpendicular to the O(1)-W(1)-F(4)-Xe(1)-F(1)-plane; thermal ellipsoids are drawn at the 50% probability level; and (b) the calculated geometry (APFD/Def2-TZVPD) of F_3XeF_b---WOF_4, viewed perpendicular to the O(1)-W(1)-F(4)-Xe(1)-F(1)-plane. Also see Figure 8.1.

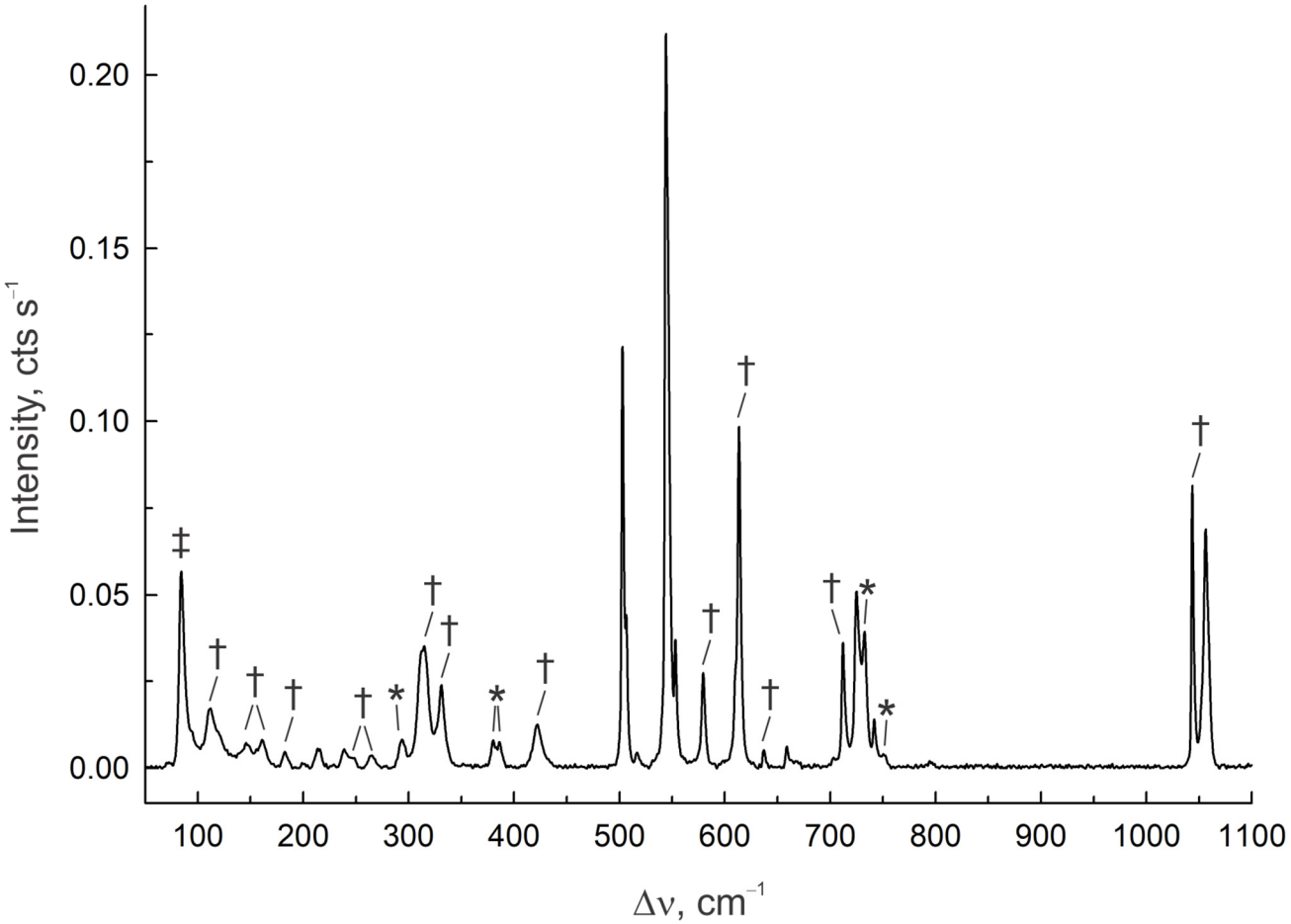

Figure A5.3. The Raman spectrum of a mixture of crystalline F_3XeF_b---WOF_4, XeF_4, and $(WOF_4)_4$ recorded at −150 °C using 1064-nm excitation. Symbols denote bands assigned to F_3XeF_b---WOF_4 (†), FEP sample tube bands (*), and an instrumental artifact (‡). Unmarked bands corresponding to XeF_4 and $(WOF_4)_4$ are listed in footnote [a] of Table A5.2.

Table A5.2. Experimental and calculated frequencies, intensities, and assignments for F_3XeF_b---WOF_4

exptl[a]	calcd[b]	**assgnts** [c]
1044(83)	1096(39)[150]	ν(W–O)
712(36)	727(12)[60]	$[\nu(W–F_5) + \nu(W–F_6)] + [\nu(W–F_7) + \nu(W–F_8)]$
	693(<0.1)[223]	$[\nu(W–F_5) + \nu(W–F_6)] - [\nu(W–F_7) + \nu(W–F_8)]$
	681(<1)[228]	$[\nu(W–F_5) + \nu(W–F_6)] – [\nu(W–F_7) + \nu(W–F_8)]_{small}$
637(5)	631(2)[85]	$[\nu(W–F_5) - \nu(W–F_6)] + [\nu(W–F_7) - \nu(W–F_8)]_{small}$
614(100)	604(32)[152]	$\nu(Xe–F_1)$
610(sh)	600(<1)[127]	$[\nu(Xe–F_2) – \nu(Xe–F_3)] + [\nu(W–F_5) – \nu(W–F_6)]_{small}$
580(27)	564(26)[31]	$[\nu(Xe–F_2) + \nu(Xe–F_3)]$
422(13)	472(17)[132]	$\nu(Xe–F_4)$
331(24)	333(2)[32]	$[\delta_{umb}(XeF_1F_2F_3F_4)] + \delta(OWF_5F_6)_{i.p.\ small}$
315(35)	321(1)[5]	$[\delta(F_6WF_7) + \delta(F_5WF_8)]$
302(sh)	309(2)[8]	$[\delta(OWF_6F_7)_{o.o.p.} – \delta(OWF_8F_5)_{o.o.p.}]$
296(sh)	307(3)[13]	$[\delta(OWF_5F_6)_{i.p.} – \delta(OWF_7F_8)_{i.p.}]$
265(4)	257(<1)[68]	$\delta_{umb}(WF_5F_6F_7F_8) + \rho_w(F_2XeF_3)_{i.p.}$
248(sh)	239(1)[2]	$[\delta(F_1XeF_2) + \delta(F_3XeF_4)]$
	226(<1)[13]	$[\delta(F_6WF_7) – \delta(F_8WF_5)] + [\delta(F_1XeF_2) – \delta(F_1XeF_3)]$
	226(<1)[18]	$[\delta(F_5WF_6) – \delta(F_7WF_8)]$
	221(1)[10]	$\rho_t(F_1XeF_2) + \rho_t(F_1XeF_3)$
200(1)	186(<1)[<1]	$[\rho_t(F_7WF_8) – \rho_t(F_5WF_6)] + \delta(F_1XeF_4)$
161(8)	153(<1)[1]	$\delta(F_2XeF_3)$
156(sh)	150(<1)[<1]	$[\rho_t(F_7WF_8) – \rho_t(F_5WF_6)] – \delta(F_1XeF_4)$
	127(1)[1]	$\rho_t(F_1XeF_4)$
	97(<1)[<1]	$\rho_r(WOF_{(4)})$
	85(<1)[<1]	$[\rho_r(XeF_1F_2F_3) + \rho_t(WOF_{(4)})]$
	61(<1)[<1]	$\delta(WF_4Xe)$
	57(1)[<1]	$[\rho_t(F_2XeF_3) – \rho_t(WOF_{(4)})_{small}]$
	28(<1)[<1]	$[\rho_r(WF_{(4)}) – \rho_r(XeF_{(4)})]$

continued …

Table A5.2. (continued)

[a] The Raman spectrum of a dry crystalline sample was recorded in an FEP sample tube at −150 °C using 1064-nm excitation. Frequencies are given in cm^{-1}. Values in parentheses denote relative Raman intensities. The abbreviation, sh, denotes a shoulder. Additional bands were observed and assigned to XeF_4 (214(6), 239(6), 503(123), 505(sh), 544(214), and 553(37) cm^{-1}) and $(WOF_4)_4$ (311(sh), 315(sh), 331(sh), 517(5), 659(6), 725(52), 742(14), and 1056(70) cm^{-1}). Bands at 112(17), 119(sh), 126(sh), and 182(5) cm^{-1} are tentatively assigned to lattice modes. [b] Values in parentheses and square brackets denote calculated Raman intensities ($Å^4$ amu^{-1}) and infrared intensities (km mol^{-1}), respectively. [c] Assignments are for the energy-minimized gas-phase geometry (C_s) calculated at the APFD/def2-TZVPD level of theory. The atom labeling scheme corresponds to that used in Figure 8.1. Abbreviations denote stretch (ν), bend (δ), rock (ρ_r), twist (ρ_t), and wag (ρ_w), umbrella (umb), $XeF_{(4)}$ ($XeF_1F_2F_3F_4$), $WOF_{(4)}$ ($W_1O_1F_5F_6F_7F_8$), in-plane (i.p.), and out-of-plane (o.o.p.). Bond elongations and angle openings are denoted by plus (+) signs, and bond contractions and angle compressions are denoted by minus (−) signs. The in-plane and out-of-plane bending modes are relative to the $O_1W_1F_4Xe_1F_1$-plane.

Table A5.3. Observed and calculated frequencies, intensities, and assignments for XeF_4

exptl[a]	calcd[b]	assgnts[c]
	590(0)[289]	$\nu_6(E_u)$
	590(0)[289]	
553(17)	570(49)[0]	$\nu_1(A_{1g})$
544(100)		
505(sh)	525(26)[0]	$\nu_4(B_{1g})$
503(57)		
	292(0)[33]	$\nu_3(A_{2u})$
239(6)[d]	218(3)[0]	$\nu_2(B_{2g})$
214(3)		
	166(0)[0]	$\nu_5(B_{2u})$
	153(0)[1]	$\nu_7(E_u)$
	153(0)[1]	

[a] The Raman spectrum of XeF_4 was obtained from a dry crystalline mixture of F_3XeF_b---WOF_4, XeF_4, and $(WOF_4)_4$ in an FEP sample tube at −150 °C using 1064-nm excitation. Frequencies are given in cm^{-1} and values in parentheses denote relative Raman intensities. The abbreviation, sh, denotes a shoulder. [b] APFD/Def2-TZVPD. Values in parentheses and square brackets denote calculated Raman intensities ($Å^4$ amu^{-1}) and infrared intensities [km mol^{-1}], respectively. [c] Assignments for XeF_4 were made under D_{4h} symmetry. [d] The band overlaps with a $(WOF_4)_4$ band.

Table A5.4. Observed and calculated frequencies, intensities, and assignments for crystalline $(WOF_4)_4$; and calculated frequencies and intensities for gas-phase WOF_4

$(WOF_4)_4$ (s)	WOF_4 (g)	
exptl[a]	calcd (C_{4v})[b]	assgnts (C_{4v})[c]
1056(100)	1096(24)[105]	$\nu_1(A_1)$
742(20) 725(52)	737(15)[46]	$\nu_2(A_1)$
	704(<1)[227] 704(<1)[227]	$\nu_7(E)$
659(6) 517(5)	648(3)[0]	$\nu_5(B_2)$
331(sh)	336(2)[0]	$\nu_4(B_1)$
315(sh) 311(sh)	299(2)[7] 299(2)[7]	$\nu_8(E)$
239(6)[d]	242(<1)[12]	$\nu_3(A_1)$
	237(<1)[21] 237(<1)[21]	$\nu_9(E)$
	99(<1)[0]	$\nu_6(B_2)$

[a] The Raman spectrum of $(WOF_4)_4$ was obtained from a dry crystalline mixture of F_3XeF_b---WOF_4, XeF_4, and $(WOF_4)_4$ in an FEP sample tube at −150 °C using 1064-nm excitation. Frequencies are given in cm^{-1}. Values in parentheses denote relative Raman intensities. The abbreviation denotes a shoulder (sh). [b] APFD/Def2-TZVPD. Values in parentheses and square brackets denote calculated Raman intensities ($Å^4$ amu^{-1}) and infrared intensities (km mol^{-1}), respectively. [c] Assignments for the WOF_4 moiety were made under C_{4v} symmetry. [d] The band overlaps with a XeF_4 band.

Quantum-chemical Calculations

Natural Atomic Orbital (NAO) and Natural Bond Orbital (NBO) Analyses

The NAO and NBO analyses of XeF_4, WOF_4, and F_3XeF_b---WOF_4 show that coordination of XeF_4 to WOF_4 results in significant polarity changes for the Xe–F, W–F, and W–O bonds of F_3XeF_b---WOF_4 (Table A5.5). The degree of charge transfer (±0.064) from XeF_4 to WOF_4 is somewhat less than for $FNgF_b$---WOF_4 (Xe, ±0.077; Kr, ±0.074),[S1] in accordance with the relative fluorobasicities of the noble-gas fluorides, $KrF_2 \approx XeF_2 > XeF_4$. The atom charges, Wiberg bond indices, and valences of the F atoms bonded to Xe in F_3XeF_b---WOF_4 reflect the relative Xe–F bond covalences, $Xe–F_b < Xe–F_{2,3} < Xe–F_1$. The $W–F_{5,6}$ bonds of WOF_4 that are proximate to XeF_4 in F_3XeF_b---WOF_4 are polarized by the high charge on Xe(IV), +2.332 (also see AIM and ELF Analyses), and are therefore somewhat less covalent than the $W–F_{7,8}$ bonds that are farthest from the Xe(IV) atom. The $Xe–F_b$ and $Xe–F_{1–3}$ Wiberg bond indices of F_3XeF_b---WOF_4 are respectively lower and higher than those of XeF_4, in accordance with their relative bond covalences. The Wiberg bond index of the W---F_b bond (0.097) is somewhat less than those calculated for the W---F_b bonds of $FNgF_b$---WOF_4 (Xe, 0.117; Kr, 0.110),[S1] in accordance with the lower fluorobasicity of XeF_4 relative to NgF_2. The W---F_b bond is best described as a primarily electrostatic σ-hole bond with a smaller, but significant degree of covalency. The covalent component accounts for the non-linear $Xe–F_b$---W angle calculated for the gas-phase structure (114.5°) and, in part, for the non-linear $Xe–F_b$---W angle observed in the X-ray crystal structure (145.2(2)°).

Table A5.5. Wiberg bond indices, natural population analysis (NPA) charges, and valence indices for F_3XeF_b---WOF_4[a]

F_3XeF_b---WOF_4 (C_s)					**XeF_4 (D_{4h})**				
Bond Indices			NPA Charges [Valence Indices]		Bond Indices			NPA Charges [Valence Indices]	
Xe1−F1	0.598	Xe1	2.332	[2.139]	Xe1−F1	0.541	Xe1	2.301	[2.165]
Xe1−F2	0.561	F1	−0.528	[0.768]	Xe1−F2	0.541	F1	−0.575	[0.715]
Xe1−F3	0.561	F2	−0.560	[0.738]	Xe1−F3	0.541	F2	−0.575	[0.715]
Xe1−F4	0.406	F3	−0.560	[0.738]	Xe1−F4	0.541	F3	−0.575	[0.715]
		F4	−0.620	[0.689]			F4	−0.575	[0.715]
		$\sum_{XeF_4}$	**0.064**				$\sum_{XeF_4}$	**0.000**	
					WOF_4 (C_{4v})				
W1---F4	0.097	W1	2.512	[4.883]	W1−F5	0.737	W1	2.534	[4.839]
W1−F5	0.685	F5	−0.528	[0.870]	W1−F6	0.737	F5	−0.491	[0.928]
W1−F6	0.685	F6	−0.528	[0.870]	W1−F7	0.737	F6	−0.491	[0.928]
W1−F7	0.750	F7	−0.483	[0.943]	W1−F8	0.737	F7	−0.491	[0.928]
W1−F8	0.750	F8	−0.483	[0.943]	W1−O1	1.892	F8	−0.491	[0.928]
W1−O1	1.911	O1	−0.554	[2.224]			O1	−0.569	[2.201]
		$\sum_{WOF_4}$	**−0.064**				$\sum_{WOF_4}$	**0.001**	
		$\sum_{total}$	**0.000**						

[a] APFD/Def2-TZVPD. [b] See Figure 8.1 for the atom labeling schemes.

Electron Localization Function (ELF) Analyses

ELF analyses were carried out for XeF_4, WOF_4, and F_3XeF_b---WOF_4. ELF parameters are provided in Table A5.6 and ELF isosurface plots are depicted in Figure 8.2. In the ensuing discussion and Figures 8.2 and A5.4, the following denote atomic basin populations, $\bar{N}$[A]; electron localization function, η(r); core basin, C(A); monosynaptic valence basin, V(A); and closed isosurface, where η(r) = f and η(r) is defined as the isosurface contour. The Def2-TZVPD basis set only explicitly represents the 4s, 5p, 5d, and 5s electrons of W, consequently, discrimination of sub-valence and valence electrons for these atoms cannot be achieved by ELF.

The $\bar{N}$[C(Xe)], $\bar{N}$[C(F)], and $\bar{N}$[C(O)] ELF core basin populations are close to the ideal charges, and hardly change upon complex formation. The ELF valence basin populations, $\bar{N}$[V(F)] and $\bar{N}$[V(O)], also do not vary significantly upon coordination, including $\bar{N}$[V(F_b)] (7.58 versus 7.59 in free XeF_4). This contrasts with the $FXeF_b$---WOF_4 and FXe–F_b---W(OF_3)–F_b'---W'OF_4 complexes which show significant increases in their $\bar{N}$[V(F_b)] basin populations relative to those of XeF_2 (7.76 and 7.80 versus 7.54 in free XeF_2),[S1] consistent with the lower fluorobasicity of XeF_4.

The localization domain reduction tree diagrams for XeF_4, WOF_4, and F_3XeF_b---WOF_4 (Figure A5.4) provide the hierarchies of ELF basins and the corresponding basin separation values for the basin isosurfaces (f_{sep}). The ELF reduction of the localization diagram of F_3XeF_b---WOF_4 separates into XeF_4 and WOF_4 domains at f_{sep} = 0.07, which is somewhat less than that of $FXeF_b$---WOF_4 (0.08)[S1] and consistent with the relative fluorobasicities, XeF_2 > XeF_4, and their relative W---F_b bond covalencies. The valence

basins separate in order of increasing covalency of their Xe–F bonds; $V(F_b) < V(F_{2,3}) < V(F_1)$, in accordance with the AIM and NBO analyses (vide supra). The core and valence basins of the F_5 and F_6 atoms of coordinated WOF_4 that are proximate to the XeF_4 moiety separate prior to F_7 and F_8, which are directed away from XeF_4 (also see NBO, NAO, and AIM Analyses). The O and W valence basins separate last, consistent with the double bond character of the W–O bond.

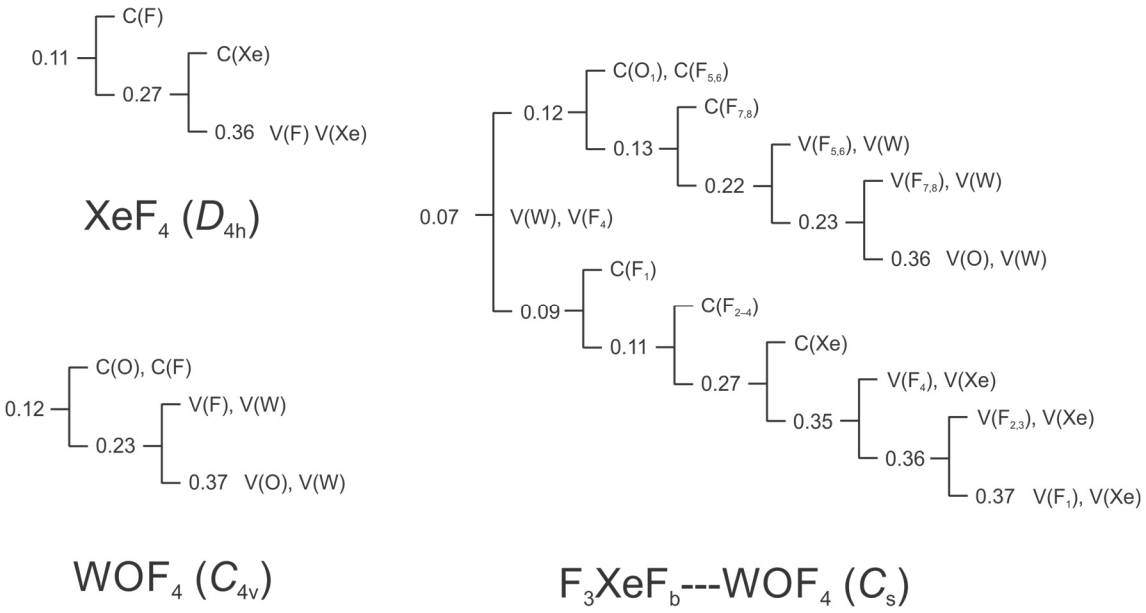

Figure A5.4. Reduction of localization diagrams for WOF_4, XeF_4, and F_3XeF_b---WOF_4 showing the ordering of localization nodes and the boundary isosurface values, $\eta(r)$, at which the reproducible domains separate. The atom numbering scheme corresponds to that used in Figure 8.1. The APFD/Def2-TZVPD level of theory was used.

Table A5.6. Laplacian of electron density ($\nabla^2\rho_b$), the density of all electrons (ρ_b), the energy density (H_b), delocalization indices (δ), QTAIM atomic populations ($\bar{N}$), and ELF basin populations ($\bar{N}$) of F_3XeF_b---WOF_4, XeF_4, and WOF_4[a,b]

	F_3XeF_b---WOF_4	XeF_4	WOF_4
$\nabla^2\rho_b$ [c]			
Xe1−F1	0.259	0.251	
Xe1−F2	0.261	0.251	
Xe1−F3	0.261	0.251	
Xe1−F4	0.223	0.251	
W1---F4	0.210		
W1−F5	0.918		0.974
W1−F6	0.918		0.974
W1−F7	0.988		0.974
W1−F8	0.988		0.974
W1−O1	1.066		1.030
ρ_b [d]			
Xe1−F1	0.152	0.142	
Xe1−F2	0.146	0.142	
Xe1−F3	0.146	0.142	
Xe1−F4	0.116	0.142	
W1---F4	0.065		
W1−F5	0.245		0.258
W1−F6	0.245		0.258
W1−F7	0.260		0.258
W1−F8	0.260		0.258
W1−O1	0.423		0.423
H_b [e]			
Xe1−F1	−0.087	−0.076	
Xe1−F2	−0.080	−0.076	
Xe1−F3	−0.080	−0.076	
Xe1−F4	−0.050	−0.076	
W1---F4	−0.001		
W1−F5	−0.067		−0.074
W1−F6	−0.067		−0.074
W1−F7	−0.075		−0.074
W1−F8	−0.075		−0.074
W1−O1	−0.262		−0.265
δ			
Xe1−F1	0.875	0.839	
Xe1−F2	0.854	0.839	
Xe1−F3	0.854	0.839	
Xe1−F4	0.679	0.839	
W1---F4	0.192		
W1−F5	0.875		0.948
W1−F6	0.875		0.948
W1−F7	0.947		0.948
W1−F8	0.947		0.948
W1−O1	2.105		2.114

continued…

Table A5.6. (continued…)

	F_3XeF_b---WOF_4	XeF_4	WOF_4
QTAIM Atom Populations			
$\bar{N}$(Xe1)	51.65	51.66	
$\bar{N}$(F1)	9.55	9.58	
$\bar{N}$(F2)	9.57	9.58	
$\bar{N}$(F3)	9.57	9.58	
$\bar{N}$(F4)	9.72	9.58	
$\bar{N}$(W1)	69.62		69.72
$\bar{N}$(F5)	9.84		9.82
$\bar{N}$(F6)	9.84		9.82
$\bar{N}$(F7)	9.82		9.82
$\bar{N}$(F8)	9.82		9.82
$\bar{N}$(O1)	8.99		8.99
ELF Basin Populations [f]			
$\bar{N}$[C(Xe1)] [g]	45.87	45.95	
$\bar{N}$[V(Xe1)]	5.21	5.17	
$\bar{N}$[C(F1)]	2.15	2.13	
$\bar{N}$[V(F1)]	7.58	7.59	
$\bar{N}$[C(F2)]	2.15	2.13	
$\bar{N}$[V(F2)]	7.58	7.59	
$\bar{N}$[C(F3)]	2.15	2.13	
$\bar{N}$[V(F3)]	7.58	7.59	
$\bar{N}$[C(F4)]	2.15	2.13	
$\bar{N}$[V(F4)]	7.58	7.59	
$\bar{N}$[C(F5)]	2.15		2.14
$\bar{N}$[V(F5)]	8.18		8.23
$\bar{N}$[C(F6)]	2.15		2.14
$\bar{N}$[V(F6)]	8.18		8.23
$\bar{N}$[C(F7)]	2.15		2.14
$\bar{N}$[V(F7)]	8.20		8.23
$\bar{N}$[C(F8)]	2.15		2.14
$\bar{N}$[V(F8)]	8.20		8.23
$\bar{N}$[C(O1)]	2.13		2.13
$\bar{N}$[V(O1)]	8.11		8.11

continued…

[a] APFD/Def2-TZVPD. [b] See Figure 8.1 for the atom labeling scheme. [c] The atomic unit (au) for $\nabla^2\rho_b$ is e/a_0^5 (1 au = 24.098 e Å^{-5}). [d] The au for ρ_b is e/a_0^3 (1 au = 6.748 e Å^{-3}, a_0 = Bohr radius = 0.52918 Å, e = charge on an electron). [e] The total energy density of Cremer and Kraka (H_b) is defined as the sum of G_b and V_b, in which G_b is the Lagrangian kinetic energy and V_b is the potential energy density. The au for H_b is e^2/a_0^4 (1 au = E_h/a_0^3 = 6.748 E_h/Å^3, E_h = hartree = e^2/a_0). In covalent bonds, G_b is dominated by V_b, which gives a negative value for H_b. [f] The Def2-TZVPD basis set only explicitly represents the 4s, 5p, 5d, and 5s electrons of W, so the separation of sub-valence and valence electrons cannot be detected by ELF. Consequently, $\bar{N}$[C(W)] and $\bar{N}$[V(W)] are not reported. [g] $\bar{N}$[C(Xe)] = 90 − $\bar{N}$[V(Xe)] − $\Sigma\bar{N}$[C(F_{1-4})] − $\Sigma\bar{N}$[V(F_{1-4})].

Atoms in Molecules (AIM) Analyses

Bond covalency in an AIM analysis is assessed at bond critical points by evaluating the Laplacian of electron density ($\nabla^2\rho_b$), Cremer-Kraka total energy density (H_b), the densities of all electrons (ρ_b), and the bond delocalization indices (δ).[S2] The AIM properties of F_3XeF_b---WOF_4 were calculated at the APFD/Def2-TZVPD level of theory to enable comparisons with the published values of $FXeF_b$---WOF_4.[S1] The AIM properties for the Xe–F, W–O, and W–F bonds of F_3XeF_b---WOF_4 (Table A5.6) show enhanced bond polarizations upon complex formation that are analogous to those described for $FXeF_b$---WOF_4.[S1]

The Xe–F bonds in F_3XeF_b---WOF_4 are polar-covalent, as indicated by their small positive ρ_b- and $\nabla^2\rho_b$-values, very small negative H_b-values, and their delocalization indices, δ_{Xe-F}. Although these values are similar to those of free XeF_4, several changes occur upon coordination, The most notable changes are those for Xe–F_b, where ρ_b (0.116

au), $\nabla^2\rho_b$ (0.223 au), and $\delta_{Xe\text{-}Fb}$ (0.679 au) decrease and H_b (−0.050 au) increases relative to free XeF_4 (0.142, 0.251, 0.839, −0.076 au, respectively), indicating that the Xe---F_b bond of F_3XeF_b---WOF_4 is more ionic. The opposite trend is observed for the Xe–F_1 bond (0.152, 0.259, 0.875, −0.080 au, respectively), which indicates the Xe–F_1 bond covalency has increased. Similar trends have been observed for the Xe–F_b and Xe–F_t bonds of F_tXeF_b---MOF_4 (M = Cr, Mo, W) upon coordination of XeF_2 to MOF_4.[S1,S3] In contrast, the AIM properties of Xe–F_{ax} (0.146, 0.261, 0.854, −0.076 au, respectively) are little affected by coordination. The Xe–F_1, Xe–F_b, and Xe–$F_{2,3}$ bond properties of F_3XeF_b---WOF_4 are consistent with their associated bond lengths and respective Wiberg indices (Table A5.5) and valence bond descriptions in which one of the two orthogonal 3-center 2-electron bonded F–Xe–F moieties of XeF_4 deformed by coordination to WOF_4, resulting in an elongated Xe–F_b bond and a contracted Xe–F_1 bond trans to the Xe–F_b bond. The NBO and AIM properties and bond lengths of the F_2–Xe–F_3 moiety are less affected by coordination.

The AIM properties of the W---F_b bond in F_3XeF_b---WOF_4 are consistent with weak W---F_b covalent bonding, i.e., very small positive values of ρ_b (0.065 au), $\nabla^2\rho_b$ (0.210 au), $\delta_{W\text{---}Fb}$ (0.192 au), and a small negative H_b-value (−0.10 x10^{-3} au), which are in accordance with a predominantly electrostatic W---F_b bond (see MEPS). The latter AIM properties are all less than those of the W---F_b bond in $FXeF_b$---WOF_4 (0.073, 0.237, 0.219, −0.30 au, respectively), which indicates the W---F_b bond of F_3XeF_b---WOF_4 is significantly less covalent than that of $FXeF_b$---WOF_4.

The large charge density (ρ_b, 0.423 au) and large negative energy density (H_b, −0.262 au) for the W–O bond of F_3XeF_b---WOF_4 indicate strong, shared interactions. The large positive electron densities ($\nabla^2\rho_b$, 1.066 au) are indicative of substantial polarization of electron density from tungsten to oxygen and a short, strongly covalent W=O bond. The charge and energy densities of the W–O bond remain essentially unchanged upon XeF_4 coordination, whereas the $\nabla^2\rho_b$ increases slightly. The δ_{W-O} value (2.105) is close to the formal bond order (Table A5.6) and is consistent with the covalent character of the W=O bond. The H_b-values of the W–F bonds are significantly less negative, which is consistent with considerably less shared density in these bonds than in the W=O double bond.

Upon coordination, the AIM properties, ρ_b, $\nabla^2\rho_b$, δ_{W-F}, and H_b, of the two W–$F_{5,6}$ bonds that are proximate to the Xe atom change more (0.245, 0.918, 0.875, −0.067 au, respectively) when compared with those of free WOF_4 (0.258, 0.974, 0.948, −0.074 au). In contrast, the AIM properties of the W–$F_{7,8}$ bonds, which are farther from XeF_4, are little affected by coordination (0.260, 0.988, 0.947, −0.075 au). The changes are consistent with more polar-covalent characters for the W–$F_{5,6}$ bonds proximate to the Xe atom (also see NBO, NAO, and ELF Analyses). Similar behavior has been noted for $FXeF_b$---WOF_4 upon coordination of XeF_2 to WOF_4.[S1]

Energy Decomposition Analyses

The energy decomposition analysis (EDA) method developed by Ziegler and Rauk[S4] provides a quantitative interpretation of chemical bonds. The instantaneous interaction

energy, ΔE_{int}, between two fragments A and B in the molecule AB is described by (1) the quasiclassical electrostatic interaction energy between the charge densities of the fragments, ΔE_{elstat}, (2) the exchange repulsion between fragments due to the Pauli principle, ΔE_{Pauli}, (3) the energy gain due to orbital mixing (covalency) between the fragments, ΔE_{orb}, and (4) a dispersion term, ΔE_{disp}, when dispersion energy corrections are included in the calculation (Eq **A5.1**).

$$\Delta E_{int} = \Delta E_{Pauli} + \Delta E_{elstat} + \Delta E_{orb} + \Delta E_{disp} \qquad \textbf{(A5.1)}$$

The total energy that is required to distort and electronically excite fragments A and B from their equilibrium geometries and wave functions to the states they possess in the molecule AB is the preparation energy, ΔE_{prep}, where the sum of the interaction energy and preparation energy provides $-D_E$, (Eq **A5.2**) where D_E is the bond dissociation energy for the A−B bond.

$$-D_E = \Delta E_{int} + \Delta E_{prep} \qquad \textbf{(A5.2)}$$

Because ΔE_{prep} and ΔE_{Pauli} are always positive, the stabilization of molecule AB requires that the absolute value of the sum of the ΔE_{elstat}, ΔE_{orb}, and ΔE_{disp} terms exceeds the sum of the ΔE_{prep} and ΔE_{Pauli} terms. The parameters described by the EDA method provide useful information regarding discussions of ionicity, covalency, aromaticity, donation, back donation, and hybridization.[S5]

The bonding in gas-phase F_3XeF_b---WOF_4 was analyzed using EDA, calculated at the hybrid PBE0 level of theory using the TZ2P basis set with Grimme4 dispersion (Table A5.7). The coordination complex was described in terms of two fragments, XeF_4 and WOF_4,

to obtain a quantitative breakdown of the relative bonding contributions that comprise the W---F_b bonding interaction.

The EDA analysis shows that the W---F_b bond is primarily electrostatic (57.4%), with a significant contribution from orbital mixing (35.4%) of the total attractive interactions. The orbital and electrostatic bonding components, and corresponding bond association energy, $-D_E$, for the W---F_b bond of F_3XeF_b---WOF_4 are significantly less negative than for the known FNgF---WOF_4 coordination complexes[S1] (Table A5.7) and the more negative than the hypothetical F_3XeF_b---MOF_4 (M = Cr, Mo) complexes (Table A5.7).

Table A5.7. Energy decomposition analyses of the M---F_b bond in F_3XeF_b---MOF_4 (M = Cr, Mo, W; C_s point symmetry)[a]

	Cr	Mo	W
ΔE_{int}	−24.25	−42.64	−49.03
ΔE_{orb}[b]	–17.02 (26.6%)	–39.89 (33.8%)	–52.15 (35.4%)
ΔE_{elstat}[b]	–37.14 (57.9%)	–68.03 (57.7%)	–84.32 (57.4%)
ΔE_{disp}[b]	–9.93 (15.5%)	–9.97 (8.5%)	–10.64 (7.2%)
ΔE_{Pauli}	39.84	75.25	98.08
Total ΔE_{prep}[c]	3.31	9.71	12.13
ΔE_{prep} XeF_4	1.26	5.02	6.65
ΔE_{prep} MOF_4	2.05	4.69	5.48
D_E	20.94	32.93	36.90

[a] Calculated using the PBE0-D4/TZ2P level of theory. Values are given in kJ mol^{-1}. [b] Values in parentheses give the percentages of attractive interactions. [c] Total ΔE_{prep} F_3XeF_b---MOF_4 = (ΔE_{prep} XeF_4) + (ΔE_{prep} MOF_4).

Extended-Transition-State Natural Orbitals for Chemical Valence (ETS-NOCV) Analysis

The ETS-NOCV analysis[S6] partitions the total orbital interaction described by the EDA method into pairwise contributions of fragment molecular orbitals, called symmetry fragment orbitals (SFOs). The difference between the electron densities of the interacting fragments before and after bond formation is represented by the deformation density term, $\Delta\rho$, which is expressed in terms of pairs of NOCV eigenfunctions; Ψ_k and Ψ_{-k} that have eigenvalues, ν_k and ν_{-k}, which possess the same absolute value but opposite sign. The total charge deformation, visualized in Figure 8.4, shows the change in electronic structure upon bond formation, so that visual inspection of the NOCVs allows assignment to a particular type of interaction (σ, π, δ), where the eigenvalues, ν_k and ν_{-k}, provide quantitative means to compare the relative amount of electron density that is deformed by an interaction and the energy gain (kJ mol^{-1}) associated with the interaction.

Table A5.8. Calculated[a] geometric parameters for F_3XeF_b---WOF_4 and the hypothetical F_3XeF_b---MOF_4 (M = Cr, Mo) coordination complexes (C_s point symmetry)

	Cr	Mo	W
Bond Lengths (Å)			
Xe(1)–F(1)	1.9335	1.9187	1.9153
Xe(1)–F(2)	1.9428	1.9362	1.9337
Xe(1)–F(3)	1.9428	1.9362	1.9337
Xe(1)–F(4)	1.9767	2.0153	2.0284
M(1)---F(4)	2.6751	2.5016	2.4552
M(1)–F(5)	1.7281	1.8525	1.8624
M(1)–F(6)	1.7281	1.8525	1.8624
M(1)–F(7)	1.7100	1.8333	1.8435
M(1)–F(8)	1.7100	1.8333	1.8435
M(1)–O(1)	1.5088	1.6412	1.6669
Bond angles (º)			
F(1)–Xe(1)–F(2)	89.33	88.42	88.40
F(1)–Xe(1)–F(3)	89.33	88.42	88.40
F(1)–Xe(1)–F(4)	178.83	179.30	179.58
F(2)–Xe(1)–F(3)	178.65	176.62	176.48
F(2)–Xe(1)–F(4)	90.66	91.57	91.59
F(3)–Xe(1)–F(4)	90.66	91.57	91.59
Xe(1)–F(4)---W(1)	116.90	122.53	122.64
O(1)–M(1)---F(4)	177.60	177.50	177.71
O(1)–M(1)–F(5)	103.59	102.83	102.67
O(1)–M(1)–F(6)	103.59	102.83	102.67
O(1)–M(1)–F(7)	103.87	103.15	102.80
O(1)–M(1)–F(8)	103.87	103.15	102.80
F(5)–M(1)---F(4)	74.70	75.38	75.68
F(5)–M(1)–F(6)	85.45	85.00	85.10
F(5)–M(1)–F(7)	152.50	153.95	154.46
F(5)–M(1)–F(8)	86.88	87.40	87.54
F(6)–M(1)---F(4)	74.70	75.38	75.68
F(6)–M(1)–F(7)	86.88	87.40	87.54
F(6)–M(1)–F(8)	152.50	153.95	154.46
F(7)–M(1)---F(4)	77.81	78.60	78.80
F(7)–M(1)–F(8)	87.87	88.61	88.66
F(8)–M(1)---F(4)	77.81	78.60	78.80
Dihedral Angles (º)			
F(5)-M-Xe-F(2)	35.98	37.15	37.25

[a] PBE0-D4/TZ2P.

References

[S1] Bortolus, M. R.; Mercier, H. P. A.; Brock, D. S.; Schrobilgen, G. J. *Chem. Eur. J.* **2022**, *28*, e202103729.

[S2] Bader, R. F. W. *Atoms in Molecules: A Quantum Theory*; Oxford University Press, Oxford, **1990**.

[S3] Mercier, H. P. A.; Breddemann, U.; Brock, D. S.; Bortolus, M. R.; Schrobilgen, G. J. *Chem. Eur. J.* **2019**, *25*, 12105–12119.

[S4] Ziegler, T.; Rauk, A. *Theor. Chim. Acta* **1977**, *46*, 1–10.

[S5] Zhao, L.; Hopffgarten, M.; Andrada, D. M.; Frenking, G. *WIREs Comput. Mol. Sci.* **2018**, *8*, 1345.

[S6] Mitoraj, M. P.; Michalak, A.; Ziegler, T. *J. Chem. Theory Comput.* **2009**, *5*, 962–975.

APPENDIX 6

CHAPTER 9 Supporting Information

Chromium Oxide Tetrafluoride and Its Reactions with Xenon Hexafluoride; the $[XeF_5]^+$ and $[Xe_2F_{11}]^+$ Salts of the $[Cr^{VI}OF_5]^-$, $[Cr^{V}OF_5]^{2-}$, $[Cr^{V}_2O_2F_8]^{2-}$, and $[Cr^{IV}F_6]^{2-}$ Anions

Adapted with permission from: Goettel, J. T.; Bortolus, M. R.; Stuart, D. G.; Mercier, H. P. A.; Schrobilgen, G. J. *Chem. Eur. J.* **2019**, *25*, 15815–15829.

Table A6.1. Raman frequencies and intensities for $[XeF_5][Xe_2F_{11}][CrOF_5]\cdot 2CrOF_4$ (**6**), $CrOF_4$, $[CrOF_5]^-$, and products of the reaction between XeF_6 and $CrOF_4$ (1:1) at various temperatures [a]

$CrOF_4$ [b]	$[CrOF_5]^-$ in $Cs[CrOF_5]$ [c]	$[CrOF_5]^-$ in $[NO][CrOF_5]$ [d]	Compd. (6) [e,f]	$3XeF_6 + 3CrOF_4 \longrightarrow [XeF_5][Xe_2F_{11}][CrOF_5]\cdot 2CrOF_4$ (6) + ½F_2 [g]						
				–30 °C [e,h,i]	–16 °C [e,h,j]	0 °C [e,h,k]	15 °C [e,h,l]	18 °C [e,h,m]	RT [e,h,m]	RT [e,h,m]
			1001(33)					1001, sh	1001(14)	1001(31)
995(29)				997(27)	997(6)	998(8)	996(16)	996(15)		
	[955]	**993, vs [980, s]**		**951(10)**	**951(21)**	**951(21)**	**951(19)**	**951(19)**	**951(18)**	**951(3)**
792(4)				792(3)	790(1)	793(1)	792(2)	791(1)	792(1)	
			750, sh							751, sh
			746(3)							746(1)
			727(3)							726(1)
716(7)	**[720]**			716, sh	715(2)	715(3)	715(7)	715(4)	715(6)	
	↑		707(8)							707(6)
702(31)				702(26)	702(4)	703(6)	702(17)	703(12)	702(12)	701, sh
			700, sh							
								692, sh		
688(22)				689(16)	689(2)	689(3)	688(12)	688(7)	688(9)	
	[n]		675(100)		677(4)	676(5)	675(19)	675(20)	675(32)	675(100)
			672, sh	673, sh				672, sh		672, sh
663(15)			662(33)	664(14)			663(16)	663(11)	662(18)	662(34)
			659, sh							659(31)
655, sh										
	↓									
	[650]		650(17)	**652, sh**	**651(63)**	**651(71)**	**651, sh**	**651, sh**	**651, sh**	**651(24)**
647(100)				649(100)	649, sh	649, sh	648(77)	649(72)	648(64)	
			644(12)							644(21)
		613, s		**640(49)**	**640(100)**	**640(100)**	**640(100)**	**640(100)**	**640(100)**	**641, sh**
			634(14)							634(21)
				632(29)	**632(63)**	**632(63)**	**633(61)**	**633(61)**	**633(59)**	
				628, sh	**628, sh**	**628, sh**	**628, sh**	**628(16)**	**628, sh**	
			608, sh	**609(4)**	**609(9)**	**609(10)**	**609(13)**	**609(10)**	**608(14)**	**608, sh**
			604(31)					604, sh		604(28)
			597(37)							597(36)
			595, sh							595, sh
				591(14)	**591(29)**	**591(31)**	**592(33)**	**592(31)**	**592(34)**	
			587, sh	**587(16)**	**587(31)**	**587(33)**	**587(33)**	**587(32)**	**587(33)**	**587, sh**
			584(32)	**584(16)**	**584(33)**	**584(33)**	**584(35)**	**584(36)**	**584(37)**	**584(34)** [o]
			576, sh							576, sh
		577, m		**568(7)**	**568(16)**	**568(16)**	**568(17)**	**568(16)**	**568(17)**	**568, sh**
			555(12)					555(2)	555(4)	555(10)
530(2)										

continued …

Table A6.1. (continued)

$CrOF_4$ [b]	$[CrOF_5]^-$ in $Cs[CrOF_5]$[c]	$[CrOF_5]^-$ in $[NO][CrOF_5]$[d]	Compd. (6)[e,f]	$3XeF_6 + 3CrOF_4 \longrightarrow [XeF_5][Xe_2F_{11}][CrOF_5]\cdot 2CrOF_4$ (6) + $\frac{1}{2}F_2$ [g]						
				–30 °C[e,h,i]	–16 °C[e,h,j]	0 °C[e,h,k]	15 °C[e,h,l]	18 °C[e,h,m]	RT [e,h,m]	RT[e,h,m]
		530, sh [520, sh]		**527(3), br**	**527(3), br**	**527(3)**	**527(4)**	**527(3)**	**527(4)**	**527(1), vbr**
				515(3), br				514(1)		
511(3)										
			470(4)							**470(2)**
									468(1)	
			419(6)	**419(1)**	**419(3)**	**419(3)**	**419(3)**	**419(3)**	**419(4)**	**419(4)**[o]
			411(5)					411(1)		411(3)
					407(1)	**407(1)**	**408(2)**	**408(2)**	**407(2)**	
			400(4)							400(2)
								397, sh		
								394(<1)		
385(1)										
380, sh										
374(11)			375, sh					375, sh		375, sh
			372(8)	**373(11)**	**371(8)**	**371(9)**	**372(13)**	**372(11)**	**372(12)**	**371(7)**[o]
362(9)				**361(15)**	**361(16)**	**361(17)**	**362(18)**	**361(18)**	**362(17)**	**362(3)**
357(11)				357, sh						
350(15)			351(19)	**350(17)**	**350(8)**	**350(10)**	**350(16)**	**350(15)**	**350(17)**	**351(18)**[o]
345(14)				346(14)				346(10)		
			343, sh							343, sh
		346, mw		**341, sh**	**341(7)**		**341(9)**	**341(8)**	**340(9)**	
			325, sh	326, sh						325, sh
				322(1)	**322(4)**	**322(4)**	**323(6)**	**322(4)**	**322(6)**	
			319(5)					317, sh		319(3)
		302, m		**314(1)**	**313, sh**	**313, sh**	**313(5)**	**314(3)**		
			305, sh							
			298, sh					298, sh		298, sh
297(1)				296(7)				295(3)		
			288, sh							
				283, sh				282, sh		
276(7)		**277, m**		275(6)	275(1)	275(2)	275(5)	275(3)	275(5)	
			271, sh							271, sh
269(5)				270, sh				269(2)		
			266(8)	265, sh				264, sh		265(5)

continued …

Table A6.1. (continued)

$CrOF_4$ [b]	$[CrOF_5]^-$ in $Cs[CrOF_5]$ [c]	$[CrOF_5]^-$ in $[NO][CrOF_5]$ [d]	Compd. (6) [e,f]	$3XeF_6 + 3CrOF_4 \longrightarrow [XeF_5][Xe_2F_{11}][CrOF_5]\cdot 2CrOF_4$ (6) + $\frac{1}{2}F_2$ [g]						
				–30 °C [e,h,i]	–16 °C [e,h,j]	0 °C [e,h,k]	15 °C [e,h,l]	18 °C [e,h,m]	RT [e,h,m]	RT [e,h,m]
			262, sh							262, sh
261(4)			258, sh	**260(5), br**	**259(2)**	**260(2)**	**260(6)**	**259(4)**	**260(6)**	**258, sh**
257, sh										
			250(3)							250(1)
				238(1), br			237(3)	237(1)	237(3)	
					235(2)	235(2)		234(1)		
			231(3)					232, sh		232(1)
								226, sh		
								219, sh		
			215, sh	**216(1)**	**215(3)**	**215(2)**	**216(3)**	**215(2)**	**215(4)**	
			212(3)							213(1)
								207, sh		
			203(3)		**203(1)**		**203(2)**	**203(<1)**	**203(2)**	**203(1)** [o]
194(3)										
186(2)				**188(3)**			**188(3)**	**189(2), br**		
					181(1)	**180(1)**		**182(2), br**		
			174(9)							174(7)
171(2)							**172(3)**	**172(3)**	**173(5)**	
				168(2)						
			164, sh							164, sh
153(2)			152(3)					151(<1)		151(<1)
				150(2)						
					144(1)	**143(1)**	**145(1)**	**144(<1)**	**144(2)**	
			139(2)							
125(2)			126, sh, br							128, sh
								119(3)		**119, sh**
			111(4), br	111(2), vbr	110(3)	109(3)		111(3)	112(5)	111(2), br
							106(4)	105(3)		
			95, sh							
								90, sh		

continued …

Table A6.1. (continued)

[a] Frequencies are given in cm^{-1}. Abbreviations denote shoulder (sh), broad (br), very broad (vbr), very strong (vs), strong (s), medium (m), medium weak (mw). Values in parentheses denote relative Raman intensities. Bolded values denote $[CrOF_5]^-$ bands. [b] Raman frequencies and relative intensities from ref. [4]. [c] Infrared frequencies and intensities (in square brackets) from ref. [4]. [d] Raman and infrared frequencies and intensities (infrared values are in square brackets) from ref. [6]. [e] The Raman spectrum was recorded in an FEP sample tube using 1064-nm excitation. [f] The Raman spectrum was recorded in an FEP sample tube on the dry crystalline compound at −140 °C. Unit cell determinations showed that crystals taken from this sample were compound (**6**). [g] Bolded frequencies are assigned to $[Xe_2F_{11}][CrOF_5]$ bands. The remaining bands are assigned to $CrOF_4$ and compound (**6**) by comparison with values given in columns 1 and 4 of this Table. The frequencies of the $[CrOF_5]^-$ anion bands were assigned by comparison with the calculated frequencies: ν(Cr-O), 1127 cm^{-1}; $[\nu_s(Cr\text{-}F_{4e}) + \nu(Cr\text{-}F_{ax})]$, 659 cm^{-1}; $\nu_{as}(Cr\text{-}F_{4e})$ and $\nu(Cr\text{-}F_{ax})$, 513 and 494 cm^{-1}; $[\delta(OCrF_e) + \delta(F_eCrF_{ax})]$, 380 cm^{-1}; $[\delta(F_eCrF_e) + \delta(F_eCrF_e)]$, 346 cm^{-1}; $[\rho_w(OCrF_{ax}) + \rho_w(F_eCrF_e)]$, 320 cm^{-1}; $[\rho_t(F_eCrF_e) + \rho_t(F_eCrF_e)]$, 226 cm^{-1} (see Computational Results). [h] Reaction conditions are provided in the Results and Discussion section of the manuscript under *"Syntheses; **[XeF5][Xe2F11][CrOF5]·2CrOF4 (6) and [Xe2F11][CrOF5]**"*. Spectra were recorded at: [i] −91 °C, [j] −96 °C, [k] −92 °C, [l] −135 °C, and [m] −120 °C. [n] A broad band was observed between 650 and 720 cm^{-1} (ref. [4]). [o] This band overlaps with a band of compound (**6**).

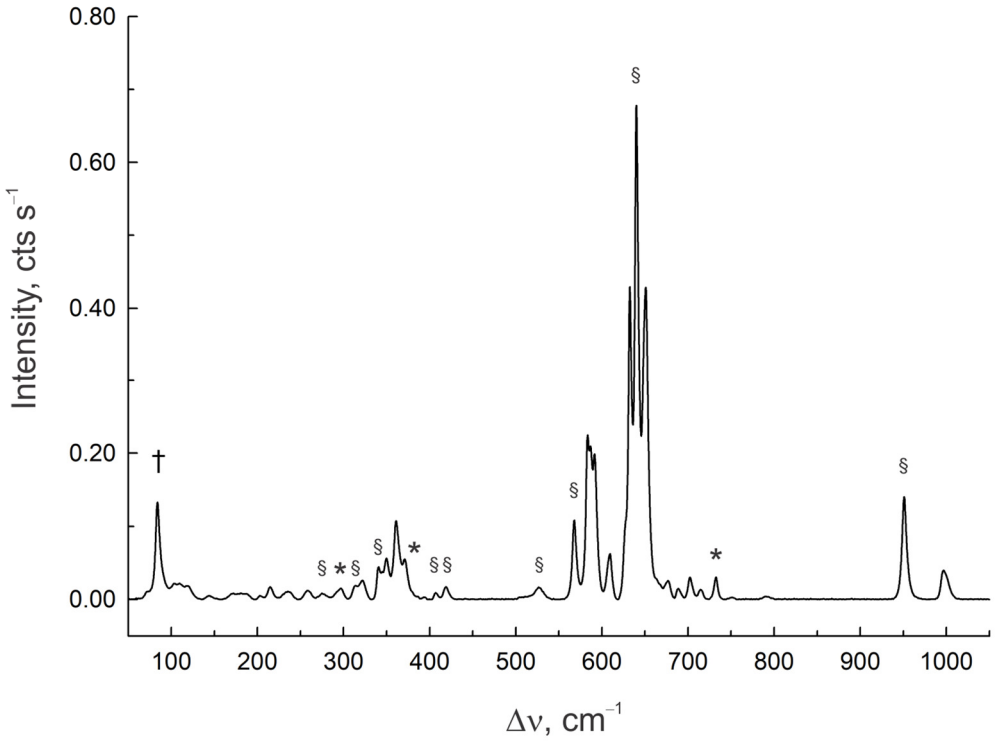

Figure A6.1. Raman spectrum obtained after an equimolar mixture of XeF_6 and $CrOF_4$ had been warmed to –16 °C and then quenched at –196 °C (see Results and Discussion; *Syntheses*, ***[XeF$_5$][Xe$_2$F$_{11}$][CrOF$_5$]·2CrOF$_4$ (6)*** and Table A6.1). The spectrum was recorded at −150 °C using 1064-nm excitation. The symbols denote; (†) an instrumental artifact, (*) FEP sample tube bands, and (§) bands assigned to the $[CrOF_5]^-$ anion.

Table A6.2. Experimental geometric parameters for $[XeF_5]_2[CrF_6]\cdot 2CrOF_4$ (**1**)

Bond Lengths and Contacts (Å)			
Cr(2)−O(1)	1.571(4)	Cr(2)−F(6)	1.749(3)
Cr(2)−F(4)	1.753(3)	Cr(2)−F(7)	1.740(3)
Cr(2)−F(5)	1.752(3)	Cr(2)---F(1)	2.216(3)
Xe(1)−F(8)	1.852(3)	Xe(1)−F(12)	1.825(3)
Xe(1)−F(9)	1.855(3)	Xe(1)---F(2)	2.447(3)
Xe(1)−F(10)	1.851(3)	Xe(1)---F(3A)	2.436(3)
Xe(1)−F(11)	1.854(3)	Xe(1)---F(4)	3.084(3)
		Xe(1)---F(5A)	3.044(3)

Bond Angles (deg)			
O(1)−Cr(2)−F(4)	98.1(2)	F(4)−Cr(2)---F(1)	81.8(1)
O(1)−Cr(2)−F(5)	98.2(2)	F(5)−Cr(2)−F(6)	88.0(2)
O(1)−Cr(2)−F(6)	99.4(2)	F(5)−Cr(2)−F(7)	162.5(2)
O(1)−Cr(2)−F(7)	99.3(2)	F(5)−Cr(2)---F(1)	81.5(1)
O(1)−Cr(2)---F(1)	179.7(2)	F(6)−Cr(2)−F(7)	88.2(2)
F(4)−Cr(2)−F(5)	90.2(2)	F(6)−Cr(2)---F(1)	80.8(1)
F(4)−Cr(2)−F(6)	162.5(2)	F(7)−Cr(2)---F(1)	81.0(1)
F(4)−Cr(2)−F(7)	88.3(2)	Cr(1)−F(1)---Cr(2)	143.4(2)
F(12)−Xe(1)−F(8)	78.8(2)	F(8)−Xe(1)−F(10)	158.0(2)
F(12)−Xe(1)−F(9)	79.4(2)	F(8)−Xe(1)−F(11)	87.3(2)
F(12)−Xe(1)−F(10)	79.3(2)	F(8)−Xe(1)−F(9)	89.3(2)
F(12)−Xe(1)−F(11)	78.6(2)	F(8)−Xe(1)---F(3A)	122.9(1)
F(12)−Xe(1)---F(2)	140.8(1)	F(8)−Xe(1)---F(2)	74.1(1)
F(12)−Xe(1)---F(3A)	144.0(1)	F(10)−Xe(1)−F(11)	88.4(1)
F(9)−Xe(1)−F(10)	86.8(2)	F(10)−Xe(1)---F(3A)	76.4(1)
F(9)−Xe(1)−F(11)	158.0(2)	F(10)−Xe(1)---F(2)	124.8(1)
F(9)−Xe(1)---F(3A)	124.7(1)	F(11)−Xe(1)---F(3A)	74.6(1)
F(9)−Xe(1)---F(2)	72.6(1)	F(11)−Xe(1)---F(2)	126.9(1)
Cr(1)−F(3)−Xe(1A)	145.3(2)	F(3A)---Xe(1)---F(2)	75.19(9)
Cr(1)−F(2)−Xe(1)	162.4(2)		

Table A6.3. Experimental geometric parameters for $[Xe_2F_{11}]_2[CrF_6]$ (**2**)

Bond Lengths and Contacts (Å)			
Xe(1)−F(1)	1.862(6)	Xe(2)−F(6)	1.863(6)
Xe(1)−F(2)	1.855(6)	Xe(2)−F(7)	1.856(6)
Xe(1)−F(3)	1.860(6)	Xe(2)−F(8)	1.863(6)
Xe(1)−F(4)	1.877(6)	Xe(2)−F(9)	1.858(6)
Xe(1)−F(5)	1.833(6)	Xe(2)−F(10)	1.833(6)
Xe(1)−F(11)	2.262(6)	Xe(2)−F(11)	2.250(6)
Xe(1)---F(12)	2.588(6)	Xe(2)---F(13)	2.583(6)
Xe(1)---F(14)	2.711(5)	Xe(2)---F(14)	2.712(5)

Bond Angles (deg)			
F(1)−Xe(1)−F(2)	86.0(3)	F(6)−Xe(2)−F(7)	86.3(3)
F(1)−Xe(1)−F(3)	160.0(3)	F(6)−Xe(2)−F(8)	153.5(3)
F(1)−Xe(1)−F(4)	91.4(3)	F(6)−Xe(2)−F(9)	84.4(3)
F(1)−Xe(1)−F(5)	79.7(3)	F(6)−Xe(2)−F(10)	76.5(3)
F(1)−Xe(1)−F(11)	85.9(3)	F(6)−Xe(2)−F(11)	72.0(3)
F(1)−Xe(1)---F(12)	125.7(2)	F(6)−Xe(2)---F(13)	129.5(2)
F(1)−Xe(1)---F(14)	69.04(3)	F(6)−Xe(2)---F(14)	133.4(3)
F(2)−Xe(1)−F(3)	84.7(3)	F(7)−Xe(2)−F(8)	90.3(3)
F(2)−Xe(1)−F(4)	154.2(3)	F(7)−Xe(2)−F(9)	159.7(3)
F(2)−Xe(1)−F(5)	76.9(3)	F(7)−Xe(2)−F(10)	79.8(3)
F(2)−Xe(1)−F(11)	71.4(2)	F(7)−Xe(2)−F(11)	86.5(2)
F(2)−Xe(1)---F(12)	129.1(7)	F(7)−Xe(2)---F(13)	126.2(2)
F(2)−Xe(1)---F(14)	132.7(3)	F(7)−Xe(2)---F(14)	69.5(3)
F(3)−Xe(1)−F(4)	89.3(3)	F(8)−Xe(2)−F(9)	90.0(3)
F(3)−Xe(1)−F(5)	80.9(3)	F(8)−Xe(2)−F(10)	77.0(3)
F(3)−Xe(1)−F(11)	107.8(3)	F(8)−Xe(2)−F(11)	134.1(2)
F(3)−Xe(1)---F(12)	73.4(2)	F(8)−Xe(2)---F(13)	72.5(2)
F(3)−Xe(1)---F(14)	129.3(3)	F(8)−Xe(2)---F(14)	68.6(3)
F(4)−Xe(1)−F(5)	77.4(3)	F(9)−Xe(2)−F(10)	80.5(3)
F(4)−Xe(1)−F(11)	134.1(2)	F(9)−Xe(2)−F(11)	107.6(3)
F(4)−Xe(1)---F(12)	72.3(2)	F(9)−Xe(2)---F(13)	72.9(2)
F(4)−Xe(1)---F(14)	69.0(3)	F(9)−Xe(2)---F(14)	128.9(3)
F(5)−Xe(1)−F(11)	145.9(3)	F(10)−Xe(2)−F(11)	146.3(3)
F(5)−Xe(1)---F(12)	140.0(3)	F(10)−Xe(2)---F(13)	139.1(2)
F(5)−Xe(1)---F(14)	132.6(3)	F(10)−Xe(2)---F(14)	132.9(3)
F(11)−Xe(1)---F(12)	72.6(2)	F(11)−Xe(2)---F(13)	72.9(2)
F(11)−Xe(1)---F(14)	67.4(3)	F(11)−Xe(2)---F(14)	67.5(3)
F(12)---Xe(1)---F(14)	56.7(3)	F(13)---Xe(2)---F(14)	56.7(3)

Table A6.4. Experimental geometric parameters for $[XeF_5]_2[Cr_2O_2F_8]$ (**3**) and $[XeF_5]_2[Cr_2O_2F_8]\cdot 2HF$ (**4**)

	(3)	(4)		(3)	(4)
Bond Lengths and Contacts (Å)					
Xe(1)−F(5)	1.8511(9)	1.8564(9)	Xe(1)---F(2A)	3.0227(9)	2.4837(8)
Xe(1)−F(6)	1.848(1)	1.8550(9)	Xe(1)---F(2B)	2.6560(9)	
Xe(1)−F(7)	1.8582(9)	1.8577(9)	Xe(1)---F(3B)	2.6573(9)	
Xe(1)−F(8)	1.855(1)	1.8601(8)	Xe(1)---F(1A)		3.0719(8)
Xe(1)−F(9)	1.8251(9)	1.8217(8)	Xe(1)---F(11A)		2.7986(9)
Xe(1)---F(4)	2.4272(9)	2.4831(8)	F(10)---F(11)		2.508(1)
Bond Angles (deg)					
F(5)−Xe(1)−F(6)	89.40(5)	85.34(4)	F(7)−Xe(1)−F(8)	85.53(5)	90.90(4)
F(5)−Xe(1)−F(7)	155.99(5)	157.94(4)	F(7)−Xe(1)−F(9)	78.16(5)	78.86(4)
F(5)−Xe(1)−F(8)	86.19(5)	87.51(4)	F(7)−Xe(1)---F(4)	130.23(4)	76.77(4)
F(5)−Xe(1)−F(9)	78.15(5)	79.23(4)	F(7)−Xe(1)---F(2A)	125.60(4)	128.93(4)
F(5)−Xe(1)---F(4)	72.14(4)	120.82(4)	F(7)−Xe(1)---F(2B)	74.59(4)	
F(5)−Xe(1)---F(2A)	68.42(4)	72.24(3)	F(7)−Xe(1)---F(3B)	66.52(4)	
F(5)−Xe(1)---F(2B)	124.77(4)		F(7)−Xe(1)---F(1A)		128.86(3)
F(5)−Xe(1)---F(3B)	134.60(4)		F(7)−Xe(1)---F(11A)		65.52(3)
F(5)−Xe(1)---F(1A)		66.47(3)	F(8)−Xe(1)−F(9)	79.01(5)	78.95(4)
F(5)−Xe(1)---F(11A)		132.66(4)	F(8)−Xe(1)---F(4)	125.44(4)	128.27(4)
F(6)−Xe(1)−F(7)	89.56(5)	87.95(4)	F(8)−Xe(1)---F(2A)	61.27(4)	78.62(4)
F(6)−Xe(1)−F(8)	157.20(4)	157.80(4)	F(8)−Xe(1)---F(2B)	75.77(4)	
F(6)−Xe(1)−F(9)	78.18(5)	79.08(4)	F(8)−Xe(1)---F(3B)	127.87(4)	
F(6)−Xe(1)---F(4)	73.84(4)	72.91(4)	F(8)−Xe(1)---F(1A)		129.41(3)
F(6)−Xe(1)---F(2A)	136.66(4)	118.74(4)	F(8)−Xe(1)---F(11A)		66.56(3)
F(6)−Xe(1)---F(2B)	124.22(4)		F(9)−Xe(1)---F(4)	138.91(4)	143.19(4)
F(6)−Xe(1)---F(3B)	69.21(4)		F(9)−Xe(1)---F(2A)	128.52(4)	144.19(4)
F(6)−Xe(1)---F(1A)		65.83(3)	F(9)−Xe(1)---F(2B)	143.95(4)	
F(6)−Xe(1)---F(11A)		131.82(3)	F(9)−Xe(1)---F(3B)	131.12(4)	
Cr(1)−F(4)---Xe(1)	156.70(4)	132.05(4)	F(9)−Xe(1)---F(1A)		131.81(4)
Cr(1)−F(2A)---Xe(1)	132.93(4)	121.60(4)	F(9)−Xe(1)---F(11A)		128.71(4)

Table A6.5. Experimental and calculated geometric parameters for $[XeF_5]_2[Cr_2O_2F_8]\cdot 2XeOF_4$ (**5**)

	exptl	**calcd[a]**		**exptl**	**calcd[a]**
Bond Lengths and Contacts (Å)					
Xe(1)−F(5)	1.855(1)	1.930	Xe(1)---F(2A)	2.518(1)	2.449
Xe(1)−F(6)	1.850(1)	1.924	Xe(1)---F(4)	2.475(1)	2.410
Xe(1)−F(7)	1.852(1)	1.925	Xe(1)---F(1A)	3.039(1)	3.291
Xe(1)−F(8)	1.856(1)	1.928	Xe(1)---F(12)	3.262(1)	2.733
Xe(1)−F(9)	1.814(1)	1.907			
Xe(2)–O(2)	1.711(2)	1.772	Xe(2)---F(2A)	2.986(1)	2.958
Xe(2)–F(10)	1.898(1)	1.949	Xe(2)---F(1)	2.968(1)	2.956
Xe(2)–F(11)	1.907(1)	1.963	Xe(2)---F(3A)	3.337(1)	3.169
Xe(2)–F(12)	1.933(1)	2.029	Xe(2)---F(4)	3.496(1)	3.567
Xe(2)–F(13)	1.900(1)	1.955			
Bond Angles (deg)					
F(9)−Xe(1)−F(5)	80.58(7)	79.81	F(5)−Xe(1)−F(6)	87.51(7)	84.98
F(9)−Xe(1)−F(6)	79.86(7)	79.19	F(5)−Xe(1)−F(7)	160.78(6)	159.08
F(9)−Xe(1)−F(7)	80.20(6)	79.47	F(5)−Xe(1)−F(8)	88.56(6)	87.76
F(9)−Xe(1)−F(8)	80.00(7)	78.71	F(6)−Xe(1)−F(7)	89.63(7)	88.38
F(9)−Xe(1)---F(1A)	135.67(6)	133.64	F(6)−Xe(1)−F(8)	159.85(6)	157.63
F(9)−Xe(1)---F(2A)	145.17(6)	143.81	F(7)−Xe(1)−F(8)	87.61(6)	90.97
F(9)−Xe(1)---F(4)	145.46(6)	144.79	F(9)−Xe(1)---F(12)	130.15(6)	131.19
O(2)−Xe(2)−F(10)	91.45(9)	92.95	F(10)−Xe(2)−F(11)	88.94(7)	89.93
O(2)−Xe(2)−F(11)	90.07(8)	90.40	F(10)−Xe(2)−F(12)	179.03(6)	176.89
O(2)−Xe(2)−F(12)	89.52(8)	89.81	F(10)−Xe(2)−F(13)	89.65(8)	90.16
O(2)−Xe(2)−F(13)	90.00(9)	90.56	F(11)−Xe(2)−F(12)	91.00(6)	89.62
O(2)−Xe(2)−F(1)	155.96(7)	154.97	F(11)−Xe(2)−F(13)	178.59(7)	178.71
O(2)−Xe(2)−F(2A)	147.57(7)	143.79	F(12)−Xe(2)−F(13)	90.41(7)	91.25
O(2)−Xe(2)−F(3A)	146.34(7)	151.60	O(2)−Xe(2)−F(4)	130.27(7)	125.85

[a] The PBE1PBE/aug-ccpVDZ (Xe)-Def2-SVP (F, O, Cr) level was used.

Table A6.6. Experimental and calculated geometric parameters for $[XeF_5][Xe_2F_{11}][CrOF_5]\cdot 2CrOF_4$ (**6**)

	exptl	calcd [a]		exptl	calcd [a]
Bond Lengths and Contacts (Å)					
Cr(2)−O(3)	1.547(2)	1.499	Cr(3)−O(2)	1.530(3)	1.499
Cr(2)−F(26)	1.740(2)	1.713	Cr(3)−F(22)	1.740(2)	1.712
Cr(2)−F(27)	1.741(2)	1.717	Cr(3)−F(23)	1.746(2)	1.710
Cr(2)−F(28)	1.740(2)	1.708	Cr(3)−F(24)	1.732(2)	1.707
Cr(2)−F(29)	1.741(2)	1.711	Cr(3)−F(25)	1.736(3)	1.719
Cr(2)---F(3)	2.393(2)	2.514	Cr(3)---F(4)	2.483(2)	2.530
Xe(1)−F(10)	1.814(2)	1.910	Xe(1)−F(9)	1.847(2)	1.929
Xe(1)−F(6)	1.859(2)	1.935	Xe(1)---F(1)	2.463(2)	2.351
Xe(1)−F(7)	1.862(2)	1.930	Xe(1)---F(3)	2.632(2)	2.573
Xe(1)−F(8)	1.860(2)	1.931	Xe(1)---F(4)	2.624(2)	2.618
Xe(2)−F(12)	1.825(2)	1.914	Xe(3)−F(21)	1.833(2)	1.912
Xe(2)−F(11)	1.868(2)	1.943	Xe(3)−F(19)	1.879(2)	1.940
Xe(2)−F(13)	1.865(2)	1.935	Xe(3)−F(20)	1.868(2)	1.940
Xe(2)−F(14)	1.856(2)	1.930	Xe(3)−F(18)	1.852(2)	1.931
Xe(2)−F(15)	1.858(2)	1.931	Xe(3)−F(17)	1.852(2)	1.932
Xe(2)−F(16)	2.333(2)	2.282	Xe(3)−F(16)	2.247(2)	2.249
Xe(2)---F(2)	2.575(2)	2.464	Xe(3)---F(5)	2.660(2)	2.436
Xe(2)---F(1)	2.822(2)	2.752	Xe(3)---F(1)	2.826(2)	3.047
Bond Angles (deg)					
O3−Cr2−F26	100.9(1)	103.13	O2−Cr3−F22	100.92(1)	103.11
O3−Cr2−F27	100.4(1)	103.25	O2−Cr3−F23	100.42(1)	103.31
O3−Cr2−F28	101.4(1)	103.17	O2−Cr3−F24	101.28(1)	103.13
O3−Cr2−F29	100.4(1)	103.28	O2−Cr3−F25	100.46(1)	103.19
O3−Cr2---F3	178.4(1)	179.01	O2−Cr3---F4	178.42(1)	178.15
F26−Cr2−F27	88.2(1)	86.44	F22−Cr3−F23	88.45(1)	87.38
F26−Cr2−F28	157.8(1)	153.70	F22−Cr3−F24	157.79(9)	153.75
F26−Cr2−F29	88.5(1)	87.16	F22−Cr3−F25	88.28(1)	86.56
F26−Cr2---F3	78.00(8)	75.92	F22−Cr3---F4	78.00(8)	75.11
F27−Cr2−F28	88.4(1)	87.00	F23−Cr3−F24	86.90(1)	86.79
F27−Cr2−F29	159.2(1)	153.46	F23−Cr3−F25	159.11(1)	153.50
F27−Cr2---F3	78.48(8)	76.50	F23−Cr3---F4	80.75(8)	77.25
F28−Cr2−F29	86.9(1)	87.42	F24−Cr3−F25	88.38(9)	86.79
F28−Cr2---F3	79.81(9)	77.79	F24−Cr3---F4	79.82(8)	78.64
F29−Cr2---F3	80.73(8)	76.97	F25−Cr3---F4	78.39(8)	76.26
F10−Xe1−F6	79.12(9)	78.59	F7−Xe1−F9	159.67(9)	160.27
F10−Xe1−F7	79.78(9)	80.61	F7−Xe1---F1	93.17(9)	101.30
F10−Xe1−F8	79.60(9)	78.70	F7−Xe1---F3	71.14(8)	72.11
F10−Xe1−F9	80.39(9)	80.43	F7−Xe1---F4	127.62(8)	127.47

continued…

Table A6.6. (continued)

	exptl	calcd [a]		exptl	calcd [a]
		Bond Angles (deg)			
F10−Xe1---F1	151.50(8)	150.85	F8−Xe1−9	85.8(1)	85.82
F10−Xe1---F3	139.56(8)	143.13	F8−Xe1---F1	72.37(8)	72.55
F10−Xe1---F4	143.87(8)	139.92	F8−Xe1---F3	124.42(8)	121.92
F6−Xe1−F7	91.39(9)	90.18	F8−Xe1---F4	120.40(8)	125.80
F6−Xe1−F8	158.67(9)	157.26	F9−Xe1---F1	102.19(8)	92.64
F6−Xe1−F9	89.24(9)	91.40	F9−Xe1---F3	128.31(7)	127.34
F6−Xe1---F1	128.96(7)	130.17	F9−Xe1---F4	72.27(7)	71.67
F6−Xe1---F3	74.25(7)	77.21	F1---Xe1---F3	59.59(6)	61.37
F6−Xe1---F4	77.39(7)	74.03	F1---Xe1---F4	60.11(6)	60.48
F7−Xe1−F8	85.2(1)	85.15	F3---Xe1---F4	56.52(6)	55.71
F12−Xe2−F11	78.41(9)	78.00	F21−Xe3−F19	78.31(9)	79.05
F12−Xe2−F13	79.14(9)	80.12	F21−Xe3−F20	78.65(9)	80.23
F12−Xe2−F14	78.66(9)	78.44	F21−Xe3−F18	78.2(1)	79.23
F12−Xe2−F15	78.63(9)	79.67	F21−Xe3−F17	78.44(9)	79.99
F12−Xe2−F16	142.11(8)	144.84	F21−Xe3−F16	140.80(8)	146.34
F12−Xe2---F2	140.76(7)	142.27	F21−Xe3---F5	145.80(8)	142.42
F11−Xe2−F13	88.01(9)	89.78	F19−Xe3−F20	87.3(1)	91.62
F11−Xe2−F14	156.97(8)	156.33	F19−Xe3−F18	156.40(9)	158.28
F11−Xe2−F15	88.74(9)	89.54	F19−Xe3−F17	86.3(1)	87.43
F11−Xe2−F16	129.24(8)	130.78	F19−Xe3−F16	127.95(8)	125.91
F11−Xe2---F2	73.79(7)	78.95	F19−Xe3---F5	86.89(7)	77.25
F13−Xe2−F14	85.64(9)	83.99	F20−Xe3−F18	86.2(1)	84.90
F13−Xe2−F15	157.74(9)	159.46	F20−Xe3−F17	157.01(9)	160.01
F13−Xe2−F16	121.24(8)	114.57	F20−Xe3−F16	124.96(8)	116.78
F13−Xe2---F2	72.83(7)	70.32	F20−Xe3---F5	69.94(7)	71.77
F14−Xe2−F15	85.64(9)	88.47	F18−Xe3−F17	91.0(1)	88.63
F14−Xe2−F16	72.24(8)	72.05	F18−Xe3−F16	73.51(8)	74.08
F14−Xe2---F2	124.80(8)	119.70	F18−Xe3---F5	111.93(8)	121.41
F15−Xe2−F16	77.06(8)	80.84	F17−Xe3−F16	75.56(8)	79.24
F15−Xe2---F2	127.04(7)	129.53	F17−Xe3---F5	131.59(7)	127.18
F16−Xe2---F2	76.93(6)	71.27	F16−Xe3---F5	71.56(6)	70.67
Xe2−F16−Xe3	135.79(9)	140.08			

[a] The PBE1PBE/aug-ccpVDZ (Xe)-Def2-SVP (F, O, Cr) level was used.

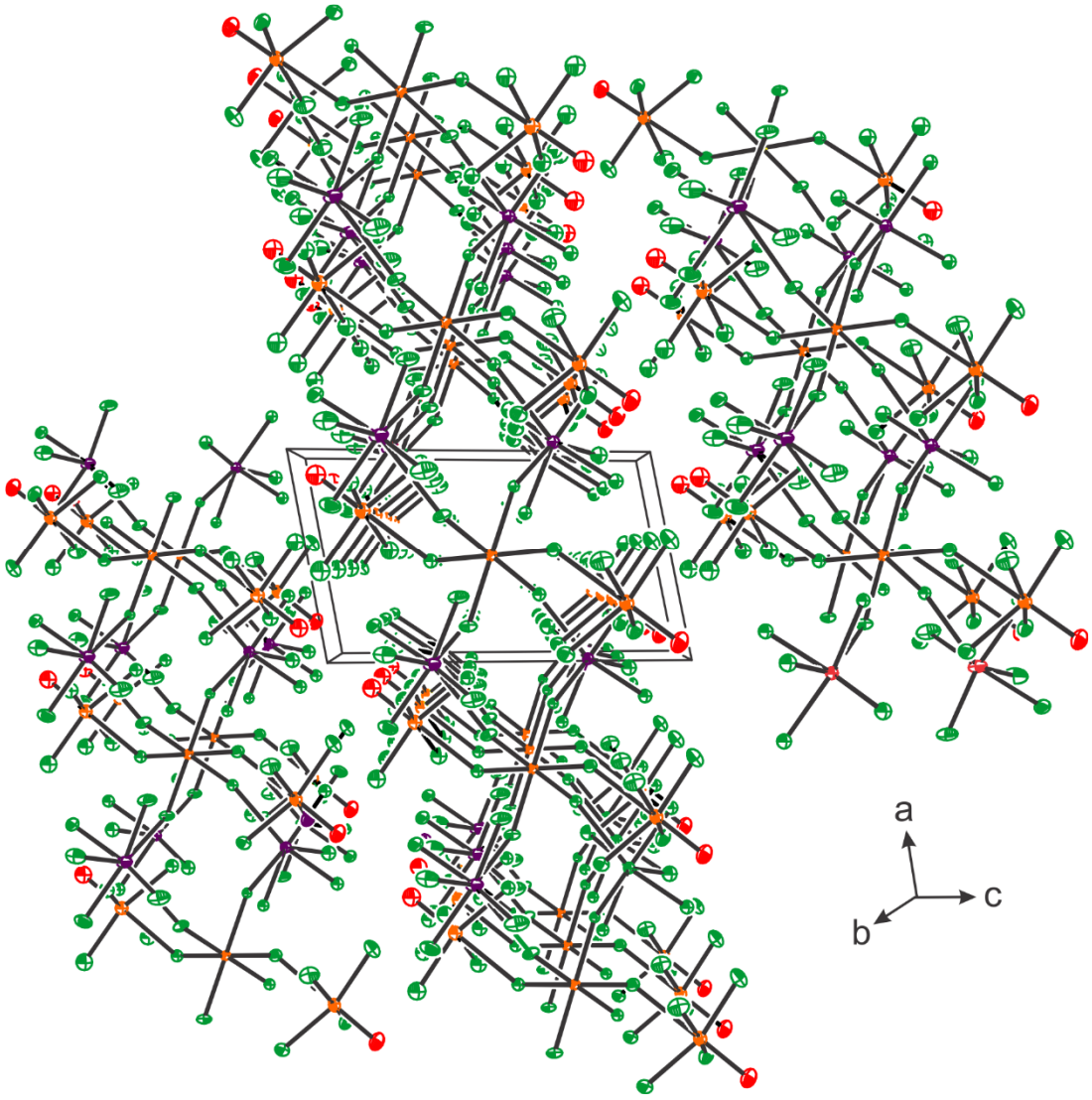

Figure A6.2. A packing diagram showing the chain structure in the X-ray crystal structure of **[**$XeF_5]_2[CrF_6]\cdot 2CrOF_4$ (**1**) viewed along the *b*-axis of the unit cell; thermal ellipsoids are drawn at the 50% probability level.

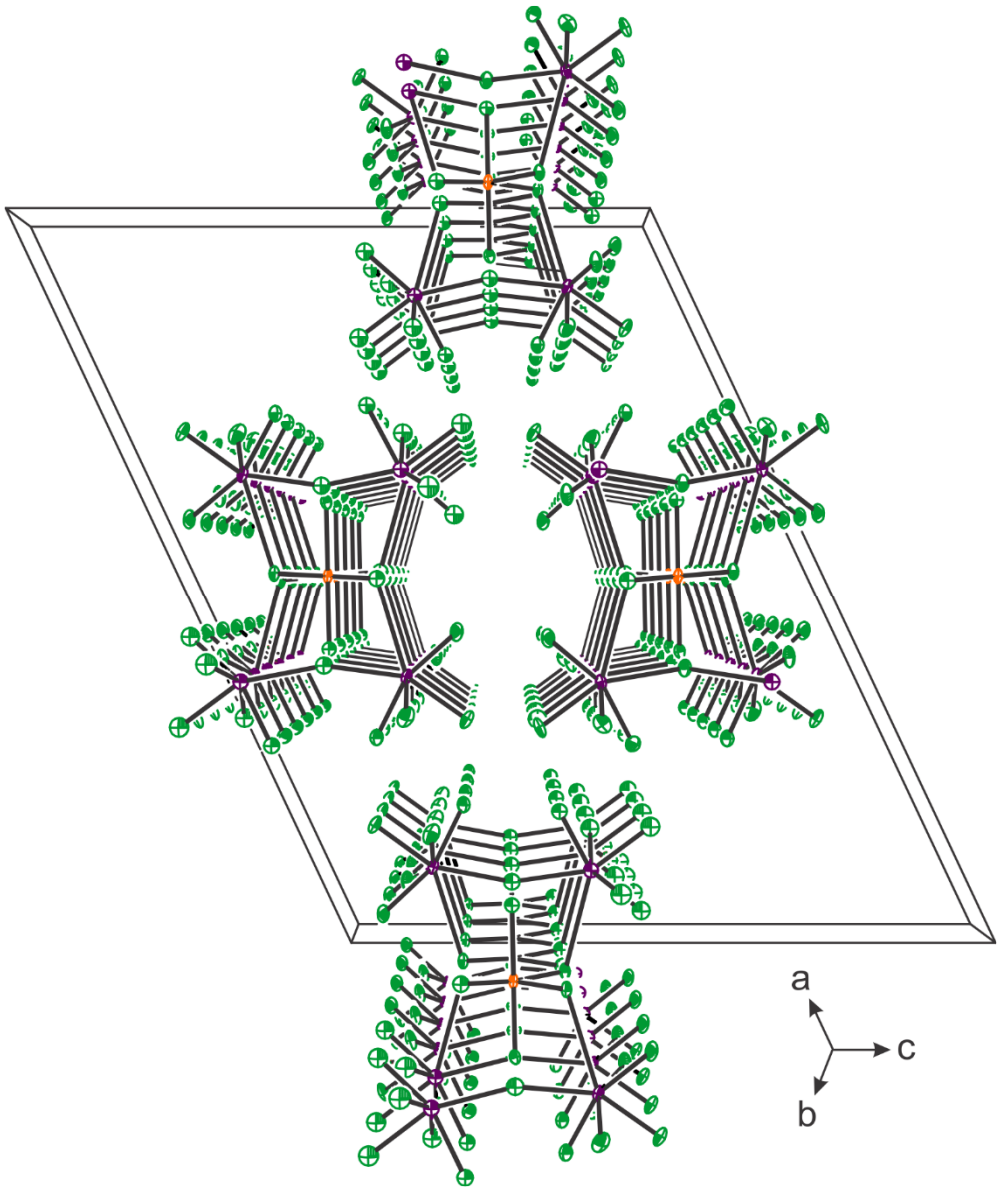

Figure A6.3. A packing diagram showing the chain structure in the X-ray crystal structure of $[Xe_2F_{11}]_2[CrF_6]$ (**2**) viewed along the *b*-axis of the unit cell; thermal ellipsoids are drawn at the 50% probability level.

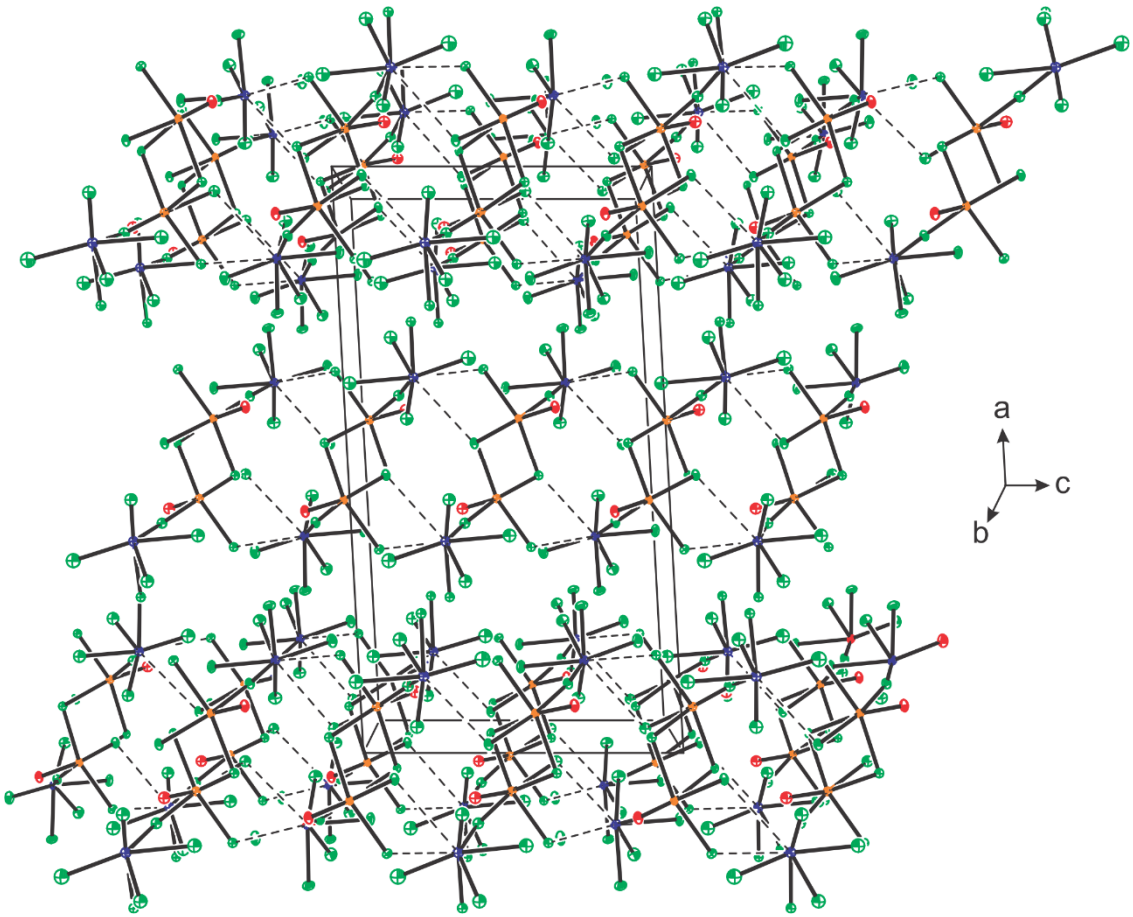

Figure A6.4. A packing diagram showing the chain structure in the X-ray crystal structure of $[XeF_5]_2[Cr_2O_2F_8]$ (**3**) viewed along the *b*-axis of the unit cell; thermal ellipsoids are drawn at the 50% probability level.

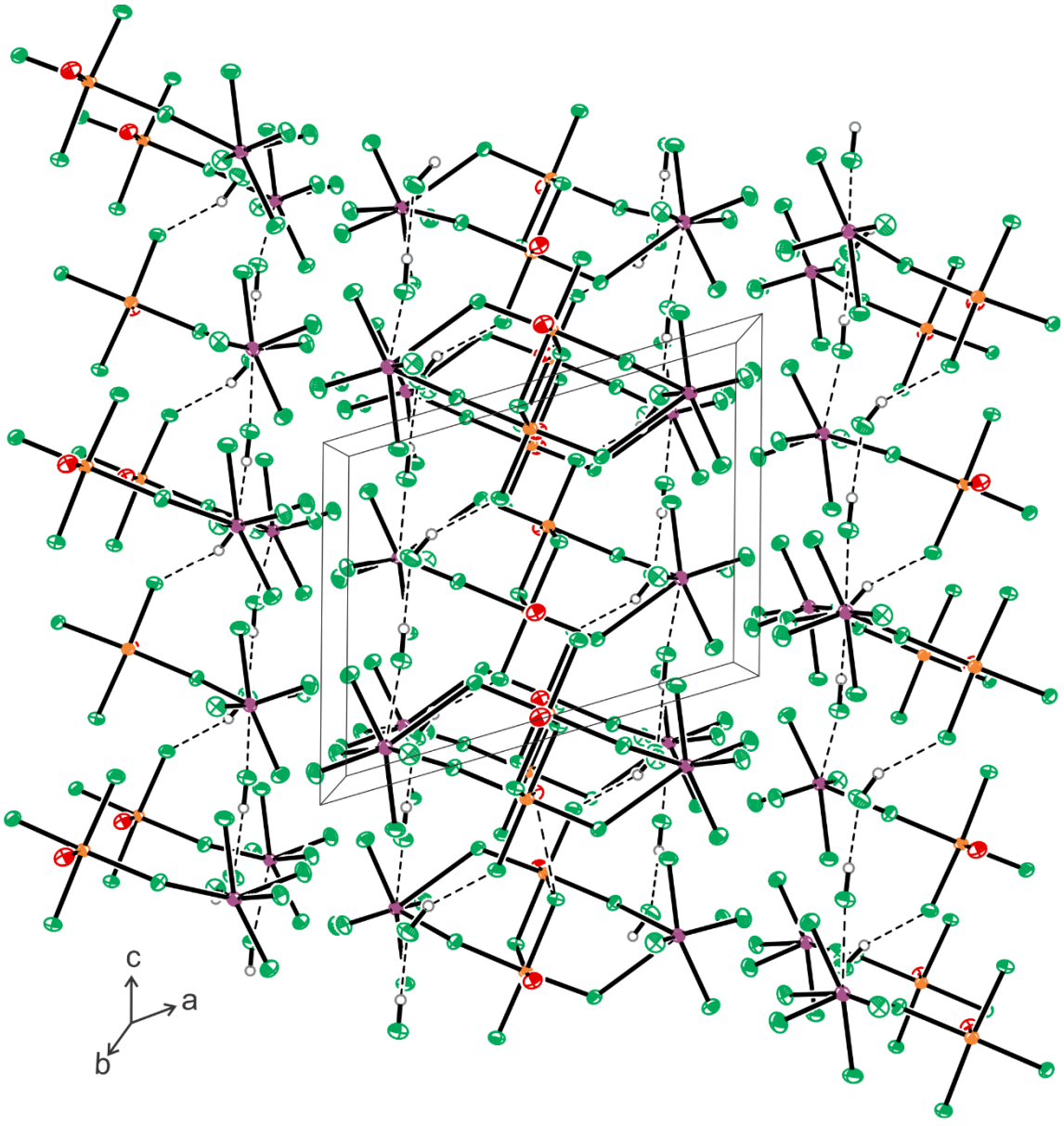

Figure A6.5. A packing diagram showing the chain structure in the X-ray crystal structure of $[XeF_5]_2[Cr_2O_2F_8]\cdot 2HF$ (**4**) viewed along the *b*-axis of the unit cell; thermal ellipsoids are drawn at the 50% probability level.

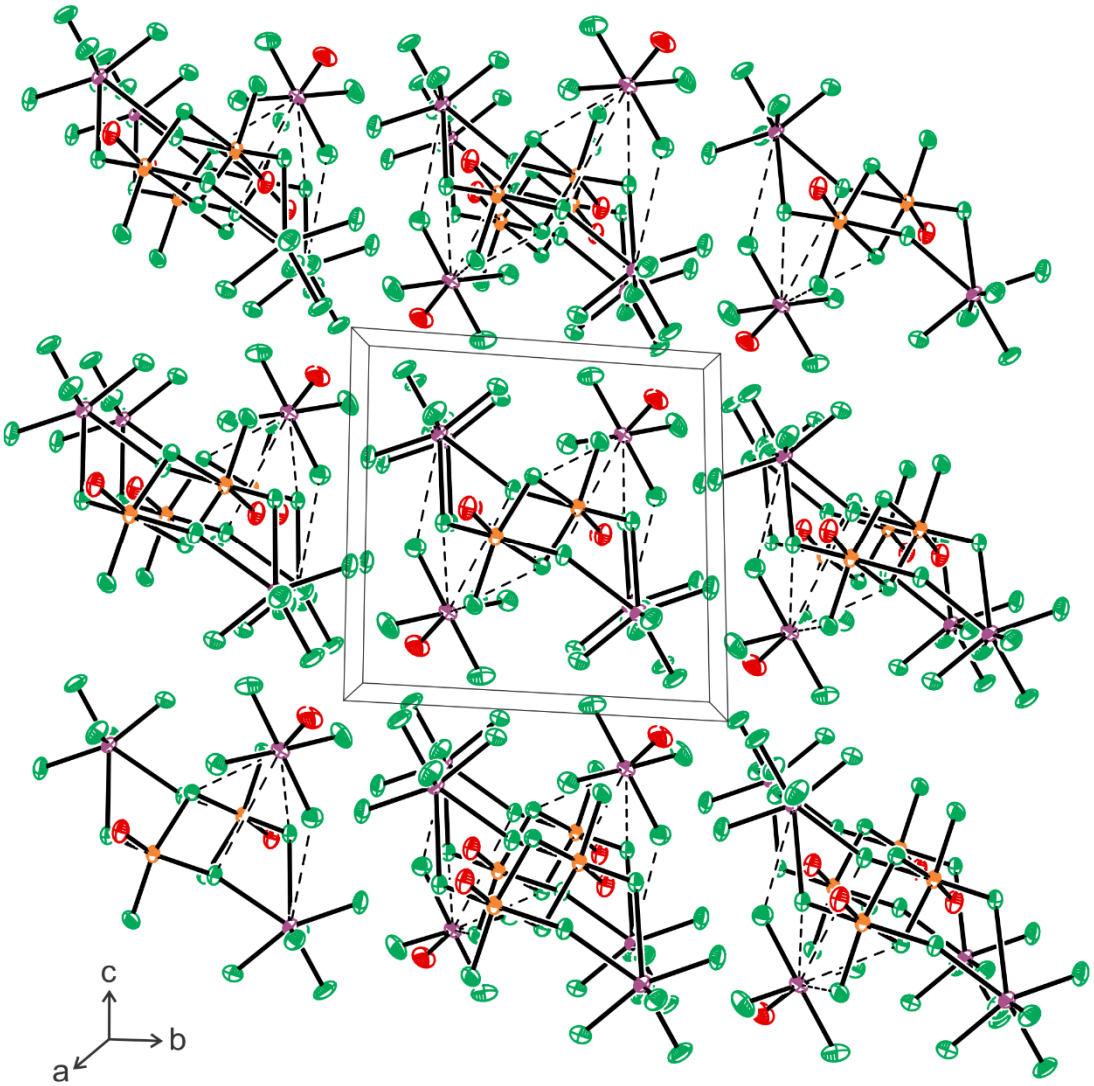

Figure A6.6. A packing diagram showing the X-ray crystal structure of $[XeF_5]_2[Cr_2O_2F_8]\cdot 2XeOF_4$ (**5**) viewed along the *a*-axis of the unit cell; thermal ellipsoids are drawn at the 50% probability level.

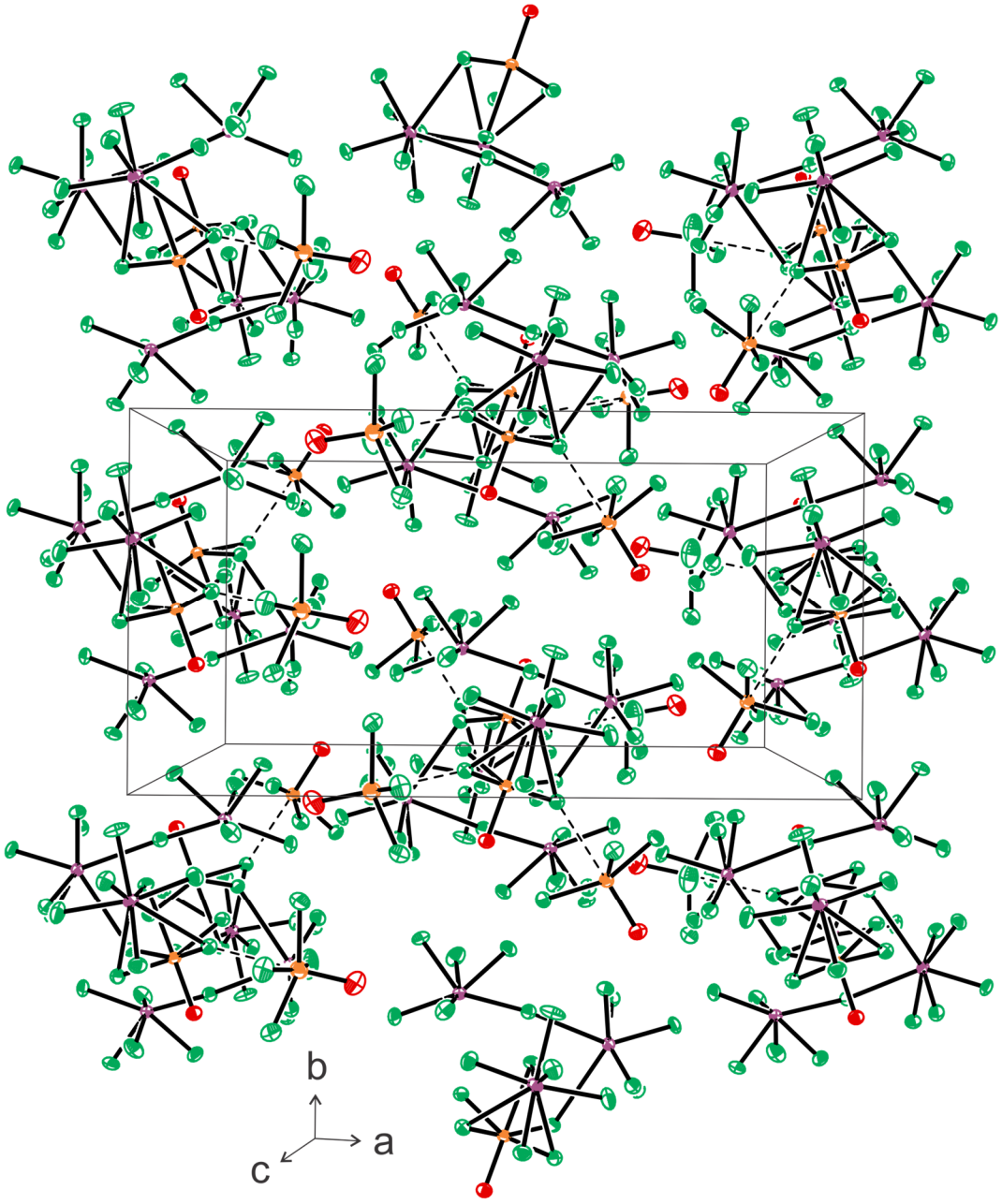

Figure A6.7. A packing diagram showing the X-ray crystal structure of $[XeF_5][Xe_2F_{11}][CrOF_5]\cdot 2CrOF_4$ (**6**) viewed along the *c*-axis of the unit cell; thermal ellipsoids are drawn at the 50% probability level.

Table A6.7. Experimental (Raman) and calculated vibrational frequencies, intensities, and assignments for $[XeF_5]_2[Cr_2O_2F_8]\cdot 2XeOF_4$ (**5**)

exptl [a,b]	calcd [a,c]	assgnts [d]
1026(17)	1206(56)[0]	$\nu(Cr_1\text{-}O_1) + \nu(Cr_{1A}\text{-}O_{1A})$
	1204(0)[206]	$\nu(Cr_1\text{-}O_1) - \nu(Cr_{1A}\text{-}O_{1A})$
922(34)	857(66)[0]	$\nu(Xe_2\text{-}O_2) + \nu(Xe_{2A}\text{-}O_{2A})$
	857(0)[50]	$\nu(Xe_2\text{-}O_2) - \nu(Xe_{2A}\text{-}O_{2A})$
	731(0)[397]	$\nu(Cr_1\text{-}F_3) - \nu(Cr_{1A}\text{-}F_{3A})$
700(22)	720(11)[0]	$\nu(Cr_1\text{-}F_3) + \nu(Cr_{1A}\text{-}F_{3A})$
677(44)	667(9)[0]	$[\nu(Xe_1\text{-}F_6) - \nu(Xe_1\text{-}F_8)] + [\nu(Xe_{1A}\text{-}F_{6A}) - \nu(Xe_{1A}\text{-}F_{8A})]$
	666(14)[0]	$[\nu(Xe_1\text{-}F_5) - \nu(Xe_1\text{-}F_7)] + [\nu(Xe_{1A}\text{-}F_{5A}) - \nu(Xe_{1A}\text{-}F_{7A})]$
653(9)	669(0)[406]	$[\nu(Xe_1\text{-}F_5) - \nu(Xe_1\text{-}F_7)] - [\nu(Xe_{1A}\text{-}F_{5A}) - \nu(Xe_{1A}\text{-}F_{7A})]$
	665(0)[305]	$[\nu(Xe_1\text{-}F_6) - \nu(Xe_1\text{-}F_8)] - [\nu(Xe_{1A}\text{-}F_{6A}) - \nu(Xe_{1A}\text{-}F_{8A})]$
	651(0)[11]	$\nu(Xe_1\text{-}F_9) - \nu(Xe_{1A}\text{-}F_{9A})$
668(63)	642(174)[0]	$\nu(Xe_1\text{-}F_9) + \nu(Xe_{1A}\text{-}F_{9A})$
591(4)	636(0)[263]	$[\nu(Xe_2\text{-}F_{11}) - \nu(Xe_2\text{-}F_{13})] - [\nu(Xe_{2A}\text{-}F_{11A}) - \nu(Xe_{2A}\text{-}F_{13A})]$
	632(2)[0]	$[\nu(Xe_2\text{-}F_{11}) - \nu(Xe_2\text{-}F_{13})] + [\nu(Xe_{2A}\text{-}F_{11A}) - \nu(Xe_{2A}\text{-}F_{13A})]$
	619(0)[661]	$[\nu(Xe_1\text{-}F_9) - \nu(Xe_{1A}\text{-}F_{9A})] - [\nu(Xe_2\text{-}F_{10}) - \nu(Xe_{2A}\text{-}F_{10A})]$
617(69)	610(4)[0]	$[\nu(Xe_1\text{-}F_9) + \nu(Xe_{1A}\text{-}F_{9A})] - [\nu(Xe_2\text{-}F_{10}) + \nu(Xe_{2A}\text{-}F_{10A})]_{small}$
	601(0)[77]	$[\nu(Xe_1\text{-}F_9) - \nu(Xe_1\text{-}F_{4e})] - [\nu(Xe_{1A}\text{-}F_{9A}) - \nu(Xe_{1A}\text{-}F_{4e'})] + [\nu(Xe_2\text{-}F_{10}) - \nu(Xe_{2A}\text{-}F_{10A})]$
606(46)	598(20)[0]	$[\nu(Xe_1\text{-}F_9) - \nu(Xe_1\text{-}F_{4e})] + [\nu(Xe_{1A}\text{-}F_{9A}) - \nu(Xe_{1A}\text{-}F_{4e'})] + [\nu(Xe_2\text{-}F_{10}) - \nu(Xe_{2A}\text{-}F_{10A})]_{small}$
	582(0)[5]	$\{[\nu(Xe_1\text{-}F_5) + \nu(Xe_1\text{-}F_7)] - [\nu(Xe_1\text{-}F_6) + \nu(Xe_1\text{-}F_8)]\} - \{[\nu(Xe_{1A}\text{-}F_{5A}) + \nu(Xe_{1A}\text{-}F_{7A})] - [\nu(Xe_{1A}\text{-}F_{6A}) + \nu(Xe_{1A}\text{-}F_{8A})]\}$
580(14)	582(4)[0]	$\{[\nu(Xe_1\text{-}F_5) + \nu(Xe_1\text{-}F_7)] - [\nu\ (Xe_1\text{-}F_6) + \nu(Xe_1\text{-}F_8)]\} + \{[\nu(Xe_{1A}\text{-}F_{5A}) + \nu(Xe_{1A}\text{-}F_{7A})] - [\nu(Xe_{1A}\text{-}F_{6A}) + \nu(Xe_{1A}\text{-}F_{8A})]\}$
562(32)	572(27)[0]	$\nu(Cr_1\text{-}F_1) + \nu(Cr_{1A}\text{-}F_{1A})$
553(34)		
547(62)	559(0)[52]	$[\nu(Xe_2\text{-}F_{11}) + \nu(Xe_2\text{-}F_{13})] - [\nu(Xe_{2A}\text{-}F_{11A}) + \nu(Xe_{2A}\text{-}F_{13A})]$
544(100)	553(61)[0]	$[\nu(Xe_2\text{-}F_{11}) + \nu(Xe_2\text{-}F_{13})] + [\nu(Xe_{2A}\text{-}F_{11A}) + \nu(Xe_{2A}\text{-}F_{13A})]$
539, sh	551(0)[592]	$[\nu(Cr_1\text{-}F_4) - \nu(Cr_1\text{-}F_2)] - [\nu(Cr_{1A}\text{-}F_{4A}) - \nu(Cr_{1A}\text{-}F_{2A})]$
523(29)	509(10)[0]	$[\nu(Cr_1\text{-}F_4) + \nu(Cr_{1A}\text{-}F_{4A})] + [\nu(Xe_2\text{-}F_{12}) + \nu(Xe_{2A}\text{-}F_{12A})]$
511(9)	499(0)[53]	$[\nu(Cr_1\text{-}F_3) - \nu(Cr_1\text{-}F_1)] - [\nu\ (Cr_{1A}\text{-}F_{3A}) - \nu(Cr_{1A}\text{-}F_{1A})]$

continued…

Table A6.7. (continued)

exptl [a,b]	calcd [a,c]	assgnts [d]
507(21)	491(52)[0]	$[\nu(Cr_1\text{-}F_2) + \nu(Cr_{1A}\text{-}F_{2A})] + [\nu(Xe_2\text{-}F_{12}) + \nu(Xe_{2A}\text{-}F_{12A})]$
	483(0)[143]	$[\nu(Xe_2\text{-}F_{12}) - \nu(Xe_{2A}\text{-}F_{12A})]$
503(57)	467(20)[0]	$\{[\nu(Cr_1\text{-}F_4) + \nu(Cr_1\text{-}F_2)] + [\nu(Cr_{1A}\text{-}F_{4A}) + \nu(Cr_{1A}\text{-}F_{2A})]\} - [\nu\ (Xe_2\text{-}F_{12}) - \nu(Xe_{2A}\text{-}F_{12A})]$
405(6)	456(0)[14]	$[\nu(Cr_1\text{-}F_4) + \nu(Cr_1\text{-}F_2)] - [\nu(Cr_{1A}\text{-}F_{4A}) + \nu(Cr_{1A}\text{-}F_{2A})]$
	374(0)[32]	$\{[\delta(F_2Cr_1O_1) - \delta(F_4Cr_1O_1)] / \rho(F_1Cr_1F_3)\} - \{[\delta(F_{2A}Cr_{1A}O_{1A}) - \delta(F_{4A}Cr_{1A}O_{1A})] / \rho(F_{1A}Cr_{1A}F_{3A})\}$
398(5)	369(3)[0]	$[\nu(Cr_1F_1) + \nu(Cr_1F_{1A})] + [\nu(Cr_{1A}F_1) + \nu(Cr_{1A}F_{1A})]$
375(12)	365(3)[0]	$[\delta(F_3Cr_1O_1) + \delta(F_{3A}Cr_{1A}O_{1A})] / [\delta(F_2Cr_1O_1) + \delta(F_{2A}Cr_{1A}O_{1A})]$
370(11)	358(3)[0]	$[\delta(F_2Cr_1O_1) + \delta(F_{2A}Cr_{1A}O_{1A})] / [\rho(F_1Cr_1O_1) + \rho(F_{1A}Cr_{1A}O_{1A})]$
	359(0)[26]	$[\delta(F_3Cr_1O_1) + \delta(F_{3A}Cr_{1A}O_{1A})] / [\delta(F_1Cr_1F_2) + \delta(F_{1A}Cr_{1A}F_{2A})]$
	355(0)[13]	$[\delta(F_9Xe_1F_6) - \delta(F_9Xe_1F_8)] - [\delta(F_{9A}Xe_{1A}F_{6A}) - \delta(F_{9A}Xe_{1A}F_{8A})]$
349(11)	354(2)[0]	$[\delta(F_9Xe_1F_6) - \delta(F_9Xe_1F_8)] + [\delta(F_{9A}Xe_{1A}F_{6A}) - \delta(F_{9A}Xe_{1A}F_{8A})]$
341(8)	344(3)[0]	$[\delta(F_9Xe_1F_5) - \delta(F_9Xe_1F_7)] + [\delta(F_{9A}Xe_{1A}F_{5A}) - \delta(F_{9A}Xe_{1A}F_{7A})]$
	343(0)[8]	$[\delta(F_9Xe_1F_5) - \delta(F_9Xe_1F_7)] - [\delta(F_{9A}Xe_{1A}F_{5A}) - \delta(F_{9A}Xe_{1A}F_{7A})]$
	338(0)[24]	$[\delta(F_3Cr_1O_1) - \delta(F_{3A}Cr_{1A}O_{1A})] / [\rho_w(F_1Cr_1O_1) - \rho_w(F_{1A}Cr_{1A}O_{1A})]$
	336(6)[0]	$[\delta(F_{11}Xe_2O_2) - \delta(F_{13}Xe_2O_2)] + [\delta(F_{11A}Xe_{2A}O_{2A}) - \delta(F_{13A}Xe_{2A}O_{2A})]$
	334(0)[10]	$[\delta(F_{11}Xe_2O_2) - \delta(F_{13}Xe_2O_2)] - [\delta(F_{11A}Xe_{2A}O_{2A}) - \delta(F_{13A}Xe_{2A}O_{2A})]$
	333(3)[0]	$[\delta(F_3Cr_1O_1) + \delta(F_{3A}Cr_{1A}O_{1A})] / [\rho_w(F_1Cr_1O_1) + \rho_w(F_{1A}Cr_{1A}O_{1A})]$
	321(0)[62]	$[\delta(F_{10}Xe_2O_2) - \delta(F_{12}Xe_2O_2)] - [\delta(F_{10A}Xe_{2A}O_{2A}) - \delta(F_{12A}Xe_{2A}O_{2A})]$
	322(7)[0]	$[\delta(F_{10}Xe_2O_2) - \delta(F_{12}Xe_2O_2)] + [\delta(F_{10A}Xe_{2A}O_{2A}) - \delta(F_{12A}Xe_{2A}O_{2A})]$
323(6)	317(6)[0]	$\delta_{umb}(Xe_1F_{4e}) + \delta_{umb}(Xe_{1A}F_{4e'})$
	314(0)[84]	$\delta_{umb}(XeF_{4e}) - \delta_{umb}(Xe_{1A}F_{4e'})$
276(6)	307(0)[1]	$[\delta(F_2Cr_1O_1) - \delta(F_5Cr_1O_1)] - [\delta(F_{2A}Cr_{1A}O_{1A}) + \delta(F_{5A}Cr_{1A}O_{1A})]\} / [\rho_w(F_1Cr_1F_3) - \rho_w(F_{1A}Cr_{1A}F_{3A})]$
	297(0)[94]	$[\delta(F_3Cr_1F_4) - \delta(F_{3A}Cr_{1A}F_{4A})]$
266(3)	277(1)[0]	$[\rho_w(F_4Cr_1O_1) + \rho_w(F_{4A}Cr_{1A}O_{1A})]$
	277(3)[0]	$\delta_{umb}(Xe_2F_4) + \delta_{umb}(Xe_{2A}F_{4A'})$
	274(0)[186]	$\delta_{umb}(Xe_2F_4) - \delta_{umb}(Xe_{2A}F_{4A'})$
252(3)	257(3)[0]	$[\delta(F_6Xe_1F_7) + \delta(F_5Xe_1F_8)] + [\delta(F_{6A}Xe_{1A}F_{7A}) + \delta(F_{5A}Xe_{1A}F_{8A})]$
	252(0)[4]	$[\delta(F_6Xe_1F_7) + \delta(F_5Xe_1F_8)] - [\delta(F_{6A}Xe_{1A}F_{7A}) + \delta(F_{5A}Xe_{1A}F_{8A})]$
243(3)	251(2)[0]	$[\rho_t(F_1Cr_1O_1) + \rho_t(F_{1A}Cr_{1A}O_{1A})]$

continued…

Table A6.7. (continued)

exptl [a,b]	calcd [a,c]	assgnts [d]
	260(0)[22]	$\delta(F_6Xe_1F_7) - \delta(F_{6A}Xe_{1A}F_{7A})$
238(3)	236(1)[0]	$[\delta(F_2Cr_1F_3) - \delta(F_{2A}Cr_{1A}F_{3A})] / [\rho_w(F_6Xe_1F_8) - \rho_w(F_5Xe_1F_7)] + [\rho_w(F_{6A}Xe_{1A}F_{8A}) - \rho_w(F_{5A}Xe_{1A}F_{7A})]$
230(3)	231(0)[<1]	$[\rho_w(F_6Xe_1F_8) - \rho_w(F_5Xe_1F_7)] - [\rho_w(F_{6A}Xe_{1A}F_{8A}) - \rho_w(F_{5A}Xe_{1A}F_{7A})]$
	231(0)[13]	$[\nu(Cr_1F_1) + \nu(Cr_1F_{1A})] - [\nu(Cr_{1A}F_1) + \nu(Cr_{1A}F_{1A})]$
	220(<1)[0]	$[\rho_w(F_6Xe_1F_8) - \rho_w(F_5Xe_1F_7)] + [\rho_w(F_{6A}Xe_{1A}F_{8A}) - \rho_w(F_{5A}Xe_{1A}F_{7A})]$
215(5)	211(1)[0]	$[\delta(F_{10}Xe_2F_{13}) + \delta(F_{11}Xe_2F_{12})] + [\delta(F_{10A}Xe_{2A}F_{13A}) + \delta(F_{11A}Xe_{2A}F_{12A})]$
	210(0)[<1]	$[\delta(F_{10}Xe_2F_{13}) + \delta(F_{11}Xe_2F_{12})] - [\delta(F_{10A}Xe_{2A}F_{13A}) + \delta(F_{11A}Xe_{2A}F_{12A})]$
	205(2)[0]	$[\delta(F_5Xe_1F_8) - \delta(F_6Xe_1F_7)] + [\delta(F_{5A}Xe_{1A}F_{8A}) - \delta(F_{6A}Xe_{1A}F_{7A})]$
209(2)	203(2)[0]	$[\rho_w(F_{10}Xe_2F_{12}) - \rho_w(F_{11}Xe_2F_{13})] + [\rho_w(F_{10A}Xe_{2A}F_{12A}) - \rho_w(F_{11A}Xe_{2A}F_{13A})]$
	202(0)[12]	$[\rho_w(F_{10}Xe_2F_{12}) - \rho_w(F_{11}Xe_2F_{13})] - [\rho_w(F_{10A}Xe_{2A}F_{12A}) - \rho_w(F_{11A}Xe_{2A}F_{13A})]$
	192(0)[3]	$[\delta(F_5Xe_1F_8) - \delta(F_6Xe_1F_7)] - [\delta(F_{5A}Xe_{1A}F_{8A}) - \delta(F_{6A}Xe_{1A}F_{7A})]$
188(2)	190(11)[0]	$[\delta(F_7Xe_1F_8) + \delta(F_{7A}Xe_1F_{8A})]$
	186(0)[13]	
178(4)	174(<1)[0]	
171(4)	170(<1)[0]	
	174(0)[5]	
	158(0)[17]	
159(3)	157(<1)[0]	
	154(<1)[0]	
	154(0)[3]	
	144(0)[3]	
143(4)	140(13)[0]	coupled deformation modes
	138(0)[24]	
121(7)	128(<1)[0]	
112(6)	118(<1)[0]	
	112(0)[6]	
	101(0)[5]	
	97(<1)[0]	
	95(0)[8]	
98(7)	92(2)[0]	
	86(0)[<1]	
	85(0)[3]	

continued…

Table A6.7. (continued)

exptl [a,b]	calcd [a,c]	assgnts [d]
72(3)	78(2)[0]	coupled deformation modes
	75(<1)[0]	
	66(0)[4]	
	60(<1)[0]	
	60(0)[3]	
	55(<1)[0]	
	47(<1)[0]	
	43(0)[5]	
	41(<1)[0]	
	42(0)[3]	
	30(<1)[0]	
	30(0)[2]	
	21(<1)[0]	
	18(0)[<1]	
	9(0)[<1]	

[a] Frequencies are given in cm^{-1}. [b] Values in parentheses denote relative Raman intensities. The Raman spectrum was recorded on the dry crystalline compound in an FEP sample tube at −140 °C. Several crystals were subsequently shown to be compound (**5**) by a single-crystal X-ray structure determination and crystallographic unit cell determinations. Weak, unassigned bands were also observed at 763(2), 806(2), 959(2), 973(5), 1001(10), 1006(3), and 1009(5) cm^{-1}. [c] Values in parentheses and square brackets denote calculated Raman intensities ($Å^4$ amu^{-1}) and infrared intensities (km mol^{-1}), respectively. [d] Assignments are for the energy-minimized geometry (C_i) calculated using the uPBE1PBE/aug-ccpVDZ (Xe)-Def2-SVP (F, O, Cr) level of theory. Abbreviations denote stretch (ν), bend (δ), twist (ρ_t), and wag (ρ_w), umbrella (umb), Xe_1F_{4e} ($Xe_1F_5F_6F_7F_8$), $Xe_{1A}F_{4e'}$ ($Xe_{1A}F_{5A}F_{6A}F_{7A}F_{8A}$), Xe_2F_4 ($Xe_2F_{10}F_{11}F_{12}F_{13}$), and $Xe_{2A}F_{4A'}$ ($Xe_{2A}F_{10A}F_{11A}F_{12A}F_{13A}$). The atom labeling scheme corresponds to that used in Figure 9.5.

Table A6.8. Experimental (Raman) and calculated vibrational frequencies, intensities, and assignments for $[XeF_5][Xe_2F_{11}][CrOF_5]\cdot 2CrOF_4$ (**6**)

exptl [a, b]	calcd [b, c]	assgnts [d]
1000(33)	1232(40)[173]	$\nu(Cr_3–O_2) + \nu(Cr_2–O_3)$
	1230(26)[204]	$\nu(Cr_3–O_2) – \nu(Cr_2–O_3)$
	1192(41)[102]	$\nu(Cr_1–O_1)$
750, sh	762(2)[222]	$[\nu(Cr_3–F_{24}) – \nu(Cr_3–F_{22})] + [\nu(Cr_2–F_{28}) – \nu(Cr_2–F_{26})]$
746(3)	752(<0.1)[214]	$[\nu(Cr_3–F_{24}) – \nu(Cr_3–F_{22})] – [\nu(Cr_2–F_{28}) – \nu(Cr_2–F_{26})]$
727(3)	750(<1](400)	$[\nu(Cr_3–F_{23}) – \nu(Cr_3–F_{25})] + [\nu(Cr_2–F_{29}) – \nu(Cr_2–F_{27})]$
707(8)	745(<1)[18]	$[\nu(Cr_3–F_{23}) – \nu(Cr_3–F_{25})] – [\nu(Cr_2–F_{29}) – \nu(Cr_2–F_{27})]$
700, sh	723(23)[24]	$[\nu(Cr_3–F_{24}) + \nu(Cr_3–F_{22})] + [\nu(Cr_3–F_{23}) + \nu(Cr_2–F_{25})] + [\nu(Cr_2–F_{28}) + \nu(Cr_2–F_{26})] + [\nu(Cr_2–F_{29}) + \nu(Cr_2–F_{27})]$
	722(<1)[48]	$[\nu(Cr_3–F_{24}) + \nu(Cr_3–F_{22})] + [\nu(Cr_3–F_{23}) + \nu(Cr_3–F_{25})] – [\nu(Cr_2–F_{28}) + \nu(Cr_2–F_{26})] + [\nu(Cr_2–F_{29}) + \nu(Cr_2–F_{27})]$
675(100)	644(136)[49]	$[\nu(Xe_2–F_{12}) + \nu(Xe_3–F_{21}) + \nu(Xe_1–F_{10})]$
662(33)	639(30)[119]	$\nu(Xe_1–F_6) + \nu(Xe_1–F_{10})$
	633(11)[116]	$[\nu(Xe_2–F_{12}) – \nu(Xe_3–F_{21})] / [\nu(Xe–F_{e\ ([Xe_2F_{11}]^+)})_{o.o.p.}]_{small}$
659, sh	668(7)[258]	
650(17)	666(8)[242]	
644(12)	654(13)[25]	$\nu(Xe–F_{e\ ([Xe_2F_{11}]^+)})_{o.o.p.} / \nu(Xe–F_{e\ ([XeF_5]^+)})_{o.o.p.}$
634(14)	644(15)[49]	
	661(7)[396]	
	653(9)[73]	$\nu(Xe–F_{e\ ([Xe_2F_{11}]^+)})_{o.o.p.}$
608, sh	602(7)[106]	$\{[\nu(Cr_1–F_2) + \nu(Cr_1–F_5)] + [\nu(Cr_1–F_3) + \nu(Cr_1–F_4)]\} + \{[\nu(Xe_2–F_{12}) + \nu(Xe_3–F_{21})] – [\nu(Xe_2–F_{13}) + \nu(Xe_3–F_{20})]\}$
604(31)	596(4)[54]	$[\nu(Cr_1–F_2) + \nu(Cr_1–F_3)] – [\nu(Cr_1–F_5) + \nu(Cr_1–F_4)] / [\nu(Xe_2–F_{12}) – \nu(Xe_3–F_{21})] / \nu(Xe–F_{e\ ([Xe_2F_{11}]^+)})_{o.o.p.}$
597(37)	593(3)[29]	$[\nu(Cr_1–F_3) + \nu(Cr_1–F_4)] + [\nu(Xe_1–F_3) + \nu(Xe_1–F_4)] + \nu(Xe_1–F_{10}) – [\nu(Xe_1–F_7) + \nu(Xe_1–F_9)]$
595, sh	587(50)[3]	$[\nu(Cr_1–F_3) + \nu(Cr_1–F_4)] + [\nu(Cr_1–F_3) + \nu(Cr_1–F_4)] – \nu(Xe_1–F_{10}) + [\nu(Xe_1–F_7) + \nu(Xe_1–F_9)]$
587, sh	578(9)[15]	$[\nu(Cr_2–F_{29}) + \nu(Cr_2–F_{27})] – [\nu(Cr_2–F_{26}) + \nu(Cr_2–F_{28})] / \nu(Xe–F_{e\ ([Xe_2F_{11}]^+)})_{i.p.} – \nu(Xe–F_{e\ ([XeF_5]^+)})_{i.p.}$
	575(5)[17]	$\nu(Cr_3–F_{24}) + \nu(Cr_3–F_{22})] – [\nu(Cr_3–F_{25}) + \nu(Cr_3–F_{23})] / \nu(Xe–F_{e\ ([Xe_2F_{11}]^+)})_{i.p.}$
584(32)	574(7)[6]	$\nu(Xe–F_{e\ ([XeF_5]^+)})_{o.o.p.}$
	574(7)[23]	$[\nu(Cr_2–F_{29}) + \nu(Cr_2–F_{27})] – [\nu(Cr_2–F_{26}) + \nu(Cr_2–F_{28})] / \nu(Xe–F_{e\ ([Xe_2F_{11}]^+)})_{o.o.p.}$
576, sh	572(10)[11]	$\nu(Xe–F_{e\ ([Xe_2F_{11}]^+)})_{o.o.p.}$
	570(19)[41]	$\nu(Xe–F_{e\ ([Xe_2F_{11}]^+)})_{o.o.p.} / [\nu(Cr_1–F_2) – \nu(Xe_2–F_2)] – [\nu(Cr_1–F_4) – \nu(Cr_3–F_4)]$
555(12)	562(14)[172]	$[\nu(Cr_1–F_5) – \nu(Cr_1–F_3)] / \nu(Xe–F_{e\ ([Xe_2F_{11}]^+)})_{o.o.p.} – \nu(Xe–F_{e\ ([XeF_5]^+)})_{o.o.p.}$
470(4)	469(10)[34]	$[\nu(Cr_1–F_2) + \nu(Cr_1–F_4)] – [\nu(Cr_1–F_5) + \nu(Cr_1–F_3)] – [\nu(Xe_2–F_2) + \nu(Cr_3–F_4)] + [\nu(Xe_3–F_5) + \nu(Cr_2–F_3)]$

continued…

Table A6.8. (continued)

exptl [a, b]	calcd [b, c]	assgnts [d]
	413(1)[<0.1]	$[\delta(F_{24}Cr_3F_{25}) + \delta(F_{23}Cr_3F_{22})] + [\delta(F_{28}Cr_2F_{27}) + \delta(F_{26}Cr_2F_{29})]$
	413(1)[<1]	$[\delta(F_{24}Cr_3F_{25}) + \delta(F_{23}Cr_5F_{22})] - [\delta(F_{28}Cr_2F_{27}) + \delta(F_{26}Cr_2F_{29})]$
419(6)	389(4)[58]	$[\delta(F_1Cr_1O_1) - \delta(F_3Cr_1F_4)]$
411(5)	383(3)[9]	$[\delta(O_2Cr_3F_{22}) - \delta(O_2Cr_3F_{24})]$
	382(3)[9]	$[\delta(O_3Cr_2F_{28}) - \delta(O_3Cr_2F_{26})]$
400(4)	380(3)[13]	$[\delta(O_3Cr_2F_{29}) - \delta(O_3Cr_2F_{27})] - [\delta(O_2Cr_3F_{23}) - \delta(O_2Cr_3F_{25})]$
	380(3)[3]	$[\delta(O_3Cr_2F_{29}) - \delta(O_3Cr_2F_{27})] + [\delta(O_2Cr_3F_{23}) - \delta(O_2Cr_3F_{25})]$
375, sh	367(2)[122]	$\delta(FXeF_{([Xe_2F_{11}]^+)})$
372(8)	365(3)[63]	$[\delta(Cr_1F_1F_2F_5) + [\delta(F_8Xe_1F_{10}) - \delta(F_6Xe_1F_{10})]$
	357(3)[22]	$\delta(Cr_1O_1F_3F_4)$
	354(4)[60]	$\delta(FXeF_{([Xe_2F_{11}]^+)}) / \delta(FXeF_{([XeF_5]^+)})$
	350(3)[42]	$\delta_{umb}[Cr_3F_{4e}] / \delta(FXeF_{([Xe_2F_{11}]^+)}) / \delta(FXeF_{([XeF_5]^+)})$
351(19)	349(5)[5]	$\delta_{umb}[Cr_2F_{4e}] / \delta(FXeF_{([Xe_2F_{11}]^+)}) / \delta(FXeF_{([XeF_5]^+)})$
343, sh	346(1)[12]	$\delta_{umb}[Cr_2F_{4e}] / \delta(FXeF_{([Xe_2F_{11}]^+)})$
	344(1)[24]	$\delta_{umb}[Cr_3F_{4e}] + \delta_{umb}[Cr_2F_{4e}] / \delta(FXeF_{([Xe_2F_{11}]^+)}) / \delta(FXeF_{([XeF_5]^+)})$
	341(<1)[54]	$\delta(F_2Cr_1F_3) - \delta(F_4Cr_1F_5)_{small} / \rho_w(O_1Cr_1F_1)$
	337(<1)[2]	$\delta(FXeF_{([Xe_2F_{11}]^+)})$
	332(2)[17]	$\delta(FXeF_{([XeF_5]^+)})$
	331(3)[11]	$\delta(FXeF_{([Xe_2F_{11}]^+)})$
325, sh	328(1)[31]	$\delta(F_2Cr_1F_3)_{small} - \delta(F_4Cr_1F_5) / \rho_w(O_1Cr_1F_1)$
319(5)	327(3)[22]	$\delta(F_2Cr_1F_5) - \delta(F_4Cr_1F_3) / \rho_w(O_1Cr_1F_1)$
	311(1)[122]	$\delta_{umb}[Xe_2F_{11}]^+$
305, sh	306(2)[21]	$\delta_{umb}[XeF_5]^+ / \delta(F_2Cr_1F_5) + \delta(F_4Cr_1F_3)$
298, sh	297(1)[1]	$\delta(Cr_2O_3F_{4e}) - \delta(Cr_3O_2F_{4e})$
293(6)	293(2)[26]	$\delta(Cr_2O_3F_{4e}) + \delta(Cr_3O_2F_{4e})$
288, sh	289(2)[4]	$\delta(Cr_2O_3F_{4e}) - \delta(Cr_3O_2F_{4e})$
	286(3)[3]	
	285(2)[4]	
271, sh	276(1)[35]	
266(8)	269(2)[45]	
262, sh	258(<1)[6]	coupled deformation modes
258, sh	256(1)[10]	
250(3)	254(2)[6]	
	246(0)[5]	

continued…

Table A6.8. (continued)

exptl [a, b]	calcd [b, c]	assgnts [d]
231(3)	243(1)[20]	
	223(1)[9]	
	221(<1)[13]	
212(3)	214(1)[5]	
	210(1)[4]	
203(3)	201(<1)[<1]	
	196(<1)[<1]	
	194(<1)[<1]	
	186(<1)[2]	
	183(<1)[<1]	
	179(<1)[<1]	
174(9)	174(1)[2]	
	171(1)[1]	
164, sh	169(<1)[<1]	
152(3)	157(1)[1]	
	142(<1)[6]	
139(2)	138(<1)[14]	coupled deformation modes
	136(<1)[11]	
126, sh, br	129(<1)[10]	
	128(<1)[3]	
111(4), br	106(<0.1)[<0.1]	
	100(<1)[<1]	
	97(<1)[<1]	
95, sh	96(<1)[<1]	
	92(<1)[3]	
	87(<1)[1]	
	82(<1)[<1]	
	78(<1)[1]	
	74(<1)[6]	
	67(<1)[<1]	
	63(<1)[<1]	
	61(<1)[<1]	
	58(<0.1)[<1]	
	52(<0.1)[<1]	

continued…

Table A6.8. (continued)

exptl [a, b]	calcd [b, c]	assgnts [d]
	42(<1)[1]	coupled deformation modes
	40(<1)[<1]	
	39(<0.1)[<0.1]	
	35(<0.1)[<0.1]	
	28(<0.1)[<0.1]	
	23(<0.1)[<0.1]	
	22(<0.1)[<0.1]	
	19(<0.1)[<0.1]	
	15(<0.1)[<0.1]	
	10(<0.1)[<0.1]	

[a] Frequencies are given in cm^{-1}. [b] Values in parentheses denote relative Raman intensities. The Raman spectrum was recorded on the dry crystalline compound in an FEP sample tube at −140 °C. Several crystals were subsequently shown to be compound (**6**) by a single-crystal X-ray structure determination and crystallographic unit cell determinations. [c] Values in parentheses and square brackets denote calculated Raman intensities ($Å^4$ amu^{-1}) and infrared intensities (km mol^{-1}), respectively. [d] Assignments are for the energy-minimized geometry (C_1) calculated using the uPBE1PBE/aug-ccpVDZ (Xe)-Def2-SVP (F, O, Cr) level of theory. Abbreviations denote stretch (ν), bend (δ), and wag (ρ_w), umbrella (umb), out-of-phase (o.o.p.), in-phase (i.p.), F equatorial (F_e). The atom labeling scheme corresponds to that used in Figure 9.6.

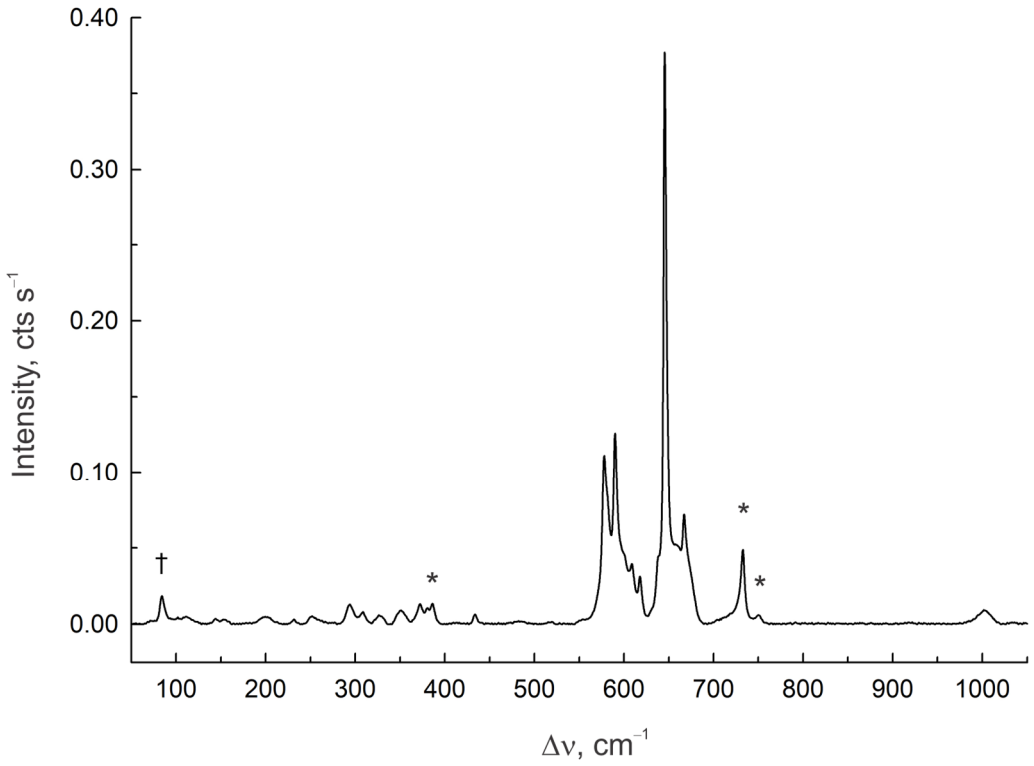

Figure A6.8. Raman spectrum obtained from the product resulting from the reaction of $[XeF_5]_2[CrF_6]\cdot 2CrOF_4$ (**1**) with excess XeF_6 at 30 °C in a melt. The spectrum of the resulting product was recorded at −150 °C using 1064-nm excitation. The dagger (†) denotes an instrumental artefact and asterisks (*) denote FEP sample tube bands. The product bands (FEP sample tube lines are not included) and their relative intensities are: 1002(3), 710(sh), 675(sh), 667(<1), 658(sh, br), 645(100), 639(12), 632(sh), 621(sh), 618(8), 609(11), 600(12), 594(sh), 590(34), 580(sh), 578(30), 554(<1), 518(<1), 484(<1), 434(2), 386(<1), 372(4), 351(2), 328(2), 309(1), 261(sh), 251(1), 232(1), 200(1,br), 154(1), 144(1), 118(sh), 111(1, br), and 102(1) cm^{-1}.

Figure A6.9. Factor-group analysis for $[XeF_5]_2[Cr_2O_2F_8]\cdot 2XeOF_4$ [a]

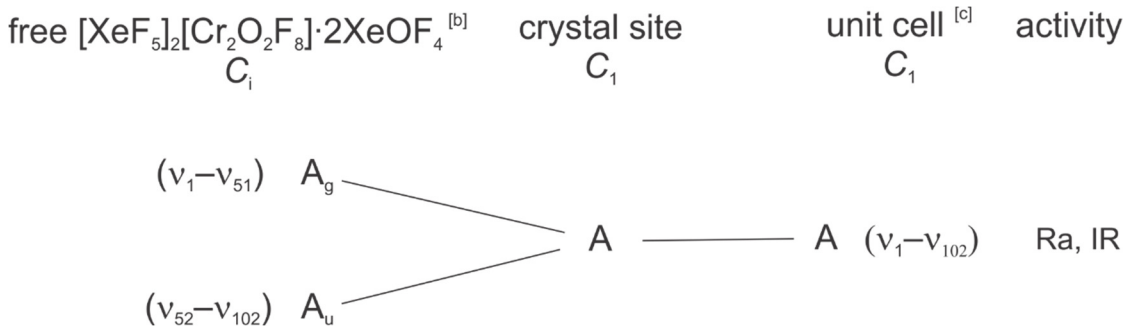

[a] The external modes have not been treated in this analysis. [b] The vibrational irreducible representation for gas-phase $[XeF_5]_2[Cr_2O_2F_8]\cdot 2XeOF_4$ is $\Gamma = 51\ A_g + 51\ A_u$. [c] Space group; $P\bar{1}$, Z = 1.

Table A6.9. Calculated geometric parameters for $Cr^{VI}OF_4$, $[Cr^{VI}OF_5]^-$, $[Cr^{V}OF_5]^{2-}$, and $[Cr^{V}_2O_2F_8]^{2-}$

	$CrOF_4$ [a] C_{4v}	**$[CrOF_5]^-$** [a] C_{4v}	**$[CrOF_5]^{2-}$** [b] C_{4v}	**$[Cr_2O_2F_8]^{2-}$** [b,c] C_2
Cr–O	1.499	1.540	1.559	1.526
Cr–F1	1.705	1.762	1.844	1.827
Cr–F2	1.705	1.762	1.844	1.771
Cr–F3	1.705	1.762	1.844	1.779
Cr–F4	1.705	1.762	1.844	1.771
Cr–F5		1.823	1.887	
Cr–F1A				2.373
O–Cr–F1	104.95	94.25	94.21	100.79
O–Cr–F2	104.95	94.25	94.21	100.95
O–Cr–F3	104.95	94.25	94.21	102.63
O–Cr–F4	104.95	94.25	94.21	100.95
O–Cr–F5		180.00	180.00	
O–Cr–F1A				172.19
F1–Cr–F2	86.18	89.69	89.69	88.53
F1–Cr–F3	150.10	171.50	171.58	156.58
F1–Cr–F4	86.18	89.69	89.69	88.53
F1–Cr–F5		85.75	85.79	
F1–Cr–F1A				71.40
F2–Cr–F3	86.18	89.69	89.69	87.05
F2–Cr–F4	150.10	171.50	171.58	158.07
F2–Cr–F5		85.75	85.79	
F2–Cr–F1A				79.24
F3–Cr–F4	86.18	89.69	89.69	87.05
F3–Cr–F5		85.75	85.79	
F3–Cr–F1A				85.18
F4–Cr–F5		85.75	85.79	
F4–Cr–F1A				79.24

[a] The PBE1PBE/aug-ccpVDZ (Xe)-Def2-SVP (F, O, Cr) level of theory was used. [b] The uPBE1PBE/aug-ccpVDZ (Xe)-Def2-SVP (F, O, Cr) level of theory was used. [c] The Cr···Cr distance was fixed at the value calculated for the $[XeF_5]_2[Cr_2O_2F_8]\cdot 2XeOF_4$ ion-pair (3.43 Å).

Table A6.10. Calculated[a] vibrational frequencies and intensities for $Cr^{VI}OF_4$, $[Cr^{VI}OF_5]^-$, $[Cr^{V}OF_5]^{2-}$, and $[Cr^{V}{}_2O_2F_8]^{2-}$

$CrOF_4$ [b] C_{4v}	**$[CrOF_5]^-$** [b] C_{4v}	**$[CrOF_5]^{2-}$** [c] C_{4v}	**$[Cr_2O_2F_8]^{2-}$** [c,d] C_2
1233(13)[111]	1127(13)[230]	1009(63)[199]	1148(79)[0]
776(<1)[226]	659(21)[41]	565(15)[63]	1141(0)[461]
741(18)[22]	633(<0.1)[278]	544(<0.1)[302]	702(0)[448]
585(6)[0]	513(6)[0]	439(3)[0]	667(<0.1)[0]
429(2)[0]	494(7)[53]	406(2)[56]	657(0)[352]
372(2)[11]	381(<1)[7]	360(3)[10]	647(11)[0]
352(2)[7]	380(4)[8]	329(<1)[4]	620(0)[221]
300(2)[14]	346(3)[0]	312(1)[<1]	610(15)[0]
116(<1)[0]	320(<0.1)[38]	279(3)[0]	502(<0.1)[17]
	226(<1)[0]	202(<0.1)[0]	502(7)[<0.1]
	111(<1)[1]	158(<1)[5]	387(0)[6]
			385(4)[0]
			377(3)[0]
			373(0)[5]
			358(4)[0]
			333(0)[1]
			332(4)[0]
			298(0)[49]
			296(0)[<1]
			270(5)[0]
			251(3)[0]
			245(0)[22]
			195(0)[4]
			192(<1)[0]
			155(<1)[0]
			115(<1)[0]
			84(0)[4]
			81(0)[<1]
			80(<1)[0]
			69(0)[<1]

[a] Values in parentheses and square brackets denote calculated Raman intensities ($Å^4$ amu^{-1}) and infrared intensities (km mol^{-1}), respectively. [b] The PBE1PBE/aug-ccpVDZ (Xe)-Def2-SVP (F, O, Cr) level of theory was used. [c] The uPBE1PBE/aug-ccpVDZ (Xe)-Def2-SVP (F, O, Cr) level of theory was used. [d] The Cr···Cr distance was fixed at the value calculated for the $[XeF_5]_2[Cr_2O_2F_8]\cdot 2XeOF_4$ ion pair (3.43 Å).

APPENDIX 7

CHAPTER 10 Supporting Information

Syntheses and Structural Characterizations of $[Cr_2O_4F_6]^{2-}$ and $[CrO_2F_4]^{2-}$ Salts

Table A7.1. Experimental and calculated (C_{2h}) geometric parameters for $[XeF_5]_2[Cr_2O_4F_6]$ (**1,1′**)

	exptl (1)	**calcd (1′)**		**exptl (1)**	**calcd (1′)**
Bond Lengths and Contacts (Å)					
Cr(1)−O(1)	1.585(5)	1.520	Xe(1)−F(5)	1.876(5)	1.878
Cr(1)−O(2)	1.590(5)	1.520	Xe(1)−F(6)	1.868(5)	1.880
Cr(1)−F(1)	2.082(5)	2.135	Xe(1)−F(7)	1.864(4)	1.880
Cr(1)−F(1A)	2.065(4)	2.135	Xe(1)−F(8)	1.820(3)	1.850
Cr(1)−F(2)	1.861(4)	1.831	Xe(1)---F(3)	2.410(5)	2.421
Cr(1)−F(3)	1.870(4)	1.831	Xe(1)---F(2A)	2.430(5)	2.421
Xe(1)−F(4)	1.874(5)	1.878	Xe(1)---F(1A)	2.762(3)	2.522
Bond Angles (deg)					
O(1)−Cr(1)−O(2)	104.5(2)	105.5	F(2)−Cr(1)−F(3)	163.23(15)	156.4
O(1)−Cr(1)−F(1)	163.4(2)	160.9	Cr(1)−F(1)−Cr(1A)	108.71(14)	110.0
O(1)−Cr(1)−F(1A)	93.4(2)	92.7	Cr(1)−F(3)---Xe(1)	120.5(2)	117.0
O(1)−Cr(1)−F(2)	94.2(2)	95.6	Cr(1A)−F(2A)---Xe(1)	120.1(2)	117.0
O(1)−Cr(1)−F(3)	96.0(2)	98.7	F(4)−Xe(1)−F(5)	90.53(16)	90.9
O(2)−Cr(1)−F(1)	91.5(3)	92.7	F(4)−Xe(1)−F(6)	158.6(2)	157.4
O(2)−Cr(1)−F(1A)	161.2(3)	160.9	F(4)−Xe(1)−F(7)	88.4(2)	88.0
O(2)−Cr(1)−F(2)	97.1(2)	98.7	F(4)−Xe(1)−F(8)	79.1(2)	78.6
O(2)−Cr(1)−F(3)	93.2(2)	95.6	F(5)−Xe(1)−F(6)	88.8(2)	88.0
F(1)−Cr(1)−F(1A)	71.29(14)	70.0	F(5)−Xe(1)−F(7)	158.2(2)	157.4
F(1)−Cr(1)−F(2)	79.18(18)	75.5	F(5)−Xe(1)−F(8)	79.1(2)	78.6
F(1)−Cr(1)−F(3)	87.36(18)	85.1	F(6)−Xe(1)−F(7)	84.41(16)	84.6
F(1A)−Cr(1)−F(2)	87.31(18)	85.1	F(6)−Xe(1)−F(8)	79.8(2)	79.1
F(1A)−Cr(1)−F(3)	78.85(18)	75.5	F(7)−Xe(1)−F(8)	79.4(2)	79.1

[a] The PBE1PBE/Def2-SVP level of theory was used.

Table A7.2. Experimental and calculated (C_{2h}) geometric parameters for $[XeF_5]_2[Cr_2O_4F_6]\cdot 4HF$ (**2,2′**)

	exptl (2)	**calcd (2′)**		**exptl (2)**	**calcd (2′)**
Bond Lengths and Contacts (Å)					
Cr(1)−O(1)	1.5765(11)	1.5202	F(10)···F(1)	2.4774(15)	2.4090
Cr(1)−O(2)	1.5822(11)	1.5202	Xe(1)−F(4)	1.8564(10)	1.8774
Cr(1)−F(1)	2.1146(9)	2.1501	Xe(1)−F(5)	1.8557(9)	1.8774
Cr(1)−F(1A)	2.1314(9)	2.1501	Xe(1)−F(6)	1.8505(10)	1.8699
Cr(1)−F(2)	1.8509(9)	1.8180	Xe(1)−F(7)	1.8562(9)	1.8699
Cr(1)−F(3)	1.8451(9)	1.8180	Xe(1)−F(8)	1.8200(10)	1.8489
F(9)−H(9)	0.77(4)	0.9814	Xe(1)---F(3)	2.4795(9)	2.4798
F(9)···F(10)	2.5431(17)	2.4025	Xe(1)---F(2A)	2.4813(9)	2.4798
F(10)−H(10)	0.73(11)	0.9732	Xe(1)---F(9)$_H$	2.7868(11)	2.4771
			Xe(1)---F(1)	3.1624(9)	3.1502
Bond Angles (deg)					
O(1)−Cr(1)−O(2)	104.82(6)	105.74	F(2)−Cr(1)−F(3)	159.29(4)	154.37
O(1)−Cr(1)−F(1)	161.65(5)	161.71	Cr(1)−F(1)−Cr(1A)	110.24(5)	110.70
O(1)−Cr(1)−F(1A)	91.40(5)	92.50	Cr(1)−F(3)---Xe(1)	129.66(5)	132.02
O(1)−Cr(1)−F(2)	95.12(5)	96.94	Cr(1A)−F(2A)---Xe(1)	130.01(5)	132.02
O(1)−Cr(1)−F(3)	97.66(5)	98.45	H(9)−F(9)---Xe(1)	112.43(5)	116.90
O(2)−Cr(1)−F(1)	93.43(5)	92.50	F(4)−Xe(1)−F(5)	85.32(5)	85.75
O(2)−Cr(1)−F(1A)	163.75(5)	161.71	F(4)−Xe(1)−F(6)	158.24(5)	156.89
O(2)−Cr(1)−F(2)	96.67(5)	98.45	F(4)−Xe(1)−F(7)	88.00(5)	86.56
O(2)−Cr(1)−F(3)	95.73(5)	96.94	F(4)−Xe(1)−F(8)	79.29(5)	78.77
F(1)−Cr(1)−F(1A)	70.39(4)	69.30	F(5)−Xe(1)−F(6)	87.25(5)	86.56
F(1)−Cr(1)−F(2)	80.67(4)	78.70	F(5)−Xe(1)−F(7)	158.48(5)	156.89
F(1)−Cr(1)−F(3)	82.09(4)	80.27	F(5)−Xe(1)−F(8)	79.59(5)	78.77
F(1A)−Cr(1)−F(2)	82.59(4)	80.27	F(6)−Xe(1)−F(7)	91.52(5)	92.11
F(1A)−Cr(1)−F(3)	80.87(4)	78.70	F(6)−Xe(1)−F(8)	79.26(5)	78.37
			F(7)−Xe(1)−F(8)	79.07(5)	78.37

[a] The PBE1PBE/Def2-SVP level of theory was used.

Table A7.3. Experimental and calculated (C_{2h}) geometric parameters for $[XeF_5]_2[Cr_2O_4F_6]\cdot 2XeOF_4$ (**3,3′**)

	exptl (3)	**calcd (3′)**		**exptl (3)**	**calcd (3′)**		**exptl (3)**	**calcd (3′)**
Bond Lengths and Contacts (Å)								
Cr(1)−O(1)	1.5822(10)	1.5185	Xe(1)−F(6)	1.8512(9)	1.8679	Xe(2)−O(3)	1.7068(11)	1.7066
Cr(1)−O(2)	1.5758(10)	1.5185	Xe(1)−F(7)	1.8493(9)	1.8679	Xe(2)−F(9)	1.9024(10)	1.9130
Cr(1)−F(1)	2.0660(8)	2.1499	Xe(1)−F(8)	1.8186(9)	1.8415	Xe(2)−F(10)	1.9202(9)	1.9355
Cr(1)−F(1A)	2.1337(8)	2.1499	Xe(1)---F(2A)	2.4790(9)	2.4642	Xe(2)−F(11)	1.9070(9)	1.9130
Cr(1)−F(2)	1.8488(8)	1.8281	Xe(1)---F(3)	2.4842(8)	2.4642	Xe(2)−F(12)	1.9008(9)	1.9093
Cr(1)−F(3)	1.8668(8)	1.8281	Xe(1)---F(1)	2.8592(9)	2.6655	Xe(2)---F(1A)	2.9965(8)	2.9894
Xe(1)−F(4)	1.8542(9)	1.8712	Xe(1)---F(10)	3.3940(11)	3.3951	Xe(2)---F(3)	3.0036(9)	3.1128
Xe(1)−F(5)	1.8527(10)	1.8712				Xe(2)---F(2A)	3.2685(9)	3.1128
Bond Angles (deg)								
O(1)−Cr(1)−O(2)	104.69(6)	105.64	F(1A)−Cr(1)−F(3)	83.16(3)	82.26	F(5)−Xe(1)−F(8)	79.53(5)	79.27
O(1)−Cr(1)−F(1)	160.23(5)	161.59	F(2)−Cr(1)−F(3)	159.47(4)	154.15	F(6)−Xe(2)−F(7)	87.22(5)	86.36
O(1)−Cr(1)−F(1A)	90.00(5)	92.44	Cr(1)−F(1)−Cr(1A)	109.31(4)	110.23	F(6)−Xe(2)−F(8)	79.85(5)	79.66
O(1)−Cr(1)−F(2)	97.00(5)	96.90	Cr(1)−F(3)---Xe(1)	110.68(3)	119.11	F(7)−Xe(2)−F(8)	80.05(5)	79.66
O(1)−Cr(1)−F(3)	94.26(5)	98.64	Cr(1A)−F(2A)---Xe(1)	121.20(4)	119.11	O(3)−Xe(2)−F(9)	90.08(6)	90.97
O(2)−Cr(1)−F(1)	94.75(5)	92.44	Cr(1)−F(1)---Xe(1)	99.49(3)	100.41	O(3)−Xe(2)−F(10)	90.24(6)	90.76
O(2)−Cr(1)−F(1A)	165.26(5)	161.59	Cr(1)−F(3)---Xe(2)	106.65(3)	108.51	O(3)−Xe(2)−F(11)	90.23(6)	90.97
O(2)−Cr(1)−F(2)	96.93(5)	98.64	F(4)−Xe(1)−F(5)	88.80(5)	90.19	O(4)−Xe(2)−F(12)	91.19(6)	91.78
O(2)−Cr(1)−F(3)	96.73(5)	96.90	F(4)−Xe(1)−F(6)	159.46(4)	158.83	F(9)−Xe(2)−F(10)	90.18(5)	91.13
F(1)−Cr(1)−F(1A)	70.69(4)	69.77	F(4)−Xe(1)−F(7)	88.45(5)	87.88	F(9)−Xe(2)−F(11)	178.38(5)	177.00
F(1)−Cr(1)−F(2)	84.03(4)	82.26	F(4)−Xe(1)−F(8)	79.63(5)	79.27	F(9)−Xe(2)−F(12)	90.09(5)	88.82
F(1)−Cr(1)−F(3)	79.63(3)	76.56	F(5)−Xe(1)−F(6)	88.29(5)	87.88	F(10)−Xe(2)−F(11)	91.41(5)	91.13
F(1A)−Cr(1)−F(2)	79.74(3)	76.56	F(5)−Xe(1)−F(7)	159.55(4)	158.83	F(10)−Xe(2)−F(12)	178.54(5)	177.46
						F(11)−Xe(2)−F(12)	88.31(5)	88.82

[a] The PBE1PBE/Def2-SVP level of theory was used.

Table A7.4. Experimental geometric parameters for $[XeF_5][Xe_2F_{11}][CrO_2F_4]$ (**4**)

Bond lengths (Å)					
Cr(1)−O(1)	1.504(16)	Xe(1)−F(9)	1.787(13)	Xe(2)---F(1)	2.417(11)
Cr(1)−O(2)	1.595(16)	Xe(1)---F(1)	2.414(12)	Xe(2)---F(4)	2.779(12)
Cr(1)−F(1)	2.105(12)	Xe(1)---F(2)	2.447(12)	Xe(3)−F(15)	1.914(13)
Cr(1)−F(2)	2.081(13)	Xe(1)---F(3)	2.687(14)	Xe(3)−F(16)	1.835(12)
Cr(1)−F(3)	1.812(14)	Xe(2)−F(10)	1.795(14)	Xe(3)−F(17)	1.845(12)
Cr(1)−F(4)	1.838(13)	Xe(2)−F(11)	1.909(14)	Xe(3)−F(18)	1.864(13)
Xe(1)−F(5)	1.941(16)	Xe(2)−F(12)	1.899(14)	Xe(3)−F(19)	1.826(12)
Xe(1)−F(6)	1.865(14)	Xe(2)−F(13)	1.788(15)	Xe(3)---F(20)	2.266(12)
Xe(1)−F(7)	1.776(16)	Xe(2)−F(14)	1.749(14)	Xe(3)---F(2)	2.544(13)
Xe(1)−F(8)	1.857(16)	Xe(2)---F(20)	2.368(13)	Xe(3)---F(4)	2.830(13)

Bond angles (º)					
O(1)–Cr(1)–O(2)	101.2(11)	F(7)–Xe(1)---F(2)	76.0(6)	F(13)–Xe(2)–F(14)	79.9(8)
O(1)–Cr(1)–F(1)	94.3(9)	F(7)–Xe(1)---F(3)	129.2(6)	F(14)–Xe(2)---F(20)	139.6(6)
O(1)–Cr(1)–F(2)	169.8(9)	F(7)–Xe(1)–F(8)	89.3(8)	F(14)–Xe(2)---F(1)	148.1(6)
O(1)–Cr(1)–F(3)	103.1(10)	F(7)–Xe(1)–F(9)	79.0(7)	F(14)–Xe(2)---F(4)	137.4(6)
O(1)–Cr(1)–F(4)	97.4(9)	F(8)–Xe(1)---F(1)	127.8(6)	F(15)–Xe(3)---F(20)	129.5(5)
O(2)–Cr(1)–F(1)	164.5(8)	F(8)–Xe(1)---F(2)	81.2(6)	F(15)–Xe(3)---F(2)	74.4(5)
O(2)–Cr(1)–F(2)	89.0(8)	F(8)–Xe(1)---F(3)	70.8(7)	F(15)–Xe(3)---F(4)	68.4(5)
O(2)–Cr(1)–F(3)	98.8(8)	F(8)–Xe(1)–F(9)	75.7(8)	F(15)–Xe(3)–F(16)	88.4(5)
O(2)–Cr(1)–F(4)	98.2(8)	F(9)–Xe(1)---F(1)	149.9(6)	F(15)–Xe(3)–F(17)	155.0(5)
F(1)–Cr(1)–F(2)	75.5(5)	F(9)–Xe(1)---F(2)	146.0(6)	F(15)–Xe(3)–F(18)	87.7(6)
F(1)–Cr(1)–F(3)	78.0(5)	F(9)–Xe(1)---F(3)	134.5(6)	F(15)–Xe(3)–F(19)	79.1(6)
F(1)–Cr(1)–F(4)	79.1(5)	F(10)–Xe(2)---F(20)	130.2(5)	F(16)–Xe(3)---F(20)	83.4(5)
F(2)–Cr(1)–F(3)	75.6(6)	F(10)–Xe(2)---F(1)	81.5(6)	F(16)–Xe(3)---F(2)	128.9(5)
F(2)–Cr(1)–F(4)	80.4(6)	F(10)–Xe(2)---F(4)	68.9(5)	F(16)–Xe(3)---F(4)	72.8(5)
F(3)–Cr(1)–F(4)	150.2(6)	F(10)–Xe(2)–F(11)	88.0(7)	F(16)–Xe(3)–F(17)	88.5(5)
F(5)–Xe(1)---F(1)	81.1(6)	F(10)–Xe(2)–F(12)	156.1(7)	F(16)–Xe(3)–F(18)	155.1(6)
F(5)–Xe(1)---F(2)	124.3(6)	F(10)–Xe(2)–F(13)	91.3(8)	F(16)–Xe(3)–F(19)	78.5(6)
F(5)–Xe(1)---F(3)	69.6(6)	F(10)–Xe(2)–F(14)	81.6(7)	F(17)–Xe(3)---F(20)	74.7(5)
F(5)–Xe(1)–F(6)	86.4(7)	F(11)–Xe(2)---F(20)	78.2(6)	F(17)–Xe(3)---F(2)	125.5(5)
F(5)–Xe(1)–F(7)	159.2(7)	F(11)–Xe(2)---F(1)	127.1(5)	F(17)–Xe(3)---F(4)	133.7(5)
F(5)–Xe(1)–F(8)	89.5(7)	F(11)–Xe(2)---F(4)	70.3(5)	F(17)–Xe(3)–F(18)	84.8(6)
F(5)–Xe(1)–F(9)	80.6(7)	F(11)–Xe(2)–F(12)	85.7(7)	F(17)–Xe(3)–F(19)	75.9(6)
F(6)–Xe(1)---F(1)	71.4(5)	F(11)–Xe(2)–F(13)	158.8(7)	F(18)–Xe(3)---F(20)	117.6(5)
F(6)–Xe(1)---F(2)	117.5(6)	F(11)–Xe(2)–F(14)	79.0(7)	F(18)–Xe(3)---F(2)	73.4(5)
F(6)–Xe(1)---F(3)	125.9(6)	F(12)–Xe(2)---F(20)	70.7(6)	F(18)–Xe(3)---F(4)	127.8(5)
F(6)–Xe(1)–F(7)	87.4(7)	F(12)–Xe(2)---F(1)	120.3(6)	F(18)–Xe(3)–F(19)	76.6(6)
F(6)–Xe(1)–F(8)	159.5(7)	F(12)–Xe(2)---F(4)	129.5(6)	F(19)–Xe(3)---F(20)	145.7(5)
F(6)–Xe(1)–F(9)	83.8(7)	F(12)–Xe(2)–F(13)	86.5(8)	F(19)–Xe(3)---F(2)	140.3(5)
F(7)–Xe(1)---F(1)	115.6(6)	F(12)–Xe(2)–F(14)	74.7(7)	F(19)–Xe(3)---F(4)	136.6(5)
		F(13)–Xe(2)---F(20)	117.5(7)		
		F(13)–Xe(2)---F(1)	73.7(6)		
		F(13)–Xe(2)---F(4)	128.8(6)		

continued…

Table A7.4. (continued) Experimental geometric parameters for $[XeF_5][Xe_2F_{11}][CrO_2F_4]$ (**4**)

Bond lengths (Å)					
Cr(2)−O(3)	1.560(16)	Xe(4)−F(29)	1.827(14)	Xe(5)---F(21)	2.419(11)
Cr(2)−O(4)	1.520(17)	Xe(4)---F(21)	2.453(12)	Xe(5)---F(24)	2.838(12)
Cr(2)−F(21)	2.178(12)	Xe(4)---F(22)	2.438(11)	Xe(6)−F(35)	1.833(15)
Cr(2)−F(22)	2.146(12)	Xe(4)---F(23)	2.695(15)	Xe(6)−F(36)	1.826(13)
Cr(2)−F(23)	1.834(14)	Xe(5)−F(30)	1.844(11)	Xe(6)−F(37)	1.868(13)
Cr(2)−F(24)	1.823(12)	Xe(5)−F(31)	1.844(11)	Xe(6)−F(38)	1.852(14)
Xe(4)−F(25)	1.856(16)	Xe(5)−F(32)	1.884(13)	Xe(6)−F(39)	1.876(14)
Xe(4)−F(26)	1.758(16)	Xe(5)−F(33)	1.906(11)	Xe(6)---F(40)	2.357(12)
Xe(4)−F(27)	1.810(16)	Xe(5)−F(34)	1.857(12)	Xe(6)---F(22)	2.502(11)
Xe(4)−F(28)	1.899(16)	Xe(5)---F(40)	2.296(12)	Xe(6)---F(24)	2.822(12)

Bond angles (°)					
O(3)–Cr(2)–O(4)	107.2(10)	F(27)–Xe(4)---F(22)	73.1(6)	F(33)–Xe(5)---F(24)	125.4(4)
O(3)–Cr(2)–F(21)	90.4(8)	F(27)–Xe(4)---F(23)	126.0(6)	F(33)–Xe(5)–F(34)	80.3(5)
O(3)–Cr(2)–F(22)	164.3(7)	F(27)–Xe(4)–F(28)	86.9(8)	F(34)–Xe(5)---F(40)	146.6(5)
O(3)–Cr(2)–F(23)	104.2(9)	F(27)–Xe(4)–F(29)	80.9(8)	F(34)–Xe(5)---F(21)	141.8(5)
O(3)–Cr(2)–F(24)	96.3(8)	F(28)–Xe(4)---F(21)	126.1(6)	F(34)–Xe(5)---F(24)	134.8(5)
O(4)–Cr(2)–F(21)	162.0(8)	F(28)–Xe(4)---F(22)	80.6(6)	F(35)–Xe(6)---F(40)	128.4(6)
O(4)–Cr(2)–F(22)	88.5(7)	F(28)–Xe(4)---F(23)	69.6(6)	F(35)–Xe(6)---F(22)	78.6(6)
O(4)–Cr(2)–F(23)	96.2(10)	F(28)–Xe(4)–F(29)	76.5(8)	F(35)–Xe(6)---F(24)	68.0(5)
O(4)–Cr(2)–F(24)	104.1(9)	F(29)–Xe(4)---F(21)	149.3(6)	F(35)–Xe(6)–F(36)	88.8(7)
F(21)–Cr(2)–F(22)	74.0(5)	F(29)–Xe(4)---F(22)	146.1(6)	F(35)–Xe(6)–F(37)	156.8(6)
F(21)–Cr(2)–F(23)	75.4(6)	F(29)–Xe(4)---F(23)	133.9(6)	F(35)–Xe(6)–F(38)	87.9(7)
F(21)–Cr(2)–F(24)	77.0(5)	F(30)–Xe(5)---F(40)	128.4(5)	F(35)–Xe(6)–F(39)	79.9(7)
F(22)–Cr(2)–F(23)	74.4(5)	F(30)–Xe(5)---F(21)	77.8(5)	F(36)–Xe(6)---F(40)	79.3(5)
F(22)–Cr(2)–F(24)	78.4(5)	F(30)–Xe(5)---F(24)	67.7(5)	F(36)–Xe(6)---F(22)	127.4(5)
F(23)–Cr(2)–F(24)	145.4(6)	F(30)–Xe(5)–F(31)	88.9(5)	F(36)–Xe(6)---F(24)	71.8(5)
F(25)–Xe(4)---F(21)	81.4(6)	F(30)–Xe(5)–F(32)	158.2(5)	F(36)–Xe(6)–F(37)	88.9(7)
F(25)–Xe(4)---F(22)	128.5(6)	F(30)–Xe(5)–F(33)	89.6(5)	F(36)–Xe(6)–F(38)	158.2(6)
F(25)–Xe(4)---F(23)	73.4(6)	F(30)–Xe(5)–F(34)	77.2(5)	F(36)–Xe(6)–F(39)	80.8(7)
F(25)–Xe(4)–F(26)	90.7(8)	F(31)–Xe(5)---F(40)	79.8(5)	F(37)–Xe(6)---F(40)	73.7(5)
F(25)–Xe(4)–F(27)	157.8(7)	F(31)–Xe(5)---F(21)	128.0(4)	F(37)–Xe(6)---F(22)	120.4(5)
F(25)–Xe(4)–F(28)	91.4(8)	F(31)–Xe(5)---F(24)	72.1(4)	F(37)–Xe(6)---F(24)	132.6(5)
F(25)–Xe(4)–F(29)	77.2(8)	F(31)–Xe(5)–F(32)	88.3(5)	F(37)–Xe(6)–F(38)	85.8(6)
F(26)–Xe(4)---F(21)	75.0(6)	F(31)–Xe(5)–F(33)	159.9(5)	F(37)–Xe(6)–F(39)	77.0(6)
F(26)–Xe(4)---F(22)	113.9(6)	F(31)–Xe(5)–F(34)	79.8(5)	F(38)–Xe(6)---F(40)	119.1(6)
F(26)–Xe(4)---F(23)	130.9(6)	F(32)–Xe(5)---F(40)	72.3(5)	F(38)–Xe(6)---F(22)	72.8(5)
F(26)–Xe(4)–F(27)	83.2(8)	F(32)–Xe(5)---F(21)	120.3(5)	F(38)–Xe(6)---F(24)	126.2(5)
F(26)–Xe(4)–F(28)	158.9(7)	F(32)–Xe(5)---F(24)	131.4(5)	F(38)–Xe(6)–F(39)	77.5(7)
F(26)–Xe(4)–F(29)	83.5(7)	F(32)–Xe(5)–F(33)	85.6(5)	F(39)–Xe(6)---F(40)	144.6(6)
F(27)–Xe(4)---F(21)	117.2(6)	F(32)–Xe(5)–F(34)	81.0(5)	F(39)–Xe(6)---F(22)	143.6(5)
		F(33)–Xe(5)---F(40)	116.3(5)	F(39)–Xe(6)---F(24)	137.5(6)
		F(33)–Xe(5)---F(21)	71.1(5)		

Table A7.5. Calculated geometric parameters for $[XeF_5][Xe_2F_{11}][CrO_2F_4]$ (**4′**) (C_s)

Bond lengths and contacts (Å)			
Cr(1)−O(1)	1.520	Xe(2)−F(11)	1.880
Cr(1)−O(2)	1.520	Xe(2)−F(12)	1.878
Cr(1)−F(1)	2.208	Xe(2)−F(13)	1.885
Cr(1)−F(2)	2.208	Xe(2)−F(14)	1.853
Cr(1)−F(3)	1.797	Xe(2)---F(20)	2.285
Cr(1)−F(4)	1.799	Xe(2)---F(1)	2.398
Xe(1)−F(5)	1.879	Xe(2)---F(4)	2.857
Xe(1)−F(6)	1.891	Xe(3)−F(15)	1.891
Xe(1)−F(7)	1.891	Xe(3)−F(16)	1.880
Xe(1)−F(8)	1.879	Xe(3)−F(17)	1.878
Xe(1)−F(9)	1.851	Xe(3)−F(18)	1.885
Xe(1)---F(1)	2.387	Xe(3)---F(19)	1.853
Xe(1)---F(2)	2.387	Xe(3)---F(2)	2.398
Xe(1)---F(3)	2.536	Xe(3)---F(4)	2.857
Xe(2)−F(10)	1.891	Xe(3)−F(20)	2.285

Bond angles (deg)			
O(1)−Cr(1)−O(2)	105.4	F(6)−Xe(1)−F(7)	84.1
O(1)−Cr(1)−F(1)	91.3	F(6)−Xe(1)−F(8)	157.4
O(1)−Cr(1)−F(2)	163.2	F(6)−Xe(1)−F(9)	78.8
O(1)−Cr(1)−F(3)	100.6	F(7)−Xe(1)−F(8)	88.0
O(1)−Cr(1)−F(4)	100.8	F(7)−Xe(1)−F(9)	78.8
O(2)−Cr(1)−F(1)	163.2	F(8)−Xe(1)−F(9)	78.8
O(2)−Cr(1)−F(2)	91.3	F(10)−Xe(2)−F(11)	88.6
O(2)−Cr(1)−F(3)	100.6	F(10)−Xe(2)−F(12)	157.3
O(2)−Cr(1)−F(4)	100.8	F(10)−Xe(2)−F(13)	89.5
F(1)−Cr(1)−F(2)	71.9	F(10)−Xe(2)−F(14)	78.6
F(1)−Cr(1)−F(3)	74.4	F(10)−Xe(2)---F(20)	128.3
F(1)−Cr(1)−F(4)	76.8	F(11)−Xe(2)−F(12)	89.0
F(2)−Cr(1)−F(3)	74.4	F(11)−Xe(2)−F(13)	158.7
F(2)−Cr(1)−F(4)	76.8	F(11)−Xe(2)−F(14)	79.2
F(3)−Cr(1)−F(4)	144.2	F(11)−Xe(2)---F(20)	79.8
Cr(1)−F(1)---Xe(1)	97.7	F(12)−Xe(2)−F(13)	84.6
Cr(1)−F(2)---Xe(1)	97.7	F(12)−Xe(2)−F(14)	78.8
Cr(1)−F(3)---Xe(1)	104.8	F(12)−Xe(2)---F(20)	73.3
F(5)−Xe(1)−F(6)	88.0	F(13)−Xe(2)−F(14)	79.6
F(5)−Xe(1)−F(7)	157.4	F(13)−Xe(2)---F(20)	117.4
F(5)−Xe(1)−F(8)	91.2	F(14)−Xe(2)---F(20)	145.1
F(5)−Xe(1)−F(9)	78.8		

continued…

Table A7.5. (continued…) Calculated geometric parameters for $[XeF_5][Xe_2F_{11}][CrO_2F_4]$ (**4′**) (C_s)

Bond angles (deg)			
F(15)−Xe(3)−F(16)	88.6	F(16)−Xe(3)---F(20)	79.8
F(15)−Xe(3)−F(17)	157.3	F(17)−Xe(3)−F(18)	84.6
F(15)−Xe(3)−F(18)	89.5	F(17)−Xe(3)−F(19)	78.8
F(15)−Xe(3)−F(19)	78.6	F(17)−Xe(3)---F(20)	73.3
F(15)−Xe(3)---F(20)	128.3	F(18)−Xe(3)−F(19)	79.6
F(16)−Xe(3)−F(17)	89.0	F(18)−Xe(3)---F(20)	117.4
F(16)−Xe(3)−F(18)	158.7	F(19)−Xe(3)---F(20)	145.1
F(16)−Xe(3)−F(19)	79.2		

[a] The PBE1PBE/Def2-SVP level of theory was used.

Table A7.6. Experimental[a] and calculated[b] vibrational frequencies, intensities, and assignments[c] for $[XeF_5]_2[Cr_2O_4F_6]$ (**1** and **1′**)

exptl[a]	calcd[b]	assgnts (C_{2h})[c,d]
940(57)	1182(51)[0]	$[\nu(Cr_1\text{-}O_1) + \nu(Cr_1\text{-}O_2)] + [\nu(Cr_{1A}\text{-}O_{1A}) + \nu(Cr_{1A}\text{-}O_{2A})]$
	1173(0)[192]	$[\nu(Cr_1\text{-}O_1) + \nu(Cr_1\text{-}O_2)] - [\nu(Cr_{1A}\text{-}O_{1A}) + \nu(Cr_{1A}\text{-}O_{2A})]$
	1165(0)[309]	$[\nu(Cr_1\text{-}O_1) - \nu(Cr_1\text{-}O_2)] - [\nu(Cr_{1A}\text{-}O_{1A}) - \nu(Cr_{1A}\text{-}O_{2A})]$
919(25)	1148(39)[0]	$[\nu(Cr_1\text{-}O_1) - \nu(Cr_1\text{-}O_2)] + [\nu(Cr_{1A}\text{-}O_{1A}) - \nu(Cr_{1A}\text{-}O_{2A})]$
	666(0)[220]	$[\nu(Xe_1\text{-}F_4) + \nu(Xe_1\text{-}F_5) + \nu(Xe_1\text{-}F_8)] - [\nu(Xe_{1A}\text{-}F_{4A}) + \nu(Xe_{1A}\text{-}F_{5A}) + \nu(Xe_{1A}\text{-}F_{8A})]$
	663(0)[433]	$[\nu(Xe_1\text{-}F_4) + \nu(Xe_1\text{-}F_7)] - [\nu(Xe_1\text{-}F_5) + \nu(Xe_1\text{-}F_6)] + [\nu(Xe_{1A}\text{-}F_{5A}) + \nu(Xe_{1A}\text{-}F_{6A})] - [\nu(Xe_{1A}\text{-}F_{4A}) + \nu(Xe_{1A}\text{-}F_{7A})]$
655(100)	661(135)[0]	$[\nu(Xe_1\text{-}F_8) + \nu(Xe_{1A}\text{-}F_{8A})]$
644(13)	661(9)[0]	$[\nu(Xe_1\text{-}F_4) + \nu(Xe_1\text{-}F_7)] - [\nu(Xe_1\text{-}F_5) + \nu(Xe_1\text{-}F_6)] + [\nu(Xe_{1A}\text{-}F_{4A}) + \nu(Xe_{1A}\text{-}F_{7A})] - [\nu(Xe_{1A}\text{-}F_{5A}) + \nu(Xe_{1A}\text{-}F_{6A})]$
628(11)	659(14)[0]	$[\nu(Xe_1\text{-}F_4) + \nu(Xe_1\text{-}F_5)] - [\nu(Xe_1\text{-}F_6) + \nu(Xe_1\text{-}F_7)] + [\nu(Xe_{1A}\text{-}F_{4A}) + \nu(Xe_{1A}\text{-}F_{5A})] - [\nu(Xe_{1A}\text{-}F_{6A}) + \nu(Xe_{1A}\text{-}F_{7A})]$
	657(0)[350]	$[\nu(Xe_1\text{-}F_6) + \nu(Xe_1\text{-}F_7)] - [\nu(Xe_1\text{-}F_4) + \nu(Xe_1\text{-}F_5)] + [\nu(Xe_{1A}\text{-}F_{4A}) + \nu(Xe_{1A}\text{-}F_{5A})] - [\nu(Xe_{1A}\text{-}F_{6A}) + \nu(Xe_{1A}\text{-}F_{7A})] + [\nu(Xe_1\text{-}F_8) - \nu(Xe_{1A}\text{-}F_{8A})]$
	611(0)[113]	$[\nu(Xe_1\text{-}F_4) + \nu(Xe_1\text{-}F_5) + \nu(Xe_1\text{-}F_6) + \nu(Xe_1\text{-}F_7)] + [\nu(Xe_{1A}\text{-}F_{8A}) - \nu(Xe_1\text{-}F_8)] - [\nu(Xe_{1A}\text{-}F_{4A}) + \nu(Xe_{1A}\text{-}F_{5A}) + \nu(Xe_{1A}\text{-}F_{6A}) + \nu(Xe_{1A}\text{-}F_{7A})]$
600(57)	608(22)[0]	$[\nu(Xe_1\text{-}F_4) + \nu(Xe_1\text{-}F_5) + \nu(Xe_1\text{-}F_6) + \nu(Xe_1\text{-}F_7)] + [\nu(Xe_{1A}\text{-}F_{4A}) + \nu(Xe_{1A}\text{-}F_{5A}) + \nu(Xe_{1A}\text{-}F_{6A}) + \nu(Xe_{1A}\text{-}F_{7A})] - [\nu(Xe_1\text{-}F_8) + \nu(Xe_{1A}\text{-}F_{8A})]$
	591(0)[<1]	$[\nu(Xe_1\text{-}F_4) + \nu(Xe_1\text{-}F_6)] - [\nu(Xe_1\text{-}F_5) + \nu(Xe_1\text{-}F_6)] + [\nu(Xe_{1A}\text{-}F_{5A}) + \nu(Xe_{1A}\text{-}F_{6A})] - [\nu(Xe_{1A}\text{-}F_{4A}) + \nu(Xe_{1A}\text{-}F_{6A})]$
584(37)	591(20)[0]	$[\nu(Xe_1\text{-}F_4) + \nu(Xe_1\text{-}F_6)] - [\nu(Xe_1\text{-}F_5) + \nu(Xe_1\text{-}F_7)] + [\nu(Xe_{1A}\text{-}F_{4A}) + \nu(Xe_1\text{-}F_{6A})] - [\nu(Xe_{1A}\text{-}F_{5A}) + \nu(Xe_{1A}\text{-}F_{7A})]$
	579(0)[125]	$[\nu(Cr_1\text{-}F_2) + \nu(Cr_1\text{-}F_3)] - [\nu(Cr_{1A}\text{-}F_{2A}) + \nu(Cr_{1A}\text{-}F_{3A})] + [\delta(O_1Cr_1O_2) - \delta(O_{1A}Cr_{1A}O_{2A})]_{small}$
534(31)	565(52)[0]	$[\nu(Cr_1\text{-}F_2) + \nu(Cr_1\text{-}F_3)] + [\nu(Cr_{1A}\text{-}F_{2A}) + \nu(Cr_{1A}\text{-}F_{3A})] + [\delta(O_1Cr_1O_2) + \delta(O_{1A}Cr_{1A}O_{2A})]_{small}$
	557(0)[530]	$[\nu(Cr_1\text{-}F_2) - \nu(Cr_1\text{-}F_3)] - [\nu(Cr_{1A}\text{-}F_{2A}) - \nu(Cr_{1A}\text{-}F_{3A})]$
520(5)	520(8)[0]	$[\nu(Cr_1\text{-}F_2) - \nu(Cr_1\text{-}F_3)] + [\nu(Cr_{1A}\text{-}F_{3A}) - \nu(Cr_1\text{-}F_{2A})]$
445(3)	481(4)[0]	$[\delta(O_1Cr_1O_2) + \delta(O_{1A}Cr_{1A}O_{2A})] + [\nu(Cr_1\text{-}F_2) + \nu(Cr_1\text{-}F_3)]_{small} + [\nu(Cr_{1A}\text{-}F_{2A}) + \nu(Cr_{1A}\text{-}F_{3A})]_{small}$
	478(0)[11]	$[\delta(O_1Cr_1O_2) - \delta(O_{1A}Cr_{1A}O_{2A})] - [\nu(Cr_1\text{-}F_2) + \nu(Cr_1\text{-}F_3)]_{small} - [\nu(Cr_{1A}\text{-}F_{2A}) + \nu(Cr_{1A}\text{-}F_{3A})]_{small}$

continued…

Table A7.6. (continued) Experimental[a] and calculated[b] vibrational frequencies, intensities, and assignments[c] for $[XeF_5]_2[Cr_2O_4F_6]$ (**1** and **1′**)

exptl[a]	calcd[b]	assgnts (C_{2h})[c,d]
408(sh)	410(2)[0]	$[\nu(Cr_1\text{-}F_1) + \nu(Cr_1\text{-}F_{1A})] + [\nu(Cr_{1A}\text{-}F_1) + \nu(Cr_{1A}\text{-}F_{1A})]$
	404(6)[0]	$[\delta(Xe_1F_5F_6F_8) + \delta(Xe_{1A}F_{5A}F_{6A}F_{8A})] + [\nu(Cr_1\text{-}F_1) - \nu(Cr_1\text{-}F_{1A})] - [\nu(Cr_{1A}\text{-}F_1) - \nu(Cr_{1A}\text{-}F_{1A})]$
404(11)	401(0)[25]	$[\delta(Xe_1F_6F_7F_8) - \delta(Xe_{1A}F_{6A}F_{7A}F_{8A})]$
	401(0)[16]	$[\delta(Xe_1F_5F_6F_8) - \delta(Xe_{1A}F_{5A}F_{6A}F_{8A})]$
	399(3)[0]	$[\delta(Xe_1F_6F_7F_8) + \delta(Xe_{1A}F_{6A}F_{7A}F_{8A})]$
	395(0)[134]	$[\nu(Xe_1\text{-}F_{1A}) + \nu(Xe_1\text{-}F_{2A}) + \nu(Xe_1\text{-}F_3)] - [\nu(Xe_{1A}\text{-}F_1) + \nu(Xe_{1A}\text{-}F_2) + \nu(Xe_{1A}\text{-}F_{3A})]$
401(sh)	390(1)[0]	$[\nu(Cr_1\text{-}F_1) - \nu(Cr_1\text{-}F_{1A})] + [\nu(Cr_{1A}\text{-}F_1) - \nu(Cr_{1A}\text{-}F_{1A})] - [\delta(Xe_1F_5F_6F_8) + \delta(Xe_{1A}F_{5A}F_{6A}F_{8A})]$
	374(0)[3]	$[\nu(Cr_1\text{-}F_1) + \nu(Cr_1\text{-}F_{1A})] - [\nu(Cr_{1A}\text{-}F_1) + \nu(Cr_{1A}\text{-}F_{1A})] + [\rho_t(F_2Cr_1F_3) + \rho_t(F_{2A}Cr_{1A}F_{3A})]$
356(5)	371(0)[21]	$[\rho_w(O_1Cr_1O_2) - \rho_w(O_{1A}Cr_{1A}O_{2A})] + [\rho_w(F_1Cr_1F_{1A}) + \rho_w(F_1Cr_{1A}F_{1A})]$
	368(3)[0]	$[\rho_t(F_1Cr_1F_{1A}) - \rho_t(F_1Cr_{1A}F_{1A})] + [\rho_t(O_1Cr_1O_2) + \rho_t(O_{1A}Cr_{1A}O_{2A})] + [\rho_t(F_2Cr_1F_3) + \rho_t(F_{2A}Cr_{1A}F_{3A})]_{small}$
	363(3)[0]	$[\rho_w(O_1Cr_1O_2) + \rho_w(O_{1A}Cr_{1A}O_{2A})] + [\nu(Cr_1\text{-}F_1) - \nu(Cr_1\text{-}F_{1A})] + [\nu(Cr_{1A}\text{-}F_1) - \nu(Cr_{1A}\text{-}F_{1A})]$
343(5)	353(0)[24]	$[\delta_{umb}(Xe_1F_{4\text{-}7}) - \delta_{umb}(Xe_{1A}F_{4A\text{-}7A})]$
	352(3)[0]	$\delta_{umb}(Xe_1F_{4\text{-}7}) + \delta_{umb}(Xe_{1A}F_{4A\text{-}7A})$
	330(0)[58]	$[\nu(Cr_1\text{-}F_1) + \nu(Cr_1\text{-}F_{1A})] - [\nu(Cr_{1A}\text{-}F_{1A}) + \nu(Cr_{1A}\text{-}F_1)] + [\rho_t(F_2Cr_1F_3) - \rho_t(F_{2A}Cr_{1A}F_{3A})]_{small}$
	330(0)[294]	$[\rho_r(O_1Cr_1O_2) - \rho_r(O_{1A}Cr_{1A}O_{2A})] + [\rho_w(F_2Cr_1F_3) - \rho_w(F_{2A}Cr_{1A}F_{3A})]$
296(11)	294(2)[0]	$[\delta(F_2Cr_1F_3) + \delta(F_{2A}Cr_{1A}F_{3A})]$
	287(0)[5]	$[\delta(F_4Xe_1F_7) + \delta(F_5Xe_1F_6)] + [\delta(F_{4A}Xe_{1A}F_{5A}) + \delta(F_{6A}Xe_{1A}F_{7A})]$
	286(0)[14]	$[\rho_t(O_1Cr_1O_2) - \rho_t(O_{1A}Cr_{1A}O_{2A})] + [\delta(F_2Cr_1F_3) - \delta(F_{2A}Cr_{1A}F_{3A}]$
274(5)	275(3)[0]	$[\rho_t(F_1Cr_1F_{1A}) + \rho_t(F_1Cr_{1A}F_{1A})] + [\delta(F_6Xe_1F_7) + \delta(F_{6A}Xe_{1A}F_{7A})] + [\delta(F_2Cr_1F_3) + \delta(F_{2A}Cr_{1A}F_{3A})]_{small}$
	267(<1)[0]	$[\rho_t(F_4Xe_1F_5) + \rho_t(F_6Xe_1F_7)] + [\rho_t(F_{4A}Xe_{1A}F_{5A}) + \rho_t(F_{6A}Xe_{1A}F_{7A})]$
242(1)	261(1)[0]	$[\rho_t(O_1Cr_1O_2) + \rho_t(O_{1A}Cr_{1A}O_{2A})] - [\rho_t(F_1Cr_1F_{1A}) + \rho_t(F_1Cr_{1A}F_{1A})]$
	258(0)[<1]	$[\rho_t(F_4Xe_1F_5) + \rho_t(F_6Xe_1F_7)] - [\rho_t(F_{6A}Xe_{1A}F_{7A}) + \rho_t(F_{4A}Xe_{1A}F_{5A})]$
226(4)	231(<1)[0]	$[\rho_w(F_2Cr_1F_3) + \rho_w(F_{2A}Cr_{1A}F_{3A})] + [\nu(Cr_1\text{-}F_1) - \nu(Cr_1\text{-}F_{1A})] - [\nu(Cr_{1A}\text{-}F_1) - \nu(Cr_{1A}\text{-}F_{1A})]$
	231(0)[19]	$[\nu(Cr_1\text{-}F_1) - \nu(Cr_1\text{-}F_{1A})] + [\nu(Cr_{1A}\text{-}F_1) - \nu(Cr_{1A}\text{-}F_{1A})] + [\rho_w(F_2Cr_1F_3) - \rho_w(F_{2A}Cr_{1A}F_{3A})]$
	225(<1)[0]	$[\rho_t(F_4Xe_1F_5) - \rho_t(F_6Xe_1F_7)] + [\rho_t(F_{4A}Xe_{1A}F_{5A}) - \rho_t(F_{6A}Xe_{1A}F_{7A})] + [\rho_w(F_2Cr_1F_3) + \rho_w(F_{2A}Cr_{1A}F_{3A})]$
	204(0)[<1]	$[\delta(F_4Xe_1F_7) - \delta(F_5Xe_1F_6)] - [\delta(F_{4A}Xe_{1A}F_{7A}) - \delta(F_{5A}Xe_{1A}F_{7A})]$
191(4)	197(1)[0]	$[\delta(F_4Xe_1F_7) - \delta(F_5Xe_1F_6)] + [\delta(F_{4A}Xe_{1A}F_{7A}) - \delta(F_{5A}Xe_{1A}F_{7A})] + [\rho_r(F_2Cr_1F_3) + \rho_r(F_{2A}Cr_{1A}F_{3A})]$

continued…

Table A7.6. (continued) Experimental[a] and calculated[b] vibrational frequencies, intensities, and assignments[c] for $[XeF_5]_2[Cr_2O_4F_6]$ (**1** and **1′**)

exptl.[a]	**calcd.**[b]	**assgnts (C_{2h})**[c,d]
184(1)	196(<1)[0]	deformation and lattice modes
	192(0)[37]	
	175(0)[86]	
178(1)	167(2)[0]	
148(5)	146(2)[0]	
	140(0)[<1]	
	136(0)[<1]	
136(2)	133(<1)[0]	
	129(0)[15]	
	116(0)[1]	
124(1)	115(<1)[0]	
115(4)	114(<1)[0]	
	114(0)[1]	
	73(0)[<1]	
	72(<1)[0]	
	54(<1)[0]	
	30(0)[<1]	
	29(0)[<1]	
	27(<1)[0]	

continued…

Table A7.6. (continued) [a] Frequencies are given in cm^{-1}. Values in parentheses denote relative Raman intensities. Abbreviations denote shoulder (sh). The Raman spectrum was recorded under frozen aHF solution at −150 °C using 1064-nm excitation on a mixture of solid $[XeF_5]_2[Cr_2O_4F_6]$ (**1**), $[XeF_5]_2[Cr_2O_4F_6]\cdot 4HF$ (**2**), and $[XeF_5]_2[Cr_2O_4F_6]\cdot 2XeOF_4$ (**3**), where **1** was the dominant species. Weak bands and shoulders assigned to **3** were observed at 951(2), 926(sh), 665(5), 611(sh), and 563(3) cm^{-1}. Bands of **3** also overlap with the following bands of **1**: 655(100), 600(57), and 534(31) cm^{-1}. A weak band assigned to **2** was observed at 613(5) cm^{-1}. Bands of **2** also overlap with the following bands of **1**: 940(57), 655(100), 644(13), 600(57), 584(37), and 534(31) cm^{-1}. [b] Values in parentheses and square brackets denote calculated Raman intensities ($Å^4$ amu^{-1}) and infrared intensities (km mol^{-1}), respectively. [c] Assignments are for the energy-minimized geometry of **1′** (C_{2h}) calculated at the PBE1PBE/Def2-SVP (F, O, Cr, Xe) level of theory. [d] Abbreviations denote stretch (ν), bend (δ), rock (ρ_r), twist (ρ_t), wag (ρ_w), umbrella (umb). The atom labeling scheme corresponds to that used in Figure 10.1.

Table A7.7. Experimental[a] and calculated[b] vibrational frequencies, intensities, and assignments[c] for $[XeF_5]_2[Cr_2O_4F_6]\cdot 4HF$ (**2** and **2′**)

exptl[a]	calcd[b]	assgnts (C_{2h})[c,d]
	3250(51)[0]	$[\nu(F_9\text{-}H_9) - \nu(F_{10}\text{-}H_{10})] + [\nu(F_{9A}\text{-}H_{9A}) - \nu(F_{10A}\text{-}H_{10A})]$
	3241(0)[2694]	$[\nu(F_9\text{-}H_9) - \nu(F_{10}\text{-}H_{10})] - [\nu(F_{9A}\text{-}H_{9A}) - \nu(F_{10A}\text{-}H_{10A})]$
	2896(133)[0]	$[\nu(F_9\text{-}H_9) + \nu(F_{10}\text{-}H_{10})] + [\nu(F_{9A}\text{-}H_{9A}) + \nu(F_{10A}\text{-}H_{10A})]$
	2895(0)[3373]	$[\nu(F_9\text{-}H_9) + \nu(F_{10}\text{-}H_{10})] - [\nu(F_{9A}\text{-}H_{9A}) + \nu(F_{10A}\text{-}H_{10A})]$
951(31)	1189(35)[0]	$[\delta(H_9F_{10}H_{10}) + \delta(H_{9A}F_{10A}H_{10A})] + [\nu(Cr_1\text{-}O_1) + \nu(Cr_1\text{-}O_2)] + [\nu(Cr_{1A}\text{-}O_{1A}) + \nu(Cr_{1A}\text{-}O_{2A})]$
	1175(0)[206]	$[\nu(Cr_1\text{-}O_1) + \nu(Cr_1\text{-}O_2)] - [\nu(Cr_{1A}\text{-}O_{1A}) + \nu(Cr_{1A}\text{-}O_{2A})]$
	1169(0)[685]	$[\delta(H_9F_{10}H_{10}) - \delta(H_{9A}F_{10A}H_{10A})] + [\nu(Cr_1\text{-}O_1) + \nu(Cr_1\text{-}O_2)] - [\nu(Cr_{1A}\text{-}O_{1A}) + \nu(Cr_{1A}\text{-}O_{2A})]$
	1165(0)[28]	$[\delta(H_9F_{10}H_{10}) - \delta(H_{9A}F_{10A}H_{10A})]$
933(13)	1164(22)[0]	$[\delta(H_9F_{10}H_{10}) + \delta(H_{9A}F_{10A}H_{10A})]$
912(7)	1153(32)[0]	$[\nu(Cr_1\text{-}O_1) - \nu(Cr_1\text{-}O_2)] + [\nu(Cr_{1A}\text{-}O_{1A}) - \nu(Cr_{1A}\text{-}O_{2A})]$
	958(0)[324]	$[\rho_w(H_9F_{10}H_{10}) - \rho_w(H_{9A}F_{10A}H_{10A})]$
	944(<1)[0]	$[\rho_w(H_9F_{10}H_{10}) + \rho_w(H_{9A}F_{10A}H_{10A})]$
	884(0)[155]	$[\rho_r(H_9F_{10}H_{10}) - \rho_r(H_{9A}F_{10A}H_{10A})]$
745(4)	883(1)[0]	$[\rho_r(H_9F_{10}H_{10}) + \rho_r(H_{9A}F_{10A}H_{10A})]$
	845(0)[127]	$[\rho_t(H_9F_{10}H_{10}) - \rho_t(H_{9A}F_{10A}H_{10A})]$
	844(<1)[0]	$[\rho_t(H_9F_{10}H_{10}) + \rho_t(H_{9A}F_{10A}H_{10A})]$
	668(0)[326]	$[\nu(Xe_1\text{-}F_5) + \nu(Xe_1\text{-}F_6)] - [\nu(Xe_1\text{-}F_4) + \nu(Xe_1\text{-}F_7)] - [\nu(Xe_{1A}\text{-}F_{5A}) + \nu(Xe_{1A}\text{-}F_{6A})] + [\nu(Xe_{1A}\text{-}F_{4A}) + \nu(Xe_{1A}\text{-}F_{7A})]$
671(sh)	668(9)[0]	$[\nu(Xe_1\text{-}F_5) + \nu(Xe_1\text{-}F_6)] - [\nu(Xe_1\text{-}F_4) + \nu(Xe_1\text{-}F_7)] + [\nu(Xe_{1A}\text{-}F_{5A}) + \nu(Xe_{1A}\text{-}F_{6A})] - [\nu(Xe_{1A}\text{-}F_{4A}) + \nu(Xe_{1A}\text{-}F_{7A})]$
	667(0)[99]	$[\nu(Xe_1\text{-}F_8) - \nu(Xe_{1A}\text{-}F_{8A})]$
659(100)	666(92)[0]	$[\nu(Xe_1\text{-}F_8) + \nu(Xe_{1A}\text{-}F_{8A})] + [\nu(Xe_1\text{-}F_6) + \nu(Xe_1\text{-}F_7)] + [\nu(Xe_{1A}\text{-}F_{6A}) + \nu(Xe_{1A}\text{-}F_{7A})]$
	663(0)[392]	$[\nu(Xe_1\text{-}F_4) + \nu(Xe_1\text{-}F_5)] - [\nu(Xe_1\text{-}F_6) + \nu(Xe_1\text{-}F_7)] - [\nu(Xe_{1A}\text{-}F_{4A}) + \nu(Xe_{1A}\text{-}F_{5A})] + [\nu(Xe_{1A}\text{-}F_{6A}) + \nu(Xe_{1A}\text{-}F_{7A})]$
646(19)	660(38)[0]	$[\nu(Xe_1\text{-}F_8) + \nu(Xe_{1A}\text{-}F_{8A})] + [\nu(Xe_1\text{-}F_4) + \nu(Xe_1\text{-}F_5)] + [\nu(Xe_{1A}\text{-}F_{4A}) + \nu(Xe_{1A}\text{-}F_{5A})]$
	615(0)[252]	$[\nu(Xe_1\text{-}F_{4\text{–}7}) - \nu(Xe_1\text{-}F_8)] - [\nu(Xe_{1A}\text{-}F_{4A\text{–}7A}) - \nu(Xe_{1A}\text{-}F_{8A})] + [\nu(Cr_1\text{-}F_2) - \nu(Cr_1\text{-}F_3)] - [\nu(Cr_{1A}\text{-}F_{2A}) - \nu(Cr_{1A}\text{-}F_{3A})]$
613(52)	611(14)[0]	$[\nu(Xe_1\text{-}F_{4\text{–}7}) - \nu(Xe_1\text{-}F_8)] + [\nu(Xe_{1A}\text{-}F_{4A\text{–}7A}) - \nu(Xe_{1A}\text{-}F_{8A})] + [\nu(Cr_1\text{-}F_2) + \nu(Cr_1\text{-}F_3)] + [\nu(Cr_{1A}\text{-}F_{2A}) + \nu(Cr_{1A}\text{-}F_{3A})]$
	596(0)[19]	$[\nu(Xe_1\text{-}F_4) + \nu(Xe_1\text{-}F_6)] - [\nu(Xe_1\text{-}F_5) + \nu(Xe_1\text{-}F_7)] - [\nu(Xe_{1A}\text{-}F_{4A}) + \nu(Xe_{1A}\text{-}F_{6A})] - [\nu(Xe_{1A}\text{-}F_{5A}) + \nu(Xe_{1A}\text{-}F_{7A})]$
599(84)	595(24)[0]	$[\nu(Xe_1\text{-}F_4) + \nu(Xe_1\text{-}F_6)] - [\nu(Xe_1\text{-}F_5) + \nu(Xe_1\text{-}F_7)] + [\nu(Xe_{1A}\text{-}F_{4A}) + \nu(Xe_{1A}\text{-}F_{6A})] - [\nu(Xe_{1A}\text{-}F_{5A}) + \nu(Xe_{1A}\text{-}F_{7A})]$

continued…

Table A7.7. (continued) Experimental[a] and calculated[b] vibrational frequencies, intensities, and assignments[c] for $[XeF_5]_2[Cr_2O_4F_6]\cdot 4HF$ (**2** and **2′**)

exptl[a]	calcd[b]	assgnts (C_{2h})[c,d]
	585(0)[129]	$[\nu(Cr_1\text{-}F_2) + \nu(Cr_1\text{-}F_3)] - [\nu(Cr_{1A}\text{-}F_{2A}) + \nu(Cr_{1A}\text{-}F_{3A})] + [\delta(O_1Cr_1O_2) - \delta(O_{1A}Cr_{1A}O_{2A})]_{small}$
585(25)	575(73)[0]	$[\nu(Cr_1\text{-}F_2) + \nu(Cr_1\text{-}F_3)] + [\nu(Cr_{1A}\text{-}F_{2A}) + \nu(Cr_{1A}\text{-}F_{3A})] + [\delta(O_1Cr_1O_2) + \delta(O_{1A}Cr_{1A}O_{2A})]_{small}$
	565(0)[664]	$[\nu(Cr_1\text{-}F_2) - \nu(Cr_1\text{-}F_3)] - [\nu(Cr_{1A}\text{-}F_{2A}) - \nu(Cr_{1A}\text{-}F_{3A})] + [\nu(Xe_1\text{-}F_{4\text{–}7}) - \nu(Xe_{1A}\text{-}F_{4A\text{–}7A})]_{small}$
540(39)	521(13)[0]	$[\nu(Cr_1\text{-}F_2) - \nu(Cr_1\text{-}F_3)] + [\nu(Cr_{1A}\text{-}F_{2A}) - \nu(Cr_{1A}\text{-}F_{3A})]$
439(4)	483(8)[0]	$[\delta(O_1Cr_1O_2) + \delta(O_{1A}Cr_{1A}O_{2A})] + [\nu(Cr_1\text{-}F_2) + \nu(Cr_1\text{-}F_3)]_{small} + [\nu(Cr_{1A}\text{-}F_{2A}) + \nu(Cr_{1A}\text{-}F_{3A})]_{small}$
	474(0)[13]	$[\delta(O_1Cr_1O_2) - \delta(O_{1A}Cr_{1A}O_{2A})] - [\nu(Cr_1\text{-}F_2) + \nu(Cr_1\text{-}F_3)]_{small} - [\nu(Cr_{1A}\text{-}F_{2A}) + \nu(Cr_{1A}\text{-}F_{3A})]_{small}$
433(sh)	466(2)[0]	$[\nu(F_1\text{-}H_{10}) + \nu(F_{1A}\text{-}H_{10A})] - [\nu(F_{10}\text{-}H_9) + \nu(F_{10A}\text{-}H_{9A})]$
	459(0)[45]	$[\nu(F_1\text{-}H_{10}) - \nu(F_{1A}\text{-}H_{10A})] - [\nu(F_{10}\text{-}H_9) - \nu(F_{10A}\text{-}H_{9A})]$
409(10)	410(3)[0]	$\delta(Xe_1F_5F_6F_8) + \delta(Xe_{1A}F_{5A}F_{6A}F_{8A})$
	410(0)[15]	$\delta(Xe_1F_5F_6F_8) - \delta(Xe_{1A}F_{5A}F_{6A}F_{8A})$
405(7)	407(2)[0]	$\delta(Xe_1F_6F_7F_8) + \delta(Xe_{1A}F_{6A}F_{7A}F_{8A})$
	405(0)[35]	$\delta(Xe_1F_6F_7F_8) - \delta(Xe_{1A}F_{6A}F_{7A}F_{8A})$
397(sh)	396(5)[0]	$[\nu(F_{10}\text{-}H_9) + \nu(F_{10A}\text{-}H_{9A})] + [\delta(Xe_1F_4F_5F_8) + \delta(Xe_{1A}F_{4A}F_{5A}F_{8A})] + [\nu(Cr_1\text{-}F_1) + \nu(Cr_1\text{-}F_{1A})]_{small} + [\nu(Cr_{1A}\text{-}F_1) + \nu(Cr_{1A}\text{-}F_{1A})]_{small}$
	382(0)[27]	$[\nu(F_{10}\text{-}H_9) + \nu(F_{10A}\text{-}H_{9A})] - [\rho_w(F_1Cr_1F_{1A}) - \rho_w(F_1Cr_{1A}F_{1A})] - [\rho_w(O_1Cr_1O_2) - \rho_w(O_{1A}Cr_{1A}O_{2A})]$
	378(0)[42]	$[\nu(F_{10}\text{-}H_9) + \nu(F_{10A}\text{-}H_{9A})] - [\rho_w(F_1Cr_1F_{1A}) - \rho_w(F_1Cr_{1A}F_{1A})] + [\rho_w(O_1Cr_1O_2) - \rho_w(O_{1A}Cr_{1A}O_{2A})]$
	373(2)[0]	$[\rho_w(O_1Cr_1O_2) + \rho_w(O_{1A}Cr_{1A}O_{2A})] + [\nu(Cr_1\text{-}F_1) - \nu(Cr_1\text{-}F_{1A})]_{small} + [\nu(Cr_{1A}\text{-}F_1) - \nu(Cr_{1A}\text{-}F_{1A})]_{small}$
339(5)	365(2)[0]	$[\delta_{umb}(Xe_1F_{4\text{–}7}) + \delta_{umb}(Xe_{1A}F_{4A\text{–}7A})] - [\rho_t(F_1Cr_1F_{1A}) - \rho_t(F_1Cr_{1A}F_{1A})]$
	362(3)[0]	$[\nu(Cr_1\text{-}F_1) - \nu(Cr_1\text{-}F_{1A})] + [\nu(Cr_{1A}\text{-}F_1) - \nu(Cr_{1A}\text{-}F_{1A})] + [\rho_t(O_1Cr_1O_2) + \rho_t(O_{1A}Cr_{1A}O_{2A})]_{small} + [\rho_t(F_2Cr_1F_3) + \rho_t(F_{2A}Cr_{1A}F_{3A})]_{small}$
331(2)	353(2)[0]	$[\delta_{umb}(Xe_1F_{4\text{–}7}) + \delta_{umb}(Xe_{1A}F_{4A\text{–}7A})] + [\rho_t(F_1Cr_1F_{1A}) - \rho_t(F_1Cr_{1A}F_{1A})]$
	353(0)[113]	$[\delta_{umb}(Xe_1F_{4\text{–}7}) - \delta_{umb}(Xe_{1A}F_{4A\text{–}7A})]$
	342(0)[<1]	$[\rho_t(O_1Cr_1O_2) - \rho_t(O_{1A}Cr_{1A}O_{2A})] + [\nu(Cr_1\text{-}F_1) + \nu(Cr_1\text{-}F_{1A})] - [\nu(Cr_{1A}\text{-}F_1) + \nu(Cr_{1A}\text{-}F_{1A})] + [\rho_t(F_3Xe_1F_{2A}) - \rho_t(F_2Xe_{1A}F_{3A})]$
	336(0)[172]	$[\rho_w(F_2Cr_1F_3) - \rho_w(F_{2A}Cr_{1A}F_{3A})] + [\rho_r(O_1Cr_1O_2) - \rho_r(O_{1A}Cr_{1A}O_{2A})]$
	327(0)[5]	$[\rho_t(O_1Cr_1O_2) - \rho_t(O_{1A}Cr_{1A}O_{2A})] - [\nu(Cr_1\text{-}F_1) + \nu(Cr_1\text{-}F_{1A})] - [\nu(Cr_{1A}\text{-}F_1) + \nu(Cr_{1A}\text{-}F_{1A})] + [\rho_t(F_3Xe_1F_{2A}) - \rho_t(F_2Xe_{1A}F_{3A})]$
304(6)	306(3)[0]	$[\rho_t(F_1Cr_1F_{1A}) - \rho_t(F_1Cr_{1A}F_{1A})] + [\rho_t(O_1Cr_1O_2) + \rho_r(O_{1A}Cr_{1A}O_{2A})]$
	291(0)[14]	$[\delta(F_4Xe_1F_5) + \delta(F_6Xe_1F_7)] - [\delta(F_{4A}Xe_{1A}F_{5A}) + \delta(F_{6A}Xe_{1A}F_{7A})]$
	288(<1)[0]	$[\delta(F_4Xe_1F_7) + \delta(F_5Xe_1F_6)] + [\delta(F_{4A}Xe_{1A}F_{7A}) + \delta(F_{5A}Xe_{1A}F_{6A})]$
	279(<1)[0]	$[\rho_t(F_4Xe_1F_5) + \rho_t(F_6Xe_1F_7)] + [\rho_t(F_{4A}Xe_{1A}F_{5A}) + \rho_t(F_{6A}Xe_{1A}F_{7A})]$
	270(0)[3]	$[\rho_t(F_4Xe_1F_5) + \rho_t(F_6Xe_1F_7)] - [\rho_t(F_{4A}Xe_{1A}F_{5A}) + \rho_t(F_{6A}Xe_{1A}F_{7A})]$
261(2)	265(2)[0]	$[\delta(F_2Cr_1F_3) + \delta(F_{2A}Cr_{1A}F_{3A})]$

continued…

Table A7.7. (continued) Experimental[a] and calculated[b] vibrational frequencies, intensities, and assignments[c] for $[XeF_5]_2[Cr_2O_4F_6]\cdot 4HF$ (**2** and **2′**)

exptl[a]	calcd[b]	assgnts (C_{2h})[c,d]
	265(0)[33]	$[\rho_r(F_9H_9F_{10}) - \rho_r(F_{9A}H_{9A}F_{10A})]$
	258(0)[28]	$[\delta(F_2Cr_1F_3) - \delta(F_{2A}Cr_{1A}F_{3A})]$
	241(0)[22]	$[\nu(Cr_1\text{-}F_1) - \nu(Cr_1\text{-}F_{1A})] + [\nu(Cr_{1A}\text{-}F_1) - \nu(Cr_{1A}\text{-}F_{1A})] - [\rho_r(F_1H_{10}F_{10}) - \rho_r(F_{1A}H_{10A}F_{10A})]$
244(1)	237(<1)[0]	$[\rho_w(F_2Cr_1F_3) + \rho_w(F_{2A}Cr_{1A}F_{3A})] + [\nu(Cr_1\text{-}F_2) - \nu(Cr_1\text{-}F_3)] - [\nu(Cr_{1A}\text{-}F_{2A}) - \nu(Cr_{1A}\text{-}F_{3A})]$
232(3)	223(<1)[0]	$[\delta(F_4Xe_1F_7) - \delta(F_5Xe_1F_6)] + [\delta(F_{4A}Xe_{1A}F_{7A}) - \delta(F_{5A}Xe_{1A}F_{6A})]$
	223(<1)[0]	$\nu(Xe_1\text{-}F_9) + \nu(Xe_{1A}\text{-}F_{9A})$
	217(0)[<1]	$[\delta(F_4Xe_1F_7) - \delta(F_5Xe_1F_6)] - [\delta(F_{4A}Xe_{1A}F_{7A}) - \delta(F_{5A}Xe_{1A}F_{6A})]$
210(2)	214(2)[0]	$[\delta(F_4Xe_1F_5) - \delta(F_6Xe_1F_7)] + [\delta(F_{4A}Xe_{1A}F_{5A}) - \delta(F_{6A}Xe_{1A}F_{7A})]$
	211(0)[<1]	$[\delta(F_4Xe_1F_5) - \delta(F_6Xe_1F_7)] - [\delta(F_{4A}Xe_{1A}F_{5A}) - \delta(F_{6A}Xe_{1A}F_{7A})]$
	203(0)[26]	
	202(<1)[0]	
187(3)	191(<1)[0]	
	180(0)[<1]	
172(1)	173(<1)[0]	
	161(0)[36]	
168(2)	156(<1)[0]	
	146(0)[1]	
	142(<1)[0]	Deformation and lattice modes
	140(0)[14]	
121(4)	134(<1)[0]	
	130(<1)[0]	
	130(0)[5]	
	108(0)[<1]	
	106(0)[2]	
114(3)	100(<1)[0]	
	95(<1)[0]	

continued…

Table A7.7. (continued) Experimental[a] and calculated[b] vibrational frequencies, intensities, and assignments[c] for $[XeF_5]_2[Cr_2O_4F_6]\cdot 4HF$ (**2** and **2′**)

calcd[b]	assgnts (C_{2h})[c,d]
94(0)[23]	deformation modes
71(0)[0]	
70(<1)[0]	
59(<1)[0]	
48(<1)[0]	
47(<1)[0]	
44(0)[<1]	
41(0)[<1]	
25(0)[<1]	

Table A7.7. (continued) [a] Frequencies are given in cm^{-1}. Values in parentheses denote relative Raman intensities. Abbreviations denote shoulder (sh). The Raman spectrum was recorded under frozen aHF solution at −150 °C using 1064-nm excitation on a mixture of solid $[XeF_5]_2[Cr_2O_4F_6]$ (**1**), $[XeF_5]_2[Cr_2O_4F_6]\cdot 4HF$ (**2**), and $[XeF_5]_2[Cr_2O_4F_6]\cdot 2XeOF_4$ (**3**), where **2** was dominant. Bands and shoulders assigned to **1** were observed at 941(24), 918(10), 628(5), 642(sh), 531(19), 520(sh), 444(sh), 225(sh), 191(2), and 148(2) cm^{-1}. Bands of **1** also overlap with the following bands of **2**: 646(19), 599(84), 585(25), and 405(7) cm^{-1}. Bands and shoulders assigned to **3** were observed at 926(7), 665(sh), 563(11), 531(19), 373(2), 365(2), and 238(2) cm^{-1}. Bands of **3** also overlap with the following bands of **2**: 951(31), 613(52), 599(84), 540(39), and 405(7) cm^{-1}. [b] Values in parentheses and square brackets denote calculated Raman intensities ($Å^4$ amu^{-1}) and infrared intensities (km mol^{-1}), respectively. [c] Assignments are for the energy-minimized geometry of **2′** (C_{2h}) calculated at the PBE1PBE/Def2-SVP (F, O, Cr, Xe) level of theory. [d] Abbreviations denote stretch (ν), bend (δ), rock (ρ_r), twist (ρ_t), wag (ρ_w), umbrella (umb). The atom labeling scheme corresponds to that used in Figure 10.2.

Table A7.8. Experimental[a] and calculated[b] vibrational frequencies, intensities, and assignments[c] for $[XeF_5]_2[Cr_2O_4F_6]\cdot 2XeOF_4$ (**3** and **3′**)

exptl[a]	calcd[b]	assgnts (C_{2h})[c,d]
951(50)	1185(44)[0]	$[\nu(Cr_1\text{-}O_1) + \nu(Cr_1\text{-}O_2)] + [\nu(Cr_{1A}\text{-}O_{1A}) + \nu(Cr_{1A}\text{-}O_{2A})]$
	1177(0)]157]	$[\nu(Cr_1\text{-}O_1) + \nu(Cr_1\text{-}O_2)] - [\nu(Cr_{1A}\text{-}O_{1A}) + \nu(Cr_{1A}\text{-}O_{2A})]$
	1168(0)[304]	$[\nu(Cr_1\text{-}O_1) - \nu(Cr_1\text{-}O_2)] - [\nu(Cr_{1A}\text{-}O_{1A}) - \nu(Cr_{1A}\text{-}O_{2A})]$
922(34)	1151(28)[0]	$[\nu(Cr_1\text{-}O_1) - \nu(Cr_1\text{-}O_2)] + [\nu(Cr_{1A}\text{-}O_{1A}) - \nu(Cr_{1A}\text{-}O_{2A})]$
926(49)	969(53)[0]	$\nu(Xe_2\text{-}O_3) + \nu(Xe_{2A}\text{-}O_{3A})$
	968(0)[91]	$\nu(Xe_2\text{-}O_3) - \nu(Xe_{2A}\text{-}O_{3A})$
	678(0)[513]	$[\nu(Xe_1\text{-}F_5) + \nu(Xe_1\text{-}F_6)] - [\nu(Xe_1\text{-}F_4) + \nu(Xe_1\text{-}F_7)] - [\nu(Xe_{1A}\text{-}F_{5A}) + \nu(Xe_{1A}\text{-}F_{6A})] + [\nu(Xe_{1A}\text{-}F_{4A}) + \nu(Xe_{1A}\text{-}F_{7A})]$
	676(0)[345]	$[\nu(Xe_1\text{-}F_4) + \nu(Xe_1\text{-}F_5)] - [\nu(Xe_1\text{-}F_6) + \nu(Xe_1\text{-}F_7)] - [\nu(Xe_{1A}\text{-}F_{4A}) + \nu(Xe_{1A}\text{-}F_{5A})] - [\nu(Xe_{1A}\text{-}F_{6A}) + \nu(Xe_{1A}\text{-}F_{7A})] + [\nu(Xe_1\text{-}F_8) - \nu(Xe_{1A}\text{-}F_{8A})]$
665(100)	670(111)[0]	$[\nu(Xe_1\text{-}F_8) + \nu(Xe_{1A}\text{-}F_{8A})]$
655(41)	675(22)[0]	$[\nu(Xe_1\text{-}F_6) + \nu(Xe_1\text{-}F_7)] - [\nu(Xe_1\text{-}F_4) + \nu(Xe_1\text{-}F_5)] + [\nu(Xe_{1A}\text{-}F_{6A}) + \nu(Xe_{1A}\text{-}F_{7A})] - [\nu(Xe_{1A}\text{-}F_{4A}) + \nu(Xe_{1A}\text{-}F_{5A})]$
	674(7)[0]	$[\nu(Xe_1\text{-}F_5) + \nu(Xe_1\text{-}F_6)] - [\nu(Xe_1\text{-}F_4) + \nu(Xe_1\text{-}F_7)] + [\nu(Xe_{1A}\text{-}F_{5A}) + \nu(Xe_{1A}\text{-}F_{6A})] - [\nu(Xe_{1A}\text{-}F_{4A}) + \nu(Xe_{1A}\text{-}F_{7A})]$
	670(0)[220]	$[\nu(Xe_1\text{-}F_6) + \nu(Xe_1\text{-}F_7)] - [\nu(Xe_{1A}\text{-}F_{6A}) + \nu(Xe_{1A}\text{-}F_{7A})] + [\nu(Xe_1\text{-}F_8) - \nu(Xe_{1A}\text{-}F_{8A})]$
	630(0)[277]	$[\nu(Xe_2\text{-}F_9) - \nu(Xe_2\text{-}F_{11})] - [\nu(Xe_{2A}\text{-}F_{9A}) - \nu(Xe_{2A}\text{-}F_{11A})]$
	629(0)[647]	$[\nu(Xe_2\text{-}F_{10}) - \nu(Xe_2\text{-}F_{12})] - [\nu(Xe_{2A}\text{-}F_{10A}) - \nu(Xe_{2A}\text{-}F_{12A})]$
	627(<1)[0]	$[\nu(Xe_2\text{-}F_9) - \nu(Xe_2\text{-}F_{11})] + [\nu(Xe_{2A}\text{-}F_{9A}) - \nu(Xe_{2A}\text{-}F_{11A})]$
611(87)	618(22)[0]	$[\nu(Xe_1\text{-}F_4) + \nu(Xe_1\text{-}F_5) + \nu(Xe_1\text{-}F_6) + \nu(Xe_1\text{-}F_7)] + [\nu(Xe_{1A}\text{-}F_{4A}) + \nu(Xe_{1A}\text{-}F_{5A}) + \nu(Xe_{1A}\text{-}F_{6A}) + \nu(Xe_{1A}\text{-}F_{7A})] - [\nu(Xe_1\text{-}F_8) + \nu(Xe_{1A}\text{-}F_{8A})]$
	617(0)[45]	$[\nu(Xe_1\text{-}F_4) + \nu(Xe_1\text{-}F_5) + \nu(Xe_1\text{-}F_6) + \nu(Xe_1\text{-}F_7)] - [\nu(Xe_{1A}\text{-}F_{4A}) + \nu(Xe_{1A}\text{-}F_{5A}) + \nu(Xe_{1A}\text{-}F_{6A}) + \nu(Xe_{1A}\text{-}F_{7A})] - [\nu(Xe_1\text{-}F_8) - \nu(Xe_{1A}\text{-}F_{8A})]$
602(65)	611(3)[0]	$[\nu(Xe_2\text{-}F_{10}) - \nu(Xe_2\text{-}F_{12})] + [\nu(Xe_{2A}\text{-}F_{10A}) - \nu(Xe_{2A}\text{-}F_{12A})]$
	603(0)[<1]	$[\nu(Xe_1\text{-}F_4) + \nu(Xe_1\text{-}F_6)] - [\nu(Xe_1\text{-}F_5) + \nu(Xe_1\text{-}F_7)] - [\nu(Xe_{1A}\text{-}F_{4A}) + \nu(Xe_{1A}\text{-}F_{6A})] + [\nu(Xe_{1A}\text{-}F_{5A}) + \nu(Xe_{1A}\text{-}F_{7A})]$
	603(17)[0]	$[\nu(Xe_1\text{-}F_4) + \nu(Xe_1\text{-}F_6)] - [\nu(Xe_1\text{-}F_5) + \nu(Xe_1\text{-}F_7)] + [\nu(Xe_{1A}\text{-}F_{4A}) + \nu(Xe_{1A}\text{-}F_{6A})] - [\nu(Xe_{1A}\text{-}F_{5A}) + \nu(Xe_{1A}\text{-}F_{7A})]$

continued…

Table A7.8. (continued) Experimental[a] and calculated[b] vibrational frequencies, intensities, and assignments[c] for $[XeF_5]_2[Cr_2O_4F_6]\cdot 2XeOF_4$ (**3** and **3′**)

exptl[a]	calcd[b]	assgnts (C_{2h})[c,d]
	577(0)[50]	$[\nu(Cr_1\text{-}F_2) + \nu(Cr_1\text{-}F_3)] - [\nu(Cr_{1A}\text{-}F_{2A}) + \nu(Cr_{1A}\text{-}F_{3A})] + [\delta(O_1Cr_1O_2) - \delta(O_{1A}Cr_{1A}O_{2A})]_{small}$
591(7)	576(12)[0]	$[\nu(Xe_2\text{-}F_{10}) + \nu(Xe_2\text{-}F_{12})] + [\nu(Xe_2\text{-}F_9) + \nu(Xe_2\text{-}F_{11})] + [\nu(Xe_{2A}\text{-}F_{10A}) + \nu(Xe_{2A}\text{-}F_{12A})] + [\nu(Xe_{2A}\text{-}F_{9A}) + \nu(Xe_{2A}\text{-}F_{11A})]$
	576(0)[26]	$[\nu(Xe_2\text{-}F_{10}) + \nu(Xe_2\text{-}F_{12})] + [\nu(Xe_2\text{-}F_9) + \nu(Xe_2\text{-}F_{11})] - [\nu(Xe_{2A}\text{-}F_{10A}) + \nu(Xe_{2A}\text{-}F_{12A})] + [\nu(Xe_{2A}\text{-}F_{9A}) + \nu(Xe_{2A}\text{-}F_{11A})]$
563(95)	569(65)[0]	$[\nu(Cr_1\text{-}F_2) + \nu(Cr_1\text{-}F_3)] + [\nu(Cr_{1A}\text{-}F_{2A}) + \nu(Cr_{1A}\text{-}F_{3A})] + [\delta(O_1Cr_1O_2) + \delta(O_{1A}Cr_{1A}O_{2A})]_{small}$
	558(0)[232]	$[\nu(Cr_1\text{-}F_2) - \nu(Cr_1\text{-}F_3)] - [\nu(Cr_{1A}\text{-}F_{2A}) - \nu(Cr_{1A}\text{-}F_{3A})]$
542(28)	528(4)[0]	$[\nu(Cr_1\text{-}F_2) - \nu(Cr_1\text{-}F_3)] + [\nu(Cr_{1A}\text{-}F_{2A}) - \nu(Cr_{1A}\text{-}F_{3A})]$
	535(0)[12]	$[\nu(Xe_2\text{-}F_{10}) + \nu(Xe_2\text{-}F_{12})] - [\nu(Xe_2\text{-}F_9) + \nu(Xe_2\text{-}F_{11})] - [\nu(Xe_{2A}\text{-}F_{10A}) + \nu(Xe_{2A}\text{-}F_{12A})] - [\nu(Xe_{2A}\text{-}F_{9A}) + \nu(Xe_{2A}\text{-}F_{11A})]$
531(69)	535(13)[0]	$[\nu(Xe_2\text{-}F_{10}) + \nu(Xe_2\text{-}F_{12})] - [\nu(Xe_2\text{-}F_9) + \nu(Xe_2\text{-}F_{11})] + [\nu(Xe_{2A}\text{-}F_{10A}) + \nu(Xe_{2A}\text{-}F_{12A})] - [\nu(Xe_{2A}\text{-}F_{9A}) + \nu(Xe_{2A}\text{-}F_{11A})]$
440(3)	481(4)[0]	$[\delta(O_1Cr_1O_2) + \delta(O_{1A}Cr_{1A}O_{2A})] + [\nu(Cr_1\text{-}F_2) + \nu(Cr_1\text{-}F_3)]_{small} + [\nu(Cr_{1A}\text{-}F_{2A}) + \nu(Cr_{1A}\text{-}F_{3A})]_{small}$
	478(0)[7]	$[\delta(O_1Cr_1O_2) - \delta(O_{1A}Cr_{1A}O_{2A})] - [\nu(Cr_1\text{-}F_2) + \nu(Cr_1\text{-}F_3)]_{small} - [\nu(Cr_{1A}\text{-}F_{2A}) + \nu(Cr_{1A}\text{-}F_{3A})]_{small}$
405(12)	401(6)[0]	$[\nu(Cr_1\text{-}F_1) + \nu(Cr_1\text{-}F_{1A})] + [\nu(Cr_{1A}\text{-}F_1) + \nu(Cr_{1A}\text{-}F_{1A})]$
	400(4)[0]	$\delta(Xe_1F_4F_7F_8) + \delta(Xe_{1A}F_{4A}F_{7A}F_{8A})$
	398(0)[13]	$\delta(Xe_1F_4F_7F_8) + \delta(Xe_{1A}F_{5A}F_{6A}F_{8A})$
	397(0)[26]	$\delta(Xe_1F_4F_5F_8) + \delta(Xe_{1A}F_{6A}F_{7A}F_{8A})$
398(3)	396(3)[0]	$\delta(Xe_1F_6F_7F_8) + \delta(Xe_{1A}F_{6A}F_{7A}F_{8A})$
373(15)	384(2)[0]	$[\nu(Cr_1\text{-}F_1) - \nu(Cr_1\text{-}F_{1A})] + [\nu(Cr_{1A}\text{-}F_1) - \nu(Cr_{1A}\text{-}F_{1A})] + [\rho_r(O_1Cr_1O_2) + \rho_r(O_{1A}Cr_{1A}O_{2A})]_{small}$
	383(0)[63]	$[\rho_w(O_1Cr_1O_2) - \rho_w(O_{1A}Cr_{1A}O_{2A})]$
	372(0)[10]	$[\delta(O_3Xe_2F_9) - \delta(O_3Xe_2F_{11})] - [\delta(O_{3A}Xe_{2A}F_{9A}) - \delta(O_{3A}Xe_{2A}F_{11A})]$
366(13)	372(5)[0]	$[\delta(O_3Xe_2F_9) - \delta(O_3Xe_2F_{11})] + [\delta(O_{3A}Xe_{2A}F_{9A}) - \delta(O_{3A}Xe_{2A}F_{11A})]$
	367(0)[27]	$[\delta(O_3Xe_2F_{10}) - \delta(O_3Xe_2F_{12})] - [\delta(O_{3A}Xe_{2A}F_{10A}) - \delta(O_{3A}Xe_{2A}F_{12A})]$

continued…

Table A7.8. (continued) Experimental[a] and calculated[b] vibrational frequencies, intensities, and assignments[c] for $[XeF_5]_2[Cr_2O_4F_6]\cdot 2XeOF_4$ (**3** and **3′**)

exptl[a]	calcd[b]	assgnts (C_{2h})[c,d]
353(5)	365(7)[0]	$[\delta(O_3Xe_2F_{10}) - \delta(O_3Xe_2F_{12})] + [\delta(O_{3A}Xe_{2A}F_{10A}) - \delta(O_{3A}Xe_{2A}F_{12A})]$
	364(6)[0]	$[\rho_t(F_2Cr_1F_3) - \rho_t(F_{2A}Cr_{1A}F_{3A})] + [\rho_t(O_1Cr_1O_2) - \rho_t(O_{1A}Cr_{1A}O_{2A})] + [\rho_t(F_{1A}Cr_1F_1) - \rho_t(F_{1A}Cr_{1A}F_1)]$
	364(0)[16]	$[\rho_w(F_1Cr_1F_{1A}) - \rho_w(F_1Cr_{1A}F_{1A})] + [\delta(O_3Xe_2F_{10}) - \delta(O_3Xe_2F_{12})] - [\delta(O_{3A}Xe_{2A}F_{10A}) - \delta(O_{3A}Xe_{2A}F_{12A})]$
	360(3)[0]	$[\rho_w(O_1Cr_1O_2) + \rho_w(O_{1A}Cr_{1A}O_{2A})] + [\nu(Cr_1\text{-}F_1) - \nu(Cr_1\text{-}F_{1A})]_{small} + [\nu(Cr_{1A}\text{-}F_1) - \nu(Cr_{1A}\text{-}F_{1A})]_{small}$
344(7)	358(0)[<1]	$[\nu(Cr_1\text{-}F_1) + \nu(Cr_1\text{-}F_{1A})] - [\nu(Cr_{1A}\text{-}F_1) + \nu(Cr_{1A}\text{-}F_{1A})]$
	350(1)[0]	$\delta_{umb}(Xe_1F_{4\text{-}7}) + \delta_{umb}(Xe_{1A}F_{4A\text{-}7A})$
	347(0)[44]	$[\delta_{umb}(Xe_1F_{4\text{-}7}) - \delta_{umb}(Xe_{1A}F_{4A\text{-}7A})]$
	331(0)[231]	$[\delta_{umb}(Xe_1F_{4\text{-}7}) - \delta_{umb}(Xe_{1A}F_{4A\text{-}7A})] + [\rho_r(O_1Cr_1O_2) - \rho_r(O_{1A}Cr_{1A}O_{2A})] + [\rho_w(F_2Cr_1F_3) - \rho_w(F_{2A}Cr_{1A}F_{3A})]$
	327(0)[23]	$[\nu(Cr_1\text{-}F_1) + \nu(Cr_1\text{-}F_{1A})] - [\nu(Cr_{1A}\text{-}F_1) + \nu(Cr_{1A}\text{-}F_{1A})] - [\rho_t(O_1Cr_1O_2) + \rho_t(O_{1A}Cr_{1A}O_{2A})] - [\rho_t(F_{3A}Xe_1F_2)] + \rho_t(F_{2A}Xe_{1A}F_3)]$
295(13)	300(2)[0]	$\delta_{umb}(Xe_2F_{9\text{-}12}) + \delta_{umb}(Xe_{2A}F_{9A\text{-}12A})$
	294(0)[173]	$\delta_{umb}(Xe_2F_{9\text{-}12}) - \delta_{umb}(Xe_{2A}F_{9A\text{-}12A})$
	292(2)[0]	$[\delta(F_4Xe_1F_7) + \delta(F_5Xe_1F_6)] + [\delta(F_{4A}Xe_{1A}F_{7A}) + \delta(F_{5A}Xe_{1A}F_{6A})] + [\delta(F_2Cr_1F_3) + \delta(F_{2A}Cr_{1A}F_{3A})]_{small}$
	286(0)[8]	$[\delta(F_4Xe_1F_7) + \delta(F_5Xe_1F_6)] + [\delta(F_{4A}Xe_{1A}F_{5A}) + \delta(F_{6A}Xe_{1A}F_{7A})]$
	281(0)[21]	$[\rho_t(O_1Cr_1O_2) - \rho_t(O_{1A}Cr_{1A}O_{2A})] - [\delta(F_2Cr_1F_3) - \delta(F_{2A}Cr_{1A}F_{3A})]$
275(7)	272(2)[0]	$[\delta(F_4Xe_1F_7) + \delta(F_5Xe_1F_6)] + [\delta(F_{4A}Xe_{1A}F_{7A}) + \delta(F_{5A}Xe_{1A}F_{6A})] + [\delta(F_2Cr_1F_3) + \delta(F_{2A}Cr_{1A}F_{3A})]$
	258(<1)[0]	$[\rho_t(F_4Xe_1F_5) - \rho_t(F_6Xe_1F_7)] + [\rho_t(F_{4A}Xe_{1A}F_{5A}) - \rho_t(F_{6A}Xe_{1A}F_{7A})]$
	252(0)[<1]	$[\rho_t(F_4Xe_1F_5) - \rho_t(F_6Xe_1F_7)] - [\rho_t(F_{4A}Xe_{1A}F_{5A}) - \rho_t(F_{6A}Xe_{1A}F_{7A})]$
239(7)	245(<1)[0]	$[\rho_t(O_1Cr_1O_2) + \rho_t(O_{1A}Cr_{1A}O_{2A})] - [\rho_t(F_1Cr_1F_{1A}) + \rho_t(F_1Cr_{1A}F_{1A})]$
	241(0)[24]	$[\nu(Cr_1\text{-}F_1) - \nu(Cr_1\text{-}F_{1A})] + [\nu(Cr_{1A}\text{-}F_1) - \nu(Cr_{1A}\text{-}F_{1A})]$
231(4)	239(<1)[0]	$[\nu(Cr_1\text{-}F_1) - \nu(Cr_1\text{-}F_{1A})] - [\nu(Cr_{1A}\text{-}F_1) - \nu(Cr_{1A}\text{-}F_{1A})] + [\rho_w(F_2Cr_1F_3) + \rho_w(F_{2A}Cr_{1A}F_{3A})]_{small}$
	231(0)[<1]	$[\delta(F_9Xe_2F_{12}) + \delta(F_{10}Xe_1F_{11})] + [\delta(F_{9A}Xe_{2A}F_{10A}) + \delta(F_{11A}Xe_{1A}F_{12A})]$
222(4)	228(2)[0]	$[\delta(F_9Xe_2F_{12}) + \delta(F_{10}Xe_2F_{11})] + [\delta(F_{9A}Xe_{2A}F_{12A}) + \delta(F_{10A}Xe_{2A}F_{11A})]$

continued…

Table A7.8. (continued) Experimental[a] and calculated[b] vibrational frequencies, intensities, and assignments[c] for $[XeF_5]_2[Cr_2O_4F_6]\cdot 2XeOF_4$ (**3** and **3′**)

exptl[a]	**calcd**[b]	**assgnts (C_{2h})**[c,d]
	223(<1)[0]	deformation and lattice modes
	209(0)[<1]	
	205(<1)[0]	
	204(0)[2]	
	199(<1)[0]	
	194(<1)[0]	
	191(0)[2]	
193(2)	174(2)[0]	
184(2)	171(0)[39]	
173(3)	164(<1)[0]	
161(1)	164(0)[<1]	
133(3)	163(<1)[0]	
123(4)	161(0)[20]	
109(3)	143(0)[2]	
	139(0)[<1]	
	137(0)[0]	
	125(0)[33]	
	122(0)[<1]	
	122(<1)[0]	
	117(<1)[0]	
	110(0)[2]	
	103(<1)[0]	

continued…

Table A7.8. (continued) Experimental[a] and calculated[b] vibrational frequencies, intensities, and assignments[c] for $[XeF_5]_2[Cr_2O_4F_6]\cdot 2XeOF_4$ (**3** and **3′**)

calcd[b]	assgnts (C_{2h})[c,d]
77(<1)[0]	deformation modes
77(0)[<1]	
74(0)[<1]	
70(<1)[0]	
68(0)[<1]	
67(<1)[0]	
66(<1)[0]	
62(0)[2]	
60(<1)[0]	
48(0)[<1]	
45(<1)[0]	
43(<1)[0]	
37(0)[<1]	
25(0)[1]	
22(<1)[0]	
17(0)[1]	
14(0)[<1]	
13(<1)[0]	

Table A7.8. [a] Frequencies are given in cm^{-1}. Values in parentheses denote relative Raman intensities. The Raman spectrum was recorded on a sample of solid **3** under frozen aHF solution at −150 °C using 1064-nm excitation. [b] Values in parentheses and square brackets denote calculated Raman intensities ($Å^4$ amu^{-1}) and infrared intensities (km mol^{-1}), respectively. [c] Assignments are for the energy-minimized geometry of **3′** (C_{2h}) calculated at the PBE1PBE/Def2-SVP (F, O, Cr, Xe) level of theory. [d] Abbreviations denote stretch (ν), bend (δ), rock (ρ_r), twist (ρ_t), wag (ρ_w), umbrella (umb). The atom labeling scheme corresponds to that used in Figure 10.3.

Table A7.9. Experimental[a] and calculated[b] vibrational frequencies, intensities, and assignments[c] for $[XeF_5][Xe_2F_{11}][CrO_2F_4]$ (**4** and **4′**)

exptl[a]	calcd[b]	assgnts (C_s) [c,d]
954(14)	1183(22)[108]	$\nu(Cr_1\text{-}O_1) + \nu(Cr_1\text{-}O_2)$
950(9)	1164(16)[166]	$\nu(Cr_1\text{-}O_1) - \nu(Cr_1\text{-}O_2)$
654(100)	667(117)[14]	$[\nu(Xe_2\text{-}F_{11}) + \nu(Xe_3\text{-}F_{16})] + [\nu(Xe_2\text{-}F_{14}) + \nu(Xe_3\text{-}F_{19})] + [\nu(Xe_1\text{-}F_5) + \nu(Xe_1\text{-}F_8)] + \nu(Xe_1\text{-}F_9)$
642(16)	669(18)[305]	$[\nu(Xe_2\text{-}F_{11}) + \nu(Xe_3\text{-}F_{16})] - [\nu(Xe_2\text{-}F_{13}) + \nu(Xe_3\text{-}F_{18})]$
629(8)	665(10)[500]	$[\nu(Xe_2\text{-}F_{10}) + \nu(Xe_3\text{-}F_{15})] - [\nu(Xe_2\text{-}F_{12}) + \nu(Xe_3\text{-}F_{17})] - [\nu(Xe_1\text{-}F_6) + \nu(Xe_1\text{-}F_7) + \nu(Xe_1\text{-}F_9)]$
620(10)	661(14)[207]	$[\nu(Xe_1\text{-}F_5) + \nu(Xe_1\text{-}F_6)] - [\nu(Xe_1\text{-}F_7) + \nu(Xe_1\text{-}F_8)] + [\nu(Xe_2\text{-}F_{13}) + \nu(Xe_3\text{-}F_{16})] - [\nu(Xe_2\text{-}F_{11}) + \nu(Xe_3\text{-}F_{18})]$
596(35)	653(24)[326]	$[\nu(Xe_1\text{-}F_5) + \nu(Xe_1\text{-}F_8)] + \nu(Xe_1\text{-}F_9) - [\nu(Xe_2\text{-}F_{14}) + \nu(Xe_3\text{-}F_{19})]$
	652(10)[13]	$[\nu(Xe_1\text{-}F_5) + \nu(Xe_1\text{-}F_8)] - [\nu(Xe_1\text{-}F_6) + \nu(Xe_1\text{-}F_7)] - \nu(Xe_1\text{-}F_9) + [\nu(Xe_2\text{-}F_{12}) + \nu(Xe_3\text{-}F_{17})] - [\nu(Xe_2\text{-}F_{10}) + \nu(Xe_3\text{-}F_{15})] + \nu(Cr_1\text{-}F_3)_{small}$
587(35)	651(20)[184]	$[\nu(Xe_2\text{-}F_{12}) + \nu(Xe_2\text{-}F_{14})] - [\nu(Xe_3\text{-}F_{17}) + \nu(Xe_3\text{-}F_{19})]$
	644(5)[102]	$[\nu(Xe_2\text{-}F_{10}) + \nu(Xe_2\text{-}F_{14}) + \nu(Xe_3\text{-}F_{17})] - [\nu(Xe_2\text{-}F_{12}) + \nu(Xe_3\text{-}F_{15}) + \nu(Xe_3\text{-}F_{19})]$
	634(<1)[1]	$[\nu(Xe_1\text{-}F_5) + \nu(Xe_1\text{-}F_6)] - [\nu(Xe_1\text{-}F_8) + \nu(Xe_1\text{-}F_7)] + [\nu(Xe_2\text{-}F_{11}) + \nu(Xe_3\text{-}F_{18})] - [\nu(Xe_2\text{-}F_{13}) + \nu(Xe_3\text{-}F_{16})]$
	606(5)[24]	$[\nu(Xe_1\text{-}F_5) + \nu(Xe_1\text{-}F_6) + \nu(Xe_1\text{-}F_7) + \nu(Xe_1\text{-}F_8)] - \nu(Xe_1\text{-}F_9) - \nu(Cr_1\text{-}F_3)$
	603(9)[24]	$[\nu(Xe_2\text{-}F_{10}) + \nu(Xe_2\text{-}F_{11}) + \nu(Xe_2\text{-}F_{12}) + \nu(Xe_2\text{-}F_{13})] + [\nu(Xe_3\text{-}F_{15}) + \nu(Xe_3\text{-}F_{16}) + \nu(Xe_3\text{-}F_{17}) + \nu(Xe_3\text{-}F_{18})] - [\nu(Xe_2\text{-}F_{14}) + \nu(Xe_3\text{-}F_{19})] - \nu(Cr_1\text{-}F_4)$
	601(2)[1]	$[\nu(Xe_2\text{-}F_{10}) + \nu(Xe_2\text{-}F_{11}) + \nu(Xe_2\text{-}F_{12}) + \nu(Xe_2\text{-}F_{13}) - \nu(Xe_2\text{-}F_{14})] - [\nu(Xe_3\text{-}F_{15}) + \nu(Xe_3\text{-}F_{16}) + \nu(Xe_3\text{-}F_{17}) + \nu(Xe_3\text{-}F_{18}) - \nu(Xe_3\text{-}F_{19})]$
579(20)	591(34)[57]	$[\nu(Cr_1\text{-}F_3) + \nu(Cr_1\text{-}F_4)] + [\nu(Xe_2\text{-}F_{11}) + \nu(Xe_2\text{-}F_{13})] + [\nu(Xe_3\text{-}F_{16}) + \nu(Xe_3\text{-}F_{18})]$

continued…

Table A7.9. (continued) Experimental[a] and calculated[b] vibrational frequencies, intensities, and assignments[c] for $[XeF_5][Xe_2F_{11}][CrO_2F_4]$ (**4** and **4′**)

exptl[a]	calcd[b]	assgnts (C_s) [c,d]
573(21)	587(4)[15]	$[\nu(Cr_1\text{-}F_3) - \nu(Cr_1\text{-}F_4)] + [\nu(Xe_1\text{-}F_6) + \nu(Xe_1\text{-}F_7)] - [\nu(Xe_2\text{-}F_{10}) + \nu(Xe_2\text{-}F_{12})] - [\nu(Xe_3\text{-}F_{15}) + \nu(Xe_3\text{-}F_{17})]$
	584(5)[<1]	$[\nu(Xe_2\text{-}F_{10}) + \nu(Xe_2\text{-}F_{12})] + [\nu(Xe_3\text{-}F_{16}) + \nu(Xe_3\text{-}F_{18})] - [\nu(Xe_3\text{-}F_{15}) + \nu(Xe_3\text{-}F_{17})] - [\nu(Xe_2\text{-}F_{11}) + \nu(Xe_2\text{-}F_{13})]$
	582(24)[5]	$[\nu(Xe_2\text{-}F_{10}) + \nu(Xe_2\text{-}F_{12})] + [\nu(Xe_3\text{-}F_{15}) + \nu(Xe_3\text{-}F_{17})] - [\nu(Xe_3\text{-}F_{15}) + \nu(Xe_3\text{-}F_{17})] - [\nu(Xe_2\text{-}F_{11}) + \nu(Xe_2\text{-}F_{13})] + [\nu(Xe_1\text{-}F_6) + \nu(Xe_1\text{-}F_7)] + \nu(Cr_1\text{-}F_3)$
557(8)	580(10)[3]	$[\nu(Xe_1\text{-}F_5) + \nu(Xe_1\text{-}F_7)] - [\nu(Xe_1\text{-}F_8) + \nu(Xe_1\text{-}F_6)]$
441(3)	483(3)[2]	$\delta(O_1Cr_1O_2)$
408(4)	401(2)[36]	$[\delta(F_{12}Xe_2F_{14}) - \delta(F_{10}Xe_2F_{14})] + [\delta(F_{15}Xe_3F_{19}) - \delta(F_{17}Xe_3F_{19})] + [\nu(Xe_2\text{-}F_{20}) - \nu(Xe_3\text{-}F_{20})]_{small}$
	400(3)[27]	$\delta(Xe_1F_9F_6F_7)$
	398(2)[10]	$[\delta(F_{12}Xe_2F_{14}) - \delta(F_{10}Xe_2F_{14})] - [\delta(F_{15}Xe_3F_{19}) - \delta(F_{17}Xe_3F_{19})] + \delta(Xe_1F_9F_5F_8)_{small}$
	397(1)[23]	$[\delta(Xe_1F_9F_5F_6) - \delta(Xe_1F_9F_7F_8)]$
	394(2)[142]	$\delta(Xe_1F_9F_5F_8) + [\delta(F_{12}Xe_2F_{14}) + \delta(F_{17}Xe_3F_{19})] + \delta(Cr_1F_1F_2F_3)$
373(3)	386(<1)[4]	$[\delta(F_{13}Xe_2F_{14}) - \delta(F_{11}Xe_2F_{14})] + [\delta(F_{16}Xe_3F_{19}) - \delta(F_{18}Xe_3F_{19})]$
	382(3)[45]	$[\delta(F_{11}Xe_2F_{14}) + \delta(F_{16}Xe_3F_{19})] + \delta(Cr_1F_1F_2F_3)$
358(3)	374(2)[201]	$[\rho_t(F_1Cr_1F_2) + \rho_t(F_3Cr_1F_4)] + [\nu(Xe_2\text{-}F_{20}) - \nu(Xe_3\text{-}F_{20})]$
	365(2)[<1]	$[\rho_w(O_1Cr_1O_2) + \rho_r(F_3Cr_1F_4)]$
334(2)	361(2)[19]	$\rho_r(O_1Cr_1O_2) + \rho_r(F_1Cr_1F_2) + \rho_w(F_3Cr_1F_4)$
323(2)	359(3)[44]	$\rho_w(O_1Cr_1O_2) + \rho_r(F_3Cr_1F_4) + [\delta_{umb}(Xe_2F_{10-13}) + \delta_{umb}(Xe_3F_{15-18}))$
303(2)	348(2)[<1]	$\delta(Cr_1F_1F_2F_4)$
	346(3)[121]	$\delta_{umb}(Xe_1F_{5\text{-}8}) + [\delta(F_3Cr_1F_4) + \rho_w(F_1Cr_1F_2)]$
	338(<1)[148]	$\delta_{umb}(Xe_2F_{10\text{-}13}) - \delta_{umb}(Xe_3F_{15\text{-}18})$
294(6)	316(2)[123]	$\rho_t(O_1Cr_1O_2) + \rho_t(F_3Cr_1F_4) + [\nu(Xe_2\text{-}F_{20}) - \nu(Xe_3\text{-}F_{20})]$
283(3)	305(2)[48]	$[\nu(Cr_1\text{-}F_1) + \nu(Cr_1\text{-}F_2)] + \delta(F_3Cr_1F_4)$
	296(<1)[6]	$\delta(F_1Cr_1F_2) + [\nu(Xe_2\text{-}F_{20}) + \nu(Xe_3\text{-}F_{20})]$
279(3)	287(1)[37]	$[\delta(F_{10}Xe_2F_{13}) + \delta(F_{11}Xe_2F_{12})] + [\delta(F_{15}Xe_3F_{18}) + \delta(F_{16}Xe_3F_{17})] + \delta(F_3Cr_1F_4)$

continued…

Table A7.9. (continued) Experimental[a] and calculated[b] vibrational frequencies, intensities, and assignments[c] for $[XeF_5][Xe_2F_{11}][CrO_2F_4]$ (**4** and **4′**)

exptl[a]	**calcd**[b]	**assgnts (C_s)**[c,d]
255(1)	281(2)[8]	$[\delta(F_{18}Xe_3F_{20}) - \delta(F_{13}Xe_2F_{20}) - \rho_t(F_6Xe_1F_7)] - [\rho_w(F_3Cr_1F_4) + \rho_r(F_1Cr_1F_2) + \rho_r(O_1Cr_1O_2)]_{small}$
249(1)	275(1)[3]	$\delta(F_5Xe_1F_6) + \delta(F_7Xe_1F_8)$
	274(<1)[5]	$[\rho_t(F_5Xe_1F_6) - [\rho_t(F_7Xe_1F_8)] + [\delta(F_{10}Xe_2F_{11}) + \delta(F_{12}Xe_2F_{13})] + [\delta(F_{15}Xe_3F_{18}) + \delta(F_{16}Xe_3F_{17})] + [\nu(Xe_1\text{-}F_1) - \nu(Xe_1\text{-}F_2)]$
	265(<1)[23]	$[\delta(F_1Cr_1F_2) - \delta(F_3Cr_1F_4)] + [\delta(F_{11}Xe_2F_{12}) + \delta(F_{10}Xe_2F_{13})] + [\delta(F_{16}Xe_3F_{17}) + \delta(F_{15}Xe_3F_{18})]$
	262(<1)[5]	$[\rho_t(F_5Xe_1F_6) - \rho_t(F_7Xe_1F_8)] + [\delta(F_{10}Xe_2F_{11}) + \delta(F_{12}Xe_2F_{13})] + [\rho_t(O_1Cr_1O_2) - \rho_t(F_1Cr_1F_2)] + [\delta(F_{15}Xe_3F_{16}) + \delta(F_{17}Xe_3F_{18})]$
	247(<1)[4]	$\rho_t(O_1Cr_1O_2) + \rho_t(F_1Cr_1F_2)$
225(1)	243(1)[8]	$[\rho_w(F_{10}Xe_2F_{20}) + \rho_t(F_{11}Xe_2F_{12})] + [\rho_w(F_{15}Xe_3F_{20}) + \rho_t(F_{16}Xe_3F_{17})]$
	235(<1)[8]	$[\rho_t(F_{10}Xe_2F_{13}) - \rho_t(F_{11}Xe_2F_{12})] + [\rho_t(F_{16}Xe_3F_{17}) - \rho_t(F_{15}Xe_3F_{18})] + \rho_r(F_1Cr_1F_2) + [\rho_t(O_1Cr_1O_2) - \rho_w(F_3Cr_1F_4)]_{small}$
201(3)	216(<1)[2]	$[\rho_w(F_3Cr_1F_4) + \rho_r(F_1Cr_1F_2)] + [\rho_t(F_5Xe_1F_8) - \rho_t(F_6Xe_1F_7)]$
	213(<1)[2]	$\nu(Xe_2\text{-}F_{20}) + \nu(Xe_3\text{-}F_{20})$
182(1)	201(<1)[7]	deformation and lattice modes
	199(<1)[<1]	
	194(<1)[3]	
	192(<1)[<1]	
	181(<1)[<1]	

continued…

Table A7.9. (continued) Experimental[a] and calculated[b] vibrational frequencies, intensities, and assignments[c] for $[XeF_5][Xe_2F_{11}][CrO_2F_4]$ (**4** and **4′**)

exptl[a]	calcd[b]	assgnts (C_s) [c,d]
153(1)	160(<1)[4]	
147(1)	156(<1)[18]	
139(1)	146(1)[4]	
122(1)	135(<1)[3]	
	125(<1)[2]	
111(1)	120(1)[<1]	
	108(<1)[<1]	
	108(<1)[<1]	
	104(<1)[1]	
	101(<1)[<1]	deformation and lattice modes
	93(<1)[<1]	
	79(<1)[2]	
	69(<1)[<1]	
	69(<1)[<1]	
	50(<1)[<1]	
	48(<1)[<1]	
	37(<1)[<1]	
	32(<1)[<1]	
	22(<1)[<1]	

continued…

Table A7.9. (continued) [a] Frequencies are given in cm^{-1}. Values in parentheses denote relative Raman intensities. The Raman spectrum was recorded on dry crystalline **4** at −150 °C using 1064-nm excitation. [b] Values in parentheses and square brackets denote calculated Raman intensities ($Å^4$ amu^{-1}) and infrared intensities (km mol^{-1}), respectively. [c] Assignments are for the energy-minimized geometry of **4′** (C_s) calculated at the PBE1PBE/Def2-SVP (F, O, Cr, Xe) level of theory. [d] Abbreviations denote stretch (ν), bend (δ), rock (ρ_r), twist (ρ_t), wag (ρ_w), and umbrella (umb). The atom labeling scheme corresponds to that used in Figure 10.5.

Table A7.10. Calculated geometric parameters for CrO_2F_2 (C_{2v}), $[Cr_2O_4F_6]^{2-}$ (C_{2h}), and $[CrO_2F_4]^{2-}$ (C_{2v})[a]

	CrO_2F_2	$[Cr_2O_4F_6]^{2-}$	$[CrO_2F_4]^{2-}$
Bond Lengths and Contacts (Å)			
Cr(1)–O(1)	1.5249	1.5515	1.5702
Cr(1)–O(2)	1.5249	1.5515	1.5702
Cr(1)–F(1)	1.6847	2.0683	1.9303
Cr(1)–F(2)	1.6847	1.7805	1.9303
Cr(1)–F(3)		1.7805	1.8555
Cr(1)–F(4)			1.8555
Bond Angles (deg)			
O(1)–Cr(1)–O(2)	108.20	105.17	102.85
O(1)–Cr(1)–F(1)	109.60	162.91	88.70
O(1)–Cr(1)–F(2)	109.60	95.86	168.46
O(1)–Cr(1)–F(3)		95.87	93.51
O(1)–Cr(1)–F(4)			93.51
O(2)–Cr(1)–F(1)	109.60	91.92	168.46
O(2)–Cr(1)–F(2)	109.60	95.87	88.70
O(2)–Cr(1)–F(3)		95.86	93.51
O(2)–Cr(1)–F(4)			93.51
F(1)–Cr(1)–F(2)	110.20	82.13	79.76
F(1)–Cr(1)–F(3)		82.13	85.68
F(1)–Cr(1)–F(4)			85.68
F(2)–Cr(1)–F(3)		160.64	85.68
F(2)–Cr(1)–F(4)			85.68
F(3)–Cr(1)–F(4)			168.73
Cr(1)–F(1)–Cr(1A)		109.00	

[a] The PBE1PBE/Def2-SVP (F, O, Cr) level of theory was used.

Table A7.11. Calculated geometric parameters for $[XeF_5]^+$ (C_{4v}) and $[Xe_2F_{11}]^+$ (C_2)[a]

	$[XeF_5]^+$	$[Xe_2F_{11}]^+$
Bond lengths (Å)		
Xe(1)–F(1)	1.839	1.874
Xe(1)–F(2)	1.839	1.856
Xe(1)–F(3)	1.839	1.856
Xe(1)–F(4)	1.839	1.874
Xe(1)–F(5)	1.807	1.823
Xe(1)–F(6)		2.293
Bond angles (°)		
F(1)–Xe(1)–F(2)	89.20	88.05
F(1)–Xe(1)–F(3)	166.44	164.14
F(1)–Xe(1)–F(4)	89.20	90.99
F(1)–Xe(1)–F(5)	83.22	82.21
F(1)–Xe(1)–F(6)		114.59
F(2)–Xe(1)–F(3)	89.20	88.31
F(2)–Xe(1)–F(4)	166.44	163.90
F(2)–Xe(1)–F(5)	83.22	81.87
F(2)–Xe(1)–F(6)		79.41
F(3)–Xe(1)–F(4)	89.20	88.25
F(3)–Xe(1)–F(5)	83.22	81.99
F(3)–Xe(1)–F(6)		79.84
F(4)–Xe(1)–F(5)	83.22	82.08
F(4)–Xe(1)–F(6)		115.39
F(5)–Xe(1)–F(6)		154.18

[a] The PBE1PBE/Def2-SVP (F, Xe) level of theory was used.

Table A7.11. Calculated[a] vibrational frequencies,[b] intensities, and assignments[c] for CrO_2F_2

calcd[a,b]	assgnts (C_{2v})[c]
1186(7)[185]	$\nu(Cr–O_1) - \nu(Cr–O_2)$
1182(17)[89]	$\nu(Cr–O_1) + \nu(Cr–O_2)$
832(2)[155]	$\nu(Cr–F_1) - \nu(Cr–F_2)$
780(9)[69]	$\nu(Cr–F_1) + \nu(Cr–F_2)$
448(4)[<1]	$\delta(O_1CrO_2)$
337(1)[11]	$\rho_w(O_1CrO_2) + \rho_r(F_1CrF_2)$
311(8)[2]	$\rho_w(F_1CrF_2) + \rho_r(O_1CrO_2)$
298(4)[0]	$\rho_t(O_1CrO_2) + \rho_t(F_1CrF_2)$
229(2)[6]	$\delta(F_1CrF_2)$

[a] The PBE1PBE/Def2-SVP (F, O, Cr) level of theory was used. [b] Values in parentheses and square brackets denote calculated Raman intensities ($Å^4$ amu^{-1}) and infrared intensities (km mol^{-1}), respectively. [c] Abbreviations denote stretch (ν), bend (δ), rock (ρ_r), twist (ρ_t), and wag (ρ_w).

Table A7.12. Calculated[a] vibrational frequencies,[b] intensities, and assignments[c] for $[CrO_2F_4]^{2-}$

calcd[a,b]	assgnts (C_{2v}) [c]
1058(27)[190]	$\nu(Cr\text{-}O_1) + \nu(Cr\text{-}O_2)$
1042(9)[356]	$\nu(Cr\text{-}O_1) - \nu(Cr\text{-}O_2)$
558(11)[85]	$[\nu(Cr\text{-}F_1) + \nu(Cr\text{-}F_2)] + [\nu(Cr\text{-}F_3) + \nu(Cr\text{-}F_4)]$
501(<1)[255]	$\nu(Cr\text{-}F_3) - \nu(Cr\text{-}F_4)$
453(5)[1]	$\delta(O_1CrO_2)$
404(3)[32]	$[\nu(Cr\text{-}F_1) + \nu(Cr\text{-}F_2)] - [\nu(Cr\text{-}F_3) + \nu(Cr\text{-}F_4)]$
397(<1)[17]	$[\nu(Cr\text{-}F_1) - \nu(Cr\text{-}F_2)] + \rho_r(O_1CrO_2)$
361(2)[60]	$\rho_w(O_1CrO_2)$
340(5)[0]	$[\rho_t(O_1CrO_2) + \rho_t(F_1CrF_2)] + \rho_t(F_3CrF_4)$
336(3)[52]	$[\rho_r(O_1CrO_2) + \rho_r(F_1CrF_2)] - \rho_w(F_3CrF_4)$
335(1)[<1]	$\delta(F_1CrF_2) + \delta(F_3CrF_4)_{small}$
298(2)[3]	$\rho_w(F_1CrF_2) + \rho_r(F_3CrF_4)$
220(<1)[3]	$\delta(F_3CrF_4) - \delta(F_1CrF_2)_{small}$
192(<1)[6]	$[\rho_r(O_1CrO_2) + \rho_r(F_1CrF_2)] + \rho_w(F_3CrF_4)$
122(<1)[0]	$\rho_t(O_1CrO_2) + \rho_t(F_1CrF_2)$

[a] The PBE1PBE/Def2-SVP (F, O, Cr) level of theory was used. [b] Values in parentheses and square brackets denote calculated Raman intensities ($Å^4$ amu^{-1}) and infrared intensities (km mol^{-1}), respectively. [c] Abbreviations denote stretch (ν), bend (δ), rock (ρ_r), twist (ρ_t), and wag (ρ_w).

Table A7.13. Calculated[a] vibrational frequencies,[b] intensities, and assignments[c] for $[Cr_2O_4F_6]^{2-}$

calcd[a,b]	assgnts (C_{2h}) [c]
1106(66)[0]	$[\nu(Cr_1\text{-}O_1) + \nu(Cr_1\text{-}O_2)] + [\nu(Cr_{1A}\text{-}O_{1A}) + \nu(Cr_{1A}\text{-}O_{2A})]$
1106(0)[520]	$[\nu(Cr_1\text{-}O_1) - \nu(Cr_1\text{-}O_2)] - [\nu(Cr_{1A}\text{-}O_{1A}) - \nu(Cr_{1A}\text{-}O_{2A})]$
1085(0)[431]	$[\nu(Cr_1\text{-}O_1) + \nu(Cr_1\text{-}O_2)] - [\nu(Cr_{1A}\text{-}O_{1A}) + \nu(Cr_{1A}\text{-}O_{2A})]$
1075(46)[0]	$[\nu(Cr_1\text{-}O_1) - \nu(Cr_1\text{-}O_2)] + [\nu(Cr_{1A}\text{-}O_{1A}) - \nu(Cr_{1A}\text{-}O_{2A})]$
646(0)[417]	$[\nu(Cr_1\text{-}F_2) - \nu(Cr_1\text{-}F_3)] - [\nu(Cr_{1A}\text{-}F_{2A}) - \nu(Cr_{1A}\text{-}F_{3A})]$
605(0)[116]	$[\nu(Cr_1\text{-}F_2) + \nu(Cr_1\text{-}F_3)] - [\nu(Cr_{1A}\text{-}F_{2A}) + \nu(Cr_{1A}\text{-}F_{3A})]$
602(<1)[0]	$[\nu(Cr_1\text{-}F_2) - \nu(Cr_1\text{-}F_3)] + [\nu(Cr_{1A}\text{-}F_{2A}) - \nu(Cr_{1A}\text{-}F_{3A})]$
602(19)[0]	$[\nu(Cr_1\text{-}F_2) + \nu(Cr_1\text{-}F_3)] + [\nu(Cr_{1A}\text{-}F_{2A}) + \nu(Cr_{1A}\text{-}F_{3A})]$
476(6)[0]	$[\delta(O_1Cr_1O_2) + \delta(O_{1A}Cr_{1A}O_{2A})]$
466(0)[8]	$[\delta(O_1Cr_1O_2) - \delta(O_{1A}Cr_{1A}O_{2A})]$
414(1)[0]	$[\nu(Cr_1\text{-}F_1) + \nu(Cr_1\text{-}F_{1A})] + [\nu(Cr_{1A}\text{-}F_1) + \nu(Cr_{1A}\text{-}F_{1A})]$
400(0)[56]	$[\rho_w(O_1Cr_1O_2) - \rho_w(O_{1A}Cr_{1A}O_{2A})]$
396(3)[0]	$[\nu(Cr_1\text{-}F_1) - \nu(Cr_1\text{-}F_{1A})] - [\nu(Cr_{1A}\text{-}F_1) - \nu(Cr_{1A}\text{-}F_{1A})] + [\rho_r(O_1Cr_1O_2) + \rho_r(O_{1A}Cr_{1A}O_{2A})]_{small}$
393(6)[0]	$[\rho_w(O_1Cr_1O_2) + \rho_w(O_{1A}Cr_{1A}O_{2A})]$
388(0)[119]	$[\nu(Cr_1\text{-}F_1) + \nu(Cr_1\text{-}F_{1A})] - [\nu(Cr_{1A}\text{-}F_1) + \nu(Cr_{1A}\text{-}F_{1A})]$
366(7)[0]	$[\rho_t(O_1Cr_1O_2) + \rho_t(O_{1A}Cr_{1A}O_{2A})] + [\rho_t(F_2Cr_1F_3) - \rho_t(F_{2A}Cr_{1A}F_{3A})] + \rho_t(F_1Cr_1F_{1A})$
361(0)[16]	$[\rho_r(O_1Cr_1O_2) - \rho_r(O_{1A}Cr_{1A}O_{2A})] + [\rho_w(F_2Cr_1F_3) - \rho_w(F_{2A}Cr_{1A}F_{3A})]$
349(0)[<1]	$\rho_w(F_1Cr_1F_{1A}) + [\rho_r(F_2Cr_1F_3) - \rho_r(F_{2A}Cr_{1A}F_{3A})]$
344(0)[0]	$[\rho_t(O_1Cr_1O_2) - \rho_t(O_{1A}Cr_{1A}O_{2A})] + [\rho_t(F_2Cr_1F_3) - \rho_t(F_{2A}Cr_{1A}F_{3A})]$
275(4)[0]	$\delta(F_2Cr_1F_3) + \delta(F_{2A}Cr_{1A}F_{3A})$
258(0)[10]	$[\nu(Cr_1\text{-}F_1) - \nu(Cr_1\text{-}F_{1A})] + [\nu(Cr_{1A}\text{-}F_1) - \nu(Cr_{1A}\text{-}F_{1A})] + [\rho_w(F_2Cr_1F_3) + \rho_w(F_{2A}Cr_{1A}F_{3A})]_{small}$

continued…

Table A7.13. (continued) Calculated[a] vibrational frequencies,[b] intensities, and assignments[c] for $[Cr_2O_4F_6]^{2-}$

calcd[a,b]	**assgnts (C_{2h}) [c]**
245(0)[46]	$[\delta(F_2Cr_1F_3) - \delta(F_{2A}Cr_{1A}F_{3A})]$
241(1)[0]	$[\rho_t(O_1Cr_1O_2) + \rho_t(O_{1A}Cr_{1A}O_{2A})] - [\rho_t(F_1Cr_1F_{1A}) + \rho_t(F_1Cr_{1A}F_{1A})]$
210(1)[0]	$[\rho_w(F_2Cr_1F_3) + \rho_w(F_{2A}Cr_{1A}F_{3A})] + [\nu(Cr_1\text{-}F_1) - \nu(Cr_1\text{-}F_{1A})]_{small} - [\nu(Cr_{1A}\text{-}F_1) - \nu(Cr_{1A}\text{-}F_{1A})]_{small}$
204(1)[0]	$[\rho_r(F_2Cr_1F_3) + \rho_r(F_{2A}Cr_{1A}F_{3A})$
180(2)[0]	$\delta(Cr_1F_1Cr_{1A}) + \delta(Cr_1F_{1A}Cr_{1A})$
132(0)[<1]	$[\rho_r(O_1Cr_1O_2) - \rho_r(O_{1A}Cr_{1A}O_{2A})]$
101(0)[2]	$[\rho_r(F_2Cr_1F_3) - \rho_r(F_{2A}Cr_{1A}F_{3A})] + \rho_w(F_1Cr_1F_{1A})$
91(0)[0]	$[\rho_t(O_1Cr_1O_2) - \rho_t(O_{1A}Cr_{1A}O_{2A})] + [\rho_t(F_2Cr_1F_3) + \rho_t(F_{2A}Cr_{1A}F_{3A})]_{small}$
−46(<1)[0]	$[\rho_r(O_1Cr_1O_2) + \rho_r(O_{1A}Cr_{1A}O_{2A})] + \rho_t(F_1Cr_1F_{1A})$

[a] The PBE1PBE/Def2-SVP (F, O, Cr) level of theory was used. [b] Values in parentheses and square brackets denote calculated Raman intensities ($Å^4$ amu^{-1}) and infrared intensities (km mol^{-1}), respectively. [c] Abbreviations denote stretch (ν), bend (δ), rock (ρ_r), twist (ρ_t), and wag (ρ_w).

Table A7.14. Calculated[a] vibrational frequencies,[b] intensities, and assignments[c] for $[XeF_5]^+$

calcd[a,b]	assgnts (C_{4v}) [c]
731(<1)[157]	$\nu(Xe_1\text{-}F_1) - \nu(Xe_1\text{-}F_3)$
731(<1)[157]	$\nu(Xe_1\text{-}F_2) - \nu(Xe_1\text{-}F_4)$
707(12)[29]	$\nu(Xe_1\text{-}F_5)$
659(23)[<1]	$[\nu(Xe_1\text{-}F_1) + \nu(Xe_1\text{-}F_2) + \nu(Xe_1\text{-}F_3) + \nu(Xe_1\text{-}F_4)] - \nu(Xe_1\text{-}F_5)$
651(14)[0]	$[\nu(Xe_1\text{-}F_1) + \nu(Xe_1\text{-}F_3)] - [\nu(Xe_1\text{-}F_2) + \nu(Xe_1\text{-}F_4)]$
372(2)[11]	$\delta(F_1Xe_1F_5) - \delta(F_3Xe_1F_5)$
372(2)[11]	$\delta(F_2Xe_1F_5) - \delta(F_4Xe_1F_5)$
331(<1)[38]	$\delta_{umb}(Xe_1F_{1\text{–}4})$
289(3)[0]	$\delta(F_1Xe_1F_2) + \delta(F_3Xe_1F_4)$
213(<1)[0]	$\rho_t(F_1Xe_1F_2) + \rho_t(F_3Xe_1F_4)$
209(<1)[4]	$\rho_w(F_1Xe_1F_3)$
209(<1)[4]	$\rho_w(F_2Xe_1F_4)$

[a] The PBE1PBE/Def2-SVP (F, Xe) level of theory was used. [b] Values in parentheses and square brackets denote calculated Raman intensities ($Å^4$ amu^{-1}) and infrared intensities (km mol^{-1}), respectively. [c] Abbreviations denote stretch (ν), bend (δ), umbrella mode (δ_{umb}), twist (ρ_t), and wag (ρ_w).

Table A7.15. Calculated[a] vibrational frequencies,[b] intensities, and assignments[c] for $[Xe_2F_{11}]^+$

calcd[a,b]	assgnts (C_{4v}) [c]
696(83)[39]	$[\nu(Xe_1\text{-}F_1) + \nu(Xe_1\text{-}F_2) + \nu(Xe_1\text{-}F_5)] - [\nu(Xe_1\text{-}F_3) + \nu(Xe_1\text{-}F_4)] + [\nu(Xe_{1A}\text{-}F_{2A}) + \nu(Xe_{1A}\text{-}F_{3A}) + \nu(Xe_{1A}\text{-}F_{5A})] - [\nu(Xe_{1A}\text{-}F_{1A}) + \nu(Xe_{1A}\text{-}F_{4A})]$
694(<1)[350]	$[\nu(Xe_1\text{-}F_2) - \nu(Xe_1\text{-}F_4)] + [\nu(Xe_{1A}\text{-}F_{1A}) + \nu(Xe_{1A}\text{-}F_{2A})] - [\nu(Xe_{1A}\text{-}F_{3A}) + \nu(Xe_{1A}\text{-}F_{4A})]$
693(35)[220]	$[\nu(Xe_1\text{-}F_3) + \nu(Xe_1\text{-}F_4) + \nu(Xe_1\text{-}F_5)] - \nu(Xe_1\text{-}F_1) + [\nu(Xe_{1A}\text{-}F_{4A}) + \nu(Xe_{1A}\text{-}F_{5A})] - [\nu(Xe_{1A}\text{-}F_{2A})]$
686(10)[11]	$[\nu(Xe_1\text{-}F_3) + \nu(Xe_1\text{-}F_5)] - \nu(Xe_1\text{-}F_1) - [\nu(Xe_{1A}\text{-}F_{4A}) + \nu(Xe_{1A}\text{-}F_{5A})] + [\nu(Xe_{1A}\text{-}F_{2A})]$
686(6)[2]	$[\nu(Xe_1\text{-}F_2) - \nu(Xe_1\text{-}F_4)] + [\nu(Xe_{1A}\text{-}F_{3A}) + \nu(Xe_{1A}\text{-}F_{4A})] - [\nu(Xe_{1A}\text{-}F_{1A}) + \nu(Xe_{1A}\text{-}F_{2A})]$
682(<1)[312]	$[\nu(Xe_1\text{-}F_1) + \nu(Xe_1\text{-}F_2) + \nu(Xe_1\text{-}F_5)] - [\nu(Xe_1\text{-}F_3) + \nu(Xe_1\text{-}F_4)] - [\nu(Xe_{1A}\text{-}F_{2A}) + \nu(Xe_{1A}\text{-}F_{3A}) + \nu(Xe_{1A}\text{-}F_{5A})] + [\nu(Xe_{1A}\text{-}F_{1A}) + \nu(Xe_{1A}\text{-}F_{4A})]$
630(5)[6]	$[\nu(Xe_1\text{-}F_1) + \nu(Xe_1\text{-}F_2) + \nu(Xe_1\text{-}F_3) + \nu(Xe_1\text{-}F_4)] - [\nu(Xe_1\text{-}F_5) - \nu(Xe_{1A}\text{-}F_{5A})] - [\nu(Xe_{1A}\text{-}F_{1A}) + \nu(Xe_{1A}\text{-}F_{2A}) + \nu(Xe_{1A}\text{-}F_{3A}) + \nu(Xe_{1A}\text{-}F_{4A})]$
630(46)[3]	$[\nu(Xe_1\text{-}F_1) + \nu(Xe_1\text{-}F_2) + \nu(Xe_1\text{-}F_3) + \nu(Xe_1\text{-}F_4)] + [\nu(Xe_{1A}\text{-}F_{1A}) + \nu(Xe_{1A}\text{-}F_{2A}) + \nu(Xe_{1A}\text{-}F_{3A}) + \nu(Xe_{1A}\text{-}F_{4A})] - [\nu(Xe_1\text{-}F_5) + \nu(Xe_{1A}\text{-}F_{5A})]$
612(10)[7]	$[\nu(Xe_1\text{-}F_1) + \nu(Xe_1\text{-}F_3)] - [\nu(Xe_1\text{-}F_2) + \nu(Xe_1\text{-}F_4)] + [\nu(Xe_{1A}\text{-}F_{1A}) + \nu(Xe_{1A}\text{-}F_{3A})] - [\nu(Xe_{1A}\text{-}F_{2A}) + \nu(Xe_{1A}\text{-}F_{4A})]$
612(21)[1]	$[\nu(Xe_1\text{-}F_1) + \nu(Xe_1\text{-}F_3)] - [\nu(Xe_1\text{-}F_2) + \nu(Xe_1\text{-}F_4)] - [\nu(Xe_{1A}\text{-}F_{1A}) + \nu(Xe_{1A}\text{-}F_{3A})] + [\nu(Xe_{1A}\text{-}F_{2A}) + \nu(Xe_{1A}\text{-}F_{4A})]$
371(66)[<1]	$[\delta(F_1Xe_1F_5) - \delta(F_3Xe_1F_5)] - [\delta(F_{2A}Xe_{1A}F_{5A}) - \delta(F_{4A}Xe_{1A}F_{5A})]$
369(2)[8]	$[\delta(F_1Xe_1F_5) - \delta(F_3Xe_1F_5)] + [\delta(F_{2A}Xe_{1A}F_{5A}) - \delta(F_{4A}Xe_{1A}F_{5A})]$
368(<1)[20]	$[\delta(F_2Xe_1F_5) - \delta(F_4Xe_1F_5)] + [\delta(F_{1A}Xe_{1A}F_{5A}) - \delta(F_{3A}Xe_{1A}F_{5A})]$
366(<1)[5]	$[\delta(F_2Xe_1F_5) - \delta(F_4Xe_1F_5)] - [\delta(F_{1A}Xe_{1A}F_{5A}) - \delta(F_{3A}Xe_{1A}F_{5A})]$
328(<1)[568]	$[\nu(Xe_1\text{-}F_6) - \nu(Xe_{1A}\text{-}F_{6A})] + [\delta_{umb}(Xe_1F_{1\text{–}4}) - \delta_{umb}(Xe_{1A}F_{1A\text{–}4A})]$
325(16)[9]	$[\delta_{umb}(Xe_1F_{1\text{–}4}) + \delta_{umb}(Xe_{1A}F_{1A\text{–}4A})]$
301(<1)[24]	$[\nu(Xe_1\text{-}F_6) - \nu(Xe_{1A}\text{-}F_{6A})] - [\delta_{umb}(Xe_1F_{1\text{–}4}) - \delta_{umb}(Xe_{1A}F_{1A\text{–}4A})]$
277(2)[2]	$[\delta(F_1Xe_1F_2) + \delta(F_3Xe_1F_4) + \delta(F_{1A}Xe_{1A}F_{4A}) + \delta(F_{2A}Xe_{1A}F_{3A})]$

continued…

Table A7.15. (continued) Calculated[a] Raman frequencies,[b] intensities, and assignments[c] for $[Xe_2F_{11}]^+$

calcd[a,b]	assgnts (C_{4v}) [c]
274(2)[9]	$[\delta(F_1Xe_1F_2) + \delta(F_3Xe_1F_4) + \delta(F_{1A}Xe_{1A}F_{2A}) - \delta(F_{3A}Xe_{1A}F_{4A})]$
230(<1)[1]	$[\rho_t(F_1Xe_1F_2) + \rho_t(F_3Xe_1F_4)] - [\rho_t(F_{1A}Xe_{1A}F_{2A}) + \rho_t(F_{3A}Xe_{1A}F_{4A})]$
223(<1)[1]	$\rho_t(F_1Xe_1F_2) + \rho_t(F_3Xe_1F_4) + \rho_t(F_{1A}Xe_{1A}F_{2A}) + \rho_t(F_{3A}Xe_{1A}F_{4A})$
197(<1)[2]	$[\rho_w(F_1Xe_1F_3) + \rho_w(F_2Xe_1F_4)] - [\rho_w(F_{1A}Xe_{1A}F_{3A}) + \rho_w(F_{2A}Xe_{1A}F_{4A})]$
196(<1)[<1]	$\rho_w(F_1Xe_1F_3) + \rho_w(F_2Xe_1F_4) + \rho_w(F_{1A}Xe_{1A}F_{3A}) + \rho_w(F_{2A}Xe_{1A}F_{4A})$
190(<1)[7]	$[\rho_w(F_1Xe_1F_3) - \rho_w(F_2Xe_1F_4)] - [\rho_w(F_{1A}Xe_{1A}F_{3A}) - \rho_w(F_{2A}Xe_{1A}F_{4A})]$
180(<1)[10]	$[\rho_w(F_1Xe_1F_3) - \rho_w(F_2Xe_1F_4)] + [\rho_w(F_{1A}Xe_{1A}F_{3A}) - \rho_w(F_{2A}Xe_{1A}F_{4A})]$
170(2)[3]	$\nu(Xe_1\text{-}F_6) + \nu(Xe_{1A}\text{-}F_{6A})$
122(<1)[4]	$\delta(F_2Xe_1F_6) - \delta(F_{3A}Xe_{1A}F_6)$
96(<1)[<1]	$\delta(Xe_1F_1F_2F_6) + \delta(Xe_{1A}F_{1A}F_{2A}F_6)$
62(<1)[<1]	$\rho_r(Xe_1F_1F_3F_5) - \rho_r(Xe_{1A}F_{2A}F_{4A}F_{5A})$
46(1)[<1]	$\rho_r(Xe_1F_2F_4F_5) - \rho_r(Xe_{1A}F_{1A}F_{3A}F_{5A})$
24(<1)[<1]	$\rho_r(Xe_1F_1F_3F_5) + \rho_r(Xe_{1A}F_{2A}F_{4A}F_{5A})$
18(<1)[<1]	$\rho_r(Xe_1F_2F_4F_5) + \rho_r(Xe_{1A}F_{1A}F_{3A}F_{5A})$
9(<1)[<1]	$\rho_r(F_1Xe_1F_2) + \rho_r(F_3Xe_1F_4) + \rho_r(F_{1A}Xe_{1A}F_{2A}) + \rho_r(F_{3A}Xe_{1A}F_{4A})$

[a] The PBE1PBE/Def2-SVP (F, Xe) level of theory was used. [b] Values in parentheses and square brackets denote calculated Raman intensities ($Å^4$ amu^{-1}) and infrared intensities (km mol^{-1}), respectively. [c] Abbreviations denote stretch (ν), bend (δ), umbrella mode (δ_{umb}), twist (ρ_t), and wag (ρ_w).

Figure A7.1. Factor-Group Analysis of $[XeF_5][Cr_2O_4F_6]$[a]

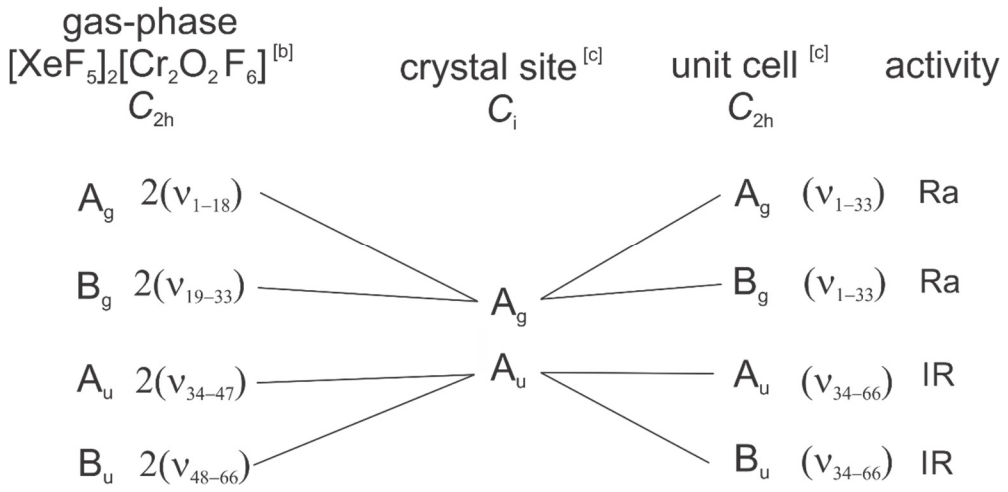

[a] The external modes have not been treated in this analysis. [b] The vibrational irreducible representation for gas-phase $[XeF_5][Cr_2O_4F_6]$ is $\Gamma = 18\ A_g + 15\ B_g + 14\ A_u + 19\ B_u$. [c] Space group; $P2_1/n$, Z = 2.

Figure A7.2. Factor-Group Analysis of $[XeF_5][Cr_2O_4F_6]\cdot 4HF$[a]

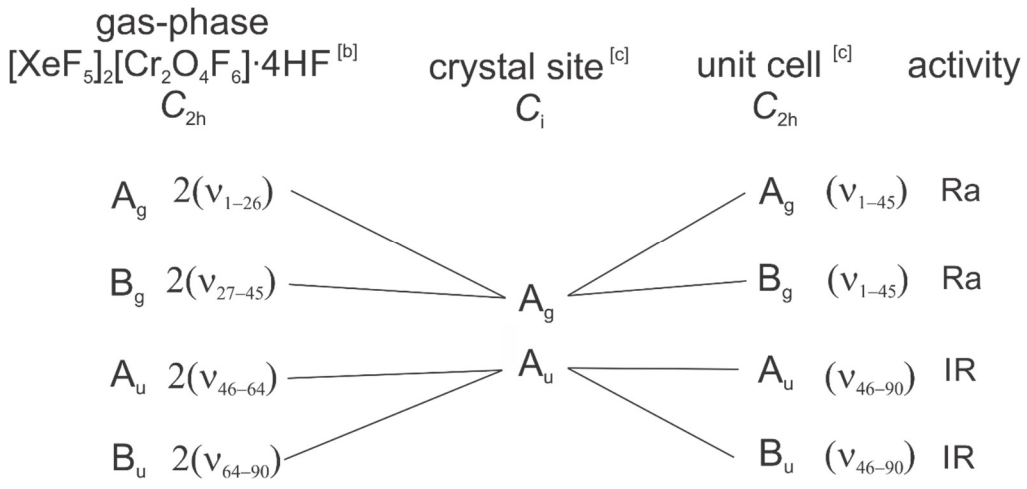

[a] The external modes have not been treated in this analysis. [b] The vibrational irreducible representation for gas-phase $[XeF_5][Cr_2O_4F_6]\cdot 4HF$ is $\Gamma = 26\ A_g + 19\ B_g + 19\ A_u + 26\ B_u$. [c] Space group; $P2_1/c$, Z = 2.

Figure A7.3. Factor-Group Analysis of $[XeF_5][Cr_2O_4F_6]\cdot 2XeOF_4$[a]

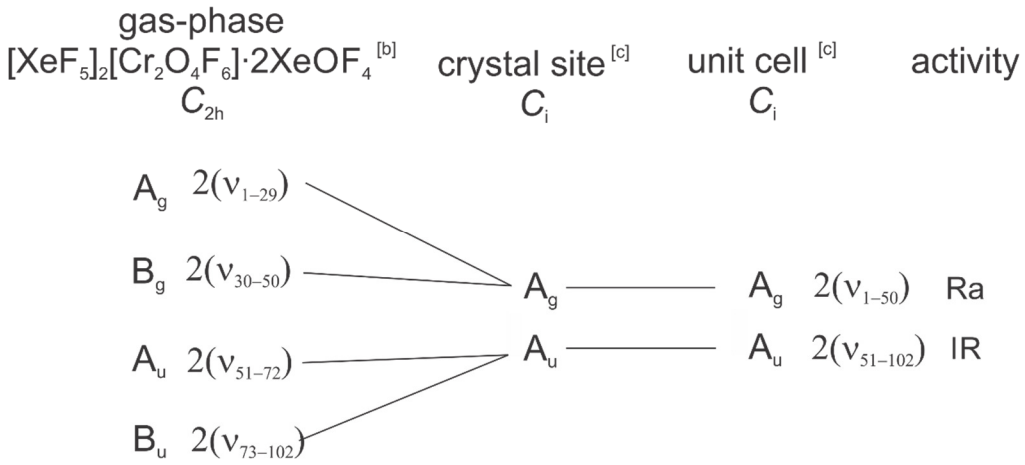

[a] The external modes have not been treated in this analysis. [b] The vibrational irreducible representation for gas-phase $[XeF_5][Cr_2O_4F_6]\cdot 2XeOF_4$ is $\Gamma = 29\ A_g + 21\ B_g + 22\ A_u + 30\ B_u$. [c] Space group; $P\bar{1}$, Z = 2.

Figure A7.4. Factor-Group Analysis of $[XeF_5][Xe_2F_{11}][CrO_2F_4]$[a]

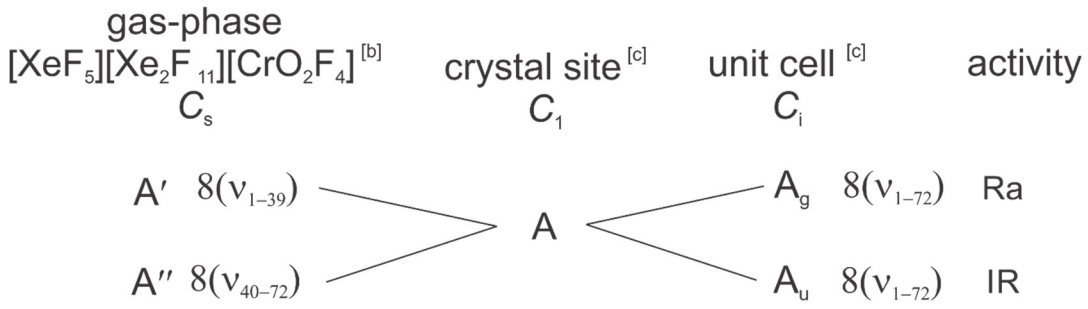

[a] The external modes have not been treated in this analysis. [b] The vibrational irreducible representation for gas-phase $[XeF_5][Cr_2O_4F_6]\cdot 4HF$ is $\Gamma = 39\ A' + 33\ A''$ [c] Space group; $P2/c$, Z = 8.

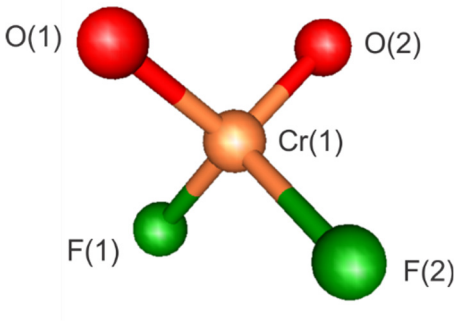

Figure A7.5. Calculated geometry of CrO_2F_2 (C_{2v}) (PBE1PBE/Def2-SVP-(F, O, Cr)). See Table A7.10 for bond lengths and bond angles.

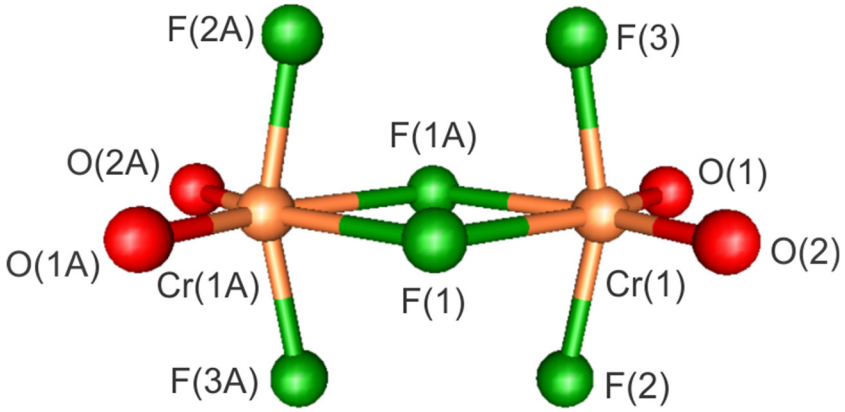

Figure A7.6. Calculated geometry of $[Cr_2O_4F_6]^{2-}$ (C_{2h}) (PBE1PBE/Def2-SVP-(F, O, Cr)). See Table A7.10 for bond lengths and bond angles.

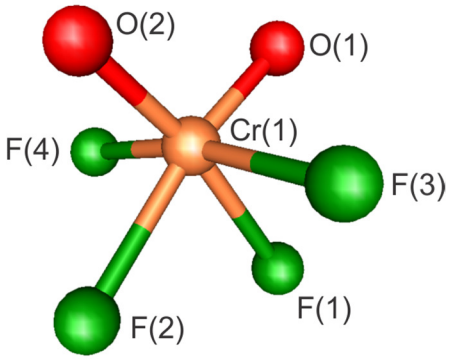

Figure A7.7. Calculated geometry of $[CrO_2F_4]^{2-}$ (C_{2v}) (PBE1PBE/Def2-SVP-(F, O, Cr)). See Table A7.10 for bond lengths and bond angles.

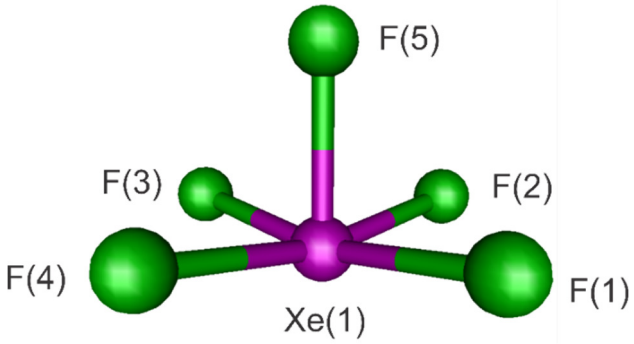

Figure A7.8. Calculated geometry of $[XeF_5]^+$ (PBE1PBE/Def2-SVP-(F, Xe)). See Table A7.11 for bond lengths and bond angles.

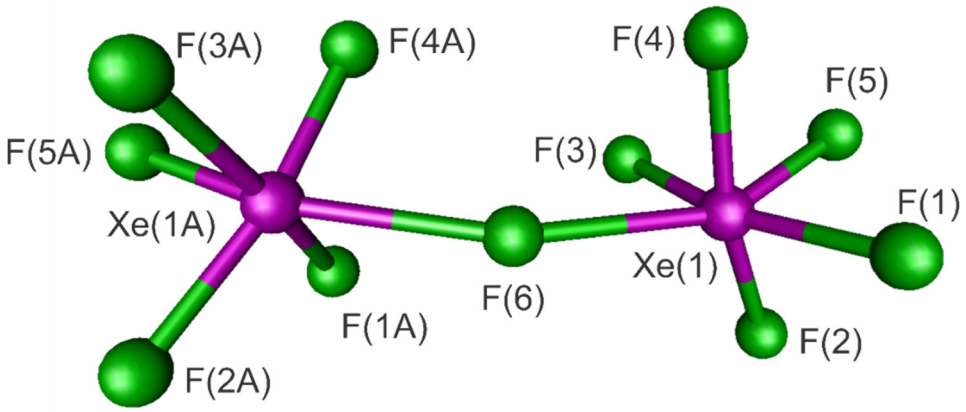

Figure A7.9. Calculated geometry of $[Xe_2F_{11}]^+$ (PBE1PBE/Def2-SVP-(F, Xe)). See Table A7.11 for bond lengths and bond angles.

Table A7.16. Wiberg bond indices, Natural Population Analysis (NPA) Charges, and Valence Indices for CrO_2F_2 (C_{2v})[a]

Bond Indices		NPA Charges [Valence Indices]		
Cr−O	1.913	Cr	1.220	[5.371]
Cr−F	0.773	O	−0.241	[2.512]
		F	−0.369	[1.124]
		$\sum_{CrO2F2}$	**0.000**	

[a] The PBE1PBE/Def2-SVP (O, F, Cl) level of theory was used. The sum $\sum_{CrO2F2}$ = Cr + 2(O + F).

Table A7.17. Wiberg bond indices, Natural Population Analysis (NPA) Charges, and Valence Indices for $[Cr_2O_4F_6]^{2-}$ (C_{2h})[a]

Bond Indices		NPA Charges [Valence Indices]		
Cr1−O1	1.860	Cr1	1.051	[5.582]
Cr1−O2	1.860	O1	−0.302	[2.473]
Cr1−F1	0.268	O2	−0.302	[2.473]
Cr1−F2	0.654	F1	−0.552	[0.838]
Cr1−F3	0.654	F2	−0.448	[0.978]
		F3	−0.448	[0.978]
		$\sum_{[Cr2O4F6]2-}$	**−2.002**	

[a] The PBE1PBE/Def2-SVP (O, F, Cl) level of theory was used. The labeling scheme is the same as in Figure A7.6. The sum $\sum_{[Cr2O4F6]2-}$ = 2(Cr_1 + O_1 + O_2 + F_1 + F_2 + F_3).

Table A7.18. Wiberg bond indices, Natural Population Analysis (NPA) Charges, and Valence Indices for $[CrO_2F_4]^{2-}$ (C_{2v})[a]

Bond Indices		NPA Charges [Valence Indices]		
Cr−O	1.809	Cr	1.036	[5.617]
Cr−$F_{1,2}$	0.460	O	−0.361	[2.406]
Cr−$F_{3,4}$	0.540	$F_{1,2}$	−0.604	[0.726]
		$F_{3,4}$	−0.553	[0.794]
		$\sum_{[CrO2F4]2-}$	**−2.000**	

[a] The PBE1PBE/Def2-SVP (O, F, Cl) level of theory was used. The labeling scheme is the same as in Figure A7.7. The sum $\sum_{[CrO2F4]2-}$ = Cr + 2(O + $F_{1,2}$ + $F_{3,4}$).

Table A7.19. Wiberg bond indices, natural population analysis (NPA) charges, and valence indices for $[XeF_5]_2[Cr_2O_4F_6]$ (**1′**) (C_{2h})[a]

Bond Indices		NPA Charges [Valence Indices]		
Xe1−F4	0.615	Xe1	3.192	[3.384]
Xe1−F5	0.609	F4	−0.490	[0.850]
Xe1−F6	0.609	F5	−0.495	[0.841]
Xe1−F7	0.615	F6	−0.495	[0.841]
Xe1−F8	0.617	F7	−0.490	[0.850]
Xe1---F1	0.085	F8	−0.463	[0.859]
Xe1---F2	0.108			
Xe1---F3A	0.108	$\sum_{[XeF5]+}$	**0.759**	
Cr1−O1	2.037	Cr1	1.067	[5.526]
Cr1−O2	2.037	O1	−0.114	[2.609]
Cr1−F1	0.203	O2	−0.114	[2.609]
Cr1−F2	0.506	F1	−0.601	[0.908]
Cr1−F3	0.506	F2	−0.499	[0.841]
		F3	−0.499	[0.841]
		$\sum_{[Cr2O4F6]2-}$	**−1.520**	
		$\sum_{total}$	**−0.002**	

[a] The PBE1PBE/Def2-SVP (F, O, Cr, Xe) level of theory was used. The sums, $\sum_{[XeF5]+} = Xe_1 + F_4 + F_5 + F_6 + F_7 + F_8$, $\sum_{[Cr2O4F6]2-} = 2(Cr_1 + O_1 + O_2 + F_1 + F_2 + F_3)$, and $\sum_{total} = 2\sum_{[XeF5]+} + \sum_{[Cr2O4F6]2-}$. The labeling scheme is the same as in Figure 10.1.

Table A7.20. Wiberg bond indices, natural population analysis (NPA) charges, and valence indices for $[XeF_5]_2[Cr_2O_4F_6]\cdot 4HF$ (**2′**) (C_{2h})

Bond Indices		NPA Charges [Valence Indices]		
Xe1−F4	0.608	Xe1	3.204	[3.378]
Xe1−F5	0.624	F4	−0.496	[0.840]
Xe1−F6	0.624	F5	−0.484	[0.854]
Xe1−F7	0.608	F6	−0.484	[0.854]
Xe1−F8	0.618	F7	−0.496	[0.840]
Xe1---F1	0.011	F8	−0.462	[0.859]
Xe1---F2	0.084			
Xe1---F3A	0.084			
Xe1---F9	0.103	$\sum_{[XeF5]+}$	**0.782**	
Cr1−O1	2.041	Cr1	1.068	[5.516]
Cr1−O2	2.041	O1	−0.107	[2.618]
Cr1−F1	0.181	O2	−0.107	[2.618]
Cr1−F2	0.515	F1	−0.617	[0.738]
Cr1−F3	0.515	F2	−0.507	[0.897]
		F3	−0.507	[0.897]
		$\sum_{[Cr2O4F6]2-}$	**−1.554**	
H9−F9	0.515	H1	0.576	[0.675]
H(10)---F(10)	0.148	F6	−0.589	[0.714]
		$\sum_{HF(1)}$	**−0.013**	
H10−F10	0.536	H2	0.571	[0.680]
F(1)---H(2)	0.131	F7	−0.564	[0.753]
		$\sum_{HF(2)}$	**0.007**	
		$\sum_{total}$	**−0.002**	

[a] The PBE1PBE/Def2-SVP (F, O, Cr, Xe) level of theory was used. The sums, $\sum_{[XeF5]+} = Xe_1 + F_4 + F_5 + F_6 + F_7 + F_8$, $\sum_{[Cr2O4F6]2-} = 2(Cr_1 + O_1 + O_2 + F_1 + F_2 + F_3)$, and $\sum_{total} = 2(\sum_{[XeF5]+} + \sum_{HF(1)} + \sum_{HF(2)}) + \sum_{[Cr2O4F6]2-}$. The labeling scheme is the same as in Figure 10.2.

Table A7.21. Wiberg bond indices, natural population analysis (NPA) charges, and valence indices for $[XeF_5]_2[Cr_2O_4F_6]\cdot 2XeOF_4$ (**3′**) (C_{2h})[a]

Bond Indices		NPA Charges [Valence Indices]		
Xe1−F4	0.620	Xe1	3.198	[3.381]
Xe1−F5	0.625	F4	−0.486	[0.856]
Xe1−F6	0.625	F5	−0.483	[0.857]
Xe1−F7	0.620	F6	−0.483	[0.857]
Xe1−F8	0.627	F7	−0.486	[0.856]
Xe1---F1	0.061	F8	−0.453	[0.856]
Xe1---F2	0.090			
Xe1---F3A	0.090	$\sum_{[XeF5]+}$	**0.807**	
Cr1−O1	2.053	Cr1	1.051	[5.534]
Cr1−O2	2.053	O1	−0.093	[2.627]
Cr1−F1	0.188	O2	−0.093	[2.627]
Cr1−F2	0.501	F1	−0.637	[0.702]
Cr1−F3	0.501	F2	−0.515	[0.886]
		F3	−0.515	[0.886]
		$\sum_{[Cr2O4F6]2-}$	**−1.604**	
Xe2−O3	1.306	Xe2	3.040	[3.435]
Xe2−F9	0.500	O3	−0.817	[1.670]
Xe2−F10	0.530	F9	−0.575	[0.737]
Xe2−F11	0.530	F10	−0.552	[0.769]
Xe2−F12	0.534	F11	−0.552	[0.769]
Xe2---F1	0.016	F12	−0.550	[0.768]
Xe2---F2	0.007			
		$\sum_{XeOF4}$	**−0.006**	
		$\sum_{total}$	**−0.002**	

[a] The PBE1PBE/Def2-SVP (F, O, Cr, Xe) level of theory was used. The sums, $\sum_{[XeF5]+} = Xe_1 + F_4 + F_5 + F_6 + F_7 + F_8$, $\sum_{[Cr2O4F6]2-} = 2(Cr_1 + O_1 + O_2 + F_1 + F_2 + F_3)$, and $\sum_{total} = 2(\sum_{[XeF5]+} + \sum_{XeOF4}) + \sum_{[Cr2O4F6]2-}$. The labeling scheme is the same as in Figure 10.3.

Table A7.22. Wiberg bond indices, natural population analysis (NPA) charges, and valence indices for $[XeF_5][Xe_2F_{11}][CrO_2F_4]$ (**4′**) (C_s)[a]

Bond Indices		NPA Charges [Valence Indices]		
Xe1−F5	0.612	Xe1	3.183	[3.389]
Xe1−F6	0.589	F5	−0.492	[0.847]
Xe1−F7	0.589	F6	−0.511	[0.819]
Xe1−F8	0.612	F7	−0.511	[0.819]
Xe1−F9	0.617	F8	−0.492	[0.847]
Xe1---F1	0.134	F9	−0.465	[0.857]
Xe1---F2	0.134	$\sum_{[XeF5]+}$	**0.712**	
Xe1---F3	0.079			
Xe2−F10	0.596	Xe2	3.186	[3.387]
Xe2−F11	0.608	F10	−0.503	[0.836]
Xe2−F12	0.611	F11	−0.496	[0.841]
Xe2−F13	0.603	F12	−0.493	[0.841]
Xe2−F14	0.613	F13	−0.501	[0.834]
Xe2---F20	0.184	F14	−0.468	[0.854]
Xe2---F1	0.125	F20	−0.689	[0.857]
Xe2---F4	0.026	$\sum_{[Xe2F11]+}$	**0.761**	
Cr1−O1	2.024	Cr1	1.070	[5.513]
Cr1−O2	2.024	O1	−0.123	[2.612]
Cr1−F1	0.151	O2	−0.123	[2.612]
Cr1−F2	0.151	F1	−0.665	[0.642]
Cr1−F3	0.568	F2	−0.665	[0.642]
Cr1−F4	0.566	F3	−0.468	[0.956]
		F4	−0.498	[0.910]
		$\sum_{[CrO2F4]2-}$	**−1.472**	
		$\sum_{total}$	**0.001**	

[a] The PBE1PBE/Def2-SVP (F, O, Cr, Xe) level of theory was used. The sums, $\sum_{[XeF5]+} = Xe_1 + F_4 + F_5 + F_6 + F_7 + F_8$, and $\sum_{[Xe2F11]+} = 2(Xe_2 + F_{10} + F_{11} + F_{12} + F_{13} + F_{14}) + F_{20}$. The labeling scheme is the same as in Figure 10.5.

APPENDIX 8

CHAPTER 11 Supporting Information

Group 6 Oxyfluoro-anion Salts of $[XeF_5]^+$ and $[Xe_2F_{11}]^+$; Syntheses and Structures of $[XeF_5][M_2O_2F_9]$ (M = Mo, W), $[Xe_2F_{11}][M'OF_5]$ (M' = Cr, Mo, W), $[XeF_5][HF_2]\cdot CrOF_4$, and $[XeF_5][WOF_5]\cdot XeOF_4$

Adapted with permission from: Bortolus, M. R.; Mercier, H. P. A.; Schrobilgen, G. J. *Chem. Eur. J*. **2020**, *26*, 8935–8950.

LIST OF FIGURES

page

LIST OF TABLES

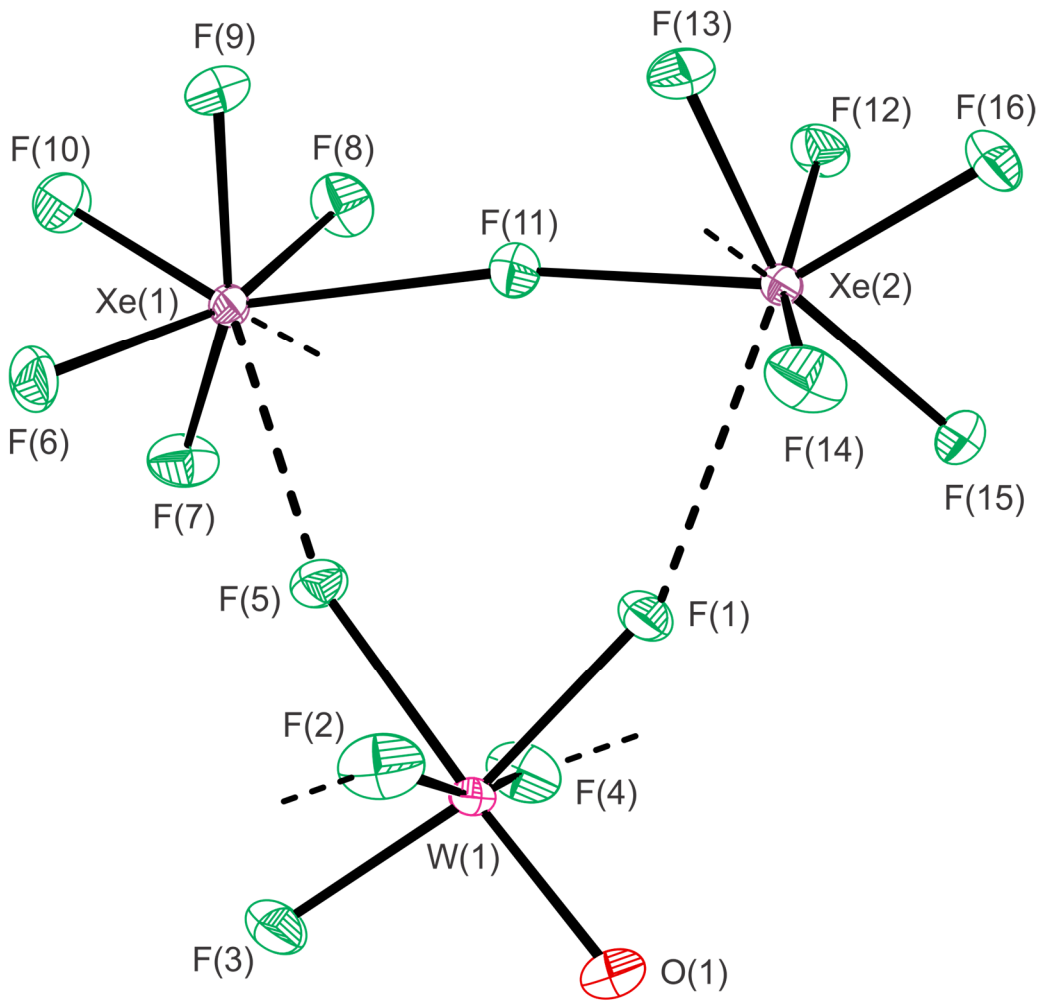

Figure A8.1. The X-ray crystal structure of $[Xe_2F_{11}][WOF_5]$ (**4**), with thermal ellipsoids drawn at the 50% probability level. Secondary Xe---F and W---F bonding interactions are indicated by dashed lines.

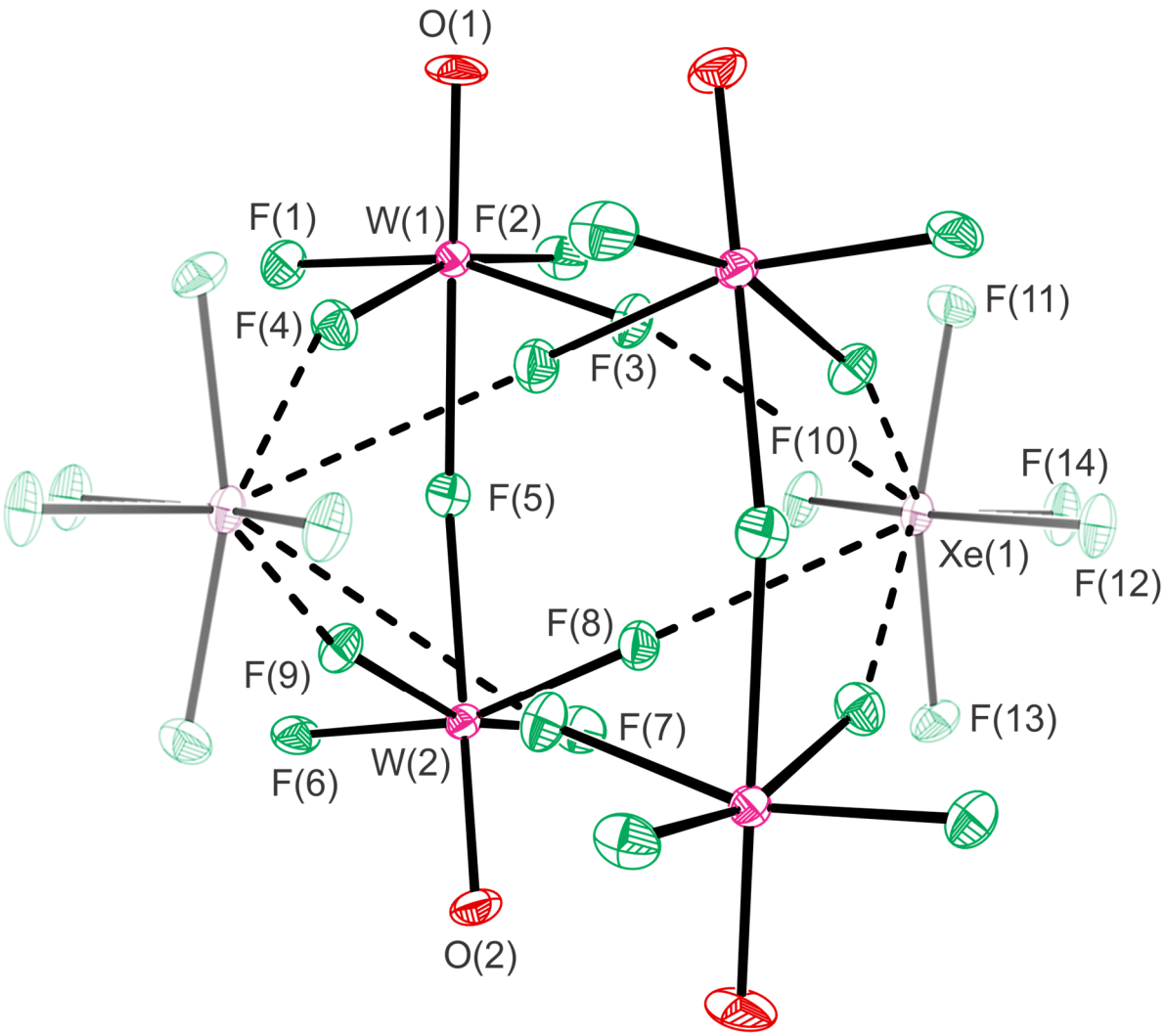

Figure A8.2. The X-ray crystal structure of the dimeric unit of $[XeF_5][W_2O_2F_9]$ (**6**) with thermal ellipsoids drawn at the 50% probability level. The $[XeF_5]^+$ cations have been faded to emphasize the anion. Secondary Xe---F and W---F bonding interactions are indicated by dashed lines.

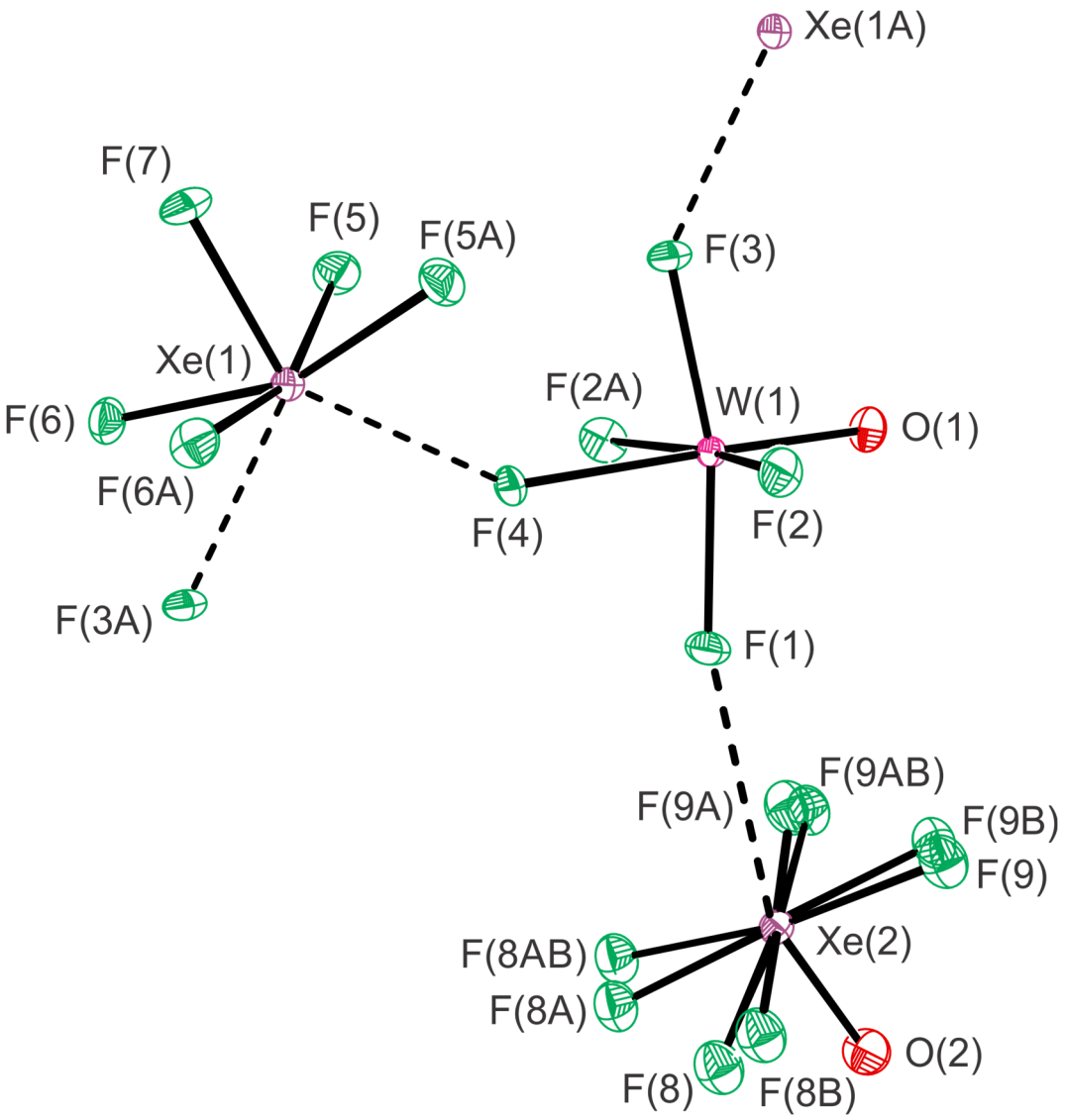

Figure A8.3. The structural unit in the X-ray crystal structure of $[XeF_5][WOF_5]\cdot XeOF_4$ (**7**) with thermal ellipsoids drawn at the 50% probability level. The two orientations of the disordered $XeOF_4$ molecule in the cocrystal are shown. Secondary Xe---F and W---F bonding interactions are indicated by dashed lines.

Table A8.1. Experimental and calculated geometric parameters for $[Xe_2F_{11}]^+$ in $[Xe_2F_{11}][CrOF_5]$ (**1**) and $\{[Xe_2F_{11}][CrOF_5]\}_2$ (**1'**) (C_i)

	1	**1'**		**1**	**1'**
	exptl	calcd [a]		exptl	calcd [a]
Bond Lengths (Å)					
Xe(1)---F(5)	2.5065(9)	2.433	Xe(2)---F(5A)	2.5687(9)	2.434
Xe(1)–F(6)	1.8330(9)	1.857	Xe(2)–F(11)	2.2167(9)	2.246
Xe(1)–F(7)	1.8700(9)	1.882	Xe(2)–F(12)	1.840(1)	1.857
Xe(1)–F(8)	1.869(1)	1.890	Xe(2)–F(13)	1.859(1)	1.881
Xe(1)–F(9)	1.8604(9)	1.881	Xe(2)–F(14)	1.884(1)	1.890
Xe(1)–F(10)	1.8633(9)	1.881	Xe(2)–F(15)	1.877(1)	1.883
Xe(1)–F(11)	2.2778(9)	2.247	Xe(2)–F(16)	1.859(1)	1.881
Xe(1)---F(1)	2.862(1)	2.849	Xe(2)---F(3A)	2.814(1)	2.850
Bond Angles (deg)					
F(5)---Xe(1)–F(6)	143.86(4)	144.1	F(5A)---Xe(2)–F(12)	143.33(4)	143.9
F(5)---Xe(1)–F(7)	74.93(4)	75.9	F(5A)---Xe(2)–F(13)	124.89(4)	124.9
F(5)---Xe(1)–F(8)	76.65(4)	76.3	F(5A)---Xe(2)–F(14)	75.77(4)	76.0
F(5)---Xe(1)–F(9)	125.14(4)	125.0	F(5A)---Xe(2)–F(15)	75.59(4)	75.9
F(5)---Xe(1)–F(10)	123.41(4)	123.4	F(5A)---Xe(2)–F(16)	124.88(4)	123.8
F(5)---Xe(1)–F(11)	74.84(3)	72.8	F(11)–Xe(2)–F(12)	144.56(4)	143.1
F(6)–Xe(1)–F(7)	79.13(5)	79.0	F(11)–Xe(2)–F(13)	79.39(4)	77.6
F(6)–Xe(1)–F(8)	78.29(5)	78.2	F(11)–Xe(2)–F(14)	130.23(4)	128.6
F(6)–Xe(1)–F(9)	78.72(5)	78.6	F(11)–Xe(2)–F(15)	116.93(5)	120.4
F(6)–Xe(1)–F(10)	78.16(5)	78.3	F(11)–Xe(2)–F(16)	73.39(4)	73.6
F(6)–Xe(1)–F(11)	141.19(4)	143.0	F(12)–Xe(2)–F(13)	79.14(6)	78.6
F(7)–Xe(1)–F(8)	89.27(6)	89.3	F(12)–Xe(2)–F(14)	77.38(5)	78.2
F(7)–Xe(1)–F(9)	157.84(5)	157.5	F(12)–Xe(2)–F(15)	79.64(6)	79.0
F(7)–Xe(1)–F(10)	85.08(5)	84.1	F(12)–Xe(2)–F(16)	77.99(5)	78.3
F(7)–Xe(1)–F(11)	122.63(5)	120.6	F(13)–Xe(2)–F(14)	89.69(5)	88.2
F(8)–Xe(1)–F(9)	87.09(5)	88.3	F(13)–Xe(2)–F(15)	158.43(5)	157.5
F(8)–Xe(1)–F(10)	156.42(5)	156.4	F(13)–Xe(2)–F(16)	87.98(5)	89.2
F(8)–Xe(1)–F(11)	128.35(4)	128.6	F(14)–Xe(2)–F(15)	89.42(6)	89.4
F(9)–Xe(1)–F(10)	89.57(5)	89.3	F(14)–Xe(2)–F(16)	155.26(5)	156.3
F(9)–Xe(1)–F(11)	75.74(4)	77.6	F(15)–Xe(2)–F(16)	83.89(5)	84.0
F(10)–Xe(1)–F(11)	72.97(4)	73.5	Xe(1)–F(11)–Xe(2)	162.92(5)	160.9
F(5A)---Xe(2)–F(11)	71.82(3)	72.9	Xe(1)---F(5)---Xe(2)	137.75(3)	140.7

[a] The PBE1PBE/Def2-SVP (F, O, Cr, Xe) level of theory was used.

Table A8.2. Experimental geometric parameters for $[XeF_5][HF_2]\cdot CrOF_4$ (**2**)

Bond Lengths (Å)			
Cr(1)–O(1)	1.5547(9)	Xe(1)---F(6)	2.4231(7)
Cr(1)–F(1)	1.7444(8)	Xe(1)---F(6A)	2.4320(7)
Cr(1)–F(2)	1.7794(8)	Xe(1)–F(7)	1.8579(7)
Cr(1)–F(3)	1.7384(8)	Xe(1)–F(8)	1.8657(7)
Cr(1)–F(4)	1.7305(8)	Xe(1)–F(9)	1.8657(7)
Cr(1)---F(5)	2.2378(7)	Xe(1)–F(10)	1.8528(7)
F(5)---F(6)	2.386(1)	Xe(1)–F(11)	1.8191(7)
F(5)–H(1)	0.74(3)	Xe(1)---F(2A)	3.0592(8)
F(6)–H(1)	1.65(3)	Xe(1A)---F(2)	3.1707(8)

Bond Angles (deg)			
O(1)–Cr(1)–F(1)	99.45(5)	F(6)---Xe(1)–F(10)	121.43(3)
O(1)–Cr(1)–F(2)	98.82(5)	F(6)---Xe(1)–F(11)	145.53(3)
O(1)–Cr(1)–F(3)	100.13(5)	F(6A)---Xe(1)–F(7)	122.97(3)
O(1)–Cr(1)–F(4)	99.71(5)	F(6A)---Xe(1)–F(8)	122.62(3)
O(1)–Cr(1)---F(5)	178.89(5)	F(6A)---Xe(1)–F(9)	75.90(3)
F(1)–Cr(1)–F(2)	86.97(4)	F(6A)---Xe(1)–F(10)	76.09(3)
F(1)–Cr(1)–F(3)	160.28(4)	F(6A)---Xe(1)–F(11)	145.66(3)
F(1)–Cr(1)–F(4)	89.83(5)	F(7)–Xe(1)–F(8)	88.75(4)
F(1)–Cr(1)---F(5)	81.52(4)	F(7)–Xe(1)–F(9)	158.86(4)
F(2)–Cr(1)–F(3)	87.78(4)	F(7)–Xe(1)–F(10)	87.46(4)
F(2)–Cr(1)–F(4)	161.47(4)	F(7)–Xe(1)–F(11)	79.52(4)
F(2)–Cr(1)---F(5)	80.66(4)	F(8)–Xe(1)–F(9)	87.69(4)
F(3)–Cr(1)–F(4)	89.15(4)	F(8)–Xe(1)–F(10)	159.10(4)
F(3)–Cr(1)---F(5)	78.88(3)	F(8)–Xe(1)–F(11)	79.25(4)
F(4)–Cr(1)---F(5)	80.82(4)	F(9)–Xe(1)–F(10)	88.48(4)
Cr(1)---F(5)---F(6)	128.62(4)	F(9)–Xe(1)–F(11)	79.34(4)
Xe(1)---F(6)---Xe(1A)	111.19(2)	F(10)–Xe(1)–F(11)	79.85(4)
Xe(1)---F(6)---F(5)	129.35(3)	H(1)–F(5)–Cr(1)	124(3)
F(6)---Xe(1)---F(6A)	68.81(2)	H(1)–F(6)–Xe(1)	126(1)
F(6)---Xe(1)–F(7)	75.18(3)	H(1)–F(6)–Xe(1A)	120(1)
F(6)---Xe(1)–F(8)	77.19(3)	F(5)–H(1)–F(6)	170(3)
F(6)---Xe(1)–F(9)	124.09(3)		

Table A8.3. Experimental and calculated geometric parameters for $[Xe_2F_{11}]^+$ in $[Xe_2F_{11}][MoOF_5]$ (**3** and **3'** (C_1))

	3	**3'**		**3**	**3'**
	exptl	calcd [a]		exptl	calcd [a]
Bond Lengths (Å)					
Xe(1)---F(5)	2.348(2)	2.251	Xe(2)---F(1)	2.640(2)	2.547
Xe(1)–F(6)	1.860(3)	1.876	Xe(2)–F(11)	2.170(2)	2.171
Xe(1)–F(7)	1.866(3)	1.879	Xe(2)–F(12)	1.843(2)	1.871
Xe(1)–F(8)	1.869(2)	1.893	Xe(2)–F(13)	1.853(2)	1.869
Xe(1)–F(9)	1.866(3)	1.892	Xe(2)–F(14)	1.890(2)	1.894
Xe(1)–F(10)	1.821(2)	1.852	Xe(2)–F(15)	1.882(3)	1.905
Xe(1)–F(11)	2.356(2)	2.373	Xe(2)–F(16)	1.832(2)	1.850
Xe(1)---F(2)	2.969(3)	-------	Xe(2)---F(4)	3.072(2)	-------
Bond Angles (deg)					
F(5)---Xe(1)–F(6)	73.1(1)	75.0	F(1)---Xe(2)–F(11)	74.62(8)	71.3
F(5)---Xe(1)–F(7)	76.4(1)	77.2	F(1)---Xe(2)–F(12)	125.9(1)	125.3
F(5)---Xe(1)–F(8)	126.9(1)	124.1	F(1)---Xe(2)–F(13)	129.4(1)	126.1
F(5)---Xe(1)–F(9)	121.6(1)	120.8	F(1)---Xe(2)–F(14)	73.6(1)	73.0
F(5)---Xe(1)–F(10)	143.1(1)	145.3	F(1)---Xe(2)–F(15)	70.1(1)	73.6
F(5)---Xe(1)–F(11)	74.33(8)	72.0	F(1)---Xe(2)–F(16)	137.4(1)	140.4
F(6)–Xe(1)–F(7)	89.9(2)	89.3	F(11)–Xe(2)–F(12)	75.3(1)	80.1
F(6)–Xe(1)–F(8)	158.3(1)	158.7	F(11)–Xe(2)–F(13)	80.2(1)	75.6
F(6)–Xe(1)–F(9)	84.9(1)	85.3	F(11)–Xe(2)–F(14)	126.3(1)	115.5
F(6)–Xe(1)–F(10)	79.5(1)	79.4	F(11)–Xe(2)–F(15)	116.1(1)	124.9
F(6)–Xe(1)–F(11)	121.3(1)	123.2	F(11)–Xe(2)–F(16)	147.5(1)	148.2
F(7)–Xe(1)–F(8)	87.5(1)	86.4	F(12)–Xe(2)–F(13)	87.4(1)	87.9
F(7)–Xe(1)–F(9)	158.3(1)	158.8	F(12)–Xe(2)–F(14)	156.6(1)	160.4
F(7)–Xe(1)–F(10)	79.3(1)	79.4	F(12)–Xe(2)–F(15)	84.6(1)	87.4
F(7)–Xe(1)–F(11)	127.1(1)	125.3	F(12)–Xe(2)–F(16)	78.4(1)	80.3
F(8)–Xe(1)–F(9)	89.6(1)	91.2	F(13)–Xe(2)–F(14)	88.0(1)	85.0
F(8)–Xe(1)–F(10)	78.8(1)	79.3	F(13)–Xe(2)–F(15)	159.0(1)	157.7
F(8)–Xe(1)–F(11)	76.5(1)	75.5	F(13)–Xe(2)–F(16)	79.8(1)	78.9
F(9)–Xe(1)–F(10)	79.0(1)	79.4	F(14)–Xe(2)–F(15)	91.7(1)	92.3
F(9)–Xe(1)–F(11)	72.8(1)	74.1	F(14)–Xe(2)–F(16)	78.2(1)	80.4
F(10)–Xe(1)–F(11)	142.3(1)	142.6	F(15)–Xe(2)–F(16)	79.6(1)	78.7
			Xe(1)–F(11)–Xe(2)	163.8(1)	152.3

[a] The PBE1PBE/Def2-SVP (F, O, Mo, Xe) level of theory was used.

Table A8.4. Experimental and calculated geometric parameters for $[Xe_2F_{11}]^+$ in $[Xe_2F_{11}][WOF_5]$ (**4** and **4'** (C_1))

	4	**4'**		**4**	**4'**
	exptl	calcd [a]		exptl	calcd [a]
		Bond Lengths (Å)			
Xe(1)---F(5)	2.404(2)	2.266	Xe(2)---F(1)	2.661(2)	2.546
Xe(1)–F(6)	1.870(2)	1.880	Xe(2)–F(11)	2.186(2)	2.183
Xe(1)–F(7)	1.865(2)	1.877	Xe(2)–F(12)	1.851(2)	1.869
Xe(1)–F(8)	1.859(2)	1.890	Xe(2)–F(13)	1.849(2)	1.871
Xe(1)–F(9)	1.868(2)	1.890	Xe(2)–F(14)	1.882(2)	1.902
Xe(1)–F(10)	1.820(2)	1.851	Xe(2)–F(15)	1.891(2)	1.891
Xe(1)–F(11)	2.340(2)	2.357	Xe(2)–F(16)	1.832(2)	1.849
Xe(1)---F(2)	3.057(2)	---------	Xe(2)---F(4)	2.966(2)	---------
		Bond Angles (deg)			
F(5)---Xe(1)–F(6)	76.03(9)	76.8	F(1)---Xe(2)–F(11)	73.73(8)	71.2
F(5)---Xe(1)–F(7)	72.51(9)	75.1	F(1)---Xe(2)–F(12)	129.46(8)	125.8
F(5)---Xe(1)–F(8)	121.8(1)	121.3	F(1)---Xe(2)–F(13)	125.37(9)	125.3
F(5)---Xe(1)–F(9)	127.02(9)	123.8	F(1)---Xe(2)–F(14)	69.88(9)	73.8
F(5)---Xe(1)–F(10)	142.7(1)	145.1	F(1)---Xe(2)–F(15)	73.74(8)	73.0
F(5)---Xe(1)–F(11)	73.79(8)	71.6	F(1)---Xe(2)–F(16)	137.53(9)	140.6
F(6)–Xe(1)–F(7)	90.2(1)	89.7	F(11)–Xe(2)–F(12)	80.90(9)	75.4
F(6)–Xe(1)–F(8)	158.5(1)	159.0	F(11)–Xe(2)–F(13)	75.1(1)	80.0
F(6)–Xe(1)–F(9)	87.7(1)	86.2	F(11)–Xe(2)–F(14)	115.2(1)	125.2
F(6)–Xe(1)–F(10)	79.5(1)	79.6	F(11)–Xe(2)–F(15)	126.4(1)	115.6
F(6)–Xe(1)–F(11)	126.8(1)	124.3	F(11)–Xe(2)–F(16)	148.2(1)	148.0
F(7)–Xe(1)–F(8)	84.9(1)	85.5	F(12)–Xe(2)–F(13)	87.3(1)	88.0
F(7)–Xe(1)–F(9)	158.9(1)	158.8	F(12)–Xe(2)–F(14)	159.3(1)	157.7
F(7)–Xe(1)–F(10)	79.9(1)	79.5	F(12)–Xe(2)–F(15)	88.3(1)	85.0
F(7)–Xe(1)–F(11)	120.1(1)	123.2	F(12)–Xe(2)–F(16)	80.0(1)	78.9
F(8)–Xe(1)–F(9)	89.4(1)	90.9	F(13)–Xe(2)–F(14)	84.8(1)	87.5
F(8)–Xe(1)–F(10)	79.0(1)	79.5	F(13)–Xe(2)–F(15)	157.0(1)	160.5
F(8)–Xe(1)–F(11)	73.06(9)	74.7	F(13)–Xe(2)–F(16)	78.8(1)	80.3
F(9)–Xe(1)–F(10)	79.1(1)	79.4	F(14)–Xe(2)–F(15)	91.5(1)	92.1
F(9)–Xe(1)–F(11)	77.17(9)	75.5	F(14)–Xe(2)–F(16)	79.8(1)	78.8
F(10)–Xe(1)–F(11)	143.2(1)	143.3	F(15)–Xe(2)–F(16)	78.2(1)	80.5
			Xe(1)–F(11)–Xe(2)	165.1(1)	155.3

[a] The PBE1PBE/Def2-SVP (F, O, W, Xe) level of theory was used.

Table A8.5. Experimental and calculated[a] geometric parameters for $[XeF_5]^+$ in $[XeF_5][M_2O_2F_9]$ (M = Mo (**5**), W (**6**)) and $\{[XeF_5][M_2O_2F_9]\}_2$ (M = Mo (**5'**) (C_{2h}), W (**6'**) (C_2))

	5	**5'**	**6**	**6'**
	exptl	calcd	exptl	calcd
Bond Lengths (Å)				
Xe(1)–F(10)	1.8415(8)	1.859	1.836(5)	1.860
Xe(1)–F(11)	1.8433(9)	1.860	1.837(5)	1.858
Xe(1)–F(12)	1.8420(8)	1.861	1.835(4)	1.859
Xe(1)–F(13)	1.8375(9)	1.860	1.849(5)	1.858
Xe(1)–F(14)	1.8167(8)	1.844	1.813(4)	1.842
Xe(1)---F(8)	2.6438(9)	2.638	2.677(5)	2.657
Xe(1)---F(9A)	2.6553(8)	2.645	2.681(5)	2.650
Xe(1)---F(4A)	2.8987(9)	2.642	2.888(5)	2.645
Xe(1)---F(3)	2.9828(9)	2.635	2.990(5)	2.652
Bond Angles (deg)				
F(3)---Xe(1)---F(4A)	82.54(3)	92.0	94.2(2)	91.8
F(3)---Xe(1)---F(8)	59.60(3)	61.7	59.5(2)	61.8
F(3)---Xe(1)---F(9A)	59.81(3)	60.6	59.6(2)	60.5
F(3)---Xe(1)–F(10)	70.27(3)	69.0	66.0(2)	69.1
F(3)---Xe(1)–F(11)	71.62(4)	68.7	66.0(2)	68.6
F(3)---Xe(1)–F(12)	127.44(3)	129.4	129.1(2)	129.1
F(3)---Xe(1)–F(13)	125.30(3)	129.8	129.6(2)	129.8
F(3)---Xe(1)–F(14)	138.42(4)	133.9	132.2(2)	134.1
F(4A)---Xe(1)---F(8)	59.67(3)	60.6	59.8(2)	60.5
F(4A)---Xe(1)---F(9A)	59.24(3)	61.8	58.6(2)	61.8
F(4A)---Xe(1)–F(10)	125.57(3)	129.1	128.7(2)	129.1
F(4A)---Xe(1)–F(11)	126.04(3)	129.9	128.1(2)	129.8
F(4A)---Xe(1)–F(12)	71.02(3)	69.3	67.9(2)	69.1
F(4A)---Xe(1)–F(13)	70.83(3)	68.4	67.0(2)	68.6
F(4A)---Xe(1)–F(14)	139.02(4)	134.1	133.6(2)	134.1
F(8)---Xe(1)---F(9A)	95.30(3)	92.1	82.6(2)	92.2
F(8)---Xe(1)–F(10)	65.90(3)	69.0	69.8(2)	69.0
F(8)---Xe(1)–F(11)	130.07(4)	129.9	125.0(2)	129.9
F(8)---Xe(1)–F(12)	129.16(3)	129.4	127.7(2)	129.1
F(8)---Xe(1)–F(13)	65.70(3)	68.7	71.6(2)	68.5
F(8)---Xe(1)–F(14)	131.45(4)	133.9	138.3(2)	133.9
F(9A)---Xe(1)–F(10)	129.03(3)	129.1	125.5(2)	129.2
F(9A)---Xe(1)–F(11)	66.82(3)	68.6	70.4(2)	68.5
F(9A)---Xe(1)–F(12)	67.63(3)	69.3	71.0(2)	69.0

continued …

Table A8.5. (continued)

F(9A)---Xe(1)–F(13)	129.02(3)	129.9	125.6(2)	129.9
F(9A)---Xe(1)–F(14)	133.24(4)	134.1	139.1(2)	133.9
F(10)–Xe(1)–F(11)	89.21(4)	87.8	88.1(2)	87.7
F(10)–Xe(1)–F(12)	159.78(4)	157.0	160.0(2)	157.3
F(10)–Xe(1)–F(13)	87.56(4)	87.8	89.3(2)	87.7
F(10)–Xe(1)–F(14)	79.87(4)	78.5	80.2(2)	78.7
F(11)–Xe(1)–F(12)	88.25(4)	87.7	87.7(2)	87.8
F(11)–Xe(1)–F(13)	159.98(4)	157.0	160.7(2)	157.2
F(11)–Xe(1)–F(14)	79.90(4)	78.5	80.7(3)	78.6
F(12)–Xe(1)–F(13)	88.00(4)	87.7	88.2(2)	87.8
F(12)–Xe(1)–F(14)	79.94(4)	78.5	79.8(2)	78.7
F(13)–Xe(1)–F(14)	80.08(4)	78.5	80.0(2)	78.6
M(1)–F(5)–M(2)	147.40(4)	148.2	147.7(2)	148.9
M(1)–F(3)---Xe(1)	148.22(4)	168.9	148.0(2)	165.7
M(1A)–F(4A)---Xe(1A)	164.14(4)	158.7	161.0(2)	169.9
M(2A)–F(9A)---Xe(1A)	159.89(4)	158.8	164.5(2)	169.7
M(2)–F(8)---Xe(1)	147.14(4)	168.8	148.6(2)	165.8

[a] The PBE1PBE/Def2-SVP (F, O, Mo, W, Xe) level of theory was used.

Table A8.6. Experimental geometric parameters for $[XeF_5][WOF_5]\cdot XeOF_4$ (**7**)

Bond Lengths (Å)					
W(1)–O(1)	1.686(5)	Xe(1)---F(2A)	3.131(3)	Xe(2)–F(8A)	1.881(7)
W(1)–F(1)	1.862(4)	Xe(1)–F(5)	1.853(3)	Xe(2)–F(9)	1.881(8)
W(1)–F(2)	1.864(3)	Xe(1)–F(5A)	1.853(3)	Xe(2)–F(9A)	1.881(8)
W(1)–F(2A)	1.864(3)	Xe(1)–F(6)	1.855(3)	Xe(2)−F(8B)	1.921(7)
W(1)–F(3)	1.890(4)	Xe(1)–F(6A)	1.855(3)	Xe(2)–F(8AB)	1.921(7)
W(1)−F(4)	2.063(4)	Xe(1)–F(7)	1.811(4)	Xe(2)–F(9B)	1.920(8)
Xe(1)---F(4)	2.357(4)	Xe(2)−O(2)	1.698(5)	Xe(2)–F(9AB)	1.920(8)
Xe(1)---F(3)	2.689(4)	Xe(2)−F(8)	1.881(7)	Xe(2)---F(1)	2.890(7)
Xe(1)---F(2)	3.131(3)				
Bond Angles (deg)					
O(1)–W(1)–F(1)	95.8(2)	F(4)---Xe(1)–F(7)	145.0(3)	F(8)−Xe(2)–F(9)	92.2(7)
O(1)–W(1)–F(2)	97.81(9)	F(3A)---Xe(1)–F(5)	124.7(2)	F(8)−Xe(2)–F(9AB)	178.3(3)
O(1)–W(1)–F(2A)	97.81(9)	F(3A)---Xe(1)–F(5A)	124.7(2)	F(8)−Xe(2)–O(2)	88.0(2)
O(1)–W(1)–F(3)	98.4(2)	F(3A)---Xe(1)–F(6)	72.5(2)	F(8AB)−Xe(2)–F(9)	176.8(4)
O(1)–W(1)−F(4)	178.8(2)	F(3A)---Xe(1)–F(6A)	72.5(2)	F(8AB)−Xe(2)–F(9AB)	88.3(3)
F(1)–W(1)–F(2)	89.3(1)	F(3A)---Xe(1)–F(7)	141.6(3)	F(8AB)−Xe(2)–O(2)	94.0(2)
F(1)–W(1)–F(2A)	89.3(1)	F(5)–Xe(1)–F(5A)	88.6(4)	F(9)−Xe(2)–F(9AB)	89.4(4)
F(1)–W(1)–F(3)	165.8(2)	F(5)–Xe(1)–F(6)	88.1(3)	F(9)−Xe(2)–O(2)	88.2(4)
F(1)–W(1)−F(4)	82.9(2)	F(5)–Xe(1)–F(6A)	160.1(3)	F(9AB)−Xe(2)–O(2)	92.5(3)
F(2)–W(1)–F(2A)	164.4(2)	F(5)–Xe(1)–F(7)	79.9(3)	F(1)---Xe(2)–F(8B)	98.6(1)
F(2)–W(1)–F(3)	88.8(1)	F(5A)–Xe(1)–F(6)	160.1(3)	F(1)---Xe(2)–F(8AB)	109.3(4)
F(2)–W(1)−F(4)	82.20(9)	F(5A)–Xe(1)–F(6A)	88.1(3)	F(1)---Xe(2)–F(9B)	78.5(4)
F(2A)–W(1)–F(3)	88.8(1)	F(5A)–Xe(1)–F(7)	79.9(3)	F(1)---Xe(2)–F(9AB)	70.5(1)
F(2A)–W(1)−F(4)	82.20(9)	F(6)–Xe(1)–F(6A)	88.4(4)	F(8B)−Xe(2)–F(8A)	90.1(6)
F(3)–W(1)−F(4)	82.9(2)	F(6)–Xe(1)–F(7)	80.3(3)	F(8B)−Xe(2)–F(9B)	176.8(4)
W(1)−F(4)---Xe(1)	148.6(3)	F(6A)–Xe(1)–F(7)	80.3(3)	F(8B)−Xe(2)–F(9A)	88.2(3)
W(1)−F(3)---Xe(1A)	158.1(4)	F(1)---Xe(2)–F(8)	109.3(4)	F(8B)−Xe(2)–O(2)	94.0(2)
W(1)−F(1)---Xe(2)	164.0(4)	F(1)---Xe(2)–F(8A)	98.6(1)	F(8A)−Xe(2)–F(9B)	178.3(3)
F(4)---Xe(1)---F(3A)	73.4(2)	F(1)---Xe(2)–F(9)	78.5(4)	F(8A)−Xe(2)–F(9A)	92.2(3)
F(4)---Xe(1)–F(5)	75.3(2)	F(1)---Xe(2)–F(9A)	70.5(1)	F(8A)−Xe(2)–O(2)	88.0(3)
F(4)---Xe(1)–F(5A)	75.3(2)	F(1)---Xe(2)–O(2)	158.3(4)	F(9B)−Xe(2)–F(9A)	89.4(4)
F(4)---Xe(1)–F(6)	122.6(2)	F(8)−Xe(2)–F(8AB)	90.1(6)	F(9B)−Xe(2)–O(2)	92.5(3)
F(4)---Xe(1)–F(6A)	122.6(2)			F(9A)−Xe(2)–O(2)	88.2(3)

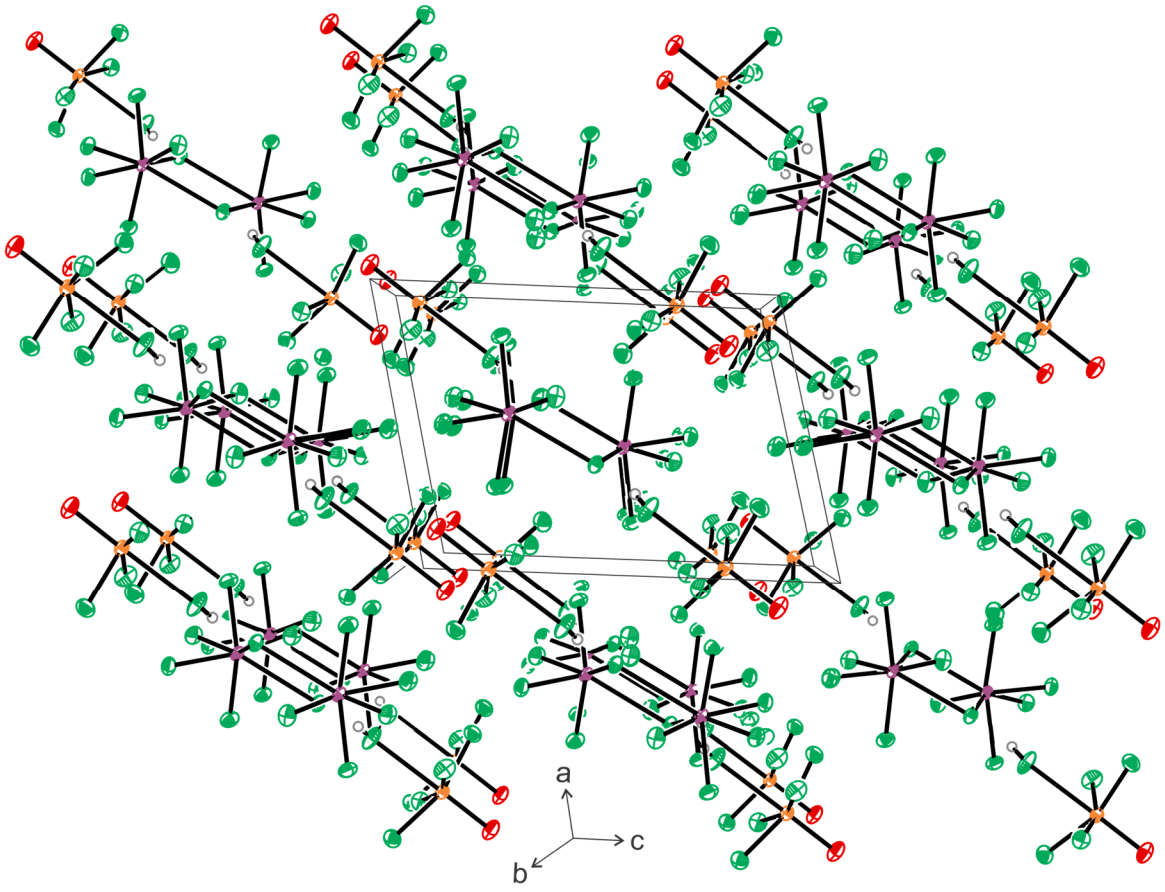

Figure A8.4. A packing diagram showing the X-ray crystal structure of $[XeF_5][HF_2]\cdot CrOF_4$ (**2**) viewed along the *b*-axis of the unit cell; thermal ellipsoids are drawn at the 50% probability level.

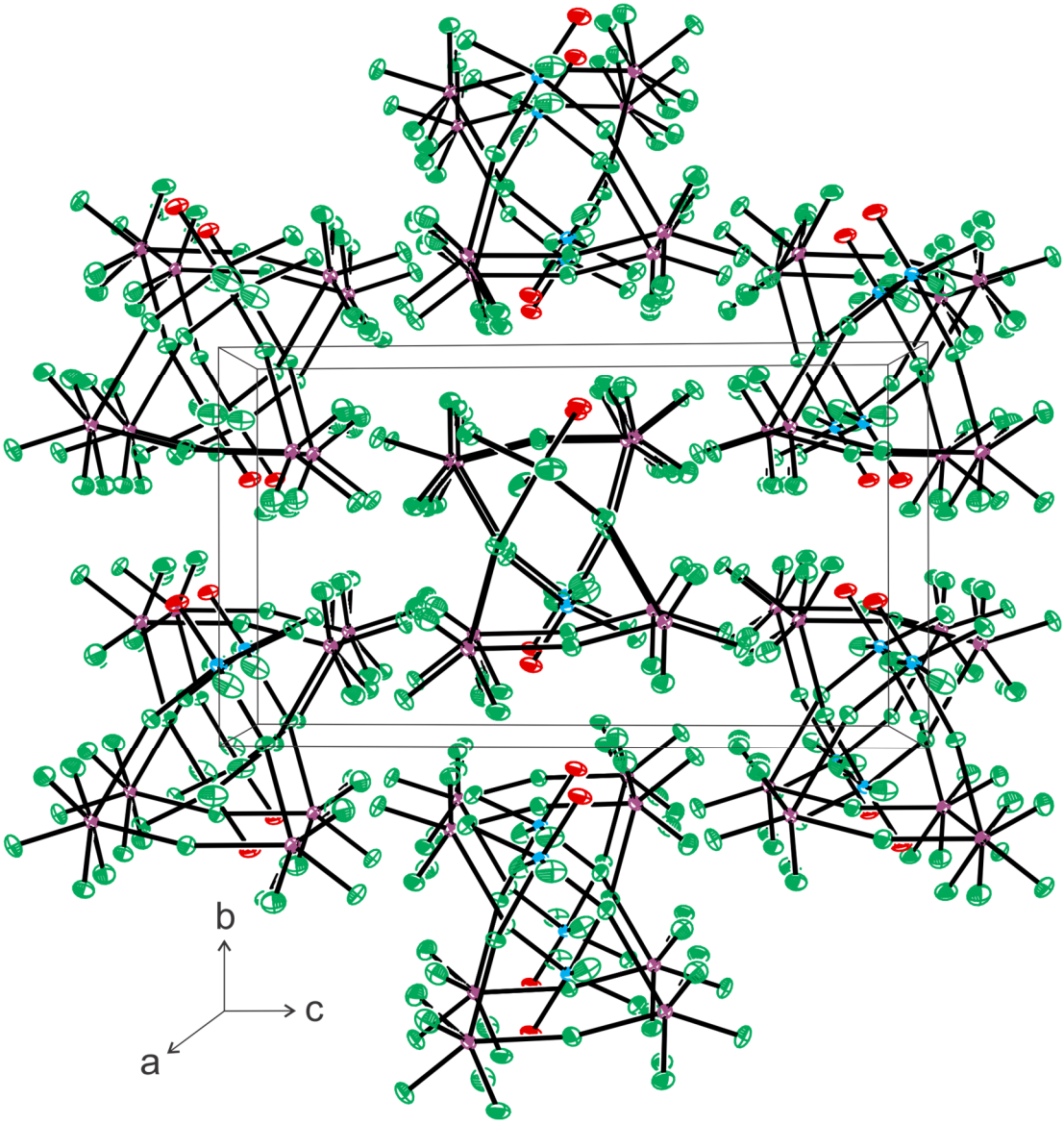

Figure A8.5. A packing diagram showing the X-ray crystal structure of $[Xe_2F_{11}][MoOF_5]$ (**3**) viewed along the *a*-axis of the unit cell; thermal ellipsoids are drawn at the 50% probability level. The packing diagram of isotypic **4** is not shown.

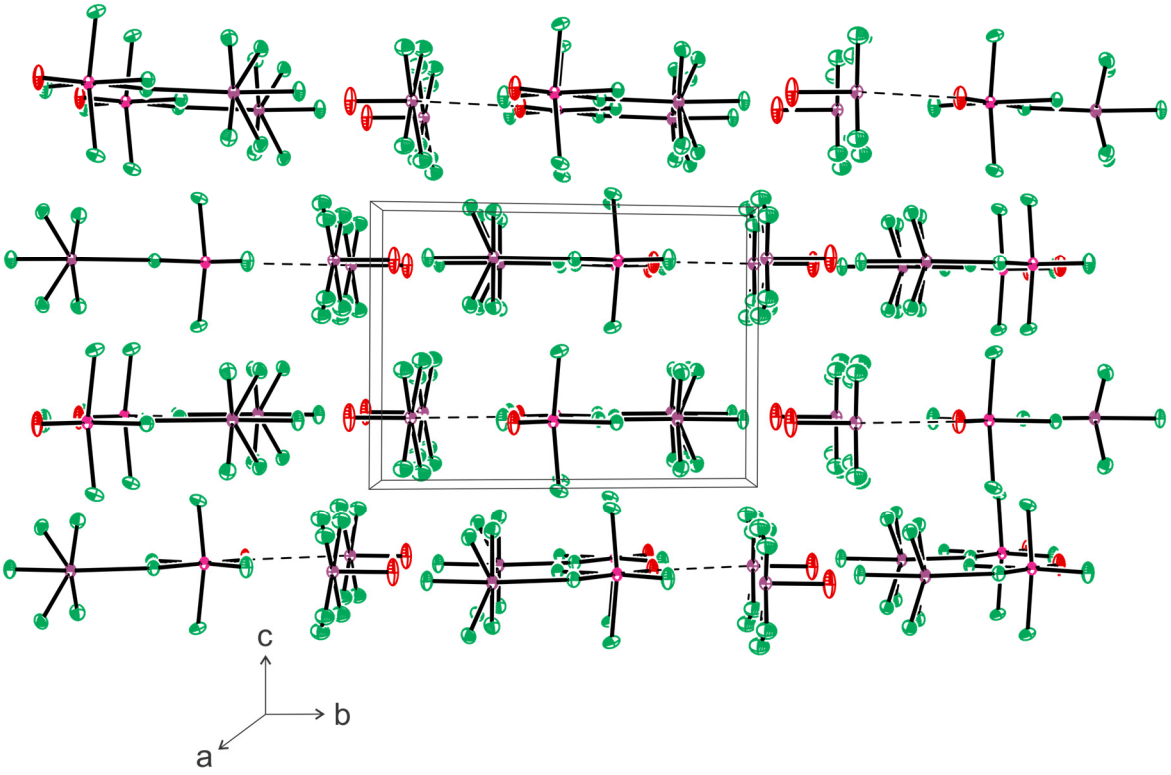

Figure A8.6. A packing diagram showing the X-ray crystal structure of $[XeF_5][WOF_5]\cdot XeOF_4$ (**7**) viewed along the *a*-axis of the unit cell; thermal ellipsoids are drawn at the 50% probability level.

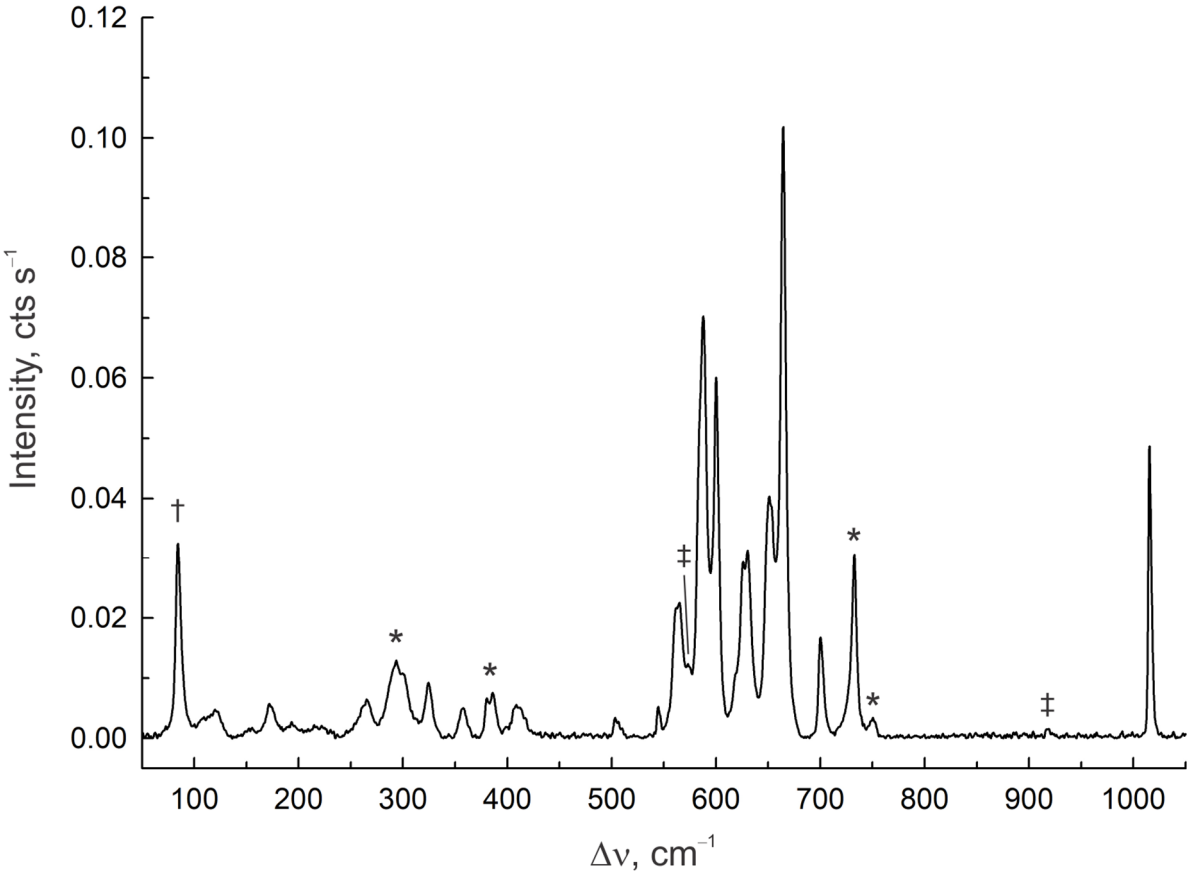

Figure A8.7. Raman spectrum of crystalline $[Xe_2F_{11}][WOF_5]$ (**4**) recorded at −140 °C using 1064-nm excitation. Symbols denote an instrumental artifact (†), FEP sample tube bands (*) and bands assigned to a trace amount of $XeOF_4$ impurity (‡).

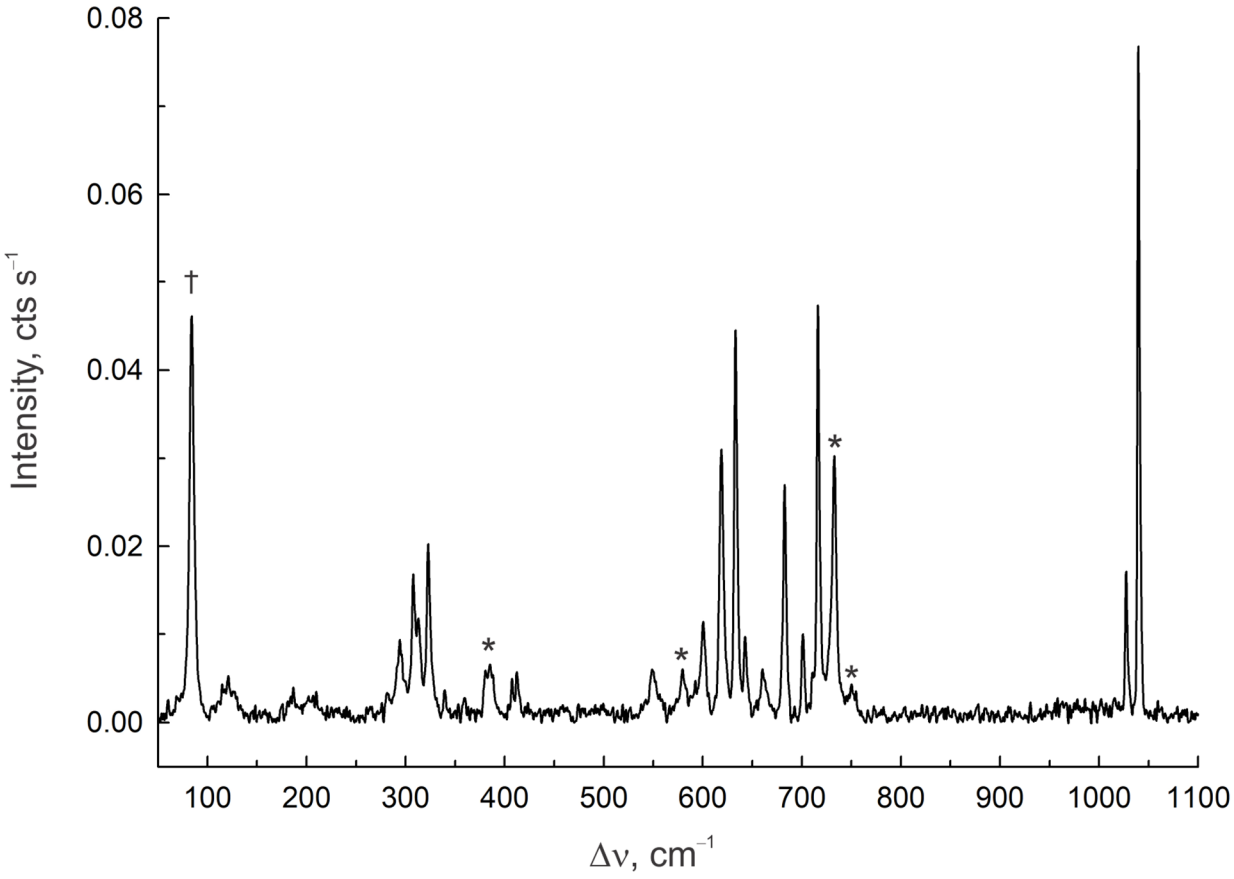

Figure A8.8. Raman spectrum of crystalline $[XeF_5][W_2O_2F_9]$ (**6**) recorded at −140 °C using 1064-nm excitation. Symbols denote an instrumental artifact (†) and FEP sample tube bands (*).

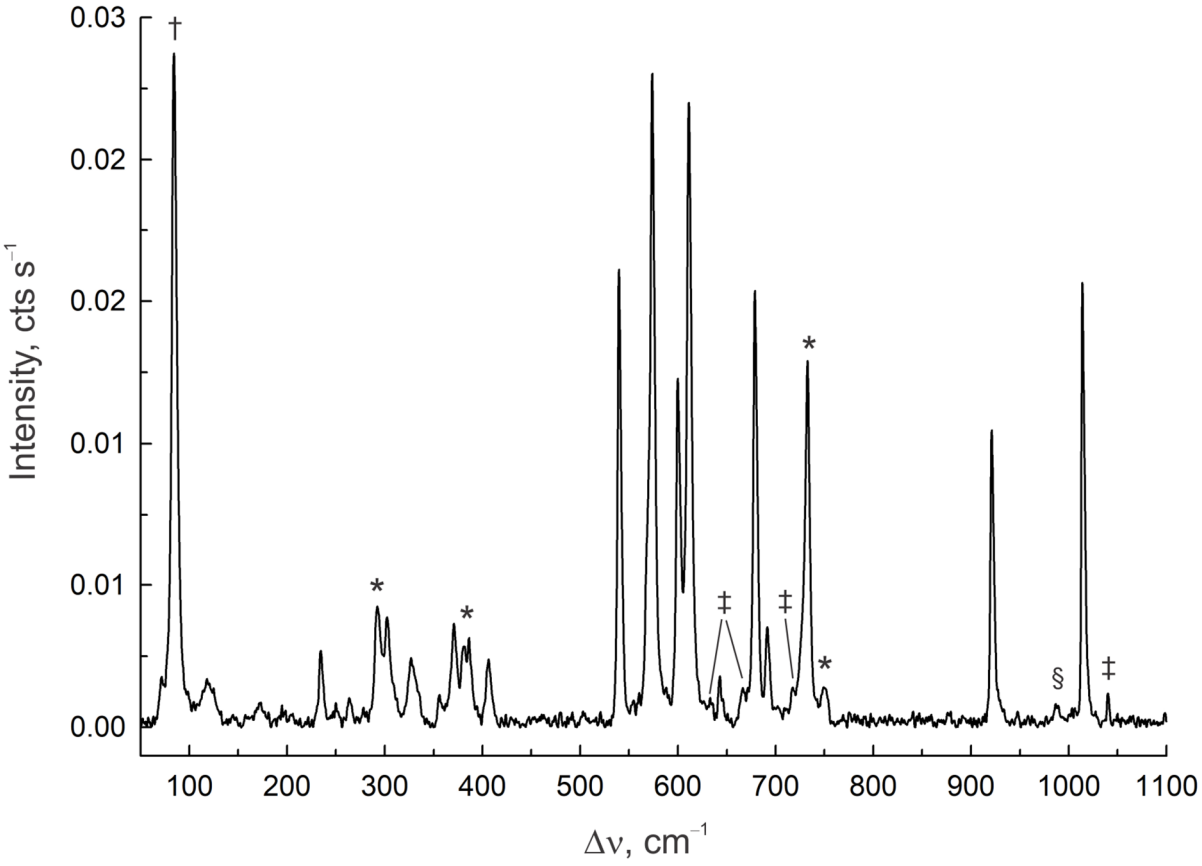

Figure A8.9. Raman spectrum of crystalline $[XeF_5][WOF_5]\cdot XeOF_4$ (**7**) recorded at −140 °C using 1064-nm excitation. Symbols denote an instrumental artifact (†), FEP sample tube bands (*), Raman bands assigned to $[XeF_5][W_2O_2F_9]$ and $[Xe_2F_{11}][WOF_5]$ (‡) impurities, and a W–O stretching band tentatively assigned to the $[WOF_6]^{2-}$ salt of $[XeF_5]^+$ or $[Xe_2F_{11}]^+$ (§). The latter band was assigned by comparison to the ν(W-O) stretching band reported for $[NO]_2[WOF_6]$ in *Inorg. Chem.* **1975**, *14*, 1822–1830.

Table A8.7. Experimental Raman frequencies and calculated[a] vibrational frequencies, intensities, and assignments for $[Xe_2F_{11}][CrOF_5]$ (**1**) and $\{[Xe_2F_{11}][CrOF_5]\}_2$ (**1'**)

1 [a,b]	**1'** [a,c]	**assgnts (*C*i)** [d]
951(19)	1225(63)[0]	[ν(Cr_1-O_1) + ν(Cr_{1A}-O_{1A})]
	1225(0)[339]	[ν(Cr_1-O_1) – ν(Cr_{1A}-O_{1A})]
	750(0)[510]	[ν(Cr_1-F_4) + ν(Cr_{1A}-F_{2A})] – [ν(Cr_{1A}-F_{4A}) + ν(Cr_1-F_2)]
715(3)	750(6)[0]	[ν(Cr_1-F_4) + ν(Cr_{1A}-F_{4A})] – [ν(Cr_1-F_2) + ν(Cr_{1A}-F_{2A})]
	706(0)[631]	[ν(Cr_1-F_3) + ν(Cr_{1A}-F_{1A})] – [ν(Cr_{1A}-F_{3A}) + ν(Cr_1-F_1)]
677(4)	699(<1)[0]	[ν(Cr_1-F_3) + ν(Cr_{1A}-F_{3A})] – [ν(Cr_1-F_1) + ν(Cr_{1A}-F_{1A})]
652(55)[e]	698(22)[0]	[ν(Cr_1-F_{4eq}) + ν(Cr_{1A}-F_{4eq})]
	696(0)[124]	[ν(Cr_1-F_{4eq}) – ν(Cr_{1A}-F_{4eq})]
652(55)[e]	672(30)[0]	[ν(Xe_1-F_9) + ν(Xe_2-F_{13}) + ν(Xe_{1A}-F_{9A}) + ν(Xe_{2A}-F_{13A})] – [ν(Xe_1-F_7) + ν(Xe_2-F_{15}) + ν(Xe_{1A}-F_{7A}) + ν(Xe_{2A}-F_{15A})]
	669(0)[639]	[ν(Xe_1-F_7) + ν(Xe_2-F_{13}) + ν(Xe_{1A}-F_{9A}) + ν(Xe_{2A}-F_{15A})] – [ν(Xe_1-F_9) + ν(Xe_2-F_{15}) + ν(Xe_{1A}-F_{7A}) + ν(Xe_{2A}-F_{13A})]
640(100)	659(241)[0]	[ν(Xe_1-F_6) + ν(Xe_2-F_{12}) + ν(Xe_{1A}-F_{6A}) + ν(Xe_{2A}-F_{12A})]
	654(0)[110]	[ν(Xe_1-F_6) + ν(Xe_1-F_9) + ν(Xe_1-F_{10}) + ν(Xe_2-F_{14}) + ν(Xe_2-F_{15}) + ν(Xe_{1A}-F_{7A}) + ν(Xe_{1A}-F_{8A}) + ν(Xe_{2A}-F_{12A}) + ν(Xe_{2A}-F_{13A}) + ν(Xe_{2A}-F_{16A})] – [ν(Xe_1-F_7) + ν(Xe_1-F_8) + ν(Xe_2-F_{12}) + ν(Xe_2-F_{13}) + ν(Xe_2-F_{16}) + ν(Xe_{1A}-F_{6A}) + ν(Xe_{1A}-F_{9A}) + ν(Xe_{1A}-F_{10A}) + ν(Xe_{2A}-F_{14A}) + ν(Xe_{2A}-F_{15A})]
	651(0)[91]	[ν(Xe_1-F_6) + ν(Xe_1-F_8) + ν(Xe_2-F_{12}) + ν(Xe_2-F_{14})] – [ν(Xe_{1A}-F_{6A}) + ν(Xe_{1A}-F_{8A}) + ν(Xe_{2A}-F_{12A}) + ν(Xe_{2A}-F_{14A})]
	646(0)[468]	[ν(Xe_1-F_6) + ν(Xe_2-F_{16}) + ν(Xe_{2A}-F_{12A}) + ν(Xe_{2A}-F_{14A}) + ν(Xe_{2A}-F_{15A})] – [ν(Xe_{1A}-F_{6A}) + ν(Xe_{2A}-F_{16A}) + ν(Xe_2-F_{12}) + ν(Xe_2-F_{14}) + ν(Xe_2-F_{15})]
	646(0)[388]	[ν(Xe_1-F_7) + (Xe_1-F_8) + ν(Xe_{1A}-F_{9A}) + ν(Xe_{1A}-F_{10A}) + ν(Xe_{2A}-F_{12A}) + ν(Xe_{2A}-F_{13A}) + ν(Xe_{2A}-F_{16A})] – [ν(Xe_1-F_9) + ν(Xe_1-F_{10}) + ν(Xe_2-F_{12}) + ν(Xe_2-F_{13}) + ν(Xe_2-F_{16}) + ν(Xe_{1A}-F_{7A}) + ν(Xe_{1A}-F_{8A})]
627(15)	644(12)[0]	[ν(Xe_1-F_8) + (Xe_2-F_{14}) + ν(Xe_{1A}-F_{8A}) + ν(Xe_{2A}-F_{14A})] – [ν(Xe_1-F_{10}) + (Xe_2-F_{16}) + ν(Xe_{1A}-F_{10A}) + ν(Xe_{2A}-F_{16A})]
633(64)	643(56)[0]	[ν(Xe_1-F_6) + ν(Xe_{1A}-F_{6A})] – [ν(Xe_2-F_{12}) + ν(Xe_{2A}-F_{12A})]
	637(0)[6]	[ν(Xe_1-F_7) + (Xe_1-F_{10}) + ν(Xe_2-F_{15}) + ν(Xe_2-F_{16}) + ν(Xe_{1A}-F_{9A}) + ν(Xe_{2A}-F_{13A})] – [ν(Xe_1-F_9) + ν(Xe_2-F_{13}) + ν(Xe_{1A}-F_{7A}) + ν(Xe_{1A}-F_{10A}) + ν(Xe_{2A}-F_{15A}) + ν(Xe_{2A}-F_{16A})]

continued…

Table A8.7. (continued)

1 [a,b]	**1'** [a,c]	**assgnts (C_i)** [d]
610(10)	634(9)[0]	$[\nu(Xe_1\text{-}F_7) + (Xe_1\text{-}F_{10}) + \nu(Xe_2\text{-}F_{13}) + \nu(Xe_2\text{-}F_{14}) + \nu(Xe_{1A}\text{-}F_{7A}) + \nu(Xe_{1A}\text{-}F_{10A}) + \nu(Xe_{2A}\text{-}F_{13A}) + \nu(Xe_{2A}\text{-}F_{14A})] - [\nu(Xe_1\text{-}F_8) + \nu(Xe_1\text{-}F_9) + \nu(Xe_2\text{-}F_{15}) + \nu(Xe_2\text{-}F_{16}) + \nu(Xe_{1A}\text{-}F_{8A}) + \nu(Xe_{1A}\text{-}F_{9A}) + \nu(Xe_{2A}\text{-}F_{15A}) + \nu(Xe_{2A}\text{-}F_{16A})]$
608(10)	628(2)[0]	$[\nu(Xe_1\text{-}F_7) + (Xe_1\text{-}F_8) + \nu(Xe_2\text{-}F_{13}) + \nu(Xe_2\text{-}F_{16}) + \nu(Xe_{1A}\text{-}F_{7A}) + \nu(Xe_{1A}\text{-}F_{8A}) + \nu(Xe_{2A}\text{-}F_{13A}) + \nu(Xe_{2A}\text{-}F_{16A})] - [\nu(Xe_1\text{-}F_9) + \nu(Xe_1\text{-}F_{10}) + \nu(Xe_2\text{-}F_{14}) + \nu(Xe_2\text{-}F_{15}) + \nu(Xe_{1A}\text{-}F_{9A}) + \nu(Xe_{1A}\text{-}F_{10A}) + \nu(Xe_{2A}\text{-}F_{14A}) + \nu(Xe_{2A}\text{-}F_{15A})]$
	603(0)[33]	$[\nu(Xe_1\text{-}F_6) + \nu(Xe_2\text{-}F_{13}) + \nu(Xe_2\text{-}F_{15}) + \nu(Xe_{2A}\text{-}F_{12A}) + \nu(Xe_{1A}\text{-}F_{7A}) + \nu(Xe_{1A}\text{-}F_{9A})] - [\nu(Xe_1\text{-}F_7) + \nu(Xe_1\text{-}F_9) + (Xe_2\text{-}F_{12}) + \nu(Xe_{1A}\text{-}F_{6A}) + \nu(Xe_{2A}\text{-}F_{13A}) + \nu(Xe_{2A}\text{-}F_{15A})]$
592(32)	599(33)[0]	$[\nu(Xe_1\text{-}F_6) + (Xe_2\text{-}F_{12}) + \nu(Xe_{1A}\text{-}F_{6A}) + \nu(Xe_{2A}\text{-}F_{12A})] - [\nu(Xe_1\text{-}F_7) + \nu(Xe_1\text{-}F_9) + \nu(Xe_2\text{-}F_{13}) + \nu(Xe_2\text{-}F_{15}) + \nu(Xe_{1A}\text{-}F_{7A}) + \nu(Xe_{1A}\text{-}F_{9A}) + \nu(Xe_{2A}\text{-}F_{13A}) + \nu(Xe_{2A}\text{-}F_{15A})]$
587(32)	599(5)[0]	$[\nu(Xe_1\text{-}F_6) + (Xe_2\text{-}F_{4eq}) + \nu(Xe_{2A}\text{-}F_{4eq}) + \nu(Xe_{1A}\text{-}F_{6A})] - [\nu(Xe_1\text{-}F_{4eq}) + (Xe_2\text{-}F_{12}) + \nu(Xe_{1A}\text{-}F_{4eq}) + \nu(Xe_{2A}\text{-}F_{12A})]$
	595(0)[1]	$[\nu(Xe_1\text{-}F_6) + (Xe_2\text{-}F_{12}) + \nu(Xe_{1A}\text{-}F_{4eq}) + \nu(Xe_{2A}\text{-}F_{4eq})] - [\nu(Xe_1\text{-}F_{4eq}) + (Xe_2\text{-}F_{4eq}) + \nu(Xe_{1A}\text{-}F_{6A}) + \nu(Xe_{2A}\text{-}F_{12A})]$
	587(0)[1]	$[\nu(Xe_1\text{-}F_7) + \nu(Xe_1\text{-}F_9) + \nu(Xe_2\text{-}F_{14}) + \nu(Xe_2\text{-}F_{16}) + \nu(Xe_{1A}\text{-}F_{8A}) + \nu(Xe_{1A}\text{-}F_{10A}) + \nu(Xe_{2A}\text{-}F_{13A}) + \nu(Xe_{2A}\text{-}F_{15A})] - [\nu(Xe_1\text{-}F_6) + \nu(Xe_1\text{-}F_8) + \nu(Xe_2\text{-}F_{13}) + \nu(Xe_2\text{-}F_{15}) + \nu(Xe_{1A}\text{-}F_{7A}) + \nu(Xe_{1A}\text{-}F_{9A}) + \nu(Xe_{2A}\text{-}F_{14A}) + \nu(Xe_{2A}\text{-}F_{16A})]$
584(39)	585(41)[0]	$[\nu(Xe_1\text{-}F_7) + \nu(Xe_1\text{-}F_9) + \nu(Xe_2\text{-}F_{13}) + \nu(Xe_2\text{-}F_{15}) + \nu(Xe_{1A}\text{-}F_{7A}) + \nu(Xe_{1A}\text{-}F_{9A}) + \nu(Xe_{2A}\text{-}F_{14A}) + \nu(Xe_{2A}\text{-}F_{16A})] - [\nu(Xe_1\text{-}F_6) + \nu(Xe_1\text{-}F_8) + \nu(Xe_2\text{-}F_{14}) + \nu(Xe_2\text{-}F_{16}) + \nu(Xe_{1A}\text{-}F_{8A}) + \nu(Xe_{1A}\text{-}F_{10A}) + \nu(Xe_{2A}\text{-}F_{13A}) + \nu(Xe_{2A}\text{-}F_{15A})]$
568(22)	582(11)[0]	$[\nu(Xe_1\text{-}F_7) + \nu(Xe_1\text{-}F_9) + \nu(Xe_2\text{-}F_{14}) + \nu(Xe_2\text{-}F_{16}) + \nu(Xe_{1A}\text{-}F_{8A}) + \nu(Xe_{1A}\text{-}F_{10A}) + \nu(Xe_{2A}\text{-}F_{13A}) + \nu(Xe_{2A}\text{-}F_{15A})] - [\nu(Xe_1\text{-}F_6) + \nu(Xe_1\text{-}F_8) + \nu(Xe_2\text{-}F_{13}) + \nu(Xe_2\text{-}F_{15}) + \nu(Xe_{1A}\text{-}F_{7A}) + \nu(Xe_{1A}\text{-}F_{9A}) + \nu(Xe_{2A}\text{-}F_{14A}) + \nu(Xe_{2A}\text{-}F_{16A})]$
	581(0)[<0.1]	$[\nu(Xe_1\text{-}F_7) + \nu(Xe_1\text{-}F_9) + \nu(Xe_2\text{-}F_{13}) + \nu(Xe_2\text{-}F_{15}) + \nu(Xe_{1A}\text{-}F_{8A}) + \nu(Xe_{1A}\text{-}F_{10A}) + \nu(Xe_{2A}\text{-}F_{14A}) + \nu(Xe_{2A}\text{-}F_{16A})] - [\nu(Xe_1\text{-}F_6) + \nu(Xe_1\text{-}F_8) + \nu(Xe_2\text{-}F_{14}) + \nu(Xe_2\text{-}F_{16}) + \nu(Xe_{1A}\text{-}F_{7A}) + \nu(Xe_{1A}\text{-}F_{9A}) + \nu(Xe_{2A}\text{-}F_{13A}) + \nu(Xe_{2A}\text{-}F_{15A})]$
	556(0)[24]	$[\nu(Cr_1\text{-}F_1) + \nu(Cr_1\text{-}F_3) + \nu(Cr_{1A}\text{-}F_{2A}) + \nu(Cr_{1A}\text{-}F_{4A})] - [\nu(Cr_1\text{-}F_2) + \nu(Cr_1\text{-}F_4) + \nu(Cr_{1A}\text{-}F_{1A}) + \nu(Cr_{1A}\text{-}F_{3A})]$
527(3)	553(8)[0]	$[\nu(Cr_1\text{-}F_1) + \nu(Cr_1\text{-}F_3) + \nu(Cr_{1A}\text{-}F_{1A}) + \nu(Cr_{1A}\text{-}F_{3A})] - [\nu(Cr_1\text{-}F_2) + \nu(Cr_1\text{-}F_4) + \nu(Cr_{1A}\text{-}F_{2A}) + \nu(Cr_{1A}\text{-}F_{4A})]$
	410(0)[88]	$[\delta(F_6Xe_1F_{10}) + \delta(F_{12A}Xe_{2A}F_{16A}) + \delta(F_{11}Xe_2F_{16})] - [\delta(F_{6A}Xe_{1A}F_{8A}) + \delta(F_{12}Xe_2F_{16}) + \delta(F_{11A}Xe_{1A}F_{16A})]$
421, sh	406(4)[0]	$[\delta(F_6Xe_1F_{10}) - \delta(F_{12}Xe_2F_{16})] + [\delta(F_{6A}Xe_{1A}F_{10A}) - \delta(F_{12A}Xe_{2A}F_{16A})]$
419(3)	405(4)[0]	$[\delta(Xe_1F_6F_7F_{10}) + \delta(Xe_2F_{12}F_{15}F_{16}) + \delta(Xe_{1A}F_{6A}F_{7A}F_{10A}) + \delta(Xe_{2A}F_{12A}F_{15A}F_{16A})$
	403(0)[3]	$[\delta(F_6Xe_1F_{10}) + \delta(F_{12}Xe_2F_{16})] - [\delta(F_{6A}Xe_{1A}F_{10A}) + \delta(F_{12A}Xe_{2A}F_{16A})]$

continued…

Table A8.7. (continued)

1 [a,b]	**1'** [a,c]	**assgnts (*C*i)** [d]
407(2)	401(4)[0]	$[\delta(F_1Cr_1F_2) + \delta(F_3Cr_1F_4)] + [\delta(F_{1A}Cr_{1A}F_{2A}) + \delta(F_{3A}Cr_{1A}F_{4A})]$
	399(0)[142]	$[\delta(F_6Xe_1F_7) - \delta(F_{12}Xe_2F_{15})] - [\delta(F_{6A}Xe_{1A}F_{7A}) - \delta(F_{12A}Xe_{2A}F_{15A})]$
	398(0)[<0.1]	$[\delta(F_1Cr_1F_2) + \delta(F_3Cr_1F_4)] - [\delta(F_{1A}Cr_{1A}F_{2A}) + \delta(F_{3A}Cr_{1A}F_{4A})]$
	396(2)[0]	$[\delta(F_6Xe_1F_9) + \delta(F_{12}Xe_2F_{13}) + \delta(F_{6A}Xe_{1A}F_{9A}) + \delta(F_{12A}Xe_{2A}F_{13A})]$
	394(0)[11]	$[\delta(O_1Cr_1F_4) + \delta(O_{1A}Cr_{1A}F_{2A})] - [\delta(O_1Cr_1F_2) + \delta(O_{1A}Cr_{1A}F_{4A})]$
371(7)	393(5)[0]	$[\delta(O_1Cr_1F_4) + \delta(O_{1A}Cr_{1A}F_{4A})] - [\delta(O_1Cr_1F_2) + \delta(O_{1A}Cr_{1A}F_{2A})]$
	392(0)[47]	$[\delta(F_6Xe_1F_9) + \delta(F_{12}Xe_2F_{13})] - [\delta(F_{6A}Xe_{1A}F_{9A}) + \delta(F_{12A}Xe_{2A}F_{13A})]$
	391(<1)[0]	$[\delta(F_6Xe_1F_7) - \delta(F_{12}Xe_2F_{13})] + [\delta(F_{6A}Xe_{1A}F_{7A}) - \delta(F_{12A}Xe_{2A}F_{13A})]$
	377(0)[22]	$[\delta(O_1Cr_1F_1) + \delta(O_{1A}Cr_{1A}F_{3A})] - [\delta(O_1Cr_1F_3) + \delta(O_{1A}Cr_{1A}F_{1A})]$
365, sh	377(7)[0]	$[\delta(O_1Cr_1F_1) + \delta(O_{1A}Cr_{1A}F_{1A})] - [\delta(O_1Cr_1F_3) + \delta(O_{1A}Cr_{1A}F_{3A})]$
362(12)	373(9)[0]	$[\delta_{umb}(O_1Cr_1F_{4eq}) + \delta_{umb}(O_{1A}Cr_{1A}F_{4eq})]$
	374(0)[34]	$[\delta_{umb}(O_1Cr_1F_{4eq}) - \delta_{umb}(O_{1A}Cr_{1A}F_{4eq})]$
350(5)	360(6)[0]	$[\delta_{umb}(Xe_1F_{4eq}) + \delta_{umb}(Xe_2F_{4eq})] + [\delta_{umb}(Xe_{1A}F_{4eq}) + \delta_{umb}(Xe_{2A}F_{4eq})]$
	358(3)[0]	$[\nu(Xe_1\text{-}F_5) + \nu(Xe_1\text{-}F_{11}) + \nu(Xe_{1A}\text{-}F_{5A}) + \nu(Xe_{1A}\text{-}F_{11A})] - [\nu(Xe_2\text{-}F_{5A}) + \nu(Xe_2\text{-}F_{11}) + \nu(Xe_{2A}\text{-}F_5) + \nu(Xe_{2A}\text{-}F_{11A})]$
	353(0)[86]	$[\nu(Xe_{1A}\text{-}F_{11A}) + \nu(Xe_2\text{-}F_{11})] - [\nu(Xe_1\text{-}F_{11}) + \nu(Xe_{2A}\text{-}F_{11A})] + [\nu(Cr_1\text{-}F_5) - \nu(Cr_{1A}\text{-}F_{5A})]$
	352(0)[30]	$[\delta_{umb}(Xe_1F_{4eq}) + \delta_{umb}(Xe_2F_{4eq})] - [\delta_{umb}(Xe_{1A}F_{4eq}) + \delta_{umb}(Xe_{2A}F_{4eq})]$
	346(0)[666]	$[\delta_{umb}(Xe_1F_{4eq}) + \delta_{umb}(Xe_{2A}F_{4eq})] - [\delta_{umb}(Xe_2F_{4eq}) + \delta_{umb}(Xe_{1A}F_{4eq})] + [\nu(Xe_{1A}\text{-}F_{11A}) + \nu(Xe_2\text{-}F_{11})] - [\nu(Xe_1\text{-}F_{11}) + \nu(Xe_{2A}\text{-}F_{11A})]$
341(6)	341(<1)[0]	$[\delta_{umb}(Xe_1F_{4eq}) + \delta_{umb}(Xe_{1A}F_{4eq})] - [\delta_{umb}(Xe_2F_{4eq}) + \delta_{umb}(Xe_{2A}F_{4eq})]$
	329(0)[383]	$[\nu(Xe_1\text{-}F_5) + \nu(Xe_2\text{-}F_{5A})] - [\nu(Xe_{2A}\text{-}F_5) + \nu(Xe_{1A}\text{-}F_{5A})]$

continued…

Table A8.7. (continued)

1 [a,b]	**1'** [a,c]	**assgnts (C_i)** [d]
	318(0)[<0.1]	$[\rho_w(F_1Cr_1F_3) - \rho_w(F_{1A}Cr_{1A}F_{3A})] / [\delta(F_2Cr_1F_5) + \delta(F_5Cr_1F_4)] + [\delta(F_{2A}Cr_{1A}F_{5A}) + \delta(F_{5A}Cr_{1A}F_{4A})]$
323(5)	318(7)[0]	$[\rho_w(F_1Cr_1F_3) + \rho_w(F_{1A}Cr_{1A}F_{3A})] / \{[\delta(F_5Xe_1F_{11}) + \delta(F_{11}Xe_2F_{5A})] + [\delta(F_{5A}Xe_{1A}F_{11A}) + \delta(F_{11A}Xe_{2A}F_5)]\}_{small}$
314(4)	301(4)[0]	$[\nu(Xe_1\text{-}F_{11}) + \nu(Xe_2\text{-}F_{11})] - [\nu(Xe_{1A}\text{-}F_{11A}) + \nu(Xe_{2A}\text{-}F_{11A})]$
312, sh	293(3)[0]	$[\delta(F_7Xe_1F_8) + \delta(F_9Xe_1F_{10})] + [\delta(F_{14}Xe_2F_{15}) + \delta(F_{13}Xe_2F_{16})] + [\delta(F_{7A}Xe_{1A}F_{8A}) + \delta(F_{9A}Xe_{1A}F_{10A})] + [\delta(F_{14A}Xe_{2A}F_{15A}) + \delta(F_{13A}Xe_{2A}F_{16A})]$
	292(0)[34]	$[\delta(F_7Xe_1F_8) + \delta(F_9Xe_1F_{10})] + [\delta(F_{14}Xe_2F_{15}) + \delta(F_{13}Xe_2F_{16})] + [\delta(F_{7A}Xe_{1A}F_{10A}) + \delta(F_{8A}Xe_{1A}F_{9A})] + [\delta(F_{13A}Xe_{2A}F_{14A}) + \delta(F_{15A}Xe_{2A}F_{16A})]$
	291(0)[19]	$[\delta(F_{10}Xe_1F_{11}) - \delta(F_{11}Xe_2F_{16})] - [\delta(F_{10A}Xe_{2A}F_{11A}) - \delta(F_{11A}Xe_{2a}F_{16A})] / [\delta(F_7Xe_1F_5) + \delta(F_{7A}Xe_{1A}F_{5A})] + [\delta(F_{15}Xe_2F_{5A}) + \delta(F_{15A}Xe_{2A}F_5)]$
	274(0)[22]	$[\delta(F_7Xe_1F_8) + \delta(F_9Xe_1F_{10}) + \delta(F_{13}Xe_2F_{14}) + \delta(F_{15}Xe_2F_{16})] - [\delta(F_{7A}Xe_{1A}F_{8A}) + \delta(F_{9A}Xe_{1A}F_{10A}) + \delta(F_{13A}Xe_{2A}F_{14A}) + \delta(F_{15A}Xe_{2A}F_{16A})]$
278, sh	274(1)[0]	$[\delta(F_7Xe_1F_8) + \delta(F_9Xe_1F_{10}) + \delta(F_{13}Xe_2F_{14}) + \delta(F_{15}Xe_2F_{16})] + [\delta(F_{7A}Xe_{1A}F_{8A}) + \delta(F_{9A}Xe_{1A}F_{10A}) + \delta(F_{13A}Xe_{2A}F_{14A}) + \delta(F_{15A}Xe_{2A}F_{16A})]$
275(2)	273(4)[0]	$[\rho_t(F_7Xe_1F_{10}) + \rho_t(F_{15}Xe_2F_{16})] - [\rho_t(F_{7A}Xe_{1A}F_{10A}) + \rho_t(F_{15A}Xe_{2A}F_{16A})]$
261(2)	261(4)[0]	$[\nu(Xe_1\text{-}F_{11}) + \nu(Xe_{1A}\text{-}F_{11A})] - [\nu(Xe_2\text{-}F_{11}) + \nu(Xe_{2A}\text{-}F_{11A})]$
259(2)	258(3)[0]	$[\rho_r(F_5Xe_1F_{11}) + \rho_r(F_{5A}Xe_{1A}F_{11A})] / [\rho_t(F_8Xe_1F_9) + \rho_t(F_{8A}Xe_{1A}F_{9A})] - [\rho_w(F_{13}Xe_2F_{14}) + \rho_w(F_{13A}Xe_{2A}F_{14A})]$
	255(0)[2]	$[\rho_w(F_7Xe_1F_9) + \rho_w(F_8Xe_1F_{10}) + \rho_w(F_{13}Xe_2F_{15}) + \rho_w(F_{14}Xe_2F_{16})] + [\rho_w(F_{7A}Xe_{1A}F_{9A}) + \rho_w(F_{8A}Xe_{1A}F_{10A}) + \rho_w(F_{13A}Xe_{2A}F_{15A}) + \rho_w(F_{14A}Xe_{2A}F_{16A})]$
	251(0)[30]	$[\delta(F_5Xe_1F_8) + \delta(F_{5A}Xe_{1A}F_{8A})] - [\delta(F_5Xe_{2A}F_{14A}) + \delta(F_{5A}Xe_2F_{14})]$
	249(0)[31]	$[\rho_w(F_7Xe_1F_{11}) + \rho_w(F_{11}Xe_2F_{15})] - [\rho_w(F_{7A}Xe_{1A}F_{11A}) + \rho_w(F_{11A}Xe_{2A}F_{15A})]$
238(2)	246(2)[0]	$[\delta(F_5Xe_1F_{11}) + \delta(F_{11}Xe_2F_{5A})] + [\delta(F_{5A}Xe_{1A}F_{11A}) + \delta(F_{11A}Xe_{2A}F_5)]$
	238(0)[68]	$[\delta(F_{11}Xe_2F_{5A}) - \delta(F_{11A}Xe_{2A}F_5)$
	227(0)[13]	$[\rho_w(O_1Cr_1F_5) + \rho_w(F_{2A}Cr_{1A}F_{4A})] - [\rho_w(O_{1A}Cr_{1A}F_{5A}) + \rho_w(F_2Cr_1F_4)]$
233(2)	227(3)[0]	$[\nu(Cr_1\text{-}F_5) + \nu(Cr_{1A}\text{-}F_{5A})] - [\rho_w(F_1Cr_1F_3) + \rho_w(F_{1A}Cr_{1A}F_{3A})]$

continued…

Table A8.7. (continued)

1 [a,b]	**1'** [a,c]	**assgnts (C_i)** [d]
	221(<1)[0]	$[\nu(Xe_1\text{-}F_5) - \nu(Xe_1\text{-}F_{11})] + [\nu(Xe_{1A}\text{-}F_{5A}) - \nu(Xe_{1A}\text{-}F_{11A})] + [\nu(Xe_2\text{-}F_{11}) - \nu(Xe_2\text{-}F_5)] + [\nu(Xe_{2A}\text{-}F_{11A}) - \nu(Xe_{2A}\text{-}F_{5A})]$
	216(0)[4]	$[\rho_w(F_1Cr_1F_3) + \rho_w(F_{2A}Cr_{1A}F_{4A})] - [\rho_w(F_{1A}Cr_{1A}F_{3A}) + \rho_w(F_2Cr_1F_4)]$
	212(<1)[0]	$[\rho_t(F_7Xe_1F_8) + \rho_t(F_9Xe_1F_{10}) + \rho_t(F_{13}Xe_2F_{16}) + \rho_t(F_{14}Xe_2F_{15})] + [\rho_t(F_{7A}Xe_{1A}F_{8A}) + \rho_t(F_{9A}Xe_{1A}F_{10A}) + \rho_t(F_{13A}Xe_{2A}F_{16A}) + \rho_t(F_{14A}Xe_{2A}F_{15A})]$
216(3)	209(5)[0]	$[\nu(Cr_1\text{-}F_5) + \nu(Cr_{1A}\text{-}F_{5A})] - [\rho_w(F_2Cr_1F_4) + \rho_w(F_{2A}Cr_{1A}F_{4A})] + [\rho_w(F_1Cr_1F_3) + \rho_w(F_{1A}Cr_{1A}F_{3A})]_{small}$
	208(0)[13]	$[\rho_w(F_7Xe_1F_9) + \rho_w(F_{13}Xe_2F_{15})] + [\rho_w(F_{7a}Xe_{1a}F_{9a}) + \rho_w(F_{13a}Xe_{2a}F_{15a})]$
	204(0)[<1]	$[\delta(F_8Xe_1F_9) - \delta(F_{13A}Xe_{2A}F_{14A})] + [\delta(F_{13}Xe_2F_{14}) - \delta(F_{8A}Xe_{1A}F_{9A})]$
203(1)	201(3)[0]	$[\delta(F_8Xe_1F_9) - \delta(F_{13A}Xe_{2A}F_{14A})] - [\delta(F_{13}Xe_2F_{14}) - \delta(F_{8A}Xe_{1A}F_{9A})]$
	201(0)[3]	$[\delta(Xe_{1A}F_{5A}Xe_2) - \delta(Xe_1F_5Xe_{2A})]$
	197(1)[0]	$[\rho_w(O_1Cr_1F_5) + \rho_w(F_{2A}Cr_{1A}F_{4A}) + \rho_w(F_7Xe_1F_9) + \rho_w(F_{7A}Xe_{1A}F_{9A})] - [\rho_w(O_{1A}Cr_{1A}F_{5A}) + \rho_w(F_2Cr_1F_4) + \rho_w(F_{13}Xe_2F_{15}) + \rho_w(F_{13A}Xe_{2A}F_{15A})]$
	190(0)[<1]	$[\nu(Xe_1\text{-}F_{11}) + \nu(Xe_2\text{-}F_{11})] + [\nu(Xe_{1A}\text{-}F_{11A}) + \nu(Xe_{2A}\text{-}F_{11A})]$
	182(<1)[0]	$[(F_8Xe_1F_{11}) + \rho_w(F_{8A}Xe_{1A}F_{11A})] - [\rho_w(F_{11}Xe_2F_{14}) + \rho_w(F_{11A}Xe_{2A}F_{14A})]$
	180(0)[1]	$[\rho_t(F_8Xe_1F_{10}) + \rho_t(F_{14A}Xe_{2A}F_{16A}) + \delta(Xe_1F_{11}Xe_2)] - [\rho_t(F_{8A}Xe_{1A}F_{10A}) + \rho_t(F_{14}Xe_2F_{16}) + \delta(Xe_{1A}F_{11A}Xe_{2A})]$
174(2)	168(2)[0]	$[\delta(Xe_{1A}F_{5A}Xe_2) + \delta(Xe_1F_5Xe_{2A})] + [\delta(Xe_1F_{11}Xe_2) + \delta(Xe_{1A}F_{11A}Xe_{2a})]$
	137(<1)[0]	coupled deformation modes
	136(0)[7]	
	121(0)[6]	
	120(0)[27]	
	114(0)[2]	
	114(<1)[0]	

continued…

Table A8.7. (continued)

1 [a,b]	**1'** [a,c]	**assgnts (C_i)** [d]
	113(<1)[0]	
	108(<1)[0]	
	107(<1)[0]	
	103(0)[<1]	
	102(0)[2]	
	94(<1)[0]	
	94(<1)[0]	
	87(0)[1]	
	86(0)[<1]	
	77(<0.1)[0]	
	76(<1)[0]	
	72(0)[<1]	
	60(0)[<0.1]	coupled deformation modes
	58(<1)[0]	
	56(<1)[0]	
	50(0)[2]	
	47(0)[<0.1]	
	45(<1)[0]	
	38(<0.1)[0]	
	35(<1)[0]	
	34(0)[<1]	
	26(0)[<0.1]	
	11(<1)[0]	
	-4(0)[<0.1]	

continued…

Table A8.7. (continued)

[a] Frequencies are given in cm^{-1} and anion frequencies and mode descriptions are gray-highlighted. [b] Values in parentheses denote relative Raman intensities. Abbreviations denote shoulder (sh). The Raman spectrum was recorded in a FEP sample tube at −150 °C using 1064-nm excitation. A weak band and a shoulder were also observed at 1006(2), 667(6), 658(sh), and 374(sh) cm^{-1} and were tentatively assigned to a Cr oxide fluoride reduction product. [c] Values in parentheses and square brackets denote calculated Raman intensities ($Å^4$ amu^{-1}) and infrared intensities (km mol^{-1}), respectively. [d] Assignments are for the energy-minimized geometry (C_i) calculated using the PBE1PBE/Def2-SVP (F, O, Cr, Xe) levels of theory. [e] This band is attributed to overlapping ν(Cr-F_{4eq}) and ν(Xe-F_{eq}) stretching modes. Abbreviations denote stretch (ν), bend (δ), rock (ρ_r), twist (ρ_t), wag (ρ_w), umbrella (umb), and equatorial (eq). Bond elongations and angle openings are denoted by plus (+) signs, and bond contractions and angle compressions are denoted by minus (–) signs. The atom labeling scheme corresponds to that used in Figure 11.9.

Table A8.8. Experimental Raman frequencies and calculated vibrational frequencies, intensities, and assignments for $[Xe_2F_{11}][MoOF_5]$ (**3** and **3'**) and $[Xe_2F_{11}][WOF_5]$ (**4** and **4'**)

3' [a,b]	**3** [a,c]	**assgnts (C_1)** [d]	**4** [a,c,d]	**4'** [a,b]
1087(30)[186]	1002(31)	$\nu(M_1–O_1)$	1015(48)	1060(30)[160]
733(12)[195]	698, sh	$[\nu(Mo_1–F_2) + \nu(Mo_1–F_3)_{small}]$ // $[\nu(W_1–F_2) + \nu(W_1–F_3)]$	703, sh	717(15)[99]
727(5)[216]	695(35)	$[\nu(Mo_1–F_3) – \nu(Mo_1–F_2)_{small}]$ // $[\nu(W_1–F_3) – \nu(W_1–F_2)]$	700(17)	705(2)[212]
668(50)[65]	664(76)	$[\nu(Xe_1–F_6) + \nu(Xe_1–F_{10}) + \nu(Xe_2–F_{14}) + \nu(Xe_2–F_{16})] – [\nu(Xe_1–F_8) + \nu(Xe_2–F_{12})] – \nu(M_1–F_4)_{small}$	664(100)	669(47)[108]
664(34)[201]		$[\nu(Xe_1–F_8) + \nu(Xe_1–F_{10}) + \nu(Xe_2–F_{12}) + \nu(Xe_2–F_{16})] – [\nu(Xe_1–F_6) + \nu(Xe_2–F_{14})]$		666(48)[162]
661(6)[307]		$[\nu(Xe_1–F_9) – \nu(Xe_1–F_7)] + [\nu(Xe_2–F_{13}) – \nu(Xe_2–F_{15})]$		662(7)[282]
654(26)[142]	650(43)	$[\nu(Xe_1–F_{10}) + \nu(Xe_1–F_9)_{small}] – \nu(Xe_2–F_{16})_{small}$	653, sh	656(27)[127]
652(7)[80]	644(31)	$[\nu(Xe_1–F_8) + \nu(Xe_2–F_{13})] + [\nu(Xe_1–F_7) + \nu(Xe_2–F_{14})]_{small} – [\nu(Xe_1–F_6) + \nu(Xe_2–F_{12})] – [\nu(Xe_1–F_9) + \nu(Xe_2–F_{14})]_{small}$	651(39)	654(6)[97]
645(4)[228]		$[\nu(Xe_1–F_9) + \nu(Xe_2–F_{15}) + \nu(Xe_2–F_{16})] – [\nu(Xe_1–F_7) + \nu(Xe_1–F_{10}) + \nu(Xe_2–F_{13})] + \nu(M_1–F_4)_{small}$		647(3)[250]
637(21)[130]	626(44) 623, sh	$[\nu(M_1–F_4) + \nu(M_1–F_1)_{small}]$	630(30) 626(28)	637(12)[127]
604(5)[7]	618, sh 613(15)	$[\nu(Xe_1–F_{4eq}) + \nu(Xe_1–F_{11}) + \nu(Xe_2–F_{16})] – [\nu(Xe_2–F_{4eq}) + \nu(Xe_2–F_{11}) + \nu(Xe_1–F_{10})]$	619, sh 613, sh	606(5)[7]
601(35)[5]	601, sh 599(80)	$[\nu(Xe_1–F_{4eq}) + \nu(Xe_2–F_{4eq})] – [\nu(Xe_1–F_{10}) + \nu(Xe_2–F_{16})]$	600(59)	603(34)[5]
583(13)[2]	585(100) 581, sh	$[\nu(Xe_1–F_6) + \nu(Xe_1–F_8)] – [\nu(Xe_1–F_7) + \nu(Xe_1–F_9)]$	588(69) 585, sh	585(14)[<1]
579(11)[19]	569, sh 566(31)	$[\nu(Xe_2–F_{13}) + \nu(Xe_2–F_{15})] – [\nu(Xe_2–F_{12}) + \nu(Xe_2–F_{14})]$	573(12) 562(22)	582(10)[20]

continued…

Table A8.8. (continued)

3' [a,b]	**3** [a,c]	**assgnts (C_1)** [d]	**4** [a,c,d]	**4'** [a,b]
525(8)[98]	538(7) 535(6)	$[\nu(M_1–F_1) – \nu(Xe_2–F_1)] – \nu(M_1–F_4)$	554, sh 545(5)	538(9)[114]
405(5)[307]	412(4)	$[\nu(Xe_1–F_5) – \nu(M_1–F_5)] + [\nu(Xe_1–F_{11}) – \nu(Xe_2–F_{11})] + [\delta(F_{13}Xe_2F_{16}) – \delta(F_{15}Xe_2F_{16})]_{small}$	411(6)	411(3)[388]
394(1)[21]	402(3)	$[\delta(F_6Xe_1F_{10}) – \delta(F_5Xe_1F_6)] + [\delta(F_{13}Xe_2F_{16}) – \delta(F_{15}Xe_2F_{16})]$	402(4)	396(1)[11]
388(<1)[64]	393, sh 391, sh	$[\delta(F_9Xe_1F_{10}) – \delta(F_7Xe_1F_{10})] + [\nu(Xe_1–F_5) – \nu(M_1–F_5)]$	392, sh 390, sh	389(<1)[30]
381(3)[137]	384, sh	$[\nu(Xe_1–F_{11}) – \nu(Xe_2–F_{11})] + [\delta(Xe_1F_{10}F_8F_9) – \delta(Xe_1F_{10}F_6F_7)]$		381(2)[98]
371(1)[22]		$[\delta(F_{12}Xe_2F_{16}) – \delta(F_{16}Xe_2F_{14})]$		373(<1)[6]
359(9)[71]	361, sh	$[\delta_{umb}(Xe_1F_{4eq}) + \delta_{umb}(Xe_2F_{4eq})]$	362, sh	355(10)[88]
350(5)[94]	358(6)	$[\nu(Xe_1–F_5) + \nu(M_1–F_5)] + [\nu(Xe_1–F_{11}) – \nu(Xe_2–F_{11})] – \delta(O_1M_1F_4)$	358(5)	349(3)[142]
335(<1)[6]		$\delta_{umb}(Xe_2F_{4eq}) + \delta(F_1M_1F_4)$		335(<1)[7]
326(3)[41]	323, sh	$[\nu(M_1–F_1) + \nu(Xe_2–F_1)] – \delta_{umb}(Xe_1F_{4eq}) – \rho_t(F_1M_1F_{11}) – \delta(F_5M_1F_4)$	327, sh	325(3)[57]
320(4)[50]	319(15)	$\delta(MoO_1F_1F_2)$	301(8)	308(6)[54]
312(4)[36]	301, sh	$\delta(O_1M_1F_3)$	324(9)	319(3)[15]
294(3)[22]	290, sh	$\rho_w(O_1M_1F_5) / \rho_t(F_2M_1F_4) / \delta(F_6Xe_1F_7)$	290, sh	286(2)[30]
280(2)[18]	276(9)	$[\delta(F_{12}Xe_2F_{13}) + \delta(F_{14}Xe_2F_{15})]$	265(5)	277(2)[17]
273(2)[13]	271, sh	$[\delta(F_8Xe_1F_9) + \delta(F_6Xe_1F_7)]$	260, sh	271(3)[7]
268(<0.1)[1]		$[\nu(Xe_1–F_{11}) + \nu(Xe_2–F_{11})] / [\rho_w(F_6Xe_1F_8) + \rho_w(F_{12}Xe_2F_{14})]$		265(<1)[4]

continued…

Table A8.8. (continued)

3' [a,b]	**3** [a,c]	**assgnts (C_1)** [d]	**4** [a,c,d]	**4'** [a,b]
261(2)[33]		$\delta_{umb}(M_1F_{4eq}) + [\rho_t(F_{13}Xe_2F_{14}) - \rho_t(F_{12}Xe_2F_{15})]$		254(<1)[41]
252(2)[20]		$\delta(F_3M_1F_4) + \delta(F_8Xe_1F_9)$		247(1)[10]
240(<1)[2]		$[\rho_w(F_7Xe_1F_9) - \rho_w(F_6Xe_1F_8)] + \rho_w(F_{11}Xe_2F_{14})$		238(1)[11]
230(2)[25]	223(3)	$[\rho_t(F_6Xe_1F_8) + \rho_t(F_{11}Xe_1F_9)] - [\rho_t(F_{12}Xe_2F_{15}) + \rho_t(F_{11}Xe_2F_{13})]$	223(2)	230(1)[25]
211(<1)[4]		$[\rho_w(F_1M_1F_3) + \rho_w(F_2M_1F_4)] + [\rho_w(F_7Xe_1F_9) - \rho_w(F_6Xe_1F_8)]$		209(<0.1)[4]
209(<1)[3]		$\rho_w(F_7Xe_1F_9) + \rho_w(F_{12}Xe_2F_{14}) + [\rho_w(F_1M_1F_3) - \rho_w(F_2M_1F_4)]$		206(<1)[4]
206(<1)[<1]	201(4)	$[\rho_w(F_6Xe_1F_8) - \rho_w(F_7Xe_1F_9)] + [\rho_w(F_{13}Xe_2F_{15}) - \rho_w(F_{12}Xe_2F_{14})] + [\rho_w(F_1M_1F_3) - \rho_w(F_2M_1F_4)]_{small}$		205(<1)[<1]
196(<1)[<1]		$[\rho_w(F_6Xe_1F_8) + \rho_w(F_{14}Xe_2F_{15})] + \rho_t(F_3M_1F_4)$	193(2)	193(<1)[2]
187(<1)[1]		$[\rho_w(F_1M_1F_3) - \rho_w(F_2M_1F_4)] / \delta(F_5Xe_1F_{11})$		183(<1)[3]
174(<1)[5]	171(6)	$[\delta(F_7Xe_1F_{11}) + \delta(F_1Xe_2F_{11})]$	171(4)	171(<1)[4]
161(<1)[<1]		$[\rho_w(O_1M_1F_5) + \rho_w(F_2M_1F_4)] + [\rho_t(F_{11}Xe_2F_{14}) + \rho_w(F_{13}Xe_2F_{15})] + \delta(F_5Xe_1F_{11})$		159(<1)[2]
141(<1)[2]		$\rho_t(F_5Xe_1F_{11}) + [\rho_w(F_6Xe_1F_8) - \rho_w(F_{13}Xe_2F_{15})]$		141(<1)[2]
126(<1)[6]	127(4)	$\rho_r(M_1O_1F_1F_2)$	121(4)	121(<1)[4]
109(<1)[1]		$[\rho_r(Xe_1F_7F_9F_{10}) - \rho_r(Xe_2F_{13}F_{16}F_{15})] - \rho_r(M_1F_1O_1F_3)$		105(<1)[<1]
102(<1)[3]		$\rho_t(Xe_1F_{10}F_{4eq})$		100(<1)[3]
89(<1)[<1]		$\rho_t(Xe_2F_{16}F_{4eq})$		89(<1)[<1]
88(<1)[<1]		$\delta(Xe_1F_{11}Xe_2)$		83(<1)[<1]

continued…

Table A8.8. (continued)

3' [a,b]	**3** [a,c]	**assgnts (C_1)** [d]	**4** [a,c,d]	**4'** [a,b]
78(<1)[<1]				78(<1)[<1]
67(<1)[<0.1]				68(<1)[<1]
60(<1)[<1]				58(<1)[<1]
49(<1)[<0.1]		coupled deformation modes		47(<0.1)[<0.1]
36(<0.1)[<0.1]				34(<0.1)[<0.1]
27(<1)[<1]				21(<1)[<1]
16(<0.1)[<0.1]				8(<0.1)[<0.1]

[a] Frequencies are given in cm^{-1} and anion frequencies and mode descriptions are gray-highlighted. [b] Values in parentheses and square brackets denote calculated Raman intensities ($Å^4$ amu^{-1}) and infrared intensities (km mol^{-1}), respectively. [c] Values in parentheses denote relative Raman intensities. Abbreviations denote shoulder (sh). The Raman spectrum was recorded in a FEP sample tube at −150 °C (Mo) and −110 °C (W) using 1064-nm excitation. [d] Assignments are for the energy-minimized geometry (C_1) calculated using the PBE1PBE/Def2-SVP (F, O, M, Xe) level of theory. Abbreviations denote stretch (ν), bend (δ), rock (ρ_r), twist (ρ_t), wag (ρ_w), umbrella (umb), and equatorial (eq). Bond elongations and angle openings are denoted by plus (+) signs, and bond contractions and angle compressions are denoted by minus (–) signs. The atom labeling scheme corresponds to those used in Figure 11.10. [d] The bands observed at 565(23) and 917(1) cm^{-1} are attributed to small amount of $XeOF_4$ immpurity. Unassigned weak bands were observed at 506(2) and 503(3) cm^{-1}.

Table A8.9. Experimental Raman frequencies and calculated vibrational frequencies, intensities, and assignments for $[XeF_5][Mo_2O_2F_9]$ (**5**), $[XeF_5][W_2O_2F_9]$ (**6**), $\{[XeF_5][Mo_2O_2F_9]\}_2$ (**5'**) (C_{2h}), and $\{[XeF_5][W_2O_2F_9]\}_2$ (**6'**) (C_2)

5' [a,b]	**5** [a,c]	**assgnts (C_1)** [d]	**6** [a,c]	**6'** [a,b]
1123(88)[0]	1023(63)	$[\nu(M_1\text{-}O_1) + \nu(M_2\text{-}O_2)] + [\nu(M_{1A}\text{-}O_{1A}) + \nu(M_{2A}\text{-}O_{2A})]$	1040(100)	1103(85)[<0.1]
1117(0)[50]		$[\nu(M_1\text{-}O_1) + \nu(M_2\text{-}O_2)] - [\nu(M_{1A}\text{-}O_{1A}) + \nu(M_{2A}\text{-}O_{2A})]$		1099(<0.1)[40]
1111(0)[640]		$[\nu(M_1\text{-}O_1) - \nu(M_2\text{-}O_2)] - [\nu(M_{1A}\text{-}O_{1A}) - \nu(M_{2A}\text{-}O_{2A})]$		1095(<0.1)[528]
1102(2)[0]	1009(8)	$[\nu(M_1\text{-}O_1) - \nu(M_2\text{-}O_2)] + [\nu(M_{1A}\text{-}O_{1A}) - \nu(M_{2A}\text{-}O_{2A})]$	1027(22)	1088(1)[<0.1]
750(43)[0]	720(49)	$[\nu(M_1\text{-}F_1) + \nu(M_1\text{-}F_2)] + [\nu(M_2\text{-}F_6) + \nu(M_2\text{-}F_7)] + [\nu(M_{1A}\text{-}F_{1A}) + \nu(M_{1A}\text{-}F_{2A})] + [\nu(M_{2A}\text{-}F_{6A}) + \nu(M_{2A}\text{-}F_{7A})]$	716(61)	743(42)[<0.1]
742(0)[957]]		$\{[\nu(M_1\text{-}F_1) - \nu(M_1\text{-}F_2)] + [\nu(M_2\text{-}F_6) - \nu(M_2\text{-}F_7)]\} - \{[\nu(M_{1A}\text{-}F_{1A}) - \nu(M_{1A}\text{-}F_{2A})] + [\nu(M_{2A}\text{-}F_{6A}) - \nu(M_{2A}\text{-}F_{7A})]\}$		724(0)[695)
741(0)[7]		$\{[\nu(M_1\text{-}F_1) + \nu(M_1\text{-}F_2)] - [\nu(M_2\text{-}F_6) + \nu(M_2\text{-}F_7)]\} - [\nu(M_{1A}\text{-}F_{1A}) + \nu(M_{1A}\text{-}F_{2A})] - [\nu(M_{2A}\text{-}F_{6A}) + \nu(M_{2A}\text{-}F_{7A})]\}$		741(<0.1)[33]
740(0)[623]		$\{[\nu(M_1\text{-}F_1) + \nu(M_1\text{-}F_2)] + [\nu(M_2\text{-}F_6) + \nu(M_2\text{-}F_7)]\} - \{[\nu(M_{1A}\text{-}F_{1A}) + \nu(M_{1A}\text{-}F_{2A})] + [\nu(M_{2A}\text{-}F_{6A}) + \nu(M_{2A}\text{-}F_{7A})]\}$		738(<0.1)[354]
735(5)[0]	713(38)	$\{[\nu(M_1\text{-}F_1) + \nu(M_1\text{-}F_2)] - [\nu(M_2\text{-}F_6) + \nu(M_2\text{-}F_7)]\} + \{[\nu(M_{1A}\text{-}F_{1A}) + \nu(M_{1A}\text{-}F_{2A})] - [\nu(M_{2A}\text{-}F_{6A}) + \nu(M_{2A}\text{-}F_{7A})]\}$	711(8)	736(4)[<0.1]
729(5)[0]	694(14)	$[\nu(M_1\text{-}F_1) - \nu(M_1\text{-}F_2)] + [\nu(M_2\text{-}F_6) - \nu(M_2\text{-}F_7)]\} + \{[\nu(M_{1A}\text{-}F_{1A}) - \nu(M_{1A}\text{-}F_{2A})] + [\nu(M_{2A}\text{-}F_{6A}) - \nu(M_{2A}\text{-}F_{7A})]\}$	701(13)	719(7)[<0.1]
722(<1)[0]		$\{[\nu(M_1\text{-}F_1) - \nu(M_1\text{-}F_2)] - [\nu(M_2\text{-}F_6) - \nu(M_2\text{-}F_7)]\} + \{[\nu(M_{1A}\text{-}F_{1A}) - \nu(M_{1A}\text{-}F_{2A})] - [\nu(M_{2A}\text{-}F_{6A}) - \nu(M_{2A}\text{-}F_{7A})]\}$		712(1)[<0.1]
716(0)[<0.1]		$\{[\nu(M_1\text{-}F_1) - \nu(M_1\text{-}F_2)] - [\nu(M_2\text{-}F_6) - \nu(M_2\text{-}F_7)]\} - \{[\nu(M_{1A}\text{-}F_{1A}) - \nu(M_{1A}\text{-}F_{2A})] - [\nu(M_{2A}\text{-}F_{6A}) - \nu(M_{2A}\text{-}F_{7A})]\}$		710(<0.1)[<0.1]
685(0)[282]		$[\nu(Xe_1\text{-}F_{10}) - \nu(Xe_1\text{-}F_{12})] - [\nu(Xe_{1A}\text{-}F_{10A}) - \nu(Xe_{1A}\text{-}F_{12A})]$		688(<0.1)[246]
683 (0)[249]		$[\nu(Xe_1\text{-}F_{11}) - \nu(Xe_1\text{-}F_{13})] - [\nu(Xe_{1A}\text{-}F_{11A}) - \nu(Xe_{1A}\text{-}F_{13A})]$		685(<0.1)[282]

continued…

Table A8.9. (continued)

5' [a,b]	**5** [a,c]	**assgnts (C_1)** [d]	**6** [a,c]	**6'** [a,b]
682(12)[0]	679(11)	[ν(Xe_1-F_{14}) + ν(Xe_{1A}-F_{14A})] + {[ν(Xe_1-F_{10}) + ν(Xe_1-F_{12})] + [ν(Xe_{1A}-F_{10A}) + ν(Xe_{1A}-F_{12A})]} + {[ν(Xe_1-F_{11}) + ν(Xe_1-F_{13})] + [ν(Xe_{1A}-F_{11A}) + ν(Xe_{1A}-F_{13A})]} + {[ν(Xe_1-F_3) + ν(Xe_1-F_8)] + [ν(Xe_1-F_{4A}) + ν(Xe_1-F_{9A})]} + {[ν(Xe_{1A}-F_{3A}) + ν(Xe_{1A}-F_{8A})] + [ν(Xe_{1A}-F_4) + ν(Xe_{1A}-F_9)]} – {[νM_1-F_3) + ν(M_2-F_8)] + [ν(M_{1A}-F_{4A}) + ν(M_{2A}-F_{9A})]} – {[ν(M_{1A}-F_{3A}) + ν(M_{2A}-F_{8A})] + [νM_1-F_4) + ν(M_2-F_9)]}	683(35)	684(27)[<0.1]
678(4)[0]	672(3)	[ν(Xe_1-F_{11}) – ν(Xe_1-F_{13})] + [ν(Xe_{1A}-F_{11A}) – ν(Xe_{1A}-F_{13A})]	662, sh	684(3)[<0.1]
676(5)[0]	658(3)	[ν(Xe_1-F_{10}) – ν(Xe_1-F_{12})] + [ν(Xe_{1A}-F_{10A}) – ν(Xe_{1A}-F_{12A})]	660(8)	679(2)[<0.1]
671(0)[121]		[ν(Xe_1-F_{14}) – ν(Xe_{1A}-F_{14A})]		675(<0.1)[48]
648(90)[0]	632(100)	[ν(Xe_1-F_{14}) + ν(Xe_{1A}-F_{14A})] – {[ν(Xe_1-F_3) + ν(Xe_1-F_8)] + [ν(Xe_1-F_{4A}) + ν(Xe_1-F_{9A})]} – {[ν(Xe_{1A}-F_{3A}) + ν(Xe_{1A}-F_{8A})] + [ν(Xe_{1A}-F_4) + ν(Xe_{1A}-F_9)]} + {[ν(M_{1A}-F_{4A}) + ν(M_{2A}-F_{9A})] + [νM_1-F_4) + ν(M_2-F_9)]} + {[ν(M_{1A}-F_{3A}) + ν(M_{2A}-F_{8A})] + [νM_1-F_3) + ν(M_2-F_8)]}	633(58)	649(62)[<0.1]
631(0)[825]		{[ν(Xe_1-F_3) + ν(Xe_1-F_{9A})] – [ν(Xe_1-F_8) + ν(Xe_1-F_{4A})]} + {[ν(Xe_{1A}-F_{8A}) + ν(Xe_{1A}-F_4)] – [ν(Xe_{1A}-F_{3A}) + ν(Xe_{1A}-F_9)]} – {[ν(M_1-F_3) + ν(M_{2A}-F_{9A})] – [ν(M_2-F_8) + ν(M_{1A}-F_{4A})]} – {[ν(M_{2A}-F_{8A}) + ν(M_1-F_4)] – {[ν(M_{1A}-F_{3A}) + ν(M_2-F_9)]} – {[ν(M_1-F_5) – ν(M_2-F_5)] – [ν(M_{1A}-F_{5A}) + ν(M_{2A}-F_{5A})]}		627(<0.1)[741]
624(0)[780]		[ν(Xe_1-F_{14}) – ν(Xe_{1A}-F_{14A})] – {[ν(Xe_1-F_{4A}) + ν(Xe_1-F_{9A})] – [ν(Xe_{1A}-F_4) + ν(Xe_{1A}-F_9)]} + {[ν(M_{1A}-F_{4A}) + ν(M_{2A}-F_{9A})] – [ν(M_1-F_4) + ν(M_2-F_9)]}		620(<0.1)[1010]
620(6)[0]	646(24)	{[ν(Xe_1-F_3) + ν(Xe_1-F_{4A})] – [ν(Xe_1-F_8) + ν(Xe_1-F_{9A})]} + {[ν(Xe_{1A}-F_{3A}) + ν(Xe_{1A}-F_4)] – [ν(Xe_{1A}-F_{8A}) + ν(Xe_{1A}-F_9)]} – {[ν(M_1-F_3) + ν(M_{1A}-F_{4A})] – [ν(M_2-F_8) + ν(M_{2A}-F_{9A})]} – {[ν(M_{1A}-F_{3A}) + ν(M_1-F_4)] – [ν(M_{2A}-F_{8A}) + ν(M_2-F_9)]} – {[ν(M_1-F_5) – ν(M_2-F_5)] + [ν(M_{1A}-F_{5A}) – ν(M_{2A}-F_{5A})]}	643(13)	615(4)[3]

continued…

Table A8.9. (continued)

5' [a,b]	**5** [a,c]	**assgnts (C_1)** [d]	**6** [a,c]	**6'** [a,b]
618(0)[291]		$[\nu(Xe_1\text{-}F_{14}) - \nu(Xe_{1A}\text{-}F_{14A})] - \{[\nu(Xe_1\text{-}F_3) + \nu(Xe_1\text{-}F_8)] - [\nu(Xe_{1A}\text{-}F_{3A}) + \nu(Xe_{1A}\text{-}F_{8A})]\} + + \{[\nu(M_1\text{-}F_3) + \nu(M_2\text{-}F_8)] - [\nu(M_{1A}\text{-}F_{3A}) + \nu(M_{2A}\text{-}F_{8A})]\} - \{[\nu(Xe_1\text{-}F_{10}) + \nu(Xe_1\text{-}F_{12})] - [\nu(Xe_{1A}\text{-}F_{10A}) + \nu(Xe_{1A}\text{-}F_{12A})]\}$		630(<0.1)[357]
611(18)[0]	619(41)	$\{[\nu(Xe_1\text{-}F_{10}) + \nu(Xe_1\text{-}F_{12})] + [\nu(Xe_{1A}\text{-}F_{10A}) + \nu(Xe_{1A}\text{-}F_{12A})]\} - \{[\nu(Xe_1\text{-}F_{11}) + \nu(Xe_1\text{-}F_{13})] + [\nu(Xe_{1A}\text{-}F_{11A}) + \nu(Xe_{1A}\text{-}F_{13A})]$	619(40)	612(18)[<0.1]
610(0)[3]		$\{[\nu(Xe_1\text{-}F_{10}) + \nu(Xe_1\text{-}F_{12})] - [\nu(Xe_{1A}\text{-}F_{10A}) + \nu(Xe_{1A}\text{-}F_{12A})]\} + \{[\nu(Xe_1\text{-}F_{11}) + \nu(Xe_1\text{-}F_{13})] - [\nu(Xe_{1A}\text{-}F_{11A}) + \nu(Xe_{1A}\text{-}F_{13A})]\}$		612(<0.1)[2]
602(92)[0]	601(23)	$[\nu(Xe_1\text{-}F_{14}) + \nu(Xe_{1A}\text{-}F_{14A})] - \{[\nu(Xe_1\text{-}F_{10}) + \nu(Xe_1\text{-}F_{12})] + [\nu(Xe_{1A}\text{-}F_{10A}) + \nu(Xe_{1A}\text{-}F_{12A})]\} - \{[\nu(Xe_1\text{-}F_{11}) + \nu(Xe_1\text{-}F_{13})] + [\nu(Xe_{1A}\text{-}F_{11A}) + \nu(Xe_{1A}\text{-}F_{13A})]\}$	601(14)	604(80)[<0.1]
580(0)[277]		$[\nu(Xe_1\text{-}F_{14}) + \nu(Xe_{1A}\text{-}F_{14A})] + \{[\nu(Xe_1\text{-}F_3) + \nu(Xe_1\text{-}F_8)] + [\nu(Xe_1\text{-}F_{4A}) + \nu(Xe_1\text{-}F_{9A})]\} + \{[\nu(Xe_{1A}\text{-}F_{3A}) + \nu(Xe_{1A}\text{-}F_{8A})] + [\nu(Xe_{1A}\text{-}F_4) + \nu(Xe_{1A}\text{-}F_9)]\} - \{[\nu(M_{1A}\text{-}F_{4A}) + \nu(M_{2A}\text{-}F_{9A})] + [\nu M_1\text{-}F_4) + \nu(M_2\text{-}F_9)]\} - \{[\nu(M_{1A}\text{-}F_{3A}) + \nu(M_{2A}\text{-}F_{8A})] + [\nu M_1\text{-}F_3) + \nu(M_2\text{-}F_8)]\}$	593(3)	597(<0.1)[218]
529(17)[0]	556(7)	$\{[\nu(Xe_1\text{-}F_3) + \nu(Xe_1\text{-}F_{9A})] - [\nu(Xe_1\text{-}F_8) + \nu(Xe_1\text{-}F_{4A})]\} - \{[\nu(Xe_{1A}\text{-}F_{8A}) + \nu(Xe_{1A}\text{-}F_4)] - [\nu(Xe_{1A}\text{-}F_{3A}) + \nu(Xe_{1A}\text{-}F_9)]\} - \{[\nu(M_1\text{-}F_3) + \nu(M_{2A}\text{-}F_{9A})] - [\nu(M_2\text{-}F_8) + \nu(M_{1A}\text{-}F_{4A})]\} + \{[\nu(M_{2A}\text{-}F_{8A}) + \nu(M_1\text{-}F_4)] - \{[\nu(M_{1A}\text{-}F_{3A}) + \nu(M_2\text{-}F_9)]\}$	549(8)	545(27)[<0.1]
523(32)[0]	523(6)	$\{[\nu(Xe_1\text{-}F_3) + \nu(Xe_1\text{-}F_8)] + [\nu(Xe_{1A}\text{-}F_{3A}) + \nu(Xe_{1A}\text{-}F_{8A})]\} - \{[\nu(Xe_1\text{-}F_{4A}) + \nu(Xe_1\text{-}F_{9A})] + [\nu(Xe_{1A}\text{-}F_4) + \nu(Xe_{1A}\text{-}F_9)]\} - \{[\nu(M_{1A}\text{-}F_{3A}) + \nu(M_{2A}\text{-}F_{8A})] + [\nu M_1\text{-}F_3) + \nu(M_2\text{-}F_8)]\} + \{[\nu(M_{1A}\text{-}F_{4A}) + \nu(M_{2A}\text{-}F_{9A})] + [\nu M_1\text{-}F_4) + \nu(M_2\text{-}F_9)]\}$		555(15)[<0.1]
512(0)[1]		$\{[\nu(Xe_1\text{-}F_3) + \nu(Xe_1\text{-}F_{4A})] - [\nu(Xe_1\text{-}F_8) + \nu(Xe_1\text{-}F_{9A})]\} - \{[\nu(Xe_{1A}\text{-}F_{3A}) + \nu(Xe_{1A}\text{-}F_4)] - [\nu(Xe_{1A}\text{-}F_{8A}) + \nu(Xe_{1A}\text{-}F_9)]\} - \{[\nu(M_1\text{-}F_3) + \nu(M_{1A}\text{-}F_{4A})] - [\nu(M_2\text{-}F_8) + \nu(M_{2A}\text{-}F_{9A})]\} + \{[\nu(M_{1A}\text{-}F_{3A}) + \nu(M_1\text{-}F_4)] - [\nu(M_{2A}\text{-}F_{8A}) + \nu(M_2\text{-}F_9)]\}$		537(<0.1)[<0.1]

continued…

Table A8.9. (continued)

5' [a,b]	**5** [a,c]	**assgnts (C_1)** [d]	**6** [a,c]	**6'** [a,b]
447(0)[153]		$[\nu(M_1\text{-}F_5) - \nu(M_2\text{-}F_5)] - [\nu(M_{1A}\text{-}F_{5A}) - \nu(M_{2A}\text{-}F_{5A})]$		466(<0.1)[181]
440(<1)[0]		$[\nu(M_1\text{-}F_5) - \nu(M_2\text{-}F_5)] + [\nu(M_{1A}\text{-}F_{5A}) - \nu(M_{2A}\text{-}F_{5A})]$		459(<1)[<0.1]
416(0)[18]		$[\delta(F_{10}Xe_1F_{14}) - \delta(F_{12}Xe_2F_{14})] - [\delta(F_{10A}Xe_{1A}F_{14A}) - \delta(F_{12A}Xe_{1A}F_{14A})]$		415(<0.1)[18]
416(3)[0]	419(8)	$[\delta(F_{11}Xe_1F_{14}) - \delta(F_{13}Xe_2F_{14})] + [\delta(F_{11A}Xe_{1A}F_{14A}) - \delta(F_{13A}Xe_{1A}F_{14A})]$	412(8)	416(3)[<0.1]
416(0)[8]		$[\delta(F_{11}Xe_1F_{14}) - \delta(F_{13}Xe_2F_{14})] - [\delta(F_{11A}Xe_{1A}F_{14A}) - \delta(F_{13A}Xe_{1A}F_{14A})]$		416(<0.1)[11]
416(3)[0]	409(4)	$[\delta(F_{10}Xe_1F_{14}) - \delta(F_{12}Xe_2F_{14})] + [\delta(F_{10A}Xe_{1A}F_{14A}) - \delta(F_{12A}Xe_{1A}F_{14A})]$	407(6)	415(3)[<0.1]
363(2)[0]	360(1)	$[\delta_{umb}(Xe_1F_{4eq}) + \delta_{umb}(Xe_{1A}F_{4eq})]$	360(1)	363(1)[0]
359(0)[250]		$[\delta_{umb}(Xe_1F_{4eq}) - \delta_{umb}(Xe_{1A}F_{4eq})]$		360(0)[240]
347(5)[0]	335(7)	$\{[\delta(M_1O_1F_3F_4) - \delta(M_1F_5F_8F_9)] + [\delta(M_2O_2F_8F_9) - \delta(M_2F_5F_8F_9)]\} + \{[\delta(M_{1A}O_{1A}F_{3A}F_{4A}) - \delta(M_{1A}F_{5A}F_{8A}F_{9A})] + [\delta(M_{2A}O_{2A}F_{8A}F_{9A}) - \delta(M_{2A}F_{5A}F_{8A}F_{9A})]\}$	339(6)	351(3)[0]
343(0)[<1]		$\{[\delta(M_1O_1F_3F_4) - \delta(M_1F_5F_8F_9)] + [\delta(M_2O_2F_8F_9) - \delta(M_2F_5F_8F_9)]\} - \{[\delta(M_{1A}O_{1A}F_{3A}F_{4A}) - \delta(M_{1A}F_{5A}F_{8A}F_{9A})] + [\delta(M_{2A}O_{2A}F_{8A}F_{9A}) - \delta(M_{2A}F_{5A}F_{8A}F_{9A})]\}$		346(0)[<1]
337(0)[<1]		$[\delta(O_1M_1F_5) + \delta(O_2M_2F_5)] - [\delta(O_{1A}M_{1A}F_{5A}) - \delta(O_{2A}M_{2A}F_{5A})]$		340(0)[<0.1]
333(<1)[0]		$[\delta(O_1M_1F_5) + \delta(O_2M_2F_5)] + [\delta(O_{1A}M_{1A}F_{5A}) - \delta(O_{2A}M_{2A}F_{5A})]$		335(<1)[0]
329(0)[<1]		$[\delta(M_1O_1F_3F_4) - \delta(M_2O_2F_8F_9)] - [\delta(M_{1A}O_{1A}F_{3A}F_{4A}) - \delta(M_{2A}O_{2A}F_{8A}F_{9A})]$		327(0)[<1]
325(3)[0]		$[\delta(F_3M_1F_4) + \delta(F_8M_2F_9)] + [\delta(F_{3A}M_{1A}F_{4A}) + \delta(F_{8A}M_{2A}F_{9A})]$		323(3)[0]
322(7)[0]	320(25)	$[\delta(O_1M_1F_2) - \delta(O_2M_2F_7)] + [\delta(O_{1A}M_{1A}F_{2A}) - \delta(O_{2A}M_{2A}F_{7A})]$	323(26)	320(7)[<0.1]
321(1)[0]		$[\delta_{umb}(M_1F_{4eq}) + \delta_{umb}(M_2F_{4eq})] + [\delta_{umb}(M_{1A}F_{4eq}) + \delta_{umb}(M_{2A}F_{4eq})]$		302(<1)[0]
319(9)[0]	312(27)	$[\delta(O_1M_1F_1) - \delta(O_2M_2F_6)] + [\delta(O_{1A}M_{1A}F_{1A}) - \delta(O_{2A}M_{2A}F_{6A})]$	313(16)	315(8)[<0.1]

continued…

Table A8.9. (continued)

5' [a,b]	**5** [a,c]	**assgnts (C_1)** [d]	**6** [a,c]	**6'** [a,b]
319(0)[<0.1]		$[\delta(O_1M_1F_2) - \delta(O_2M_2F_7)] - [\delta(O_{1A}M_{1A}F_{2A}) - \delta(O_{2A}M_{2A}F_{7A})]$		317(<0.1)[<0.1]
317(0)[1]		$[\delta_{umb}(M_1F_{4eq}) + \delta_{umb}(M_2F_{4eq})] - [\delta_{umb}(M_{1A}F_{4eq}) + \delta_{umb}(M_{2A}F_{4eq})]$		291(<0.1)[2]
308(0)[8]		$\{[\delta(F_1M_1F_4) + \delta(F_2M_1F_3)] - [\delta(F_7M_2F_8) + \delta(F_6M_2F_9)]\} - \{[\delta(F_{1A}M_{1A}F_{4A}) + \delta(F_{2A}M_{1A}F_{3A})] - [\delta(F_{7A}M_{2A}F_{8A}) + \delta(F_{6A}M_{2A}F_{9A})]\} / [\delta(O_1M_1F_5) - \delta(O_2M_2F_5)] + [\delta(O_{1A}M_{1A}F_{5A}) - \delta(O_{2A}M_{2A}F_{5A})]$		306(<1)[<0.1]
306(<1)[0]	305(14)	$[\delta(F_{11}Xe_1F_{12}) + \delta(F_{10}Xe_2F_{13})] + [\delta(F_{11A}Xe_{1A}F_{12A}) + \delta(F_{10A}Xe_{1A}F_{13A})]$	308(22)	306(<0.1)[2]
305(0)[64]		$[\delta(F_3M_1F_4) + \delta(F_8M_2F_9)] - [\delta(F_{3A}M_{1A}F_{4A}) + \delta(F_{8A}M_{2A}F_{9A})]$		303(<0.1)[24]
297(0)[81]		$[\rho_w(O_1M_1F_5) + \rho_w(O_2M_2F_5)] + [\rho_w(O_{1A}M_{1A}F_{5A}) + \rho_w(O_{2A}M_{2A}F_{5A})]$		288(<0.1)[65]
295(0)[<1]		$[\delta(F_{11}Xe_1F_{12}) + \delta(F_{10}Xe_2F_{13})] - [\delta(F_{11A}Xe_{1A}F_{12A}) + \delta(F_{10A}Xe_{1A}F_{13A})]$		297(0)[<0.1]
291(3)[0]		$[\delta(O_1M_1F_5) + \delta(O_2M_2F_5)] + [\delta(O_{1A}M_{1A}F_{5A}) + \delta(O_{2A}M_{2A}F_{5A})]$		283(2)[0]
288(0)[77]		$[\delta(O_1M_1F_5) + \delta(O_2M_2F_5)] - [\delta(O_{1A}M_{1A}F_{5A}) + \delta(O_{2A}M_{2A}F_{5A})]$		277(<0.1)[122]
285(<1)[0]		$[\rho_w(O_1M_1F_5) + \rho_w(O_2M_2F_5)] + [\rho_w(O_{1A}M_{1A}F_{5A}) + \rho_w(O_{2A}M_{2A}F_{5A})]$		272(<1)[0]
283(2)[0]		$[\delta(F_{11}Xe_1F_{12}) + \delta(F_{10}Xe_2F_{13})] + [\delta(F_{11A}Xe_{1A}F_{12A}) + \delta(F_{10A}Xe_{1A}F_{13A})] + \{[\delta(F_1M_1F_4) + \delta(F_2M_1F_3)] - [\delta(F_7M_2F_8) + \delta(F_6M_2F_9)]\} + \{[\delta(F_{1A}M_{1A}F_{4A}) + \delta(F_{2A}M_{1A}F_{3A})] - [\delta(F_{7A}M_{2A}F_{8A}) + \delta(F_{6A}M_{2A}F_{9A})]\}$		282(2)[<0.1]
279(0)[173]		$[\delta_{umb}(M_1F_{4eq}) - \delta_{umb}(M_2F_{4eq})] - [\delta_{umb}(M_{1A}F_{4eq}) - \delta_{umb}(M_{2A}F_{4eq})]$		268(0)[58]
273(0)[18]		$[\rho_w(F_{10}Xe_1F_{12}) - \rho_w(F_{11}Xe_1F_{13})] - [\rho_w(F_{10A}Xe_{1A}F_{12A}) - \rho_w(F_{11A}Xe_{1A}F_{13A})]$		267(<1)[<0.1]
271(<1)[0]		$[\rho_w(F_{10}Xe_1F_{12}) - \rho_w(F_{11}Xe_1F_{13})] + [\rho_w(F_{10A}Xe_{1A}F_{12A}) - \rho_w(F_{11A}Xe_{1A}F_{13A})]$		266(<0.1)[175]
257(1)[0]		$[\rho_w(F_9Xe_1F_{8A}) + \rho_w(F_4Xe_{1A}F_{3A})] - [\rho_w(F_{4A}Xe_1F_3) + \rho_w(F_{9A}Xe_{1A}F_8)]$		248(<1)[<0.1]
245(<1)[0]		$[\rho_w(F_9Xe_1F_{8A}) + \rho_w(F_4Xe_{1A}F_{3A})] + [\rho_w(F_{4A}Xe_1F_3) + \rho_w(F_{9A}Xe_{1A}F_8)]$		240(<0.1)[<0.1]

continued…

Table A8.9. (continued)

5' [a,b]	**5** [a,c]	**assgnts (C_1)** [d]	**6** [a,c]	**6'** [a,b]
236(<0.1)[0]	232(3)	$[\rho_w(F_{11}Xe_1F_{13}) + \rho_w(F_{11A}Xe_{1A}F_{13A})]$		236(<0.1)[<0.1]
230(0)[<1]		$[\delta(F_1M_1F_2) - \delta(F_6M_2F_7)] - [\delta(F_{1A}M_{1A}F_{2A}) - \delta(F_{6A}M_{2A}F_{7A})]$ / $[\rho_w(F_{10}Xe_1F_{12}) - \rho_w(F_{10A}Xe_{1A}F_{12A})]$		226(<0.1)[2]
228(0)[28]		$[\rho_w(F_{11}Xe_1F_{13}) - \rho_w(F_{11A}Xe_{1A}F_{13A})]$		228(0)[31]
222(0)[1]		$[\rho_w(F_2M_1F_4) - \rho_w(F_7M_2F_9)] - [\rho_w(F_{2A}M_{1A}F_{4A}) - \rho_w(F_{7A}M_{2A}F_{9A})]\}$		208(<0.1)[<1]
216(<1)[0]	218(3)	$[\rho_w(F_{11}Xe_1F_{13}) + \rho_w(F_{11A}Xe_{1A}F_{13A})]$		212(<0.1)[<0.1]
216(0)[<0.1]		$[\rho_w(F_{10}Xe_1F_{12}) - \rho_w(F_{10A}Xe_{1A}F_{12A})]$		209(<0.1)[2]
214(0)[7]		$\{[\rho_w(F_1M_1F_3) - \rho_w(F_2M_1F_4)] + [\rho_w(F_6M_2F_8) - \rho_w(F_7M_2F_9)]\} - \{[\rho_w(F_{1A}M_{1A}F_{3A}) - \rho_w(F_{2A}M_{1A}F_{4A})] + [\rho_w(F_{6A}M_{2A}F_{8A}) - \rho_w(F_{7A}M_{2A}F_{9A})]\}$		216(0)[12]
213(<1)[0]	213(4)	$\{[\delta(F_1M_1F_2) - \delta(F_3M_1F_4)] - [\delta(F_6M_2F_7) - \delta(F_8M_2F_9)]\} + \{[\delta(F_{1A}M_{1A}F_{2A}) - \delta(F_{3A}M_{1A}F_{4A})] - [\delta(F_{6A}M_{2A}F_{7A}) - \delta(F_{8A}M_{2A}F_{9A})]\}$		204(<1)[0]
206(2)[0]	209(4)	$\{[\rho_w(F_1M_1F_3) - \rho_w(F_2M_1F_4)] + [\rho_w(F_6M_2F_8) - \rho_w(F_7M_2F_9)]\} + \{[\rho_w(F_{1A}M_{1A}F_{3A}) - \rho_w(F_{2A}M_{1A}F_{4A})] + [\rho_w(F_{6A}M_{2A}F_{8A}) - \rho_w(F_{7A}M_{2A}F_{9A})]\}$	210(4)	202(2)[0]
200(1)[0]	202(3)	$\{[\rho_t(F_1M_1F_2) - \rho_t(F_3M_1F_4)] + [\rho_t(F_6M_2F_7) - \rho_t(F_8M_2F_9)]\} + \{[\rho_t(F_{1A}M_{1A}F_{2A}) - \rho_t(F_{3A}M_{1A}F_{4A})] + [\rho_t(F_{6A}M_{2A}F_{7A}) - \rho_t(F_{8A}M_{2A}F_{9A})]\}$	202(4)	201(<1)[<0.1]
199(1)[0]	199(3)	$\{[\rho_w(F_1M_1F_3) - \rho_w(F_2M_1F_4)] - [\rho_w(F_6M_2F_8) - \rho_w(F_7M_2F_9)]\} + \{[\rho_w(F_{1A}M_{1A}F_{3A}) - \rho_w(F_{2A}M_{1A}F_{4A})] - [\rho_w(F_{6A}M_{2A}F_{8A}) - \rho_w(F_{7A}M_{2A}F_{9A})]\}$	187(5)	198(<1)[<0.1]
193(0)[4]		$\{[\delta(F_1M_1F_2) - \delta(F_3M_1F_4)] + [\delta(F_6M_2F_7) - \delta(F_8M_2F_9)]\} - \{[\delta(F_{1A}M_{1A}F_{2A}) - \delta(F_{3A}M_{1A}F_{4A})] + [\delta(F_{6A}M_{2A}F_{7A}) - \delta(F_{8A}M_{2A}F_{9A})]\}$ / $\{[\delta(O_1M_1F_5) + \delta(O_2M_2F_5)] - [\delta(O_{1A}M_{1A}F_{5A}) + \delta(O_{2A}M_{2A}F_{5A})]\}$		189(0)[10]
189(0)[19]		$\{[\rho_w(F_1M_1F_3) - \rho_w(O_1M_1F_5)] + [\rho_w(F_6M_2F_8) - \rho_w(O_2M_2F_5)]\} - \{[\rho_w(F_{1A}M_{1A}F_{3A}) - \rho_w(O_{1A}M_{1A}F_{5A})] + [\rho_w(F_{6A}M_{2A}F_{8A}) - \rho_w(O_{2A}M_{2A}F_{5A})]\}$		191(0)[16]

continued…

Table A8.9. (continued)

5' [a,b]	**5** [a,c]	**assgnts (C_1)** [d]	**6** [a,c]	**6'** [a,b]
189(0)[<0.1]		$\{[\rho_w(F_1M_1F_3) - \rho_w(F_2M_1F_4)] - [\rho_w(F_6M_2F_8) - \rho_w(F_7M_2F_9)]\} - \{[\rho_w(F_{1A}M_{1A}F_{3A}) - \rho_w(F_{2A}M_{1A}F_{4A})] - [\rho_w(F_{6A}M_{2A}F_{8A}) - \rho_w(F_{7A}M_{2A}F_{9A})]\}$		192(<0.1)[<0.1]
179(<0.1)[0]		$\{[\rho_w(F_4M_1F_5) - \rho_w(F_8M_2F_5)] + [\rho_w(F_{4A}M_{1A}F_{5A}) - \rho_w(F_{8A}M_{2A}F_{5A})]\}$		177(<0.1)[<0.1]
140(<0.1)[0]	135(3)	$[\rho_t(Xe_1F_{11}F_{14}F_{13}) - \rho_t(Xe_{1A}F_{11A}F_{14A}F_{13A})]$		136(<0.1)[<0.1]
140(0)[9]		$[\rho_r(Xe_1F_{10}F_{14}F_{12}) - \rho_r(Xe_{1A}F_{10A}F_{14A}F_{12A})]$		137(<0.1)[5]
136(0)[<1]		$[\rho_t(Xe_1F_{11}F_{14}F_{13}) - \rho_t(Xe_{1A}F_{11A}F_{14A}F_{13A})]$		132(0)[<1]
131(<1)[0]	131(4)	$[\nu(M_1\text{-}F_5) + \nu(M_2\text{-}F_5)] + [\nu(M_{1A}\text{-}F_{5A}) + \nu(M_{2A}\text{-}F_{5A})]$	127(5)	122(<0.1)[<0.1]
128(0)[6]		$[\nu(M_1\text{-}F_5) + \nu(M_2\text{-}F_5)] - [\nu(M_{1A}\text{-}F_{5A}) + \nu(M_{2A}\text{-}F_{5A})]$	121(6)	116(<1)[0]
125(<1)[0]	126(4)	$[\rho_r(Xe_1F_{10}F_{14}F_{12}) + \rho_r(Xe_{1A}F_{10A}F_{14A}F_{12A})]$		116(<0.1)[<0.1]
120(<0.1)[0]	120(6)	$\{[\rho_r(M_1F_{4eq}) + \rho_r(M_2F_{4eq})] - [\rho_r(M_{1A}F_{4eq_A}) + \rho_r(M_{2A}F_{4eq_A})]\} / [\rho_r(Xe_1F_{4eq}) + \rho_r(Xe_{1A}F_{4eq_A})]$		113(0)[<1]
120(0)[19]		coupled deformation modes		115(0)[14]
119(0)[2]				111(0)[2]
110(0)[<1]				105(<1)[<0.1]
109(<1)[0]				104(<0.1)[<0.1]
93(<0.1)[0]				87(<0.1)[<0.1]
89(<0.1)[0]				87(<0.1)[0]
86(0)[<0.1]				83(<0.1)[<0.1]
83(0)[1]				81(<0.1)[3]
79(<0.10)[0]				78(<0.1)[<0.1]
77(<0.1)[0]				77(<0.1)[<0.1]

continued…

Table A8.9. (continued)

5' [a,b]	**5** [a,c]	**assgnts (C_1)** [d]	**6** [a,c]	**6'** [a,b]
72(0)[3]				72(0)[2]
72(<0.10)[0]				72(<0.1)[<0.1]
67(0)[9]				63(0)[8]
61(0)[2]				54(<0.1)[4]
54(<1)[0]				51(0)[11]
52(0)[1]				50(<0.1)[<1]
50(0)[9]		coupled deformation modes		48(<1)[<0.1]
50(<1)[0]				47(<1)[<0.1]
42(<0.1)[0]				40(<0.1)[<0.1]
27(<0.1)[0]				25(0)[<1]
26(0)[<1]				24(<0.1)[<0.1]
19(<0.1)[0]				11(<0.1)[<0.1]
11(0)[<0.1]				6(<0.1)[0]

[a] Frequencies are given in cm^{-1} and anion frequencies and mode descriptions are gray-highlighted. [b] Values in parentheses and square brackets denote calculated Raman intensities ($Å^4$ amu^{-1}) and infrared intensities (km mol^{-1}), respectively. [c] Values in parentheses denote relative Raman intensities. Abbreviations denote shoulder (sh) and broad (br). The Raman spectrum was recorded in a FEP sample tube at −155 (Mo) and −150 (W) °C using 1064-nm excitation. [d] Assignments are for the energy-minimized geometry (C_1) calculated using the PBE1PBE/Def2-SVP (F, O, M, Xe) levels of theory. Abbreviations denote stretch (ν), bend (δ), rock (ρ_r), twist (ρ_t), wag (ρ_w), umbrella (umb), equatorial (eq), axial (ax), in-plane (i.p.), and out-of-plane (o.o.p.). Bond elongations and angle openings are denoted by plus (+) signs, and bond contractions and angle compressions are denoted by minus (–) signs. The in-plane and out-of-plane bending modes are relative to the XYZT-plane, where the atom labeling scheme corresponds to that used in Figure 11.11.

Table A8.10. Calculated[a] vibrational frequencies, intensities, and assignments for $[M'OF_5]^-$ (M' = Cr, Mo, W)

$[CrOF_5]^-$ [b]	$[MoOF_5]^-$ [b]	$[WOF_5]^-$ [b]		assgnts (C_{4v}) [c]
1127(13)[230]	1018(20)[232]	994(22)[200]	A_1	ν(M'–O)
659(21)[40]	664(17)[54]	673(13)[46]	A_1	$\nu(M'–F_{4eq}) + \nu(M'–F_{ax})_{small}$
634(<0.1)[278]	671(<0.1)[292]	649(<0.1)[251]	E	$\nu(M'–F_1) – \nu(M'–F_3)$
514(6)[0]	580(3)[0]	605(2)[0]	B_2	$[\nu(M'–F_1) + \nu(M'–F_3)] – [\nu(M'–F_2) + \nu(M'–F_4)]$
492(7)[54] [d]	556(2)[79] [d]	565(<1)[96]	A_1	$\nu(M'–F_{ax})$
381(<1)[7]	292(<1)[15]	269(<0.1)[22]	A_1	$\delta_{umb}(M'–F_{4eq})$
380(4)[8]	324(4)[5]	325(4)[5]	E	$\delta(OM'F_3) + \delta(F_1M'F_5)$
346(3)[0]	278(3)[0]	275(2)[0]	B_1	$\delta(F_1M'F_2) + \delta(F_3M'F_4)$
320(<0.1)[38]	241(<0.1)[39]	222(<0.1)[48]	E	$\rho_w(OM'F_5) + \rho_w(F_2M'F_4)$
225(<1)[0]	190(<0.1)[0]	187(<0.1)[0]	B_2	$\rho_w(F_1M'F_3) – \rho_w(F_2M'F_4)$
112(<1)[1]	95(<1)[<1]	93(<1)[<1]	E	$\rho_w(OM'F_5) – \rho_w(F_2M'F_4)$

[a] Frequencies are given in cm^{-1}. [b] Values in parentheses and square brackets denote calculated Raman intensities ($Å^4$ amu^{-1}) and infrared intensities (km mol^{-1}), respectively. The PBE1PBE/Def2-SVP (F, O, M') level of theory was used. [c] Abbreviations denote stretch (ν), bend (δ), wag (ρ_w), umbrella (umb), equatorial (eq), axial (ax). Bond elongations and angle openings are denoted by plus (+) signs, and bond contractions and angle compressions are denoted by minus (–) signs. The atoms labeling scheme corresponds to that used in Figure A8.13. [d] These modes also have a small contribution from $\nu(M'–F_{4eq})$.

Table A8.11. Calculated vibrational frequencies, intensities, and assignments for $[M'_2O_2F_9]^-$ (M = Cr, Mo, W).

$[Cr_2O_2F_9]^-$ [a,b]	$[Mo_2O_2F_9]^-$ [a,b]	$[W_2O_2F_9]^-$ [a,b]		assgnts (*C*4) [c]
1177(65)[0]	1069(70)[<0.1]	1073(65)[<0.1]	A	$\nu(M'_1–O_1) + \nu(M'_2–O_2)$
1150(0)[630]	1053(<0.1)[499]	1068(<0.1)[409]	A	$\nu(M'_1–O_1) – \nu(M'_2–O_2)$
710(0)[477]	714(0)[508]	695(0)[479]	E	$[\nu(M'_1–F_1) + \nu(M'_1–F_2)] – [\nu(M'_1–F_3) + \nu(M'_1–F_4)] + [\nu(M'_2–F_6) – \nu(M'_2–F_8)]$
688(<0.1)[<0.1]	698(<0.1)[<0.1]	679(<0.1)[<0.1]	E	$[\nu(Cr_1–F_1) – \nu(Cr_1–F_3)] + [\nu(Cr_2–F_6) + \nu(Cr_2–F_9)] – [\nu(Cr_2–F_7) + \nu(Cr_2–F_8)]$ // $[\nu(M_1–F_1) + \nu(M_1–F_2)] – [\nu(M_1–F_3) + \nu(M_1–F_4)] – [\nu(M_2–F_6) – \nu(M_2–F_8)]$
689(<0.1)[77]	687(<0.1)[94]	716(<0.1)[90]	A	$\nu(M'_1–F_{4eq}) – \nu(M'_2–F_{4eq})$
680(52)[<0.1]	680(32)[<0.1]	712(21)[<0.1]	A	$\nu(M'_1–F_{4eq}) + \nu(M'_2–F_{4eq})$
551(6)[0]	607(3)[0]	649(2)[0]	B	$[\nu(Cr_1–F_1) + \nu(Cr_1–F_3)] + [\nu(Cr_2–F_6) + \nu(Cr_2–F_8)] – [\nu(Cr_1–F_2) + \nu(Cr_1–F_4)] – [\nu(Cr_2–F_7) + \nu(Cr_2–F_9)]$ // $[\nu(Mo_1–F_1) + \nu(Mo_1–F_3)] + [\nu(Mo_2–F_6) + \nu(Mo_2–F_8)] – [\nu(Mo_1–F_2) + \nu(Mo_1–F_4)] – [\nu(Mo_2–F_7) + \nu(Mo_2–F_9)]$ // $[\nu(W_1–F_1) + \nu(W_1–F_3)] – [\nu(W_1–F_2) + \nu(W_1–F_4)]$
550(5)[0]	606(2)[0]	649(2)[0]	B	$[\nu(Cr_1–F_1) + \nu(Cr_1–F_3)] + [\nu(Cr_2–F_7) + \nu(Cr_2–F_9)] – [\nu(Cr_1–F_2) + \nu(Cr_1–F_4)] – [\nu(Cr_2–F_6) + \nu(Cr_2–F_8)]$ // $[\nu(Mo_1–F_1) + \nu(Mo_1–F_3)] + [\nu(Mo_2–F_7) + \nu(Mo_2–F_9)] – [\nu(Mo_1–F_2) + \nu(Mo_1–F_4)] – [\nu(Mo_2–F_6) + \nu(Mo_2–F_8)]$ // $[\nu(W_2–F_7) + \nu(W_2–F_9)] – [\nu(W_2–F_6) + \nu(W_2–F_8)]$
459(0)[130]	468(0)[311]	484(0)[332]	A	$[\nu(M'_1–F_5) – \nu(M'_2–F_5)]$
389(<0.1)[35]	326(<0.1)[15]	336(0)[13]	E	$\delta(O_1M'_1F_5) – [\delta(O_2M'_2F_6) – \delta(F_8M'_2F_5)]$
386(8)[<0.1]	318(8)[<0.1]	325(6)[0]	E	$[\delta(O_1M'_1F_5) – \delta(O_1M'_1F_4)] + [\delta(O_2M'_2F_6) – \delta(F_8M'_2F_5)]$
376(5)[<0.1]	298(1)[<0.1]	278(<1)[<0.1]	A	$\delta_{umb}(M'_1F_{4eq}) + \delta_{umb}(M'_2F_{4eq})$
375(2)[0]	294(3)[0]	300(2)[0]	B	$[\delta(F_2M'_1F_3) + \delta(F_1M'_1F_4)] + [\delta(F_7M'_2F_8) + \delta(F_6M'_2F_9)]$
374(2)[0]	294(2)[0]	300(2)[0]	B	$[\delta(F_2M'_1F_3) + \delta(F_1M'_1F_4)] – [\delta(F_7M'_2F_8) + \delta(F_6M'_2F_9)]$
350(0)[8]	272(0)[37]	270(0)[49]	E	$[\rho_w(O_1M'_1F_5) + \rho_w(O_2M'_2F_5)] + [\rho_w(F_1M'_1F_3) + \rho_w(F_6M'_2F_8)]$
278(3)[<0.1]	210(1)[<0.1]	206(<1)[0]	E	$\rho_w(F_1M'_1F_3) + \rho_t(F_8M'_2F_9) + \rho_t(F_6M'_2F_7)$
271(0)[364]	253(0)[164]	242(0)[146]	A	$\delta_{umb}(M'_1F_{4eq}) – \delta_{umb}(M'_2F_{4eq})$

continued…

Table A8.11. (continued)

$[Cr_2O_2F_9]^-$ [a,b]	$[Mo_2O_2F_9]^-$ [a,b]	$[W_2O_2F_9]^-$ [a,b]		assgnts (C_4) [c]
206(1)[0]	169(<1)[0]	176(<0.1)[0]	B	$[\rho_w(F_1Cr_1F_3) + \rho_w(F_7Cr_2F_9)] - [\rho_w(F_2Cr_1F_4) + \rho_w(F_6Cr_2F_8)]$ // $[\rho_w(F_1Mo_1F_3) + \rho_w(F_7Mo_2F_9)] - [\rho_w(F_2Mo_1F_4) + \rho_w(F_6Mo_2F_8)]$ // $[\rho_w(F_7W_2F_9) - \rho_w(F_6W_2F_8)]$
204(<1)[0]	170(<1)[0]	176(<0.1)[0]	B	$[\rho_w(F_1Cr_1F_3) + \rho_w(F_6Cr_2F_8)] - [\rho_w(F_2Cr_1F_4) + \rho_w(F_7Cr_2F_9)]$ // $[\rho_w(F_1Mo_1F_3) + \rho_w(F_6Mo_2F_8)] - [\rho_w(F_2Mo_1F_4) + \rho_w(F_7Mo_2F_9)]$ // $[\rho_w(F_1W_1F_3) - \rho_w(F_2W_1F_4)]$
200(0)[3]	155(0)[4]	164(0)[5]	E	$[\rho_w(O_1M'_1F_5) + \rho_w(O_2M'_2F_5)] - [\rho_w(F_2M'_1F_4) + \rho_w(F_7M'_2F_9)]$
134(2)[0]	123(<1)[0]	108(<0.1)[0]	A	$[\nu(M'_1–F_5) + \nu(M'_2–F_5)]$
127(<0.1)[<0.1]	94(<0.1)[0]	97(<0.1)[0]	E	$\rho_r(O_1M'_1F_{4eq}) + \rho_r(O_2M'_2F_{4eq})$
11(0)[0]	11(0)[0]	4(0)[0]	A	$[\rho_t(M'_1F_{4eq}) - \rho_t(M'_2F_{4eq})]$
-24(0)[2]	14(0)[<1]	13(0)[<0.1]	E	$[\rho_r(O_1M'_1F_1F_3F_5) + \rho_r(O_2M'_2F_6F_8F_5)]$

[a] Frequencies are given in cm^{-1}. [b] Values in parentheses and square brackets denote calculated Raman intensities ($Å^4$ amu^{-1}) and infrared intensities (km mol^{-1}), respectively. The PBE1PBE/Def2-SVP (F, O, M') level of theory was used. [c] Abbreviations denote stretch (ν), bend (δ), rock (ρ_r), twist (ρ_t), wag (ρ_w), umbrella (umb), equatorial (eq), and axial (ax). Bond elongations and angle openings are denoted by plus (+) signs, and bond contractions and angle compressions are denoted by minus (–) signs. The atom labeling scheme corresponds to that used in Figure A8.13.

Table A8.12. Experimental vibrational frequencies, intensities, and assignments for $[XeF_5][WOF_5]\cdot XeOF_4$ (**7**)

7 [a,b]	assgnts
1014(68)	ν(W–O) of $[WOF_5]^-$
921(45)	ν(Xe–O) of $XeOF_4$
718(6) 691(15)	ν(W–F) of $[WOF_5]^-$
681, sh 679(66)	ν(W–F) of $[WOF_5]^-$ / ν(Xe–F) of $[XeF_5]^+$
667(6)	ν(Xe–F) of $[XeF_5]^+$
643(7)	ν(W–F) of $[WOF_5]^-$ / ν(Xe–F) of $[XeF_5]^+$
611(96) 600(53)	ν(Xe–F) of $[XeF_5]^+$
574(100)	ν(Xe–F) of $XeOF_4$
569, sh 561(5)	ν(W–F) of $[WOF_5]^-$ / ν(Xe–F) of $[XeF_5]^+$
540(70)	ν(Xe–F) of $XeOF_4$
406(10)	ν(Xe–F) of $[XeF_5]^+$
371(16)	δ(OXeF) of $XeOF_4$
356(5) 334, sh 327(11) 303(17) 296(7) 264(4) 235(12) 173(4) 119(7)	deformation modes of $[XeF_5][WOF_5]$ and $XeOF_4$

[a] Frequencies are given in cm^{-1}. [b] Values in parentheses denote relative Raman intensities. Abbreviations denote shoulder (sh). The Raman spectrum was recorded in a FEP sample tube at −110 °C using 1064-nm excitation. The band observed at 1039(6) cm^{-1} is attributed to trace amount of $[XeF_5][W_2O_2F_9]$ impurity, and the band observed at 987(4) cm^{-1} was tentatively assigned to the W–O stretching band of a $[WOF_6]^{2-}$ salt of $[XeF_5]^+$ or $[Xe_2F_{11}]^+$.

Figure A8.10. Factor-Group Analysis of $[Xe_2F_{11}][MOF_5]$ (M = Mo, W)[a]

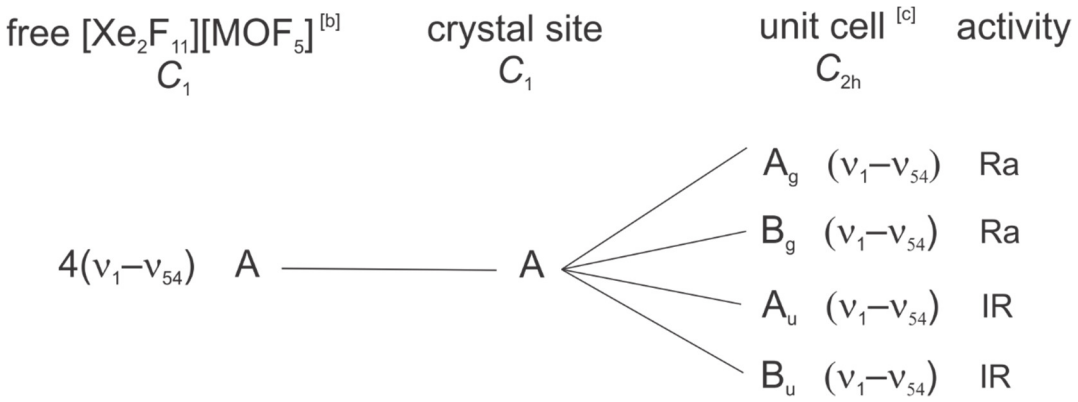

[a] The external modes have not been treated in this analysis. [b] The vibrational irreducible representation for gas-phase $[Xe_2F_{11}][MOF_5]$ is Γ = 54 A. [c] Space group; $P2_1/n$, Z = 4.

Figure A8.11. Factor-Group Analysis of $[Xe_2F_{11}][CrOF_5]$[a]

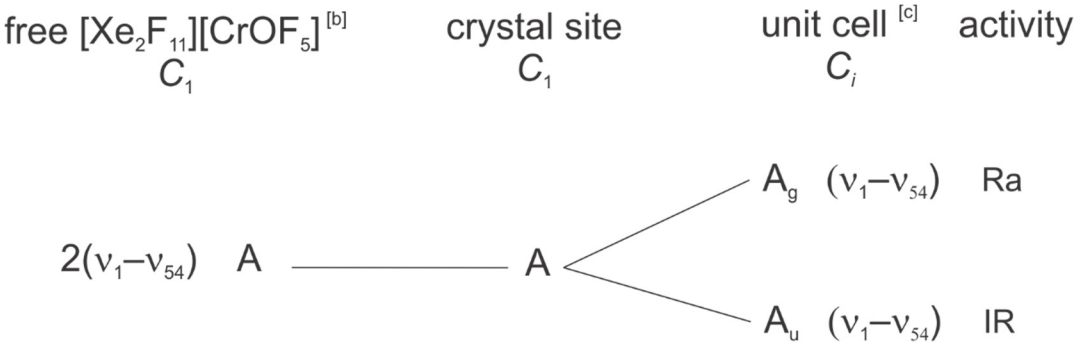

[a] The external modes have not been treated in this analysis. [b] The vibrational irreducible representation for gas-phase $[Xe_2F_{11}][CrOF_5]$ is Γ = 54 A. [c] Space group; $P1$, Z = 2.

Figure A8.12. Factor-Group Analysis of $[XeF_5][M_2O_2F_9]$ (M = Mo, W)[a]

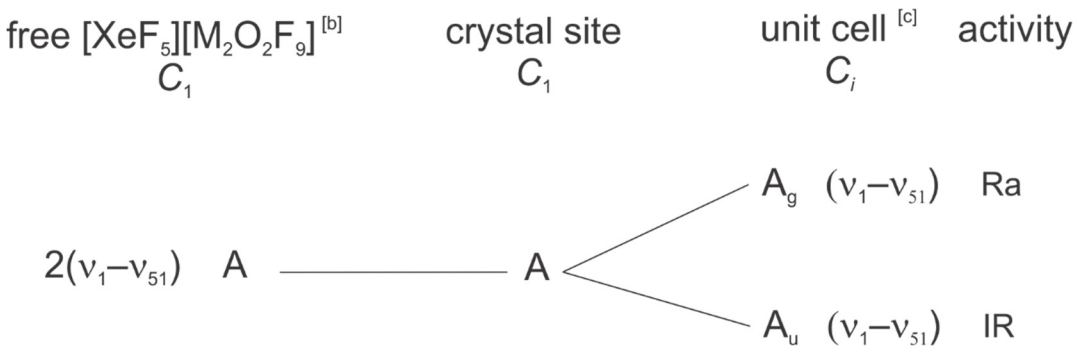

[a] The external modes have not been treated in this analysis. [b] The vibrational irreducible representation for gas-phase $[XeF_5][M_2O_2F_9]$ is $\Gamma = 51$ A. [c] Space group; $P1$, $Z = 2$.

Table A8.13. Calculated[a] geometric parameters for $[M'OF_5]^-$ (C_{4v}) and $[M'_2O_2F_9]^-$ (C_4) (M' = Cr, Mo, W)

	$[CrOF_5]^-$	$[MoOF_5]^-$	$[WOF_5]^-$	$[Cr_2O_2F_9]^-$	$[Mo_2O_2F_9]^-$	$[W_2O_2F_9]^-$
M'1–O1	1.540	1.702	1.729	1.519	1.678	1.689
M'1–F1	1.761	1.893	1.908	1.731	1.873	1.871
M'1–F2	1.761	1.893	1.908	1.731	1.873	1.871
M'1–F3	1.761	1.893	1.908	1.731	1.873	1.871
M'1–F4	1.761	1.893	1.908	1.731	1.873	1.871
M'1–F5	1.824	1.955	1.972	2.026	2.125	2.129
M'2–O2				1.519	1.678	1.689
M'2–F5				2.026	2.125	2.129
M'2–F6				1.731	1.873	1.871
M'2–F7				1.731	1.873	1.871
M'2–F8				1.731	1.873	1.871
M'2–F9				1.731	1.873	1.871
O1–M'1–F1	94.3	94.5	94.7	97.5	97.4	97.6
O1–M'1–F2	94.3	94.5	94.7	97.5	97.4	97.6
O1–M'1–F3	94.3	94.5	94.7	97.5	97.4	97.6
O1–M'1–F4	94.3	94.5	94.7	97.5	97.4	97.6
O1–M'1–F5	180.0	180.0	180.0	180.0	180.0	180.0
O2–M'2–F5				180.0	180.0	180.0
O2–M'2–F6				97.5	97.4	97.6
O2–M'2–F7				97.5	97.4	97.6
O2–M'2–F8				97.5	97.4	97.6
O2–M'2–F9				97.5	97.4	97.6
F1–M'1–F2	85.7	85.5	85.3	89.0	89.1	89.0
F1–M'1–F3	85.7	85.5	85.3	165.0	165.3	164.9
F1–M'1–F4	85.7	85.5	85.3	89.0	89.1	89.0
F1–M'1–F5	85.7	85.5	85.3	82.5	82.6	82.5
F2–M'1–F3	85.7	85.5	85.3	89.0	89.1	89.0
F2–M'1–F4	85.7	85.5	85.3	165.0	165.3	164.9
F2–M'1–F5	85.7	85.5	85.3	82.5	82.6	82.5
F3–M'1–F4	85.7	85.5	85.3	89.0	89.1	89.0
F3–M'1–F5	85.7	85.5	85.3	82.5	82.6	82.5
F4–M'1–F5	85.7	85.5	85.3	82.5	82.6	82.5
F5–M'1–F6				82.5	82.6	82.5
F5–M'1–F7				82.5	82.6	82.5
F5–M'1–F8				82.5	82.6	82.5
F5–M'1–F9				82.5	82.6	82.5
F6–M'1–F7				89.0	89.1	89.0
F6–M'1–F8				165.0	165.3	164.9
F6–M'1–F9				89.0	89.1	89.0
F7–M'1–F8				89.0	89.1	89.0
F7–M'1–F9				165.0	165.3	164.9
F8–M'1–F9				89.0	89.1	89.0

[a] The PBE1PBE/Def2-SVP (F, O, M') level of theory was used.

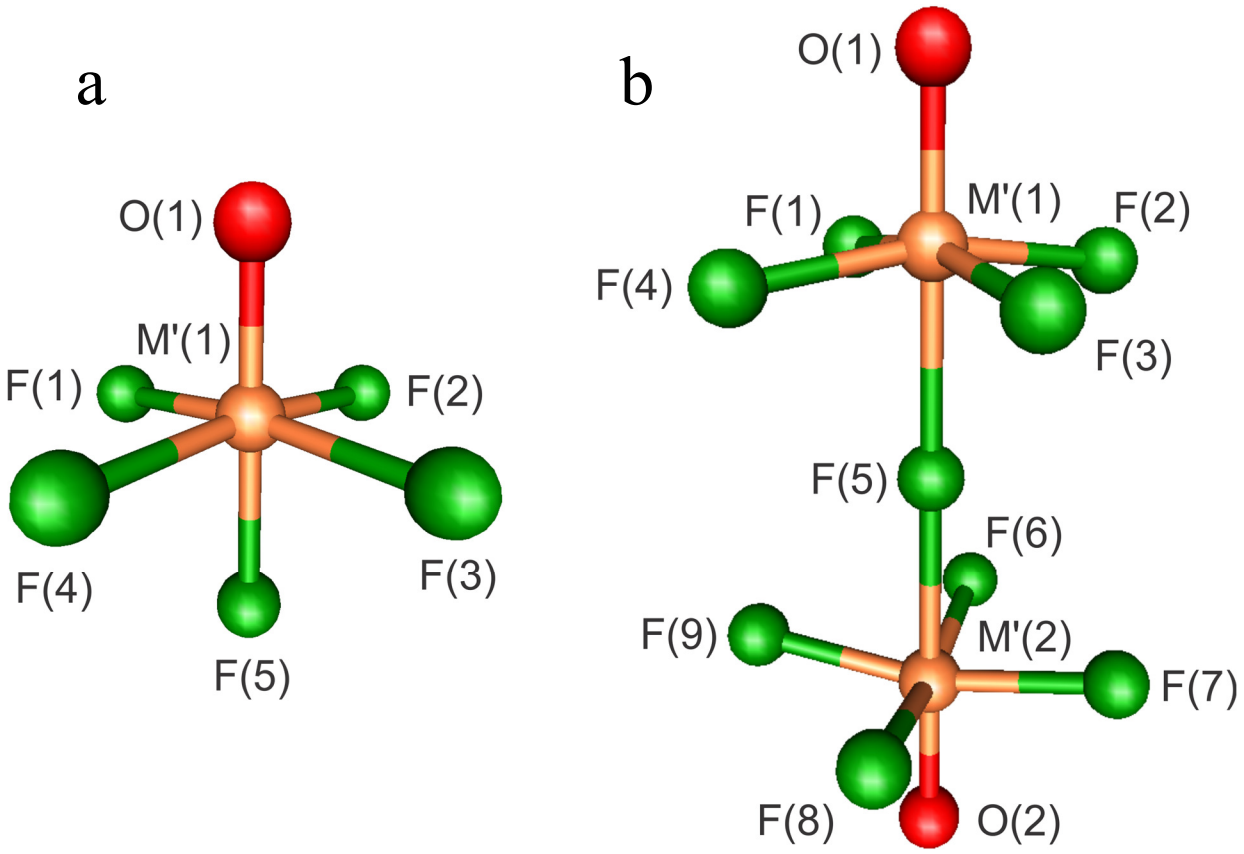

Figure A8.13. The calculated gas-phase geometries of (a) the $[M'OF_5]^-$ and (b) the $[M'_2O_2F_9]^-$ anions (M' = Cr, Mo, W). The PBE1PBE/Def2-SVP (F, O, M') level of theory was used.

Table A8.14. Calculated[a] geometric parameters for M'OF_4 (M' = Cr, Mo, W) (C_{4v}).

	$CrOF_4$	$MoOF_4$	WOF_4
M'1–O1	1.499	1.656	1.683
M'1–F1	1.705	1.854	1.872
O1–M'1–F1	104.9	105.1	105.0
F1–M'1–F2	86.2	86.1	86.2

[a] The PBE1PBE/Def2-SVP (F, O, M') level of theory was used.

Table A8.15. Calculated[a] vibrational frequencies, intensities, and assignments for M'OF_4 (M' = Cr, Mo, W)

$CrOF_4$ [b]	$MoOF_4$ [b]	WOF_4 [b]		assgnts (C_{4v}) [c]
1233(13)[111]	1108(16)[126]	1079(17)[110]	A_1	ν(M'–O)
775(<1)[226]	746(<1)[228]	715(<1)[195]	E	ν(M'–F_1) – ν(M'–F_3)
740(18)[22]	723(16)[32]	727(14)[33]	A_1	ν(M'–F_{4eq})
585(6)[0]	632(3)[0]	654(3)[0]	B_2	[ν(M'–F_1) + ν(M'–F_3)] – [ν(M'–F_2) + ν(M'–F_4)]
429(2)[0]	330(3)[0]	322(3)[0]	B_1	δ(F_1M'F_2) + δ(F_3M'F_4)
372(2)[11]	299(3)[7]	297(3)[7]	E	δ(OM'F_1) – δ(O_1M'F_3)
352(2)[7]	263(1)[16]	240(<1)[16]	A_1	δ_{umb}(M'–F_{4eq})
300(2)[14]	236(<1)[20]	223(<1)[24]	E	ρ_w(F_1M'F_3)
117(<1)[0]	101(<1)[0]	108(<1)[0]	B_2	ρ_t(F_1M'F_2) – ρ_t(F_3M'F_4)

[a] Frequencies are given in cm^{-1}. [b] Values in parentheses and square brackets denote calculated Raman intensities ($Å^4$ amu^{-1}) and infrared intensities (km mol^{-1}), respectively. The PBE1PBE/Def2-SVP (F, O, M') level of theory was used. [c] Abbreviations denote stretch (ν), bend (δ), wag (ρ_w), umbrella (umb), equatorial (eq), and axial (ax). Bond elongations and angle openings are denoted by plus (+) signs, and bond contractions and angle compressions are denoted by minus (–) signs. The atom labeling scheme corresponds to that used in Figure A8.13. [d] These modes also have a small contribution from ν(M'–F_{4eq}).

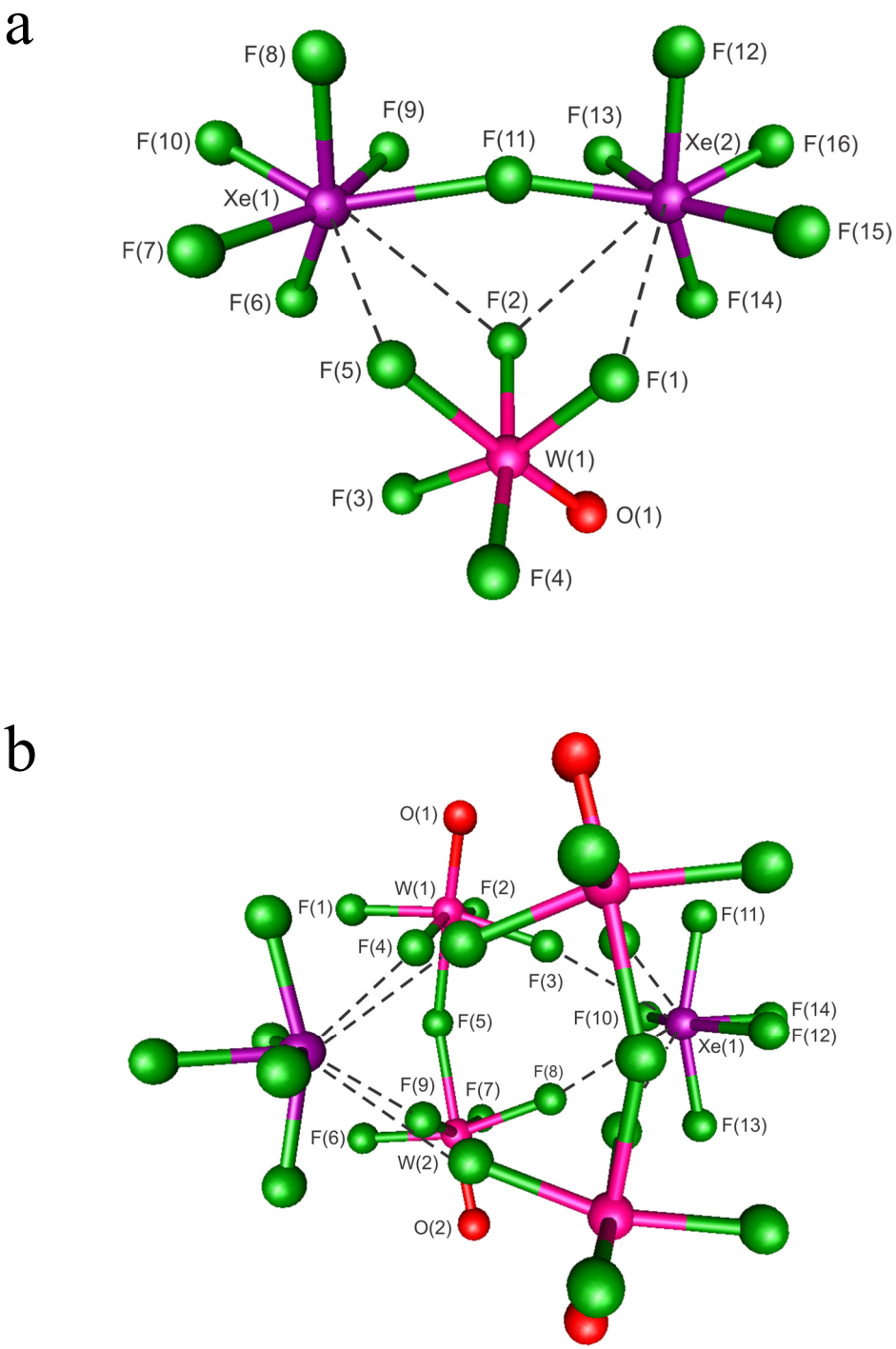

Figure A8.14. The calculated gas-phase geometries of (a) $[Xe_2F_{11}][WOF_5]$ and (b) $\{[XeF_5][W_2O_2F_9]\}_2$. The PBE1PBE/Def2-SVP (F, O, W, Xe) level of theory was used.

Table A8.16. Natural Population Analysis (NPA) Charges, Valence Indices, and Wiberg Bond Indices[a] for M'OF_4 (M' = Cr, Mo, W), $[M'OF_5]^-$, $\{[Xe_2F_{11}][CrOF_5]\}_2$, $[Xe_2F_{11}][MOF_5]$ (M = Mo, W), $\{[XeF_5][M_2O_2F_9]\}_2$, and $[M'_2O_2F_9]^-$

$\{[Xe_2F_{11}][CrOF_5]\}_2$				
Bond Indices		NPA Charges [Valence Indices]		
Cr1---F5	0.125	Cr1	1.173	[5.500]
Cr1−F1	0.765	F1	–0.340	[1.167]
Cr1−F2	0.797	F2	–0.325	[1.198]
Cr1−F3	0.765	F3	–0.341	[1.167]
Cr1−F4	0.881	F4	–0.256	[1.297]
Cr1−O1	2.134	F5	–0.686	[0.601]
		O1	0.006	[2.744]
		$\sum_{[CrOF_5]^-}$	**–0.769**	
Xe1---F5	0.127	Xe1	3.191	[3.385]
Xe1–F6	0.608	F6	–0.471	[0.849]
Xe1–F7	0.600	F7	–0.503	[0.832]
Xe1–F8	0.596	F8	–0.503	[0.834]
Xe1–F9	0.607	F9	–0.496	[0.839]
Xe1–F10	0.606	F10	–0.496	[0.836]
Xe1–F11	0.190	F11	–0.675	[0.601]
Xe1---F1	0.020	Xe2	3.191	[3.385]
Xe2---F5a	0.128	F12	–0.471	[0.849]
Xe2–F11	0.189	F13	–0.496	[0.839]
Xe2–F12	0.608	F14	–0.503	[0.834]
Xe2–F13	0.607	F15	–0.503	[0.832]
Xe2–F14	0.597	F16	–0.496	[0.836]
Xe2–F15	0.600	$\sum_{[Xe_2F_{11}]^+}$	**0.769**	
Xe2–F16	0.606			
Xe2---F3a	0.020			

$[Xe_2F_{11}][MoOF_5]$				
Bond Indices		NPA Charges [Valence Indices]		
Mo1---F5	0.278	Mo1	2.176	[5.154]
Mo1−F1	0.560	F1	–0.552	[0.836]
Mo1−F2	0.815	F2	–0.417	[1.058]
Mo1−F3	0.814	F3	–0.419	[1.054]
Mo1−F4	0.670	F4	–0.515	[0.897]
Mo1−O1	1.986	F5	–0.627	[0.704]
		O1	–0.422	[2.369]
		$\sum_{[MoOF_5]^-}$	**–0.776**	
Xe1---F5	0.207	Xe1	3.187	[3.386]
Xe1–F6	0.613	F6	–0.491	[0.844]
Xe1–F7	0.610	F7	–0.492	[0.845]
Xe1–F8	0.595	F8	–0.508	[0.828]
Xe1–F9	0.596	F9	–0.506	[0.830]
Xe1–F10	0.615	F10	–0.467	[0.855]
Xe1–F11	0.123	F11	–0.677	[0.597]
Xe1---F4	0.006	Xe2	3.184	[3.390]
Xe2–F11	0.262	F12	–0.487	[0.849]
Xe2–F12	0.619	F13	–0.483	[0.849]
Xe2–F13	0.620	F14	–0.507	[0.832]
Xe2–F14	0.597	F15	–0.515	[0.823]
Xe2–F15	0.581	F16	–0.463	[0.859]
Xe2–F16	0.619	$\sum_{[Xe_2F_{11}]^+}$	**0.776**	
Xe2---F1	0.064			
Xe2---F4	0.008			

$[Xe_2F_{11}][WOF_5]$				
Bond Indices		NPA Charges [Valence Indices]		
W1---F5	0.282	W1	2.504	[4.949]
W1−F1	0.537	F1	–0.586	[0.777]
W1−F2	0.774	F2	–0.472	[0.967]
W1−F3	0.776	F3	–0.472	[0.967]
W1−F4	0.647	F4	–0.554	[0.831]
W1−O1	1.901	F5	–0.644	[0.674]
		O1	–0.567	[2.212]
		$\sum_{[WOF_5]^-}$	**–0.791**	
Xe1---F5	0.191	Xe1	3.190	[3.386]
Xe1–F6	0.610	F6	–0.492	[0.845]
Xe1–F7	0.613	F7	–0.491	[0.845]
Xe1–F8	0.599	F8	–0.504	[0.831]
Xe1–F9	0.598	F9	–0.505	[0.830]
Xe1–F10	0.617	F10	–0.465	[0.857]
Xe1–F11	0.130	F11	–0.681	[0.590]
Xe1---F4	0.004	Xe2	3.187	[3.390]
Xe2–F11	0.250	F12	–0.483	[0.849]
Xe2–F12	0.621	F13	–0.487	[0.850]
Xe2–F13	0.620	F14	–0.512	[0.827]
Xe2–F14	0.585	F15	–0.504	[0.835]
Xe2–F15	0.600	F16	–0.462	[0.860]
Xe2–F16	0.620	$\sum_{[Xe_2F_{11}]^+}$	**0.791**	
Xe2---F1	0.063			
Xe2---F4	0.008			

$\{[XeF_5][Mo_2O_2F_9]\}_2$				
Bond Indices		NPA Charges [Valence Indices]		
Mo1---F5	0.282	Mo1	2.255	[5.119]
Mo1−F1	0.813	F1	–0.427	[1.041]
Mo1−F2	0.807	F2	–0.431	[1.035]
Mo1−F3	0.591	F3	–0.553	[0.837]
Mo1−F4	0.599	F4	–0.548	[0.845]
Mo1−O1	1.990	F5	–0.596	[0.774]
Mo2---F5	0.282	O1	–0.437	[2.356]
Mo2−F6	0.813	Mo2	2.255	[5.119]
Mo2−F7	0.807	F6	–0.427	[1.041]
Mo2−F8	0.591	F7	–0.431	[1.035]
Mo2−F9	0.599	F8	–0.553	[0.837]
Mo2−O2	1.990	F9	–0.548	[0.845]
		O2	–0.437	[2.356]
		$\sum_{[Mo_2O_2F_9]^-}$	**–0.878**	
Xe1–F10	0.636	Xe1	3.232	[3.349]
Xe1–F11	0.635	F10	–0.475	[0.865]
Xe1–F12	0.637	F11	–0.476	[0.863]
Xe1–F13	0.635	F12	–0.474	[0.866]
Xe1–F14	0.623	F13	–0.476	[0.863]
Xe1---F3	0.042	F14	–0.453	[0.867]
Xe1---F4a	0.042	$\sum_{[XeF_5]^+}$	**0.878**	
Xe1---F8	0.042			
Xe1---F9a	0.042			

continued …

Table A8.16. (continued)

$\{[XeF_5][W_2O_2F_9]\}_2$				
Bond Indices		NPA Charges [Valence Indices]		
W1---F5	0.272	W1	2.595	[4.901]
W1−F1	0.771	F1	–0.483	[0.948]
W1−F2	0.772	F2	–0.482	[0.949]
W1−F3	0.573	F3	–0.586	[0.778]
W1−F4	0.573	F4	–0.587	[0.777]
W1−O1	1.902	F5	–0.626	[0.719]
W2---F5	0.272	O1	–0.587	[2.194]
W2−F6	0.770	W2	2.595	[4.901]
W2−F7	0.772	F6	–0.483	[0.948]
W2−F8	0.574	F7	–0.482	[0.950]
W2−F9	0.572	F8	–0.586	[0.779]
W2−O2	1.902	F9	–0.587	[0.776]
		O2	–0.587	[2.194]
		$\sum_{[W_2O_2F_9]^-}$	**–0.886**	
Xe1–F10	0.638	Xe1	3.234	[3.348]
Xe1–F11	0.639	F10	–0.474	[0.866]
Xe1–F12	0.636	F11	–0.474	[0.867]
Xe1–F13	0.639	F12	–0.475	[0.865]
Xe1–F14	0.625	F13	–0.474	[0.867]
Xe1---F3	0.040	F14	–0.451	[0.870]
Xe1---F4a	0.039	$\sum_{[XeF_5]^+}$	**0.886**	
Xe1---F8	0.039			
Xe1---F9a	0.038			

$CrOF_4$				
Bond Indices		NPA Charges [Valence Indices]		
Cr1−F1	0.838	Cr1	1.243	[5.417]
Cr1−F2	0.838	F1	–0.296	[1.232]
Cr1−F3	0.838	F2	–0.296	[1.232]
Cr1−F4	0.838	F3	–0.296	[1.232]
Cr1−O1	2.066	F4	–0.296	[1.232]
		O1	–0.061	[2.687]
		$\sum_{CrOF_4}$	**0**	

$MoOF_4$				
Bond Indices		NPA Charges [Valence Indices]		
Mo1−F1	0.765	Mo1	2.300	[5.012]
Mo1−F2	0.765	F1	–0.456	[0.993]
Mo1−F3	0.765	F2	–0.456	[0.993]
Mo1−F4	0.765	F3	–0.456	[0.993]
Mo1−O1	1.952	F4	–0.456	[0.993]
		O1	–0.475	[2.317]
		$\sum_{MoOF_4}$	**0**	

WOF_4				
Bond Indices		NPA Charges [Valence Indices]		
W1−F1	0.735	W1	2.607	[4.825]
W1−F2	0.735	F1	–0.502	[0.917]
W1−F3	0.735	F2	–0.502	[0.917]
W1−F4	0.735	F3	–0.502	[0.917]
W1−O1	1.887	F4	–0.502	[0.917]
		O1	–0.601	[2.176]
		$\sum_{WOF_4}$	**0**	

$[CrOF_5]^-$				
Bond Indices		NPA Charges [Valence Indices]		
Cr1---F5	0.600	Cr1	1.078	[5.547]
Cr1−F1	0.741	F1	–0.376	[1.101]
Cr1−F2	0.741	F2	–0.376	[1.101]
Cr1−F3	0.741	F3	–0.376	[1.101]
Cr1−F4	0.741	F4	–0.376	[1.101]
Cr1−O1	1.983	F5	–0.449	[1.006]
		O1	–0.123	[2.642]
		$\sum_{[CrOF_5]^-}$	**–1.000**	

$[MoOF_5]^-$				
Bond Indices		NPA Charges [Valence Indices]		
Mo1---F5	0.582	Mo1	2.123	[5.228]
Mo1−F1	0.706	F1	–0.502	[0.915]
Mo1−F2	0.706	F2	–0.502	[0.915]
Mo1−F3	0.706	F3	–0.502	[0.915]
Mo1−F4	0.706	F4	–0.502	[0.915]
Mo1−O1	1.822	F5	–0.562	[0.817]
		O1	–0.555	[2.229]
		$\sum_{[MoOF_5]^-}$	**–1.000**	

continued …

Table A8.16. (continued)

$[WOF_5]^-$				
Bond Indices		NPA Charges [Valence Indices]		
W1---F5	0.557	W1	2.465	[5.013]
W1−F1	0.679	F1	–0.542	[0.847]
W1−F2	0.679	F2	–0.542	[0.847]
W1−F3	0.679	F3	–0.542	[0.847]
W1−F4	0.679	F4	–0.542	[0.847]
W1−O1	1.740	F5	–0.603	[0.747]
		O1	–0.695	[2.068]
		$\sum_{[WOF_5]^-}$	**–1.000**	

$[Cr_2O_2F_9]^-$				
Bond Indices		NPA Charges [Valence Indices]		
Cr1---F5	0.270	Cr1	1.124	[5.530]
Cr1−F1	0.799	F1	–0.319	[1.197]
Cr1−F2	0.799	F2	–0.319	[1.197]
Cr1−F3	0.799	F3	–0.319	[1.197]
Cr1−F4	0.799	F4	–0.319	[1.197]
Cr1−O1	2.052	O1	–0.081	[2.680]
Cr2---F5	0.270	F5	–0.531	[0.885]
Cr2−F6	0.799	Cr2	1.124	[5.530]
Cr2−F7	0.799	F6	–0.319	[1.197]
Cr2−F8	0.799	F7	–0.319	[1.197]
Cr2−F9	0.799	F8	–0.319	[1.197]
Cr2−O2	2.052	F9	–0.319	[1.197]
		O2	–0.081	[2.680]
		$\sum_{[Cr_2O_2F_9]^-}$	**–1.000**	

$[M_2O_2F_9]^-$				
Bond Indices		NPA Charges [Valence Indices]		
Mo1---F5	0.289	Mo1	2.179	[5.168]
Mo1−F1	0.740	F1	–0.472	[0.968]
Mo1−F2	0.740	F2	–0.472	[0.968]
Mo1−F3	0.740	F3	–0.472	[0.968]
Mo1−F4	0.740	F4	–0.472	[0.968]
Mo1−O1	1.907	O1	–0.501	[2.289]
Mo2---F5	0.289	F5	–0.583	[0.797]
Mo2−F6	0.740	Mo2	2.179	[5.168]
Mo2−F7	0.740	F6	–0.472	[0.968]
Mo2−F8	0.740	F7	–0.472	[0.968]
Mo2−F9	0.740	F8	–0.472	[0.968]
Mo2−O2	1.907	F9	–0.472	[0.968]
		O2	–0.501	[2.289]
		$\sum_{[Mo_2O_2F_9]^-}$	**–1.000**	

$[W_2O_2F_9]^-$				
Bond Indices		NPA Charges [Valence Indices]		
W1---F5	0.276	W1	2.587	[4.932]
W1−F1	0.706	F1	–0.527	[0.874]
W1−F2	0.706	F2	–0.527	[0.874]
W1−F3	0.706	F3	–0.527	[0.874]
W1−F4	0.706	F4	–0.527	[0.874]
W1−O1	1.818	O1	–0.666	[2.107]
W2---F5	0.276	F5	–0.624	[0.722]
W2−F6	0.706	W2	2.587	[4.932]
W2−F7	0.706	F6	–0.527	[0.874]
W2−F8	0.706	F7	–0.527	[0.874]
W2−F9	0.706	F8	–0.527	[0.874]
W2−O2	1.818	F9	–0.527	[0.874]
		O2	–0.666	[2.107]
		$\sum_{[W_2O_2F_9]^-}$	**–1.000**	

[a] Calculated at the PBE1PBE/Def2-SVP (F, O, Cr, Mo, W, Xe) level of theory.

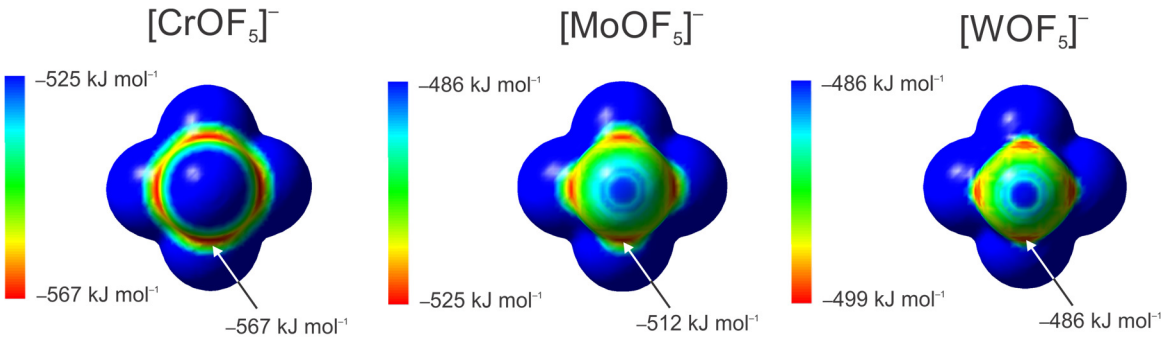

Figure A8.15. Molecular electrostatic potential surface (MEPS) contours calculated at 0.001 e $bohr^{-3}$ isosurfaces for $[M'OF_5]^-$ (M = Cr, Mo, W). The lowest electrostatic potentials (indicated by arrows) are located at the intersections of the F_{ax} and F_{eq} isosurfaces. The optimized geometries and MEPs were calculated at the PBE1PBE/Def2-SVP (O, F, M') level of theory.

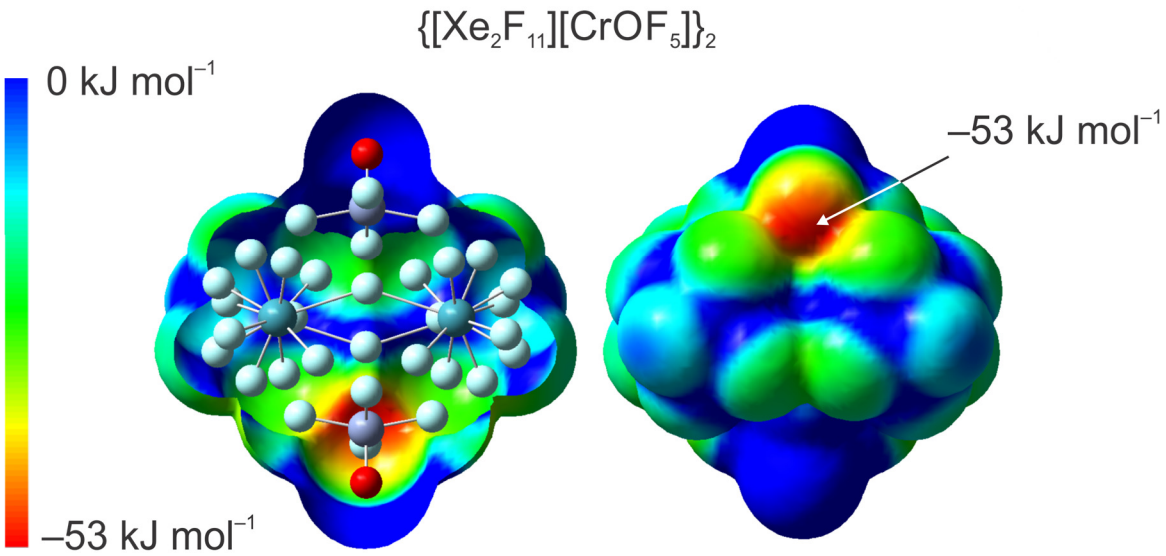

Figure A8.16. Molecular electrostatic potential surface (MEPS) contours calculated at the 0.001 e bohr^{-3} isosurface for $\{[Xe_2F_{11}][CrOF_5]\}_2$. The arrow indicates the lowest EP on the isosurface of an exposed F_{eq} atom in the $[CrOF_5]^-$ anion. The optimized geometries and MEPs were calculated at the PBE1PBE/Def2-SVP (O, F, Cr, Xe) level of theory.

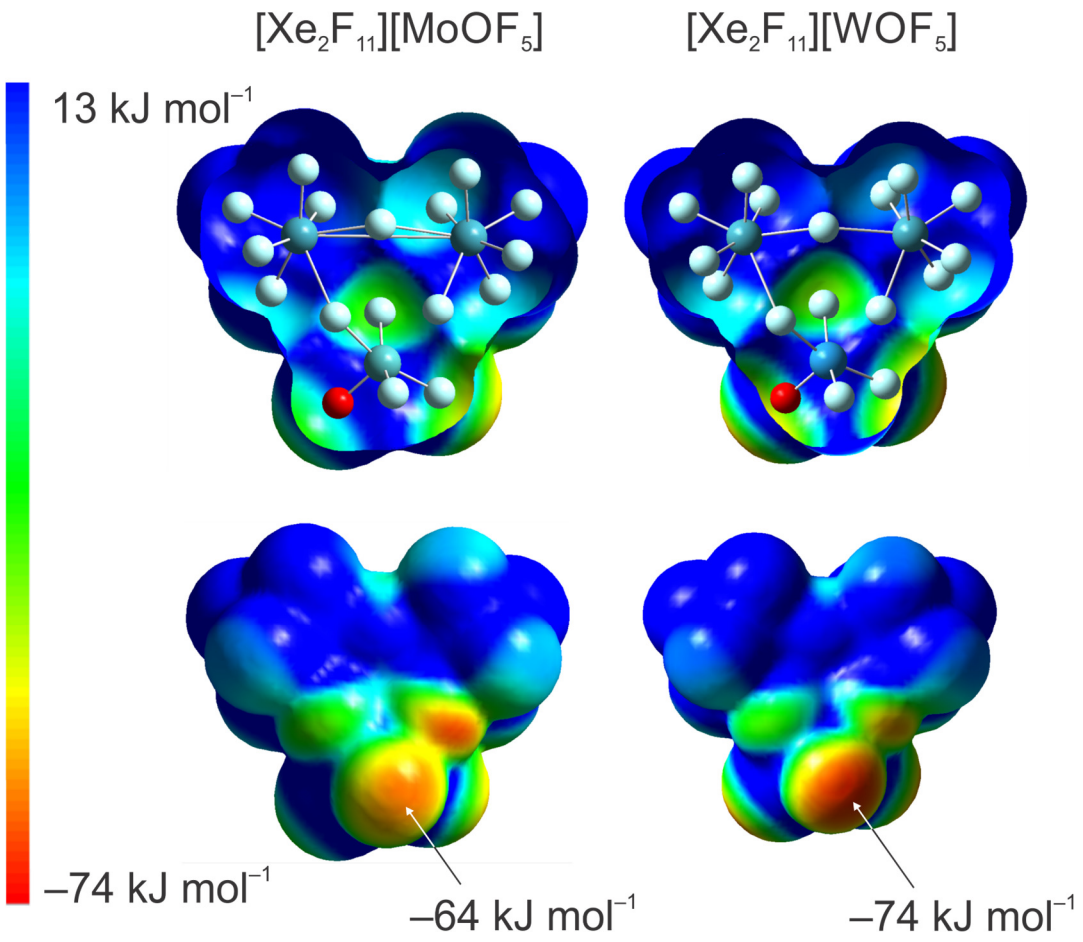

Figure A8.17. Molecular electrostatic potential surface (MEPS) contours calculated at the 0.001 e bohr^{-3} isosurface for $[Xe_2F_{11}][MOF_5]$ (M = Mo, W). The lowest electrostatic potential extrema for one exposed F_{eq} atom in each $[MOF_5]^-$ anion are indicated by arrows. The optimized geometries and MEPs were calculated at the PBE1PBE/Def2-SVP (O, F, M, Xe) level of theory.